**Energy, Environment, and Sustainability**
*Series Editors:* Avinash Kumar Agarwal · Ashok Pandey

Himanshu Tyagi
Avinash Kumar Agarwal
Prodyut R. Chakraborty
Satvasheel Powar *Editors*

# Advances in Solar Energy Research


Springer

# Energy, Environment, and Sustainability

This books series publishes cutting edge monographs and professional books focused on all aspects of energy and environmental sustainability, especially as it relates to energy concerns. The Series is published in partnership with the International Society for Energy, Environment, and Sustainability. The books in these series are editor or authored by top researchers and professional across the globe. The series aims at publishing state-of-the-art research and development in areas including, but not limited to:

- Renewable Energy
- Alternative Fuels
- Engines and Locomotives
- Combustion and Propulsion
- Fossil Fuels
- Carbon Capture
- Control and Automation for Energy
- Environmental Pollution
- Waste Management
- Transportation Sustainability

More information about this series at http://www.springer.com/series/15901

Himanshu Tyagi · Avinash Kumar Agarwal
Prodyut R. Chakraborty · Satvasheel Powar
Editors

# Advances in Solar Energy Research

Springer

*Editors*
Himanshu Tyagi
Department of Mechanical Engineering
Indian Institute of Technology Ropar
Rupnagar, India

Prodyut R. Chakraborty
Department of Mechanical Engineering
Indian Institute of Technology Jodhpur
Jodhpur, Rajasthan, India

Avinash Kumar Agarwal
Department of Mechanical Engineering
Indian Institute of Technology Kanpur
Kanpur, Uttar Pradesh, India

Satvasheel Powar
Department of Mechanical Engineering
Indian Institute of Technology Mandi
Mandi, Himachal Pradesh, India

ISSN 2522-8366 ISSN 2522-8374 (electronic)
Energy, Environment, and Sustainability
ISBN 978-981-13-3301-9 ISBN 978-981-13-3302-6 (eBook)
https://doi.org/10.1007/978-981-13-3302-6

Library of Congress Control Number: 2018961729



This Springer imprint is published by the registered company Springer Nature Singapore Pte Ltd.
The registered company address is: 152 Beach Road, #21-01/04 Gateway East, Singapore 189721, Singapore

# Foreword

## Why Do We Need Solar Energy Research?

This volume includes excellent overviews of a number of traditional and emerging areas of solar research, such as solar photovoltaic cells and systems, solar fuels, concentrating solar power, solar thermal applications. It is clear, even with decades of solar energy research behind us, that there remains an urgent need for continued scientific and technological advances, particularly in India. Data and forecasts available from the International Energy Agency (https://www.iea.org/) suggest that from 2016 to 2040, India will be the single largest contributor ($\sim$30%) to growth in worldwide energy demand, overtaking China and leading to an estimated $\sim$11% of global energy consumption in 2040. The total primary energy supply (TPES) of India, defined as the net difference between local production and imports (+) and exports and storage (−), is growing at an average rate of $\sim$5%/year since 2006, compared with a negative TPES growth rate for China in 2016. Interestingly, relatively few articles in this volume discuss concentrating solar power (CSP), which for some time has been the main driver behind solar *thermal* engineering research. It is quite possible that the authors represented here recognize that CSP will increasingly lose market share to utility-scale photovoltaic power, especially with continued advances in utility-scale batteries. This means that the solar thermal research community, in India and elsewhere, needs to turn their attention to other pressing issues for which solar thermal energy can be better suited.

Returning our attention to the title of this Foreword, it is worthwhile to consider the potential impacts of solar energy research beyond simply substituting for fossil fuels. Of course, the greenhouse gas (GHG) implications of renewable energy are apparent, although often these are not well quantified by solar researchers. But, GHG emissions are just one environmental impact of fossil fuels. Burning coal, in particular, releases heavy metals, particulates, and NOx into the environment, not to

mention the deleterious environmental and health impacts of coal mining.[1] But sometimes, what is overlooked is the economic impact of solar energy development and technology deployment. Solar energy, as well as other renewable energy technologies such as wind energy, tends to create local jobs in both manufacturing and assembly and in installation and maintenance. For example, in the USA, the US Bureau of Labor Statistics forecasts an employment growth rate of 105% for solar PV installers from 2016 to 2026.[2] On the macroeconomic level, money that (usually) flows out of an area (or country) to purchase fossil fuels will instead remain local, once the need for those fossil fuels is eliminated. In short, solar energy research is needed for many reasons—micro- and macroeconomic, environmental, and health—and solar energy researchers need to understand these motivations to better position their research agendas in this wider context.

What areas of solar energy research may, in particular, require more attention? One area is industrial process heating, which can be divided into low-temperature (<100 °C), medium-temperature (100–400 °C), and high-temperature (>400 °C) applications. Such industrial heating represents ~20% of global energy consumption, and India is poised to once again overtake China as the greatest single contributor to growth in the need for high-temperature industrial heat.[3] Innovations in both solar thermal engineering and high-temperature heat pumps are necessary to reduce the huge amount of GHG emissions that will be generated by simply burning fossil fuels to produce heat. Other applications may well involve the combined use of solar thermal energy and solar photovoltaics, as well as solar-driven chemistry such as photocatalysis. Whatever the application, the solar energy research community is ready, capable, and willing to address these outstanding global problems.

Tempe, Arizona, USA

Prof. Patrick E. Phelan
Professor, Mechanical &
Aerospace Engineering &
Assistant Dean of Graduate Programs,
Ira A. Fulton Schools of Engineering
Arizona State University

[1] See, e.g., Munawer, M.E., 2018, "Human health and environmental impacts of coal combustion and post-combustion wastes," Journal of Sustainable Mining, Vol. 17, pp. 87–96.
[2] https://www.bls.gov/ooh/construction-and-extraction/solar-photovoltaic-installers.htm.
[3] https://www.iea.org/newsroom/news/2018/january/commentary-clean-and-efficient-heat-for-industry.html.

# Preface

Energy demand has been rising remarkably due to increasing population and urbanization. Global economy and society are significantly dependent on energy availability because it touches every facet of human life and its activities. Transportation and power generation are two major examples. Without the transportation by millions of personalized and mass transport vehicles and availability of $24 \times 7$ power, human civilization would not have reached contemporary living standards.

The International Society for Energy, Environment, and Sustainability (ISEES) was founded at Indian Institute of Technology Kanpur (IIT Kanpur), India, in January 2014 with the aim of spreading knowledge/awareness and catalyzing research activities in the fields of energy, environment, sustainability, and combustion. The society's goal is to contribute to the development of clean, affordable, and secure energy resources and a sustainable environment for the society and to spread knowledge in the above-mentioned areas and create awareness about the environmental challenges, which the world is facing today. The unique way adopted by the society was to break the conventional silos of specializations (engineering, science, environment, agriculture, biotechnology, materials, fuels, etc.) to tackle the problems related to energy, environment, and sustainability in a holistic manner. This is quite evident by the participation of experts from all fields to resolve these issues. ISEES is involved in various activities such as conducting workshops, seminars, and conferences in the domains of its interest. The society also recognizes the outstanding works done by the young scientists and engineers for their contributions in these fields by conferring them awards under various categories.

The second international conference on "Sustainable Energy and Environmental Challenges" (SEEC-2018) was organized under the auspices of ISEES from December 31, 2017, to January 3, 2018, at JN Tata Auditorium, Indian Institute of Science, Bangalore. This conference provided a platform for discussions between eminent scientists and engineers from various countries including India, USA, South Korea, Norway, Finland, Malaysia, Austria, Saudi Arabia, and Australia. In this conference, eminent speakers from all over the world presented their views

related to different aspects of energy, combustion, emissions, and alternative energy resources for sustainable development and a cleaner environment. The conference presented five high-voltage plenary talks from globally renowned experts on topical themes, namely "Is It Really the End of Combustion Engines and Petroleum?" by Prof. Gautamkalghatgi, Saudi Aramco; "Energy Sustainability in India: Challenges and Opportunities" by Prof. Baldev Raj, NIAS, Bangalore; "Methanol Economy: An Option for Sustainable Energy and Environmental Challenges" by Dr. Vijay Kumar Saraswat, Hon. Member (S&T), NITI Ayog, Government of India; "Supercritical Carbon Dioxide Brayton Cycle for Power Generation" by Prof. Pradip Dutta, IISc Bangalore; and "Role of Nuclear Fusion for Environmental Sustainability of Energy in Future" by Prof. J. S. Rao, Altair Engineering.

The conference included 27 technical sessions on topics related to energy and environmental sustainability including 5 plenary talks, 40 keynote talks, and 18 invited talks from prominent scientists, in addition to 142 contributed talks, and 74 poster presentations by students and researchers. The technical sessions in the conference included Advances in IC Engines: SI Engines, Solar Energy: Storage, Fundamentals of Combustion, Environmental Protection and Sustainability, Environmental Biotechnology, Coal and Biomass Combustion/Gasification, Air Pollution and Control, Biomass to Fuels/Chemicals: Clean Fuels, Advances in IC Engines: CI Engines, Solar Energy: Performance, Biomass to Fuels/Chemicals: Production, Advances in IC Engines: Fuels, Energy Sustainability, Environmental Biotechnology, Atomization and Sprays, Combustion/Gas Turbines/Fluid Flow/Sprays, Biomass to Fuels/Chemicals, Advances in IC Engines: New Concepts, Energy Sustainability, Waste to Wealth, Conventional and Alternate Fuels, Solar Energy, Wastewater Remediation, and Air Pollution. One of the highlights of the conference was the rapid-fire poster sessions in (i) Energy Engineering, (ii) Environment and Sustainability, and (III) Biotechnology, where more than 75 students participated with great enthusiasm and won many prizes in a fiercely competitive environment. More than 200 participants and speakers attended this four-day conference, which also hosted Dr. Vijay Kumar Saraswat, Hon. Member (S&T), NITI Ayog, Government of India, as the chief guest for the book release ceremony, where 16 ISEES books published by Springer, under a special dedicated series "Energy, Environment, and Sustainability" were released. This is the first time that such significant and high-quality outcome has been achieved by any society in India. The conference concluded with a panel discussion on "Challenges, Opportunities & Directions for Future Transportation Systems," where the panelists were Prof. Gautam Kalghatgi, Saudi Aramco; Dr. Ravi Prashanth, Caterpillar Inc.; Dr. Shankar Venugopal, Mahindra and Mahindra; Dr. Bharat Bhargagava, DG, ONGC Energy Center; and Dr. Umamaheshwar, GE Transportation, Bangalore. The panel discussion was moderated by Prof. Ashok Pandey, Chairman, ISEES. This conference laid out the road map for technology development, opportunities, and challenges in energy, environment, and sustainability domains. All these topics are very relevant for the country and the world in the present context. We acknowledge the support received from various funding agencies and organizations for the successful conduct of the second ISEES

conference SEEC-2018, where these books germinated. We would therefore like to acknowledge SERB, Government of India (special thanks to Dr. Rajeev Sharma, Secretary); ONGC Energy Center (special thanks to Dr. Bharat Bhargava); TAFE (special thanks to Sh. Anadrao Patil); Caterpillar (special thanks to Dr. Ravi Prashanth); Progress Rail, TSI, India (special thanks to Dr. Deepak Sharma); Tesscorn, India (special thanks to Sh. Satyanarayana); GAIL, VOLVO; and our publishing partner Springer (special thanks to Swati Meherishi).

The editors would like to express their sincere gratitude to a large number of authors from all over the world for submitting their high-quality work in a timely manner and revising it appropriately at short notice. We would like to express our special thanks to all the reviewers (Dr. Eric Anderson, Dr. Vishal Bhalla, Dr. Anirban Bhattacharya, Dr. Muhammad Burhan, Dr. Prodyut Chakraborty, Dr. Deepak Ganta, Dr. Manas Gartia, Dr. Ankur Gupta, Dr. Khairul Habib, Dr. M. Kum Ja, Dr. Dinesh Kabra, Dr. Vikrant Khullar, Dr. E. Anil Kumar, Dr. Atul Lanjewar, Dr. Rudrodip Majumdar, Dr. Balkrishna Mehta, Dr. Amaresh Mishra, Dr. Sourav Mitra, Dr. Dhiraj Patil, Dr. Smarat Rao, Dr. Bidyut Baran Saha, Dr. Sandip Saha, Dr. Marie-Pierre Santoni, Dr. Soumitra Satapathi, Dr. Sanjeev Soni, Dr. Vijay Kumar Soni, Dr. K. R. Justin Thomas, Dr. Ponnulakshmi VK, Dr. Vivek Vishwakarma), who reviewed various chapters of this book and provided very valuable suggestions to the authors to improve their manuscript.

This monograph is intended for researchers working in the field of solar energy, and we hope that the book would be of great interest to the professionals and post-graduate students involved in the study of solar thermal collectors, solar radiation forecasting, dye-sensitized solar cells, concentrated photovoltaics, energy storage systems, solar fuels, and various solar-based applications (such as desalination, cooling, gasification, cooking). The main objective of this monograph is to promote a better and more accurate understanding of the various aspects of research in the field of solar energy.

Rupnagar, India — Himanshu Tyagi
Kanpur, India — Avinash Kumar Agarwal
Jodhpur, India — Prodyut R. Chakraborty
Mandi, India — Satvasheel Powar

# Contents

# Editors and Contributors

## About the Editors

**Himanshu Tyagi** is Associate Professor of Mechanical Engineering at IIT Ropar. He has previously worked at Siemens (Germany and India) and Intel (USA). He received his Ph.D. from Arizona State University, his master's from University of Windsor, Canada, and his Bachelor's from IIT Delhi. His research interests include thermo-fluids, bio-heat transfer, nanofluids, nanoscale heat transfer, clean and sustainable energy, solar energy, energy storage, ignition properties of fuels containing nanoparticles, thermodynamics, thermal management, and packaging of micro-electronic devices. At present, he is working with a team to develop nanotechnology-based, clean and sustainable energy sources. He is a member of multiple professional bodies including ASME, ISHMT, and ISEES and has published six books, together with more than 50 research articles in the reputed journals and international conferences.

**Avinash Kumar Agarwal** is Professor in the Department of Mechanical Engineering at Indian Institute of Technology Kanpur. His areas of interest are IC engines, combustion, alternative fuels, conventional fuels, optical diagnostics, laser ignition, HCCI, emission and particulate control, and large bore engines. He has published 24 books and more than 230 international journal and conference papers. He is Fellow of SAE (2012), ASME (2013), ISEES (2015), and INAE (2015). He has received several awards such as the prestigious Shanti Swarup Bhatnagar Award in Engineering Sciences (2016), Rajib Goyal Prize (2015), and NASI-Reliance Industries Platinum Jubilee Award (2012).

**Prodyut R. Chakraborty** is currently working as Assistant Professor of Mechanical Engineering at IIT Jodhpur. He has previously worked at the German Aerospace Center (DLR), Cologne, and the GE Global Research Center, Bangalore, India. He received his Ph.D. and master's from the Department of Mechanical Engineering, IISc Bangalore, and his bachelor's from North Bengal University. His primary areas of research are numerical modeling of alloy solidification, latent-heat-based energy storage systems for high-temperature applications, thermal management and thermal comfort, and sorption cooling.

**Satvasheel Powar** is currently working as Assistant Professor at the School of Engineering, IIT Mandi. He has previously worked at Greatcell Solar SA in Switzerland and at G24i in the UK. He received his Ph.D. in chemistry/materials engineering from Monash University, Australia, in 2013. Before joining IIT Mandi, he worked at Nanyang Technological University, Singapore, as a postdoctoral research fellow. His primary areas of research are new-generation solar photovoltaic and solar thermal utilization.

## Contributors

**Haneen Aburub** Department of Electrical and Computer Engineering, Florida International University, Miami, FL, USA

**Avinash Kumar Agarwal** Department of Mechanical Engineering, Indian Institute of Technology Kanpur, Kanpur, UP, India

**Ankit Bansal** Mechanical and Industrial Engineering Department, IIT Roorkee, Roorkee, India

**Muhammad Burhan** Water Desalination and Reuse Centre, Biological and Environmental Science and Engineering (BESE), King Abdullah University of Science and Technology, Thuwal, Saudi Arabia

**Prodyut R. Chakraborty** Department of Mechanical Engineering, Indian Institute of Technology Jodhpur, Jheepasani, Jodhpur, India

**K. Combrink** Department of Biology and Chemistry, Texas A&M International University, Laredo, TX, USA

**Sarit K. Das** School of Mechanical, Materials and Energy Engineering, Indian Institute of Technology Ropar, Rupnagar, Punjab, India

**Atul Dhar** School of Engineering, Indian Institute of Technology Mandi, Mandi, Himachal Pradesh, India

**Brian M. Fronk** School of Mechanical Industrial and Manufacturing Engineering, Oregon State University, Corvallis, OR, USA

**D. Ganta** School of Engineering, Texas A&M International University, Laredo, TX, USA

**Kapil Garg** School of Mechanical, Materials and Energy Engineering, Indian Institute of Technology Ropar, Rupnagar, Punjab, India

**G. Gokul** Photosciences and Photonics Section, Chemical Sciences and Technology Division, CSIR-National Institute for Interdisciplinary Science and Technology, Thiruvananthapuram, Kerala, India

**Gurudayal** Joint Center for Artificial Photosynthesis and Chemical Sciences Division, Lawrence Berkeley National Laboratory, Berkeley, CA, USA; Department of Materials Science and Engineering, University of California Berkeley, Berkeley, CA, USA

**C. V. Hettiarachchi** Department of Chemistry, Faculty of Science, University of Peradeniya, Peradeniya 20400, Sri Lanka

**Swapnik Jagarlapudi** Department of Computer Science and Engineering, Indian Institute of Technology Dharwad, Dharwad, KA, India

**Raj Krishna Jha** School of Engineering, Indian Institute of Technology Mandi, Mandi, Himachal Pradesh, India

**Yashwant Kashyap** Department of Electrical and Electronics Engineering, NIT Surathakal, Surathakal, India

**Ankur Kaundal** School of Engineering, Indian Institute of Technology Mandi, Mandi, Himachal Pradesh, India

**Vikrant Khullar** Mechanical Engineering Department, Thapar Institute of Engineering and Technology, Patiala, Punjab, India

**Shigeru Koyama** Kyushu University Program for Leading Graduate School, Green Asia Education Center Interdisciplinary Graduate School of Engineering Sciences, International Institute of Carbon-Neutral Energy Research (WPI-I2CNER), Kyushu University, Fukuoka, Japan

**Thomas L'Estrange** SpaceX Corporation, Hawthorne, CA, USA

**Rudrodip Majumdar** Department of Energy Science and Engineering, Indian Institute of Technology Bombay, Mumbai, India

**Akriti Masoom** Mechanical and Industrial Engineering Department, IIT Roorkee, Roorkee, India

**Amaresh Mishra** School of Chemistry, Sambalpur University, Sambalpur, India

**Ayushi Mishra** School of Engineering, Indian Institute of Technology Mandi, Mandi, Himachal Pradesh, India

**Vinod Narayanan** Department of Mechanical and Aerospace Engineering, University of California, Davis, CA, USA

**Kim Choon Ng** Water Desalination and Reuse Centre, Biological and Environmental Science and Engineering (BESE), King Abdullah University of Science and Technology, Thuwal, Saudi Arabia

**Virender Ohri** Mechanical Engineering Department, Thapar Institute of Engineering and Technology, Patiala, Punjab, India

**Amlan K. Pal** Organic Semiconductor Centre, EaStCHEM School of Chemistry, University of St Andrews, St Andrews, Fife, UK

**Dhiraj V. Patil** Department of Mechanical Engineering, Indian Institute of Technology Dharwad, Dharwad, KA, India

**I. R. Perera** Department of Chemistry, Faculty of Science, University of Peradeniya, Peradeniya, Sri Lanka

**Hannah C. Potter** Organic Semiconductor Centre, EaStCHEM School of Chemistry, University of St Andrews, St Andrews, Fife, UK

**Satvasheel Powar** School of Engineering, Indian Institute of Technology Mandi, Mandi, Himachal Pradesh, India

**Sourava C. Pradhan** Photosciences and Photonics Section, Chemical Sciences and Technology Division, CSIR-National Institute for Interdisciplinary Science and Technology, Thiruvananthapuram, Kerala, India

**Shahinur Rahman** Department of Electrical and Computer Engineering, Florida International University, Miami, FL, USA

**R. J. K. U. Ranatunga** Department of Chemistry, Faculty of Science, University of Peradeniya, Peradeniya, Sri Lanka

**Erfan Rasouli** Department of Mechanical and Aerospace Engineering, University of California, Davis, CA, USA

**Bidyut Baran Saha** International Institute of Carbon-Neutral Energy Research (WPI-I2CNER), Kyushu University, Fukuoka, Japan; Kyushu University Program for Leading Graduate School, Green Asia Education Center Interdisciplinary Graduate School of Engineering Sciences, Kyushu University, Fukuoka, Japan; Mechanical Engineering Department, Kyushu University, Fukuoka, Japan

**Sandip K. Saha** Department of Mechanical Engineering, Indian Institute of Technology Bombay, Mumbai, India

**Satya Narayan Sahu** School of Chemistry, Sambalpur University, Sambalpur, India

**Arif I. Sarwat** Department of Electrical and Computer Engineering, Florida International University, Miami, FL, USA

**Muhammad Wakil Shahzad** Water Desalination and Reuse Centre, Biological and Environmental Science and Engineering (BESE), King Abdullah University of Science and Technology, Thuwal, Saudi Arabia

**Amit Shrivastava** Department of Mechanical Engineering, Indian Institute of Technology Jodhpur, Jheepasani, India

**Sudheer Siddapureddy** Department of Mechanical Engineering, Indian Institute of Technology Dharwad, Dharwad, KA, India

**Anirudh Singh** School of Engineering, Indian Institute of Technology Mandi, Mandi, Himachal Pradesh, India

**Suraj Soman** Photosciences and Photonics Section, Chemical Sciences and Technology Division, CSIR-National Institute for Interdisciplinary Science and Technology, Thiruvananthapuram, Kerala, India

**Kyaw Thu** International Institute of Carbon-Neutral Energy Research (WPI-I2CNER), Kyushu University, Fukuoka, Japan; Kyushu University Program for Leading Graduate School, Green Asia Education Center Interdisciplinary Graduate School of Engineering Sciences, Kyushu University, Fukuoka, Japan

**Himanshu Tyagi** School of Mechanical, Materials and Energy Engineering, Indian Institute of Technology Ropar, Rupnagar, Punjab, India

**Kutub Uddin** International Institute of Carbon-Neutral Energy Research (WPI-I2CNER), Kyushu University, Fukuoka, Japan; Faculty of Physics, Jagannath University, Dhaka, Bangladesh

**R. Villanueva** School of Engineering, Texas A&M International University, Laredo, TX, USA

# Part I
# General

# Chapter 1
# Introduction to Advances in Solar Energy Research


**Himanshu Tyagi, Avinash Kumar Agarwal, Prodyut R. Chakraborty and Satvasheel Powar**

**Abstract** A lot of activity has been taking place in the research community over the decades to efficiently harness solar energy. One way this is fuelled is by the support from the governments which promote the implementation of large-scale projects—whether it be for electric power generation (using PV), or for water heating using solar thermal collectors. These activities involve the efforts of the industry, which keep pace with the latest technology in the world, and are in a race to provide the most reliable technological solution to the customer for harnessing solar energy in an economical and robust manner. This has been the backdrop theme of almost all the chapters included in this book, which have been contributed by various authors from across the world. This is the first chapter of the book, and thus provides an overview of the various topics that will be covered in this book, ranging from an energy roadmap for the future, to technologies advances in the field of photovoltaics and solar cells (DSSC—Dye-Sensitized Solar Cells). It also includes details of solar thermal collector, along with the discussion about its heat transfer aspects. Apart from the two primary uses of solar energy—electric power generation and water

H. Tyagi (✉)
Department of Mechanical Engineering, Indian Institute of Technology Ropar, Rupnagar, Punjab, India
e-mail: himanshu.tyagi@iitrpr.ac.in

A. K. Agarwal
Department of Mechanical Engineering, Indian Institute of Technology Kanpur, Kanpur, UP, India

P. R. Chakraborty
Department of Mechanical Engineering, Indian Institute of Technology Jodhpur, Jodhpur 342037, India

S. Powar
School of Engineering, Indian Institute of Technology Mandi, Mandi, Himachal Pradesh, India



H. Tyagi et al. (eds.), *Advances in Solar Energy Research*, Energy, Environment, and Sustainability, https://doi.org/10.1007/978-981-13-3302-6_1

heating—there are numerous applications for which it has been used over the years. Several such applications are also discussed in some of the subsequent chapters, such as refrigeration, desalination, gasification, and cooking.

**Keywords** Solar energy · Solar cells · Photovoltaics · DSSC · Applications Solar thermal systems

Photovoltaic systems generate electricity with minimum environmental impact, as compared to conventional fossil fuel sources. Large-scale solar deployment reduces greenhouse gas emission and consequently reduces the effects of global warming. In 2014, the Indian government announced an ambitious target of 100 GW installation capacity of solar PV systems by 2022. Since then, India has achieved notable progress towards this goal and has installed 20 GW cumulative solar capacity with 9.6 GW in 2017 alone. Based on the 2015 MIT Energy Initiative, by 2050, a major fraction of the world's electric power is expected to come from solar sources. However, this poses many technical and economic challenges on the electrical infrastructure. It is important to study the technical and economic potentials of large-scale deployment of the most commonly recognized types of solar; photovoltaic (PV) and concentrated solar power (CSP) at different locations in the US. This allows the assessment of technical potential based on grid interconnection topologies and solar collector performance. Moreover, it is important to evaluate the economic potential of such systems based on various metrics such as the levelized avoided cost of energy (LACE) and levelized cost of electricity (LCOE), along with the possibility of integration into the electricity markets. The evaluation of economic potential also involves assessment of subsidies, taxes, policies, and incentives for large-scale solar deployment.

One of the challenges in the use of renewable energy sources (such as solar energy, wind energy) is the estimation and measurement of its availability. It is especially useful if such measurements are available at various locations as well as varying time intervals—such as on an hourly basis, daily basis, as well as on a seasonal basis. Since the availability of ground data is very sparse, satellite data provides an alternative method to estimate solar irradiation. Satellites data across various spectral bands may be employed to distinguish weather signatures, such as dust, aerosols, fog, and clouds. For a tropical country like India, which is potentially rich in solar energy resources, the study of these parameters is of crucial importance from the perspective of solar energy. Furthermore, a complete utilization of solar energy depends on its proper integration with power grids. Incorporation of large amounts of photovoltaic energy into electricity grid suffers technical challenges because of its variable nature. Solar radiation is subjected to reflection scattering and absorption by air molecules, clouds, and aerosols in the atmosphere. Clouds can block most of the direct radiation. Modern solar energy forecasting systems relies on real-time Earth Observation from satellite for cloud and aerosols.

In recent times, a lot of advancements have taken place in traditional and modern solar cell technologies, notably, (a) silicon solar cells, (b) multi-junction solar cells

(c) Perovskite solar cells and (d) dye-sensitized solar cells. Research efforts have focused on improvement of the stability and the efficiency of each type of cells. While the current industrial market is predominantly dominated by silicon solar cells, other photovoltaic cells (b–d) show immense promise to overtake the silicon-PV market in near future. The most efficient silicon solar cell reported reaches an efficiency of over 26%. This efficiency was achieved by fabricating a cell, an interdigitated back contact, combining n-type and p-type amorphous silicon to collect both holes and electrons. The back contact is separated from the front contact by crystalline silicon, with the front contact covered by an amorphous silicon passivation layer and an antireflective coating. A close competitor of silicon solar cells, known as multi-junction solar cells, display power conversion efficiency as high as 46% using a solar concentrator. However, due to difficulty in cell fabrication with elevated cost, application of this type of cell is mostly limited to extra-terrestrial purposes. A low-cost alternative of multi-junction cell is a Perovskite solar cell. The best efficient Perovskite solar cell with a power conversion efficiency of 23.9% was achieved by using a complex semitransparent organic–inorganic Perovskite material with a high bandgap absorber, $Cs_{0.1}(H_2NCHNH_2)_{0.9}PbI_{2.865}Br_{0.135}$ combined with a low bandgap absorber, *c*-Si, for the back contact. While the Perovskite solar cells are promising candidates as low-cost substitute to silicon solar cells, stability remains an issue for the former. On the other hand, dye-sensitized solar cells are cost-effective and chemically stable, with a best reported efficiency of 13% using a panchromatic donor-π-acceptor based designed SM315 as an organic sensitizer, power conversion efficiencies of this type of cell is still to be improved to overtake the silicon-PV market.

Bioinspired dye-sensitized solar cells (DSSCs) from natural plant-based dyes gained importance due to their low cost of manufacturing and environmental friendliness. Not all plants are candidates for DSCCs; they should contain certain pigments such as chlorophyll, anthocyanin, and betalains. Titanium oxide nanoparticles play an important role as electron transporter in the DSSCs. The efficiency is still low in comparison with traditional silicon-based solar cells. There are several challenges to improve the efficiency such as the photodegradation of the dye, the stability of the electrolyte over time, and adhesion of dye with titanium oxide nanoparticles. It is important to review methods for fabricating DSSCs, and to understand the science behind the working principle. Various microscopic and spectroscopic analysis methods such as Fourier transform infrared spectroscopy, and confocal microscopy are in use, for investigating optical properties, surface chemistry of the dyes and in structural characterization of the plant cells. The photoelectrochemical properties such as conversion efficiency measure the performance of the DSSCs. They are usually in the range of 0.05–3.9% depending on the plant dye used, including plant dyes modified. A critical feature in the design of dye-sensitized solar cells is the attachment of the photosensitizing dye to the titanium oxide surface.

The single junction based conventional PV panels are dominating almost the entire photovoltaic market. In addition, they can only offer limited solar conversion efficiency due to limitations of the bandgap of their single pn-junction. On the other hand, third generation multi-junction solar cell offers the highest solar energy

conversion efficiency as their multiple pn-junctions can absorb a larger portion of solar spectrum. Despite such high potential, their share in current photovoltaic market is still negligible, even though, they have been used in form of concentrated photovoltaic (CPV) systems to reduce the use of expensive solar cell material. The main reason for such low market share is due to the gigantic design of commercial PV system which is only suitable to install in the open desert regions, thereby limiting its customers and application scope. It is important to analyze a compact CPV system with the motivation for its rooftop application and installation. Moreover, the long-term performance of CPV needs to be compared with conventional PV system in tropical conditions, to highlight its potential in low solar energy areas.

In 1991, the very first high efficiency dye-sensitized solar cell (DSC) was reported by Brian O'Regan and Michael Grätzel. Since then these devices have been steadily developed around the world. Environment friendliness, cost effectiveness, easy fabrication, and significant performance under indoor light condition, encourage researchers to explore the possibility of commercializing DSCs. Numerous materials have been tested to improve the overall device performance leading to efficiencies over 14%. Metal organic frameworks (MOFs) are one such material that have been utilized to further improve device performance. Although this field is only in its incipiency, MOF integrated DSCs have demonstrated the possibility of fabricating devices as efficient as conventional devices. It is hoped that by establishing robust structure–property relationships, future design, and synthesis of MOF-based DSCs will converge to desired commercialization goals.

Solution-processed bulk-heterojunction solar cells (BHJSCs) are the focus of photovoltaic research for the last 20 years due to new materials development, bandgap tunability through molecular design, high efficiency, and cost-effective fabrication, and optimization. Much attention has been paid to the design and development of donor materials whereas the development of new electron accepting materials is at its infancy. For a long time fullerene and its derivatives have dominated the field as electron acceptor materials. In last few years, a significant progress has been made towards the development of fullerene-free acceptors (FFA) which in combination with conjugated polymers/oligomers as the donors reached power conversion efficiencies (PCE) up to 14% and exceeded those of the fullerene-based OSCs. These sharp growths in PCE make OSCs as one of the fastest growing solar technology. Specifically, in these devices, the choice of FFAs and corresponding complementary donor materials plays critical role in achieving high efficiencies.

Dye-Sensitized Solar Cell (DSC) technology has carved a recognizable space in the PV arena owing to its unique merits like roll-to-roll compatibility, relatively inexpensive fabrication techniques using cheap and readily available materials, workability on flexible substrates, and excellent low/diffused light performance. Semitransparent multi-colored Dye Solar Panels stands as a potential candidate in the Building Integrated Photovoltaic (BIPV) sector, while the small form-factor devices show an excellent performance in indoor/artificial light, thus paving way for the self-powered indoor light-harvesting Internet of Things (IoT) applications.

Solar cells are widely used in the space where solar energy is a readily available source of energy. Reentry vehicles and satellites harness the radiation from the sun using an array of solar panels. These panels are folded compactly, and are quickly unfolded for operations once the satellite is in outer space. During reentry into the Earth's atmosphere, the solar panels must be folded and re-stowed. For efficient folding and unfolding of the solar panels, a concept of origami called Miura folding has been utilized, which is achieved with the help of robots. These solar panels have been developed primarily at NASA's Jet Propulsion Laboratory. Origami, the art of paper folding involving the creation of two and/or three-dimensional shapes, can be of paramount importance when space is limited and can be used as a compactly stowed system that transforms into a 3D structure with variable functionality. It is important to review the attempts made so far by the scientific community in applying the principles of origami in solar panel arrays. A few studies suggest the possibility of using rigid origami in the manufacture of stretchable electronics without employing elastomeric materials. They specifically fabricated origami-enabled stretchable solar cells, which can achieve significant deformability.

In addition to solar PV, solar thermal systems are increasingly being used all across the world. The supercritical carbon dioxide ($sCO_2$) power cycle is being considered for solar thermal central receiver systems in the United States. The cycle lends to increased high-temperature input that is expected of the next-generation concentrating solar thermal power (CSP) systems. Power block efficiencies of about fifty percent can be achieved for recompression cycles at an input temperature of approximately 700 °C. Additionally, the power block is compact and less complex, raising the possibility of using thermal-storage-coupled CSP $sCO_2$ technologies for modular ($\sim$100 MW) peak-load power plants. Three pathways towards providing solar thermal input to the $sCO_2$ cycle have been proposed by various research groups—the molten salt receiver pathway, the solid particle receiver pathway, and the gas-phase receiver pathway. The first two technologies have the advantage of sensible thermal storage within the solid/fluid medium passing through the receiver. In the gas receiver pathway, there is a need for coupling a sensible or latent heat storage technology. Several key technologies are needed to enable the realization of the $sCO_2$ solar thermal technology, key among them being the receiver and thermal storage.

Pivotal heat transfer components of solar thermal systems may involve single-phase flow of the working fluid in some unit (e.g., single phase solar collector), whereas, two-phase flow of the working fluid occurs in the other units (e.g., two-phase solar collector coupled directly to the turbine, boilers, and evaporators). Modeling of these systems is important to understand the heat transfer behavior, as well as, to develop the system level control among many other attributes. A detailed analysis of single-phase and two-phase systems is possible using mathematical models to characterize the fluid flow and heat transfer. Detailed description of the fluid flow and heat transfer become computationally very expensive with such models, and also a very high level of precision may not be required in large time ($\sim$few hours) simulations of the systems, as well as, in controlling the entire solar thermal power plant. Hence there is a need to develop computationally fast, low

order dynamic models. Among many other modeling approaches, a particular class of heat exchanger model, namely the moving boundary lumped-parameter model, has emerged as an efficient and effective tool for simulating dynamic characteristics of the two-phase solar collectors and the evaporators, pertinent to organic Rankine cycle (ORC) systems. These models are efficient in locating the continuously moving working fluid phase change boundary without requiring any sophisticated, well-trained formulation pertinent to the starting solutions. Even a simplified, reduced order quasi-steady state model is capable of demonstrating moving boundary characteristics in a narrow evaporator tube that is employed to carry organic refrigerant (working fluid) into the two-phase ORC heat exchanger in the medium temperature solar thermal applications ($\sim$200 °C). The model is capable of predicting the variation in working fluid mass flow rates with time-varying temperature of the heat transfer fluid (usually a commercial thermic oil) that transfers energy into the organic refrigerant. The variation in wall temperatures of the evaporator tube for three distinct flow regimes of the working fluid (subcooled, two-phase, and superheated) can be evaluated with changing average heat transfer fluid (HTF) temperature, corresponding to the varying levels of solar radiation incident on the collectors; and therefore, the model provides an avenue for ascertaining the practicability of the operating conditions based on the variation of the driving parameters values. By using the results of the quasi-steady model as the initial guess in the detailed dynamic model, the sharp transient characteristics can be explored by introducing time-dependent fluctuations in the subcooled refrigerant flow at the heat exchanger entry. Further complexity can be added to the modeling by incorporating axial variation in the heat transfer fluid temperature profile in the prevalent shell and tube heat exchanger.

Thermal energy storage (TES) unit has become an integral part of energy conservation. As the name implies, the device simply stores heat when energy from the source is available in excess, and releases the same when energy from the source falls short of the requirement. By doing so, such devices deliver heat energy across the temporal barrier, making thermal energy available for extended working hours of solar thermal power plants (STPP). High energy density and stable operation for long duration are desirable qualities which may be found in latent heat thermal energy storage (LHTES) system. To exploit the advantage of LHTES, the most common design reported in literature is shell and tube type latent heat thermal energy storage (ST-LHTES) systems with phase change material filled in shell side, while (heat transfer fluid) HTF flows in the tubes (or vice versa). It is important to perform a detailed classification of ST-LHTES systems based on geometry, orientation and relative position of PCM and HTF in heat exchanger along with the classification of phase change materials.

Solar to fuel conversion, if it could be performed in a sustainable manner, could provide an alternative to mankind's currently unsustainable use of fossil fuels. Solar fuel generation by photoelectrochemical (PEC) methods is a potentially promising approach to address this fundamental and important challenge. To date, research into these approaches has been primarily focused on solar water splitting, which produces hydrogen. Thus, the conversion of $CO_2$ to hydrocarbons that could

displace currently used fossil fuels remains as an unmet challenge. Various photoelectrode materials such as $Fe_2O_3$, $BiVO_4$, $WO_3$, $TiO_2$, and $Cu_2O$ have been discussed for solar water splitting. However, their performance for PEC water splitting is limited by poor electronic properties and sluggish charge transfer kinetics that lead to high charge carrier recombination. Nanostructuring, elemental doping, surface passivation, conducting template, cocatalyst, and heterostructure are possible pathways to improve their performance. Whereas only few reports are available on PEC $CO_2$ reduction, a number of semiconducting photocathodes including Si, GaP, InP, and CdTe have been explored for PEC $CO_2$ reduction reaction ($CO_2RR$). Although most of these photocathodes produce only two electron products such as carbon monoxide or formate. It is important to review the state-of-the-art limitations of various semiconducting photoelectrodes for PEC water splitting and $CO_2$ reduction. Other emerging photoelectrode materials and tandem cell strategies also need to be studied for efficient solar fuel production.

Refrigerant significantly influences the performance of air conditioning and refrigeration system as well as it has some environmental issues need to be considered before selection. These systems can be made eco-friendly if it is powered by solar energy or low-grade thermal energy and they use environment-friendly refrigerants. Thus, it is important to explore low-GWP (global warming potential) refrigerants for the domestic air conditioning applications. Refrigerants with high GWP are mostly used in environment control applications such as heating, ventilation, air conditioning (HVAC) and refrigeration systems. Some refrigerants contribute to significant environmental issues and the Montreal Protocol and Kyoto Protocol have been signed to address the threats of ozone layer depletion and global warming potential. To fulfill the commitments of Kyoto Protocol, meanwhile, governments in many countries instituted phaseout plan for the use of environmentally harmful gasses in heat pump systems. For instance, EU MAC Directives, F-gas regulation, and Japan METI directives, which clearly declared their target year to use new refrigerant of GWP below 150 for mobile air conditioner and GWP below 750 for the residential air conditioner. Research interest has been stimulated to find alternative refrigerants with low or ultralow GWP for energy conservation and environmental sustainability. Hydrofluoroolefins (HFOs) have very low environmental impact and thus HFOs are considering as potential candidates to replace the hydrofluorocarbon (HFC) refrigerants such as R410A, a near-azeotropic mixture of difluoromethane (R-32) and pentafluoroethane (R-125) and is commonly used refrigerant in air conditioning applications. The limited number of pure fluid sometimes cannot meet the excellent heat transfer criteria due to their low volumetric capacity and moderate flammability or toxicity. Mixing of HFOs and HFCs refrigerants, in this case, allows the adjustment of the most desirable properties of the refrigerant by varying the molar fraction of the components. Different combination of these mixtures cannot be claimed as the best option, but it might be a good choice for further study. It is important to focus on the research trend in finding low-GWP refrigerants and its application in different heat pump system considering the system performance, safety, and the overall environmental impact. The

conventional vapor compression system, thermally driven adsorption system and sorption–compression hybrid systems also need to be taken into consideration.

Multistage flash (MSF) desalination technique is one of the simplest of thermal desalination methods which requires thermal energy in order to desalinate seawater. This thermal energy can be provided by solar energy harnessed by a direct absorption solar collector (DASC), in which a nanofluid while flowing through the collector absorbs the incident irradiation directly, and gets heated to higher temperatures. These collectors are having a relatively higher thermal efficiency (10% higher) as compared to conventional surface absorption-based solar collectors. A direct absorption solar collector (DASC) can be used as a heat source for multistage flash (MSF) desalination system having once-through (OT) configuration, and these two systems may be coupled using a counterflow type heat exchanger. This direct absorption collector is replaced by surface absorption-based collector in order to prevent the degradation of thermal performance of surface absorption-based collector due to high salinity of seawater. It is important to evaluate the thermal performance of the combined system by a quantity known as gained output ratio (GOR). The thermal performance or efficiency of the solar collector depends upon the various parameters such as thickness of nanofluid layer inside DASC, length of the collector, particle volume fraction of nanoparticles, and incident solar energy which will affect the performance of the MSF system also. Hence, the performance of the combined system can be evaluated as a function of these parameters.

In recent years, solar energy driven water desalination/purification systems have been extensively researched with the objective of improving the distillate yield. In these conventional solar-driven systems, solar energy heats the water indirectly, i.e., in these systems, the solar energy is transferred to the water through conduction, resulting in evaporation and hence purification of the water. Researchers have explored the idea of adding nanoparticles into the wastewater so that solar energy is transferred to water volumetrically, which considerably improves the evaporation rate. Amorphous carbon nanoparticles are used owing to their high solar weighted absorptivity values.

Gasification is a thermo-chemical conversion process, which is used to gasify any carbonaceous substance. On the application of heat, and/or under a controlled amount of oxygen, carbonaceous substances break down to form the synthetic gas. Use of gasification may be attributed to a wide range of applications, from biomass conversion for energy production to municipal solid waste management. The gasification process is endothermic with an operating temperature range of 480–1650 °C. In conventional gasification process, some part ($\sim$5–20%) of feedstock is burnt in controlled air to supply the process heat. Any auxiliary heating source such as solar heating reduces the heat requirements from partial combustion. Moreover, the side effects of combustion, viz., product gas contamination, need for purification attachments, etc. can be partially averted. Higher temperatures of the concentrated solar radiations drive the chemical reaction to the near-complete utilization of carbonaceous content.

Solar energy can often be used for cooking purposes. For instance, the bakery process, out of all the food making processes, requires the highest range of processing temperature. Therefore the energy consumption in bakery is also high. The baking process alone consumes about 73% of the total energy consumed in bread production. Currently utilized conventional energy sources affect the surroundings detrimentally. Shifting to renewable energy sources can be a sustainable way. Considering the fact that the process temperature requirements can be fulfilled by the solar thermal energy, a solar thermal based system can be used for bakery oven.

The topics in this book have been organized in four different sections: (i) General, (ii) Solar Cells, (iii) Solar Thermal Systems, and (iv) Applications of Solar Energy.

Specific topics covered in this book include:

Introduction to Advances in Solar Energy Research
Techno-Economic Potential of Large-Scale Solar Deployment in the US
Solar Radiation Assessment and Forecasting Using Satellite Data
Solar Cells and Their Applications
Natural Dye-Sensitized Solar Cells: Fabrication, Characterization, and Challenges
Concentrated Photovoltaic (CPV) for Rooftop—Compact System Approach
Metal Organic Frameworks in Dye-sensitized Solar Cells
Fullerene-Free Molecular Acceptors for Organic Photovoltaics
Dye-Sensitized Solar Cells as Potential Candidate for Indoor/ Diffused Light-Harvesting Applications: from BIPV to self-powered IoTs
On the Use of Origami for Solar Energy Harvesting
Supercritical Carbon dioxide Solar Thermal Power Generation—Overview of the Technology and Microchannel Receiver Development
Reduced Order Heat Exchanger Models for Low-to-Medium Temperature Range Solar Thermal Applications
Shell and Tube Latent Heat Thermal Energy Storage (ST-LHTES)
Current Trends and Future Roadmap for Solar Fuels
Low-GWP Refrigerants for Energy Conservation and Environmental Sustainability
Application of Nanofluid based Direct Absorption Solar Collector in Once-through Multistage Flash Desalination System
Experimental Investigation into the Applicability of Nanoparticles in Purification of Sewage Water Through Usage of Solar Energy
Solar Assisted Gasification
Solar Thermal Powered Bakery Oven

To summarize, this book contains information about various aspects of solar energy and its applications. Different techniques of harness solar energy have been discussed in detail, along with the detailed analysis of direct electricity generation (using solar cells). Moreover, description of solar thermal systems, including applications such as cooling, desalination, gasification, cooking, etc. has been provided.

# Chapter 2
# Techno-Economic Potential of Large-Scale Solar Deployment in the US


**Shahinur Rahman, Arif I. Sarwat and Haneen Aburub**

**Abstract** PV system generates electricity with minimum environmental impact than conventional fossil fuel sources. Large-scale solar deployment reduces greenhouse gas emission and consequently reduces the effects of global warming. In late of 2014, the Indian government announced an ambitious target of 100 GW installation capacity of solar PV systems by 2022. Since then, India has achieved notable progress towards this goal and has installed 20 GW cumulative solar capacity with 9.6 GW in 2017 alone. Based on the 2015 MIT Energy Initiative, by 2050, a major fraction of the world's electric power will come from solar sources. However, this poses many technical and economic challenges on the electrical infrastructure. In this chapter, we focus on the US case, by studying the technical and economic potentials of large-scale deployment of the most commonly recognized types of solar; photovoltiac (PV) and concentrated solar power (CSP) at different locations in the US. The technical potential is assessed based on grid interconnection topologies, and solar system performance. The economic potential is evaluated based on several metrics such as the levelized avoided cost of energy (LACE) and levelized cost of electricity (LCOE), and the possibility of integration into the electricity markets. The economic potential also covers the subsidies, taxes, policies, and incentives for large-scale solar deployment. Two simulation case studies are implemented on two large-scale solar PV and CSP projects at different locations in the US to evaluate their techno-economic potentials.

**Keywords** Concentrated solar power · Photovoltaic system · Mounting system Heat transfer fluid · Thermal energy storage · LACE · LCOE · NPV Payback period

S. Rahman · A. I. Sarwat (✉) · H. Aburub
Department of Electrical and Computer Engineering,
Florida International University, Miami, FL 33174, USA
e-mail: asarwat@fiu.edu

S. Rahman
e-mail: srahm026@fiu.edu

H. Aburub
e-mail: haburub@fiu.edu



H. Tyagi et al. (eds.), *Advances in Solar Energy Research*, Energy, Environment, and Sustainability, https://doi.org/10.1007/978-981-13-3302-6_2

## 2.1 Introduction

The worldwide energy consumption has continued to increase with the fast and consistent growth of the economy and is estimated to rise 28% within next 20 years because of increasing residential and commercial energy demand (International energy outlook 2017). Per capita electricity consumption has been increased by 50 times since independence in India but energy generation growth is insufficient in comparison.[1] In several remote areas of India, the power grid network is unavailable and fuel transportation is difficult and expensive. Generally, electric power plants use fossil fuels, such as oil, natural gas, and coal to generate electricity that severely pollutes the environment and thus, hinders sustainable economic development. The trend of increasing fuel cost, $CO^2$ emission rate, and gradual decline of the fossil fuel reserve has brought different countries and organizations of the world together to give emphasis on large-scale renewable energy deployment and its integration to the power grid (Schmalensee 2015). It is highly needed to promote clean energy technologies to confront the global challenges of climate change, energy security, and overall economic development (Mendelsohn et al. 2012).

Solar power has the potential to meet increasing energy demand, without being dependent on imports and the associated vagaries for fossil fuels. Solar electric systems, such as concentrated solar power (CSP) (Sharma 2011) and photovoltaic (PV) (Salasovich et al. 2013) systems, are very popular technology due to the abundant solar resources, lower operation, and maintenance cost in comparison to conventional power plants and longer lifespan of system components. PV systems are implemented as stand-alone microgrids, grid-connected, or hybrid systems for electrification of local communities, especially in the developing countries like India. The government provides subsidies to solar energy systems to make it competitive with other energy sources. In the US, Renewable Energy Tax Credit (RETC) programs support the installation and operation of residential and industrial solar energy facilities and decrease about 30% tax liability, paid by solar energy users (Brown et al. 2016). Moreover, many European countries introduce a Feed-In-Tariff (Fouquet 2007) scheme to increase the appeal of clean energy and encourage ordinary people to invest more in the solar energy sector. According to feed-in-tariff projects, the government pays solar system owners for electricity generation from their own systems. Due to abundant production capacity, massive technological potential, environmental concerns, and government subsidies, solar energy gets easy entrance into the electricity market as a substitute of conventional power sources.

In this chapter, we will discuss briefly two popular and recognized solar power plant technologies, their advantages, and limitations. We will also explain solar cell materials, PV plant components, grid connection topologies, and major solar power plant performance indicators. We will describe several financial metrics and risk assessment tools to evaluate the economic potential of solar energy projects.

[1]Applications of solar energy—https://www.springer.com/series/15901.

Finally, we will simulate two solar power plants at different locations of the USA to evaluate plant performance and economic potential.

## 2.2 Solar Power Plant Technology

Solar power technology can be commonly categorized into two major groups:

1. **Concentrated Solar Power (CSP) Technology**: Usually, solar energy is used to heat water to produce steam, which drives a steam turbine and produces electricity indirectly.
2. **Solar Photovoltaic (PV) Technology**: Solar energy is directly converted into electricity using solar panels.

Again, CSP technology is subdivided into four groups while PV technology has three other topologies. The detailed classification is clearly depicted in Fig. 2.1.

### *2.2.1 Concentrated Solar Power (CSP) Technology*

CSP plants accumulate a large area of solar irradiation and indirectly generate electric power using mirrors and reflectors. Concentrated sunlight heats a working fluid to produce steam, which rotates a steam turbine or drives a heat engine and generate electricity. Thermal Energy Storage (TES) in CSP technology provides flexibility in energy use and balances energy supply and demand during intermittent sunlight. Nowadays, most commercially available CSP plants are Parabolic Trough, Solar Towers, Parabolic Dishes, and Linear Fresnel Reflectors. The details of four main CSP technologies are briefly discussed below:

**Parabolic Trough Solar Power Plant**: The parabolic trough solar power plant is the most developed CSP plant that has been operated commercially since 2008. A group of large, parabolic-shaped mirrors gathers solar energy and reflects it on receiver tubes that are placed along the mirrors' focal line. The mirrors usually track

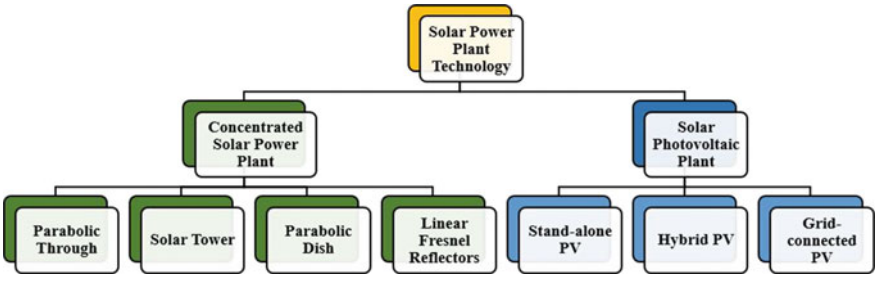


**Fig. 2.1** Details classification of solar power plant technology

the sun along north–south axes. Many parallel rows of mirrors are connected in series to receiver tubes in large utility-scale CSP plants. Solar energy heats up Heat Transfer Fluids (HTFs), such as synthetic thermal oil or molten salt, to approximately 400 °C when HTFs are flowing through the receiver tube. A heat exchanger transfers the heat to a water-steam Rankine cycle, which in a result rotates the turbine to generate electric power. According to the record of 2014, the largest parabolic trough solar power plants using CSP technology include SEGS plants (354 MW) in California, Solana Generating Station (280 MW), Genesis Solar Energy Project (250 MW), and Solaben Solar Power Station (200 MW) in Spain. Parabolic trough solar plants face some difficulties during operation with different HTFs. Synthetic fuels and molten salts remain viscous at low temperatures, which in a result reduces the efficiency of the heat transfer process at night and on cloudy days. Molten salts or synthetic fuels cannot rotate a steam turbine directly and therefore, a heat exchanger is required to heat water and drive a heat engine. It is possible to produce superheated steam directly using steam as an HTF, which reduces the cost of expensive HTFs and heat exchangers. However, it is an inefficient approach because it cannot reach sufficiently high temperature like other HTFs.

**Solar Tower Power Plant**: The solar tower power plant has a central receiver tower to absorb focused sunlight. A circular array of flat mirrors (called heliostats) surrounds the 100–200 m high central tower. The heliostats have two axes tackers to follow the sun the whole day. A heat transfer fluid at receiver assimilates high concentrated reflected radiation (600–1000 times higher) and achieves extremely high temperature (500–800 °C or 930–1470 °F). HTFs transfer heat to produce superheated steam for the heat engine, which eventually generates electric power. Solar tower power plants can use various HTFs, including air, steam, mineral oil, liquid metal, and molten nitrate salts. This system possesses approximately 15–20% higher efficiency than parabolic trough technology due to the high temperature and concentration ratio. However, high operation and construction cost of heliostats and towers is a big challenge for the installation of solar tower power plants. The largest solar tower system, PS20 station (20 MW), is located in Seville, Spain. Abengoa Solar designed the facility, which has 1255 heliostats and 531 ft. central solar tower.

**Parabolic Dish Solar Plant**: The parabolic dish solar plant has a satellite-like reflective surface to gather sunlight on a central receiver. The paraboloid surface has two axes trackers to follow the sun throughout the day. A central receiver positioned at the dish focal point absorbs accumulated sunlight and heats a working fluid or gas to nearly 750 °C. The thermal energy of fluid or gas eventually is converted to electric power. Comparing with other CSP plants, they have the highest heat–electricity conversion efficiencies (up to 30%). Additionally, the dish systems require a small amount of water for washing purposes only. Generally, parabolic dish systems are 10–25 kW in size. The highly flexible design of this system allows small-scale (up to 10 kW) remote applications, as well as large-scale deployment (300 MW or more) for utility applications. However, the dish system has no energy storage, so the produced power need to be used instantly or sent to the utility grid. Sufficient storage capacity in the design could make the parabolic dish solar plant more desirable and attractive technology in the future.

**Linear Fresnel Reflectors Solar Plant**: Linear Fresnel reflectors solar plants use many long, thin, and nearly flat mirror arrays to concentrate sunlight onto elevated linear receiver tube. The concentrated solar energy converts water into steam while water is flowing through the receiver tubes. Flat mirrors used in this plant allow more reflective surface, which in a result capture more sunlight. Compared to other CSP technologies, the investment costs of this plant tend to be lower because of simple solar field construction, less expensive reflector materials, and absorber components. In addition, the stationary receiver does not need the rotating mechanism that provides further design flexibility. Therefore, the linear Fresnel reflectors solar plant offers high thermal performance as well as low cost. In addition, the system creates a shaded area that is especially good for agriculture in dry weather. The shaded space protects the plants from excessive evaporation and provides safety from the cold climate of the desert region at night. In addition to electricity generation, this technology is also used for direct thermal applications, such as cooling, hybrid STE—fuel fired combined cycle, enhanced oil recovery, and industrial process heat applications. Fresnel reflectors more than 200 MW size are in operation or under construction in different places in the world.

Concentrated solar power facilities require a consistent source of fresh water to cool the whole system during operation. A dry cooling or air-cooled system is also observed that uses air to condense heat in order to minimize water consumption. However, the construction of dry cooling systems is very expensive and less effective in the very hot atmosphere. To optimize plant efficiency, construction cost, and water consumption, some power plants combine dry and wet cooling systems to make hybrid cooling systems. The hybrid cooling system minimizes water consumption about 50–85%, with a 1–3% drop in output power.

### *2.2.2 Solar Photovoltaic (PV) Technology*

Solar Photovoltaic (PV) technology converts sunlight directly into electric power using solar panels. Solar panels are made of solar cells that contain multiple layers of semiconductor materials. When these materials absorb sunlight, solar energy causes electrons to go out from their atoms and flow within the material, which in result produces electric energy. Generally, the size of solar cells is very small and each cell generates a small amount of electric power. Therefore, several cells are combined to form a solar module and several modules are congregated into a PV array. Generally, PV arrays are mounted either at a fixed angle inclined to the south or on a solar tracker device. PV arrays with tracking devices track the sun throughout the day to maximize captured sunlight. Many arrays are connected to build a large system, suitable for utility applications.

Photovoltaic systems are classified broadly into three different groups according to their operational method, component configurations, and components connections to electrical loads and other generation sources. The details of different PV systems are explained in the next subsection.

**Stand-alone PV System**: The stand-alone PV system is a self-governing electric network that produces sufficient energy to meet its own electricity demand. It consists of PV arrays with single or multiple PV modules, converters, and electrical loads (illustrated in Fig. 2.2). Depending on the design, energy storage can be included with a stand-alone PV system to minimize system intermittent output power. During bright sunshine hours of a day, the PV system supplies power directly to the electric load and stocks excess energy into storages for later use. On the contrary, energy storage feeds power to the load during the night or low sunshine periods of cloudy days. An inverter is employed to the system that converts DC power to the required 120 or 240 VAC for household AC applications. Stand-alone PV systems are appropriate for the remote application for providing free and reliable electric power supply. These systems are environmentally friendly and require low maintenance, and are easily expanded with multiple solar modules and storage. However, high initial capital cost of PV modules and bulk energy storage, intermittent power generation, and the possible electrical hazard of system components limit its application.

**Hybrid PV System**: Photovoltaic systems, along with other energy sources, form a hybrid PV system that allows continuous power supply in a more economical and efficient way (D'Rozario et al. 2015). A common wind-PV hybrid

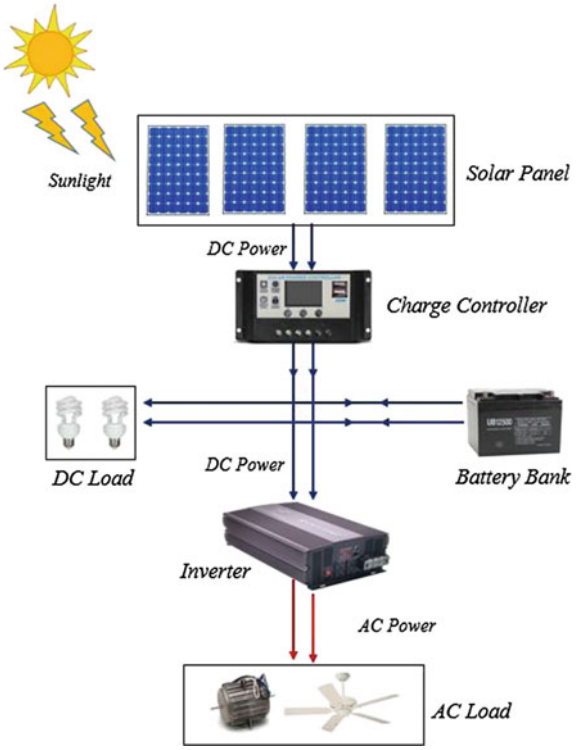


**Fig. 2.2** Simplified diagram of stand-alone PV system

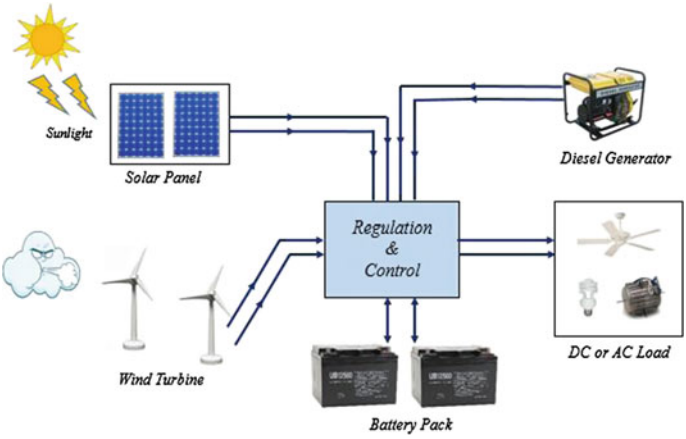


**Fig. 2.3** A hybrid wind-PV-battery–diesel generator system

system (shown in Fig. 2.3) combines solar and wind energy and offers several advantages over a single system. In the USA, summer has the brightest and longest period of sunshine but has low wind speed, where winter is completely opposite. Thus, hybrid wind-PV systems act more reliably to supply electric power due to the opposite peak operating times of individual wind and solar sources. A diesel generator or energy storage systems are connected with most hybrid systems as a backup when neither the PV nor wind system is capable of producing power. Moreover, the diesel generator or storage device reduces the system component ratings. However, an addition of diesel generator or storage complicate the overall system connection, but advanced power electronic devices make easier connectivity. Most hybrid systems act as a stand-alone system, which is not integrated into the utility power grid.

**Grid-connected PV System**: A grid-connected PV system illustrated in Fig. 2.4 operates in conjunction with the existing utility grid. The main components of this system are solar arrays, power converters, a transformer, and other equipment for metering and connection purposes (Rahman et al. 2018a). A grid-connected system does not include any expensive and bulky energy storage systems, like the stand-alone PV. Power converters generate grid-compatible AC power from PV output. A transformer creates a bidirectional interface between the PV system and the electric power grid to provide galvanic isolation and steps up voltage compatible to the grid. When the PV system generation energy is more than the load demand, the PV system feeds power into the utility grid after running the electrical loads. Besides, the utility balances the power requirement of the load during low generation of the PV system. It is expected that the PV system automatically stops to feed energy into the feeder during grid disturbance. Rooftop residential PV systems connected to the large utility power grid are a perfect example of this system.

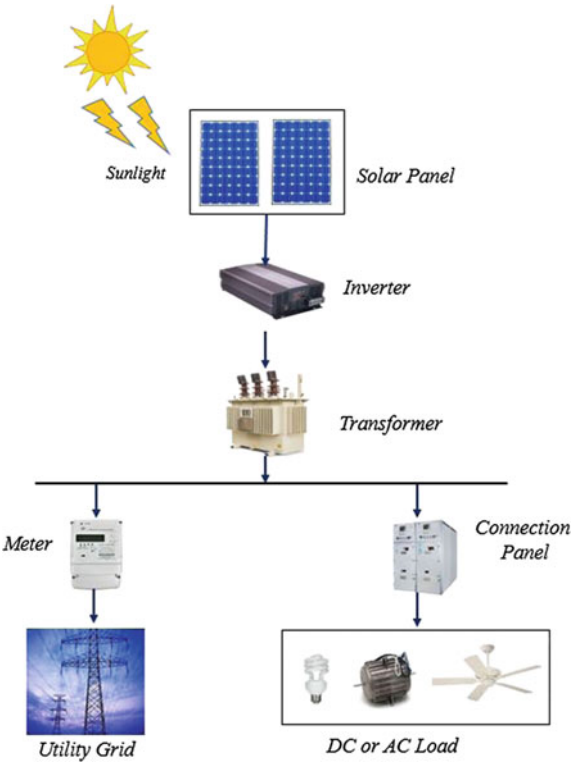


**Fig. 2.4** Simplified diagram of grid-connected PV systems

## 2.3 Photovoltaic System Components

The design of a solar photovoltaic (PV) plant is not complex. The basic components of PV systems are PV panels, PV inverters, transformers, and mounting systems (Salasovich et al. 2013). PV modules convert sunlight into DC power, which is then fed to an inverter to generate grid-compatible AC power. Electrical wires, breakers, fuses, and disconnect switches are needed for connection, safety, and equipment protection. In this section, details of different PV system components are described as follows.

**PV Panel**: Solar panels are considered the core of a PV system. It is composed of several solar modules, which are in turn composed of many solar cells. Due to nonlinear voltage and current properties of PV panels, a maximum power point tracker (MPPT) is desired to track the maximum power point, which delivers about 10–25% more power for the same array. Solar panels vary in cell material, size, type, color, shape, design, and manufacturing method. The most common PV cells are made of crystalline silicon (c–Si) that covers about 85–90% of the solar market due to its efficiency, abundant primary resources, stable, and reliable operation (Ruiz 2011). c–Si modules are classified as single crystalline (sc–Si) and

**Table 2.1** Efficiencies of photovoltaic modules available in global solar market

| Technology | Cell materials | Efficiency (%) |
|---|---|---|
| Wafer-based c–Si | Mono-Si | 15–20 |
| | Multi-Si | 15–17 |
| Thin films | a–Si; a–Si/μc–Si | 6–9 |
| | CdTe | 9–11 |
| | CIS/CIGS | 10–12 |
| Advanced technology | DSSC | 15 |
| | CNT | 30 |
| | QD | 13.4 |

multi-crystalline (mc–Si) modules. However, the main drawbacks of this technology are the manufacturing price and the quality of material used. Thin film solar cells currently occupy about 10–15% of the global sales. Amorphous (a–Si), micromorph silicon (a–Si/μc–Si), Cadmium Telluride (CdTe), Copper–Indium–Gallium–Diselenide (CIGS), and Copper–Indium–Diselenide (CIS) are the most popular thin film solar technologies. Thin film solar cells are comparatively cheap, have a low temperature coefficient, and are effective at lower sunlight. However, the main shortcomings are low efficiency, unstable operation, and the scarcity of cell materials. Dye-sensitized solar cells (DSSC) and other advanced technologies, such as carbon nanotube (CNT), quantum dots (QD), and silicon nanoparticle ink, are also available in the solar cell market. Solar cell materials affect overall efficiency and required land area of PV sites. Table 2.1 depicts some available commercial efficiencies of different PV modules. For the same output power, PV systems having low efficient panels require a large installation area, which affect installation, transportation, maintenance, and mounting cost. Several solar panels are combined to achieve large and required power rating. Generally, 12 or 24 V PV panels are chosen for the stand-alone PV system, where 18, 42, or 60 V panels are used in utility-scale applications.

**Inverter**: PV inverters convert dc power to AC power, which is used to run the most common electrical appliances. PV panels produce dc power, which is fed into a PV inverter to generate AC power that allows its integration to the utility grid. Inverters are key components in both grid-connected and stand-alone PV power applications. Maximum load demand and PV system size determine the ratings of an inverter. Inverters are connected directly to the electric loads in an off-grid system, where grid-tied inverters are coupled to the power grid with net metering infrastructure. Inverters connected in large PV systems must have galvanic isolation to avoid an unsafe operation. They must maintain the operational characteristics, power quality, and electrical standards (ANSI C84, 150 UL1741 and IEEE 1547) for interconnection with the distribution network (Photovoltaics and Storage 2018). Most AC grid-tied inverters should have an anti-islanding feature that disconnects them from the grid during a disturbance, low–voltage, or fault condition. However, the use of inverters causes energy loss due to harmonics of PWM switching. Typical efficiency of an inverter well matched to the array is around 90%. For the

future development, PV inverters should upgrade control characteristics to support grid operation by regulating voltage and providing inertia response (Rahman et al. 2018b).

**Transformer**: Industrial, commercial, and utility PV systems have substation and distribution transformers to step up inverter voltage to a grid-compatible one. Transformers provide isolation between a PV system and the power grid to improve equipment safety. Large-scale PV systems install two transformers: the first one steps up the PV inverter voltage to medium voltage (MV) and the second one steps up to high-voltage (HV) and provides galvanic isolation. Generally, a three windings transformer is employed in 500 kW or higher PV power systems, where two windings are connected to the low-voltage (LV) side and the third one is for MV connection. PV systems less than 500 kW power rating have a two windings transformer, where the windings are connected to the LV and HV side, accordingly. Transformer selection depends on efficiency, rated power, and cost. A technique has been developed in Testa et al. (2010) to choose the right size of a transformer for reliable and successful PV system operation.

**Mounting Systems**: Solar panel mounting systems refer to a framework that attaches a PV array to a pole, a roof, or the ground permanently. Mounting system selection depends on installed system size, land constraints, and local weather. In ground-mounted PV systems, PV panels are directly attached to the ground via concrete footers or fixed panels on the surface without ground penetration. Wind speed, ice loading, and snow are important design considerations of this mounting system. The ground mounting system must tolerate 90–120 mph local wind speeds depending on geographical location. A solar tracker is employed with the mounting system to maximize system output throughout the year. Single-axis tracking (PV panels track the sun on one axis) increases output power up to 25%, where dual-axes tracking increases output up to 35% or more. However, the tracking system increases maintenance and equipment cost slightly. Another type of mounting system, PV panels ballasted or fixed to the roof is termed rooftop mounting. A relatively new roof should be recommended for PV system installation to avoid the movement of PV panels in the future due to roof impairment or replacement. Several design techniques can make residential and commercial buildings suitable for the rooftop mounting. Building orientation at southern exposure can maximize PV output and reduce the mechanical support requirement (Gagnon et al. 2016).

## 2.4 Performance of PV Systems

The measurement of system performance is required for operation and maintenance planning, commissioning, performance guarantees, and making investment decisions. A PV system performance depends on both system component parameters and weather factors. Usually, solar power plant performance is measured by Capacity Utilization Factor (CUF) or Performance Ratio (PR). CUF or PR is

defined as the ratio of actual electric power output from a PV system to the system nameplate output ratings over the years. CUF gives emphasis on geographical areas, where PR focuses on the component losses, instead of location and site potential. Generally, a PV system performance is observed under Standard Test Conditions (STC), when solar insolation, AM solar spectrum, and module temperature are 1000 W/m$^2$, 1.5, and 25 °C, respectively. The PV plant performance can be calculated using standard software, such as HOMER, RETScreen, PVsyst, etc. The key performance indicators are described as follows.

### 2.4.1 Location Performance Parameters

Variations in weather factor such as solar radiation, wind velocity, humidity, and ambient temperature from month-to-month and year-to-year influence the PV system performance. The details are described below.

**Solar Radiation**: Solar radiation is a fundamental input of PV systems for electric power generation. It depends on various parameters, such as sunshine duration, relative humidity, temperature, latitude, and altitude. During low sunshine in the morning, evening, and especially in winter, the output power from a PV system decreases compared to other times of the day and year. Depending on the installation location, plants and buildings can throw shade on PV modules and hence, degrade overall system performance. The primary design requirement of a PV plant is precise solar irradiation data that is available in different sources, such as NREL, IMD, NASA, Meteonorm, and WRDC. Some agencies provide data without any cost while from others, data needs to be purchased.

**Temperature**: Performance and efficiency of a solar cell depend on module temperature. A PV module operates more efficiently at a low-temperature range. The PV output power is reduced at elevated temperature. The system output power loss depends on temperature coefficients of cell materials, which determines the change of power generation with different temperatures. Table 2.2 presents temperature coefficients of different PV Modules, available in the global solar market. Thin film PV modules perform better than crystalline silicon at a high temperature due to the low-temperature coefficient.

**Table 2.2** Temperature coefficient of different photovoltaic modules

| Module types | Temperature coefficient (%/K) |
|---|---|
| Crystalline modules | −0.4 ~ 0.45 |
| Amorphous modules | −0.2 ~ 0.23 |
| Thin film CdTe modules | −0.24 ~ 0.25 |

### 2.4.2 Component Performance Parameters

Component performance parameters, such as inverter efficiency, module mismatch, module degradation due to aging, module efficiency, and soiling have a significant impact on PV power generation. While designing a PV system, all possible losses should be considered.

**Inverter Efficiency**: A solar inverter efficiency determines conversion competence from DC power into AC. The quality of the inverter influences solar plant performance. High efficient inverters improve the plant's performance ratio. Inverters operate in a less efficient way below their rated power. Therefore, choosing the correct size of an inverter is crucial to the design process. 96 to 98.5% efficient grid-tied PV inverters are available in the current solar market. Besides, there are also less efficient inverters below 95% available in the industry.

**Module Degradation due to Aging**: The operating life of a PV module depends on the stability and resistance to corrosion of the constructed materials. Manufacturers offer a warranty of 25 years or more on their PV panels but no PV system exists for such a long period. Several module degradation mechanisms, such as water ingress or temperature pressure, reduce generation output and cause module failure. The degradation losses entirely relate to short circuit current losses, concluded by NREL investigations. The drop in current production is attributed by visual physical defects, such as module delamination, EVA browning, and localized hot spots that reduce efficiency about 15–20%. However, researchers are working hard to find long-term reliable PV modules to reduce degradation loss.

**Module Mismatch**: Solar modules with identical properties are connected in series and parallel to form a large PV array. The modules, which have different properties, experience module mismatch losses. Mismatch losses are one of the major problems of a PV system because it may cause the entire system output to be lowest under the worst scenario. When one solar cell is shaded, while the remainder of the array is not, power generated by the good solar cells can be dissipated through the shaded cell rather than the load. This results in high localized power dissipation and damages to the module by heating. Therefore, module selection is a primary design consideration that affects the overall plant performance.

**Soiling Loss**: The PV module soiling loss refers to output power reduction, resulting from dust, dirt, snow, and other particles. Dust generated from heavy wind, vehicular movements, and pedestrian volcanic eruptions makes a thin coating on the module's surface. In most cases, rainfall washes away the accumulated dust on the panel surface. However, dirt, such as bird droppings, stays on the surface of the PV module, even after heavy rains that reduce PV power generation. Generally, soiling losses are about 1%, however, the reduced power is restored after cleaning the module's surface.

**Reflection Loss**: PV module power ratings are determined at standard test conditions that use perpendicular incident sunlight. In the practical case, sunlight falls on the module's surface at larger incidence angles, which results in high reflection loss and reduces output power. Calculations show that reflection losses

are about 1%, relative to STC for the equator faced modules with a tilt angle equivalent to the latitude. A variety of antireflection technologies have been deployed with PV modules to minimize reflection losses of solar cells.

## 2.5 Grid Connection Topology

PV output power depends on the connection of internal components and grid collection topologies. It is very important to choose the right topology based on system location, power ratings, component efficiency, cost, and system reliability. In this section, different internal PV inverter connections and grid integration topologies will be discussed with their advantages and limitations.

### *2.5.1 Internal Connection Topology*

According to the connection between PV modules, inverters, and transformers, large-scale PV plants have four basic topologies: (i) central, (ii) string, (iii) multi-string, and (iv) module integrated (Hassaine et al. 2014; Deshpande and Bhasme 2017). The detailed architecture of the four topologies is given below.

**Central Inverter Topology**: In the central topology, illustrated in Fig. 2.5a, thousands of PV arrays are connected to an inverter to form a large system. Several PV modules are connected in series to form a string and then strings are connected in parallel through string diodes to achieve high power (10–250 kW). Each string produces a sufficiently high voltage that does not need further amplification. The centralized inverter offers advantages on large-scale, three phase, and high power PV applications due to easy and robust structure with the convenient operation technique. However, centralized inverters have several serious shortcomings, such as power losses due to a centralized MPPT, high-voltage DC cables between the inverter and PV panels, string diode losses, and mismatch losses. Moreover, the bulky and heavy inverter of this system generates high harmonic content and a poor power factor that lead to integration difficulties. In this connection topology, partial shading or cloud movement affects the overall system performance significantly. Besides, many parallel connected strings cause high dc voltage variation. This topology is less reliable because the central inverter failure stops the whole plant's operation. However, the majority of large-scale PV systems developed in the world prefer central topology due to an easy installation and fewer component requirement in the overall system.

**String Inverter Topology**: String inverters, illustrated in Fig. 2.5b, have been evolved as a standard for grid-connected PV plants. It is a modified form of the centralized topology, where each PV string is connected to a separate inverter. The string inverter minimizes some limitations of the central inverter topology. There is no loss associated with string diodes in this topology. Each string has its own

MPPT control that ensures more accurate maximum power point operation than the centralized ones. In this topology, power generation is increased due to less PV modules' mismatch effect and partial shading loss. The superior technical potentials of this structure lead to output power generation increase, more efficient operation and an enhanced reliable system. However, there are still some drawbacks, such as low power ratings and clouding or shading effect on the PV module. The shading on one PV module of a string reduces the overall energy production of that string. The installation and system maintenance cost also increase due to an increased number of the inverter.

**Multi-string Inverter Topology**: A multi-string inverter, illustrated in Fig. 2.5c, is a compact, efficient, and cost-effective connection topology, which integrates the benefits of both central and string inverters. Each string of a PV module is connected to low power DC–DC converters with individual MPPT control that is interfaced to an identical DC–AC inverter. Advantages and limitations of this topology are similar to the string inverter, though it is applicable for a high rated system. The multi-string inverter harvests more energy than other inverters because of the individual MPPT control per string. This topology permits the integration of distinct PV modules at different orientations (north, south, east, and west). Those technical specifications allow time-shifted power generation that increases operational efficiency of each string. However, installation complexity and a large number of installed inverters make this connection less appealing to developers. Deeper investigation on the system cost, overall production efficiency, and technical challenges are necessary for the future.

**Module-integrated Inverter Topology**: A module-integrated connection topology, depicted in Fig. 2.5d, develops to overcome the shortcomings and losses associated with the string and centralized inverter system. In this topology, each PV module is connected to a small and low-rated inverter with its own MPPT control. The main advantage of this connection is to eliminate the effect of clouding, shading, and mismatch losses in the overall system production. Partial shading affects the PV module's performance, which faces shadow only. Hence, PV systems using this connection topology produce more power than the string and central inverter system. However, the voltage is highly unbalanced due to the parallel connection of many inverters in this system. Therefore, a central regulation mechanism is essential to decrease the voltage variation and enhance the system balance. Module-integrated inverter design is flexible and compact, which provides an advantage of easy installation and integration to the grid. Compact design, reliable system operation, maximum energy yield, low maintenance, longer lifespan, and easy expansion in the future have made this topology more attractive and favorable in small, medium and large-scale applications.

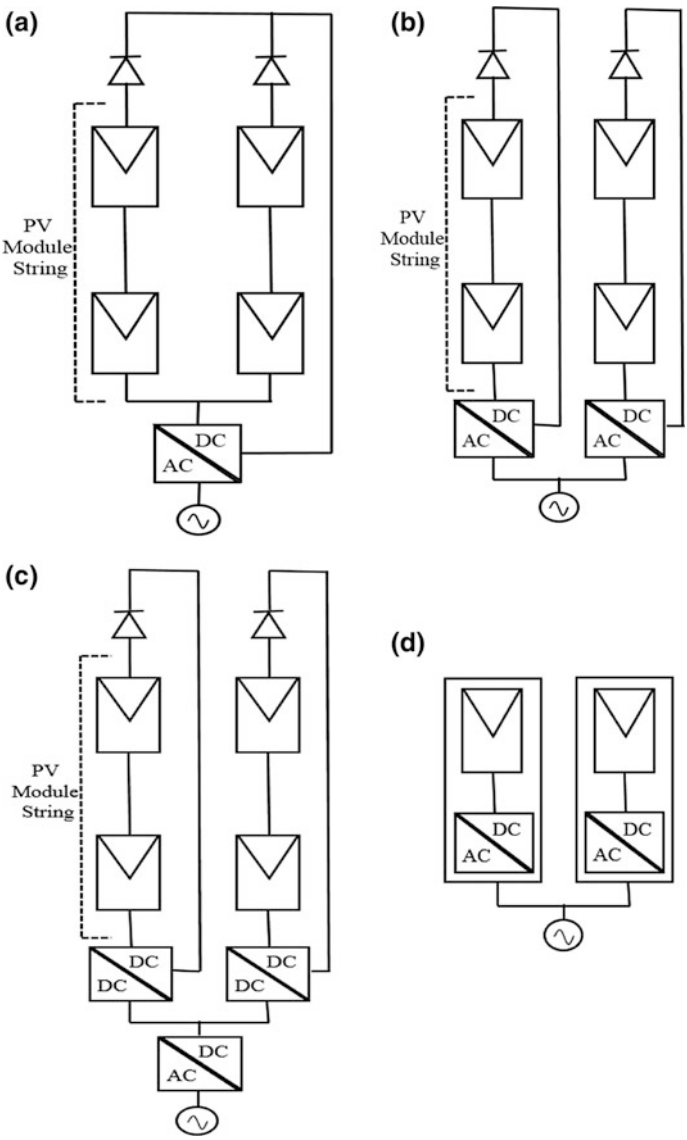


**Fig. 2.5** PV panel-inverter connection topologies. **a** Central, **b** string, **c** multi-string, **d** module integrated

### *2.5.2 AC Collection Topology*

This section explains three basic AC power collection topologies for the large-scale PV plant. They are (i) Radial, (ii) Ring, and (iii) Star (Cabrera-Tobar et al. 2016).

The connection of PV panels inverters and transformers commonly is termed as PV generator in the following discussion.

**Radial Topology**: In this topology, several PV generators are connected to one bus radially, illustrated in Fig. 2.6. Most of the large-scale PV plants use this topology due to low cost and simplicity in design. However, this connection topology is less reliable. Failure of one PV generator connected to the main bus causes power loss of the full string in the worst case scenario. A detailed example of a 12 MW PV plant connected to multi-string inverters is presented in Fig. 2.6. The plant has two 6 MW feeders; and each of them has three transformer stations of 2 MW rating. All three transformers with PV generators are connected in parallel. If one transformer station fails in operation, the whole system generation will be affected largely. Failure of the PV generator close to the main feeder (worst case scenario) would interrupt the entire feeder's power and the overall power production will decrease to 50%.

**Ring Topology**: A ring collection topology is quite similar to the radial architecture but it connects one more bus on the opposite side of the string, depicted in Fig. 2.7a, b. In case of one PV generator failure, the other PV generators can still give power to the feeder through the other side. This collection topology improves the reliability of a large-scale PV plant. However, high cost and installation complexity are the main drawbacks of this connection. An example of a 12 MW

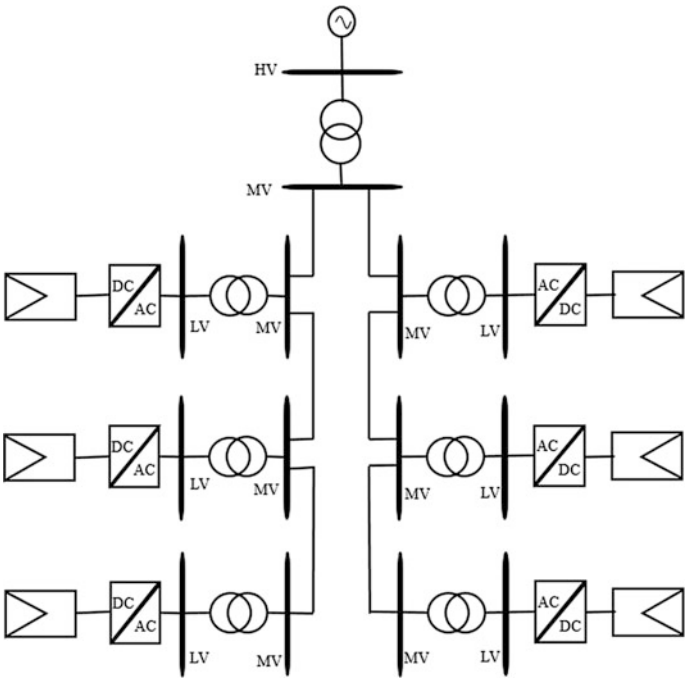


**Fig. 2.6** Radial collection configuration of a 12 MW PV plant

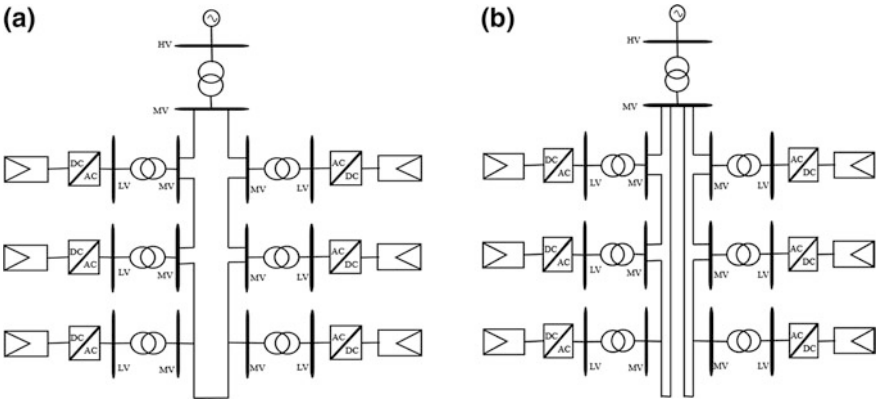


**Fig. 2.7** Ring collection configuration of a 12 MW PV plant

large-scale PV plant with 6 transformer stations is presented in Fig. 2.7. The transformer's low-voltage side is coupled to six multi-string inverters. In this configuration, one transformer station failure causes a reduction of power production by 16.6%.

**Star Topology**: In star collection topology, each PV generator is connected directly to the main feeder, illustrated in Fig. 2.8. This topology reduces cable length and causes identical line losses for all PV generators. This collection topology offers higher system reliability than others but increases the total installation cost. An example of a 18 MW PV plant with 6 transformer stations is explained in Fig. 2.8 for grid integration. Each transformer's low-voltage side is linked to the individual PV generator of 3 MW rating. In this topology, one transformer station failure causes a reduction of power production at about 16.6%.

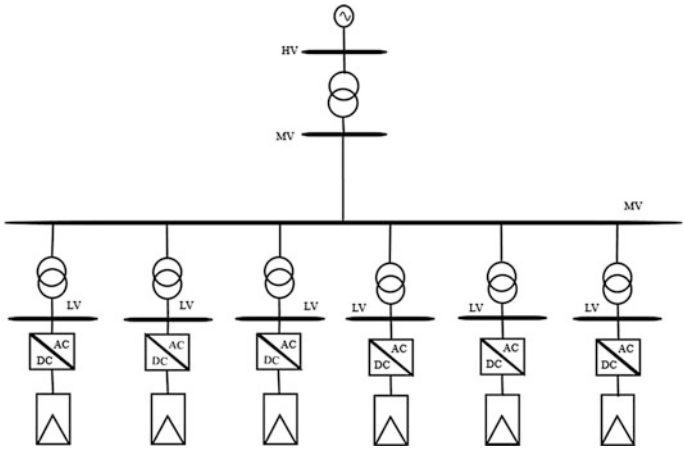


**Fig. 2.8** Star collection configuration of a 18 MW PV plant

## 2.6 Economic Potential of Solar Energy

Economic potential is a financing metric that demonstrates the economic viability of renewable generation within an area. It is defined as the difference between expected revenues and generation costs, considering an expected lifetime of system components and production costs relative to other conventional generation costs, such as fuel price, capital cost, plant efficiency, and market potential. Market potential is the amount of expected energy collection considering the present and future market factors, such as investor response, market regulations, incentives, energy policies, and economic competition with conventional energy sources. In this section, the economic potential of solar energy systems is investigated by targeting risk assessment, cost estimation, and profitability indicators, such as payback period, internal rate of return (IRR), and net present value (NPV).

### *2.6.1 Cost Estimation*

The economic competitiveness of solar electricity depends on generation cost and electricity price relative to other energy sources in the power market. The generation cost depends on design, construction method, and material specification used in a power plant. Proper design with efficient component use increases output power generation and minimizes per unit electricity cost. Levelized Cost of Electricity (LCOE) and Levelized Avoidable Cost of Electricity (LACE) are commonly used to analyze the economic feasibility of different power sources. Indirect factors, such as $CO^2$ emission avoiding credits, may be considered in some economic evaluations. The comparison between LACE and LCOE provides an inherent indicator of economic attractiveness, where a net positive value of LACE − LCOE indicates the economic feasibility of a power plant at a specific location.

**Levelized Cost of Electricity (LCOE)**: LCOE refers to the average revenue required per unit of energy production to recover all investment and operation costs. It is measured for specific site and technology under a variety of cost assumptions and depreciation benefits. The LCOE is estimated using Eq. 1 that includes annual fuel cost, capital cost, fixed, and variable O&M cost.

$$\text{LCOE } (\$/\text{MWh}) = \frac{\text{FCF} \times \text{CC} + \text{O\&M}_{\text{Fixed}}}{\text{AEGH}} + \text{O\&M}_{\text{Variable}} + \text{FC} \qquad (1)$$

where

- Capital Cost (CC)—Estimated construction cost.
- Fixed charge factor (FCF)—Annualized capital costs calculated with project lifetime and interest rate.

- Annual Expected Generation Hours (AEGH)—The expected no of hours in a year when a plant is in operation.
- Fixed O&M Cost—Operating and maintenance cost of a plant, which does not depend on plant output.
- Variable O&M Cost—Operating and maintenance cost of a plant, which depends on plant output.
- Fuel Cost (FC)—The cost related to fuel consumption.

LCOE is a crucial indicator to investors of the solar energy to determine a project's feasibility and design tax and subsidies. However, LCOE is an inadequate measure for comparison of different PV technologies with other conventional generation sources. It does not consider many features of the regional electricity market, including PV penetration level, where the availability of PV capacity in a given market indicates less revenue with an increment of PV generation.

**Levelized Avoidable Cost of Electricity (LACE)**: LACE developed by EIA is a method to assess the economic competitiveness of different power sources. It is estimated by the potential revenues available from a renewable generation project at a given site with regard to the replaced energy capacity. It is the amount that a project would be given for its generation, what a utility would not have to purchase from other sources. The following general formula in Eq. 2 is used to estimate LACE.

$$\text{LACE } (\$/\text{MWh}) = \frac{\text{AMGP} \times \text{AEGH} + \text{CP} \times \text{CC}}{\text{AEGH}} \tag{2}$$

where

| | |
|---|---|
| AMGP | Average Marginal Generation Price |
| AEGH | Average Expected Generation Hours |
| CP | Capacity Payment |
| CC | Capacity Credit |

LACE estimation depends on the regional marginal generation price and capacity value. Marginal generation price relates to the associated cost of serving load to meet energy demand in a certain time interval. Locational Marginal Price (LMP) is the best available term to measure marginal generation prices. It reflects generation value at different geographical areas, load profile variation, and projected per-unit electricity cost over the plant lifetime. Market Marginal Cost (MMC) data is used (basically in the Southwest and Southeast mountain areas) to estimate LACE, when LMP is not available. In the absence of both LMP and MMC data (Pacific Northwest and Mountain areas), cost estimation is done with the LMP price data of regions close to it. The second LACE assessment component comprises two parts—capacity credit and capacity payment. The product of these two terms represents a capacity value of a generation plant. Capacity payment relates to the value of a generation plant in meeting a reliable reserve margin, where capacity credit reveals the potential to provide a reliable system reserve.

### 2.6.2 Risk Assessment

Risks are inherited within every solar project, which affects it throughout the entire project lifetime. The technical risks associated with energy price change, inflation, and currency uncertainties have an economic impact on the electricity price of a solar plant. These risks need to be quantitatively and qualitatively assessed, managed, and controlled through financial instruments and insurance products (Masters 2013). This assessment creates a new dimension in the economic analysis to evaluate the value of a generating unit. In this section, financial risks in terms of uncertain energy price, inflation, currency depreciation, and financial opportunities are briefly discussed.

**Energy Price Change**: Electricity selling price is volatile in the most deregulated power markets. It is essential to estimate the unstable electricity price in the upcoming 10–20 years to minimize potential risk. It is quite impossible to anticipate price with a 100% precision. However, current electricity price with inflation rates can be applied to deduce the projected future price. In this way, future revenues can be calculated more precisely, which decreases the overestimated cash flow risk in the future.

**Inflation and Currency Depreciation**: Inflation occurs when the general price of products in a country increases. It causes the value of money to depreciate, which in a result reduces the purchasing power. The main driver of inflation in large-scale PV projects is an increase in fossil fuel cost and utility electricity price. High inflation creates a potential risk due to the increase of PV plant operation costs. If power transmission rate is higher than the currency depreciation, future revenue will be shrinking largely. The net cash flow will remain unchanged until inflation rates become higher than the currency depreciation. A clear, signed, and long-term agreement between all parties is required to mitigate this risk. Both PV developers and the utility company should agree with a written document not to increase charges or the selling price of electricity within a long time period.

**Incentive and Financial Opportunities**: In the USA, Department of Energy (DOE) and Office of Energy Efficiency and Renewable Energy (EERE) provide technical assistance to support the development of solar projects (Salasovich and Mosey 2011). They provide information and encourage the commercial investors and general public to spread out solar energy applications. In some cases, state incentives are offered to the development of commercial and residential solar projects. Moreover, a tax-paying PV system can capture about 30% federal tax credit incentives. Another solar energy financing source is tax increment financing (TIF) that is paid as a subsidy for the infrastructure, redevelopment, and other improvement projects in many countries. In the USA, Connecticut, Iowa, Michigan, and Wisconsin have a TIF financing opportunity as an effective and efficient way to increase site redevelopment and reuse programs.

### 2.6.3 Profitability Indicators

Profitability indicators analyze the economic potential of a solar project and help an investor to identify good opportunities and keep away from risky ones in the future. The details of profitability indicators are given below.

**Cash Flow Statement**: A cash flow statement is one type of financial evidence that depicts the cash flows inside and outside of a project over a specific time period. An Excel sheet is used to record all cash flows for the whole project lifetime plus year zero. The net cash flow is negative and equivalent to the total capital cost at year zero, which indicates the project is not in operation and under the construction stage. A cash flow statement contains the following information: sales revenue at the positive side and capital cost, tax liability, and O&M cost at the negative side. The revenue collected from electricity sell can be calculated simply by the product of monthly total generation ($P_{sys}$) and per unit selling price of electricity ($S$).

$$R = P_{sys} \times S \tag{3}$$

Tax Liability ($\tau$) can be measured by the following formula, which includes asset depreciation cost ($D_p$), revenue ($R$), O&M cost ($C_{op}$), and tax rate = 25%.

$$\tau = \left(R - C_{op} - D_p\right) \times 25\% \tag{4}$$

The Net Cash Flow (NCF) is evaluated from the below equation.

$$\text{NCF} = R - C_{op} - \tau \tag{5}$$

Eventually, the whole project net cash flow will be equivalent to the aggregation of all year cash flows. The cash flow series requires a graphical representation in order to become fully understood.

**Net Present Value (NPV)**: NPV estimation helps to assess the practical implementation possibility of a PV plant. It is defined as the value of all estimated future revenues of a project in today's dollars. Higher NPV indicates more profitable investment. NPV can be calculated by Eq. 6. The function requires net cash flow input (NCF) of all years, when a solar plant was in operation, capital expenditure ($C_i$), and discount rate ($r$), which will be increased exponentially over the years ($n$).

$$\text{NPV} = \sum_{1}^{n} \frac{\text{NCF}}{(1+r)^n} - C_i \tag{6}$$

**Internal Rate of Return (IRR)**: IRR refers to an interest rate of an investment that tells how much a PV project will earn annually. It is important to track the IRR throughout a project lifetime to achieve good returns. The project's NPV becomes

zero at IRR rate, meaning a breakeven point is achieved. IRR calculation is done via Excel iteratively. It should have a minimum acceptable value to make a solar project viable.

**Payback Period and B/C Ratio**: The payback period represents how long a PV project will take to recover its initial investment. The first year, in which the cumulative benefits exceed the cumulative cost, is called the payback period. This type of analysis reveals that in years after the payback period, the plant will start to make profit. The B/C ratio considers a monetary gain, achieved by a project performance versus costs related to the project execution, where all monetary terms should be expressed in the present values. Higher BCR value indicates a good investment. This is measured by Eq. 7.

$$\text{BCR} = \frac{\text{Incremental Benefits}}{\text{Incremental Cost}} \tag{7}$$

## 2.7 Techno-Economic Potential Assessment: Simulation Case Study

In this section, we will present two simulation studies on large-scale solar PV and CSP projects at different locations in the USA to evaluate their techno-economic potentials.

### *2.7.1 Techno-Economic Potential Assessment of CSP Technology*

To assess the solar energy potential of CSP technology, we select five cities in different states in the USA. Table 2.3 presents those city names with their geographical coordinates. The annual average Global Horizontal Irradiation (GHI) data is determined to evaluate the solar insolation potential of the above cities using System Advisor Model (SAM) software, developed at NREL (Gilman and Dobos 2012). The monthly average GHI values per unit area of the selected cities are illustrated in Fig. 2.9a. It is observed that all considered cities have more than 100 kWh/m$^2$ monthly mean GHI value. The monthly GHI value, calculated by SAM software, follows a similar trend with the solar map provided by SolarAnywhere organization, presented in Fig. 2.9b. Due to the high monthly mean GHI and favorable climate conditions, such as humidity and wind velocity, the five mentioned city areas: Sandberg in California, Prescott in Arizona, Raleigh in North Carolina, Newark in New Jersey, and Nellis in Nevada are the best locations in the USA for solar power plant installation.

**Table 2.3** Five main cities of the USA with their geographical coordinates (longitude and latitude) in degrees

| State | City | Latitude | Longitude |
|---|---|---|---|
| California | Sandberg | 34.75° N | −118.717° E |
| Arizona | Prescott | 34.65° N | −112.433° E |
| North Carolina | Raleigh | 35.86° N | −78.783° E |
| New Jersey | Newark | 40.70° N | −74.16° E |
| Nevada | Nellis | 36.25° N | −115.033° E |

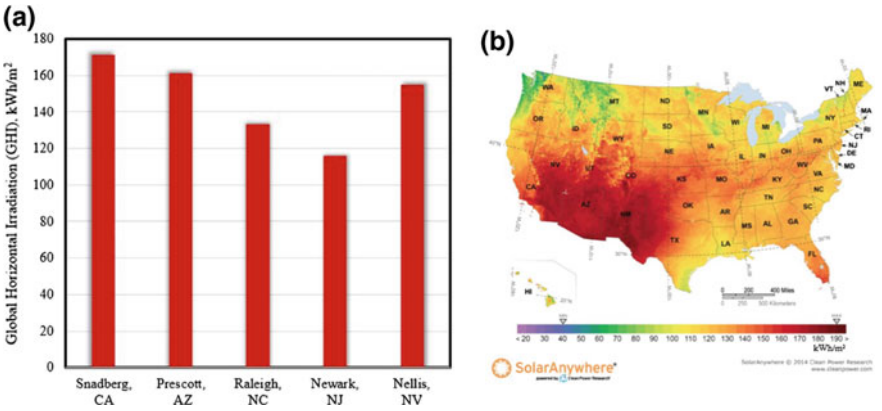


**Fig. 2.9** **a** Monthly mean solar radiation (GHI) of the considered cities listed in Table 2.3. **b** Solar map of the USA with selected states location

We will analyze the performance of a parabolic trough CSP plant located at five mentioned cities with the help of SAM software, developed by National Renewable Energy Laboratory (NREL). SAM has several solar plant modeling features, including parabolic trough CSP technology. SAM integrates the performance and economic parameters to calculate output generation, energy costs per unit, and cash flows over the years. We consider a 100 MW capacity of parabolic trough CSP plant with a 6-h thermal storage, located at selected five areas. Other plant modeling parameters are given in Table 2.4.

The results from the simulation are shown in Figs. 2.10 and 2.11. Figure 2.10 depicts the annual incident solar radiation, and annual net energy production forms the parabolic trough CSP plants of five selected city areas in the USA. The annual electric energy production is nearly 333, 298, 162, 121, and 264 GWh in Sandberg, Prescott, Raleigh, Newark, and Nellis CSP plants, respectively. It is clearly observed that Sandberg and Prescott have higher production output than other cities due to the high received solar insolation and favorable climate conditions. Electric energy output per month of five selected locations is plotted in 11. The amount of electricity generation follows in proportion to the solar radiation over different

**Table 2.4** Design specifications of parabolic trough CSP plant for simulation

| Characteristics | Value |
|---|---|
| Plant capacity | 100 MW |
| Land area | 3,294,141 $m^2$ |
| Condenser type | Air-cooled |
| *Solar Field and Collectors* | |
| Collector type | Luz LS-3 |
| Reflective aperture area | 545 $m^2$ |
| Aperture width | 5.75 m |
| Single module length | 8.33 m |
| Assembly module No. | 12 |
| Collector length | 100 m |
| Mirror reflectivity | 0.94 |
| Focal length | 2.1 m |
| Total field reflector area | 949,888 $m^2$ |
| Single loop aperture | 5248 $m^2$ |
| No of loops | 181 |
| Solar multiple | 2 |
| *Thermal Receiver and HTF Properties* | |
| Receiver type | Schott PTR70 |
| Absorber tube inner diameter | 0.066 m |
| Absorber material type | 304L |
| Absorber tube outer diameter | 0.07 m |
| Glass envelope outer diameter | 0.12 m |
| Storage volume | 22796.8 $m^3$ |
| HTF type | VP-1 |
| Tank loss coefficient | 0.4 w/$m^2$ K |
| Tank diameter | 38.0958 m |
| Design loop inlet temperature | 293 °C |
| Design loop outlet temperature | 391 °C |
| *Thermal Energy Storage (TES)* | |
| Storage type | 2 bank |
| Storage fluid | Solar salt |
| TES capacity | 6 h |

months of a year and the highest generation was obtained from June due to the highest solar irradiation.

SAM software is used to access the economic potential of a 100 MW parabolic trough CSP technology of five states in the USA. In the simulation, 150, 60 \$/$m^2$, and 65 \$/kWh are considered for the solar field, HTF, and storage cost, accordingly. Another 150 \$/$m^2$ is kept for site improvement, mounting system, and other direct and indirect capital cost. Risk assessment factors, such as inflation rate, escalation rate, and real discount rate are considered 2.5, 1, and 5.5%, respectively.

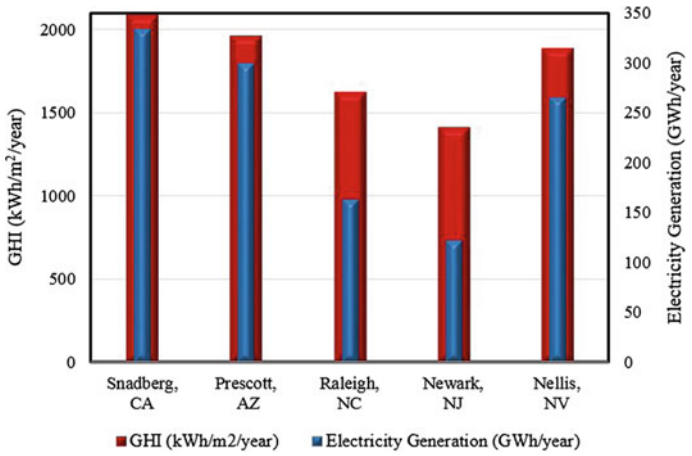


**Fig. 2.10** Comparison of solar irradiation (GHI) and annual electric power production in the selected States of the USA

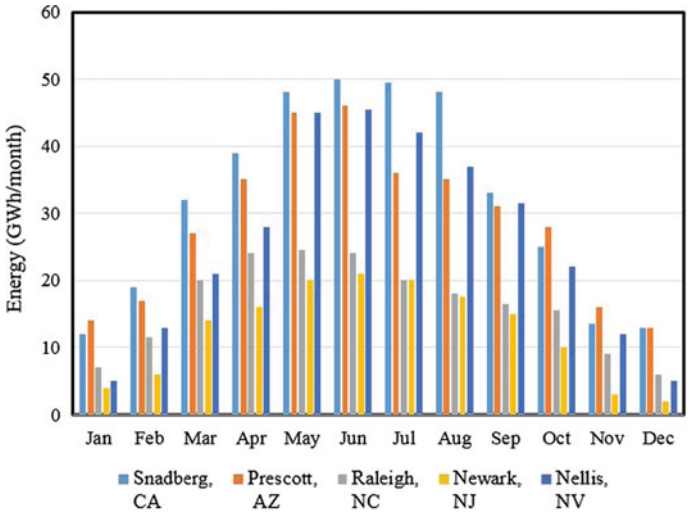


**Fig. 2.11** Energy production per month of five selected CSP plants over a year

Federal investment tax credit (ITC) and sales income tax are kept 30 and 7%, accordingly. The simulation results obtained from the financial study of the parabolic trough CSP plant, are summarized in Table 2.5 for the selected five cities in the USA. Levelized costs of per unit electricity at California, Arizona, and Nevada are comparatively low due to the higher solar potential than other states.

**Table 2.5** Annual performance and financial index of parabolic trough CSP plant in five cities based on Table 2.4 Parameters

| Parameters | Sandberg, CA | Prescott, AZ | Raleigh, NC | Newark, NJ | Nellis, NV |
|---|---|---|---|---|---|
| Annual energy (GWh) | 333 | 298 | 162 | 121 | 264 |
| Gross-to-net conversion (%) | 91.1 | 90.7 | 87.1 | 84.3 | 89.6 |
| Capacity factor (%) | 42.3 | 37.9 | 20.6 | 15.4 | 33.5 |
| Annual water usage ($m^3$) | 73,181 | 69,777 | 56,102 | 51,979 | 67,447 |
| Levelized COE (cent/kWh) | 11.46 | 12.75 | 23.13 | 30.71 | 14.34 |
| NPV (million $) | 45.34 | 45.35 | 45.38 | 45.39 | 45.36 |
| Net capital cost (million $) | 598.978 | 598.898 | 598.585 | 598.492 | 598.820 |

### 2.7.2 *Techno-Economic Potential Assessment of Photovoltaic Technology*

Sandberg, California is a good choice for the large-scale photovoltaic plant deployment due to the abundant solar energy potential. In this section, we will evaluate the techno-economic potential of a 21 MW PV plant in Sandberg, California using the SAM software. The SAM software tool is employed to calculate the solar irradiation data based on the weather database for the considered location. It allows the designers to specify parallel connected string and module no per string. It also has options to select an appropriate inverter model based on the PV plant size. The designed PV power plant has a capacity of 21 MW, including 22 modules per string and 5374 strings in parallel. Other system configuration parameters are presented in Table 2.6.

Inputs, such as solar irradiation data, PV module and inverter specifications are applied to the System Advisor Model (SAM) to design and optimize the PV system. To observe the performance of the PV plant, simulation is carried out using SAM software with the system information of Table 2.6. Calculated monthly solar irradiation data and system output AC energy are plotted in Figs. 2.12 and 2.13, respectively. The maximum AC energy is obtained from May due to the abundant solar energy potential and favorable weather conditions. Component parameters, such as inverter efficiency, PV module mismatch, module degradation over years, module efficiency, shading, and soiling influence solar plant performance. Different types of losses, found in simulation, are listed in Table 2.7. Figure 2.14 illustrates the annual degradation of electric power production by the PV plant over years. The PV plant production was highest in the first year and gradually decreased over the plant lifetime. The main reason behind the gradual performance decrease is due to temperature stress, water ingress, and performance degradation of inverters, PV modules, wires, and other components.

The economic model of the SAM software computes financial metrics of the designed PV plant and system's cash flow over the years. In the simulation, $1.5 and $0.5 are considered for per-kW dc module and AC inverter cost respectively.

**Table 2.6** System design parameter of a 21 MW DC photovoltaic power plant

| Parameters | Value |
|---|---|
| *System Overview* | |
| Module per string | 22 |
| Strings in parallel | 5374 |
| DC/AC ratio | 1.26 |
| Mounting system | Ground |
| Tracking | Fixed axis |
| Total module area | 153,696 $m^2$ |
| Total land area | 126.6 acres |
| *PV Module Specification* | |
| T-Cell type | CdTe |
| Module efficiency | 13.85% |
| Per Module area | 1.3 $m^2$ |
| Power | 180 Wdc |
| Nominal operating cell temp | 460 |
| MPP voltage ($V_{mp}$) | 6 A |
| MPP current ($I_{mp}$) | 3456 |
| Short circuit current ($I_{SC}$) | 7 A |
| Open circuit voltage ($V_{OC}$) | 37 V |
| Temp. coefficient of $V_{OC}$ | −0.11 V/°C |
| Temp. coefficient of MPP | −0.41 V/°C |
| No of cells in series | 60 |
| *Inverter Specification* | |
| Model No. | SMA:SC750CP |
| Efficiency | 98.28% |
| Number of inverters | 22 |

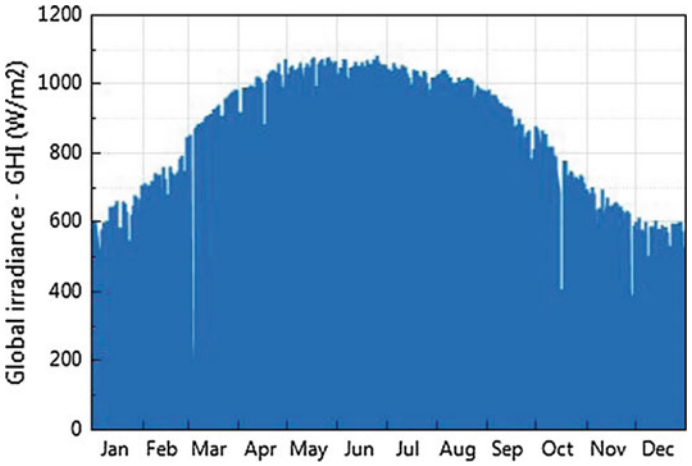


**Fig. 2.12** Hourly solar irradiance in Sandberg, California, calculated by SAM software

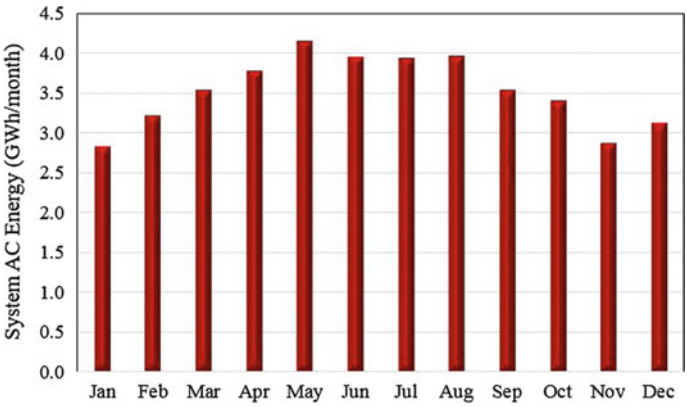


**Fig. 2.13** Monthly AC energy production of a 21 MW PV plant in Sandberg, California during a year

**Table 2.7** Different losses of the designed PV system found from simulation results

| | |
|---|---|
| Shading and soiling loss | 5% |
| DC module modeled loss | 4.98% |
| DC mismatch loss | 1.97% |
| Diodes and connection loss | 0.49% |
| DC wiring loss | 1.97% |
| AC inverter switching loss | 1.24% |
| AC inverter efficiency loss | 1.73% |

Risk assessment parameters, such as annual inflation rate, escalation rate, and real discount rate are kept as 2.5, 1, and 5.5, accordingly. Federal investment tax credit (ITC), federal income tax and sales tax are considered 30, 35, and 7% respectively. Other expenses for regular maintenance, construction work, and BOS equipment are added to the system cost during simulation. The financial metrics from the simulation of the designed PV plant are summarized in Table 2.8. The annual energy generation of the designed PV plant is about 42 GWh and per-unit electricity cost calculated as $10.41. Figure 2.15 shows the system's cash flow over the years. At year zero, the system cost was negative due to the investment and construction expenditure, and after the year, the plant started to gain revenue.

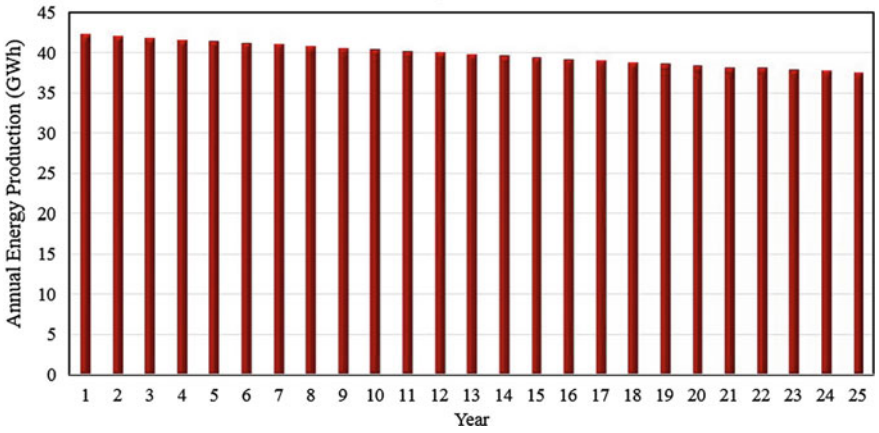


**Fig. 2.14** Annual electricity production of the designed PV plant over the years

**Table 2.8** Financial metrics of a 21 MW PV plant in Sandberg, California

| | |
|---|---|
| Annual energy yield | 42.162 GWh |
| Capacity factor | 22.6% |
| Performance ratio | 0.83 |
| Levelized COE | 10.41 cent/kWh |
| Net present value | $4,569,218 |
| IRR at the end of the project | 12.72% |
| Net capital cost | $63,917,932 |

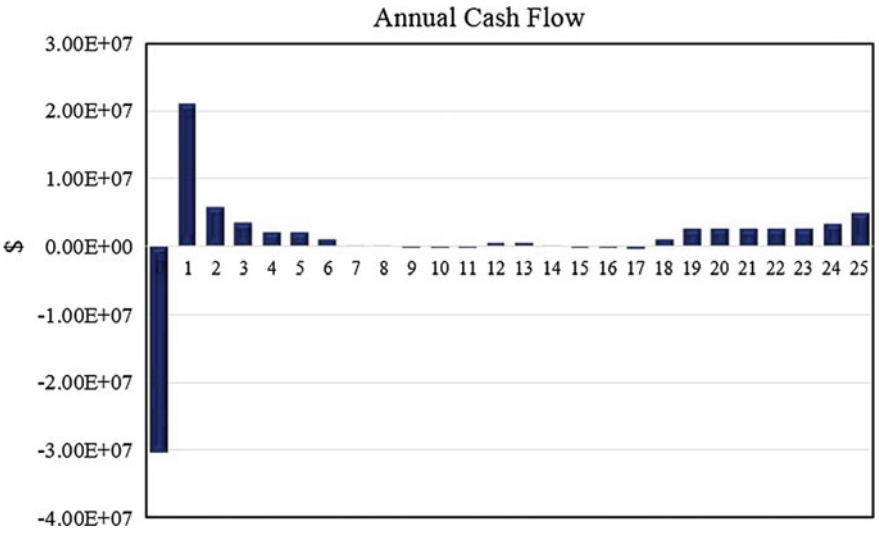


**Fig. 2.15** Cash flow of a 21 MW PV plant in Sandberg, California over the years

## 2.8 Conclusion

This chapter focuses on the technical potential and economic viability of two popular solar power technologies: CSP and Photovoltaic plant, with their advantages and limitations. The basic system components and connection topologies of a large-scale PV power plant have been discussed in detail. It is worth pointing out the importance of a right component and topology choice because they affect performance index, implementation cost, efficiency, and reliability of the overall system. To estimate the economic potential of a large-scale solar system, two financial terms, LCOE and LACE, are briefly covered in this chapter. Different risk assessment parameters are sincerely considered to ensure the viability of a project and better revenue earned from the solar power plant. The implementation of a solar project means a huge amount of cash flow into the green energy technology, which creates direct, indirect, and induced jobs that develop a country's economy. The future of a large-scale solar energy deployment depends on the prices and size reduction of PV modules and efficiency improvement of different components, such as PV panels, transformers, and inverters. Additionally, the internal component connection and grid collection topology are the primary future design concern of large-scale applications considering cost, system robustness, reliable, and flexible plant operation. Improving component efficiency, along with their control and energy management should be given importance. Solar energy plants should be controlled in such a way so that they behave like conventional power plants and fulfill the power grid code requirements.

**Acknowledgments** This work is supported by the National Science Foundation under Grant CAREER No. 1553494. Any opinions, findings, and conclusions or recommendations expressed in this material are those of the authors and do not necessarily reflect the views of the National Science Foundation.

## References

Brown A, Beiter P, Heimiller D, Davidson C, Denholm P, Melius J, Lopez A, Hettinger D, Mulcahy D, Porro G (2016) Estimating renewable energy economic potential in the United States: methodology and initial results. https://www.nrel.gov/docs/fy15osti/64503.pdf

Cabrera-Tobar A, Bullich-Massagué E, Aragüés-Peñalba M, Gomis-Bellmunt O (2016) Topologies for large scale photovoltaic power plants. https://pdfs.semanticscholar.org/473f/5e3a2fab05660130c736ca0ff88c\\66b66358.pdf

D'Rozario J, Shams S, Rahman S, Sharif A, Basher E (2015) Cost-effective solar-biogas hybrid power generation system. In: IEEE international conference on industrial technology (ICIT)

Deshpande S, Bhasme NR (2017) A review of topologies of inverter for grid connected PV systems. In: 2017 innovations in power and advanced computing technologies (i-PACT), pp 1–6

Fouquet D (2007) Prices for renewable energies in Europe: feed in tariffs versus quota systems—a comparison. http://citeseerx.ist.psu.edu/viewdoc/download?doi=10.1.1.189.4011\&rep=rep1\&type=pdf

Gagnon P, Margolis R, Melius J, Phillips C, Elmore R (2016) Rooftop solar photovoltaic technical potential in the United States: a detailed assessment. https://www.nrel.gov/docs/fy16osti/65298.pdf

Gilman P, Dobos A (2012) System advisor model (SAM) software of national renewable energy laboratory (NREL). https://sam.nrel.gov/

Hassaine L, OLias E, Quintero J, Salas V (2014) Overview of power inverter topologies and control structures for grid connected photovoltaic systems. Renew Sustain Energ Rev 30: 796–807

International energy outlook (2017) https://www.eia.gov/outlooks/ieo/. Release date: 14 Sept 2017

Masters G (2013) Renewable and efficient electric power systems. Wiley, Hoboken

Mendelsohn M, Lowder T, Canavan B (2012) Utility-scale concentrating solar power and photovoltaics projects: a technology and market overview. https://www.nrel.gov/docs/fy12osti/51137.pdf

Photovoltaics DG, Storage E (2018) IEEE standard for interconnection and interoperability of distributed energy resources with associated electric power systems interfaces. In: IEEE Std 1547-2018, pp. 1–138, 6 Apr 2018

Rahman S, Aburub H, Moghaddami M, Sarwat AI (2018a) Reverse power flow protection in grid connected PV systems. In: IEEE SoutheastCon 2018, St. Petersburg, Florida, USA

Rahman S, Moghaddami M, Sarwat AI, Olowu T, Jafaritalarposthi M (2018b) Flicker estimation associated with PV integrated distribution network. In: IEEE SoutheastCon 2018, St. Petersburg, Florida, USA

Ruiz A (2011) System aspects of large scale implementation of a photovoltaic power plant

Salasovich J, Mosey G (2011) Feasibility study of economics and performance of solar photovoltaics in the commonwealth of Puerto Rico. https://www.nrel.gov/docs/fy11osti/49237.pdf

Salasovich J, Geiger J, Healey V, Mosey G (2013) Feasibility study of economics and performance of solar photovoltaics at the Brisbane Baylands Brownfield Site in Brisbane, California. https://www.nrel.gov/docs/fy13osti/57357.pdf

Schmalensee R (2015) The future of solar energy—an interdisciplinary MIT study. http://energy.mit.edu/wp-content/uploads/2015/05/MITEI-The-Future-of-Solar-Energy.pdf

Sharma BD (2011) Performance of solar power plants in India. http://www.cercind.gov.in/2011

Testa A, De Caro S, La Torre R, Scimone T (2010) Optimal size selection of step-up transformers in PV plants. In: XIX International Conference on Electrical Machine—ICEM 2010, IEEE, pp 1–6

# Chapter 3
# Solar Radiation Assessment and Forecasting Using Satellite Data


**Akriti Masoom, Yashwant Kashyap and Ankit Bansal**

**Abstract** Since the availability of ground data is very sparse, satellite data provides an alternative method to estimate solar irradiation. Satellite data across various spectral bands may be employed to distinguish weather signatures, such as dust, aerosols, fog, and clouds. For a tropical country like India, which is potentially rich in solar energy resources, the study of these parameters is of crucial importance from the perspective of solar energy. Furthermore, a complete utilization of the solar energy depends on its proper integration with power grids. Because of its variable nature, incorporation of photovoltaic energy into electricity grids suffers technical challenges. Solar radiation is subjected to reflection, scattering and absorption by air molecules, clouds, and aerosols in the atmosphere. Clouds can block most of the direct radiation. Modern solar energy forecasting systems rely on real-time Earth observation from the satellite for detecting clouds and aerosols.

**Keywords** Numerical weather prediction · GHI · Forecasting · Image processing

## Nomenclature

| | |
|---|---|
| ADI | All-Day index |
| AI | Artificial Intelligence |
| ANN | Artificial Neural Network |
| ARIMA | Auto-Regressive Integrated Moving Averages |
| ARMA | Auto-Regressive Moving Averages |
| BTD | Brightness Temperature Difference |
| COG | Center of Gravity |

A. Masoom · A. Bansal (✉)
Mechanical and Industrial Engineering Department, IIT Roorkee, Roorkee, India
e-mail: abansfme@iitr.ac.in

A. Masoom
e-mail: akritimasoom@gmail.com

Y. Kashyap
Department of Electrical and Electronics Engineering, NIT Surathakal, Surathakal, India
e-mail: yashwant.kashyap@nitk.edu.in



H. Tyagi et al. (eds.), *Advances in Solar Energy Research*, Energy, Environment, and Sustainability, https://doi.org/10.1007/978-981-13-3302-6_3

| | |
|---|---|
| CS | Cloud Shadow |
| DHI | Direct Horizontal Irradiance |
| DNI | Direct Normal Irradiance |
| DWT | Discrete Wavelet Transform |
| ECMRWF | European Centre for Medium Range Weather Forecasts |
| EKF | Extended Kalman Filter |
| GFS | Global Forecast System |
| GHI | Global Horizontal Irradiance |
| IMD | Indian Meteorological Department |
| MT | METEOSAT |
| NAM | North American Mesoscale |
| NCEP | National Centers for Environmental Prediction |
| NWP | Numerical Weather Prediction |
| PBL | Planetary Boundary Layer |
| RTE | Radiative Transfer Equation |
| RUC | Rapid Update Cycle |
| SMARTS | Simple Model of Atmospheric Radiative Transfer of Sunshine |
| WRF | Weather Research and Forecasting |
| WT | Wavelet Transform |

## 3.1 Introduction

Solar energy is one of the most attractive forms of renewable energy; however, its availability is subjected to weather disturbances. The effect of aerosols, dust, clouds, and fog on solar energy availability are still not properly understood and quantified. A singe dust storms event may result in a quick blackout of sunlight and significantly affects the operation of a photovoltaic power plant (Mekhilef et al. 2012).

About 50% of solar radiation lies in the visible part of the electromagnetic spectrum and remaining in the near-infrared portion. The solar radiation is subjected to reflection, scattering, and absorption by air molecules, clouds, and aerosols in the atmosphere. Clouds can block most of the direct radiation. Atmospheric aerosols not only scatter and absorb radiation but also affect the amount and lifetime of clouds. Predicting all these phenomena accurately is a very complex and difficult task.

This monograph presents an overview of various techniques used in the assessment and forecasting of solar irradiance for solar energy applications. We present state-of-the-art models that process satellite data and prepare accurate estimation and forecast of Global Horizontal Irradiance (GHI) for time horizon varying from a few hours to several days.

### 3.1.1 GHI Estimation Models

Models for estimating GHI from satellite data may be classified into physical models and statistical models. Physical models are based on the interaction between the solar radiation and atmospheric gases and aerosols. These models solve the Radiative Transfer equation (RTE) (Liang et al. 2010; Tapiador 2009). Physical models show better results in clear sky conditions; however, they fail to give accurate result under cloudy conditions. The input to the radiative transfer model includes cloud images and measurements of aerosol and water vapor. The uncertainty in these measurements is estimated to be 3% in case of direct irradiance and 5% in the global and diffuse irradiance (Gueymard 2012).

Many physical models have been developed to evaluate GHI, such as Möser and Raschke model (MR) (1984) based on the METEOSAT images and the RTE model of Kerschgens et al. (1978) and Dedieu, Deschamps and Kerr model (DDK) based on single equation applicable to both clear and cloudy conditions (Dedieu et al. 1987).

Statistical models, on the other hand, depends on straightforward statistical regressions between ground measurements and satellite data (Salcedo-Sanz et al. 2014). A number of statistical and empirical methods have been developed to assess the radiation values from clear sky irradiance and cloud indices derived from satellite data. One of the earliest models, developed by Tarpley (1979), used ground pyranometer and satellite data along with statistical regressions against measurements to obtain the value of cloud index. The HELIOSAT method is a widely used and accurate statistical model (Cano et al. 1986; Beyer et al. 1996; Rigollier et al. 2004) to estimate GHI. The original HELIOSAT model employed METEOSAT satellite data (visible band). The model proposed a simple linear relationship between the cloud index derived from satellite and the clearness index.

### 3.1.2 Clear Sky Models

In statistical models, the GHI values at a particular location and time are calculated by correlating the local atmospheric conditions with the clear sky irradiance. The clear sky irradiance is obtained by solving the RTE with various meteorological inputs. The SOLIS model is a spectrally resolved clear sky transmittance model. It solves the Radiative Transfer equation with meteorological inputs of ozone content, aerosol optical depth, and water vapor at 550 nm (Mueller et al. 2004). European Solar Radiation Atlas (ESRA) model was developed for the HELIOSAT-II project by Rigollier et al. (2000). McClear model is another fast clear sky model which is entirely based on the physical laws of radiative transfer. Under clear sky conditions, it estimates downwelling shortwave global and direct irradiances at ground level (Lefevre et al. 2013). Simple Model of Atmospheric Radiative Transfer of Sunshine (SMARTS) is the most widely used software for solving the RTE. SMARTS

parameterizes absorption and scattering parameters and generate detailed solar intensity spectrum at the ground level (Gueymard 1995).

Alternatively, the clear sky radiation may be treated approximately based on the available ground data from the network of meteorological stations (Kashyap et al.) In press). The clear sky irradiance usually does not vary significantly over a short period (a month). The variation in clear sky GHI over a period of one month was observed to be about 1%. The same magnitude of uncertainty would manifest in the estimation of actual GHI as well. Thus, the clear sky radiation may be estimated from the ground measured GHI data for the entire month. The maximum value of the GHI data for over a month may be taken as the representative clear sky radiation at a given time of the day. For example, the clear sky GHI at 11:00 AM in May would be equal to the maximum value of GHI at 11:00 AM for all the days of the May.

### *3.1.3 Forecasting Models*

The simplest solar radiation forecasting models were based on regression model. These were followed by more advanced stochastic time series models and models based on Artificial Intelligence (AI). The effect of local weather phenomena, including the effect of dust and clouds, has been included with satellite data and ground measurements with various data assimilation techniques such as the Kalman Filter. Depending on the time horizon of the forecasts, simple time series models, or more advanced models with numerical weather prediction tools, can be employed to achieve varying degree of accuracy.

The forecasting methods for solar irradiance may be classified as Statistical, Physical and Hybrid (Kashyap et al. In press). Statistical method is based upon time series analysis of global irradiance. Many times, the accuracy of these methods may be improved by employing time series data of exogenous meteorological variables such as wind, humidity, air temperature, etc. Physical methods employ numerical weather prediction (NWP) tools along with cloud imagery and motion tracking techniques. These models are used to prepare extended forecasts of solar irradiance for more than a day. Hybrid models may employ physical as well as statistical techniques to improve the accuracy of the forecasted value.

In statistical methods, historical data is used in the prediction of the future values. It uses mathematical equations to determine patterns and trends in the time series data. Statistical models may again be classified into the persistence model and the time series model. A persistence model predicts the value by considering it to be the same as the previous value. In contrast to this, the time series models use historical sequence of observations measured over a set time (weekly, daily or hourly). It is a stochastic process as the observations can be random.

Auto-Regressive Moving Averages (ARMA) model, Auto-Regressive Integrated Moving Averages (ARIMA) model, Fuzzy Logic, Artificial Neural Network (ANN) models, and many hybrid systems such as ANFIS, ANN-wavelet, and ANN-genetic algorithm provide the basis for many problems internal and external

to the domain of solar radiation forecasting (Al-Alawi and Al-Hinai 1998; Mellit and Pavan 2010; Mantzari and Mantzaris 2012; Ong et al. 2005; Ji and Chee 2011). Use of meteorological parameters in solar energy forecast has been identified as a key step in increasing the accuracy and time horizons of the solar radiation forecasts. Al-Alawi et al. used climatological variables as input to the ANN model for the prediction of monthly GHI values for a year (Al-Alawi and Al-Hinai 1998).

However, the limitation of simple time series models is that they employ only the locally measured/estimated data. The effect of weather over a wider geographical area, which might affect solar irradiance at various time horizons, is not accounted in these models. For example, in the case of a dust storm, it might be useful to understand and forecast the occurrence and movement of clouds and dust. Tracking of such weather phenomena over a wider land mass is possible only through satellite data or ground-based sky imagers.

Crispim et al. (2008) used the ANN model with the cloudiness index obtained from the TSI images to predict solar irradiance. Similarly, Chow et al. (2011) used the Sky Imager to produce intra-hour GHI forecasting. Cross-correlation of two consecutive images was used to generate motion vectors which were used to propagate cloud fields forward in time. Similarly, Marquez et al. used the SI for intra-hour Direct Normal Irradiance (DNI) forecasts (Marquez and Coimbra 2013), employing detailed image processing with the help of Particle Image Velocimetry (PIV). However, time horizon for SI forecasts is limited to 15–30 min because of small residence time of the clouds over a region in strong winds.

While statistical models are good for solar irradiance forecasts in the range of time horizon zero to six hours ahead, long-term forecasting is best achieved by physical models which are based on Numerical Weather Prediction (NWP) (Perez et al. 2002, 2013). NWP models are based on the equations of flow dynamics and heat transfer and forecast state of the atmosphere and its evolution for up to few days in advance. This model discretizes the inputs and the governing equations on a 3-D grid covering the Earth's surface and extending vertically (Kleissl 2013). However, most of the clouds remain unresolved in NWP model.

Hybrid models combine the superiority of both the physical and the statistical models to improve the accuracy of the forecasts and increase the time horizon of the forecasts. The combined models are constructed to overcome the deficiencies of individual models and reduce forecast errors. As an example, a combination of NWP and ANN models may be used, where the output from the NWP model is fed to the ANN model as input.

Figure 3.1 shows the various elements of forecasting method for solar energy forecasting. Clouds form the major hurdles in accurate forecasting models. Depending on the forecast horizon, the cloud description may be based on observations from the ground, from the satellite instruments or from estimates based on numerical weather prediction.

Furthermore, ground-based solar irradiance measurements at the power generation site may provide additional data for the forecast model input and validation. Data assimilation is a process that refines the estimates of model's initial states for improved model forecast performance.

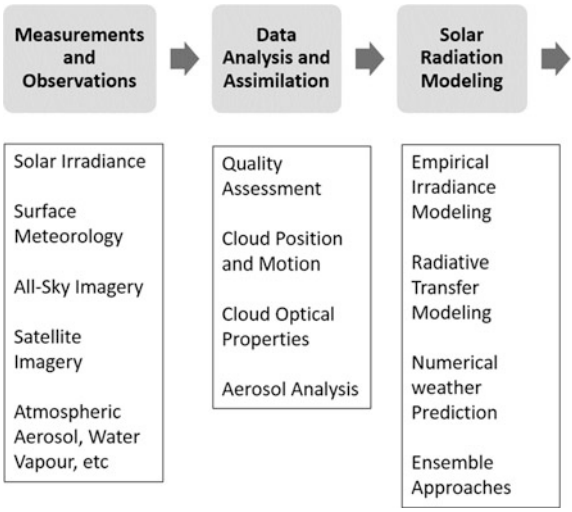


**Fig. 3.1** Elements of the solar irradiance forecasting process

## 3.2 Satellite Data and Processing

The satellite and cloud imagery play an important role in extending the time horizon of forecasting models based on physical as well as empirical approach. Generally, the visible band satellite images are employed to detect cloud patterns. The reflectance measured by the satellite imager may be employed to calculate the cloud index that can be used in solar resource mapping. Cloud motion vectors are prepared by correlating two subsequent images, which are then used to extrapolate future cloud pattern. In Numerical Weather Models, cloud data obtained from satellites may be directly assimilated into the model to improve the forecasts.

Geostationary satellites like METEOSAT, GOES, INSAT 3D, etc. provide images in high temporal and spatial resolution. The radiation reflected by clouds and aerosols is the basis for calculation of irradiance. Scheme like SOLIS is based upon atmospheric information retrieved from satellites and radiative transfer models (RTM).

Indian Meteorological Department (IMD) maintains and controls the distributions of data from INSAT-3D satellite. The satellite's imager consists of six spectral bands as listed in Table 3.1. IMD generates multiple data products in Hierarchical Data Format 'HDF'. The data is available with half-hour temporal and 4 km spatial resolution. The uncertainty in data taken from INSAT-3D is reported to be 2% in the case of brightness temperature and outgoing long-wave radiation (http://satellite.imd.gov.in/dynamic/INSAT3D_Catalog.pdf). The data from the satellite in each band is available in the form of reflection digital count. The digital reflection count is converted into Radiance, Reflectance, and Brightness temperature using calibration coefficients. Brightness temperature is defined as the temperature of a black

**Table 3.1** INSAT-3D imagery channels, respective wavelength, and application

| INSAT-3D imager bands | Wavelength range (μm) | Central wavelength (μm) | Usage | | | | |
|---|---|---|---|---|---|---|---|
| | | | Day | Night | Dust | Fog | Cloud |
| 1. Visible (VIS) | 0.55–0.75 | 0.65 | ✓ | ✗ | ✓ | ✓ | ✓ |
| 2. Shortwave infrared (SWIR) | 1.55–1.70 | 1.625 | ✗ | ✗ | ✗ | ✗ | ✗ |
| 3. Middle infrared (MIR) | 3.80–4.00 | 3.9 | ✓ | ✓ | ✓ | ✓ | ✓ |
| 4. Water vapor (WVIR) | 6.50–7.10 | 6.8 | ✗ | ✗ | ✗ | ✗ | ✗ |
| 5. Thermal infrared 1 (TIR1) | 10.30–11.30 | 10.8 | ✓ | ✓ | ✓ | ✓ | ✓ |
| 6. Thermal infrared (TIR2) | 11.50–12.50 | 12 | ✓ | ✓ | ✓ | ✓ | ✓ |

body which emits the same amount of radiation as observed from a gray body object at a given wavelength (Kashyap et al. In press).

### *3.2.1 Image Processing*

The models that estimate GHI from satellite data rely on various indices. These indices are derived from the interactions between the solar radiation and the atmospheric gases and aerosols. The Brightness Temperature Difference (BTD) is calculated by taking the difference between the brightness temperatures of two different spectral bands. Features like dust, cloud, and fog are extracted or segmented from the BTD images. The $BTD_{31}$ is the difference between MIR (central wavelength 3 μm) and TIR-1 (central wavelength 10 μm) band (King et al. 1992). It is employed to detect and quantify nighttime clouds (Hammer et al. 2015). It is defined as

$$BTD_{21} = MIR - TIR_1 \tag{1}$$

$BTD_{31}$ parameter may also be employed to detect fog during winter (Yoo et al. 2010). Similarly, $BTD_{12}$ and $BTD_{30}$ are defined as

$$BTD_{12} = TIR_1 - TIR_2 \tag{2}$$

$$BTD_{30} = MIR_{ob} - MIR_{ref} \tag{3}$$

where $MIR_{ob}$ and $MIR_{ref}$ are observed and reference mid-infrared signal, respectively. The reference signal, $MIR_{ref}$, is taken as the minimum signal over a 15-day period. The outgoing long-wave radiation and temperature of surface are affected by the presence of dust. It can be employed to define the infrared difference dust index (IDDI) as follows (Legrand et al. 2001):

$$\mathrm{IDDI} = \mathrm{TIR}_{\mathrm{ref}} - \mathrm{TIR1}_{\mathrm{ob}} \tag{4}$$

where $TIR_{ob}$ and $TIR1_{ref}$ are the observed and reference signals of the thermal infrared band, where the reference signal is taken as maximum over a 15-day period. Furthermore, $BRD_{30}$ is the difference in radiance of MIR and VIS channels. High $BRD_{30}$ index shows strong scattering by airborne dust, and therefore $BRD_{30}$ index is used to distinguish dust clouds from water and ice clouds.

$$\mathrm{BRD}_{30} = \mathrm{MIR} - \mathrm{VIS} \tag{5}$$

One can observe the effect of dust in all BTD images in different segments.

As can be observed, the IDDI, $BTD_{30}$, and $BTD_{31}$ images clearly show the presence of dust and cloud, as shown in Fig. 3.2 (Kashyap 2017). While using the visible channel only, dust can be recognized above dark surfaces but shows no contrast above bright surfaces such as deserts. Therefore, six different indices are combined to overcome this difficulty.

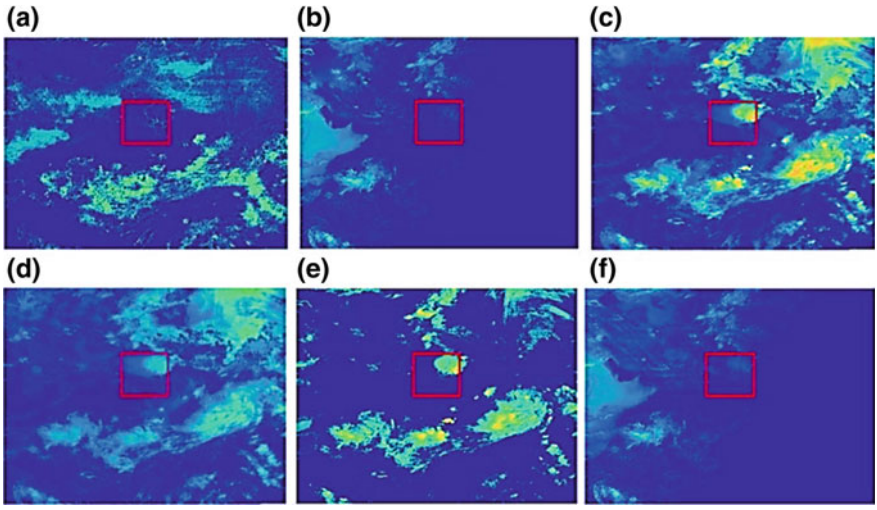


**Fig. 3.2** Post-processed satellite images **a** $BTD_{12}$, **b** VIS, **c** IDDI, **d** $BTD_{30}$, **e** $BTD_{31}$, **f** $RAT_{30}$

### 3.2.2 *Image Segmentation*

The different postprocessed images obtained from the above steps contain multiple geographical features such as ocean, desert, land, etc. Segmentation is a procedure of dividing an image in multiple zones identified by different color schemes. One has to define the number of segments/clusters based on the desired features to be extracted from the image. The *k*-mean clustering method was originally developed for signal processing and is now widely used in the field of image processing (Ng et al. 2006). It is a simple unsupervised learning algorithm and is a type of partition clustering algorithms. It divides the data set into non-overlapping groups. The method employs an iterative method to club the data into a number of clusters by minimizing the cost function.

Figure 3.3 shows TIR-1 image before and after the segmentation. The method is applied to all BTD images. The segmented images are passed through a filtering process that removes unwanted segments from the image. Table 3.2 identifies the segments in each BTD image that may be employed to detect dust.

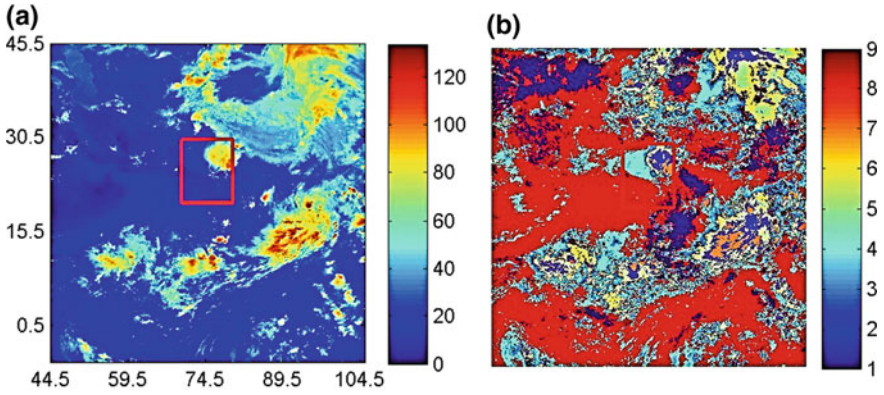


**Fig. 3.3** Image segmentation using *k*-means clustering, **a** original, **b** segmented

**Table 3.2** The selected segments for dust detection

| | $BTD_{12}$ | VIS | IDDI | $BTD_{33}$ | $BTD_{31}$ | $BTD_{30}$ |
|---|---|---|---|---|---|---|
| K1 | ✓ | ✗ | ✓ | ✓ | ✗ | ✗ |
| K2 | ✗ | ✗ | ✓ | ✓ | ✓ | ✓ |
| K3 | ✓ | ✓ | ✓ | ✓ | ✓ | ✓ |
| K4 | ✓ | ✓ | ✓ | ✓ | ✓ | ✗ |
| K5 | ✗ | ✗ | ✓ | ✓ | ✓ | ✗ |
| K6 | ✗ | ✓ | ✓ | ✓ | ✗ | ✓ |
| K7 | ✓ | ✗ | ✓ | ✓ | ✗ | ✓ |
| K8 | ✗ | ✓ | ✗ | ✗ | ✗ | ✓ |
| K9 | ✓ | ✓ | ✓ | ✓ | ✓ | ✓ |

## 3.3 Numerical Weather Prediction

Numerical Weather Prediction deals with the physics of atmosphere and uses recent weather observations and data to predict the future states. NWP is a tool used for forecasting the solar irradiance with time horizon of few hours to few days. It is generally used for day ahead irradiance forecasting. Hence, it can be used for the scheduling of solar power plants.

A physical domain is selected and discretized at a chosen resolution. The NWP model requires specification of boundary conditions from worldwide observations as the initial step. The initial state of the atmosphere is determined from satellites and ground observations. This is followed by integrating the governing equations forward in time. The governing equations include radiative transfer equations, dynamical equations (like Newton's second law for fluid flow) and thermodynamic equations (equations governing cloud-droplet formation). These equations are solved on a mesh of grid points of the region of interest.

In order to enhance the accuracy of the NWP models, statistical postprocessing tools are employed; wherein, the output of the NWP model is compared with observations, and corrections in biases are implemented. The main source of error in these models is cloud, as due to their relatively coarser resolution, the NWP model is unable to resolve microscale physics of cloud formation as well as not able to predict the actual location of the cloud fields (Kleissl 2013). NWP models can be subdivided into two groups on the basis of the domain size: global models and regional models.

### *3.3.1 Global Models*

Global NWP models are run on scales covering the entire Earth to predict the future state of the atmosphere. Few Global models are: the European Centre for Medium Range Weather Forecasts (ECMRWF) and the Global Forecast System (GFS). Global models have coarse resolution in the range of 16–50 $km^2$.

GFS is a weather forecast model created by the National Centers for Environmental Prediction (NCEP). Many variables like winds, temperatures, atmospheric ozone concentration, precipitation, and soil moisture are available through the dataset. It is one of the most popular global models; and has a time horizon of 16 days and spatial resolution of 28 km.

### *3.3.2 Regional Models*

Mesoscale or regional models solve same governing equations as that of Global models but are run only over a part of the Earth. Regional models depend on global

models for initial and boundary conditions. Since they cover only small part of the Earth's area, they employ higher spatial and temporal resolution. These models are run by various national meteorological services. Most popular mesoscale models are: Rapid Update Cycle (RUC), North American Mesoscale (NAM) and Weather Research and Forecasting (WRF) models.

RUC model has a temporal resolution of 1 h and a spatial resolution of 13 km. The model comprises of a model independent of wavelength for scattering and absorption of radiation by water vapor. The atmospheric gases and aerosols are neglected. It is not very accurate in capturing the relationship between wavelengths of the radiation and scattering intensity. The North American Mesoscale model has a resolution of 12 km and 6 h. The model accounts for variation in water vapor, ozone, and carbon dioxide concentrations; however, explicit consideration of aerosols is not implemented. WRF model is a flexible model with user specific temporal and spatial resolution. The model has parameterizations for physical processes that helps in adapting the configuration of the model to some specific climatic condition. WRF models are capable of integrating local measurements and thus improves the forecast accuracy.

For the forecasting of solar radiation, the model characterization of cloud formation and dissipation is critical. Parameterizations of cloud microphysics, subgrid scale vertical mixing (cumulus), and turbulent Planetary Boundary Layer (PBL) mixing are the primary model components influencing cloud and solar irradiance forecasting. Thompson microphysics package predicts the interaction between six phases of water that are water vapor, rain, cloud water, snow, cloud ice, and graupel (Kleissl 2013). It is one of the most advanced models for cloud formation in NWP models. Alternatively, "Direct cloud assimilation" is a procedure wherein the cloud information derived from satellite imagery is directly assimilated into the model initial conditions through direct modification of water vapor mixing ratio.

The NWP models cannot predict the exact position of dust aerosol fields and clouds. The usability of NWP to estimate GHI has been extensively tested. Differences over a specific location arise in the regions with varying weather and partially cloudy days. However, there is a significant potential for improvements of solar forecasts from the NWP models. Since solar output is strongly associated with cloud cover, increased spatial resolution, and high-frequency data assimilation are the key to successfully implement the NWP based solar forecasting.

Perez et al. (2010) evaluated the ECMWF global model and the WRF mesoscale model. These were initialized with GFS forecasts in order to forecast solar irradiance. The global models were found to outperform the mesoscale models. Heinemann has evaluated a hybrid model for irradiance forecasts based upon forecast data of two NWP systems and cloud motion vectors from satellite images. They observed that combined forecast is better than forecasts based on single model (Heinemann et al. 2006).

## 3.4 Modified HELIOSAT Model

The HELIOSAT model—originally developed for data from METEOSAT satellite—may be extended to data from other satellites, such as INSAT 3D and to other regions of the globe. We refer this model as HT model; while the HELIOSAT model applied to the METEOSAT satellite data would be referred as MT model.

The HELIOSAT method estimates the GHI over a region using clear sky radiance and clear sky index ***k*** as

$$\mathrm{GHI_G} = k \cdot \mathrm{GHI_{CS}} \tag{6}$$

where $\mathrm{GHI_G}$ and $\mathrm{GHI_{CS}}$ are ground measured global irradiance (horizontal) and clear sky irradiance, respectively. Clear sky GHI may be taken as the maximum GHI value over a period of one month as measured from ground. It is not possible to obtain a clear sky index directly from satellite data because it is based on ground measured GHI. To overcome this difficulty, the HELIOSAT model proposes the following correlation between the clear sky index ($k^*$) and the cloud index (***ci***) as follows:

$$k^* = \begin{cases} 1.2 & \text{if} \quad ci \leq -0.2 \\ 1 - ci & \text{if} \quad -0.2 < ci \leq 0.8 \\ 1.66 - 1.78ci + 0.725ci^2 & \text{if} \quad 0.8 < ci \leq 1.05 \\ 0.09 & \text{if} \quad 1.05 < ci \end{cases} \tag{7}$$

where the cloud index ***ci*** is a satellite-derived quantity and $k^*$ is the derived value of clear sky index.

### *3.4.1 All-Day Index*

The original HELIOSAT method employed the cloud index derived from the visible band solar radiation data only. The model was later modified by Hammer et al. (2003, 2015), Yoo et al. (2010), Legrand et al. (2001), Ng et al. (2006), Perez et al. (2010), Heinemann et al. (2006) to include nighttime data using brightness temperature difference ($\mathrm{BTD_{31}}$). The cloud index value normally varies from −0.2 to 1.2. The negative index represents the absorption of radiation, a characteristic of oceans; while the large positive value of the index means reflection of the radiation from desert or snow.

There is a difficulty in differentiating desert with dust, as they both tend to have similar reflection property. Therefore, six different BTD indices are combined to overcome this difficulty. IDDI and $\mathrm{BTD_{30}}$ provide good resolution for dust in both day and night time. The VIS and $\mathrm{RAT_{30}}$ indices provide good resolution for dust and cloud in daytime only (Kashyap et al. In press).

The segmented BTD images are combined into one single index (ADI) to represent the combined attenuation of solar radiation by dust, fog, and clouds. The cloud index for a given image is defined as

$$ci = \frac{\mathrm{BTD} - \mathrm{BTD}_{\min}}{\mathrm{BTD}_{\max} - \mathrm{BTD}_{\min}} \tag{8}$$

where BTD is the actual measured brightness temperature difference from the satellite. $\mathrm{BTD}_{\min}$ and $\mathrm{BTD}_{\max}$ are the minimum and the maximum values of the brightness temperature difference over a 15-day period. Using BTD in the evaluation of the cloud index instead of actual reflectance avoids the problem of separate filtering of day and nighttime clouds, fog, and dust index. With this definition, the low stratus clouds and fog have a lower index than ocean or land surface.

While using the visible channel only, dust can be recognized above dark surfaces but shows no contrast above bright surfaces such as deserts. Therefore, in this work, six different indices are combined to overcome this difficulty. Based on relevant spectral bands required to capture the effect of dust or fog, cloud indices calculated from Eq. 8 separately for various images are combined to determine an All-Day index (ADI) as

$$\overline{ci} = \frac{1}{N}\sum_{i=1}^{N} ci_i \tag{9}$$

ADI is analogous to cloud index proposed for the original HELIOSET model. In the context of atmospheric conditions presented in this paper (dust, fog, and cloud), the ADI presents a significant improvement over the cloud index, as it incorporates satellite data from six different satellite bands. This ADI, $\overline{ci}$, replaces the cloud index, *ci,* in Eq. 7 to obtain clear sky index. All-Day Index is determined such as to capture the effect of fog, dust, and clouds on radiation for the entire day. Although the ADI values for the night time are not used in the assessment model, they are useful for tracking and forecasting of GHI over extended time horizons. The final All-Day Index is shown in Fig. 3.4. This ADI is able to capture the effect of

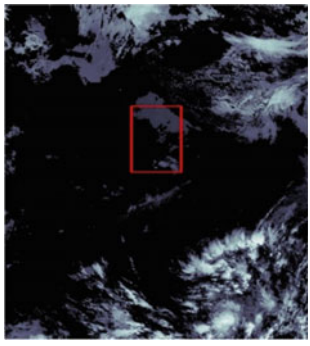

**Fig. 3.4** All-day index at 11:00 IST 16 Jan 2016

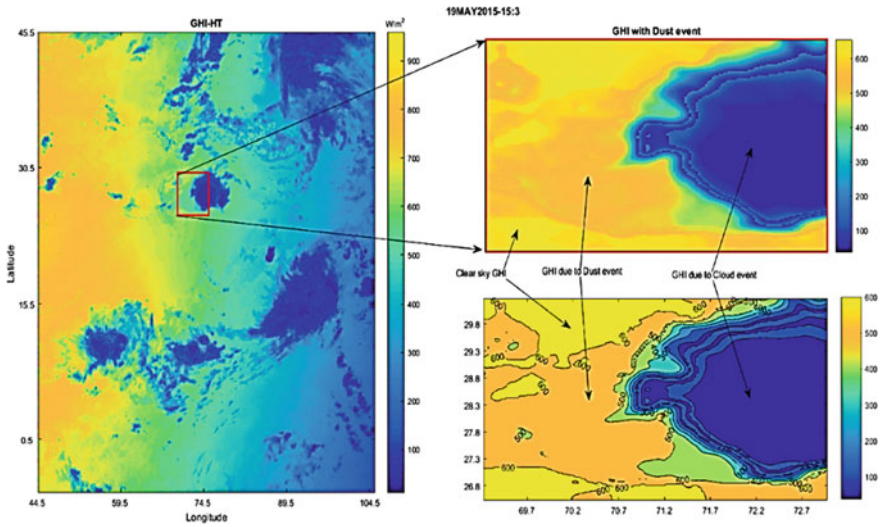


**Fig. 3.5** GHI maps on 18:00 IST 19/01/15

morning fog and evening dust, which is not possible with the cloud index based on just visible band data.

The GHI on a particular day and time is estimated using Eq. 6. The GHI maps as estimated from the HT model proposed in this work are presented in Fig. 3.5. It can be observed from these figures that the presence of dust reduces the GHI by around 20%, which is about 200 W/m$^2$.

The RMSE and $R^2$ in the assessment of GHI for the entire day are given in Table 3.3 for 12 different locations, selected from all geographical regions of India. For comparison, results obtained from the METEOSAT (MT) model for the same locations are also given in the table. It should be noted that the MT model employed by Hammer et al. employs more accurate values of clear sky radiation, calculated with the McClear model. However, their model employs only VIS and TIR data and does not account for dust and fog. Therefore, the All-Day index based on multiple-band data proposed in this work should give a better estimation of GHI. The RMSE error is in the range of 75–182 W/m$^2$ as compared to 21–179 W/m$^2$ reported by Hammer et al. It is clear from results listed in Table 3.3 that the GHI values obtained from the proposed model at most of the locations are comparable with those obtained by Hammer et al. However, there are disagreements at a few places due to mismatch in the clear sky radiation data. Further, significant errors compared to ground data are observed at a few location with both the models. This might be due to errors in the ground data itself.

The accuracy of the estimated GHI from the HT model can be further improved by assimilating the ground data using the Kalman Filter. The GHI, DNI and DHI ground data is available from 32 locations across India from IMD network stations. In this work, only the GHI data is assimilated for 27 sites. The remaining five

**Table 3.3** Error in estimation model for 19 MAY 2015

| STATION | | 'AHMEDABAD' | 'VISAKHAPATNAM' | 'MACHILIPATNAM' | 'BHOPAL' | 'CHENNAI' | 'KOLKATA' | 'JAISALMER' | 'JODHPUR' | 'PUNE' | 'JAIPUR' | 'PANJIM' | 'KARAIKAL' |
|---|---|---|---|---|---|---|---|---|---|---|---|---|---|
| CO-ORDINATES | LAT | 23.0225 | 17.6868 | 16.1905 | 23.2827 | 13.0827 | 22.5726 | 26.9157 | 26.2389 | 18.5204 | 26.9124 | 15.4909 | 10.9254 |
| | LOG | 72.5714 | 83.2185 | 81.1362 | 77.4142 | 80.2707 | 88.3639 | 70.9083 | 73.0243 | 73.8567 | 75.7873 | 73.8278 | 79.838 |
| HOLIOSAT-INSAT 3D | RMSE | 86.88 | 82.81 | 102.08 | 81.23 | 72.52 | 97.79 | 117.85 | 93.85 | 134.13 | 147.94 | 81.46 | 80.19 |
| HOLIOSAT-METEOSAT | | 62.96 | 109.31 | 20.45 | 88.93 | 104.26 | 144.85 | 122.33 | 113.74 | 28.88 | 98.35 | 127.11 | 140.73 |
| KALMAN FILTER | | 59.65 | 34.26 | 42.68 | 37.99 | 39.12 | 147.82 | 52.73 | 45.94 | 114.29 | 62.14 | 57.56 | 163.87 |
| HOLIOSAT-INSAT 3D | $R^2$ | ✓ 0.93 | ✓ 0.94 | ✓ 0.92 | ✓ 0.94 | ✓ 0.94 | ✓ 0.88 | ✓ 0.88 | ✓ 0.92 | ✓ 0.88 | ! 0.81 | ✓ 0.93 | ✓ 0.93 |
| HOLIOSAT-METEOSAT | | ✓ 0.96 | ✓ 0.89 | ✓ 1 | ✓ 0.93 | ✓ 0.89 | ✗ 0.75 | ✓ 0.88 | ✓ 0.89 | ✓ 0.99 | ✓ 0.91 | ! 0.82 | ! 0.78 |
| KALMAN FILTER | | ✓ 0.97 | ✓ 0.99 | ✓ 0.99 | ✓ 0.99 | ✓ 0.98 | ✗ 0.72 | ✓ 0.98 | ✓ 0.98 | ✓ 0.92 | ✓ 0.97 | ✓ 0.97 | ✗ 0.7 |

locations are employed for assessing the accuracy of the model. As the developed model utilize stochastic techniques, the effect of missing data could be easily accommodated in the model.

The estimated values after assimilating the ground data into the proposed model are also given in Table 3.3. Out of 12 locations listed in the table, the data from first seven-locations (Ahmedabad, Visakhapatnam, Machilipatnam, Bhopal, Chennai, Kolkata, and Jaisalmer) is assimilated into the model, and last five locations (Jodhpur, Pune, Jaipur, Panjim, and Karaikal) employ the KF corrections. It is clear that the GHI estimates significantly improve after the assimilation of ground data. The RMSE error improves to 26–110 W/m$^2$.

The estimated and assimilated GHI values for a location in Jaipur are shown in Fig. 3.6. Both the estimated and assimilated results obtained from the ADI-Heliosat model show excellent agreement with the ground measured data. It is observed that the HT model is able to capture the effect of a dust storm on GHI at these locations.

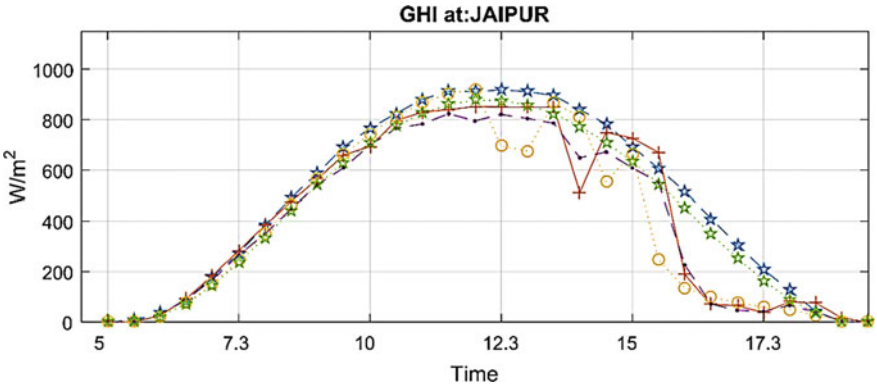


**Fig. 3.6** GHI assessment on 19 May 2015

## 3.5 Simple Forecast Model

Solar radiation suffers from interim and frequent fluctuations in DNI due to presence of clouds and their movement over a geographical region. The clouds may vary in shape, volume, and composition of water particles; which in turn affects their reflection, absorption, and scattering properties. The spatial distribution of GHI may provide important information about the presence of clouds at a specific site. The movement of cloud is tracked over the geographical location with a dynamic model and data assimilation. When the ground network is rather sparse, satellite data may provide an attractive alternative to track cloud features and forecast their effect on GHI. The time series satellite data of GHI over a wide spatial grid may be employed to simulate the effect of cloud and forecast GHI for short time horizons.

Figure 3.7 shows the GHI map obtained from a satellite on a typical cloudy day. The clear sky region in the image is shown in red adjacent to cloudy conditions shown in blue regions. The regions with colors between these two extremes may represent thin and scattered clouds. We employed hourly averaged time series data obtained from morning 7:00 to evening 19:00 IST (Indian Standard Time). The data is taken for the monsoon period, which observes the highest cloud activity over India. The satellite estimated GHI represents the reflectance of clouds over a geographical location. The reflection is high at locations with significant cloud. The satellite-derived images of GHI are processed to determine the possible location of cloud or cloud clusters. The cluster of cloud is then tracked in space to determine the movement of clouds and its effect on GHI.

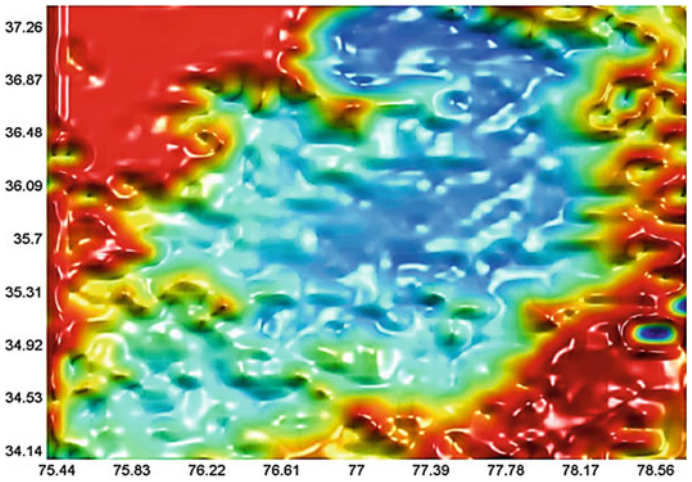


**Fig. 3.7** GHI map over India on 13/07/2007, 13:00 IST

The image is divided pixel by pixel in clear and cloudy parts, based on the blue and red values. A threshold criterion is applied to each pixel considering its Red/Blue fraction. Red pixel is assigned maximum radiation (1) and blue is assigned minimum radiation (0) (Kashyap et al. 2015). The image is smoothened using a Gaussian filter of matrix size 3 × 3. Mathematically, the Cloud shadow (CS) index is written as

$$\mathrm{CS}_{(x,y,t)} = \begin{cases} 0 & \text{if } \left|rb_{(x,y,t)}\right| \geq \in, \\ 1 & \text{if } \left|rb_{(x,y,t)}\right| < \in, \end{cases} \tag{10}$$

where $\boldsymbol{rb}_{(x,y,t)}$ is the Blue/Red value of the pixel. If R/B fraction is more than $\epsilon$, the threshold value, then it is regarded as clear, otherwise, the pixel is classified as cloudy. The value of $\epsilon$ depends upon the cloud type and the radiation value. The threshold value can differ for different times and locations. A lower threshold value would mean that some thin clouds are left out; while a larger threshold value would mean that radiation is completely blocked by even thinner clouds. It is important to capture the most dominant clouds and therefore, the threshold value is adjusted according to time and location. The main limitation of this method is that it does not distinguish various types of clouds. The cloud images are converted into grayscale and are shown in Fig. 3.8. The black regions in the image represent clouds.

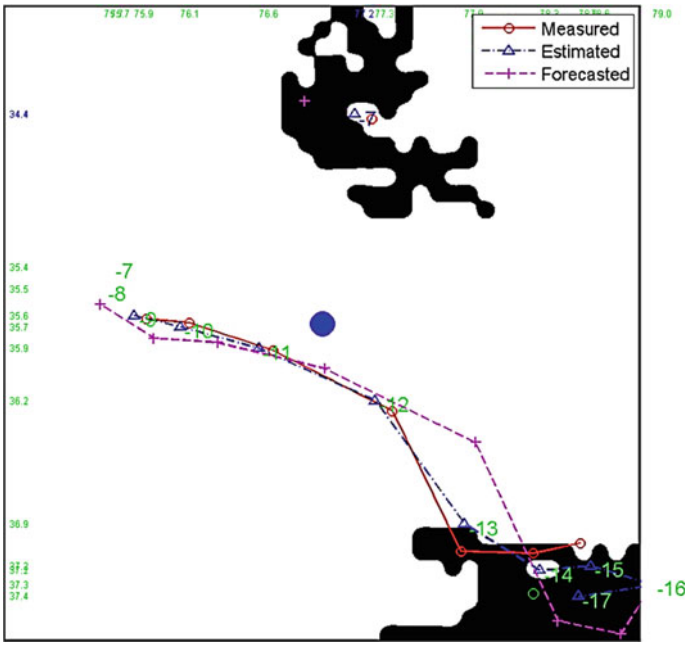


**Fig. 3.8** Tracking of multiple shadow object from 7:00 to 19:00 IST

Next, the geometric features of the cloud such as its size and location are extracted. To avoid the difficulty of dealing with small clouds, smaller objects are combined with bigger objects to create a large object. All the objects are numbered and the bounding box of the cloud object with the coordinates of the Center of Gravity (COG) are determined.

Finally, the cloud objects are moved over the domain. It is assumed that the shape and size of the clouds do not change in two successive images or time steps. If between successive time steps a cloud is broken into a number of smaller clouds, then the mean of the COG of all smaller clouds is taken same as the COG of combined object. Similarly, in the case of integration of small clouds into a bigger one, effective COG of combined cloud is taken into consideration.

The movement of clouds in space is modeled with a dynamic state space model. The governing equation for an object moving with speed $V$ at any point $\boldsymbol{X}$ is given by

$$X_{t+1} = X_t + V_t \cdot \Delta t \tag{11}$$

$$V_{t+1} = V_t \tag{12}$$

where $\boldsymbol{X}_t, \boldsymbol{X}_{t+1}, \boldsymbol{V}_t$ and $\boldsymbol{V}_{t+1}$ are positions and velocities of the object at time $\boldsymbol{t}$ and $\boldsymbol{t+1}$, respectively. The estimated values of position and velocities from the above equations are updated with the Kalman filter. The Kalman Filter assimilates the latest data of cloud images and returns improved estimate of the cloud position and the velocity. The posterior updated value of the cloud position is represented by $\boldsymbol{X}_t^+$ and is given as follows:

$$X_t^+ = X_t^- + K_t\left(Z_t - HX_t^-\right) \quad t = 1, \ldots, N, \tag{13}$$

where $\boldsymbol{X}_t^-$ is the priori estimated cloud position, $\boldsymbol{Z}_{t+1}$ is the new observation and $\boldsymbol{K}_t$ is the Kalman gain, written as:

$$K_t = P_t^- H^T \left(HP_t^- H^T + R_t\right)^{-1} = \frac{P_t^- H_t^T}{H_t P_t^- H_t^T + R_t} \tag{14}$$

where the prior and posterior predicted error covariance is defined by

$$P_t^- = E\left[e_t^- e_t^{-T}\right] = A \cdot P_{t-1} \cdot A^T + Q_{t-1} \tag{15}$$

$$P_t^+ = E\left[e_t^+ e_t^{+T}\right] = (1 - K_t H) P_t^- \tag{16}$$

where $e_t^- = X_t - X_t^-, e_t^+ = X_t - X_t^+, P_t^-, P_t^+$ are the priori and posteriori estimated error, priori and posteriori estimated covariance matrix with covariance $R_t$ and $Q_t$, respectively (Kashyap et al. 2015).

The state space model projects the movement of shadow at time $t + 1$, and Kalman Filter updates the forecast by assimilating the features of the cloud from latest data. The trajectory of clouds on a typical day is shown in Fig. 3.8, which shows the trajectory of COGs of clouds from 7:00–17:00 IST. Three different sets of track points are plotted in the figure, namely: the measured, forecast (prior estimates of the coordinate $X_t^-$), and estimated (posterior estimate $X_t^+$). It is clear from the figure that the data assimilation significantly improves the predictions of cloud images.

## 3.6 Hybrid Model

During summer seasons, when energy available from solar radiation is maximum, India observes extreme weather events like dust storms and western disturbances. These events result in quick blackout of available solar radiation. Hybrid model exploits satellite-derived cloud/dust information and combines it with statistical models to forecast solar radiation in the presence of significant dust and cloud activity. The model extends the concept of All-Day index discussed in Sect. 3.4 to forecasting of GHI using tracking algorithms and time series models.

The hybrid model incorporates the concepts of ADI, Wavelet Transform (WT), ARIMA, ANN, and KF. The model is applied to forecast GHI for time horizons up to 7 h. The key procedure in the model include:

1. Reduction of image resolution using WT to increase computational efficiency and reduce calculation time.
2. Cloud and dust tracking over a spatial domain as well as data assimilation using KF.
3. The tracking model is combined with the time series forecasts based on ARMA and ANN model.

Each processed satellite image comprises of 1616 × 1618 pixels, and size of each image is around 20 MB. The ADI is taken as the basic parameter for forecasting as well as tracking. To forecast GHI from time series, ADI images for multiple time delays are required to be stored in memory, which makes the method very computationally demanding. To overcome this difficulty, the resolution of the image is reduced using WT.

### 3.6.1 Wavelet Transform

Wavelet Transform is a method of image compression. The Discrete Wavelet Transform (DWT) considers the image as the sum of wavelet functions with different scale and location. WT represents data in a set of low-pass (approximate) and high-pass (detail) coefficients. The input data is passed through sets of high-pass and low-pass filters. Haar WT is applied to reduce the resolution of ADI images. The *haar2* function in MATLAB performs the 2-D Haar DWT of the high-resolution image; and returns the low-resolution image (Kour and Singh 2013; Talukder and Harada 2010). The resolution of each of the image is reduced to $25 \times 25$ pixels before the simulation, and original resolution is recovered by applying inverse wavelet transform after forecasting as shown in Fig. 3.9.

### 3.6.2 Image Tracking

ADI image may be tracked during day as well as nighttime to determine the position of clouds and dust storms over a geographical area. It is desirable to forecast position of cloud and dust over a geographic area up to seven hours in advance. The tracking of clouds during nighttime, especially, gives a method to

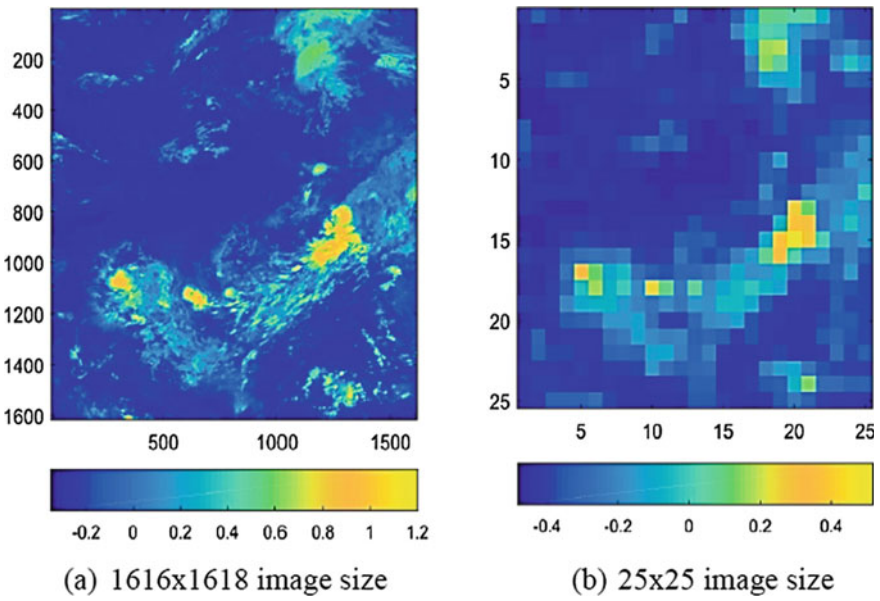


**Fig. 3.9** Wavelet decomposition of ADI image

forecast GHI for morning hours of the next day. The same method as discussed in Sect. 3.5 is employed for tracking. However, to overcome the inherent limitations of image-based tracking methods in the absence of wind profile, a hybrid methodology is implemented that links the time series forecasting with the spatial tracking. The accuracy of the forecast based on simple tracking method can be improved by utilizing the time series models such as ANN and ARIMA. These models try to capture the dynamic nature of the variability of ADI at a given pixel. In the proposed hybrid model, the ADI, as well as GHI, at a particular location is assumed to be influenced not only by moving clouds and dust patches from neighboring pixels but also by time history of the ADI at that particular location.

The ARIMA models are reported to have limited success with nonlinear problems. On the other hand, the application of ANNs to linear problems may not give excellent results. A hybrid methodology that has both linear and nonlinear modeling capabilities may be a good strategy to solve practical time series problems (Kashyap 2017). Thus, time series modeling of ADI is accomplished with the combined ARIMA and ANN models. Let a time series is composed of a linear component and a nonlinear element as

$$\mathrm{ADI}_t = \mathrm{L}_t + \mathrm{NL}_t \tag{17}$$

where $\boldsymbol{L_t}$ denotes linear component and $\boldsymbol{NL_t}$ denotes nonlinear component of the time series, $\boldsymbol{ADI}$. In the present case, the time series is represented by recently estimated ADI values from the tracking model and ADI values from three previous times at the same location. The linear and nonlinear components are separately modeled with the ANN and ARIMA models, respectively. First, the ARIMA model is applied to forecast the linear component, then the residuals from the linear model, containing only nonlinear part, are forecasted with the ANN model. The residuals after the ARIMA forecasting at time $\boldsymbol{t}$ are given as

$$e_t = \mathrm{ADI}_t - \widehat{\mathrm{L}_t} \tag{18}$$

where $\widehat{\boldsymbol{L_t}}$ is the ARIMA forecast at time $\boldsymbol{t}$. If residuals from the ARIMA forecast are very small, it highlights the linearity in the time series data. On the other hand, higher residual imply highly nonlinear time series data. The nonlinear part of the time series, $\boldsymbol{NL_t}$ is modeled with the ANN model.

Both the ARIMA and the ANN models are trained with a variation of Kalman Filter. Generally, the networks are trained using the traditional Back Propagation and Levenberg–Marquardt algorithms, which are based on the gradient descent algorithm to determine the weights of the network. These methods are rather slow due to their linear convergence. A much faster algorithm based on Extended Kalman Filter (EKF) may be adopted for training the network (Singhal and Wu 1988).

The model learns from the satellite and ground data and then forecasts the effect of storm, dust, and cloud on GHI. The model produces the first forecast of GHI for 7:00 AM. Due to unavailability of daytime data for training the model in early hours, only the nighttime data is utilized and the accuracy of the model is relatively poor. However, as more and more data is available with time, the model is better trained and produces more accurate forecasts later in the day.

Together, cloud and dust can block 70–80% of GHI on a typical stormy day. Even on a normal cloudy day, the reduction in GHI could be as high as 50%. If the forecast model is able to predict GHI reduction with 10–20% uncertainty, the model may be accepted. The acceptable range depends on time horizon of the forecast. As the time horizon increases, the uncertainties in the forecast also increase. A good forecast model should be able to reduce the uncertainties in GHI by half at any time and location. The GHI forecasts are prepared for time horizons varying from 30 min to a maximum of seven hours ahead. A total of 14 points with thirty minutes interval is taken for the time horizon. In other words, the time horizon values such as 120, 90, 60, 30 min, etc. are chosen for comparison. The forecasts of GHI are made from 7:00 h in the morning to 18:00 h in the evening. For each day, a total of 22 forecasts is done, with a gap of 30 min. For the case of 7-h time horizon, for example, the first forecast at 7:00 h is made at 00:00 h and last forecast at 18:00 h is made at 11:00 h. There is one forecast every 30 min. The RMSE is calculated for the forecasts of the entire day for each location and time horizon. The algorithm for the hybrid forecast model is shown in Fig. 3.10.

Figure 3.11 shows the contour maps of (a) actual and (b) forecasted GHI, and variation along (c) latitude, and (d) longitude for five hour time horizon. The intersection of the dashed blackened lines marks the center of the dust storm. There is a dip in GHI values near the storm regions. The figures also show low GHI values at other locations away from the center of the dust storm. These dips are due to the presence of clouds. The figures also show error along horizontal and vertical lines passing through the center of a dust storm.

The model can capture the trend in GHI very well. However, the error at certain locations increases up to 400 W/m$^2$. It is observed that all the locations which witness a complete blackout of solar radiation due to storm give significant errors. Since across the storm, the meteorological parameters change abruptly, the higher errors are expected (Kashyap et al. In press; Kashyap 2017).

Figure 3.12 shows the RMSE values for the selected locations. These sites are chosen based on the extent of a dust storm that had its origin in Rajasthan, a northwestern region of the country. The errors for Ahmedabad and Jaisalmer are lower compared to other locations, as these sites are not affected by the dust storm activity. Jaipur sees the highest error in GHI forecasts, as it lies in the path of the dust storm. The RMSE values for Jaipur, the worst dust storm affected location, are consistently above 100 W/m$^2$. Although the absolute error was found to be very high for the dust storm affected locations, the RMSE values calculated for the entire day are in good agreement.

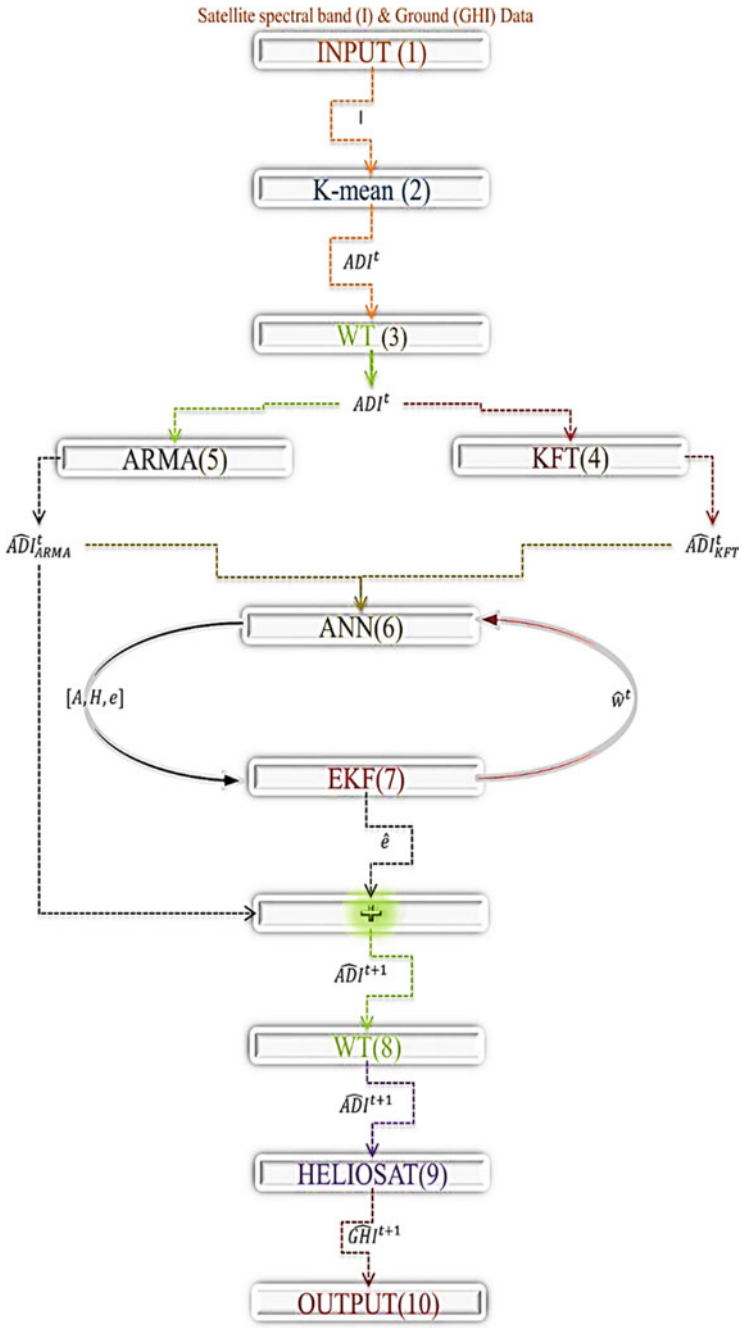


**Fig. 3.10** Flow chart for the hybrid forecasting model

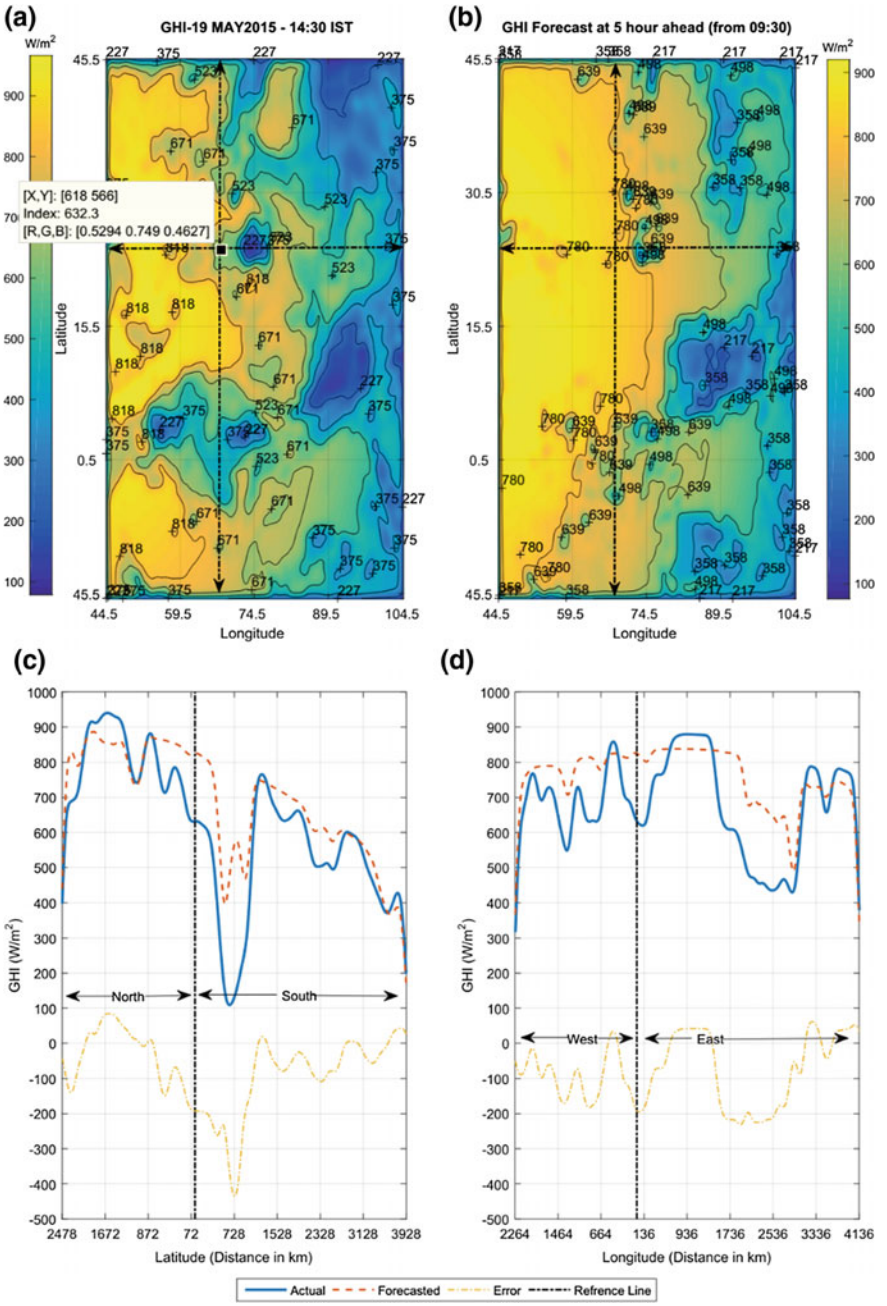


**Fig. 3.11** GHI map: **a** actual, **b** forecast and line plots, **c** along Latitude, **d** along Longitude for 5-h time horizon

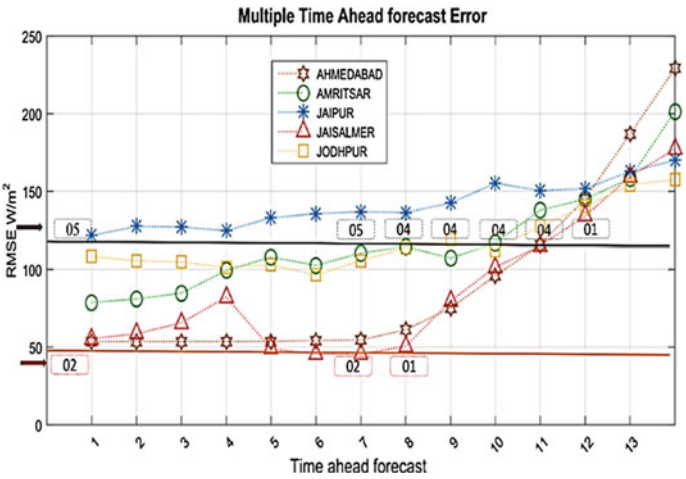


**Fig. 3.12** RMSE in GHI forecast at 5 locations

## 3.7 Conclusion

Accurate estimation and forecasting of GHI requires state-of-the-art models that process satellite data. Empirical models have an advantage over the physical models as they do not require complex modeling of underlying physical processes. These models directly work on the satellite data and capture the effect of clouds, dust, and fog. A hybrid model employing multispectral satellite data, image processing tools, time tracking model, and time series models is discussed to forecast GHI for time horizons up to 5 to 7 h.

## References

Al-Alawi S, Al-Hinai H (1998) An ANN-based approach for predicting global radiation in locations with no direct measurement instrumentation. Renew Energy 14:199–204

Beyer HG, Costanzo C, Heinemann D (1996) Modifications of the Heliosat procedure for irradiance estimates from satellite images. Sol Energy 56(3):207–212

Cano D, Monget J-M, Albuisson M et al (1986) A method for the determination of the global solar radiation from meteorological satellite data. Sol Energy 37(1):31–39

Chow CW, Urquhart B, Lave M, Dominguez A, Kleissl J, Shields J et al (2011) Intra-hour forecasting with a total sky imager at the UC San Diego solar energy testbed. Sol Energy 85:2881–2893

Crispim EM, Ferreira PM, Ruano AE (2008) Prediction of the solar radiation evolution using computational intelligence techniques and cloudiness indices. Training 2:2

Dedieu G, Deschamps P, Kerr Y (1987) Satellite estimation of solar irradiance at the surface of the earth and of surface albedo using a physical model applied to Metcosat Data. J Climate Appl Meteorol 26(1):79–87

Gueymard C (1995) SMARTS2: a simple model of the atmospheric radiative transfer of sunshine: algorithms and performance assessment. Florida Solar Energy Center, Cocoa, FL

Gueymard CA (2012) Clear-sky irradiance predictions for solar resource mapping and large-scale applications: improved validation methodology and detailed performance analysis of 18 broadband radiative models. Sol Energy 86:2145–2169

Hammera A, Heinemanna D, Hoyera C, Kuhlemanna R, Lorenza E, Mullera R, Beyerb HG (2003) Solar energy assessment using remote sensing technologies. Remote Sens Environ 86:423–432

Hammer A, Kühnert J, Weinreich K et al (2015) Short-term forecasting of surface solar irradiance based on Meteosat-SEVIRI data using a nighttime cloud index. Remote Sens 7(7):9070–9090

Heinemann D, Lorenz E, Girodo (2006) Forecasting of solar radiation. In: Solar energy resource management for electricity generation from local level to global scale. Nova Science Publishers, pp 223–233

http://satellite.imd.gov.in/dynamic/INSAT3D_Catalog.pdf. Last Accessed on 6 June 2018

Ji W, Chee KC (2011) Prediction of hourly solar radiation using a novel hybrid model of ARMA and TDNN. Sol Energy 85:808–817

Kashyap Y (2017) Solar radiation assessment and forecasting over india in the presence of dust and fog activity. Ph.D. Dissertation, IIT Mandi

Kashyap Y, Bansal A, Sao AK (2015) The spatial approach of artificial neural network on solar radiation forecasting: modeling issues; Hindawi Publishing Corporation. J Solar Energy 13 pages. Article ID 410684, http://dx.doi.org/10.1155/2015/410684

Kashyap Y, Bansal A, Sao AK, Hammer A (In press) Model for estimation of global horizontal irradiance in presence of dust, fog and clouds. IEEE Trans Geosci Remote Sens, https://doi.org/10.1109/tgrs.2018.2847047

Kleissl J (2013) Solar energy forecasting and resource assessment. Center for Renewable Resources and Integration, University of California, San Diego

Kour G, Singh SP (2013) Image decomposition using wavelet transform. Int J Eng Comput Sci 2:3477–3480

Kerschgens M, Pilz U, Raschke E (1978) A modified two-stream approximation for computations of the solar radiation budget in a cloudy atmosphere. Tellus 30(5):429–435

King MD, Kaufman YJ, Menzel WP et al (1992) Remote sensing of cloud, aerosol, and water vapor properties from the moderate resolution imaging spectrometer (MODIS). IEEE Trans Geosci Remote Sens 30(1):2–27

Lefevre M, Oumbe A, Blanc P et al (2013) McClear: a new model estimating downwelling solar radiation at ground level in clear-sky conditions. Atmos Measure Tech 6:2403–2418

Legrand M, Plana-Fattori A, N'doumé C (2001) Satellite detection of dust using the IR imagery of Meteosat. I- Infrared difference dust index. J Geophys Res 106(D16):18251–18274

Liang S, Wang K, Zhang X et al (2010) Review on estimation of land surface radiation and energy budgets from ground measurement, remote sensing and model simulation. IEEE J Sel Top Appl Earth Observations Remote Sens 3(3):225–240

Marquez R, Coimbra CF (2013) Intra-hour DNI forecasting based on cloud tracking image analysis. Sol Energy 91:327–336

Mantzari VH, Mantzaris DH (2012) Solar radiation: cloudiness forecasting using a soft computing approach. Artif Intell Res 2:69

Mellit A, Pavan AM (2010) A 24-h forecast of solar irradiance using artificial neural network: application for performance prediction of a grid-connected PV plant at Trieste, Italy. Sol Energy 84:807–821

Möser W, Raschke E (1984) Incident solar radiation over Europe estimated from Meteosat data. J Climate Appl Meteorol 23(1):166–170

Mekhilef S, Saidur R, Kamalisarvestani M (2012) Effect of dust, humidity and air velocity on efficiency of photovoltaic cells. Renew Sustain Energy Rev 16(5):2920–2925

Mueller R, Dagestad K-F, Ineichen P et al (2004) Rethinking satellite-based solar irradiance modelling: the SOLIS clear-sky module. Remote Sens Environ 91(2):160–174

Ng H, Ong S, Foong K et al. (2006) Medical image segmentation using k-means clustering and improved watershed algorithm, pp 61–65

Ong C-S, Huang J-J, Tzeng G-H (2005) Model identification of ARIMA family using genetic algorithms. Appl Math Comput 164:885–912

Perez R, Kivalov S, Schlemmer J, Hemker K Jr, Renne D, Hoff TE (2010) Validation of short and medium term operational solar radiation forecasts in the US. Solar Energy 84:2161–2172

Perez R, Ineichen P, Moore K, Kmiecik M, Chain C, George R et al (2002) A new operational model for satellite-derived irradiances: description and validation. Sol Energy 73:307–317

Perez R, Lorenz E, Pelland S, Beauharnois M, Van Knowe G, Hemker K et al (2013) Comparison of numerical weather prediction solar irradiance forecasts in the US, Canada and Europe. Sol Energy 94:305–326

Rigollier C, Bauer O, Wald L (2000) On the clear sky model of the ESRA—European solar radiation atlas—with respect to the Heliosat method. Sol Energy 68(1):33–48

Rigollier C, Lefevre M, Wald L (2004) The method Heliosat-2 for deriving shortwave solar radiation from satellite images. Sol Energy 77(2):159–169

Singhal S, Wu L (1988) Training multilayer perceptrons with the extende Kalman algorithm. In: NIPS, pp 133–140

Salcedo-Sanz S, Casanova-Mateo C, Muñoz-Marí J et al (2014) Prediction of daily global solar irradiation using temporal gaussian processes. IEEE Geosci Remote Sens Lett 11(11):1936–1940

Tapiador FJ (2009) Assessment of renewable energy potential through satellite data and numerical models. Energy Environ Sci 2(11):1142–1161

Tarpley J (1979) Estimating incident solar radiation at the surface from geostationary satellite data. J Appl Meteorol 18(9):1172–1181

Talukder KH, Harada K (2010) Haar wavelet based approach for image compression and quality assessment of compressed image. arXiv preprint arXiv:1010.4084

Yoo J-M, Jeong M-J, Hur YM et al (2010) Improved fog detection from satellite in the presence of clouds. Asia-Pacific J Atmos Sci 46(1):29–40

# Part II
# Solar Cells

# Chapter 4
# Advances in Solar Energy: Solar Cells and Their Applications


**Amlan K. Pal and Hannah C. Potter**

**Abstract** This chapter will focus on the recent advances on the traditional and modern solar cell technologies, notably, (a) silicon solar cells, (b) multi-junction solar cells, (c) perovskite solar cells, and (d) dye-sensitized solar cells. Research efforts focused on improvement of the stability and the efficiency of each type of cells will be mentioned. While the current industrial market is predominantly dominated by silicon solar cells, other photovoltaic cells (b–d) show immense promise to overtake the silicon PV market in near future. The most efficient silicon solar cell reported reaches an efficiency of over 26%. This efficiency was achieved by fabricating a cell with an interdigitated back contact, combining n-type and p-type amorphous silicon to collect both holes and electrons. The back contact is separated from the front contact by crystalline silicon, with the front contact covered by an amorphous silicon passivation layer and an antireflective coating. A close competitor of silicon solar cells, known as multi-junction solar cells, displays power conversion efficiency as high as 46% using a solar concentrator. However, due to difficulty in cell fabrication with elevated cost, application of this type of cell is mostly limited to extraterrestrial purposes. A low-cost alternative of multi-junction cell is a perovskite solar cell. The best efficient perovskite solar cell with a power conversion efficiency of 23.9% was achieved by using a complex semitransparent organic–inorganic perovskite material with a high bandgap absorber, $Cs_{0.1}(H_2NCHNH_2)_{0.9}PbI_{2.865}Br_{0.135}$ combined with a low bandgap absorber, *c*-Si, for the back contact. While the perovskite solar cells are promising candidates as low-cost substitute to silicon solar cells, stability remains an issue for the former. On the other hand, dye-sensitized solar cells are cost-effective and chemically stable, with a best reported efficiency of 13% using a panchromatic donor–$\pi$–acceptor-based designed **SM315** as an organic sensitizer; power conversion efficiency of this type of cell is still to be improved to overtake the silicon PV market.

A. K. Pal (✉) · H. C. Potter
Organic Semiconductor Centre, EaStCHEM School of Chemistry,
University of St Andrews, St Andrews, Fife KY16 9ST, UK
e-mail: akp5@st-andrews.ac.uk



H. Tyagi et al. (eds.), *Advances in Solar Energy Research*, Energy, Environment, and Sustainability, https://doi.org/10.1007/978-981-13-3302-6_4

**Keywords** Renewable energy · Photovoltaic or solar cells · Power conversion efficiency

## 4.1 Introduction

Many of the world's greatest problems could be solved with readily available and inexpensive energy, provided that these additional resources do not contribute to global warming (Olah et al. 2011). The 2014 Climate Change Act requires at least 40% reduction in greenhouse gas emissions from the 1990 baseline in the European Union by 2030 (European Union Homepage 2018). According to a report by the International Energy Agency (IEA), artificial lighting consumed around 3500 TW hours of electricity in 2012, corresponding to 1900 Mt of equivalent $CO_2$ emissions and corresponding to about 20% of world electricity consumption (International Energy Agency Light's Labour's Lost 2018). The worldwide power consumption is expected to double in the next three decades because of the increase in world population and the rising demand of energy in the developing countries. Because of diminishing resources, a huge power shortage of 14 terawatts is expected to rise by year 2050 equalling today's entire consumption (Grätzel 2009). On this note, the strategy of adopting renewable energy sources is well accepted, yet not fully functional to address this demanding and challenging requirement. According to a current study, about 16% of global final energy presently originates from renewable resources, in which 3 and 10% are contributed by hydroelectricity and biomass, respectively (International Energy Agency 2018).

Solar energy offers a clean, climate-friendly, very abundant, and inexhaustible energy resource to mankind, which is relatively well spread over the globe. The sun provides about 120,000 terawatts to the earth's surface, which amounts to 6000 times the present rate of the world's energy consumption (Grätzel 2009). However, capturing solar energy and converting it to electricity or chemical fuels, such as hydrogen, at low cost and using abundantly available raw materials remains a huge challenge. The high-renewable scenario variant of IEA showed that solar photovoltaic (PV) devices and solar thermal electricity together could provide up to 25% of global electricity by 2050 (International Energy Agency Light's Labour's Lost 2018). With the global cumulative installation of 301 GW power capacity solar panels by the end of 2016, solar photovoltaics is now, after hydro and wind power, the third most important renewable energy source and has seen a tremendous 33.2% increase versus that at the end of 2015 (BP Global Homepage 2018). Although negligible, with rapid past and foreseeable promising advances in solar technologies, power generated from solar contributed to 1.3% of global power (BP Global Homepage 2018).

A solar cell or a photovoltaic (PV) cell is an electrical device that converts light directly into electricity by photovoltaic effect. The photovoltaic effect is closely related to the photoelectric effect where when the light is absorbed excitation of an electron or other charge carrier to a higher energy state is created. A PV or a solar

cell is typically consisted of a p–n junction, where illumination of the material creates an electric current as excited electrons and the remaining holes are swept in different directions by the built-in electric field of the depletion region. In the context of converting solar energy into electrical energy using a PV cell, intense research has led to the development of distinct categories of solar cells, such as silicon solar cells, thin-film solar cells, multi-junction solar cells, quantum dot solar cells, organic/polymer solar cells, etc. (Fig. 4.1). This chapter will focus on the recent advances on the traditional and modern four major solar cell technologies, notably, (a) silicon solar cells, (b) multi-junction solar cells, (c) dye-sensitized solar cells, and (d) perovskite solar cells. Research efforts focused on improvement of the stability and the efficiency of each type of cells will be mentioned, with a note on the best performing solar cell to date.

## 4.2 Silicon Solar Cells

### *4.2.1 Background of Silicon Solar Cells*

The first silicon cell was reported and patented in 1941 (Ohl 1942). These silicon solar cells were discovered by Russell Ohl, using junctions formed by melted silicon (Green 2009). The recrystallization of pure silicon melts led to impurity segregation leading to the "grown-in" junctions (Green 1993). Upon illumination or heating, one side of the junction was found to reach a negative potential and therefore named "n-type" silicon, whereas the opposite side was titled the "p-type"

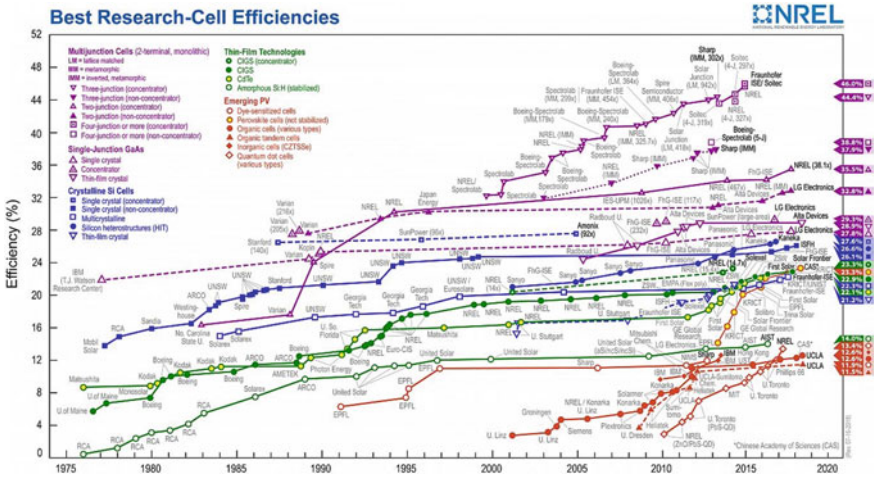


**Fig. 4.1** Advancement of best efficient solar cells with progression of time. Figure courtesy—National Renewable Energy Laboratory (NREL), July 2018, Colorado, USA

material (Green 1993). Efficiency of these silicon solar cells was found to be less than 1% (Green 2009). The next step in the development of silicon cells was reported by Kingsbury and Ohl in 1952 (Kingsbury and Ohl 1952). The naturally formed potential barrier previously found by Ohl was now produced in silicon devices by forming junctions through bombardment by helium ions (Kingsbury and Ohl 1952). These silicon devices were not tested under sunlight but did show desirable properties such as reasonable spectral responsivity, with a theoretical efficiency of 1% (Green 2009).

From 1952 onwards, the efficiency of solar cells rapidly improved. In 1954, Chapin et al. produced electron–hole pairs that were separated in the presence of p–n junctions and in an external circuit, this cell shows an efficiency of 6% (Chapin et al. 1954). The efficiency of this type of cell rapidly increased to 10% and was most commonly used in space vehicle power supplies (Goetzburger et al. 2002). The use of phosphorus-doped silicon solar cells achieved efficiencies of above 10% in 1962 (Mandelkorn et al. 1962). Phosphorous-doped cells were found to have a higher resistance to radiation compared to boron-doped cells making them useful for applications in space (Mandelkorn et al. 1962). Cosmat Laboratories developed the first cells that successfully exceeded efficiencies of 14.5% using a "violet" cell and later, a nonreflecting cell using textured surfaces (Rittner and Arndt 1976). Efficiencies of silicon solar cells were not adequately improved until the mid-1980s when two different cell types, one with a metal-insulator p–n junction and a passivated emitter solar cell, were developed, reaching efficiencies of around 19% (Green et al. 1985). Further improvements of the earlier passivated emitted solar cells included the use of microgrooved surfaces with experimental efficiencies around 20%, for the first time in history (Blakers and Green 1986).

Since the production of the first useful silicon cell in 1954, with 6% efficiency, silicon solar cell technology has advanced rapidly. Up until this point, the cost of silicon cells was so high that only companies using them for applications in space could afford them, which deferred the development of cheaper and terrestrial solar cells (Green 2005). Production of crystalline silicon solar cells required ultrahigh purity silicon via crystal growth and vapor deposition (Jacoby 2016). Silicon cells also required a thick layer of silicon to achieve higher sunlight absorption, which was supported by heavy glass, further contributing to the cost of the cell (Szlufcik et al. 1997). From the 1970s onward, terrestrial applications became of more importance and so production of cheaper silicon solar cells was the main interest in the development of the solar cell industry (Szlufcik et al. 1997).

In 1976, Carlson and Wronski developed an efficient thin-film solar cell from amorphous silicon, with a decrease in solar cell cost in comparison to the previous solar cells formed from monocrystalline silicon (Carlson and Wronski 1976). Petroleum shortages crisis in the 1970s led to the formation of new smaller companies investigating and producing lower cost photovoltaics suitable for terrestrial use (Green 2005). This resulted in the modern era of photovoltaics, where large government-sponsored programs in the USA became interested in the development of more affordable solar cells (Green 2005). According to data from CleanTechnica, the pricing of silicon solar cells rapidly dropped from $101.05 per watt per solar

panel in the mid-1970 s to $0.61 per watt in 2015, further decreasing to $0.37 in 2017 (CleanTechnica 2018). This large decline in cost over the years can be accredited to the significant popularity of the silicon solar cell compared to other photovoltaic cell types, such as dye-sensitized and perovskite cells. Crystalline silicon solar cells have represented approximately 90% of the world total production of photovoltaic cells in recent years (Sago 2010).

As mentioned earlier, the first practical silicon cell was produced by Chapin et al. at Bell Telephone Laboratories in 1954 (Chapin et al. 1954). Their work investigated the ability of photons with an energy of 1.02 eV to produce electron–hole pairs in silicon. These electron–hole pairs could then be separated in the proximity of a p–n junction, which allowed them to do work in an external circuit. A theoretical computation of this silicon solar cell over the whole solar spectrum calculated a limiting efficiency of 22% (Chapin et al. 1954). However, the silicon cell did not display this level of efficiency due to two principal factors that included the untreated silicon surface reflecting 50% of the photons and recombination of electron–hole pairs before separating upon reaching the p–n junction. This silicon solar cell made use of a thin layer of p-type silicon assembled over an n-type base, achieving an experimentally measured efficiency of 6% (Chapin et al. 1954). Efficiencies increased above 10% in 1962 due to the work of Mandelkorn et al. on phosphorous diffused cells at United States Army Signal Research and Development Laboratory. Before the development of this silicon solar cell, previous cells were made by boron doping into the n-type silicon, whereas the cell in question was made by phosphorous diffusion (Mandelkorn et al. 1962). Phosphorous-doped silicon solar cells allowed for more resistance to radiation damage due to the "slower rate of degradation of minority carriers in p-type silicon compared to n-type silicon", making them better suited for use in space (Mandelkorn et al. 1962).

Carlson and Wronski later developed the first amorphous silicon solar cell at RCA laboratories in 1976 (Carlson and Wronski 1976). Noncrystalline deposits were formed from a glow discharge of silane, this amorphous silicon was then used to fabricate the thin-film solar cell (1 μm thick) (Carlson and Wronski 1976). The p–n junction was created by using the dopants in gas phase during the glow discharge in silane. Use of noncrystalline thin-film solar cells led to a noticeable decrease in cell cost when compared to crystalline silicon devices (Carlson and Wronski 1976). The conversion efficiency of the cell was lower than previous silicon cells at 2.4%, but the production of an efficient, more competitively priced silicon solar cell which could compete with conventional sources of power kick-started the development of cheaper and more efficient photovoltaic cells (Carlson and Wronski 1976). Leading on from this fact, Tawada et al. developed a new silicon thin-film cell, a methane-based *a*-SiC:H/*a*-Si:H film (*a* = amorphous, $C{=}CH_4$), achieving 8% efficiency (Tawada et al. 1982). These *a*-SiC:H films were formed by the decomposition of silane and methane gas (Tawada et al. 1982). By the late 1980s, efficiencies increased to 22.8% with the creation of a new silicon solar cell structure with a passivated emitter and rear cell (PERC cell) (Fig. 4.2) (Blakers et al. 1989). One major difference compared to previous cells arose from

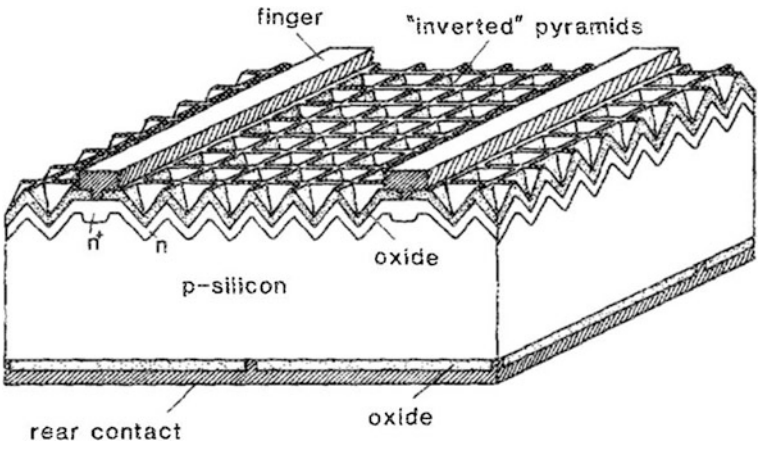


**Fig. 4.2** Diagram of PERC cell. Reprinted with permission from Blakers et al. (1989). Copyright (1989) AIP Publishing

contacting the cell rear by using a considerable amount of contact holes through a passivating oxide layer while the old cells contained an alloyed aluminum rear surface (Blakers et al. 1989). The top layer was lightly diffused with phosphorous to help prevent recombination of electron–hole pairs (Blakers et al. 1989). By the next year, passivated emitter cells had reached maximum efficiencies of 24% under terrestrial conditions. In general, PERC cells increased open-circuit voltage ($V_{OC}$) and short-circuit current density ($J_{SC}$) due to their low recombination rates but exhibited low fill factor (FF) due to resistance loss in the substrate. Improvements were made due to the introduction of the passivated emitter rear locally diffused cell (PERL); the only difference being that boron was locally diffused in rear contact areas (Wang et al. 1990). This factor allowed slower recombination rates and reduction in spacing of the rear contact points, decreasing resistance and therefore having the ability to achieve better fill factor values (Wang et al. 1990).

Moving forward to the current solar cell market, the demand for cheaper power alternatives to fossil fuels is the main driving force in production. Although cheaper amorphous silicon cells have been designed, the implementation of these on a large scale was not feasible when prices were compared to those of more conventional sources of power (i.e., fossil fuels) (Garnett and Yang 2010). One of the main ways to decrease the cost of silicon solar cells is to use thin-film structures, that use inexpensive substrates and a lower quantity and quality of semiconductor silicon. In 2010, Garnett and Yang concentrated their research on scalable and simple assembly of silicon solar cells using silicon nanowires with radial p–n junctions (Garnett and Yang 2010). The fabrication of these cells required dip coating of silicon substrate to form silica spheres, followed by deep reactive ion etching (DRIE) to form the nanowires. Finally, the p–n junction was formed via boron diffusion into the starting n-type silicon (Garnett and Yang 2010). Efficiencies achieved were only between 5 and 6% for these cells but a simple method with the

ability to be implemented on a large scale was achieved (Garnett and Yang 2010). Use of ultrathin silicon cells became of significant interest due to their ability to reduce cost, but efficiencies of these cells needed to be improved. Improvements in efficiency for ultrathin silicon solar could be achieved by surface treatments, such as antireflective coatings and use of more effective light trapping techniques (Garnett and Yang 2010).

Over the last 60 years, the solar industry has focused on increasing the efficiency of sunlight conversion into electrical energy, leading to characteristic changes in solar cell architecture over time. Incorporation of boron and phosphorous diffusions in the 1950s led to the first significant improvement of efficiencies whereas the 1980s and 1990s introduced more complex cell structures, in particular the PERC and PERL solar cells, with the PERL cell reaching an impressive efficiency of 25% in 1999 (Zhao et al. 1999). This 25% efficiency was defined as the limit for single junction silicon cells and so over the next 15 years, interests changed from improving efficiency to scalability and lowering costs (Smith et al. 2014). However, to solve the challenge of high efficiencies as well the viability of implementation on a larger scale, new solar cell technologies were sought after, and multi-junction solar cells were developed and will be discussed in more detail in this chapter (Smith et al. 2014). The periods in which significant advancement in the silicon solar cell was made show a greater output of research publications in the field. The substantial increase in publications in the 1980s compared to the 1970s can be attributed to the development of the passivated emitter cells that increased the efficiency of solar cells immensely (Fig. 4.3). However, the considerable rise in the number of publications in the last 8 years can be accredited to the development of new solar cell technologies, including multi-junction, dye-sensitized, and perovskite solar cells.

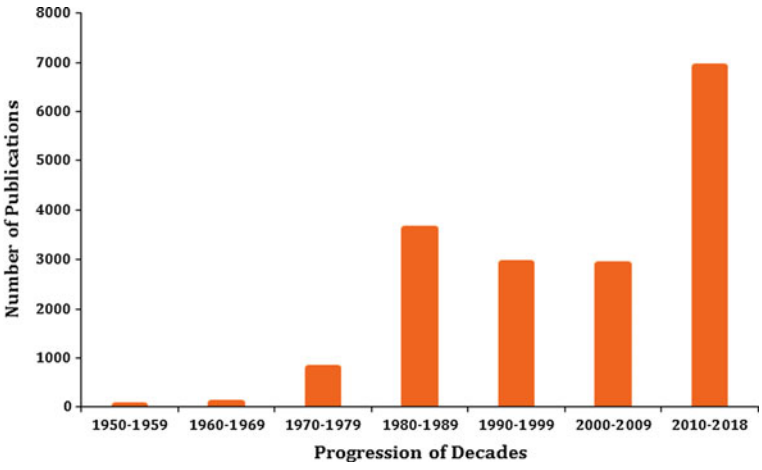


**Fig. 4.3** A graph representing the number of publications for the search item "silicon solar cells" in SciFinder for each decade until June 2018 since the first useful cell was discovered

### 4.2.2 *Fabrication of a Silicon Solar Cell*

A silicon solar cell is a device that converts energy from the sun into electrical energy. Through the absorption of light, excitation of an electron in the valence band to a higher energy state is instigated, thus creating an electron–hole pair; these are free to migrate and will recombine when they are in the close vicinity of one and other (Lincot 2017). In the presence of an electric field, however, the electrons and holes will be separated preventing recombination, with the electrons moving toward a positive electrode and holes toward a negative electrode. This produces a potential difference known as an open circuit and when the electron–hole pairs recombine in the external circuit, current flows. An electric field can be built in by use of a p–n junction. Diffusion of an electron donor into the silicon produces an n-type region while doping an electron acceptor into silicon will create a p-type region, the p–n junction lies between these two regions. Due to the n-type region displaying a negative charge and the p-type region displaying a positive charge, an electric field is produced.

The basic structure of a solar cell is shown in Fig. 4.4 (Green 2000). Light enters the cell by passing through the gaps in the top contact metal. The solar cell serves as a "quantum device, exchanging photons for electrons" (Green 2000). Not all photons reaching the cell will promote an electron, some photons will be reflected by the cell surface or are absorbed by the metal contact. Strategies such as antireflective coatings and the use of thin layers of metal can help the cell to absorb a higher percentage of photons. Following this, the p–n junction described earlier

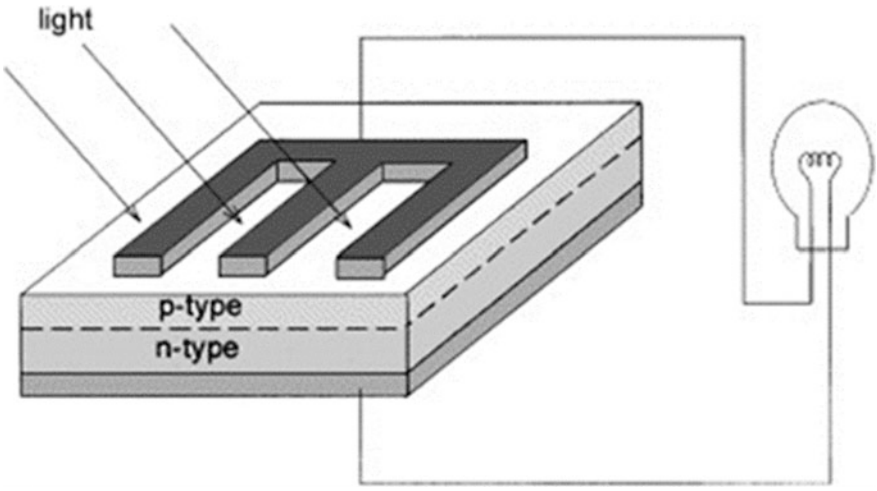


**Fig. 4.4** Illustration of light passing through the top contact metal in a basic solar cell which utilizes a p-n junction to produce an electrical current. Reprinted with permission from Green (2000). Copyright (2000) Elsevier

ensures the separation of the newly produced electrons and holes, guiding the electrons into the external circuit, which produces an electrical current (Green 2000).

For the use of silicon in photovoltaic cells, silicon is first extracted from quartz and then processed to an "ultrahigh purity" before being melted. The melted silicon is drawn into a large cylindrical crystal or "ingot" and then sliced into wafers of silicon (Green 2000). Subsequent steps in the process etch the silicon wafer surface with chemicals to ensure damage produced when slicing is removed. Following the removal of the damage, the wafer surface is etched again at different rates and directions leaving pyramid type shapes on the surface which help to minimize the reflection of photons and maximizing photon absorption (Fig. 4.5) (Green 2000). P-type impurities such as boron, introduced during silicon crystal growth are present in the wafer before etching (Green 2000). Heating the P-type wafer in the presence of an n-type impurity, such as phosphorous, produces an n-type material, creating the p–n junction (Green 2000). Finally, top and bottom contacts are applied to the solar cell, followed by the addition of any desirable features, such as an antireflective coating. An upper theoretical limit for the efficiencies of silicon solar cells with p–n junctions can be calculated, named the Shockley–Queisser efficiency limit (Shockley and Queisser 1961). However, cells do not reach their maximum efficiencies due to a series of loss mechanisms decreasing the performance of the cell; these mechanisms include blackbody radiation, optical losses, recombination, and parasitic resistive losses (Rose et al. 2013). Blackbody radiation is a loss mechanism that affects any object above 0 K. Optical losses are associated with the

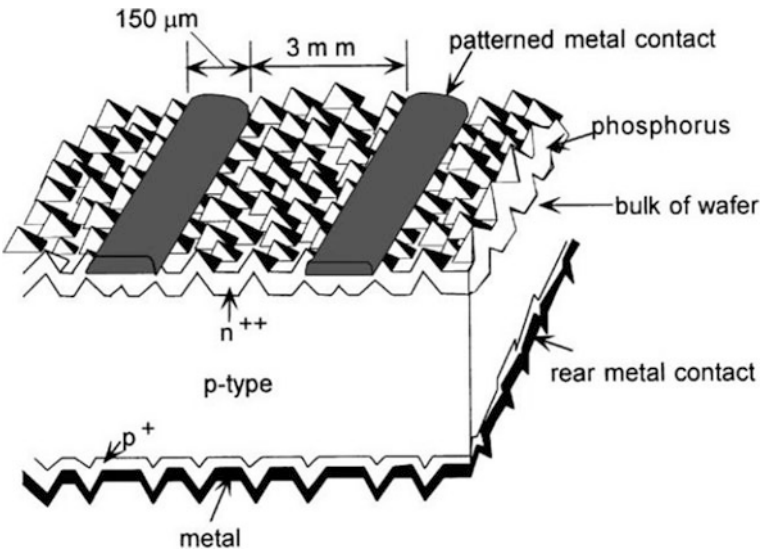


**Fig. 4.5** Illustration of a typical silicon commercial textured surface. Reprinted with permission from Green (2000). Copyright (2000) Elsevier

decrease in the number of photons absorbed into the cell. Factors like reflection of photons on the cell surface, transmission losses by captured photons escaping the cell, and area losses from the front metal contact causing shading preventing absorption of photons contribute to the reduction of photons absorbed (Rose et al. 2013). Efficiency loss caused by recombination is described by the number of electron–hole pairs that recombine within the cell before reaching the p–n junction and separating to the different cell contacts, whereas resistive losses are generated by the existence of "shunt and series resistance effects" (Rose et al. 2013). To achieve higher efficiencies, a number of techniques can be employed. As mentioned earlier, the use of etching in different directions and rates can cause a textured surface, minimizing reflection of photons (Green 2000). Using boron-doped silicon as the starting material can lead to severe degradation of minority carrier lifetimes. Reduction of the degradation can be achieved by use of thinner silicon wafers and decreasing boron concentration (Glunz 2006). The use of surface passivation using a dielectric layer was incorporated in the first silicon cell achieving over 20% efficiency, these being the PERC and PERL cells. Surface passivation allowed the reduction of recombination of electron–hole pairs, improving the efficiencies of solar cells at the time remarkably (Blakers et al. 1989).

### *4.2.3 Crystalline Versus Amorphous Silicon Solar Cells*

Silicon is still primarily used for the fabrication of solar cells today due to a number of factors including its considerable abundance in nature and relatively high and stable conversion efficiencies (Blakers et al. 2013). Declining costs and increasing efficiencies can be accredited to the development of techniques which help in the maintenance of high minority carrier lifetimes, reduction of recombination of electron–hole pair and minimization of optical losses (Blakers et al. 2013). Crystalline silicon is the dominant material with the highest cell stabilities and efficiencies, with a Shockley–Queisser limit of 29% (Blakers et al. 2013). First-generation monocrystalline silicon has a bandgap of 1.12 eV corresponding to 1160 nm (near-infrared radiation) (Battaglia et al. 2016). A bandgap of this value coincides well with the solar spectrum (Battaglia et al. 2016).

The solar cells developed by Chapin et al. and Mandelkorn et al., with efficiencies of 6 and 10%, respectively, were made from monocrystalline silicon (Chapin et al. 1954; Mandelkorn et al. 1962). Passivated emitter silicon solar cells, **PERC** (Blakers et al. 1989), **PERL** (Wang et al. 1990; Zhao et al. 1998), and **PERL FZ** (Zhao et al. 1999) with increased efficiencies of 22–25%, also made use of monocrystalline silicon. Panasonic developed a HIT® solar cell in 2014 achieving an efficiency of 25.6% with a cell area of 143.7 $cm^2$ (com/global/press/data/ 2014). Monocrystalline silicon solar panels are the most inert and stable thus increasing the lifetime warranty and are more space efficient due to higher power outputs. However, crystalline silicon's bandgap is indirect, requiring a thick layer of silicon to allow the absorption of the full solar spectrum (Bruton 2002). Therefore,

the main concern about the crystalline solar cells is the inflated costs associated with their production, resulting in multi-crystalline alternatives, beginning to increase in popularity.

Production of multi-crystalline silicon differs from monocrystalline by allowing molten silicon to cool rather than drawing it into a large cylindrical crystal. This cooling forms crystal defects on the surface of silicon. However, efficiencies of multi-crystalline silicon solar cells are lower than those found for monocrystalline cells due to the defects formed upon formation decreasing the absorption of light. By texturing the surface, efficiencies of multi-crystalline solar cells are increasing with the added benefit of lower costs. Green et al. were able to produce a multi-crystalline solar cell with a laboratory efficiency of 19.8%, etching the surface to form a hexagonally symmetrical honeycomb surface texture compared to the pyramid type shapes on the surface of monocrystalline silicon solar cells (Green 2000; Zhao et al. 1998). Texturizing the surface in this way reduced the reflection of photons and trapped absorbed light, decreasing optical losses, therefore increasing efficiency (Zhao et al. 1998). The development of multi-crystalline silicon cells was at the forefront of solar cell research for the next decade, achieving mass-produced solar cells with efficiencies of up to 17.5% in 2015 and 18.2% in 2017 (Lin et al. 2015; Jiang et al. 2017).

A newer technology used in the production of solar cells is the incorporation of amorphous silicon. Fabrication of these solar cells can be completed at lower temperatures leading to lower cost substrate materials, such as glass. This fact, alongside the ability to use ultrathin layers of silicon, signify the cost of these cells low in comparison to monocrystalline cells (Rech and Wagner 1999). The first amorphous silicon solar cell produced by Carlson and Wronski, mentioned previously, was cheaply and simply fabricated using noncrystalline silicon deposits with p–n dopants (Carlson and Wronski 1976). However, efficiencies only reached 2.4%, and the bandgap for these amorphous cells was found to be 1.7 eV (Cheng et al. 2012). A high bandgap can result in light-induced degradation, so in general, amorphous silicon solar cells have the lowest stability of all the silicon solar cells, giving them the shortest lifetime warranty. Development of the *a*-SiC:H solar cell showed improvements in efficiency, increasing to 8% in 1982 (Tawada et al. 1982). By 2014, efficiencies only increased to 10.2%, confirming the difficulties that amorphous silicon cells have in achieving good cell efficiency. However, a different class of thin-film photovoltaics known as a CIGS cell, a semiconductor material composed of copper indium gallium and selenium, has achieved efficiencies of 19.9% (Repins et al. 2008). This fact allows for the development of more efficient but cost-effective thin-film solar cells.

There are numerous advantages and disadvantages for each class of silicon solar cell. Higher efficiency and stability alongside the higher manufacturing costs of monocrystalline silicon solar cell devices make them suitable for use in space, whereas multi-crystalline cells with slightly lower efficiencies but more affordable prices increase their popularity for the use in terrestrial applications. Amorphous cells are considerably behind the previous classes of silicon solar cells in terms of efficiency, but their much cheaper and simpler fabrication methods will allow for

easier large-scale implementation and potential to rival costs of fossil fuels. A range of silicon solar cells and their module efficiencies are tabulated in Table 4.1. These results emphasize the difference in efficiencies across the range of different classes of silicon solar cells.

**Table 4.1** Confirmed terrestrial module efficiencies under the global AM1.5 spectrum (1000 W/$m^2$) at a cell temperature of 25 °C

| Class[a] | Eff.[b] (%) | Area ($cm^2$) | $V_{OC}$ (V) | $J_{SC}$ (mA/$cm^2$) | FF[c] (%) | Test center[d] (date) |
|---|---|---|---|---|---|---|
| Si (thin-film *a*-Si) (Carlson and Wronski 1976) | 2.4 | 3.5 | 0.8 | 22 | <45 | RCA (2/76) |
| Si (thin-film *a*-SiC:H/*a*-Si:H) (Tawada et al. 1982) | 8 | 1 | 0.88 | 15.2 | 62.4 | Osaka (1/82) |
| Si (*c*-PERC cell) (Blakers et al. 1989) | 22.8 | 0.2 | 0.7 | 40.3 | 81.4 | SPL-JMRC (9/89) |
| Si (*c*-PERL cell) (Wang et al. 1990) | 24.2 | 4 | 0.7 | 42.9 | 81 | SNL (8/90) |
| Si (a-Si:H) (Wakisaka et al. 1997) | 8.9 | 1 | 0.85 | 16.1 | 65 | Sanyo (/97) |
| Si (*a*-Si:H) (Yang 1998) | 9.2 | 0.25 | 0.95 | 15 | 64 | USSC (11/98) |
| Si (*c*-PERL cell) (Zhao et al. 1998) | 24.4 | 4 | 0.7 | 42 | 83.6 | SNL (10/98) |
| Si (*mc*-Si) (Zhao et al. 1998) | 19.8 | 1 | 0.65 | 38.1 | 79.5 | SNL (10/98) |
| Si (*c*-PERL FZ) (Zhao et al. 1999) | 24.7 | 4 | 0.71 | 42.2 | 82.8 | SNL (10/99) |
| Si (amorphous) (Meier et al. 2004) | 9.5 | 1 | 0.86 | 17.5 | 63 | NREL (4/03) |
| Si (*mc*-Si) (Schultz et al. 2004) | 20.4 | 1 | 0.66 | 38 | 80.9 | NREL (5/04) |
| CIGS (Repins et al. 2008) | 19.9 | 0.4 | 0.69 | 35.5 | 81.2 | NREL (11/07) |
| Si (*a*-20 μm nanowire) (Garnett and Yang 2010) | 5.3 | 0.002 | 0.52 | 16.8 | 60.7 | California (1/10) |
| Si (*mc*-Si) (Green et al. 2012) | 18.5 | 14,661 (ap)[e] | – | – | 76.2 | FhG-ISE (1/12) |
| Si (*mc*-Si) (Verlinden et al. 2014) | 20.8 | 243.9 | 0.66 | 39 | 80.3 | TrinaSolar (11/14) |
| Si (amorphous) (Matsui et al. 2013) | 10.2 | 1 | 0.89 | 16.3 | 69.8 | AIST (7/14) |
| Si (*c*-HIT®) (Panasonic 2014) | 25.6 | 143.7 | 0.74 | – | 82.7 | Panasonic (4/14) |

(continued)

**Table 4.1** (continued)

| Class[a] | Eff.[b] (%) | Area ($cm^2$) | $V_{OC}$ (V) | $J_{SC}$ (mA/$cm^2$) | FF[c] (%) | Test center[d] (date) |
|---|---|---|---|---|---|---|
| Si (*mc*-Si) (Lin et al. 2015) | 17.5 | – | 0.62 | 87.6 | 78.1 | −0.0666667 |
| Si (*c*-HIT®) (Panasonic 2018) | 23.8 | 11,562 (ap)[e] | 0.54 | – | 81.6 | Panasonic (2/16) |
| Si (*mc*-Si) (Benick et al. 2017) | 21.9 | 4 | 0.67 | 40.76 | 79.7 | FhG-ISE (2/17) |
| Si (*c*-silicon) (Yoshikawa et al. 2017) | 26.7 | 79.0 (da)[f] | 0.74 | 42.7 | 84.9 | AIST (3/17) |
| Si (*mc*-Si) (Jiang et al. 2017) | 18.2 | 15.6 | 0.64 | 35.8 | 79.7 | Nanjing (8/17) |

[a]*a* = amorphous, *c* = monocrystalline, *mc* = multi-crystalline. [b]Eff. = power conversion efficiency (PCE). [c]FF = fill factor. [d]SPL-JMRC = Solar Photovoltaic Laboratory, Joint Microelectronics Research Centre; SNL = Sandia National Laboratories; USSC = United Solar Systems Corporation; AIST = Japanese Institute of Advanced Industrial Science and Technology, FhG-ISE = Fraunhofer Institut fur Solare Energiesysteme. [e]ap = aperture area. [f]da = designated illumination area

## 4.3 Multi-junction Solar Cells

The highest efficiencies to date have been achieved by multi-junction solar cells, composed of compounds of elements in groups III and V to produce a III–V multi-junction solar cell (Phillips et al. 2012). Stacking a variety of solar cells composed of different III–V semiconductors containing multiple p–n junctions with distinct size bandgaps, thus allowing the solar cell to absorb a broader spectral range, and thus increasing the overall efficiency of the cell. For efficient stacking, the material with the highest bandgap should be placed on top, with decreasing bandgap size descending the solar cell, this allows for wavelengths of light corresponding to smaller bandgaps to pass through the cell until the suitable material is reached (Phillips et al. 2012). A solar cell containing a variety of bandgaps will allow for a higher proportion of the solar spectrum to be absorbed by the cell. Figure 4.6a shows the bandgaps for a triple-junction solar cell composed of GaInP, GaInAs, and Ge. These materials have a variety of bandgaps, resulting in the majority of the solar spectrum being absorbed by the multi-junction solar cell, leading to higher efficiencies. The maximum efficiencies that can be achieved for 1, 2, 3, and 36 junctions are 37, 50, 56, and 72%, respectively, overtaking those of silicon solar cells by a substantial measure (Henry 1980). Three layers of semiconductor materials are the most popular approach in the production of multi-junction solar cells, balancing the practicality of fabrication and efficiency (Wolf 1960).

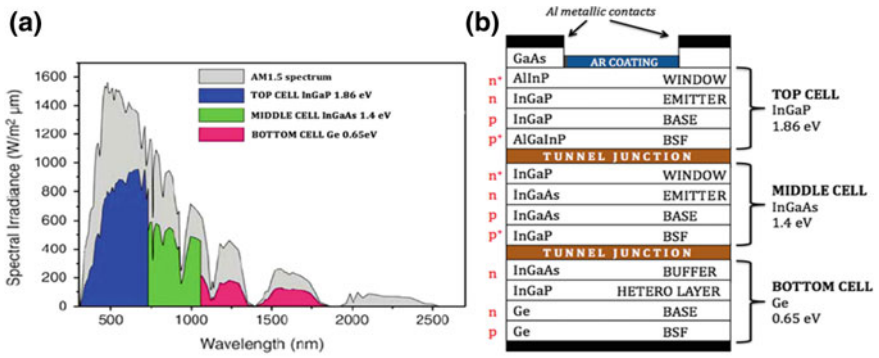


**Fig. 4.6** **a** Graph of solar AM1.5 spectrum shown together with the maximum electricity conversion efficiency for every junction as a function of the wavelength. **b** The structure of an MJ solar cell. There are six important types of layers: p–n junctions, back-surface field (BSF) layers, window layers, tunnel junctions, antireflective coating, and metallic contacts. Figure courtesy, Ncouniot—Fraunhofer Institute for Solar Energy Systems, January 2010, CC BY-SA 3.0

### 4.3.1 Fabrication of a Multi-junction Solar Cell

In general, III–V multi-junction solar cells are assembled via an epitaxial monolithic stack, with each sub-cell of different semiconductor material connected by tunnel junctions. To allow the ordered growth of crystals, each material being used must have compatible crystal lattice constants to create lattice-matched devices (Friedman 2010). However, if the lattices contain a small amount of mismatch, a metamorphic solar cell is made. More mismatch can cause crystal defects and therefore degradation of electronic properties. To fabricate these devices, the entire device must contain materials with similar atomic structures, ensuring similar atomic spacing and crystal lattice constants (Cotal et al. 2009). As well as this, the materials used should be of high quality to ensure efficient collection of electrons and holes. Inactive layers, such as front and back passivation layers, within the structure should be present with larger bandgaps, to help decrease recombination (Cotal et al. 2009). Lastly, the use of tunnel junctions is essential to interconnect each sub-cell in the device in the forward/backward bias, window layers to reduce surface recombination, and a back-surface field (BSF) to reduce scattering of carriers toward the tunnel junction (Fig. 4.6b) (Cotal et al. 2009).

### 4.3.2 Production Issues

Monolithic devices are connected in series as they only have contacts at the top and the bottom of the cell. The cell being in a series setup dictates that the current density of a multi-junction solar cell is limited by the sub-cell which produces the

lowest individual current (Bonnet-Eymard et al. 2013; Liao et al. 2013; Feng et al. 2014). It is of extreme importance that the photocurrent of each sub-cell in a multi-junction solar cell is matched to prevent the performance of the device being impacted (Bonnet-Eymard et al. 2013; Liao et al. 2013; Feng et al. 2014).

Several factors affect the photocurrent in each sub-cell, including the material and its associated absorption coefficient and the thickness of the sub-cell (Warmann et al. 2011; Yastrebova 2007). Therefore, sub-cells which exhibit higher absorption coefficients must be made thinner to bring their photocurrent in line with sub-cells with lower absorption coefficients (Warmann et al. 2011; Yastrebova 2007).

Another crucial factor to consider when producing monolithic multi-junction solar cells is that each layer is grown on top of each other. It is therefore important that the lattices of each adjacent layer are matched, as failure to do so can lead to lattice strain and dislocations which impact on the cell's efficiency (Yastrebova 2007). In order to achieve lattice matching in monolithic multi-junction solar cells, metal organic chemical vapor deposition (MOCVD) techniques are most commonly implemented (Schmieder et al. 2011). This technique has led to solar cells with the highest efficiencies, such as 40.8% (Geisz et al. 2008), however, it becomes expensive upon upscaling (Schmieder et al. 2011).

The requirement to achieve lattice matching has limited the possible number of material combinations when growing a multi-junction solar cell. This has often meant that semiconductors with optimum bandgaps have not been coupled (Garcia et al. 2016). More recently, however, the emergence of efficient lattice-mismatched (metamorphic) multi-junction solar cells has led to research into the coupling of semiconductors with slightly different lattice constants, such as in a GaInP/GaInAs/Ge cell, achieving an 40.7% efficiency, thus, allowing more favorable bandgap absorbers to be combined (King et al. 2007).

When choosing the potential materials for multi-junction solar cells, the former must have the properties which allow the device to achieve high optical performance. High-quality optical materials generally have high absorption coefficients as to absorb all incoming light (a property which silicon does not display) (Connolly et al. 2013; Steiner et al. 2013). For multi-junction solar cells to be most efficient, it is important that the material exhibits both high minority charge carrier lifetime and mobility (Steiner et al. 2013; Xuan 2011). The effect of increasing the lifetime and mobility of minority charge carriers is that long diffusion lengths are ensured, indicating that all the charges produced from the incident photons can reach the depletion region, thus, increasing efficiency (Xuan 2011). Achieving these optimum characteristics demands that high-quality materials and fabrication methods must be employed leading to a high cost of production.

### *4.3.3 Examples of Multi-junction Solar Cells*

Multi-junction III-V cells containing crystalline semiconductor sub-cells are natural candidates as they contain bandgaps ranging over the optimal values for absorption

of the solar spectrum. The first multi-junction solar cell consisted of AlGaAs and GaAs with two p–n junctions. Fabrication of the first multi-junction cell was successful, however, at 9%, the efficiency was too low to be practical (Bedair et al. 1979). To improve efficiency, insertion of a window layer and use of materials with more favorable bandgap combinations were adopted. An example of a higher performing multi-junction cell is the GaInP/GaAs cell (Bertness et al. 1994). In 1994, Olsen et al. developed a two-junction solar cell containing $Ga_{0.52}In_{0.48}P$ (GaInP) as the top cell, connected to the bottom cell, GaAs, via a tunnel junction. An antireflection coating of ZnS and $MgF_2$ was also used, with the cell achieving an efficiency of 29.5% (Bertness et al. 1994). The efficiency of this cell was improved in 1996 by the introduction of a double heterostructure InGaP tunnel junction, surrounded by high bandgap AlInP barriers (Fig. 4.7) (Takamoto et al. 1997).

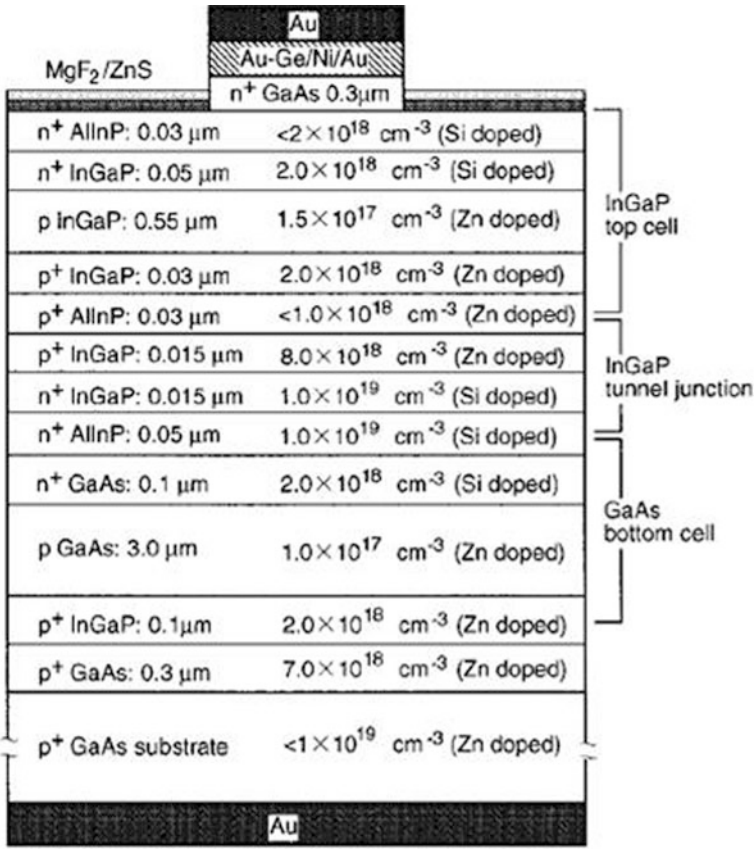


**Fig. 4.7** Illustration of an InGaP/GaAs cell with an InGaP tunnel junction surrounded by AlInP layers. Reprinted with permission from Takamoto et al. (1997). Copyright (1994) AIP Publishing

The inclusion of these features allowed an increase in the peak current of the tunnel junction, effective reflection of minority carriers in the top cell and reduction in absorbance losses, leading to an efficiency above 30% (Takamoto et al. 1997). InGaP materials have a bandgap of 1.9 eV, allowing wavelengths corresponding to smaller bandgaps to pass through, making it suitable for use as the top cell in multi-junction solar cells (Feng et al. 2014). The AlInP layer prevented Zn diffusion from the tunnel junction, increasing efficiency of the top cell, whereas the InGaP tunnel junction helped eliminate absorption losses, increasing efficiency of the bottom cell (Takamoto et al. 1997). One of the first three-junction solar cells contained $In_{0.49}Ga_{0.51}P/In_{0.01}GaAs/Ge$ using a C-doped AlGa/Si-doped InGaP tunnel junction. Such solar cells have reached efficiencies of 31.2% (Takamoto et al. 2000).

Concentrator photovoltaics became of interest with the use of multi-junction solar cells in the early 2000s achieving efficiencies far beyond those achievable by solar cells without them. Concentrator photovoltaics aim to use concentrating optics to reduce the area of the cell, therefore allowing the use of higher quality materials to produce solar cells with higher efficiencies but at lower costs (Last accessed May 29, 2018). Lenses and curved mirrors are used to direct sunlight onto the small cell, increasing the amount of sunlight reaching the cell, hence increasing efficiency (Fig. 4.8) (Last accessed May 29, 2018). An example a concentrator cell with high efficiencies is shown in the research of King et al. in 2007, when a GaInP/GaInAs/Ge concentrator cell led to an efficiency of 40.7% (King et al. 2007). To achieve more efficient solar cell structures, improved bandgap combinations are required.

**Fig. 4.8** Illustration of a parabolic disk concentrator solar cell, some specification: diameter 8.5 m, aperture 56.7 $m^2$, and average concentration factor 2500. Photo courtesy: Schlaich Bergermann and Partner

This fact means that the use of lattice mismatching in solar cells is becoming more popular, forming metamorphic multi-junction solar cells with low crystal defects (Geisz et al. 2008). Both lattice-matched (InGaP/InGaAs/Ge) and metamorphic cells (GaInP/GaAs/GaInAs) have been found to reach efficiencies of 42 and 44.4%, respectively (Guter et al. 2011; Dimroth et al. 2016). To compare efficiencies of a cell with and without concentrators, an inverted triple-junction solar cell, InGaP/GaAs/InGaAs, was used. An efficiency of 43.5% was achieved with concentrators for a 0.2 $cm^2$ sized cell, compared to an efficiency of 37.7% without concentrators, with a larger area of 1.0 $cm^2$ (Sasaki et al. 2013).

New research into multi-junction solar cells has led to the development of the next generation of highly efficient photovoltaic devices, four-junction solar cells. The world record for sunlight conversion into electrical energy is 46% (see Table 4.2) (Fraunhofer ISE 2014). This four-junction cell used in concentrator photovoltaics employs the use of Fresnel lenses to concentrate sunlight onto the cell (Fraunhofer ISE 2014).

**Table 4.2** Confirmed terrestrial module efficiencies under the global AM1.5 spectrum (1000 W/$m^2$) at a cell temperature of 25 °C

| Class[a] | Eff.[b] (%) | Area ($cm^2$) | $V_{OC}$ (V) | $J_{SC}$ (mA/$cm^2$) | FF[c] (%) | Test center[d] (date) |
|---|---|---|---|---|---|---|
| AlGaAs/GaAs (Xuan 2011) | 9.0 | – | 2.0 | 7.0 | 70.0 | NCU (11/78) |
| GaInP/GaAs (Bedair et al. 1979) | 29.5 | 0.25 | 2.4 | 16.4 | 88.2 | NASA (6/94) |
| GaInP/GaAs (Bertness et al. 1994) | 30.3 | 4.0 | 2.5 | 67.4 | 88.1 | NSDA (11/96) |
| InGaP/InGaAs/Ge (Takamoto et al. 1997) | 31.2 | 5.0 | 2.4 | 38.3 | 84.2 | JEC (9/00) |
| GaInP/GaInAs/Ge-*conc* (Garcia et al. 2016) | 40.7 | 0.27 | 2.9 | 15.96 | 87.5 | Sprectrolab (4/07) |
| GaInP/GaInAs/Ge-*conc* (Geisz et al. 2008) | 40.8 | 0.1 | 3.3 | – | 88.4 | NREL (8/08) |
| InGaP/GaAs/InGaAs (Sasaki et al. 2013) | 37.5 | 1.0 | 3.0 | 14.56 | 85.5 | AIST (2/12) |
| InGaP/GaAs/InGaAs-*conc* (Sasaki et al. 2013) | 43.5 | 0.2 | 3.5 | – | 87.0 | AIST (2/12) |
| GaInP/GaAs;GaInAsP/GaInAs (Fraunhofer ISE 2014) | 46.0 | 0.05 | 4.2 | – | 85.1 | AIST (10/14) |
| GaInP/GaAs/GaInAsP/GaInAs (NREL 2014) | 45.7 | 0.09 | – | – | – | NREL (9/14) |
| GaInp/GaInAs/Ge; Si (Green et al. 2015) | 40.6 | 0.05 | – | – | – | NREL (4/16) |

[a]*conc* = concentrator cell. [b]Eff. = power conversion efficiency (PCE). [c]FF = fill factor. [d]NCU = North Carolina University; NASA = NASA Lewis Research Centre; NSDA = National Space Development Agency; JEC = Japan Energy Corporation; NREL = National Renewable Energy Laboratory; AIST = Japanese Institute of Advanced Industrial Science and Technology. [e]ap = aperture area

Although multi-junction solar cells show extremely high efficiencies compared to other classes of photovoltaic cells, the cost of production is too high (15–23 $ panel cost per watt) (Solar Energy For Us 2018) to compete with other sources of electricity for terrestrial uses (Paquette et al. 2016). Current applications involve use in satellites as these high efficiencies are essential and can only be afforded by the wealthiest aerospace companies. Concentrator photovoltaic cells have higher costs than thin-film and silicon photovoltaic cells, which only cost 1.1–1.4 $ (Solar Energy For Us 2018), 0.8–0.9 $ (Solar Energy For Us 2018), and 0.45–0.53 $ (Solar Energy For Us 2018) for crystalline, multi-crystalline, and amorphous silicon solar cells, respectively. These high concentrator cell costs are due to the increased cost of the internal optical devices and the incorporated tracking system to follow the most intense sunlight (Vossier et al. 2012). The number of research papers published in recent years for multi-junction solar cells is significantly less than the number that was published on silicon solar cells (Fig. 4.9). This could be attributed to the fabrication of multi-junction cells being significantly more expensive than crystalline, multi-crystalline, and amorphous silicon solar cells, leading to less research on the production of terrestrial photovoltaic cells.

Research into multi-junction cells mainly focuses on increasing the efficiency by developing the four-junction cell (Dimroth et al. 2016), and examples include the GaInP/GaAs; GaInAsP/GaInAs cell with an efficiency of 46.0% (Fraunhofer ISE 2014), or the GaInP/GaAs/GaInAsP/GaInAs cell with 45.7% efficiency (NREL 2014), optimizing bandgaps (King et al. 2012) and more recently the addition of quantum dots (Wheeldon et al. 2010). As well as increasing efficiencies of cells, the potential for reduction in multi-junction concentrator photovoltaics costs could be achieved by increasing the concentration ratio of the cells (Wheeldon et al. 2010). Even though multi-junction III-V solar cells are not currently ready to outcompete

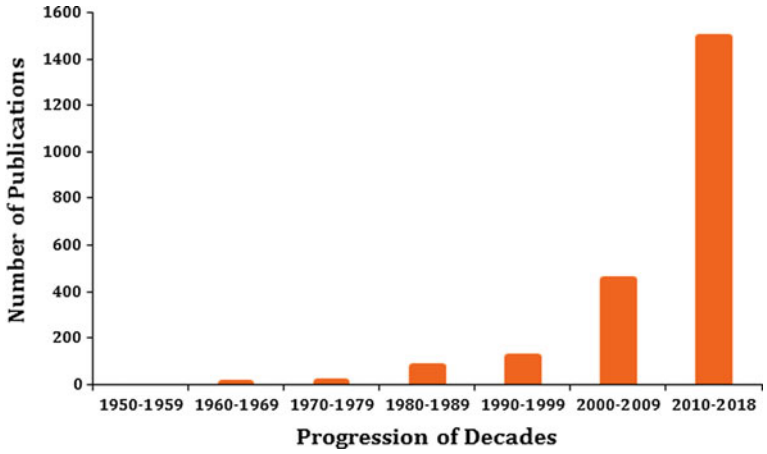


**Fig. 4.9** A graph representing the number of publications for the search item "multi-junction solar cells" in SciFinder for each decade until June 2018 since the first useful multi-junction solar cell was discovered

the use of fossil fuels and be implemented large scale, there is evidence to suggest that prices could start to decline and so could become more applicable to terrestrial uses in the future. The change in efficiencies between two-, three-, and four-junction solar cells, along with the efficiency increase by use of concentrators, can be seen in Table 4.2.

## 4.4 Perovskite Solar Cells

### *4.4.1 Background of a Perovskite*

"Perovskite" was the name the German crystallographer Gustav Rose gave to the mineral calcium titanium oxide ($CaTiO_3$) in honor of the Russian mineralogist Lev Aleksevich von Perovski, who first discovered the mineral in the Ural Mountains (Attfield et al. 2015). Today, the name perovskite relates to a wide range of materials based on the general $ABX_3$ crystalline structure of the original perovskite, $CaTiO_3$. A standard perovskite exhibits the aforementioned $ABX_3$ general formula in a three-dimensional structure of corner-sharing $BX_6$ octahedra while the A component neutralizes the overall charge (Fig. 4.10) (Eperon et al. 2014).

In typical inorganic perovskites, the A and B components can consist of most cationic metal species in the periodic table, with the A cation being significantly larger than the B cation (Fig. 4.10) (Lufaso and Woodward 2001). The X component can consist of a variety of anionic species. The most common inorganic perovskites have been oxides or fluorides; however, a diverse range of perovskites have been synthesized including oxyfluorides, sulfides, hydrides, and heavier halides (Carlson et al. 2000; Clearfield 1963; Gingl et al. 1999; Luaña et al. 1997). The first metal halide perovskites (MHPs) were synthesized as $CsPbX_3$ (X=Cl, Br, I) by reacting $PbX_2$ and CsX salts under aqueous conditions over 50 years after the discovery of $CaTiO_3$ (Wells 1893).

Given the chemical, and therefore, structural diversity of perovskite materials, their physical properties are distinct and have found a broad range of applications in material science. Perovskites have become prominent in the fields of ferroelectrics

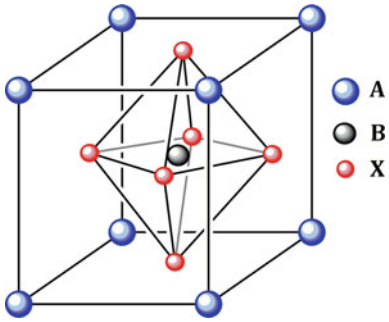


**Fig. 4.10** Illustration of the general $ABX_3$ crystal structure of a perovskite (Eperon et al. 2014)

(Attfield et al. 2015), superconductors (Attfield et al. 2015) and more recently in photovoltaics (Attfield et al. 2015).

### 4.4.2 Perovskites in Photovoltaic Devices

Perovskite solar cells are named as such due to their absorber materials exhibiting an $ABX_3$ crystal structure. The use of perovskites in solar cells is a new, although rapidly emerging field, with the research area becoming one of significant interest since the initial incorporation of perovskite compounds into photovoltaic devices in 2009 by Kojima et al. (2009). The perovskites used in photovoltaic devices are closely related to the original synthetically produced $CsPbX_3$ compounds. Variations of this structure in the earliest devices most commonly replaced caesium with an alternative organic cation as the A component of the perovskite structure. The first perovskite-containing photovoltaic devices produced by Miyasaka et al. were methylammonium lead trihalides ($CH_3NH_3PbBr_3$ and $CH_3NH_3PbI_3$) and displayed an efficiency of up to 3.8% (Kojima et al. 2009). Although the efficiency of these initial perovskite solar cells was poor, they still presented an exciting prospect within the field of photovoltaics for reasons which are discussed as follows.

One reason for the use of perovskite compounds in photovoltaic devices being of great interest is the low cost of fabrication thanks to cheap production methods coupled with readily available raw materials (Werner et al. 2018). Compared to an expensive and multistep processing of a traditional silicon solar cell which often requires high temperature (>1000 °C) in a high vacuum in laboratory special clean room facilities, the perovskite material can be synthesized in a wet chemistry and can be processed both by various solvent evaporation and vapor coating techniques (Saidaminov et al. 2015). The economic viability and simplicity of organic–inorganic perovskite photovoltaic device production methods also arise from the propensity of the compounds to self-assemble with solvent evaporation when using the low-cost production method of spin coating in dimethyl sulfoxide (DMSO) (Cheng and Lin 2010). In conjunction with the low-cost nature of perovskite photovoltaic devices, importantly, they also exhibit high defect tolerance and provide a highly tuneable bandgap across a wide spectral range, along with high $V_{oc}$ with low potential loss, the ability for charge carriers to diffuse across long distances greater than one micrometer and photon recycling (Werner et al. 2018; Unger et al. 2017; Tress 2017; Stranks et al. 2013; Pazos-Outón et al. 2016).

The organic–inorganic perovskite devices have most commonly been based on methylammonium lead trihalides $CH_3NH_3PbX_3$ (X=Cl, Br, I), with some advances in efficiency being made using the larger formamidinium cation in place of methylammonium cation to form $H_2NCHNH_2PbX_3$ perovskites, which exhibits a greater spectral absorption, up to 780 nm compared to 750 nm for the methylammonium cation (Eperon et al. 2014). More recently, the original synthetic inorganic perovskite ($CsPbX_3$) from 1892 has been used to produce perovskite photovoltaic

devices with improved optical and thermal stability compared to organic–inorganic perovskite-based devices (Beal et al. 2016; Kulbak et al. 2015); (Eperon et al. 2014b). From the initial 3.8% efficiency of Miyasaka's first perovskite solar cell, significant improvements have been made through the composition of cells which absorb a wider portion of the solar spectrum, with the best research cell achieving an efficiency of 22.7% in the NREL efficiency chart (Last accessed May 26, 2018).

### *4.4.3 Early Perovskite Photovoltaic Devices*

As previously eluded to, the first perovskite photovoltaic devices produced were done so in the laboratory of Miyasaka in 2009. The devices in question were produced by coating mesoporous $TiO_2$ films with $CH_3NH_3PbBr_3$ and $CH_3NH_3PbI_3$ perovskites, which sensitized $TiO_2$ for visible-light conversion, where $TiO_2$ acts as an n-type semiconductor (Fig. 4.11) (Kojima et al. 2009). The devices produced had a heterojunction cell architecture. The first insight into bandgap tunability in organic–inorganic perovskites was indicated in the work of Miyasaka et al., as changing the halide ion from bromide to chloride saw a marked change in the photovoltaic characteristics of the perovskite-based cells (Kojima et al. 2009).

In the $CH_3NH_3PbBr_3$ perovskite-based cell, a high open-circuit voltage ($V_{oc}$) of 0.96 V compared to the $CH_3NH_3PbI_3$ perovskite-based cell with a $V_{oc}$ of 0.61 V was found (Kojima et al. 2009). However, the efficiency of $CH_3NH_3PbI_3$ was superior at 3.81% compared to $CH_3NH_3PbBr_3$ at 3.16% (Kojima et al. 2009). The differences in photovoltaic characteristics induced by the halide used clearly indicated the highly adaptable nature of perovskite devices. The ability of perovskite materials to effectively sensitize $TiO_2$ along with the possibility of achieving high $V_{oc}$ has driven research into a large number of perovskite photovoltaic devices since 2009.

In the years following 2009, a number of further attempts were made to make use of the favorable characteristics of perovskites in solar cells. Advances were made by Park et al. when they fabricated a quantum dot-sensitized solar cell based

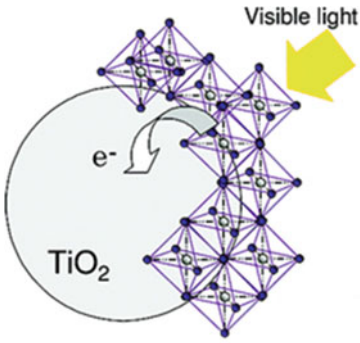


**Fig. 4.11** A $TiO_2$ film coated in nanocrystalline perovskite sensitizers ($CH_3NH_3PbBr_3$ or $CH_3NH_3PbI_3$) for visible-light conversion. Reprinted with permission from Kojima et al. (2009). Copyright (2009) American Chemical Society

on the perovskite $CH_3NH_3PbI_3$ with which an efficiency of 6.54% was achieved in 2011 (Im et al. 2011). An alternative approach in perovskite-based solar cells in which $CsSnI_3$ was utilized by Chung et al. in 2012, proved the material was an effective hole conductor in solid-state dye-sensitized solar cells with 8.5% efficiency (Chung et al. 2012).

However, the breakthrough in perovskite photovoltaic devices was made in 2012 when insulating mesoporous nanostructures such as $Al_2O_3$ with a wide bandgap of 7–9 eV was used instead of n-type $TiO_2$ (bandgap of 3.3 eV) (Lee et al. 2012; Zhan et al. 2012). The work of Snaith et al. found that using $Al_2O_3$ as an insulating scaffold for the perovskite $CH_3NH_3PbI_2Cl$ in a photovoltaic device achieved a significantly improved $V_{oc}$ of 1.1 eV and 10.9% efficiency (Lee et al. 2012). It was found that the perovskite not only acted as an absorber (as seen in sensitized $TiO_2$) cells but also as an n-type semiconductor which transferred charge out of the device in the cells investigated with $Al_2O_3$ scaffold (Lee et al. 2012). Since the $Al_2O_3$ in the devices was not an n-type oxide as the devices with $TiO_2$, these cells could no longer be termed "sensitized", but became known as "two-component hybrid solar cells" instead (Lee et al. 2012).

More recently, advances have been made in planar heterojunction perovskite-sensitized $TiO_2$ solar cells by replacing the methylammonium cation in methylammonium lead trihalides with a formamidinium cation. The larger cation indicates a smaller bandgap of 1.48 eV in $H_2NCHNH_2PbI_3$ compared to $\sim$1.57 eV in $CH_3NH_3PbI_3$, which is closer to the optimum of 1.1–1.4 eV, was present in these new cells (Eperon et al. 2014). Improvements in photovoltaic characteristics of heterojunction perovskite solar cells have been marked with the introduction of the formamidinium cation, with short current circuits of over 23 mA $cm^{-2}$ being achieved leading to efficiencies of up to 14.2% due to lowering the bandgap (Eperon et al. 2014).

### 4.4.4 *Improving Efficiency with Tandem Perovskite Solar Cells*

Organic–inorganic perovskites have become extremely important in photovoltaic cells as they are highly efficient absorbers with a high bandgap and can be simply fabricated at low cost. The production of tandem solar cells combining high bandgap materials with an optimum bandgap of 1.7–1.9 eV (organic–inorganic perovskites) and low bandgap materials with an optimum bandgap of 0.9–1.2 eV (traditional silicon solar cells and more recently low bandgap perovskites) has become a focus in the field of photovoltaics (Bailie et al. 2015; Forgács et al. 2017; Albrecht et al. 2016; Lal et al. 2014; Eperon et al. 2016; Jaysankar et al. 2018).

Fabrication of tandem solar cells can be achieved through two different architectures, mechanically stacked (four-terminal) (Fig. 4.12, left) or the monolithic (two-terminal) stacking approach (Fig. 4.12, right) (Bailie et al. 2015). Mechanical

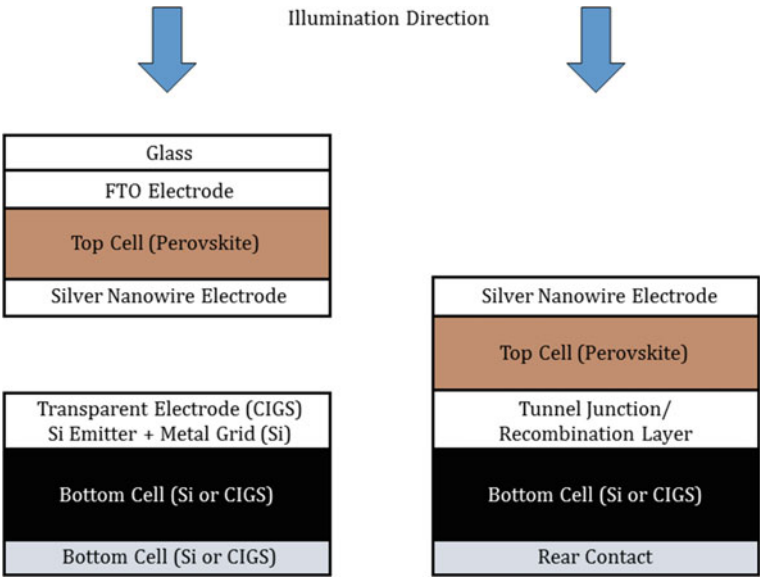


**Fig. 4.12** Illustration of a mechanically stacked (four-terminal) tandem solar cell architecture (left) and a monolithic crystalline tandem solar cell (two-terminal, right). Reprinted with permission from Bailie et al. (2015). Copyright (2015) Royal Society of Chemistry

stacking reduces the requirements for current density matching and tunnel junctions, and allows the front, high bandgap absorber to be optimized separately from rear, low bandgap absorber, meaning they have been more commonly fabricated (Bailie et al. 2015; Forgács et al. 2017). However, monolithic stacking leads to higher potential efficiencies as it reduces the number of "transparent" electrodes which can parasitically absorb light (Bailie et al. 2015).

### *4.4.5 Perovskites as a Single Absorber in a Tandem Stack*

Tandem solar cells can be fabricated through the deposition of high energy photon crystalline absorbers, such as organic–inorganic perovskites, on top of low energy photon absorbing materials, such as Si or copper indium gallium diselenide (CIGS) (Bailie et al. 2015). By combining absorbers with variable bandgaps, such as silicon (optimum bandgap 0.9–1.2 eV) (Eperon et al. 2016) and organic–inorganic perovskites (optimum bandgap 1.6–1.9 eV) (Eperon et al. 2016), the region of the spectrum absorbed can be broadened, thus, increasing the efficiency (Bailie et al. 2015). One example of a successful monolithic tandem solar cell in the initial stages of this technology is described in the work of Albrecht et al. (Albrecht et al. 2016). A combination of a $CH_3NH_3PbI_3$ front cell and a silicon heterojunction rear cell to obtain an impressive $V_{oc}$ of 1.78 V and an efficiency of 18% has been produced

(Albrecht et al. 2016). In 2015, Bailie et al. used a four-terminal configuration in which the two sub-cells are electrically isolated to obtain a 17 and 18.6% efficient tandem cell with *mc*-Si (eff. ~11%) and copper indium gallium selenide (CIGS, eff. ~17%) bottom cells, respectively (Bailie et al. 2015). In the same year, Philipp et al. obtained a 13.4% efficient tandem cell with a highly efficient *a*-Si:H/*c*-Si heterojunction bottom cell using the same configuration (Löper et al. 2015) and Mailoa et al. used a *c*-Si bottom cell in a two-terminal design to obtain a 13.7% tandem cell (Mailoa et al. 2015).

To date, the most advanced perovskite–silicon tandem solar cell in this rapidly progressing field was fabricated by a team at Interuniversity Micro Electronics Center (IMEC) in Belgium, in 2018 (Jaysankar et al. 2018). The cell made use of a complex semitransparent organic–inorganic perovskite material as the high bandgap absorber with the formula, $Cs_{0.1}(H_2NCHNH_2)_{0.9}PbI_{2.865}Br_{0.135}$ (CsFAPbIBr) (Jaysankar et al. 2018). This perovskite is a clear example of the ability to precisely tune photovoltaic characteristics by implementing small compositional alterations. As the low bandgap absorber, an integrated back contact *c*-Si solar cell was used (Jaysankar et al. 2018). By combining these efficient absorbers at opposite ends of the visible spectrum, an efficiency of 23.9% was achieved (Jaysankar et al. 2018). Although a tandem cell with an efficiency of 23.9% has been achieved in practice, it has been calculated that this exciting technology could theoretically achieve up to 35% (Lal et al. 2014; Meillaud et al. 2006).

### *4.4.6 Perovskites as Both Absorbers in a Tandem Stack*

The fabrication of tandem solar cells has become advantageous in the quest for highly efficient photovoltaic devices. However, to achieve a rear absorber bandgap in the region of 1 eV in most tandem solar cells to date, a rear absorber consisting of a silicon or a CIGS-based cell has been utilized (Bailie et al. 2015; Albrecht et al. 2016; Lal et al. 2014; Jaysankar et al. 2018). The issue associated with the inflated cost of silicon cells in many of these devices indicating that expensive fabrication costs remain problematic when considering production on a larger scale.

One promising alternative to the high-cost silicon and CIGS-based rear absorbers has come in the form of low bandgap perovskite materials, which could lead to low-cost tandem cells. Advances made in perovskite bandgap tuning have allowed perovskite–perovskite tandem solar cells to be fabricated with the low energy light absorber also consisting of a perovskite (Forgács et al. 2017; Albrecht et al. 2016). One of the cells in question was fabricated by Snaith et al. using highly tuned perovskite absorbers (Eperon et al. 2016). The front cell, with a bandgap of 1.8 eV, which absorbed high energy photons, consisted of the perovskite $(H_2NCHNH_2)_{0.83}Cs_{0.17}PbI_{1.5}Br_{1.5}$ (Eperon et al. 2016). Since solely lead-based organic–inorganic perovskites cannot be tuned to a bandgap below 1.48 eV, a novel lead–tin composite perovskite was fabricated with a bandgap of ~1.2 eV, $(H_2NCHNH_2)_{0.75}Cs_{0.25}Pb_{0.5}$ $Sn_{0.5}I_3$ as the rear, low bandgap absorber (Eperon

et al. 2016). When combined in a tandem perovskite–perovskite solar cell, this approach led to a monolithic two-terminal solar cell with a $V_{oc}$ of 1.66 eV and an efficiency of 17.0%, along with an even more efficient mechanically stacked four-terminal solar cell with an efficiency of 20.3% (Eperon et al. 2016). In 2017, Zhao et al. fabricated low bandgap ($\sim$1.25 eV) mixed Sn–Pb perovskite solar cell achieving a maximum power conversion efficiency of 17.6% (Zhao et al. 2017). This fact is attributed to the thickness of 620 nm of the cell that enables larger grains and higher crystallinity to extend the career lifetimes to more than 250 ns. This low bandgap cell reached an external quantum efficiency of more than 70% in the near-infrared wavelength range (700–900 nm). Subsequently combining this low bandgap perovskite cell at the bottom with a $\sim$1.58 eV high bandgap perovskite cell at the top, a steady-state power conversion efficiency of 21% was obtained (Zhao et al. 2017). The high efficiencies of these cells are intrinsically related to their ability to absorb light from across the visible spectrum. All-perovskite tandem cells offer the first solution-processable architecture that shows promise to surpass the efficiencies of *c*-Si, GaAs, and other expensive III–V semiconductor solar cells.

### *4.4.7 Commercial Viability*

Perovskite-based photovoltaic devices offer a lower cost alternative to the current silicon-based solar cells which dominate the market (Werner et al. 2018). In the brief period since the field of perovskite photovoltaic devices emerged in 2009, their efficiencies have seen a dramatic rise from an initial maximum efficiency of 3.81 to 23.9% in 2018 (Table 4.3) (Kojima et al. 2009; Jaysankar et al. 2018). Perovskites have been at the center of impressive advances in solar cell technology and could theoretically outperform the maximum efficiency of silicon-based cells in tandem setups (Lal et al. 2014; Meillaud et al. 2006). These advances can be attributed to the highly favorable characteristics of organic–inorganic perovskite materials including high defect tolerance, highly tuneable bandgaps, high $V_{oc}$ with low potential loss, long diffusion distances, and photon recycling (Werner et al. 2018; Unger et al. 2017; Tress 2017; Stranks et al. 2013; Pazos-Outón et al. 2016). Not only perovskite solar cells offer beneficial physical characteristics which lead to high potential efficiencies, the fact that they are easily fabricated from solution using simple techniques such as spin coating, along with the abundance of the constituent elements making them cheap to produce is highly advantageous (Werner et al. 2018).

Although perovskites are an exciting prospect in the field of photovoltaics, there are several significant drawbacks still associated with implementing them commercially. First, organic–inorganic-based perovskite solar cells are generally associated with poor stability toward humidity and oxygen, heat, light (UV), and electrical stresses (Niu et al. 2014; Leijtens et al. 2015). Rapid degradation of perovskite solar cells indicates that they cannot compete in this area with the highly

**Table 4.3** Confirmed terrestrial module efficiencies under the global AM1.5 spectrum (1000 W/$m^2$) at a cell temperature of 25 °C

| Class[a] | Eff.[b] (%) | Area ($cm^2$) | $V_{OC}$ (V) | $J_{SC}$ (mA/$cm^2$) | FF[c] (%) | Test center[d] (date) |
|---|---|---|---|---|---|---|
| Perovskite (sensitized) ($CH_3NH_3PbBr_3$) (Kojima et al. 2009) | 3.13 | 0.24 | 0.96 | 5.57 | 59.0 | TU (4/09) |
| Perovskite (sensitized) ($CH_3NH_3PbI_3$) (Kojima et al. 2009) | 3.81 | 0.24 | 0.61 | 11.0 | 57.0 | TU (4/09) |
| Perovskite (QD-sensitized) ($CH_3NH_3PbI_3$) (Im et al. 2011) | 6.20 | 0.31 | 0.63 | 16.0 | 61.7 | SU (8/11) |
| Perovskite ($Al_2O_3$) ($CH_3NH_3PbI_2Cl_3$) (Lee et al. 2012) | 10.9 | – | 0.98 | 17.8 | 63.0 | Oxford (11/12) |
| Perovskite (sensitized) ($CH_3NH_3SnIBr_2$) (Hao et al. 2014) | 5.73 | 0.1 | 0.82 | 12.3 | 57.0 | NWU (5/14) |
| Perovskite (sensitized) ($CH_3NH_3SnBr_3$) (Hao et al. 2014) | 4.27 | 0.1 | 0.88 | 8.26 | 59.0 | NWU (5/14) |
| Tandem (4 -T) ($CH_3NH_3PbI_3$:SHJ)[e], (Chen et al. 2016) | 23.0 | 0.075: 4[e] | – | – | – | UNL/ASU (7/16) |
| Tandem (2 -T) ($CH_3NH_3PbI_3$:SHJ)[e], (Werner et al. 2016) | 20.9 | 0.17 | 1.69 | 15.9 | 77.6 | EPFL/CSEM (12/15) |
| Tandem (4 -T) ($RbCs(CH_3NH_3)(H_2NCHNH_2)PbI_{3-x}Br_x$:IBC)[e], (Duong et al. 2017) | 26.4 | 0.16: 4[e] | – | – | – | ANU (4/17) |
| Tandem (2 -T) ($Cs(H_2NCHNH_2)PbI_{3-x}Br_x$:SHJ)[e], (Bush et al. 2017) | 23.6 | 1 | 1.65 | 18.1 | 79 | Stanford/ASU (2/17) |
| Tandem (4 -T) ($(H_2NCHNH_2)_{0.83}Cs_{0.17}PbI_{1.5}Br_{1.5}$: $(H_2NCHNH_2)_{0.75}Cs_{0.25}Pb_{0.5}Sn_{0.5}I_3$)[e], (Eperon et al. 2016) | 20.1 | 0.2: 0.2[e] | – | – | – | Stanford/Oxford (11/16) |
| Tandem (2 -T) ($(H_2NCHNH_2)_{0.83}Cs_{0.17}PbI_{1.5}Br_{1.5}$: $(H_2NCHNH_2)_{0.75}Cs_{0.25}Pb_{0.5}Sn_{0.5}I_3$)[e], (Eperon et al. 2016) | 16.9 | 0.2 | 1.66 | 14.5 | 70.0 | Stanford/Oxford (11/16) |
| Tandem (4 -T) ($(Cs_{0.1}(H_2NCHNH_2)_{0.9}PbI_{2.865}Br_{0.135}$: IBC)[e], (Jaysankar et al. 2018) | 23.9 | 4: 4[e] | – | – | – | Imec (3/18) |

[a]QD = quantum dot; 4 – T = four terminals; 2 – T = two terminals, SHJ = silicon heterojunction. [b]Eff. = power conversion efficiency (PCE). [c]FF = fill factor. [d]TU = Tokyo University; SU = Sungkyunkwan University; NWU = North Western University; UNL = University of Nebraska-Lincoln; ASU = Arizona State University, EPFL = Ecole Polytechnique Fédérale de Lausanne; ANU = Australian National University. [e]front cell:back cell

resilient, long lifetime silicon solar cells on the market. The device degradation due to moisture can be reduced by optimizing the constituent materials, cell architecture and cell interface, and environmental conditions during fabrication. Cells encapsulated with carbon nanotube and an inert fluorinated photopolymer have shown promise to prevent immediate degradation in a moist and elevated temperature

atmosphere (Habisreutinger et al. 2014; Bella et al. 2016). Another issue with perovskite-based photovoltaic devices is that some of the most efficient solar cells to date contain a lead component (Eperon et al. 2016; Meillaud et al. 2006). In terms of commercialization, this is a drawback due to the toxicity of lead, and although attempts have been made to fabricate lead free perovskite-based photovoltaic devices, they have not been successful in achieving efficiencies capable of competing with lead-containing devices (Table 4.3) (Noel et al. 2014; Hao et al. 2014). For perovskite-based solar cells to displace silicon as the primary solar cell on the market, their production must be reproducible over a larger surface area. Although progress has been made in scaling-up this technology, the cells produced struggle to achieve high efficiencies due to pinholes and other inhomogeneities (Razza et al. 2016). For the reasons presented, silicon solar cells still dominate the market. The $PbI_2$ residue in perovskite film has been experimentally demonstrated to have a negative effect on the long-term stability of devices (Zhang et al. 2015). The stabilization problem is claimed to be solved by replacing the organic transport layer with a metal-oxide layer, allowing the cell to retain 90% capacity after 60 days (Zhang et al. 2016; You et al. 2016). Advancements in the engineering of interfaces allowed the creation of a 2D/3D mixed perovskite, which enabled the creation of a solar cell with over 10,000 h (more than 1 year) stable performance without any loss in efficiency, pointing toward the viability of commercialization (Grancini et al. 2017). However, as the field of perovskite photovoltaic devices rapidly develops, it is not inconceivable that perovskite-based devices may one day surpass silicon solar cells as the market leader. For this reason, the number of publications published in recent years on perovskite solar cells has overtaken numbers for multi-junction solar cell publications despite the first device being fabricated in 2009 (Fig. 4.13).

## 4.5 Dye-Sensitized Solar Cells (DSSCs)

### *4.5.1 Background of DSSCs*

DSSCs are third-generation photovoltaic solar cells. Unlike conventional first-generation photovoltaic solar cells, the photoreceptor and charge carrier are implemented by different components in DSSCs like the photosynthetic system in plants where chlorophyll absorbs photons but does not participate in charge transfer kinetics. The separation of functions in light absorption and electron/hole transport leads to low demand on purity of raw materials of DSSC components, thus making them a low-cost alternative (Grätzel 2001, 2009). Despite the high efficiency associated with the first-generation silicon solar cells (efficiency $\sim$25%) and second-generation compound III-IV film solar cells, such as GaAs (efficiency $\sim$28%), CdTe (efficiency $\sim$20%), copper indium gallium selenide (CIGS, efficiency $\sim$20%), the disadvantages of high production and environment cost

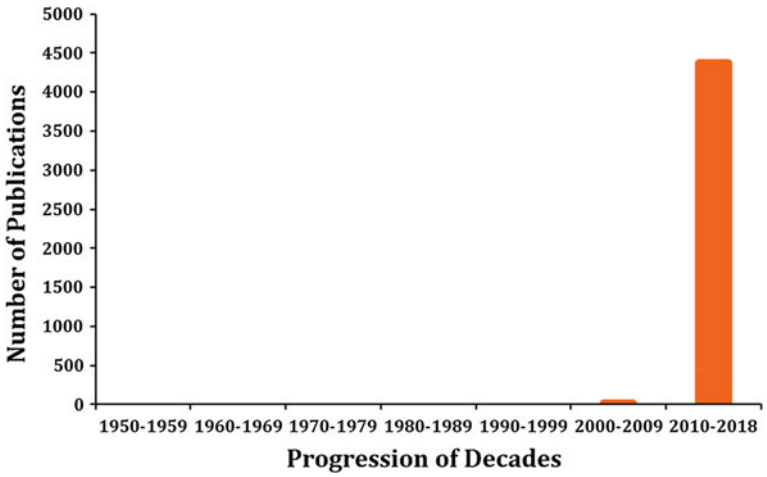


**Fig. 4.13** A graph representing the number of publications for the search item "perovskite solar cells" in SciFinder for each decade until June 2018 since the first useful perovskite solar cell was discovered

associated with these cells prompted the search for third-generation solar cells, such as DSSC, quantum dot, and perovskite solar cells. These third-generation solar cells have lower processing cost with ease of preparation, minor environmental impact, and shorter payback time. Until now, although the power conversion efficiencies (PCEs) of DSSC are lower than first- and second-generation PV solar cells, the former shows immense potential to outperform the PCEs of the later, with almost five publications coming out each day related to DSSCs (Fig. 4.14) (Wu et al. 2015; Green et al. 2014).

### *4.5.2 Operating Principle of a DSSC*

A schematic illustration of a DSSC is shown in Fig. 4.15 (Grätzel 2001; O'Regan and Grätzel 1991; Hagfeldt et al. 2010). A typical DSSC has five main ingredients. (i) Conductive indium-doped tin oxide (ITO) or fluorine-doped tin oxide (FTO) coated transparent glass anode that allows light to pass through and charge collection. (ii) A mesoporous metal-oxide layer (typically $TiO_2$, NiO) deposited on the glass as an electron transporting layer; (iii) a monomolecular layer of a dye (typically panchromatic ruthenium complexes and organic dyes) adsorbed on the surface of the mesoporous metal-oxide layer to harvest incident light, (iv) an electrolyte (usually an organic solvent containing a redox mediator, such as iodide/triiodide couple); (v) a cathode made of an ITO or FTO conductive glass sheet coated with a catalyst (typically platinum).

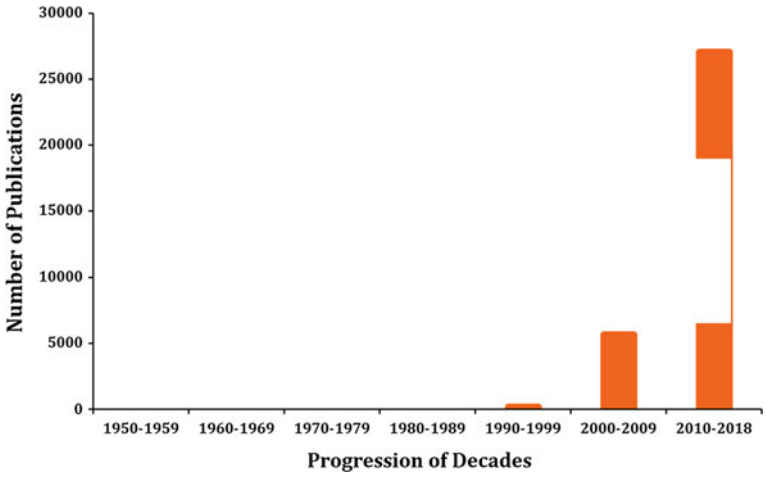


**Fig. 4.14** A graph representing the number of publications for the search item "dye-sensitized solar cells" in SciFinder for each decade until June 2018 since the first DSSC was discovered

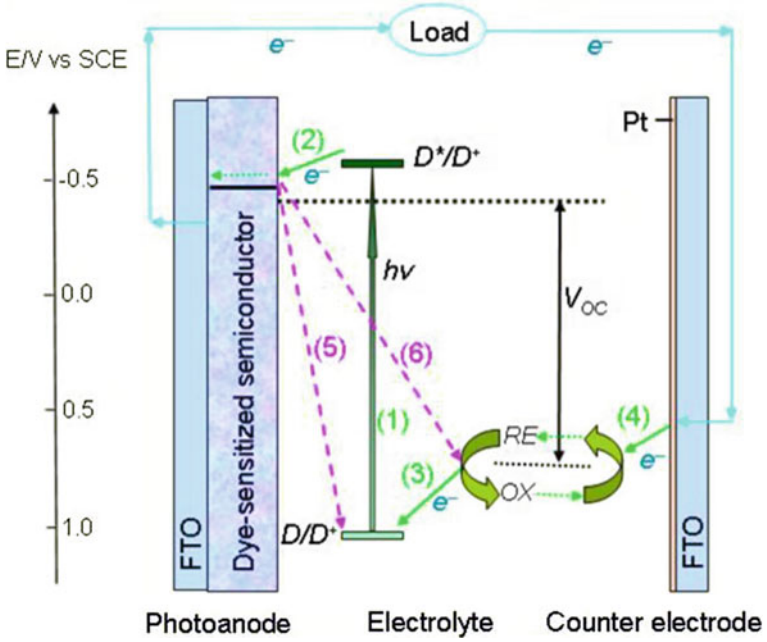


**Fig. 4.15** Operating principle of a DSSC. Reprinted with permission from Wu et al. (2015). Copyright (2009) American Chemical Society

In a typical mechanism (Wu et al. 2015), upon harvesting photons, the dye molecule (D) promotes an electron from its highest occupied molecular orbital (HOMO) to the lowest unoccupied molecular orbital (LUMO) (process 1). The LUMO of the dye injects the electron into the conduction band of the $TiO_2$ film to form oxidized dye ($D^+$) and the electron eventually drifts to the conducting anode in a timescale of $10^{-11}$ to $10^{-13}$ s (process 2). The oxidized dye ($D^+$) is then regenerated by receiving electrons from the reduced component of the redox electrolyte (RE) (timescale $10^{-6}$ s, process 3), the RE is then oxidized into the oxidized component (OX) of the redox couple. The circuit is completed when the electron in the anode from process two circulates through an external load to reach the cathode and the migrated OX is reduced back to RE at the cathode at a timescale of $10^{-5}$ to $10^{-6}$ s (process 4).

There are two competitive reactions in the entire process: (i) recombination of the electrons generated in process 1 with $D^+$ at a timescale of $10^{-4}$ s (process 5); (ii) the electrons in $TiO_2$ film are captured by OX of the redox couple, also leading to the recombination of electrons (timescale $10^{-2}$ s, process 6). Processes 5 and 6 are termed as dark reactions in a DSSC. While processes $1 - 4$ are requirements and advantageous reactions the light-to-electric conversion, the dark reactions are disadvantageous for the efficiency of DSSCs. However, due to slower reaction kinetics compared to those of processes $1 - 4$, the dark reactions do not play a remarkable negative effect.

The photovoltage generated under illumination corresponds to the potential difference between the Fermi level of the electron in the $TiO_2$ and the redox potential of the electrolyte, and the photocurrent depends on the incident sunlight harvest efficiency, charge carrier transportation, and collection efficiencies. The overall sunlight-to-electric power conversion efficiency ($\eta$ or PCE) of the DSSC is determined by the ratio of the maximum obtainable power and the intensity of the incident light. The maximum obtainable power is the product of photocurrent density measured at short circuit ($J_{sc}$), open-circuit photovoltage ($V_{oc}$), and fill factor (FF, typically between 0 and 1 and reflects the electrical (Ohmic) and electrochemical (overvoltage) losses occurring during operation of the DSSC).

The light-harvesting dye is a crucial part in a DSSC and the former should have some characteristics (Clifford et al. 2011):

(a) Panchromatic ($\lambda_{abs}$ = 300–800 nm) and optimum absorption that overlaps with that of the incident light for efficient light harvesting.
(b) Anchoring groups such as carboxylates or phosphonates which are capable of covalently bonding on the $TiO_2$ surface.
(c) Higher energy level of the LUMO of the dye than the energy of the conduction band of the $TiO_2$ for efficient electron injection and lower energy level of the HOMO of the dye than that of the redox electrolyte for efficient dye regeneration.
(d) High thermal and chemical stability of the dye.

Optimization of DSSC efficiency is addressed in a variety of ways, e.g., by designing different semiconducting metal oxides with different nanostructures (Galoppini et al. 2006), by the development of different redox electrolytes (Bai et al. 2008) and solid-state hole conducting materials (Mor et al. 2009; Snaith et al. 2007). This part of the chapter, however, will focus principally on how optimization of DSSC performance can be achieved through structural design of the dye sensitizer.

### 4.5.3 Development of Ruthenium-Based DSSCs

Efforts have been gathered to improve the PCE of DSSCs on the development of combination of new dyes, redox couples, and photoanode/cathode. The pioneering work of B. O'Regan and M. Grätzel in 1991 incorporated the first successful fabrication of a DSSC using a monolayer of a trimeric ruthenium complex $RuL_2(\mu\text{-}(CN)Ru(CN)L'_2)_2$ (L = 2,2′-bipyridine-4,4′-dicarboxylic acid; L′ = 2,2′-bipyridine) onto nanostructured $TiO_2$ films with $I^-/I_3^-$ electrolyte and Pt-FTO cathode. The absorption onset of the dye onto $TiO_2$ surface was shifted to 750 nm with the light-harvesting efficiency reading almost 100% in the whole visible region below 550 nm. The DSSC obtained an efficiency of 7.9 and 7.12% under one-tenth and full sunlight irradiation, with FFs of 0.76 and 0.685, respectively (O'Regan and Grätzel 1991). In 1993, **N3** dye [$RuL_2(NCS)_2{\cdot}2H_2O$ (L = 2,2′-bipyridyl-4,4′-dicarboxylic acid)] with $I^-/I_3^-$ electrolyte and Pt cathode was developed (see Chart 4.1 for some benchmark ruthenium-based sensitizers under discussion, unless otherwise mentioned the photocathodes used for the DSSCs are Pt-coated FTO/ITO electrodes), the spectral response of the solar cell was extended to the 800 nm, and the efficiency of the solar cell was enhanced to 10% (Table 4.4). Water contamination was found to show a detrimental effect on the PCE of the DSSC and thus the long-term stability was determined to have more than $10^7$ turnovers with respect to the dye without significant decomposition since the beginning of the illumination (Nazeeruddin et al. 1993). Indeed, this was the dye *par excellence* for many years in the field. In 2001, Nazeeruddin et al. reported the synthesis of **black dye**, **N749**, [$RuL'(NCS)_3$:3TBA (L = 2,2′,2″-terpyridyl-4,4′,4″-tricarboxylic acid; TBA = tetrabutylammonium)]. In comparison to the **N3** sensitizer, the absorption spectrum of the black dye extends up to the near IR region, with the lowest energy absorption maxima trailing up to 920 nm. Due to high extinction coefficient (molar absorptivity $\sim 6 \times 10^3$ $M^{-1}$ $cm^{-1}$ at around 610 nm) in the visible wavelength region, the incident photon to current conversion efficiency (IPCE) of 80% was obtained using medium haze $TiO_2$. The DSSC with the black dye achieved an impressive certified efficiency of 10.4%, with $J_{sc}$ = 20.5 mA/cm$^2$ and $V_{oc}$ = 0.72 V (data from NREL calibration laboratory, USA) (Nazeeruddin et al. 2001). The PCE of the **N749** dye was later improved to 11.1% by Chiba and co-workers in 2006 (Chiba et al. 2006). To address the stability of a DSSC device, in 2005, amphiphilic dye **K19** was grafted with 1-decylphosphonic acid as co-adsorbent onto

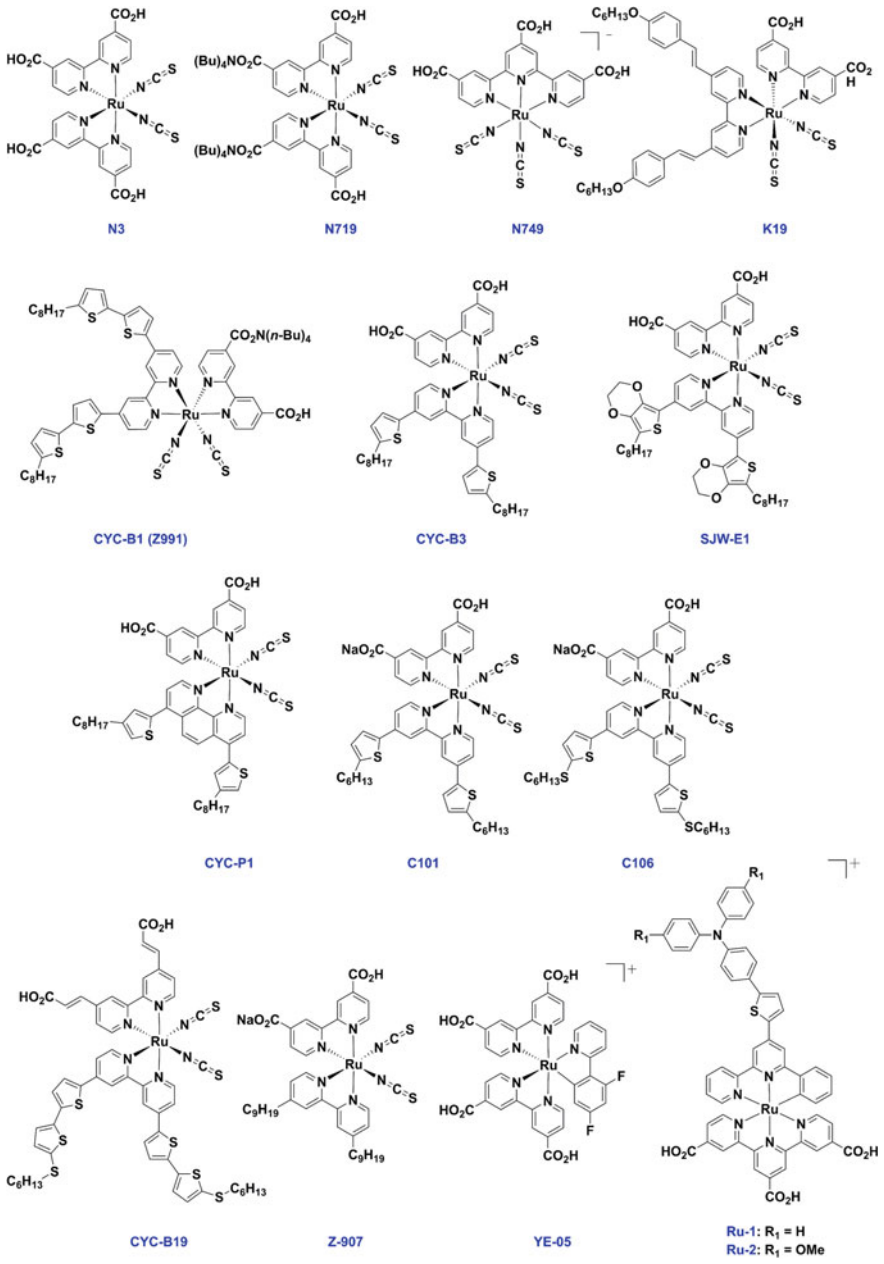


**Chart 4.1** Benchmark ruthenium photosensitizers used in DSSCs

**Table 4.4** Cell parameters of ruthenium photosensitizer-based DSSCs under the global AM1.5 spectrum (1000 W/m$^2$)

| Dye | Eff.[a] (%) | Area (cm$^2$) | $V_{OC}$ (V) | $J_{SC}$ (mA/cm$^2$) | FF[b] (%) |
|---|---|---|---|---|---|
| **N3** (under 0.556 mW/cm$^2$)[c], (Nazeeruddin et al. 1993) | 10.3 | 0.31 | 0.67 | 11.5 | 74.0 |
| **N749**[d], (Nazeeruddin et al. 2001) | 11.1 | 0.219 | 0.74 | 20.9 | 72.2 |
| **K19**[e], (Wang et al. 2005) | 8.0 | 0.158 | 0.75 | 15.1 | 69.9 |
| **CYC-B1 (Z991)**[f], (Chen et al. 2006) | 8.54 | 0.25 | 0.65 | 23.9 | 55.0 |
| **CYC-B3**[f], (Chen et al. 2007) | 7.39 | 0.16 | 0.69 | 15.7 | 70.5 |
| **SJW-E1**[f], (Chen et al. 2007) | 9.02 | 0.16 | 0.67 | 21.6 | 62.6 |
| **CYC-P1**[f], (Chen et al. 2007) | 6.01 | 0.25 | 0.64 | 14.92 | 63.0 |
| **C-101** [g], (Cao et al. 2009) | 10.33 | 0.158 | 0.75 | 17.75 | 77.7 |
| **C-106** [g], (Cao et al. 2009) | 11.29 | 0.158 | 0.776 | 19.20 | 75.9 |
| **CYC-B19** [h], (Chen et al. 2012) | 8.4 | 0.158 | 0.70 | 16.6 | 72.0 |
| **Z-907** [g], (Cao et al. 2009) | 9.05 | 0.2 | 0.73 | 17.13 | 72.4 |
| **YE-05**[i], (Bessho et al. 2009) | 10.1 | 0.152 | 0.80 | 17.00 | 74.0 |
| **Ru-1**[j], (Robson et al. 2011) | 7.13 | – | 0.67 | 14.95 | 71.0 |
| **Ru-2**[j], (Robson et al. 2011) | 8.02 | – | 0.68 | 16.74 | 71.0 |

[a]Eff. = power conversion efficiency (PCE). [b]FF = fill factor. [c]Using electrolyte = mixture of acetonitrile/NMO (90/10, v/v) [Li] = 0.3 M, [$I_2$] = 0.03 M. [d]Using electrolyte = dimethyl propyl imidazolium iodide (0.6 M), lithium iodide (0.1 M), iodine (0.05 M), and tert-butylpyridine (0.5 M). [e]Using electrolyte = 0.8 M 1-propyl-3-methylimidazolium iodide, 0.15 M $I_2$, 0.1 M guanidinium thiocyanate, and 0.5 M *N*-methylbenzimidazole in 3-methoxypropionitrile. [f]Using electrolyte = 0.5 M lithium iodide, 0.05 M iodine, 0.5 M tert-butylpyridine in acetonitrile. [g]Using electrolyte = 1.0 M 1,3-dimethylimidazolium iodide (DMII), 50 mM LiI, 30 mM $I_2$, 0.5 M *tert*-butylpyridine, and 0.1 M guanidium thiocyanate in the mixed solvent of acetonitrile and valeronitrile (V/V, 85/15). [h]Using electrolyte = 0.1 M LiI, 1.0 M 1,3-dimethylimidazolium iodide (DMII), 30 mM $I_2$, 0.5 M *tert* -butylpyridine, and 0.1 M guanidinium thiocyanate (GNCS) in the mixed solvent of acetonitrile and valeronitrile (v/v, 85/15). [i]Using electrolyte = 0.60 M butylmethylimidazolium iodide (BMII), 0.03 M I2, 0.10 M guanidinium thiocyanate, and 0.50 M *tert*-butylpyridine in a mixture of acetonitrile and valeronitrile volume ratio, 85:15 (A6141). [j]Using electrolyte = 1.0 M1,3-dimethylimidazolium iodide (DMII), 60 mM I2, 0.5 M tert-butylpyridine, 0.05 M NaI and 0.1 M GuNCS in a mixed solvent system of acetonitrile and valeronitrile (v/v, 85/15)

FTO-mesoporous $TiO_2$ surface with Pt cathode. The electrolyte contained 0.8 M 1-propyl-3-methylimidazolium iodide, 0.15 M $I_2$, 0.1 M guanidinium thiocyanate, and 0.5 M *N*-methylbenzimidazole in 3-methoxypropionitrile (Wang et al. 2005). Under AM 1.5G condition, this device showed a PCE value of 8% (Table 4.4). This device was found to maintain a strikingly stable performance under thermal stress and long-term light soaking. the $V_{oc}$ of such a device drops only by 25 mV during 1000 h of aging at 80 °C. The stabilizing effect of co-grating is attributed to the formation of a robust and compact molecular monolayer at the mesoscopic $TiO_2$ surface, stabilizing the quasi-Fermi level of the semiconductor electrode. Another key issue is the limited extinction coefficients of the sensitizers (**N3** has a molar

absorptivity of 14,500 $M^{-1}$ $cm^{-1}$ at 530 nm; **N719**, di-tetrabutylammonium analogue of **N3** dye, has a molar absorptivity of 13,900 $M^{-1}$ $cm^{-1}$ at 541 nm) (Nazeeruddin et al. 1999). This requires thick layering $TiO_2$ films (typically over 8 mm) to efficiently capture all the incident light. Thicker films result in both lower $V_{oc}$ (due to increased dark current) and lower fill factor (due to an increase in electrolyte resistance) (Clifford et al. 2011). In this regard, several amphiphilic heteroleptic ruthenium sensitizers, e.g., **CYC-B1** (**Z991**) (Chen et al. 2006), **CYC-B3** (Chen et al. 2007), **SJW-E1** (Chen et al. 2007), **CYC-P1** (Chen et al. 2007), **C101** (Cao et al. 2009), **C106** (Chen et al. 2012), **CYC-B19** (Chen et al. 2012) that contain alkyl-mono/bis-thiophene and/or phenylenevinylene moieties tethered to an ancillary 2,2′-bpy ligand have been developed and their DSSC PCEs have been tested. The introduction of the alkylthiophene moiety produces a strong new band centered at around 410 nm (Grätzel 2009). Borrowing intensity from this transition, the maximum of the metal-to-ligand charge transfer (MLCT) band in the visible region is shifted from 530 (in **N3**) to 554 nm (in **CYC-B1**) and the extinction coefficient is increased from 14,500 (in **N3**) to 24,200 (in **CYC-B1**) $M^{-1}$ $cm^{-1}$ (Clifford et al. 2011). Apart from increasing the light-harvesting capacity, the presence of alkylthiophene moiety also shifts the absorption spectra to the red, thus enabling to efficiently capturing the NIR region of the solar spectrum. Within the year 2006–2012, the PCEs of the DSSCs made of these dyes vary in the range of 6.01–10.57% with a special mentioning of the "champion" double layer (9 + 5 μm) C106 dye that offers a record high PCE of 11.29% under 1 Sun illumination (Cao et al. 2009). An analogous dye **C101** offers a PCE of 11.30% at 29.72 mW/$cm^2$ light intensity (Table 4.4). This PCE value slightly decreases to 11.0% under a light intensity of 99.39 mW/$cm^2$ with corresponding $J_{SC}$, $V_{OC}$, and FF values of 17.94 mA/$cm^2$, 0.777 V, and 0.785, respectively. More importantly, based on a low volatility 3-methoxypropionitrile electrolyte and a solvent-free ionic liquid electrolyte, cells have corresponding > 9.0% and ~7.4% efficiencies retained over 95% of their initial performances after 1000 h full sunlight soaking at 60 °C (Gao et al. 2008).

Sensitizer **Z-907** with its structural simplicity was used with 10 μm + 5 μm thick anatase $TiO_2$ layer by Wang and co-workers with the concept that the second titania layer would act as a light-scattering layer such the saturated absorption in the green region and enhanced external quantum efficiency of the yellow and red region would be observed. Such a design successfully produced a PCE of 9.05% with corresponding $J_{SC}$, $V_{OC}$, and fill factor values of 17.13 mA/$cm^2$, 0.73 V, and 0.724, respectively (Cao et al. 2009). In light of device stability, attempts have been made to replace the thiocyanate donor ligand in the series of ruthenium complexes mentioned above, as monodentate $SCN^-$ is believed to be the weakest coordinating ligand in view of chemical stability. However, thus far, the PCE of cells that contain a sensitizer without the $SCN^-$ ligand remained well below 10%. In this respect, cyclometalated ruthenium dyes, e.g., **YE-05** (Bessho et al. 2009), **Ru-1** (Robson et al. 2011), and **Ru-**2 (Robson et al. 2011), have emerged recently as a new paradigm in the molecular engineering of sensitizers for solar cell applications. As the cyclometalated ligand is a stronger donor than two thiocyanate groups, the

HOMO-LUMO gap is decreased and consequently, a significant redshift in the absorption spectrum of **YE-05** is observed compared to that of **N719** (Grätzel 2009). In a standard DSC configuration, the **YE-05** sensitizer showed an IPCE spectrum with a maximum of over 80% at 600 nm extending to 800 nm. Under AM 1.5 standard sunlight, the **YE-05** produces a short-circuit photocurrent of 17 mA/cm$^2$, a $V_{oc}$ of 0.80 V, and a fill factor of 0.74, corresponding to an overall conversion efficiency of 10.1%. Cyclometalated ruthenium dyes, **Ru-1** and **Ru-2** based on tridentate "push–pull" system show PCE values of 7.13 and 8.02% (Table 4.4), respectively, both with a specially designed electrolyte system containing 1.0 M 1,3-dimethylimidazolium iodide, 60 mM $I_2$, 0.5 M *tert*-butylpyridine, 0.05 M NaI and 0.1 M guanidium thiocyanate in a mixed solvent system of acetonitrile and valeronitrile (v/v, 85/15) (Robson et al. 2011).

An often-encountered problem in a DSSC fabrication is the volatilization and leakage of liquid electrolyte, the instability of the iodine specimen leading to the corrosion of the electrodes, thus decreasing the device efficiency and lifetime. Other alternatives for avoiding liquid electrolyte include (a) use of ionic liquids (Freitas et al. 2009; Welton 2004), due to good thermal and chemical stability, tunable viscosity, relative nonflammability, high ionic conductivity, broad electrochemical potential window, and extremely low vapor pressure; (b) use of pseudohalogen redox couples (Oskam et al. 2001; Bergeron et al. 2004), such as $(SCN)^-/(SCN)_3^-$, $(SeCN)^-/(SeCN)_3^-$; (c) use of polymer (thermoplastic, thermosetting, composite) electrolyte (Lan et al. 2007; Stergiopoulos et al. 2002; Han et al. 2005); (d) use of an inorganic hole transport material (Tennakone et al. 1998; Tennakone et al. 1995); and (e) use of a redox mediator (Nusbaumer et al. 2001; Daeneke et al. 2011). While approaches (a)–(c) show moderate efficiency with poor device lifetime, approaches (d) and (e) is promising. In light of approach (d), solution-processable p-type direct bandgap semiconductor $CsSnI_3$ can be used for hole conduction in lieu of a liquid electrolyte. The resulting solid-state dye-sensitized solar cells consist of $CsSnI_{2.95}F_{0.05}$ doped with $SnF_2$, nanoporous $TiO_2$ and the dye **N719**, and show conversion efficiencies of up to 10.2% with associated $J_{SC}$ = 19.2 mA/cm$^2$, $V_{OC}$ = 0.732 V, and fill factor = 0.727 (Chung et al. 2012). Following approach (e) and using **Z-907** as the sensitizer and $[Co(bpy)_3]^{3+/2+}$ as the redox mediator, PCE value of 6.5% was obtained under AM 1.5 1 Sun illumination (Liu et al. 2011). Regarding the device cost, a platinum counter electrode is the most expensive component in DSSCs. To minimize the photocathode fabrication cost based on platinum, studies revealed development of nanoscaled early transition metal-carbides, metal-nitrides, and metal-oxide, such as $Cr_3C_2$, CrN, VN, TiC, $V_2O_3$ as potential photocathodes in combination with **N719** dye, where only in one case, VC embedded in mesoporous carbon (synthesized in situ) outperformed the catalytic activity (PCE = 7.63%) of a Pt photocathode (PCE = 7.50%) (Wu et al. 2012).

### 4.5.4 Development of DSSCs Based on Organic Dyes

Transition metal-based photosensitizers are often toxic and contain toxic metals. In this regard, organic chromophores are appealing substitutes to metal-based dyes and their optoelectronic properties can often be tuned by facile structural adjustments (Mishra et al. 2009). Organic dyes that exhibit molar absorptivity over 100,000 $M^{-1}$ $cm^{-1}$ are promising applicants for thin-film solid-state DSSCs with hole transporting materials, e.g., P3HT (Mor et al. 2009) or OMeTAD (Snaith et al. 2007). However, organic sensitizers have a number of limitations, e.g., narrow and sharp absorption bands that do not encompass the visible spectral range (350–800 nm), aggregation due to planarity of the chromophores that inhibits the kinetics of electron transfer, poor absorption in red, and poor stability. Pioneering work by Arakawa and Hara in 2003 with coumarin-based dyes reported an organic sensitizer, **NKX-2677**, that exhibited a maximum PCE of 7.7% (Hara et al. 2001, 2003a, b, 2005). This PCE value was comparable to that of Ru-based **N719** dye (PCE = 7.8–8.0%) under identical measurement conditions (see Chart 4.2 for the structures of the organic photosensitizers under discussion, unless otherwise mentioned the photocathodes used for the DSSCs are Pt-coated FTO/ITO electrodes and Table 4.5 for important solar cell parameters). Using indoline-based bye, **D149**, Horiuchi, and Uchida achieved an impressive PCE of 9.03% in 2006 (Table 4.5) (Horiuchi et al. 2003, 2004; Ito et al. 2006). The high PCE and associated high photocurrent ($J_{SC}$ = 16.13 mA/$cm^2$) were attributed to the high absorption coefficient of the **D149** dye. In 2008, Ito and Grätzel improved the PCE of an indoline-based dye **D205** to 9.52% using an anti-aggregation agent, chenodeoxycholic acid (Table 4.5) (Ito et al. 2008). Later in the year 2013, DSSCs containing the imidazolium functionalized TEMPO/PMII (TEMPO = 2,2,6,6-tetramethyl-piperidine-1-oxyl and PMII = 1-propyl-3-methylimidazolium iodide) hybrid redox couple in combination with organic dye **D205** exhibited average overall power conversion efficiencies of 8.2 and 9.1% under simulated air mass 1.5 solar spectrum illumination at 100 and 50 mW/$cm^2$, respectively, which are higher than that of the traditional PMII/$I_2$-based electrolyte at 6.8% (at 100 mW/$cm^2$) and 7.6% (at 50 mW/$cm^2$) (Chen et al. 2013). Since the device stability associated with the indoline-based dyes was arguable, researchers were interested to develop a chemically robust dye, such as **C217** or **C219**, which contain a donor-(π-bridge)-acceptor (D-π-A) system. These dyes typically contain a donor system, e.g., an aryl amine group, an acceptor system, such as a cyanoacrylate group and one/multiple thiophene moiety(ies) as a π-conducting bridge. Molecular orbital calculations show that the electron density of the HOMO of the sensitizer to be mainly located on the aryl amine, while the LUMO it is centered at the cyanoacrylate moiety. Hence, during light excitation, electrons are transferred from the triarylamine through the thiophene bridge to the surface-bound cyanoacrylate, producing strong coupling of the excited state wave function with the Ti(3d, t2g) orbitals that form the conduction band of titanium dioxide. Therefore, efficient and rapid electron injection from the excited state of the sensitizer into the conduction band of the

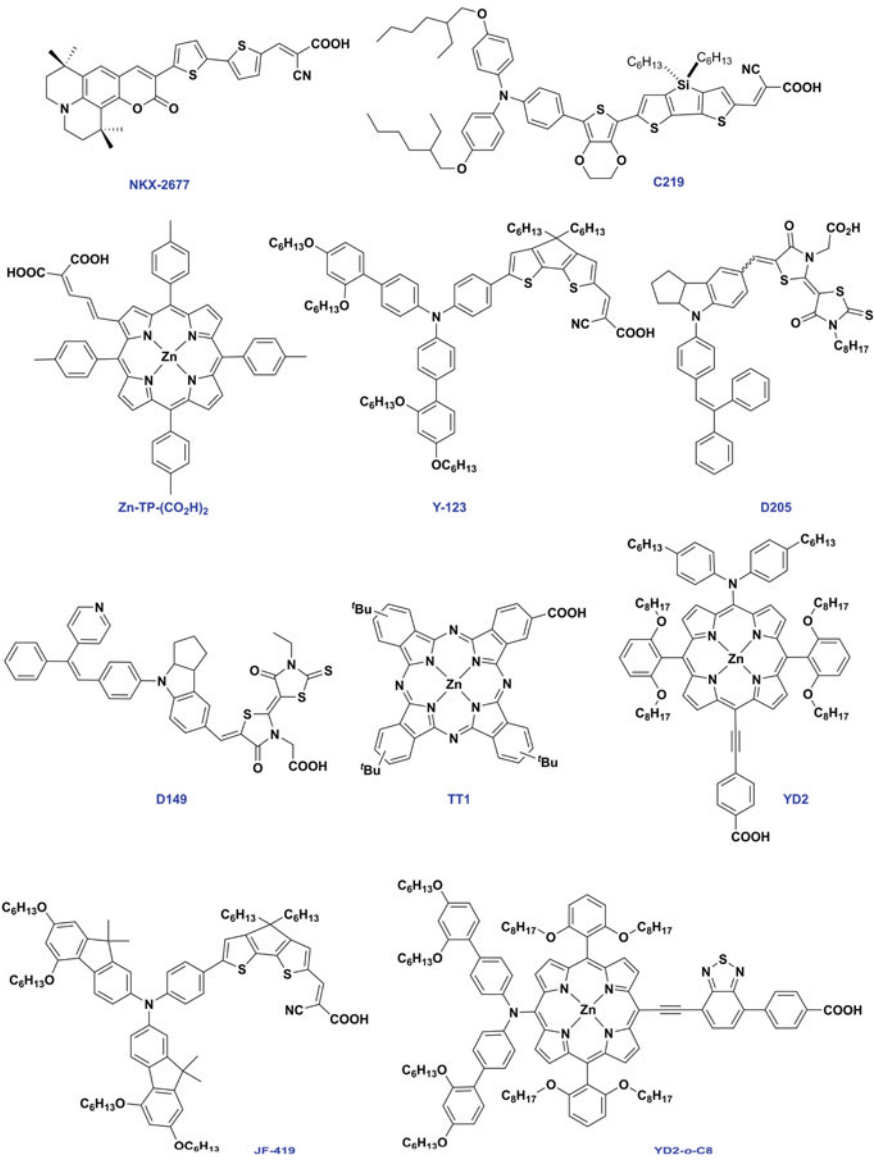


**Chart 4.2** Benchmark organic photosensitizers used in DSSCs

oxide can be achieved (Grätzel 2009). In 2010, Wang and co-workers reported a PCE of 10.1% using **C219** as the sensitizer under standard AM1.5G illumination (Zeng et al. 2010). Along with **C219** other chemically and photochemically robust D-π-A dyes have been developed, resisting degradation over 1000 h of light soaking at full solar intensity and elevated temperatures (Zhang et al. 2009; Yum

**Table 4.5** Cell parameters of organic photosensitizer-based DSSCs under the global AM1.5 spectrum (1000 W/m$^2$)

| Dye | Eff.[a] (%) | Area (cm$^2$) | $V_{OC}$ (V) | $J_{SC}$ (mA/cm$^2$) | FF[b] (%) |
|---|---|---|---|---|---|
| **NKX-2677**[c], (Hara et al. 2003) | 7.70 | 0.25 | 0.73 | 14.3 | 74.0 |
| **D149**[d], (Ito et al. 2006) | 9.03 | – | 0.653 | 19.96 | 69.4 |
| **D205**[e], (Ito et al. 2008) | 9.40 | – | 0.71 | 18.68 | 70.7 |
| **C-219**[f], (Zeng et al. 2010) | 10.10 | 0.158 | 0.77 | 17.94 | 73.0 |
| **Y-123** [g], (Polander et al. 2013) | 9.77 | 0.20 | 0.876 | 14.1 | 78.0 |
| **JF-419** [g], (Polander et al. 2013) | 10.30 | 0.20 | 0.84 | 16.2 | 76.0 |
| **TT1** [h], (Cid et al. 2009) | 3.56 | – | 0.611 | 7.78 | 75.0 |
| **Zn-TP-($CO_2H$)$^i_2$**, (Campbell et al. 2007) | 7.10 | – | 0.68 | 14.00 | 74.0 |
| **YD2-*o*-C8**[j], (Yella et al. 2009) | 11.90 | – | 0.965 | 17.3 | 71.0 |
| **SM315** [k], (Mathew et al. 2014) | 13.00 | 0.28 | 0.91 | 18.1 | 78.0 |

[a]Eff. = power conversion efficiency (PCE). [b]FF = fill factor. [c]Using electrolyte = 0.6 M DMPImI–0.1 M LiI–0.05 M $I_2$–1.0 M 4-tert-butylpyridine in acetonitrile. [d]Using electrolyte = 0.10 M lithium iodide, 0.60 M butylmethylimidazolium iodide, 0.05 M $I_2$, and 0.05 M 4-*tert*-butylpyridine in MeCN:valeronitrile (v/v, 85:15). [e]Using electrolyte = 0.10 M lithium iodide, 0.60 M butylmethylimidazolium iodide, 0.05 M $I_2$, and 0.05 M 4-tert-butylpyridine in MeCN:valeronitrile (v/v, 85 : 15). [f]Using electrolyte = 1.0 M DMII, 50 mM LiI, 30 mM $I_2$, 0.5 M 4-*tert*-butylpyridine (TBP), and 0.1 M guanidinium thiocyanate in the 85/15 mixture of acetonitrile and valeronitrile. [g]Using electrolyte = 0.25 M $[Co(bpy)_3](TFSI)_2$, 0.05 M $[Co(bpy)_3](TFSI)_3$, 0.25 M TBP, and 0.1 M LiTFSI in acetonitrile (TFSI = trifluoromethanesulfony limide). [h]Using electrolyte = 0.6 M M-methyl-N-butyl imidazolium iodide, 0.04 M iodine, 0.025 M LiI, 0.05 M guanidinium thiocyanate and 0.28 M tertiary butylpyridine in 15/85 (v/v) mixture of valeronitrile and acetonitrile. [i]Using electrolyte = 0.6 M BMII, 0.05 M $I_2$, 0.1 M LiI, and 0.5 M 4-*tert*-butyl pyridine in 1:1 acetonitrile/valeronitrile. [j]Using electrolyte = 0.165 M $[Co^{II}(bpy)_3](B(CN)_4)_2$, 0.045 M $[Co^{III}(bpy)_3](B(CN)_4)_3$ along with 0.8 M tert-butyl pyridine (TBP), and 0.1 M $LiClO_4$ in acetonitrile. [k]Using electrolyte = 0.25 M $[Co(bpy)_3](TFSI)_2$, 0.06 M $[Co(bpy)_3](TFSI)_3$, 0.1 M LiTFSI, and 0.5 M 4-*tert*-butylpyridine in acetonitrile

et al. 2009). In 2013, Nazeeruddin, Grätzel, and co-workers improved the PCEs of two other D-π-A systems, **Y-123** and **JF-419**, which in combination with $[Co(bpy)_3]^{3/2+}$ based redox mediator produced PCE values of 9.77 and 10.3%, respectively (Table 4.5) (Polander et al. 2013). Their previous research on using graphene nanoplatelets-coated FTO as a photocathode reported that the PCE of the DSSC containing the former (9.4% under 1 Sun illumination) outperforms the efficiency of a DSSC containing Pt-coated FTO photocathode (8.2% under 1 Sun illumination) using **Y-123** and $[Co(bpy)_3]^{3/2+}$ based redox mediator, thus providing opportunity to mitigate the fabrication cost (Kavan et al. 2011). Recently, Cao and co-workers developed a low-cost solid-state DSSC based on **Y-123** as the sensitizer and $[Cu(4,4',6,6'$-tetramethyl-2,2′-bipyridine$)_2]^{2+/+}$ as the hole conductor to achieve a maximum PCE of 11.0% under standard AM1.5G 1000 W/m$^2$ condition. The amorphous Cu(II/I) conductors that conduct holes by rapid hopping infiltrated in a

6.5-mm-thick mesoscopic $TiO_2$ scaffold are crucial for achieving such a high efficiency (Cao et al. 2017).

The D-π-A sensitizers often have limited and insufficient absorption above 700 nm. This fact makes them less useful for overall solar to power conversion compared to ruthenium-based photosensitizers. In this respect, porphyrins and phthalocyanines are interesting candidates as sensitizers for DSSCs. They are robust and photo- and electrochemically stable compounds. The absorption spectrum of porphyrin exhibits a typical Soret band at 400 nm with high absorption coefficient and moderate Q-bands at 600 nm, while the intense Q-bands of phthalocyanines are located at around 700 nm. Since unsubstituted porphyrins and phthalocyanines are highly symmetrical, their frontier molecular orbitals are distributed all over the molecule and thus directional electron transfer toward the semiconducting $TiO_2$ layer is less favorable, rendering them unsuitable for a DSSC fabrication. Also, aggregation of these molecules in device provides a detrimental effect in the device efficiency and lifetime. Seminal work on phthalocyanine-based DSSC includes **TT1** (0.1 mM) that displayed a PCE of 3.5% when used with chenodeoxycholic acid (10 mM) (Cid et al. 2009). In one of the early works including porphyrin dyes in 2007, such as **Zn-TP-($CO_2H$)$_2$**, an unprecedented PCE of 7.1% was observed under illumination AM1.5G 100 mW/cm$^2$ (Table 4.5) (Campbell et al. 2007). **YD2**, a class of D-π-A porphyrin dye reached a PCE of 11% when used with iodide/triiodide redox electrolyte (Bessho et al. 2010). The panchromatic porphyrin chromophore in **YD2** acts as the π-bridge, while the diarylamine group and the ethynylbenzoic acid moiety attached to the porphyrin ring act as an electron donor and an acceptor, respectively. **YD2-*o*-C8**, an analogue of **YD2,** includes two octyloxy groups in the ortho positions of each *meso*-phenyl ring and a π-accepting benzothiadiazole unit. These changes brought a striking amelioration of the photo-induced charge separation, so that high PCE values reaching 11.9% have been achieved with a $V_{OC}$ of 965 mV, a $J_{SC}$ of 17.3 mA/cm$^2$, and a fill factor of 0.71 under standard AM1.5 sunlight at 995 W/m$^2$ intensity using $[Co(bpy)_3]^{3+/2+}$ based redox mediator. In presence of a co-sensitizer **Y123**, **YD2-*o*-C8** yielded an efficiency of 12.3% with the same cobalt-based redox mediator (Yella et al. 2009). The high PCE of **YD2-*o*-C8** is due to the molecular design that harvest sunlight throughout the visible spectrum so that the dark reactions are retarded and large photocurrent and photovoltage are attained. The generation of high photocurrent is supported by high IPCE values, exceeding 80% from 450 nm to 680 nm. Recently, Mathew and Grätzel used a panchromatic D-π-A porphyrin dye, **SM315**, featuring a bulky bis(2′,4′-bis(hexyloxy)-[1,1′-biphenyl]-4-yl) amine donor, porphyrin as π-bridge, and pro-quinoidal benzothiadiazole (BTD) unit as the acceptor (Mathew et al. 2014). Due to the broadening of the Soret and Q-band absorptions, the **SM315** dye features a high light-harvesting nature. Without the use of any co-sensitizer, this dye exhibited strikingly record high PCE of 13% with a $[Co(bpy)_3]^{3+/2+}$ based redox shuttle at full sun illumination (Table 4.5). The dye exhibited a high IPCE value of 80% throughout the entire visible electromagnetic spectrum (450–750 nm). The spectral mismatch between the simulated and true AM1.5G sunlight is negligibly small for the DSSC comprising of **SM315**. This fact

is supported by less than 2% of the measured photocurrent overlap integral of the photocurrent action spectrum with the standard AM1.5G solar emission spectrum. During the 500 h of light-soaking experiment, devices using **SM315** underwent over one million turnovers without showing any significant loss in stability. Thus, with judicious molecular designing, the DSSC can exhibit improved PCE and can one day surpass those of first and second-generation photovoltaic solar cells.

### *4.5.5 Viability of a DSSC*

A DSSC can be fabricated in a relatively simple way than a first- or second-generation solar cell in a wet laboratory without employing a glove box or high vacuum steps. By taking appropriate precautions and adopting a rigorous protocol, relative variations of PCE of less than 2–3% can be easily achieved in laboratory cells. A vast amount of efforts has been focused on accessing the long-term stability of a DSSC over the last 15 years. Accelerated light-soaking experiments performed over many thousands of hours under full or even concentrated sunlight have confirmed the intrinsic stability of current DSSC substituents. Stable operation under high-temperature stress at 80–85 °C as well as under damp heat and temperature cycling has been achieved by judicious molecular engineering of the sensitizers with the use of robust and nonvolatile electrolytes, such as ionic liquids, and adequate sealing materials. Appropriate sealing of a DSSC has been problematic in the early experiments causing leakage of a volatile electrolyte, which now has been overcome by many experienced research groups and industrial enterprises. Satisfactory results on device durability and efficiency are currently being confirmed under real outdoor conditions. Considering the extensive studies, a minimum 20 years stability for a DSSC is expected to match the stability requirements to sustain outdoor operations. With a steady growth in PCE (maximum achieved so far for ruthenium-based sensitizer, **C106** is 11.29% and organic dye-based sensitizer, **SM-315** is 13%) and durability, commercialization is underway for DSSCs.

## 4.6 Conclusion

As previously mentioned, crystalline silicon photovoltaic cell production dominates the field of solar energy, occupying 90% of total solar cells (Sago 2010). The use of monocrystalline silicon solar cells leads to higher stabilities and efficiencies compared to multi-crystalline and amorphous silicon solar cells. Although the multi-crystalline and amorphous silicon solar cells have lower efficiencies than monocrystalline solar cells, the lower costs and easier fabrication methods can lead to the development of solar cells that can be implemented on a large scale for terrestrial uses. The most efficient silicon solar cell reported reaches an efficiency of

over 26% (Yoshikawa et al. 2017). This efficiency was achieved by fabricating a cell with a designated area of 180.4 $cm^2$ with an interdigitated back contact, combining n-type and p-type amorphous silicon to collect both holes and electrons (Yoshikawa et al. 2017). The back contact is separated from the front contact by crystalline silicon, with the front contact covered by an amorphous silicon passivation layer and an antireflective coating (Yoshikawa et al. 2017). These higher efficiencies can be achieved in silicon solar cells by improving lifetime, series resistance, and optical properties to allow for the reduction of recombination and optical losses.

However, these silicon solar cell efficiencies are strongly rivaled by those achieved from multi-junction photovoltaic cells. With experimental efficiencies reaching 46% by use of concentrator photovoltaics, costs are however dramatically increased compared to all forms of silicon solar cells. The most efficient multi-junction solar cell was achieved by Fraunhofer Institute for Solar Energy Systems ISE by combining a four-junction cell (GaInP/GaAs; GaInAsP/GaInAs) with a Fresnel lens (Fraunhofer ISE 2014). For multi-junction cells to be more applicable to terrestrial uses, research into lowering the cost is of primary interest with the potential of increasing the concentration ratio of the cells leading the way to decreasing highly efficient multi-junction cell prices. If prices can be markedly reduced, these cells have the potential to outcompete the use of fossil fuels.

Development of lower cost alternatives in the field of solar cells has led to the production of perovskite-based photovoltaic cells. Although efficiencies have only reached 23.9%, the use of tandem cells show that perovskite solar cells can theoretically outperform silicon solar cell efficiencies but at a much lower price. The best efficient perovskite solar cell was achieved by using a complex semitransparent organic–inorganic perovskite material with a high bandgap absorber, $Cs_{0.1}(H_2NCHNH_2)_{0.9}PbI_{2.865}Br_{0.135}$ (CsFAPbIBr) combined with a low bandgap absorber, *c*-Si, for the back contact (Jaysankar et al. 2018). This cell showed that by incorporating efficient absorbers with bandgaps absorbing at opposite ends of the visible spectrum allows to produce perovskite solar cells with efficiencies approaching those achieved from silicon solar cells. However, the implementation of such cells on a large scale is not currently practical due to a number of reasons including poor stability toward oxygen, heat, light, and humidity (Niu et al. 2014; Leijtens et al. 2015). Silicon solar cells are very stable in comparison and so perovskite solar cells cannot yet compete with the use of silicon solar cells in terrestrial applications. Research efforts based on perovskite solar cells have now been gathered in improving stability, such as the cells being encapsulated with carbon nanotube and an inert fluorinated photopolymer showing the prevention of immediate degradation of perovskite solar cells (Habisreutinger et al. 2014; Bella et al. 2016).

Alike perovskite solar cells, research into lower cost and environmentally-friendly alternatives has led to the development of DSSCs. With best efficiencies achieved so far as 11.29% with ruthenium-based dyes and 13% with organic photosensitizers, the technology based on DSSCs is not yet as mature as the silicon photovoltaics. The best efficient ruthenium dye **C-106** was developed

by tethering two thiophene moieties in a 2,2′-bpy ancillary ligand to increase the panchromatic absorption. The designing of the best efficient organic sensitizer **SM-315** depends on the efficient electron relay from a donating alkoxy substituted aryl amine to the accepting benzothiadiazine moiety through the porphyrin π-bridge. With the development of various ionic liquids, Co(III/II)-polypyridyl-based redox shuttle, polymer electrolytes, the typical problem of leakage of volatile liquid electrolyte can now be avoided. The device fabrication cost can be lowered down by using graphene nanoplatelets, early transition metal-carbide, metal-nitride, and metal-oxide-based photocathode instead of a Pt-coated FTO/ITO. With these modifications and steady increase in the PCE, the DSSCs and especially thin-film DSSCs show immense potential to outperform the silicon PV-based market in future. Due to the difference in operating mechanism compared to other PV solar cells as mentioned earlier, a DSSC can also work at a low-light or non-direct sunlight condition. Although the DSSCs exhibit high chemical stability, thermal tolerance (up to 80–85 °C) the technology has not been fully commercialized yet for a fair price-to-performance point of view.

In summary, silicon solar cells are still the dominant class of photovoltaic cells in practical aspects. Despite this fact, ongoing research into multi-junction solar cells, perovskite solar cells, and DSSCs is promising with the potential of cost reductions and increased stability, respectively, allowing for these cells to out-compete the use of fossil fuels.

**Acknowledgements** AKP and HCP gratefully acknowledge the financial support from University of St Andrews. AKP also thanks the Leverhulme Trust for an Early Career Fellowship (ECF-2017-326) and ScotCHEM for a short-term Postgraduate and Early Career Researcher Exchange (PECRE) fellowship.

**Conflict of Interest** The authors declare no conflict of interest.

## References

Albrecht S, Saliba M, Baena JPC, Lang F, Kegelmann L, Mews M, Steier L, Abate A, Korte JL, Schlatmann R, Nazeeruddin MK, Hagfeldt A, Grätzel M, Rech B (2016) Monolithic perovskite/silicon-heterojunction tandem solar cells processed at low temperature. Energy Environ Sci 9(1):81–88

Attfield JP, Lightfoot P, Morris RE (2015) Perovskites. Dalton Trans 44(23):10541–10542

Bai Y, Cao YM, Zhang J, Wang M, Li RZ, Wang P, Zakeeruddin SM, Grätzel M (2008) High-performance dye-sensitized solar cells based on solvent-free electrolytes produced from eutectic melts. Nat Mater 7(8):626–630

Bailie CD, Christoforo MG, Mailoa JP, Bowring AR, Unger EL, Nguyen WH, Burschka J, Pellet N, Lee JZ, Grätzel M, Noufi R, Buonassisi T, Salleo A, McGehee MD (2015) Semi-transparent perovskite solar cells for tandems with silicon and CIGS. Energy Environ Sci 8(3):956–963

Battaglia C, Cuevas A, Wolf SD (2016) High-efficiency crystalline silicon solar cells: status and perspectives. Energy Environ Sci 9(5):1552–1576

Beal RE, Slotcavage DJ, Leijtens T, Bowring AR, Belisle RA, Nguyen WH, Burkhard G, Hoke ET, McGehee MD (2016) Cesium Lead Halide Perovskites with improved stability for tandem solar cells. J Phys Chem Lett 7(5):746–751

Bedair SM, Lamorte MF, Hauser JR (1979) A two-junction cascade solar-cell structure. Appl Phys Lett 34(1):38–39

Bella F, Griffini G, Correa-Baena JP, Saracco G, Grätzel M, Hagfeldt A, Turri S, Gerbaldi C (2016) Improving efficiency and stability of perovskite solar cells with photocurable fluoropolymers. Science 354(6309):203–206

Benick J, Richter A, Muller R, Hauser H, Feldmann F, Krenckel P, Riepe S, Schindler F, Schubert MC, Hermle M, Bett AW, Glunz SW (2017) High-efficiency n-Type HP mc silicon solar cells. IEEE J Photovoltaics 7(5):1171–1175

Bergeron B, Marton A, Oskam G, Meyer G (2004) Dye-sensitized $SnO_2$ electrodes with iodide and pseudohalide redox mediators. J Phys Chem B 109(2):937–943

Bertness KA, Kurtz SR, Friedman DJ, Kibbler AE, Kramer C, Olson JM (1994) 29.5%-efficient GaInP/GaAs tandem solar cells. Appl Phys Lett 65(8):989–991

Bessho T, Yoneda E, Yum J-H, Guglielmi M, Tavernelli I, Imai H, Rothlisberger U, Nazeeruddin MK, Grätzel M (2009) New paradigm in molecular engineering of sensitizers for solar cell applications. J Am Chem Soc 131(16):5930–5934

Bessho T, Zakeeruddin SM, Yeh CY, Diau EWG, Grätzel M (2010) Highly efficient mesoscopic dye-sensitized solar cells based on donor–acceptor-substituted porphyrins. Angew Chem Int Ed 49(37):6646–6649

Blakers AW, Green MA (1986) 20% efficiency silicon solar cells. Appl Phys Lett 48(3):215–217

Blakers AW, Wang A, Milne AM, Zhao J, Green MA (1989) 22.8% efficient silicon solar cell. Appl Phys Lett 55(13):1363–1365

Blakers A, Zin N, McIntosh KR, Fong K (2013) High efficiency silicon solar cells. Energy Proc 33:1–10

Bonnet-Eymard M, Boccard M, Bugnon G, Meillaud F, Despeisse M, Haug FJ, Ballif C (2013) Current matching optimization in high-efficiency thin-film silicon tandem solar cells. In: 39th Photovoltaic Specialists Conference (PVSC). IEEE, Tampa, pp 0184–0187

BP Global Homepage. https://www.bp.com/en/global/corporate/energy-economics/statistical-review-of-world-energy/renewable-energy/solar-energy.html. Last accessed 28 June 2018

Bruton TM (2002) General trends about photovoltaics based on crystalline silicon. Sol Energy Mater Sol Cells 72(1–4):3–10

Bush KA, Palmstrom AF, Yu Z, Boccard M, Cheacharoen R, Mailoa JP, McMeekin DP, Hoye RLZ, Bailie CD, Leijtens T, Peters IM, Minichetti MC, Rolston N, Prasanna R, Sofia SE, Harwood D, Ma W, Moghadam F, Snaith HJ, Buonassisi T, Holman ZC, Bent SF, McGehee MD (2017) 23.6%-efficient monolithic perovskite/silicon tandem solar cells with improved stability. Nat Energy 2, article number 17009

Campbell WM, Jolley KW, Wagner P, Wagner K, Walsh PJ, Gordon KC, Schmidt-Mende L, Nazeeruddin MK, Wang Q, Grätzel M, Officer DL (2007) Highly efficient porphyrin sensitizers for dye-sensitized solar cells. J Phys Chem C 111(32):11760–11762

Cao Y, Bai Y, Yu Q, Cheng Y, Liu S, Shi D, Gao F, Wang P (2009) Dye-sensitized solar cells with a high absorptivity ruthenium sensitizer featuring a 2-(Hexylthio)thiophene conjugated bipyridine. J Phys Chem C 113(15):6290–6297

Cao Y, Saygili Y, Ummadisingu A, Teuscher J, Luo J, Pellet N, Giordano F, Zakeeruddin SM, Moser J-E, Freitag M, Hagfeldt A, Grätzel M (2017) 11% efficiency solid-state dye-sensitized solar cells with copper(II/I) hole transport materials. Nat Commun 8, article number 15390

Carlson DE, Wronski CR (1976) Amorphous silicon solar cell. Appl Phys Lett 28(11):671–673

Carlson S, Larsson AK, Rohrer FE (2000) High-pressure transformations of $NbO_2F$. Acta Cryst B56:189–196

Chapin DM, Fuller CS, Pearson GL (1954) A new silicon p-n junction photocell for converting solar radiation into electrical power. J Appl Phys 25(5):676–677

Chen C-Y, Wu S-J, Wu C-G, Chen J-G, Ho K-C (2006) A Ruthenium complex with superhigh light-harvesting capacity for dye-sensitized solar cells. Angew Chem Int Ed 45(35):5822–5825

Chen C-Y, Wu S-J, Li J-Y, Wu C-G, Chen J-G, Ho K-C (2007a) A new route to enhance the light-harvesting capability of ruthenium complexes for dye-sensitized solar cells. Adv Mater 19 (22):3888–3891

Chen C-Y, Lu H-C, Wu C-G, Chen J-G, Ho K-C (2007b) New Ruthenium complexes containing oligoalkylthiophene-substituted 1,10-phenanthroline for nanocrystalline dye-sensitized solar cells. Adv Func Mater 17(1):29–36

Chen C-Y, Pootrakulchote N, Chen M-Y, Moehl T, Tsai H-H, Zakeeruddin SM, Wu C-G, Grätzel M (2012) A new heteroleptic ruthenium sensitizer for transparent dye-sensitized solar cells. Adv Energy Mater 2(12):1503–1509

Chen X, Xu D, Qiu L, Li S, Zhang W, Yan F (2013) Imidazolium functionalized TEMPO/iodide hybrid redox couple for highly efficient dye-sensitized solar cells. J Mater Chem A 1 (31):8759–8765

Chen B, Bai Y, Yu Z, Li T, Zheng X, Dong Q, Shen L, Boccard M, Gruverman A, Holman Z, Huang J (2016) Efficient semitransparent Perovskite solar cells for 23.0%-efficiency Perovskite/Silicon four-terminal tandem cells. Adv Energy Mater 6(19), article number 1601128

Cheng Z, Lin J (2010) Layered organic–inorganic hybrid perovskites: structure, optical properties, film preparation, patterning and templating engineering. CrystEngComm 12(10):2646–2662

Cheng YY, Fückel B, MacQueen RW, Khoury T, Clady RGCR, Schulze TF, Ekins-Daukes NJ, Crossley MJ, Stannowski B, Lips K, Schmidt TW (2012) Improving the light-harvesting of amorphous silicon solar cells with photochemical upconversion. Energy Environ Sci 5:6953–6959

Chiba Y, Islam A, Watanabe Y, Komiya R, Koide N, Han L (2006) Dye-sensitized solar cells with conversion efficiency of 11.1%. Jpn J Appl Phys 45(2):24–28

Chung I, Lee B, He J, Chang RPH, Kanatzidis MG (2012a) All-solid-state dye-sensitized solar cells with high efficiency. Nature 485(7399):486–489

Chung I, Lee B, He J, Chang RPH, Kanatzidis MG (2012b) All-solid-state dye-sensitized solar cells with high efficiency. Nature 485(7399):486–489

Cid JJ, Garcia-Iglesias M, Yum JH, Forneli A, Albero J, Martinez-Ferrero E, Vazquez P, Grätzel M, Nazeeruddin MK, Palomares E, Torres T (2009) Structure-function relationships in unsymmetrical zinc phthalocyanines for dye-sensitized solar cells. Chem Eur J 15(20):5130–5137

Clearfield A (1963) The synthesis and crystal structures of some alkaline earth titanium and zirconium sulphides. Acta Cryst 16:135–142

Clifford JN, Martínez-Ferrero E, Viterisi A, Palomares E (2011) Sensitizer molecular structure-device efficiency relationship in dye sensitized solar cells. Chem Soc Rev 40 (3):1635–1646

CleanTechnica. https://cleantechnica.com/2018/02/11/solar-panel-prices-continue-falling-quicker-expected-cleantechnica-exclusive. Last accessed 28 May 2018

Connolly JP, Mencaraglia D, Renard C, Bouchier D (2013) Designing III-V multijunction solar cells on silicon. In: 28th European photovoltaic solar energy conference and exhibition. EEA, Villepinte, pp 219–228

Cotal H, Fetzer C, Boisvert J, Kinsey G, King R, Herbert P, Yoon H, Karam N (2009) III–V multijunction solar cells for concentrating photovoltaics. Energy Environ Sci 2:174–192

Daeneke T, Kwon T, Holmes A, Duffy N, Bach U, Spiccia L (2011) High-efficiency dye-sensitized solar cells with ferrocene-based electrolytes. Nat Chem 3(3):211–215

Dimroth F, Tibbits TND, Niemeyer M, Predan F, Beutal P, Karcher C, Oliva E, Siefer G, Lackner D, Fuß-Kailuweit P, Bett AW, Krause R, Drazek C, Guiot E, Wasselin J, Tauzin A, Signamarcheix T (2016) Four-junction wafer-bonded concentrator solar cells. IEEE J Photovolatics 6(1):343–349

Duong T, Wu Y, Shen H, Peng J, Fu X, Jacobs D, Wang E, Kho TC, Fong KC, Stocks M, Franklin E, Blakers A, Zin N, McIntosh K, Li W, Cheng Y, White TP, Weber K, Catchpole K (2017) Rubidium multication Perovskite with optimized bandgap for Perovskite-Silicon tandem with over 26% efficiency. Adv Energy Mater 7(14), article number 1700228

Eperon GE, Stranks SD, Menelaou C, Johnston MB, Herz LM, Snaith HJ (2014a) Formamidinium lead trihalide: a broadly tunable perovskite for efficient planar heterojunction solar cells. Energy Environ Sci 7:982–988

Eperon GE, Burlakov VM, Docampo P, Goriely A, Snaith HJ (2014b) Morphological control for high performance, solution-processed planar heterojunction Perovskite solar cells. Adv Funct Mater 24(1):151–157

Eperon GE, Leijtens T, Bush KA, Prasanna R, Green T, Wang JTW, McMeekin DP, Volonakis G, Milot RL, May R, Palmstrom A, Slotcavage DJ, Belisle R, Patel JB, Parrott ES, Sutton RJ, Ma W, Moghadam F, Conings B, Babayigit A, Boyen H-G, Bent S, Giustino F, Herz LM, Johnston MB, McGehee MD, Snaith HJ (2016) Perovskite-perovskite tandem photovoltaics with optimized band gaps. Science 354(6314):861–865

European Union Homepage. https://europa.eu/european-union/topics/climate-action_en. Last accessed 28 June 2018

Feng S-W, Lai C-M, Tsai C-Y, Tu L-W (2014) Numerical simulations of the current-matching effect and operation mechanisms on the performance of InGaN/Si tandem cells. Nanoscale Res Lett 9:652–661

Forgács D, Gil-Escrig L, Pérez-Del-Rey D, Momblona C, Werner J, Niesen B, Ballif C, Sessolo M, Bolink HJ (2017) Efficient monolithic Perovskite/Perovskite tandem solar cells. Adv Energy Mater 7(8), article number 1602121

Fraunhofer ISE. https://www.ise.fraunhofer.de/en/press-media/press-releases/2014/new-world-record-for-solar-cell-efficiency-at-46-percent.html. Last accessed 30 May 2018

Fraunhofer ISE. https://www.ise.fraunhofer.de/content/dam/ise/de/documents/publications/studies/cpv-report-ise-nrel.pdf. Last accessed 29 May 2018

Freitas J, Nogueira A, De Paoli M (2009) New insights into dye-sensitized solar cells with polymer electrolytes. J Mater Chem 19(30):5279–5294

Friedman DJ (2010) Progress and challenges for next-generation high-efficiency multijunction solar cells. Curr Opin Solid State Mater Sci 14(6):131–138

Galoppini E, Rochford J, Chen HH, Saraf G, Lu YC, Hagfeldt A, Boschloo G (2006) Fast electron transport in metal organic vapor deposition grown dye-sensitized ZnO nanorod solar cells. J Phys Chem B 110(33):16159–16161

Gao F, Wang Y, Shi D, Zhang J, Wang M, Jing X, Humphry-Baker R, Wang P, Zakeeruddin SM, Grätzel M (2008) Enhance the optical absorptivity of nanocrystalline $TiO_2$ film with high molar extinction coefficient ruthenium sensitizers for high performance dye-sensitized solar cells. J Am Chem Soc 130(32):10720–10728

Garcia I, France RM, Geisz JF, McMahon WE, Steiner MA, Johnston S, Friedman DJ (2016) Metamorphic III–V solar cells: recent progress and potential. IEEE J Photovoltaics 6(1):366–373

Garnett E, Yang P (2010) Light trapping in silicon nanowire solar cells. Nano Lett 10(3):1082–1087

Geisz JF, Friedman DJ, Ward JS, Duda A, Olavarria WJ, Moriarty TE, Kiehl JT, Romero MJ, Norman AG, Jones KM (2008) 40.8% efficient inverted triple-junction solar cell with two independently metamorphic junctions. Appl Phys Lett 93(12):123505–123507

Gingl F, Vogt T, Akiba E, Yvon K (1999) Cubic $CsCaH_3$ and hexagonal $RbMgH_3$: new examples of fluoride-related perovskite-type hydrides. J Alloys Compd 282(1–2):125–129

Glunz SW (2006) New concepts for high-efficiency silicon solar cells. Sol Energy Mater Sol Cells 90(18–19):3276–3284

Goetzburger A, Luther J, Willeke G (2002) Solar cells: past, present, future. Sol Energy Mater Sol Cells 74:1–11

Grancini G, Roldán-Carmona C, Zimmerman I, Mosconi E, Lee X, Martineau D, Narbey S, Oswald F, De Angelis F, Gräetzel M, Nazeeruddin MK (2017) Nat Commun 8, article number 15684

Grätzel M (2001) Photoelectrochemical cells. Nature 414(6861):338–344

Grätzel M (2009) Recent advances in sensitized mesoscopic solar cells. Acc Chem Res 42 (11):1788–1798

Green MA (1993) Silicon solar cells: evolution, high-efficiency design and efficiency enhancements. Semicond Sci Technol 8(1):1–12
Green MA (2000) Photovoltaics: technology overview. Energy Policy 28(14):989–998
Green M (2005) A: silicon photovoltaic modules: a brief history of the first 50 years. Prog Photovolt Res Appl 13(5):447–455
Green MA (2009) The path to 25% silicon solar cell efficiency: history of silicon cell evolution. Prog Photovolt Res Appl 17(3):183–189
Green MA, Blakers AW, Osterwald CR (1985) Characterization of high-efficiency silicon solar cells. J Appl Phys 58(11):4402–4408
Green MA, Emery K, Hishikawa Y, Warta W, Dunlop ED (2012) Solar cell efficiency tables (version 40). Prog Photovolt Res Appl 20(5):606–614
Green MA, Emery K, Hishikawa Y, Warta W, Dunlop E (2014) Solar cell efficiency tables (version 43). Prog Photovolts Res Appl 22(1):1–11
Green MA, Keevers MJ, Thomas I, Lasich JB, Emery K, King RR (2015) Solar cell efficiency tables (version 47). Prog Photovolt Res Appl 23(6):685–691
Guter W, Kern R, Köstler W, Kubera T, Löckenoff R, Meusel M, Shirnow M, Strobl G (2011) III-V multijunction solar cells–new lattice-matched products and development of upright metamorphic 3 J cells. In: 7th international conference on concentrating photovoltaic systems. AIP, Las Vegas, pp 5–8
Habisreutinger SN, Leijtens T, Eperon GE, Stranks SD, Nicholas RJ, Snaith HJ (2014) Carbon nanotube/polymer composites as a highly stable hole collection layer in Perovskite solar cells. Nano Lett 14(10):5561–5568
Hagfeldt A, Boschloo G, Sun L, Kloo L, Pettersson H (2010) Dye-sensitized solar cells. Chem Rev 110(11):6595–6663
Han H, Liu W, Zhang J, Zhao X (2005) A hybrid poly(ethylene oxide)/poly(vinylidene fluoride)/$TiO_2$ nanoparticle solid-state redox electrolyte for dye-sensitized nanocrystalline solar cells. Adv Funct Mater 15(12):1940–1944
Hao F, Stoumpos CC, Cao DH, Chang RPH, Kanatzidis MG (2014) Lead-free solid-state organic–inorganic halide perovskite solar cells. Nat Photonics 8:489–494
Hara K, Sayama K, Ohga Y, Shinpo A, Suga S, Arakawa H (2001) A coumarin-derivative dye sensitized nanocrystalline $TiO_2$ solar cell having a high solar-energy conversion efficiency up to 5.6%. Chem Commun 0(6):569–570
Hara K, Kurashige M, Dan-oh Y, Kasada C, Shinpo A, Suga S, Sayama K, Arakawa H (2003a) Design of new coumarin dyes having thiophene moieties for highly efficient organic-dye-sensitized solar cells. New J Chem 27(5):783–785
Hara K, Sato T, Katoh R, Furube A, Ohga Y, Shinpo A, Suga S, Sayama K, Sugihara H, Arakawa H (2003b) Molecular design of coumarin dyes for efficient dye-sensitized solar cells. J Phys Chem B 107(2):597–606
Hara K, Sato T, Katoh R, Furube A, Yoshihara T, Murai M, Kurashige M, Ito S, Shinpo A, Suga S, Arakawa H (2005) Novel conjugated organic dyes for efficient dye-sensitized solar cells. Adv Funct Mater 15(2):246–252
Henry CH (1980) Limiting efficiencies of ideal single and multiple energy gap terrestrial solar cells. J Appl Phys 51(8):4494–4500
Horiuchi T, Miura H, Uchida S (2003) Highly-efficient metal-free organic dyes for dye-sensitized solar cells. Chem Commun 0(24):3036–3037
Horiuchi T, Miura H, Sumioka K, Uchida S (2004) High efficiency of dye-sensitized solar cells based on metal-free indoline dyes. J Am Chem Soc 126(39):12218–12219
Im JH, Lee CR, Lee JW, Park SW, Park NG (2011) 6.5% efficient perovskite quantum-dot-sensitized solar cell. Nanoscale 3(10):4088–4093
International Energy Agency. Chapter 15 - Energy for cooking in developing countries, pp 419–445. http://www.iea.org/publications/freepublications/publication/cooking.pdf. Last accessed 28 June 2018
International Energy Agency Light's Labour's Lost. http://www.iea.org. Last accessed 28 June 2018

Ito S, Zakeeruddin SM, Humphry-Baker R, Liska P, Charvet R, Comte P, Nazeeruddin MK, Pechy P, Takata M, Miura H, Uchida S, Grätzel M (2006) High-efficiency organic-dye-sensitized solar cells controlled by nanocrystalline-$TiO_2$ electrode thickness. Adv Mater 18 (9):1202–1205

Ito S, Miura H, Uchida S, Takata M, Sumioka K, Liska P, Comte P, Péchyb P, Grätzel M (2008) High-conversion-efficiency organic dye-sensitized solar cells with a novel indoline dye. Chem Commun 0(41):5194–5196

Jacoby M (2016) The future of low-cost solar cells. Chem Eng News 94(18):30–35

Jaysankar M, Filipič M, Zielinski B, Schmager R, Song W, Qiu W, Paetzold UW, Aernouts T, Debucquoy M, Gehlhaara R, Poortmans J (2018) Energy Environ Sci 11(6):1489–1498

Jiang Y, Shen H, Pu T, Zheng C, Tang Q, Gao K, Wu J, Rui C, Li Y, Liu Y (2017) High efficiency multi-crystalline silicon solar cell with inverted pyramid nanostructure. Sol Energy 142:91–96

Kavan L, Yum J-H, Grätzel M (2011) Graphene nanoplatelets outperforming platinum as the electrocatalyst in co-bipyridine-mediated dye-sensitized solar cells. Nano Lett 11(12):5501–5506

King RR, Law DC, Edmondson KM, Fetzer CM, Kinsey GS, Yoon H, Sherif RA, Karam NH (2007) 40% efficient metamorphic GaInP/GaInAs/Ge multijunction solar cells. Appl Phys Lett 90(18):183516–183518

King RR, Bhusari D, Larrabee D, Liu XQ, Rehder E, Edmonson K, Cotal H, Jones RK, Ermer JH, Fetzer CM, Law DC, Karam NH (2012) Solar cell generations over 40% efficiency. Prog Photovolt Res Appl 20(6):801–815

Kingsbury EF, Ohl RS (1952) Photoelectric properties of ionically bombarded silicon. Bell Syst Tech J 31(4):802–815

Kojima A, Teshima K, Shirai Y, Miyasaka T (2009) Organometal Halide Perovskites as visible-light sensitizers for photovoltaic cells. J Am Chem Soc 131(17):6050–6051

Kulbak M, Cahen D, Hodes G (2015) How important is the organic part of lead halide perovskite photovoltaic cells? Efficient CsPbBr 3 cells. J Phys Chem Lett 6(13):2452–2456

Lal NN, White TP, Catchpole KR (2014) Optics and light trapping for tandem solar cells on silicon. IEEE J Photovoltaics 4(6):1380–1386

Lan Z, Wu J, Wang D, Hao S, Lin J, Huang Y (2007) Quasi-solid-state dye-sensitized solar cells based on a sol–gel organic–inorganic composite electrolyte containing an organic iodide salt. Sol Energy 81(1):117–122

Lee MM, Teuscher J, Miyasaka T, Murakami TN, Snaith HJ (2012) Efficient hybrid solar cells based on meso-superstructured Organometal Halide Perovskites. Science 338(6107):643–647

Leijtens T, Eperon GE, Noel NK, Habisreutinger SN, Petrozza A, Snaith HJ (2015) Stability of metal Halide Perovskite solar cells. Adv Energy Mater 5(20), article number 1500963

Liao X, Xiang X, Zeng X (2013) International conference on Electro-Information Technology (EIT). IEEE, Rapid City, USA

Lin XX, Zeng Y, Zhong SH, Huang ZG, Qian HQ, Ling J, Zhu JB, Shen WZ (2015) Realization of improved efficiency on nanostructured multicrystalline silicon solar cells for mass production. Nanotechnology 26(12):125401–125410

Lincot D (2017) The new paradigm of photovoltaics: From powering satellites to powering humanity. C R Phys 18(7–8):381–390

Liu Y, Jennings JR, Huang Y, Wang Q, Zakeeruddin SM, Grätzel M (2011) Cobalt redox mediators for ruthenium-based dye-sensitized solar cells: a combined impedance spectroscopy and near-ir transmittance study. J Phys Chem C 115(38):18847–18855

Luaña V, Costales A, Pendás AM (1997) Ions in catalysis: the topology of the electron density in ionic materials II. The cubic halide perovskites. Phys Rev B 55:4285–4297

Lufaso MW, Woodward PM (2001) Prediction of the crystal structures of perovskites using the software program SPuDS. Acta Cryst B57:725–738

Löper P, Moon S, Nicolas SMD, Niesen B, Ledinsky M, Nicolay S, Bailat J, Yum J, Wolf SD, Ballif C (2015) Organic–inorganic halide perovskite/crystalline silicon four-terminal tandem solar cells. Phys Chem Chem Phys 17(3):1619–1629

Mailoa JP, Bailie CD, Johlin EC, Hoke ET, Akey AJ, Nguyen WH, McGehee MD, Buonassisi T (2015) A 2-terminal perovskite/silicon multijunction solar cell enabled by a silicon tunnel junction. Appl Phys Lett 106(12), article number 121105

Mandelkorn J, McAfee C, Kesperis J, Schwartz L, Pharo W (1962) Fabrication and characteristics of phosphorous-diffused silicon solar cells. J Electrochem Soc 109(4):313–318

Mathew S, Yella A, Gao P, Humphry-Baker R, Curchod BFE, Ashari-Astani N, Tavernelli I, Rothlisberger U, Nazeeruddin MK, Grätzel M (2014) Dye-sensitized solar cells with 13% efficiency achieved through the molecular engineering of porphyrin sensitizers. Nat Chem 6 (3):242–247

Matsui T, Sai H, Suezaki T, Matsumoto M, Saito K, Yoshida I, Kondo M (2013) Development of highly stable and efficient amorphous silicon based solar cells. In: 28th European photovoltaic solar energy conference and exhibition. EU PVSEC, Paris, pp 2213–2217

Meier J, Spitznagel J, Kroll U, Bucher C, Fay S, Moriarty T, Shah A (2004) Potential of amorphous and microcrystalline silicon solar cells. Thin Solid Films 451–452:518–524

Meillaud F, Shah A, Droz C, Vallat-Sauvain E, Miazza C (2006) Efficiency limits for single-junction and tandem solar cells. Sol Energy Mater Sol Cells 90(18–19):2952–2959

Mishra A, Fischer MKR, Bauerle P (2009) Metal-free organic dyes for dye-sensitized solar cells: from structure: property relationships to design rules. Angew Chem Int Ed 48(14):2474–2499

Mor GK, Kim S, Paulose M, Varghese OK, Shankar K, Basham J, Grimes CA (2009) Visible to near-infrared light harvesting in $TiO_2$ nanotube array − P3HT based heterojunction solar cells. Nano Lett 9(12):4250–4257

Nazeeruddin MK, Kay A, Rodicio I, Humpbry-Baker R, Miiller E, Liska P, Vlachopoulos N, Grätzel M (1993) Conversion of light to electricity by cis-$X_2$bis(2,2'-bipyridyl-4,4'-dicarboxylate)ruthenium(II) charge-transfer sensitizers (X = $Cl^-$, $Br^-$, $I^-$, $CN^-$, and $SCN^-$) on nanocrystalline titanium dioxide electrodes. J Am Chem Soc 115(14):6382–6390

Nazeeruddin MK, Zakeeruddin SM, Humphry-Baker R, Jirousek M, Liska P, Vlachopoulos N, Shklover V, Fischer CH, Grätzel M (1999) Acid − base equilibria of (2,2′-Bipyridyl-4,4′-dicarboxylic acid)ruthenium(II) complexes and the effect of protonation on charge-transfer sensitization of nanocrystalline titania. Inorg Chem 38(26):6298–6305

Nazeeruddin MK, Péchy P, Renouard T, Zakeeruddin SM, Humphry-Baker R, Comte P, Liska P, Cevey L, Costa E, Shklover V, Spiccia L, Deacon GB, Bignozzi CA, Grätzel M (2001) Engineering of efficient panchromatic sensitizers for nanocrystalline $TiO_2$-based solar cells. J Am Chem Soc 123(8):1613–1624

Niu G, Li W, Meng F, Wang L, Dong H, Qiu Y (2014) Study on the stability of $CH_3NH_3PbI_3$ films and the effect of post-modification by aluminum oxide in all-solid-state hybrid solar cells. J Mater Chem A 2(3):705–710

Noel NK, Stranks SD, Abate A, Wehrenfennig C, Guarnera S, Haghighirad A, Sadhanala A, Eperon GE, Pathak SK, Johnston MB, Petrozza A, Herza LM, Snaith HJ (2014) Lead-free organic–inorganic tin halide perovskites for photovoltaic applications. Energy Environ Sci 7 (9):3061–3068

NREL. https://www.nrel.gov/news/press/2014/15436.html. Last accessed 25 May 2018

NREL. https://www.nrel.gov/pv/assets/images/efficiency-chart.png. Last accessed 26 May 2018

Nusbaumer H, Moser J, Zakeeruddin S, Nazeeruddin M, Grätzel M (2001) $Co^{II}(dbbip)_2^{2+}$ complex rivals tri-iodide/iodide redox mediator in dye-sensitized photovoltaic cells. J Phys Chem B 105 (43):10461–10464

O'Regan B, Grätzel M (1991) A low-cost, high-efficiency solar cell based on dye-sensitized colloidal $TiO_2$ films. Nature 353(6346):737–740

Ohl R (1942) Light-sensitive electric device including silicon. US Patent 2402662

Olah GA, Prakash GKS, Goeppert A (2011) Anthropogenic chemical carbon cycle for a sustainable future. J Am Chem Soc 133(33):12881–12898

Oskam G, Bergeron B, Meyer G, Searson P (2001) Pseudohalogens for dye-sensitized $TiO_2$ photoelectrochemical cells. J Phys Chem B 105(29):6867–6873

Panasonic https://news.panasonic.com/global/press/data/2014/04/en140410-4/en140410-4.html#top. Last accessed 28 May 2018

Panasonic. https://eu-solar.panasonic.net/en/2337.htm. Last accessed 28 May 2018
Paquette B, Boucherif A, Aimez V, Arès R (2016) Novel multijunction solar cell design for low cost, high concentration systems. Prog Photovolt Res Appl 24(2):150–158
Pazos-Outón LM, Szumilo M, Lamboll R, Richter JM, Crespo-quesada M, Abdi-Jalebi M, Beeson HJ, Vrucinic M, Alsari M, Snaith HJ, Ehrler B, Friend RH, Deschler F (2016) Photon recycling in lead iodide perovskite solar cells. Science 351(6280):1430–1433
Phillips SP, Dimroth F, Bett AW (2012) High efficiency III–V multijunction solar cells. In: McEvoy A, Castaner L, Markvart T (eds) Solar cells—materials, manufacture and operation, 2nd edn, ch. 1C-6. Elsevier, Amsterdam, pp 353–381
Polander LE, Yella A, Teuscher J, Humphry-Baker R, Curchod BFE, Astani NA, Gao P, Moser J-E, Tavernelli I, Rothlisberger U, Grätzel M, Nazeeruddin MK, Frey J (2013) Unravelling the potential for dithienopyrrole sensitizers in dye-sensitized solar cells. Chem Mater 25(13):2642–2648
Razza S, Castro-Hermosa S, Carlo AD, Brown TM (2016) Large-area deposition, coating, printing, and processing, techniques for the upscaling of perovskite solar cell technology. APL Mater 4(9), article number 091508
Rech B, Wagner H (1999) Potential of amorphous silicon for solar cells. Appl Phys A 69(2):155–167
Repins I, Contreras MA, Egaas B, DeHart C, Scharf J, Perkins CL, To B, Noufi R (2008) 19.9%-efficient ZnO/CdS/$CuInGaSe_2$ solar cell with 81.2% fill factor. Prog Photovolt Res Appl 16 (3):235–239
Rittner ES, Arndt RA (1976) Comparison of silicon solar cell efficiency for space and terrestrial use. J Appl Phys 47(7):2999–3002
Robson KCD, Koivisto BD, Yella A, Sporinova B, Nazeeruddin MK, Baumgartner T, Grätzel M, Berlinguette CP (2011) Design and development of functionalized cyclometalated ruthenium chromophores for light-harvesting applications. Inorg Chem 50(12):5494–5508
Rose RD, Magnone P, Zanuccoli M, Sangiorgi E, Fiegna C (2013) Loss analysis of silicon solar cells by means of numerical device simulation. In: 14th international conference on ultimate integration on silicon. IEEE, Coventry, UK, pp 205–208
Sago T (2010) Advances in crystalline silicon solar cell technology for industrial mass production. Asia Mater 2(3):96–102
Saidaminov MI, Abdelhady AL, Murali B, Alarousu E, Burlakov VM, Peng W, Dursun I, Wang L, He Y, MacUlan G, Goriely A, Wu T, Mohammed OF, Bakr OM (2015) High-quality bulk hybrid perovskite single crystals within minutes by inverse temperature crystallization. Nat Commun 6, article number 7586
Sasaki K, Agui T, Nakaido K, Takahashi N, Onitsuku R, Takamoto T (2013) Development of InGaP/GaAs/InGaAs inverted triple junction concentrator solar cells. In: 9th international conference on concentrator photovoltaic systems. AIP, Japan, pp 22–25
Schmieder EK, Haughn C, Pulwin Z, Dyer D, Mutitu J, Doty M, Ebert C, Barnett A (2011) Analysis of high growth rate MOCVD structures by solar cell device measurements. In: 37th Photovoltaic Specialists Conference (PVSC). IEEE, Seattle, pp 000542–000545
Schultz O, Glunz SW, Willeke GP (2004) Multicrystalline silicon solar cells exceeding 20% efficiency. Prog Photovolt Res Appl 12(7):553–558
Shockley W, Queisser HJ (1961) Detailed balance limit of efficiency of p-n junction solar cells. J Appl Phys 32:510–519
Smith DD, Cousins P, Westerberg S, Jesus-Tabajonda RD, Aniero G, Shen Y (2014) Toward the practical limits of silicon solar cells. IEEE J Photovoltaics 4(6):1465–1469
Snaith HJ, Moule AJ, Klein C, Meerholz K, Friend RH, Grätzel M (2007) efficiency enhancements in solid-state hybrid solar cells via reduced charge recombination and increased light capture. Nano Lett 7(11):3372–3376
Solar Energy For Us. https://solarenergyforus.com/amorphous-silicon-thin-film. Last accessed 03 June 2018
Solar Energy For Us. https://solarenergyforus.com/monocrystalline-silicon-solar-panel. Last accessed 03 June 2018

Solar Energy For Us. https://solarenergyforus.com/multijunction-solar-panel. Last accessed 03 June 2018

Solar Energy For Us. https://solarenergyforus.com/polycrystalline-silicon-solar-panel. Last accessed 03 June 2018

Steiner MA, Geisz JF, García I, Friedman DJ, Kurtz SR (2013) Experimental and modeling analysis of internal luminescence in III–V solar cells. In: 9th international conference on concentrator photovoltaic systems. AIP, Miyazaki, pp 57–61

Stergiopoulos T, Arabatzis IM, Katsaros G, Falaras P (2002) Binary polyethylene oxide/titania solid-state redox electrolyte for highly efficient nanocrystalline $TiO_2$ photoelectrochemical cells. Nano Lett 2(11):1259–1261

Stranks SD, Eperon GE, Grancini G, Menelaou C, Alcocer MJP, Leijtens T, Herz LM, Petrozza A, Snaith HJ (2013) Electron-hole diffusion lengths exceeding 1 micrometer in an organometal trihalide perovskite absorber. Science 342(3156):341–343

Szlufcik J, Sivothaman S, Nijs JF, Mertens RP, Overstraeten RV (1997) Low-cost industrial technologies of crystalline silicon solar cells. Proc IEEE 85(5):711–730

Takamoto T, Ikeda E, Kurita H, Ohmori M (1997) Over 30% efficient InGaP/GaAs tandem solar cells. Appl Phys Lett 70(3):381–383

Takamoto T, Agui T, Ikeda E, Kurita H (2000) High-efficiency InGaP/InGaAs tandem solar cells on Ge substrates. In: 28th IEEE photovoltaic specialists conference. IEEE, Anchorage, USA, pp 976–981

Tawada Y, Tsuge K, Kondo M, Okamoto H, Hamakawa Y (1982) Properties and structure of a-SiC: H for high-efficiency a-Si solar cell. J Appl Phys 53(7):5273–5281

Tennakone K, Kumara G, Kumarasinghe A, Wijayantha K, Sirimanne PM (1995) A dye-sensitized nano-porous solid-state photovoltaic cell. Semicond Sci Technol 10(12):1689–1693

Tennakone K, Kumara G, Kottegoda I, Wijayantha K, Perrera V (1998) A solid-state photovoltaic cell sensitized with a ruthenium bipyridyl complex. J Phys D Appl Phys 31(12):1492–1496

Tress W (2017) Perovskite solar cells on the way to their radiative efficiency limit—insights into a success story of high open-circuit voltage and low recombination. Adv Energy Mater 7(14), article number 1602358

Unger EL, Kegelmann L, Suchan K, Sörell D, Korte L, Albrecht S (2017) Roadmap and roadblocks for the band gap tunability of metal halide perovskites. J Mater Chem A 5 (23):11401–11409

Verlinden P, Deng W, Zhang X, Yang Y, Xu J, Shu Y, Quan P, Sheng J, Zhang S, Bao J, Ping F, Zhang Y, Feng Z (2014) The 6th world conference on photovoltaic energy conversion, WCPEC-6, Kyoto

Vossier A, Chemisana D, Flamant G, Dollet A (2012) Very high fluxes for concentrating photovoltaics: considerations from simple experiments and modelling. Renew Energy 38 (1):31–39

Wakisaka K, Sayama K, Tanaka M, Isomura M, Haku H, Kiyma S, Tsuda S (1997) Development of high-efficiency a-Si solar cell submodule with a size of 30 cm $\times$ 40 cm. Sol Energy Mat Sol Cells 49(1–4):121–125

Wang A, Zhao J, Green MA (1990) 24% efficient silicon solar cells. Appl Phys Lett 57:602–604

Wang P, Klein C, Humphry-Baker R, Zakeeruddin SM, Grätzel M (2005) Stable $\geq$ 8% efficient nanocrystalline dye-sensitized solar cell based on an electrolyte of low volatility. Appl Phys Lett 86(12):article number 123508

Warmann EC, Leite MS, Atwater HA (2011) Photovoltaic efficiencies in lattice-matched III-V multijunction solar cells with unconventional lattice parameters. In: 37th Photovoltaic Specialists Conference (PVSC). IEEE, Seattle, pp 000570–000574

Wells HL (1893) Uber die Caesium- und Kalium-Bleihalogenide. Zeitschrift für Anorg. Chemie 3 (1):195–210

Welton T (2004) Ionic liquids in catalysis. Coord Chem Rev 248(21–24):2459–2477

Werner J, Weng C-H, Walter A, Fesquet L, Seif JP, De Wolf S, Niesen B, Ballif C (2016) Efficient monolithic Perovskite/Silicon tandem solar cell with cell area > 1 $cm^2$. J Phys Chem Lett 7 (1):161–166

Werner J, Niesen B, Ballif C (2018) Perovskite/silicon tandem solar cells: marriage of convenience or true love story?—an overview. Adv Mater Interfaces 5(1), article number 1700731

Wheeldon JF, Valdivia CE, Masson D, Proulx F, Riel B, Puetz N, Desfonds E, Farard S, Rioux B, SpringThorpe AJ, Arès R, Aimez V, Armstrong M, Swinton M, Cook J, Shepherd F, Hall TJ, Hinzer K (2010) High-efficiency commercial grade 1 $cm^2$ AlGaInP/GaAs/Ge solar cells with embedded InAs quantum dots for concentrator demonstration system. In: Photonics North. SPIE, Niagara Falls, Canada, pp 77502Q-(1-9)

Wolf M (1960) Limitations and possibilities for improvement of photovoltaic solar energy converters: Part I: considerations for earth's surface operation. Proc IRE 48(7):1246–1263

Wu M, Lin X, Wang Y, Wang L, Guo W, Qi D, Peng X, Hagfeldt A, Grätzel M, Ma T (2012) Economical Pt-free catalysts for counter electrodes of dye-sensitized solar cells. J Am Chem Soc 134(7):3419–3428

Wu J, Lan Z, Lin J, Huang M, Huang Y, Fan L, Luo G (2015) Electrolytes in dye-sensitized solar cells. Chem Rev 115(5):2136–2173

Xuan OZ (2011) Transport imaging of multi-junction and CIGS solar cell materials. Master's thesis, Naval Postgraduate School

Yang JC (1998) Advances in amorphous silicon alloy technology—the achievement of high–efficiency multijunction solar cells and modules. Prog Photovolt Res Appl 6:181–186

Yastrebova NV (2007) High-efficiency multi-junction solar cells: current status and future potential. University of Ottawa

Yella A, Lee H-W, Tsao HN, Yi C, Chandiran AK, Nazeeruddin MK, Diau W-G, Yeh C-Y, Zakeeruddin SM, Grätzel M (2009) Porphyrin-sensitized solar cells with cobalt (II/III)-based redox electrolyte exceed 12 percent efficiency. Science 334(6056):629–634

Yoshikawa K, Kawasaki H, Yoshida W, Irie T, Konishi K, Nakano K, Uto T, Adachi D, Kanematsu M, Uzu H, Yamamoto K (2017) Silicon heterojunction solar cell with interdigitated back contacts for a photoconversion efficiency over 26%. Nat Energy 2, article number 17032

You J, Meng L, Song T, Guo T, Yang Y, Chang W, Hong Z, Chen H, Zhou H, Chen Q, Liu Y, Marco ND, Yang Y (2016) Improved air stability of perovskite solar cells via solution-processed metal oxide transport layers. Nat Nanotechnol 11(1):75–82

Yum J-H, Hagberg DP, Moon S-J, Karlsson KM, Marinado T, Sun L, Hagfeldt A, Nazeeruddin MK, Grätzel M (2009) A light-resistant organic sensitizer for solar-cell applications. Angew Chem Int Ed 48(9):1576–1580

Zeng W, Cao Y, Bai Y, Wang Y, Shi Y, Zhang M, Wang F, Pan C, Wang P (2010) Efficient dye-sensitized solar cells with an organic photosensitizer featuring orderly conjugated ethylenedioxythiophene and dithienosilole blocks. Chem Mater 22(5):1915–1925

Zhan Z, An J, Zhang H, Hansen RV, Zheng L (2012) Three-dimensional plasmonic photoanodes based on Au-embedded $TiO_2$ structures for enhanced visible-light water splitting. Appl Mater Interfaces 6(2):1139–1144

Zhang G, Bala H, Cheng Y, Shi D, Lv X, Yu Q, Wang P (2009) High efficiency and stable dye-sensitized solar cells with an organic chromophore featuring a binary π-conjugated spacer. Chem Commun 0(16):2198–2200

Zhang H, Mao J, He H, Zhang D, Zhu HL, Xie F, Wong KS, Grätzel M, Choy WCH (2015) A smooth $CH_3NH_3PbI_3$ film via a new approach for forming the $PbI_2$ nanostructure together with strategically high $CH_3NH_3I$ concentration for high efficient planar-heterojunction solar cells. Adv Energy Mater 5(3), article number 1501354

Zhang H, Cheng J, Lin F, He H, Mao J, Wong KS, Jen AKY, Choy WCH (2016) Pinhole-free and surface-nanostructured $NiO_x$ film by room-temperature solution process for high-performance flexible perovskite solar cells with good stability and reproducibility. ACS Nano 10(1):1503–1511

Zhao J, Wang A, Green MA (1998) 19.8% efficient "honeycomb" textured multicrystalline and 24.4% monocrystalline silicon solar cells. Appl Phys Lett 73(14):1991–1993

Zhao J, Wang A, Green MA (1999) 24.5% efficiency silicon PERT cells on MCZ substrates and 24.7% efficiency PERL cells on FZ substrates. Prog Photovolt Res Appl 7(6):471–474

Zhao D, Yu Y, Wang C, Liao W, Shrestha N, Grice CR, Cimaroli AJ, Guan L, Ellingson RJ, Zhu K, Zhao X, Xiong R, Yan Y (2017) Low-bandgap mixed tin–lead iodide perovskite absorbers with long carrier lifetimes for all-perovskite tandem solar cells. Nat Energy 2, article number 17018

# Chapter 5
# Natural Dye-Sensitized Solar Cells: Fabrication, Characterization, and Challenges


**D. Ganta, K. Combrink and R. Villanueva**

**Abstract** Bio-inspired dye-sensitized solar cells (DSSCs) from natural plant-based dyes gained importance due to their low cost of manufacturing and environmental friendliness. Not all plants are candidates for DSCCs; they should contain certain pigments such as chlorophyll, anthocyanin, and betalains. Titanium oxide nanoparticles play an important role as electron transporter in the DSSCs. The efficiency is still low in comparison with traditional silicon-based solar cells. There are several challenges to improve the efficiency such as the photodegradation of the dye, the stability of the electrolyte over time, and adhesion of dye with titanium oxide nanoparticles. We reviewed methods for fabricating DSSCs, and the science behind the working principle. Various microscopic and spectroscopic analysis methods such as Fourier transform infrared spectroscopy and confocal microscopy were presented, for investigating optical properties, surface chemistry of the dyes, and in structural characterization of the plant cells. The photoelectrochemical properties such as conversion efficiency measure the performance of the DSSCs. They are usually in the range of 0.05–3.9% depending on the plant dye used, including plant dyes modified. A critical feature in the design of dye-sensitized solar cells is the attachment of the photosensitizing dye to the titanium oxide surface. We reviewed and summarized the design of binding elements that enhance the binding of the sensitizing dye to the titanium dioxide surface. The efficiencies of covalent linkage of the dye to the titanium surface versus non-covalent binding were discussed, including a survey of functional groups and geometries, to determine the most effective reported.

**Keywords** Plant dye solar cells · Titanium oxide · Nanomaterials FTIR · Photovoltaics

D. Ganta (✉) · R. Villanueva
School of Engineering, Texas A&M International University, Laredo, TX 78041, USA
e-mail: deepak.ganta@tamiu.edu

K. Combrink
Department of Biology and Chemistry, Texas A&M International University, Laredo, TX 78041, USA



H. Tyagi et al. (eds.), *Advances in Solar Energy Research*, Energy, Environment, and Sustainability, https://doi.org/10.1007/978-981-13-3302-6_5

## 5.1 Introduction

Energy sustainability strongly depends on utilization of renewable natural resources available such as sunlight and water, including the methods to reduce carbon dioxide emissions. Sunlight is sustainable, inexpensive, and abundant and the use of potential systems mimicking photosynthesis in the plants is underutilized. The solar energy needed to be adequately utilized to prevent pollution and global warming from other nonrenewable energy conversion methods such as coal and fossil fuels. Photovoltaic cell fabricated from silicon and thin film gained importance as first- and second-generation energy devices. The cost of manufacturing is still high and recycling the hardware after use is still a problem causing environmental pollution. There is a huge demand for organic, sustainable, and inexpensive photovoltaic devices, environmentally friendly that mimic plants in energy conversion.

In 1960s, Hishiki and others developed the DSSCs by using zinc oxide and plant dyes (Gerischer et al. 1968; Namba and Hishiki 1965). Later in 1991, Gratzel et al. developed the first DSSCs using nanocrystalline $TiO_2$ replacing the zinc oxide (O'Regan and Gratzel 1991). DSSCs from ruthenium were metal-based dyes and not organic; they recorded high efficiency of 11–12% (Buscaino et al. 2008; Chiba et al. 2006). They are still not environmentally friendly and not safe to handle, and platinum metal used for the cathode is also very expensive. There are three essential parts in DSSCs: cathode or counter electrode, dye, anode or working electrode, and electrolyte. Inexpensive materials such as carbon or graphite are replacing platinum. Currently, the highest efficiency reported in DSSC is 13% (Mathew et al. 2014). Initially, the majority of the dyes were chemical based, used were not green, readily available in nature or sustainable, this motivated many researchers to investigating next-generation bio-based photovoltaic devices, mimicking photosynthesis and utilizing the pigments in the dyes for DSSCs.

Plant-based DSSCs are inexpensive and nontoxic and do not cause harm to the environment in comparison with the chemical-based DSSCs. Plant dyes serve as a sensitizer, which absorbs sunlight and converts solar energy into electric energy. Several plant-based dyes were reported to be used as sensitizers in DSSCs, and the performance results were reported in Table 5.1. The maximum conversion efficiency is still lower ($\sim$3.9%) in comparison with the start-of-the-art non-plant-based or chemical-based DSSCs (13%). The ultimate goal moving forward in the natural bio-based DSSC research is to design and develop DSSCs which are stable and have high conversion efficiency comparable to the silicon-based solar cells. The pigments in the dyes such as chlorophyll, anthocyanin, and betalains are developed in the plants naturally, and it is difficult to vary the surface chemistry or be able to control it over time. Anchoring of those plant pigments to working electrode or titanium oxide film properly with strong adhesion is a significant challenge to the researchers. Researchers are now able to extract pigments of interest, modify the extraction process of the dye with solvents, be able to control the pH of the resultant dye solutions, and further be able to co-sensitize

**Table 5.1** Photoelectrochemical parameters of selected natural plant dyes reported for DSSCs

| Plant source | Structure | $J_{sc}$ (mA/cm$^2$) | $V_{oc}$ (V) | FF (%) | $\eta$ (%) | References |
|---|---|---|---|---|---|---|
| Black rice | Anthocyanin | 2.09 | 0.47 | 57 | 0.56 | Noor et al. (2014) |
| Lawsonia inermis seed | Lawsone | 2.99 | 0.50 | 70 | 1.47 | Ananth et al. (2014) |
| Brown seaweed | Chlorophylls | 0.8 | 0.36 | 69 | 0.18 | Calogero et al. (2014) |
| Red Frangipani | Anthocyanin | 0.94 | 0.49 | 65 | 0.30 | Shanmugam et al. (2013) |
| Ixora sp. (Rubiaceae) | Anthocyanin | 6.26 | 0.35 | 47 | 0.96 | Kumara et al. (2013a) |
| Rhododendron | Anthocyanin | 1.61 | 0.58 | 61 | 0.57 | Zhou et al. (2011) |
| Yellow rose | Xanthophyll | 0.74 | 0.6 | 57 | 0.26 | Zhou et al. (2011) |
| Petunia | Chlorophyll | 0.85 | 0.61 | 61 | 0.32 | Zhou et al. (2011) |
| Violet | Anthocyanin | 1.02 | 0.49 | 65 | 0.33 | Zhou et al. (2011) |
| Rosella | Anthocyanin | 1.63 | 0.4 | 57 | 0.37 | Wongcharee et al. (2007) |
| Blue pea | Anthocyanin | 0.37 | 0.37 | 33 | 0.05 | Wongcharee et al. (2007) |
| Red Bougainvillea spectabilis | Betalain | 2.29 | 0.28 | 76 | 0.48 | Hernandez-Martinez et al. (2011) |
| Hibiscus rosa-sinensis | Anthocyanin | 3.31 | 0.14 | 55 | 1.08 | Yusoff et al. (2014) |
| Blueberry | Anthocyanin | 4.1 | 0.3 | 55 | 0.69 | Teoli et al. (2016) |
| Tangerine peel | Flavone | 0.74 | 0.59 | 63 | 0.28 | Zhou et al. (2011) |
| Fructus lycii | Carotene | 0.53 | 0.68 | 46 | 0.17 | Zhou et al. (2011) |
| Mangosteen pericarp | ∝-Mangostin/ β-mangostin | 2.55 | 0.62 | 58 | 0.92 | Zhou et al. (2011) |
| Wild Sicilian prickly pear | Etalain | 8.20 | 0.38 | 38 | 1.19 | Calogero et al. (2010) |
| Nephelium lappaceum (F: Sapindaceae) | Anthocyanin | 3.88 | 0.41 | 35 | 0.56 | Kumara et al. (2013b) |
| Mulberry fruit | Anthocyanin | 1.89 | 0.56 | 49 | 0.55 | Chang and Lo (2010) |
| Ivy gourd fruits | β-carotene | 0.24 | 0.64 | 49 | 0.08 | Wongcharee et al. (2007) |
| Codiaeum variegatum | Anthocyanin | 4.03 | 0.44 | 55 | 1.08 | Yusoff et al. (2014) |
| Ipomoea | Chlorophyll | 0.91 | 0.54 | 56 | 0.28 | Chang et al. (2010) |
| Rhoeo spathacea | Chlorophyll, carotenoids | 10.9 | 0.5 | 27 | 1.49 | Lai et al. (2008) |
| Red cabbage | Anthocyanin | 2.25 | 0.62 | 70 | 0.97 | Chien and Hsu (2014) |

(continued)

**Table 5.1** (continued)

| Plant source | Structure | $J_{sc}$ (mA/cm$^2$) | $V_{oc}$ (V) | FF (%) | $\eta$ (%) | References |
|---|---|---|---|---|---|---|
| Pandan leaves | Chlorophyll | 1.91 | 0.48 | 56 | 0.51 | Noor et al. (2014) |
| Spinach | Modified chlorophyll/ neoxanthin | 11.8 | 0.55 | 60 | 3.9 | Wang et al. (2006) |
| Aloe vera | Anthocyanin | 0.11 | 0.67 | 50 | 0.38 | Ganta et al. (2017) |
| Cladode of cactus | Chlorophyll | 0.24 | 0.64 | 48 | 0.74 | Ganta et al. (2017) |

the $TiO_2$ film, all of which lead to an improvement in the performance of the natural plant-based DSSCs (Hug et al. 2014; Kumara et al. 2017).

A critical feature in the design of dye-sensitized solar cells is the attachment of the photosensitizing dye to the titanium oxide surface. The effort was devoted to exploring the structural features needed for efficient dye-sensitized solar cells (Hagfeldt et al. 2010). Despite the vast variety of structures for the donor–π-bridge–acceptor motifs of organic dye-sensitized molecules, there are a small set of acceptor groups used in the dyes. The acceptor portion of the dye serves several critical functions. The first is to participate in the transfer of electrons in the donor–acceptor motif to facilitate the rapid charge transfer of the hole to the redox mediator and the second is to bind to the titanium oxide layer to facilitate the transfer of charge into the titanium oxide conduction band. The binding of the dye to the titanium layer should be strong and should favor the formation of a tightly packed monolayer that is devoid of aggregates. The most common acceptor functional group is a carboxylic acid which has several common binding modes (Hagfeldt et al. 2010). The binding mode of the carboxylic acid was determined by analysis of the carbonyl (C=O) stretch frequency as well as the O–C–O asymmetric stretch of the carboxylic acid (Hagfeldt et al. 2010).

In this chapter, we discuss and review methods reported to develop natural plant-based DSSCs and the challenges in the surface adhesion chemistry. In Sect. 5.2, we discuss the structure and operation of the DSSCs and the science behind it followed by Sect. 5.3 where we will discuss the methods used in the fabrication of DSSCs. In Sect. 5.4, we review the challenges in the adhesion of plant dye in the DSSCs, comparing covalent versus intermolecular bonding in the dyes, and a discussion on the solvent systems which will aid the adsorption of the dye onto $TiO_2$. In Sect. 5.5, we will discuss various analytical methods used for characterization of the plant dye, including characterization of its interaction with titanium oxide; followed by methods and results on testing the performance of the DSSCs in Sect. 5.6. In Sects. 5.7 and 5.8, we conclude with a summary or discussion on the future direction and perspectives.

## 5.2 Structure and Operating Principle of DSSCs

There are four main components in $TiO_2$-based natural plant dye solar cells: (1) conducting oxide (CO) glass slide coated with monocrystalline titanium oxide film (working electrode or anode), (2) counter electrode or cathode (carbon or platinum coated conductive glass), (3) plant dye, and (4) electrolyte. In this section, we will discuss the science involved in them to operate as a simple DSSCs. The nanoscale $TiO_2$ nanopowder in the form of a film coated on the conducting glass slide and the glass slide is immersed in the plant dye solution for the proper amount of time to dye the $TiO_2$ film properly. Here, the electrolyte which contains ($I_3^-/I^-$) acts as a redox mediator in the entire operation of the DSSCs. The plant dyes should have the required chemical bonds to anchor such as carboxyl group to attach onto the $TiO_2$ film. Figure 5.1 shows the schematic diagram of the components in DSSCs.

The entire operation involves transport of electrons generated by absorption of photons from sunlight through the photoexcitation of the plant dye. Plant dye absorbs photons from sunlight; electrons are generated from the photoexcitation of the plant dye. Electrons were further energized enough to move from highest energy occupied molecular orbital (HOMO) to lowest energy occupied molecular orbital (LUMO). The difference between HOMO and LUMO has a more significant

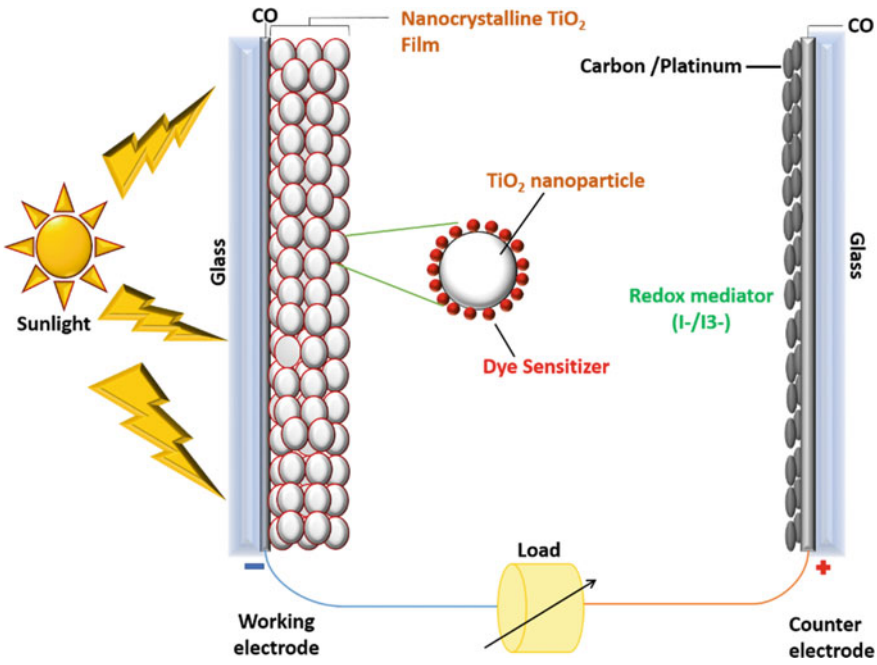


**Fig. 5.1** Schematic of the structure of the DSSCs

influence on the absorption properties, including the range of the absorption of the plant dye. Electrons then jump or transport to the conduction band (CB) of $TiO_2$ and are further transported further via $TiO_2$ nanoparticles mesh through an external load to reach the cathode, thereby completing the electrical circuit, leading to the conversion of energy from sunlight to electric energy.

It is crucial that the LUMO energy level of the dye be higher than the energy of the (CB) of $TiO_2$ and the HOMO should also be lower than the redox potential of the electrolyte used. It is also crucial to have a uniform and crack-free $TiO_2$ coating on the surface of a conductive glass slide. The final step in the operation of DSSCs is the dye regeneration as the result of oxidation of the dye; electrolyte plays a vital role in supplying the required electrons from the $I^-$ ions. Figure 5.2 shows a simplified schematic illustrating the operation principle of DSSCs.

There are also challenges involved in the undesirable recombination processes involving electrons generated and oxidized dye within the dye, trying to hinder the electron transport but that process is not kinetically favorable to dominate the regular electron transport (Ning et al. 2010; Preat et al. 2010; Meng et al. 2008; Maurya et al. 2016; Maiaugree et al. 2015). The efficiency of the DSSC is strongly dependent on the electron transport kinetics happening at the interfaces across of the main components of the DSSCs. Conversion efficiency is highly dependent on the anchoring groups, electrolyte, cathode material, and anode material. Band structure (especially bandgap between HOMO and LUMO) also plays a vital role in the absorption of the sunlight. LUMO energy level of the dye not being higher than

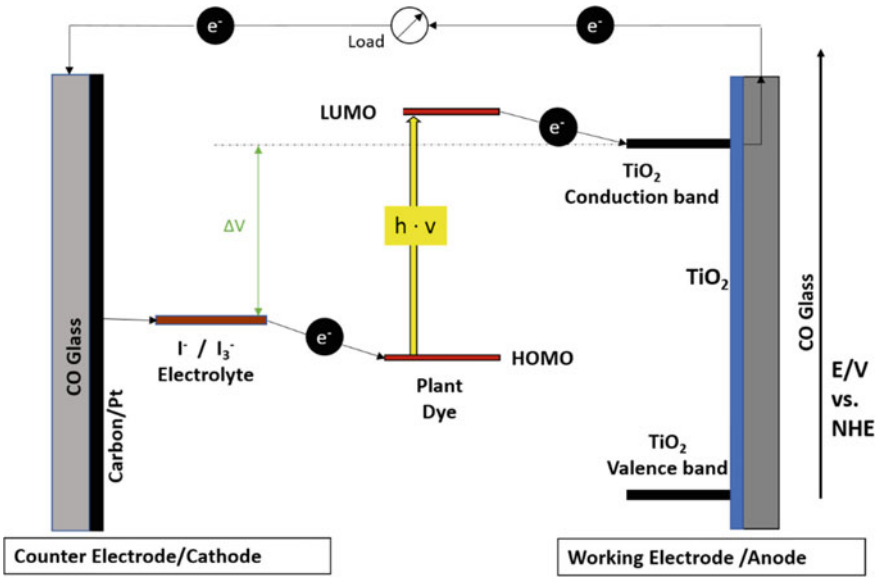


**Fig. 5.2** Schematic of the operation of the DSSCs, describing the energy levels and electron transfer from the anode to cathode across various interfaces such as dye–$TiO_2$ and electrolyte–dye

the energy of the conduction band (CB) reduces the overall conversion efficiency. In summary, the electron generation, electron transport, and dye regeneration are three crucial steps in the operation of the DSSCs.

## 5.3 Methods of Fabrication of DSSCs

In this section, we would discuss the selection of the plant dye, fabrication methods reported in the assembly of the DSSCs, with an example on how we assembled the DSSC with the cladode (*nopal*) of the prickly pear cactus (*optunia ficus–indica*) plant dye.

### *5.3.1 Selection and Preparation of the Natural Dye Sensitizers*

Natural plant-based dyes are inexpensive, nontoxic, environmentally friendly, and readily available. The dyes are usually extracted through a cost-effective and straightforward process mostly from the flowers and leaves of the plants. The color of the dye depends on the pigments present in the dye such as chlorophyll, anthocyanin, and betalains. The plant dyes should have absorption in the visible or near-infrared region in order to be suitable for energy conversion.

Figure 5.3 shows a simple design of the dye which acts as a photosensitizer. A π bridge connects the donor and acceptor part of dye and has donor and acceptor

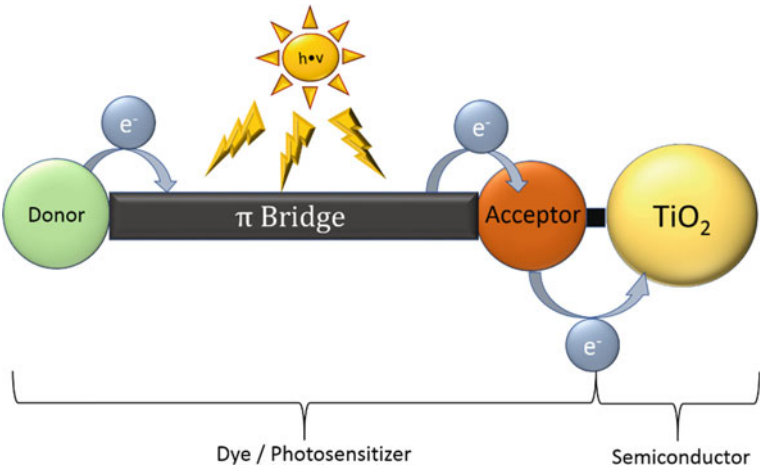


**Fig. 5.3** Simple design (donor–π–acceptor) structure of the dye

part for electrons. The functional groups present in the dye which anchor to the $TiO_2$ are present on the acceptor part of the dye. The chemical adsorption or adhesion of the natural dyes on the surface of the $TiO_2$ film occurs due to the presence of the anchoring functional groups present in the dye such as hydroxyl (–OH) groups, esters, and carbonyl (C=O) groups (Meng et al. 2008; Maurya et al. 2016; Maiaugree et al. 2015). For example, in the case of anthocyanin molecule, it binds with $TiO_2$ via carbonyl and hydroxyl groups; these anchors transfer the electrons from the photo-excited dye to $TiO_2$ film.

There are several methods reported where dyes are either modified, mixed to form a cocktail or used in the side-by-side configuration, including several factors which must be taken into account such as pH of the plant dye extract solution (Hug et al. 2014; Kumara et al. 2017; Teoli et al. 2016). Figure 5.4 shows a simple schematic of the chemical structure of the selective dyes most commonly used in DSSC fabrication, anthocyanin, β-mangostin, and chlorophyll a. Instability of the plant-based dye under exposure to sunlight is a significant concern. Two steps were considered, including solar cell assembly under an inert atmosphere and protection from sunlight, and still, they do not last more than a year (Hug et al. 2014; Calogero et al. 2012). One of the quick solutions for the problem would be to find ways to add new dye or exchange it with similar or another dye without disturbing the adhesion of the dye to $TiO_2$. Another approach would be to find ways to modify the surface chemistry of the dye to prevent photodecay while the efficiency is varied over time. In nature, plant and other biological species can regrow the pigments internally as they get damaged, and the damaged ones get replaced, without any external support.

The inexpensive and straightforward plant dye extraction procedures for cladodes of prickly pear cactus are discussed. First, the cladodes are cleaned and rinsed with water. Next, small pieces of them were blended in a blender until we were able to obtain a liquid natural plant dye solution. The plant dye is diluted with ethanol to give a final ratio of ethanol to dye of 1:1. The plant dye solutions were further filtered to remove any solid residue present in the solution. The dye can decay over time under exposure to sunlight. In the next step, care was taken to cover the dye with aluminum foil and stored in the refrigerator to prevent any contamination or photodecay. We have attempted to image the cells in the plant dye using confocal microscopy, upon excitation with a light source of 500–560 nm, as illustrated in Fig. 5.5. The information on the cells structural integrity can be beneficial in the design of DSCCs, thereby improving their efficiency. The dye is clear and ready for use, as illustrated in Fig. 5.6. The plant dyes are usually used within 48 h. Still, systematic study needed to be conducted to investigate how chemical bonds change with time under exposure to the sunlight over a period of few hours or months to estimate the lifetime of the cell.

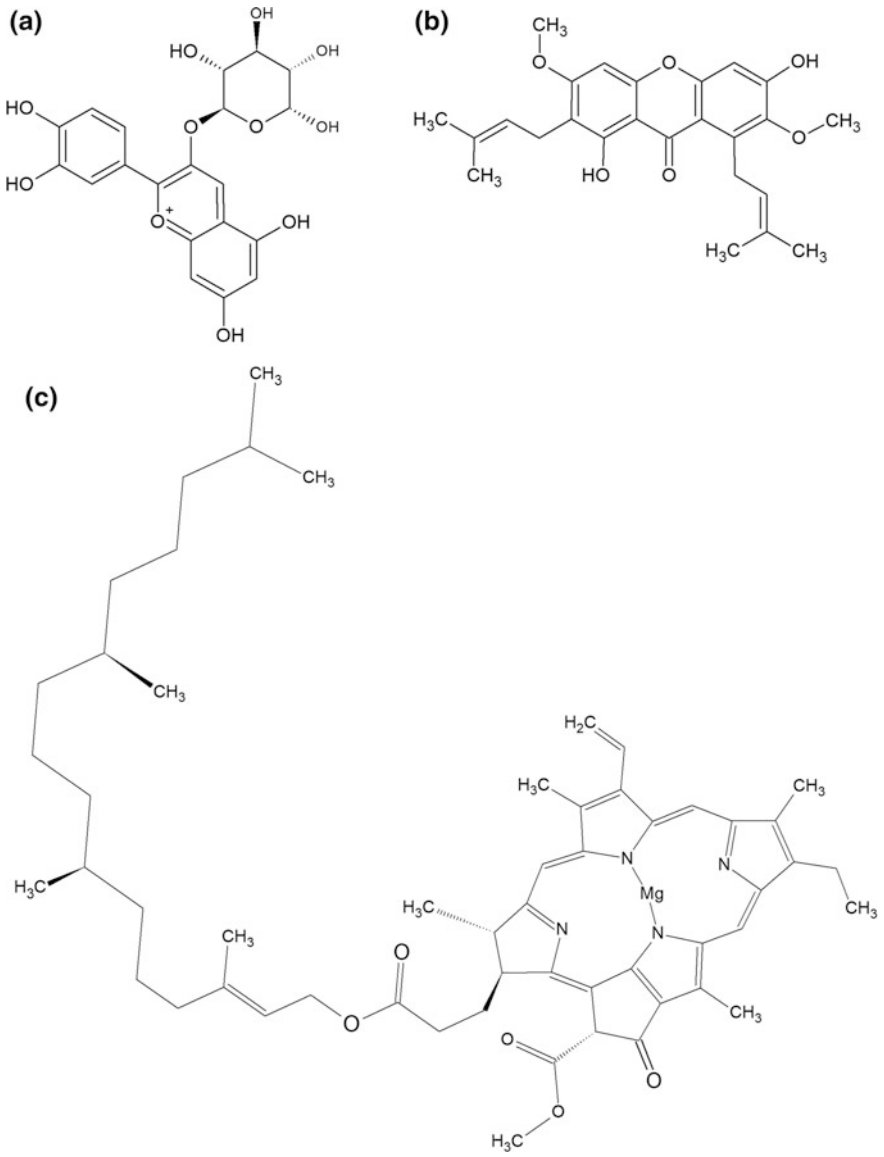


**Fig. 5.4** Chemical structure of the most commonly used dye classes: **a** cyanin (an anthocyanin), **b** β-mangostin, **c** chlorophyll a

## *5.3.2 Working Electrode and Fabrication Method*

$TiO_2$ is the choice of semiconductor material used for photoelectrode in the DSSCs. It is nontoxic, inexpensive, and can be handled safely. The nanopowder of $TiO_2$ is

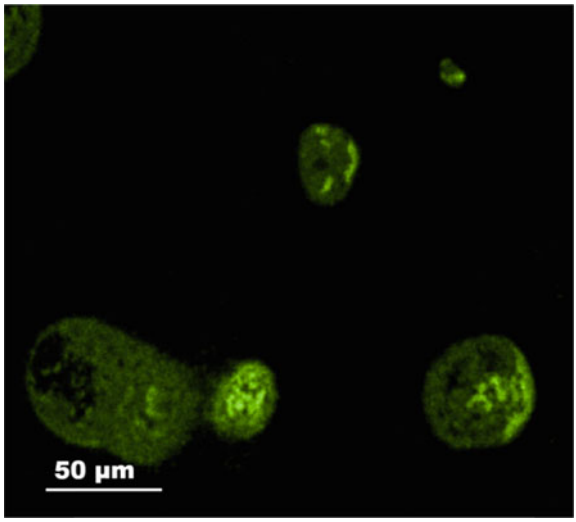


**Fig. 5.5** Confocal microscopy image of the cells present in a plant dye (cladode) used for DSSCs

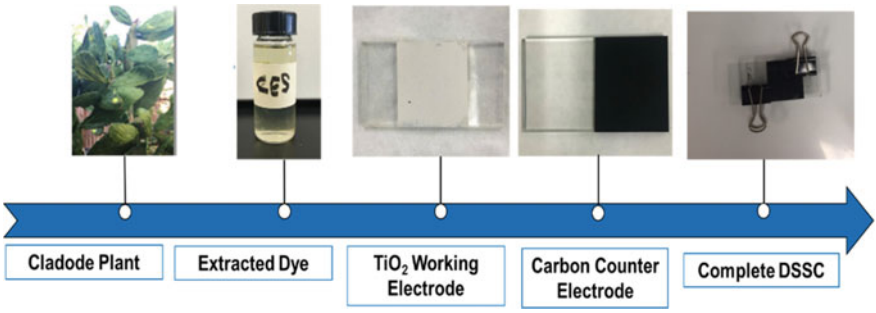


**Fig. 5.6** Steps in the fabrication of DSSCs from the extraction of cladode, to the complete assembly of the solar cell

used to increase the surface area for natural dye absorption. The LUMO of many dyes is compatible with $TiO_2$. $TiO_2$ is also available in a crystalline form to increase the surface area. Usually, X-ray diffraction methods are used to test the crystallinity (anatase) for the in-house prepared nanopowder. Other conditions which are met by $TiO_2$ include having high carrier mobility to be able to collect the photoelectrons efficiently. Other materials such as zinc oxide, stannic oxide, and magnesium oxide are used for the working electrode fabrication (Fukai et al. 2007; Sakai et al. 2013; Kumara et al. 2004).

For the fabrication of the working electrode, transparent CO glass was chosen with right resistance; in our case, we have chosen fluorine-doped tin oxide (FTO) glass with a sheet resistance of 14 Ω/sq obtained commercially. FTO glass is cleaned to ensure no impurities or contaminants on the surface using acetone and ethanol in an ultrasonic bath and preheated to test for cracking. Next, a thin film of $TiO_2$ was deposited from nanopowder paste using a combination of blade and tape casting to ensure proper height and uniformity, followed by annealing at a high temperature of around 390 °C. It is essential to ensure that there is no aggregation in the $TiO_2$ particles. The coating should be uniform without any cracks and nicely spread over the conductive side of the FTO glass slide, and the nonconductive side left for the electrical contact.

The titanium oxide-coated FTO glass is then immersed in the plant dye, inside a petri dish and left undisturbed for ~24 h and the petri dish is covered to prevent any photodecay of the dye. The immersion time of the natural dye plays a vital role in the performance of the DSSCs, and we should ensure the titanium oxide film is dyed correctly by observing the color change on the surface by simple inspection.

### *5.3.3 Preparation of Counter Electrode*

The requirements for a counter electrode or cathode include being a good conductor, electron donor to the oxidized electrolyte reducing it with low overvoltage, low resistance to charge transport, entire surface should be able to respond to charge transport, and highly stable under the influence of light over time (Kumara et al. 2017). In summary, the triiodide is formed from the plant dye reduced at the cathode.

The materials used for the counter electrode are platinum and carbon. Although platinum is a better material as a counter electrode for reduction reaction and most commonly used for electrochemistry experiments, carbon or graphite coating is inexpensive, readily available in many forms and easy to handle. The conductive glass slide is coated with the material of choice, in our case we used carbon or graphite, and FTO glass slides cleaned in an ultrasonic bath with acetone and ethanol for 10 min.

The conductive glass is simply burned with an electric lighter to form a nice and uniform coating of carbon black on the surface. The carbon coating should be stable and adhered correctly to the glass slide and not washed out in the presence of an electrolyte. Another method is to either deposit carbon soot or paint the conductive glass with colloidal graphite (Ghann et al. 2017). The platinum electrode is prepared by the sputtering method, where a thin film of platinum is deposited on the surface of the conductive glass slide, and the thickness of the film can be controlled (Hug et al. 2014; Kumara et al. 2017; Maiaugree et al. 2015).

### 5.3.4 Electrolyte Preparation and Assembly of DSSCs

The primary function of the electrolyte is the redox reaction, where the electron is transferred from the electrolyte to the oxidized dye, to complete the dye regeneration process. There are three type of electrolytes usually used for DSSCs, liquid, solid, and quasi-solid and should have properties such as (1) nontoxic and noncorrosive, (2) high ionic/electrical conductivity, (3) does not photodegrade, (4) good contact with both monocrystalline $TiO_2$ on one side and counter electrode on the other side, and (5) does not react with either dye or electrodes and lead to unwanted byproducts from the chemical reaction. The most widely used electrolyte is iodide–triiodide ($I^-/I_3^-$). The lack of stability and the need to refill the electrolyte in the DSSCs over time is still a significant issue in the development of DSSCs.

We prepared the electrolyte solution from 0.5 M potassium iodide, 0.5 M iodine, water, and ethylene glycol. Both counter and working electrodes are brought closer and held together with clips with a tiny gap in between for the electrolyte solution. Finally, using a pipette or a dropper electrolyte, drops are injected into the tiny gap between the electrodes. Proper care must be taken to ensure the electrolyte gently seeps inside the cell upon injection into the small space between the electrodes, filling it entirely with the capillary action. Visual inspection must be done to ensure there is either no carbon black washout or titanium oxide nanoparticles removed and dissolved in the electrolyte. Figure 5.6 shows the simple illustration of the steps involved in the DSSCs fabrication. The main steps in the development of DSSCs, as shown in the figure, include extraction of the dye, titanium oxide working electrode fabrication, carbon counter electrode fabrication, and assembly of working and counter electrode together sandwiched with electrolyte in between them.

## 5.4 Dye Adsorption on Titanium Oxide and Challenges

### 5.4.1 Covalent Versus Intermolecular Bonding Dyes

Catechols are the most common anchoring group found in natural product-derived sensitizing dyes. The anchoring group can mimic mussel adhesion proteins that can bind strongly to a variety of surfaces including wet surfaces (Sidharam et al. 2014). Electron-withdrawing groups added to the catechol can be used to tune the bond strength. However, this approach has not been widely used in dye solar cells (Sidharam et al. 2014). Four binding modes are possible including several hydrogen bonding arrangements, chelative, and binuclear dentate binding (Fig. 5.7) (Sidharam et al. 2014).

For synthetic dyes, the most common acceptor–anchoring functional groups are the carboxylic acid and the cyanoacrylate groups (Hagfeldt et al. 2010). In examples where a direct comparison can be made, the cyanoacrylate anchor gave slightly

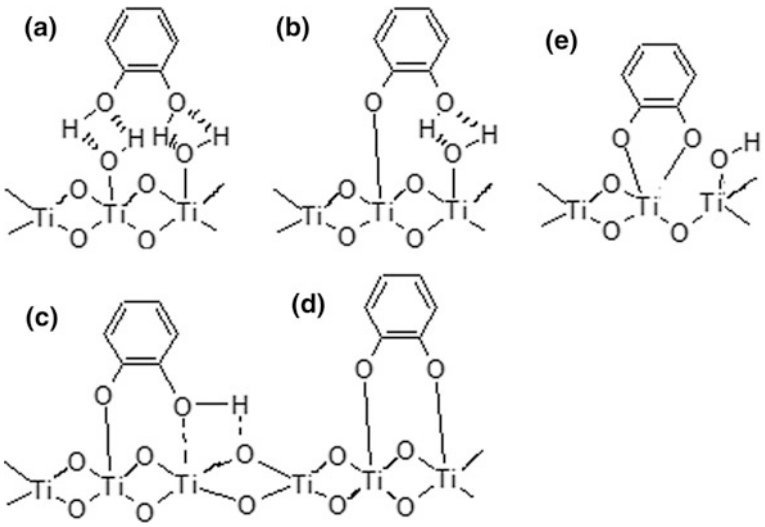


**Fig. 5.7** Binding modes for catechols (Sidharam et al. 2014). **a** Hydrogen bonding, **b** monodentate w/bridging hydrogen bonding, **c** binuclear bidentate, **d** chelative bridging, **e** bidentate chelating

better solar cell efficiency than the carboxylic acid (Prauzner-Bechcicki et al. 2016a). Dyes with acids are typically soaked with the titanium dioxide layer in a polar aprotic solvent such as THF or $CH_3CN$ (Sidharam et al. 2014). This procedure often gives initial weak hydrogen bonding interaction with the titanium dioxide surface (Sidharam et al. 2014). Heating after adsorption can improve the stability of the binding due to the formation of bidentate adsorption (Fig. 5.8) (Sidharam et al. 2014). As was observed in the catechol dyes, the electron-withdrawing nitrile is likely contributing stronger binding due to increased acidity of the acrylic acid in this system. Carboxylic acids have several documented binding modes (Hagfeldt et al. 2010; Sidharam et al. 2014; Murakoshi et al. 1995). The binding mode achieved is dependent on the conditions used for the adsorption process (Sidharam et al. 2014). A hydrogen bonding arrangement is often first formed between the carboxylic acid and the titanium dioxide surface that can be further strengthened by heating the adsorbed acid to form an ester-like bond to the $TiO_2$ surface (Sidharam et al. 2014). In an example with a porphyrin dye using scanning probe microscopy, the orientation of the dye changes from a flat orientation to an edge orientation on heating (Prauzner-Bechcicki et al. 2016a).

It cannot be assumed that the polar acceptor groups are the only functional groups interacting with the titanium dioxide surface. Pretreating the titanium nanoparticles with nitric acid has been reported to reduce the time required for adsorption when compared to conventional soaking methods (Kim et al. 2013). Although the dye adsorption process was faster, the stability over time was similar (Kim et al. 2013). Several papers explore adding a second or third acceptor–anchoring system, and in some cases, the multi-anchored systems do show

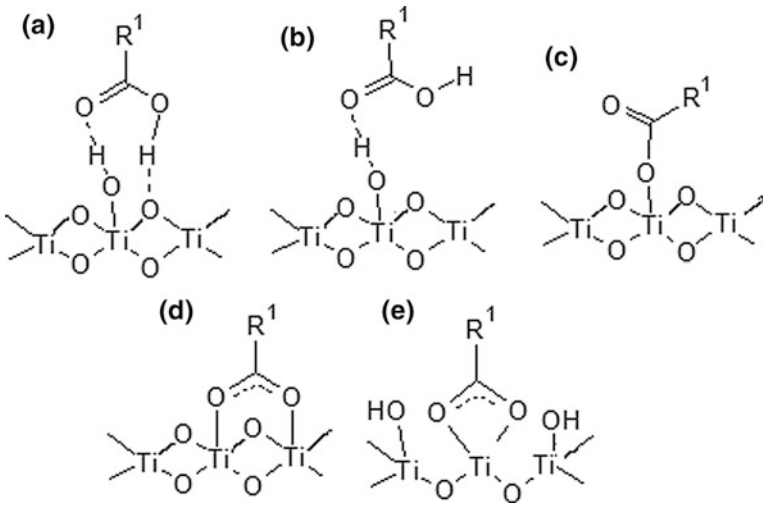


**Fig. 5.8** Binding modes of carboxylate groups to metal oxides (Sidharam et al. 2014). **a** Hydrogen bonding to the bridging oxygen, **b** hydrogen bonding to the carbonyl oxygen, **c** monodentate methyl ester, **d** bidentate bridging, **e** bidentate chelating

enhanced efficiency when compared to the single-anchor systems (Lee et al. 2016; Song et al. 2018). In other systems, there is no trend toward multi-anchor systems being superior (Chen and Lin 2017). Aggregation of the dye can limit the efficiency of the binding, and some compounds showed improved binding due to the addition of branched or aliphatic chains to limit aggregation (Song et al. 2018). The study also explored the aqueous stability of nine representative dyes. The nine compounds represented only the carboxylic acid and cyanoacrylate acceptor–anchoring groups. In this study, the superior binding compound in the aqueous solution used a carboxylic acid anchor, but the authors noted that the lipophilicity of the compounds due to added alkyl side chains away from the carboxylic acid anchor played a role in the added stability due to reduced aggregation (Song et al. 2018).

Since nonaqueous electrolyte solutions are commonly used, poor stability in aqueous solution may not necessarily be a fatal flaw for a dye-sensitized molecule. A study looking at multi-anchoring sensitizers indicated that di- and tri-anchored dyes had better long-term stability (Lee et al. 2016). In this study, the electrolyte solution was a nonaqueous ionic liquid with lithium iodide–iodine system and an acetonitrile/valeronitrile as a solvent (Lee et al. 2016). The triple-anchored dye was reported to be stable to desorption in concentrated aqueous KOH solution which the authors speculated would result in an improved lifetime of the cell (Lee et al. 2016). The acceptor–anchoring group in this study was the cyanoacrylate, and the authors showed with IR data that the cyano group did not contribute to the binding of the dye to the titanium dioxide layer (Lee et al. 2016). A study looking at several porphyrin derivatives by scanning probe microscopy found that the binding mode varied from the edge on to a flat-lying geometry depending on how the dye is

attached to the titanium dioxide layer (Prauzner-Bechcicki et al. 2016a). This study demonstrates that the conditions and solvent used to adsorb the dye to the titanium dioxide substrate are critical for determining the binding mode, efficiency, and possibly the longevity of the cell (Prauzner-Bechcicki et al. 2016a).

Dye adsorption conditions vary from several hours at room temperature (Hagfeldt et al. 2010) to elevated temperatures for one to several hours at temperatures ranging from 50 to 80 °C (Prauzner-Bechcicki et al. 2016a). Dye aggregation can also be addressed by using coadsorbents such as chenodeoxycholic acid (cheno) and deoxycholic acid usually directly in the dye solution during the adsorption process (Sidharam et al. 2014). The coadsorbant in cases where aggregation is not a problem can limit the amount of dye loading which may reduce the efficiency of the system (Sidharam et al. 2014).

Some effort has been devoted to finding additional acceptor groups that have a high affinity for the titanium dioxide layer. Most of the functional group acceptor studies used a porphyrin motif for the dye (Higashino et al. 2017; Tomohiro et al. 2015, 2017). Non-covalent titanium-binding acceptors such as tropolone, 8-hydroxyquinoline, hydroxamic acid, pyridine, and phosphinic acid anchoring groups have been reported (Higashino et al. 2017; Tomohiro et al. 2015, 2017; He et al. 2012; Ismael et al. 2012; Kakiage et al. 2015; Mai et al. 2015).

Infrared (IR) spectroscopy is the primary tool for determining the binding mode for acceptor groups. For the tropolone derivative, the binding mode is reported as bidentate as evidenced by broadening of the OH and C=O stretches in the IR spectra of the unbound and bound forms of the acceptor indicating a symmetrical bidentate binding mode (Tomohiro et al. 2015). A similar observation is reported for the hydroxamic acids with the hydroxy IR peak disappearing and the C=O peak shifting to low wavenumbers indicating the formation of a bidentate keto form of the hydroxamic acid (Tomohiro et al. 2017). Both papers also report that the compounds are very strongly bound to silica gel which eliminates silica gel chromatography as a method for purification. Three pyridine acceptors were evaluated and had several possible binding modes (Mai et al. 2015). The unsubstituted 4-pyridyl derivative can directly interact with the metal in a Lewis acid–base interaction or through a hydrogen bonding interaction with the oxide metal surface and the Lewis basic pyridine nitrogen. Both binding modes are monodentate (Mai et al. 2015). A second 2-pyridone (2-hydroxypyridine) motif takes advantage of pyridones ability to form a bidentate ligand based on the pyridine nitrogen and the pyridone oxygen acting as a Lewis base that can interact with the titanium metal surface (Mai et al. 2015). The third pyridine derivative is a 2-carboxypyridine that acts as carboxylic acid and does not appear to involve the pyridine nitrogen in the binding mode resulting in the normal carboxylic acid binding with no evidence for ester formation with the titanium oxide surface (Mai et al. 2015). A pyridine ring is more electron deficient than a benzene ring resulting in a strong binding interaction with good long-term stability (Mai et al. 2015). A phosphinic acid anchoring group has also been described as a new anchoring group (Ismael et al. 2012). The phosphinic acid group was a tight binder to the titanium dioxide which translated to better long-term stability. The authors noted some aggregation issues that were

improved with coadsorption with cheno with a slight enhancement in efficiency despite lower sensitizer binding.

A slightly different approach has been reported with a silyl anchor that forms a covalent bond to the titanium surface (Higashino et al. 2017; Kakiage et al. 2015). The propargyl silyl group gave the fastest surface coverage while the aryl silyl groups required (Ghann et al. 2017) hours to reach constant surface coverage. The conditions used to attach the silane to the surface were critical as well as the ethanol solution gave poor results while a mixture of toluene/acetonitrile (9/1) gave the best results (Higashino et al. 2017). A comparison of a carboxylic acid derivative versus the silyl adsorped anchor showed impressive retention of the dye in aqueous solution with the silyl groups remaining after 7 h in an aqueous solution (Higashino et al. 2017). The second series of silyl anchored dyes were reported using a diphenylamine and indazole donor-based dyes (Kakiage et al. 2015). Both silyl compounds showed similar improvements in dye adsorption when compared to their carboxylic acid and cyanoacrylate analogs (Higashino et al. 2017; Kakiage et al. 2015).

All of the anchoring group explorations did not significantly improve the efficiency of the devices. The tighter binding compounds, as well as the covalently linked compounds, appear to improve the stability of the devices significantly. A robust screening method to determine the strength of binding to a titanium dioxide substrate could allow more rapid screening of additional functional groups that could be used as anchoring groups. Titanium dioxide affinity columns have been reported to be useful for enriching samples with phosphorylated proteins (Engholm-Keller and Larsen 2011). Although commercial titanium dioxide chromatography columns do not exist, a thin layer system should provide a quick screening method to explore additional anchoring groups and different solvent systems that could be used to improve dye binding. New anchoring groups have focused on known metal binding groups such as hydroxamic acids, 8-hydroxyquinolines, 2-hydroxypyridines, phosphinic acids, and tropolones. Acid isosteres such as sulfonamides, sulphonic acids, acyl sulfonamides, tetrazoles, or covalent linkers such as a phosphoramidite have not been explored. These groups could be screened for titanium dioxide binding efficiency quickly, and the strongest binders could be incorporated into current or new dyes. A similar approach was used to measure the protein binding for drug candidates (Cheng et al. 2004). This method uses an HPLC column with human albumin-bound as the stationary to estimate the binding of compounds based on the retention time of the compounds on this chromatography column and compounds with known binding values and retention times (Cheng et al. 2004).

Dyes for solar cells are typically dissolved in water, or a polar organic solvent such as chloroform, ethanol, acetonitrile, dimethyl sulfoxide (DMSO), dimethylformamide (DMF), or supercritical carbon dioxide and titanium dioxide coated plates are dipped or soaked in these solutions for various amounts of time depending on the dye used. The solvent used, time, and method of soaking vary and

are critical for the effective formation of the dye titanium dioxide interface (Song et al. 2018; Rajab 2016; Tedla and Tai 2018; Tian et al. 2008). Since most dyes rely on hydrogen bonding or dipole interactions with the titanium dioxide layer for adsorption, solvents that do not compete with the dye for titanium dioxide binding would be expected to have the most extended cell life. Water is a poor solvent choice for the electrolyte solution because desorption of the dye commonly observed with carboxylic acid acceptors (Tian et al. 2008). Several researchers report that polar aprotic solvents give better adsorption than polar protic solvents like methanol or ethanol (Sidharam et al. 2014; Tian et al. 2008; Ali Shah et al. 2017). For this reason, the electrolyte solution is often different from the solution used to adsorb the dye to the titanium dioxide surface. Polar aprotic solvents such as chloroform, acetonitrile, or a higher boiling valeronitrile were often used alone, or in combination with polyethylene glycol (PEG), ion liquids (1,2-dimethyl-3-propylimidazolium iodide or 1-butyl-3-methylimidizoliumbromide), or 4-tert-butylpyridine for the electrolyte solution in dye-sensitized solar cells (Prauzner-Bechcicki et al. 2016a; Higashino et al. 2017; Nurrisma et al. 2017).

### *5.4.2 Solvent Systems for Dye Absorption*

The solvent choice and time for the adsorption process influence the amount of dye adsorbed, the type of bonding achieved, and the stability of the deposited monolayer obtained (Sidharam et al. 2014; Rajab 2016; Tedla and Tai 2018; Tian et al. 2008; Prauzner-Bechcicki et al. 2016b). Since the key binding modes of acceptors rely on hydrogen bonding or dipole–dipole interactions, solvents that can also bind to the titanium dioxide layer using these binding modes will decrease the binding efficiency of the dye for the titanium dioxide layer, thus reducing efficiency and durability of the system. A solvent is also necessary to allow the electrolyte to interact with the plant dye in the recycle process. The electrolyte solvent must solvate the electrolyte system as well as maintain the dye monolayer on the titanium surface. Modest improvements in the efficiency of DSSCs have been made, but less effort has been devoted to DSSCs long-term stability. Recent reports of stronger titanium dioxide binding acceptor groups as well as new covalent dye $TiO_2$ anchors indicate that progress is being made to improve the long-term stability of these new solar cells.

## 5.5 Analysis Methods

In this section, we would provide a brief overview of the commonly used methods to test the natural plant dye and the $TiO_2$ film.

### 5.5.1 Characterization of the Dye

It is important to test the dye for its optical properties and chemical structure, if it is suitable for the fabrication of the DSSCs and the two methods used for that purpose are optical absorption and Fourier transform infrared spectroscopy (FTIR). If the solution is dilute which is the case for dye solution, absorbance is then described by the Beer–Lambert Law:

$$A = \varepsilon(\lambda)CL \tag{5.1}$$

where $L$ is the path length in cm, $A$ is the absorbance, $C$ is the molar concentration of the material absorbing (dye in our case) in $M$, and $\varepsilon(\lambda)$ is the extinction coefficient or molar absorptivity in $cm^{-1}$ $M^{-1}$, strongly dependent on the wavelength of the light or laser used.

Figure 5.9 illustrates the UV–Vis absorption spectra obtained in the wavelength range of 500–800 nm for the dye ethanol extracts of cladode. A stronger absorption peak at 662 nm was observed for the cladode extract, confirming the presence of chlorophyll. Similarly, for aloe vera dye extract, an absorption peak was observed at 524 nm, a signature showing the presence of anthocyanins. Normally, strong absorption peaks were seen near-visible and near-infrared region for plant dyes used in the DSSCs.

While absorption spectra verify the presence of the right pigments present in the dye, we need to verify the presence of the chemical bonds or anchors needed for adhesion onto the $TiO_2$ film, and for that purpose, FTIR spectroscopy technique is used. The fundamental principle behind FTIR is that several wavelengths or frequencies of infrared light are incident or exposed on the sample; some of the light is absorbed by the sample, and rest is transmitted and molecular fingerprint of the

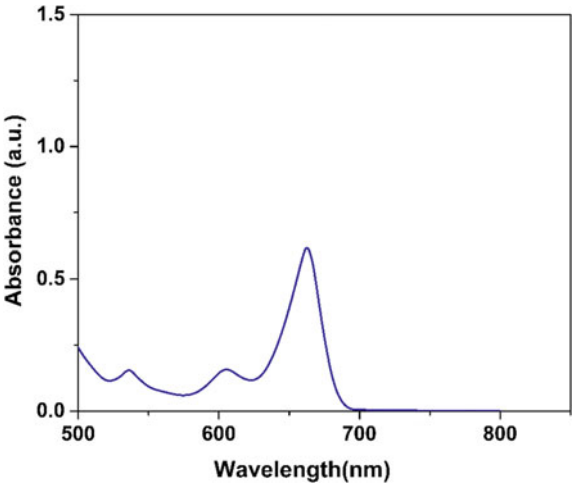


**Fig. 5.9** Absorption spectra in the UV–Vis region of the natural plant dye and ethanol extracts of cladode of prickly pear

sample for various chemicals from the signal data. The raw data is proceeded further using Fourier transform algorithm to get the FTIR spectra (wavenumber vs. intensity). Absorption means there is a match between the frequency of incident light and vibrational frequency of the molecule. The spectra are then compared with the existing library from the software for various chemical bonds to find a match and identify the chemical bonds present on the surface. Thus details on the surface chemistry can be obtained.

FTIR spectra were obtained for both the aloe vera and cladode plant dye extracts in the range of 2800–3500 $cm^{-1}$, showing the presence of hydroxyl functional group (3300 $cm^{-1}$). Carbonyl groups and ester functional groups (1050 $cm^{-1}$) and other functional groups are also shown, but these are most important for serving as anchors for adhesion onto the $TiO_2$ film. There is variation in the peak intensities for both dyes that differ at different frequencies as both of them have different chemical structures associated with the presence of different plant pigments. FTIR results also support the absorption spectroscopy results, which verifies the presence of anthocyanin and chlorophyll pigment molecules. Figure 5.10 shows the illustration of the FTIR spectra for the cladode dye.

### 5.5.2 *Characterization of the Titanium Oxide and Dye*

It is essential to perform structural analysis of the $TiO_2$ nanopowder in order to be suitable for working electrode fabrication. A simple scanning electron microscopy (SEM) images can show if there is aggregation in the titanium oxide nanopowder, but they do not provide high-resolution imaging information with atomic resolution, and the defects in the crystalline planes and the interfaces cannot be obtained. The crystallinity of the $TiO_2$ nanopowder could be verified from the X-ray powder

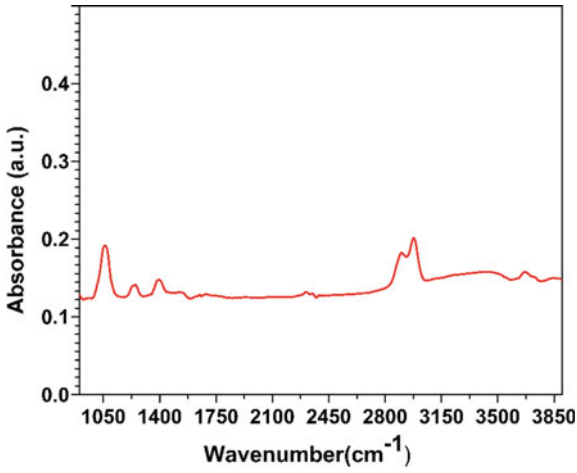


**Fig. 5.10** FTIR of the dye ethanol extracts of the cladode of prickly pear (Ganta et al. 2017)

diffraction method. The size of the nanoparticles of $TiO_2$ can be obtained from high-resolution transmission electron microscopy (HR-TEM) method, including the in situ information on crystallography with the selected area electron diffraction (SAED) method. Majority of the TEMs can obtain SAED patterns or diffraction rings with the inbuilt feature. SAED technique can obtain information on the defects in the crystalline planes and the grain boundaries.

There is a need to study the interaction with the dye, as the dye molecules decorate the $TiO_2$ nanoparticles. The HR-TEM images reported showed the interaction between the pomegranate dye and $TiO_2$ nanoparticles, including the information on their lattice planes, d-spacing, and the interaction between the $TiO_2$ nanoparticles and the dye, which could be the result of hydroxyl-containing dye being deprotonated or transfer of proton (Ghann et al. 2017).

## 5.6 Performance of the DSSCs

The DSSCs are illuminated under standard AM 1.5 standard sunlight; it depended on the beam characteristics and intensity was measured from the irradiance measurements, using a simple irradiance meter. Current density versus voltage (*J-V*) curve is obtained upon illumination of the DSSC sample from a sun simulator using a potentiostat. Five main parameters govern the performance of DSSCs and described in detail:

(1) Short-circuit current density ($J_{sc}$): It is the photocurrent incident on the sample per unit area in mA/cm$^2$. The values are obtained from a *J-V* curve as shown in Fig. 5.11 for the cladode-based DSSC. The strength of current density is dependent on the strong interaction between the sunlight, dye and $TiO_2$, and the absorption coefficient of the dye. Higher current densities usually lead to higher

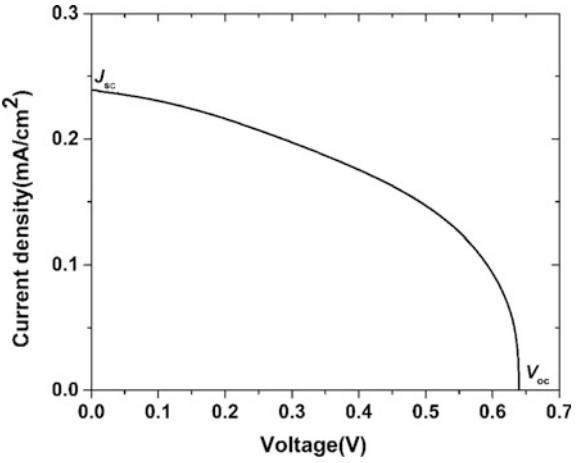


**Fig. 5.11** The *J-V* curve for the cladode DSSC, measured under the illumination from the sun simulator, indicating open-circuit voltage ($V_{oc}$) and short-circuit current density ($J_{sc}$) along the *y*- and *x*-axes, respectively (Ganta et al. 2017)

light-to-energy conversion efficiency. In the case of natural plant-based DSSCs, the $J$ values do vary with time as the plant dye losses its stability or they photodecay over time, and several groups are investigating on finding a solution for the problem.

(2) Open-circuit voltage ($V_{oc}$): The open-circuit voltage values can be obtained in the $J$-$V$ curve when the solar cell is illuminated when the circuit is open. A rough estimate of the voltages can be obtained by simply measuring the solar cell in sunlight with a multimeter and under darkness it should not give any voltage values. It can also be obtained from the following expression given by (Kumara et al. 2017).

$$V_{oc} = \frac{E_{cb}}{e} + \frac{K_b T}{e} \ln\left(\frac{n}{N_{cb}}\right) - \frac{E_{redox}}{e} \tag{5.2}$$

where $K_b$ is the Boltzmann constant, $T$ is the absolute temperature, $e$ is the charge, $n$ is the number of electrons in the conduction band, $E_{cb}$ is the energy of the conduction band, $E_{redox}$ is the redox potential, and $N_{cb}$ is the density of the states in the conduction band.

(3) Fill factor (FF): Fill factor is defined as the ratio of the maximum power ($J_{max} \cdot V_{max}$) and the product of open-circuit voltage and current density. The values are obtained from the $J$-$V$ curve and is given by,

$$FF = \frac{V_{max} \cdot J_{max}}{J_{sc} \cdot V_{oc}} \tag{5.3}$$

The maximum value of the FF is unity, and the unsuccessful fabrication of the DSSCs can lead to a reduced value.

(4) Photovoltaic energy conversion efficiency ($n$): This is an important parameter to test for the successful fabrication of the DSSCs, verifying if the dye was suitable for DSSCs. The first step would be to test the solar cell in darkness, showing no energy conversion efficiency; the solar cell was illuminated with sunlight from sun simulator and the parameters in the $J$-$V$ curve and $F$; we can calculate the energy conversion efficiency. The expression for efficiency is given by,

$$n = \frac{J_{sc} \cdot V_{oc} \cdot FF}{I_{inc}} \tag{5.4}$$

where $I_{inc}$ is the incident light intensity or irradiance usually measured from the incident light source, usually it is measured to be either 100 mW/cm$^2$ or intensity can be reduced to 100 W/m$^2$ with appropriate optics. The beam from a sun simulator usually diverges and it is recommended to perform the measurement with a circular beam and by placing the DSSCs closer to the sun simulator.

The photoelectrochemical parameters of the selected dye DSSCs are listed in Table 5.1. The efficiencies are usually in the range of 0.05–3.9% based on the plant dye and modified plant dyes used for fabrication of DSSCs. It also includes our reported experimental data. Strong adhesion of dye molecules on $TiO_2$, uniform coating of the $TiO_2$ film, plays a vital role in the efficiency of the DSSCs.

(5) Incident photon-to-current conversion efficiency (IPCE): It is also referred to as external quantum efficiency and the measurement checks on how efficient the conversion of photons to electrons occurs at various wavelengths. It also gave information on the stability of the solar cell over time. The monochromator is used to select a specific wavelength from the monochromatic sunlight source before being incident on the DSSC. The standard expression for it is given by,

$$\mathrm{IPCE}(\%) = \frac{1240 \cdot J_{sc}}{I_{inc} \cdot \lambda} \tag{5.5}$$

where $\lambda$ is the wavelength of the monochromatic light incident on the DSSCs.

## 5.7 Perspective and Challenges

In future, three significant issues lower efficiency, the stability of the plant dye over time, and an electrolyte which needs to be refilled over time needed to be addressed for the DSSCs to be commercialized. Research is needed on ways to modify the plant dyes chemical structure or functionalize them in order to prevent the photodecay from UV rays; experimentally, we can filter out the UV rays, but in reality, natural sunlight does have UV rays, and it is impossible to avoid them. Another option would be to discover new plant dyes extracted from various parts of the plant not reported to be used for DSSCs, but that option is challenging given the amount of literature reported on the usage of almost all of the plant dyes readily available. A cocktail of dyes, a combination of the dye in the side-by-side configuration without mixing them and also the addition of graphene to the dye, did not provide a boost in the conversion efficiency (Ganta et al. 2017; San Esteban and Enriquez 2013; Chang et al. 2013).

Another major issue is the lack of the choice of electrolytes used for the DSSCs assembly. Research is needed on the discovery of novel electrolytes which are compatible with both the plant dye and $TiO_2$ film in the charge transport without comprising on the efficiency. The electrolytes should not be volatile under the exposure to the sun or decay with time. Temperature changes also affect their electrolyte stability as they expand due to stress causing leakage from the DSSCs. Integration of electrolyte inside the DSSCs is another major issue with limited spacing between the cathode and anode to accommodate the electrolyte and the difficulty in covering the entire area between them for better interaction.

Finally, the low efficiency of the DSSCs is a significant concern in comparison with silicon and metal-based DSSCs. Proper selection of materials for dyes, electrolyte, cathode, and anode, including the discovery of new materials for that purpose, was required in future to improve the energy conversion efficiency. Materials such as graphene provided a boost in efficiency when used as an additive, but still, the materials research needs additional work. The interaction between the materials is also essential to study the energy transport kinetics. Designing a heterojunction DSSCs of various materials might be able to provide a boost in the efficiency by taking advantage of different materials, controlling the optical properties such as absorption and further be able to engineer the energy levels and the bandgaps, and minimizing the recombination reactions.

## 5.8 Conclusions

In summary, the methods and results presented in this chapter on DSSCs were reported using natural plant-based dyes as sensitizers. The dyes were extracted from parts of the plant and carefully analyzed both microscopy and spectroscopy methods as discussed in Sect. 5.4. Detailed discussion on the surface chemistry of the plant dye upon interaction with the $TiO_2$ film is also presented, including discussion on the various anchoring groups involved in the process. It was studied that adhesion promoters or anchoring groups played an important role in solar energy conversion, by helping in adsorption of the dye onto $TiO_2$ film, leading to improved light-to-energy conversion. In Sect. 5.6, the photoelectrochemical performance of the DSSCs is determined by the conversion efficiency and are in the range of 0.05–3.9% depending on the plant dye used and design of the solar cell.

The lower cost and environmental friendliness make DSSCs strong candidates for green energy, and they respond to very low-intensity sunlight and not dependent on the intensity of the sunlight or the angle of the incidence. In future, with improvements in the efficiency and stability over time, DSSCs can be integrated into the wearable devices especially in textiles and also occupy very low area making them suitable to be used on building for light-to-energy conversion, especially in big cities where space is major concern.

**Acknowledgements** The TAMIU faculty startup funds and U.S. National Science Foundation (Award number: 17268800) supported this work. We would also like to thank Luis Carrasco and Carlos Guzman for assisting in electrode fabrication and the selection of materials.

## References

Ali Shah Z, Zaib KMK, Qureshi M (2017) Dye sensitized solar cells based on different solvents: comparative study, 07

Ananth S, Vivek P, Arumanayagam T, Murugakoothan P (2014) Natural dye extract of lawsonia inermis seed as photo sensitizer for titanium dioxide based dye sensitized solar cells. Spectrochim Acta Part A Mol Biomol Spectrosc 128:420–426

Buscaino R, Baiocchi C, Barolo C, Medana C, Grätzel M, Nazeeruddin MK, Viscardi G (2008) A mass spectrometric analysis of sensitizer solution used for dye-sensitized solar cell. Inorg Chim Acta 361(3):798–805

Calogero G, Di Marco G, Cazzanti S, Caramori S, Argazzi R, Di Carlo A, Bignozzi CA (2010) Efficient dye-sensitized solar cells using red turnip and purple wild sicilian prickly pear fruits. Int J Mol Sci 11(1):254

Calogero G, Yum J-H, Sinopoli A, Di Marco G, Grätzel M, Nazeeruddin MK (2012) Anthocyanins and betalains as light-harvesting pigments for dye-sensitized solar cells. Sol Energ 86(5):1563–1575

Calogero G, Citro I, Di Marco G, Armeli Minicante S, Morabito M, Genovese G (2014) Brown seaweed pigment as a dye source for photoelectrochemical solar cells. Spectrochim Acta Part A Mol Biomol Spectrosc 117:702–706

Chang H, Lo Y-J (2010) Pomegranate leaves and mulberry fruit as natural sensitizers for dye-sensitized solar cells. Sol Energ 84(10):1833–1837

Chang H, Wu HM, Chen TL, Huang KD, Jwo CS, Lo YJ (2010) Dye-sensitized solar cell using natural dyes extracted from spinach and ipomoea. J Alloy Compd 495(2):606–610

Chang H, Kao M-J, Chen C-H, Chen C-H, Cho K-C, Lai X-R (2013) Characterization of natural dye extracted from wormwood and purple cabbage for dye-sensitized solar cells. Int J Photoenerg 2013:1–8

Chen Y-C, Lin JT (2017) Multi-anchored sensitizers for dye-sensitized solar cells. Sustain Energ Fuels 1(5):969–985

Cheng Y, Ho E, Subramanyam B, Tseng J-L (2004) Measurements of drug–protein binding by using immobilized human serum albumin liquid chromatography–mass spectrometry. J Chromatogr B 809(1):67–73

Chiba Y, Islam A, Watanabe Y, Komiya R, Koide N, Han L (2006) Dye-sensitized solar cells with conversion efficiency of 11.1%. Jpn J Appl Phys 45(7L):L638

Chien C-Y, Hsu B-D (2014) Performance enhancement of dye-sensitized solar cells based on anthocyanin by carbohydrates. Sol Energ 108:403–411

Engholm-Keller K, Larsen MR (2011) Titanium dioxide as chemo-affinity chromatographic sorbent of biomolecular compounds—applications in acidic modification-specific proteomics. J Proteomics 75(2):317–328

Fukai Y, Kondo Y, Mori S, Suzuki E (2007) Highly efficient dye-sensitized $SnO_2$ solar cells having sufficient electron diffusion length. Electrochem Commun 9(7):1439–1443

Ganta D, Jara J, Villanueva R (2017) Dye-sensitized solar cells using aloe vera and cladode of cactus extracts as natural sensitizers. Chem Phys Lett 679:97–101

Gerischer H, Michel-Beyerle ME, Rebentrost F, Tributsch H (1968) Sensitization of charge injection into semiconductors with large band gap. Electrochim Acta 13(6):1509–1515

Ghann W, Kang H, Sheikh T, Yadav S, Chavez-Gil T, Nesbitt F, Uddin J (2017) Fabrication, optimization and characterization of natural dye sensitized solar cell. Sci Rep-Uk 7:41470

Hagfeldt A, Boschloo G, Sun L, Kloo L, Pettersson H (2010) Dye-sensitized solar cells. Chem Rev 110(11):6595–6663

He H, Gurung A, Si L (2012) 8-Hydroxylquinoline as a strong alternative anchoring group for porphyrin-sensitized solar cells. Chem Commun 48(47):5910–5912

Hernandez-Martinez AR, Estevez M, Vargas S, Quintanilla F, Rodriguez R (2011) New dye-sensitized solar cells obtained from extracted bracts of Bougainvillea Glabra and Spectabilis Betalain pigments by different purification processes. Int J Mol Sci 12(9):5565

Higashino T, Nimura S, Sugiura K, Kurumisawa Y, Tsuji Y, Imahori H (2017) Photovoltaic properties and long-term durability of porphyrin-sensitized solar cells with silicon-based anchoring groups. ACS Omega 2(10):6958–6967

Hug H, Bader M, Mair P, Glatzel T (2014) Biophotovoltaics: natural pigments in dye-sensitized solar cells. Appl Energ 115:216–225

Ismael L-D, Mingkui W, Robin H-B, Mine I, Victoria M-D, Nazeeruddin MK, Tomás T, Michael G (2012) Molecular engineering of zinc phthalocyanines with phosphinic acid anchoring groups. Angewandte Chemie Int Ed 51(8):1895–1898

Kakiage K, Aoyama Y, Yano T, Oya K, Fujisawa J-I, Hanaya M (2015) Highly-efficient dye-sensitized solar cells with collaborative sensitization by silyl-anchor and carboxy-anchor dyes. Chem Commun 51(88):15894–15897

Kim B, Park SW, Kim J-Y, Yoo K, Lee JA, Lee M-W, Lee D-K, Kim JY, Kim B, Kim H, Han S, Son HJ, Ko MJ (2013) Rapid dye adsorption via surface modification of $TiO_2$ photoanodes for dye-sensitized solar cells. ACS Appl Mater Interfaces 5(11):5201–5207

Kumara GRA, Okuya M, Murakami K, Kaneko S, Jayaweera VV, Tennakone K (2004) Dye-sensitized solid-state solar cells made from magnesiumoxide-coated nanocrystalline titanium dioxide films: enhancement of the efficiency. J Photochem Photobiol, A 164(1):183–185

Kumara NTRN, Ekanayake P, Lim A, Liew LYC, Iskandar M, Ming LC, Senadeera GKR (2013a) Layered co-sensitization for enhancement of conversion efficiency of natural dye sensitized solar cells. J Alloy Compd 581:186–191

Kumara NTRN, Ekanayake P, Lim A, Iskandar M, Ming LC (2013b) Study of the enhancement of cell performance of dye sensitized solar cells sensitized with Nephelium lappaceum (F: Sapindaceae). J Sol Energ Eng 135(3):031014

Kumara NTRN, Lim A, Lim CM, Petra MI, Ekanayake P (2017) Recent progress and utilization of natural pigments in dye sensitized solar cells: a review. Renew Sustain Energ Rev 78:301–317

Lai WH, Su YH, Teoh LG, Hon MH (2008) Commercial and natural dyes as photosensitizers for a water-based dye-sensitized solar cell loaded with gold nanoparticles. J Photochem Photobiol A 195(2):307–313

Lee YH, Yun HJ, Choi SK, Yang YS, Park T, Ahn K-S, Suresh T, Kim JH (2016) Triphenylamine-based tri-anchoring organic dye with enhanced electron lifetime and long-term stability for dye sensitized solar cells. Synth Met 217:248–255

Mai C-L, Moehl T, Hsieh C-H, Décoppet J-D, Zakeeruddin SM, Grätzel M, Yeh C-Y (2015) Porphyrin sensitizers bearing a pyridine-type anchoring group for dye-sensitized solar cells. ACS Appl Mater Interfaces 7(27):14975–14982

Maiaugree W, Lowpa S, Towannang M, Rutphonsan P, Tangtrakarn A, Pimanpang S, Maiaugree P, Ratchapolthavisin N, Sang-Aroon W, Jarernboon W (2015) A dye sensitized solar cell using natural counter electrode and natural dye derived from mangosteen peel waste. Sci Rep-Uk 5:15230

Mathew S, Yella A, Gao P, Humphry-Baker R, Curchod BFE, Ashari-Astani N, Tavernelli I, Rothlisberger U, Nazeeruddin MK, Grätzel M (2014) Dye-sensitized solar cells with 13% efficiency achieved through the molecular engineering of porphyrin sensitizers. Nat Chem 6:242

Maurya IC, Srivastava P, Bahadur L (2016) Dye-sensitized solar cell using extract from petals of male flowers Luffa cylindrica L. as a natural sensitizer. Opt Mater 52:150–156

Meng S, Ren J, Kaxiras E (2008) Natural dyes adsorbed on $TiO_2$ nanowire for photovoltaic applications: enhanced light absorption and ultrafast electron injection. Nano Lett 8(10):3266–3272

Murakoshi K, Kano G, Wada Y, Yanagida S, Miyazaki H, Matsumoto M, Murasawa S (1995) Importance of binding states between photosensitizing molecules and the $TiO_2$ surface for efficiency in a dye-sensitized solar cell. J Electroanal Chem 396(1):27–34

Namba S, Hishiki Y (1965) Color sensitization of zinc oxide with cyanine dyes1. J Phys Chem 69 (3):774–779

Ning Z, Fu Y, Tian H (2010) Improvement of dye-sensitized solar cells: what we know and what we need to know. Energ Environ Sci 3(9):1170–1181

Noor MM, Buraidah MH, Careem MA, Majid SR, Arof AK (2014) An optimized poly(vinylidene fluoride-hexafluoropropylene)–NaI gel polymer electrolyte and its application in natural dye sensitized solar cells. Electrochim Acta 121:159–167

Nurrisma P, Silviyanti SNA, Gatut Y (2017) Endarko, effect of mixing dyes and solvent in electrolyte toward characterization of dye sensitized solar cell using natural dyes as the sensitizer. IOP Conf Ser Mater Sci Eng 214(1):012022

O'Regan B, Gratzel M (1991) A low-cost, high-efficiency solar cell based on dye-sensitized colloidal $TiO_2$ films. Nature 353(6346):737–740

Prauzner-Bechcicki JS, Zajac L, Olszowski P, Jöhr R, Hinaut A, Glatzel T, Such B, Meyer E, Szymonski M (2016a) Scanning probe microscopy studies on the adsorption of selected molecular dyes on titania. Beilstein J Nanotechnol [Online] 7:1642–1653

Prauzner-Bechcicki JS, Zajac L, Olszowski P, Jöhr R, Hinaut A, Glatzel T, Such B, Meyer E, Szymonski M (2016b) Scanning probe microscopy studies on the adsorption of selected molecular dyes on titania. Beilstein J Nanotechnol 7:1642–1653

Preat J, Jacquemin D, Perpete EA (2010) Towards new efficient dye-sensitised solar cells. Energ Environ Sci 3(7):891–904

Rajab FM (2016) Effect of solvent, dye-loading time, and dye choice on the performance of dye-sensitized solar cells. J Nanomater 2016:8

Sakai N, Miyasaka T, Murakami TN (2013) Efficiency enhancement of ZnO-based dye-sensitized solar cells by low-temperature $TiCl_4$ treatment and dye optimization. J Phys Chem C 117 (21):10949–10956

San Esteban ACM, Enriquez EP (2013) Graphene–anthocyanin mixture as photosensitizer for dye-sensitized solar cell. Sol Energ 98:392–399

Shanmugam V, Manoharan S, Anandan S, Murugan R (2013) Performance of dye-sensitized solar cells fabricated with extracts from fruits of ivy gourd and flowers of red frangipani as sensitizers. Spectrochim Acta Part A Mol Biomol Spectrosc 104:35–40

Sidharam PP, Luc S, Marcelis TM, Han Z (2014) Covalent surface modification of oxide surfaces. Angewandte Chemie Int Ed 53(25):6322–6356

Song H, Liu Q, Xie Y (2018) Porphyrin-sensitized solar cells: systematic molecular optimization, coadsorption and cosensitization. Chem Commun 54(15):1811–1824

Tedla A, Tai Y (2018) Influence of binary solvent system on the stability and efficiency of liquid dye sensitized solar cells, 358

Teoli F, Lucioli S, Nota P, Frattarelli A, Matteocci F, Carlo AD, Caboni E, Forni C (2016) Role of pH and pigment concentration for natural dye-sensitized solar cells treated with anthocyanin extracts of common fruits. J Photochem Photobiol A 316:24–30

Tian H, Yang X, Chen R, Zhang R, Hagfeldt A, Sun L (2008) Effect of different dye baths and dye-structures on the performance of dye-sensitized solar cells based on triphenylamine dyes. J Phys Chem C 112(29):11023–11033

Tomohiro H, Yamato F, Kenichi S, Yukihiro T, Seigo I, Hiroshi I (2015) Tropolone as a high-performance robust anchoring group for dye-sensitized solar cells. Angew Chem Int Ed 54(31):9052–9056

Tomohiro H, Yuma K, Ning C, Yamato F, Yukihiro T, Shimpei N, Packwood DM, Jaehong P, Hiroshi I (2017) A hydroxamic acid anchoring group for durable dye-sensitized solar cells incorporating a cobalt redox shuttle. ChemSusChem 10(17):3347–3351

Wang X-F, Matsuda A, Koyama Y, Nagae H, Sasaki S-I, Tamiaki H, Wada Y (2006) Effects of plant carotenoid spacers on the performance of a dye-sensitized solar cell using a chlorophyll derivative: enhancement of photocurrent determined by one electron-oxidation potential of each carotenoid. Chem Phys Lett 423(4):470–475

Wongcharee K, Meeyoo V, Chavadej S (2007) Dye-sensitized solar cell using natural dyes extracted from rosella and blue pea flowers. Sol Energy Mater Sol Cells 91(7):566–571

Yusoff A, Kumara NTRN, Lim A, Ekanayake P, Tennakoon KU (2014) Impacts of temperature on the stability of tropical plant pigments as sensitizers for dye sensitized solar cells. J Biophys 2014:8

Zhou H, Wu L, Gao Y, Ma T (2011) Dye-sensitized solar cells using 20 natural dyes as sensitizers. J Photochem Photobiol A 219(2):188–194

# Chapter 6
# Concentrated Photovoltaic (CPV) for Rooftop—Compact System Approach


**Muhammad Burhan, Muhammad Wakil Shahzad and Kim Choon Ng**

**Abstract** The single-junction-based conventional PV panels are dominating almost the entire photovoltaic market. In addition, they can only offer a limited solar conversion efficiency due to limitations of the band gap of their single pn-junction. On the other hand, third-generation multi-junction solar cell offers the highest solar energy conversion efficiency as their multiple pn-junctions can absorb a larger portion of solar spectrum. Despite such high potential, their share in current photovoltaic market is still negligible, even though, they have been used in form of concentrated photovoltaic (CPV) systems to reduce the use of expensive solar cell material. The main reason for such low market share is due to the gigantic design of commercial PV system which is only suitable to install in the open desert regions, thereby limiting its customers and application scope. In this chapter, a compact CPV system design is discussed with the motivation for its rooftop application and installation. Moreover, the long-term performance of CPV is also compared with conventional PV system in tropical conditions to highlight its potential in low solar energy areas.

**Keywords** Long-term CPV potential · CPV · Concentrated photovoltaic Compact · Solar tracker · Multi-junction cell

## 6.1 Background

The global ambient temperature is reaching a drastic limit rapidly, due to emissions from excessive use of fossil fuel based systems, which will have irreversible impact on our planet. Such situation demands change in our energy needs to be shifted to sustainable resources (Desideri and Campana 2014; Shahzad et al. 2018a, b;

M. Burhan (✉) · M. W. Shahzad · K. C. Ng
Water Desalination and Reuse Centre, Biological and Environmental Science and Engineering (BESE), King Abdullah University of Science and Technology, Thuwal 23955-6900, Saudi Arabia
e-mail: muhammad.burhan@kaust.edu.sa



H. Tyagi et al. (eds.), *Advances in Solar Energy Research*, Energy, Environment, and Sustainability, https://doi.org/10.1007/978-981-13-3302-6_6

Desideri et al. 2013; Ng et al. 2017). Many renewable energy resources, such as wind, biomass, geothermal have been reported to sustainably fulfill a part of our energy needs. However, none of the energy sources has potential greater than the solar radiations hitting the earth surface, which is many times higher than our global energy needs (Solanki et al. 2009; IPCC 2012). The only need is to capture it efficiently and effectively.

Due to low energy density and quality of received solar radiations, they have to be converted into a high-grade energy form such as electricity, and photovoltaic system or solar cell provides the best and most simple method of sunlight to electricity conversion (Burhan et al. 2016a, b, c, d, e, 2017a). As mentioned before, the most important factor regarding the sustainability of any renewable energy sources is that how efficiently its potential is captured. In the current market trend of photovoltaic systems, first and second generations of solar cells, comprising of monocrystalline, polycrystalline and thin film, are contributing to 99% of the total installed capacity. However, due to their material characteristics of single-junction-based semiconductor, they offer very low solar energy conversion efficiency. This is because of the fact that they respond to a certain portion of solar radiations, depending upon the band gap of the pn-junction (Green et al. 2015; Burhan et al. 2017b). On the other hand, the third generation solar cells are based upon multi-junction solar cells, offering highest efficiency of 46% so far (National Renewable Energy Laboratory (NREL) 2016). The main reason for such high efficiency is their material characteristics which are based upon a stack of multiple pn-junction of the semiconductor material. Each junction is designed to have a certain band gap such that they can respond to a certain portion of solar spectrum. As a result, whole solar spectrum is absorbed from short wavelength of ultraviolet radiations to the large wavelength infrared radiations (Cherucheril et al. 2011). Despite higher efficiency, multi-junction solar cells are still unable to make the prominent contribution in the photovoltaic market.

The multi-junction solar cells still cannot be fabricated as flat panels like conventional single-junction solar cells, because of high cost of material. Therefore, concentrated photovoltaic (CPV) concept is used which utilizes low-cost concentrators to concentrate solar radiations to an intensity of 500–1000 times onto a small area of cell. This reduces the use of expensive solar cell material with low-cost optical material (Mathur et al. 1990; Muhammad et al. 2016). The concentrated photovoltaic system was firstly developed in 1976 at National Sandia Laboratories. Later, many system design prototypes were developed to be installed in different locations across the globe (Sala et al. 1979; Claverie et al. 1980; Giuffrida et al. 1980; Salim and Eugenio 1990). The CPV system evolved in many phases, i.e., from development of high performance multi-junction solar cells (Garboushian et al. 1996; Shahzad et al. 2018c; Tsadka et al. 2009; Singh and Liburdy 1993; Clemens 1997; Walter and John 1994; Burhan et al. 2018a; Burhan 2015) to the compact solar concentrators for cost-effective fabrication and system assembly (Burhan et al. 2018b; Garboushian et al. 2007; David and Stephen 2007). However, till now, the concentrated photovoltaic systems are aimed to install in open deserts field due to their operational needs as they can only respond to solar beam

radiations. Therefore, these systems are commercially available in gigantic design which can only be installed in open field conditions, with limited applications and customers. As CPV system requires highly accurate solar tracking to capture solar beam radiations (McConnell 2008), therefore, multiple CPV modules are mounted onto a gigantic tracker to lower the need of sophisticated tracking units.

If installations trends of conventional single-junction PV panels are notice, then it can be seen that large number rooftop units contribute to a significant share of overall installed capacity which is targeted to be increased to 40–50% (Burhan et al. 2018c). On the other hand, there is no such provision available for the concentrated photovoltaic system, which makes their share negligible in the market due to such limited applications and customers. Due to their current commercial design, their production potential is still utilized despite their highest energy conversion efficiency. Therefore, compact CPV design is needed, which can remove all such installation related restrictions to boost their market potential and application scope, especially for rooftop installation. However, as mentioned before, the CPV system requires very sophisticated and highly accurate solar tracking units, therefore, it is not that simple to have compact CPV system design. With such compact design, more number of sophisticated tracking units will be needed, which will increase the overall cost of the system. This chapter discuss the design and development of compact CPV system with cost-effective and highly accurate solar tracking methodology and sensor. Detailed operations methodologies and construction design are discussed for such compact CPV system development which will also be able to be installed for rooftop operation.

## 6.2 Compact Solar Tracking Unit Design for CPV

Owing to the need of large number of tracking units for the compact CPV system design; low cost, simple but highly accurate tracking units are needed for its feasible and economical operation. There are many systems and techniques discussed in the literature regarding design and operation of solar tracking systems for conventional PV systems. These conventional solar tracking units range from fixed speed single axis systems to the two-axis controlled systems. However, if concentrated photovoltaic systems are considered, there are very few studies discussing the tracking requirements of CPV. It must be noted that the solar tracking units required and designed for conventional PV systems cannot be used for CPV due to their poor tracking accuracy of 10–12°. CPV system demands tracking accuracy of order 0.1–0.3°. In addition, the solar tracking units for CPV cannot only rely on the passive tracking methodologies, due to high accuracy requirements. As passively tracked solar tracker can incur error due to mechanical backlash and wind disturbance related problems, therefore, tracking accuracy can only be insured through feedback from solar tracking sensor. Such hybrid tracking can only work for concentrated photovoltaic system. A detailed design of compact solar tracking unit for CPV application with proposed hybrid tracking algorithm and tracking sensor is discussed in this section.

### 6.2.1 Passive/Astronomical Solar Tracking

The solar radiations hitting earth's surface change their incident angle throughout the day, due to its continuous motion around the sun. However, such motion follows a certain profile which can be easily and accurately traced through predefined astronomical models of solar geometry. With known information of date, time, latitude, and longitude, the position of sun can be determined through these defined models, at any location throughout the globe. The position of sun is defined by two planer angle, i.e., azimuth and zenith, presented in the horizontal plane and the vertical plane, respectively. The azimuth angle is reference from the south. On the other hand, zenith is reference from horizontal surface with movement in vertical plane. Such tracking methodology, based upon predefined solar coordinates from reference planes, obtained from solar astronomical models, is called as astronomical tracking. As it does not have any feedback regarding actual position of the tracker, instead of calculated motion from reference plane, therefore, it is also called as passive tracking. As per the solar geometry model, azimuth "$\theta_{az}$" and zenith "$\theta_z$" angles are given by Eqs. (6.1) and (6.2a) or (6.2b), respectively.

$$\theta_z = \cos^{-1}\{\sin\phi \sin\delta + \cos\phi \cos\delta \cos\omega\} \tag{6.1}$$

If $\omega < 0$,

$$\theta_{az} = 90 + \cos^{-1}\left\{\frac{\sin\delta - \sin(90-\theta_z)\sin\phi}{\cos(90-\theta_z)\cos\phi}\right\} \tag{6.2a}$$

If $\omega > 0$,

$$\theta_{az} = 360 - \left[90 + \cos^{-1}\left\{\frac{\sin\delta - \sin(90-\theta_z)\sin\phi}{\cos(90-\theta_z)\cos\phi}\right\}\right] \tag{6.2b}$$

where "$\omega$", "$\delta$", and "$\phi$" are hour angle, declination angle and latitude respectively, as explained in detailed in Oh et al. (2015).

### 6.2.2 Master–Slave Configuration for CPV Field

To implement the defined astronomical or passive solar tracking strategy and to compute the tracking angles through mentioned solar geometry model, a control circuit is needed which also control the motion of the tracker in two axis as per given instructions or pulses. On the other hand, for compact CPV field configuration, larger number of tracking units are needed and so as these sophisticated and expensive control box. Therefore, for cost-effective operation, a master–slave configuration is presented in which control box of single master tracking unit is

equipped with all required electronic modules which are expensive and sophisticated, and needed to get the necessary real-time data to implement astronomical tracking methodology. However, when the computations are done by the master tracker, the required information of solar position in form of azimuth and zenith angles is transmitted to the slave tracker which only have transceiver module to receive and implement the received information. As a result, most of expensive modules are save from slave tracker control circuit, as shown in Fig. 6.1, reducing the overall capital cost of the CPV field.

A wireless communication protocol of Zigbee network is utilized for such configuration, in which radio frequency waves are used for data transmission. As per Zigbee network, illustrated in Fig. 6.1, the master tracker acts as coordinator "C" which creates its own network of communication. However, rest of the trackers in the field acts as slave which join the created communication network as router "R" or end devices "ED" as per their communication preferences. The router can receive and further transmits the information. However, end devices only act as receiver and normally, the devices in the last circle of the zigbee network act as end devices. The number and address to each of the tracking unit in the zigbee network are defined by Eqs. (6.3) and (6.4), as explained in Farahani (2011). Such wireless communication is very important for compact CPV field configuration which can be easily set up at rooftop of multiple and distant residential or commercial buildings, without any need of horizontal level ground.

$$\mathrm{C}_{skip} = 1 + C_m(L_m - d - 1) \quad \text{if } R_m = 1, \text{for } d < L_m \tag{6.3}$$

$$\mathrm{C}_{skip} = \frac{1 + C_m - R_m - (C_m R_m^{(L_m - d - 1)})}{1 - R_m}, \text{otherwise, for } d < L_m \tag{6.4}$$

### 6.2.3 Development of Solar Feedback Sensor

As explained before, to achieve high level accuracy of solar tracking for concentrated photovoltaic system, hybrid solar tracking algorithm is needed in which the accurate position of the solar tracker is ensured through real-time solar position feedback from solar tracking sensor. Therefore, the sensor is of prime importance here which must also have very high accuracy and sensitivity but at low cost due to the need of large number of solar tracking units for compact CPV field.

There are many studies available in literature regarding design and working principle of solar tracking sensor for conventional PV system (Luque-Heredia et al. 2007), e.g., shadow rod, wedge shape and quadrant designs. Although, they are workable for conventional PV tracking their accuracy is not as per CPV tracking requirements (Yao et al. 2014). In addition, the response of optical sensor employed in such solar tracking sensor configuration is not steady and uniform under same light intensity. For CPV tracking, there is only one commercial solar tracking

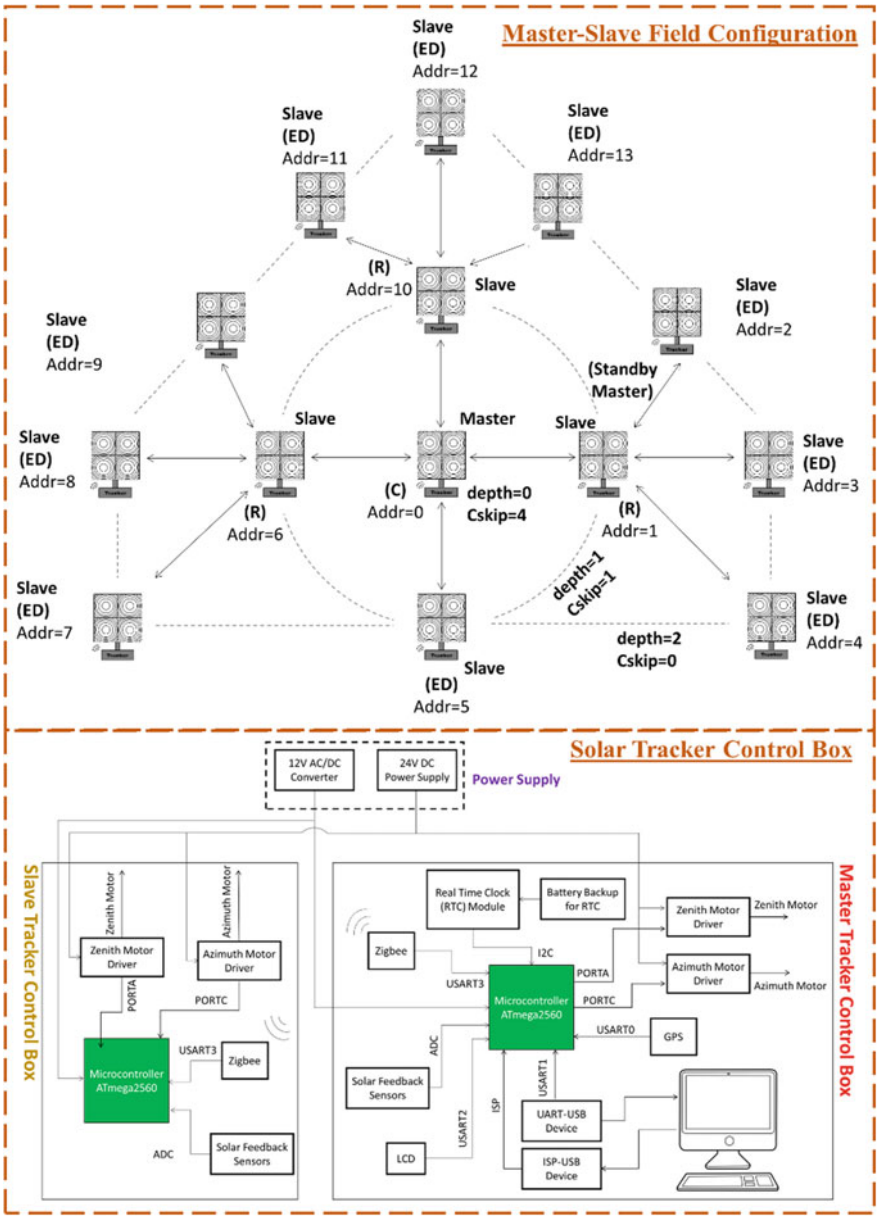


**Fig. 6.1** Master slave configuration and control box for compact CPV field

sensor available which utilizes highly accurate position sensitive diode (PSD) (Luque-Heredia et al. 2006; Xu et al. 2013). Though such sensor can provide the solar tracking feedback in the range of CPV requirements, however, due to its

high cost, it is not suitable to be used for compact CPV field configuration. In addition, larger number of such tracking sensor will be needed for compact CPV as compared to conventional configuration, thereby, increasing overall capital cost of the system. Therefore, a simple solar tracking sensor is needed at fraction of the cost of its commercial alternative, but with same accuracy and sensitivity response, so that overall cost of the system is not affected by it.

A simple schematic of proposed solar tracking sensor, for CPV application, is shown in Fig. 6.2. The proposed configuration is based upon a twin lens collimator which provides a collimated and concentrated beam at the center of photo-sensors array. Parallel solar rays, after being refracted through convex–concave lens collimator, become parallel but as a concentrated beam which creates a bright spot at the center of photo-sensors array. The focal point of both lenses must coincide for better collimated effect. Therefore, the rays become parallel after being refracted through concave lens. The proposed solar tracking sensor configuration works in such a way that the when the sensor position is aligned with solar position then the solar radiations parallel to the collimator axis creates a bright spot at the center of the photo-sensor array. When tracking error is induced, received solar radiation deviates from collimator axis, causing the bright spot to move from its center position. The deviation of bright spot from its center position depends upon the angular deviation of solar radiation from the collimator axis. When this angular deviation increases from a certain limit, the concentrated spot hits any sensor of the photo-sensors array. The feedback of photo-sensors is given to the microcontroller of the control box, which translated its analogue signal to digital value, using ADC (analogue to digital converter). The microcontroller processes the feedback signal in such a way that it moves tracker to bring back bright spot at the center of photo-sensor array.

The feedback from photo-sensors to microcontroller works in binary mode, i.e., high or low. The concentrated radiations falling onto the photo-sensor are higher than its saturation limit. When bright spot hits any of the photo-sensor, a high feedback signal is given to the microcontroller. Depending upon the position of the photo-sensor, giving high feedback signal, the direction of tracker movement is decided to bring back the bright spot in between photo-sensors array. As long as bright spot remains within photo-sensor array, the feedback signal to microcontroller is low, indicating that the tracker is operating within defined tracking accuracy. This depicts that the distance between photo-sensor array and the bright spot defines the tracking error limit, higher the distance, lower the tracking accuracy. Therefore, based upon the relationship between the deviation of the parallel rays from collimator axis and corresponding deviation of bright spot from its center position, the distance between photo-sensors array and bright spot is adjusted. However, thickness "$b_t$" of collimated beam also need to be considered while selecting photo-sensors spacing. As far as, the concentrated bright spot remains within the photo-sensors array, the tracker is ensured to be operated with required

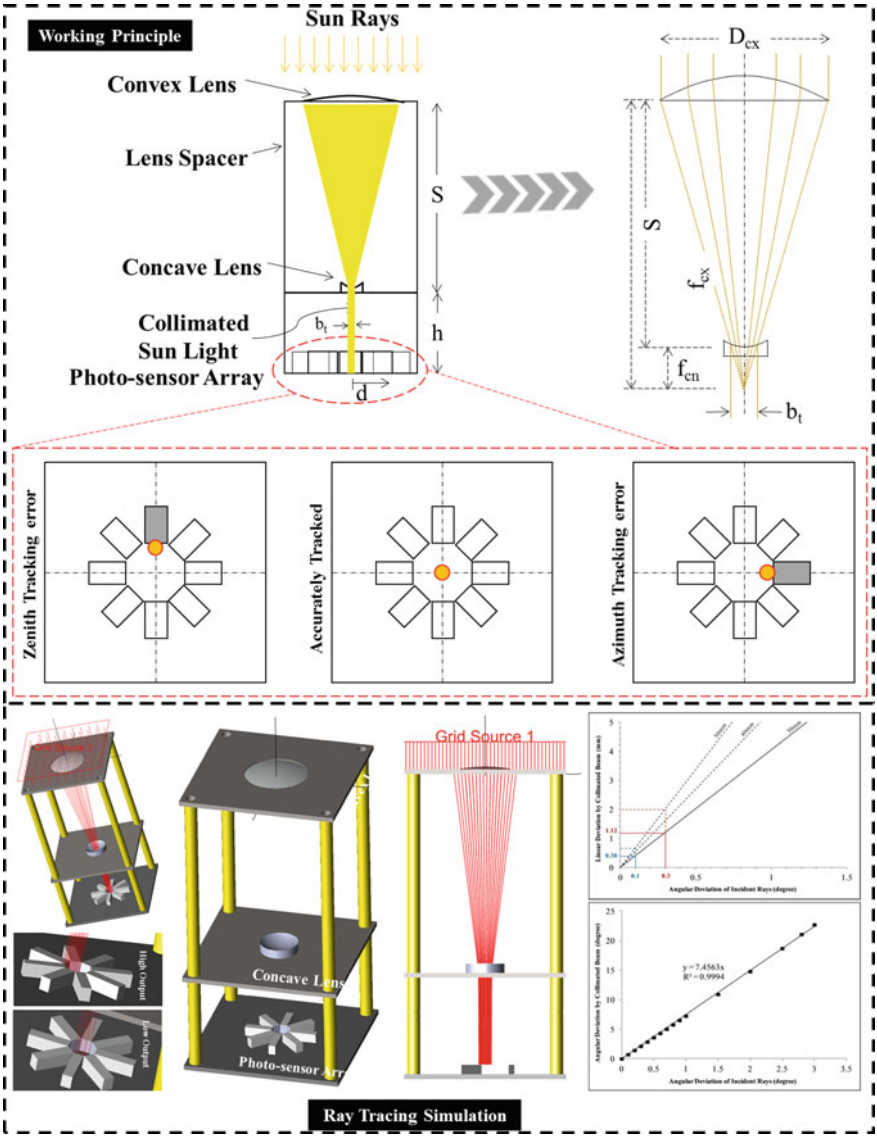


**Fig. 6.2** Collimator based solar tracking sensor schematic and ray tracing simulation

tracking accuracy. If the diameter of primary convex lens is "$D_{cx}$" and the focal lengths of convex and concave lenses are "$f_{cx}$" and "$f_{cn}$", respectively, then the thickness "$b_t$" of collimated beam and the distance "$S$" between collimated lenses can be found mathematically by using Eqs. (6.5) and (6.6).

$$S = f_{cx} + (-f_{cn}) \tag{6.5}$$

$$b_t = \frac{D_{cx}}{f_{cx}} \cdot f_{cn} \tag{6.6}$$

It must be noted that the focal length of concave lens is negative. Therefore, the distance between the collimated lenses is actually the sum of their focal lengths, in which one component is negative.

Besides tracking error limit, another important feature of solar tracking sensor is its sensitivity to tracking error. Due to high tracking accuracy, it is very important to have high sensitivity, so that even a small tracking error can be detected by the sensor. To investigate the sensitivity of proposed solar tracking sensor configuration, the optical simulation of a prototype is conducted with components details as $f_{cx}$ = 80 mm, $D_{cx}$ = 20 mm, and $f_{cn}$ = −12 mm. The raytracing simulation results, performed using Tracepro, are shown in Fig. 6.2. The performance graphs show the response of sensor in terms of linear deviation of concentrated bright spot and angular deviation of collimated beam against incident radiations. It can be seen that even for 0.1° incident ray deviation, there is a significant linear deviation of bright spot. Moreover, from angular deviation of collimated beam graph, it can be seen that there is 7.4° deviation in collimated beam for one-degree deviation in incident radiations, which also represents the slope of the graph. For the mentioned configuration, a sensitivity of 7.4° is offered by the solar tracking sensor. On the other hand, such sensitivity can be further increased by increasing distance between concave lens and photo-sensors array. Thus, simple, highly sensitive and accurate solar tracking sensor is proposed and designed, which has tracking accuracy and sensitivity of 0.1°. In addition, as the radiations interacting with photo-sensors are higher than their saturation limit, therefore, ordinary photo-sensors can be used without worrying about their nonuniform response at same intensity.

### 6.2.4 Development of Tracking Algorithm for CPV Field

After designing the solar tracking algorithms, the next step is the development of solar tracking algorithm which is used by the microcontroller to implement the solar tracking methodologies. In the proposed compact CPV tracking system, a hybrid tracking algorithm (passive/astronomical + active/optical) is developed using C-language programming and CodevisionAVR compiler. In the developed hybrid algorithm, astronomical/passive tracking methodology (Oh et al. 2015) is executed first, which acts as the main primary tracking methodology. The actual position of the tracker is compared with the calculated position of the sun. If the difference between actual position and calculated value is greater than the required tracking limit, then the tracker is rotated either in azimuth and zenith direction, accordingly. When such difference is within the acceptable range then the tracker is stopped or it

remains stationary. When execution of astronomical method is completed, then the optical/active tracking method is implemented to ensure the tracking accuracy. During optical tracking execution, the feedback from solar tracking sensor is obtained. If high feedback signal is obtained from any of the sensor then the tracker is adjusted accordingly, till a low feedback signal is obtained and the loop starts again with the astronomical tracking.

The hybrid tracking algorithm, as explained above, is shown in Fig. 6.3. At the start of the loop, the data from RTC (Real Time Clock) and GPS (Global Positioning System) modules is obtained and sorted to get local date, time, latitude, and longitude which are transmitted continuously through Zigbee to the slave trackers. Such communication is time independent and whenever a new data set is received by the slave tracker, it is replaced with old value. However, the slave tracker does not have any movement unless difference between actual solar position of the tracker and the received coordinates is greater than the tracking accuracy, even though the data transmission is always happening in the background. When there is time of sunset, the solar tracker returns to its initial reference position, i.e., horizontal module while facing south. The operation starts again when there is time for sunrise.

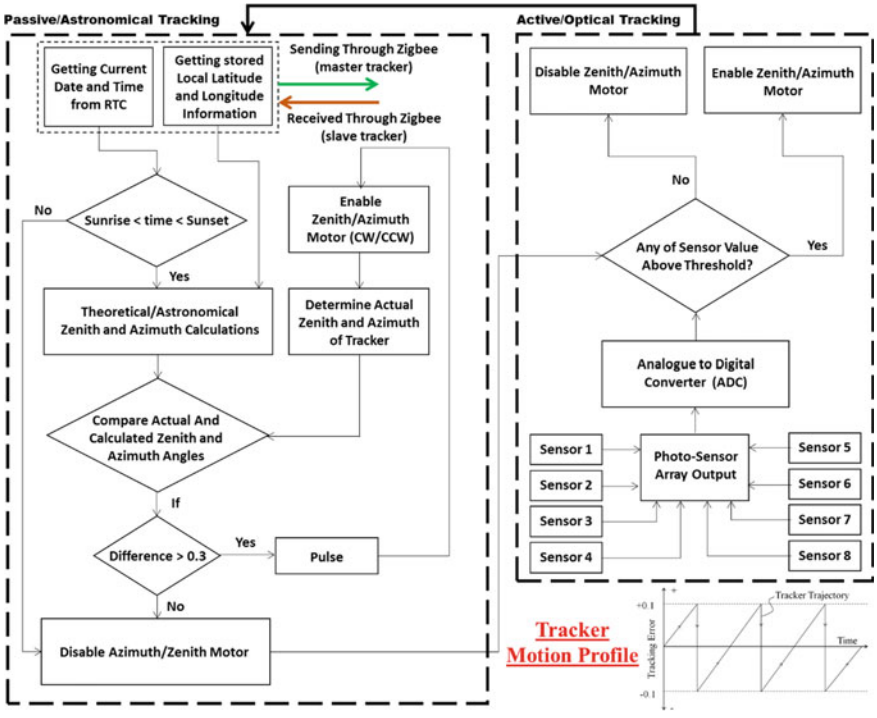


**Fig. 6.3** Hybrid solar tracking algorithm for compact CPV field

## 6.3 Development of CPV System

As per tracking methodology and design discussed, a compact CPV system prototype is developed for CPV field at the rooftop, as shown in Fig. 6.4. The shown system is consisting of four compact CPV units in which there is one master tracker with three slave trackers. Each CPV unit is also equipped with the proposed solar tracking sensor for CPV, for which the developed prototype is shown in Fig. 6.4. It can be seen that there is a perfect bright spot at the center of photo-sensors array, which verifies the proposed design and configuration. It must be noted that four developed CPV system are also equipped with four different types of CPV concentrating assemblies, refractive and reflective both, to analyze their performance. However, only the performance of Fresnel lens based CPV unit will be discussed here as other systems design are not under the scope of current discussion.

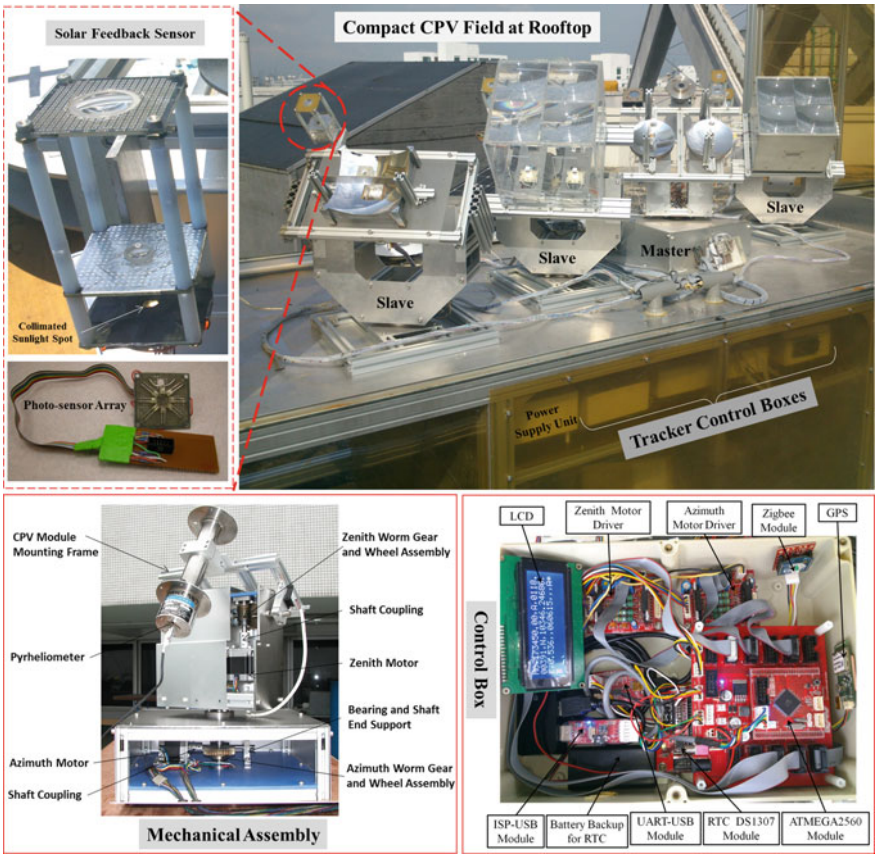


**Fig. 6.4** Experimental prototype of compact CPV field for rooftop operation

The Fresnel lens based CPV systems are using primary concentrator as Fresnel lens. The CPV unit consists of two parts: CPV module and solar tracker. The construction of CPV module is such that the incident solar radiations, after being refracted from Fresnel lens, are converged and focused at its focal point which is placed at the inlet aperture of secondary optical element, known as homogenizer. The homogenizer rod further guides and uniformly distributes radiations at its outlet aperture where multi-junction solar cell (MJC) InGaP/InGaAs/Ge is placed. The heat spreader and heat sink are place at the back side of the MJC for heat dissipation during operation so that the cell temperature remain with optimum limits.

The solar tracking unit also consists of two parts: control box and mechanical system. The developed control box of CPV prototype is also shown in Fig. 6.4, based upon Atmega2560 microcontroller. It also contains power supply, Zigbee transceivers, and motor drivers. The mechanical system of solar tracker further consists of two parts; support structure with top frame where CPV module is mounted, and mechanical drive. The mechanical drive is constructed using motors and gear assembly, for physical movement of the solar tracker. The motor receives signal from motor drivers which receive instructions from microcontroller. The gear assembly contains worm gear and wheel. Each of the tracking unit has two gear assemblies, on for each axis tracking, i.e., azimuth and zenith. In the developed prototype of CPV system, the zenith and azimuth gear assemblies have gear ratio of 60 and 40, respectively. However, motor drivers have capability of further reduction of motor step in 16 steps. Therefore, as per the Eq. (6.7), the overall step size of 0.001875° and 0.0028125° can be obtained for zenith and azimuth drives, respectively.

$$\text{Tracker Movement/Step} = \frac{\text{Motor Step}}{\text{Driver Step} \times \text{Gear Ratio}} \tag{6.7}$$

## 6.4 Field Testing and Analysis

In order to analyze the performance of developed compact CPV unit, in terms of its tracking accuracy and efficiency/power production, an outdoor field operation was conducted at the rooftop of Engineering-EA building of National University of Singapore (NUS), in tropical weather conditions. First of all, the performance of developed solar tracking system was investigated for the whole day operation and the comparison of calculated solar coordinates was made with the solar position data obtained from US Naval Observatory (Astronomical Applications Department of the U.S. Naval Observatory 2015); one of the oldest scientific agency which provides data related to date, time, and position for navigation. Figure 6.5 shows the graphs for error between calculated azimuth and zenith values with the data obtained from US Naval Observatory. The comparison is made for coordinates of 1.229°N latitude and 103.771°E longitude, and date January 1, 2015. From the

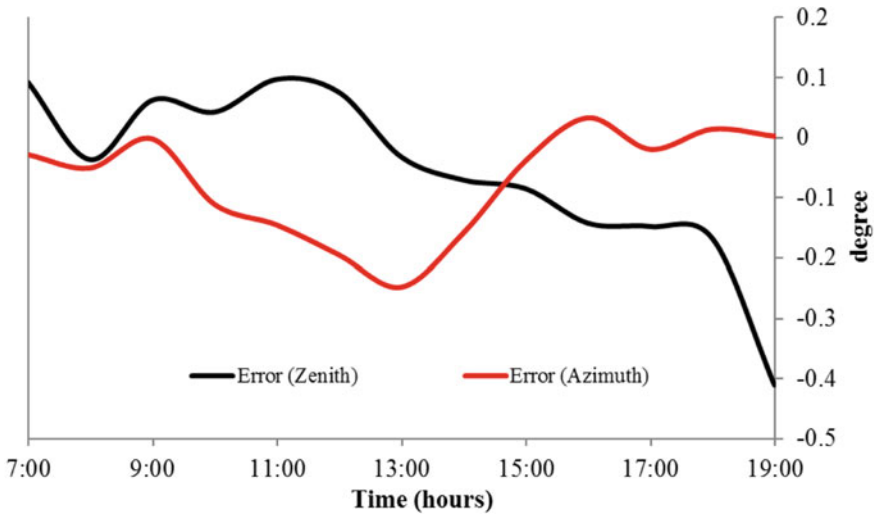


**Fig. 6.5** Calculated and actual solar position angles comparison

graph, it can be seen that the graphs of both calculated and obtained values are overlapping. Therefore, from the difference of these position coordinates, it is evident that for most of the time, the tracking error is with ±0.1°. However, maximum error for azimuth and zenith axis are −0.225° and −0.4°, respectively.

To analyze CPV system performance and production, under tropical weather conditions, it was operated under field conditions of Singapore. Figure 6.6 shows

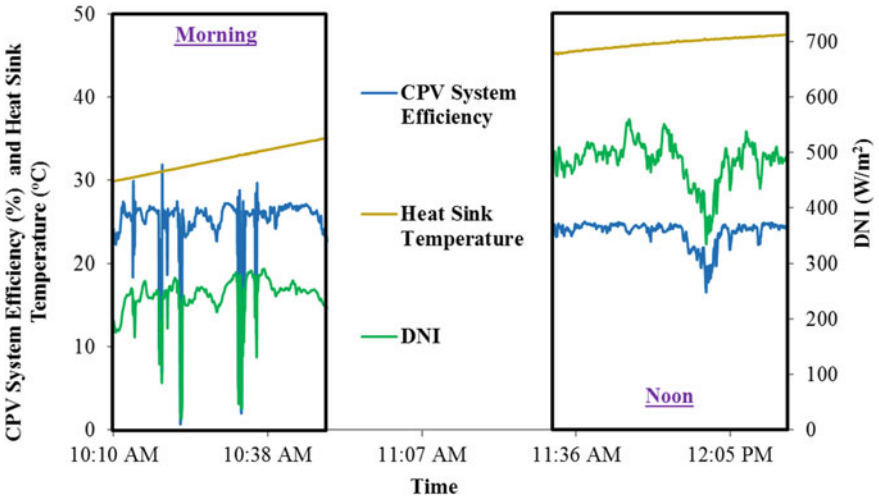


**Fig. 6.6** Maximum efficiency curve for CPV module

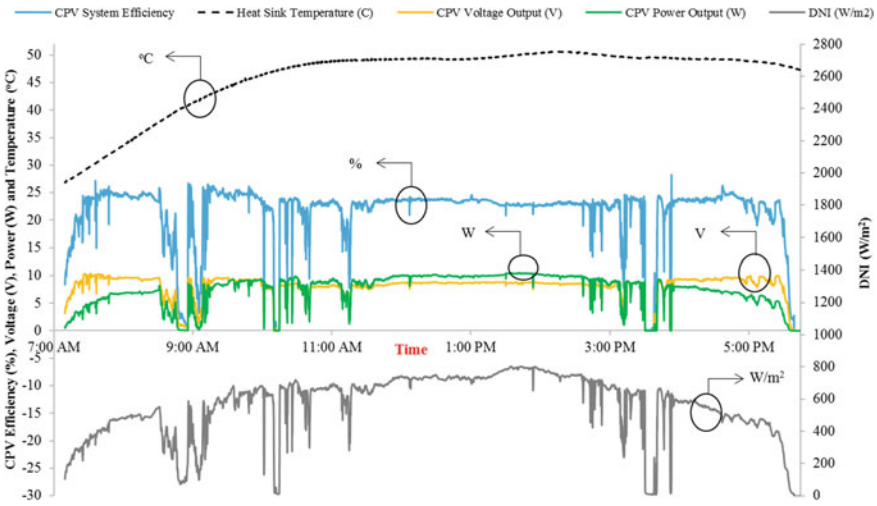


**Fig. 6.7** Field performance curves of CPV system

the maximum CPV system efficiency. It can be clearly seen that the maximum efficiency of 28% is recorded during daytime. However, the system efficiency drops to 25–26% during the noon period. To understand such efficiency variations, the system performance curves, for whole day operation are shown in Fig. 6.7. The efficiency value seems to increase with increase in direct normal irradiance (DNI) in the morning. However, when DNI increases further, the efficiency of the system decreases. Such drop in efficiency can be attributed to cell temperature increment which can be predicted from heat sink temperature as shown in Fig. 6.7. With increase in DNI, the concentration at the cell area increases, which also increases the heat loss, causing an increase in cell temperature and decrease in its efficiency. On the other hand, in the afternoon, with drop in DNI, the heat sink temperature also decreases with increase in efficiency. However, after certain drop in DNI, the efficiency also starts to drop as the concentration at cell area decrease. If we look at the power out curve, it varies in proportion to the received DNI.

As mentioned before, the concentrated photovoltaic (CPV) system are normally considered to be feasible in open desert field, from performance point of view, as they only absorb beam radiations. As the main motivation of this study is the development of compact CPV unit which is targeted to be installed on the rooftops of urban regions. Therefore, to analyze the performance of CPV system in tropical weather conditions, the performance of the CPV and different types of conventional PV systems (Monocrystalline of size 6.86 $m^2$ with efficiency of 17.2% at STC, Polycrystalline of size 19.4 $m^2$ with efficiency of 16.2% at STC, and Thin Film-CIS of size 21.27 $m^2$ with efficiency of 17% at STC) were analyzed for one period in terms of their energy output, presented in Fig. 6.8 as kWh/$m^2$/year (Burhan et al. 2017c). As CPV only absorbs beam radiations while conventional PV can respond to both, diffuse and beam radiations. Therefore, to access their performance

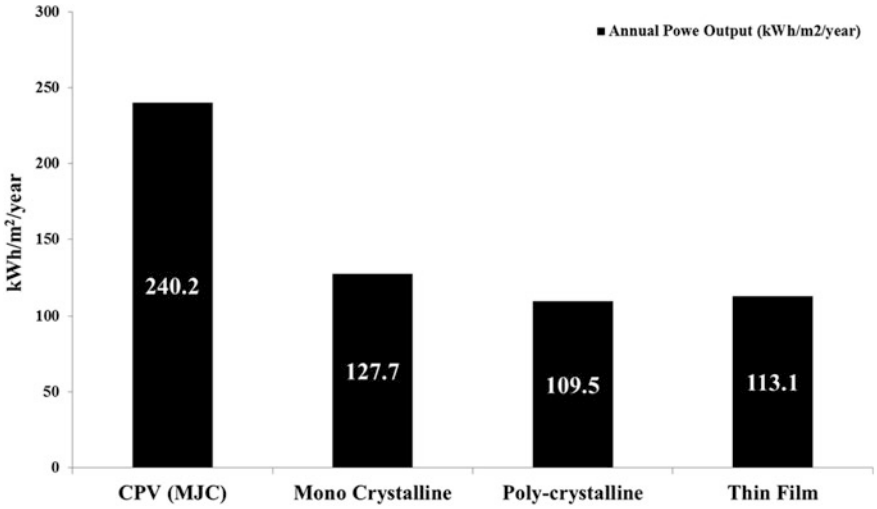


**Fig. 6.8** Long-tem energy production potential of photovoltaic systems under tropical weather conditions

feasibility, efficiency is not an appropriate parameter of comparison. At the end, it is the total energy produced, which is supplied to the customer. In such scenario, energy output is the true performance indicator which is used here. The long-term energy output of all types of photovoltaic systems is analyzed under conditions of Singapore, as shown in Fig. 6.8. It can be seen that the energy output of photovoltaic system is almost two times higher than the conventional PV. Such double production is observed in weather conditions where only 66% of total received solar energy was in form of beam radiations. It shows that CPV not only has great production potential in desert field but it is also feasible to be installed in urban region, which justifies the concept of compact CPV for rooftop operation as discussed in this chapter.

## 6.5 Summary of Chapter

Despite highest energy efficiency, third-generation multi-junction solar cells are still unable to make significant in the photovoltaic market. Their cost-effective use in the form of concentrated photovoltaic (CPV) is also unable to boost their market share due to limited market and customers of current gigantic CPV units. A novel design of compact CPV system is developed and discussed for efficient and cost-effective rooftop operation of MJC, in urban region. By keeping in mind the need of large number of solar trackers, a master–slave control technique is proposed for cost-effective operation compact CPV field tracking. Moreover, to ensure high accuracy need of CPV tracking unit, a solar tracking sensor which is optically

sensitive, is designed, analyzed, developed, and tested for field operation. The proposed sensor is a unique design of its own type with fraction of the cost of commercial unit. The proposed design made it possible to have high accurate two-axis solar tracking with extreme low cost. The simple construction and algorithm of compact CPV will boost its customers and share in photovoltaic market. Moreover, the double energy production of CPV system, even in tropical weather, will also negate the general perspective that CPV system is only feasible to operate in open desert conditions.

## References

Astronomical Applications Department of the U.S. Naval Observatory. http://aa.usno.navy.mil/data/docs/AltAz.php. Date retrieved: 10-05-2015

Burhan M (2015) Theoretical and experimental study of concentrated photovoltaic (CPV) system with hydrogen production as energy storage, Doctoral dissertation

Burhan M, Chua KJE, Ng KC (2016a) Simulation and development of a multi-leg homogeniser concentrating assembly for concentrated photovoltaic (CPV) system with electrical rating analysis. Energy Convers Manage 116:58–71

Burhan M, Chua KJE, Ng KC (2016b) Sunlight to hydrogen conversion: design optimization and energy management of concentrated photovoltaic (CPV-Hydrogen) system using micro genetic algorithm. Energy 99:115–128

Burhan M, Oh SJ, Chua KJE, Ng KC (2016c) Double lens collimator solar feedback sensor and master slave configuration: development of compact and low cost two axis solar tracking system for CPV applications. Sol Energy 137:352–363

Burhan M, Chua KJE, Ng KC (2016d) Long term hydrogen production potential of concentrated photovoltaic (CPV) system in tropical weather of Singapore. Int J Hydrogen Energy 41 (38):16729–16742

Burhan M, Chua KJE, Ng KC (2016e) Electrical rating of concentrated photovoltaic (CPV) systems: long-term performance analysis and comparison to conventional PV systems. Int J Technol 7(2):189–196. https://doi.org/10.14716/ijtech.v7i2.2983

Burhan M, Shahzad MW, Ng KC (2017a) Development of performance model and optimization strategy for standalone operation of CPV-hydrogen system utilizing multi-junction solar cell. Int J Hydrogen Energy 42(43):26789–26803

Burhan M, Oh SJ, Chua KJ, Ng KC (2017b) Solar to hydrogen: compact and cost effective CPV field for rooftop operation and hydrogen production. Appl Energy 194:255–266

Burhan M, Shahzad MW, Ng KC (2017c) Long-term performance potential of concentrated photovoltaic (CPV) systems. Energy Convers Manage 148:90–99

Burhan M, Shahzad MW, Choon NK (2018a) Hydrogen at the rooftop: compact CPV-hydrogen system to convert sunlight to hydrogen. Appl Therm Eng 132:154–164

Burhan M, Shahzad MW, Ng KC (2018b) Sustainable cooling with hybrid concentrated photovoltaic thermal (CPVT) system and hydrogen energy storage. Int J Comput Phys Ser 1 (2):40–51

Burhan M, Shahzad MW, Oh SJ, Ng KC (2018c) A pathway for sustainable conversion of sunlight to hydrogen using proposed compact CPV system. Energy Convers Manage 165:102–112

Cherucheril G, March S, Verma A (2011) Multijunction solar cells. Department of Electrical Engineering, Iowa State University

Claverie M, Dupas A, Esteve A (1980) Proceedings of 3rd E.C. photovoltaic solar energy conference, p 381, Reidel, Dordrecht, CNRS, France

Clemens DD (1997) Photovoltaic concentrator system. US Patent 5,660,644

David FK, Stephen HJ (2007) Laminated solar concentrating photovoltaic device. US Patent application publication, pp US2007/0256726
Desideri U, Campana PE (2014) Analysis and comparison between a concentrating solar and a photovoltaic power plant. Appl Energy 113:422–433
Desideri U, Zepparelli F, Morettini V, Garroni E (2013) Comparative analysis of concentrating solar power and photovoltaic technologies: technical and environmental evaluations. Appl Energy 102:765–784
Farahani S (2011) ZigBee wireless networks and transceivers. Newnes
Garboushian V, Roubideaux D, Yoon S (1996) Proceedings of 25th photovoltaic specialists conference, p 1373, IEEE, New York
Garboushian V, Stone KW, Slade A (2007) The amonix high-concentration photovoltaic system. Concentrator Photovoltaics 130:253
Giuffrida M, Tornielli GP, Pidatella S, Repetto A, Bellafronte E, Zani PE (1980) Proceedings of 3rd E.C. photovoltaic solar energy conference, p 391, Reidel, Dordrecht
Green MA, Emery K, Hishikawa Y, Warta W, Dunlop ED (2015) Solar cell efficiency tables (Version 45). Prog Photovoltaics Res Appl 23(1):1–9
IPCC (2012) Renewable energy sources and climate change mitigation. Special report of the Intergovernmental Panel on Climate Change
Luque-Heredia I, Cervantes R, Quemere G (2006) A sun tracking error monitor for photovoltaic concentrators. In: Photovoltaic energy conversion, conference record of the 2006 IEEE 4th world conference on 2006, vol 1, pp 706–709
Luque-Heredia I, Moreno JM, Magalhaes PH, Cervantes R, Quemere G, Laurent O (2007) Inspira's CPV sun tracking. Concentrator Photovoltaics 130:221
Mathur SS, Negi BS, Kandpal TC (1990) Geometrical designs and performance analysis of a linear Fresnel reflector solar concentrator with a flat horizontal absorber. Int J Energy Res 14 (1):107–124
McConnell R (2008) A solar concentrator pathway to low-cost electrolytic hydrogen. In: Solar hydrogen generation. Springer, New York, pp 65–86
Muhammad B, Seung JO, Ng KC, Chun W (2016) Experimental investigation of multijunction solar cell using two axis solar tracker. In: Applied mechanics and materials, vol 819, pp 536–540. https://doi.org/10.4028/www.scientific.net/AMM.819.536
National Renewable Energy Laboratory (NREL) (2016) http://www.nrel.gov/ncpv/images/efficiency_chart.jpg. Date retrieved: 01-08-2016
Ng KC, Burhan M, Shahzad MW, Ismail AB (2017) A universal isotherm model to capture adsorption uptake and energy distribution of porous heterogeneous surface. Sci Rep 7(1):10634
Oh SJ, Burhan M, Ng KC, Kim Y, Chun W (2015) Development and performance analysis of a two-axis solar tracker for concentrated photovoltaics. Int J Energy Res 39(7):965–976
Sala G, Araújo GL, Luque A, Ruiz J, Coello MA, Lorenzo E, Chenlo F, Sanz J, Alonso A (1979) Proceedings of ISES international solar energy society silver jubilee congress, p 1737, Pergamon, New York
Salim A, Eugenio N (1990) A comprehensive report on the performance of the longest operating 350 kW concentrator photovoltaic power system. Solar Cells 29(1):1–24
Shahzad MW, Burhan M, Ang L, Ng KC (2018a) Adsorption desalination—principles, process design, and its hybrids for future sustainable desalination. In: Emerging technologies for sustainable desalination handbook, pp 3–34
Shahzad MW, Burhan M, Son HS, Oh SJ, Ng KC (2018b) Desalination processes evaluation at common platform: a universal performance ratio (UPR) method. Appl Therm Eng 134:62–67
Shahzad MW, Burhan M, Ghaffour N, Ng KC (2018c) A multi evaporator desalination system operated with thermocline energy for future sustainability. Desalination 435:268–277
Singh P, Liburdy JA (1993) A solar concentrator design for uniform flux on a flat receiver. Energy Convers Manage 34:533–543
Solanki SC, Dubey S, Tiwari A (2009) Indoor simulation and testing of photovoltaic thermal (PV/T) air collectors. Appl Energy 86(11):2421–2428

Tsadka S, Segev R, Migalovich P, Levin O, Tarazi E, Whelan R (2009) Solar electricity generation system. US Patent application publication, p US2009/0065045

Walter L, John L (1994) Multiple reflector concentrator solar electric power system. US Patent 5,374,317

Xu G, Zhong Z, Wang B, Guo R, Tian Y (2013) Design of PSD based solar direction sensor. In: Sixth international symposium on precision mechanical measurements, International Society for Optics and Photonics, pp 89162–89162

Yao Y, Hu Y, Gao S, Yang G, Du J (2014) A multipurpose dual-axis solar tracker with two tracking strategies. Renew Energy 72:88–98

# Chapter 7
# Metal–Organic Frameworks in Dye-Sensitized Solar Cells


**I. R. Perera, C. V. Hettiarachchi and R. J. K. U. Ranatunga**

**Abstract** In 1991, the very first high-efficiency dye-sensitized solar cell (DSC) was reported by Brian O'Regan and Michael Grätzel. Since then these devices have been steadily developed around the world. Environment friendliness, cost-effectiveness, easy fabrication, and significant performance under indoor light conditions encourage researchers to explore the possibility of commercializing DSCs. Numerous materials have been tested to improve the overall device performance leading to efficiencies over 14%. Metal–organic frameworks (MOFs) are one such material that has been utilized to further improve device performance. Although this field is only in its incipiency, MOF-integrated DSCs have demonstrated the possibility of fabricating devices as efficient as conventional devices. This chapter is focused on MOF-based DSCs with a brief introduction on MOFs and DSCs, separately. The basic requirements of MOFs to be utilized in DSCs are then discussed. Further, the up-to-date state of MOF research in the area of DSCs will be reviewed. Finally, directions of future research on MOF-based DSCs are identified, with emphasis on reaching the desired properties of MOFs that impact device performance. It is hoped that by establishing robust structure–property relationships, future design and synthesis of MOF-based DSCs will converge to desired commercialization goals.

I. R. Perera (✉) · C. V. Hettiarachchi · R. J. K. U. Ranatunga
Department of Chemistry, Faculty of Science, University of Peradeniya, Peradeniya 20400, Sri Lanka
e-mail: ishanieperera@pdn.ac.lk

C. V. Hettiarachchi
e-mail: champikav@pdn.ac.lk

R. J. K. U.Ranatunga
e-mail: udyranatunga@pdn.ac.lk



H. Tyagi et al. (eds.), *Advances in Solar Energy Research*, Energy, Environment, and Sustainability, https://doi.org/10.1007/978-981-13-3302-6_7

## 7.1 Introduction

### *7.1.1 Dye-Sensitized Solar Cells*

In this chapter, Sects. 7.1.1 and 7.1.2 comprise a brief introduction to dye-sensitized solar cells (DSCs) and metal–organic frameworks (MOF), respectively. Here, the structure and properties of both aspects will be discussed. In Sect. 7.2, a detailed review is presented on the status of the research carried out on MOF-based DSCs. There, the research based on individual components of a DSC is discussed separately. Finally, in Sect. 7.3, general problems associated with DSCs and MOF-based solar cells will be summarized and the chapter will be concluded by stating the further improvements that could enhance the device performance.

Energy demand is increasing rapidly with the growth of human population, and electricity has become the fastest growing end-use energy in modern human life. Statistics from the International Energy Agency (IEA), World Energy Outlook (WEO), and European Photovoltaic Industry Association (EPIA) have predicted a one-third increase in energy consumption from 2011 to 2030 (2015, 2015). Since currently the highest proportion of energy is supplied by fossil fuels, the growth in energy consumption is accompanied by large increase in combustion of fossil fuel and extensive emission of greenhouse gases like carbon dioxide (2014). The rapid increase in the atmospheric carbon dioxide concentration since the beginning of the indicated revolution is impacting on the earth's climate, and by extension, our lives (2014).

Finding ways to minimize the hazardous effects from the present day energy utilization on our climate, environment, and health by replacing the declining fossil fuel supplies with sustainable and renewable energy resources is thus a key challenge. Among the available renewable energy sources, solar energy is expected to play a key role in the future as the amount of sunlight that strikes the earth in an hour could generate more energy than which is annually consumed by human beings (Lewis 2007). Numerous technologies are being developed to harvest solar energy, among which the DSCs have been recognized as a potentially cheaper alternative to other, high-cost photovoltaics.

Since the publication of the paper by Brian O'regan and Michael Grätzel in 1991, the development of dye-sensitized solar cells has been a steady journey. A tremendous amount of research is being carried out around the world to improve individual components as well as the whole device in order to achieve the ultimate goal of fabricating stable and highly efficient devices. At first, how these devices worked was unclear as there was no built-in electric field present. Over the years, they have been thoroughly studied and their operation is now well understood (Hagfeldt et al. 2010). One interesting feature of DSCs is the Low requirement for highly pure starting materials. Thus, the energy payback time would be significantly shorter and the production costs are believed to be much lower compared to the other types of solar cells (Grätzel 2001; Grätzel 2003; Perera et al. 2015; Nattestad et al. 2010; Kakiage et al. 2015).

A typical DSC consists of an electrolyte which is sandwiched between two transparent electrodes made out of fluorine-doped tin oxide (FTO) glass and is illustrated in Fig. 7.1. On one side is the working electrode (WE) in which a sensitizer is adsorbed on to a wide band gap semiconductor. On the other side is the counter electrode (CE) which is commonly platinized by the thermal decomposition of platinic acid. Electrolyte may appear as liquid, quasi-solid, or solid which is discussed in detail under Sect. 7.2.2 (Grätzel 2001; Hagfeldt and Grätzel 2000).

DSCs can be constructed as single-junction n- or p-type and multi-junction pn-type. In n-DSCs, photocurrent results from the photoexcited electron injection by the sensitizer into the n-type semiconductor. In p-DSCs, the operation principle is inverted. That is, the photoexcited sensitizer accepts electrons from the p-type semiconductor. Integrated structures of n- and p-DSCs are known as tandem DSCs (pn-DSCs).

In n-type devices, an n-type semiconductor (typically $TiO_2$) is used as the wide bandgap semiconductor and electrons are considered the majority charge carriers. Figure 7.2 shows a schematic diagram of an n-DSC with the trail of electron transport.

Initially, photoexcitation of the sensitizer/dye ($D$) from the highest occupied molecular orbital (HOMO) to the lowest unoccupied molecular orbital (LUMO), results in the injection of an electron into the conduction band (CB) of the oxide generating the dye cation ($D^+$). The lifetime of the excited state of the dye is in the nanosecond to microsecond range, whereas the corresponding injection rate constants are in the femtosecond range (Hagfeldt and Grätzel 2000; Koops et al. 2009; Ramakrishna et al. 2005; Asbury et al. 1999; Benkö et al. 2001; Kuang et al. 2006). For efficient electron injection, the LUMO level of the dye should be at least 0.10–0.15 V above the $TiO_2$ CB edge, which is approximately −0.50 to −0.80 V versus Normal Hydrogen Electrode (NHE) (Koops et al. 2009). Then, the electron

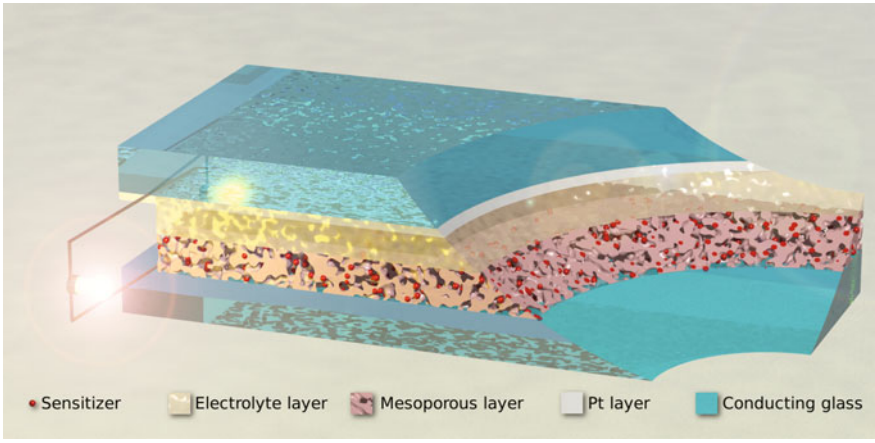


**Fig. 7.1** Assembly of a typical dye-sensitized solar cell

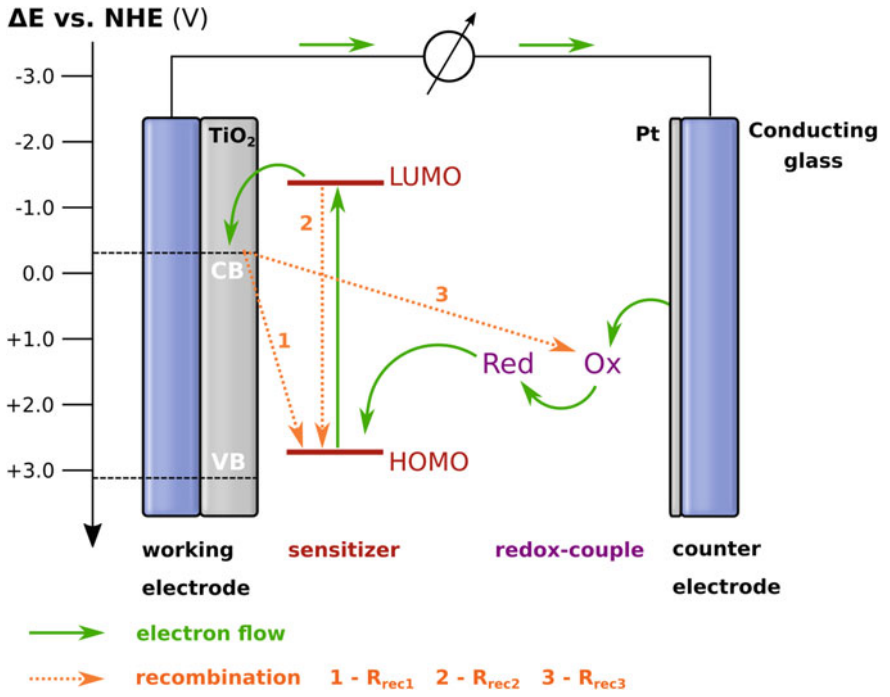


**Fig. 7.2** Schematic illustration of the electron flow in n-DSCs

donation of the reduced species of a redox couple restores the original state of the dye (dye regeneration), which occurs on the microsecond or millisecond timescale. To avoid energy losses due to charge recombination, dye regeneration must be faster than the rate of back reaction of the injected electrons with $D^+$ (Fig. 7.2, $R_{rec1}$). This difference in lifetime is the main requirement for the efficient electron–hole separation in the device. The reduced form of the redox couple is then restored by reduction of the oxidized species of the redox couple at the counter electrode. The electron flow through the external circuit completes the electrical circuit.

The overall performance of DSC depends on the ability to suppress the unfavorable recombination pathways shown in Fig. 7.2 ($R_{rec1}$, $R_{rec2}$, and $R_{rec3}$). Two out of the three paths ($R_{rec1}$ and $R_{rec3}$) are interfacial charge recombination reactions limiting the charge collection efficiency at the device contacts. The injected electrons could recombine with the oxidized dye ($R_{rec1}$) or oxidized redox mediator of the electrolyte ($R_{rec3}$). These reactions will reduce the maximum current and the voltage that could be generated within the device, leading to a lower than expected device performance. The third, and least likely, phenomenon that may limit the device performance is the relaxation of the excited dye without injecting the electron to the CB of the semiconductor ($R_{rec2}$) (Kalyanasundaram and Gratzel 1998; Kebede and Lindquist 1999; Palomares et al. 2002). This process is unlikely because of the fast rate of electron injection into the semiconductor.

To date, the highest efficiency for n-DSCs is 14.7% achieved by Kakiage et al. using a cobalt complex, tris(1,10-phenanthroline)cobalt(II/III) ($[Co(phen)_3]^{3+/2+}$), in conjunction with a carbazole/hexyl-functionalized oligothiophene/trimethoxysilyl-anchor dye, ADEKA-1, and a dibiphenylmonophenylamine dye, LEG4 (Kakiage et al. 2015).

In p-type DSCs, the device fabrication and the materials used are similar to those of n-DSCs except for the material used as the mesoporous metal oxide layer. Here, NiO, a p-type semiconductor, is typically used instead of $TiO_2$ (Nattestad et al. 2010; Powar et al. 2012; He et al. 1999).

In p-DSCs (Fig. 7.3), once the dye molecules (*D*) are photoexcited an electron is transferred from the valence band (VB) of the semiconductor to the HOMO level of the dye (in other words, a hole is injected from D to the VB of the semiconductor). The holes in the semiconductor diffuse toward the CE via the external circuit. At the CE, the reduced form of the redox couple is oxidized and the dye is then regenerated by electron transfer from the reduced dye to the oxidized form of the redox

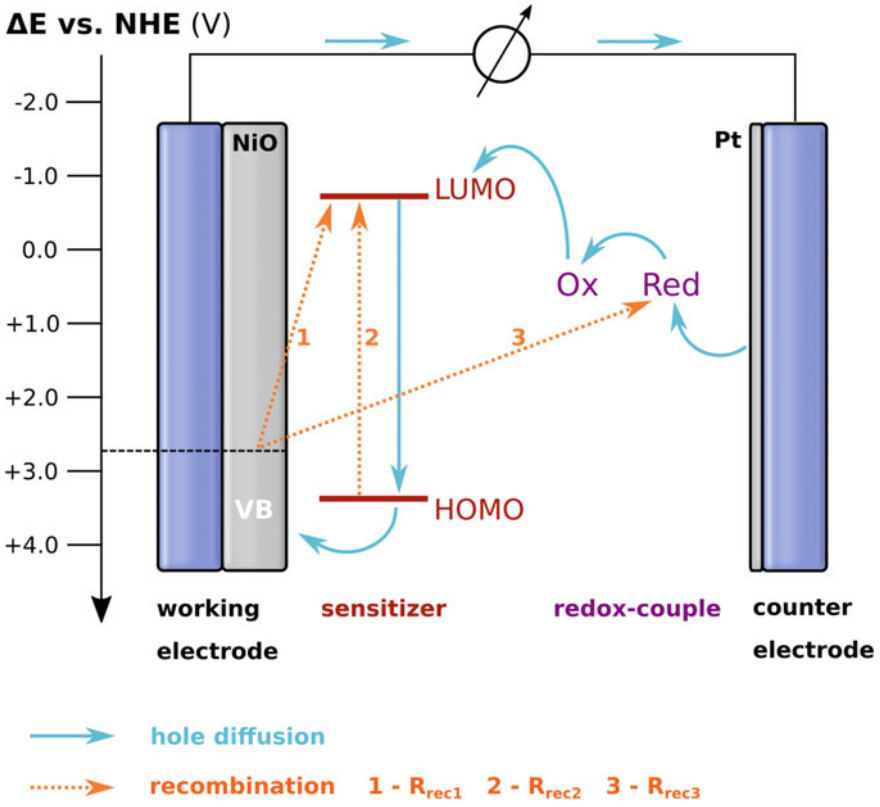


**Fig. 7.3** Schematic illustration of the holes diffusion in p-DSCs

couple. The reduction potential of the redox mediator must be more positive than that of the dye to provide a significant driving force for the dye regeneration reaction.

As for n-DSCs, unfavorable recombination reactions (Fig. 7.3) limit the device performance in p-DSCs ($R_{rec1}$, $R_{rec2}$, and $R_{rec3}$) (Perera et al. 2015; Nattestad et al. 2010; Powar et al. 2012).

Due to the slow development and the complexity of some of the materials used in p-DSCs, the maximum efficiency attained so far has been limited. In 2015, an efficiency of 2.5% was reported by Perera et al. for devices constructed with a tris (acetylacetonate)iron(III)/(II) ($[Fe(acac)_3]^{-1/0}$) redox shuttle in conjunction with PMI-6T-TPA sensitizer (Perera et al. 2015). This represented a significant improvement over the 0.61% reached with the $I^-/I_3^-$ redox couple (Zhang et al. 2012).

The tandem DSCs/pn-DSCs is a multi-junction photovoltaic in which a photocathode and a photoanode are combined into a single device (Fig. 7.4) (Nattestad et al. 2016). This allows a broader spectral absorption while maintaining a high voltage leading to a higher theoretical energy conversion efficiency ($\sim$43%) than that achievable with single-junction DSCs (Shockley and Queisser 1961). Due to the slow development of p-DSCs, progress on pn-DSCs has been limited, since they were first introduced in 2000 (He et al. 2000).

A variety of construction concepts for tandem devices has been described in literature (Dürr et al. 2004; Kubo et al. 2004; Murayama and Mori 2007). The simplest and, so far, the best-performing pn-DSC architecture is shown in Fig. 7.4 (He et al. 1999). This pn-DSC is constructed simply by connecting a dye-sensitized photocathode and a dye-sensitized photoanode. Upon illumination, simultaneous light absorption occurs at both electrodes. At the photoanode, excited dye molecules inject electrons to the CB of the n-type semiconductor and, at the

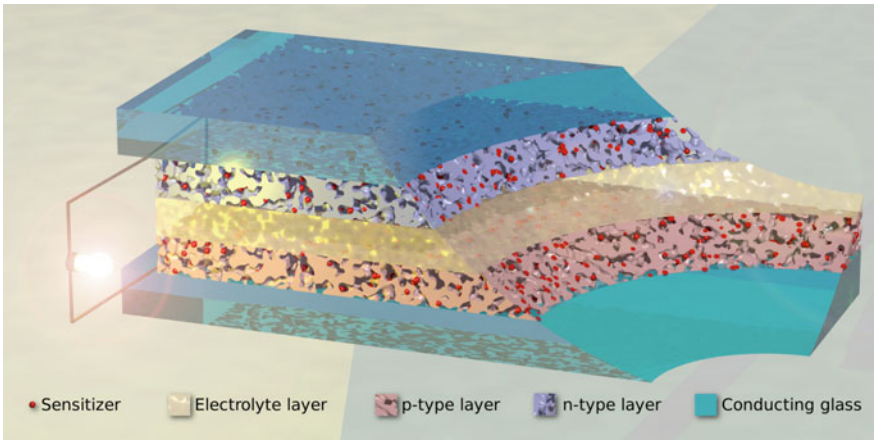


**Fig. 7.4** Structure of a typical pn-DSCs

photocathode, excited dye molecules inject holes into the VB of p-type semiconductor. These charges then propagate through the external circuit in opposite directions. To complete the cycle, reduced and oxidized form of the redox couple in the electrolyte will regenerate the oxidized and reduced dye molecules at the anode and cathode, respectively (Gibson et al. 2009).

The series connection used in pn-DSCs increases the maximum attainable voltage compared to single-junction devices. The overall voltage of the tandem solar cell is typically close to the arithmetic sum of those achievable by the individual p- and n-type devices. In contrast, the overall photocurrent generated in the device is limited by the least efficient photoelectrode. Hence, matching of the current generated at each of the electrodes is crucial. The recombination reactions that occur in both n- and p-DSCs, have a major influence on the overall performance of tandem DSCs.

In 2010, Nattestad et al. achieved 1.9% efficiency with the $I_3^-/I^-$ redox mediator in conjunction with the PMI-6T-TPA sensitizer at the photocathode and the N719 sensitizer at the photoanode (Nattestad et al. 2010).

Current density–voltage ($J$–$V$) curves (Fig. 7.5) of these devices are used as the preliminary characterization method. Photovoltaic parameters such as short-circuit current density ($J_{SC}$), open-circuit voltage ($V_{OC}$), fill factor (FF), and overall energy conversion efficiency ($\eta$) can be derived from a typical $J$–$V$ curve.

The intercept of the $Y$ axis in a $J$–$V$ curve at zero applied bias conditions represents the $J_{SC}$ of a device, and is defined as the photocurrent per unit area under short-circuit condition. The $V_{OC}$ is the difference between the Fermi level of the semiconductor and the redox potential of the electrolyte. In a $J$–$V$ curve, the voltage at open-circuit condition (intercept of X axis) represent the $V_{OC}$. The FF (see Eq. 7.1) of a device is defined as the maximum power output ($P_{max} = J_{max} \times V_{max}$) divided by the product of $J_{SC}$ and $V_{OC}$ and is often described as a measure of the "rectangularity" of the $J$–$V$ curve. The power output of the device reaches its maximum at one specific combination of current and voltage. This current and voltage points are labeled as $J_{max}$, $V_{max}$, respectively, in the $J$–$V$ curve. Hence, the efficiency, $\eta$, (see Eq. 7.2) of a DSC is calculated by the ratio of the maximum output electrical power to the energy of incident sunlight ($I_S$).

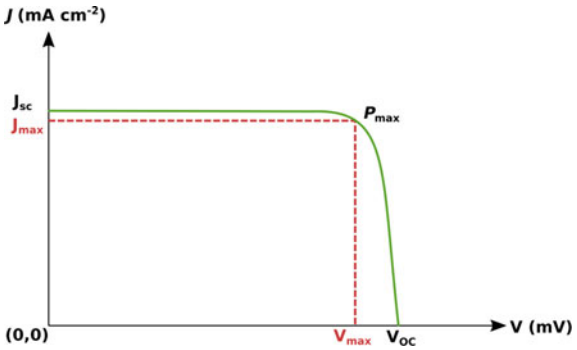


**Fig. 7.5** Typical current–voltage characteristics of a DSC

$$\mathrm{FF} = (J_{\max} \times V_{\max})/(V_{\mathrm{OC}} \times J_{\mathrm{SC}}) \tag{7.1}$$

$$\eta = (J_{\mathrm{SC}} \times V_{\mathrm{OC}} \times \mathrm{FF})/I_S = (J_{\max} \times V_{\max})/I_{\mathrm{S}} \tag{7.2}$$

### 7.1.2 Metal–Organic Frameworks (MOFs)

Porous materials have become very useful owing to a wide range of technological applications in many areas of science and society. In this regard, porous coordination polymers, and among these metal–organic frameworks, have attracted consideration among different other materials.

Initially, coordination polymers (CP) were introduced by Shibatha in 1916 by synthesizing dimers and trimers of cobalt(II) with ammine nitrates and since then, thousands of CPs have been reported, including straight-chain 1D, branched network 2D, and framework 3D coordination polymers. However, the origin of the word Metal–Organic Frameworks (MOF) is fairly new; Yaghi et al. used this word first in 1995 to explain the open microporous crystalline framework, obtained between copper metal and 4,4-bipyridine ligand via hydrothermal synthesis, as a subgroup of 3D coordination polymers (Yaghi and Li 1995). According to the IUPAC definition released in 2013 after conducting a survey, *MOF is a coordination network with organic ligands containing potential voids* (Batten et al. 2013). Thus, to be considered as a MOF, though porosity is essential, crystallinity is not required.

MOFs are constructed to obtain permanent porosity by linking metal cations or metal clusters (referred to as nodes) with organic ligands, through strong coordinate bonds. If a cluster of metals occupies the node, Secondary Building Units (SBU) are formed with different geometries. Even though the first reported MOF does not contain an SBU, most others reported since which have become popular as prototypes of MOFs have SBUs creating a vast variety of rigid pore architectures. MOFs containing oxygen-ligating sites in carboxylate groups can form robust and more stable frameworks compared to nitrogen-containing ligands like bipyridines due to the very strong M–O bonds in SBUs which cannot be created strongly by N ligating sites.

Flexibility in the metal SBUs, length, geometry, and number of electron donors in organic linkers can build up periodic nets via reticular synthesis. Once the network is designed based on the reaction conditions, with the concept of isoreticular expansion, high porosity can be achieved using longer ligands with the same topology. As revealed in Fig. 7.6, MOF-177, synthesized using Zn(II) and 4,4′,4″-benzene-1,3,5-triyl-tribenzoate (Chae et al. 2004), was expanded to give the same pore structure with ultrahigh porosity in MOF-180 and MOF-200 using 4,4′,4″-(benzene-1,3,5-triyl-tris(ethyne-2,1-diyl)) tribenzoate and 4,4′,4″-(benzene-1,3,5-triyl-tris(benzene-4,1-diyl))tribenzoate, respectively, by changing the length of the linker only (Furukawa et al. 2010).

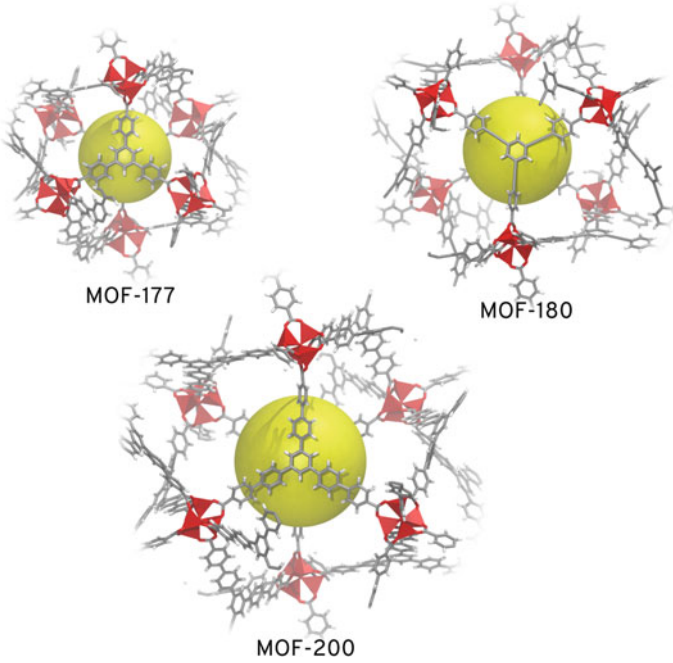


**Fig. 7.6** Isoreticular expansion of the pore architecture in MOF-177 by extending the linker length. Crystal structures were taken from published data from (Chae et al. 2004; Furukawa et al. 2010), through the Cambridge crystallographic database center, CCDC deposit numbers: MOF-177 -230642, MOF-180-775690, MOF-200-775691

Thus, in the past two decades, an explosive growth in preparation and characterization methods of MOFs has been observed fueled by the anticipation of utilizing them in a large number of applications, using organic linkers shown in Fig. 7.7. Further, mixed-metal MOFs and mixed-ligand MOFs have also been synthesized depending on the application type.

Most MOFs are composed of a large number of bonds such as C–C, C–H, C–O, and M–O bonds and as a result they show very high thermal stability above 300 °C and some even above 500 °C (Eddaoudi et al. 2002). Along with this high thermal stability, high chemical stability, tunability in pore or channel architecture, and ability of changing chemical properties after synthesis via post-synthetic techniques are the most attractive properties in MOFs. These properties have motivated researchers to explore them in a wide range of potential applications; in gas storage, separations, heterogeneous catalysis, sensing, in energy-related technologies like fuel cells, supercapacitors, and as molecular vessels and drug carriers.

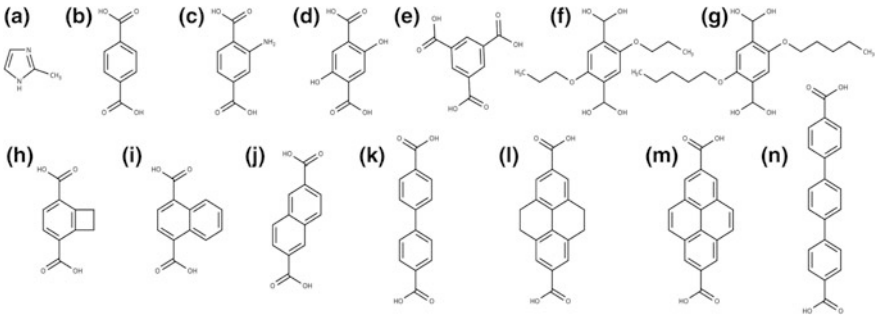


**Fig. 7.7** Common organic linkers used for synthesis of MOFs. **a** 2-methylimidazole; **b** BDC (benzene dicarboxylic acid); **c** R3-BDC; **d** 2,5-dihydroxyterephthalic acid; **e** trimesic acid; **f** R4-BDC; **g** R5-BDC; **h** R6-BDC; **i** R7-BDC; **j** 2,6-NDC; **k** BPDC; **l** HPDC; **m** PDC; and **n** TPDC

#### 7.1.2.1 Synthesis and Characterization

For the synthesis of metal–organic frameworks, numerous synthetic methods have been developed in recent past covering a wide range of temperatures, solvent mixtures, pH, metal-to-linker ratios and concentrations, and pressures and reaction times (Stock and Biswas 2012). However, the greatest challenge in preparing a new or a reported MOF lies in attaining the optimized reaction conditions which give the desired MOF in high yield and correct crystal sizes are required for a particular application. Hence, all these parameters should be fine tuned individually to obtain the desired MOF. Actually, among all the reported synthetic procedures, solvothermal synthesis using autoclaves was the first reported successful method (Yaghi and Li 1995) giving crystalline MOFs and later on, other alternative methods; microwave synthesis, spray pyrolysis, mechanochemical methods, sonication-assisted synthesis, layer-by-layer deposition, and chemical bath deposition have also been utilized. Generally, in MOFs, solvent molecules used for synthesis occupy voids in channels/pores, and upon heating or vacuuming, they are removed leaving large pore volumes and large surface area. In fact, a single metal and a di- or tri- or polydentate ligand can combine in various ways to form a large number of 1D, 2D, or 3D coordination polymers; many of which are nonporous and not MOFs. Thus, the discovery of optimized conditions that afford the desired MOF can involve a large number of trial reactions by changing reaction parameters carefully.

The best characterization method for new MOFs is Single Crystal X-ray Diffraction (SCXRD) which can unambiguously determine the geometry of SBU, shape and size of the pores and channels, and other structural information of interest (Wang et al. 2018). However, the major challenge here is to obtain good quality single crystals with high crystallinity and required size. Thus, for partially crystalline samples, the Powder X-ray Diffraction (PXRD) technique can be used to identify the degree of crystallinity and to obtain a characteristic diffraction pattern

of the MOF (Wang et al. 2014). Further, nitrogen gas adsorption and desorption isotherms can be used at cryogenic conditions to determine the pore volume and size and thereby the surface area of the MOF (Thommes et al. 2015; Thommes 2010). Scanning Electron Microscopy (SEM) can provide the morphology and size of the MOF crystals and if SEM is coupled with Energy Dispersive X-ray Spectroscopy (EDXS), qualitative information about the metal distribution in MOFs also can be obtained. If the MOF product is not crystalline enough to obtain a structure using SCXRD analysis, solid-state NMR (SS-NMR) spectroscopy is the next best option to get information about the molecular and crystal structure. Local chemical environment inside a MOF and supramolecular interactions between small molecules and the internal walls of MOF and oxidation state of ions can be elucidated based on the SS-NMR data (Hoffmann et al. 2012; Sutrisno and Huang 2013). On the other hand, Diffuse Reflectance Infrared Fourier Transform Spectroscopy (DRIFTS) can also be used to identify functional groups in linkers, and to elucidate the interaction between MOF and molecules inside the pores (Howarth et al. 2017). However, DRIFT is not a successful method to deduce the structure of the MOF accurately. Thus, if the structure of the MOF is reported earlier along with its crystal structure, to confirm the synthesis of the same MOF later, only PXRD can be used, because it can give a characteristic diffraction pattern and from which unknown MOF can be identified. Apart from experimental analysis, theoretical and computational techniques have been used to study various facets of MOFs. These have ranged from structure prediction and refining, to characterization of mechanical, thermal, and optoelectronic properties (Coudert and Fuchs 2016).

#### 7.1.2.2 Light Harvesting Properties

Other than aforementioned main properties, recently MOFs were identified with light harvesting properties as well dependent on the properties of linker/s. Since the linkers are organic molecules having p-electrons, they absorb energy from the UV and blue regions in the electromagnetic spectrum for electronic transitions. As a result, metal-to-ligand or ligand-to-metal energy transfer processors are possible depending on the selection of the linker and metal type. Specially, MOFs made up of ligands like 2,5-dihydroxyterephthalic acid and 2-amino terephthalic acid can impart a color to the MOF even composed of cations Zn(II) and Ti(IV) having $d^{10}$ and $d^0$ electronic configurations, and those MOFs can harvest energy from the visible spectrum (Gao et al. 2014; Hendon et al. 2013).

Further, Kent et al. reported that long-distance energy migration is possible in a Ru(II)-based MOF composed of bipyridine as the ligand only upon doped with Os(II) (Kent et al. 2010). Later, Lee et al. prepared a black mixed-ligand MOF containing Zn(II) as the node tetra-acid porphyrin as the primary ligand and pyridine-functionalized boron dipyrromethene as the secondary ligand. Here, the second ligand is capable of behaving as a black chromophore or an antenna by

absorbing effectively the energy within the entire visible region and passing the energy absorbed to the other ligand. This strut-to-strut energy transfer process occurs effectively, due to well-ordered donor–acceptor assembly in MOF lattices (Lee et al. 2011).

#### 7.1.2.3 Semiconductor Properties

Materials showing insulating properties at low temperatures and low conductivity at higher temperatures are called semiconductors. These materials can be characterized by considering their bandgaps which fall in the range of 0.7–4.0 eV. Based on the carrier type, there are n-type and p-type semiconductors in which electrons and holes are carriers, respectively. UV-Visible spectroscopy, photoluminescence (PL) analysis, and Mott–Schottky data can be used to determine the bandgap and the type of semiconductor, respectively. Accordingly, most MOFs are insulators. However, MOF-5 has exhibited semiconductor behavior due to the geometric type of metal clusters containing ZnO units in the network which can act as quantum dots (Alvaro et al. 2007; Llabrés i Xamena et al. 2007). Further, it was reported that a mixed-metal MOF composed of Cu and Ni with pyrazine-2,3-dithiolate as linkers showed p-type semiconductivity and its conductivity was able to enhance significantly upon doping $I_2$ (Kobayashi et al. 2010).

## 7.2 Current Research on MOF-Based DSCs

Controllable architectures, adjustable pore sizes, high surface areas, and unique thermal behavior of MOFs allow investigation of these materials for any component of a DSC. So far, MOF-based DSC research has only focused on n-DSCs. Therefore, in this section each component of a DSC will be discussed separately and n-DSCs will be referred as DSCs.

### *7.2.1 Working Electrode Material*

In DSCs, the semiconductor/dye interface provides the platform for charge separation after photoexcitation of the dye. Further, injected charge carriers are diffused toward the external circuit. In general, prerequisites of the semiconductor materials used in DSCs are large surface area, high surface chemical affinity for the dyes, suitable CB/VB potentials, and high charge mobility.

In a semiconductor material, the majority charge carriers are electrons and the Fermi level lies closer to the CB of the semiconductor. A variety of materials, such as $TiO_2$, (Nowotny et al. 2008; Park et al. 2000; Barbé et al. 1997; Wang et al. 2006) ZnO, (Fan et al. 2013; Quintana et al. 2006; Zhang et al. 2008) $Fe_2O_3$,

(Bjoerksten et al. 1994) $Nb_2O_5$, (Sayama et al. 1998; Ou et al. 2012; Le Viet et al. 2010) $CeO_2$, (Corma et al. 2004) $Zn_2SnO_4$, (Tan et al. 2007) $SrTiO_3$, (Burnside et al. 1999; Daeneke et al. 2012) $BaSnO_3$, (Shin et al. 2013) and $Zn_2SnO_4$, (Tan et al. 2007) have been tested as photoanodes in DSCs (Jose et al. 2009). $TiO_2$ is by far, the most commonly used semiconductor material in DSC (Kakiage et al. 2015) where it can exist in three crystalline polymorphs, namely, rutile (bandgap energy, Eg = 3.05 eV), anatase (Eg = 3.23 eV), and brookite (Eg = 3.26 eV). Both anatase and rutile have been tested in DSCs, and rutile has been found to scatter light more efficiently and is more stable than anatase. The drawback is that rutile has a lower surface area which limits the dye adsorption, and hence lowers the device performance (Park et al. 2000). Therefore, anatase has been preferred over rutile as the semiconductor material for DSCs.

Devices based on $TiO_2$ have been studied extensively and the best-performing devices known to date typically consist of several $TiO_2$ layers with different morphologies. On FTO, a thin blocking layer of $TiO_2$ is typically generated (100–200 nm) that prevents the unfavorable recombination reactions at the substrate/electrolyte interface. On top of this, a transparent $TiO_2$ layer (particle size ~20–30 nm) is applied to provide the surface for the dye molecules to be adsorbed. The thickness of the layer used depends on the light absorption characteristics of the dye and can range from as low as 1 to >10 μm. A scattering layer (particle size ~300–400 nm) is then coated on the transparent layer to enhance the light absorption as it backscatters the light which has not been absorbed by dye molecules (Barbé et al. 1997; Wang et al. 2006). Finally, a post-treatment with $TiCl_4$ is applied to increase the connection between $TiO_2$ particles in both the transparent and the scattering layers (Sommeling et al. 2006).

Apart from $TiO_2$, ZnO is another competitive candidate that has been used in DSCs. Although ZnO has a faster charge transport compared to $TiO_2$, the devices based on ZnO have shown faster recombination kinetics (Zhang et al. 2008). On the other hand, $TiO_2$ has a slower recombination, better dye loading, and faster electron injection that makes it the best candidate for n-type semiconductors up to date (Jose et al. 2009; Chandiran et al. 2014). The devices based on ZnO photoanodes have reached a conversion efficiency of 7.5% (Nafiseh et al. 2011) compared to 14.7% for devices based on $TiO_2$ (Kakiage et al. 2015).

In 2011, Li et al. introduced a zeolite imidazolate framework (ZIF-8, see Fig. 7.8), a metal–organic framework reticulated using a nitrogen-containing ligand, 2-methylimidazole, and zinc metal for the very first time, into DSCs. A thin layer (2 nm) of ZIF-8 was fabricated on top of the $TiO_2$ layer which demonstrated an enhancement in $V_{OC}$ (Li et al. 2011). ZIF-8 has been the choice of MOF in this study due to its attractive features such as high specific area (>1400 $m^2\ g^{-1}$), thermal stability, being a chemically robust compound, small pore apertures (3.4 Å), and large cavities (11.6 Å). XPS confirmed the deposition of ZIF-8 and high-resolution TEM confirmed the formation of core/shell nanostructure. The growth time of the MOF was controlled in order to vary the thickness of the MOF layer where a linear relationship between the $V_{OC}$ and the thickness of ZIF-8 layer was observed until 40 min of growth time. *I–V* measurements under dark

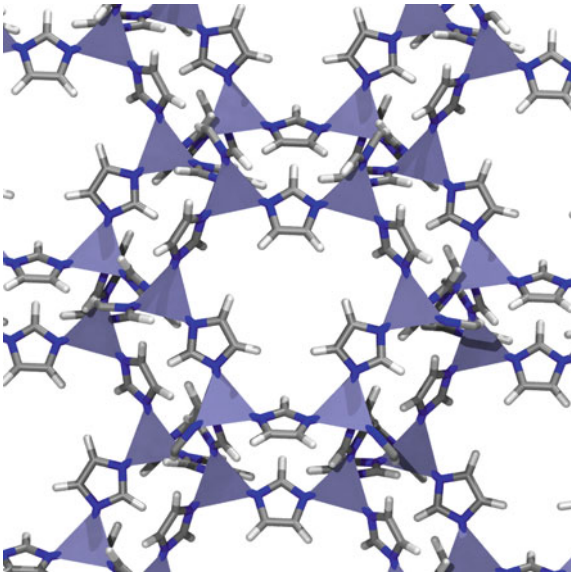

**Fig. 7.8** Structure of ZIF-8. Crystal structures were taken from published data from (Morris et al. 2012), through the Cambridge crystallographic database center, CCDC deposit number [864309]

conditions revealed the requirement of higher voltage for the motion of electrons for ZIF-8-coated $TiO_2$ electrodes. Further, the charge transfer resistance ($R_{REC}$) derived from EIS has shown a higher resistance for ZIF-8-coated $TiO_2$. Thus, the interfacial charge recombination reactions were inhibited by the thicker layer of ZIF-8 which ascribed to the enhancement in $V_{OC}$. In contrast, no significant effect was observed by the improved dye loading due to the high surface area of ZIF-8/$TiO_2$ electrode as the quantum yields of electron injection was low. Therefore, a significant decrease in both the $J_{SC}$ and $\eta$ was observed as the thickness of ZIF-8 layer increased even though the $V_{OC}$ was enhanced. According to the Mott–Schottky measurements, coordination of the organic ligand of the MOF (2-methyl imidazole) to $Ti^{4+}$ did not affect the Fermi level of $TiO_2$. So, the increase in $V_{OC}$ of the devices with $TiO_2$/ZIF-8 electrode was purely due to the inhibition of interfacial charge recombination reactions.

Same group proposed an improved post-treatment method in which the negative effect on $J_{SC}$ and $\eta$ was lessened (Yafeng et al. 2014). Figure 7.9 depicts the two different methods, wherein the pre-treatment method, the MOF layer was introduced before sensitization of the $TiO_2$ layer ($TiO_2$/ZIF-8/Dye), whereas in the post-treatment method ZIF-8 was introduced after the sensitization of the $TiO_2$ layer and the ZIF-8 layer itself was sensitized after the deposition ($TiO_2$/Dye/ZIF-8/Dye). According to the UV-visible spectra, an enhancement in the amount of anchored dye was observed due to the increased surface area by the deposition of ZIF-8. This led to an improvement in light harvesting efficiency and charge collection efficiency of the photoanode. But, the thickness of the MOF layer was

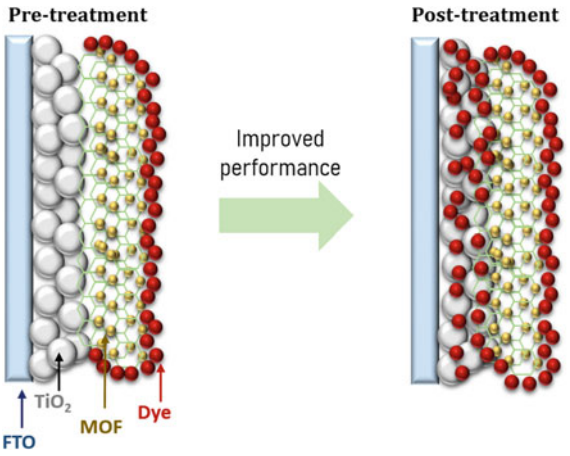


**Fig. 7.9** The possible photoanode statuses after sensitization in pre-treatment and post-treatment approaches

controlled as the charge injection efficiency decreased due to the retarded dye regeneration which was a result of obstructed electron penetration. Although the electron injection was hampered for dyes adsorbed onto ZIF-8 layer, in the post-treatment, dye anchored onto $TiO_2$ layer ensured the efficient photocurrent output of the electrode.

Another interesting study was reported by Lopez et al, where the photochemical response of commercially available MOFs was studied using laser flash photolysis (Lopez et al. 2011). This was used as a tool to identify transient species upon irradiation of the MOF. Out of the MOFs they studied, only $Al_2(BDC)_3$ (MIL-53-Al) composed of terephthalic linter generated a signal indicating charge-separated states. The lifetime of the charge-separated state was then modulated by the inclusion of guest molecules such as anthracene, methylviologen, and dimethoxybenzene. These guest molecules were expected to trap electrons or holes and increase the lifetime. Application of these modified $Al_2(BDC)_3$ MOFs as the semiconductor material in DSCs demonstrated higher efficiencies with better photocurrent response and $V_{OC}$ than that of the unmodified $Al_2(BDC)_3$ MOF.

MOFs have also been used to derive most commonly used metal oxides such as ZnO and $TiO_2$. In 2012, Kundu et al. studied the synthesis of ZnO by calcination of a zinc-based MOF (Kundu et al. 2012). The change in anion of the organic ligand changed the morphology of the calcined product. Further, the shape of ZnO crystals was controlled by applying different calcination environments (under $N_2$ or air). ZnO microstructures derived in air, from the precursors that consist of $Cl^-$ and $Br^-$ exhibited efficiencies 0.14 and 0.15%, respectively, in liquid-state DSCs. Authors claim this method as advantageous over the other synthesis processes owing to its simplicity as one-step thermolysis technique without using any template, surfactant, or other additives.

A similar work was reported by Li et al. (2014), where MOF-5 (with terephthalate ligand) derived ZnO particles were used as the scattering layer of the photoanode (Li et al. 2014). ZnO scattering layer was obtained by the calcination of MOF-5 which was then deposited on the ZnO mesoporous layer. For further improvement, on top of this ZIF-8 was deposited as reported by Kundu et al. Charge transfer resistance ($R_{rec}$) of these devices (8.4 Ω) was lower than that of the devices that consist of pure ZnO mesoporous layer (10.1 Ω). Increase in new pathways for charge recombination after the deposition of the scattering layer may ascribe for reduced $R_{rec}$. However, the obvious improvement in light harvesting efficiency is gained due to the bilayer structure of the device which surpassed the negative effect caused by charge recombination loses. After the modifications, the device efficiency was enhanced by 16.5% when compared to the devices with pure ZnO mesoporous layer.

Apart from ZnO, $TiO_2$ has also been derived from MOFs, since it permits control over the shape and the morphology of $TiO_2$ particles. For the very first time, Chi et al. reported a method of converting the MOF, MIL-125(Ti) again with the same linker terephthalate, into hierarchical $TiO_2$ (her-$TiO_2$) with anatase phase (Chi et al. 2015). In this method, poly(ethylene glycol) diglycidyl ether (PEGDGE) was used as a structure directing agent. Synthesized her-$TiO_2$ was applied as the scattering layer. As described above for ZnO scattering layer, $R_{rec}$ was increased as the application of the scattering layer opened up new pathways for charge recombination. In contrast, enhanced dye loading capacity was observed due to higher thickness and surface area after the application of the scattering layer. Synergistic effect enhances the $J_{SC}$ that improved the overall device performance.

Dou et al. reported a similar study where MIL-125 has been used to synthesize $TiO_2$ nanoparticles that are applied in DSCs as the mesoporous layer (Dou et al. 2016). Simple decomposition of MIL-125 was done instead of using any template molecules. An improvement in $J_{SC}$ was observed for the devices with MIL-125-derived $TiO_2$ layer compared to the devices with P25. The enhanced efficiency was clearly explained by three observations. First was the longer electron lifetime that was derived from EIS studies. Second was the high dye loading calculated from desorption studies. Third was the improved charge collection efficiency that was observed in IPCE measurements. High dye loading also proved the enhanced surface area of MOF-derived $TiO_2$ nanoparticles compared to P25.

Both studies with MOF-derived $TiO_2$ nanoparticles reported efficiencies over 7% due to the enhancement in $J_{SC}$ compared to state-of-the-art devices.

Polyoxometalates (POMs) are another class of materials that have been utilized in DSCs as they are good electron acceptors which improves the charge separation within a device, and some of the POMs have the ability to absorb visible light (He et al. 2016; Sun et al. 2013; Luo et al. 2012). In 2018, Zhang et al. modified the ZnO layer using dendritic Fe-based polyoxometalates@metal–organic framework [POM@MOF(Fe)] (Zhang et al. 2018). Upon application of this material as a modifier layer on ZnO enhanced the energy conversion efficiency by 28% as the light absorption was improved due to ligand-to-metal and ligand-to-ligand charge transfer transition that undergoes within POM@MOF(Fe).

### 7.2.2 Sensitizer (Dye)

The role of the sensitizer in DSCs is to capture incident light. The sensitizer photoexcites and then injects the resultant charge carriers into the CB of the semiconductor. The oxidized sensitizer is then regenerated by the redox mediator present in the electrolyte. In DSCs, for efficient injection and regeneration to occur, the sensitizer should meet a number of requirements including; (i) it should absorb at all the wavelengths within the visible and the UV spectral regions, ideally reaching the near infrared (NIR); (ii) for an efficient charge injection the LUMO level should have a more reducing potential ($\sim$100–150 mV) than the CB potential of the semiconductor; and (iii) for efficient dye regeneration, the HOMO level of the sensitizer should have a more oxidizing potential than the redox potential of the electrolyte (Grätzel 2001).

Ruthenium-based sensitizers have been the main interest since the introduction of DSCs owing to the favorable photochemical properties and high chemical stability (Kohle et al. 1997). An important step in the development of sensitizers was the introduction of the N3 dye (Fig. 7.10) in 1993 (Nazeeruddin et al. 1993). The high absorption by N3 covers the visible-to-near-IR region of the solar spectrum with an absorption threshold around 800 nm. Nazeeruddin et al. then introduced an improved version of N3, N719, in which tert-butylammonium cations balanced the negative charge on two carboxylate groups in N3 (Fig. 7.10) (Nazeeruddin et al. 1997). Application of this dye in DSCs resulted in improvement in the $V_{OC}$ and a $\eta$ of 10.2% was reported in 2004 (Wang et al. 2004). The discovery of the black dye (N749, Fig. 7.10) (Nazeeruddin et al. 1997) in 1997 was another breakthrough in the field of sensitizers for n-DSCs, (Nazeeruddin et al. 2001) which led to a record energy conversion efficiency of 11% in 2006 (Chiba et al. 2006). The advantage of the black dye is that it absorbs light over the whole UV-visible-to-near-IR region (up to 920 nm), thereby converting more photons to electricity.

Despite the excellent performance of the ruthenium-based sensitizers, researchers investigated more abundant and cheaper alternatives as the rarity of ruthenium may limit application of large-scale production DSCs. Zinc-based sensitizers containing large and stable π-aromatic molecules, like porphyrins, have been applied extensively in DSCs (Mathew et al. 2014; Yella et al. 2011). Porphyrin sensitizers such as YD2, YD2-o-C8, and SM3 have resulted in highly efficient (around 13%) DSCs (Mathew et al. 2014).

Apart from ruthenium- and zinc-based sensitizers, other metal-based complexes such as copper, (Linfoot et al. 2010; Bessho et al. 2008) nickel, (Linfoot et al. 2011; Miao et al. 2011) platinum, (Bisquert et al. 2009; Kwok et al. 2010) iridium, (Baranoff et al. 2010) iron (Chauhan et al. 2011), and osmium (Kinoshita et al. 2012) have been tested. None of these metal-based complexes have shown device performances comparable to those based on ruthenium or zinc complexes.

In addition to metal-based sensitizers, a variety of organic sensitizers have been developed as they demonstrate higher molar extinction coefficients than that of metal-based sensitizers and a good light absorption extending into the near-IR

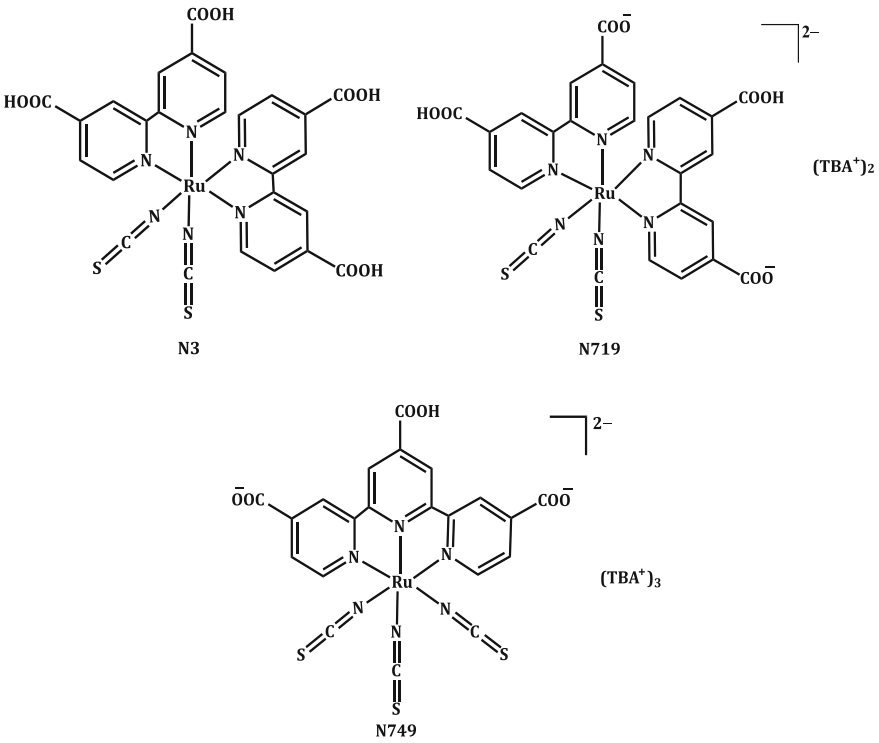


**Fig. 7.10** Structure of; N3- cis-dithiocyanatobis(2,2′-bipyridyl-4,4′-dicarboxylic acid) ruthenium (II), N719- Bis(tetrabutylammonium)cis-di(thiocyanato)bis(2,2′-bipyridyl-4,4′-dicarboxylate) ruthenium(II), N749- trithiocyanato(terpyridyl)ruthenium(II) (Black dye)

spectral region (Obotowo et al. 2016). Increasing the molar extinction coefficient is beneficial, as it allows the use of thinner $TiO_2$ films. A thinner film decreases interfacial charge recombination reactions by shortening the path of the electron flow through the semiconductor. This leads to a decrease in the dark current and increases the maximum voltage attainable at short circuit. Among these organic sensitizers, in 2015, Kakige et al. reported more than 14% efficiencies with an alkoxysilyl-anchor dye of ADEKA-1 and a carboxy-anchor organic dye of LEG4 which give the highest reported efficiency for DSCs up to date (Kakiage et al. 2015).

Though high efficiencies have been achieved with these sensitizers, a significant amount of these sensitizers are desorbed when incorporated into the device. Further, there could be distribution of binding modes and strengths, varied interactions among absorber molecules, and aggregation of dye molecules that lower the device performance. To circumvent these drawbacks, owing to their tunable architecture and strong photoresponse, MOFs have been utilized as sensitizers in DSCs. In 2013, Lee et al. introduced a MOF-199 (copper(II) benzene-1,3,5-tricarboxylate, see Fig. 7.11) as the sensitizer. This was fabricated on top of the mesoporous layer

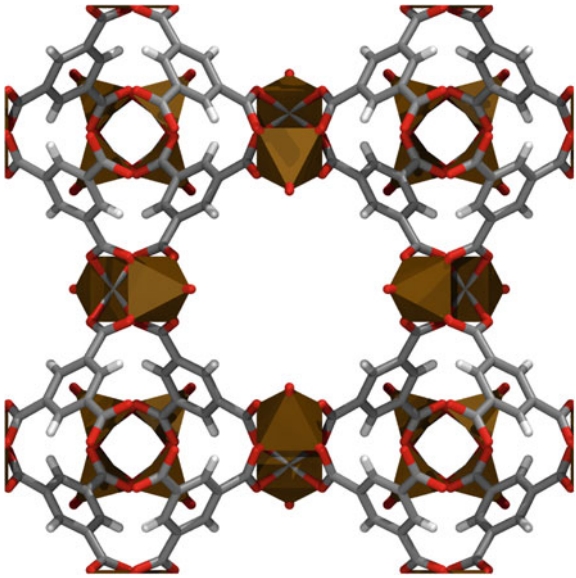

**Fig. 7.11** Structure of MOF-199. Crystal structures were taken from published data from (Chui et al. 1999), through the Cambridge crystallographic database center, CCDC deposit number [12954]

using layer-by-layer technique (Lee et al. 2014). Even though the estimated HOMO (−5.37 eV vs. vacuum) and LUMO levels (−3.82 eV vs. vacuum) of the MOF were compatible with the energy levels of $TiO_2$ a poor conductivity was observed. By doping $I_2$ within the MOF-199 which is a neutral coordination polymer with a 3D porous network, the conductivity was improved. It is postulated to form intermolecular interactions with the π electron cloud of the benzene ring of the organic linker molecule in the MOF-199. The observed increment in cooperative electrical conductivity was higher than that of bare $I_2$ which implies that the intermolecular interactions may have ascribed to the enhanced performance. Hence, for the very first time, MOF-sensitized DSCs reported an efficiency of 0.26%. In early 2014, a modification to the abovementioned system was done by the same group of scientists. In that study, the MOF-199 was deposited on top of a composite of $TiO_2$ and carbon nanotubes (Lee et al. 2014). According to the EIS measurements, modification of the $TiO_2$ layer with multi-walled carbon nanotubes (MWCNT) improved the charge transfer resistance at the working electrode which in turn enhanced the $J_{SC}$ generated. An overall efficiency improvement of 60% was observed when compared to the devices without MWCNT. Further, the same group reported a successful application of a Ru-MOF composed of the ligand benzene-1,3,5-tricarboxylates as the sensitizer in DSCs (Lee et al. 2014). A thin layer of Ru-MOF was fabricated on top of the mesoporous $TiO_2$ layer using layer-by-layer deposition. Electronic absorption data along with cyclic voltammetry were used to derive HOMO and LUMO levels of this 3D network. Both HOMO (−5.47 vs. vacuum) and LUMO (−3.21 vs. vacuum) levels are in position with the CB and VB of $TiO_2$, which leads to feasible electron flow. However, the photoluminescence studies indicated an intense peak for the electrode FTO/$TiO_2$/

Ru-MOF which implies low or no charge transfer within the electrode. As in MOF-199, once $I_2$ was doped, the peak intensity was lowered significantly demonstrating an improvement in the conductivity of MOF. This was further proved by EIS measurements where a significantly high charge transfer resistance was observed at the WE/electrolyte interface before the modification with $I_2$. The doping reduced the charge transfer resistance allowing the electron flow through the interface, $TiO_2$/Ru-MOF. They were able to enhance the device performance from 0.46 to 1.22% after the substitution of MOF-199 with Ru-MOF with a $I_{SC}$ 2.56 mA, a $V_{OC}$ 0.63 V, and a FF 0.63.

In a different approach to enhance the conductivity of MOF-based photoanodes, Kaur et al. reported the fabrication of a Eu-MOF (with the same ligand benzene-1,3,5-tricarboxylates) in the presence of graphene. Owing to its superior conductivity, graphene has been reported to enhance charge transfer by lowering recombination losses. Thus, incorporation of graphene with the Eu-MOF that was barely conducting, a composite with a significant conductivity has been fabricated on top of $TiO_2$ to serve as the sensitizer. In this study, Eu-MOF was first synthesized and electrodeposition was used to coat graphene MOF composite on the mesoporous $TiO_2$ layer. The presence of graphene was confirmed with FT-IR spectra in which the appearance of bands at C–O–C (at 1150 $cm^{-1}$), C–H bending (at 1310 and 1380 $cm^{-1}$), and C = C stretching (at 1650 $cm^{-1}$) were observed. Further, confirmation was done with Raman spectrum where the characteristic bands for graphene (G band at 1617 $cm^{-1}$ and D band at 1367 $cm^{-1}$) were recognized. DSCs consisting of this composite demonstrated an outstanding overall energy conversion efficiency of 2.2% due to the reduced charge transfer resistance which enhanced the current generated within the device.

A study was performed by Liu et al. as a proof of concept, where the authors propose that MOFs could be used as an efficient sensitizer due to the indirect bandgap they present (Jinxuan et al. 2015). The authors use a layer-by-layer liquid phase epitaxy method to "surface graft" Zn and porphyrin MOFs on FTO glass to generate a rudimentary photovoltaic device. They found the free MOF-based device and Pd loaded MOF devices showed high charge carrier generation efficiencies, two orders of magnitude higher than previously reported. To investigate electronic structure calculations using density functional theory calculations, one in particular being the GGA–DFT band structure calculation of the Pd-inserted MOF. The authors find a small ($\sim$5 meV) dispersion in the valence and conduction band edges. They propose that although this is not significant enough to initiate separation between the charges, it may have a positive effect on deterring recombination. The authors further extended this study later (Liu et al. 2016) to include porphyrin-based organic linkers substituted with phenyl or diphenylamine. The energy bandgap for Zn porphyrin linker was again studied using GGA–DFT methods (PBE functional, with the D3 correction). Here, it was found that substitution of the porphyrin with the diphenylamine lowered the bandgap significantly, while the dispersion of the band edges was 2.5–3.6 meV.

In 2016, Maza et al. reported the effect of preparative method of dye-incorporated MOFs on the performance of the device (Maza et al. 2016). Ru(II)

$L_2L'$ (L = 2,2′-bipyridyl, L′ = 2,2′-bipyridine-5,5′-dicarboxylic acid), RuDCBPY containing zirconium(IV)-based MOFs (UiO-67) were grown as thin films on $TiO_2$ under solvothermal conditions (Scheme 7.1). RuDCBPY-UiO-67-DCBPY-X [route (b) and (c)] has been synthesized in two different methods, namely, one-pot synthesis, where all the starting materials were incubated at 120 °C for 24 h and post-synthetic modification, where the UiO-67-DCBPY film has been incubated in an ethanolic solution of $Ru(bpy)_2Cl_2$. The overall performance was found to be dependent on the preparative method of the MOF. A significant difference was observed in terms of resonance energy transfer that takes place by coupling between RuDCBPY centers and interacting pairs. Lower power conversion efficiency was observed in post-synthetic route [route (c)] which ascribes to the nonuniform distribution of the dye. They claim that the nonuniform distribution may be due to diffusional limitations of the $Ru(bpy)_2Cl_2$ that inhibits penetration of RuDCBPY into the bulk of the MOF. Further, the encapsulation of dye molecules within the pore of the MOF may block the diffusion of the redox couple into the MOF, restricting the regeneration of the dye. This effect was clearly shown by the low $J_{SC}$ and $V_{OC}$ observed. However, it was reported that the mechanisms of excited state energy migration and electron transfer into $TiO_2$ were similar between materials regardless of the synthetic route.

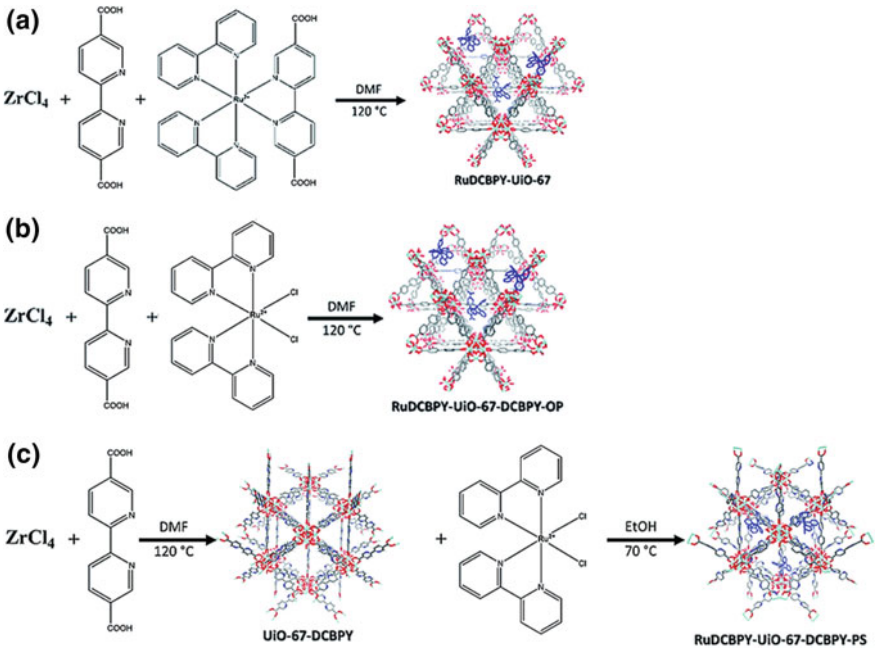


**Scheme 7.1** Synthesis route **a** RuDCBPY–UiO-67; **b** RuDCBPY–UiO-67–DCBPY-OP (OP-One pot); **c** RuDCBPY–UiO-67–DCBPY-PS (PS-post-synthetic) (Maza et al. 2016). Reproduced by permission of the royal society of chemistry

The most commonly used techniques to improve conductivity of MOFs involve either to incorporate a guest molecule or a highly conducting material. Thus, the actual contribution of the pure MOF is not known. In order to study the real effect of pure MOF, Spoerke et al. constructed DSCs with pillared porphyrin framework (Spoerke et al. 2017). In this study, authors have confirmed the exclusion of solvent molecules and unreacted linker molecules within this framework. A thin layer of $TiO_2$ fabricated using atomic layer deposition was used to deposit the MOF. As anticipated, low efficiencies were on observed due to the lack of surface area. But, a higher efficiency was observed for the MOF-incorporated device than that of the bare $TiO_2$ which implies the contribution of pure MOF toward the enhanced performance. Improved device efficiency was further characterized using EIS measurements where a significant reduction in interfacial charge transfer resistance was observed after the addition of MOF. Electronic structure calculations performed using DFT (HSE06 functional), predict a HOMO–LUMO gap of the MOF of 1.9 eV, with the HOMO 0.9 eV above the CB edge of $TiO_2$, indicating electron transfer from the excited MOF is feasible.

### *7.2.3 Electrolyte Material*

In DSCs, the electrolyte is one of the components that determines the stability and the efficiency of the device. The electrolyte is made out of a redox couple (redox shuttle or redox mediator), additives, and a solvent. The main function of the electrolyte is to transport charge carriers from the CE to the oxidized dye at the working electrode where the dye regeneration occurs. Prerequisites of an efficient electrolyte are the fast dye regeneration kinetics, slow recombination reactions, and low light absorbance within the visible region. To meet these prerequisites, the electrolyte should be readily soluble and has a high ionic mobility in the solvent of interest. Further, the dye should be regenerated at minimal overpotential (Hamann and Ondersma 2011; Wang and Hu 2012).

Until recently, triiodide/iodide ($I_3^-/I^-$) has been the most widely used redox shuttle in DSCs. An efficiency of 11% was achieved with $I_3^-/I^-$ in conjunction with the N749 sensitizer (Chiba et al. 2006). The kinetic properties of this redox shuttle are favorable as $I^-$ has a sufficiently high dye regeneration rate and on the other hand, reduction of $I_3^-$ at the CE is relatively slow and allows a high charge collection efficiency with limited interfacial charge recombination reactions. The devices constructed with $I_3^-/I^-$ have shown a high stability at ambient conditions which makes it a potential candidate for commercial applications. Although this redox couple has been widely applied and studied within DSCs, researchers began to investigate alternatives due to disadvantages, such as absorption of $I_3^-/I^-$ in the blue wavelength region (competition with the sensitizer), and also the corrosive nature of $I_3^-/I^-$ on silver and copper which are used as the current collectors in large modules (Boschloo and Hagfeldt 2009; Grätzel and Moser 2001). Further, the energy mismatch between the redox shuttle ($E_{red/ox}$ = 0.35 V vs. NHE) and the

sensitizer (typically about $E_{red/ox}$ = 1.00 V vs. NHE) leads to high energy loss within the device. A reduction in this loss could be achieved using redox shuttles with redox potentials closer to those of the dyes.

Attempts to replace the $I_3^-/I^-$ redox couple have been highly successful in recent years. From the very beginning, transition metal complexes stood out due to the ability to fine tune the redox potential simply by altering the structure of the ligand. Among transition metals, cobalt ($[Co(dbbip)_2]^{2+/3+}$, $[Co(bpy)_3]^{2+/3+}$, $[Co(bpy\text{-}pz)_2]^{2+/3+}$, ($[Co(phen)_3]^{3+/2+}$) (Kakiage et al. 2015; Nusbaumer et al. 2001; Feldt et al. 2010; Yum et al. 2012) has been the most widely investigated. In addition, nickel (bis(dicarbollides)nickel(IV/III)) (Li et al. 2010), iron (ferrocenium/ferrocene) (Daeneke et al. 2011), manganese (tris(acetylacetonato)manganese(III)/(IV)) (Perera et al. 2014), and copper ($[Cu(dmp)_2]^{2+/1+}$) (Hattori et al. 2005) complexes have been used in DSCs. The highest reported efficiency of 14.7% was achieved with the cobalt complex, tris(1,10-phenanthroline)cobalt(II/III) ($[Co(phen)_3]^{3+/2+}$) (Kakiage et al. 2015). Additives are utilized in DSCs to enhance the device performance by affecting the redox potential of the electrolyte, the position of the conduction band (CB) edge of $TiO_2$, recombination kinetics in the device, and also the photovoltaic parameters (Kambe et al. 2002; Nakade et al. 2003). As additives, heterocyclic compounds that contain nitrogen have been studied in DSCs since 1993 (Nazeeruddin et al. 1993). The most widely used heterocyclic compound is tert-butylpyridine (tBP). It was reported that tBP decreases the charge recombination losses at the electrolyte/semiconductor interface (Huang et al. 1997). Extensive studies revealed that the decrease in charge recombination reaction is attributed to the surface passivation by tBP (Shi et al. 2005). Schlichthorl et al. also observed that tBP causes a shift in the CB edge of $TiO_2$ to a more negative potential (vs. NHE) that leads to a significant improvement in $V_{OC}$ (Schlichthörl et al. 1997). According to Boschloo et al., the enhanced performance is a combination effect of the favorable shift in the CB of $TiO_2$ and increased electron lifetime (Boschloo et al. 2006).

The other nitrogen-containing heterocyclic compounds tested, such as derivatives of pyridine, alkylaminopryridine, alkylpyridine, benzimidazole, pyrazole, and quinolone, have been found to function similar to tBP in DSCs (Gorlov and Kloo 2008; Shi et al. 2008; Bella et al. 2014).

Other commonly used additives are cations, such as $Li^+$ or guanidium, $[C(NH_2)_3]^+$, typically abbreviated as $G^+$, and are typically utilized as the following salts: lithium bis-trifluoromethanesulfonimide (LiTFSI), lithium tetrafluoroborate ($LiBF_4$), and guanidinium thiocyanate (GSCN). The addition of $Li^+$ improves the charge injection from the photoexcited dye molecules to the CB of $TiO_2$ by shifting the CB edge to a more positive potential (vs. NHE) (Liu et al. 1998; Kelly et al. 1999; Haque et al. 2005). This is a result of $Li^+$ ions being intercalated into $TiO_2$ surface irreversibly (Kopidakis et al. 2003). Similar effects have been observed in the devices that have used $G^+$ as an additive (Kopidakis et al. 2003; Zhang et al. 2009).

Even though the function of nitrogen-containing heterocyclic compounds and cations ($Li^+$, $G^+$) appears to be opposite to each other, the presence of both additives

improves the device performance compared to the devices consisting of only one type of additive (Lewis 2007; Shi et al. 2008; Bai et al. 2008).

Moreover, to further enhance the device performance, additives such as deoxycholic acids and phosphonic acids have been utilized in DSCs (Daeneke et al. 2011; Wang et al. 2007). Most commonly used acid is chenodeoxycholic acid (cheno), which has been reported to significantly improve the current generated in the device (Xie and Hamann 2013). Cheno found to passivate the semiconductor surface and form a supramolecular aggregation on the surface that suppress the interfacial charge recombination reactions improving $J_{SC}$ in DSCs (Salvatori et al. 2013).

The solvent of the electrolyte is the medium that provides a platform for diffusion of ionic conductors. An efficient solvent should have a melting point less than −20 °C to minimize solvent freezing and a boiling point over 100 °C to avoid evaporation. These properties may improve the long-term stability of the device in outdoor applications. Further, a solvent with a high dielectric constant may ensure complete dissolution of the redox couple and the additives. To improve the conductivity, an ideal solvent should have a low viscosity that leads to a high diffusion coefficient of the redox mediator. Inertness toward metal contacts, low light absorption within the visible region, low toxicity and abundance are some other characteristics of an ideal solvent (Fischer et al. 2007; Xu 2004; Yu et al. 2011; Wu et al. 2015).

In liquid-state devices, a variety of organic solvents have been tested (Hagfeldt et al. 2010; Nazeeruddin et al. 1993; Yu et al. 2011; O'Regan and Grätzel 1991). Among them, acetonitrile has shown the most suitable properties to be the solvent of choice. High solubility of salt components, low viscosity, and excellent chemical stability are some attractive properties of acetonitrile. Use of acetonitrile avoids mass transport limitations within the electrolyte and leads to high efficiencies. To date, the highest conversion efficiency of 14.7% was achieved in DSCs based on acetonitrile (Kakiage et al. 2015). However, low boiling point ($\sim$82 °C) and toxicity limit its application in large scale. This problem has been overcome using mixtures of nitriles (Wu et al. 2015).

Water has also been a solvent of choice for DSC electrolytes which still stimulates research due to its nontoxicity, nonflammability, and excellent solvation of most of the redox shuttles (Daeneke et al. 2012; Tsubomura et al. 1976; Xiang et al. 2013; Dong et al. 2014). To date, $\geq$5% overall energy conversion efficiencies were achieved with devices based on water (Dong et al. 2014). It is believed that the poor interaction between the working electrode and the electrolyte attributes to low efficiencies reported compared to organic-solvent-based DSCs. Hydrophilicity at the sensitized working electrode surface enables the sensitizer desorption that reduces the $J_{SC}$ and the long-term stability of the device. On the other hand, hydrophobic sensitizers decrease the electrolyte infiltration at the working electrode, limiting the effective dye regeneration (Bella et al. 2015). It is important to achieve an optimum condition between these two extremes in order to increase the interactions at the working electrode/electrolyte interface that may improve the performance of DSCs based on aqueous electrolytes.

Ionic liquids (ILs) have been studied in DSCs as an alternative to overcome the volatility related to electrolytes based on organic solvents. These are room temperature molten solvents with attractive properties such as nonvolatility, high ionic conductivity, high thermal stability, and electrochemical stability (Gorlov and Kloo 2008; Zakeeruddin and Grätzel 2009). ILs are formed by organic salts containing cations, for example, imidazolium, pyridinium or quaternary alkyl ammonium ions and anions from the halide or pseudohalide family, and non-coordinating ions such as $BF_4^-$ and $PF_6^-$. Thus, the physical and chemical properties of ILs are found to be tunable by varying the composition of these cationic and anionic components of the solvent. They have been intensively tested in DSCs and efficiencies of >8% have been reported (Kuang et al. 2006; Bai et al. 2008; Wang et al. 2005, 2004, 2005). Despite all these attractive properties, the high viscosity of ILs has been found to cause mass transport limitations on the photocurrent in the device (Zakeeruddin and Grätzel 2009). Therefore, development of low-viscous ILs has become the next goal of researchers (Gorlov and Kloo 2008; Zakeeruddin and Grätzel 2009).

Quasi-solid-state (QSS) electrolytes are another class of electrolytes that have been utilized in DSCs (Lewis 2007). Limitation of solvent leakage under thermal stress which is vital in outdoor application of DSCs encourages the extensive research on QSS electrolytes. DSCs based on these electrolytes have demonstrated extraordinary stability under prolonged thermal stress and light soaking (Wang et al. 2003). Polyethylene glycol, (Upadhyaya et al. 2006; Wu et al. 2007; Gao et al. 2010) polyacrylonitrile, (Cao et al. 1995) polymers based on acrylate or methacrylate (Roh et al. 2010), and Poly(vinylidene) fluoride-co-hexauo ropropylene (Wang et al. 2003) are a few examples of polymer materials that have been tested in QSS DSCs. Recently, a new class of material, low molecular mass organogelators (LMOG), was introduced for gel electrolyte preparation. They exhibit three-dimensional networks and possess higher ionic conductivity, good pore filling, and better stability compared to other QSS materials. 1,2-hyd roxystearic acid, cyclohexanecarboxylic acid-[4-(3-octadecylureido)phenyl]amide, (Yu et al. 2012) 1-ethyl-3-methylimidazolium thiocyanate, (Mohmeyer et al. 2006) tetradodecyl-ammonium bromide, and (Huo et al. 2010) *N,N′*-1,5-pentan ediylbis-dodecanamide (Mohmeyer et al. 2004) are few examples of LMOGs applied in DSCs. Up to date, a maximum energy conversion efficiency of 9.6% has been achieved for QSS DSCs using *N,N′*-1,5-pentanediylbis-dodecanamide (Tao et al. 2015).

MOF has also been utilized in QSS DSCs as the medium for the redox couple. To use MOF as the medium special kinds of supramolecular gels were formed by introducing metal into the organic gel systems, forming metal–organic gels (MOGs). MOGs are mainly assembled from bridging organic ligands and metal ions, which is more similar to the formation of MOFs. These MOGs demonstrate more metal-specific features where the properties could be fine tuned by changing the organic ligands and metals. Due to their sponge-like porous matrix, they accommodate constituents of the electrolyte while preserving the properties of a liquid electrolyte. Further, MOGs successfully penetrate through the mesoporous layer allowing better contact between the WE and the electrolyte.

In 2013, Bella et al. were the first to introduce MOF in DSCs as the medium for electrolyte (Bella et al. 2013). A Mg-MOF was introduced into a mixture of poly (ethylene glycol) methyl ether methacrylate (PEGMA) and polyethylene glycol diacrylate (PEGDA) (80: 20 weight ratio). Under UV-light, the formation of polymer matrix was observed. Then, it was activated by soaking in the $I^-/I_3^-$-based electrolyte. The EIS spectra of the DSCs which incorporated this gel polymer electrolyte demonstrated an increase in the effective electron lifetime when the amount of Mg-MOF synthesized with benzene-1,3,5-tricarboxylate was increased. This indicated the lowering of recombination losses at the WE/polymer electrolyte. Further, by increasing the amount of Mg-MOF, the long-term stability of the device was enhanced where they postulated that the Mg-MOF may act as a filler in the polymer matrix. Consequently, optimized devices achieved an energy conversion efficiency of 4.8%.

In another study, $Al^{3+}$ and 1,3,5-benzenetricarboxylate ($H_3BTC$) containing MOG was used as the medium for gel polymer electrolyte (Fan et al. 2014). Penetration of the $I^-/I_3^-$-based electrolyte was confirmed with UV-visible spectra where the transparent color of the matrix was turned brown and the intensity of the color was varied with the amount of the electrolyte. Further, according to the EDX analysis, the cross section of the electrode after soaking in the electrolyte has indicated a homogeneous and thorough penetration of I and Al which confirms the proper distribution of the electrolyte within the mesoporous layer. A comparison of the *J–V* characteristics has been done between the devices with $I^-/I_3^-$-based liquid electrolyte and gel polymer electrolyte. MOG-based devices demonstrated a maximum efficiency of 8.69% with $J_{SC}$ of 16.67 mA $cm^{-2}$, $V_{OC}$ of 756 mV, and FF of 0.69, whereas the liquid-electrolyte-based devices reached an efficiency of 9.13% with $J_{SC}$ of 16.75 mA $cm^{-2}$, $V_{OC}$ of 789 mV, and FF of 0.69. The reasons for lower $V_{OC}$ of MOG-based devices were studied in depth. The low $V_{OC}$ was observed for all MOG-based devices compared to state-of-the-art devices due to the high amount of $Al^{3+}$ present in the matrix. It is well studied and reported that the addition of cations tends to shift the CB of $TiO_2$ to a positive potential (vs. NHE) decreasing the $V_{OC}$ of the device. Apart from $Al^{3+}$, these devices consist of both $Li^+$ and guanidinium ion which were added as additives in the electrolyte. Thus, the shift in CB was significant. Nevertheless, this effect was counterbalanced by the addition of tBP with which a negative potential shift in CB is expected. Though the content of $Li^+$, guanidinium ion, and tBP is the same for both devices, high content of $Al^{3+}$ in MOG-based DSCs reduced the $V_{OC}$. Further, the high recombination losses that were confirmed with *J–V* measurements under dark conditions may ascribe to lower $V_{OC}$ and lower efficiencies of MOG-based DSCs. In contrast, the positive shift in CB may be the reason for observed high $J_{SC}$ where the positive shift enhances the electron injection by providing a large driving force.

Recently, Dong et al. introduced another Al-based MOG into quasi-solid-state DSCs. $Al^{3+}$ and tBP were used to synthesize the desired MOG (Dong et al. 2017). In this matrix, tBP acts as a gelator as well as an active additive to enhance the performance of the device. The advantage of this Al–tBP gel electrolyte is that it preserves the properties of the liquid electrolyte and avoids the addition of extra

gelator. IMVS measurements have indicated a longer electron lifetime with the increasing concentration of tBP. This is due to the surpassed electron recombination by the adsorption of tBP onto the surface. Complete optimization of the device has led to an overall efficiency of 8.25%.

### 7.2.4 Counter Electrode Material

The counter electrode (CE) is the back contact of the DSC at which the charge carriers that pass through the external load, enter the device to complete the circuit. A typical CE consists of a catalyst that is fabricated on a transparent conducting oxide glass and the choice of catalyst depends on the redox mediator in use. The function of the catalyst is to accelerate the regeneration of the reduced redox mediator using the charge carriers from the external circuit. The CE must exhibit a high catalytic activity and thereby be capable of promoting a fast reaction at low overpotential (Thomas et al. 2014).

A large number of different CE materials have been tested in DSCs in recent years. The most commonly and widely used CE material is Pt due to its good electrocatalytic activity, stability in air and water even at high temperatures, and excellent electrical and thermal conductivity (Thomas et al. 2014; Maiaugree et al. 2015). A variety of Pt materials have been tested in DSCs, among them Pt nanoparticles standout, owing to their exceptionally good properties such as corrosion resistance, low charge transfer resistance, high transmittance, high electrical conductivity, and high surface area (Lee et al. 2010). Pt nanoparticles can be synthesized by thermal decomposition of chloroplatinic acid and electrochemical reduction of hexachloroplatinic acid (Fu et al. 2012). For example, Yella et al. reported a DSC with 12.3% efficiency in which thermally decomposed Pt was used as the CE material (Yella et al. 2011). Pt composite materials are another type of CE material that has been tested in DSCs (Xu et al. 2008; Yen et al. 2012; Huang et al. 2010). Even though Pt-based CE shows a high performance in DSCs, its high cost ($\sim$\$4900 per 100 g) (Thomas et al. 2014) and low abundance have encouraged the search for alternatives.

One of the attractive alternatives is carbon due to its abundance, environment friendliness, excellent catalytic activity toward most redox mediators, corrosion resistance, and cost-effectiveness. A variety of carbon-based CE materials was tested in DSCs (Ghann et al. 2017; Ganta et al. 2017). One such material is carbon black. Incomplete combustion of petroleum is used to produce carbon black which features attractive properties such as high surface area, excellent conductivity, and electrocatalytic activity (Thomas et al. 2014). The use of a thicker carbon layer at the CE increases the FF by decreasing the charge transfer resistance at the CE/electrolyte interface. Using carbon black, efficiencies around 9% have been achieved (Murakami et al. 2006; Zhang et al. 2008). Other carbon-based CE materials that have been used within DSCs are mesoporous carbon, (Plonska-Brzezinska et al. 2011) graphene, (Kavan et al. 2010) graphene-based

composite materials, (Dou et al. 2012) and carbon nanotubes (Nair et al. 2008). Of these materials, graphene is the most promising substitute for Pt due to its many advantages such as high carrier mobility ($\sim 1 \times 104\ cm^2\ V^{-1}\ s^{-1}$), (Novoselov et al. 2004; Du et al. 2008) high specific area (2630 $m^2\ g^{-1}$), (Peigney et al. 2001) excellent thermal conductivity ($\sim 3000\ W\ m^{-1}\ K^{-1}$), (Stankovich et al. 2006) and high optical transparency (97.7%) (Nair et al. 2008). The best-performing DSC, which was reported by Kakiage et al., applied graphene and gold as the CE material and achieved an energy conversion efficiency of 14.7% (Kakiage et al. 2015).

The other popular CE materials that have been used in DSCs are polymer based. These include polyethylene dioxythiophene (PEDOT), polyaniline (PANI), polypyrrole (PPy), and PEDOT doped with p-toluenesulfonate (PEDOT-TsO) or polystyrenesulfonate (PEDOT-PSS) (Thomas et al. 2014; Hou et al. 2012; Yohannes and Inganäs 1998; Lee et al. 2010; Tang et al. 2013). Polymer–carbon and polymer–Pt composites have also been used in DSCs. But, the performance of the device was not as good as with other polymer materials alone (Ikeda et al. 2006). A few studies were also carried out on transition-metal-based materials for CEs (Hou et al. 2013). In 2012, Kung et al. introduced a very stable CoS film as a CE material that achieved a 7.7% efficiency (Kung et al. 2012). WS and $MoS_2$ are two other metal sulfides that have been tested by Wu et al. and have shown to achieve efficiencies of over 7.5% (Wu et al. 2011). These materials have interesting properties such as electrical and thermal conductivities, high melting temperature of the ionic crystal, durability, and, most importantly, platinum-like catalytic activity (Levy and Boudart 1973).

In addition, MOFs are used to derive carbonaceous materials to utilize in photovoltaics. A simple preparation process has to be followed in order to obtain these porous carbonaceous materials (Fig. 7.12). The tunnel structure is beneficial for the electrolyte penetration and the high surface area enhances the catalytic activity. For the very first time, Sun et al. introduced a carbonaceous material that was derived from a ZIF-8 in DSCs (Sun et al. 2016). A comparable efficiency (7.32%) with Pt electrode was reported. In this study, properties of ZIF-8 samples that were calcined at different temperatures were investigated. The samples that were calcined beyond 1000 °C lost the original morphology of the MOF, whereas the samples that were calcined at or below 1000 °C demonstrated a consistent morphology with that of the MOF. Thus, the ZIF-8 samples that were calcined at 1000 °C were reported as the best choice with the highest device efficiencies. The Raman spectroscopy data

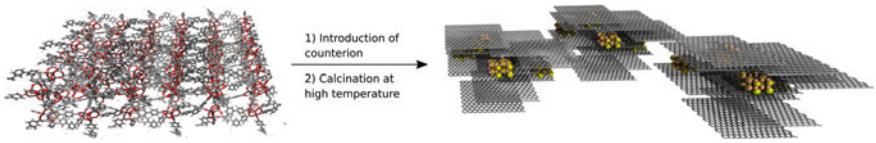


**Fig. 7.12** Illustration of the preparation process for the $Co_3O_4$-WC-CN/rGO

indicated the conversion of carbonaceous material into graphite crystallites. Further, cyclic voltammetry studies indicated comparable catalytic activity of MOF-derived carbonaceous material with Pt.

As an improvement of this study, Jing et al. reported the synthesis of a nitrogen-doped porous graphitic carbon with surface-oxidized CoO species where the metal nanoparticles were enveloped. The significance of this synthesis was that the ZIF-67 (based on Co and 2-methylimidazolate, see Fig. 7.13) acted as a self-template where the process was faster and inexpensive compared to using a separate template. Further, the aggregation of Co species was avoided by the framework structure. Catalytic activity and the stability of the carbonized material were improved due to the enveloped metal particles. The charge density, which improves the electron transfer properties and enhances the surface wettability of the materials, was increased by doping nitrogen. ZIF-67 was calcined at 650, 750, and 850 °C. The framework structure was completely collapsed at 850 °C. Formation of two types of Co centers (Co/CoS) was also identified using XRD patterns. Thus, ZIF-67 calcined at 850 °C demonstrated the highest device efficiency (7.92%) and this performance was postulated to be a synergistic effect of both the Co and CoS centers that were present within the matrix.

Around same time, Cui et al. introduced a facile solution process to synthesize $CoS_2$ embedded carbon nanocages using ZIF-67 as the template (Cui et al. 2016). Even though $CoS_2$ has exceptional electrocatalytic properties, its poor electrical conductivity and chemical instability limit the application in high-performance photovoltaics. Therefore, in this study, $CoS_2$ was embedded within carbon

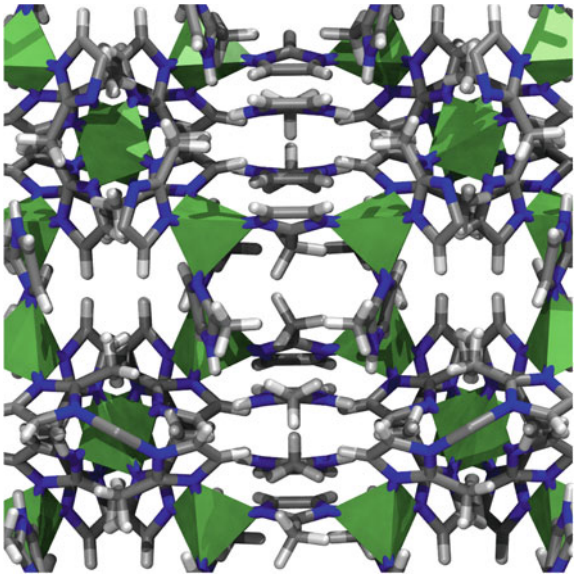

**Fig. 7.13** Structure of ZIF-67. Crystal structures were taken from published data from (Banerjee et al. 2008), through the Cambridge crystallographic database center, CCDC deposit number 671073

nanocages in which the $CoS_2$ nanoparticles provide a superior catalytic activity while they are protected by the matrix. Further, the carbon nanocages improve the electrical conductivity and avoid $CoS_2$ aggregation. To obtain this composite first, the ZIF-67 samples were sulfurized. Uniform hollow spheres were obtained for the samples that were sulfurized for 4 h. Increasing the sulfurization time caused deformation of the hollow structure while creating $CoS_2$ aggregation as the organic linker is replaced by S atoms. Then, the sulfurized organic scaffold was annealed at 450 °C under $N_2$ to form conducting carbon matrix. Annealing for 4 h converted the samples completely to nanocages due to the carbonization of the organic species. Excess annealing time yield significant stacking and aggregation of $CoS_2$ nanoparticles. Application of this composite as the CE material in DSCs demonstrated an outstanding efficiency of 8.2% which surpassed the efficiency of the devices that used Pt.

A similar work was reported by Jian et al. in early 2018, where ZnSe embedded N-doped carbon cubes were synthesized using a MOF consisting of Zn nodes and benzimidazole linkers (ZIF-7) (Jiang et al. 2018). The optimum ZnSe embedded carbon cubes were obtained by calcination of ZIF-7 at 900 °C and then selanization at 450 °C. Carbon cubes ascribed good electrical conductivity, whereas the ZnSe within the matrix provides the catalytic activity. EIS revealed a lower charge transfer resistance ($R_{ct}$) and a lower series resistance ($R_s$) for these electrodes compared to Pt. Low $R_{ct}$ implies a better electron transfer at the CE/electrolyte interface indicating a faster electron flow within the matrix and low $R_s$ implies a better ohmic contact between the substrate and the electrocatalytic film. Further, the higher value of the exchange current density obtained from the Tafel polarization curves explained the better electrocatalytic activity of ZnSe embedded N-doped carbon cube matrix. Due to the outstanding electrocatalytic activity, DSCs consisting of ZnSe carbon cube matrices outperformed the DSCs with Pt as the CE. An overall energy conversion efficiency of 8.69% was obtained.

Recently, ZIF-67 has been used to synthesize $Co_3O_4$-WC-CN/rGO (Fig. 7.13) (Chen et al. 2018). FT-IR spectra as well as TGA curves confirmed the encapsulation of $H_2W_{12}$. After calcination, ZIF-67 and ZIF-67GO (GO-graphene oxide) consisted of $Co_3O_4$. Further, ZIF-67 @$H_2W_{12}$ and ZIF-67@ $H_2W_{12}$/GO consist of $Co_3O_4$-WC. From EDX spectra, it was clear that $Co_3O_4$ and WC are evenly distributed among graphene. EIS was used to investigate the catalytic activity. Lower charge transfer resistance at the CE/electrolyte interface indicated a high catalytic activity. This was further confirmed by the Tafel polarization curves in which a higher exchange current density was observed. Incorporation of this material, $Co_3O_4$-WC-CN/rGO, as the CE in DSC demonstrated an energy conversion efficiency of 7.38% which was superior to the DSCs that used Pt as the CE material.

Table 7.1 summarizes the reported *J–V* characteristics of the devices based on MOFs.

**Table 7.1** Summary of *J–V* characteristics of the devices where MOF has been incorporated

| Component | MOF | $J_{SC}$/ mA cm$^{-2}$ | $V_{OC}$/ mV | FF | $\eta$/% |
|---|---|---|---|---|---|
| WE | ZIF-8 (Li et al. 2011) | 10.28 | 753 | 0.69 | 5.34 |
| | ZIF-8 (Yafeng et al. 2014) | 10.89 | 789 | 0.74 | 6.35 |
| | MIL-53-Al (Lopez et al. 2011) | 0.0036 | 361 | 0.40 | – |
| | Zn-MOF (Kundu et al. 2012) | – | – | – | 0.15 |
| | MOF-5 (Li et al. 2014) | 8.13 | 663 | 0.68 | 3.67 |
| | MIL-125(Ti) (Chi et al. 2015) | 19.1 | 660 | 0.55 | 7.1 |
| | MIL-125(Ti) (Dou et al. 2016) | 13.99 | 768 | 0.67 | 7.20 |
| | POM@MOF(Fe) (Zhang et al. 2018) | 0.71 | 410 | 0.25 | 0.073 |
| Sensitizer | MOF-199 (Lee et al. 2014) | 1.25 | 490 | 0.43 | 0.26 |
| | Ru-MOF (Lee et al. 2014) | 2.56 | 630 | 0.63 | 1.22 |
| | Eu-MOF (Kaur et al. 2017) | 20.0 | 449 | 0.46 | 2.3 |
| | Pd porphyrin Zn-SURMOF 2 (Jinxuan et al. 2015) | 0.71 | 700 | 0.65 | 0.45 |
| | Zn(II)porphyrin Zn-SURMOF 2 (Liu et al. 2016) | 0.023 | 267 | – | 0.017 |
| | RuDCBPY-ZrMOF (Maza et al. 2016) | 0.564 | 482 | 0.47 | 0.125 |
| | RuDCBPY-ZrMOF (Spoerke et al. 2017) | 8.50 | 521 | 0.48 | 0.0023 |
| | Cu-MOF (Lee et al. 2014) | 1.95 | 480 | 0.51 | 0.46 |
| Electrolyte medium | Mg-MOF (Bella et al. 2013) | 12.6 | 690 | 0.55 | 4.80 |
| | Al-MOG (Fan et al. 2014) | 17.1 | 734 | 0.68 | 8.49 |
| | Al-TBP-MOG (Dong et al. 2017) | 17.08 | 704 | 0.70 | 8.25 |
| CE | ZIF-8 (Sun et al. 2016) | 13.56 | 770 | 0.68 | 7.32 |
| | ZIF-67 (Jing et al. 2016) | 13.29 | 740 | 0.80 | 7.92 |
| | ZIF-67 (Cui et al. 2016) | 16.9 | 730 | 0.66 | 8.20 |
| | ZIF-67 (Jian et al. 2018) | 12.27 | 740 | 0.66 | 6.02 |

## 7.3 Conclusion and Future Prospects

Although the continued development of DSCs has reached efficiencies of over 14% recently, recombination losses, poor stability, and leakage of the electrolyte (in liquid-state devices) have limited the enhancement of the device performance and commercialization.

Over the years, numerous efforts have been made to minimize the recombination losses within the device. Out of the three recombination pathways (as explained in Sect. 7.1.1), the relaxation of the excited sensitizer prior to injecting an electron to the CB of the semiconductor has been suppressed, through modifications, and is unlikely to occur. The rate of injection of electrons is faster than the relaxation time of the sensitizer. Out of the other two recombination pathways, back reaction of the injected electrons with the oxidized dye has been minimized by fine tuning the

structure of the sensitizer. Here, the common approach is to distance the donor and the acceptor moieties by connecting through a spacer ligand. Through modifications, the injection time has been shortened to femtoseconds, whereas the lifetime of an excited dye is in nanoseconds to milliseconds. The third recombination pathway, where the oxidized redox mediator of the electrolyte recombines with the injected electrons, has been suppressed by application of various techniques: (1) addition of a dense/blocking layer, to block the access of the oxidized species to the semiconductor; (2) surface passivation by molecules such as tBP and deoxycholic acids; and (3) addition of an insulating layer on top of the semiconductor. Moreover, over the years, $I^-/I_3^-$ redox mediator has been substituted with coordination complexes with bulky ligands which make the molecules too large to access to the WE. Even though many strategies have been implemented, still the recombination reactions lower the device performance. This has directed researchers on quasi-solid-state and solid-state devices that together solve the long-term stability issue and the leakage problems associated with the liquid-state devices.

In constructing the solid-state devices, the ability to fine tune the device components is important. Particularly, a smooth electron flow to avoid back reactions is desirable. In this regard, the architectural flexibility and the diversity of metal–organic frameworks afford the opportunity to fine tune and utilize for every single component of DSC. As described above, date research efforts have been carried out to develop individual components, while using conventional (non-MOF) materials for the rest of the components in the cell. However, many challenges exist, limiting the realization of high efficiency in MOF-based DSCs.

Development of MOF-based semiconductors that are suitable for the application in DSCs is still in its primitive stage. The main limitations are the poor electrical conductivity and the large particle size resulting from common synthesis techniques. Most MOFs are either insulators or weak semiconductors. However, this property can be fine tuned by changing the metal type present in nodes. There are mixed-metal MOFs that are composed of metal couples and they are randomly or systematically distributed in the MOF lattice. On the other hand, mixed-ligand MOFs containing two ligand types as linkers with different ligand sites can be utilized to tailor the electronic properties in the MOF. These two types of MOFs might be an excellent option to fabricate DSCs by replacing mesoporous layer in the future, as they might be able to show better conducting properties. Doping is another technique that has been practiced in order to fine tune the bandgap of an MOF. Even though various methods have been developed to dope pure MOFs, in the field of DSCs doping with $I_2$ has been the only successful practice for improving the electrical conductivity. Yet, this may not always provide the necessary shifts in the VB and CB of the framework. Therefore, to fine tune the bandgap of a MOF according to the requirement, encapsulation of other inorganic and organic molecules could be more effective. Further, doping with colored materials may enhance the light harvesting properties of the MOF in which these frameworks could function as both the semiconductor and the sensitizer simultaneously. When it comes to the particle size of the MOF obtained from solvothermal

synthesis, due to the high pressure and high temperature usually the particle size is greater than 1 μm. For an MOF to be successfully applied as the mesoporous layer, the size of a particle should be in nanometer range (10–100 nm). Therefore, a development of new synthesis routes that produce smaller particles is a necessity. Attempts have been made to substitute the sensitizer of a DSC with colored MOFs with compatible HOMO and LUMO levels. It is well known that the coverage of the entire visible and near-IR regions in the electromagnetic spectrum is a pre-requisite of a successful sensitizer. Thus, synthesis of MOFs that satisfy the above requirement may enhance the quantum yield of the device. The poor conductivity of MOFs could also be a limiting a factor even when it has the potential to absorb the entire visible and near-IR regions. Thus, the improvement in electrical conductivity of an MOF is a critical factor in their development.

On the other hand, MOFs are also utilized as the medium for quasi-solid-state electrolytes. The drawback of this process is that it still uses $I^-/I_3^-$ redox mediator, with which several disadvantages are associated. The $I^-/I_3^-$ redox couple has a two-electron redox process where the intermediate process results in a significant loss of internal energy. It also absorbs the blue part of the spectrum which results in a small photocurrent. Thus, the use of other single-electron redox shuttles that have demonstrated better device performances may lift the device performance to another level. So far, application of MOF-derived CE materials has been successful and high efficiencies have been reported. But, an improvement that is necessary for CE materials is the low charge transfer resistance at the CE/electrolyte interface.

In addition, fabrication of devices with more than one MOF-based constituents will be challenging. However, addition of more than one MOF may enhance the long-term stability and leakage problem associated with the liquid phase devices. Thus, the versatile tunable properties of MOFs may allow fabrication of DSCs that are suitable for specific requirements. Further, the stability of the device may substantially improve as most of the MOFs are stable.

Even though many studies have been carried out to utilize MOFs in n-type DSCs, no reports are available for the application of MOFs within p-type DSCs. The discovery of MOFs that are suitable for p-type DSCs may pave the way to fabricate tandem DSCs that have a higher energy conversion efficiency.

## References

(2015) International energy agency, https://www.iea.org/

(2015) European photovoltaic industry association https://ec.europa.eu/energy/intelligent/projects/en/partners/epia

(2014) British petroleum statistical review of world energy

Alvaro M, Carbonell E, Ferrer B, Llabrés i Xamena FX, Garcia H (2007) Semiconductor behavior of a metal-organic framework (MOF). Chem Eur J 13 (18):5106–5112. https://doi.org/10.1002/chem.200601003

Asbury JB, Ellingson RJ, Ghosh HN, Ferrere S, Nozik AJ, Lian T (1999) Femtosecond IR study of excited-state relaxation and electron-injection dynamics of $Ru(dcbpy)_2(NCS)_2$ in solution and

on nanocrystalline $TiO_2$ and $Al_2O_3$ thin films. J Phys Chem B 103(16):3110–3119. https://doi.org/10.1021/jp983915x

Bai Y, Cao Y, Zhang J, Wang M, Li R, Wang P, Zakeeruddin SM, Grätzel M (2008) High-performance dye-sensitized solar cells based on solvent-free electrolytes produced from eutectic melts. Nat Mater 7 (8):626–630. http://www.nature.com/nmat/journal/v7/n8/suppinfo/nmat2224_S1.html

Banerjee R, Phan A, Wang B, Knobler C, Furukawa H, O'Keeffe M, Yaghi OM (2008) High-throughput synthesis of zeolitic imidazolate frameworks and application to $CO_2$ capture. Science 319(5865):939–943. https://doi.org/10.1126/science.1152516

Baranoff E, Yum J-H, Jung I, Vulcano R, Grätzel M, Nazeeruddin MK (2010) Cyclometallated iridium complexes as sensitizers for dye-sensitized solar cells. Chem-Asian J 5(3):496–499. https://doi.org/10.1002/asia.200900429

Barbé CJ, Arendse F, Comte P, Jirousek M, Lenzmann F, Shklover V, Grätzel M (1997) Nanocrystalline titanium oxide electrodes for photovoltaic applications. J Am Ceram Soc 80 (12):3157–3171. https://doi.org/10.1111/j.1151-2916.1997.tb03245.x

Batten SR, Champness NR, Chen X-M, Garcia-Martinez J, Kitagawa S, Öhrström L, O'Keeffe M, Paik SM, Reedijk J (2013) Terminology of metal–organic frameworks and coordination polymers (IUPAC Recommendations 2013). Pure Appl Chem 85. https://doi.org/10.1351/pac-rec-12-11-20

Bella F, Bongiovanni R, Kumar RS, Kulandainathan MA, Stephan AM (2013) Light cured networks containing metal organic frameworks as efficient and durable polymer electrolytes for dye-sensitized solar cells. J Mater Chem A 1(32):9033–9036. https://doi.org/10.1039/c3ta12135f

Bella F, Sacco A, Pugliese D, Laurenti M, Bianco S (2014) Additives and salts for dye-sensitized solar cells electrolytes: what is the best choice? J Power Sources 264:333–343. https://doi.org/10.1016/j.jpowsour.2014.04.088

Bella F, Gerbaldi C, Barolo C, Grätzel M (2015) Aqueous dye-sensitized solar cells. Chem Soc Rev 44(11):3431–3473. https://doi.org/10.1039/c4cs00456f

Benkö G, Kallioinen J, Korppi-Tommola JEI, Yartsev AP, Sundström V (2001) Photoinduced ultrafast dye-to-semiconductor electron injection from nonthermalized and thermalized donor states. J Am Chem Soc 124(3):489–493. https://doi.org/10.1021/ja016561n

Bessho T, Constable EC, Grätzel M, Hernandez Redondo A, Housecroft CE, Kylberg W, Nazeeruddin MK, Neuburger M, Schaffner S (2008) An element of surprise-efficient copper-functionalized dye-sensitized solar cells. Chem Commun 32:3717–3719. https://doi.org/10.1039/b808491b

Bisquert J, Fabregat-Santiago F, Mora-Seró I, Garcia-Belmonte G, Giménez S (2009) Electron lifetime in dye-sensitized solar cells: theory and interpretation of measurements. J Phys Chem C 113(40):17278–17290. https://doi.org/10.1021/jp9037649

Bjoerksten U, Moser J, Grätzel M (1994) Photoelectrochemical studies on nanocrystalline hematite films. Chem Mater 6(6):858–863. https://doi.org/10.1021/cm00042a026

Boschloo G, Hagfeldt A (2009) Characteristics of the iodide/triiodide redox mediator in dye-sensitized solar cells. Acc Chem Res 42(11):1819–1826. https://doi.org/10.1021/ar900138m

Boschloo G, Häggman L, Hagfeldt A (2006) Quantification of the effect of 4-tert-butylpyridine addition to $I^-/I^3$-redox electrolytes in dye-sensitized nanostructured $TiO_2$ solar cells. J Phys Chem B 110(26):13144–13150

Burnside S, Moser J-E, Brooks K, Grätzel M, Cahen D (1999) Nanocrystalline mesoporous strontium titanate as photoelectrode material for photosensitized solar devices: increasing photovoltage through flatband potential engineering. J Phys Chem B 103(43):9328–9332. https://doi.org/10.1021/jp9913867

Cao F, Oskam G, Searson PC (1995) A solid state, dye sensitized photoelectrochemical cell. J Phys Chem 99(47):17071–17073. https://doi.org/10.1021/j100047a003

Chae HK, Siberio-Pérez DY, Kim J, Go Y, Eddaoudi M, Matzger AJ, O'Keeffe M, Yaghi OM (2004) A route to high surface area, porosity and inclusion of large molecules in crystals.

Nature 427:523. https://doi.org/10.1038/nature02311. https://www.nature.com/articles/nature02311#supplementary-information

Chandiran AK, Abdi-Jalebi M, Nazeeruddin MK, Grätzel M (2014) Analysis of electron transfer properties of ZnO and $TiO_2$ photoanodes for dye-sensitized solar cells. ACS Nano 8(3):2261–2268. https://doi.org/10.1021/nn405535j

Chauhan R, Trivedi M, Bahadur L, Kumar A (2011) Application of π-extended ferrocene with varied anchoring groups as photosensitizers in $TiO_2$-based dye-sensitized solar cells (DSSCs). Chem-Asian J 6(6):1525–1532. https://doi.org/10.1002/asia.201000845

Chen L, Chen W, Wang E (2018) Graphene with cobalt oxide and tungsten carbide as a low-cost counter electrode catalyst applied in Pt-free dye-sensitized solar cells. J Power Sources 380:18–25. https://doi.org/10.1016/j.jpowsour.2017.11.057

Chi WS, Roh DK, Lee CS, Kim JH (2015) A shape-and morphology-controlled metal organic framework template for high-efficiency solid-state dye-sensitized solar cells. J Mater Chem A 3 (43):21599–21608. https://doi.org/10.1039/c5ta06731f

Chiba Y, Islam A, Watanabe Y, Komiya R, Koide N, Han LY (2006) Dye-sensitized solar cells with conversion efficiency of 11.1%. Jpn J Appl Phys Part 2 45 (24–28):L638–L640. https://doi.org/10.1143/jjap.45.l638

Chui SS-Y, Lo SM-F, Charmant JPH, Orpen AG, Williams ID (1999) A chemically functionalizable nanoporous material $[Cu_3(TMA)_2(H_2O)_3]_n$. Science 283(5405):1148–1150. https://doi.org/10.1126/science.283.5405.1148

Corma A, Atienzar P, Garcia H, Chane-Ching J-Y (2004) Hierarchically mesostructured doped $CeO_2$ with potential for solar-cell use. Nat Mater 3(6):394–397

Coudert F-X, Fuchs AH (2016) Computational characterization and prediction of metal–organic framework properties. Coordinat Chem Rev 307:211–236. https://doi.org/10.1016/j.ccr.2015.08.001

Cui X, Xie Z, Wang Y (2016) Novel $CoS_2$ embedded carbon nanocages by direct sulfurizing metal-organic frameworks for dye-sensitized solar cells. Nanoscale 8(23):11984–11992. https://doi.org/10.1039/c6nr03052a

Daeneke T, Kwon TH, Holmes AB, Duffy NW, Bach U, Spiccia L (2011) High-efficiency dye-sensitized solar cells with ferrocene-based electrolytes. Nat Chem 3(3):211–215. https://doi.org/10.1038/nchem.966

Daeneke T, Uemura Y, Duffy NW, Mozer AJ, Koumura N, Bach U, Spiccia L (2012) Aqueous dye-sensitized solar cell electrolytes based on the ferricyanide-ferrocyanide redox couple. Adv Mat 24(9):1222–1225. https://doi.org/10.1002/adma.201104837

Dong C, Xiang W, Huang F, Fu D, Huang W, Bach U, Cheng Y-B, Li X, Spiccia L (2014) Controlling interfacial recombination in aqueous dye-sensitized solar cells by octadecyltrichlorosilane surface treatment. Angew Chem Int Ed 53(27):6933–6937. https://doi.org/10.1002/anie.201400723

Dong Y-J, Rao H-S, Cao Y, Chen H-Y, Kuang D-B, Su C-Y (2017) In situ gelation of Al(III)-4-tert-butylpyridine based metal-organic gel electrolyte for efficient quasi-solid-state dye-sensitized solar cells. J Power Sources 343:148–155. https://doi.org/10.1016/j.jpowsour.2017.01.051

Dou YY, Li GR, Song J, Gao XP (2012) Nickel phosphide-embedded graphene as counter electrode for dye-sensitized solar cells. Phys Chem Chem Phys 14(4):1339–1342. https://doi.org/10.1039/c2cp23775j

Dou J, Li Y, Xie F, Ding X, Wei M (2016) Metal-organic framework derived hierarchical porous anatase $TiO_2$ as a photoanode for dye-sensitized solar cell. Cryst Growth Des 16(1):121–125. https://doi.org/10.1021/acs.cgd.5b01003

Du X, Skachko I, Barker A, Andrei EY (2008) Approaching ballistic transport in suspended graphene. Nat Nano 3 (8):491–495. http://www.nature.com/nnano/journal/v3/n8/suppinfo/nnano.2008.199_S1.html

Dürr M, Bamedi A, Yasuda A, Nelles G (2004) Tandem dye-sensitized solar cell for improved power conversion efficiencies. Appl Phys Lett 84(17):3397–3399. http://dx.doi.org/10.1063/1.1723685

Eddaoudi M, Kim J, Rosi N, Vodak D, Wachter J, O'Keeffe M, Yaghi OM (2002) Systematic design of pore size and functionality in isoreticular MOFs and their application in methane storage. Science 295(5554):469–472. https://doi.org/10.1126/science.1067208

Fan J, Hao Y, Cabot A, Johansson EMJ, Boschloo G, Hagfeldt A (2013) Cobalt(II/III) redox electrolyte in zno nanowire-based dye-sensitized solar cells. ACS Appl Mater Interfaces 5 (6):1902–1906. https://doi.org/10.1021/am400042s

Fan J, Li L, Rao H-S, Yang Q-L, Zhang J, Chen H-Y, Chen L, Kuang D-B, Su C-Y (2014) A novel metal-organic gel based electrolyte for efficient quasi-solid-state dye-sensitized solar cells. J Mater Chem A 2(37):15406–15413. https://doi.org/10.1039/c4ta03120b

Feldt SM, Gibson EA, Gabrielsson E, Sun L, Boschloo G, Hagfeldt A (2010) Design of organic dyes and cobalt polypyridine redox mediators for high-efficiency dye-sensitized solar cells. J Am Chem Soc 132(46):16714–16724. https://doi.org/10.1021/ja1088869

Fischer A, Pettersson H, Hagfeldt A, Boschloo G, Kloo L, Gorlov M (2007) Crystal formation involving 1-methylbenzimidazole in iodide/triiodide electrolytes for dye-sensitized solar cells. Sol Energy Mater Sol Cells 91(12):1062–1065

Fu D, Huang P, Bach U (2012) Platinum coated counter electrodes for dye-sensitized solar cells fabricated by pulsed electrodeposition—Correlation of nanostructure, catalytic activity and optical properties. Electrochim Acta 77:121–127. https://doi.org/10.1016/j.electacta.2012.05.158

Furukawa H, Ko N, Go YB, Aratani N, Choi SB, Choi E, Yazaydin AÖ, Snurr RQ, O'Keeffe M, Kim J, Yaghi OM (2010) Ultrahigh porosity in metal-organic frameworks. Science 329 (5990):424–428. https://doi.org/10.1126/science.1192160

Ganta D, Jara J, Villanueva R (2017) Dye-sensitized solar cells using Aloe Vera and Cladode of Cactus extracts as natural sensitizers. Chem Phys Lett 679:97–101. https://doi.org/10.1016/j.cplett.2017.04.094

Gao R, Wang L, Ma B, Zhan C, Qiu Y (2010) $Mg(OOCCH_3)_2$ interface modification after sensitization to improve performance in quasi-solid dye-sensitized solar cells. Langmuir 26 (4):2460–2465. https://doi.org/10.1021/la902688a

Gao J, Miao J, Li P-Z, Teng WY, Yang L, Zhao Y, Liu B, Zhang Q (2014) A p-type Ti(iv)-based metal-organic framework with visible-light photo-response. Chem Commun 50(29):3786–3788. https://doi.org/10.1039/c3cc49440c

Ghann W, Kang H, Sheikh T, Yadav S, Chavez-Gil T, Nesbitt F, Uddin J (2017) Fabrication, optimization and characterization of natural dye sensitized solar cell. Sci Rep 7:41470. https://doi.org/10.1038/srep41470; https://www.nature.com/articles/srep41470#supplementary-information

Gibson EA, Smeigh AL, Le Pleux L, Fortage J, Boschloo G, Blart E, Pellegrin Y, Odobel F, Hagfeldt A, Hammarström L (2009) A p-type NiO-based dye-sensitized solar cell with an open-circuit voltage of 0.35 V. Angew Chem Int Ed 48(24):4402–4405. https://doi.org/10.1002/anie.200900423

Gorlov M, Kloo L (2008) Ionic liquid electrolytes for dye-sensitized solar cells. Dalton Trans 20:2655–2666. https://doi.org/10.1039/b716419j

Grätzel M (2001) Photoelectrochemical cells. Nature 414(6861):338–344. https://doi.org/10.1038/35104607

Grätzel M (2003) Dye-sensitized solar cells. J Photochem Photobiol C: Photochem Rev 4(2):145–153. https://doi.org/10.1016/S1389-5567(03)00026-1

Grätzel M, Moser J-E (2001) Solar energy conversion, vol 5. Wiley-VCH, Weinheim

Hagfeldt A, Grätzel M (2000) Molecular photovoltaics. Acc Chem Res 33(5):269–277. https://doi.org/10.1021/ar980112j

Hagfeldt A, Boschloo G, Sun L, Kloo L, Pettersson H (2010) Dye-sensitized solar cells. Chem Rev 110(11):6595–6663. https://doi.org/10.1021/cr900356p

Hamann TW, Ondersma JW (2011) Dye-sensitized solar cell redox shuttles. Energy Environ Sci 4 (2):370–381. https://doi.org/10.1039/c0ee00251h

Haque SA, Palomares E, Cho BM, Green AN, Hirata N, Klug DR, Durrant JR (2005) Charge separation versus recombination in dye-sensitized nanocrystalline solar cells: the minimization of kinetic redundancy. J Am Chem Soc 127(10):3456–3462

Hattori S, Wada Y, Yanagida S, Fukuzumi S (2005) Blue copper model complexes with distorted tetragonal geometry acting as effective electron-transfer mediators in dye-sensitized solar cells. J Am Chem Soc 127(26):9648–9654. https://doi.org/10.1021/ja0506814

He J, Lindström H, Hagfeldt A, Lindquist S-E (1999) Dye-sensitized nanostructured p-type nickel oxide film as a photocathode for a solar cell. J Phys Chem B 103(42):8940–8943. https://doi.org/10.1021/jp991681r

He J, Lindström H, Hagfeldt A, Lindquist S-E (2000) Dye-sensitized nanostructured tandem cell-first demonstrated cell with a dye-sensitized photocathode. Sol Energ Mat Sol 62(3):265–273. https://doi.org/10.1016/S0927-0248(99)00168-3

He L, Chen L, Zhao Y, Chen W, Shan C, Su Z, Wang E (2016) $TiO_2$ film decorated with highly dispersed polyoxometalate nanoparticles synthesized by micelle directed method for the efficiency enhancement of dye-sensitized solar cells. J Power Sources 328:1–7. https://doi.org/10.1016/j.jpowsour.2016.07.085

Hendon CH, Tiana D, Fontecave M, Sanchez C, D'arras L, Sassoye C, Rozes L, Mellot-Draznieks C, Walsh A (2013) Engineering the optical response of the titanium-MIL-125 metal–organic framework through ligand functionalization. J Am Chem Soc 135 (30):10942–10945. https://doi.org/10.1021/ja405350u

Hoffmann H, Debowski M, Müller P, Paasch S, Senkovska I, Kaskel S, Brunner E (2012) Solid-state NMR spectroscopy of metal-organic framework compounds (MOFs). Materials 5 (12):2537

Hou S, Cai X, Wu H, Lv Z, Wang D, Fu Y, Zou D (2012) Flexible, metal-free composite counter electrodes for efficient fiber-shaped dye-sensitized solar cells. J Power Sources 215:164–169. https://doi.org/10.1016/j.jpowsour.2012.05.002

Hou Y, Wang D, Yang XH, Fang WQ, Zhang B, Wang HF, Lu GZ, Hu P, Zhao HJ, Yang HG (2013) Rational screening low-cost counter electrodes for dye-sensitized solar cells. Nat Commun 4:1583. http://www.nature.com/ncomms/journal/v4/n3/suppinfo/ncomms2547_S1.html

Howarth AJ, Peters AW, Vermeulen NA, Wang TC, Hupp JT, Farha OK (2017) Best practices for the synthesis, activation, and characterization of metal-organic frameworks. Chem Mater 29 (1):26–39. https://doi.org/10.1021/acs.chemmater.6b02626

Huang SY, Schlichthörl G, Nozik AJ, Grätzel M, Frank AJ (1997) Charge recombination in dye-sensitized nanocrystalline $TiO_2$ solar cells. J Phys Chem B 101(14):2576–2582. https://doi.org/10.1021/jp962377q

Huang K-C, Wang Y-C, Dong R-X, Tsai W-C, Tsai K-W, Wang C-C, Chen Y-H, Vittal R, Lin J-J, Ho K-C (2010) A high performance dye-sensitized solar cell with a novel nanocomposite film of PtNP/MWCNT on the counter electrode. J Mater Chem 20(20):4067–4073. https://doi.org/10.1039/b925245b

Huo Z, Zhang C, Fang X, Cai M, Dai S, Wang K (2010) Low molecular mass organogelator based gel electrolyte gelated by a quaternary ammonium halide salt for quasi-solid-state dye-sensitized solar cells. J Power Sources 195(13):4384–4390. https://doi.org/10.1016/j.jpowsour.2009.12.107

Ikeda N, Teshima K, Miyasaka T (2006) Conductive polymer-carbon-imidazolium composite: a simple means for constructing solid-state dye-sensitized solar cells. Chem Commun 16:1733–1735. https://doi.org/10.1039/b516417f

Jian S-L, Huang Y-J, Yeh M-H, Ho K-C (2018) A zeolitic imidazolate framework-derived ZnSe/N-doped carbon cube hybrid electrocatalyst as the counter electrode for dye-sensitized solar cells. J Mater Chem A 6(12):5107–5118. https://doi.org/10.1039/c8ta00968f

Jiang X, Li H, Li S, Huang S, Zhu C, Hou L (2018) Metal-organic framework-derived Ni–Co alloy@carbon microspheres as high-performance counter electrode catalysts for dye-sensitized solar cells. Chem Eng J 334:419–431. https://doi.org/10.1016/j.cej.2017.10.043

Jing H, Song X, Ren S, Shi Y, An Y, Yang Y, Feng M, Ma S, Hao C (2016) ZIF-67 derived nanostructures of Co/CoO and Co@N-doped graphitic carbon as counter electrode for highly efficient dye-sensitized solar cells. Electrochim Acta 213:252–259. https://doi.org/10.1016/j.electacta.2016.07.129

Jinxuan L, Wencai Z, Jianxi L, Ian H, Goran K, Sabine S, Damien C, Matthew A, Satoru Y, Yusuke T, Tsuneaki S, Shu S, Zhengbang W, Peter L, Engelbert R, Thomas H, Christof W (2015a) Photoinduced charge-carrier generation in epitaxial mof thin films: high efficiency as a result of an indirect electronic band gap? Angew Chem Int Ed 54(25):7441–7445. https://doi.org/10.1002/anie.201501862

Jinxuan L, Wencai Z, Jianxi L, Ian H, Goran K, Sabine S, Damien C, Matthew A, Satoru Y, Yusuke T, Tsuneaki S, Shu S, Zhengbang W, Peter L, Engelbert R, Thomas H, Christof W (2015b) Photoinduced charge-carrier generation in epitaxial MOF thin films: high efficiency as a result of an indirect electronic band gap? Angew Chem Int Ed 54(25):7441–7445. https://doi.org/10.1002/anie.201501862

Jose R, Thavasi V, Ramakrishna S (2009) Metal oxides for dye-sensitized solar cells. J Am Ceram Soc 92(2):289–301. https://doi.org/10.1111/j.1551-2916.2008.02870.x

Kakiage K, Aoyama Y, Yano T, Oya K, Fujisawa J-I, Hanaya M (2015) Highly-efficient dye-sensitized solar cells with collaborative sensitization by silyl-anchor and carboxy-anchor dyes. Chem Commun 51(88):15894–15897. https://doi.org/10.1039/c5cc06759f

Kalyanasundaram K, Gratzel M (1998) Dye-sensitized solar cells based on redox active monolayers adsorbed on nanocrystalline oxide semiconductor films. In: International symposium on micelles, microemulsions, and monolayers, pp 579–603

Kambe S, Nakade S, Kitamura T, Wada Y, Yanagida S (2002) Influence of the electrolytes on electron transport in mesoporous $TiO_2$—electrolyte systems. J Phys Chem B 106(11):2967–2972. https://doi.org/10.1021/jp013397h

Kaur R, Kim K-H, Deep A (2017) A convenient electrolytic assembly of graphene-MOF composite thin film and its photoanodic application. Appl Surf Sci 396:1303–1309. https://doi.org/10.1016/j.apsusc.2016.11.150

Kavan L, Yum JH, Grätzel M (2010) Optically transparent cathode for dye-sensitized solar cells based on graphene nanoplatelets. ACS Nano 5(1):165–172. https://doi.org/10.1021/nn102353h

Kebede Z, Lindquist S-E (1999) Donor–acceptor interaction between non-aqueous solvents and I2 to generate I–3, and its implication in dye sensitized solar cells. Sol Energ Mat Sol 57(3):259–275. https://doi.org/10.1016/S0927-0248(98)00178-0

Kelly CA, Farzad F, Thompson DW, Stipkala JM, Meyer GJ (1999) Cation-controlled interfacial charge injection in sensitized nanocrystalline TiO2. Langmuir 15(20):7047–7054

Kent CA, Mehl BP, Ma L, Papanikolas JM, Meyer TJ, Lin W (2010) Energy transfer dynamics in metal − organic frameworks. J Am Chem Soc 132(37):12767–12769. https://doi.org/10.1021/ja102804s

Kinoshita T, J-i Fujisawa, Nakazaki J, Uchida S, Kubo T, Segawa H (2012) Enhancement of near-IR photoelectric conversion in dye-sensitized solar cells using an osmium sensitizer with strong spin-forbidden transition. J Phys Chem Lett 3(3):394–398. https://doi.org/10.1021/jz2016445

Kobayashi Y, Jacobs B, Allendorf MD, Long JR (2010) Conductivity, doping, and redox chemistry of a microporous dithiolene-based metal − organic framework. Chem Mater 22(14):4120–4122. https://doi.org/10.1021/cm101238m

Kohle O, Grätzel M, Meyer AF, Meyer TB (1997) The photovoltaic stability of, bis(isothiocyanato)rlutheniurn(II)-bis-2, 2′bipyridine-4, 4′-dicarboxylic acid and related sensitizers. Adv Mater 9(11):904–906. https://doi.org/10.1002/adma.19970091111

Koops SE, O'Regan BC, Barnes PRF, Durrant JR (2009) Parameters Influencing the efficiency of electron injection in dye-sensitized solar cells. J Am Chem Soc 131(13):4808–4818. https://doi.org/10.1021/ja8091278

Kopidakis N, Benkstein KD, van de Lagemaat J, Frank AJ (2003) Transport-limited recombination of photocarriers in dye-sensitized nanocrystalline $TiO_2$ solar cells. J Phys Chem B 107(41):11307–11315. https://doi.org/10.1021/jp0304475

Kuang D, Ito S, Wenger B, Klein C, Moser J-E, Humphry-baker R, Zakeeruddin SM, Grätzel M (2006) High molar extinction coefficient heteroleptic ruthenium complexes for thin film dye-sensitized solar cells. J Am Chem Soc 128(12):4146–4154. https://doi.org/10.1021/ja058540p

Kubo W, Sakamoto A, Kitamura T, Wada Y, Yanagida S (2004) Dye-sensitized solar cells: improvement of spectral response by tandem structure. J Photochem Photobiol, A 164(1–3):33–39. https://doi.org/10.1016/j.jphotochem.2004.01.024

Kundu T, Sahoo SC, Banerjee R (2012) Solid-state thermolysis of anion induced metal-organic frameworks to ZnO microparticles with predefined morphologies: facile synthesis and solar cell studies. Cryst Growth Des 12(5):2572–2578. https://doi.org/10.1021/cg300174f

Kung C-W, Chen H-W, Lin C-Y, Huang K-C, Vittal R, Ho K-C (2012) CoS acicular nanorod arrays for the counter electrode of an efficient dye-sensitized solar cell. ACS Nano 6(8):7016–7025. https://doi.org/10.1021/nn302063s

Kwok EC-H, Chan M-Y, Wong KM-C, Lam WH, Yam VW-W (2010) Functionalized alkynylplatinum(II) polypyridyl complexes for use as sensitizers in dye-sensitized solar cells. Chem-Eur J 16(40):12244–12254. https://doi.org/10.1002/chem.201001424

Le Viet A, Jose R, Reddy MV, Chowdari BVR, Ramakrishna S (2010) $Nb_2O_5$ photoelectrodes for dye-sensitized solar cells: choice of the polymorph. J Phys Chem C 114(49):21795–21800. https://doi.org/10.1021/jp106515k

Lee Y-L, Chen C-L, Chong L-W, Chen C-H, Liu Y-F, Chi C-F (2010a) A platinum counter electrode with high electrochemical activity and high transparency for dye-sensitized solar cells. Electrochem Commun 12(11):1662–1665. https://doi.org/10.1016/j.elecom.2010.09.022

Lee KS, Lee HK, Wang DH, Park N-G, Lee JY, Park OO, Park JH (2010b) Dye-sensitized solar cells with Pt- and TCO-free counter electrodes. Chem Commun 46(25):4505–4507. https://doi.org/10.1039/c0cc00432d

Lee CY, Farha OK, Hong BJ, Sarjeant AA, Nguyen ST, Hupp JT (2011) Light-harvesting metal-organic frameworks (MOFs): efficient strut-to-strut energy transfer in bodipy and porphyrin-based MOFs. J Am Chem Soc 133(40):15858–15861. https://doi.org/10.1021/ja206029a

Lee DY, Shinde DV, Yoon SJ, Cho KN, Lee W, Shrestha NK, Han S-H (2014a) Cu-based metal-organic frameworks for photovoltaic application. J Phys Chem C 118(30):16328–16334. https://doi.org/10.1021/jp4079663

Lee DY, Shin CY, Yoon SJ, Lee HY, Lee W, Shrestha NK, Lee JK, Han S-H (2014b) Enhanced photovoltaic performance of Cu-based metal-organic frameworks sensitized solar cell by addition of carbon nanotubes. Sci Rep 4:3930. https://doi.org/10.1038/srep03930

Lee DY, Kim E-K, Shin CY, Shinde DV, Lee W, Shrestha NK, Lee JK, Han S-H (2014c) Layer-by-layer deposition and photovoltaic property of Ru-based metal-organic frameworks. RSC Adv 4(23):12037–12042. https://doi.org/10.1039/c4ra00397g

Levy RB, Boudart M (1973) Platinum-like behavior of tungsten carbide in surface catalysis. Science 181(4099):547–549. https://doi.org/10.2307/1736506

Lewis NS (2007) Toward cost-effective solar energy use. Science 315(5813):798–801. https://doi.org/10.1126/science.1137014

Li TC, Spokoyny AM, She C, Farha OK, Mirkin CA, Marks TJ, Hupp JT (2010) Ni (III)/(IV) bis (dicarbollide) as a fast, noncorrosive redox shuttle for dye-sensitized solar cells. J Am Chem Soc 132(13):4580–4582

Li Y, Pang A, Wang C, Wei M (2011) Metal-organic frameworks: promising materials for improving the open circuit voltage of dye-sensitized solar cells. J Mater Chem 21(43):17259–17264. https://doi.org/10.1039/c1jm12754c

Li Y, Che Z, Sun X, Dou J, Wei M (2014) Metal-organic framework derived hierarchical ZnO parallelepipeds as an efficient scattering layer in dye-sensitized solar cells. Chem Commun 50(68):9769–9772. https://doi.org/10.1039/c4cc03352c

Linfoot CL, Richardson P, Hewat TE, Moudam O, Forde MM, Collins A, White F, Robertson N (2010) Substituted [Cu(i)(POP)(bipyridyl)] and related complexes: Synthesis, structure,

properties and applications to dye-sensitised solar cells. Dalton Trans 39(38):8945–8956. https://doi.org/10.1039/c0dt00190b

Linfoot CL, Richardson P, McCall KL, Durrant JR, Morandeira A, Robertson N, Linfoot CL, Richardson P, McCall KL, Durrant JR, Morandeira A, Robertson N (2011) A nickel-complex sensitiser for dye-sensitised solar cells. Sol Energy 85(6):1195–1203. https://doi.org/10.1016/j.solener.2011.02.023

Liu Y, Hagfeldt A, Xiao X-R, Lindquist S-E (1998) Investigation of influence of redox species on the interfacial energetics of a dye-sensitized nanoporous $TiO_2$ solar cell. Sol Energy Mater Sol Cells 55(3):267–281

Liu J, Zhou W, Liu J, Fujimori Y, Higashino T, Imahori H, Jiang X, Zhao J, Sakurai T, Hattori Y, Matsuda W, Seki S, Garlapati SK, Dasgupta S, Redel E, Sun L, Woll C (2016) A new class of epitaxial porphyrin metal-organic framework thin films with extremely high photocarrier generation efficiency: promising materials for all-solid-state solar cells. J Mater Chem A 4 (33):12739–12747. https://doi.org/10.1039/c6ta04898f

Llabrés i Xamena FX, Corma A, Garcia H (2007) Applications for metal − organic frameworks (MOFs) as quantum dot semiconductors. J Phys Chem C 111 (1):80–85. https://doi.org/10.1021/jp063600e

Lopez HA, Dhakshinamoorthy A, Ferrer B, Atienzar P, Alvaro M, Garcia H (2011) Photochemical response of commercial MOFs: $Al_2(BDC)_3$ and its use as active material in photovoltaic devices. J Phys Chem C 115(45):22200–22206. https://doi.org/10.1021/jp206919m

Luo X, Li F, Xu B, Sun Z, Xu L (2012) Enhanced photovoltaic response of the first polyoxometalate-modified zinc oxide photoanode for solar cell application. J Mater Chem 22 (30):15050–15055. https://doi.org/10.1039/c2jm16018h

Maiaugree W, Lowpa S, Towannang M, Rutphonsan P, Tangtrakarn A, Pimanpang S, Maiaugree P, Ratchapolthavisin N, Sang-aroon W, Jarernboon W, Amornkitbamrung V (2015) A dye sensitized solar cell using natural counter electrode and natural dye derived from mangosteen peel waste. Sci Rep 5:15230. https://doi.org/10.1038/srep15230; https://www.nature.com/articles/srep15230#supplementary-information

Mathew S, Yella A, Gao P, Humphry-Baker R, CurchodBasile FE, Ashari-Astani N, Tavernelli I, Rothlisberger U, NazeeruddinMd K, Grätzel M (2014) Dye-sensitized solar cells with 13% efficiency achieved through the molecular engineering of porphyrin sensitizers. Nat Chem 6 (3):242–247. https://doi.org/10.1038/nchem.1861; http://www.nature.com/nchem/journal/v6/n3/abs/nchem.1861.html#supplementary-information

Maza WA, Haring AJ, Ahrenholtz SR, Epley CC, Lin SY, Morris AJ (2016) Ruthenium(ii)-polypyridyl zirconium(iv) metal-organic frameworks as a new class of sensitized solar cells. Chem Sci 7(1):719–727. https://doi.org/10.1039/c5sc01565k

Miao Q, Gao J, Wang Z, Yu H, Luo Y, Ma T (2011) Syntheses and characterization of several nickel bis(dithiolene) complexes with strong and broad Near-IR absorption. Inorg Chim Acta 376(1):619–627. https://doi.org/10.1016/j.ica.2011.07.046

Mohmeyer N, Wang P, Schmidt H-W, Zakeeruddin SM, Gratzel M (2004) Quasi-solid-state dye sensitized solar cells with 1,3:2,4-di-O-benzylidene-d-sorbitol derivatives as low molecular weight organic gelators. J Mat Chem 14(12):1905–1909

Mohmeyer N, Kuang D, Wang P, Schmidt H-W, Zakeeruddin SM, Gratzel M (2006) An efficient organogelator for ionic liquids to prepare stable quasi-solid-state dye-sensitized solar cells. J Mater Chem 16(29):2978–2983. https://doi.org/10.1039/b604021g

Morris W, Stevens CJ, Taylor RE, Dybowski C, Yaghi OM, Garcia-Garibay MA (2012) NMR and X-ray study revealing the rigidity of zeolitic imidazolate frameworks. J Phys Chem C 116 (24):13307–13312. https://doi.org/10.1021/jp303907p

Murakami TN, Ito S, Wang Q, Nazeeruddin MK, Bessho T, Cesar I, Liska P, Humphry-Baker R, Comte P, Péchy P, Grätzel M (2006) Highly efficient dye-sensitized solar cells based on carbon black counter electrodes. J Electrochem Soc 153(12):A2255–A2261. https://doi.org/10.1149/1.2358087

Murayama M, Mori T (2007) Dye-sensitized solar cell using novel tandem cell structure. J Phys D Appl Phys 40(6):1664

Nafiseh M, Isabella C, Antonio B, Mohammad RS, Alberto V, Giorgio S (2011) Hierarchically assembled ZnO nanocrystallites for high-efficiency dye-sensitized solar cells. Angew Chem Int Ed 50(51):12321–12325. https://doi.org/10.1002/anie.201104605

Nair RR, Blake P, Grigorenko AN, Novoselov KS, Booth TJ, Stauber T, Peres NMR, Geim AK (2008) Fine structure constant defines visual transparency of graphene. Science 320 (5881):1308. https://doi.org/10.1126/science.1156965

Nakade S, Saito Y, Kubo W, Kanzaki T, Kitamura T, Wada Y, Yanagida S (2003) Enhancement of electron transport in nano-porous $TiO_2$ electrodes by dye adsorption. Electrochem Commun 5(9):804–808. https://doi.org/10.1016/j.elecom.2003.07.008

Nattestad A, Mozer AJ, Fischer MKR, Cheng YB, Mishra A, Bäuerle P, Bach U (2010) Highly efficient photocathodes for dye-sensitized tandem solar cells. Nat Mat 9(1):31–35. https://doi.org/10.1038/nmat2588

Nattestad A, Perera I, Spiccia L (2016) Developments in and prospects for photocathodic and tandem dye-sensitized solar cells. J Photochem Photobiol C: Photochem Rev 28:44–71. https://doi.org/10.1016/j.jphotochemrev.2016.06.003

Nazeeruddin MK, Kay A, Rodicio I, Humphry-Baker R, Mueller E, Liska P, Vlachopoulos N, Grätzel M (1993) Conversion of light to electricity by cis-X2bis(2,2′-bipyridyl-4,4′-dicarboxylate)ruthenium(II) charge-transfer sensitizers (X = Cl-, Br-, I-, CN-, and SCN-) on nanocrystalline titanium dioxide electrodes. J Am Chem Soc 115(14):6382–6390. https://doi.org/10.1021/ja00067a063

Nazeeruddin MK, Pechy P, Gratzel M (1997) Efficient panchromatic sensitization of nanocrystalline $TiO_2$ films by a black dye based on a trithiocyanato-ruthenium complex. Chem Commun 18:1705–1706. https://doi.org/10.1039/a703277c

Nazeeruddin MK, Péchy P, Renouard T, Zakeeruddin SM, Humphry-Baker R, Comte P, Liska P, Cevey L, Costa E, Shklover V, Spiccia L, Deacon GB, Bignozzi CA, Grätzel M (2001) Engineering of efficient panchromatic sensitizers for nanocrystalline $TiO_2$-based solar cells. J Am Chem Soc 123(8):1613–1624. https://doi.org/10.1021/ja003299u

Novoselov KS, Geim AK, Morozov SV, Jiang D, Zhang Y, Dubonos SV, Grigorieva IV, Firsov AA (2004) Electric field effect in atomically thin carbon films. Science 306(5696):666–669. https://doi.org/10.1126/science.1102896

Nowotny MK, Sheppard LR, Bak T, Nowotny J (2008) Defect chemistry of titanium dioxide. Application of defect engineering in processing of $TiO_2$-based photocatalysts†. J Phys Chem C 112 (14):5275–5300. https://doi.org/10.1021/jp077275m

Nusbaumer H, Moser J-E, Zakeeruddin SM, Nazeeruddin MK, Grätzel M (2001) CoII(dbbip)22 + complex rivals tri-iodide/iodide redox mediator in dye-sensitized photovoltaic cells. J Phys Chem B 105(43):10461–10464. https://doi.org/10.1021/jp012075a

Obotowo IN, Obot IB, Ekpe UJ (2016) Organic sensitizers for dye-sensitized solar cell (DSSC): properties from computation, progress and future perspectives. J Mol Struct 1122:80–87. https://doi.org/10.1016/j.molstruc.2016.05.080

O'Regan B, Grätzel M (1991) A low-cost, high-efficiency solar cell based on dye-sensitized colloidal $TiO_2$ films. Nature 353(6346):737–740

Ou JZ, Rani RA, Ham M-H, Field MR, Zhang Y, Zheng H, Reece P, Zhuiykov S, Sriram S, Bhaskaran M, Kaner RB, Kalantar-zadeh K (2012) Elevated temperature anodized $Nb_2O_5$: a photoanode material with exceptionally large photoconversion efficiencies. ACS Nano 6 (5):4045–4053. https://doi.org/10.1021/nn300408p

Palomares E, Clifford JN, Haque SA, Lutz T, Durrant JR (2002) Control of charge recombination dynamics in dye sensitized solar cells by the use of conformally deposited metal oxide blocking layers. J Am Chem Soc 125(2):475–482. https://doi.org/10.1021/ja027945w

Park NG, van de Lagemaat J, Frank AJ (2000) Comparison of dye-sensitized rutile- and anatase-based $TiO_2$ solar cells. J Phys Chem B 104(38):8989–8994. https://doi.org/10.1021/jp9943651

Peigney A, Laurent C, Flahaut E, Bacsa RR, Rousset A (2001) Specific surface area of carbon nanotubes and bundles of carbon nanotubes. Carbon 39(4):507–514. https://doi.org/10.1016/s0008-6223(00)00155-x

Perera IR, Gupta A, Xiang W, Daeneke T, Bach U, Evans RA, Ohlin CA, Spiccia L (2014) Introducing manganese complexes as redox mediators for dye-sensitized solar cells. Phys Chem Chem Phys 16(24):12021–12028. https://doi.org/10.1039/c3cp54894e

Perera IR, Daeneke T, Makuta S, Yu Z, Tachibana Y, Mishra A, Bäuerle P, Ohlin CA, Bach U, Spiccia L (2015) Application of the tris(acetylacetonato)iron(III)/(II) redox couple in p-type dye-sensitized solar cells. Angew Chem Int Ed 54(12):3758–3762. https://doi.org/10.1002/anie.201409877

Plonska-Brzezinska ME, Lapinski A, Wilczewska AZ, Dubis AT, Villalta-Cerdas A, Winkler K, Echegoyen L (2011) The synthesis and characterization of carbon nano-onions produced by solution ozonolysis. Carbon 49(15):5079–5089. https://doi.org/10.1016/j.carbon.2011.07.027

Powar S, Wu Q, Weidelener M, Nattestad A, Hu Z, Mishra A, Bäuerle P, Spiccia L, Cheng Y-B, Bach U (2012) Improved photocurrents for p-type dye-sensitized solar cells using nano-structured nickel(ii) oxide microballs. Energy Environ Sci 5(10):8896–8900. https://doi.org/10.1039/c2ee22127f

Quintana M, Edvinsson T, Hagfeldt A, Boschloo G (2006) Comparison of dye-sensitized ZnO and $TiO_2$ solar cells: studies of charge transport and carrier lifetime. J Phys Chem C 111(2):1035–1041. https://doi.org/10.1021/jp065948f

Ramakrishna G, Jose DA, Kumar DK, Das A, Palit DK, Ghosh HN (2005) Strongly coupled ruthenium—polypyridyl complexes for efficient electron injection in dye-sensitized semiconductor nanoparticles. J Phys Chem B 109(32):15445–15453. https://doi.org/10.1021/jp051285a

Roh DK, Park JT, Ahn SH, Ahn H, Ryu DY, Kim JH (2010) Amphiphilic poly(vinyl chloride)-g-poly(oxyethylene methacrylate) graft polymer electrolytes: Interactions, nanostructures and applications to dye-sensitized solar cells. Electrochim Acta 55(17):4976–4981. https://doi.org/10.1016/j.electacta.2010.03.106

Salvatori P, Marotta G, Cinti A, Anselmi C, Mosconi E, De Angelis F (2013) Supramolecular interactions of chenodeoxycholic acid increase the efficiency of dye-sensitized solar cells based on a cobalt electrolyte. J Phys Chem C 117(8):3874–3887. https://doi.org/10.1021/jp4003577

Sayama K, Sugihara H, Arakawa H (1998) Photoelectrochemical properties of a porous $Nb_2O_5$ electrode sensitized by a ruthenium dye. Chem Mater 10(12):3825–3832. https://doi.org/10.1021/cm9801111

Schlichthörl G, Huang S, Sprague J, Frank A (1997) Band edge movement and recombination kinetics in dye-sensitized nanocrystalline $TiO_2$ solar cells: a study by intensity modulated photovoltage spectroscopy. J Phys Chem B 101(41):8141–8155

Shi C, Dai S, Wang K, Pan X, Kong F, Hu L (2005) The adsorption of 4-tert-butylpyridine on the nanocrystalline $TiO_2$ and Raman spectra of dye-sensitized solar cells in situ. Vib Spectrosc 39 (1):99–105

Shi D, Pootrakulchote N, Li R, Guo J, Wang Y, Zakeeruddin SM, Grätzel M, Wang P (2008) New efficiency records for stable dye-sensitized solar cells with low-volatility and ionic liquid electrolytes. J Phys Chem C 112(44):17046–17050. https://doi.org/10.1021/jp808018h

Shin SS, Kim JS, Suk JH, Lee KD, Kim DW, Park JH, Cho IS, Hong KS, Kim JY (2013) Improved quantum efficiency of highly efficient perovskite $BaSnO_3$-based dye-sensitized solar cells. ACS Nano 7(2):1027–1035. https://doi.org/10.1021/nn305341x

Shockley W, Queisser HJ (1961) Detailed balance limit of efficiency of p-n junction solar cells. J Appl Phys 32 (3):510–519. http://dx.doi.org/10.1063/1.1736034

Sommeling PM, O'Regan BC, Haswell RR, Smit HJ, Bakker NJ, Smits JJ, Kroon JM, van Roosmalen JA (2006) Influence of a $TiCl_4$ post-treatment on nanocrystalline $TiO_2$ films in dye-sensitized solar cells. J Phys Chem B 110(39):19191–19197

Spoerke ED, Small LJ, Foster ME, Wheeler J, Ullman AM, Stavila V, Rodriguez M, Allendorf MD (2017) MOF-sensitized solar cells enabled by a pillared porphyrin framework. J Phys Chem C 121(9):4816–4824. https://doi.org/10.1021/acs.jpcc.6b11251

Stankovich S, Dikin DA, Dommett GHB, Kohlhaas KM, Zimney EJ, Stach EA, Piner RD, Nguyen ST, Ruoff RS (2006) Graphene-based composite materials. Nature 442 (7100):282–286. http://www.nature.com/nature/journal/v442/n7100/suppinfo/nature04969_S1.html

Stock N, Biswas S (2012) Synthesis of metal-organic frameworks (MOFs): routes to various MOF topologies, morphologies, and composites. Chem Rev 112(2):933–969. https://doi.org/10.1021/cr200304e

Sun Z, Fang S, Li F, Xu L, Hu Y, Ren J (2013) Enhanced photovoltaic performance of copper phthalocyanine by incorporation of polyoxometalate. J Photochem Photobiol A: Chem 252:25–30. https://doi.org/10.1016/j.jphotochem.2012.11.007

Sun X, Li Y, Dou J, Shen D, Wei M (2016) Metal-organic frameworks derived carbon as a high-efficiency counter electrode for dye-sensitized solar cells. J Power Sources 322:93–98. https://doi.org/10.1016/j.jpowsour.2016.05.025

Sutrisno A, Huang Y (2013) Solid-state NMR: a powerful tool for characterization of metal–organic frameworks. Solid State Nucl Mag Reson 49–50:1–11. https://doi.org/10.1016/j.ssnmr.2012.09.003

Tan B, Toman E, Li Y, Wu Y (2007) Zinc stannate ($Zn_2SnO_4$) dye-sensitized solar cells. J Am Chem Soc 129(14):4162–4163. https://doi.org/10.1021/ja070804f

Tang Q, Cai H, Yuan S, Wang X (2013) Counter electrodes from double-layered polyaniline nanostructures for dye-sensitized solar cell applications. J Mater Chem A 1(2):317–323. https://doi.org/10.1039/c2ta00026a

Tao L, Huo Z, Ding Y, Li Y, Dai S, Wang L, Zhu J, Pan X, Zhang B, Yao J, Nazeeruddin MK, Grätzel M (2015) High-efficiency and stable quasi-solid-state dye-sensitized solar cell based on low molecular mass organogelator electrolyte. J Mater Chem A 3(5):2344–2352. https://doi.org/10.1039/c4ta06188h

Thomas S, Deepak TG, Anjusree GS, Arun TA, Nair SV, Nair AS (2014) A review on counter electrode materials in dye-sensitized solar cells. J Mater Chem A 2(13):4474–4490. https://doi.org/10.1039/c3ta13374e

Thommes M (2010) Physical adsorption characterization of nanoporous materials. Chem Ing Tech 82 (7):1059–1073. https://doi.org/10.1002/cite.201000064

Thommes M, Kaneko K, Neimark AV, Olivier JP, Rodriguez-Reinoso F, Rouquerol J, Sing KSW (2015) Physisorption of gases, with special reference to the evaluation of surface area and pore size distribution (IUPAC Technical Report). Pure Appl Chem 87 (9–10). https://doi.org/10.1515/pac-2014-1117

Tsubomura H, Matsumura M, Nomura Y, Amamiya T (1976) Dye sensitised zinc oxide: aqueous electrolyte: platinum photocell. Nature 261(5559):402–403

Upadhyaya HM, Hirata N, Haque SA, de Paoli M-A, Durrant JR (2006) Kinetic competition in flexible dye sensitised solar cells employing a series of polymer electrolytes. Chem Commun 8:877–879. https://doi.org/10.1039/b515240b

Wang H, Hu YH (2012) Graphene as a counter electrode material for dye-sensitized solar cells. Energy Environ Sci 5(8):8182–8188. https://doi.org/10.1039/c2ee21905k

Wang P, Zakeeruddin SM, Moser JE, Nazeeruddin MK, Sekiguchi T, Grätzel M (2003) A stable quasi-solid-state dye-sensitized solar cell with an amphiphilic ruthenium sensitizer and polymer gel electrolyte. Nat Mater 2(6):402–407

Wang Z-S, Kawauchi H, Kashima T, Arakawa H (2004a) Significant influence of $TiO_2$ photoelectrode morphology on the energy conversion efficiency of N719 dye-sensitized solar cell. Coord Chem Rev 248(13–14):1381–1389. https://doi.org/10.1016/j.ccr.2004.03.006

Wang P, Zakeeruddin SM, Humphry-Baker R, Grätzel M (2004b) A binary ionic liquid electrolyte to achieve $\geq 7\%$ power conversion efficiencies in dye-sensitized solar cells. Chem Mater 16 (14):2694–2696. https://doi.org/10.1021/cm049916l

Wang P, Wenger B, Humphry-Baker R, Moser J-E, Teuscher J, Kantlehner W, Mezger J, Stoyanov EV, Zakeeruddin SM, Grätzel M (2005a) Charge separation and efficient light energy conversion in sensitized mesoscopic solar cells based on binary ionic liquids. J Am Chem Soc 127(18):6850–6856. https://doi.org/10.1021/ja042232u

Wang P, Klein C, Humphry-Baker R, Zakeeruddin SM, Grätzel M (2005) Stable ⩾8% efficient nanocrystalline dye-sensitized solar cell based on an electrolyte of low volatility. Appl Phys Lett 86 (12):123508. http://dx.doi.org/10.1063/1.1887825

Wang Q, Ito S, Grätzel M, Fabregat-Santiago F, Mora-Seró I, Bisquert J, Bessho T, Imai H (2006) Characteristics of high efficiency dye-sensitized solar cells†. J Phys Chem B 110(50):25210–25221. https://doi.org/10.1021/jp064256o

Wang ZS, Cui Y, Dan-oh Y, Kasada C, Shinpo A, Hara K (2007) Thiophene-functionalized coumarin dye for efficient dye-sensitized solar cells: electron lifetime improved by coadsorption of deoxycholic acid. J Phys Chem C 111(19):7224–7230. https://doi.org/10.1021/jp067872t

Wang LJ, Deng H, Furukawa H, Gándara F, Cordova KE, Peri D, Yaghi OM (2014) Synthesis and characterization of metal-organic framework-74 containing 2, 4, 6, 8, and 10 different metals. Inorg Chem 53(12):5881–5883. https://doi.org/10.1021/ic500434a

Wang S, Kitao T, Guillou N, Wahiduzzaman M, Martineau-Corcos C, Nouar F, Tissot A, Binet L, Ramsahye N, Devautour-Vinot S, Kitagawa S, Seki S, Tsutsui Y, Briois V, Steunou N, Maurin G, Uemura T, Serre C (2018) A phase transformable ultrastable titanium-carboxylate framework for photoconduction. Nature Commun 9(1):1660. https://doi.org/10.1038/s41467-018-04034-w

Wu JH, Hao SC, Lan Z, Lin JM, Huang ML, Huang YF, Fang LQ, Yin S, Sato T (2007) A thermoplastic gel electrolyte for stable quasi-solid-state dye-sensitized solar cells. Adv Funct Mater 17(15):2645–2652. https://doi.org/10.1002/adfm.200600621

Wu M, Wang Y, Lin X, Yu N, Wang L, Wang L, Hagfeldt A, Ma T (2011) Economical and effective sulfide catalysts for dye-sensitized solar cells as counter electrodes. Phys Chem Chem Phys 13(43):19298–19301. https://doi.org/10.1039/c1cp22819f

Wu J, Lan Z, Lin J, Huang M, Huang Y, Fan L, Luo G (2015) Electrolytes in dye-sensitized solar cells. Chem Rev 115(5):2136–2173. https://doi.org/10.1021/cr400675m

Xiang W, Huang F, Cheng YB, Bach U, Spiccia L (2013) Aqueous dye-sensitized solar cell electrolytes based on the cobalt(ii)/(iii) tris(bipyridine) redox couple. Energy Environ Sci 6:121–127

Xie Y, Hamann TW (2013) Fast low-spin cobalt complex redox shuttles for dye-sensitized solar cells. J Phys Chem Lett 4(2):328–332. https://doi.org/10.1021/jz301934e

Xu K (2004) Nonaqueous liquid electrolytes for lithium-based rechargeable batteries. Chem Rev 104(10):4303–4418. https://doi.org/10.1021/cr030203g

Xu M, Li R, Pootrakulchote N, Shi D, Guo J, Yi Z, Zakeeruddin SM, Grätzel M, Wang P (2008) Energy-level and molecular engineering of organic D-π-A sensitizers in dye-sensitized solar cells. J Phys Chem C 112(49):19770–19776. https://doi.org/10.1021/jp808275z

Yafeng L, Caiyun C, Xun S, Jie D, Mingdeng W (2014) Metal-organic frameworks at interfaces in dye-sensitized solar cells. Chemsuschem 7(9):2469–2472. https://doi.org/10.1002/cssc.201402143

Yaghi OM, Li H (1995) Hydrothermal synthesis of a metal-organic framework containing large rectangular channels. J Am Chem Soc 117(41):10401–10402. https://doi.org/10.1021/ja00146a033

Yella A, Lee HW, Tsao N, Yi C, Chandiran AK, Nazeeruddin MK, Diau EW, Yeh CY, Zakeeruddin SM, Grätzel M (2011) Porphyrin-sensitized solar cells with cobalt (II/III)-based redox electrolyte exceed 12% efficiency [science (629)]. Science 334(6060):1203

Yen Y-S, Chou H-H, Chen Y-C, Hsu C-Y, Lin JT (2012) Recent developments in molecule-based organic materials for dye-sensitized solar cells. J Mater Chem 22(18):8734–8747. https://doi.org/10.1039/c2jm30362k

Yohannes T, Inganäs O (1998) Photoelectrochemical studies of the junction between poly[3-(4-octylphenyl)thiophene] and a redox polymer electrolyte. Sol Energy Mater Sol Cells 51(2):193–202. https://doi.org/10.1016/S0927-0248(97)00213-4

Yu Z, Vlachopoulos N, Gorlov M, Kloo L (2011) Liquid electrolytes for dye-sensitized solar cells. Dalton Trans 40(40):10289–10303

Yu Q, Yu C, Guo F, Wang J, Jiao S, Gao S, Li H, Zhao L (2012) A stable and efficient quasi-solid-state dye-sensitized solar cell with a low molecular weight organic gelator. Energy Environ Sci 5(3):6151–6155. https://doi.org/10.1039/c2ee03128k

Yum J-H, Baranoff E, Kessler F, Moehl T, Ahmad S, Bessho T, Marchioro A, Ghadiri E, Moser J-E, Yi C, Nazeeruddin MK, Grätzel M (2012) A cobalt complex redox shuttle for dye-sensitized solar cells with high open-circuit potentials. Nat Commun 3:631. http://www.nature.com/ncomms/journal/v3/n1/suppinfo/ncomms1655_S1.html

Zakeeruddin SM, Grätzel M (2009) Solvent-free ionic liquid electrolytes for mesoscopic dye-sensitized solar cells. Adv Funct Mater 19(14):2187–2202. https://doi.org/10.1002/adfm.200900390

Zhang Q, Chou TP, Russo B, Jenekhe SA, Cao G (2008a) Aggregation of ZnO nanocrystallites for high conversion efficiency in dye-sensitized solar cells. Angew Chem 120(13):2436–2440. https://doi.org/10.1002/ange.200704919

Zhang Z, Chen P, Murakami TN, Zakeeruddin SM, Grätzel M (2008b) The 2,2,6,6-Tetramethyl-1-piperidinyloxy radical: an efficient, iodine- free redox mediator for dye-sensitized solar cells. Adv Funct Mater 18(2):341–346. https://doi.org/10.1002/adfm.200701041

Zhang C, Huang Y, Huo Z, Chen S, Dai S (2009) Photoelectrochemical effects of guanidinium thiocyanate on dye-sensitized solar cell performance and stability. J Phys Chem C 113 (52):21779–21783. https://doi.org/10.1021/jp909732f

Zhang XL, Zhang Z, Chen D, Bauerle P, Bach U, Cheng Y-B (2012) Sensitization of nickel oxide: improved carrier lifetime and charge collection by tuning nanoscale crystallinity. Chem Commun 48(79):9885–9887. https://doi.org/10.1039/c2cc35018a

Zhang W, Li W, He X, Zhao L, Chen H, Zhang L, Tian P, Xin Z, Fang W, Zhang F (2018) Dendritic Fe-based polyoxometalates @ metal–organic framework (MOFs) combined with ZnO as a novel photoanode in solar cells. J Mater Sci Mater in Electronics 29(2):1623–1629. https://doi.org/10.1007/s10854-017-8073-1

# Chapter 8
# Fullerene-Free Molecular Acceptors for Organic Photovoltaics


**Amaresh Mishra and Satya Narayan Sahu**

**Abstract** Solution-processed bulk-heterojunction solar cells (BHJSCs) are the focus of photovoltaic research for the last 20 years due to new materials development, bandgap tunability through molecular design, high efficiency, and cost-effective fabrication and optimization. Much attention has been paid to the design and development of donor materials whereas the development of new electron accepting materials is at its infancy. For a long time fullerene and its derivatives have dominated the field as electron acceptor materials. In last few years, a significant progress has been made towards the development of fullerene-free acceptors (FFA) which in combination with conjugated polymers/oligomers as the donors reached power conversion efficiencies (PCE) up to 14% and exceed those of the fullerene-based OSCs. These sharp growth in PCE makes OSCs as one of the fastest growing solar technology. Specifically, in these devices the choice of FFAs and corresponding complementary donor materials plays critical role in achieving high efficiencies. This chapter summarizes recent development in the design principles of FFAs for BHJSCs. The role of FFAs in binary and ternary devices is discussed as a way to improve the device performance. A special attention is paid to the structure-activity relationships with the device performance and an approach for efficiency enhancement of OSCs.

**Keywords** Organic semiconductors · Fullerene-free acceptors · Organic solar cells

## 8.1 Introduction

In the last 20 years, solution-processed bulk heterojunction organic solar cells (BHJOSCs) have drawn significant attention due to their unique advantages of light weight, low-temperature processing, mechanical flexibility and compatibility with

A. Mishra (✉) · S. N. Sahu
School of Chemistry, Sambalpur University, Jyoti Vihar, 768019 Sambalpur, India
e-mail: amaresh.mishra@suniv.ac.in



H. Tyagi et al. (eds.), *Advances in Solar Energy Research*, Energy, Environment, and Sustainability, https://doi.org/10.1007/978-981-13-3302-6_8

roll-to-roll process (Li 2012; Dennler et al. 2009; Brabec et al. 2014; Kang et al. 2016). BHJ consists of a donor (D) and an acceptor (A) composite layer sandwiched between two metal electrodes. BHJOSCs are in intense investigation in both academic and industrial communities in an effort to increase their processability, power conversion efficiency (PCE), and stability. In solution-processed BHJSCs the utilization of D-A-based low bandgap copolymers or oligomers as donor materials has been considered as one of the most effective ways to increase PCEs of fullerene-based OSCs and the research has promoted many exciting breakthroughs in the field (Cheng et al. 2009; Mishra and Bäuerle 2012; Chen et al. 2013; Coughlin et al. 2014; Yao et al. 2016a). Among the fullerene derivaives, [6,6]-phenyl-$C_{61}$/$C_{71}$-butyric acid methyl ester ($PC_{61}BM$/$PC_{71}BM$) and indene-$C_{60}$ bis-adduct ($IC_{60}BA$) have formed an integral part as acceptor component achieving high power conversion efficiency (PCE) up to 11% (Kan et al. 2015; Deng et al. 2016; Zhang et al. 2017; Zhao et al. 2016a; Cai et al. 2017). Although significant progress has been accomplished, the inherent limitations of fullerene derivatives are their synthetic flexibility, cost, stability, weak light absorption in the visible region, limited energy level variation and poor structural tunability via chemical modifications. Furthermore, fullerene-based devices always suffers from a trade-off between short circuit current ($J_{SC}$) and open-circuit voltage ($V_{OC}$). An increase in the $J_{SC}$ value has mostly been realized by a decrease in the $V_{OC}$, thus restricting the overall PCE improvement. Therefore, to overcome the trade-off between the $J_{SC}$ and $V_{OC}$, fullerene-free acceptors (FFA) with tunable optical properties and energy levels were developed and employed in OSCs as alternative replacements to the conventional fullerene acceptors. Since then the field of OSCs has created a passion among the researchers and the PCEs have been constantly increasing form $\sim$1% in 2011 to >14% by the evolution of many promising materials (Zhang et al. 2018a; Xiao et al. 2017a; Zhang et al. 2018b). To date, several high and low bandgap n-type molecular acceptors have been developed which includes perylene diimide, naphthalene diimide, diketopyrrolopyrrole and ladder type conjugated molecules containing fused heterocycles (Lin and Zhan 2016; Wadsworth et al. 2018; Zhang et al. 2018c; Xu and Gao 2018). However, it is quite difficult to rationally classify the acceptor materials because of their rapid development.

Ladder-type conjugated molecules containing fused aromatic or heterocyclic rings are important building blocks to develop donor and acceptor materials for OSCs (Wu et al. 2014). The major advantages of ladder-type coplanar building blocks are: (1) the extended π-systems which reduce the bandgaps and enhance light-harvesting ability of the molecules; (2) to facilitate π–π-stacking and improve the charge-transport property (Xu et al. 2012; Mishra et al. 2014). Moreover, the intrinsic electron disorder and the low dielectric constant of fullerene derivatives is the origin of geminate and nongeminate recombination during the charge transport process, which induces major photon-energy losses ($E_{loss}$) thus can limit the open-circuit voltage ($V_{OC}$). The typical energy losses in fullerene-based solar cells are between 0.6–1.0 eV which significantly lower the $V_{OC}$ and thus, the PCE. In comparison to fullerenes, the FFAs can further reduce the $E_{loss}$ and simultaneously

increase the photocurrent density in the devices. $E_{loss}$ is defined as the difference between the lowest optical bandgap of either donor or acceptor and $V_{OC}$ of the devices ($E_{loss} = E_g - eV_{OC}$). The $E_{loss}$ can be reduced by suppressing the nonradiative recombination losses.

The basic requirements for molecular design of high performance donor and acceptor materials have been discussed and summarized in several reviews (Mishra and Bäuerle 2012; Wadsworth et al. 2018; Yip and Jen 2012; Li et al. 2017). In this chapter, we will start with the basic development of OSCs and then provide insights for molecular design and evolution of high-performance of conjugated molecular electron acceptor materials. First, we summarize about various champion perylene derivatives and then comprehensively discuss the design concept for the development of FFAs in the last 2–3 years using ladder-type building block and their use to construct high performance OSCs. Finally, the concept and the usage of FFAs in ternary blend OSCs will be briefly discussed.

## 8.2 Basic Principles of Organic Solar Cells

Figure 8.1 presents the device architecture of both conventional and inverted devices. PCE is the important parameter used for the evaluation of solar cell performance. It is determined by three parameters, i.e. open-circuit voltage ($V_{OC}$), short-circuit current density ($J_{SC}$), and fill factors (FF), represented by the PCE = $(J_{SC} \times V_{OC} \times FF)/P_{in}$, where $P_{in}$ is the power of input light. The photoactive materials should show a broad and strong absorption in order to match with the solar irradiation spectrum, and to achieve high $J_{sc}$. Solar irradiation spectrum is very broad, spanning from visible to infrared region with maximum at around 700 nm. Therefore, an ideal absorption region for photoactive materials is from 400 to 900 nm. The $V_{OC}$ is typically related to the energy difference between the highest occupied molecular orbital (HOMO) of the donor and the lowest unoccupied molecular orbital (LUMO) of the acceptor and strongly depends on the balance between the photogeneration and recombination processes. The organic materials should have appropriate HOMO/LUMO energy levels for efficient charge separation and to reduce the energy losses. The FF depends on the morphology of the composite layer and efficient extraction of photogenerated charge carriers from the device. Morphology of the active layer plays a key role in determining the device performance. It has been stated earlier that 3-dimensional (3D) or twisted conformation is very important for suppression of molecular aggregates but that reduces the charge transport process. On the other hand, planar geometry can enhance the electron mobility but form strong π–π stacking. Therefore, a balance between the molecular structure and their aggregation behaviour should be maintained.

Another important parameter to be taken care of in organic material is the bandgap ($E_g$), which is the difference between HOMO and LUMO. Majority of the photoactive materials have $E_g$ values between 1.5 and 2.5 eV. Therefore, these conjugated oligomers/polymers are known as organic semiconductors. From the

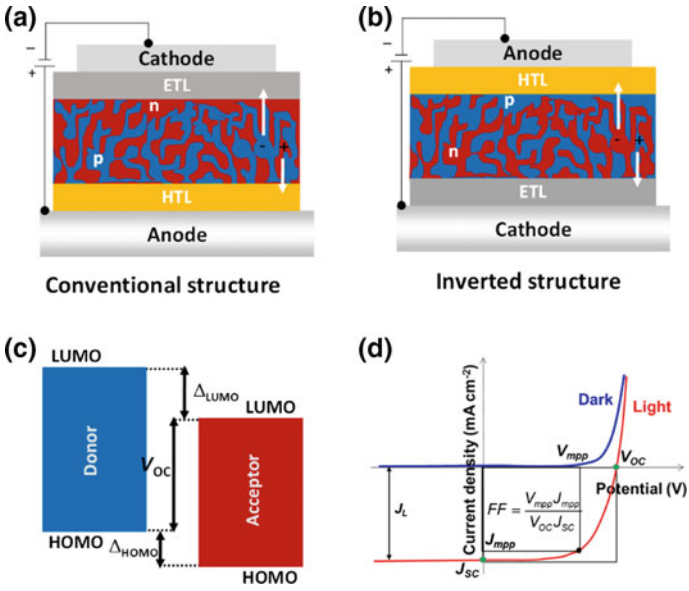


**Fig. 8.1** **a** Conventional and **b** inverted device structures employed in bulk heterojunction organic solar cells, electron donor is denoted by blue and acceptor by red. **c** Schematic energy levels diagram of electron donors and acceptors in OSCs. **d** Typical current density-voltage (*J-V*) curve showing different parameters

absorption spectra the optical bandgap ($E_g^{opt}$) value can be calculated using the equation $E_g = 1240/\lambda_{onset}$ (eV). The optical bandgap can also be measured from the crossing point between absorption and emission spectra. The HOMO/LUMO are generally estimated from the onset of oxidation and reduction waves measured by cyclic voltammetry.

## 8.3 Fullerene-Free Acceptors

In this section we will discuss the concept of different fullerene-free acceptors and their implementation as electron acceptor materials in conjunction with different polymer and oligomer donors. Figures 8.2 and 8.3 presents the structure of the polymer donors used in fullerene-free devices presented in this chapter.

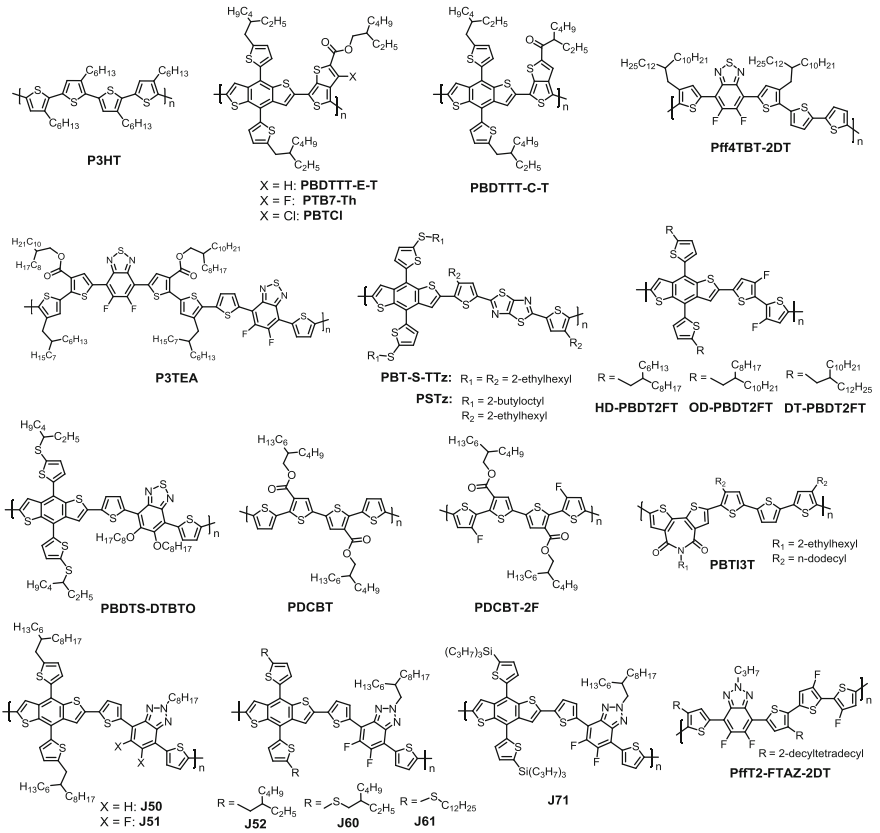


**Fig. 8.2** Structure of polymer donors used in fullerene-free solar cells

### *8.3.1 Perylene-Derivatives as Acceptor*

In the last 6–7 years, the number of publications about functional perylene tetracarboxylic diimides (PDI) derivatives, which can be considered as strong electron acceptor, dramatically increased. By varying the functional groups various perylene derivatives with different geometry have been developed and reviewed (Li and Wonneberger 2012; Fernandez-Lazaro et al. 2016; Liu et al. 2016a). In this section we will briefly discuss examples of some PDI derivatives used as electron acceptor materials in high performance OSCs (Fig. 8.4). PDI derivatives have shown to be one of the most important building blocks exhibiting high electron mobility and high electron affinity. Therefore, they can be attractive alternatives to replace fullerenes as electron transport layer in BHJSCs. However, despite these interesting properties the use of mono-PDI derivatives in OSC resulted in a dramatic reduction of PCEs due to strong aggregation tendencies of the PDI moieties. Therefore, in order to break the aggregation, it is important to reduce the

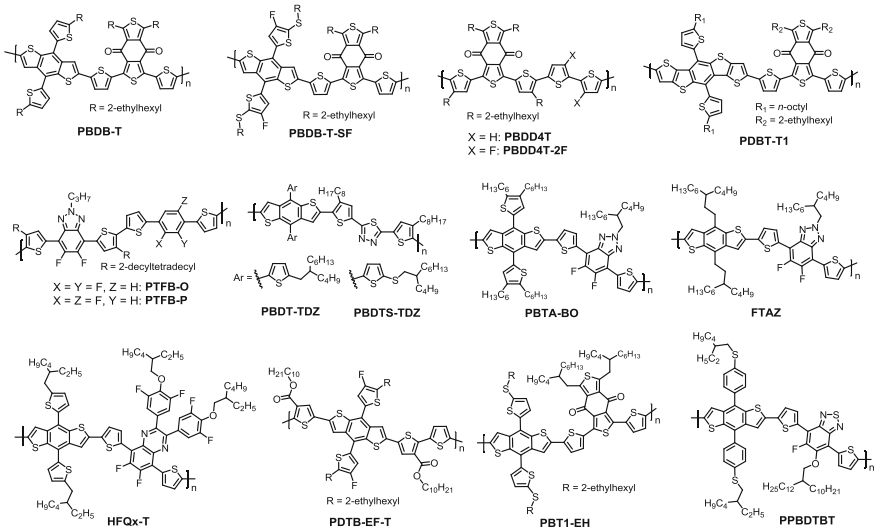


**Fig. 8.3** Structure of polymer donors used in fullerene-free solar cells

crystallinity of PDI units without affecting the charge transport properties. Narayan and co-workers reported a nonplanar PDI derivative namely, *N*,*N*-di-PDI which in combination with a donor polymer PBDTTT-C-T showed a PCE of 2.77% in comparison to 0.13% for planar mono-PDI (Table 8.1) (Rajaram et al. 2012). The enhancement was mainly due to almost 10 fold increase in the $J_{SC}$ value and FF. Marks and co-workers attached four phenyl groups at the ortho positions of PDI unit to prepare Ph-PDI which formed a slip-stacked packing structure (Hartnett et al. 2014). The bulky phenyl groups decrease germinate recombination and increase the driving force for charge separation. BHJSCs using Ph-PDI as acceptor and PBTI3T as donor afforded a PCE of 3.67% and high FF of 0.55. Sun group reported a twisted bay-substituted tetraphenyl-functionalized PDI monomer (TP-PDI) which exhibited a weak aggregation tendency in solid state and blend films (Cai et al. 2015). When blended with PTB7-Th a respectable PCE of 4.1% was achieved using 1% chloronaphthalene (CN) as solvent additive which is higher than the 3.3% obtained without additive. The results indicated that lowering of aggregation tendency of PDI moiety is a useful way of designing high performance FFAs.

Wang and co-workers reported a bay-linked twisted PDI dimer (di-PDI) with a twist angle of 70° which exhibited PCE of 3.63% using PBDTTT-C-T as donor and 1.5% DIO/1.5% CN as mixed additive (Jiang et al. 2014). The PCE was further improved to 5.9% when the polymer donor was replaced with PBDTT-F-TT in an inverted device structure (Zang et al. 2014). The polymer has a deeper HOMO and red-shifted absorption compared to that of PBDTTT-C-T, therefore match well with the di-PDI acceptor.

Wang and co-workers inserted a thiophene (Sun et al. 2015) and selenophene (Meng et al. 2016) units at the bay position of perylene unit to prepare SdiPDI-S

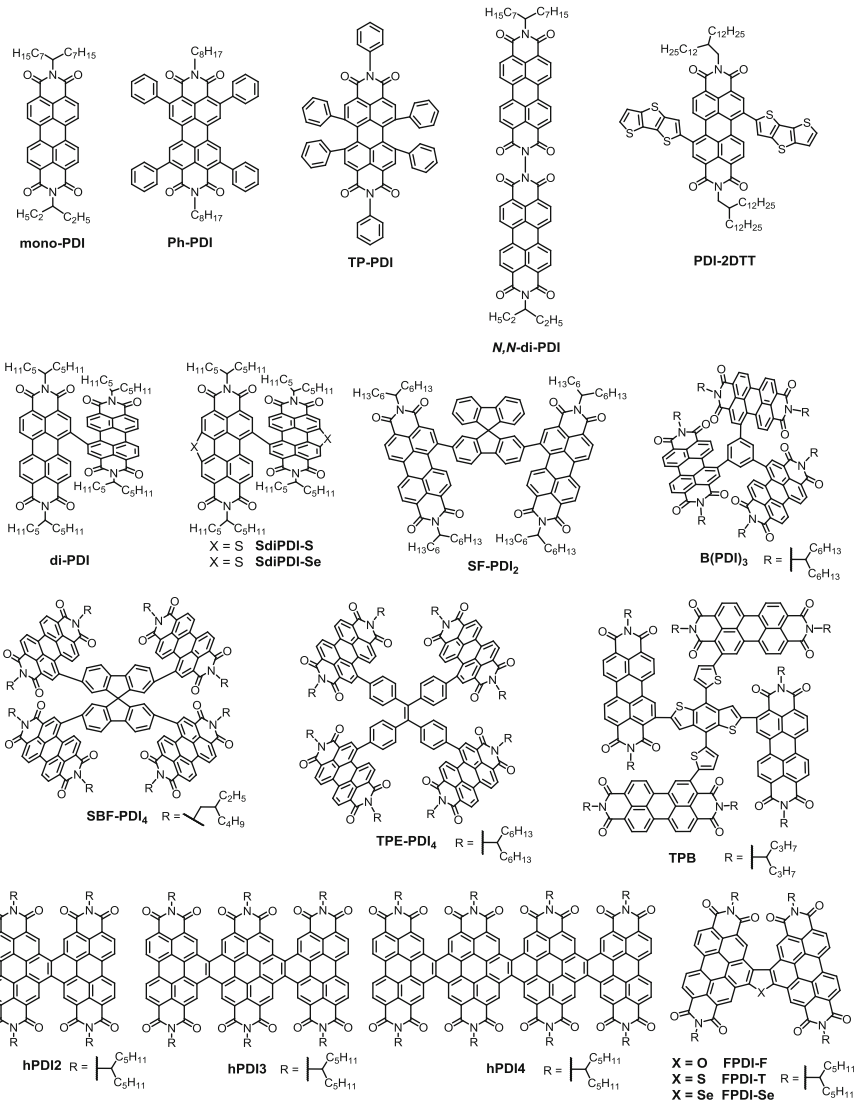


**Fig. 8.4** Structure of perylene diimide-based acceptors

and SdiPDI-Se. The introduction of heteroatoms increased the twisted conformation leading to higher LUMO energy level. BHJ solar cells using PDBT-T1:SdiPDI-S and PDBT-T1:SdiPDI-Se generated PCEs of 7.16 and 8.4%, respectively with 0.25% DIO as processing solvent additive. Yan and co-workers reported OSCs based on P3TEA/SF-PDI$_2$, which demonstrated an excellent PCE of 9.5% along with a high $V_{OC}$ of 1.11 V and a low $E_{loss}$ of 0.61 eV. Despite of negligible driving

**Table 8.1** Device parameters for perylene diimide based electron acceptor using various polymer donors

| Acceptor | Donor | $J_{SC}$ (mA cm$^{-2}$) | $V_{OC}$ (V) | FF | PCE (%) | References |
|---|---|---|---|---|---|---|
| mono-PDI | PBDTTT-C-T | 0.80 | 0.62 | 0.30 | 0.13 | Rajaram et al. (2012) |
| Ph-PDI | PBTI3T | 6.56 | 1.02 | 0.55 | 3.67 | Hartnett et al. (2014) |
| TP-PDI | PTB7-Th | 10.1 | 0.87 | 0.46 | 4.10 | Cai et al. (2015) |
| *N,N*-di-PDI | PBDTTT-C-T | 9.50 | 0.76 | 0.46 | 2.77 | Rajaram et al. (2012) |
| di-PDI | PBDTTT-C-T | 10.58 | 0.73 | 0.47 | 3.63 | Jiang et al. (2014) |
| di-PDI | PBDTT-F-TT | 12.30 | 0.80 | 0.59 | 5.90 | Zang et al. (2014) |
| SdiPDI-S | PDBT-T1 | 11.98 | 0.90 | 0.66 | 7.16 | Sun et al. (2015) |
| SdiPDI-Se | PDBT-T1 | 12.49 | 0.96 | 0.70 | 8.40 | Meng et al. (2016) |
| SF-PDI$_2$ | P3TEA | 13.27 | 1.11 | 0.64 | 9.50 | Liu et al. (2016a) |
| B(PDI)$_3$ | PTB7-Th | 13.12 | 0.83 | 0.52 | 5.65 | Li et al. (2016) |
| SBF-PDI$_4$ | PTB7-Th | 13.08 | 0.85 | 0.48 | 5.34 | Yi et al. (2016) |
| TPE-PDI$_4$ | PBDTT-F-TT | 11.70 | 0.91 | 0.52 | 5.53 | Liu et al. (2015) |
| TPB | PTB7-Th | 17.90 | 0.79 | 0.58 | 8.47 | Wu et al. (2016) |
| hPDI$_2$ | PTB7-Th | 11.0 | 0.79 | 0.59 | 5.21 | Zhong et al. (2014) |
| hPDI$_3$ | PTB7-Th | 14.50 | 0.81 | 0.67 | 7.90 | Zhong et al. (2015) |
| hPDI$_4$ | PTB7-Th | 15.20 | 0.80 | 0.68 | 8.30 | Zhong et al. (2015) |
| FPDI-F | PTB7-Th | 8,60 | 0.92 | 0.40 | 3.18 | Zhong et al. (2016) |
| FPDI-T | PTB7-Th | 12.48 | 0.94 | 0.58 | 6.72 | Zhong et al. (2016) |
| FPDI-Se | PTB7-Th | 11.10 | 0.92 | 0.56 | 5.77 | Zhong et al. (2016) |

force, the device exhibited fast and efficient charge separation, thus a minimal detrimental effects on charge transfer dynamics of solar cells (Liu et al. 2016b).

Yan group developed a 3D molecular acceptor TPE-PDI$_4$ using tetraphenylethylene core and PDI terminal units. The molecule exhibited weak molecular aggregation and small domains (≈20 nm) when blended with PBDTT-F-TT polymer showing PCE of 5.5% (Liu et al. 2015). A PDI derivative B(PDI)$_3$ containing central benzene unit tends to form twisted molecular geometry and suppressed the aggregation. A blend of PTB7-Th:B(PDI)$_3$ gave a good PCE of 5.65% (Li et al. 2016). A structurally non-planar SBF-PDI$_4$ containing a 9,9′-spirobi[9H-fluorene] (SBF) core and four peripheral PDIs achieved a PCE of 5.34% in BHJSCs using a low bandgap PTB7-Th as donor. The PCE was lower compared to PTB7-Th:PC$_{61}$BM device (7.03%) (Yi et al. 2016).

Yu and co-workers prepared a FFA, TPB in which four PDI units attached to BDT-Th core forming a conjugated structure. The blend of PTB7-Th:TPB films show favorable morphology and efficient charge separation. Inverted solar cells with 8% diphenylether (DPE) as solvent additive demonstrated a high PCE of 8.47% with an excellent high $J_{SC}$ values >18 mA cm$^{-2}$ (Wu et al. 2016).

Nuckolls and co-workers reported a series of fused helical PDI derivatives that showed red-shifted absorption with increase in the molecular length (Zhong et al. 2014; Zhong et al. 2015). A PCE of 5.2% was achieved using helical PDI dimer hPDI2 as the electron acceptor and PTB7-Th as donor. Femtosecond transient absorption spectroscopy revealed both electron and hole transfer processes at the donor-acceptor interfaces, indicating exciton generation in both the donor and acceptor phases. BHJSCs using PTB7-Th:hPDI3 and PTB7-Th:hPDI4 exhibited PCEs of 7.9 and 8.3%, respectively.

Jen and co-workers synthesized fused PDI dimers bridged with furan, thiophene and selenophene (FPDI-F, FPDI-T, FPDI-Se) (Zhong et al. 2016). The twist angle gradually increases with increasing chalcogen atoms in the bridge. Grazing incidence wide-angle X-ray scattering (GIWAXS) study revealed strong π–π stacking with favourable phase separation and appropriate length-scale domain in solid state. The molecule FPDI-T with thiophene bridge achieved the best PCE of 6.72% PTB7-Th as the donor.

### 8.3.2 *Pentafused Indacenodithiophene as Core Unit*

A major development in the design of A-D-A-type molecular acceptor was made by the use of multi-fused indaceno[2,1-*b*:6,5-*b*′]dithiophene (IDT) unit as the central donor block. IDT have been extensively used as building block to develop various high performance polymeric and oligomeric donors for OSCs owing to their excellent light-absorbing and hole transporting properties. Zhan and co-workers synthesized a new acceptor DC-IDT2T by using IDT as central donor block flanked with 3-dicyanomethyleneindan-1-one (DCI) electron acceptor (Bai et al. 2015). The compound was synthesized using a Stille-type cross-coupling reaction between 5-bromothiophene-2-carbaldehyde **2** and stannylated IDT **1** followed by Knoevenagel condensation with DCI unit (Scheme 8.1). The molecule exhibited a strong absorption with maximum at ∼720 nm and optical bandgap ($E_g^{opt}$) of 1.55 eV in thin films. The HOMO and LUMO energy levels of the DC-IDT2T were estimated to be −5.43 and −3.85 eV respectively. The solar cell device based on a low bandgap polymer donor PBDTTT-C-T (Huo et al. 2011) and DC-IDT2T acceptor (1.2:1, w/w) blend in ITO/PEDOT:PSS/active layer/Ca/Al structure exhibited a $V_{OC}$ of 0.90 V, $J_{SC}$ of 8.33 mA cm$^{-2}$, FF of 0.52%, and PCE of 3.93% without any post-treatment (Table 8.2).

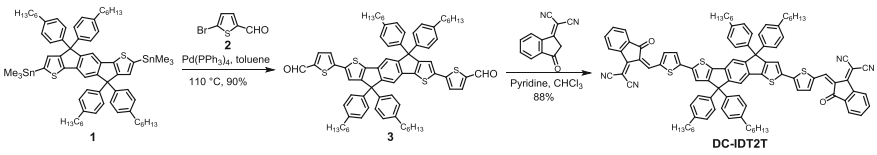


**Scheme 8.1** Synthesis pathway of DC-IDT2T molecular acceptor

**Table 8.2** Device parameters for multi-fused fullerene-free electron acceptor using various polymer donors

| Acceptor | Donor | $J_{SC}$ (mA cm$^{-2}$) | $V_{OC}$ (V) | FF | PCE (%) | References |
|---|---|---|---|---|---|---|
| DC-IDT2T | PBDTTT-C-T | 8.33 | 0.90 | 0.52 | 3.93 | Bai et al. (2015) |
| IDT-2BR | P3HT | 8.91 | 0.84 | 0.68 | 5.12 | Wu et al. (2015) |
| O-IDTBR | P3HT | 13.90 | 0.72 | 0.60 | 6.30 | Holliday et al. (2016) |
| EH-IDTBR | P3HT | 12.10 | 0.76 | 0.62 | 6.00 | Holliday et al. (2016) |
| O-IDTBR | P3HT | 12.55 | 0.72 | 0.67 | 6.05 | Gasparini et al. (2017) |
| IDT-2BR1 | PTB7-Th | 15.20 | 0.95 | 0.60 | 8.70 | Jia et al. (2017) |
| IDT-2BR | PTB7-Th | 13.00 | 0.99 | 0.60 | 7.70 | Jia et al. (2017) |
| O-IDTBR | PffBT4T-2DT | 15.00 | 1.07 | 0.62 | 9.95 | Baran et al. (2016) |
| IDT-2BM | PBDTTT-C-T | 10.10 | 0.77 | 0.55 | 4.26 | Bai et al. (2015) |
| IEIC | PTB7-Th | 13.55 | 0.97 | 0.48 | 6.31 | Lin et al. (2015a) |
| IEIC | PffT2-FTAZ-2DT | 12.20 | 1.0 | 0.59 | 7.30 | Lin et al. (2015b) |
| IEICO | PBDTTT-E-T | 17.70 | 0.82 | 0.58 | 8.40 | Yao et al. (2016b) |
| IEIC | PBDTTT-E-T | 11.70 | 0.90 | 0.47 | 4.90 | Yao et al. (2016b) |
| IEICO-4F | PTB7-Th | 25.30 | 0.73 | 0.59 | 10.9 | Yao et al. (2017a) |
| IEICO-4F | PBDTTT-E-T | 22.30 | 0.69 | 0.59 | 9.08 | Yao et al. (2017a) |
| IEICO-4F | J52 | 21.9 | 0.73 | 0.59 | 9.40 | Yao et al. (2017a) |
| IEICO-4F | PBDTS-DTBTO | 24.70 | 0.72 | 0.51 | 9.10 | Yao et al. (2017a) |
| IEICO-4F | PTB7-Th | 27.30 | 0.71 | 0.66 | 12.8 | Song et al. (2018) |
| IffBR | PBTA-BO | 11.77 | 1.01 | 0.53 | 6.34 | Zhong et al. (2017) |
| IDT-BTT1 | PTB7-Th | 12.54 | 0.89 | 0.52 | 5.79 | Xu et al. (2018) |
| IDT-BTT2 | PTB7-Th | 20.33 | 0.71 | 0.63 | 9.07 | Xu et al. (2018) |
| DC-IDTTz | PTB7-Th | 15.94 | 0.80 | 0.66 | 8.40 | Yu et al. (2017a) |
| IDTCR | PTB7-Th | 11.00 | 1.11 | 0.50 | 6.10 | Ye et al. (2017) |
| IDTzCR | PTB7-Th | 13.80 | 1.04 | 0.61 | 8.71 | Ye et al. (2017) |
| IDT-BOC6 | PBDB-T | 17.52 | 1.01 | 0.54 | 9.60 | Liu et al. (2017) |
| IDT-BC6 | PBDB-T | 5.63 | 0.92 | 0.44 | 2.30 | Liu et al. (2017) |
| ATT-1 | PTB7-Th | 16.48 | 0.87 | 0.70 | 10.07 | Liu et al. (2016c) |
| ATT-2 | PTB7-Th | 20.75 | 0.73 | 0.63 | 9.58 | Feng et al. (2017) |
| IDIC | PDBT-T1 | 15.05 | 0.89 | 0.65 | 8.71 | Lin et al. (2016a) |
| IDIC | FTAZ | 20.80 | 0.84 | 0.72 | 12.50 | Lin et al. (2018) |
| IDIC | PDBT-T1 | 15.85 | 0.85 | 0.68 | 9.20 | Lin et al. (2016b) |
| IDT-IC | PDBT-T1 | 13.39 | 0.92 | 0.60 | 7.39 | Lin et al. (2016b) |
| IDIC | PSTZ | 16.39 | 0.88 | 0.70 | 10.11 | Zhang et al. (2017) |
| IDIC8-M | PBDB-T | 15.70 | 0.86 | 0.72 | 9.65 | Zhang et al. (2018d) |
| IDT-2B | PBDB-T | 13.30 | 0.89 | 0.54 | 6.42 | Feng et al. (2017) |
| IDT-OB | PBDB-T | 16.18 | 0.88 | 0.71 | 10.12 | Feng et al. (2017) |

Since then many new molecular acceptors were developed using IDT core (Fig. 8.5). The compound IDT-2BR containing IDT core and 3-ethylrhodanine terminal units separated by benzo[*c*] [1,2,5] thiadiazole (BT) spacer (Wu et al. 2015). The HOMO and LUMO energy levels were at −5.52 and −3.69 eV, respectively that fits well with the energy levels of P3HT. The hexylphenyl groups attached to the IDT moiety exhibit a dihedral angle of ∼115° to the molecular plane. OSCs prepared using P3HT:IDT-2BR (1:0.6, w/w) processed with 3 vol% chloronaphthalene (CN) as solvent additive demonstrated an improved PCE of 5.12%, which was higher than that of P3HT:$PC_{61}BM$ device (3.63%).

McCulloch and co-workers modified the IDT group by replacing hexylphenyl groups with *n*-octyl in O-IDTBR and 2-ethylhexyl group in EH-IDTBR (Holliday et al. 2016). In thin films both O-IDT-BR ($\lambda_{max}$ = 690 nm) and EH-IDTBR ($\lambda_{max}$ = 673 nm) showed red-shifted absorption compared to IDT-2BR ($\lambda_{max}$ = 658 nm). Most interestingly, when the films were annealed at 130 °C for 10 min. the absorption band of O-IDTBR significantly shifted to 731 nm while no change was observed for EH-IDTBR showing the effect of alkyl chain on intermolecular packing. OSC devices prepared using O-IDTBR:P3HT and EH-IDTBR:P3HT blend in an inverted device ITO/ZnO/P3HT:IDTBR/$MoO_3$/Ag structure promoted by thermal annealing at 130 °C for 10 min. afforded PCE of 6.3 and 6.0%,

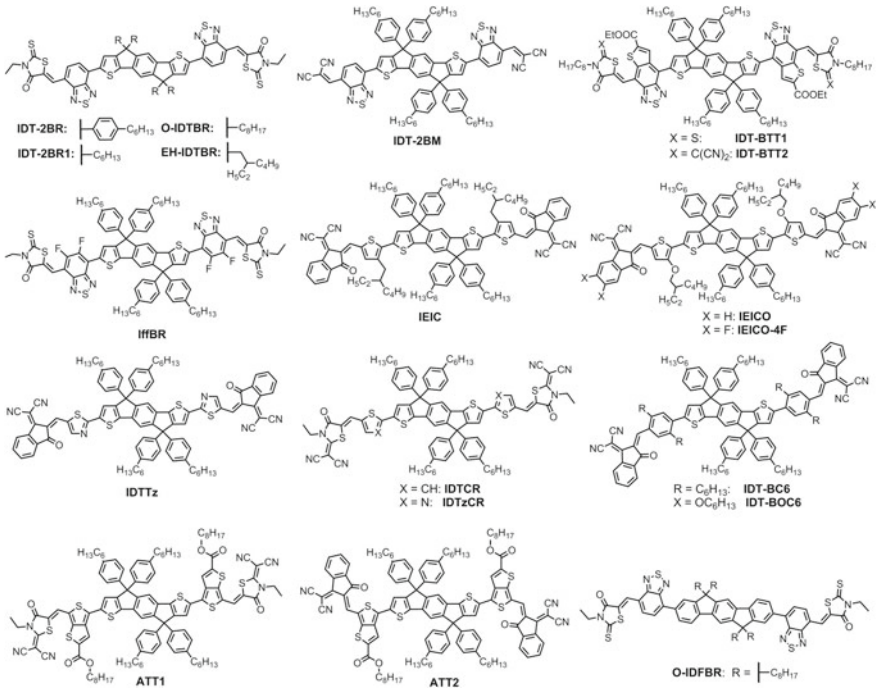


**Fig. 8.5** Structure of A-D-A oligomers with pentafused core units

respectively. This is significantly higher than the P3HT:$PC_{61}BM$ devices (3.7%). A good thermal stability was observed for O-IDTBR:P3HT device in ambient condition compared to P3HT:$PC_{61}BM$ device. Hexyl-substituted analogue IDT-2BR1 in combination with PTB7-Th polymer donor exhibited a higher PCE of 8.7% compared to 7.7% for PTB7-Th:IDT-2BR device due to the reduced steric hindrance and stronger molecular packing (Jia et al. 2017). IDT-2BR1 showed a higher electron mobility ($2.2 \times 10^{-3}$ $cm^2$ $V^{-1}$ $s^{-1}$) than IDT-2BR ($3.4 \times 10^{-4}$ $cm^2$ $V^{-1}$ $s^{-1}$) due to the reduced steric hindrance and ordered molecular packing. The PCE of O-IDTBR was further improved by using a highly crystalline low band gap polymer PffBT4T-2DT as donor (Baran et al. 2016). Device based on PffBT4T-2DT: O-IDTBR (1:1 w/w) gave a higher PCE of 9.95% and outperform PffBT4T-2DT: $PC_{71}BM$ devices (7.5%) mostly due to significant increase in the $V_{OC}$ to 1.07 V from 0.76 V. The fullerene-free devices showed low voltage loss ($E_{loss}$) of 0.55 eV due to suppressed non-radiative recombination without compromising the $J_{SC}$ value.

Brabec and co-wokers recently demonstrated a very low burn-in loss in P3HT: O-IDTBR-based fullerene-free solar cell. After 2000 h light soaking the device loss about 5% of its initial PCE of 6.05% (Gasparini et al. 2017). In contrast, P3HT: $P_{61}BM$ device showed a severe burn-in extended up to few hundred hours and levels off at ~34% of initial value. The loss is mainly due to reduction of $J_{SC}$ values due to dimerization of fullerene derivative under light soaking.

The replacement of terminal 3-ethylrhodanine groups of IDT-2BR with dicyanovinyl goups in IDT-2BM resulted in a decrease in PCE to 4.26% using PBDTTT-C-T as donor polymer. The lower performance was due to lower $V_{OC}$ and $J_{SC}$ values and unbalanced hole and electron mobilities ($\mu_e/\mu_h$ = 25) (Bai et al. 2015).

The solubility of DC-IDT2T was further improved by introduction of alkyl groups on the thiophene rings in IEIC which improves the solution-processability as well as molecular crystallinity in film state (Lin et al. 2015a). The introduction of alkyl groups slightly blue-shifted the absorption band with maximum at 720 nm and optical bandgap of 1.57 eV. The HOMO and LUMO energy levels were at −5.42 and −3.82 eV respectively. Solar cells prepared with PTB7-Th:IEIC blend (1:1.5 w/w) and a perylene diimide (PDIN) derivative as a cathode interlayer in a device structure ITO/PEDOT:PSS/active layer/PDIN/Al, gave PCEs of up to 6.31%, compared to 5.24% when Ca was used as the cathode interlayer. Despite low FF of 0.48, the device generated a high $V_{OC}$ of 0.97 V and $J_{SC}$ of 13.55 mA $cm^{-2}$.

Yan and co-workers used a highly crystalline large bandgap fluorinated polymer PffT2-FTAZ-2DT which has a complementary absorption to IEIC acceptor, achieving broad spectral coverage and strong temperature dependent aggregation (TDA) (Lin et al. 2015b). Solar cell devices were fabricated with an inverted structure of ITO/ZnO/PffT2-FTAZ-2DT:IEIC (1:1.5 w/w)/$V_2O_5$/Al and generated best PCE of 7.3% and $V_{OC}$ of 1.0 V. The result demonstrated that a HOMO energy offset of 0.17 eV between the donor and acceptor is sufficient for efficient hole transfer from IEIC to PffT2-FTAZ-2DT. The PffT2-FTAZ-2DT:IEIC device generated a balanced electron and hole mobilities ($\mu_h/\mu_e$ = 1.1) which is very important for reducing build-up space charge density and bimolecular recombination achieving high FF of 0.59.

Hou and co-workers substituted the 2-ethylhexyl chain of thiophene groups in IEIC by electron donating alkoxy groups in IEICO acceptor (Yao et al. 2016b). The introduction of oxygen atom red-shifted the absorption maximum to near-IR region (805 nm) with an absorption onset of 925 nm, corresponding to an $E_g^{opt}$ of 1.34 eV, which is 0.16 eV lower than that of IEIC (1.50 eV). In comparison with IEIC, the HOMO level of IEICO was shifted upward by 0.15 eV while the LUMO level slightly lowered by 0.05 eV. A low band gap polymer PBDTTT-E-T was chosen as donor material which provide a sufficient driving force for exciton dissociation and to obtain a complementary absorption with IEICO. The devices were prepared using ITO/PEDOT:PSS/BHJ/PFN-Br/Al, exhibiting impressive PCE of 8.4% compared to 4.9% measured for PBDTTT-E-T:IEIC devices. The higher PCE was mainly due to enhanced $J_{SC}$ and FF values. The PBDTTT-E-T:IEICO-based device exhibited a $V_{OC}$ as high as 0.82 V, which is a remarkable value considering low optical gap of 1.34 eV, representing an low energy loss ($E_{loss}$) of 0.52 eV. The external quantum efficiency (EQE) spectra of PBDTTT-E-T:IEICO device displayed a broad and higher spectral response from 300–900 nm, while it is limited to about 800 nm for the PBDTTT-E-T:IEIC device.

The introduction of electronegative fluorine atoms into the organic molecule can have numerous advantages. For instance, reduce the bandgap and stabilize the HOMO/LUMO energy levels, (Zhang et al. 2013; Kawashima et al. 2016) improve both inter/intramolecular interactions as a result of the noncovalent F···H, S···F, C–F···π interactions, increase face-on crystalline orientation and π–π stacking with larger domain purity, thus facilitate charge transport (Reichenbächer et al. 2005). It has been reported earlier that in fullerene-based solar cell the introduction of fluorine atom in the molecular backbone can improve the degree of orientation of the backbone and thus the crystalline properties and optimize domain size in the active layer (Liu et al. 2014). In order to make compatible with low bandgap polymers, such as PTB7-Th also called as PBDTTT-EFT, Hou group introduced fluorine atoms on the terminal DCI groups in IEICO (Yao et al. 2017a). The introduction of fluorine atoms down-shifted the LUMO energy level (−4.19 eV) of IEICO-4F and exhibited an ultra-small optical bandgap of 1.24 eV with a strong absorption band extended up to 1000 nm due to enhanced intramolecular charge transfer (ICT). Using PTB7-Th as the donor polymer, the IEICO-4F-based device enable a high PCE of 10.9% using device structure ITO/PEDOT:PSS/BHJ/PFN-Br/Al. Interestingly, despite low $E_{loss}$ of 0.51 eV, the device gave an impressive $J_{SC}$ value of 22.8 mA $cm^{-2}$. IEICO-4F was also found to be compatible with various other donor polymers J52, PBDTTT-E-T, PBDTS-DTBTO and PBDB-T generating PCEs close to 9% and $J_{SC}$ values over 20 mA $cm^{-2}$.

Very recently, using an inverted device structure with ZnO and $MoO_3$ as electron and hole transport layers and CN as solvent additive the PCE of PTB7-Th:IEICO:4F device was significantly improved to 12.8% with an outstanding record $J_{SC}$ of 27.3 mA $cm^{-2}$ and FF of 0.66 with an active layer thickness of 200 nm (Song et al. 2018). The high photocurrent was mainly ascribed to the increased π–π

coherence length of the acceptor, the domain purity and a balanced hole and electron mobility.

Cao and co-workers reported a novel electron acceptor IffBR by introducing fluorine atoms at the BT bridge of IDT-2BR to further lower the energy levels. The HOMO and LUMO energy levels were down-shifted to −5.71 and −3.77 eV, respectively. Using a ITO/PEDOT:PSS/BHJ/PFN-Br/Al device structure PBTA-BO:IffBR showed a PCE of 6.34% compared to 4.73% for PBTA-BO: $PC_{71}BM$ (Zhong et al. 2017).

Xu et al. prepared two molecular acceptor IDT-BTT1 and IDT-BTT2 consisting of a thiophene-fused benzothiadiazole (BTT) as bridge unit connected to IDT core and 3-otcylrhodanine or 3-otcyl-2-(1,1-dicyanomethylene)rhodanine as the terminal groups (Xu et al. 2018). Compared to IDT-2BR ($\lambda_{max}$ = 656 nm), the fusion of a thiophene ring into the BT unit helps to stabilize the quiniod structure, thus red-shifted and broaden the intramolecular charge transfer (ICT) absorption bands and reduce the bandgap in thin films ($\lambda_{max}$ = 785 nm, $E_g^{opt}$ = 1.40 eV for IDT-BTT1 and $\lambda_{max}$ = 770 nm, $E_g$ = 1.36 eV for IDT-BTT2). The HOMO/LUMO levels of these acceptors were down-shifted compared to IDT-2BR. With PTB7-Th as donor the device based on IDT-BTT1 with 1% CN obtained a PCE of 5.79%, whereas, the PCE of IDT-BTT2:PTB7-Th device with 1% DIO reached excellent PCE of 9.07% with a high $J_{SC}$ of 20.33 mA $cm^{-2}$, which is attributed to stronger intermolecular interaction between the donor and acceptor.

Yu et al. introduced thiazole units as π-bridges instead of thiophene group in IDT based molecular acceptor, IDTTz (Yu et al. 2017a). The introduction of thiazole unit increase the planarity of the backbone due to N···S non-covalent interaction, thus reduce the reorganization energy and increase charge transport properties. The absorption band was blue-shifted to 699 nm with $E_g^{opt}$ of 1.58 eV. Both HOMO/LUMO energy levels were stabilized by the introduction of thiazole unit. In an inverted device structure using ITO/ZnO/active layer/$MoO_3$/Ag the device based on PTB7-Th:IDTTz exhibited a PCE of 8.4%, which is significantly high compared to the corresponding DC-IDT2T-based device (4.08%). Despite slight reduction in the $V_{OC}$ value due to decreased $HOMO_{donor}/LUMO_{acceptor}$ offset, the IDTTz device gave an impressive $J_{SC}$ of 15.94 mA $cm^{-2}$ and FF of 0.66. The increased $J_{SC}$ could be due to larger $\Delta E_{LUMO}$ (0.28 eV) between PTB7-Th and IDT-Tz compared to DC-IDT2T ($\Delta E_{LUMO}$ = 0.15 eV), leading to a more efficient exciton dissociation and charge transport.

Two new acceptors IDTCR and IDTzCR were prepared by introducing thiophene and thiazole units as π-spacer between the IDT core and 3-ethyl-2-(1,1-dicyanomethyl-ene)rho-danine termini (Ye et al. 2017). With PTB7-Th as donor and IDTCR as acceptor the device with ITO/ZnO/PEIE/D:A/$MoO_3$/Ag structure, where PEIE was used as cathode buffer layer gave PCE of 6.1%, $J_{SC}$ of 11.0 mA $cm^{-2}$, $V_{OC}$ of 1.11 V and a FF of 0.50. Interestingly, PTB7-Th:IDTzCR device gave an improved PCE of 8,71% due to high $J_{SC}$ (13.80 mA $cm^{-2}$) and FF (0.61) values. The increase of $J_{SC}$ and FF and reduction of $V_{OC}$ (1.04 V) values were ascribed to the increased LUMO/LUMO offset (0.11 vs. 0.01 eV) and a

homogeneous morphology with small domains for IDTzCR-based device, which facilitate exciton dissociation and charge transport. Most importantly, the IDTCR- and IDTzCR-based OSCs afforded a very low $E_{loss}$ of ~0.46 and 0.43 eV, respectively, a significant value for the "narrow-Bandgap donor:wide-bandgap acceptor" systems.

Bo group introduced alkoxy-substituted benzene as π-bridge in IDT-BOC6 to lock the molecular planarity by O···H, S···O intramolecular non-covalent interactions (Liu et al. 2017). The conformational locking due to the presence of oxygen atoms effectively broaden and red-shifted the absorption spectrum by ~96 nm, decreased the bandgap, improved the electron mobility, and reduced nonradiative energy losses compared to alkylated benzene analogue IDT-BC6. Inverted OSCs based on PBDB-T:IDT-BOC6 resulted in a PCE of 9.6%. In contrast, solar cells based on IDT-BC6 acceptor with lack of planar conformation, i.e. conformational twist between the alkylated phenyl and thiophene units, gave a PCE of only 2.3%.

Zhu group extended the design strategy for IDT-based acceptor by introducing an ester-substituted thieno[3,4-*b*]thiophene spacer into IDT core and 3-ethyl-2-(1,1-dicyanomethyl-ene)rhodanine in ATT-1 and DCI group in ATT-2 (Liu et al. 2016c; Feng et al. 2017). Due to strong electron accepting ability of DCI acceptor the absorption band of ATT-2 was red-shifted ($\lambda_{max}$ = 835 nm) compared to ATT-1 ($\lambda_{max}$ = 736 nm), leading to small $E_g^{opt}$ of 1.32 eV for ATT-2 versus 1.54 eV for ATT-1. Although both molecules showed similar HOMO level, the LUMO level of ATT–2 was down-shifted by 0.27 eV. BHJ solar cells prepared using PTB7-Th as donor and ATT–1 as acceptor the device with ITO/PEDOT:PSS/BHJ/PFN/Al structure gave PCE of up to 10.07% with 1% DIO as additive. The ATT-2-based device was fabricated using an inverted device configuration of ITO/ZnO/BHJ/$MoO_3$/Ag using PTB7-Th as donor and 2% CN as solvent additive, which gave a PCE of 9.58% and $J_{SC}$ of 20.8 mA $cm^{-2}$. The addition of solvent additives improved the charge transport properties by enhancing acceptor crystallinity and reducing D:A mixing in the blend. The high $J_{SC}$ value was ascribed to the efficient exciton dissociation and negligible bimolecular recombination. However, the $V_{OC}$ value decreases to 0.73 V (0.87 V for ATT1-device) due to lowering of LUMO energy level. Benefiting from the absorption in the NIR region, a semitransparent device was prepared using PTB7-TH:ATT-2 blend which achieved a PCE of 7.74% with 37% transparency.

Lin et al. reported a planar pentafused IDT-based electron acceptor IC-C6IDT-IC also known as IDIC without any π-bridge (Fig. 8.6) (Lin et al. 2016a). The molecule showed absorption maximum at 716 nm with bandgap of 1.62 eV. High electron mobility of $1.1 \times 10^{-3}$ $cm^2$ $V^{-1}$ $s^{-1}$ was extracted from space charge limiting current (SCLC) measurement. The as-cast inverted solar cells based on IDIC as acceptor and PDBT-T1 as donor (1:1 w/w) exhibited PCEs of up to 8.71% without any additional treatments. The active layer showed appropriate phase separation, strong "face-on" π–π ordering and relatively good charge transport. The authors demonstrated that planar electron acceptors can exhibit very promising performance and further challenges the traditional opinion on FFA that

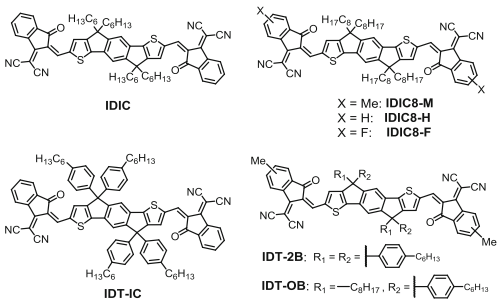


**Fig. 8.6** Molecular structure of IDT-based molecular acceptors

they must have twisted backbones to suppress self-aggregation and large phase separation. With a medium band gap polymer donor FTAZ, the IDIC-based OSC device demonstrated an outstanding PCE of 12.5% with a high $J_{SC}$ of 20.8 mA cm$^{-2}$ and $V_{OC}$ of 0.84 V and exceptional FF of 0.72 using diiodooctane (DIO) as solvent additive (Lin et al. 2018). In contrast, the control device FTAZ: $PC_{61}BM$ gave a much lower PCE of ~6%. Transient absorption spectroscopy reveals that exciting either the donor or the acceptor component efficiently generates mobile charges, and do not suffer from recombination to triplet states. This clearly shows that the proper choice of donor or acceptor components in OSCs is very import to achieve high performance. Zhan and co-workers obtained a higher PCE of 9.2% using PDBT-T1 as donor and IDIC as acceptor in an inverted device structure (Lin et al. 2016b). In comparison to the phenyl counterpart, IDT-IC obtain a lower PCE of 7.39%. The IDIC-based device showed a reduced $V_{OC}$ (0.85 V) compared to IDT-IC (0.92 V) due to lower LUMO level (IDIC: −3.91 eV; IDT-IC: −3.83 eV). However, due to better ordering of the D:A molecule a high FF and $J_{SC}$ was observed for IDIC device. Xiao et al. reached a PCE of 6.05% using PBDB-T as donor and IDT-IC as acceptor in an inverted device structure ITO/ZnO/active layer/$MoO_3$/Ag (Xiao et al. 2017b).

Zhang et al. employed an in situ solvent annealing method i.e. solvent annealing during spin-coating (SC-SVA) to improve the crystallinity of the FFA without significant interference on the domain size. BHJ device based on a wide bandgap polymer PSTZ (2.0 eV) and IDIC acceptor after SC-SVA treatment generated a PCE of 10.11% compared to 9.2% for the as cast device mostly due to the improved photocurrent (Zhang et al. 2017). The strong π–π stacking in the out-of-plane direction indicate that both PSTZ and IDIC have preferred face-on orientation relative to the substrate by SC-SVA.

Substitution of electron donating methyl group on the DCI acceptors in IDIC8-M slightly blue-shifted the absorption band with maximum around 705 nm compared to IDIC. The planar acceptor, when combined with the PBDB-T polymer donor in an inverted structure, exhibited a PCE of 9.65% with high FF of 0.72 and $J_{SC}$ of 15.70 mA cm$^{-2}$ (Zhang et al. 2018d).

Bo and co-workers reported FFA IDT-OB containing asymmetric side chains which exhibited enhanced solubility, close molecular packing and thus a better

phase separation compared to symmetrical analogue IDT-2B (Feng et al. 2017). IDT-OB showed a red-shifted absorption band ($\lambda_{max}$ = 697 nm) compared to IDT-2B ($\lambda_{max}$ = 672 nm) in thin film due to closure molecular packing resulted from the octyl chains. BHJ device based on PBDB-T:IDT-OB blend with an inverted device structure ITO/ZnO/active layer/$MoO_3$/Ag led to a high PCE of 10.12% compared to 6.42% for IDT-2B-based device. IDT-OB-based device showed a higher $J_{SC}$ (16.2 vs. 13.3 mA $cm^{-2}$) and FF (0.71 vs. 0.54) than that of IDT-2B-based device due to more balanced hole and electron mobility (1.3 vs. 4.03). Most importantly, IDT-OB-based device can maintain high PCE of 9.17% even with an active layer thickness 210 nm. Grazing-incidence wide-angle X-ray scattering (GIWAX) study revealed π–π stacking diffractions of PBDB-T:IDT-OB blends along out-of-plane direction showing face-on orientation, beneficial for charge transport. In contrast, PBDB-T:IDT-2B blends exhibit π–π stacking diffractions along both the out-of-plane and in-plane directions showing co-existence of both face-on and edge-on orientations in the film.

### 8.3.3 *Indacenodithieno[3,2-b]Thiophene-Based Multi-fused Systems*

In order to further tune the molecular properties Zhan and co-workers elongated the fused ring system in the molecular backbone by introducing indacenodithieno[3,2-*b*]thiophene core. They have synthesized an A-D-A-type organic semiconductor ITIC for use as fullerene-free acceptor (FFA) in OSCs (Lin et al. 2015). The molecule was synthesized by lithiation of fused indacenodithieno[3,2-*b*]thiophene (IT) followed by quenching with dimethylformamide (DMF) to afford IT-CHO in 93% yield. Final Knoevenagel condensation with DCI unit gave ITIC in 21% yield (Scheme 8.2). The molecule showed good thermal stability (>345 °C). In thin film ITIC exhibited strong absorption between 500 and 750 nm peaking at 702 nm with an optical bandgap of 1.59 eV. The HOMO and LUMO energy levels estimated from the onset of oxidation and reduction waves were −5.48 and −3.83 eV, respectively. BHJ OSCs were prepared using ITIC as acceptor and a low band gap polymer PTB7-Th based on benzodithiophene and thieno[3,4-*b*]thiophene units as donor (HOMO/LUMO = −5.2 eV/−3.59 eV) using device structure ITO/PEDOT:PSS/PTB7-Th:ITIC/PDIN/Al. PDIN, a perylene derivative served as a cathode

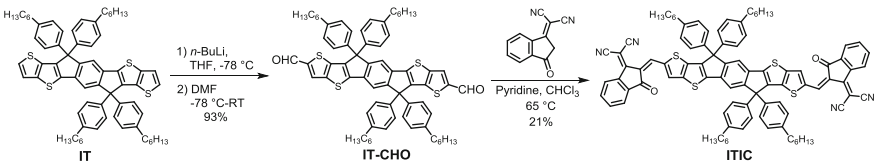


**Scheme 8.2** Synthesis pathway of heptafused ITIC molecular acceptor

interlayer which can lower the work function of the electrode. The devices with D:A weight ratio of 1:1.3 generated best PCE of 6.8%, $V_{OC}$ of 0.81 V and $J_{SC}$ of 14.21 mA cm$^{-2}$ without any post-treatment, the highest value reported at that time for A-D-A-type small molecular acceptors (Table 8.3). The PCE value is even higher compared to PTB7-Th:$PC_{61}BM$ device (PCE = 6.05%) mainly due to lower $J_{SC}$ of 11.94 mA cm$^{-2}$. The higher performance mainly attributed to good film morphology, better phase separation and balanced charge transport properties ($\mu_e/\mu_h$ = 2.6). The PTB7-Th:ITIC-based device using SC-SVA treatment exhibited a PCE of 7.51% compared to 6.25% for the as cast device and 7.17% for post-SVA processing devices (Zhang et al. 2017). The in situ SC-SVA method improve the individual crystallinity of the donor and acceptor in the blend without hampering the phase separation, thus improve the molecular ordering for better charge transport.

The initial photovoltaic performance of n-type ITIC was very impressive. To further increase the PCE of the device it is very important to develop donor material with suitable energy levels, which match well with the fullerene-free acceptor and provide complementary absorption to achieve panchromatic absorption along with suppressed bimolecular recombination and minimize energy loss. In this respect various wide band gap polymers were developed and tested with ITIC acceptor. The rational selection of polymer donor is very important to obtain high performance devices. The absorption spectrum of ITIC has a strong overlap with PTB7-Th polymer. Therefore, Hou and co-workers developed a wide bandgap (WBG) polymers PBT-S-TTz based on benzo[1,2-*b*:4,5-*b*′]dithiophene (BDT) and thiophene-thiazolothiazole (TTz) units (Zhao et al. 2016b). The polymer showed absorption peak at around 600 nm with optical gap of 1.95 eV in thin films. Fullerene-free OSCs fabricated using ITO/PEDOT:PSS /PBT-S-TTz:ITIC (1:1)/Ca/Al device structure generated high PCE of 8.22% after thermal annealing at 140 °C. A slightly lower PCE of 7.92% was observed in OSCs based on a PBT-S-TTz:$PC_{71}BM$ active layer. The same group further synthesized another WBG polymer PBDTS-DTBTO comprising alkylthio-substituted thienyl-benzodithiophene as weak donor and benzothiadiazole as acceptor unit (Yao et al. 2016c). The polymer displayed a strong absorption at ~640 nm and wide bandgap of 1.76 eV with strong π–π interaction. The HOMO/LUMO energy levels (−5.24/−3.60 eV) of the polymer matches well with ITIC. OSCs fabricated using ITO/(PEDOT:PSS/PBDTS-DTBTO:ITIC (1:1)/PFN-Br/Al structure generated PCE of 9.09% after thermal annealing at 100 °C in comparison to 6.7% for $PC_{71}BM$ based devices. The higher PCE for ITIC-based device compared to $PC_{71}BM$ was mainly due to high $V_{OC}$ of 0.84 vs. 0.77 V and $J_{SC}$ of 16.6 vs. 13.17 mA cm$^{-2}$. Grazing incident wide angle X-ray scattering (GIWAXS) study revealed that the thermal annealing promotes the inter-chain packing with considerably increased face-on π–π stacking. The device were relatively less sensitive to active layer thickness keeping PCEs over 8% between 50 and 200 nm.

When a wide bandgap polymer donor PBDB-T was used in combination with ITIC acceptor the OSC devices (ITO/ZnO/BHJ-layer (1:1 wt. ratio)/$MoO_3$/Al) demonstrated a high PCEs up to 11.21% with $V_{OC}$ of 0.90 V and $J_{SC}$ of

16.8 mA $cm^{-2}$ and excellent FF of 0.74 using 0.5 vol% DIO as solvent additive (Zhao et al. 2016c). The active layer also showed a balanced charge transport property due to low ratio of electron and hole mobility $\mu_e/\mu_h$ = 1.49. Under similar condition the control PBDB-T:$PC_{71}BM$ device gave comparatively low PCE of 7.45%.

Hou group reported a new polythiophene derivative PDCBT containing alkylester side chain as donor and ITIC as acceptor in ITO/PEDOT:PSS/PDCBT:ITIC (1:1 wt ratio)/PFN-Br/Al device structure that exhibited an excellent PCE of 10.16% after thermal annealing at 160 °C for 10 min compared to 9.5% without annealing (Qin et al. 2016). Most surprisingly, following similar optimization condition the P3HT:ITIC device generated a very poor PCE of 1.25%. Due to ester-functionality PDCBT showed deeper HOMO (−5.31 eV) and LUMO (−3.0 eV) levels compared to P3HT (HOMO/LUMO: −5.06 eV/−2.76 eV) which is beneficial for high $V_{OC}$ and efficient charge transport. In comparison to P3HT the excellent performance of PDCBT-based device is mainly attributed to well-distributed nano-fibrillar structure with face-on orientation, which is favourable for efficient charge generation and extraction as confirmed by TEM and grazing incident wide angle X-ray scattering (GIWAXS) studies. It is important to note that the edge-on orientation of pristine PDCBT polymer was changed to face-on after blending with ITIC, indicating a some kind of favourable interactions between PDCBT and ITIC, probably due to dipole–dipole interactions of the polar alkylester substituents and DCI moieties in ITIC. On the other hand, P3HT is prone to form a face-on orientation which does not change upon blend with ITIC. Furthermore, the P3HT:ITIC blend unable to form nanoscale domains due to their efficient mixing, thus leading to large nongeminate recombination losses in the device.

The same group further introduced two fluorine atoms into the $\beta$- and $\beta'$-position of the 2,2′-bithiophene segments in PBDD4T polymer (Zhang et al. 2016). The fluorine atoms helped to increase the rotation barrier and hence stabilize backbone conformation of the polymer donor and enhance interchain π–π interaction. In comparison to PBDD4T, a strong temperature dependent aggregation tendency was observed for PBDD4T-4F at low temperature. Both PBDD4T and PBDD4T-2F exhibited similar optical gap of 1.76 eV and enhanced crystallinity for the later polymer. The HOMO energy levels of PBDD4T and PBDD4T-2F were −5.30 and −5.39 eV, respectively, showing that the strong electronegative fluorine atom can lower the energy level of the polymer. Fullerene-free solar cells prepared by employing PBDD4T and PBDD4T-2F as donor and ITIC as acceptor in ITO/PFN/BHJ-active-layer/$MoO_3$/Al device structure generated PCEs of 0.45 and 8.69%, respectively. This significant enhancement is achieved by synergistic improvements in $V_{OC}$, charge generation and charge transport, thus $J_{SC}$ and FF of fluorinated polymer.

Li and co-workers studied the effect of fluorination on solar cell performance using a wide band gap polymer J51 containing benzodithiophene–alt–fluorobenzotriazole (Gao et al. 2016). Due to its complementary absorption with ITIC, a broad absorption coverage can be recognized which is a desirable parameter to increase light harvesting efficiency. The optical bandgap of fluorinated polymer J51

**Table 8.3** Device parameters for multi-fused fullerene-free electron acceptor using various polymer donors

| Acceptor | Donor | $J_{SC}$ (mA cm$^{-2}$) | $V_{OC}$ (V) | FF | PCE (%) | References |
|---|---|---|---|---|---|---|
| ITIC | PTB7-Th | 14.21 | 0.81 | 0.59 | 6.80 | Lin et al. (2015) |
| ITIC | PTB7-Th | 14.15 | 0.82 | 0.65 | 7.51 | Zhang et al. (2017) |
| ITIC | PBT-S-TTz | 14.93 | 0.97 | 0.57 | 8.22 | Zhao et al. (2016b) |
| ITIC | PBDTS-DTBTO | 16.60 | 0.84 | 0.65 | 9.09 | Yao et al. (2016c) |
| ITIC | PBDB-T | 16.80 | 0.90 | 0.74 | 11.21 | Zhao et al. (2016c) |
| ITIC | PDCBT | 16.50 | 0.94 | 0.66 | 10.16 | Qin et al. (2016) |
| ITIC | PBDD4T | 2.04 | 0.88 | 0.25 | 0.45 | Zhang et al. (2016) |
| ITIC | PBDD4T-4F | 15.04 | 0.94 | 0.61 | 8.69 | Zhang et al. (2016) |
| ITIC | J51 | 16.47 | 0.82 | 0.69 | 9.26 | Gao et al. (2016) |
| ITIC | J50 | 12.93 | 0.71 | 0.53 | 4.80 | Gao et al. (2016) |
| ITIC | J52 | 13.11 | 0.73 | 0.58 | 5.51 | Bin et al. (2016) |
| ITIC | J60 | 16.33 | 0.91 | 0.60 | 8.97 | Bin et al. (2016) |
| ITIC | J61 | 17.43 | 0.89 | 0.61 | 9.53 | Bin et al. (2016) |
| ITIC | J71 | 17.32 | 0.94 | 0.70 | 11.40 | Bin et al. (2016) |
| ITIC | HD-PBDT2FT | 14.40 | 0.92 | 0.65 | 8.70 | Xia et al. (2016) |
| ITIC | OD-PBDT2FT | 13.10 | 0.92 | 0.69 | 8.30 | Xia et al. (2016) |
| ITIC | DT-PBDT2FT | 13.10 | 0.95 | 0.57 | 7.00 | Xia et al. (2016) |
| ITIC | PBTCl | 14.53 | 0.91 | 0.58 | 7.57 | Wang et al. (2017) |
| ITIC | PBDT-TDZ | 15.91 | 1.02 | 0.58 | 9.43 | Xu et al. (2018) |
| ITIC | PBDTS-TDZ | 17.78 | 1.10 | 0.65 | 12.80 | Xu et al. (2018) |
| *m*-ITIC | J61 | 18.31 | 0.91 | 0.70 | 11.77 | Yang et al. (2016) |

(continued)

**Table 8.3** (continued)

| | | | | | | |
|---|---|---|---|---|---|---|
| ITIC-Th | PTB7-Th | 15.93 | 0.80 | 0.68 | 8.70 | Lin et al. (2016c) |
| ITIC-Th | PDBT-T1 | 16.24 | 0.88 | 0.67 | 9.60 | Lin et al. (2016c) |
| ITIC-Th | FTAZ | 15.84 | 0.92 | 0.61 | 8.88 | Fuwen et al. (2017) |
| ITIC-Th1 | FTAZ | 19.33 | 0.85 | 0.74 | 12.10 | Fuwen et al. (2017) |
| ITIC-Th | PTFB-O | 17.10 | 0.92 | 0.67 | 10.88 | Li et al. (2016) |
| ITIC | PTFB-O | 15.50 | 0.92 | 0.70 | 10.13 | Li et al. (2016b) |
| ITIC | PTFB-P | 12.80 | 0.92 | 0.65 | 7.85 | Li et al. (2016b) |
| IT-M | PBDB-T | 17.40 | 0.94 | 0.74 | 12.05 | Li et al. (2016c) |
| IT-DM | PBDB-T | 16.48 | 0.97 | 0.71 | 11.29 | Li et al. (2016c) |
| ITCC | PBDB-T | 15.90 | 1.01 | 0.71 | 11.40 | Yao et al. (2017b) |
| ITTC | HFQxT | 16.49 | 0.88 | 0.71 | 10.40 | Zhang et al. (2017) |
| ITTC | PBT1-EH | 16.50 | 0.95 | 0.75 | 11.80 | Xie et al. (2017) |
| ITIC | PBT1-EH | 15.70 | 0.99 | 0.63 | 9.80 | Xie et al. (2017) |
| IT-4F | PBDB-T-SF | 20.50 | 0.88 | 0.72 | 13.10 | Zhao et al. (2017)a |
| IT-4F | PDTB-EF-T | 20.73 | 0.90 | 0.76 | 14.20 | Li et al. (2018)a |
| IHIC | PTB7-Th | 19.01 | 0.75 | 0.68 | 9.77 | Wang et al. (2017) |
| FOIC | PTB7-Th | 24.00 | 0.74 | 0.67 | 12.0 | Li et al. (2018)b |
| ITIC-OE | PBDB-T | 14.80 | 0.85 | 0.67 | 8.50 | Liu et al. (2018) |

was ~1.94 eV and the HOMO energy level was down-shifted to −5.26 eV compared to non-fluorinated analogue J50 ($E_{HOMO}$ = −5.13 eV), benefitting high $V_{OC}$. Despite of small HOMO offset $\Delta E_{HOMO}$ = 0.22 eV) an efficient hole transfer from the ITIC acceptor to the J51 donor can be observed as confirmed from photoluminescence (PL) quenching measurement. The solar cell device with J51:ITIC (1:2) gave best PCE of 9.26% after thermal annealing at 150 °C for 10 min, which was significantly higher than that of J50:ITIC device (PCE = 4.8%). The $\mu_e/\mu_h$ values for J51 was significantly lower (1.15) than that of J50 (2.86) showing more

balanced electron and hole mobility for J51:ITIC devices. Light intensity dependent photocurrent measurements revealed the suppression of bimolecular recombination in the device with fluorinated polymer J51 showing balanced charge carrier mobility which account for the higher FF values of 0.69 vs. o.53 for J50-based devices.

Three new medium bandgap bithienyl-benzodithiophene-alt-fluorobenzotriazole copolymers were synthesized by introducing branched alkyl (J52), branched alkylthio (J60), and linear alkylthio (J61) substituent on the BDT unit and studied the effect of substituents on the OSC performance using ITIC as acceptor (Bin et al. 2016). The alkylthio-substitution red-shifted the absorption, down-shifted the HOMO level and improved crystallinity of the conjugated polymers. The OSC devices were fabricated with ITO/PEDOT:PSS/BHJ (1:1, w/w)/PDINO/Al, structure. After annealing at 100 °C for 10 min, the device based on the J61:ITIC blend exhibits an enhanced $J_{SC}$ of 17.43 mA cm$^{-2}$, a high $V_{OC}$ of 0.89 V, with a PCE of 9.53%, which was higher compared to J60 (PCE = 8.97%) and J52 (PCE = 5.51%) devices. Thermal annealing significantly increased the $J_{SC}$ values from 11.73 to 13.11 mA cm$^{-2}$ for J52-based device, from 9.78 to 16.33 mA cm$^{-2}$ for J60-based device, and from 14.95 to 17.43 mA cm$^{-2}$ for J61-based device. Due to the excitonic nature of organic semiconductors it is difficult to achieve high $V_{OC}$ and high $J_{SC}$ simultaneously in a high performance device. The PCE always suffers from a trade-off between $V_{OC}$ and $J_{SC}$. Therefore, in order to increase the PCE the energy loss ($E_{loss}$) of the OSCs should be minimized. It has been observed that the $E_{loss}$ in alkylthio-substituted polymers J60 and J61 were reduced to 0.68–0.65 eV compared to 0.83 eV for J52-based devices.

The alkyl group was further replaced by trialkylsilyl group in polymer J71 due to which the HOMO level was down-shifted due to Si–C bond interaction (Bin et al. 2016). Solar cells prepared using J71:ITIC (1:1,w/w) after thermal annealing at 150°C for 10 min. revealed a significantly high PCE of 11.41% with both high $V_{OC}$ of 0.94 V and high and $J_{SC}$ of 17.32 mA cm$^{-2}$ benefitting from the complementary absorption of the donor and acceptor components. Even if the HOMO level offset between the donor and acceptor was only 0.11 eV, the hole transfer efficiency from acceptor to donor was very high. The device exhibited an $E_{loss}$ value of 0.65 eV.

Xia et al. demonstrate the influence of branched alkyl chain length of the PBDT2FT-based polymer donor on FFA-based solar cells (Xia et al. 2016). It has shown that the length of the alkyl chain has little effect on the solar cell performance using ITIC as acceptor component. Devices based on HD-PBDT2FT:ITIC exhibited the highest PCE of 8.7%. The PCE was further slightly reduced to 8.3% for OD-PBDT2FT and to 7.0% for DT-PBDT2FT polymer mostly due to lower $J_{SC}$. In comparison, the $PC_{71}BM$-based devices gave PCE of only 3.4–4.6%. The result demonstrated that the internal quantum efficiency has only marginal influence on the fullerene-free solar cells.

A work by Wang et al. has shown that the replacement of fluorine atom of PTB7-Th by chlorine atom into the thieno[3,4 *b*]thiophene unit in PBTCl can induce subtle variations in material properties, resulting in a blue-shifted absorption

than PTB7-th and more complementary absorption with ITIC acceptor (Wang et al. 2017). Chlorine substitution also lowered the HOMO level of PBTCl (−5.43 eV), beneficial to increase the $V_{OC}$ of the corresponding devices. The 2D GIWAXS analysis demonstrated that the PBTCl:ITIC blend film exhibited a "face-on" orientation exhibiting scattering features of both PBTCl and ITIC, which suggested that the blend of PBTCl and ITIC was phase-separated and formed individual crystalline domains of the donor and acceptor due to larger size of the chlorine atom, which promoted bicontinuous charge transfer in the active layer. The PBTCl:ITIC-based devices displayed a maximum PCE of 7.57% with a $V_{OC}$ of 0.91 V, which were comparatively higher than the fluorine-analogue PTB7-Th (PCE = 6.62% $V_{OC}$ = 0.81 V).

In a recent report, Xu et al. used two wide band gap copolymers PBDT-TDZ and PBDTS-TDZ ($E_g \sim 2.1$ eV) based on 1,3,4-thiadiazole (TDZ) and benzo[1,2-*b*:4,5-*b*′]dithiophene (BDT) building blocks (Xu et al. 2018). Inverted single-junction BHJ devices using ITIC acceptor exhibited PCEs of 9.43 and 12.8%, respectively, when fabricated from a halogen-free solvent *o*-xylene without any post-treatment. Interestingly, the PBDTS-TDZ:ITIC device demonstrated an impressive $V_{OC}$ of 1.1 V and a small $E_{loss}$ of 0.48 eV without sacrificing the $J_{SC}$ and FF values. Due to the complementary absorption both the devices showed broad EQE response from 300 to 800 nm, with above 60% between 400 and 720 nm regions.

The variation of the length and position of the side chains has a significant influence on the intermolecular self-assembly of the conjugated oligomers or polymers. Li and co-workers reported a new isomeric molecular acceptor *m*-ITIC by modifying the structure of ITIC with meta-hexyl-phenyl substitution (Fig. 8.7) (Yang et al. 2016). In a comparison with its isomeric counterpart ITIC containing *p*-hexyl-phenyl substitution, *m*-ITIC showed a stronger film absorption, higher electron mobility and larger crystalline coherence. These inherent advantages of *m*-ITIC resulted in a higher PCE of 11.77% using a medium bandgap polymer J61 as donor, which is markedly improved over that of ITIC-based devices (PCE = 10.57%). Grazing incident wide-angle X-ray scattering (GIWAXS) studies revealed significantly stronger diffraction peak along with narrower peak width for J61:*m*-ITIC blend film compared to J61:ITIC blend, suggesting better defined scattering peak and intensities with predominant face-on crystalline orientation for *m*-ITIC (Fig. 8.8). It has also been reported that the *m*-ITIC-based device showed less thickness-dependent photovoltaic behaviour than ITIC-based devices in the active-layer thickness range of 80–360 nm, PCE of over 8.50%@250 nm active layer thickness and over 8.00%@360 nm, an important parameter for large area device fabrication.

In order to fine tune the molecular properties, Zhan and co-workers replaced the hexylphenyl group of ITIC with hexylthienyl-substituents in ITIC-Th at the out-of-plane side chain (Lin et al. 2016c). The molecular energy levels (HOMO = −5.66 eV, LUMO = −3.93 eV) of ITIC-Th stabilized compared to the ITIC, since 2-thienyl group possess slightly inductively electron withdrawing. The intramolecular charge transfer absorption maximum for ITIC-Th observed at

706 nm with an optical bandgap of 1.60 eV. ITIC-Th was blended with well-known low bandgap PTB7-Th and wide bandgap PBDT-T1 polymers as donor. The PTB7-Th:ITIC-Th and PDBT-T1:ITIC-Th-based OSCs with a structure of ITO/ZnO/BHJ/$MoO_3$/Ag exhibited PCEs up to 8.7 and 9.6%, respectively, using chloronaphthalene (CN) as solvent additive. Interestingly, in comparison to PTB7-Th, the PDBT-T1 polymer showed high $V_{OC}$ due to low lying HOMO level and higher $J_{SC}$ due to complementary absorption with the acceptor. The use of solvent additive CN increase the hole and electron mobilities due to improved π–π stacking and higher domain purity in the BHJ layer.

The same group developed a fluorinated FFA, ITIC-Th1, by introducing fluorine atoms onto the terminal acceptor units (Fuwen et al. 2017). The incorporation of F atoms would improve intermolecular interactions through C-F•••S, C–F···H, and C–F···π noncovalent interactions and enhance electron mobility, favourable for enhancing $J_{SC}$ and FF. In comparison to the non-fluorinated counterpart ITIC-Th, ITIC-Th1 resulted in a red-shifted absorption, slightly deeper LUMO level, and smaller bandgap. The blend film of FTAZ:ITIC-Th1 presented smaller domain sizes and longer coherence length and balanced charge carrier mobility, thus providing larger D:A interfaces for exciton dissociation and reduced monomolecular recombination. OSCs based on FTAZ:ITIC-Th1 exhibited a PCE of 12.1%, significantly higher compared to that of controlled devices based on FTAZ:ITIC-Th (8.8%) and FTAZ:$PC_{71}$BM (5.22%).

Finding a suitable donor polymer is very crucial for achieving high efficiency (>10%) in fullerene-free solar cells. It is always not necessary for donor polymers which gives best performance in fullerene cells may work well with fullerene-free acceptor. In addition, slight structural modification by changing the substituent position in the molecular backbone, the material properties and device performance can be dramatically alter. Li et al. developed two polymer PTFB-O and PTFB-P that exhibits strong temperature-dependent aggregation (Li et al. 2016b). OSC devices using PTFB-O:ITIC-Th and PTFB-O:ITIC gave PCEs of 10.88 and 10.13%, respectively. The control device PTFB-O:$PC_{71}$BM only achieved a PCE of 6.53%. The high performance of PTFB-O was ascribed to the reduced lamellar stacking and polymer crystallinity via introduction of a less symmetric fluorinated phenyl group with mirror symmetry. In comparison, an analogue polymer PTFB-P with a C2-symmetric fluorinated phenyl unit yielded highly crystalline polymer films but reduced PCE of 7.85% using ITIC as acceptor. The results clearly demonstrate that the isomerization of the fluorine atoms caused dramatic effect on the molecular properties of the polymer and their solar cell performance.

Hou and co-workers develop two molecular acceptors IT-M and IT-DM, which were based on IDT as central unit and methyl-modified DCI as end groups (Li et al. 2016). The introduction of week electron donating methyl group(s) slightly blue-shifted the absorption band and elevated the energy levels for IT-M and IT-DM in comparison to prototype ITIC. Specifically, the upward shifting of LUMO level is beneficial for high $V_{OC}$. PBDB-T:IT-M based OSC device using an inverted architecture ITO/ZnO/active-layer/$MoO_3$/Al exhibited an excellent PCE of 12.05%, $J_{SC}$ of 17.4 mA $cm^{-2}$ and an FF of 0.74 by using 1% of DIO as additive.

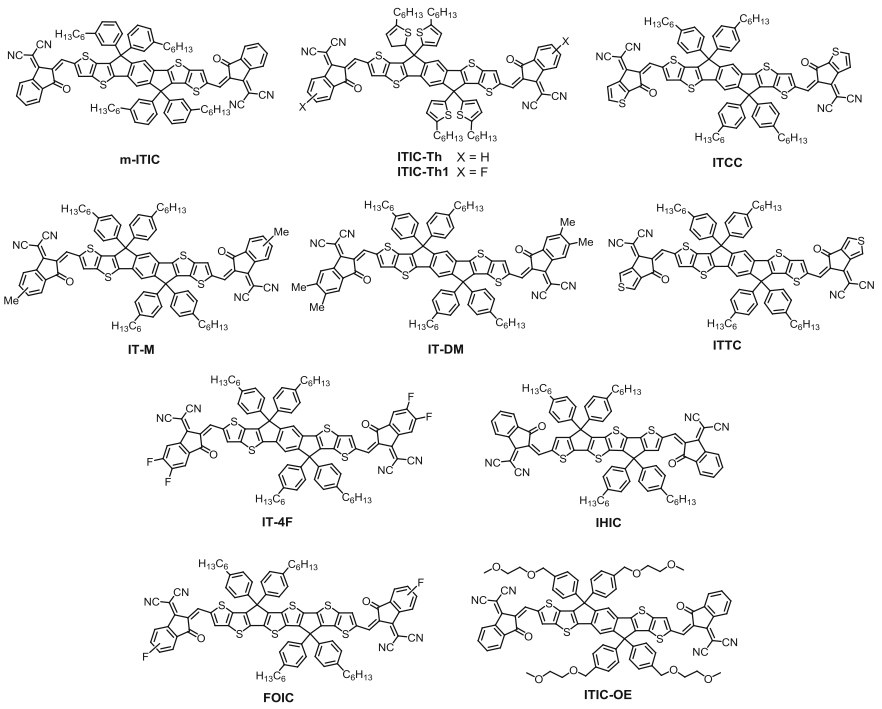


**Fig. 8.7** Structure of indacenodithieno[3,2-b]thiophene-based multi-fused systems

The IT-DM-based device under similar condition gave a PCE of 11.29% due to lower $J_{SC}$ and FF. The higher photovoltaic performance for PBDB-T:IT-M blend was ascribed to highly ordered packing of PBDB-T polymer and purer domains.

It is well known that the sulfur atom in thiophene is more easily polarized than carbon atom of phenyl group due to its more loosely held electrons relative to a benzene ring, and tend to form strong S···S interactions, and increase intermolecular interactions which facilitate π-stacking and charge transport property (Lin et al. 2016). Furthermore, the thiophene based electron donor molecules destabilize the HOMO level which reduced $V_{OC}$ of the device. On the other hand, electron acceptors with high lying HOMO level do not affect the $V_{OC}$ as it is irrelevant with the HOMO level of acceptor. Hou and co-workers prepared a new molecular acceptor ITCC based on thienyl-fused indanone as end-groups (Yao et al. 2017b). Due to enhanced intermolecular interactions due to the thiophene units, ITCC exhibits a closer π–π stacking distance (3.7 Å) compared to ITIC (3.8 Å) and expected to improve the charge transport properties. The introduction of thiophene unit at the terminal acceptors blue-shifted the absorption band ($\lambda_{max}$ = 670 nm) compared to ITIC with an $E_g^{opt}$ of 1.67 eV. The blue-shift was mainly ascribed to the decrease in intermolecular charge transfer due to electron donating thiophene units. ITCC showed improved electron-transport properties and a high-lying

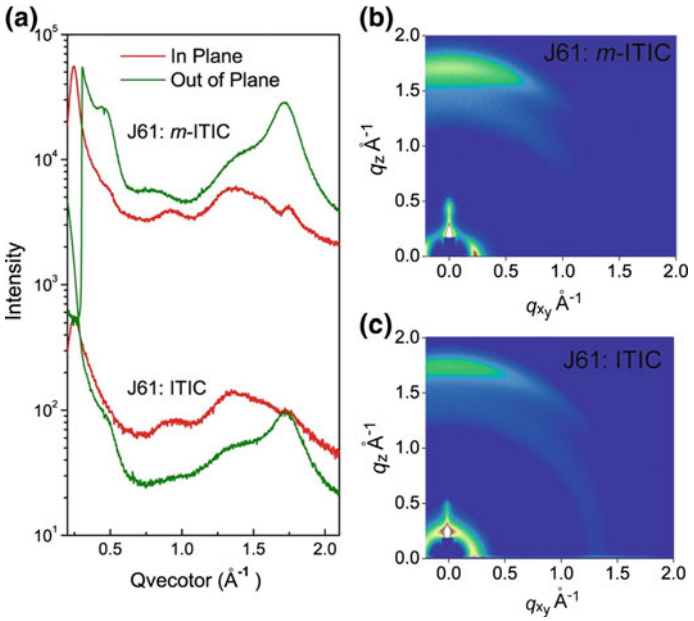


**Fig. 8.8** **a** Line cuts of the GIWAXS images of J61:*m*-ITIC (1:1, w/w) film and J61:ITIC (1:1, w/w) film. GIWAXS images of **b** J61:*m*-ITIC film and **c** J61:ITIC film. Reproduced with permission from Ref. Yang et al. (2016). Copyright (2016) American Chemical Society

LUMO level (−3.76 eV) which is beneficial for high $V_{OC}$. With PBDB-T as donor polymer in ITO/PEDOT:PSS/active layer/PFN-Br/Al structure the ITCC based device showed an impressive PCE of 11.4% with a $V_{OC}$ of 1.01 V, $J_{SC}$ of 15.9 mA cm$^{-2}$ and an FF of 0.71 was observed. Under similar condition PBDB-T:ITIC gave a PCE of 10.6% due to lower $V_{OC}$ of 0.93 V and FF of 0.67. The lower $J_{SC}$ could be due to the blue-shifted absorption of ITCC.

Zhang et al. reported a new molecular acceptor ITTC by using IDT as core and 2-(6-oxo-5,6-dihydrocyclopenta[*c*]thien-4-ylidene)malononitrile as end groups (Zhang et al. 2017). The introduction of thiophene group slightly red-shifted the absorption maximum of ITTC ($\lambda_{max}$ = 707 nm) compared to ITIC ($\lambda_{max}$ = 699 nm). The $E_{HOMO}/E_{LUMO}$ of ITTC are −5.49/−3.85 eV which are slightly up-shifted compared to ITIC. The device (ITO/PEDOT:PSS/active layer/PDINO/Al) employing a wide band gap hexafluoroquinoxaline-based polymer HFQx-T as the donor and ITTC as the acceptor delivered a PCE of 8.19% without any post-treatment. After thermal annealing 130 °C for 10 min, the devices based on HFQx-T:ITTC blend films generated an impressive PCE of 10.4% with a high FF of 0.71. This enhancement was mainly ascribed to the balanced charge transport after TA treatment ($\mu_e/\mu_h$ = 1.02) compared to the untreated devices ($\mu_e/\mu_h$ = 1.35). Xie et al. reported a PCE of 11.8% for PBT1-EH:ITTC (1:1 w/w) based device compared to 9.8% for PBT1-EH:ITIC after TA treatment at 100 °C (Xie et al.

2017). The FF of ITTC-based device was significantly higher (0.75) compared to ITIC device (0.63). The study revealed strong π–π stacking in the preferential face-on orientation, a low charge recombination and a suitable phase separation for ITTC-based device.

Recently, to fine tune the energy levels, Hou group synthesized a new acceptor IT-4F by introducing two fluorine atoms into the each terminal DCI unit of ITIC (Zhao et al. 2017a). The introduction of fluorine atom lowered the HOMO/LUMO energy levels as well the bandgap. The lower LUMO level of IT-4F (−4.14 eV) can have detrimental effect on the $V_{OC}$ using non-fluorinated polymer, and therefore, a new polymer PBDB-T-SF was developed by inserting fluorine atoms at the thiophene units. In contrast to the non-flurinated polymer, the introduction of fluorine atom lowers the energy levels which fits well with the IT-4F acceptor (Zhao et al. 2017a). The PBDB-T-SF:IT-4F-based inverted OSCs device (ITO/ZnO/active layer/$MoO_3$/Al) obtained an excellent PCE of 13.1% a record value at the time, and a high $J_{SC}$ of 20.5 mA $cm^{-2}$ $V_{OC}$ of 0.88 V and FF of 0.72. Most interestingly, an efficiency of over 12% was reported with a thickness range from 100–200 nm, an important parameter for practical applications.

Although high performance have been achieved for many polymer donor-based OSCs, the HOMO level of most of them are very high to achieve high $V_{OC}$ using low lying LUMO level of FFAs. Therefore, it is very important to prepare a donor material with low HOMO level in order to further enhance the PCE and lower the $E_{loss}$. Hou group developed a benzodithiophene-based polymer PDTB-EF-T containing electron withdrawing fluorine and ester functionalities (Li et al. 2018a). Because of the electron withdrawing groups the polymer exhibited a HOMO level of –5.5 eV. The authors prepared both conventional and inverted devices using PDTB-EF-T as donor and IT-4F as acceptor. The device with conventional structure ITO/PEDOT:PSS/active layer/PFN-Br/Al exhibited PCE of 13% using DIO as solvent additive followed by annealing at 150 °C for 10 min. The single-junction device with inverted structure of ITO/ZnO/active layer/$MoO_3$/Al achieve a record high PCE of 14.2% with a $V_{OC}$ of 0.90 V, a $J_{SC}$ of 20.73 mA $cm^{-2}$, and a FF of 0.76. The high value was ascribed to the vertical phase distribution of the active layer. Besides very similar $V_{OC}$ and $J_{SC}$ values, the lower performance of conventional device was mainly due to the lower FF of 0.71. Furthermore, the devices showed a low $E_{loss}$ of 0.62 eV.

Zhan and co-workers prepared a hexacyclic electron acceptor, IHIC, containing a strong electron donating dithienocyclopentathieno[3,2-*b*]thiophene core (Wang et al. 2017). The molecule showed a strong absorption with maximum at 800 nm extending up to near-IR region and high molar extinction coefficients, a small bandgap of 1.38 eV. When blend with a PTB7-Th donor polymer the best device using an inverted structure ITO)/ZnO/PTB7-Th:IHIC/$MoO_3$/Au/Ag demonstrated a PCE of 9.77% with CN as solvent additive. Most importantly, an average visible transmittance (AVT) of 36% was observed for the device a much higher value than fullerene-based single-junction semitransparent devices (6.2% at AVT of 21%) (Chen et al. 2012).

The authors further prepared another longer molecular acceptor FOIC comprising fused tris(thienothiophene) block (Li et al. 2018b). FOIC showed strong NIR absorption ($\lambda_{max}$ = 836 nm) with high molar extinction coefficient of up to $2 \times 10^5$ $M^{-1}$ $cm^{-1}$, low bandgap of 1.32 eV, and high electron mobility of $1.2 \times 10^{-3}$ $cm^2$ $V^{-1}$ $s^{-1}$. Optimized OSCs based on PTB7-Th:FOIC exhibited a high PCE of 12.0% with a $V_{OC}$ of 0.74 V, a $J_{SC}$ of 24.0 mA $cm^{-2}$, and an FF of 0.67 and $E_{loss}$ of 0.58 without any additional treatment. A semitransparent device based on PTB7-Th:FOIC resulted in an excellent PCE of 10.3% with an average visible transmittance of 37.4%. These results demonstrated the great potential of NIR absorbing FFAs in semitransparent devices for window applications.

Most of the organic semiconductors used in photovoltaic devices have low relative dielectric constant ($\varepsilon_r < 6$). In order to improve the device performance it is important to increase the ε of the materials. Generally, a high ε value would reduce the exciton binding energy, thus increase the charge separation and reduce recombination losses, thereby increase overall device performance. Recently, Cao and co-workers introduce oligoethylene oxide side chains to the molecular backbone and develop a FFA ITIC-OE with high $\varepsilon_r$ of $\sim$9.4 much larger value than that to ITIC ($\varepsilon_r$ = $\sim$4.5) (Liu et al. 2018). OSCs based on PBDB-T:ITIC-OE resulted in a PCE of up to 8.5%, a significant value for OSCs employing high dielectric constant materials. However, this value is lower than those of ITIC-based control devices (10.4%), due to less phase-separated morphology and reduced crystallinity of ITIC-OE. The $\mu_h/\mu_e$ ratios for ITIC-OE- and ITIC-based blend films are 28.9 and 1.0, respectively, mainly due to the low $\mu_e$ of ITIC-OE ($1.2 \times 10^{-5}$ $cm^2$ $V^{-1}$ $s^{-1}$) than the ITIC-based blend ($3.5 \times 10^{-4}$ $cm^2$ $V^{-1}$ $s^{-1}$). This imbalance hole/electron mobility is the likely reason for lower FF and $J_{SC}$.

### 8.3.4 *Longer Multi-fused Heteroacenes*

Chen and co-workers reported a fused fluorine-based FFA, FDICTF where fluorine core is fused with thiophene moieties via cyclopentadiene (Fig. 8.9) (Qiu et al. 2017). The molecule demonstrate strong absorption from 500−770 nm ($\lambda_{max}$ = 689 nm) with optical bandgap of 1.63 eV. The solar cells with conventional architecture ITO/PEDOT:PSS/active layer/PDIN/Al using PBDB-T as donor yielded a PCE of 10.06% with high $V_{OC}$ of 0.94 V which is significantly higher than the controlled PBDB-T:$PC_{71}$BM-devices (PCE = 7.33%, $V_{OC}$ = 0.86 V) and PTB7-Th:FDICTF device (PCE = 7.87%) (Table 8.4). Morphological investigations suggested that the molecular aggregation of the FFA was prevented by the long octyl chains and form nanoscale phase separation for better charge transport using complementary absorbing donor polymer PBDB-T.

Zhan and co-workers elongated the core unit and prepared a series of nona-fused electron acceptors named as INIC, INIC-F and INIC-2F based on 6,6,12,12-tetrakis (4-hexylphenyl)-indacenobis(dithieno[3,2-*b*;2′,3′-*d*]thiophene) (IBDT) as the electron-rich unit and DCI or fluorinated DCI as the electron-deficient group (Dai

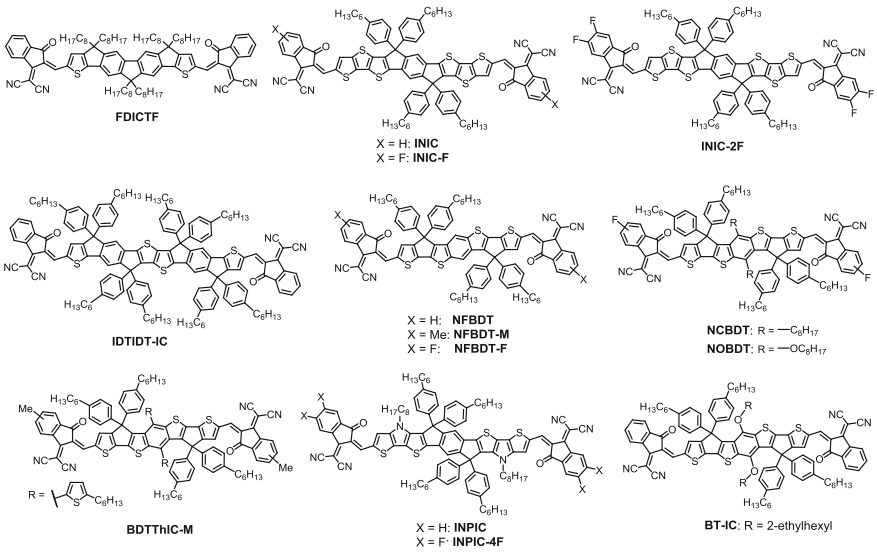


**Fig. 8.9** Structure of longer multi-fused Heteroacenes

et al. 2017). Substitution of fluorine atom(s) found to red-shifted the absorption spectrum ($\lambda_{max}$ from 704 for INIC to 744 nm for INIC-2F), down-shifted the LUMO energy level (−3.88 to −4.02 eV), and enhanced electron mobility. Because of the fluorine-induced intermolecular interactions, FTAZ:INIC-2F blend films exhibited highest crystallinity and more balanced electron/hole mobilities in comparison to other fluorinated and non-fluorinated analogues. The OSCs based on a polymer donor FTAZ and fluorinated electron acceptors (1:1.5 w/w) significantly increased the PCE to >10%, a much higher value than the non-fluorinated counterpart INIC (7.7%) using 0.25% DIO (v/v). The difluorinated molecule INIC-2F exhibited the highest PCE of 11.5% and $J_{SC}$ of 19.68 mA cm$^{-2}$. The $E_{loss}$ values of the devices were 0.61−0.63 eV.

Li et al. prepared a multi-fused decacyclic acceptor IDTIDT-IC which possessed destabilized HOMO/LUMO energy levels (−5.42/−3.82 eV) compared to IDT-IC (−5.61/−3.88 eV). The absorption band of IDTIDT-IC is red-shifted to 721 nm showing a reduced bandgap of 1.53 eV compared to 1.72 eV for IDT-IC. BHJ solar cells prepared using PTB7-Th:IDTIDT-IC blend in ITO/PEDOT:PSS/BHJ/PDINO/Al gave PCE of 6.48% and high $V_{OC}$ of 0.94 V, with an $E_{loss}$ of 0.59 (Li et al. 2016).

Kan et al. reported a molecular acceptor NFBDT which consists of a heptacyclic benzo-di(cyclo-pentadithiophene) core and DCI acceptor. (Kan et al. 2017a) The molecule showed a maximum absorption at 731 nm in thin film with bandgap of 1.56 eV. Despite of small HOMO energy offset 0.07 eV between PBDB-T (−5.33 eV) and NFBDT (−5.4 eV), the hole transfer from the NFBDT acceptor to PBDB-T donor appeared to be highly efficient as studied by photoluminiscence

**Table 8.4** Device parameters for multi-fused fullerene-free electron acceptor with polymer donors

| Acceptor | Donor | $J_{SC}$ (mA cm$^{-2}$) | $V_{OC}$ (V) | FF | PCE (%) | References |
|---|---|---|---|---|---|---|
| FDICTF | PBDB-T | 15.81 | 0.94 | 0.66 | 10.06 | Qiu et al. (2017) |
| FDICTF | PTB7-Th | 15.56 | 0.86 | 0.57 | 7.87 | Qiu et al. (2017) |
| INIC | FTAZ | 13.51 | 0.96 | 0.58 | 7.70 | Dai et al. (2017) |
| INIC-F | FTAZ | 17.56 | 0.90 | 0.67 | 10.80 | Dai et al. (2017) |
| INIC-2F | FTAZ | 19.68 | 0.85 | 0.69 | 11.50 | Dai et al. (2017) |
| IDTIDT-IC | PTB7-Th | 14.49 | 0.94 | 0.59 | 6.48 | Li et al. (2016) |
| NFBDT | PBDB-T | 17.85 | 0.87 | 0.67 | 10.42 | Kan et al. (2017) |
| NFBDT-M | PBDB-T | 17.30 | 0.91 | 0.70 | 11.00 | Ke et al. (2018) |
| NFBDT-F | PBDB-T | 19.28 | 0.79 | 0.69 | 10.62 | Ke et al. (2018) |
| NCBDT | PBDB-T | 20.33 | 0.84 | 0.71 | 12.12 | Kan et al. (2017) |
| NOBDT | PTB7-Th | 19.16 | 0.77 | 0.70 | 10.55 | Zhang et al. (2018e) |
| BDTThIC-M | PBDB-T | 18.03 | 0.94 | 0.71 | 12.12 | An et al. (2018a) |
| INPIC | PBDB-T | 8.55 | 0.96 | 0.52 | 4.31 | Sun et al. (2018) |
| INPIC-4F | PBDB-T | 21.61 | 0.85 | 0.71 | 13.13 | Sun et al. (2018) |
| BT-IC | J61 | 16.35 | 0.87 | 0.67 | 9.56 | Zhang et al. (2017) |
| BT-IC | J71 | 17.75 | 0.90 | 0.66 | 10.46 | Zhang et al. (2017) |
| FDICTF–F | PBDB-T | 17.36 | 0.88 | 0.71 | 10.85 | Wang et al. (2018a) |
| FDICTF–Cl | PBDB-T | 17.61 | 0.87 | 0.75 | 11.47 | Wang et al. (2018a) |
| FDICTF–Br | PBDB-T | 18.22 | 0.87 | 0.76 | 12.05 | Wang et al. (2018a) |
| ITIC-$Cl_2$ | PTPDBDT | 15.60 | 0.94 | 0.65 | 9.50 | Yang et al. (2017a) |
| BT-CIC | PTB7-Th | 22.50 | 0.70 | 0.71 | 11.20 | Li et al. (2017) |
| ITIC-$Cl_2$ | PBDT-T-2F | 19.08 | 0.922 | 0.75 | 13.16 | Zhang et al. (2018a) |
| ITIC-$Cl_4$ | PBDT-T-2F | 22.67 | 0.790 | 0.75 | 13.45 | Zhang et al. (2018a) |

quenching and high EQE values. With PBDB-T as the donor, NFBDT based OSCs comprising ITO/PEDOT:PSS/BHJ layer/PDIN/Al structure gave an impressive PCE of 10.42% ($J_{SC}$ of 17.85 mA cm$^{-2}$, $V_{OC}$ of 0.87 V and FF of 0.67) after solvent vapor annealing of the active layer using chloroform. The as-cast device achieved a PCE of only 8.99%. PDIN (*N,N′*-bis(propylenedimethylamine)-3,4:9,10-perylenediimide) was used as electron transport layer. The grazing-incidence X-ray diffraction (GIXRD) of the PBDB-T:NFBDT blend showed a preferred face-on orientation of the donor and acceptor phase which can be beneficial for the vertical charge transport. Recently, an inverted device using PBDB-T:NFBDT (1:1 w/w) blend gave a PCE of 9.33% after thermal annealing at 150 °C (Chang et al. 2018).

The introduction of methyl and fluorine units at the terminal DCI unit of NFBDT yielded molecular acceptors NFBDT-M and NFBDT-F. The methyl substituent slightly up-shifted the LUMO level while the fluorine unit down-shifted both HOMO/LUMO energy levels (Ke et al. 2018). The NFBDT-M and NFBDT-F acceptors were combined with well-known PBDB-T polymer donor, achieving higher PCEs of 11.0 and 10.62%, respectively compared to PBDB-T:NFBDT blend (10.42%). As expected for NFBDT-M, the PCE improvement was mainly attributed to the higher $V_{OC}$, while for NFBDT-F, the increase was mainly due to higher $J_{SC}$. The results clearly demonstrate how the PCE can be manipulated by a delicate variation of the functional group.

Judicious modification of both the donor and acceptor groups of NFBDT developed a new electron acceptor NCBDT with lower bandgap (Kan et al. 2017b). Compared to NFBDT, the HOMO energy level of NCBDT was up-shifted due to the additional octyl chain on the donor unit and the LUMO level was down-shifted due to the insertion of fluorine atom on each terminal acceptor groups. NCBDT has a red-shifted absorption ($\lambda_{max}$ = 760 nm in film) and low optical bandgap of 1.45 eV compared to NFBDT, resulting in an extended absorption to the IR region down to 860 nm. BHJ solar cells fabricated using PBDB-T:NCBDT blend and PDINO (perylene diimide functionalized with amino N-oxide) as electron transport layer achieved an enhanced $J_{SC}$ of 20.33 mA cm$^{-2}$ and FF of 0.70, thus an increased PCE of 12.12%. The 60 meV lowered LUMO level of NCBDT marginally affected the $V_{OC}$ (0.84 V), partly due to a lower $E_{loss}$ of 0.61 eV compared to 0.69 for NFBDT device. Despite high HOMO level the devices based on both acceptors displayed an efficient charge generation mediated by interfacial charge pair and subsequently suitable charge extraction as studied using transient absorption spectroscopy. The replacement of octyl group of NCBDT by octyloxy group in NOBDT further up-shifted the HOMO energy level and red-shifted the absorption maximum to 781 nm with optical bandgap of 1.37 eV (Zhang et al. 2018e). The device based on PTB7-Th:NOBDT active layer after solvent vapor annealing with chloroform, gave a PCE of 10.55%, a $V_{OC}$ of 0.77 V with a low $E_{loss}$ of 0.62 eV, a high $J_{SC}$ of 19.16 mA cm$^{-2}$, and FF of 0.70. The material was further used as rare sub-cell in a tandem device which will be discussed later.

Yang and co-workers introduced hexylthienyl side groups into the BDT core in BDTThIC-M which elevated the HOMO/LUMO energy levels compared to NFBDT-M (An et al. 2018). The PBDB-T:BDTThIC-M device exhibited an excellent PCE of 12.12% and a high $V_{OC}$ of 0.94 V which is much higher compared to NFBDT-M (PCE = 11.3% $V_{OC}$ = 0.94 V) measured under identical fabrication conditions. The optimized devices were prepared with D:A ratio of 1:1 (wt/wt) with 0.75 vol% DIO additive followed by thermal annealing of the active layers at 100 °C for 5 min. The BDTThIT-M-based device exhibited a very small $E_{loss}$ of 0.59 eV benefiting from the elevated LUMO level and narrowed bandgap, and electron mobility. The insertion of methyl group was found to be very effective for elevating the HOMO/LUMO energy levels and simultaneously realizing higher $V_{OC}$ and $J_{SC}$.

Tang and co-workers reported two nonafused FFAs, namely INPIC and INPIC-4F by incorporating electron-rich dithieno[3,2-b:2′,3′-d]pyrrole units into

the fused system (Sun et al. 2018). In comparison to INPIC (($\lambda_{max}$ = 779 nm, $E_g$ = 1.46 eV), the fluorinated derivative INPIC-4F showed a strong absorption in the near-IR region (821 nm) and lower bandgap of 1.39 eV. The acceptors and PBDB-T donor have complementary absorption and suitable energy levels. INPIC-4F possesses higher electron mobility and better crystallinity compared to INPIC. OSC devices prepared using PBDB-T:INPIC-4F with 0.5% DIO as additive achieved PCEs of up to 13.13%, which is exceptionally higher compared to INPIC-based device (4.31%). The lower efficiency of the PBDB-T:INPIC device was mainly due to severe charge recombination and poor charge extraction, while the PBDB-T:INPIC-4F device reveals favourable charge transport due to higher electron mobility and better crystallinity.

Liao and co-workers synthesized a seven membered fused heteroacene-based low bandgap FFA BT-IC ($E_g$ = 1.43 eV) (Zhang et al. 2017). When blended with different polymer donors J61 and J71 the OSC devices achieved PCEs of 9.56 ad 10.46%, respectively, with low $E_{loss}$ of 0.56 eV for J61 and 0.53 eV for J71 without sacrificing the $J_{SC}$. Interestingly, in spite of small HOMO-HOMO offset ($\Delta E_H$ = 0.10 eV), both J61:BT-IC and J71:BT-IC-based devices showed efficient charge generation as studied by femtosecond transient absorption spectroscopy, suggesting that small $\Delta E_H$ is not the limiting factor for high performance devices.

### 8.3.5 *Heteroacenes Containing Halogenated Terminal Units*

Chen group synthesized a series of halogenated FFAs, namely, FDICTF–F, FDICTF–Cl, and FDICTF–Br (Fig. 8.10) (Wang et al. 2018a). Unlike their non-halogenated analogues, the halogenated molecules possessed red-shifted absorptions, deep frontier energy levels, increased crystallinities, and improved charge carrier mobilities. This is because of the strong electronegativity and heavy atom effect of halogens. After blending with donor polymer PBDB-T, the FDICTF–

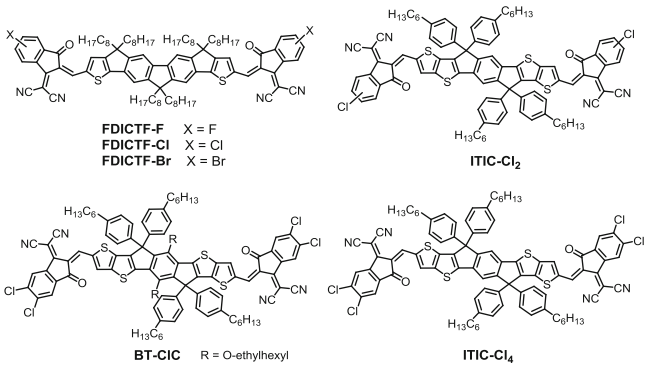


**Fig. 8.10** Structure of FFAs containing halogenated terminal units

F, FDICTF–Cl, and FDICTF–Br-based devices exhibited PCEs of 10.85, 11.47, and 12.05%, respectively, which are significantly higher than 9.59% obtained for FDICTF (Table 8.4). The results demonstrate that halogenation of acceptor molecules could be an effective way to achieve improved device performance.

Li and co-workers reported a PCE of 9.5% for PTPDBDT:ITIC-$Cl_2$ (1:1) blend using 0.5% DIO as processing additive followed by thermal annealing of the active layer at 150 °C (Yang et al. 2017a). The performance was higher compared to the corresponding F- and Br-analogues (8.8 and 9.4%, respectively). In comparison the non-halogenated analogue achieved a much lower PCE of 6.4%. The molecule also showed a high electron mobility of 0.1 $cm^2\ V^{-1}\ cm^{-1}$ when tested in field effect transistor and was significantly higher compared to the non-halogenated ($4.7 \times 10^{-2}\ cm^2\ V^{-1}\ cm^{-1}$) or fluorinated ($2 \times 10^{-3}\ cm^2\ V^{-1}\ cm^{-1}$) analogues.

Forrest and his group reported a chlorinated FFA BT-CIC with low energy gap of 1.3 eV, which exhibited PCE of 11.2% in contrast to 8.2% for non-Cl derivative using PTB7-Th as donor (Li et al. 2017). Most importantly, the EQE spectra of the solar cell reaches 75%, between 650 and 850 nm while leaving a transparency window between 400 and 600 nm. Furthermore, a semi-transparent device using an ultrathin (10 nm) Ag cathode shows PCE of 7.1%, with an average visible transmittance of 43 ± 2%.

Hou group introduced chlorine atoms into the terminal DCI acceptor units to develop FFAs ITIC-$Cl_2$ and ITIC-$Cl_4$ (Zhang et al. 2018a). The large dipole moment of the C–Cl bond enhances the intermolecular charge-transfer effect between the donor–acceptor structures, and thus expands the absorption and down shifts the molecular energy levels. The ITIC-$Cl_4$ film showed a broad absorption band with a maximum at 746 nm, which is red-shifted by ≈40 nm than the ITIC-4F film. The introduction of chlorine atoms causes more pronounced molecular stacking, and this further helped to broaden the absorption spectrum. OSCs devices based on two acceptors delivered PCEs of 13.16 and 13.45%, respectively, when blended with PBDT-T-2F with a low-lying HOMO level.

### 8.3.6 *Naphthyl-Based Fused Heteroacenes Core*

In the process of elongation of core unit, Ma et al. replaced the central phenyl group of IDT core with a naphthalene unit to prepare a ladder type dithienocyclopentanapthalene (DTN) building block (Fig. 8.11) (Ma et al. 2017). The new molecule DTNIC8 containing DTN core flanked by DCI units exhibited a $\lambda_{max}$ value of 660 nm with bandgap of 1.73 eV and a LUMO level of −3.93 eV. When combined with the prototypical polymer PBDB-T as donor, the device exhibited a PCE of 9.03%, a $V_{OC}$ of 0.96 V and FF of 0.73 using ITO/$TiO_2$:TOPD/BHJ layer/$MoO_3$/Ag configuration without any additives and posttreatments (Table 8.5). The device performance was slightly lower when ZnO was used as the electron transport layer. However, the device displayed a larger $E_{loss}$ of 0.77 eV. The GIWAXS study of

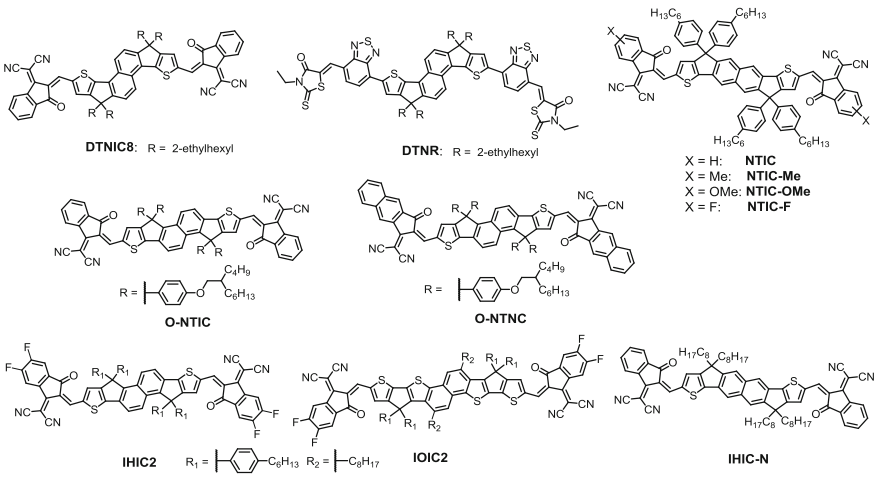


**Fig. 8.11** Structure of naphthyl-based fused heteroacenes core

**Table 8.5** Device parameters for napthyl-substituted multi-fused fullerene-free electron acceptor with polymer donors

| Acceptor | Donor | $J_{SC}$ (mA cm$^{-2}$) | $V_{OC}$ (V) | FF | PCE (%) | References |
|---|---|---|---|---|---|---|
| DTNIC8 | PBDB-T | 12.92 | 0.96 | 0.73 | 9.03 | Ma et al. (2017) |
| DTNR | PTB7-Th | 15.72 | 1.08 | 0.56 | 9.51 | Ma et al. (2017) |
| O-NTIC | PBDB-T | 13.31 | 0.98 | 0.70 | 9.10 | Huanran et al. (2018) |
| O-NTNC | PBDB-T | 15.98 | 0.94 | 0.73 | 11.0 | Huanran et al. (2018) |
| NTIC | PBDB-T | 13.55 | 0.93 | 0.68 | 8.63 | Yi et al. (2017) |
| NTIC-Me | PBDB-T | 13.03 | 0.96 | 0.66 | 8.30 | Yi et al. (2017) |
| NTIC-OMe | PBDB-T | 13.52 | 0.97 | 0.66 | 8.61 | Yi et al. (2017) |
| NTIC-F | PBDB-T | 15.04 | 0.81 | 0.66 | 8.10 | Yi et al. (2017) |
| IHIC2 | FTAZ | 16.10 | 0.77 | 0.59 | 7.30 | Zhu et al. (2017) |
| IOIC2 | FTAZ | 19.70 | 0.90 | 0.69 | 12.30 | Zhu et al. (2017) |
| IHIC-N | PTB7-Th | 13.50 | 0.85 | 0.61 | 6.91 | Zhang et al. (2018f) |
| IHIC | PTB7-Th | 19.40 | 0.75 | 0.73 | 10.60 | Zhang et al. (2018f) |
| FDNCTF | PBDB-T | 16.30 | 0.93 | 0.72 | 11.20 | Feng et al. (2017) |
| NNBDT | PBDB-T | 18.63 | 0.88 | 0.72 | 11.70 | Kan et al. (2018) |
| IDTT-BH | PBDB-T | 16.86 | 0.85 | 0.69 | 9.92 | Chang et al. (2018) |
| IDTT-OBH | PBDB-T | 17.46 | 0.87 | 0.72 | 10.93 | Chang et al. (2018) |

PBDB-T:DTNIC8 blend film revealed strong interchain π–π stacking with face-on orientation, which is beneficial for charge transport in the vertical directions.

In order to further lower the $E_{loss}$ value still maintaining high $V_{OC}$ and PCE, Ma et al. prepared a new molecular acceptor DTNR containing a weaker electron-withdrawing 3-ethylrhodanine and benzothiadiazole groups (Ma et al. 2017). The molecule exhibited a slightly blue-shifted absorption than DTNIC8 with maximum at 650 nm and optical bandgap of 1.72 eV. Furthermore, the LUMO energy level of DTNR was elevated to −3.75 eV compared to DTNIC forming a small LUMO energy offset of 0.13 eV with the donor polymer PTB7-Th. The value is much smaller compared to the widely accepted empirical value of 0.3 eV (Scharber et al. 2006). BHJ solar cells with PTB7-Th:DTNR (1:1.5 w/w) in an inverted configuration using 1% CN as solvent additive achieved a PCE of 9.51%, compared to 8.94% for PTB7-Th:$PC_{71}BM$ control device. Furthermore, the $V_{OC}$ of PTB7-Th:DTNR was 1.08 V, compared to 0.79 V for the control device due to high lying LUMO level of DTNR. The higher $V_{OC}$ lead to a small $E_{loss}$ of 0.5 eV. Despite small LUMO energy offset of 0.13 eV, photoluminescence quenching study revealed efficient photoinduced charge separation in the PTB7-Th:DTNR blend. The obtained PCE was quite high considering a bandgap of 1.73 eV. The AFM and TEM measurement demonstrate a bicontinuous interpenetrating network with nanofibrillar structure favourable for exciton separation and charge transport. Due to complementary absorption and efficient charge separation and transport of the donor and acceptor the EQE spectrum cover a broad range from 300 to 800 nm with maximum of 70% from 580 to 650 nm region.

Chen group prepared hexacyclic naphthalene(cyclopentadithiophene) core-based acceptors O-NTIC and O-NTNC with DCI and phenyl fused DCI as terminal units. Compared with O-NTIC, the introduction of additional phenyl extended end-groups in O-NTNC directed to a stronger π–π intermolecular stacking, a red-shifted absorption (706 vs. 671 nm), lowering of energy levels, good phase separation and better electron transport (Huanran et al. 2018). With PBDB-T as the donor, the conventional device with ITO/PEDOT:PSS/active layer (1:0.8 w/w)/PDINO/Al structure and DIO as solvent additive presented an outstanding PCE of 11.0% compared to 9.1% for PBDB-T:O-NTIC device. Although the $V_{OC}$ of O-NTNC-based device was slightly lower compared to O-NTIC-based device, the device achieved significantly higher $J_{SC}$ and FF, thus a higher PCE.

The authors further studied the effect of electron donating -Me and -OMe and electron withdrawing -F substitution in a series of NTIC acceptors (Yi et al. 2017). Compared to parent NTIC, the insertion of -Me or -OMe groups in NTIC-Me, NTIC-OMe blue-shifted the absorption and elevated the LUMO energy level, thus obtained a high $V_{OC}$ of 0.96 V. However, the fluorinated molecule NTIC-F gave the lowest $V_{OC}$ of 0.81 V due to its low lying LUMO level, however the strong red-shifted absorption enable high $J_{SC}$ value of 15.04 mA $cm^{-2}$ among all devices. In the series, OSC devices based on PBDB-T:NTIC achieved the highest PCE of 8.63% after SVA treatment from chloroform.

Zhan group prepared a new octacyclic naphtho[1,2-*b*:5,6-*b*′]dithiophene-based molecular acceptor IOIC2 which showed a stronger absorption ($\lambda_{max}$ = 730 nm)

and higher HOMO and LUMO energy levels relative to IHIC2 ($\lambda_{max}$ = 682 nm) (Zhu et al. 2017). In comparison to IHIC2, IOIC2 showed a larger extended π-conjugation and stronger intermolecular π–π stacking which contributed to a higher electron mobility, leading to a high FF of 0.69 than IHIC2 (FF = 0.59) in the device when blended with FTAZ polymer and 0.2% DIO as the processing additive. Along with higher $J_{SC}$ (19.7 mA cm$^{-2}$) and $V_{OC}$ (0.90 V) values the IOIC2-based device generated an excellent PCE of 12.3% compared to 7.3% ($J_{SC}$ = 16.1 mA cm$^{-2}$, $V_{OC}$ = 0.77 V) for IHIC2-based device.

Marder and co-workers recently reported a planar molecular acceptor IHIC-N which differ by solubilizing alkyl substituents in the backbone and regioisomerism of the naphthalene core (Zhang et al. 2018f). The device with PTB7-Th as donor and IHIC-N as acceptor furnished a reasonable PCE of 6.91% using 0.5% DIO as processing additive. The PCE was quite low compared to IHIC-based devices (10.6%). The $V_{OC}$ of IHIC-devices was quite low, however, the higher PCE was due to the increase in the $J_{SC}$ and FF.

### 8.3.7 *Naphthyl-Based Terminal Units*

Chen group further extended the π-system of the terminal acceptor units in FDICTF by naphthyl groups in FDNCTF with the aim to red-shift the absorption and increase the intermolecular end-to-end π−π interaction and molecular packing for better charge transport (Fig. 8.12) (Feng et al. 2017). The introduction of naphthyl-group red-shift the absorption maximum to 714 nm resulting in a slight reduction of the bandgap (1.60 eV). However, the naphthyl-substitution has a little impact on the molecular energy levels. BHJ devices based on PBDB-T:FDNCTF generated an improved PCE of 11.2% due to improvement in the both $J_{SC}$ and FF without affecting the $V_{OC}$ compared to that of the FDICTF-based device with phenyl groups at the termini (Table 8.5). Transient absorption studies revealed a

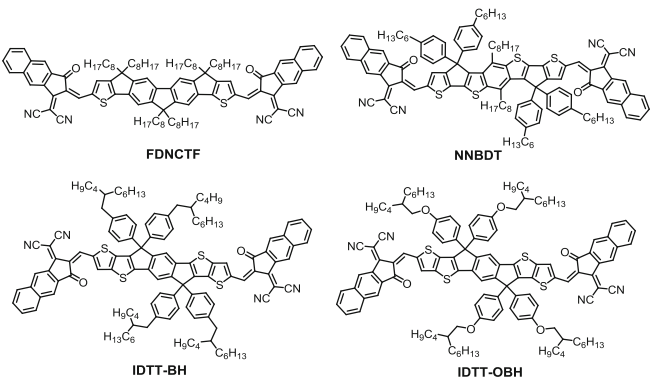


**Fig. 8.12** Molecular structures of naphthyl-based terminal units

significant improvement in the charge separation efficiency due to increase in D:A interfacial interactions. The device performance was further improved using a new low band gap FFA NNBDT ($E_g$ = 1.43 eV) which extended the absorption up to 870 nm. BHJ devices prepared using PBDB-T:NNBDT blend (0.5% vol. DIO) increased the PCE to 11.7% and FF of 0.72 with $E_{loss}$ of 0.55 eV (Kan et al. 2018).

It is always important to choose an appropriate donor material for a particular acceptor in order to achieve the best solar cell performance. Chen group prepared two FFAs, namely IDTT-BH and IDTT-OBH which differs by the side-chains attached to the phenyl groups (Chang et al. 2018). The absorption properties and energy levels of the two molecule were not influenced by the attached side-chains. However, when the two acceptors were blended with three polymer donors namely, J71, PDCBT and PBDB-T a significant difference in the device performance was observed. For J71 and PDCBT donor IDTT-BH was found to be the best acceptor showing PCEs of 11.05 and 10.35%, respectively. While for IDTT-OBH acceptor, PBDB-T polymer showed the superior PCE of 10.93% compared to 9.92% for PBDB-T:IDTT-BH blend. The results were explained by the role of side chains on tuning of the blend morphology and suggest that the choice of D:A pair is very important to achieve best solar cell performance.

### 8.3.8 *Ladder-Type Carbon-Oxygen-Bridged Heteroacenes*

As discussed, ladder-type conjugated structures with fused carbon bridge heterocycles have been widely used to develop FFAs (Fig. 8.13). In order to fine tune the properties, such as solubility, absorption property, energy levels, molecular packing etc. electron donating oxygen atom as alkoxy groups is being introduced to the

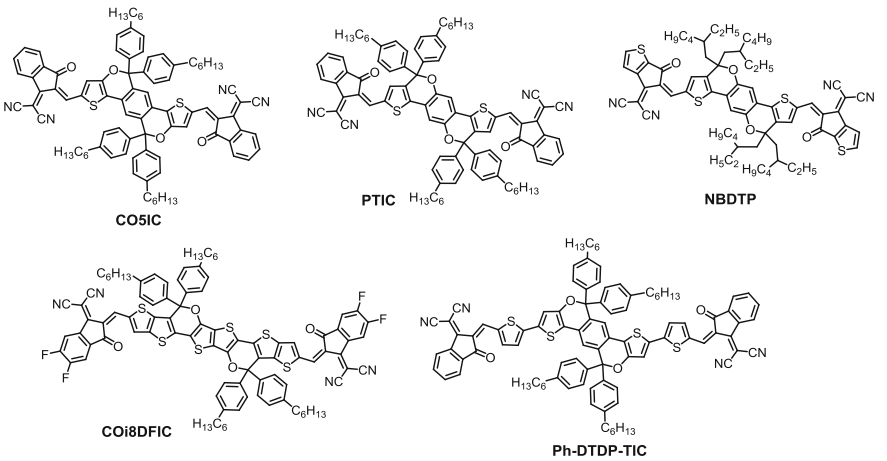


**Fig. 8.13** Structure of ladder-type carbon-oxygen-bridged heteroacenes

**Table 8.6** Solar cell parameters for C-O-bridged and selenophene-substituted fullerene-free electron acceptor with polymer donors

| Acceptor | Donor | $J_{SC}$ (mA cm$^{-2}$) | $V_{OC}$ (V) | FF | PCE (%) | References |
|---|---|---|---|---|---|---|
| CO5IC | PBDB-T | 13.31 | 0.83 | 0.68 | 7.49 | Xiao et al. (2017b) |
| COi8DFIC | PTB7-Th | 26.10 | 0.68 | 0.68 | 12.16 | Xiao et al. (2017c) |
| PTIC | PBDB-T | 14.20 | 0.84 | 0.64 | 7.66 | Wen et al. (2018) |
| NBDTP | PBDB-T | 15.72 | 0.94 | 0.66 | 10.10 | Wu et al. (2017) |
| Ph-DTDP-TIC | PBDB-T | 17.31 | 0.89 | 0.60 | 9.21 | Yang et al. (2018a) |
| IDTIDSe-IC | J51 | 15.16 | 0.91 | 0.58 | 8.02 | Li et al. (2016e) |
| IDSe-T-IC | J51 | 15.20 | 0.91 | 0.62 | 8.58 | Li et al. (2016f) |
| IDT2Se | PDBT-T | 17.49 | 0.89 | 0.61 | 9.36 | Liang et al. (2018) |
| IDT2Se-F | PDBT-T | 21.49 | 0.79 | 0.66 | 11.19 | Liang et al. (2018) |

central bridging carbon or on the conjugated moieties. In a recent report by Xiao et al. a "carbon-oxygen bridge" (CO) was introduced to replace the carbon bridge and develop a new ladder-type molecule CO5IC with stronger electron-donating ability (Xiao et al. 2017c). CO5IC showed a red-shifted absorption maximum at 698 nm compared to 687 nm for analogous IDT-IC without oxygen bridge and a lower bandgap of 1.62 eV vs. 1.70 eV. Inverted OSCs device based on PBDB-T: CO5IC blend films (1:1 w/w) gave high FF of 0.68 and PCE of 7.49% as compared to IDT-IC-blended film having FF of 0.62 and PCE of 6.05% (Table 8.6). The $V_{OC}$ of CO5IC-based device was lower compared to IDT-IC due to lower LUMO level (−4.13 vs. −3.93 eV), however, the higher $J_{SC}$ (13.31 vs. 10.94 mA cm$^{-2}$) was due to the stronger light-harvesting capability of CO5IC.

The same group further developed an octafused C-O-bridged A-D-A acceptor COi8DFIC (Xiao et al. 2017c). Oligomer COi8DFIC with electron donating planar thienothiophene units at the core and electron accepting fluorine-substituted DCI units showed a broader absorption with a smaller optical bandgap ($E_g$ = 1.26 eV) relative to that of CO5IC ($E_g$ = 1.62 eV). The solar cells based on the PTB7-Th: COi8DFIC blend (1:1, w/w, DIO additive) blend yielded a PCE of 12.16% and a very high $J_{SC}$ of 26.1 mA cm$^{-2}$, one of the highest values reported for single-junction OSCs. The device demonstrated a maximum EQE of 83% at 830 nm, corresponding to the absorption maximum of COi8DFIC in thin film.

Wen et al. reported a C-O-bridged acceptor PTIC, in which the bridging oxygen atom was facing inside (Wen et al. 2018). The pyran-core was achieved by a $BBr_3$-mediated tandem cyclization-deprotection reaction. Compared to isomeric CO5IC, PTIC showed a red-shifted absorption with maximum at 734 nm and bandgap of 1.55 eV. BHJ solar cell using PBDB-T:PTIC blend in a conventional structure achieved a PCE of 7.66% after thermal annealing at 160 °C.

Zhu group designed a new benzodi(thienopyran) unit to prepared NBDTP molecule in which the phenyl groups of terminal DCI units were replace by thiophene units (Wu et al. 2017). The ethylhexyl groups were introduced in order to

improve the solubility and morphology in the blend films. The molecule exhibited an optical bandgap of 1.58 eV with a LUMO energy level of −3.79 eV. Conventional BHJ devices using PBDB-T:NBDTP achieved a high PCE of 10.1% after thermal annealing compared to 7.25% for the as-cast device. High EQE value of 70% at 720 nm assigned to the NBDTP contribution, suggesting efficient charge transfer between the HOMO of the polymer to the acceptor.

Wang and co-workers prepared a dipyran-based ladder type molecular acceptor Ph-DTDP-TIC in which two oxygen atoms were part of the fused-conjugated bridge (Yang et al. 2018a). The molecule achieved a broad absorption with maximum at 740 nm and optical bandgap of 1.46 eV in thin film. An inverted OSC device based on PBDB-T:Ph-DTDP-TIC with 1% CN as processing additive resulted a high PCE of 9.21% with an energy loss of 0.57 eV.

### 8.3.9 Selenophene-Substituted A-D-A Type Heteroacenes

Another strategy to modify the molecular properties of an oligomer is to replace the sulfur atom by lager selenium atom (Fig. 8.14). The introduction of selenium atom in the backbone can increase orbital overlap due to its larger size and loosely bound outermost electron, reduce the bandgap, thus red-shift the absorption, improve interchain charge transfer and show better polarizability compared to thiophene analogues. Recently, Liao and co-workers have reported a decacyclic conjugated molecule IDTIDSe-IC in which the terminal thiophene units were replaced with selenophene groups (Li et al. 2016e). The molecule showed very similar optical properties and energy levels compared to IDTIDT-IC. The LUMO offset between a polymer donor J51 and IDTIDSe-IC was 0.51 eV, which is large enough for efficient electron transfer from donor to the acceptor. While the small HOMO offset of 0.12 eV could still be sufficient for hole transport from acceptor to the donor. Conventional BHJ solar cells fabricated using J51:IDTIDSe-IC blend (1:1 w/w) and PDINO as electron transport layer resulted in a PCE of 8.0% outperforming the value of control device with J51:$PC_{71}BM$ (6.0%) (Table 8.6). EQE spectra covering from 300 to 800 nm region displayed the contribution of both donor and acceptor to the photocurrent generation. The authors further prepared another selenophene containing acceptor IDSe-T-IC, which has a slightly lower bandgap of 1.52 eV compared to its thiophene analogue IEIC (1.57 eV). The reduced bandgap

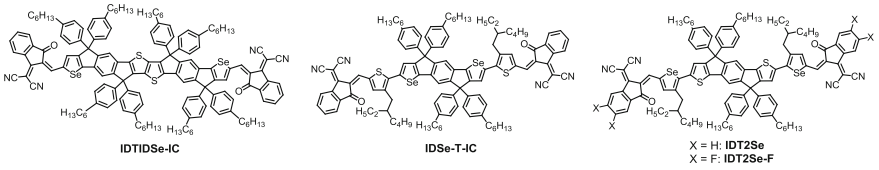


**Fig. 8.14** Structure of selenophene-substituted A-D-A type heteroacenes

is due to decreased backbone twisting and increase in quinoid character. The device exhibited a PCE of 8.58% when blended with J51 donor in 1:1 w/w ratio without an external treatment and an $E_{loss}$ of 0.61 eV (Li et al. 2016f).

When the thiophene π-bridge was exchanged by selenophene in IDT2Se the molecular planarity increases, thus led to a lower bandgap of 1.45 eV and red-shifted absorption ($\lambda_{max}$ = 747 nm) than that of the IEIC with thiophene as π-bridge (Liang et al. 2018). The bandgap was further lowered to 1.39 eV by using diflurinated DCI as terminal units in IDT2Se-F, a lower value than that of the thiophene analogue DC-IDT2T (1.55 eV). When combined with a medium bandgap donor polymer PDBT-T, IDT2Se-based device achieved a PCE of 9.36%, while IDTSe-2F displayed an outstanding PCE of 11.19% after dual SVA and TA treatments. PDBT-T:IDT2Se-F device demonstrated a lower $V_{OC}$ compared to IDT2Se-based device due to down-shifted LUMO level, while, the strong red-shifted absorption enable high $J_{SC}$ and FF. The photo-current response extended up to 850 and 900 nm for the IDT2Se and IDT2Se-4F based devices, respectively.

### *8.3.10 All Oligomer-Based Solar Cells*

The use of p-type oligomer instead of polymer as donor material is to avoid batch-to-batch variations in synthesis and thus to achieve high reproducibility in OSC devices (Mishra and Bäuerle 2012; Lin and Zhan 2016). Currently, the PCEs of oligomer-based solar cells is very much comparable to polymer-based devices using fullerene derivatives as acceptor. Therefore, it can be advantageous to use oligomeric donor in combination with n-type FFAs to prepare all oligomer solar cells. However, the major challenge in all oligomer devices could be the control of phase separation arising from well mixing of the oligomeric donor and acceptor having anisotropic structures and strong intermolecular packing. Furthermore, the phase separation is seems to be highly sensitive to processing conditions (Schulz et al. 2015). In this section we will discuss the photovoltaic characteristics of some A-D-A-type oligomers in combination with heteroacene-based A-D-A acceptors.

Zhan group prepared two oligomers BDT-2DPP and BDTS-2DPP containing benzo[1,2-*b*:4,5-*b*′]dithiophene (BDT) core connected by electron withdrawing diketopyrrolopyrrole units (Fig. 8.15) (Lin et al. 2016d). The oligomers when blended with IEIC acceptor in a ratio of 1:1 processed from chloroform:*o*-dichlorobenzene (2:1) binary solvent mixture, the corresponding BHJ devices generated PCEs of 4.0 and 5.29%, respectively (Table 8.7). The inverted OSCs based on BDTS-2DPP:IEIC resulted in an improved PCE of up to 6.03%.

Lee and co-workers used an alkylthienyl-substituted BDT-based oligomer BDT3TR as donor (Badgujar et al. 2016) which exhibit optical bandgap of 1.82 eV, complementary absorption and appropriate energy levels to the molecular acceptor O–IDTBR (Badgujar et al. 2016). BHJ solar cells were prepared using ITO/PEDOT:PSS/active layer/ZnO NPs/CPE/Al structure. The introduction of

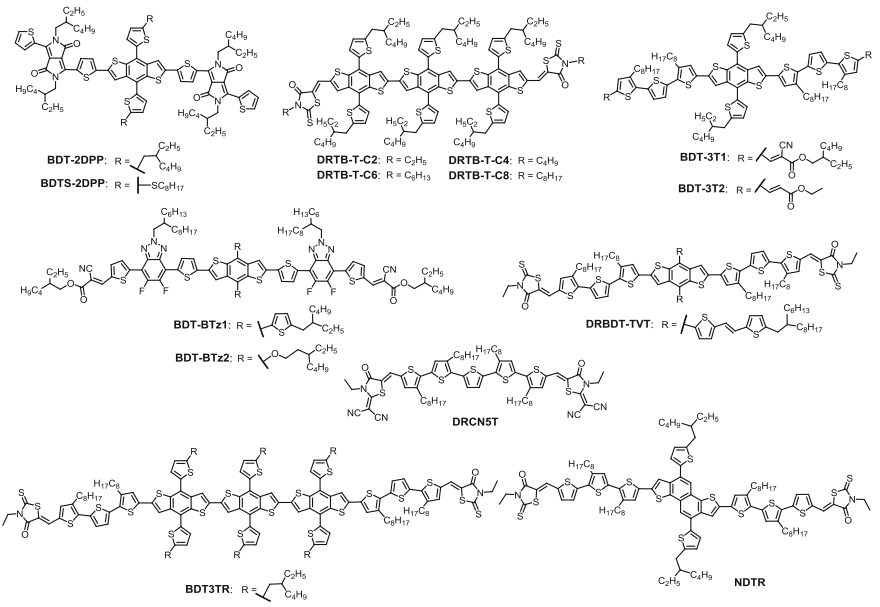


**Fig. 8.15** Structure of donor materials used in FFAs

**Table 8.7** Device parameters for fullerene-free all oligomer solar cells

| Acceptor | Donor | $J_{SC}$ (mA cm$^{-2}$) | $V_{OC}$ (V) | FF | PCE (%) | References |
|---|---|---|---|---|---|---|
| IEIC | BDT-2DPP | 8.24 | 0.90 | 0.54 | 4.00 | Lin et al. (2016d) |
| IEIC | BDTS-2DPP | 9.80 | 0.93 | 0.58 | 5.29[a] | Lin et al. (2016) |
| IEIC | BDTS-2DPP | 10.87 | 0.94 | 0.59 | 6.03[b] | Lin et al. (2016d) |
| O–IDTBR | BDT3TR | 12.10 | 1.06 | 0.55 | 7.09 | Badgujar et al. (2016) |
| IDIC | BDT-BTz1 | 15.21 | 0.98 | 0.65 | 9.73 | Bin et al. (2017) |
| IDIC | BDT-BTz2 | 10.51 | 0.96 | 0.56 | 5.51 | Bin et al. (2017) |
| IDIC | BDT-3T1 | 15.18 | 0.90 | 0.74 | 10.11 | Qiu et al. (2017) |
| IDIC | BDT-3T2 | 10.77 | 0.77 | 0.64 | 5.32 | Li et al. (2018) |
| IDIC | NDTR | 13.20 | 0.89 | 0.57 | 6.60 | Li et al. (2018) |
| IDIC | DRBDT-TVT | 12.22 | 0.84 | 0.65 | 6.63 | Huo et al. (2018) |
| IDIC | DRTB-T-C2 | 14.25 | 0.98 | 0.65 | 9.08 | Yang et al. (2017b) |
| IT-4F | DRTB-T-C2 | 16.66 | 0.89 | 0.64 | 9.52 | Yang et al. (2018b) |
| IT-4F | DRTB-T-C4 | 18.27 | 0.91 | 0.68 | 11.24 | Yang et al. (2018b) |
| IT-4F | DRTB-T-C6 | 17.92 | 0.93 | 0.63 | 10.52 | Yang et al. (2018b) |
| IT-4F | DRTB-T-C8 | 16.15 | 0.93 | 0.61 | 9.14 | Yang et al. (2018b) |
| DIC8-H | DRCN5T | 13.44 | 0.95 | 0.63 | 8.00 | Wang et al. (2018) |
| IDIC8-M | DRCN5T | 10.36 | 1.00 | 0.61 | 6.31 | Wang et al. (2018) |
| IDIC8-F | DRCN5T | 15.21 | 0.86 | 0.64 | 8.42 | Wang et al. (2018) |

[a]Conventional device structure
[b]Inverted device structure

conjugated polyelectrolyte (CPE) elevate the work function of Al electrode due to interfacial dipole of CPE and reduce the energy barrier between the cathode and the photoactive layer. ZnO was used as hole blocking layer and to facilitate electron injection and transport to the Al electrode via CPE. All oligomer solar cells based on BDT3TR:O–IDTBR exhibited a PCE of 7.09% and a high $V_{OC}$ of 1.06 V and $J_{SC}$ of 12.1 mA cm$^{-2}$. However, the FF was much lower (0.55) compared to $PC_{71}BM$-based device, thus the overall PCE was comparable to BDT3TR:$PC_{71}BM$ (7.14%).

Li group prepared two molecules BDT-BTz1 and BDT-BTz2 which when combined with IDIC acceptor (2:1 w/w) in a conventional device with PDINO as ETL generated PCEs of 9.73 and 5.51%, respectively, after thermal annealing at 120 °C for 10 min (Bin et al. 2017). The high efficiency for BDT-BTz1-based device was mainly due to dual edge-on and face-on orientation of the molecules in the blend suggesting the co-existence of both vertical and parallel charge transport pathways. On the other hand, BDT-BTz2-based blended films showed only edge-on orientation, thus hampering the charge transport and collection efficiency. The authors further prepared to oligomers BDT-3T1 and BDT-3T2 which differed by terminal acceptor groups (Qiu et al. 2017). In BHJ devices with IDIC as acceptor the cyano-substituted oligomer BDT-3T1-based blend reached PCEs of up to 10.11% and a FF of 0.73, which is significantly higher compared to BDT-3T2-based device (5.32%). Li et al. reported a naphtho[1,2-*b*:5,6-*b*′] dithiophene-based oligomer NDTR, which when blended with IDIC acceptor displayed PCE of 6.6% (Li et al. 2018). The PCE was lower than the NDTR:$PC_{71}BM$ devices (7.75%) mostly due to lower FF arising from different morphology which suffered from transport losses in the blends. Using a medium bandgap oligomer DRBDT-TVT and IDIC acceptor, BHJ solar cell exhibited a PCE of 6.63% compared to 6.87% for DRBDT-TVT:$PC_{71}BM$ after SVA treatment (Huo et al. 2018).

Hou and co-workers prepared an oligomer DRTB-T-C2 based on tris-alkylthienyl BDT terminated with 3-ethylrhodanine acceptors (Yang et al. 2017b). The oligomer resulted in a PCE of 9.08% when blended with IDIC acceptor after SVA treatment for 60s. SVA treatment improve the molecular crystallinity and thus increase the charge transport and reduce recombination. They further prepared a series of DRTB-T-Cn ($n$ = 4, 6, 8) oligomers in which the alkyl chains attached to the terminal rhodanine units were varied (Yang et al. 2018b). The study revealed that the charge transport properties were very sensitive to the molecular packing arose due to the orientation of the terminal alkyl chains. It was observed that with increasing alkyl chains from C2 to C8 the molecular orientation changes from edge-on to face-on. The inverted device based on DRTB-T-C2:IT-4F blend gave a PCE of 9.52% which exhibited edge-on orientation in the blend. In contrast, DRTB-T-C4:IT-4F blend with face-on orientation showed an enhanced PCE of 11.24% with a high $J_{SC}$ of 18.27 mA cm$^{-2}$. The device performance of longer C6 and C8-alkyl chains were slightly lowered. Most interestingly, a high PCE of 10% could be maintained with DRTB-T-C4:IT-4F active layer thickness up to 300 nm.

Very recently, Chen group described three molecules, namely IDIC8-H, IDIC8-M, IDIC8-F and used as acceptor materials with one of the high performance

donor DRCN5T (Wang et al. 2018). The acceptors displayed absorption maxima at 709, 701 and 725 nm leading to optical bandgap of 1.64, 1.66 and 1.58 eV, respectively. BHJ devices prepared using IDIC8-H:DRCN5T in a ratio of 1:1 reached a PCE of 8.0% after SVA treatment from $CS_2$:$CHCl_3$ mixture solvent. When the terminal DCI acceptors were functionalized with methyl and fluorine groups in IDIC8-M, IDIC8-F, the devices generated PCEs of 6.31 and 8.42%, respectively. The improved PCE for the fluorinated acceptor was mainly because of higher $J_{SC}$ and FF values due to higher crystalline behavior and strong face-on orientation of both the donor and acceptor. Whereas, the methyl derivative IDIC8-M gave the highest $V_{OC}$ of 1.0 V compared to 0.95 V for IDIC-H and 0.86 V for IDIC-F associated with the LUMO level alignments.

All the results discussed above demonstrated that it is very important to tune the properties of donor polymer/oligomer in order to improve the photovoltaic performance in combination with fullerene-free acceptor. Furthermore, controlling the nanoscale morphology of the active layer is most critical factor in determining the PCE and overall stability of a BHJ solar cell.

### *8.3.11 Ternary Bulk-Heterojunction Solar Cells*

Although high PCEs <13% have been reached in BHJ solar cells using binary components, there are still room for the improvement because of the missing light absorption in the either low or higher energy region of the solar spectrum. In most of the binary systems discussed above low band gap molecular acceptors were used in combination with low bandgap polymer/oligomer donors. In many cases wide bandgap donor materials having complementary absorption to the acceptors were used in order to improve the light absorption in a broad spectral region, thus to improve the photocurrent as well as the PCEs in the devices. However, it is difficult to achieve a binary system which can cover entire solar spectrum region. In order to fill the gap tandem cell concept were implemented however, this requires a tedious fabrication conditions, thus could increase the device cost (Xu et al. 2018; Li et al. 2013; Sista et al. 2011). Therefore, many research groups started to introduce a third component into the binary system in order to complement the absorption of D:A blend and at the same time provide additional cascade-type charge transfer pathway for exciton dissociation and transport (Cheng et al. 2014; An et al. 2016; Ameri et al. 2013; Huang et al. 2018). The BHJSCs fabricated using ternary blend composed of either two donors and one acceptor (D-D-A) or one donor and two acceptors (D-A-A). The ternary system could reduce the complexity in the device fabrication conditions although the addition of the third component needs to be optimized in order to achieve the best performance. The introduction of third component plays an important role in the device performance and can also modify the molecular energy levels, thus fine tune the photovoltage (Yu et al. 2018).

Because of the different energy levels of the three components and diverse morphological features, there are generally three working mechanisms that control

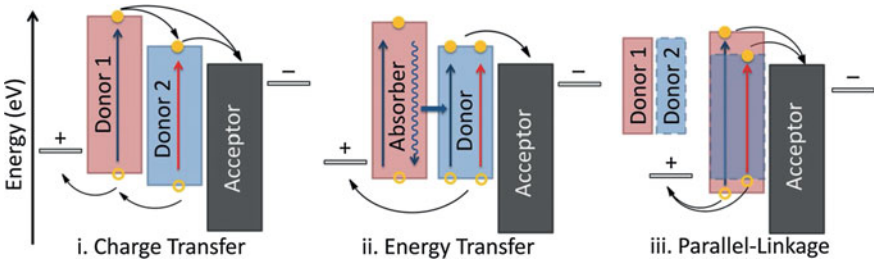


**Fig. 8.16** Three fundamentally different mechanisms that can potentially improve the efficiency of ternary organic solar cells: charge transfer, energy transfer, and parallel-linkage. Reproduced with permission from Ref. Yang et al. (2013). Copyright (2013) American Chemical Society

the photovoltaic processes in ternary devices: (i) charge transfer, (ii) energy transfer, and (iii) parallel-linkage transfer (Fig. 8.16) (Yang et al. 2013). Generally, the operating mechanisms in ternary systems are interrelated. In i) after excitation both donor can directly contribute to the charge carrier generation when interacting with acceptor. Then the electron can transfer to the cathode via the acceptor and holes transported to the anode through one donor. In ii) energy transfer process plays an important role where holes are generated within the domain of one donor and second donor acts only as light absorber which transfer the energy to the other donor via Dexter or Föster energy transfer. All this process depends on the alignment of the energy levels and bandgap. In the process iii) first the excitons generated in each donor domains and then migrate to their respective D:A interface and then dissociate into free charge carriers. Therefore, each process shown in Fig. 8.16 works differently and has its own limitations and advantages.

#### 8.3.11.1 D:D:A System Using Fullerene-Free Acceptor

In order to cover a broad spectral range, thus to improve the $J_{SC}$ value, Hou group introduced a second donor material J52 (300–650 nm) into the binary blend of PTB7-Th (400–780 nm) and IEICO-4F (600–1000 nm) (Yao et al. 2017). The corresponding ternary device using 30% of J52 polymer gave similar $V_{OC}$ and FF but a higher $J_{SC}$ of 25.3 mA cm$^{-2}$ and an impressive PCE of 10.9% compared to the binary device (Table 8.8). The insertion of J52 improved the photoresponse in the higher energy region and reduce the bimolecular recombination.

#### 8.3.11.2 D:A:A Systems with Fullerene Derivatives as a Component

Bo and co-workers presented a ternary-blend strategy to overcome the shortcomings of both fullerene derivatives and FFAs. The optimal inverted ternary device PPBDTBT:ITIC:$PC_{71}BM$ (1:1.2:0.8 w/w/w) displayed a high PCE of 10.4%,

which has of about 35–40% enhancement relative to both the binary reference devices (Lu et al. 2016). It was found that the $V_{OC}$ decreases with increasing the fullerene content in the device. In the ternary system, $PC_{71}BM$ helps to disrupt the aggregation of ITIC and thus increase the D:A interface area. Furthermore, the fullerene derivative with low lying HOMO/LUMO energy level provide a cascade energy gradient among the three components and facilitate the electron/hole transport and reduce charge recombination. ITIC used to extend the light absorption to the low energy region and act as a bridge for charge transfer.

Hou and co-workers reported a ternary BHJ device with PBDTTT-E-T as polymer donor and IEICO as oligomeric acceptor, in which 5% (w/w) bis-$PC_{71}BM$ was added as the third component (Chen et al. 2017a). The PCE of the ternary device was found to be 10.21% which is significantly higher compared to the corresponding binary device based on PBDTTT-E-T:IEICO (8.33%). The LUMO level of bis-$PC_{71}BM$ lies in between the LUMO levels of PBDTTT-E-T and IEICO, thus formed a cascade for charge transfer process. Due to their spherical shape, the fullerene derivatives can also transport electron isotropically. EQE spectra revealed that the addition of minute amount of bis-$PC_{71}BM$, instead of contributing to the photocurrent, played a role of a sensitizer and enhanced the EQE from 600-800 nm region in the ternary blend, leading to an enhancement in the $J_{SC}$ and FF. Morphological studies revealed that the small amount of bis-$PC_{71}BM$ could induce the aggregate formation of the polymer, beneficial for facilitating the charge transport and preventing the charge recombination processes in the device. The authors also introduced bis-$PC_{71}BM$ into the binary blend of PBDB-T:IT-M in order to compensate the absorption losses in the higher energy region (Zhao et al. 2017b). With a blend ratio of PBDB-T:IT-M:bis-$PC_{71}BM$ (1:1:0.2) high PCE of 12.2% and FF of 0.74 could be realized which is ∼13% higher compared to the PBDB-T:IT-M binary device. EQE spectra revealed that the addition of bis-$PC_{71}BM$ not only improve the photocurrent enhancement in the higher energy region but also improve the exciton dissociation and charge transport in the lower energy region i.e. PBDB-T:IT-M interface. The device performance was found to be insensitive to the fullerene content (0.2 to 1 wt%) in the blend.

Ternary devices constructed with PBTA-BO:$PC_{71}BM$:IffBR (1:1:0.6 w/w/w) as the photoactive layer displayed a PCE of 9.06% using 0.5 vol% diphenylether (DPE) as solvent additive. The PCE was significantly higher than those of binary devices based on either PBTA-BO:IffBR (6.34%) or PBTA-BO:$PC_{71}BM$ (4.73%) (Zhong et al. 2017). The enhancement was attributed to the broadened absorption of ternary blend, formation of cascade charge-transfer pathways, reduced non-geminate recombination, enhanced charge extraction, and more favourable morphologies of the BHJ films.

A dihydronaphthyl-based $C_{60}$ bis-adduct NCBA was introduced as third component into the binary mixture of PBDB-T:ITIC (Niu et al. 2018). The PBDB-T:NCBA:ITIC-based (1:0.1:0.9) inverted solar cells showed an optimized PCE value of 9.56% a slightly higher value compared to PBDB-T:ITIC binary device (8.45%). The LUMO level of NCBA (3.7 eV) lies between the PBDB-T (3.5 eV) and ITIC (4.0 eV) forming a favourable pathway for charge transport between the PBDB-T/

NCBA, NCBA/ITIC, and PBDB-T/ITIC interfaces. Using a PBDB-T:IDIC8-M:$PC_{71}BM$ (1:0.8:0.2) ternary blend a PCE of 10.67% has been reported due to the contribution of the fullerene derivative towards photocurrent between 300 and 400 nm region (Zhang et al. 2018) A ternary blend comprising PBDB-T:NFBDT:$PC_{71}BM$ (1:1:0.67) has achieved a PCE of 9.73% with a $J_{SC}$ of 16.84 mA $cm^{-2}$ a slightly higher value compared to the corresponding binary counterparts (Chang et al. 2018).

Xiao et al. achieved a record PCE of 14.08%, $J_{SC}$ of 28.20 mA $cm^{-2}$ and a FF of 0.71 using a ternary blend composed of PTB7-Th as donor and C-O-bridged COi8DFIC and $PC_{71}BM$ as acceptors in 1:1.05:0.45 ratio (Xiao et al. 2017a). The results demonstrate that only small amount of fullerene derivative is sufficient to obtain optimized morphology and facilitated electron transport and to reduce charge recombination in the devices. With increase in fullerene content the $V_{OC}$ was increased but the device showed a detrimental effect on $J_{SC}$ and FF leading to a lower PCE of 7.36% for PTB7-Th:$PC_{71}BM$ blend (1:1.5 w/w). This is the record value for organic solar cells reported to date and demonstrated the great potential of the use of FFAs in ternary devices.

#### 8.3.11.3 D:A:A Systems with Fullerene-Free Acceptor

McCulloch and co-workers used two FFAs O-IDTBR and O-IDFBR as components with P3HT in a ternary device which yielded a PCE of 7.7% without any post-processing treatment (Baran et al. 2016). O-IDFBR with absorption maximum at 530 nm complement to the absorption of O-IDTBR having $\lambda_{max}$ value at 690 nm. The results showed that 30% of O-IDFBR is sufficient to maintain the crystallinity of the P3HT and IDTBR component forming a cascade. Interestingly, the $V_{OC}$ of the ternary device was about 100 mV higher compared to the P3HT:O-IDTBR binary device. The three components in the ternary device maintain the microstructure crystalline domains that is favourable for photocurrent generation, reduced bimolecular recombination and enhancing charge collection efficiency. When P3HT was replaced with a low bandgap polymer PBDTTT-EFT commonly known as PTB7-Th, the PCE was improved to about 11% with a high $V_{OC}$ of 1.03 V.

Zhan and co-workers introduced a perylene derivative PDI-2DTT (1% w/w) as third component in PTB7-Th:IDT-2BR blend in ITO/PEDOT:PSS/active layer/Ca/Al device structure to enhance the driving force for charge transfer. The device with PDI-2DTT gave a PCE of 10.1% with a $V_{OC}$ of 1.03 V and low energy loss of 0.55 eV (Cheng et al. 2017). The EQE response of the ternary blend increased for PTB7-Th and IDT-2BR indicating efficient charge transfer from D to A and vice versa. The PDI-2DTT with lower HOMO/LUMO energy levels acted as an energy driver in the device.

Hou group prepared a ternary blend using a wide bandgap polymer J52 and two miscible FFAs IEICO and IT-M (Yu et al. 2017b). The two acceptors shows similar LUMO level but due to high lying HOMO level, IEICO exhibited a red-shifted

absorption complementing to the IT-M. The J52:IT-M:IEICO ternary device (1:0.8:0.2 w/w/w) obtained a PCE of 11.1% due to high $J_{SC}$ and FF compared to the binary devices. The $V_{OC}$ of the ternary device did not change due to the similar LUMO levels of both the acceptors. Furthermore, the two acceptors showed excellent compatibility in the blend due to their very similar chemical structures, and efficient energy transfer from IT-M to IEICO.

Sun group used a polymer donor PDBT-T1 and two FFAs SdiPDI-Se and ITIC-Th which possesses complementary absorption with onset of 700, 600 and 800 nm, respectively (Liu et al. 2016d). Solar cells based on PDBT-T1:SdiPDI-Se:ITIC-Th ternary blend with 50% ITIC-Th contents showed the best PCE of 10.3% with a $V_{OC}$ of 0.94 V, a $J_{SC}$ of 15.40 mA cm$^{-2}$, a FF of 0.71, a higher value than the binary counterparts. Morphological studies revealed that both FFAs exhibited reduced crystallinity in the blend without hampering the transport properties.

Marder group obtained a PCE of 11.9% using PTB7-Th:IHIC-N:IHIC ternary blend and 0.5 vol% DIO as solvent additive, which was significantly higher compared to the PTB7-Th:IHIC-N (6.9%) or PTB7-Th:IHIC (10.6%) binary device (Zhang et al. 2018f). Although INIC-N-based binary device gave the highest $V_{OC}$, the lower performance is mainly due to significantly lower $J_{SC}$ and FF. Both ternary and PTB7-Th:IHIC binary blends exhibited more balanced charge transport than PTB7-Th:IHIC-N binary blends. GIWAXS study showed broad scattering features with face-on π–π stacking for both donor (PTB7-Th) and acceptor (IHIC and/or IHIC-N) materials.

Wang and co-workers fabricated a ternary device using J71 as donor and IT-M and ITIC with an almost identical band gap as acceptors (Hu et al. 2018). The binary device fabricated using J71:IT-M and J71:ITIC devices exhibited PCEs of 10.68 and 10.65%, respectively. Although IT-M-based device exhibited higher $J_{SC}$ and $V_{OC}$, the similar PCEs are due to significantly high FF of ITIC-based device. Furthermore, the BHJ devices fabricated using optimized ternary blend of J71:IT-M:ITIC (1:0.9:0.1) reached PCEs of up to 11.6% by taking the advantages of high $J_{SC}$ and $V_{OC}$ of J71:IT-M based device and high FF of J71:ITIC based device. The ITIC acts as a morphology regulator which optimized the morphology of ternary device, thus improved the FF. It has been shown that the FF improved from 0.62 to 0.68 by increasing ITIC content from 0 to 100 wt%.

Along with the photocurrent it is also important to obtain high $V_{OC}$ in the ternary derives in order to improve the device performance. It has known that in binary devices the $V_{OC}$ depends on the difference between the HOMO of the donor and LUMO of the acceptor, however, in ternary blend the incorporation of third component plays a crucial role in tuning the $V_{OC}$ value, the mechanism of which is however unclear. The $V_{OC}$ mostly falls between the values of the respective binary devices which can be controlled by the feed ratio of the third component. Huang and co-workers demonstrated that the addition of 10% of a perylene derivative TPE-4PDI as third component into the binary mixture of PBDB-T:ITIC-Th significantly improve the PCE to 11.0% with a $V_{OC}$ of 0.87 V, $J_{SC}$ of 17.34 mA cm$^{-2}$, and FF of 0.73 (Chen et al. 2017b). The 10% of TPE-4PDI improved the $V_{OC}$ by

0.02 V. Further increase in the content of TPE-4PDI improve the $V_{OC}$ but significantly reduced the PCE due to the reduction in $J_{SC}$ and FF values.

Chen group introduced an acceptor FDNCTF as the third component to fabricate ternary devices (Kan et al. 2018). The two acceptors NNBDT and FDNCTF possess complementary absorption, same molecular orientation, and miscibility. Photolumeniscence study revealed a strong nonradiative energy transfer process from FDNCTF to NNBDT due to the overlapping of the emission of FDNCTF and absorption of NNBDT. The fullerene-free ternary cells based on PBDB-T:NNBDT:FDNCTF reached a PCE of 12.8% with an improved $J_{SC}$ of 19.9 mA $cm^{-2}$ in contrast to the binary devices. This is the highest PCE reported to date for all fullerene-free ternary OSCs.

Li and co-workers fabricated a ternary device based on two well-known FFAs IDIC and ITIC and PSTZ polymer donor (Su et al. 2017). The binary PSTZ:IDIC and PSTZ:ITIC devices gave PCEs of 8.06 and 8.13%, respectively. When 10% of ITIC was added to the PSTZ:IDIC blend the device achieved a PCE of 10.2% which was further enhanced to 11.1% by thermal annealing at 120 °C. ITIC formed a charge transport channel at the D:A interface forming a smooth energy gradient between PSTZ and IDIC. The $V_{OC}$ of the optimized ternary device was 0.95 V which was between the binary devices as it depends on the feed ratio of the second acceptor. Further increase in ITIC content increases the $V_{OC}$ but the $J_{SC}$ and FF were dramatically reduced resulting in lowering of the performance. The higher performance of the ternary device was assigned to the reduced bimolecular recombination, efficient exciton separation and cascade charge transport.

Yan and co-workers reported a novel approach towards morphology control in ternary devices in order to improve the device performance. Using a polymer donor PTFB-O which tends to show temperature dependent aggregation property and two FFAs ITIC-Th and IEIC-Th with minimized interfacial tension PCEs of up to 11.2% have been achieved (Jiang et al. 2018). The $V_{OC}$ of the ternary device strongly depend on the weight percentage of the acceptor achieving a value in between the two binary devices. Although the oligomers possessed good solubility at room temperature, the active layers were spin-coated from hot solution of chlorobenzene due to poor solubility of the polymer at room temperature. During spin-coating process the polymer aggregated/crystallized first due to fast cooling process and form polymer nanofibers and the FFAs still remain in solution. The two FFAs due to their similar interfacial tension formed mixed lamellar stacking phase and promotes a more preferential face-on orientation. The results clearly demonstrate that by minimizing the interfacial tension between the two acceptors one can control the morphology of the ternary blends similar to the binary blends and improve the device performance, specifically the FF.

**Table 8.8** Device parameters for ternary solar cells using D:D:A or D:A:A blends

| Acceptor | Donor | $J_{SC}$ (mA cm$^{-2}$) | $V_{OC}$ (V) | FF | PCE (%) | References |
|---|---|---|---|---|---|---|
| IEICO-4F | J52:PTB7-Th | 25.30 | 0.73 | 0.59 | 10.90 | Yao et al. (2017) |
| ITIC:$PC_{71}BM$ | PPBDTBT | 16.66 | 0.89 | 0.68 | 10.40 | Lu et al. (2016) |
| IEICO: bis-$PC_{71}BM$ | PBDTTT-E-T | 18.92 | 0.83 | 0.65 | 10.20 | Chen et al. (2017a) |
| IT-M: bis-$PC_{71}BM$ | PBDB-T | 17.39 | 0.95 | 0.74 | 12.20 | Zhao et al. (2017b) |
| IffBR: $PC_{71}BM$ | PBTA-BO | 14.52 | 0.91 | 0.67 | 9.06 | Zhong et al. (2017) |
| ITIC:NCBA | PBDB-T | 15.80 | 0.92 | 0.66 | 9.56 | Niu et al. (2018) |
| IDIC8-M: $PC_{71}BM$ | PBDB-T | 16.80 | 0.87 | 0.73 | 10.67 | Zhang et al. (2018) |
| NFBDT: $PC_{71}BM$ | PBDB-T | 16.84 | 0.84 | 0.69 | 9.73 | Chang et al. (2018) |
| COi8DFIC: $PC_{71}BM$ | PTB7-Th | 28.20 | 0.70 | 0.71 | 14.08 | Xiao et al. (2017a) |
| O-IDTBR: O-IDFBR | P3HT | 14.40 | 0.82 | 0.64 | 7.70 | Baran et al. (2016) |
| O-IDTBR: O-IDFBR | PTB7-Th | 17.20 | 1.03 | 0.60 | 11.00 | Baran et al. (2016) |
| IDT-2BR: PDI-2DTT | PTB7-Th | 14.50 | 1.03 | 0.65 | 10.10 | Cheng et al. (2017b) |
| IT-M:IEICO | J52 | 19.70 | 0.85 | 0.67 | 11.10 | Yu et al. (2017b) |
| SdiPDI-Se: ITIC-Th | PDBT-T1 | 15.40 | 0.94 | 0.71 | 10.30 | Liu et al. (2016d) |
| IHIC-N:IHIC | PTB7-Th | 21.30 | 0.79 | 0.71 | 11.90 | Zhang et al. (2018)f |
| IT-M:ITIC | J71 | 18.08 | 0.98 | 0.66 | 11.60 | Hu et al. (2018) |
| ITIC-Th: TPE-4PDI | PBDB-T | 17.34 | 0.87 | 0.73 | 11.04 | Chen et al. (2017b) |
| NNBDT: FDNCTF | PBDB-T | 19.90 | 0.89 | 0.72 | 12.80 | Kan et al. (2018) |
| ITIC:IDIC | PSTZ | 17.40 | 0.95 | 0.67 | 11.10 | Su et al. (2017) |
| ITIC-Th: IEIC-Th | PTFB-O | 16.40 | 0.95 | 0.72 | 11.20 | Jiang et al. (2018) |

## 8.4 Conclusion

In this chapter we have summarized the recent progress in thin film OSCs containing fullerene-free molecular acceptors (n-type semiconductors) for solution-processed OSCs, which in combination with polymer/oligomer donors achieved record PCE >14%. In order to achieve this efficiency great effort has also

been paid towards the preparation of new polymer donors. A structure-property device performance relationships have been established which is beneficial for the development of new material. Different molecular design strategies were used in order to tune the optical properties, energy levels, charge carrier mobilities. Along with these parameters solid state packing of these materials and their in-depth understanding are also highly important. Many of the FFAs discussed here can be costly because of the multistep synthesis and low yield. In order to fully realize the potential of this thin film solar cell technology for commercialization and cost effective, both PCEs and stability will have to be improved beyond the present state-of-the-art. At the same time processability of these devices without chlorinated solvents is very important for practical applications. With appropriate structural tuning of molecular acceptors and device engineering, PCEs beyond 15% is not far away to achieve.

**Acknowledgements** The authors would like to acknowledge Department of Science and Technology (DST), New Delhi (DST/TMD/SERI/D05) for financial support.

## References

Ameri T, Khoram P, Min J, Brabec CJ (2013) Organic ternary solar cells: a review. Adv Mater 25 (31):4245–4266

An Q, Zhang F, Zhang J, Tang W, Deng Z, Hu B (2016) Versatile ternary organic solar cells: a critical review. Energy Environ Sci 9(2):281–322

An Q, Gao W, Zhang F, Wang J, Zhang M, Wu K, Ma X, Hu Z, Jiao C, Yang C (2018) Energy level modulation of non-fullerene acceptors enables efficient organic solar cells with small energy loss. J Mater Chem A 6(6):2468–2475

Badgujar S, Lee G-Y, Park T, Song CE, Park S, Oh S, Shin WS, Moon S-J, Lee J-C, Lee SK (2016a) High-performance small molecule via tailoring intermolecular interactions and its application in large-area organic photovoltaic modules. Adv Energy Mater 6:1600228

Badgujar S, Song CE, Oh S, Shin WS, Moon S-J, Lee J-C, Jung IH, Lee SK (2016b) Highly efficient and thermally stable fullerene-free organic solar cells based on a small molecule donor and acceptor. J Mater Chem A 4(42):16335–16340

Bai H, Wang Y, Cheng P, Wang J, Wu Y, Hou J, Zhan X (2015a) An electron acceptor based on indacenodithiophene and 1,1-dicyanomethylene-3-indanone for fullerene-free organic solar cells. J Mater Chem A 3(5):1910–1914

Bai H, Wu Y, Wang Y, Wu Y, Li R, Cheng P, Zhang M, Wang J, Ma W, Zhan X (2015b) Nonfullerene acceptors based on extended fused rings flanked with benzothiadiazolyl-methylenemalononitrile for polymer solar cells. J Mater Chem A 3(41):20758–20766

Baran D, Kirchartz T, Wheeler S, Dimitrov S, Abdelsamie M, Gorman J, Ashraf RS, Holliday S, Wadsworth A, Gasparini N, Kaienburg P, Yan H, Amassian A, Brabec CJ, Durrant JR, McCulloch I (2016a) Reduced voltage losses yield 10% efficient fullerene free organic solar cells with >1 V open circuit voltages. Energy Environ Sci 9(12):3783–3793

Baran D, Ashraf RS, Hanifi DA, Abdelsamie M, Gasparini N, Röhr JA, Holliday S, Wadsworth A, Lockett S, Neophytou M, Emmott CJM, Nelson J, Brabec CJ, Amassian A, Salleo A, Kirchartz T, Durrant JR, McCulloch I (2016b) Reducing the efficiency–stability–cost gap of organic photovoltaics with highly efficient and stable small molecule acceptor ternary solar cells. Nat Mater 16:363–370

Bin H, Zhang Z-G, Gao L, Chen S, Zhong L, Xue L, Yang C, Li Y (2016) Non-fullerene polymer solar cells based on alkylthio and fluorine substituted 2D-conjugated polymers reach 9.5% efficiency. J Am Chem Soc 138(13), 4657–4664

Bin H, Gao L, Zhang Z-G, Yang Y, Zhang Y, Zhang C, Chen S, Xue L, Yang C, Xiao M, Li Y (2016) 11.4% Efficiency non-fullerene polymer solar cells with trialkylsilyl substituted 2D-conjugated polymer as donor. Nat Commun 7:13651

Bin H, Yang Y, Zhang Z-G, Ye L, Ghasemi M, Chen S, Zhang Y, Zhang C, Sun C, Xue L, Yang C, Ade H, Li Y (2017) 9.73% Efficiency nonfullerene all organic small molecule solar cells with absorption-complementary donor and acceptor. J Am Chem Soc 139(14):5085–5094

Brabec C, Dyakonov V, Scherf U (eds) (2014) Organic photovoltaics—materials, device physics and manufacturing technologies, 2nd edn. Wiley-VCH verlag, Weinheim

Cai Y, Huo L, Sun X, Wei D, Tang M, Sun Y (2015) High performance organic solar cells based on a twisted bay-substituted tetraphenyl functionalized perylenediimide electron acceptor. Adv Energy Mater 5(11):1500032

Cai Y, Huo L, Sun Y (2017) Recent advances in wide-bandgap photovoltaic polymers. Adv Mater 29(22):1605437

Chang S-L, Cao F-Y, Huang W-C, Huang P-K, Hsu C-S, Cheng Y-J (2018a) Highly efficient inverted d:a1:a2 ternary blend organic photovoltaics combining a ladder-type non-fullerene acceptor and a fullerene acceptor. ACS Appl Mater Interfaces 9(29):24797–24803

Chang M, Wang Y, Yi Y-Q-Q, Ke X, Wan X, Li C, Chen Y (2018b) Fine-tuning the side-chains of non-fullerene small molecule acceptors to match with appropriate polymer donors. J Mater Chem A 6(18):8586–8594

Chen K-S, Salinas J-F, Yip H-L, Huo L, Hou J, Jen AKY (2012) Semi-transparent polymer solar cells with 6% PCE, 25% average visible transmittance and a color rendering index close to 100 for power generating window applications. Energy Environ Sci 5:9551–9557

Chen Y, Wan X, Long G (2013) High performance photovoltaic applications using solution-processed small molecules. Acc Chem Res 46(11):2645–2655

Chen Y, Qin Y, Wu Y, Li C, Yao H, Liang N, Wang X, Li W, Ma W, Hou J (2017a) From binary to ternary: Improving the external quantum efficiency of small-molecule acceptor-based polymer solar cells with a minute amount of fullerene sensitization. Adv Energy Mater 7:1700328

Chen Y, Ye P, Jia X, Gu W, Xu X, Wu X, Wu J, Liu F, Zhu Z-G, Huang H (2017b) Tuning Voc for high performance organic ternary solar cells with non-fullerene acceptor alloys. J Mater Chem A 5(37):19697–19702

Cheng Y-J, Yang S-H, Hsu C-S (2009) Synthesis of conjugated polymers for organic solar cell applications. Chem Rev 109(11):5868–5923

Cheng P, Li Y, Zhan X (2014) Efficient ternary blend polymer solar cells with indene-$C_{60}$ bisadduct as an electron-cascade acceptor. Energy Environ Sci 7:2005–2011

Cheng P, Zhang M, Lau T-K, Wu Y, Jia B, Wang J, Yan C, Qin M, Lu X, Zhan X (2017) Realizing small energy loss of 0.55 ev, high open-circuit voltage >1 V and high efficiency >10% in fullerene-free polymer solar cells via energy driver. Adv Mater 29 (11):1605216

Coughlin JE, Henson ZB, Welch GC, Bazan GC (2014) Design and synthesis of molecular donors for solution-processed high-efficiency organic solar cells. Acc Chem Res 47(1):257–270

Dai S, Zhao F, Zhang Q, Lau T-K, Li T, Liu K, Ling Q, Wang C, Lu X, You W, Zhan X (2017) Fused nonacyclic electron acceptors for efficient polymer solar cells. J Am Chem Soc 139 (3):1336–1343

Deng D, Zhang Y, Zhang J, Wang Z, Zhu L, Fang J, Xia B, Wang Z, Lu K, Ma W, Wei Z (2016) Fluorination-enabled optimal morphology leads to over 11% efficiency for inverted small-molecule organic solar cells. Nat Commun 7:13740

Dennler G, Scharber MC, Brabec CJ (2009) Polymer–fullerene bulk-heterojunction solar cells. Adv Mater 21(13):1323–1338

Feng L, Zichun Z, Cheng Z, Jianyun Z, Qin H, Thomas V, Feng L, Russell TP, Xiaozhang Z (2017) Efficient semitransparent solar cells with high nir responsiveness enabled by a small-bandgap electron acceptor. Adv Mater 29(21):1606574

Feng S, Zhang C, Liu Y, Bi Z, Zhang Z, Xu X, Ma W, Bo Z (2017) Fused-ring acceptors with asymmetric side chains for high-performance thick-film organic solar cells. Adv Mater 29 (42):1703527

Feng H, Qiu N, Wang X, Wang Y, Kan B, Wan X, Zhang M, Xia A, Li C, Liu F, Zhang H, Chen Y (2017c) An A-D-A Type small-molecule electron acceptor with end-extended conjugation for high performance organic solar cells. Chem Mater 29(18):7908–7917

Fernandez-Lazaro F, Zink-Lorre N, Sastre-Santos A (2016) Perylenediimides as non-fullerene acceptors in bulk-heterojunction solar cells (BHJSCs). J Mater Chem A 4(24):9336–9346

Fuwen Z, Shuixing D, Yang W, Qianqian Z, Jiayu W, Li J, Qidan L, Zhixiang W, Wei M, Wei Y, Chunru W, Xiaowei Z (2017) Single-junction binary-blend nonfullerene polymer solar cells with 12.1% efficiency. Adv Mater 29(18):1700144

Gao L, Zhang Z-G, Bin H, Xue L, Yang Y, Wang C, Liu F, Russell TP, Li Y (2016) High-efficiency nonfullerene polymer solar cells with medium bandgap polymer donor and narrow bandgap organic semiconductor acceptor. Adv Mater 28(37):8288–8295

Gasparini N, Salvador M, Strohm S, Heumueller T, Levchuk I, Wadsworth A, Bannock JH, de Mello JC, Egelhaaf H-J, Baran D, McCulloch I, Brabec CJ (2017) Burn-in free nonfullerene-based organic solar cells. Adv Energy Mater 7(19):1700770

Hartnett PE, Timalsina A, Matte HSSR, Zhou N, Guo X, Zhao W, Facchetti A, Chang RPH, Hersam MC, Wasielewski MR, Marks TJ (2014) Slip-stacked perylenediimides as an alternative strategy for high efficiency nonfullerene acceptors in organic photovoltaics. J Am Chem Soc 136(46):16345–16356

Holliday S, Ashraf RS, Wadsworth A, Baran D, Yousaf SA, Nielsen CB, Tan C-H, Dimitrov SD, Shang Z, Gasparini N, Alamoudi M, Laquai F, Brabec CJ, Salleo A, Durrant JR, McCulloch I (2016) High-efficiency and air-stable P3HT-based polymer solar cells with a new non-fullerene acceptor. Nat Commun 7:11585

Hu Z, Zhang F, An Q, Zhang M, Ma X, Wang J, Zhang J, Wang J (2018) Ternary nonfullerene polymer solar cells with a power conversion efficiency of 11.6% by inheriting the advantages of binary cells. ACS Energy Lett 555–561

Huang W, Cheng P, Yang Y, Li G, Yang Y (2018) High-performance organic bulk-heterojunction solar cells based on multiple-donor or multiple-acceptor components. Adv Mater 30 (8):1705706

Huanran F, Yuan-Qiu-Qiang Y, Xin K, Yamin Z, Xiangjian W, Chenxi L, Yongsheng C (2018) Synergistic modifications of side chains and end groups in small molecular acceptors for high efficient non-fullerene organic solar cells. Solar RRL 1800053 (2018)

Huo L, Zhang S, Guo X, Xu F, Li Y, Hou J (2011) Replacing alkoxy groups with alkylthienyl groups: a feasible approach to improve the properties of photovoltaic polymers. Angew Chem Int Ed 50(41):9697–9702

Huo Y, Yan C, Kan B, Liu X-F, Chen L-C, Hu C-X, Lau T-K, Lu X, Sun C-L, Shao X, Chen Y, Zhan X, Zhang H-L (2018) Medium-bandgap small-molecule donors compatible with both fullerene and nonfullerene acceptors. ACS Appl Mater Interfaces 10(11):9587–9594

Jia B, Wu Y, Zhao F, Yan C, Zhu S, Cheng P, Mai J, Lau T-K, Lu X, Su C-J, Wang C, Zhan X (2017) Rhodanine flanked indacenodithiophene as non-fullerene acceptor for efficient polymer solar cells. Sci China Chem 60(2):257–263

Jiang W, Ye L, Li X, Xiao C, Tan F, Zhao W, Hou J, Wang Z (2014) Bay-linked perylene bisimides as promising non-fullerene acceptors for organic solar cells. Chem Commun 50 (8):1024–1026

Jiang K, Zhang G, Yang G, Zhang J, Li Z, Ma T, Hu H, Ma W, Ade H, Yan H (2018) Multiple cases of efficient nonfullerene ternary organic solar cells enabled by an effective morphology control method. Adv Energy Mater 8(9):1701370

Kan B, Li M, Zhang Q, Liu F, Wan X, Wang Y, Ni W, Long G, Yang X, Feng H, Zuo Y, Zhang M, Huang F, Cao Y, Russell TP, Chen Y (2015) A series of simple oligomer-like small

molecules based on oligothiophenes for solution-processed solar cells with high efficiency. J Am Chem Soc 137(11):3886–3893

Kan B, Feng H, Wan X, Liu F, Ke X, Wang Y, Wang Y, Zhang H, Li C, Hou J, Chen Y (2017a) Small-molecule acceptor based on the heptacyclic benzodi(cyclopentadithiophene) unit for highly efficient nonfullerene organic solar cells. J Am Chem Soc 139(13):4929–4934

Kan B, Zhang J, Liu F, Wan X, Li C, Ke X, Wang Y, Feng H, Zhang Y, Long G, Friend RH, Bakulin AA, Chen Y. (2017b) Fine-tuning the energy levels of a nonfullerene small-molecule acceptor to achieve a high short-circuit current and a power conversion efficiency over 12% in organic solar cells. Adv Mater 1704904

Kan B, Yi Y-Q-Q, Wan X, Feng H, Ke X, Wang Y, Li C, Chen Y (2018) Ternary organic solar cells with 12.8% efficiency using two nonfullerene acceptors with complementary absorptions. Adv Energy Mater 1800424

Kang H, Kim G, Kim J, Kwon S, Kim H, Lee K (2016) Bulk-heterojunction organic solar cells: five core technologies for their commercialization. Adv Mater 28(36):7821–7861

Kawashima K, Fukuhara T, Suda Y, Suzuki Y, Koganezawa T, Yoshida H, Ohkita H, Osaka I, Takimiya K (2016) Implication of fluorine atom on electronic properties, ordering structures, and photovoltaic performance in naphthobisthiadiazole-based semiconducting polymers. J Am Chem Soc 138(32):10265–10275

Ke X, Kan B, Wan X, Wang Y, Zhang Y, Li C, Chen Y (2018) Substituents on the end group subtle tuning the energy levels and absorptions of small-molecule nonfullerene acceptors. Dyes Pigm 155:241–248

Li Y (2012) Molecular design of photovoltaic materials for polymer solar cells: toward suitable electronic energy levels and broad absorption. Acc Chem Res 45(5):723–733

Li C, Wonneberger H (2012) Perylene imides for organic photovoltaics: yesterday, today, and tomorrow. Adv Mater 24(5):613–636

Li W, Furlan A, Hendriks KH, Wienk MM, Janssen RAJ (2013) Efficient tandem and triple-junction polymer solar cells. J Am Chem Soc 135(15):5529–5532

Li S, Liu W, Li C-Z, Liu F, Zhang Y, Shi M, Chen H, Russell TP (2016a) A simple perylene diimide derivative with a highly twisted geometry as an electron acceptor for efficient organic solar cells. J Mater Chem A 4(27):10659–10665

Li Z, Jiang K, Yang G, Lai JYL, Ma T, Zhao J, Ma W, Yan H (2016b) Donor polymer design enables efficient non-fullerene organic solar cells. Nat Commun 7:13094. https://13010.11038/ncomms13094

Li S, Ye L, Zhao W, Zhang S, Mukherjee S, Ade H, Hou J (2016c) Energy-level modulation of small-molecule electron acceptors to achieve over 12% efficiency in polymer solar cells. Adv Mater 28(42):9423–9429

Li Y, Liu X, Wu F-P, Zhou Y, Jiang Z-Q, Song B, Xia Y, Zhang Z-G, Gao F, Inganäs O, Li Y, Liao L-S (2016d) Non-fullerene acceptor with low energy loss and high external quantum efficiency: towards high performance polymer solar cells. J Mater Chem A 4(16):5890–5897

Li Y, Qian D, Zhong L, Lin J-D, Jiang Z-Q, Zhang Z-G, Zhang Z, Li Y, Liao L-S, Zhang F (2016e) A fused-ring based electron acceptor for efficient non-fullerene polymer solar cells with small HOMO offset. Nano Energy 27:430–438

Li Y, Zhong L, Wu F-P, Yuan Y, Bin H-J, Jiang Z-Q, Zhang Z, Zhang Z-G, Li Y, Liao L-S (2016f) Non-fullerene polymer solar cells based on a selenophene-containing fused-ring acceptor with photovoltaic performance of 8.6%. Energy Environ Sci 9(11):3429–3435

Li Y, Gu M, Pan Z, Zhang B, Yang X, Gu J, Chen Y (2017a) Indacenodithiophene: a promising building block for high performance polymer solar cells. J Mater Chem A 5(22):10798–10814

Li Y, Lin J-D, Che X, Qu Y, Liu F, Liao L-S, Forrest SR (2017b) High efficiency near-infrared and semitransparent non-fullerene acceptor organic photovoltaic cells. J Am Chem Soc 139 (47):17114–17119

Li S, Ye L, Zhao W, Yan H, Yang B, Liu D, Li W, Ade H, Hou J (2018a) A wide band-gap polymer with a deep homo level enables 14.2% efficiency in polymer solar cells. J Am Chem Soc 140(23):7159–7167

Li T, Dai S, Ke Z, Yang L, Wang J, Yan C, Ma W, Zhan X (2018b) Fused tris(thienothiophene)-based electron acceptor with strong near-infrared absorption for high-performance as-cast solar cells. Adv Mater 30(10):1705969

Li H, Fang J, Zhang J, Zhou R, Wu Q, Deng D, Adil MA, Lu K, Guo X, Wei Z (2018c) A novel small molecule based on naphtho[1,2-*b*:5,6-*b*′]dithiophene benefits both fullerene and non-fullerene solar cells. Mater Chem Front 2:143–148

Liang Z, Li M, Zhang X, Wang Q, Jiang Y, Tian H, Geng Y (2018) Near-infrared absorbing non-fullerene acceptors with selenophene as π-bridges for efficient organic solar cells. J Mater Chem A 6(17):8059–8067

Lin Y, Zhan X (2016) Oligomer molecules for efficient organic photovoltaics. Acc Chem Res 49 (2):175–183

Lin Y, Zhang Z-G, Bai H, Wang J, Yao Y, Li Y, Zhu D, Zhan X (2015a) High-performance fullerene-free polymer solar cells with 6.31% efficiency. Energy Environ Sci 8:610–616

Lin H, Chen S, Li Z, Lai JYL, Yang G, McAfee T, Jiang K, Li Y, Liu Y, Hu H, Zhao J, Ma W, Ade H, Yan H (2015b) High-performance non-fullerene polymer solar cells based on a pair of donor–acceptor materials with complementary absorption properties. Adv Mater 27(45):7299–7304

Lin Y, Wang J, Zhang Z-G, Bai H, Li Y, Zhu D, Zhan X (2015c) An electron acceptor challenging fullerenes for efficient polymer solar cells. Adv Mater 27(7):1170–1174

Lin Y, He Q, Zhao F, Huo L, Mai J, Lu X, Su C-J, Li T, Wang J, Zhu J, Sun Y, Wang C, Zhan X (2016a) A facile planar fused-ring electron acceptor for as-cast polymer solar cells with 8.71% efficiency. J Am Chem Soc 138(9):2973–2976

Lin Y, Li T, Zhao F, Han L, Wang Z, Wu Y, He Q, Wang J, Huo L, Sun Y, Wang C, Ma W, Zhan X (2016b) Structure evolution of oligomer fused-ring electron acceptors toward high efficiency of as-cast polymer solar cells. Adv Energy Mater 1600854

Lin Y, Zhao F, He Q, Huo L, Wu Y, Parker TC, Ma W, Sun Y, Wang C, Zhu D, Heeger AJ, Marder SR, Zhan X (2016c) High-performance electron acceptor with thienyl side chains for organic photovoltaics. J Am Chem Soc 138(14):4955–4961

Lin Y, Wang J, Li T, Wu Y, Wang C, Han L, Yao Y, Ma W, Zhan X (2016d) Efficient fullerene-free organic solar cells based on fused-ring oligomer molecules. J Mater Chem A 4 (4):1486–1494

Lin Y, Zhao F, Prasad SKK, Chen J-D, Cai W, Zhang Q, Chen K, Wu Y, Ma W, Gao F, Tang J-X, Wang C, You W, Hodgkiss JM, Zhan X (2018) Balanced partnership between donor and acceptor components in nonfullerene organic solar cells with >12% efficiency. Adv Mater 1706363

Liu Y, Zhao J, Li Z, Mu C, Ma W, Hu H, Jiang K, Lin H, Ade H, Yan H (2014) Aggregation and morphology control enables multiple cases of high-efficiency polymer solar cells. Nat Commun 5:5293

Liu Y, Mu C, Jiang K, Zhao J, Li Y, Zhang L, Li Z, Lai JYL, Hu H, Ma T, Hu R, Yu D, Huang X, Tang BZ, Yan H (2015) A tetraphenylethylene core-based 3d structure small molecular acceptor enabling efficient non-fullerene organic solar cells. Adv Mater 27(6):1015–1020

Liu Z, Wu Y, Zhang Q, Gao X (2016a) Non-fullerene small molecule acceptors based on perylene diimides. J Mater Chem A 4(45):17604–17622

Liu J, Chen S, Qian D, Gautam B, Yang G, Zhao J, Bergqvist J, Zhang F, Ma W, Ade H, Inganäs O, Gundogdu K, Gao F, Yan H (2016b) Fast charge separation in a non-fullerene organic solar cell with a small driving force. Nat Energy 1:16089

Liu F, Zhou Z, Zhang C, Vergote T, Fan H, Liu F, Zhu X (2016c) A thieno[3,4-b]thiophene-based non-fullerene electron acceptor for high-performance bulk-heterojunction organic solar cells. J Am Chem Soc 138(48):15523–15526

Liu T, Guo Y, Yi Y, Huo L, Xue X, Sun X, Fu H, Xiong W, Meng D, Wang Z, Liu F, Russell TP, Sun Y (2016d) Ternary organic solar cells based on two compatible nonfullerene acceptors with power conversion efficiency >10%. Adv Mater 28(45):10008

Liu Y, Zhang Z, Feng S, Li M, Wu L, Hou R, Xu X, Chen X, Bo Z (2017) Exploiting noncovalently conformational locking as a design strategy for high performance fused-ring electron acceptor used in polymer solar cells. J Am Chem Soc 139(9):3356–3359

Liu X, Xie B, Duan C, Wang Z, Fan B, Zhang K, Lin B, Colberts FJM, Ma W, Janssen RAJ, Huang F, Cao Y (2018) A high dielectric constant non-fullerene acceptor for efficient bulk-heterojunction organic solar cells. J Mater Chem A 6(2):395–403

Lu H, Zhang J, Chen J, Liu Q, Gong X, Feng S, Xu X, Ma W, Bo Z (2016) Ternary-blend polymer solar cells combining fullerene and nonfullerene acceptors to synergistically boost the photovoltaic performance. Adv Mater 28(43):9559–9566

Ma Y, Zhang M, Yan Y, Xin J, Wang T, Ma W, Tang C, Zheng Q (2017a) Ladder-type dithienonaphthalene-based small-molecule acceptors for efficient nonfullerene organic solar cells. Chem Mater 29(18):7942–7952

Ma Y, Zhang M, Tang Y, Ma W, Zheng Q (2017b) Angular-shaped dithienonaphthalene-based nonfullerene acceptor for high-performance polymer solar cells with large open-circuit voltages and minimal energy losses. Chem Mater 29(22):9775–9785

Meng D, Sun D, Zhong C, Liu T, Fan B, Huo L, Li Y, Jiang W, Choi H, Kim T, Kim JY, Sun Y, Wang Z, Heeger AJ (2016) High-performance solution-processed non-fullerene organic solar cells based on selenophene-containing perylene bisimide acceptor. J Am Chem Soc 138 (1):375–380

Mishra A, Bäuerle P (2012) Small molecule organic semiconductors on the move: Promises for future solar energy technology. Angew Chem Int Ed 51(9):2020–2067

Mishra A, Popovic D, Vogt A, Kast H, Leitner T, Walzer K, Pfeiffer M, Mena-Osteritz E, Bäuerle P (2014) A-D–A-type S, *N*-heteropentacenes: next-generation molecular donor materials for efficient vacuum-processed organic solar cells. Adv Mater 26(42):7217–7223

Niu S, Liu Z, Wang N (2018) Effect of dihydronaphthyl-based $C_{60}$ bisadduct as third component materials on the photovoltaic performance and charge carrier recombination of binary PBDB-T:ITIC polymer solar cells. Nanoscale 10(18):8483–8495

Qin Y, Uddin MA, Chen Y, Jang B, Zhao K, Zheng Z, Yu R, Shin TJ, Woo HY, Hou J (2016) Highly efficient fullerene-free polymer solar cells fabricated with polythiophene derivative. Adv Mater 28(42):9416–9422

Qiu N, Zhang H, Wan X, Li C, Ke X, Feng H, Kan B, Zhang H, Zhang Q, Lu Y, Chen Y (2017a) A new nonfullerene electron acceptor with a ladder type backbone for high-performance organic solar cells. Adv Mater 29(6):1604964

Qiu B, Xue L, Yang Y, Bin H, Zhang Y, Zhang C, Xiao M, Park K, Morrison W, Zhang Z-G, Li Y (2017b) All-small-molecule nonfullerene organic solar cells with high fill factor and high efficiency over 10%. Chem Mater 29(17):7543–7553

Rajaram S, Shivanna R, Kandappa SK, Narayan KS (2012) Nonplanar perylene diimides as potential alternatives to fullerenes in organic solar cells. J Phys Chem Lett 3(17):2405–2408

Reichenbächer K, Süss HI, Hulliger J (2005) Fluorine in crystal engineering—"the little atom that could". Chem Soc Rev 34:22–30

Scharber MC, Mühlbacher D, Koppe M, Denk P, Waldauf C, Heeger AJ, Brabec CJ (2006) Design rules for donors in bulk-heterojunction solar cells—towards 10% energy-conversion efficiency. Adv Mater 18(6):789–794

Schulz G, Lobert M, Ata I, Urdanpilleta M, Lindén M, Mishra A, Bäuerle P (2015) Functional tuning of A-D-A oligothiophenes: the effect of solvent vapor annealing on blend morphology and solar cell performance. J Mater Chem A 3:13738–13748

Sista S, Hong Z, Chen L-M, Yang Y (2011) Tandem polymer photovoltaic cells-current status, challenges and future outlook. Energy Environ Sci 4:1606–1620

Song X, Gasparini N, Ye L, Yao H, Hou J, Ade H, Baran D (2018) Controlling blend morphology for ultrahigh current density in nonfullerene acceptor-based organic solar cells. ACS Energy Lett 669–676

Su W, Fan Q, Guo X, Meng X, Bi Z, Ma W, Zhang M, Li Y (2017) Two compatible nonfullerene acceptors with similar structures as alloy for efficient ternary polymer solar cells. Nano Energy 38:510–517

Sun D, Meng D, Cai Y, Fan B, Li Y, Jiang W, Huo L, Sun Y, Wang Z (2015) Non-fullerene-acceptor-based bulk-heterojunction organic solar cells with efficiency over 7%. J Am Chem Soc 137(34):11156–11162

Sun J, Ma X, Zhang Z, Yu J, Zhou J, Yin X, Yang L, Geng R, Zhu R, Zhang F, Tang W (2018) Dithieno[3,2-b:2′,3′-d]pyrrol fused nonfullerene acceptors enabling over 13% efficiency for organic solar cells. Adv Mater 1707150

Wadsworth A, Moser M, Marks A, Little MS, Gasparini N, Brabec CJ, Baran D, McCulloch I (2018) Critical review of the molecular design progress in non-fullerene electron acceptors towards commercially viable organic solar cells. Chem Soc Rev. https://doi.org/10.1039/c1037cs00892a

Wang H, Chao P, Chen H, Mu Z, Chen W, He F (2017) Simultaneous increase in open-circuit voltage and efficiency of fullerene-free solar cells through chlorinated thieno[3,4-*b*]thiophene polymer donor. ACS Energy Lett 1971–1977

Wang W, Yan C, Lau T-K, Wang J, Liu K, Fan Y, Lu X, Zhan X (2017) Fused hexacyclic nonfullerene acceptor with strong near-infrared absorption for semitransparent organic solar cells with 9.77% efficiency. Adv Mater 29(31):1701308

Wang Y, Zhang Y, Qiu N, Feng H, Gao H, Kan B, Ma Y, Li C, Wan X, Chen Y (2018a) A halogenation strategy for over 12% efficiency nonfullerene organic solar cells. Adv Energy Mater 8(15):1702870

Wang Y, Chang M, Kan B, Wan X, Li C, Chen Y (2018b) All-small-molecule organic solar cells based on pentathiophene donor and alkylated indacenodithiophene-based acceptors with efficiency over 8%. ACS Appl Energy Mater 1(5):2150–2156

Wen S, Wu Y, Wang Y, Li Y, Liu L, Jiang H, Liu Z, Yang R (2018) Pyran-bridged indacenodithiophene as a building block for constructing efficient A–D–A-type nonfullerene acceptors for polymer solar cells. Chemsuschem 11(2):360–366

Wu J-S, Cheng S-W, Cheng Y-J, Hsu C-S (2014) Donor-acceptor conjugated polymers based on multifused ladder-type arenes for organic solar cells. Chem Soc Rev 44:1113–1154

Wu Y, Bai H, Wang Z, Cheng P, Zhu S, Wang Y, Ma W, Zhan X (2015) A planar electron acceptor for efficient polymer solar cells. Energy Environ Sci 8(11):3215–3221

Wu Q, Zhao D, Schneider AM, Chen W, Yu L (2016) Covalently bound clusters of alpha-substituted pdi—rival electron acceptors to fullerene for organic solar cells. J Am Chem Soc 138(23):7248–7251

Wu H, Fan H, Xu S, Zhang C, Chen S, Yang C, Chen D, Liu F, Zhu X (2017) A designed ladder-type heteroarene benzodi(thienopyran) for high-performance fullerene-free organic solar cells. Solar RRL 1(12):1700165

Xia D, Wu Y, Wang Q, Zhang A, Li C, Lin Y, Colberts FJM, van Franeker JJ, Janssen RAJ, Zhan X, Hu W, Tang Z, Ma W, Li W (2016) Effect of alkyl side chains of conjugated polymer donors on the device performance of non-fullerene solar cells. Macromolecules 49(17):6445–6454

Xiao Z, Jia X, Ding L (2017a) Ternary organic solar cells offer 14% power conversion efficiency. Sci Bull 62(23):1562–1564

Xiao Z, Liu F, Geng X, Zhang J, Wang S, Xie Y, Li Z, Yang H, Yuan Y, Ding L (2017b) A carbon-oxygen-bridged ladder-type building block for efficient donor and acceptor materials used in organic solar cells. Sci Bull 62(19):1331–1336

Xiao Z, Jia X, Li D, Wang S, Geng X, Liu F, Chen J, Yang S, Russell TP, Ding L (2017c) 26 mA $cm^{-2}$ $J_{SC}$ from organic solar cells with a low-bandgap nonfullerene acceptor. Sci Bull 62(22):1494–1496

Xie D, Liu T, Gao W, Zhong C, Huo L, Luo Z, Wu K, Xiong W, Liu F, Sun Y, Yang C (2017) A novel thiophene-fused ending group enabling an excellent small molecule acceptor for high-performance fullerene-free polymer solar cells with 11.8% efficiency. Solar RRL 1(6):1700044

Xu W, Gao F (2018) The progress and prospects of non-fullerene acceptors in ternary blend organic solar cells. Mater Horiz 5(2):206–221

Xu Y-X, Chueh C-C, Yip H-L, Ding F-Z, Li Y-X, Li C-Z, Li X, Chen W-C, Jen AKY (2012) Improved charge transport and absorption coefficient in indacenodithieno[3,2-b] thiophene-based ladder-type polymer leading to highly efficient polymer solar cells. Adv Mater 24(47):6356–6361

Xu H, Yang Y, Zhong C, Zhan X, Chen X (2018a) Narrow bandgap non-fullerene acceptor based on a thiophene-fused benzothiadiazole unit with a high short-circuit current density of over 20 mA cm-2. J Mater Chem A 6(15):6393–6401

Xu X, Yu T, Bi Z, Ma W, Li Y, Peng Q (2018b) Realizing over 13% efficiency in green-solvent-processed nonfullerene organic solar cells enabled by 1,3,4-thiadiazole-based wide-bandgap copolymers. Adv Mater 30(3):1703973

Yang L, Yan L, You W (2013) Organic solar cells beyond one pair of donor–acceptor: ternary blends and more. J Phys Chem Lett 4(11):1802–1810

Yang Y, Zhang Z-G, Bin H, Chen S, Gao L, Xue L, Yang C, Li Y (2016) Side-chain isomerization on an n-type organic semiconductor itic acceptor makes 11.77% high efficiency polymer solar cells. J Am Chem Soc 138(45):15011–15018

Yang F, Li C, Lai W, Zhang A, Huang H, Li W (2017a) Halogenated conjugated molecules for ambipolar field-effect transistors and non-fullerene organic solar cells. Mater Chem Front 1 (7):1389–1395

Yang L, Zhang S, He C, Zhang J, Yao H, Yang Y, Zhang Y, Zhao W, Hou J (2017b) New wide band gap donor for efficient fullerene-free all-small-molecule organic solar cells. J Am Chem Soc 139(5):1958–1966

Yang L, Li M, Song J, Zhou Y, Bo Z, Wang H (2018a) Molecular consideration for small molecular acceptors based on ladder-type dipyran: influences of O-functionalization and π-bridges. Adv Funct Mater 28(8):1705927

Yang L, Zhang S, He C, Zhang J, Yang Y, Zhu J, Cui Y, Zhao W, Zhang H, Zhang Y, Wei Z, Hou J (2018b) Modulating molecular orientation enables efficient nonfullerene small-molecule organic solar cells. Chem Mater 30(6):2129–2134

Yao H, Ye L, Zhang H, Li S, Zhang S, Hou J (2016a) Molecular design of benzodithiophene-based organic photovoltaic materials. Chem Rev 116(12):7397–7457

Yao H, Chen Y, Qin Y, Yu R, Cui Y, Yang B, Li S, Zhang K, Hou J (2016b) Design and synthesis of a low bandgap small molecule acceptor for efficient polymer solar cells. Adv Mater 28 (37):8283–8287

Yao H, Yu R, Shin TJ, Zhang H, Zhang S, Jang B, Uddin MA, Woo HY, Hou J (2016c) A wide bandgap polymer with strong π–π interaction for efficient fullerene-free polymer solar cells. Adv Energy Mater 6(15):1600742

Yao H, Cui Y, Yu R, Gao B, Zhang H, Hou J (2017a) Design, synthesis, and photovoltaic characterization of a small molecular acceptor with an ultra-narrow band gap. Angew Chem Int Ed 56:3045–3049

Yao H, Ye L, Hou J, Jang B, Han G, Cui Y, Su GM, Wang C, Gao B, Yu R, Zhang H, Yi Y, Woo HY, Ade H, Hou J (2017b) Achieving highly efficient nonfullerene organic solar cells with improved intermolecular interaction and open-circuit voltage. Adv Mater 1700254

Ye P, Chen Y, Wu J, Wu X, Yu S, Xing W, Liu Q, Jia X, Peng A, Huang H (2017) Wide bandgap small molecular acceptors for low energy loss organic solar cells. J Mater Chem C 5 (47):12591–12596

Yi J, Wang Y, Luo Q, Lin Y, Tan H, Wang H, Ma C-Q (2016) A 9,9′-Spirobi[9H-fluorene]-cored perylenediimide derivative and its application in organic solar cells as a non-fullerene acceptor. Chem Commun 52(8):1649–1652

Yi Y-Q-Q, Feng H, Chang M, Zhang H, Wan X, Li C, Chen Y (2017) New small-molecule acceptors based on hexacyclic naphthalene(cyclopentadithiophene) for efficient non-fullerene organic solar cells. J Mater Chem A 5(33):17204–17210

Yip H-L, Jen AKY (2012) Recent advances in solution-processed interfacial materials for efficient and stable polymer solar cells. Energy Environ Sci 5:5994–6011

Yu S, Chen Y, Yang L, Ye P, Wu J, Yu J, Zhang S, Gao Y, Huang H (2017a) Significant enhancement of photovoltaic performance through introducing S•••N conformational locks. J Mater Chem A 5(41):21674–21678

Yu R, Zhang S, Yao H, Guo B, Li S, Zhang H, Zhang M, Hou J (2017b) Two well-miscible acceptors work as one for efficient fullerene-free organic solar cells. Adv Mater 29:1700437

Yu R, Yao H, Hou J (2018) Recent progress in ternary organic solar cells based on nonfullerene acceptors. Adv Energy Mater 1702814

Zang Y, Li C-Z, Chueh C-C, Williams ST, Jiang W, Wang Z-H, Yu J-S, Jen AKY (2014) Integrated molecular, interfacial, and device engineering towards high-performance non-fullerene based organic solar cells. Adv Mater 26(32):5708–5714

Zhang M, Guo X, Zhang S, Hou J (2013) Synergistic effect of fluorination on molecular energy level modulation in highly efficient photovoltaic polymers. Adv Mater 26(7):1118–1123

Zhang S, Qin Y, Uddin MA, Jang B, Zhao W, Liu D, Woo HY, Hou J (2016) A fluorinated polythiophene derivative with stabilized backbone conformation for highly efficient fullerene and non-fullerene polymer solar cells. Macromolecules 49(8):2993–3000

Zhang G, Zhang K, Yin Q, Jiang X-F, Wang Z, Xin J, Ma W, Yan H, Huang F, Cao Y (2017a) High-performance ternary organic solar cell enabled by a thick active layer containing a liquid crystalline small molecule donor. J Am Chem Soc 139(6):2387–2395

Zhang L, Lin B, Ke Z, Chen J, Li W, Zhang M, Ma W (2017b) A universal approach to improve electron mobility without significant enlarging phase separation in IDT-based non-fullerene acceptor organic solar cells. Nano Energy 41:609–617

Zhang Z, Feng L, Xu S, Yuan J, Zhang Z-G, Peng H, Li Y, Zou Y (2017c) Achieving over 10% efficiency in a new acceptor ITTC and its blends with hexafluoroquinoxaline based polymers. J Mater Chem A 5:11286–11293

Zhang Z-G, Li Y, Zhong L, Gautam B, Bin H, Lin J-D, Wu F-P, Zhang Z, Gundogdu K, Li Y, Jiang Z-Q, Liao LS (2017d) A near-infrared non-fullerene electron acceptor for high performance polymer solar cells. Energy Environ Sci 10(7):1610–1620

Zhang H, Yao H, Hou J, Zhu J, Zhang J, Li W, Yu R, Gao B, Zhang S, Hou J (2018a) Over 14% efficiency in organic solar cells enabled by chlorinated nonfullerene small-molecule acceptors. Adv Mater 1800613

Zhang S, Qin Y, Zhu J, Hou J (2018b) Over 14% efficiency in polymer solar cells enabled by a chlorinated polymer donor. Adv Mater 30(20):1800868

Zhang G, Zhao J, Chow PCY, Jiang K, Zhang J, Zhu Z, Zhang J, Huang F, Yan H (2018c) Nonfullerene acceptor molecules for bulk heterojunction organic solar cells. Chem Rev 118 (7):3447–3507

Zhang C, Feng S, Liu Y, Ming S, Lu H, Ma D, Xu X, Wu Y, Bo Z (2018d) High efficiency ternary polymer solar cells based on a fused pentacyclic electron acceptor. J Mater Chem A 6 (16):6854–6859

Zhang Y, Kan B, Sun Y, Wang Y, Xia R, Ke X, Yi Y-Q-Q, Li C, Yip H-L, Wan X, Cao Y, Chen Y (2018e) Nonfullerene tandem organic solar cells with high performance of 14.11%. Adv Mater 1707508

Zhang J, Yan C, Wang W, Xiao Y, Lu X, Barlow S, Parker TC, Zhan X, Marder SR (2018f) Panchromatic ternary photovoltaic cells using a nonfullerene acceptor synthesized using C-H functionalization. Chem Mater 30(2):309–313

Zhao J, Li Y, Yang G, Jiang K, Lin H, Ade H, Ma W, Yan H (2016a) Efficient organic solar cells processed from hydrocarbon solvents. Nat Energy 1:15027

Zhao K, Wang Q, Xu B, Zhao W, Liu X, Yang B, Sun M, Hou J (2016b) Efficient fullerene-based and fullerene-free polymer solar cells using two wide band gap thiophene-thiazolothiazole-based photovoltaic materials. J Mater Chem A 4(24):9511–9518

Zhao W, Qian D, Zhang S, Li S, Inganäs O, Gao F, Hou J (2016c) Fullerene-free polymer solar cells with over 11% efficiency and excellent thermal stability. Adv Mater 28(23):4734–4739

Zhao W, Li S, Yao H, Zhang S, Zhang Y, Yang B, Hou J (2017a) Molecular optimization enables over 13% efficiency in organic solar cells. J Am Chem Soc 139(21):7148–7151

Zhao W, Li S, Zhang S, Liu X, Hou J (2017b) Ternary polymer solar cells based on two acceptors and one donor for achieving 12.2% efficiency. Adv Mater 29(2):1604059

Zhong Y, Trinh MT, Chen R, Wang W, Khlyabich PP, Kumar B, Xu Q, Nam C-Y, Sfeir MY, Black C, Steigerwald ML, Loo Y-L, Xiao S, Ng F, Zhu XY, Nuckolls C (2014) Efficient organic solar cells with helical perylene diimide electron acceptors. J Am Chem Soc 136 (43):15215–15221

Zhong Y, Trinh MT, Chen R, Purdum GE, Khlyabich PP, Sezen M, Oh S, Zhu H, Fowler B, Zhang B, Wang W, Nam C-Y, Sfeir MY, Black CT, Steigerwald ML, Loo Y-L, Ng F, Zhu XY, Nuckolls C (2015) Molecular helices as electron acceptors in high-performance bulk heterojunction solar cells. Nat Commun 6:8242

Zhong H, Wu C-H, Li C-Z, Carpenter J, Chueh C-C, Chen J-Y, Ade H, Jen AK-Y (2016) Rigidifying nonplanar perylene diimides by ring fusion toward geometry-tunable acceptors for high-performance fullerene-free solar cells. Adv Mater 28(5):951–958

Zhong W, Cui J, Fan B, Ying L, Wang Y, Wang X, Zhang G, Jiang X-F, Huang F, Cao Y (2017) Enhanced photovoltaic performance of ternary polymer solar cells by incorporation of a narrow-bandgap nonfullerene acceptor. Chem Mater 29(19):8177–8186

Zhu J, Ke Z, Zhang Q, Wang J, Dai S, Wu Y, Xu Y, Lin Y, Ma W, You W, Zhan X (2017) Naphthodithiophene-based nonfullerene acceptor for high-performance organic photovoltaics: effect of extended conjugation. Adv Mater 30(2):1704713

# Chapter 9
# Dye-Sensitized Solar Cells as Potential Candidate for Indoor/Diffused Light Harvesting Applications: From BIPV to Self-powered IoTs


**G. Gokul, Sourava C. Pradhan and Suraj Soman**

**Abstract** Dye-Sensitized Solar Cell (DSC) technology is a photovoltaic technology that mimics natural photosynthesis, categorically coming under third generation photovoltaics; while completing almost three decades since its invention, it has carved a recognizable space in the PV arena owing to its unique merits like roll-to-roll compatibility, relatively inexpensive fabrication techniques-using cheap and readily available materials, workability on flexible substrates, and excellent low/diffused light performance. Semitransparent Multi-coloured Dye Solar Panels stands as a potential candidate in the Building-Integrated Photovoltaic (BIPV) sector, while the small form-factor devices show an excellent performance in indoor/artificial light, thus paving way for the self-powered indoor light harvesting Internet of Things (IoT) applications. This chapter builds an understanding on the DSC technology from a device to module perspective, reviewing the progress in manufacturing technologies, outlining its evolution as a potential future candidate in photovoltaic sector.

**Keywords** Dye solar modules · BIPV · Energy harvesting IoT

## 9.1 Introduction

The dawn of the twenty-first century witnessed a phenomenal boom in the entire science and technology spectrum. This transformation pillared on automation, artificial intelligence, data analytics, and Internet of Things (IoT) has already set the stage for 'Industry 4.0', a fourth industrial revolution. According to ***statista*** (2018), The Statistics Portal, 'For 2020, the installed base of Internet of Things devices is

G. Gokul · S. C. Pradhan · S. Soman (✉)
Photosciences and Photonics Section, Chemical Sciences and Technology Division, CSIR-National Institute for Interdisciplinary Science and Technology, Thiruvananthapuram 695019, Kerala, India
e-mail: suraj@niist.res.in



H. Tyagi et al. (eds.), *Advances in Solar Energy Research*, Energy, Environment, and Sustainability, https://doi.org/10.1007/978-981-13-3302-6_9

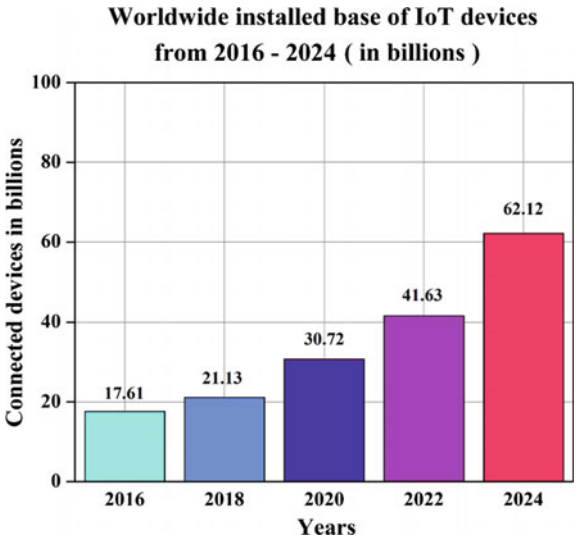


**Fig. 9.1** Present and projected status of the number of IoT devices (Statista 2018)

forecast to grow to almost 31 billion worldwide' (Fig. 9.1). Meanwhile, the projected global human population by 2030 would be 8.5 billion, according to United Nations Department of Economic and Social Affairs (UN DESA) Report (http://www.un.org/en/development/desa/news/population/2015-report.html), making it clear that there will be more connected devices than the total human population. How to power billions of these IoT devices? Is battery a reliable solution? What is the expected battery life? What environmental concerns do the depleted batteries cause? Questions are endless. The novel solution to all these concerns is, (1) to bring down the power consumption of the individual devices and/or (2) use ambient energy harvesting methods.

The evolving concept of green buildings, which adopts sustainable building practices, developed upon the notion of 'net zero energy', and involving living and restorative building concepts that improve the natural environment, has already gained momentum in developed nations. The adoption of Building Research Establishment's Environmental Assessment Method (BREEAM) (Crawley and Aho 1999), the first green building rating system in the U.K. and its counterpart in the U.S.-Leadership in Energy and Environmental Design (LEED) (Miller et al. 2008) rating system reflects this growing green commitment.

In this quest for global smart energy sufficiency, for microlevel IoTs to macro level green buildings, solar photovoltaics is the torchbearer. Progressing at the present pace, the global annual energy demand rate is projected to reach 30 TW, by the year 2050. Research reports on solar energy potential estimate the practical terrestrial, global annual solar potential value to be a whopping 600 TW; if so, usage of solar panels with 10% efficiency could easily deliver 60 TW of power (Hagfeldt 2012) (Fig. 9.2).

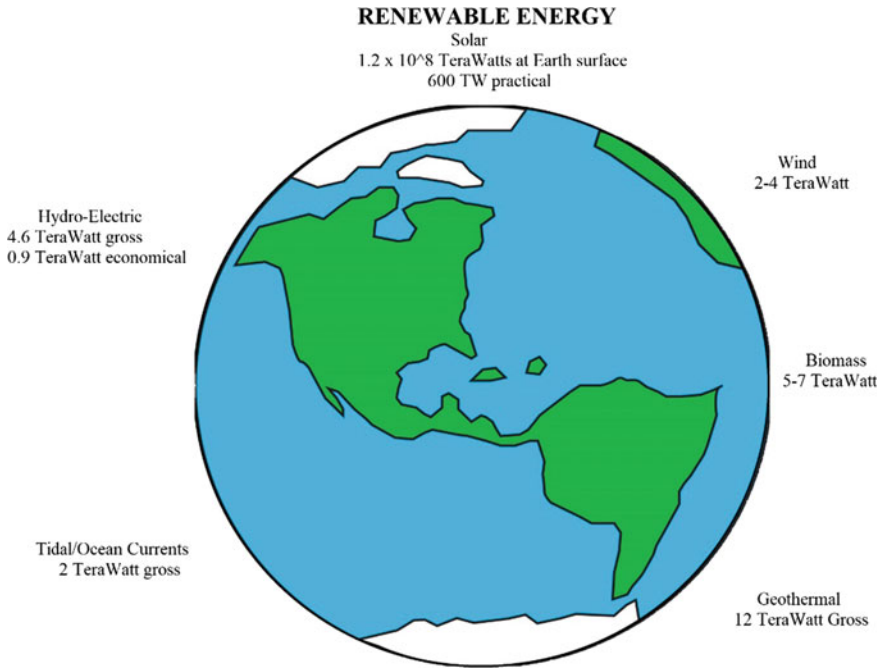


**Fig. 9.2** Global renewable energy potential (https://en.wikipedia.org/wiki/World_energy_resources)

### *9.1.1 Photovoltaic (PV) Technologies*

The progress in photovoltaic (PV) technologies can be categorized into three different generations. The silicon solar cells (both mono- and polycrystalline) belong to the first generation. PV cells of this generation require high-temperature processing and ultra clean rooms, and hence have a high cost per generated power. These solar cells are efficiency limited by the Shockley–Queisser limit (a maximum theoretical efficiency that solar cells working on the principle of a p-n junction can achieve), where the maximum achievable efficiency is 33.33%.

Thin film technologies belong to the second generation of photovoltaics. Compared to crystalline-silicon-based cells these devices are made from layers of semiconductor materials only a few micrometres thick. The production of these solar cells still include vacuum processes and high-temperature treatments, however due to lower material consumption, they offer a lower cost per generated power. Photovoltaic systems belonging to the second generation are still limited by the Shockley–Queisser limit. In pursuit of higher efficiencies, above the theoretical Shockley–Queisser limit, different new architectures like multi-junction (tandem) solar cells and other evolving technologies like downconversion (one high energy photon, is converted into two or more, lower energy photons), upconversion

(combining two lower energy photons to one higher), hot carrier capture solar cells, etc. were introduced. This was followed by the introduction of third-generation photovoltaic technology which is built on locally available materials and has less complicated fabrication processes (Green 2002).

In this chapter, we discuss dye-sensitized solar cell (DSC), a third generation, solar photovoltaic technology, fabricated using simple manufacturing techniques and easily available materials. DSC technology is yet to deliver a performance akin to that of other prominent solar cell technologies like mono/polycrystalline silicon or CIGS; the future of this technology is promising, owing to its unique merits viz., flexibility, conformability, transparency, excellent lowlight level or indoor light performance, and suitability for building-integrated photovoltaics (BIPV).

DSC Modules, unlike its first- or second-generation counterparts of the same rating, deliver 12–14% more energy, on a per day basis, due to its workability under low/diffused light (delivers better performance on cloudy days). Moreover, the DSC output is almost independent of the angle of incident radiation. Photosensitizers used in DSC are coloured, giving a unique aesthetic appearance to the semitransparent DSC modules. These features make DSC a potential candidate in the BIPV sector. The exceptional performance in low/indoor light conditions, together with its relatively lower cost, workability on flexible substrates also make DSC a potential candidate for energy harvesting IoTs (Fakharuddin et al. 2014). This chapter outlines the working principle of DSC, fabrication techniques from lab to module level, and also reviews the major progress in the application sector.

## 9.2 Dye-Sensitized Solar Cell (DSC)

Photo-electrochemical cells (PECs) were a hot research topic, since the revolutionary discovery of Photovoltaic Effect (1839) by Edmond Becquerel (Grätzel 2001). Concurrent with the research on semiconductor (p-n junction) solar cells, the different semiconductor-electrolyte junction solar cells were also studied. Heinz Gerischer did a pioneering work on the semiconductor/liquid junctions by proposing an articulated working model of the junction. This study illustrated the critical dependence of stability of PEC cells on semiconductor/liquid junction (Gerischer 1983). Researchers predicted device efficiencies as high as 10%, however, actual systems were poorly stable due to the corrosive action of the liquid electrolyte on the bulk semiconductor. Similar studies on light-activated charge separation using a monolayer of dye on a bulk semiconductor–liquid junction were also performed. Though high theoretical efficiencies were predicted Light Harvesting Efficiency (LHE) of the system was less than 1%. In 1991, a breakthrough in this field was achieved with the pioneering works of O'Regan and Gratzel (1991). By dye sensitizing a mesoporous layer of wide-bandgap semiconductor $TiO_2$, the EPFL team was able to fabricate solar cells that gave 7–8% device efficiency. By using a mesoporous layer researchers were able to tune the surface roughness by a factor of 1000, thereby allowing more dye molecule

anchoring to the semiconductor leading to more light harvesting. These devices came to be called Dye-Sensitized Solar Cells (DSCs).

### 9.2.1 Basic Working Principle

The general and functional schematic of a dye-sensitized solar cell (DSC) is illustrated in Fig. 9.3a, b. DSCs are different from conventional p-n junction devices in the sense that the photon capturing phenomenon and charge carrier transport are separated in the cell which is not the case in conventional p-n junction devices. DSCs mimic the natural photosynthesis process. Similar to the photon capture by chlorophyll, the green pigment in leaves, in DSC the light is absorbed by a sensitizer (dye), anchored on to the surface of a wide-band semiconductor. This wide-bandgap semiconductor performs the task of electron transport (Grätzel 2003). The different processes in a DSC (shown in Figs. 9.3b and 9.4) are:

1. **Light harvesting**: a monolayer of the dye molecules set adsorbed on the surface of the mesoporous semiconductor (typically $TiO_2$) absorbs photons and gets excited and the excited electrons move from the ground state (D) to the excited state (D*, $k_{11}$) of the dye:

$$D \underset{k_{12}}{\overset{h\upsilon,k_{11}}{\rightleftarrows}} D^*$$

2. **Electron injection**: the excited electrons are injected into the semiconductor conduction band ($k_{21}$), which results in the oxidation of the sensitizer ($D^+$):

$$D^* \underset{k_{22}}{\overset{k_{21}}{\rightleftarrows}} D^+ + e^-_{CB}$$

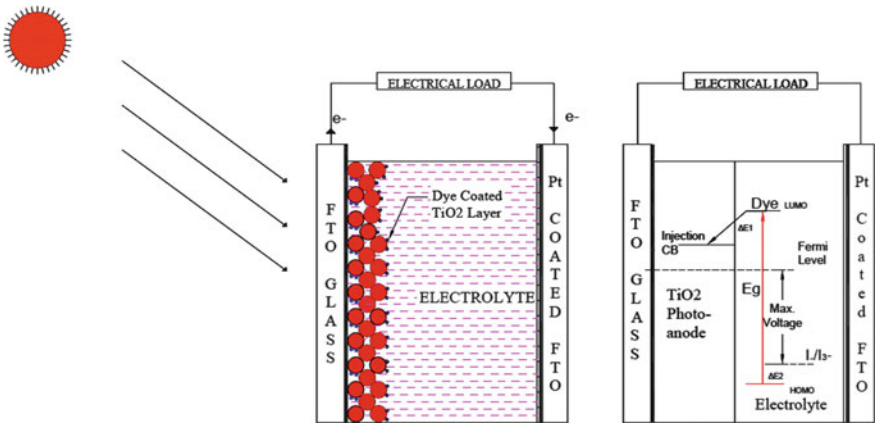


**Fig. 9.3** **a** DSC working principle and **b** energy schematic

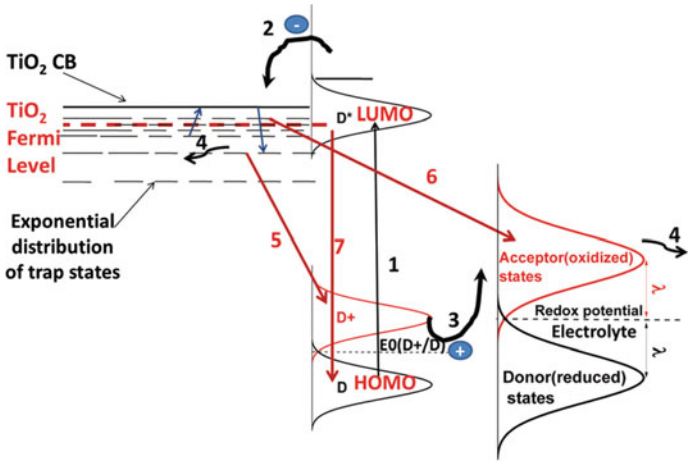


**Fig. 9.4** DSC detailed process schematic (Pazoki et al. 2017)

3. **Dye regeneration**: the oxidized sensitizer ($D^+$) is then reduced to its ground state (D) by donation of electron from iodide ion ($I^-$) present in the liquid electrolyte, producing tri-iodide ion ($I_3^-$) ($k_3$) [$I^-$ is oxidized to $I_3^-$]:

$$D^+ + \frac{3}{2}I^- \xrightarrow{k_3} \frac{1}{2}I_3^- + D$$

4. **Electron collection**: electrons from the mesoporous semiconductor get transferred to the transparent conductive oxide (TCO) [diffusive collection-trapping-detrapping-random walk (Nelson 1999) model] where they become available for electrical work in the external circuit;
5. **Electrolyte mass transfer**: the reduced tri-iodide ions ($I_3^-$) and oxidized iodide ($I^-$) undergoes a diffused transport through the pores of the semiconductor towards and from the counter electrode [Platinum, Pt-coated as catalyst on counter electrode];
6. **Regeneration of the electrolyte**: the Pt catalyst at the counter electrode reduces the oxidized tri-iodide ($I_3^-$) to iodide ($I^-$) by accepting a low energy electron from the external circuit ($k_4$):

$$I_3^- + 2e^- \xrightarrow{Pt,k_4} 3I^-$$

Processes 1–6 lists the favourable energy generation processes in a DSC. There are also competing processes that are unfavourable and limits the DSC performance (Maçaira et al. 2014):

7. **Dye de-excitation**: the dye in excited state ($D^+$) may directly decay to the original state (D) before the electron injection into the semiconductor

conduction band. This reaction rate ($k_{12}$) comes in direct opposition with the injection step ($k_{21}$);

8. **$TiO_2$ electron-dye recombination** ($k_{22}$): the oxidized dye molecules ($D^+$) can also interact with electrons in the $TiO_2$ conduction band. This reaction work against both dye regeneration ($k_3$) and with the electron collection from $TiO_2$ (Step 4);
9. **$TiO_2$ electron-electrolyte recombination**: electrons in the conduction band can also directly interact with the oxidized electrolyte species. This reaction directly opposes the electron collection (Step 4).

$$I_3^- + 2e_{CB}^- \xrightarrow{k_5} 3I^-$$

The active electrical energy generation from a DSC requires the forward electron transfer reactions ($k_{11}$, $k_{21}$, $k_3$ and $k_4$) to overcome the possible electron recombination/de-excitation processes ($k_{12}$, $k_{22}$ and $k_5$). The time constant ranges of different forward and backward reactions are illustrated in Fig. 9.5. The most important loss pathway is through the electron recombination with the electrolyte species ($k_5$), and the energy generation efficiency is delimited by this reaction rate. Since the electrolyte is present all throughout the mesoporous semiconductor, the recombination reaction is affected by the photo-electrode thickness, iodide concentration, dye structure, etc.

The approximate range of electron diffusion coefficients in anatase $TiO_2$ lies between $10^{-4}$ and $10^{-5}$ $cm^2$ $s^{-1}$. Therefore for a standard photo-electrode of 10 μm thickness, the electron transport time constant ($\tau_t$) would be in the range of few milliseconds. Figure 9.5 clearly shows that the recombination reaction constant of $k_5$ (corresponding electron lifetime ($\tau_n$) has the same order of magnitude of $\tau_t$, which results in a direct competition between these two mechanisms. The equilibrium between the charge generation and the recombination forces determines the current and voltage outputs of the DSC. DSC efficiencies can be increased by increasing the charge transport while lowering charge recombination. Researchers over the years have devoted their time and effort to understand charge recombination and controlling recombination rate constants by examining the effect of electrolyte additives, new photoanode architectures, new dyes, surface coatings, among other factors (Maçaira et al. 2014).

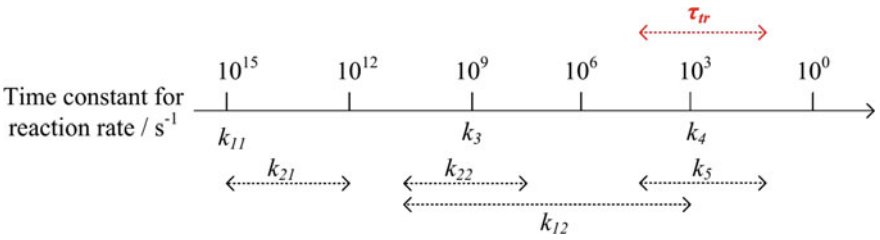


**Fig. 9.5** The reaction kinetics of different forward and backward reactions in DSC. Approximate range of values of various time constants (Maçaira et al. 2014)

### 9.2.2 DSC J–V Characteristics

*Short-Circuit Current* ($I_{SC}$)

The device current when the load resistance connected to the solar cell is decreased to zero or in other words, when the solar cell is short-circuited is called the short-circuit current ($I_{SC}$). The value of $I_{SC}$ is determined by both the photon-generated electrons and the interfacial recombination of the electrons and holes and hence is a function of the solar insolation, optical characteristics, and charge transfer probability of the cell. Short-circuit current density, $J_{SC}$, is given by $J_{SC} = I_{SC}/A$ (mA/cm$^2$), where $A$ is the solar cell effective area (Fig. 9.6).

*Open-Circuit Voltage* ($V_{OC}$)

The open-circuit voltage is defined as the maximum obtainable voltage from a solar cell, obtained when an infinite resistance load is attached to its terminals (or in other words, is open circuited). The value of $V_{OC}$ is determined by the difference between the Fermi level of electrons in the semiconductor (namely $TiO_2$) and the electrolyte redox potential.

For DSC the open-circuit voltage, $V_{OC}$ is expressed by

$$V_{oc} = \frac{E_{CB}}{q} + \frac{kT}{q}\ln\left(\frac{n}{N_{CB}}\right) - \frac{E_{redox}}{q}\ (\text{volts})$$

where '$n$' denotes the number of electrons in the $TiO_2$ conduction band (CB) and '$N_{CB}$' is the effective density of states (DOS). The first two terms in the equation describe the quasi-Fermi level of $TiO_2$ while the third term denotes the Nernst potential ($E_{redox}$) of the redox mediator.

*Series Resistance* ($R_S$)

The contact resistance and charge transfer resistance in the semiconductor material together contribute to the series resistance of a solar cell. Higher the series

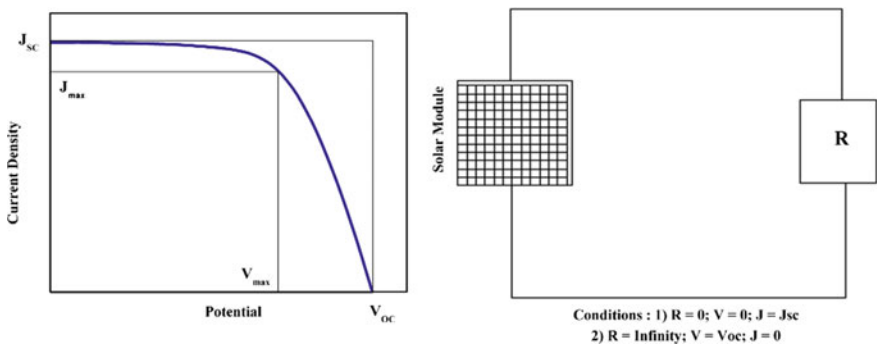


**Fig. 9.6** DSC *J–V* characteristics. Open- and short-circuit conditions

resistance lower the fill factor of the device and thus affects the maximum device power output. Excessively high value of series resistance, $R_S$ can even reduce the short-circuit current. However, $R_S$ does not affect the open-circuit voltage since at $V_{OC}$, the total current flow through cell itself is zero. The slope of the *I–V* curve at the open-circuit voltage point gives an approximate value of $R_S$.

*Shunt Resistance* ($R_{SH}$)

Shunt resistance represents the recombination or leakage current mechanisms in a solar cell. Low shunt resistance provides an alternate current path for the photo-generated current causing significant power loss, reduces the fill factor and lowers the open-circuit voltage, thereby affecting the maximum power output. However, the shunt resistance value does not affect the short-circuit current (unless otherwise too low), since at $J_{SC}$, the total current flows through the outer short-circuited path. The slope of the *I–V* curve at short-circuit current point gives an approximate value of $R_{SH}$.

*Fill Factor* (*FF*)

Fill factor is a function of the series and shunt resistances of the solar cell. It represents the squareness or the diode quality of the *I–V* curve and is defined as the ratio of the maximum power to the product of $V_{OC}$ and $J_{SC}$ for the solar cell:

$$\mathrm{FF} = \frac{V_m \times J_m}{V_{oc} \times J_{sc}}$$

where $V_m$ and $J_m$ are the voltage and current values at the maximum power point. Fill Factor (FF) is a measure of the maximum power output from a solar cell. Being a ratio of the same physical parameters, FF has no unit. For DSC, it points out the level of electrical and electrochemical losses during solar cell operation. Higher fill factor for DSC would imply a decrement of the series resistance and an improvement of the shunt resistance.

*Power Conversion Efficiency*

The power conversion efficiency of a solar cell is defined as the ratio of the maximum electrical energy output to the energy input from the sun. Thus the mathematical definition of efficiency is

$$\eta = \frac{V_{oc} \times I_{sc} \times \mathrm{FF}}{P_{in}}$$

where $P_{in}$ is the power input from the sunlight. Power Conversion Efficiency of a solar cell is dependent on the cell performance, the incident light spectrum, and intensity as well as operating temperature. The internationally recognized standard condition for the efficiency measurement of solar cells is under 'AM1.5 Global' solar irradiation and at a temperature of 25 °C.

*Quantum Efficiency or Incident Photon to Current Conversion Efficiency (IPCE)*

Quantum efficiency (QE) or 'external quantum efficiency (EQE)' also referred to as incident photon to current conversion efficiency (IPCE) represents how effectively can a solar cell create photo-generated charges at a given wavelength. It is defined as the ratio of the number of incident photons to the number of charge carriers generated and is a function of the excitation wavelength:

$$\mathrm{IPCE}(\lambda) = \frac{1240 \times J_{\mathrm{sc}}}{\lambda \times P_{\mathrm{in}}}$$

where $J_{\mathrm{SC}}$ is the short-circuit current (mA/cm$^2$), $\lambda$ is the wavelength (nm) and $P_{\mathrm{in}}$ is the incident radiative light flux (W/m$^2$).

For DSC, the term is defined as

$$\mathrm{IPCE}(\lambda) = \mathrm{LHE}(\lambda) \times \eta(\mathrm{inj}) \times \eta(\mathrm{coll}) \times \eta(\mathrm{reg})$$

where LHE($\lambda$) is the light harvesting efficiency for photons at wavelength $\lambda$, $\eta$(inj) is the quantum yield of electron injection for the excited sensitizer to the semiconductor oxide conduction band, $\eta$(coll) is the fraction of injected charges that is finally collected (i.e. able to reach the back contact) and $\eta$(reg) is the regeneration efficiency. Short-circuit current density ($J_{\mathrm{SC}}$) can be calculated by integrating the product of the incident photon to current efficiency (IPCE) and incident photon flux ($P_{\mathrm{in}}$) over the spectral distribution.

*Equivalent Circuit*

Equivalent circuits provide deep insight into the physics of dye-sensitized solar cells and have proved to be a quite useful tool to explain the various mechanisms in the cells and thereby tuning the device performance. The equivalent circuit of a general solar cell at the first level of abstraction is the single-diode model. This model could be directly applied to fit the experimental *I–V* characteristic curve of solar cells (Fig. 9.7b). The model relies on the explicit single-diode-like behaviour observed at one of the interfaces of the solar cells. In DSCs, this behaviour is visible at the $TiO_2$/dye/electrolyte interface where the resistance element related to the charge transport behaviour, similar to a diode ($R_{\mathrm{diode}}$).

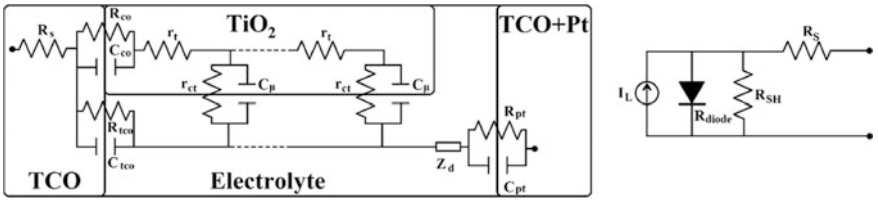


**Fig. 9.7** DSC detailed equivalent circuit and single-diode equivalent model (Chalkias et al. 2018)

However, concerning DSC technology, interpretation of the parameters obtained by single-diode equivalent model does not provide a greater insight into the fundamental physical chemistry processes governing the performance of these devices. Therefore a detailed equivalent circuit, describing the electrochemical processes at each interface is required and is provided in Fig. 9.7a.

Charge transfer at $TiO_2$/electrolyte interface can be analysed by using transmission model given by Fabregat-Santiago et al. (2007, 2011). Transmission line model consists of transport resistance ($R_t$), recombination resistance ($R_{ct}$) and chemical capacitance ($C_\mu$). $R_t$ corresponds to resistance for the diffusion of electron in $TiO_2$, $R_{ct}$ corresponds to the resistance for the recombination at $TiO_2$/electrolyte interface and $C_\mu$ is the chemical capacitance of $TiO_2$. Very often $C_\mu$ is used to represent the conduction band of $TiO_2$. $R_{co}$ and $C_{co}$ are the impedances at FTO/electrolyte interface. Similarly, $R_{tco}$ and $C_{tco}$ give the charge transfer at FTO/electrolyte interface. $R_s$ is the series resistance which includes sheet resistance of FTO and contact resistance. $Z_d$ is the impedance of the electrolyte which is used to study the diffusion of ions in electrolyte. $R_{pt}$ and $C_{pt}$ are the impedances at counter electrode-electrolyte interface.

### 9.2.3 DSC: Detailed Structure-Material Perspective

**Working Electrode**

*Transparent Conducting Oxide (TCO) Glass Substrate*

The role of a transparent conducting substrate in DSC is twin fold: (1) to serve as a current collector (2) and as a semiconductor layer supporter. Two of the important features of TCO are: high optical transparency to natural sunlight allowing the light to reach the active material without unwanted absorption of the solar spectrum, and low electrical resistivity which facilitates the electron transfer process and reduces the energy loss. The most efficient TCO material widely used in the photovoltaic application is ITO or FTO coated glass substrate. The drawback with ITO is that its conductivity decreases during the calcination process in the DSC fabrication. Considering this, FTO is the preferred transparent conducting material for DSCs. Organic films are also being developed using carbon nanotube networks and graphene, which can be fabricated to be highly transparent to infrared light, along with networks of polymers such as poly(3,4-ethylene dioxythiophene) and their derivatives. TCO films are deposited on a substrate through various deposition methods, including metal organic chemical vapour deposition (MOCVD), spray pyrolysis and pulsed laser deposition (PLD), however, the most efficient technique is magnetron sputtering of the film.

*Metal Oxide Coating*

The metal oxide nanoparticulate porous coating is generally deposited on the top of the TCO by doctor blade or screen-printing method. This coating provides a surface for the dye adsorption, and it accepts electrons from the excited dye and conducts electrons to the TCO. The choice of metal oxide can be made between different n-type oxides such as $TiO_2$, ZnO, $SnO_2$ and other ternary oxide like $Zn_2SnO_4$, etc. $TiO_2$ is the workhorse material for DSCs. It exists in three forms namely anatase, rutile and brookite. Of the three forms, rutile is the most stable phase but it suffers from slow electron transfer rate leading to the low current in DSC. Anatase $TiO_2$ is widely used as a photoanode material which renders conversion efficiency of 12% using standard materials due to greater electron transport properties and high surface area.

Two types of $TiO_2$ pastes are generally used in DSC. 20 nm nanocrystalline-$TiO_2$ used as the mesoporous transparent active layer and 400 nm microcrystalline-$TiO_2$ acting as the light-scattering layers of the photoanode. $TiO_2$ films consisting of transparent nanocrystalline and microcrystalline light-scattering anatase particles form a photon-trapping system, which results in DSC photocurrent enhancement as a result of backscattering. Figure 9.8 illustrates the effect of light harvesting layer in DSC.

Modified $TiO_2$ architectures viz., vertical/horizontal nanowires, TCO free CNT (Carbon Nanotubes) modified $TiO_x$–$TiO_2$, MWNT (Multiwalled nanotubes)-$TiO_2$ systems have been reported in the literature. Efficiency and/or fill factor improvement due to surface modifications are observed but meagre (Sharma et al. 2017).

Variation in thickness of the nanocrystalline-$TiO_2$ layer is a crucial factor in optimizing photovoltaic performances of DSC. The optimum film thickness to produce highly efficient DSC with Ruthenium Sensitizers is ~12–14 μm. With Organic dyes, the layer thickness can be even less (Fig. 9.9)

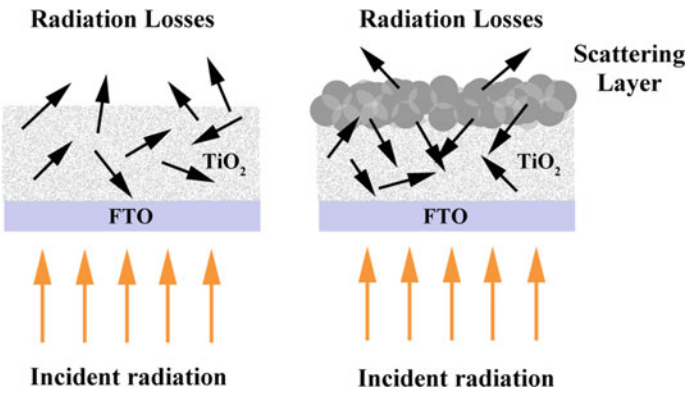


**Fig. 9.8** DSC with and without light harvesting layer (Agarkar 2014)

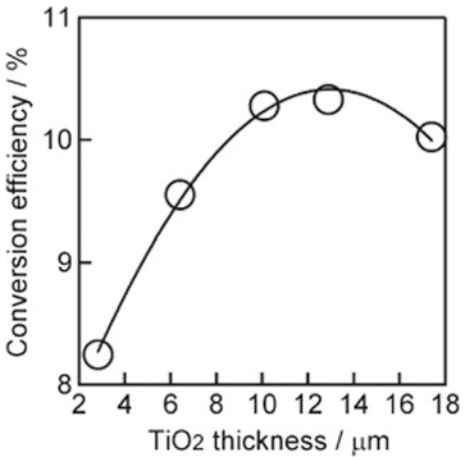


**Fig. 9.9** DSC efficiency variation with thickness (Ito et al. 2008)

## Photosensitizer (Dyes)

The ideal sensitizer (hereinafter called the 'dye') used in DSC should meet the following requirements: (i) the dye should be panchromatic, i.e. it should be capable of absorbing the entire incident light ranging from visible to near-IR region; (ii) it must possess an anchoring group either a phosphonate or carboxylate chain to anchor on the surface of the semiconductor oxide; (iii) in order to minimize the overpotential losses during the transfer of electron from the sensitizer to the metal oxide the lowest unoccupied molecular orbital (LUMO) of the dye must be in the closer range of the conduction band edge of the oxide; (iv) similarly, to facilitate the electron absorption from an electrolyte or a hole transporting material (HTM), the highest occupied molecular orbital (HOMO) of the dye must be sufficiently low (as limited by practical considerations); (v) the dye should be stable.

The sensitizer, or dye monolayer, is the layer which interacts with the sunlight and therefore is a very important part of the DSC. Typically, the metal oxide films are immersed in the dye solution for 12–24 h so that the dye molecules get adsorbed on the surface of the metal oxide nanoparticles. The addition of chenodeoxycholic acid (CDCA) helps to suppress the dye aggregation through co-adsorption with the photosensitizers in DSC.

### *Metal Complex Photosensitizers*

Absorption of these dyes in the visible and near-IR regions are attributed to the MLCT (Metal to Ligand Charge Transfer) transition. Ru based complexes have shown the highest efficiency as photosensitizers since the inception of this technology. The MLCT charge transfer occurs between the d-orbital of the Ru metal and the $\pi^*$ orbital of the ligand, respectively. N3 dye (or red dye), black dye, N719 dye and Z907 dyes are the commonly used sensitizers in DSC. Porphyrin and phthalocyanines derivatives have also been employed (Hara and Arakawa 2005).

*Organic and Natural Dye Photosensitizers*

Organic dyes whose HOMO and LUMO levels match the conduction band level of the semiconductor and the redox potential of the electrolyte can also be employed as photosensitizers. D35, MK2 and LEG4 are a few examples of organic dyes (Wang et al. 2008b, 2011; Ellis et al. 2013; Gabrielsson et al. 2013; Kakiage et al. 2015; Kusters et al. 2007; Vinayak et al. 2016; Vinayak et al. 2018; Soman et al. 2015). Organic dyes have several advantages like, they are easy to synthesize, are cheaper and also more environmentally friendly compared to metal-based dyes, have high molar extinction coefficient often higher compared to metal-based dyes and hence are suitable for solid-state solar cells where the $TiO_2$ thickness is limited (Hara and Arakawa 2005).

Natural dyes like Santalin, Coumarin and Eosin yellow have been used in DSC studies, however, the efficiency and stability of these dyes are very less.

**Electrolyte**

The electrolyte is the life vessel of dye-sensitized solar cells (DSCs). It facilitates the collection of low energy electrons from the cathode and transports them back to the dye molecules. The reaction kinetics favours the usage of the most commonly used liquid electrolyte, iodide/tri-iodide ($I^-/I_3^-$). In terms of reaction kinetics, the injection of electrons into the $TiO_2$ conduction band is favourable (femtosecond transition) and faster than the electron recombination (from dye excited state) with the oxidized electrolyte species $I_3^-$. Similarly the interaction of the oxidized dye with the reduced electrolyte species $I^-$ is more favourable than recombination with the injected electrons in $TiO_2$ conduction band. In the electrolyte, the reactant equilibrium is maintained by the forward transport of $I_3^-$ towards the cathode where it absorbs low energy electrons and the backward diffusion of $I^-$ species towards the $TiO_2$ electrode to enable dye regeneration. The recombination rates can be further suppressed by the introduction of additives such as 4-tert-butylpyridine (4-tbp), guanidinium thiocyanate (GuSCN), methyl benzimidazole (MBI), etc. These additives get absorbed on the $TiO_2$ surface and block the possibility of any electron recombination.

The overall conductivity of this electrolyte can also be increased by using different ionic liquids containing imidazolium salts. Depending on the alkyl chains attached to these imidazolium salts, the performance of the electrolyte can be varied, improving the efficiency and stability, without participating in the key photo-electrochemical processes. Lithium iodide is added in the electrolyte as it acts as a source of iodide ions required for redox couple in the electrolyte. Also, the lithium ions screen the negative charge in the semiconductor, and increase charge conductivity in the electrolyte. In the absence of these cations on the surface, the conduction band of semiconductor shows a downward shift which lowers the $V_{oc}$ of the cell. But the concentration of this Li must not be very high as the small Li cations can intercalate with the $TiO_2$ matrix and act as recombination centres thus lowering the device performance. The maximum voltage generated in DSCs is given by the difference between the quasi-Fermi level of the $TiO_2$ and the redox potential of the electrolyte [Theoretically, 0.7–0.8 V under solar illumination conditions] (Wang et al. 2012).

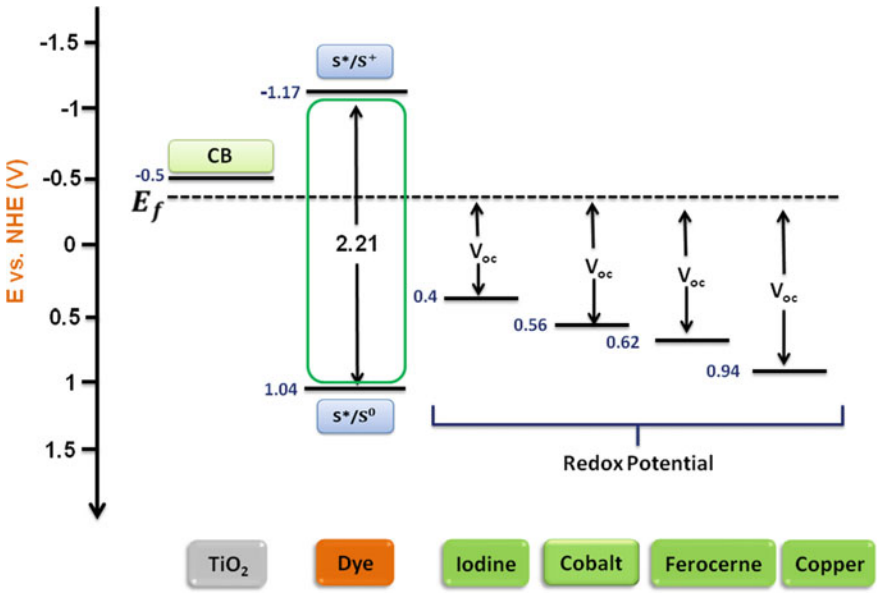


**Fig. 9.10** DSC effect of redox couple on open-circuit voltage (Pradhan et al. 2014)

Iodide/tri-iodide systems undergo redox reaction through a two-stage process. The redox potential of this system being less positive the overpotential loss for the electrolyte-dye injection is very high. In the search for alternative redox couples more positive Co(II)/Co(III) and Cu(I)/Cu(II) pairs were introduced recently, both capable of providing higher open-circuit voltages. Cobalt and copper complexes are the current hot topics of research in DSC community. Figure 9.10 illustrates the difference in redox potentials of Iodide/tri-iodide and outer sphere one electron redox shuttle like ferrocene and cobalt electrolyte and the corresponding $V_{oc}$ improvement.

### Counter Electrode

Platinum nanoparticle coated FTO obtained through chemical reduction, sputtering or thermal decomposition is used as the counter electrode due to its high efficiency in the regeneration of $I^-/I_3^-$ redox species (the $I_3^-$ to $I^-$ conversion occurs on the surface of Pt counter electrode, and is catalysed by Pt). Though the best candidate, the higher cost and lesser natural abundance has been the bottleneck in the widespread usage of Pt catalyst, and several alternate materials were sought of as a replacement. The qualities required for an efficient catalyst in DSC includes easy availability, low cost, good stability and excellent catalytic activity (Agarkar 2014). Recently, carbon in various forms, viz. mesoporous carbon, carbon nanotubes (CNTs), functionalized graphene, carbon fibres, etc. have evolved out as an alternative for Pt, delivering competing efficiencies. However, carbon counter electrodes are not devoid of de-merits due to its poor adhesion to the substrate surface and its

opaque nature. PEDOT:PSS has attracted scientific community due to its low cost and good conductivity. Spin coating and the chemical polymerization are the two major methods for the deposition of PEDOT:PSS over FTO coated glass (Wu 2017). Very recently, PEDOT has emerged alternative to Pt due to its compatibility with alternative redox mediator, viz. cobalt and copper. High catalytic property with more surface area results in fast charge transfer at PEDOT/electrolyte interface. Electropolymerization is the most used method to deposit PEDOT over FTO-coated substrate (Soman et al. 2018).

### *9.2.4 DSC-Small Device Fabrication*

The standard cell assembly procedure for a 10% efficient dye solar cell reported by Ito et al. (2008) is described here. After performing the standard cleaning procedure, the transparent conducting oxide (TCO) glass is soaked in 40 mM $TiCl_4$ (aqueous) for 30 min at 70 °C which forms a compact $TiO_2$ layer over FTO. This pre-blocking layer enhances the bonding strength between the FTO substrate and the porous-$TiO_2$ layer which also blocks the charge recombination at FTO/electrolyte interface (Sasidharan et al. 2017). The electrodes with pre-blocking layer are then annealed up to 500 °C. $TiO_2$ film which is consisting of particle size of 15–30 nm is deposited over TCO either by doctor-blading or screen-printing technique. Thickness of the $TiO_2$ layer depends upon the number of $TiO_2$ layers or mesh size of screen. A scattering layer which includes $TiO_2$ particle of size 250–400 nm is usually deposited over transparent layer. The $TiO_2$-coated electrodes are then subjected to ramped annealing up to 500 °C. Above $TiO_2$ layer another compact $TiO_2$ layer is deposited using the same procedure as adopted for deposition of pre-blocking layer. The substrates are then kept inside the dye bath for dye loading for overnight. Counter electrode preparation includes the cleaning of the predrilled TCO glasses followed by screen-printing of Pt. Screen-printed Pt is annealed at 400 °C for 30 min. Working electrode and counter electrode are assembled together with melt gasket made up of surlyn. Electrolyte is filled through the holes in counter electrode. Then the holes are sealed with cover glass. Figure 9.11 shows the standard DSC structure, while Fig. 9.12 illustrates the standard fab procedures. Figure 9.13 illustrates the device assembling stages.

## 9.3 Dye Solar Module (DSM): Scale-up Technologies

Researchers at Sharp group were able to achieve a certified efficiency of 11.9% for lab-scale DSC devices (Fakharuddin et al. 2014) [uncertified efficiencies as high as 14.3% has been reported (Kakiage et al. 2015)]. Transforming the highly efficient small area devices to large area modules through viable, repeatable, large-scale industrial production compatible processes involves a detailed introspection on the

| FTO Glass |
|---|
| $TiO_2$ blocking layer ~50-100nm thick |
| Light Absorption Layer 10~12μm thick, 15-30nm particles |
| Light Scattering Layer 3~5μm thick, 200-400nm particles |
| Ultra-thin Overcoating of $TiO_2$ using aqueous $TiCl_4$ |

**Fig. 9.11** Standard DSC photoanode structure for optimum performance (Khan 2013)

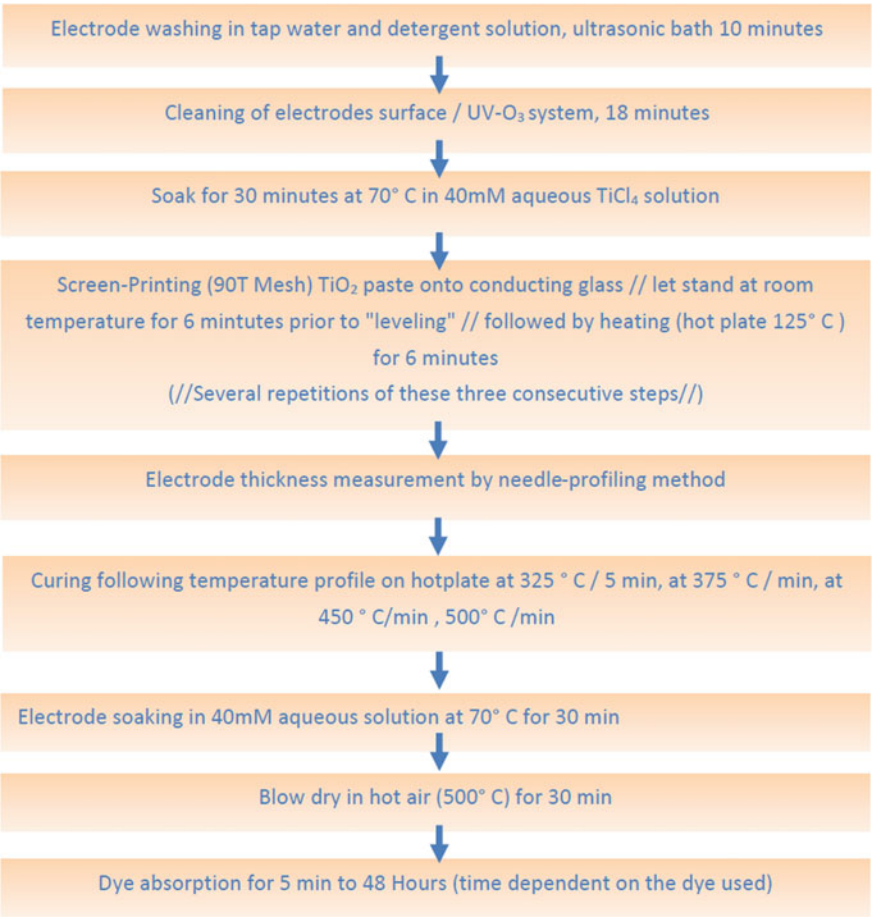


**Fig. 9.12** Fabrication Cleaning and Fabrication steps for small area DSC photoanodes (Ito et al. 2008)

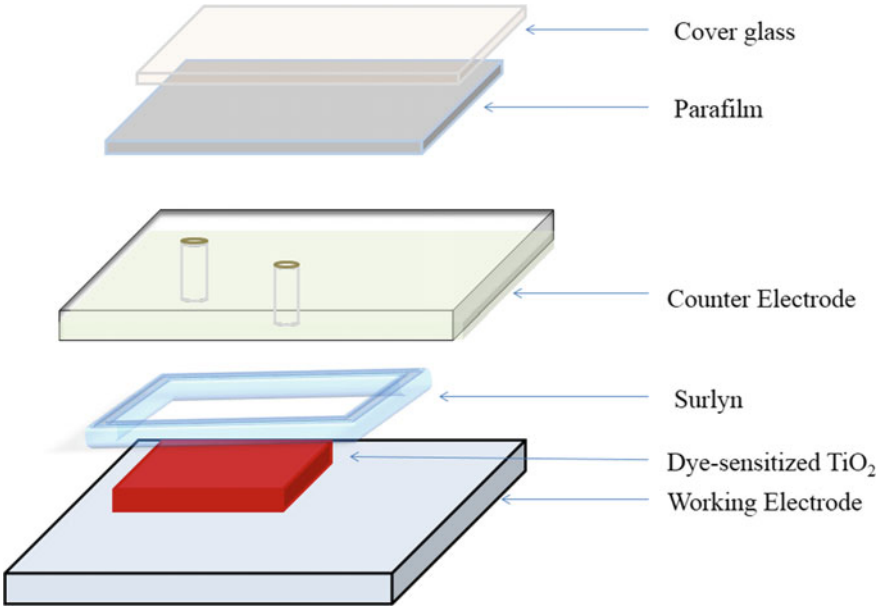


**Fig. 9.13** Internal architecture of a DSC-small device (Khan 2013)

entire technological parameters and various process stages so that stable, efficient and cheap dye-sensitized solar modules, ready for practical applications can be materialized.

The preliminary hindrance for scale-up is the high series resistance, which is the sum of transparent conducting oxide (TCO), substrate resistance ($R_{TCO}$), diffusion resistance of the redox species in the electrolyte, and the charge transfer resistance at counter electrode/electrolyte interface ($R_{CT}$). Direct scaling up of the device active area over a few square centimetres would proportionally increase $R_{TCO}$, resulting in a very high series resistance and poor fill factor (FF). Usage of silver (Ag) grid embedded TCO glass and stripe-type $TiO_2$ layers is the solution helps to reduce the ohmic losses and improve the fill factor. Efficient charge collection over the entire device is ensured by the metal grids. Now, these metal grids have to be properly insulated from the corrosive action of the electrolyte. Also, each stripe forming the module should form a completely separate compartment to prevent electrophoretic effects.

The dye solar module fabrication is significantly distinct from the assemblage of small area devices owing to the requirement for

(i) large area and patterned deposition of active layer on TCOs, creation of a sealing that prevents electrolyte leakage and drying while at the same time impervious to air and humidity,
(ii) large area air pocket free electrolyte filling,

(iii) module interconnections (parallel or serial) and provisions for external electrical contacts, and
(iv) most significantly, the fabricated devices should be stable and be able to deliver consistent performance for its entire lifetime (∼20 years) as offered by silicon-based devices

### 9.3.1 Module Architecture

Dye solar module fabrication has taken shape over time and age and has evolved out into two major practical architectures: (i) a device structure that generates high photocurrent-parallel design; and (ii) high output voltage producing devices series design (which includes monolithic, W- and Z-type interconnections).

Figure 9.14 outlines the general steps involved in the fabrication of a parallel dye solar module. Serially interconnected DSM requires etching off of the TCO for isolating individual cells. The Z-type architecture requires vertical silver interconnects to ensure serial voltage addition. In W-type interconnection, a back-to-back device architecture is adopted so that no Ag interconnection is required.

**Parallel Module**

Parallel grid type DSMs (Fig. 9.15) offers a high current, ideally equal to the sum of currents produced by individual cells in the module while offering the voltage of a

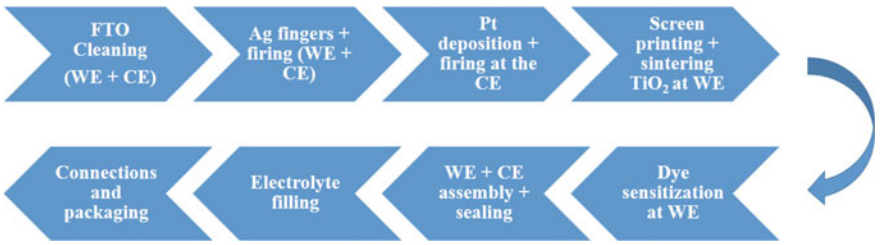


**Fig. 9.14** General fabrication steps of dye solar modules (DSMs)

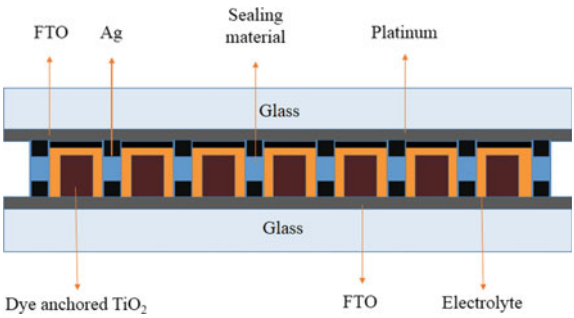


**Fig. 9.15** Parallel DSC module (Wang et al. 2010)

single cell. Parallel architecture avoids the need for an inner interconnection of the working and counter electrodes, hence offering relative ease of fabrication, compared to serial modules.

Metal grids that are provided, circumventing the active layer strips ensures faster charge collection, lowers the series resistance and improves the fill factor. This design was conceived by the researchers as early as in 1995, however the corrosive nature of the iodide electrolyte on all the known metals, which could be used for designing the grid viz., Silver (Ag), Gold (Au), Copper (Cu), Aluminium (Al), and Nickel (Ni) suspended further development, until the discovery of new materials for protecting the grid-like ceramic glazes, polymer, epoxy, glass frit, etc. Inclusion of metal grids led to a dramatic increase in the photovoltaic performance of DSM [a fivefold increase in $\eta$, FF increased greater than 200%, while $J_{SC}$ increased almost by 100% (Wang et al. 2010). Spath et al. (2003) reported the development of reproducible manufacturing processes for parallel DSM fabrication. The team developed 27 DSMs with a total area of $\sim$100 cm$^2$, and obtained an efficiency of $\sim$4.3 $\pm$ 0.07%. The same team reported an improvement in efficiency η of $\sim$7.4% using a modified fab process and with the usage of silver grids.

The drawback of this design is the availability of lower active area after allotting space provision for the current collecting grids and for the protective sealant.

## Serial Module

### *Z-Type Interconnection*

Figure 9.16 illustrates a Z-type module design. The current flow path from one cell to the other via the FTO coating resembles the English alphabet Z and hence the name for this architecture. FTO etching using procedures like manual/laser scribing is done at the relevant areas on both the working and counter electrode. The electrical interconnection connecting the adjacent cells helps in the serial addition of voltages. This interconnecting element needs to be completely protected by internal sealing, preventing corrosive action of the electrolyte on the element and for avoiding electrophoretic effects.

Toyoda et al. (2004) reported the first Z-type DSM in 2004 which comprised 64 DSM (10 $\times$ 10 cm$^2$) interconnected in series to form a large panel. Achieving the electrical interconnection between adjacent cells which are hermetically sealed was

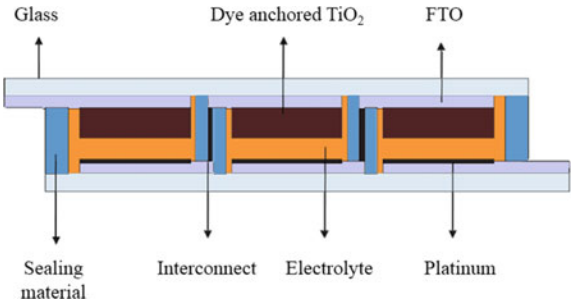


**Fig. 9.16** Z-type interconnection (Kroon and Hinsch 2003)

the immediate challenge in developing Z-architecture, which was difficult and imperfect with the conventional sealing technologies. This problem was however resolved with the usage of glass-frit sealing reported by Sastrawan et al. (2006). By carefully engineering the device architecture [width of each individual strip (<1 cm)] Jun et al. (2008) reported a 10 × 10 $cm^2$ Z-type DSM which attained an efficiency $\eta \sim 6.6\%$ ($V_{OC} \sim 8$ V, $J_{SC} \sim 1.23$ mA $cm^{-2}$, and FF $\sim 0.67$).

Poor utilization of active area due to the space provided for vertical interconnection, sealing, fabrication complexity, issues arising from the series resistance of the vertical interconnection are the drawbacks of this design. Also, the probability for the vertical interconnect to get corroded due to electrolyte action is higher in this design.

*W-Type Interconnection*

Figure 9.17 shows the W interconnected DSC architecture. In W interconnection the active layer and platinum layers are alternately deposited on each glass plate, thereby avoiding the vertical silver interconnection between cathode and anode. Simplicity in design and the elimination of vertical interconnection improves the FF of these devices. The highest reported efficiency for a dye solar module is a W-architecture as reported by SHARP Co. (8.2 and 9.3% with respect to active and total area, respectively) (Han 2009).

The drawback of the W-architecture is when the module is illuminated through the counter electrode side, a considerable portion of the light is absorbed by the Pt and the electrolyte leading to lower currents and the resulting current mismatch issues. This issue can be circumvented by widening the counter electrode layer on the frontal side.

*Monolithic Interconnection*

Monolithic architecture was first proposed by Kay and Grätzel (1996). The design was indeed innovative since it uses a single TCO-glass plate in sharp contrast to the glass/glass design used by other device architectures thus leading to a sharp reduction in production cost.

Figure 9.18 describes the device architecture of a DSC in the monolithic set-up. The first layer is formed by the nanocrystalline $TiO_2$ coated on the TCO-glass plate.

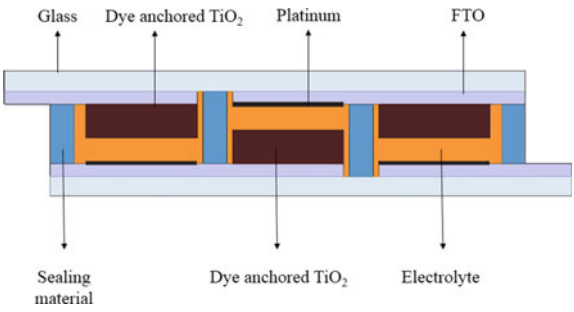


**Fig. 9.17** W-type interconnection (Kroon and Hinsch 2003)

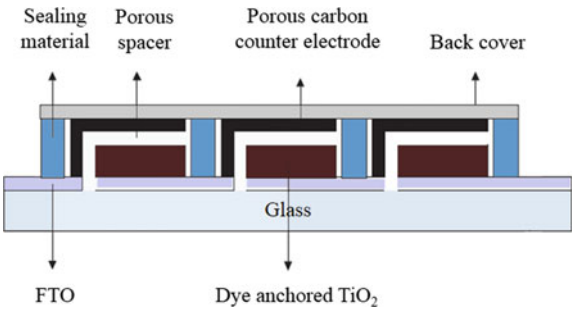


**Fig. 9.18** Monolithic interconnection (Kroon and Hinsch 2003)

A porous insulating oxide layer ($ZrO_2$) is coated on the top of the $TiO_2$ layer (to serve as a spacer). A carbon black printed porous graphite layer coated on the top acts as the counter electrode. All the three layers can be deposited by screen-printing techniques and are then subjected to annealing. Subsequent to these processes, the dye and electrolyte are applied and finally sealed and insulated using a nonfunctional material that covers the entire module (Kroon and Hinsch 2003).

Monolithic architecture is highly compatible with roll-to-roll processing of flexible DSMs. The design is more tolerant to the non-planarity of the substrates since the device fabrication progresses through a layer by layer procedure, rather than assembling one electrode over the other. The technology inspired from the architecture of series-connected amorphous-silicon solar cells also replaces the need for costly platinum by using cheaper carbon black material. The process is adaptable to large-scale production and offers 20–30% reduction in material cost. Using AM 1.5G solar light, an efficiency of 5.3% has been reported for a small module (20 $cm^2$) containing 6 series-connected monolithic cells of 4.7 $\times$ 0.7 $cm^2$.

## *9.3.2 DSM Fabrication Stages: A Technology Perspective*

### FTO Glass Preparation

The fluorine-doped tin-oxide (FTO) coated glass plates are cut into required sizes using precision cutting tools. Accuracy of the cut is critical for mechanical alignment in further processes (Fig. 9.19). For serial interconnection in Z or W or monolithic designs, laser scribing system is used to etch FTO at required locations (Fig. 9.20).

Precision holes need to be drilled on the rear side of electrode for electrolyte filling (Fig. 9.21). After the drilling and cutting steps, the probability for the presence of minute glass pieces and iron from the drill bits is very high and hence the FTO substrates are cleaned in an ultrasonic bath/industrial washing machine using deionized water and detergents.


**Fig. 9.19** Glass cutting tool

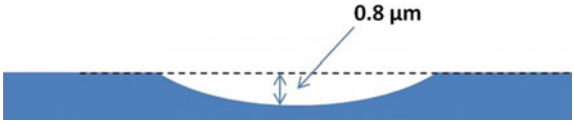


**Fig. 9.20** The surface of a scribed TCO glass plate (Mariani et al. 2015)

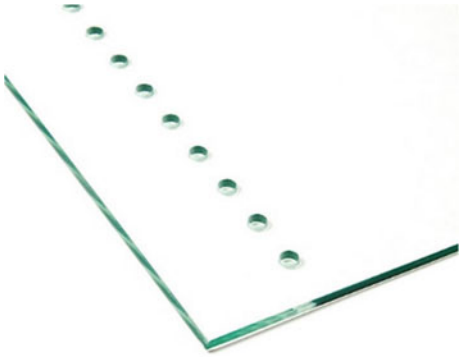

**Fig. 9.21** Drilled FTO glass

### Ag Deposition and Drying

The silver lines are either screen or pad printed or needle dispensed on the FTO screen using the predetermined pattern. The screen-printed silver grid is then subjected to a drying step at temperature specified in the Ag datasheet for ensuring proper material adhesion. The grid so formed collects the photo-electrons and reduces series resistance and improves the Fill Factor (FF). Certain device architecture proposes the application of silver grid on the counter electrode before depositing platinum to further enhance the FF.

### $TiO_2$ and Platinum (Pt) Deposition and Sintering

$TiO_2$ paste is deposited via screen printing/inkjet printing onto a glass/FTO substrate (photoanode) (Fig. 9.22). The sample is then subjected to sintering for a minimum 30 min above 500 °C to obtain a final $TiO_2$ thickness of a few µm.

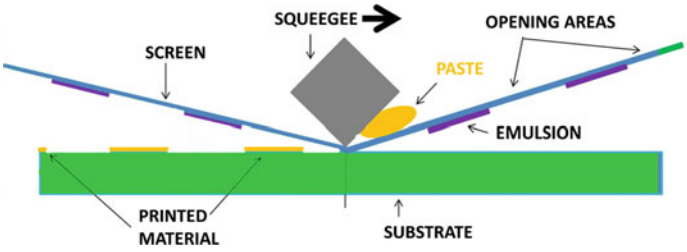


**Fig. 9.22** Screen printing mechanism (Mariani et al. 2015)

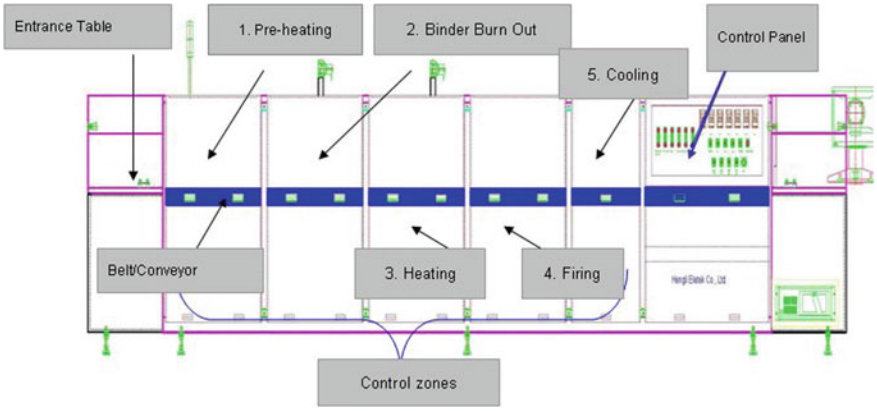


**Fig. 9.23** An automatic belt furnace for the sintering of deposited pastes (Mariani et al. 2015)

During the sintering process (Fig. 9.23), the solvents and binders are burnt off and the $TiO_2$ undergoes a phase change to the anatase crystalline phase. Coating a post-blocking layer of $TiCl_4$ (via chemical bath deposition or screen-printing) can enhance the device photocurrent. The deposition of Pt can also be done via screen-printing and the sample should be annealed at around 450 °C for 20 min (of course using a different printer and furnace to avoid cross-contamination). Laser sintering technologies have also evolved nowadays for sintering both $TiO_2$ and Pt.

### Sealing

Sealing is the most challenging process in dye solar module fabrication. The process is inevitable due to the presence of liquid electrolyte. The modules should be hermetically sealed to avoid solvent evaporation as well as to prevent the ingression of water and oxygen. The sealing materials should possess the following traits:

- the sealant should be chemically stable while coming in contact with liquid electrolyte

- the edge properties of the sealant should be excellent in order to minimize solvent losses (typically nitriles), and water/moisture/oxygen ingression
- should have stable sticking property with TCO and glass
- should be processible along with other components of the nanocrystalline-DSC.

Thermoplastic materials, resins, glass frit, anti-corrosion coatings, etc. are used to protect the conducting silver fingers (from electrolyte corrosion) and device sealing.

*Thermoplastic Polymer Sealing*

Regarding thermoplastic materials (such as Surlyn or Bynel, from Dupont), the Ag grids and the substrate perimeters are covered with the sealant foil and the module is then temperature cured in a heat-press (temperatures from 60 to 180 °C). To further enhance the durability of the sealing, heat-pressing in vacuum chamber is suggested so that moisture traps in sealing are avoided.

*UV Cured Epoxy Sealing*

The UV sealant is dispensed along the silver grid in between the stripes and covering the perimeter using a mini-robot. The counter electrode was mounted onto the anode (Pt-coated side facing the dye-stained-$TiO_2$) and the module is exposed to a strong UV light for a duration sufficient to harden the sealant.

*Glass-Frit Sealing*

Glass-frit material has offered the best sealing properties required for DSCs till date. Glass-frit material is screen printable and requires a temperature curing around 500 °C to achieve the required material strength. Tuning the thermal expansion coefficient of the glass-frit material to coincide with that of standard float glass is possible, and hence module sizes up to 30 cm × 30 cm can be hermetically sealed using Glass-frit. Due to the high-temperature sealing process, the dye staining and electrolyte filling processes follow the module assembly step (Fig. 9.24). Laser-assisted local glass-frit fusing techniques have also been reported in the literature (Sastrawan et al. 2006).

**Dye Staining**

Spath et al. (2003) describe two different methods of dye staining compatible for large-scale DSM manufacturing. The first method is applicable to hot-melt or epoxy sealed devices in which dye staining is done prior to the device assembly. In this process, the $TiO_2$ screen-printed and annealed working electrode are placed in a dye staining chamber. Heated dye solution is circulated through the chamber for several cycles followed by washing (using the dye solvent) and drying ($N_2$ purging) cycles. The concentration of the dye, rate of dye injection, applied pressure, temperature of the process, thickness and porosity of the $TiO_2$ layer are the key parameters that determine the dye adsorption. This process is more industrial compatible for faster staining of large area modules.

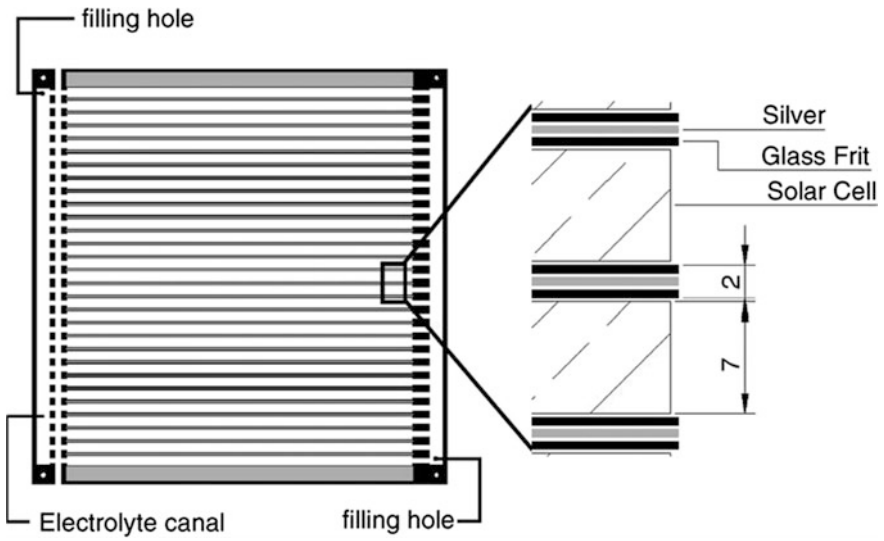


**Fig. 9.24** Glass-frit sealed system with electrolyte canals for dye and electrolyte filling (Sastrawan et al. 2006)

The second staining method was proposed for glass-frit sealed system. Here, due to the high-temperature fusing requirement of glass-frit dye staining is performed after the device assembly. In this process, the dye solution is flushed through an inlet and drained through an outlet port in the glass substrate (dedicated holes/guided paths need to be allowed in the device structure for dye staining). Also, the electrodes are moderately heated in this process to allow better dye adsorption.

### Electrolyte Filling System

Electrolyte filling is a crucial step in large area dye solar module fabrication. Two-hole electrolyte filling system, working on capillary action performs well and good with the small area devices, but introduces bubbles and voids in large area modules. Further, a two-hole electrolyte filling system is not readily scalable process from the bulk/industrial manufacturing perspective. Vacuum backfilling techniques for filling electrolyte has also been reported (Wang et al. 2005, 2008a), wherein the DSC module is dipped in electrolyte in a vacuum chamber. The disadvantages of this technique are that the electrolyte starts boiling during the application of vacuum (altering the composition) and also while dipping, large amount of electrolyte gets coated on the outside of the module resulting in wastage. Jayaweera and Kaneko (2012) report an electrolyte filling machine, which uses a single hole to fill the liquid electrolyte (including viscous ionic liquid) into an enclosed cell. This system involves a four-step filling process, namely evacuation, discharging, filling, and returning extra electrolyte. The electrolyte is not exposed to ambient conditions during the entire filling process, and the wastage of electrolyte is avoided using the return step. The advantage of this technique includes better

insertion of electrolyte into the mesoporous titanium oxide layer of dye-sensitized solar module (DSM). It helps in having an air bubble-free filling, and faster filling time (40 s with a nonvolatile liquid-based electrolyte for a 15 cm × 15 cm module).

Figure 9.25 shows the schematic of a vacuum-based electrolyte filling system developed by SPD Labs, Japan. The system relies on vacuum-based electrolyte filling through a single hole. A central controller works through various solenoid operated valves (A, B, C, D, E) to effect the electrolyte filling with minimum wastage/contamination. The electrolyte filling process can be divided into four main steps:

(1) Evacuation of the Cell—In this step, the interior of the DSC is evacuated
(2) Discharge the Electrolyte—In this step, the electrolyte is allowed to flow into the rubber tip.
(3) Fill into the cell—the pressure inside the rubber tip is increased by sending nitrogen through Port A. The electrolyte that is collected in the tip is pushed into the cell
(4) Return Extra Electrolyte—Finally, any extra electrolyte left in the middle tube and the rubber tip needs to be returned to the electrolyte bottle before the filling head is lifted off from the cell.

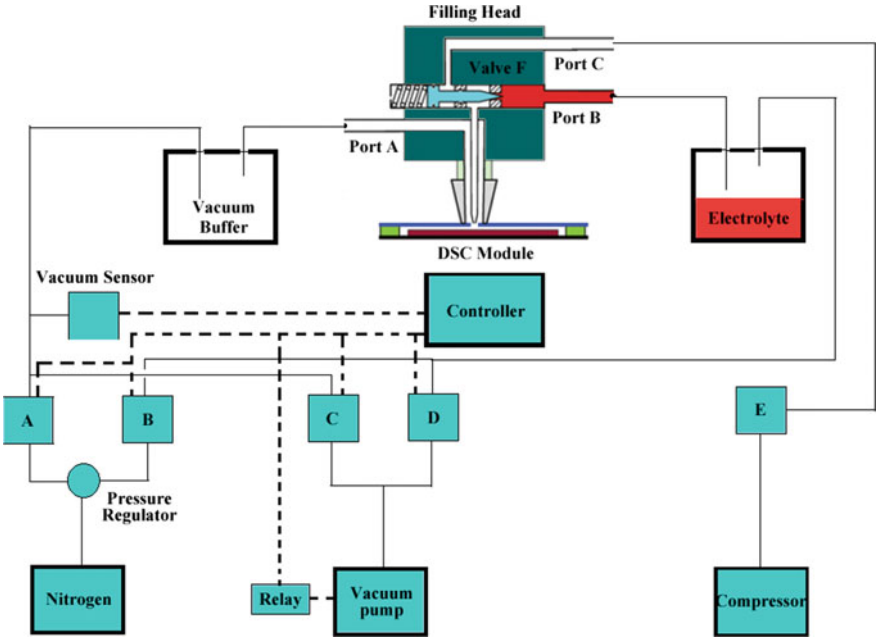


**Fig. 9.25** Schematic diagram of the electrolyte filling system showing the $N_2$, vacuum and compressed air pathways and solenoid valves with the electronic control system (Jayaweera and Kaneko 2012)

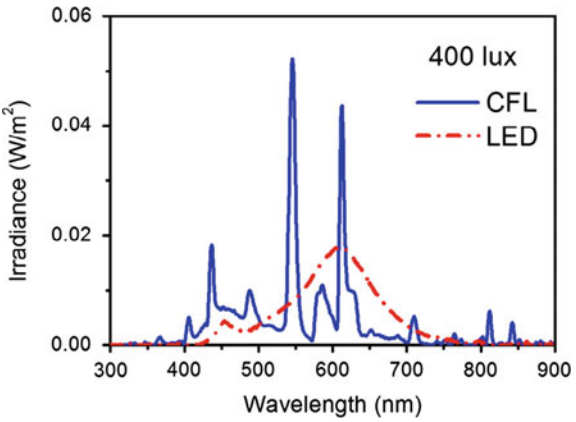


**Fig. 9.26** CFL and LED spectrum (De Rossi et al. 2015)

This technique is fast, noninvasive (does not exert excess pressure on the sealing), has provision for self-cleaning. Finally, after electrolyte filling, the hole is closed with either (1) a polymer hot-melt foil and a thin cover glass, using a hot-press sealing stamp or (2) UV epoxy resin and a thin glass piece.

## 9.4 DSC: An Application Perspective

### *9.4.1 Light Harvesting IoTs and Consumer Electronics*

Smart IoT sensors capable of performing a multitude of monitoring and control functions are all set to revolutionize the domotics and industrial automation systems. These sensor nodes require extremely low power in most applications and it would be excellent if they could be powered by indoor/lowlight harvesting systems (Fig. 9.26). Recent studies by De Rossi et al. (2015) quantitatively confirmed that small form-factor DSC devices outperform the other solar cell technologies when it comes to indoor/low/diffused light conditions as illustrated in Fig. 9.27. The efficiency under 200 lx CFL lamps for (1) a Polycrystalline Si cells was 4.4% (output power density 2.8 $\mu W/cm^2$) [the same cell was giving an outdoor efficiency of 15%], (2) amorphous-silicon cell specifically designed for indoors was 9.2% (output power density 5.9 $\mu W/cm^2$) (3) Customized flexible DSCs gave 12.4% (average output power densities of 8.0 $\mu W/cm^2$). These results reveal that customized DSCs have tremendous potential for lowlight applications. (Their lowlight efficiency is more than four times the efficiency value measured at 1 sun). These same devices delivered an efficiency of 10% under 200 lx LED illumination (output power density 6.6 $\mu W/cm^2$) (De Rossi et al. 2015).

A summary of the power consumption of different sensors and the size of DSC required to power the sensor as published by Tanabe (2013) is illustrated in Fig. 9.28. Figure 9.29 draws a concept smart home with solar energy harvesting.

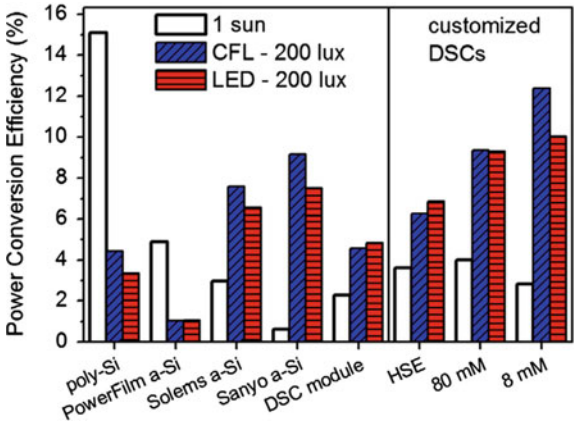


**Fig. 9.27** Lowlight performance of amorphous and dye solar cells (De Rossi et al. 2015)

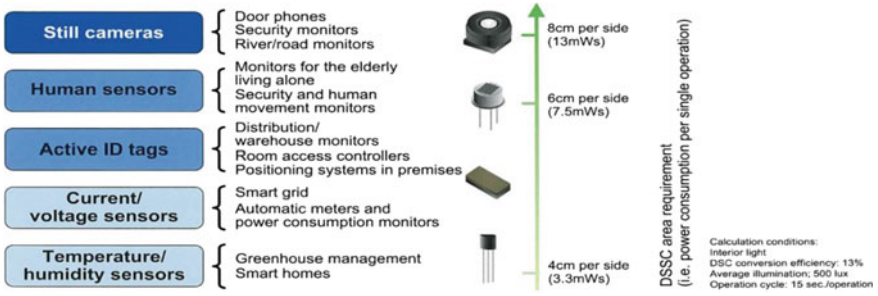


**Fig. 9.28** DSC module sizing for different sensors for lowlight applications (Tanabe 2013)

## Market Presence of DSC in Consumer Electronics and IoT Sector

GCell is well known in DSC community for its roll-to-roll flexible module fabrication facility. It offers product such as solar-powered keyboard, solar backpack, etc. GCell recently (in 2016) introduced the world's first energy harvesting iBeacon which is specially designed to be used in indoor conditions. It offers 100 ms advertising rate as default with average lifetime of 8 years (GCell 2014). Figure 9.30 illustrates the different concept devices in the consumer electronics sector put forth by GCell.

Considering the increasing power consumption in mobile electronic devices, Exeger is currently working self-powered E-readers and tablets where they want to use the sunlight and the artificial light to power those mobile electronic devices. In a recent breakthrough, Exeger has developed prototype of self-powered E-reader which has eternal life in indoor illumination alone. Exeger is also working on wearable electronic device and IoT devices in a way to charge the devices through unconscious charging thereby effectively turning them into self-powered devices.

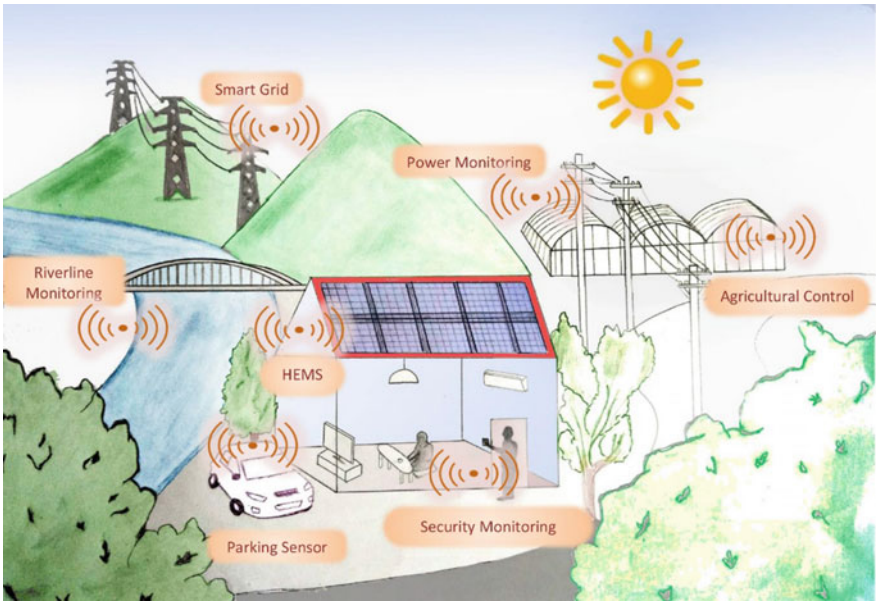


**Fig. 9.29** Energy harvesting applications using DSC (Tanabe 2013)

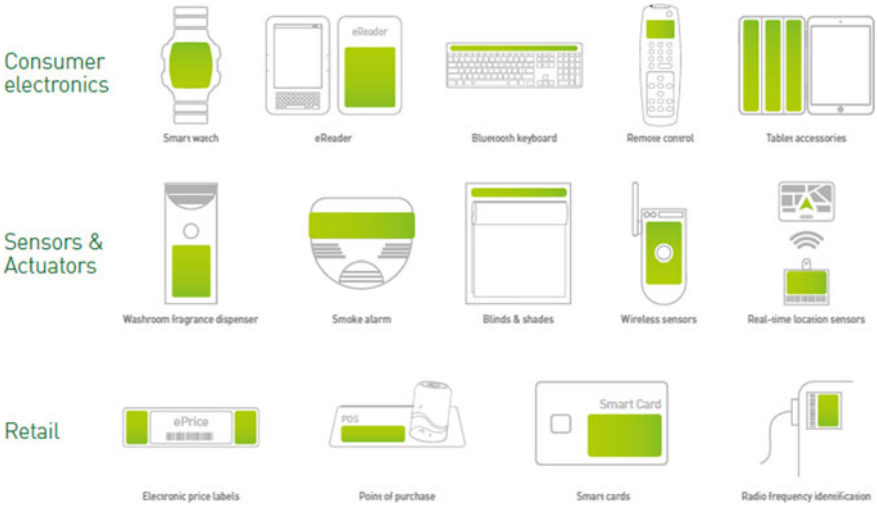


**Fig. 9.30** DSC integrated consumer electronics and sensors (GCell 2014)

3GSolar is the one of the global leader in high performance, durable DSC for wireless electronics. 3GSolar is mainly working on many electronics markets including wireless sensor networks (smart buildings, smart cities and smart homes),

medical and sports devices, security sensors and cameras, agriculture monitors, beacons and electronic signs, computer peripherals and wearable electronics (Goldstein et al. 2009).

The companies such as MKE electronics, TDP, RICOH and Solaronix are also actively working the DSC in a way to supplement power to IoT devices in artificial and ambient illumination.

### 9.4.2 Building-Integrated Photovoltaics (BIPV)

Building-Integrated Photovoltaics (BIPV) technology connotes the intelligent integration of photovoltaic cells into the climate envelope of buildings, i.e. into the roof, skylight or facades. The merits of this technology are multifold, primary advantage, of course being generation of electricity. BIPVs serve to replace the conventional building materials (e.g. roof tiles), can be cheaper, can significantly reduce conventional energy consumption (e.g. by reducing heating loads) which in turn could lead to decreased $CO_x$ emissions and lesser pressure on fuel reserves provide aesthetic and attractive appearance to buildings and overall enhancement of the functionality of the whole building space (Lee and Yoon 2018).

Do et al. (2017) evaluated a code-compliant, general BIPV system using simulation tools to analyse the potential energy benefits of the system, viz. generated power, reduction in lighting, cooling/heating loads, cooling peak loads/demands and the overall improvement in the total annual energy usage. The results of the analysis pointed that BIPVs have tremendous potential in improving the energy performance of a building. Significant light energy savings (by using BIPV with daylight dimming systems), significant reduction in the cooling loads owing to the lesser solar heat gain allowed, conjointly resulted in a 6–15% reduction in the gross annual building loads. The study also pointed out that the largest annual amount of electricity was produced by the south-facing window, however the east- and west-facing windows has tremendous scope for electricity generation during summer. The north facing window provided the least amount of electricity owing to least amount of insolation received.

To review the merits of DSC BIPV technology, one should look into the apparent shortcomings of conventional silicon PV technology: it requires a minimum 200–300 W per $m^2$ of solar irradiation for the startup operation of silicon PV; while 800–900 W per $m^2$ insolation is required to deliver the best performance. In spite of the certified $\eta$ in dye solar module (DSM) (8.2%), being lesser than what is achieved in the first two generation solar cells ($\sim$15–20%), their capability to work in lowlight conditions, relative independence of output on the angle of incidence and transparency favours their role in BIPV applications. The normalized variation in performance while varying the light intensity and angle of incidence as illustrated in Fig. 9.31a, b.

Reale et al. compared commercial PV technologies, viz. CIGS, CdTe, crystalline-silicon, amorphous-silicon, etc., with DSC technology for a generic

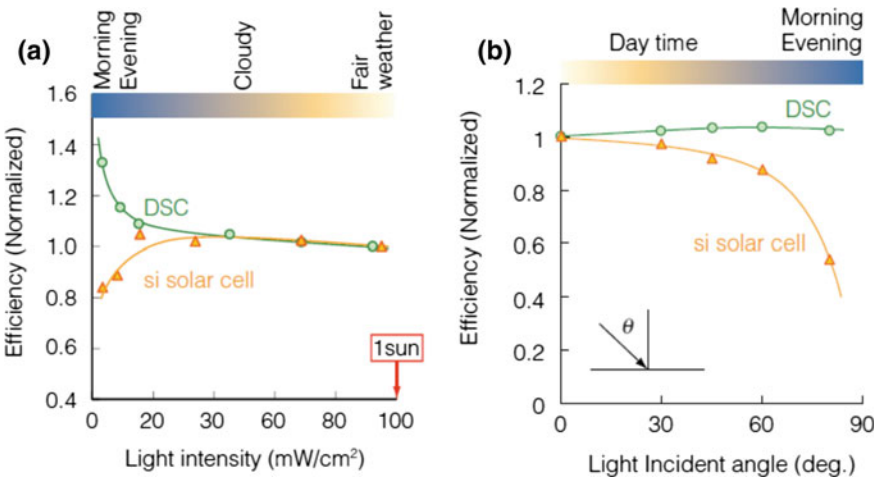


**Fig. 9.31** Relationship between normalized efficiency and **a** light intensity, **b** light incident angle (Tanabe 2013)

BIPV application (Reale et al. 2014). A concept building with a nominal available area of 1000 $m^2$ with the north, east, south and west orientations was considered. The plot of normalized producible energy on the 1000 $m^2$ facade is shown in Fig. 9.32. Expressing the yield in terms of kWh $(kWp)^{-1}$, the study concludes that for any given building orientation with respect to the sun, DSC technology stands as the champion for building-integrated photovoltaic applications, compared to standard technologies. The versatility of this technology is more obvious from the fact that DSC technology offers the best output even in nonoptimal orientations (while oriented towards north, west or east). This merit is based on the capability of DSC panels to use the diffuse component of radiation more efficiently than standard photovoltaic technologies.

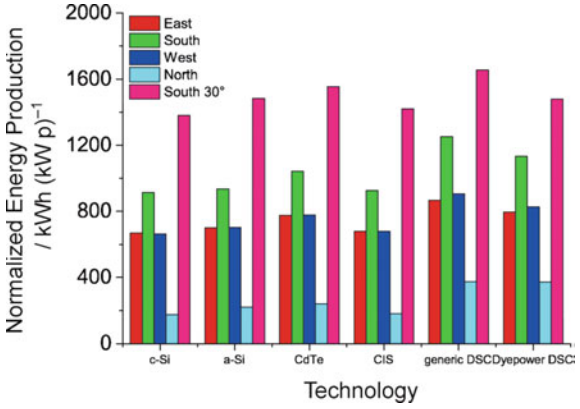


**Fig. 9.32** Comparison of BIPV performance of different PV technologies for different orientations (Reale et al. 2014)

**Market Presence of DSC in BIPV Sector**

H glass in Switzerland manufactures the most efficient glass-sealed, coloured and semitransparent solar panels for glass facades (h.glass). H Glass has developed a unique manufacturing process of glass encapsulation which masks DSC modules enough rigid to be used in direct and diffused sunlight with long-term stability.

## 9.5 Conclusion

Past few years have witnessed a paradigm shift in DSC technology. To a greater extent, this is complemented by developments that happened in electronic industry. The realization that DSC is not a replacement for silicon with respect to the power output in direct sunlight but a true champion with respect to the competing functionalities it possesses over the first- and second-generation PV technologies triggered its entry into the niche markets like self-powered IoTs, BIPVs, etc., shaping it a unique smart technology for the future smart applications. We need to adopt 'Go-to-market' strategy focusing more on application and then finding out ways to modify the devices in a way to meet the requirements is highly essential to sustain a transformation from lab to industries for DSCs.

Recent developments that happened with Cu electrolyte and the realization of DSC to be the best technology for indoor light harvesting application with an efficiency surpassing 30% in 1000 lx elevated its importance. We strongly believe that in near future itself DSC will emerge out as a potential candidate finding niche market space for commercialization particularly in BIPV and consumer electronics for indoor light harvesting applications. Future looks very bright for DSCs with a roadmap involving even the development of 'Zombies' to modules in near future. In this regard, at CSIR-NIIST we are also involved in developing a module fabrication line for DSC module manufacturing in a more affordable way through indigenization of technology. We strongly believe that our effort will pave towards a faster market entry for dye solar modules in near future in India.

**Acknowledgements** S. Soman gratefully acknowledges financial support from DST INSPIRE Faculty Award (IFA 13-CH-115). We also thank DST for the DST-SERI Project [DST/TM/SERI/D46(G)]. G. Gokul and S. C. Pradhan thank DST-SERI for research fellowships. We also extend our sincere thanks to Director, CSIR-NIIST for the motivation and support.

## References

Agarkar S (2014) Dye sensitized solar cell: optimizing materials, methods and optoelectronic effects. Ph. D ,NCL Pune, AcSIR

Chalkias DA, Laios AI, Petala A, Papanicolaou GC (2018) Evaluation of the limiting factors affecting large-sized, flexible, platinum-free dye-sensitized solar cells performance: a combined experimental and equivalent circuit analysis. J Mater Sci Mater Electron 1–14

Crawley D, Aho I (1999) Building environmental assessment methods: applications and development trends. Build Res Inf 27(4–5):300–308
De Rossi F, Pontecorvo T, Brown TM (2015) Characterization of photovoltaic devices for indoor light harvesting and customization of flexible dye solar cells to deliver superior efficiency under artificial lighting. Appl Energy 156:413–422
Do SL, Shin M, Baltazar JC, Kim J (2017) Energy benefits from semi-transparent BIPV window and daylight-dimming systems for IECC code-compliance residential buildings in hot and humid climates. Sol Energy 155:291–303
Ellis H et al (2013) Linker unit modification of triphenylamine-based organic dyes for efficient cobalt mediated dye-sensitized solar cells. J Phys Chem C 117(41):21029–21036
Fabregat-Santiago F et al (2007) Correlation between photovoltaic performance and impedance spectroscopy of dye-sensitized solar cells based on ionic liquids. J Phys Chem C 111 (17):6550–6560
Fabregat-Santiago F, Garcia-Belmonte G, Mora-Seró I, Bisquert J (2011) Characterization of nanostructured hybrid and organic solar cells by impedance spectroscopy. Phys Chem Chem Phys 13(20):9083–9118
Fakharuddin A, Jose R, Brown TM, Fabregat-Santiago F, Bisquert J (2014) A perspective on the production of dye-sensitized solar modules. Energy Environ Sci 7(12):3952–3981
Gabrielsson E et al (2013) Convergent/divergent synthesis of a linker-varied series of dyes for dye-sensitized solar cells based on the D35 donor. Adv Energy Mater 3(12):1647–1656
GCell (2014) GCell brochure. [Online]. Available: http://gcell.com/wp-content/uploads/GCell_Brochure_G0201a_Web_2014.pdf.pdf
Gerischer H (1983) The role of semiconductor structure and surface properties in photoelectrochemical processes. J Electroanal Chem Interfacial Electrochem 150(1–2):553–569
Goldstein J, Yakupov I, Breen B, Freedman S (2009) Development of large area photovoltaic dye cells at 3GSolar. In: 2009 34th IEEE photovoltaic specialists conference (PVSC), pp 000006–000008
Grätzel M (2001) Photoelectrochemical cells. Nature 414:338
Grätzel M (2003) Dye-sensitized solar cells. J Photochem Photobiol C Photochem Rev 4(2):145–153
Green MA (2002) Third generation photovoltaics: solar cells for 2020 and beyond. Phys E Low-Dimension Syst Nanostruct 14(1–2):65–70
H-Glass. h.glass. [Online]. Available: h.glass
Hagfelt, A. et. al. (2012). Dye-Sensitized Photo electrochemical cells, In: Practice Handbook of Photovoltaics. Elsevier, pp 479–542. https://doi.org/10.1016/B978-0-12-385934-1.00015-5.
Han L et al (2009) Integrated dye-sensitized solar cell module with conversion efficiency of 8.2%. Appl Phys Lett 94(1):5
Hara K, Arakawa H (2005) Dye-sensitized solar cells. In: Handbook of photovoltaic science and engineering. Wiley, Chichester, UK, pp 663–700
Ito S et al (2008) Fabrication of thin film dye sensitized solar cells with solar to electric power conversion efficiency over 10%. Thin Solid Films 516(14):4613–4619
Jayaweera PVV, Kaneko S (2012) Fabrication of automatic electrolyte filling machine for dye-sensitized solar cells. Instrum Sci Technol 40(6):490–503
Jun Y, Son JH, Sohn D, Kang MG (2008) A module of a $TiO_2$ nanocrystalline dye-sensitized solar cell with effective dimensions. J Photochem Photobiol A Chem 200(2–3):314–317
Kakiage K, Aoyama Y, Yano T, Oya K, Fujisawa JI, Hanaya M (2015) Highly-efficient dye-sensitized solar cells with collaborative sensitization by silyl-anchor and carboxy-anchor dyes. Chem Commun 51(88):15894–15897
Kay A, Grätzel M (1996) Low cost photovoltaic modules based on dye sensitized nanocrystalline titanium dioxide and carbon powder. Sol Energy Mater Sol Cells 44(1):99–117
Khan MI (2013) A study on the optimization of dye sensitized solar cell. University of South Florida

Kroon J, Hinsch A (2003) In: Brabec CJ, Dyakonov V, Parisi J, Sariciftci NS (eds) Dye-sensitized solar cells BT—organic photovoltaics: concepts and realization. Springer, Berlin, pp 273–290

Kusters J et al (2007) Design of organic dyes and cobalt polypyridine redox mediators for high efficiency dye-sensitized solar cells. J Am Chem Soc 1(46):2–7

Lee HM, Yoon JH (2018) Power performance analysis of a transparent DSSC BIPV window based on 2 year measurement data in a full-scale mock-up. Appl Energy 225:1013–1021

Maçaira J, Andrade L, Mendes A (2014) Modeling, simulation and design of dye sensitized solar cells. RSC Adv 4(6):2830–2844

Mariani P, Vesce L, Di Carlo A (2015) The role of printing techniques for large-area dye sensitized solar cells. Semicond Sci Technol 30(10):104003

Miller N, Spivey J, Florance A (2008) Does green pay off? J Real Estate Portf Manage 14(4):385–400

Nelson J (1999) Continuous-time random-walk model of electron transport in nanocrystalline $TiO_2$ electrodes. Phys Rev B Condens Matter Mater Phys 59(23):15374

O'Regan B, Gratzel M (1991) A low-cost, high-efficiency solar-cell based on dye-sensitized colloidal $TiO_2$ films. Nature 353(6346):737

Pazoki M, Cappel UB, Johansson EMJ, Hagfeldt A, Boschloo G (2017) Characterization techniques for dye-sensitized solar cells. Energy Environ Sci 10(3):672–709

Pradhan S C, Hagfeldt A, Soman S (2014) *Journal of Materials Chemistry A*, https://doi.org/10.1039/C8TA06948D

Reale A, Cinà L, Malatesta A, DeMarco R, Brown TM, DiCarlo A (2014) Estimation of energy production of dye-sensitized solar cell modules for building-integrated photovoltaic applications. Energy Technol 2(6):531–541

Sasidharan S, Soman S, Pradhan S C, Unni K N N, Mohamed A A P, Nair B N, Saraswathy H U N (2017) Fine tuning of compact ZnO blocking layers for enhanced photovoltaic performance in ZnO based DSSCs: a detailed insight using β recombination, EIS, OCVD and IMVS techniques, New Journal of Chemistry 41(3):1007–1016

Sastrawan R et al (2006) A glass frit-sealed dye solar cell module with integrated series connections. Sol Energy Mater Sol Cells 90(11):1680–1691

Sharma S, Siwach B, Ghoshal SK, Mohan D (2017) Dye sensitized solar cells: from genesis to recent drifts. Renew Sustain Energy Rev 70:529–537

Soman S, Pradhan SC, Yoosuf M, Vinayak MV, Lingamoorthy S, Gopidas KR (2018) Probing recombination mechanism and realization of Marcus normal region behavior in DSSCs employing cobalt electrolytes and triphenylamine dyes. J Phys Chem C 122(25):14113–14127

Soman S, Rahim M A, Lingamoorthy S, Suresh C H, Das S (2015) Strategies for optimizing the performance of carbazole thiophene appended unsymmetrical squaraine dyes for dye-sensitized solar cells, Phys. Chem. Chem. Phys, pp. 17(35):23095–23103

Spath M et al (2003) Reproducible manufacturing of dye-sensitized solar cells on a semi-automated baseline. Prog Photovoltaics Res Appl 11(3):207–220

Statista (2018) Internet of Things (IoT) connected devices installed base worldwide from 2015 to 2025 (in billions). [Online]. Available: https://www.statista.com/statistics/471264/iot-number-of-connected-devices-worldwide/. Accessed 28 Jun 2018

Tanabe N (2013) Dye-sensitized solar cell for energy harvesting applications. Fujikura Tech Rev 42:109–113

Toyoda T et al (2004) Outdoor performance of large scale DSC modules. J Photochem Photobiol A Chem 164(1–3):203–207

UN DESA. [Online]. Available: http://www.un.org/en/development/desa/news/population/2015-report.html

Vinayak M V, Lakshmykanth T M, Yoosuf M, Soman S, Gopidas K R (2016) Effect of recombination and binding properties on the performance of dye sensitized solar cells based on propeller shaped triphenylamine dyes with multiple binding groups, *Solar Energy*, December 2015, pp. 124:227–241

Vinayak M V, Yoosuf M, Pradhan S C, Lakshmykanth T M, Soman S, Gopidas K R (2018) A detailed evaluation of charge recombination dynamics in dye solar cells based on starburst triphenylamine dyes, *Sustainable Energy & Fuels*, 2(1):303–314

Wang P, Klein Ć, Humphry-Baker R, Zakeeruddin SM, Grätzel M (2005) Stable $\geq$ 8% efficient nanocrystalline dye-sensitized solar cell based on an electrolyte of low volatility. Appl Phys Lett 86(12):123508

Wang M et al (2008a) High-performance liquid and solid dye-sensitized solar cells based on a novel metal-free organic sensitizer. Adv Mater 20(23):4460–4463

Wang ZS et al (2008b) Hexylthiophene-functionalized carbazole dyes for efficient molecular photovoltaics: tuning of solar-cell performance by structural modification. Chem Mater 20 (12):3993–4003

Wang L, Fang X, Zhang Z (2010) Design methods for large scale dye-sensitized solar modules and the progress of stability research. Renew Sustain Energy Rev 14(9):3178–3184

Wang G, Feldt SM, Boschloo G, Hagfeldt A (2011) Effects of driving forces for recombination and regeneration on the photovoltaic performance of dye-sensitized solar cells using cobalt polypyridine redox couples. J Phys Chem C 115:21500–21507

Wang M, Grätzel C, Zakeeruddin SM, Grätzel M (2012) Recent developments in redox electrolytes for dye-sensitized solar cells. Energy Environ Sci 5(11):9394–9405

World Energy Resources. [Online]. Available: https://en.wikipedia.org/wiki/World_energy_resources

Wu J et al (2017) Counter electrodes in dye-sensitized solar cells. Chem Soc Rev 46(19):5975–6023

# Chapter 10
# On the Use of Origami for Solar Energy Harvesting


**Swapnik Jagarlapudi, Sudheer Siddapureddy and Dhiraj V. Patil**

**Abstract** Reentry vehicles and satellites harness the radiation from the Sun using an array of solar panels. These panels are folded compactly, and are quickly unfolded for operations once the satellite is in outer space. During reentry into the earth's atmosphere, the solar panels must be folded and re-stowed. For the efficient folding and unfolding of the solar panels, a concept of origami called Miura folding has been utilized, which is achieved with the help of robots. These solar panels have been developed primarily at NASA's Jet Propulsion Laboratory (Zirbel et al. in Accommodating thickness in origami-based deployable arrays. ASME. International design engineering technical conferences and computers and information in engineering conference, vol 6b: 37th mechanisms and robotics conference, 2014). Origami, the art of paper folding involving the creation of two and/or three-dimensional shapes, can be of paramount importance when space is limited and can be used as a compactly stowed system that transforms into a 3D structure with variable functionality. This chapter reviews the attempts made so far by the scientific community in applying the principles of origami in solar panel arrays. A few studies suggest the possibility of using rigid origami in the manufacture of stretchable electronics without employing elastomeric materials. They specifically fabricated origami-enabled stretchable solar cells, which can achieve significant deformability.

**Keywords** Solar panels · Origami · Solar energy

S. Jagarlapudi
Department of Computer Science and Engineering,
Indian Institute of Technology Dharwad, Dharwad 580011,
KA, India

S. Siddapureddy · D. V. Patil (✉)
Department of Mechanical Engineering, Indian Institute of Technology
Dharwad, Dharwad 580011, KA, India
e-mail: dhiraj@iitdh.ac.in



H. Tyagi et al. (eds.), *Advances in Solar Energy Research*, Energy, Environment,
and Sustainability, https://doi.org/10.1007/978-981-13-3302-6_10

## 10.1 Introduction

The development of interest in photovoltaic conversion is the result of the perceived need to discover sources of energy for the future, which will be economical and ensure the safety of the environment. Fossil fuels such as oil, coal and natural gas are exhaustible and are likely to get depleted. For countries such as India, coal remains the most affordable source of energy. Major economic growth in India has been almost entirely due to coal. The extensive use of coal threatens the quality of air due to pollutants. Even with the use of techniques such as solvent refining, pyrolysis, gasification and magnetohydrodynamic generators to enhance the quality of coal to make it relatively safer, the reserves of coal may last another 300 years or less (Nelson 2015). During World War I, oil became a major contributor to energy consumption globally (Black 2017). Currently, natural gas is being used widely in power generation. The reserves of these fuels are also limited. It is a matter of time before these fuels get exhausted. Besides, the use of fossil fuels leads to the emission of greenhouse gases (Liang et al. 2012). Under such circumstances, it is entirely conceivable for the world to be on the lookout for alternative sources of energy, which include nuclear fission, nuclear fusion, solar thermal, solar electric, wind, geothermal, hydro, ocean and biomass. Wind and solar energy have the highest potential for power generation. Inexhaustible supply of these resources makes them extremely attractive. An added advantage is that power generation using wind and photovoltaic solar energy does not lead to the direct contamination of the environment. However, the total energy output which might be tapped economically from sources wind and tides, would be a very small fraction compared to the global demand (Brown et al. 1957).

Solar energy is the most abundantly available form of renewable energy as sunlight can be tapped almost indefinitely. No other source of energy, encompassing both renewable and non-renewable sources, is as large as the solar energy reservoir with the Sun being an endless source of solar power. According to projections, if we can capture even 2% of the solar energy that reaches the earth's surface, it would be more than sufficient to meet the energy needs all over the world (Baker 2016). As far as wind power is concerned, the construction and operation of both onshore and offshore wind farms is likely to result in potential negative environmental effect on plants and animals, including birds and cetaceans, landscape, sustainable land use (including protected areas) and the marine ecosystem (The European Wind Energy Association 2009). While nuclear energy is cleaner than other energy sources like coal, the radioactive wastes generated could cause a lot of potential damage to our environment (El-Hinnawi 1978). The Chernobyl and Fukushima disasters demonstrate the dangers of nuclear energy. For more than 50 years, solar energy remained very expensive for widespread usage. Since 2008, the price of solar panels decreased by almost 80% (Baker 2016). With the cost of equipment decreasing significantly, solar power generation is becoming an attractive option for homes. By 2016, the world's solar market grew into a $100-billion business annually.

### *10.1.1 A Timeline of the Development of Solar Cells*

Becquerel discovered in 1839 that a photovoltage is created when the light falls on an electrolyte solution (Grätzel 2001). In 1873, photoconductivity in selenium was discovered by W. Smith (Cashman 1959). Subsequent work on selenium and other materials such as cuprous oxide helped in the development of the selenium photovoltaic cell, which saw widespread use in photographic exposure metres. Subsequently, the discovery by R. E. Day and W. G. Adams established that electricity could be produced by selenium from light without heat or moving parts that could break down effortlessly. This discovery confirmed that it was easy to harvest and maintain solar energy (Fahrenbruch and Bube 1983). In 1883, the first solar cell was developed by the inventor C. Fritts who coated selenium with a flimsy layer of gold (Fahrenbruch and Bube 1983).

In 1887, H. Hertz observed the photoelectric effect when light was employed to release electrons from a solid surface (usually metal). He was able to generate power using this phenomenon. Between 1953 and 1956, physicists at Bell Laboratories observed that the efficacy of silicon was greater than that of selenium and created the practical solar cell, the first of its kind (Baker 2016). Subsequently, solar cells with the capability to power electrical equipment were developed. The following experiments for many years to enhance the efficacy and exploit solar power commercially, the US government extended support to solar energy by using it in space exploration equipment in 1958. Solar power came into prominence in the 1970s when the Organization of the Petroleum Exporting Countries (OPEC) increased oil prices. In the early 1970s, research in solar power was financed by Exxon Corporation with a view to developing solar cells by employing low-grade silicon and inexpensive materials, which resulted in the cost decreasing to just $20–$40 per watt from $100 per watt. Arco Solar was the company that built the first solar park in 1982, essentially a solar power plant, in Hesperia, California. In 1994, the National Renewable Energy Laboratory used gallium indium phosphide (GaInP) and gallium arsenide (GaAs) to develop a new solar cell. Using these new composites, the conversion efficiency of the cell exceeded 30%. In 1995, T. Faludy applied for a patent for a retractable awning that contained integrated solar cells. This marked the beginning of the use of solar cells in recreational vehicles. From 2005 onwards, do-it-yourself solar panels gained prominence in the market and have found greater acceptance. In 2015, the market saw the introduction of flexible printed solar panels. Their power conversion efficiency stood at 20% with a single strip being able to produce up to 50 W/m$^2$ (Baker 2016). According to a 2018 report by the Fraunhofer Institute of Solar Energy Systems, the record efficiency for a monocrystalline cell in the laboratory is 26.7% and for a multicrystalline cell with silicon wafer-based technology, the record efficiency is 22.3%. For thin-film technology, the highest efficiency achieved in the laboratory is 21.7% for CIGS solar cells and 21.0% for CdTe solar cells. During the last decade, commercial silicon modules using wafer-based technology have seen an increase in efficiency from around 12 to 17%, and the efficiency of CdTe modules has seen an increase

from about 9 to 16%. The best performing modules are monocrystalline silicon-based, with an efficiency of 24.4%. In the laboratory, an efficiency of up to 46.0% can be reached by high-concentration multi-junction solar cells (Fraunhofer Institute for Solar Energy Systems 2001). The cost of harvesting solar energy continues to decrease, leading to an increase in solar power installations. The annual generation capacity of solar power globally grew 26% to 39 gigawatts (GW) in 2013 from 31 GW in 2012 (Miret 2014). Solar power constitutes 1.13% of the current power generation capacity in the US. It would increase substantially with the proposed addition of 1510 MW capacity by the US Department of Energy (DOE) with the completion of solar projects by the end of 2015 (Miret 2014).

## 10.2 Solar Energy Harvesting

Energy harvesting is a way of collecting, storing and using energy. This stored energy may be harnessed using different methodologies through interfaces and storage devices. The concept of harvesting renewable energy is different from conventional electricity generation process, as harvesting renewable energy does not involve fossil fuels and it is possible to decentralize the generation units. As a result, it becomes possible to reduce transmission losses and distribution cost significantly. It is possible to harvest energy from many sources, e.g. wind, solar, thermal, tidal waves, vibration, electrostatic, human body motion and electromagnetic sources. In order to overcome the constraints related to financial, ecological and geopolitical aspects on conventional energy resources, countries all over the world have been forced to hasten the harvesting and use of renewable energy. Under such circumstances, it becomes imperative to develop advanced technology so that the equipment used in harvesting energy from diverse environmentally friendly sources and converting it into electrical energy has greater efficacy. Solar energy harvesting consists of four essential methods:

1. Natural Photosynthesis (Biofuels)
2. Artificial Photosynthesis
3. Solar Thermal
4. Photovoltaic Modules.

In view of the context of the use of origami in solar panels, we shall briefly discuss the photovoltaic modules in this section.

### *10.2.1 Photovoltaic Modules*

The most prominent solar power harvesting technology consists of photovoltaic (PV) modules incorporating solar panels. With PV modules being used widely,

their performance has come to be viewed as the benchmark for the solar industry at large. For power generation in residential and commercial establishments, PV modules are being used, besides their use in utility-scale plants that generate solar power. Electricity generation by PV modules involves energizing the electrons, which are contained within their material system. Semiconductor materials are used to produce PV modules as they possess the ability to absorb sunlight and generate electric energy. When sunlight is absorbed by a semiconductor, the optical energy of the light is transmitted to the electrons. It is possible to extract the energized electrons from the semiconductor and move them into an electrical circuit, which helps in electricity generation. The reason behind the use of semiconductor materials in PV module production is their ability to separate electrons into high and low-energy states, with the separation being carried out by an energy gap inherent to the material. When the semiconductors absorb the sunlight, the energy so absorbed stimulates a low-energy electron into a high-energy electron, which subsequently moves into the external circuit. This process also produces positively charged holes and helps maintain charge balance in the total system. As the absorption of sunlight increases, high-energy electrons also grow in number, leading to the generation of flowing electric current. Voltage production by the PV module is determined by the level of energy gap, i.e. the variation in the energy between low-energy electrons and high-energy electrons. One of the biggest PV generation facilities, the Agua Caliente plant, which has a capacity of 290 MW, was built in Yuma County, Arizona (Miret 2014).

## 10.3 Solar Panels and Their Applications in Space

### *10.3.1 Introduction to Solar Panels*

Solar panels are contraptions that convert light into electricity. A solar panel is a collection of solar cells. A solar cell consists of a small disc of a semiconductor such as silicon. The cells are attached by a wire to a circuit. A number of small solar cells spread over a huge area are capable of working together to generate power. The amount of electricity produced is directly proportional to the amount of light that hits a cell. Hence, spacecraft are generally designed with solar panels that can always face the Sun even while the rest of its body moves around. As we are interested in the usage of solar panels in space, we shall discuss this aspect in more detail.

### *10.3.2 Space Applications*

The fundamental application of solar panels in space consists of powering spacecraft. Spacecraft that operate within the inner solar system usually depends on

photovoltaic cells to draw energy in order to function. Solar panels supply power that helps run the sensors and instrumentation on the spacecraft, besides its propulsion through space. The larger the surface area under the cover of solar radiation, the higher is the amount of energy generated by solar cells. However, spacecraft are designed to be small in size, which results in limitation on the amount of power that can be produced employing solar panels. The fundamental parameters of performance for solar panels in space are their conversion efficiency, cost of production, weight, maximum electrical output, the effect of solar radiation on the performance of the solar cell and operation under extreme temperatures.

Solar panels are shaped like wings and positioned the way they are because of the need for large expanses of surface area that balance on either side of the craft. It is necessary for solar panels to have a large surface area that can be pointed towards the Sun as the spacecraft moves. Exposure to greater surface area results in the conversion of light energy from the Sun into more electricity. It is also not useful to have one solar panel cast a shadow on the other one. Because of these reasons, it is better to have solar panels as flat sheets on either side of the spacecraft. The wings of solar panels also need to have large expanses of surface area and not interfere with each other, though the reasons are different. The Sun is similar to the flashlight, spreading the same amount of energy in different directions. When a spacecraft is closer to the Sun, it intercepts an abundance of light rays. When the Sun is farther, the light is more diffuse, and the solar panels receive less light.

Besides conversion efficiency and fabrication cost, it is important to ensure operational dependability under extreme thermal conditions and in the presence of solar radiation for the selection of solar panels for use on space shuttles. Silicon is one of the materials best suited for this, as it is light, and available cheaply and easily, can endure high temperatures of up to 125 °C, and more so because silicon-based solar cells have a better conversion efficiency than cells made of other materials such as gallium arsenide or cadmium sulphide. They demonstrate a conversion efficiency ranging between 15 and 18% in laboratory conditions. However, the efficiency of the cells is not likely to be in excess of 28%. The cell area and surface thickness of the material used in its manufacture determine the weight of the cell. As the dimensions of the array increase, the weight of the cell also increases. More solar cells need to be added in order to compensate for losses due to factors such as reflection, component losses, reduction in cell voltage due to increased temperatures and altitude stabilization. In order to maintain lower temperatures and to increase their resistance to radiation in space, solar cells are covered by fused silica cover slides. The cover ranges in thickness from 0.004 to 0.02 in., which conforms to the requisite level of protection from radiation and a manageable weight budget. Since silica is cheaper than other materials such as sapphire, applying silica as cover to protect solar cells is also an extremely cost-effective option. Radiation results in the reduction of open-circuit voltage, short-circuit current, power yield of the device and efficacy of the cell. It may also result in other changes in semiconductor properties. Temperature also hampers the performance of solar cells. Especially, there is a 0.5% decrease in the open-circuit voltage with one-degree increase in temperature in silicon cells. Thus, a solar cell

stack with a back surface to radiate the extra heat to space will be cooler and possesses greater operational efficiency and power output than a stack with the spacecraft or some other equipment blocking its hind surface. The integration of thin-film technology into solar cells is an extremely useful measure as it reduces costs considerably, with a significant reduction in the resultant size and weight. Cadmium Telluride (CdTe) thin-film technology is the most popular thin-film solar panel design, as it has clear benefits over silicon technology, particularly its thickness, which is one-hundredth of that needed for a silicon cell, which also facilitates reduction in cost with a shorter production time. CIGS thin-film technology has also been in limelight due to reports of increase in efficiency of up to 20% in laboratory conditions; however, in case of quick production, it has demonstrated a conversion efficiency of only 12%. Hence, the degree of its usefulness is not yet fully clear. However, improvement in thin-film technology could be a welcome development as shortage of silicon could be felt after 2025. Thin-film layers fabricated using GeAs, GeInP and GaInP constitute multi-junction solar cells, which demonstrate thrice the efficiency of CdTe thin-film solar cells. However, with their production cost being inordinately high, multi-junction solar cells are used in a limited manner in ground communication, and surveillance and reconnaissance applications using satellites (Jha 2010).

Digital signal 1 (DS1) solar panels are capable of converting 22% of their available energy into electrical power. This is much higher than what most of the solar panels are capable of. Most of the solar panels on people's houses, for instance, are fairly inefficient. They can convert less than 14% of the energy that reaches them into electricity. DS1 panels are very efficient, so much so that unless the ion propulsion drive is running, DS1 produces far more power than it requires. Ion propulsion is a kind of electric propulsion system which ionises the propellant, extracts ions from the plasma and accelerates them to a high velocity, increasing the effectiveness of the propulsion system (Goebe and Katz 2008). DS1 solar cells are relatively more efficient than regular solar panels produced for satellites because they use solar concentrators (QRG—Northwestern University 2018).

The concept of space-based solar power (SBSP) consists of solar energy harvesting in space and its transmission to earth. Peter Glaser, who proposed the concept in 1968, obtained a patent related to the concept, which consists of a microwave beam to transmit energy to large antennas on earth called rectennas. SBSP has the potential to surmount many of the constraints of harvesting solar energy on the surface of the earth, such as cloud cover, absorption of energy by the atmosphere, and very importantly, day–night cycles. While many studies have been conducted on SBSP, it has not been harnessed with seriousness and at present is looked past in favour of other more urgent needs (Caton 2015).

The solar panels, which have a large surface area by design, and thus occupy a large amount of space, need to be stowed in an efficient manner and then opened once the spacecraft is in orbit or moving into outer space (depending on the function of the craft). Their large size causes complications in this process and thus there is a need to find more efficient methods to pack solar panels on spacecraft

which are sent to orbit in space. Here, we deal with one of the methods which have the potential for a lot of use in the future, namely, the utilization of structures in origami in solar panels.

## 10.4 Origami and Its Applications in Solar Panels

Origami is the art of folding paper into various shapes. By folding them, the origamist makes papers seem like true objects. The art itself began as a trial-and-error method wherein the origamist made paper(s) seem like real objects. The earliest documented origami in Japan started after Buddhist monks brought paper to Japan, circa sixth century (Robinson 2004). Later on, origamists harnessed several mathematical principles to understand the phenomena associated with the paper created by the folding and also to assess the shape of the folded paper. One of these is the box-pleating technique developed by N. Elias and others (Lang 2012) and the circle packing technique developed by Lang (2012). Most of these methods involve the creation of crease patterns. A crease pattern is the pattern, which is formed on the paper when an origami is unfolded completely. Looking at the crease pattern, it is possible to say what its folded form looks like (but not necessarily vice versa). This is the principle used in most of the mathematical methods employed in origami design; the designer already knows what the finished product looks like, hence they try to make a crease pattern, which forms the model they aim to make. The concept of 'pure origami' is described by a series of axioms and theorems. These theorems elucidate the conditions which facilitate flat foldability and the Huzita–Hatori axioms, which depict the set of performable operations, while a sheet of paper is being folded. A crease pattern which achieves flat collapsibility is referred to as flat foldable. The following are the theorems that outline the conditions for flat foldability (Hull 1995):

1. Maekawa's theorem: the number of valley and mountain folds at any vertex invariably differs by two. It also indicates that at any vertex, the number of creases is even.
2. Kawasaki's theorem: the sum of all the odd angles totals 180° at any vertex, as happens with even angles.
3. A fold can never be penetrated by a sheet.

There are several types of origami which do not follow flat foldability, for example, those which use curves and origami made from crease patterns which do not satisfy these theorems, usually in order to achieve a 3D geometric figure.

The Huzita–Hatori axioms are (Hull 1995):

1. Given two points p1 and p2, the origamist can fold a line linking them both.
2. Given two points p1 and p2, it is possible to fold p1 onto p2.
3. Given two lines l1 and l2, the origamist can fold line l1 onto l2.

4. Given a point p1 and a line l1, the origamist can turn a fold perpendicular to l1 moving through the point p1.
5. Given two points p1 and p2 and a line l1, the origamist can create a fold that puts p1 onto l1 and moves through the point p2.
6. Given two points p1 and p2, and two lines l1 and l2, the origamist can create a fold that puts p1 onto line l1 and puts p2 onto line l2.
7. Given one point p1 and two lines l1 and l2, the origamist can create a fold that puts p1 onto l1 and makes p1 perpendicular to l2.

### *10.4.1 Examples of the Use of Origami in Engineering Applications*

The tightness and deformability of the folded structures are the central themes of origami. The principles of origami have been applied in the recent past in space exploration in the form of a foldable telescope lens, automotive safety in the form of airbags and biomedical devices in the form of a heart stent. Deformable electronics have very wide use. Deformability was achieved in them through the process of folding and unfolding at the creases, where the functional gadgets do not undergo strain (Fei and Sujan 2013).

The application of the principles of origami in engineering concepts and stacked solar panels, among others, makes the art increasingly pertinent. The concepts of origami were applied in stowing and deploying a solar cell array in the research vessel called Space Flyer Unit, a Japanese satellite. Robert Lang designed eyeglass, a foldable telescopic lens that can be folded seamlessly into a space shuttle and unfolded when in space by applying the principles of origami (Zirbel et al. 2014). However, it did not make it past the testing stages due to lack of funding (Lang 2018).

Rigid origami is applied to folding materials that have thickness. Car airbags, large solar panel arrays for space satellites (that use Miura fold), paper shopping bags are among the applications of rigid origami (Tang 2014).

Macroelectronics, which include stretchable and flexible electronics, is expected to transform the functionality of microelectronics fundamentally as they are applicable in various domains, from consumer electronics to biomedical applications. Researchers employed various approaches to evaluate stretchable and flexible electronics and devised a broad range of devices. Resultantly, an alternative approach that uses origami to fabricate stretchable electronics evolved. However, elastomeric materials are not used in this approach and the approach is in tune with the mainstream CMOS process for high-performance devices (Fei and Sujan 2013). However, in order to make a device stretchable, it is not necessary to use elastomeric substrates. An alternative method to bring about stretchability, which has been in vogue for a long time, is origami.

The ‘Miura-ori’ origami pattern connects similar parallelograms through ‘mountain’ and ‘valley’ creases. Though it is possible to collapse the Miura folding

in one direction almost completely, the parallelograms stay undeformed. As a result, the stretchability of the Miura pattern is achieved through the folding and unfolding of the creases, while preserving the rigidity of the parallelograms (Nishiyama 2012). We shall discuss this pattern in detail.

### *10.4.2 Miura Folding and Other Methods of Folding Solar Panels*

The term 'Miura' in Miura folding is eponymous as it refers to Koryo Miura, the Japanese astrophysicist who developed it. This method of folding occurred to him a few decades ago when he was researching aerospace structures. At that time, he was a student at the Institute of Space and Aeronautical Science in Tokyo University. While in motion, rockets/satellites launched into space are known to collect the Sun's energy for their functioning. Solar panels are the contraptions used to collect the solar energy. However, the solar panels are built in such a manner that they cannot be opened until the rocket/satellite is launched. To make it possible to pack them into the rocket/satellite, the solar panels are folded down to the extent that their thickness and structure allows, and subsequent to the entry of the rocket/satellite into outer space, they unfold swiftly. At the time of the return of the rocket/satellite into earth's orbit, the solar panels have to be folded and re-stowed. The application of Miura folding to achieve this series of actions was conceived with the deployment of robots as it was beyond human capabilities.

Using the Miura fold consists of accommodating two diagonally opposite corners of a paper with the folding of the Miura pattern and stretching the paper in diametric directions, with the paper closing and nudging them together to open. The fold acts as if the paper 'memorizes' it. It is possible to open or collapse a paper with Miura folding with a single movement. This becomes possible as the vertical folds are parallel, while the horizontal folds are in a zig-zag manner; however, if these folds were at a 90° angle to the vertical ones, this would not have been possible. This pattern has been depicted in Fig. 10.1a.

However, one of the complications which arise in the application of Miura folding to solar panels is that solar panels are much thicker than paper. Apart from a Miura pattern, another possible design is a six-sided flasher design. A flasher is a model devised by Shafer (2001) which is, essentially, a collapsible pattern similar to the Miura-ori pattern. Ideally, the panels must have a large stowed-to-be-deployed diameter ratio, i.e. when folded, the panel must be much smaller than when deployed. Thickness can inhibit the foldability of a given pattern, and this is an important consideration, since solar panels are thick. The material should not flex during the folding motion. This is a challenge since origami is generally designed for near-zero thickness sheets. Generally, hinges are added in order to enable folding of thick panels. Trautz and Kunstler (2009) identified two types of hinge formations—one where the hinge is placed on the surface of the

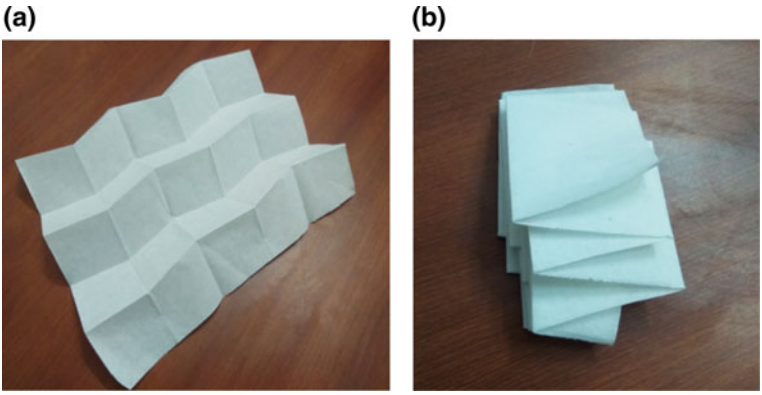


**Fig. 10.1** **a** A basic Miura-ori pattern, the zig-zag horizontal lines and the straight vertical lines may be observed; **b** the Miura-ori pattern after collapsing

panel, and another where the panels have material removed over the hinge axes. In more recent models, the hinges do not lie in the same plane, as the asymmetry helps release tensile forces built up in the panels, which enables them to collapse (Chen et al. 2015). S. A. Zirbel et al. have discussed the six-sided flasher model in detail. In their analysis, they have described two methods of folding the model—in the first, the panels are allowed to flex along their diagonals, in the second, the panels are fixed to a flexible membrane with discrete spacing between the panels. This model has a large stowed-to-deployed ratio of 9.2. However, there are unanswered questions concerning the joints and hinges in this model. Increasing the number of hinges causes an increase in the degrees of freedom the model has, but an ideal model should have a single degree of freedom. Allowing the panels in the model to fold along their diagonals would cause a loss in the usable surface area, rendering it ineffective for use in a solar array application. Another area of interest is the actuation of the model; an actuation mechanism is required for the model to be able to unfold itself once it is deployed. One possible method is to incorporate the mechanism in the model itself, using stored strain energy in shape memory alloys. However, stowing the model is slightly more difficult using this mechanism. Another aspect that could be researched more is the fabric used in the membrane (Zirbel et al. 2014).

Hoberman has described several concepts for hinges (Hoberman 2010), one of which consists of adding tapered material to the plane of zero thickness. Another concept involves offsetting panels away from the planes defined by adjacent creases. In these models, however, the surfaces are usually not entirely flat or require gaps to allow foldability. In a zero thickness sheet, the patterns are made of creases which intersect at a point. This is not possible in a rigid panel as the lines on which they are folded cannot lie on the same face. The folds must be distributed between the two faces of the panel, thus making folds which do not intersect at

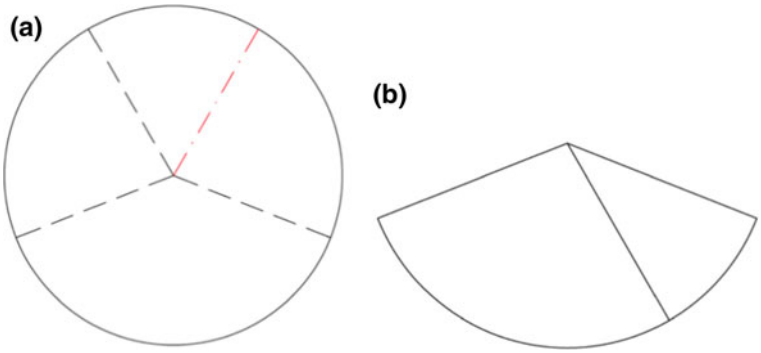


**Fig. 10.2** **a** Illustration of a four-crease pattern; **b** illustration of collapsed four-crease pattern

vertices. Such a model is a mechanical assembly with panels connected by spherical linkages (hinges) which are placed at a distance due to thickness. Most patterns in use have 4, 5 or 6 creases intersecting at a point, and hence, the corresponding rigid panel structure will have 4R, 5R or 6R spherical linkages (where R represents revolute joints). In Fig. 10.2a and b, a four-crease pattern is illustrated. In Fig. 10.2a, the black dash lines represent valley folds (where the paper is folded towards the observer), and the red dash-dot line represents mountain folds (where the paper is folded away from the observer). Figure 10.3a shows the photograph of the same four-crease pattern. Its collapsed form can be observed in Fig. 10.3b. Another example of a pattern with four concurrent creases is the Miura fold. They belong to a special family of linkages called overconstrained linkages as their Kutzbach criterion (which is a value describing the degree of freedom of rigid bodies linked by mechanical constraints, otherwise called linkages). Chen et al. (2015) found the mechanical (kinematically) equivalent linkages of origami patterns made from zero thickness sheets with 4, 5 and 6 creases and extended it to

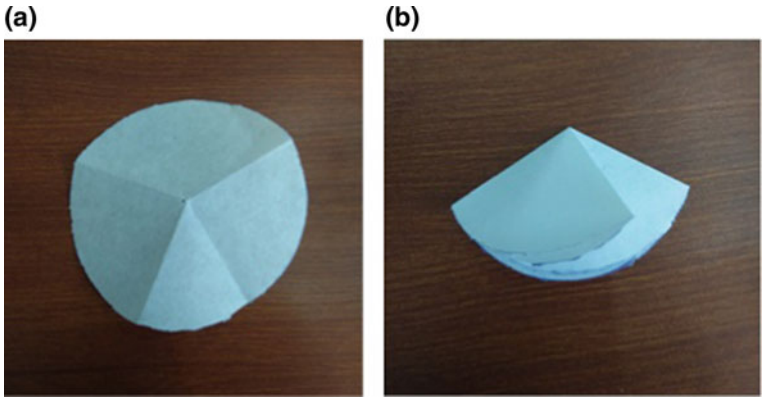


**Fig. 10.3** **a** A four-crease pattern; **b** collapsed four-crease pattern

patterns with multiple vertices by making sure that their motion is identical to that of their zero thickness equivalents. They identified spatial linkages which satisfy the angular conditions for fold arrangements identical to that of the spherical linkages and proved that their motions are exactly the same. This study deals with models which differ from the existing designs of kinematic synthesis for rigid panels, but are applicable for real engineering structures (Chen et al. 2015).

## 10.5 Final Remarks

In this review, we have looked at the current developments in the usage of origami in the solar panels. While it is a useful concept, it is still in developing stages. As packing the solar panels in this manner helps in storing them in a more compact form, it allows satellites to be of a smaller size. Some of the primary questions with regard to origami used in satellites concern the foldability and durability of material as well as the efficiency of the folding patterns used. We believe that the Miura-ori pattern may see a wider usage in space travel, exploration and energy harvesting if the answers to these questions are found.

## References

Baker A (2016) Retrieved from https://www.solarpowerauthority.com/a-history-of-solar-cells. Last accessed 8 June 2018

Black BC (2017) How World War I ushered in the century of oil. Retrieved from https://theconversation.com/how-world-war-i-ushered-in-the-century-of-oil-74585. Last accessed 12 Aug 2018

Brown H, Bonner JF, Weir JR (1957) The next hundred years. Eng Sci 20(7):19–23

Cashman RJ (1959) Film-type infA history of solar cells: how technology has evolved rared photoconductors. Proc IRE 47(9):1471–1475

Caton JL (2015) Space based solar power a technical economic and operational assessment. United States Army War College Press, Carlisle, pp 1–3

Chen Y, Peng R, You Z (2015) Origami of thick panels. Science 349(6246):396–400

El-Hinnawi EE (1978) Review of the environmental impact of nuclear energy. IAEA Bull 20 (2):32–42

Fahrenbruch AL, Bube RH (1983) Fundamentals of solar cells, photovoltaic solar energy conversion. Academic Press, London, p 9

Fei LJ, Sujan D (2013) Origami theory and its applications: a literature review. Int J Soc Hum Sci Eng 7:113–117

Fraunhofer Institute for Solar Energy Systems (2001) Photovoltaics report. (pdf). Available at: https://www.ise.fraunhofer.de/content/dam/ise/de/documents/publications/studies/Photovoltaics-Report.pdf. Last accessed 10 Aug 2018

Goebe DM, Katz I (2008) Fundamentals of electric propulsion. Wiley, London, p 4

Grätzel M (2001) *Sol-gel processed $TiO_2$ films for photovoltaic applications*. J Sol Gel Sci Technol 22(1–2):7–13

Hoberman C (2010) *Folding structures made of thick hinged sheets*. United States Patent No. 7,794,019

Hull TC (1995) On the mathematics of flat origamis. Congressus Numerantium 100:215–224
Jha AR (2010) Solar cell and array designs best suited for space applications. Solar cell technology and applications. Auerbach Publications, United States of America
Lang RJ (2012a) Box pleating. Origami design secrets: mathematical methods for an Ancient Art. CRC Press, Boca Raton
Lang RJ (2012b) Circle packing, Origami design secrets: mathematical methods for an Ancient Art. CRC Press, Boca Raton
Lang RJ (2018) Eyeglass telescope. Retrieved from https://www.langorigami.com/article/eyeglass-telescope. Last accessed 9 Aug 2018
Liang F-Y, Ryvak M, Sayeed S, Zhao N (2012) The role of natural gas as a primary fuel in the near future, including comparisons of acquisition, transmission and waste handling costs of as with competitive alternatives. Chem Cent J 6(Suppl 1):S4. https://doi.org/10.1186/1752-153X-6-S1-S4
Miret S (2014) 4 ways to do solar energy. Retrieved from http://blogs.berkeley.edu/2014/06/09/4-ways-to-do-solar-energy/. Last accessed 10 June 2018
Nelson SA (2015) Energy resources. Retrieved from https://www.tulane.edu/∼sanelson/eens1110/energy.htm. Last accessed 12 Aug 2018
Nishiyama Y (2012) Miura folding: applying origami to space exploration. Int J Pure Appl Math 79(2):269–279
QRG—Northwestern University, (n.d-e), retrieved from http://www.qrg.northwestern.edu/projects/vss/docs/power/2-how-efficient-are-solar-panels.html. Last accessed 15 June 2018
Robinson N (2004) The Origami Bible, p 10
Shafer J (2001) Origami to astonish and amuse. Martin's Griffin, St
Tang R, Huang H, Tu H, Liang H, Liang M, Sang Z, Xu Y, Jiang H, Yu H (2014) Origami-enabled deformable silicon solar cells. Appl Phys Lett 4(8)
The European Wind Energy Association (2009) Environmental Impacts. Wind energy—the facts: a guide to the technology, economics and future of wind power, Earthscan, p 328
Trautz M, Kunstler A (2009) Deployable folded plate structures: folding patterns based on 4-fold-mechanism using stiff plates. In: Proceedings of the International Association for Shell and Spatial Structures Symposium
Zirbel SA, Magleby SP, Howell LL, Lang RJ, Thomson MW, Sigel DA, Walkemeyer PE, Trease RP (2014) Accommodating thickness in origami-based deployable arrays. ASME. International design engineering technical conferences and computers and information in engineering conference, vol 6B: 37th mechanisms and robotics conference, 4–7 August 2014

# Part III
# Solar Thermal Systems

# Chapter 11
# Supercritical Carbon Dioxide Solar Thermal Power Generation—Overview of the Technology and Microchannel Receiver Development


**Vinod Narayanan, Brian M. Fronk, Thomas L'Estrange and Erfan Rasouli**

**Abstract** The supercritical carbon dioxide ($sCO_2$) power cycle is being considered for solar thermal central receiver systems in the United States. The cycle lends to increased high-temperature input that is expected of the next-generation concentrating solar thermal power (CSP) systems. Power block efficiencies of about 50% can be achieved for recompression cycles at an input temperature of approximately 720 °C. Additionally, the power block is compact and less complex, raising the possibility of using thermal-storage-coupled CSP $sCO_2$ technologies for modular ($\sim$100 MW) peak-load power plants. Three pathways toward providing solar thermal input to the $sCO_2$ cycle have been proposed by various research groups—the molten salt receiver pathway, the solid particle receiver pathway, and the gas-phase receiver pathway. The first two technologies have the advantage of sensible thermal storage within the solid/fluid medium passing through the receiver. In the gas receiver pathway, there is a need for coupling a sensible or latent heat storage technology. Several key technologies are needed to enable the realization of the $sCO_2$ solar thermal technology, key among them being the receiver and thermal storage. In this chapter, some of the key gas-phase receiver technologies are discussed. The group's past and recent work on the development of microchannel solar thermal receivers for $sCO_2$ is emphasized.

**Keywords** Solar thermal · Concentrating solar power · Supercritical carbon dioxide · Microchannel · Receiver · Efficiency

V. Narayanan (✉) · E. Rasouli
Department of Mechanical and Aerospace Engineering,
University of California, Davis, CA, USA
e-mail: vnarayanan@ucdavis.edu

B. M. Fronk
School of Mechanical, Industrial and Manufacturing Engineering,
Oregon State University, Corvallis, OR, USA

T. L'Estrange
SpaceX Corporation, Hawthorne, CA, USA



H. Tyagi et al. (eds.), *Advances in Solar Energy Research*, Energy, Environment, and Sustainability, https://doi.org/10.1007/978-981-13-3302-6_11

## 11.1 Overview of Solar Thermal Power Generation

There are two main pathways by which solar energy can be converted into electrical energy. In the first pathway, photons are directly converted to electricity in semiconductor materials by the photovoltaic (PV) effect. In the second pathway, termed concentrating solar power (CSP), solar energy is concentrated using mirrors and directed at a receiver. A heat transfer fluid flows within the receiver and absorbs heat from the concentrated solar energy and passes this energy on to a thermodynamic power cycle. The PV pathway to power generation is more prevalent than CSP because the latter requires high levels of direct normal irradiance (DNI). In the last decade, dramatic decreases in the cost of PV technology have resulted in the widespread deployment of this technology. PV scales well and can be placed on rooftops of residential buildings, as well as on a utility scale. In order to make economic sense, CSP power generation is restricted to areas of high DNI, and this technology is only relevant to utility-scale power generation.

Key subsystems of a CSP plant include the solar concentrator field, receiver including heat transfer fluid, thermal storage, and power block. Concentration could occur using parabolic troughs, parabolic dish, or central tower type receivers. In trough technology, the heat transfer fluid, typically a mineral oil, is sent through evacuated tube receivers at the focal line of a series of parabolic troughs. The heated fluid exchanges thermal energy with water in a heat exchanger to generate steam, which in turn drives a Rankine power cycle. Due to the lower concentration ratio, trough technology limits the high temperature of the fluid to approximately 350–400 °C. In the central receiver solar thermal power plant, an array of heliostats (two-axis tracking mirrors) are located in a field and surround a power tower (see Fig. 11.1). The receiver is mounted atop the tower. The heliostats reflect the sunlight onto the central receiver, thereby heating the fluid flowing within. Figure 11.1

**Fig. 11.1** Photograph of one of the power towers and heliostat fields of the Ivanpah solar thermal power plant in the Mojave Desert in California at the border with Nevada. *Photo credit* V. Narayanan

shows a picture of one of the three power towers and heliostat fields of the Ivanpah solar electric power generation system designed by BrightSource and built by Bechtel (California Energy Commission 2018).

The key advantage of solar thermal power generation technology when compared with PV technology is the lower cost of thermal storage compared with battery storage. In trough plants, the mineral oil can be used for sensible thermal storage. Solar salt, a 60–40% mixture of sodium and potassium nitrate, has been used for central receiver plants.

Several generations of solar thermal technology have been successfully commissioned around the world. A list of operational and decommissioned solar thermal plants around the world is documented by SolarPACES (SolarPACES 2018). Early parabolic trough solar thermal power plants in California's Mojave Desert—the Solar Energy Generation Systems (SEGS), were built in the 1980s. This type of solar thermal plant is most prevalent around the world. The Solar I was the first pilot plant that demonstrated the central receiver technology in the 1980s. In the mid-1990s, the plant was redesigned as Solar II to demonstrate high-temperature thermal storage using a two-tank nitrate salt system. The Solar Two receiver produced 565 °C molten salt with a receiver efficiency of 88%, including absorptivity of 95%, and an average flux of 43 W/cm$^2$ (Pacheco 2002). Commercial solar thermal power plants are being built based on this technology, such as the 110 MWe Crescent Dunes plant by SolarReserve in Nevada, which was designed to provide 10 h of thermal storage.

One key avenue to achieving cost reductions in solar thermal power generation in order to make it more cost competitive with PV technology is to increase the efficiency of solar-to-electric power conversion. One can consider ideal limits of efficiency of a solar power plant to determine the factors that influence the power plant efficiency. The Carnot cycle represents the thermodynamic limit to efficiency,

$$\eta_{\text{Carnot}} = 1 - \frac{T_{\text{amb}}}{T_{\text{h}}} \tag{11.1}$$

where $T_{\text{h}}$ is the temperature on the hot side of the cycle and $T_{\text{amb}}$ is the ambient sink temperature. Unsurprisingly, Eq. (11.1) implies that higher cycle efficiency can be gained by increasing the hot side temperature. The high side fluid temperature, $T_{\text{h}}$ is obtained by means of concentrated solar energy incident on the receiver. If one were to consider the surface of the receiver and perform an energy balance, the amount of thermal energy entering the fluid per unit time would be equal to the absorbed irradiation less the emission and convection losses, and the receiver efficiency would be given as

$$\begin{aligned}\eta_{\text{receiver}} &= \frac{q_{\text{fluid}}}{q_{\text{incident}}} = \frac{q_{\text{absorbed}} - \{q_{\text{re-radiation}} + q_{\text{convection}}\}}{q_{\text{incident}}} \\ &= \alpha_{\text{s}} - \frac{h(T_{\text{s}} - T_{\text{amb}}) + \varepsilon\sigma\left(T_{\text{s}}^4 - T_{\text{amb}}^4\right)}{I \cdot C}.\end{aligned} \tag{11.2}$$

In Eq. (11.2), $I$ represents the DNI in W/m$^2$, $C$ represents the concentration ratio enabled by the solar collector subsystem, $\alpha_s$ denotes the solar absorptivity of the receiver surface, $\varepsilon$ is the emissivity of the receiver surface, and $T_s$ is the average surface temperature of the receiver. The average surface temperature of the receiver is higher than the average fluid temperature within the receiver and would approach the latter for large internal convective heat transfer coefficients or small mass flow rate of the heat transfer fluid (i.e., large residence times). As a simplification, if one were to assume an ideal absorptivity to solar insolation, negligible external convection losses and a uniform surface temperature of $T_h$, Eq. (11.2) simplifies to

$$\eta_{\text{receiver}} = 1 - \frac{\varepsilon\sigma\left(T_h^4 - T_{amb}^4\right)}{I \cdot C}. \tag{11.3}$$

Equation (11.3) suggests that the receiver efficiency decreases with an increase in surface temperature for a fixed concentrated solar insolation. It also suggests that at a fixed surface temperature, an increase in the concentration ratio results in an increase in the receiver efficiency. The combined system efficiency including receiver and Carnot efficiency is given by combining Eqs. (11.1) and (11.3),

$$\eta_{\text{receiver}+\text{Carnot}} = \left\{1 - \frac{\varepsilon\sigma\left(T_h^4 - T_{amb}^4\right)}{I \cdot C}\right\} \cdot \left[1 - \frac{T_{amb}}{T_h}\right]. \tag{11.4}$$

Figure 11.2 shows the combined receiver and cycle efficiency plotted as a function of receiver surface temperature for various concentration ratios. Several interesting observations can be made from the trends. For any fixed concentration ratio, there is an optimum $T_h$ at which efficiency is highest. This trend is a result of the interaction between the increase in cycle efficiency and a decrease in receiver efficiency with increase in $T_h$. Additionally, the peak value of efficiency moves to higher $T_h$ with an increase in concentration ratio. At a fixed surface temperature, higher concentration ratios results in higher efficiency. The trends suggest that in order to increase the efficiency of a solar thermal plant, one needs to be able to (a) operate at high temperatures and (b) at high concentration ratios. The former is limited by the availability of materials and heat transfer fluid while the latter is limited by the solar field optics and the receiver design.

Kolb (2011) estimated that current state-of-the-art commercial molten salt technology could operate with an incident flux on the order of 80 W/cm$^2$. He also estimated that next-generation high-temperature molten salt power towers could operate at an increased flux of 100 W/cm$^2$ ($C$ = 1000) with a corresponding thermal efficiency of 94% (or 89% total receiver efficiency, including reflection losses based on an absorptivity of 95%). From Fig. 11.2, for a concentration of $C$ = 1000, the ideal system efficiency can reach 66% at $T_h$ = 1100 K (827 °C). Attaining such high-temperatures necessitates research in high-temperature heat transfer fluids and materials.

The potential to increase system efficiency using central receiver solar thermal technology has led to several research and development efforts of subsystem

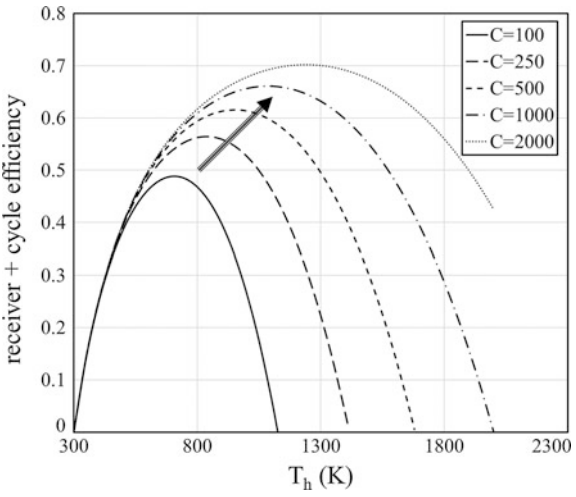


**Fig. 11.2** Combined receiver and Carnot cycle efficiency. An emissivity of 90% and an insolation of 1000 W/m$^2$ has been used in Eq. (11.4) for the plot

components in the United States under the auspices of the U.S. Department of Energy's Sunshot CSP initiative over the past decade (U.S. Department of Energy, Concentrating Solar Power 2018). The focus of development of the power block subsystem has been on a Brayton cycle employing supercritical carbon dioxide ($sCO_2$), rather than the traditional Rankine cycle. This cycle is discussed in the following section.

## 11.2 Supercritical Carbon Dioxide ($sCO_2$) Thermodynamic Cycle

The $sCO_2$ cycle is a Brayton cycle that can result in high cycle efficiency for moderate fluid temperatures ranging between 500 and 800 °C. Advantages include compactness of turbomachinery, simpler controls, and high efficiency at moderate temperatures. The efficiency gains are obtained by compressing near the critical point where density variation through the compression is minimal due to the liquid-like behavior of $sCO_2$, and by the recuperation of heat. Several researchers are investigating the use of this power cycle with varied sources such as fossil, solar, nuclear, geothermal, and moderate- to high-quality waste heat streams (Brun et al. 2017).

The $sCO_2$ power generation cycle with two stages of recuperation and two compression stages is shown in Fig. 11.3a and the corresponding T-s diagram for $sCO_2$ is depicted in Fig. 11.3b. There are seven processes in an ideal recompression cycle, namely, 1–2 isentropic compression stage 1, 2–3a isobaric heat input (low-temperature recuperator), 3–4 isobaric heat input (high-temperature recuperator), 4–5 isobaric heat input (primary heat exchanger), 5–6 isentropic expansion,

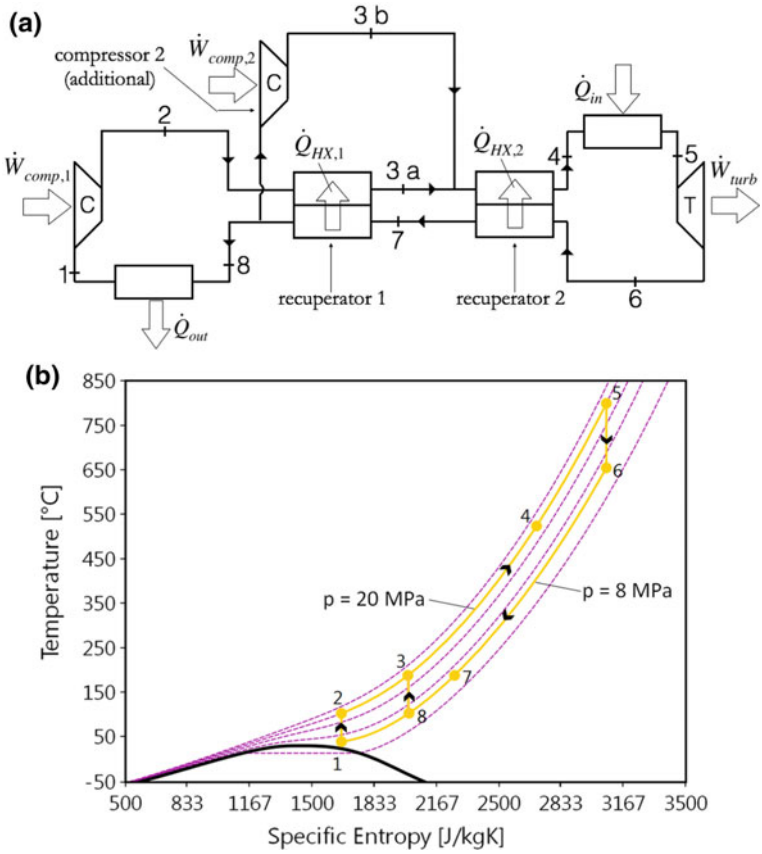


**Fig. 11.3** **a** Layout of $sCO_2$ recompression Brayton power generation cycle, **b** corresponding T-s diagram

6–7 isobaric heat removal (high-temperature recuperator), 7–8 isobaric heat removal (low-temperature recuperator), and 8–1 isobaric heat removal to the ambient through a heat exchanger. A fraction of the low-pressure $sCO_2$ is bypassed following the second recuperator and compressed in the second compressor to state point 3b such that only the remaining fraction of the flow passes through the low-temperature side of the low-temperature recuperator in process 2–3a. Both high-pressure fluid streams merge prior to entering the high-temperature recuperator.

Ideal cycle efficiency of the recompression, single recuperation, and a reheat cycle are compared in Fig. 11.4 as a function of the turbine inlet temperature. The turbine inlet temperature in this model is at 800 °C at a pressure of 200 bar. This inlet temperature is close to the ideal operating point for the solar Carnot cycle (Fig. 11.2) with a concentration ratio of 1000. The low-pressure side of the cycle is at 80 bar and the temperature at the compressor inlet (state point 1 in Fig. 11.3a) is

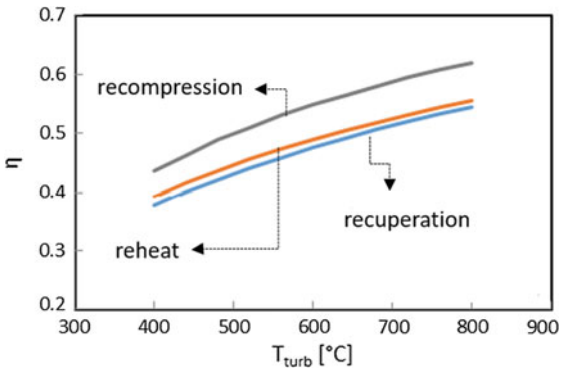


**Fig. 11.4** Ideal $sCO_2$ cycle efficiency for a recompression cycle, single recuperation cycle, and a reheat cycle

kept fixed at 40 °C. As the name suggests, the single recuperation cycle consists of a single compressor, turbine, and recuperator. It is the simplest $sCO_2$ cycle but a significant penalty in efficiency is incurred by rejecting heat to the environment at a higher temperature. The reheat cycle consists of a single compressor, a single recuperator but two heat addition and two expansion stages. The efficiency is slightly better than that of a single recuperator cycle. The recompression cycle provides higher efficiency compared with the other two cycles due to the ability to tune the pinch point in the low-temperature recuperator.

The $sCO_2$ power block subsystem described in this section interfaces with the solar thermal system through one of two methods in process 4–5 of a recompression cycle (Fig. 11.3)—1. by direct addition of heat from the receiver or 2. by means of a storage fluid-to-$sCO_2$ heat exchanger. The different configurations of integration of the receiver, storage, and power block are discussed in the next section.

## 11.3 Solar Thermal $sCO_2$ Power Generation Systems

A recent U.S. Department of Energy report (Mehos et al. 2017) has identified the $sCO_2$ cycle for next-generation solar thermal technologies. The report discusses potential pathways toward implementation of the solar $sCO_2$ power generation system. One of the most attractive application niches for the solar $sCO_2$ power plant with thermal energy storage has been identified to be that of providing peak-load power. A key requirement of such plants would be quick ramp rate and start-up times, for which the $sCO_2$ cycle, with its compact turbomachinery, is well suited. Thermal storage of around 6 h would be needed for these plants and the capacity is envisioned to be 50 MWe or larger. The report also finds that while peaking $sCO_2$ solar power plant is favored based on the current cost of natural gas, higher capacity factor plants with longer thermal storage capacity might become desirable with higher natural gas costs.

The U.S. Department of Energy report (Mehos et al. 2017) describes three different pathways toward the implementation of a solar $sCO_2$ power plant based on

the working fluid used in the central receiver, namely, (1) the molten salt receiver pathway, (2) the solid particle receiver pathway, and the (3) the gas-phase receiver pathway. Figure 11.5a–c shows simplified schematics of potential configurations of the three pathways.

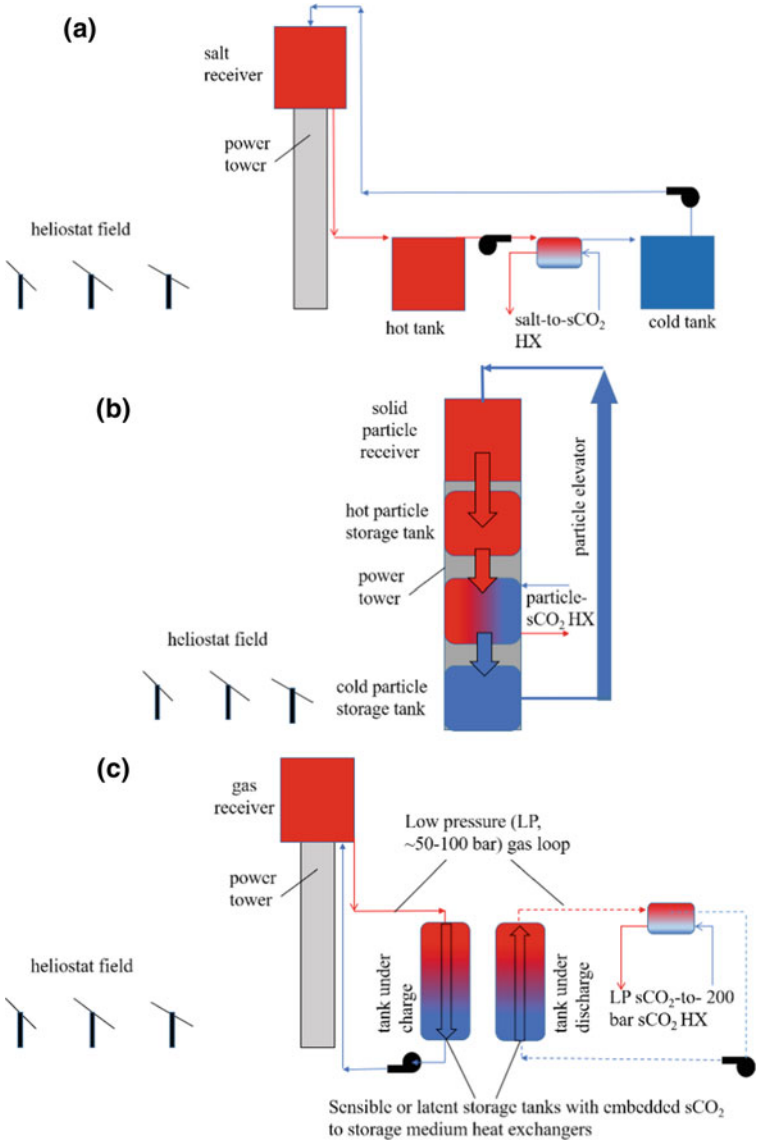


**Fig. 11.5** Simplified schematics of the three pathways to solar-$sCO_2$ power plant technology. **a** High-temperature molten salt receiver pathway, **b** solid particle receiver pathway, and **c** gas receiver pathway. Adapted from Mehos et al. (2017)

The molten salt receiver pathway architecture (Fig. 11.5a) is similar to the existing nitrate salt systems, but use a higher temperature salt mixture such as $MgCl_2$/KCl that is stable at temperatures as high as 800 °C. In the molten salt pathway, the salt mixture flows from a cold storage tank through the receiver atop the power tower, where it picks up heat from the concentrated sunlight. The hot salt is directed into a hot tank. During the time of power generation, the salt flows from the hot tank through a salt-to-$sCO_2$ heat exchanger and then into a cold tank. Salt from the cold tank is directed again through the receiver.

In the solid particle receiver pathway, shown in Fig. 11.5b, solid particles from a cold silo are transported to the top of the power tower where they fall as a sheet and are directly heated from concentrated sunlight. The heated particles fall into a hot storage tank. During times of power generation, the particles are directed from the hot storage tank through a particle-to-$sCO_2$ heat exchanger to a cold storage tank. Particles are transported from the cold storage tank through the receiver to complete the loop.

The advantages of molten salt and particle receiver pathways are that sensible storage is integrated into the heat transfer medium going through the receiver. Both pathways lend to high-temperature $sCO_2$ cycles by choice of the heat transfer media. However, several technological challenges exist and research toward retiring these challenges have been identified in the U.S. Department of Energy report (Mehos et al. 2017).

In the gas-phase receiver pathway (Fig. 11.5c), as the name suggests, a gas-phase fluid is circulated through the receiver. This heat needs to be transferred to a thermal storage medium, which could be either sensible, latent, or thermochemical. The heat is then transferred from the storage medium to $sCO_2$ via a heat exchanger. The gas-phase heat transfer fluid needs to be relatively high in density in order to reduce the pressure drop through the receiver loop. The rest of the chapter describes receiver designs for this pathway in more detail.

## 11.4 Gaseous Solar Receiver Technologies for $sCO_2$ Solar Power Cycles

One of the earliest concentrated solar power systems used a gaseous working fluid in the receiver. In the European GAST project, air was heated in tubular panels to temperatures up to 1000 °C at 9.5 bar and fluxes of <20 W $cm^{-2}$ (Romero et al. 2002). Even at an elevated operating pressure, very high volumetric flow rates of air are required to achieve suitable temperature increase and thermal capacity (Romero et al. 2002; Hyder and Fronk 2018). Thus, to minimize pressure drop, the tubular receivers had to be large, which increased capital cost, yielded poor convective heat transfer coefficients and ultimately limited incident flux.

These challenges were partially overcome by the development of volumetric receivers, where air or other gases are heated to temperatures >1500 °C inside a

porous volume (Ho and Iverson 2014). Thus, the gas-phase heat transfer performance was improved due to the increased transfer area. While volumetric receiver technology remains an area of active research, designs that use ambient air as the working fluid have the same challenge of extremely high volumetric flow rates to achieve economical thermal power. Other challenges of these gas-based receivers are difficulty integrating with commercial thermal storage (e.g., molten salt two-tank systems) and the potential for large thermal transients and reduced fatigue life of the receiver materials (Ho 2017).

However, the development of the $sCO_2$ Brayton cycle for solar thermal applications has led to another look at gas-based receivers using supercritical carbon dioxide as the working fluid. A key advantage is the significantly higher volumetric heat capacity of the fluid compared to the older air systems. As an example, the volumetric flow rate for a 300 MW thermal system heating $sCO_2$ from 550 to 720 °C is 28.3 $m^3\ s^{-1}$ and 11.3 $m^3\ s^{-1}$ for operating pressures of 80 and 200 bar, respectively, compared to flow rates for 3716 and 392 $m^3\ s^{-1}$ for air at 1 and 9.5 bar. Thus, the pumping power required for an equivalent thermal power can be significantly reduced.

Still, receivers using $sCO_2$ must overcome the challenges of relatively poor convective heat transfer coefficients of gases, and the high-pressure and high-temperature operation. Starting in 2014, the U.S. Department of Energy supported the development of multiple high-pressure gaseous receiver concepts by U.S. National Laboratories, universities, and for-profit companies (Mehos et al. 2017). Brayton Energy extended a plate-fin-style recuperative heat exchanger design to a high-pressure (>25 MPa) design (Mehos et al. 2017). A dense network of fins was brazed within an enclosed shell. The shell wall thickness combined with the fins acting as tensile support members allowed the receiver to sustain the high operating pressures. The fins also increased the heat transfer coefficient and heat transfer area, improving performance. The Brayton design envisioned developing multiple modules based on the finned-tube concept and arranging them in either cylindrical or planer open receiver depending on the heliostat field. The National Renewable Energy Laboratory developed a cellular cavity concept in which vertical and horizontal cavity panels formed a grid of unit cells. Supercritical $CO_2$ flowing through the panels would absorb incident and reflected solar radiation within the cavity. A primary challenge of the design was that the leading edges of the horizontal and vertical panels were exposed to the full incident flux and effectively uncooled, resulting in excessive temperatures if not actively cooled. Researchers at Oregon State University and University of California-Davis have been pursuing a microchannel-based receiver concept, discussed in more detail in the following sections. Here, multiple repeating unit cells containing small ($\sim$300 μm) flow features enable high heat transfer coefficient and safe containment of high pressures up to 250 bar. In addition to these high-pressure $sCO_2$ concepts, Ho (2017) reviewed recent investigations on other mid- to high-pressure gaseous receivers including volumetric, tubular, and microchannel designs. A general conclusion was that while gaseous receivers have the potential advantage of low-cost working fluids at high temperature, all must overcome the challenges of potentially low heat

transfer coefficient, high-pressure drop, and the potential for manufacturing complexity due to the requirement of multiple parallel flow paths to minimize pressure drop.

While operating at higher pressure has advantages from a volumetric flow rate and heat transfer perspective, for gaseous receivers with ground-based thermal storage and power block, it requires the use of thick-walled riser and downcomer pipes of expensive nickel-based alloys materials along the central power tower. As an example, in detailed cost-analysis of a 350 MW thermal microchannel solar receiver (Weimar 2018) (design discussed in following sections), the cost of the riser and downcomer were >35% of the total receiver system costs when operating at 250 bar and a tower height of 140 m. The required wall thickness is driven by the requirements of the ASME B31.3 process piping code and the relatively low maximum allowable stresses of qualified materials at 720 °C. Fronk and Jajja (2018) conducted a simple trade-off analysis exploring the effect of reducing gas receiver operating pressure on downcomer and riser size. For a 320 MW thermal receiver and a pumping power equal to 4% of the plant electric output, they showed that reasonable sized downcomers made with lower cost (i.e., non-nickel-based alloys) could be obtained at lower operating pressures ($\sim$80 bar) while still maintaining reasonable allowable pressure drop through the system. As will be discussed in the following section, this opens the possibility for microchannel based solar receivers using gaseous working fluids to be a viable option for a wide range of working fluids and operating conditions.

## 11.5 Microchannel Solar Receiver R&D

### *11.5.1 Microchannel Receiver Architecture*

Over the past several years, our group has been working on a different architecture for a central receiver using flow through microscale passages. The efficiency of the solar receiver depends on the radiative properties of its surface and the convective heat transfer coefficient on the internal flow passages. The latter is important as it dictates the surface temperature of the receiver and the overall size of the receiver and solar field. By reducing the diffusion length for thermal transport, microchannels increase the internal convective heat transfer coefficient thereby permitting increased flux of incident solar energy at the same fixed surface temperature of the solar receiver.

In a conventional open central tower receiver, the concentrated solar flux is incident on 2–3 cm diameter tubes that run vertically between an upper and lower headers (plena). The tubes are arranged in the form of a cylinder for an open receiver configuration with heliostats located around the receiver.

A microchannel receiver would look significantly different from the tubular receiver and would consist of several flat receiver panels that are arranged atop the

central tower. For an open configuration, the panels would be arranged in a cylindrical fashion with heliostat field surrounding the power tower. A rendition of the open receiver is shown in Fig. 11.6. Rather than tubes, the building blocks of a microchannel receiver architecture would consist of repeating regions called "unit cells" that are connected by fluid distribution regions called "headers". Within each unit cell, flow would be routed through an array of microscale flow passages, thereby increasing heat transfer rate from the concentrated solar radiation to the fluid. In order to mitigate high-pressure drop through small passages, several such unit cells would be arranged in parallel within the receiver panel.

Since the heat transfer and pressure drop occur in large part within the microscale unit cells, the focus of the numerical and experimental studies to date have been on design and demonstration of the thermofluidic performance of a unit cell or a few unit cells. A system-level model is then used to provide a design for the hundreds of MW-scale receiver. These aspects are discussed in the following sections.

### *11.5.2 Lab-Scale Unit Cell Receiver Design and Fabrication*

Lab-scale unit cell receivers (LUCRs) were designed and fabricated to demonstrate the microchannel receiver concept. The receiver has to be able to withstand temperatures of about 750 °C and a pressure of 200 bar. The LUCRs were 2 cm × 2 cm in dimension based on the limitation of the lab-scale simulator used to generate 1000 sun concentration; see L'Estrange et al. (2015) for details. Table 11.1 lists some of the

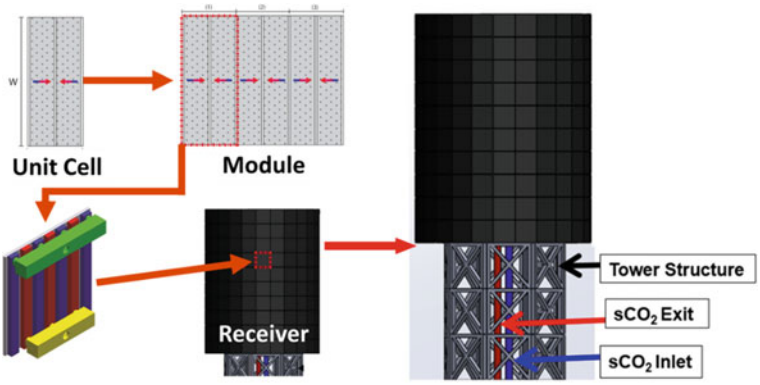


**Fig. 11.6** Representation of the microchannel receiver in an open central power tower configuration. Several microchannel receiver panels of ~1 $m^2$ would be placed alongside each other to form a cylindrical receiver. Each panel would, in turn, have fluidic headers to route hot and cold streams of $sCO_2$ into the microscale flow features. These microscale flow features are replicated as unit cells, with flow going in parallel, to make up each panel

**Table 11.1** Material Properties at temperature for select Nickel superalloys considered

| Vendor | Alloy name | $T_m$ (C) | Composition for bonding (%)[1] | Thermal conductivity (W/m-K) @700 °C | Rupture stress @100 h (Mpa) | Temperature for rupture stress @100 h (C) | Material thickness affected by oxidation after 1000 h @980 ° C (μm) |
|---|---|---|---|---|---|---|---|
| Special metals | Inconel 8OOH &HT | 1360 | 23 | 22.8 | – | – | 312 |
| Special metals | Inconel X750 | 1400 | 17 | 22.2 | 241[2] | 730 | – |
| Special metals | Inconel 751 | 1400 | 17 | – | 352 | 732 | – |
| Special metals | Inconel 718 | 1270 | 21 | 23.1 | – | | – |
| Special metals | Nimonic 80A | 1330 | 21 | 22.3 | 305[2] | 750 | – |
| Haynes International | 230 | 1350 | 36.02 | 22.4 | 185 | 760 | 20 |
| Haynes International | 214 | 1370 | 16 | 26.9 | 235 | 760 | 5 |
| Haynes International | 25 | 1365 | 35 | 22.6 | 250 | 730 | 211 |
| Haynes International | R41 | 1325 | 19 | 22 | – | – | – |
| Haynes International | Waspaloy | 1340 | 19 | 20.9 | 365 | 760 | – |

[1]Must have a % composition sum of Cr, W, and La that is <35–40%
[2]Approximated from fatigue chart to be chemically etched

Nickel superalloys shortlisted for this application. Based on material properties, cost, and vendor expertise in fabrication, Haynes 230 was chosen as the material for the LUCRs. A micro-lamination process was used to fabricate the LUCRs. In this approach, laminae with microchannels or microscale features are machined or photo-chemically etched into sheets of metal and joined together by methods such as diffusion bonding or brazing.

The LUCR designs were based on conjugate computational fluid dynamics simulations of the receiver, and on mechanical and thermal stress analysis (Rymal et al. 2013, 2014; Rymal 2015). Two types of receivers were designed- a parallel microchannel LUCR and a microscale pin array LUCR. Limited parametric analysis was performed on the variation of the receiver geometrical variables (Rymal et al. 2014).

Figure 11.7a shows the exploded isometric wireframe view of the of the pin array LUCR design. The LUCR consisted of three plates that were bonded together. The top plate had two large circular holes to which the inlet and outlet tubes of the LUCR were welded. In a multiple-unit cell receiver design, there would be another layer of headers that connected the inlet and exit tubes of each unit cell together (see Fig. 11.6). On the underside of the top plate, slots that directed the fluid to the next plate were machined. In this LUCR, two unit cells that are 2 cm wide $\times$ 1 cm long were designed. The inlet flow was therefore split into two slots, one on either end of the 2 cm length. The middle plate had three rows of slots with ribs of material in between for structural support to direct flow in and out of the pin array. The two outer rows of slots were inlet slots and the middle row of slots was for the fluid outlet. The pin array was sinker Electrical Discharge Machined (EDM) into the bottom and middle plates. The pins were designed to be 700 μm in diameter, with a height of 350 μm. One half of this depth is machined on the middle and bottom plates. The diagonal center-to-center pin spacing was 1050 μm, while the longitudinal pitch was $\sim$1800 μm. Figure 11.7b shows a picture of the bottom plate (flux plate) following the EDM process while Fig. 11.7c shows the completed pin fin LUCR after diffusion bonding, as viewed from the solar insolation side. Because this was the first attempt at creating a microscale solar receiver, large bonding areas around the 2 cm $\times$ 2 cm central microchannel regions were used (see Fig. 11.7c). In an actual receiver, the bonded regions would only be a few millimeters in dimension.

The lamination architecture of the parallel channel LUCR was similar to the pin array LUCR; ten microchannels with design width of 500 μm and height of 360 μm were micro-machined into the bottom flux plate (Fig. 11.7a) and the underside of the middle plate creating a 2 cm $\times$ 2 cm unit cell.

The LUCRs were first subjected to mechanical integrity tests to ensure that they could withstand the operating experimental conditions of 130 bar and 730 °C. Upon successful completion of integrity tests, thermofluidic experiments were performed to characterize pressure drop and efficiency using a custom-built high-flux solar simulator and a $sCO_2$ open-loop facility; see L'Estrange et al. (2015) for details.

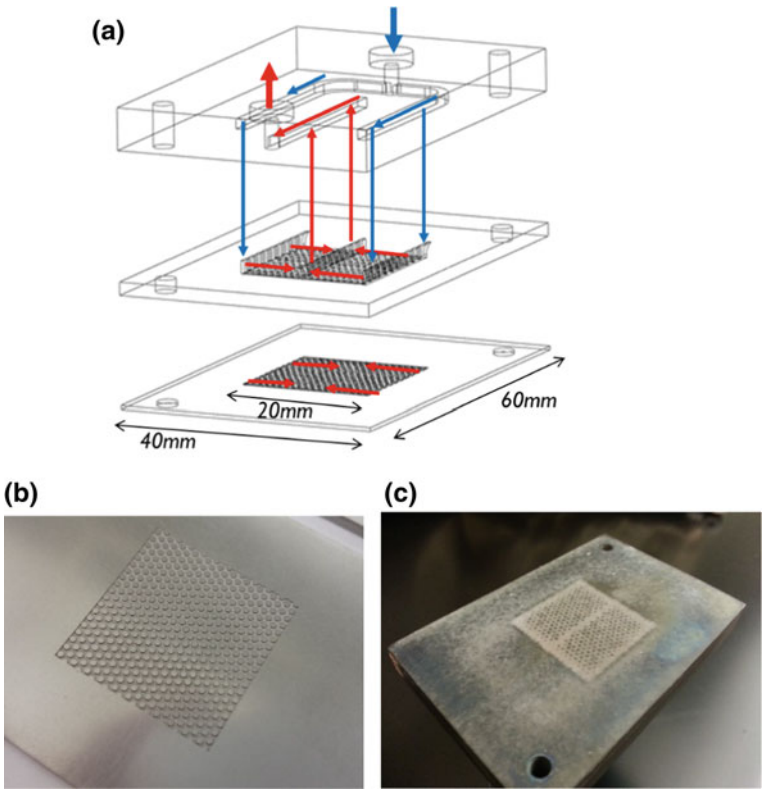


**Fig. 11.7** Pin array LUCR. **a** Exploded isometric wireframe view of the pin fin LUCR. Outer dimensions of the LUCR are 40 mm in width, 60 mm in length, and a height of 8.9 mm, **b** picture of the pin array shim, **c** completed pin array LUCR as viewed from the flux absorber plate side. The pins are visible in the 2 cm × 2 cm area upon which the concentrated simulated solar flux would be incident. *Source* L'Estrange et al. (2015), reproduced with permission from ASME

### *11.5.3 Lab-Scale Unit Cell Receiver Experimental Results*

Pressure drop experiments were performed at lower temperatures and without concentrated flux from the simulator in order to reduce heat loss in the latter experiments. Flow was held at approximately 100 °C to ensure the gas was above the critical temperature and the system pressure was matched to be identical to that in efficiency experiments. Figure 11.8 shows the results of pressure drop tests for the pin array LUCR as a function of mass flow rate and Reynolds number (based on the pin array hydraulic diameter, $\mathrm{Re}_{D_H}$). For the design flow rate of 1 g/s, the pressure drop across the LUCR is under 0.5 bar. Similar pressure drops could be expected in larger scale receivers since the flow through the micro-pin fin regions would occur in a parallel network. It is also important to note that based on $\mathrm{Re}_{D_H}$, the flow is expected to be in the transitional to turbulent regime through the pin fin receiver.

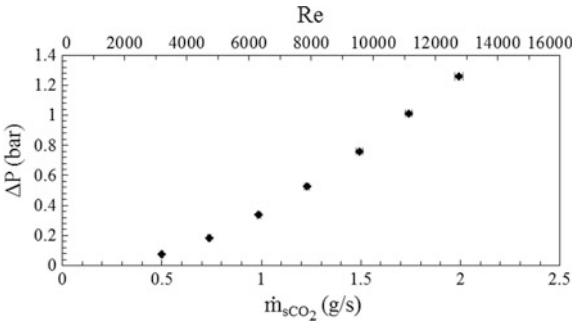


**Fig. 11.8** Experimental pin fin array lab-scale receiver pressure drop. *Source* L'Estrange et al. (2015), reproduced with permission from ASME

#### 11.5.3.1 Heat Transfer Experiments

The parallel channel and pin array LUCRs were characterized for efficiency in the laboratory $sCO_2$ open-loop test facility; details of the experimental set-up and procedures are discussed in L'Estrange et al. (2015). Briefly, compressed $CO_2$ from cylinders was preheated in a custom-built electrical heater before entering the LUCR. The LUCR was located at the focal point of a custom-built elliptical reflector. A Xenon arc lamp was located at one focal point of the reflector while the LUCR was located at the other. Upon exiting the LUCR, the heated $sCO_2$ was regulated down in pressure, cooled, and discharged into a fume hood. System pressure, mass flow rate, and inlet and exit temperatures of $sCO_2$ were measured in order to obtain an indication of the rate of heat absorbed by the fluid. Additional thermocouples were mounted in several locations on the surface to obtain an indication of average temperature of the LUCR. In a separate experiment, a heat fluxmeter, located in the same focal plane as the LUCR was traversed in two axes to map the distribution of heat flux from the concentrator. The heat fluxmeter reading provided a measure of the incident heat flux onto the LUCR.

Two efficiency measures were used-receiver (total) and thermal. Receiver efficiency was defined based on the heat transferred to the working fluid to that incident on the receiver surface,

$$\eta_{\text{receiver}} = \frac{\dot{m}_{sCO_2} \cdot (h_{\text{out}} - h_{\text{in}})}{q_{\text{incident}}}. \tag{11.5}$$

The thermal efficiency of the receiver was defined as the ratio of the heat absorbed by the working fluid to the heat absorbed by the receiver,

$$\eta_{\text{receiver,thermal}} = \frac{\dot{m}_{sCO_2} \cdot (h_{\text{out}} - h_{\text{in}})}{\alpha q_{\text{incident}}}. \tag{11.6}$$

Thermal efficiency does not include optical reflection losses, which are dependent on the applied coating to the receiver surface. Therefore, the thermal efficiency is a measure of the efficacy of using microchannels and is decoupled from the

performance of the coating on the receiver surface. This measure was defined since commercially available high-temperature coatings were found to be unreliable for the surface temperatures tested (in excess of 700 °C) and a bare receiver surface of Haynes 230 was tested. In order to obtain a value for absorptivity for Eq. 11.6, the reflectivity of the bare Haynes surface of the LUCR was assessed using a spectrophotometer following the experiments. Numerical integration of the device surface reflectivity and the spectral distribution of irradiation from the solar simulator (a Xenon arc lamp) provided a spectrally averaged reflectivity of the device of 0.172.

The results of thermal and receiver efficiency as a function of heat flux are shown in Fig. 11.9. The temperature of the surface was maintained relatively constant in these experiments so that the effect of heat flux on efficiency could be evaluated. The inlet $sCO_2$ temperature was maintained approximately constant at 400 °C using an electric preheater and the system pressure was between 81 and 86 bar.

As shown in Fig. 11.9, both thermal and receiver efficiency are seen to increase with increasing heat flux. The parallel channel LUCR efficiency varies from 60.7% at 68.1 W/cm$^2$ to about 71.6% at 120.3 W/cm$^2$, while the thermal receiver efficiency increases from 73.3 to 86.4% over this same range of heat fluxes. As for the pin array LUCR, the thermal efficiency varies from 72.3 to 83.9% with the variation in heat flux from 73 to 120 W/cm$^2$.

The trend of the receiver and thermal efficiency with heat flux follows what is to be expected from Eq. (11.3). For the same surface temperature, the convection and reradiation losses are fixed. Hence, an increase in flux would imply that a larger fraction of the incident or absorbed heat is transferred to the $sCO_2$ fluid within the

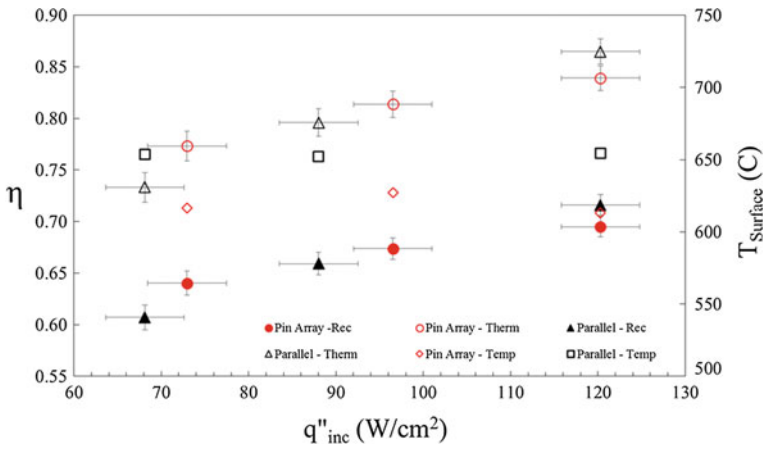


**Fig. 11.9** Receiver and thermal efficiency with a variation of incident flux at a fixed exit temperature of ~650 °C. Also plotted is the average surface temperature of the device. Data are not corrected for heat loss through the insulation

receiver. The increased ability to transfer high incident fluxes is a key advantage of the microchannel receivers.

Since the LUCR was the first prototype demonstration of microchannel receiver technology, safety margins were added during the device fabrication. To ensure that the device would be able to withstand high pressures, large bonding margins were added such that the pin array was located only in the central 2 cm × 2 cm of the 5 cm × 5 cm LUCR. During experiments with the solar concentrator, only the 2 cm × 2 cm area of the LUCR was exposed to the concentrated source while the rest of the device was insulated. Since the area for heat loss relative to the incident heat flux area was large, even with thorough insulation, heat loss on the order of 10% of incident heat, occurred through the insulation. A heat loss calibration experiment was performed, in which the 2 cm × 2 cm pin area was insulated. The solar simulator was turned off and heated $sCO_2$ from the preheater was sent into the LUCR. The difference between the inlet and exit temperatures of $sCO_2$ in the LUCR was then attributed solely to heat loss through the insulation. This heat loss experiment was performed over a range of temperatures to determine a heat loss correction (see L'Estrange et al. (2015) for details). Upon accounting for heat loss, the thermal efficiency shown in Fig. 11.9 varied between 89.9% at 68.1 W/cm$^2$ to about 96.6% at 120.3 W/cm$^2$ at a fixed surface temperature of 650 °C.

The effect of surface temperature variation at a constant heat flux on the receiver and thermal efficiency is shown in Fig. 11.10. The system pressure and $sCO_2$ inlet temperatures were kept fixed at the same values as for the varying heat flux experiments. While the variation in efficiency with exit fluid temperature is shown in Fig. 11.10, it should be borne in mind that the surface temperature varies as the exit fluid temperature for a fixed inlet fluid temperature. In the experiments, the exit fluid temperature is varied by changing the exit temperature by changing the mass flow rate of $sCO_2$. The trend in Fig. 11.10 for both receiver and thermal efficiency shows that with an increase in surface temperature, a reduction in thermal and receiver efficiency is observed. The decrease can be attributed to increase in convective and reradiative heat losses at higher surface temperature (see Eq. (11.3)). The thermal efficiency of the pin array drops from 95.5% at a receiver exit fluid

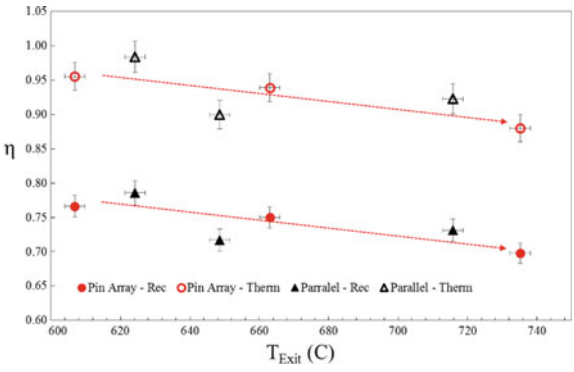


**Fig. 11.10** Receiver and thermal efficiency variation with exit temperature at a fixed incident flux of 68.1 W/cm$^2$ for the parallel channel and 72.95 W/cm$^2$ for the pin array. Data are corrected for heat loss through the insulation. *Source* L'Estrange et al. (2015), reproduced with permission from ASME

temperature of 606 °C to 89% at an exit fluid temperature of 735 °C. The thermal efficiency of the parallel channel drops from 98.3% at a gas exit temperature of 624 °C to 92.2% with an exit temperature of 715 °C. The nonuniform drop in efficiency for the parallel channel as compared to the pin array is likely due to experimental error in surface temperature data at 650 °C. Regardless, thermal efficiencies of around or above 90% was achieved for both LUCR designs at exit fluid temperatures of 735 °C.

The ability of the microchannel receiver to reduce the diffusion resistance in the fluid enables reduced surface temperature for a fixed flux, thereby resulting in an increased efficiency. Having completed characterization of the microchannel LUCR pressure drop and efficiency, a scale-up of this concept was performed.

### *11.5.4 Scaling from Microchannel to Megawatt Receiver*

The potential for the microscale receiver to be scaled to practical megawatt scale capacities was explored in Zada et al. (2016) and Hyder and Fronk (2018). To obtain the high heat transfer coefficients observed in the above sections while maintaining a reasonable pressure drop, a "numbering-up" concept was investigated, shown schematically in Fig. 11.6.

Here, the unit cell is the smallest element in the receiver, and consists of an array of micro-pin features covered with a thin flux plate to contain the fluid. The flow length of the unit cell is limited to achieve the maximum allowable pressure drop of the working fluid as determined from a system level analysis. To number-up to a megawatt scale receiver, multiple-unit cells are constructed in parallel to form a single device, referred to as a module (Fig. 11.6). In the receiver concept, each module had a surface area of approximately 1 $m^2$ which corresponds to approximately 1 MW of absorbed thermal energy at the design conditions. Finally, multiple modules connected in parallel form the full receiver. The modular design allows for the mass flow rate of $sCO_2$ to different zones within the receiver to be controlled to maintain a specified fluid temperature increase and enables arrangement of modules to tune the receiver surface area to a given heliostat field allowing for higher efficiency annualized performance.

To predict the performance of this concept, Zada et al. (2016) developed a simplified thermal network model for a single microchannel unit cell, and validated the predictive capability with the data from L'Estrange et al. (2015). They then used the unit cell model as the basis for a multi-scale model of a full-scale 250 MW thermal central receiver. The full-scale receiver consists of 3000 micro-pin fin unit cells divided into 250 modules. Using a scaled receiver flux distribution from a representative heliostat field, the local incident flux on each unit cell in the receiver could be determined and used as an input to the thermal model. The results from each individual unit cell model were then combined to assess overall receiver performance. Using this approach, different arrangements of modules were considered (cylindrical, trapezoidal, etc.). It was found that with an increase in

northern-facing panels, while still keeping the total surface area constant, the absorbed solar thermal energy can be increased while also increasing the receiver efficiency, suggesting a reduction in cost per kW of electrical power produced. Overall, a receiver built with individual modules was shown to have the ability to be tailored to adapt to a nonuniform field flux to achieve consistent efficiency and $sCO_2$ delivery temperature throughout the receiver.

A key assumption in the Zada et al. (2016) analysis is that flow is uniformly distributed between all the modules and within each module to each unit cells. Poorly distributed flow would reduce efficiency and potentially lead to device failure due to local overheating. To confirm this assumption, Hyder and Fronk (2018) conducted a simulation study to quantify the distribution and the overall efficiency of an integrated module. The developed model was used to specify the maximum allowable unit cell size and header dimensions in a 1 m × 1 m module to maintain acceptable thermal performance, pressure loss, and less than 5% flow mal-distribution. Near the design conditions of an incident flux of 140 W $cm^{-2}$, the predicted receiver efficiency was 90.2%, pressure drop 3.9 bar, and a maximum flow distribution less than 2.2% while heating $sCO_2$ from 550 to 720 °C of the specified design.

As shown in the cost model of the microchannel receiver (Weimar 2018) and in an analysis by the U.S. Department of Energy (Mehos et al. 2017), it is unlikely that a gas-based receiver with a working pressure >200 bar will be able to achieve the cost target of less than 150 $/kWth with existing materials. Thus, there is a movement to consider lower pressure (60–80 bar) gaseous receiver operation to mitigate the high cost of process pipping up and down the tall power tower.

At lower pressures, the volumetric flow rate will be significantly higher due to the lower fluid density. Furthermore, the allowable pressure drop is also less ($\sim$1 bar). These two factors would seem to potentially reduce the viability of a microchannel-based device due to nonlinear increases in pressure drop at higher volume flow rates. However, for the designs discussed above, the flow length and micro-pin heights can be varied to achieve desired performance. To demonstrate the feasibility of achieving efficiency and pressure drop targets for the microscale receiver, Fig. 11.11 shows that a large design space exists where receiver efficiency (>90%), and pressure loss (<1 bar) targets can be met by varying pin array depth and unit cell width for $sCO_2$ as the working fluid at 80 bar (Fronk and Jajja 2018). Simulated results were obtained using the thermal and hydraulic models of Hyder and Fronk (2018). Pin diameter ($D$ = 300 μm) and span ($S$ = 300 μm) remain unchanged from the 200 bar design, providing confidence that the designs will be particularly robust at lower operating pressures. The performance predictions of the scaling models at high and low pressures will be validated in ongoing experimental work by the research groups at UC-Davis and Oregon State University.

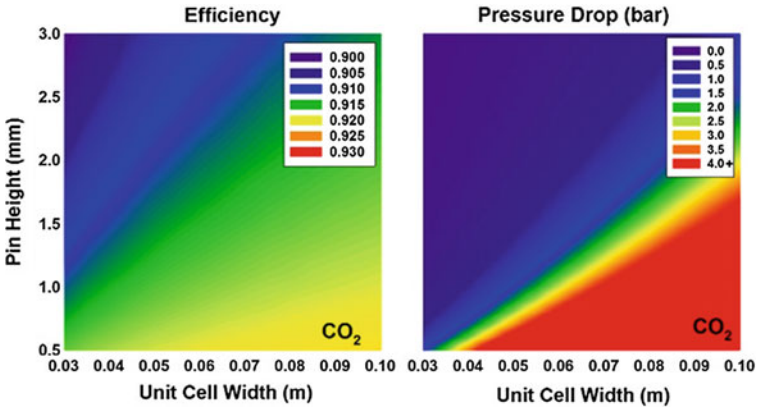


**Fig. 11.11** Receiver efficiency and pressure drop as a function of unit cell width and pin height for carbon dioxide and helium at $P$ = 80 bar, incident flux of 148 W/cm$^2$, absorptivity = 0.96 and emissivity = 0.80

## 11.6 Conclusions and Outlook

The state-of-the-art and advances in concentrated solar thermal power (CSP) generation is discussed in this chapter. Avenues to increasing the efficiency of the CSP are discussed. An overview of the supercritical $CO_2$ Brayton cycle is provided. Potential applications for CSP $sCO_2$ power plants are discussed. Three pathways, based on the heat transfer fluid flowing through the receiver, exist and are the subject of extensive research and development. These include the molten salt receiver pathway, the solid particle receiver pathway, and the gas-phase receiver pathway. An overview of the efforts of the group in development of a microchannel solar receiver for $sCO_2$ was provided. It was shown that lab-scale microchannel receivers can operate at incident fluxes in excess of 100 W/cm$^2$ at thermal efficiencies in excess of 90%. Scale-up of the lab-scale unit cells for commercial plants was presented.

An important advantage of CSP as compared to photovoltaic pathway lies in the ability to store thermal energy at relatively lower cost than as electricity in batteries. The high temperatures and pressures in CSP $sCO_2$ power cycles require the use of expensive and exotic materials such as nickel superalloys. Significant research and development efforts in multidisciplinary areas of material science, advanced fabrication and manufacturing, thermal and fluid sciences, and cost-modeling are needed to realize reliable, cost-competitive CSP $sCO_2$ technology.

**Acknowledgements** Financial support by DOE EERE grants #DE-EE0005801 and DE-EE0007108 is gratefully acknowledged. The work presented here represents the work of several students and their contributions are acknowledged here. The authors would like to acknowledge the contribution of their colleagues, Drs. Kevin Drost and Sourabh Apte. Contributions of Christian Horend for cycle analysis, Eric Truong for $sCO_2$ lab-scale receiver experiments, Charles Rymal for CFD simulations on the unit cell receiver, and Kyle Zada and Matthew Hyder for full-scale receiver design and analysis are acknowledged.

## References

Brun K, Friedman P, Dennis R (eds) (2017) Fundamentals and applications of supercritical carbon dioxide ($sCO_2$) based power cycles, 1st edn. Woodhead Publishing, UK

California Energy Commission (2018) California energy tour-Ivanpah solar electric generation system. http://www.energy.ca.gov/tour/ivanpah/, Accessed July 2018

Fronk BM, Jajja SA (2018) System and component transport considerations of micro-pin based solar receivers with high temperature gaseous working fluids. In: ASME 2018 15th international conference on nanochannels, microchannels, and minichannels, ASME, Dubrovnik, Croatia https://doi.org/10.1115/ICNMM2018-7614

Ho CK (2017) Advances in central receivers for concentrating solar applications. Sol Energy. https://doi.org/10.1016/j.solener.2017.03.048

Ho CK, Iverson BD (2014) Review of high-temperature central receiver designs for concentrating solar power. Renew Sustain Energy Rev 29:835–846. https://doi.org/10.1016/j.rser.2013.08.099

Hyder MB, Fronk BM (2018) Simulation of thermal hydraulic performance of multiple parallel micropin arrays for concentrating solar thermal applications with supercritical carbon dioxide. Sol Energy. https://doi.org/10.1016/j.solener.2018.02.035

Kolb GJ (2011) An evaluation of the next generation of high temperature molten salt power towers. Paper No. SAND11-9320, Sandia National Laboratory, PO Box 5800, Albuquerque, NM

L'Estrange T, Truong E, Rymal C, Rasouli E, Narayanan V, Apte S, Drost MK (2015) High flux microscale solar thermal receiver for supercritical carbon dioxide cycles. In: Proceedings of the ASME 2015 international technical conference and exhibition on packaging and integration of electronic and photonic microsystems and ASME 2015 12th international conference on nanochannels, microchannels, and minichannels InterPACKICNMM2015, 6–9 July 2015, San Francisco, California, USA. Paper: InterPACKICNMM2015-48233

Mehos M, Turchi C, Vidal J, Wagner M, Ma Z, Ho C, Kolb W, Andraka C, Kruizenga A (2017) Concentrating solar power Gen3 demonstration roadmap, Technical Report NREL/TP-5500-67464

Pacheco JE (2002) Final test and evaluation results from solar two project. Paper No. SAND2002-0120, Sandia National Laboratory, PO Box 5800, Albuquerque, NM

Romero M, Buck R, Pacheco JE (2002) An update on solar central receiver systems, projects, and technologies. J Sol Energy Eng. https://doi.org/10.1115/1.1467921

Rymal CJ (2015) Numerical design of a high-flux microchannel solar receiver. MS Thesis, Oregon State University, Corvallis, OR, USA

Rymal CJ, Apte SV, Narayanan V, Drost K (2013) Numerical design of a high-flux microchannel solar receiver. In: Proceedings of the ASME 2013 7th international conference on energy sustainability ES-FuelCell 2013, Minneapolis, MN, 14–19 July 2013. ES-FuelCell2013-18353

Rymal CJ, Apte SV, Narayanan V, Drost K (2014) Numerical design of a planar high-flux microchannel solar receiver. In: Proceedings of the ASME 2013 8th international conference on energy sustainability ES-FuelCell 2014, Boston, MA, 30th June–2nd July 2014. ES-FuelCell2014-6637

SolarPACES (2018) CSP projects around the world. http://www.solarpaces.org/csp-technologies/csp-projects-around-the-world/, Accessed 10th July 2018

U.S. Department of Energy, Concentrating Solar Power. https://www.energy.gov/eere/solar/concentrating-solar-power, Accessed 10th July 2018

Weimar MR (2018) Cost estimate for a commercial scale microchannel solar receiver. PNNL-SA-27252

Zada KR, Hyder MB, Drost MK, Fronk BM (2016) Numbering-up of microscale devices for megawatt-scale supercritical carbon dioxide concentrating solar power receivers. J Sol Energy Eng 138:61007. https://doi.org/10.1115/1.4034516

# Chapter 12
# Reduced Order Heat Exchanger Models for Low-to-Medium Temperature Range Solar Thermal Applications


**Rudrodip Majumdar and Sandip K. Saha**

**Abstract** Pivotal heat transfer components of solar thermal systems may involve single phase flow of the working fluid in some unit (e.g. single phase solar collector), whereas, two phase flow of the working fluid occurs in the other units (e.g. two-phase solar collector coupled directly to the turbine, boilers and evaporators). Modelling of these systems are important to understand the heat transfer behavior, as well as, to develop the system level control among many other attributes. A detailed analysis of single phase and two phase systems is possible using mathematical models to characterize the fluid flow and heat transfer. Detailed description of the fluid flow and heat transfer become computationally very expensive with such models, and also a very high level of precision may not be required in large time (∼few hours) simulations of the systems, as well as, in controlling the entire solar thermal power plant. Hence there is a need to develop computationally fast, low order dynamic models. Among many other modelling approaches, a particular class of heat exchanger model, namely the moving boundary lumped-parameter model, has emerged as an efficient and effective tool for simulating dynamic characteristics of the two-phase solar collectors and the evaporators, pertinent to organic Rankine cycle (ORC) systems. These models are efficient in locating the continuously moving working fluid phase change boundary without requiring any sophisticated, well-trained formulation pertinent to the starting solutions. Even a simplified, reduced order quasi-steady state model is capable of demonstrating moving boundary characteristics in a narrow evaporator tube that is employed to carry organic refrigerant (working fluid) into the two-phase ORC heat exchanger in the medium temperature solar thermal applications (∼200 °C). The model is capable of predicting the variation in working fluid mass flow rates with time-varying temperature of the heat transfer fluid (usually a

R. Majumdar (✉)
Department of Energy Science and Engineering, Indian Institute of Technology Bombay, Mumbai, India
e-mail: rudro.associates@gmail.com

S. K. Saha
Department of Mechanical Engineering, Indian Institute of Technology Bombay, Mumbai, India



H. Tyagi et al. (eds.), *Advances in Solar Energy Research*, Energy, Environment, and Sustainability, https://doi.org/10.1007/978-981-13-3302-6_12

commercial thermic oil), that transfers energy into the organic refrigerant. The variation in wall temperatures of the evaporator tube for three distinct flow regimes of the working fluid (subcooled, two-phase and superheated) can be evaluated with changing average heat transfer fluid (HTF) temperature, corresponding to the varying levels of solar radiation incident on the collectors; and therefore, the model provides an avenue for ascertaining the practicability of the operating conditions based on the variation of the driving parameters values. By using the results of the quasi-steady model as the initial guess in the detailed dynamic model, the sharp transient characteristics can be explored by introducing time-dependent fluctuations in the subcooled refrigerant flow at the heat exchanger entry. Further complexity can be added to the modelling by incorporating axial variation in the heat transfer fluid temperature profile in the prevalent shell and tube heat exchanger. In this monograph, we will briefly discuss about the full-fledged numerical models followed by elaborate description on reduced order models.

**Keywords** Reduced order modelling · Solar thermal system · Moving boundary model

## Nomenclature

$A$ Area of cross section ($m^2$)
$c$ Specific heat (J/kg K)
$D$ Diameter of tube (m)
$h$ Specific enthalpy (J/kg)
$\bar{h}$ Average specific enthalpy (J/kg)
$k$ Thermal conductivity (W/m K)
$L$ Length (m)
$\dot{m}$ Mass flow rate (kg/s)
$p$ Pressure (Pa or bar)
$p_o$ Steady state mean pressure (Pa or bar)
$\tilde{P}$ Solar Irradiation ($W/m^2$)
$q''$ Heat flux ($W/m^2$)
$T$ Temperature (K or °C)
$\bar{T}$ Average temperature (K or °C)
$t$ Time (s or min)
$u$ Internal energy (J/kg)
$v$ Velocity (m/s)
$z$ Distance along length (m)

## Greek Symbols

$\alpha$ Heat transfer coefficient ($W/m^2$ K)
$\delta$ Thermal boundary layer thickness in the thermic oil side (m)
$\eta$ Efficiency

$\rho$ Density (kg/m$^3$)
$\bar{\rho}$ Average density (kg/m$^3$)

## Subscripts

| | |
|---|---|
| 1 | Subcooled region |
| 2 | Two-phase region |
| 3 | Superheated region |
| 12 | Interface 1-2 |
| 23 | Interface 2-3 |
| *b* | Boiler |
| *f* | Saturated liquid |
| conv | Convective |
| *g* | Saturated gas |
| *l* | Liquid |
| HTF | Heat transfer fluid |
| HE | Heat Exchanger |
| *i* | Inner side of the tube |
| in | Inlet of tube or tank |
| *o* | Outer side of the tube |
| out | Outlet of tube or tank |
| lower | Lower end of the limit |
| Rfg | Refrigerant |
| sat | Saturation |
| Solar | Solar |
| sub | Subcooled |
| turbine | Turbine |
| upper | Upper end of the limit |
| wall | Wall |

## Abbreviation

| | |
|---|---|
| DHW | Domestic hot water |
| HE | Heat exchanger |
| HTF | Heat transfer fluid |
| NIST | National Institute of Standards and Technology |
| ORC | Organic Rankine cycle |
| PPS | Peak to peak swing |
| TPHE | Two phase heat exchanger |

## 12.1 Introduction

Earth receives more energy from the sun in just one hour than what the world consumes collectively over a period of one year (Thirugnanasambandam et al. 2010). India, in particular, receives average annual solar radiation amounting to over $5 \times 10^{15}$ kWh (MNRE Annual Report 2006), with the average diurnal incident energy varying between 4 and 7 kWh/m$^2$ depending on the location (Mani and Rangarajan 1982). Therefore, harnessing of the solar energy potential is of interest in order to address the ever increasing demand for the usable energy. Studies indicate that the largest utility expense for a household is the cost to make hot water. Typically, on an average about 20% of total energy consumption in a household is attributed to the domestic hot water applications (e.g. cooking, cleaning, bathing) and the share increases to about 50% if the hot water is also used for heating purposes (Solar Thermal Hot Water Systems and Individual Components 2018). Naturally solar thermal energy technologies in particular have emerged as lucrative options for the domestic hot water (DHW) systems as well as for the production of heat for residential space heating (Thirugnanasambandam et al. 2010; Solar Thermal Hot Water Systems and Individual Components 2018; Kalogirou and Tripanagnostopoulos 2006; Natural Resources Canada 2005; Pinel et al. 2011; Weiss 2012; Evarts and Swan 2013; Aguilar et al. 2005; Fairey and Parker 2004; Becker and Stogsdill 1990; Mills 2004; Mathioulakis and Belessiotis 2002; Davidson 2005; Sarbu and Adam 2011; Baddou 2017; Homola 2018; Renewable Energy Solutions 2018). The earliest commercial solar water heater was introduced by Clarence Kemp in the 1890s in California. This primitive heating system was a simple batch type solar water heater that combined the collector and the storage in a single box. For an investment of $25, the annual savings in the coal costs was found to be about $9 (Homola 2018). The variation in the expenses incurred depends on the size of a system, amount of the water to be heated, the type of fuel used to heat water and how the heating system fits into the existing plumbing. Generally, the solar hot water systems designed for the warmer places (e.g. thermosiphon systems) are cheaper and more efficient compared to the more complex systems used in the colder regions (e.g. systems with vacuum tube collectors, pumps, heat exchangers, antifreeze mixtures, controls). Typically, the solar domestic hot water systems in Europe are sized to provide approximately 50–70% of the annual heating load (Renewable Energy Solutions 2018).

Design of low-to-medium temperature solar thermal systems needs to consider the heat transfer fundamentals in connection with the solar radiation levels, the collector configurations, the transfer of the collected heat and the storage of the collected heat to ensure reliable long-term system performance (Lunde 1980). Solar water heating systems use heat exchangers to transfer solar energy absorbed in solar collectors to the heat transfer fluid (liquid or air) used to heat water or a space. Heat exchangers (HE) are usually made of metals with reasonably high thermal conductivity, e.g. steel, copper, bronze, stainless steel, aluminium, cast iron etc. For the domestic solar heating systems copper is prevalently used in HE, due to its high

thermal conductivity (∼386 W/m K at 20 °C) as well as higher resistance to corrosion compared to the other candidates (Heat Exchangers for Solar Water Heating Systems 2018). The simplest form of heat transfer is single-phase heat exchange, where the heat transfer fluid (HTF) remains in the same phase (i.e. liquid or gas) throughout the process. The plate heat exchangers are the most studied and prevalently used heat exchanger configuration for the single phase liquid to liquid or air to liquid heat transfer (Nilpueng and Wongwises 2015; Khan et al. 2010; Li and Hrnjak 2016; Kim and Park 2017; Muley and Manglik 1997).

In a single-phase heat exchanger (SPHE), usually a liquid is preferred over the gas for the heat transfer process, since a liquid is a better thermal conductor than a gas, and therefore it requires much less surface area for effective heat transfer. The amount of heat transfer from one fluid to another is directly proportional to the temperature difference between the fluids. By keeping the heat load unchanged, the temperature difference between the working fluids can be increased either by raising the temperature of the heat source fluid, and/or by lowering the temperature of the heat sink fluid. The temperature difference can also be enhanced by increasing the mass flow rate of one (or, ideally both) of the fluids (Single Phase Fluid Coils 2018; Mehendale 2017). Although, it is to be mentioned that in case of unchanged heat load, a large temperature difference or higher flow rate will cause reduction in heat transfer time.

An alternative way of single phase heating employs ‘thermosyphon’, where passive heat exchange takes place due to the natural convection that circulates the liquid (working fluid) without the necessity of a mechanical pump (Kalogirou 2009; Koffi et al. 2008; Hobson and Norton 1988; Tang et al. 2010; Zelzouli et al. 2014; Tchuen and Koholé 2017; Taherian et al. 2011). Several experimental as well as numerical studies pertinent to the thermosyphon systems in connection with flat plate solar collectors have been previously reported along with some performance metrics (Koffi et al. 2008; Hobson and Norton 1988; Tang et al. 2010; Zelzouli et al. 2014; Tchuen and Koholé 2017; Taherian et al. 2011). One of the key performance parameter is the energy efficiency of the solar collector, which is expressed as the ratio of the amount of useful heat collected to the total amount of solar radiation striking the collector surface during any period of time (Tchuen and Koholé 2017). The energy efficiency of the thermosyphon solar water heating (TSWH) systems with different flat-plate collector configurations (based on the position of the riser tubes) have been previously reported for the same weather conditions. For the absorber-pipe lower bond configuration (i.e. riser tubes are welded above the absorber tube), the average value of the energy efficiency was found to be about 39.47%. The reported value of energy efficiency for the absorber-pipe side bond configuration (i.e. the absorber tube is welded in a way such that each interior absorber tube segment connects two consecutive riser tubes in the array) is 34.86% and that for the absorber-pipe upper bond configuration (i.e. the riser tuber welded below the absorber tube) is 32.28% (Tchuen and Koholé 2017).

For plant-scale production of solar thermal energy (in the range of hundreds of $kW_t$ to $MW_t$) the heat exchangers are configured to work in the two-phase flow mode where latent heat of evaporation of a vapour-liquid mixture is used to improve the transport capacity as well as to enhance the heat transfer process

(Kakaç et al. 1988; Shoureshi and McLaughlin 1984; Manglik 2006; Thome 1990). Simulation of the dynamic response of two-phase heat exchangers (TPHE) is of interest in order to increase reliability of various thermofluid systems as well as to facilitate significant energy savings (Shoureshi and McLaughlin 1984). Several computer codes have been previously developed to analyze the design and operational characteristics of residential heating and cooling equipment. Significant effort has been put towards the derivation of accurate, simple dynamic models of heat exchangers (Shoureshi and McLaughlin 1984; Paynter and Takahashi 1956; Wormley and Masada 1982; Pingaud et al. 1989; Roetzel 1996; Du et al. 1996; Roetzel and Xuan 1999).

Available literature has reported very few analytical solutions pertinent to heat flow and diffusion processes that involve phase change of the working fluid in a solar thermal system in particular and in similar relevant physical systems in general (Mongibello et al. 2014; Endalew and Abebe 2012). In connection to the solar thermal applications, a few implicit as well as mixed numerical techniques can be found in the published literatures, accompanied by different solution approaches and assumptions. Transient numerical model for the solar domestic hot water (DHW) system has been reported recently, with the solar collector being simulated by a zero-dimensional analytical model (Mongibello et al. 2014). In a zero-dimensional model the collector is treated as a single point with a single average temperature. One-dimensional numerical models were employed to find the temperature profile in the heat transfer fluid as well as in the water inside the hot water tank. The finite difference implicit scheme was utilized to solve for the energy balance in the coil heat exchanger and in the hot water tank. The energy conservation equations for the different solar DHW components were numerically coupled with the help of an implicit scheme based in-house computational code (Mongibello et al. 2014).

Implementation of advanced control techniques for the energy systems that rely upon the intermittent sources of heat energy (e.g. solar radiation), as well as, improvement in the overall efficiency necessitate computationally fast and, at the same time, adequately accurate system level dynamic models. Continued research effort in the direction of control-oriented modelling has resulted in the emergence of a particular category of simplified reduced-order models, formally classified as moving-boundary models (Eldredge and Alleyne 2006). Conventionally, for the physical systems that undergo a phase change at a specified temperature, the continuously shifting phase change boundary is detected by the means of a sweeping algorithm working over a region that is approximated and represented by a finite number of points. It is to be noted that there are significant challenges in obtaining accurate phase change boundaries using such a method. In order to improve the performance of the sweeping algorithm, a few solving techniques such as moving grid points and isotherm migration have been introduced, where specified isotherms are traced during their migration through the solution space, instead of determining the temperature at the spatial location and time instant of interest (Voller and Cross 1981; Wood 1991). However, well-formulated starting solutions are required to achieve meaningful results from the above-mentioned methods even in one-dimensional problems. Moving boundary method is capable of giving very

accurate results over enthalpy methods without requiring well-formulated starting solutions, especially when the phase change takes over a very small temperature range or practically the process degenerates to a single temperature (Voller and Cross 1981). Therefore, in the context of solar thermal applications, low-order lumped parameter moving boundary models prove to be instrumental for the dynamical simulation of transient models and in determining the principal control parameters for the pivotal components, such as boilers and evaporators, where the phase change takes place in the working fluid side (Jensen and Tummescheit 2002; Zhang and Zhang 2006; Grald and MacArthur 1992; Shi et al. 2016). In such models, the flow of the working fluid inside the evaporator tube and the flow of the exhaust gas is considered to be one-dimensional. The pressure drop across the length of the evaporator is assumed to be negligible and this particular assumption leads to a reduced order model, as the need for momentum conservation goes away (Shi et al. 2016). The evaporator tube is considered to be thin, long and horizontal. The axial heat conduction is neglected in the working fluid as well as in the exhaust gas. The axial heat conduction in the tube wall is ignored as well. Another approach of convenience, in the context of renewable energy systems, is to use quasi-steady state models considering a reasonably large time step ($\sim$1 h) to facilitate ease of computation and validation, assuming the overall performance of the system to remain unfazed by the variability of the load and intermittency of the renewable sources within that time span (Hoevenaars and Crawford 2012).

## 12.2 Discussion About Specific Numerical Models

### *12.2.1 Modeling of Heat Exchanger (Boiler) in an ORC Based Solar Thermal Power Plant*

In the foregoing discussion, numerical models of heat exchanger pertinent to solar thermal applications reported in published literature are elaborated. The first model describes a heat exchanger used as a boiler in an ORC based solar thermal power plant (Fig. 12.1) with a view to understanding its interaction with other components in the power plant for extending electricity generation after sunset (Lakhani et al. 2017). The aforesaid heat exchanger is modelled by assuming that the HTF enters a heating coil that passes through a tank of saturated liquid ORC, as shown in Fig. 12.2. The temperature of HTF inside the coil varies with time and distance along the coil while the temperature of organic fluid in the boiler is assumed to be constant during phase change.

The energy balance equation for the HTF in the coil is written as follows (Powell and Edgar 2012),

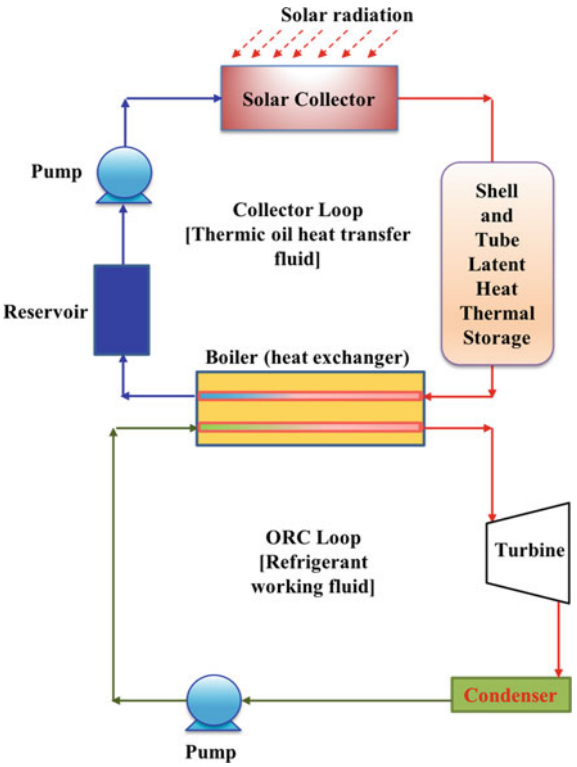


**Fig. 12.1** Schematic diagram of ORC based solar thermal power plant with latent heat thermal storage system

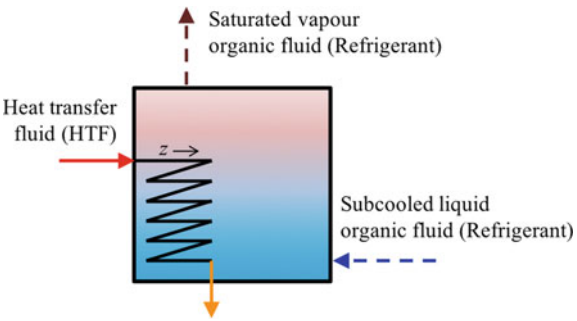


**Fig. 12.2** Schematic diagram of heat exchanger (boiler)

$$\rho_{\mathrm{HTF}} c_{p,\mathrm{HTF}} A_{b,i} \frac{\partial T_{\mathrm{HTF}}}{\partial t} + \dot{m}_{\mathrm{HTF}} c_{p,\mathrm{HTF}} \frac{\partial T_{\mathrm{HTF}}}{\partial z} = h_{\mathrm{conv},b} P_{b,i} (T_b - T_{\mathrm{HTF}}) \qquad (12.1)$$

where, $z$ represents the distance along the boiler coil, $T_b$ is the boiler organic fluid temperature and $A_{b,i}$ and $P_{b,i}$ represent the surface area and perimeter of the inner tube ($r_{p,i}$ = 0.03 m), respectively. The mass flow rate of the saturated organic fluid can be calculated from the steady-state energy balance on the boiler as,

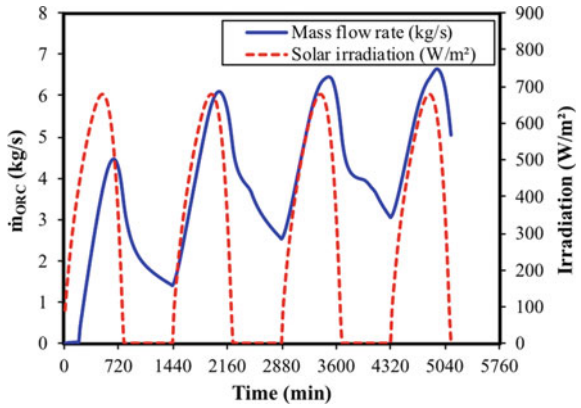


**Fig. 12.3** Transient variation of solar irradiation and mass flow rate of organic fluid to generate 200 $kWh_t$

$$\dot{m}_{\mathrm{HTF}} c_{p,\mathrm{HTF}} (T_{\mathrm{in}} - T_{\mathrm{out}}) = \dot{m}_{ORC} \left[ h_{\mathrm{fg}} + \left( h_f - h_{\mathrm{sub},l} \right) \right] \tag{12.2}$$

where, $h_{\mathrm{fg}}$ is enthalpy of vaporization of the organic fluid at temperature $T_b$, $h_f$ is the enthalpy of saturated organic fluid and $h_{\mathrm{sub},l}$ is the enthalpy of subcooled organic fluid.

Figure 12.3 shows the temporal variation in mass flow rate of organic fluid and solar radiation for four days of continuous operation of two-stage solar thermal power plant (Fig. 12.1). The parabolic solar collector of with dimensions 1500 (length) × 6 m (width) are considered for generating 200 $kWh_t$ from the turbine. A shell and tube latent heat thermal storage system with representative dimension of shell diameter ($D_i$) of 98 mm, and HTF tube of $D_{i,\mathrm{HTF}}$ = 50 mm and $D_{o,\mathrm{HTF}}$ = 56 mm and total length of 4800 m is chosen in this study. An organic fluid R134a flows through the boiler tube of length 200 m and exchanges heat with Hytherm 600 (constant mass flow rate = 13.8 kg/s) in the collector loop. The ORC loop is pressurized at 3 MPa. The mass flow rate of organic fluid is observed to be varying with time according to the power output from the turbine. Details of the analysis can be found in (Lakhani et al. 2017).

### *12.2.2 Quasi Steady-State Reduced Order Moving Boundary Model for ORC Heat Exchanger*

The second model of interest is the quasi steady-state reduced order moving boundary model for the medium temperature range (∼120–200 °C) solar thermal applications. Recently reported work (Majumdar et al. 2018a) illustrated that a simplified quasi-steady state reduced order model is adequate for exhibiting the continuously changing phase change boundary characteristics in a narrow evaporator tube of a two-phase ORC heat exchanger. The model predicts the variation in ORC working fluid (refrigerant) mass flow rates with varying temperature of the

commercial thermic oil employed as the heat transfer fluid to transfer heat content to the organic refrigerant (Majumdar et al. 2018a; Majumdar and Saha 2018) through the wall of the narrow evaporator tube. The average heat transfer fluid temperature ($T_{HTF}$) changes with the solar radiation incident on the solar collectors. The quasi-steady model enables prediction of the changes in temperature of the evaporator tube wall segments (subcooled, two-phase and superheated) with changing $T_{HTF}$. Very high tube wall segment temperatures have been predicted for the higher values of $T_{HTF}$. Additionally, the prescribed mass flow rates of the working fluid (refrigerant) have been found to very high as well, for higher values of $T_{HTF}$. Thus, the model serves as a useful tool for examining the viability of the operating conditions based on the temporal variation of the driving parameters, such as the solar radiation and $T_{HTF}$. The results of the quasi-steady model can be used as the initial guess in the computational algorithm developed for a detailed dynamic model, in order to explore the sharp transient characteristics by introducing time-dependent fluctuations in the subcooled refrigerant flow at the inlet of the two-phase ORC heat exchanger.

The quasi-steady state model was employed to investigate the moving boundary characteristics in the narrow evaporator tube of a two-phase ORC heat exchanger that carries an organic refrigerant. For the purpose of computational demonstration, a well-known and widely used hydrofluorocarbon compound named 1,1,1,2-Tetrafluoroethane (R134a), with a molecular formula: $CH_2FCF_3$ and formula weight of 102 kg/kmol, has been utilized (Vélez et al. 2014). The evaporator tube is placed inside a solar-thermal heat-exchanger (HE) reservoir (Fig. 12.4) that contains commercialized thermic oil (Hytherm 600), which is considered as HTF (Shinde et al. 2017). Fixed thermodynamic conditions of superheated refrigerant vapor have been assumed at the evaporator exit and the variation in refrigerant mass flow rate with changing temperature of heat transfer fluid ($T_{HTF}$) has been investigated for the chosen evaporator tube lengths of 5 and 10 m, respectively, with

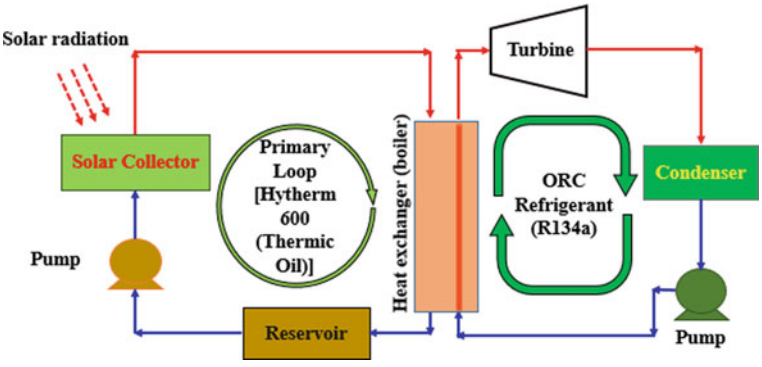


**Fig. 12.4** Representative layout of the primary and secondary loops in a simplified ORC-based solar thermal power plant (Majumdar et al. 2018a). (Reproduced with permission from © 2018 Elsevier)

suitable constraints on the lengths of distinct flow segments (subcooled, two-phase and superheated).

The temperature of the thermic oil flowing in the collector loop is dependent on the level of available solar radiation. During a bright and cloudless day in India, the magnitude of solar radiation received at the earth surface (i.e. solar collector) increases with time and eventually reaches a peak value around noon. The solar radiation level decreases in the afternoon as the daylight diminishes and eventually ceases to exist in the evening. Therefore, during a diurnal solar radiation cycle, a rise phase is followed by a fall phase and this aspect needs to be taken into account in the time-dependent solar collector models. Relevant figures presented in the work by Lakhani et al. (Lakhani et al. 2017), shows that the heat transfer fluid temperature ($T_{HTF}$) keeps increasing as the intensity of the solar radiation increases and subsequently it reaches a maximum value as the solar radiation level reaches the diurnal peak. Thereafter, as the day progresses, the value of $T_{HTF}$ decreases as the solar radiation level keeps diminishing. However, the value of $T_{HTF}$ is found be considerably higher during the fall phase of solar radiation cycle than that observed during the rise phase for the same power level, due to different heat transfer rates (Majumdar et al. 2018a). The temperature of Hytherm 600 (HTF) at the collector outlet is calculated by assuming a fixed mass flow rate of 13.8 kg/s flowing through the collector loop (Fig. 12.4). The collector is modelled by following the parabolic trough configuration as described in the previously reported works (Powell and Edgar 2012; Behar et al. 2015). Figure 12.5 exhibits the temporal variation in HTF temperature ($T_{HTF}$) for the solar radiation data of Greater Noida, Uttar Pradesh, India; collected on June 2, 2016 (Lakhani et al. 2017; Majumdar et al. 2018a). For the illustrative computational results, the solar radiation profile stretching over a total time period of 640 min is used; where 7:20 AM in the morning is considered to be the starting time ($t = 0$) and the successive sample instances are separated by a uniform interval of 20 min (Majumdar et al. 2018a).

**Conceptualization of phase change in the ORC heat exchanger**. The schematic diagram of the evaporator tube (Fig. 12.6) exhibits three distinct phase segments of the working fluid, R134a. The evaporator tube is assumed to be placed

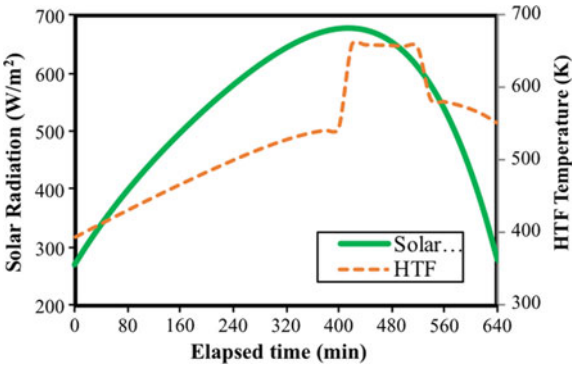


**Fig. 12.5** Variation of the temperature of Hytherm 600 ($T_{HTF}$) with the representative diurnal solar radiation profile $\left(\tilde{P}_{solar}\right)$ ($t = 0$ corresponds to 7:20 AM) (Majumdar et al. 2018a). (Reproduced with permission from © 2018 Elsevier)

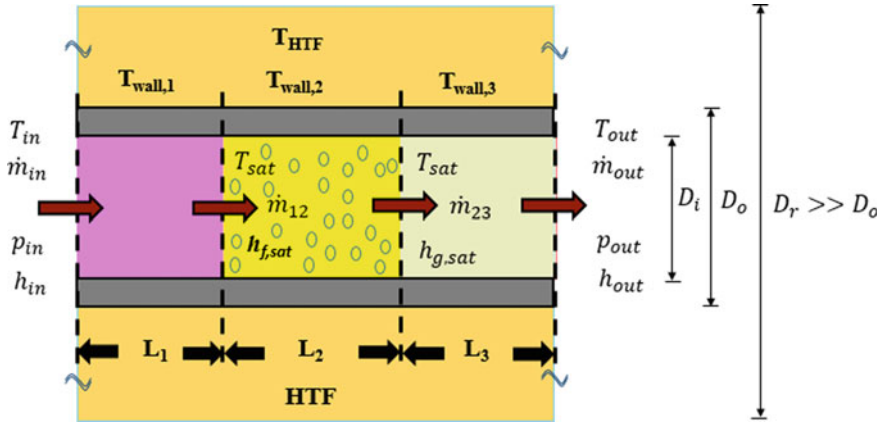


**Fig. 12.6** Representative layout of the narrow evaporator tube placed in the thermic oil reservoir ($D_r \gg D_o$), (From left to right, the colored zones represent (i) sub-cooled segment, (ii) two-phase flow segment and (iii) superheated segment, respectively) (Majumdar et al. 2018a). (Reproduced with permission from © 2018 Elsevier)

inside a thermic oil reservoir with a diameter much greater than that of the evaporator tube, i.e. ($D_r \gg D_o$). Additionally, the thermal boundary layer thickness in the thermic oil side ($\delta$) has been assumed to be considerably smaller than the annular span, i.e. $2\delta \ll (D_r - D_o)$. Furthermore, the thermic oil reservoir is assumed to be insulated on the outer surface. In an actual solar thermal power plant, a finite drop in the temperature is observed between the inlet and outlet of the thermic oil side in the heat exchanger employed in the load loop. This change in $T_{\mathrm{HTF}}$ takes place due to the transfer of heat content from the thermic oil (HTF) to the refrigerant (working fluid). However, the quasi-steady state reduced order moving boundary model assumes the simplification of an average value of the HTF temperature, and uses the linear average of the HTF temperatures at the inlet and the outlet of the ORC heat exchanger, respectively.

**Computational set-up**. For an illustrative computational demonstration of the quasi-steady reduced order moving boundary model in the two-phase load loop heat exchanger, evaporator tube lengths of 5 and 10 m have been chosen, as mentioned before. The operating pressure is assumed to be constant at 30 bar over the whole length of the heat-exchanger tube (*i.e.* $p_{\mathrm{in}} = p_{\mathrm{out}}$), and any change in pressure in the axial direction is neglected. This assumption prompts a quasi-steady operational condition. Subsequently, the mass flows across the various flow regimes can be equated to the steady state mass flow rate at the inlet of the ORC two-phase heat exchanger. The subcooled working fluid (refrigerant) enters the evaporator tube, where the subcooling margin ($T_{\mathrm{sat}} - T_{\mathrm{in}}$) is assumed to be approximately 40 °C. At length $L_1$ inside the evaporator tube (Fig. 12.6), the working fluid refrigerant becomes a saturated liquid, accompanied by a dryness fraction value of zero. The boiling begins at the axial location $L = L_1$, and the void fraction starts to increase. At the axial location $L = L_1 + L_2$, the flow becomes a completely dry, saturated

steam. Thereafter, the dry refrigerant vapor gradually becomes superheated steam at 30 bar and acquires a significantly high temperature ($T_{out}$) as well as high specific enthalpy ($h_{out}$) at the exit of the evaporator tube and this superheated vapour enters the turbine.

Thermodynamically, R134a is an isentropic fluid and therefore the fluid flow at the turbine exit is assumed to be a saturated dry steam. The ambient temperature soars to about 45 °C during the scorching summer days in the western region of India. On top of that, it is assumed that there is a margin of temperature drop of 25 °C across the condenser unit. Therefore, upon taking into consideration the peak ambient temperature, the vapor temperature at the exit of the turbine is found as 70 °C. From the database of thermodynamic properties, the pressure at the exit of the turbine ($p_{out,turbine}$) is found to be 21.2 bar and the corresponding specific enthalpy at the turbine exit ($h_{out,turbine}$) is 280.48 kJ/kg (Majumdar et al. 2018a).

The flow enthalpy at the turbine inlet can be calculated using Eq. 12.3 as,

$$\left(\frac{\dot{W}_{net}}{\eta_{isentropic}}\right) = \dot{m}\left(h_{in,turbine} - h_{out,turbine}\right) \tag{12.3}$$

where, the isentropic efficiency ($\eta_{isentropic}$) of the turbine is chosen as 68.1% for a representative output power level of 200 $kW_t$ (Sung et al. 2016). A representative steady state test mass flow rate value ($\dot{m} = 6.65 kg/s$) is used, along with $\dot{W}_{net} = 200\,kW_t$ and the aforesaid calculated value of $h_{out,turbine}$; and the value of specific enthalpy at the turbine inlet $\left(h_{in,turbine}\right)$ is found to be 324.64 kJ/kg, which is equal to the specific enthalpy at the evaporator tube exit ($h_{out}$). The corresponding temperature of the superheated vapor ($T_{out}$) at 30 bar is approximately 364.31 K (Majumdar et al. 2018a).

**Governing equations of quasi-steady moving boundary model**. As the pressure gradient in the axial direction is neglected in the evaporator tube at the two-phase ORC heat exchanger, only mass and energy balances are considered in the reduced order modelling approach. The relevant equations are solved numerically for the average values of interest in the three distinct flow segments (subcooled, two-phase and the superheated), respectively; by treating each zone as a single node.

The general differential mass balance equation for a working fluid can be written as (Jensen and Tummescheit 2002),

$$\frac{\partial \rho}{\partial t} + \nabla \cdot (\rho \vec{v}) = 0 \tag{12.4}$$

where, $\rho$ denotes density, $t$ represents time and $v$ symbolizes velocity.

For one-dimensional flow, Eq. 12.4 is reduced to,

$$\frac{\partial A\rho}{\partial t} + \frac{\partial \dot{m}}{\partial z} = 0 \tag{12.5}$$

where, $z$ represents the length traversed by the working fluid, $t$ denotes time, $\dot{m}$ is the working fluid mass flow rate and $A$ represents the cross-sectional area of the evaporator tube.

The general differential energy balance equation for a working fluid is given by,

$$\frac{\partial \rho h}{\partial t} + \nabla \cdot (\rho h \vec{v}) = -\nabla . \vec{q}'' - q''' + \frac{\mathrm{d}p}{\mathrm{d}t} + \varphi \tag{12.6}$$

where, $h$ symbolizes specific enthalpy of the working fluid, $\varphi$ denotes the dissipation function, $\vec{v}$ symbolizes the velocity, $\vec{q}''$ and $q'''$ stand for is heat flux and the volumetric energy density, respectively.

For a one dimensional flow, the axial conductivity, radiation and the viscous stress terms are neglected for the sake of simplification in the energy balance, and hence, Eq. 12.6 can be rewritten as,

$$\frac{\partial (A\rho h - Ap)}{\partial t} + \frac{\partial \dot{m} h}{\partial z} = \pi D \alpha \left(T_{\text{wall}} - T_{\text{Rfg}}\right) \tag{12.7}$$

where, $D$ is the inner diameter of the evaporator tube, $\alpha$ represents the average heat transfer coefficient, $T_{\text{wall}}$ symbolizes the wall temperature and $T_{\text{Rfg}}$ stands for the refrigerant bulk temperature.

The differential energy balance for the evaporator tube wall is obtained by simplifying Eq. 12.6, and upon neglecting the axial conductivity as well as the flow terms (Jensen and Tummescheit 2002), the required expression turns out to be,

$$c_{\text{wall}} A_{\text{wall}} \rho_{\text{wall}} \frac{\partial T_{\text{wall}}}{\partial t} = \alpha_i \pi D_i \left(T_{\text{Rfg}} - T_{\text{wall}}\right) + \alpha_o \pi D_o (T_{\text{HTF}} - T_{\text{wall}}) \tag{12.8}$$

where, $c_{\text{wall}}$ stands for the heat capacity of the tube wall material, $D_i$ and $D_o$ symbolize the inner and outer diameter of the evaporator tube, respectively; $\rho_{\text{wall}}$ represents the density of the tube wall material, $A_{\text{wall}}$ represents total area of the evaporator tube wall, $T_{\text{HTF}}$ stands for the average heat transfer fluid temperature around the evaporator tube, $\alpha_i$ and $\alpha_o$ symbolize the average inner and outer heat transfer coefficients of the evaporator tube, respectively.

Under a steady state operational condition, the conservation of fluid mass across all the flow segments, including the interfaces of the distinct flow regimes, gives,

$$\dot{m}_{\text{in}} = \dot{m}_{12} = \dot{m}_{23} = \dot{m}_{\text{out}} \tag{12.9}$$

where, $\dot{m}_{\text{in}}$ represents the mass flow rate subcooled refrigerant at the entry of the ORC two-phase heat exchanger, $\dot{m}_{12}$ and $\dot{m}_{23}$ represent the mass flow rates at the interfaces 1-2 and 2-3, respectively.

At the steady state condition, the energy balance equation in the subcooled region reduces to (Majumdar et al. 2018a; Majumdar and Saha 2018),

$$\dot{m}_{\text{in}} h_{\text{in}} - \dot{m}_{12} h_l(p) + \pi D_i \alpha_{i1} L_1 \left(T_{\text{wall},1} - \widetilde{T}_{\text{Rfg},1}\right) = 0 \tag{12.10}$$

where, $h_{\text{in}}$ denotes the specific enthalpy of the subcooled refrigerant at the evaporator inlet, $h_l(p)$ represents the enthalpy of the saturated refrigerant fluid at the fluid interface 1-2; $L_1$ denotes the length of the subcooled flow segment, $T_{\text{wall},1}$ symbolizes the constant wall temperature of the subcooled segment, $\widetilde{T}_{\text{Rfg},1}$ stands for the average refrigerant temperature in the subcooled segment, $\alpha_{i1}$ denotes the average inner heat transfer coefficient in the subcooled segment.

Similarly, the energy balance equation for the two-phase region becomes,

$$\dot{m}_{12} h_l(p) - \dot{m}_{23} h_g(p) + \pi D_i \alpha_{i2} L_2 \left(T_{\text{wall},2} - \widetilde{T}_{\text{Rfg},2}\right) = 0 \tag{12.11}$$

where, $h_g(p)$ is the specific enthalpy of the saturated steam at the fluid interface 2-3; $L_2$ denotes the length of the two-phase flow segment, $T_{\text{wall},2}$ symbolizes the constant wall temperature of the two-phase segment, $\widetilde{T}_{\text{Rfg},2}$ stands for the average refrigerant temperature in the two-phase zone and $\alpha_{i2}$ represents the average inner heat transfer coefficient in the two-phase zone.

The energy balance in the superheated segment of the working fluid flow leads to,

$$\dot{m}_{23} h_g(p) - \dot{m}_{\text{out}} h_{\text{out}} + \pi D_i \alpha_{i3} L_3 \left(T_{\text{wall},3} - \widetilde{T}_{\text{Rfg},3}\right) = 0 \tag{12.12}$$

where, $h_{\text{out}}$ stands for the specific enthalpy of the superheated steam at the outlet of the evaporator tube, $L_3$ symbolizes the length of the superheated flow segment, $T_{\text{wall},3}$ denotes tube wall temperature in the superheated segment, $\widetilde{T}_{\text{Rfg},3}$ symbolizes the average temperature of superheated refrigerant vapor and $\alpha_{i3}$ denotes the average inner heat transfer coefficient in the superheated region.

At a steady state condition, the energy balance equations for the evaporator tube wall corresponding to the three distinct flow segments can be obtained from Eq. 12.6, and are as below,

(a) In the subcooled region, the energy balance in the tube wall leads to,

$$\pi D_i \alpha_{i1} L_1 \left(\widetilde{T}_{\text{Rfg},1} - T_{\text{wall},1}\right) + \alpha_o \pi D_o L_1 \left(T_{\text{HTF}} - T_{\text{wall},1}\right) = 0 \tag{12.13}$$

(b) In the two-phase flow segment, the energy balance in the tube wall gives,

$$\pi D_i \alpha_{i2} L_2 \left(\widetilde{T}_{\mathrm{Rfg},2} - T_{\mathrm{wall},2}\right) + \alpha_o \pi D_o L_2 \left(T_{\mathrm{HTF}} - T_{\mathrm{wall},2}\right) = 0 \tag{12.14}$$

(c) In the superheated segment the relevant expression turns out to be,

$$\pi D_i \alpha_{i3} L_3 \left(\widetilde{T}_{\mathrm{Rfg},3} - T_{\mathrm{wall},3}\right) + \alpha_o \pi D_o L_3 \left(T_{\mathrm{HTF}} - T_{\mathrm{wall},3}\right) = 0 \tag{12.15}$$

The wall temperatures for the respective segments can be obtained by using Eqs. 12.13 to 12.15 for a quasi-steady operational condition. Thereafter, the wall temperatures are used to estimate the length of the respective flow regimes by utilizing Eqs. 12.10 to 12.12. For the above-mentioned calculation, the average temperature of the bulk refrigerant in each of the three flow regimes is required. The average temperatures in the flow segments of interest, $\widetilde{T}_{\mathrm{Rfg},1}$, $\widetilde{T}_{\mathrm{Rfg},2}$ and $\widetilde{T}_{\mathrm{Rfg},3}$, respectively, are calculated by utilizing the flow conditions specified at the inlet and outlet of the evaporator tube, as well as, the thermodynamic parameters corresponding to the saturation condition.

At the steady state pressure $p$, the specific volumes corresponding to the inlet temperature ($T_{\mathrm{in}}$) and the saturation temperature ($T_{\mathrm{sat}}$), respectively, can be obtained from the database of thermodynamic properties and hence, the densities can also be easily calculated as well.

Assuming the working fluid densities corresponding to the temperatures $T_{\mathrm{in}}$ and $T_{\mathrm{sat}}$ to be $\rho_1(0)$ and $\rho_1(L_1)$, respectively. The average density in the subcooled flow segment is calculated as (Majumdar et al. 2018a),

$$\overline{\rho_1} = \frac{2}{3}\rho_1(0) + \frac{1}{3}\rho_1(L_1) \tag{12.16}$$

Once the average density is found, the average temperature of the refrigerant in the subcooled flow segment, $\widetilde{T}_{\mathrm{rfg},1}$, can be obtained from the thermodynamic database. In the two-phase flow segment, the average refrigerant temperature $\widetilde{T}_{\mathrm{Rfg},2}$ is equal to the saturation temperature at the steady state pressure level $p$. In the superheated flow segment of length $L_3$, the average vapour temperature $\widetilde{T}_{\mathrm{Rfg},3}$ is calculated as (Majumdar et al. 2018a),

$$\widetilde{T}_{\mathrm{Rfg},3} = \frac{1}{3}T_{\mathrm{Rfg},3}(0) + \frac{2}{3}T_{\mathrm{Rfg},3}(L_3) \tag{12.17}$$

where, $T_{\mathrm{Rfg},3}(0)$ represents the saturation temperature at the steady state pressure level $p$, and $T_{\mathrm{Rfg},3}(L_3)$ denotes the temperature of the superheated vapour at the evaporator tube exit. These approximations are made with the assumption that the axial profiles of the temperature and the density of the ORC working fluid follow quadratic nature. However, more complicated profiles can be assumed for the

working fluid with the inclusion of axial heat conduction and dissipation terms in the energy balance equation.

The prime focus of the quasi-steady moving boundary modelling approach is to find the lengths of the subcooled, two-phase and superheated segments in the narrow evaporator tube as well as the constant wall segment temperatures. From the mathematical formulation itself, it is quite evident that the heat transfer coefficient of a particular flow segment plays a very important role in determining length of that flow regime and also the constant tube wall temperature of that flow segment. It must be mentioned that the moving boundary model for one -dimensional fluid flow assumes an average inner heat transfer coefficient for each of the distinct flow segments of interest and also an average outer heat transfer coefficient (Jensen and Tummescheit 2002; Zhang and Zhang 2006; Grald and MacArthur 1992; Shi et al. 2016), as each of the sectional segments is represented by a single node.

Previously reported work, pertinent to the modeling and simulation of two-phase flow evaporators for parabolic-trough based solar thermal installations, mentions the application of the concept of heat transfer driven by an average heat transfer coefficient in each of the flow segments and approximation of regime-specific average heat transfer coefficient values (Cruz et al. 2013). Similar concept has also been utilized in control volume based object oriented modeling (Yebra 2006).

The Dittus-Boelter correlation is used to estimate the average inner heat transfer coefficient in the subcooled and superheated flow regimes (Dittus and Boelter 1930). For an average mass flow rate of 3 kg/s through the evaporator tube, the inner heat transfer coefficient for the subcooled segment, at the pumping pressure level of 3 MPa, is calculated to be 6071 $Wm^{-2}\ K^{-1}$, and that for the superheated region is calculated as 4868 $Wm^{-2}\ K^{-1}$. The calculated heat transfer coefficients are compared with the published experimental values (Li and Hrnjak 2017; Meyer 2014) and a good agreement is found. The calculated values of the heat transfer coefficient differ from the reported experimental values, as the experimental conditions (i.e. pressure, temperature, mass flow rate etc.) under which the heat transfer coefficients were measured are very different from those considered in the illustrative computational example.

It is noteworthy that the simplified reduced order quasi-steady model does not take into account the heat-flux transferred from the thermic oil side into the refrigerant flowing through the evaporator tube in the ORC heat exchanger. Furthermore, the reduced order modeling the study utilizes a time-invariant average void fraction for the two-phase region. Therefore, the average inner heat transfer coefficient in the two-phase region is iteratively calculated using Donowski-Kandlikar correlation (Donowski and Kandlikar 1999). For an average heat flux $\sim$900 $kWm^{-2}$, an average operating refrigerant mass flow rate of 3 kg/s and by assuming an average void fraction of 0.665 (Jensen and Tummescheit 2002), the aforesaid heat transfer coefficient is estimated to be 25,058 $Wm^{-2}\ K^{-1}$.

The heat transfer coefficient of Hytherm 600 (HTF) is usually low and moreover, the thermophysical properties of this lubricant oil are not yet well characterized at temperatures in excess of 305 °C. The Gnielinski correlation (Gnielinski 1975), is used to estimate the outer heat transfer coefficient in the thermic oil side. For a

thermic oil mass flow rate of 13.8 kg/s circulating in the primary loop (collector loop) and a thermic oil reservoir diameter ($D_r$) of 0.252 m, the average outer heat transfer coefficient is calculated to be 435 $Wm^{-2}$ $K^{-1}$.

In order to ensure a sufficient length of subcooled segment ($L_1$) (for avoiding a dry out scenario), a working relationship between the refrigerant mass flow rate and the average temperature of Hytherm 600 ($T_{HTF}$) has been prescribed. The working relationship considers a finite length of the superheated region ($L_3$) as well, so that the saturated dry vapour is able to gain the required level of enthalpy at the evaporator outlet, in a gradual fashion. Once $L_1$ and $L_3$ are obtained, the length of the two-phase segment ($L_2$) can be found easily. Therefore, the length of the two-phase segment ($L_2$) is not constrained strictly. From the boundary condition applied on the rate of change of sectional lengths for evaluating the tube wall temperatures in the flow segments of interest (Jensen and Tummescheit 2002), it is quite evident that the length of the subcooled column increases with increasing refrigerant mass flux, whereas the length of the two-phase region shrinks. On the other hand, the two-phase segment broadens as soon as the subcooled segment begins to diminish due to the heat transfer from the thermic oil side and subsequent evaporation. The constraints applied on the sectional lengths depend on the several system parameters; such as the total length of the narrow evaporator tube ($L$), inner diameter of the evaporator tube ($D_i$), evaporator tube wall thickness ($D_o - D_i$), and the type of the refrigerant used. An empirical relationship is formed between the refrigerant (R134a) mass flow rate and $T_{HTF}$ by using the aforementioned boundary conditions and constraints. The refrigerant mass flow rate of can neither be allowed to reach unfeasibly high values, nor it can be allowed to fall to an impractical low value based on the regular demand of the load loop. The mass inflow to the evaporator tube also depends on the capability of the pump used. In order to incorporate the effect of several system parameters, the scalar constants $K_1$ and $K_2$ are introduced in the relationship to achieve more accurate and situation specific values. Furthermore, the formulation also introduced offset correction constants $K_3$ and $K_4$ to aid fine-tuning of the working fluid mass flow rates, and these constants are to be determined iteratively in a case-specific manner. The upper limit as well as the lower limit of the working fluid mass flow rate are estimated to obtain a feasible operating range (Majumdar et al. 2018a).

In order to enable precise estimation of the mass flow rates, the constraints imposed on the sectional lengths should be varied as $T_{HTF}$ and $\tilde{P}_{solar}$ change. However, the same set of constraints is considered for the calculation of mass flow rates, over the whole range of values of $T_{HTF}$, for the sake of simplification in the numerical analysis. The flow-chart (Fig. 12.7) schematically shows the iterative process of estimating the mass flow rate of ORC working fluid.

The constraints imposed on the sectional lengths depends on the total length of the evaporator tube. Roughly, under normal operating conditions, the longer the evaporator tube, the longer should be length of the subcooled refrigerant segment. It must be noted that the refrigerant mass flow rate needs be increased to achieve a longer subcooled segment. With a view to obtaining the lower limit of the

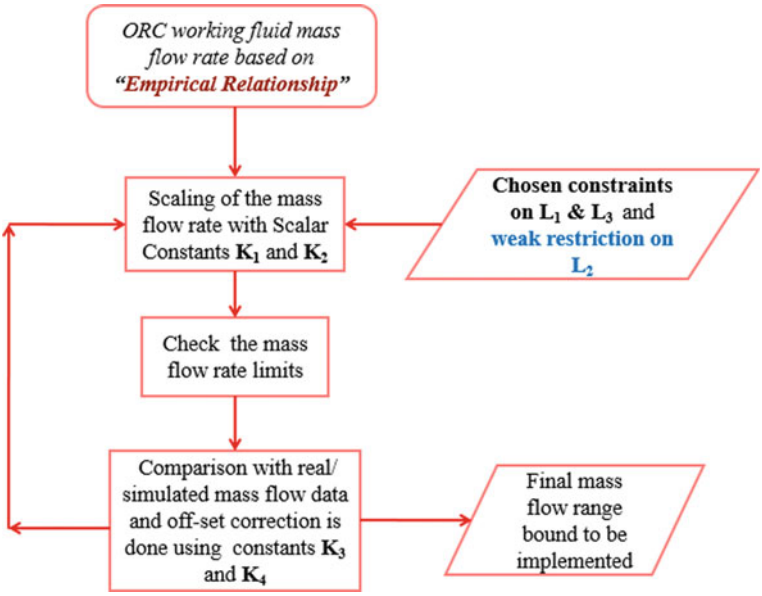


**Fig. 12.7** A flow chart describing briefly the calculation of working fluid mass flow rates (Majumdar et al. 2018a). (Reproduced with permission from © 2018 Elsevier)

refrigerant mass flow rate $(\dot{m}_{\text{in}})$ for the 5 m long heat-exchanger tube, $L_1 \geq 2.5D_i, L_2 \geq 30D_i$ and $L_3 \geq 2.6D_i$ are assumed as the constraints on the sectional lengths. The upper limit of the mass flow rate for the evaporator tube is calculated by using the constraints $L_1 \geq 4.2D_i, L_2 \geq 186D_i$ and $L_3 \geq 4.5D_i$. On the other hand, for finding the lower limit of the refrigerant mass flow rate for the 10 m long evaporator tube, the constraints on the length segments are $L_1 \geq 2.8D_i, L_2 \geq 385D_i$ and $L_3 \geq 3.1D_i$; whereas, for the corresponding upper limit of the refrigerant mass flow rate, the assumed constraints are $L_1 \geq 5.1D_i, L_2 \geq 381D_i$ and $L_3 \geq 5.5D_i$.

The working relationships between the refrigerant mass flow rates $(\dot{m}_{\text{in}})$ and $T_{\text{HTF}}$ are as follows (Majumdar et al. 2018a),

$$\dot{m}_{\text{in,lower}} = \underbrace{K_1\left(-1.019 \times 10^{-6} T_{\text{HTF}}^3 + 1.805 \times 10^{-3} T_{\text{HTF}}^2 - 0.8781 T_{\text{HTF}} + 133.1\right)}_{} + K_3 \tag{12.18}$$

$$\dot{m}_{\text{in,upper}} = \underbrace{K_2(0.237 T_{\text{HTF}} - 84.0304)}_{} + K_4 \tag{12.19}$$

In Eqs. 12.18 and 12.19, the empirical relationships between the refrigerant (R134a) mass flow rate and $T_{\text{HTF}}$ are marked with accent. The empirical relationships are fine-tuned by using the added scalar constants, as described before.

For the purpose of convenient mathematical representation, separate ratios are defined for the sectional lengths of interest, $L_1$, $L_2$ and $L_3$, respectively, at the upper end as well as the lower end of the working fluid (R134a) mass flow rate. The lower and upper ends of the working fluid mass flow rate are given by Eqs. 12.20 and 12.21, respectively.

$$\dot{m}_{\text{in}} = \dot{m}_{\text{in,lower}} \tag{12.20}$$

$$\dot{m}_{\text{in}} = \dot{m}_{\text{in,upper}} \tag{12.21}$$

The aforementioned length ratios are defined as,

$$R_{j,\text{lower}} = \left(\frac{L_{j,\text{lower}}}{D_i}\right), \quad j = 1, 2, 3 \tag{12.22}$$

and

$$R_{j,\text{upper}} = \left(\frac{L_{j,\text{upper}}}{D_i}\right), \quad j = 1, 2, 3 \tag{12.23}$$

where, $L_{j,\text{lower}}$ and $L_{j,\text{upper}}$ symbolize the respective sectional lengths corresponding to the lower and upper ends of the working fluid mass flow rate, respectively.

**Selected simulation results**. Figure 12.8 demonstrates lower end and upper end mass flow rate profiles for the refrigerant (R134a), for both 5 m as well as 10 m long evaporator tubes, for the aforementioned computational set up as well as the imposed constraints on the sectional lengths (subcooled, two-phase, superheated). Corresponding length ratios can be found from Figs. 12.9, 12.10 and 12.11

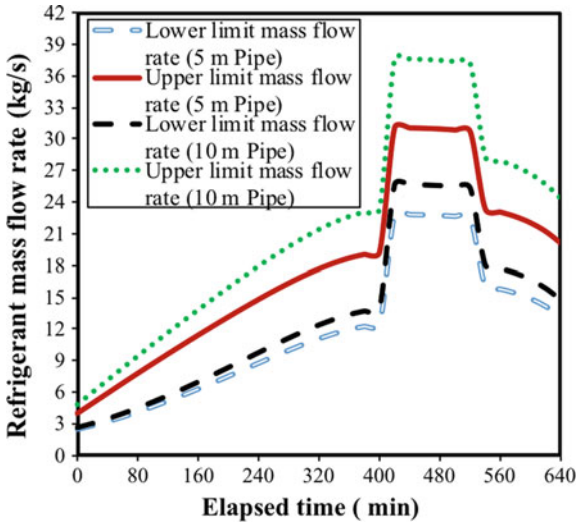


**Fig. 12.8** Variation in the ORC refrigerant (R134a) mass flow rate with time-varying profile of $T_{\text{HTF}}$ ($t$ = 0 corresponds to 7:20 AM)

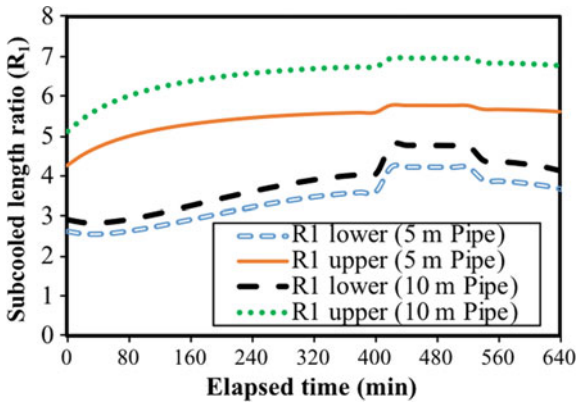


**Fig. 12.9** Variation in the subcooled length ratio ($R_1$) with time-varying profile of $T_{HTF}$ ($t$ = 0 corresponds to 7:20 AM) (Majumdar et al. 2018a). (Reproduced with permission from © 2018 Elsevier)

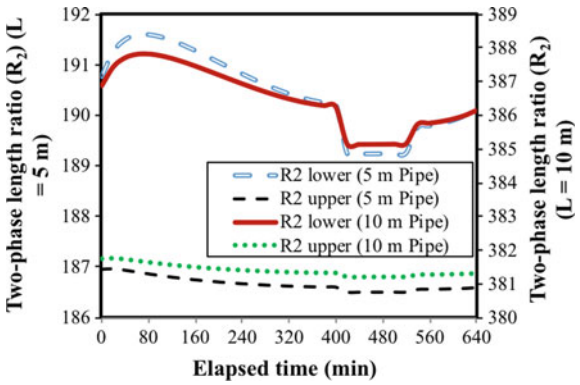


**Fig. 12.10** Variation in the two-phase length ratio ($R_2$) with time-varying profile of $T_{HTF}$ ($t$ = 0 corresponds to 7:20 AM) (Majumdar et al. 2018a). (Reproduced with permission from © 2018 Elsevier)

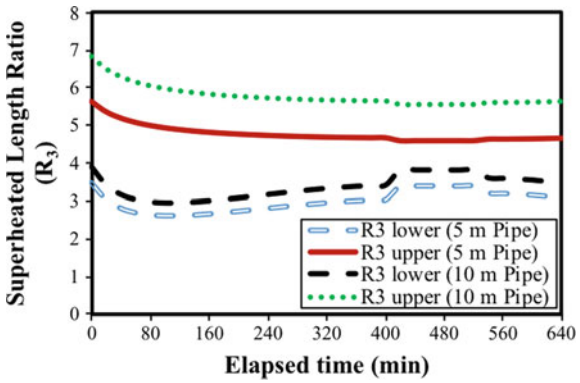


**Fig. 12.11** Variation in the superheated length ratio ($R_3$) with time-varying profile of $T_{HTF}$ ($t$ = 0 corresponds to 7:20 AM)

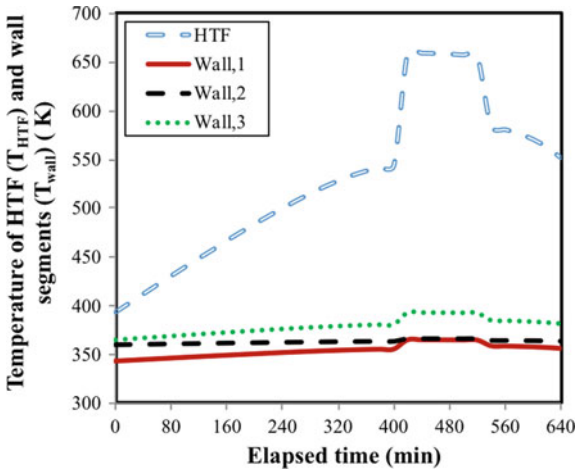


**Fig. 12.12** Variation in the temperature of the wall segments ($T_{wall,1}$, $T_{wall,2}$, $T_{wall,3}$) with time-varying profile of $T_{HTF}$ ($t$ = 0 corresponds to 7:20 AM)

respectively. The higher values of $R_{1,lower}$ and $R_{1,upper}$ in the middle region of the respective graphs in Fig. 12.9 indicate that the tube does not run dry at higher values of $T_{HTF}$. Figure 12.12 demonstrates the variation of temperatures of the wall segments ($T_{wall,1}$, $T_{wall,2}$, $T_{wall,3}$) in response to the time-varying profile of $T_{HTF}$. From Figs. 12.5 and 12.12 respectively, it can be comprehended clearly that the wall temperature of the superheated flow segment ($T_{wall,3}$) increases monotonically at the solar radiation level of about 250 W/m$^2$ during the rise phase. In the subcooled segment, the evaporator tube wall temperature ($T_{wall,1}$) exhibits a comparably lower rate of increment with increasing values $T_{HTF}$. The wall temperature in the two-phase segment ($T_{wall,2}$) hardly changes with increasing solar radiation. At the solar radiation levels of practical interest, the wall temperature of the subcooled region ($T_{wall,1}$) is found to be the lowest of all three regions, whereas the tube wall in the superheated region turns out to be the hottest, i.e. $T_{wall,1} < T_{wall,2} < T_{wall,3}$ (Fig. 12.12).

### *12.2.3 Dynamic Moving Boundary Reduced Order Model*

From the preceding discussion, it can be evidently seen that quasi-steady models are very useful and effective in describing the long-time behavioral trends of the solar thermal systems. Nevertheless, the temporal fluctuations in the pumping pressure working on the subcooled working fluid cause prominent transient changes in the wall temperature profiles of the subcooled, two-phase and superheated segments of the narrow evaporator tube in the two-phase ORC heat exchanger. In order to address these transient changes, reasonably accurate and mathematically tractable system level dynamic models are required. Due to the computational speed as well as the simplicity of formulation, the moving boundary dynamic models have

emerged as the front-runners in the context of advanced control of the solar thermal power plants (Majumdar et al. 2018b). For the dynamic moving boundary models to be applicable in the solar thermal applications as well as low-grade heat recovery systems, the assumptions of the evaporator tube and flow conditions remain the same as mentioned and discussed before (Shi et al. 2016; Majumdar et al. 2018b).

**Governing equations**. One-dimensional dynamic moving boundary model consists of the time-dependent mass balance and energy balance equations for the working fluid in each of the three distinct flow segments (subcooled, two-phase and superheated region) in the two-phase ORC heat exchanger. Additionally, three more equations are also required to account for the energy balance in the wall of the evaporator tube in each of the aforesaid segments. The time-varying operating pressure (pumping pressure), acting on the subcooled refrigerant (R134a) at the inlet of the two-phase evaporator, is considered to be the sole independent variable; whereas all other physical and thermodynamic variables of interest are taken as dependent variables (Majumdar et al. 2018b). This approach simplifies the mathematical formulation considerably and does away with the computational tediousness (Majumdar et al. 2018b), as reported in previously published work.

The mass balance equation for the subcooled region is written as,

$$A\left\{\left(\bar{\rho}_1(t)-\rho_{f,\mathrm{sat}}(t)\right)\frac{\mathrm{d}L_1(t)}{\mathrm{d}t}+L_1(t)\frac{\mathrm{d}\bar{\rho}_1(p)}{\mathrm{d}p}\frac{\mathrm{d}p(t)}{\mathrm{d}t}\right\}=\dot{m}_{\mathrm{in}}(t)-\dot{m}_{12}(t) \quad (12.24)$$

where, the time-dependent average density of the refrigerant in the subcooled segment at the pressure level $p(t)$ is expressed as, $\bar{\rho}_1(p(t))=\frac{2}{3}\rho_{f,\mathrm{in}}(p(t))+\frac{1}{3}\rho_{f,\mathrm{sat}}(p(t))$; by assuming a quadratic profile of variation in the working fluid density along the axial direction.

The mass balance equation for the two-phase flow segment is formulated as,

$$\begin{aligned}A\Bigg\{&\left(\rho_{f,\mathrm{sat}}(t)-\rho_{g,\mathrm{sat}}(t)\right)\frac{\mathrm{d}L_1(t)}{\mathrm{d}t}+(1-\bar{\gamma})\left(\rho_{f,\mathrm{sat}}(t)-\rho_{g,\mathrm{sat}}(t)\right)\frac{\mathrm{d}L_2(t)}{\mathrm{d}t}\\&+L_2(t)\left(\bar{\gamma}\frac{d\rho_{g,\mathrm{sat}}(p)}{\mathrm{d}p}+(1-\bar{\gamma})\frac{\mathrm{d}\rho_{f,\mathrm{sat}}(p)}{\mathrm{d}p}\right)\frac{\mathrm{d}p(t)}{\mathrm{d}t}\Bigg\}=\dot{m}_{12}(t)-\dot{m}_{23}(t)\end{aligned} \quad (12.25)$$

The flow qualities at the inlet as well as the at outlet of the evaporator tube are assumed to remain unchanged, and hence, the mean void fraction $(\bar{\gamma})$ can be assumed to be time-invariant (Wedekind et al. 1978; Beck and Wedekind 1981), i.e. $\frac{\mathrm{d}\bar{\gamma}}{dt}=0$.

The mass balance equation for the superheated flow segment is expressed as,

$$\begin{aligned}A\Bigg\{&L_3(t)\frac{\mathrm{d}\bar{\rho}_3(p)}{\mathrm{d}t}\frac{\mathrm{d}p(t)}{\mathrm{d}t}+\left(\rho_{g,\mathrm{sat}}(t)-\bar{\rho}_3(t)\right)\frac{\mathrm{d}L_1(t)}{\mathrm{d}t}\\&+\left(\rho_{g,\mathrm{sat}}(t)-\bar{\rho}_3(t)\right)\frac{\mathrm{d}L_2(t)}{\mathrm{d}t}\Bigg\}=\dot{m}_{23}(t)-\dot{m}_{\mathrm{out}}(t)\end{aligned} \quad (12.26)$$

The working fluid temperature at the outlet of the two-phase heat exchanger ($T_{\text{out,HE}}$) is assumed to be remain fixed irrespective of the inlet conditions (Majumdar et al. 2018b). The time-varying average temperature of the working fluid in the superheated segment $\left(\widetilde{T}_{\text{Rfg},3}(t)\right)$ is formulated as, $\widetilde{T}_{\text{Rfg},3}(t) = \frac{1}{3}T_{f,\text{sat}}(t) + \frac{2}{3}T_{\text{out,HE}}$; $T_{f,\text{sat}}(t)$ symbolizes the saturation temperature of the working fluid refrigerant corresponding to the time-varying pumping pressure $P(t)$ at the evaporator inlet.

The dynamical energy balance equation for the subcooled flow segment is formulated as,

$$
\begin{aligned}
&A\Bigg\{\left(\bar{\rho}_1(t)\bar{h}_1(t) - \rho_{f,\text{sat}}(t)h_{f,\text{sat}}(t)\right)\frac{\mathrm{d}L_1(t)}{\mathrm{d}t} \\
&\quad + \left(L_1(t)\bar{\rho}_1(t)\frac{\mathrm{d}\bar{h}_1(p)}{\mathrm{d}p} + L_1(t)\bar{h}_1(t)\frac{\mathrm{d}\bar{\rho}_1(p)}{\mathrm{d}p} - L_1(t)\right)\frac{\mathrm{d}p(t)}{\mathrm{d}t}\Bigg\} \\
&\quad + \dot{m}_{12}(t)h_{f,\text{sat}}(t) - \dot{m}_{\text{in}}(t)h_{\text{in}}(t) = \pi D_i\alpha_{i1}L_1(t)T_{\text{wall},1}(t) - \widetilde{T}_{\text{Rfg},1}(t)
\end{aligned}
\tag{12.27}
$$

The values of average specific enthalpy $(\bar{h}_1(t))$ is found by using the average density in the subcooled flow segment $(\bar{\rho}_1(t))$ (IRC Online Fluid Property Calculator 2018). The average temperature of the refrigerant in the subcooled zone $\left(T_{\text{Rfg},1}(t)\right)$ is found by utilizing the values of $(\bar{\rho}_1(t))$ (Isobaric Properties for Ethane 2018).

The dynamical energy balance equation for the two-phase flow segment is written as,

$$
\begin{aligned}
&A\Bigg[L_2(t)\Bigg\{\bar{\gamma}\rho_{g,\text{sat}}(t)\frac{\mathrm{d}h_{g,\text{sat}}(p)}{\mathrm{d}p} + \bar{\gamma}h_{g,\text{sat}}(t)\frac{\mathrm{d}\rho_{g,\text{sat}}(p)}{\mathrm{d}p} \\
&\quad + (1-\bar{\gamma})\rho_{f,\text{sat}}(t)\frac{\mathrm{d}h_{f,\text{sat}}(p)}{\mathrm{d}p} + (1-\bar{\gamma})h_{f,\text{sat}}(t)\frac{\mathrm{d}\rho_{f,\text{sat}}(p)}{\mathrm{d}p} - 1\Bigg\}\frac{\mathrm{d}p(t)}{\mathrm{d}t} \\
&\quad + \left\{\bar{\gamma}\rho_{g,\text{sat}}(t)h_{g,\text{sat}}(t) + (1-\bar{\gamma})\rho_{f,\text{sat}}(t)h_{f,\text{sat}}(t)\right\}\frac{\mathrm{d}L_1(t)}{\mathrm{d}t} \\
&\quad + \left\{(1-\bar{\gamma})\left(\rho_{f,\text{sat}}(t)h_{f,\text{sat}}(t) - \rho_{g,\text{sat}}(t)h_{g,\text{sat}}(t)\right)\right\}\frac{\mathrm{d}L_2(t)}{\mathrm{d}t}\Bigg] \\
&\quad + \dot{m}_{23}(t)h_{g,\text{sat}}(t) - \dot{m}_{12}(t)h_{f,\text{sat}}(t) = \pi D_i\alpha_{i2}L_2(t)T_{\text{wall},2}(t) - \widetilde{T}_{\text{Rfg},2}(t)
\end{aligned}
\tag{12.28}
$$

The energy balance equation pertinent to the superheated flow is formulated as,

$$
\begin{aligned}
&A\Bigg\{\bar{\rho}_3(t)\bar{h}_3(t)\frac{\mathrm{d}L_3(t)}{\mathrm{d}t} + \rho_{g,\text{sat}}(t)h_{g,\text{sat}}(t)\frac{\mathrm{d}L_2(t)}{\mathrm{d}t}L_3(t) \\
&\quad + \left(\bar{\rho}_3(t)\frac{\mathrm{d}\bar{h}_3(p)}{\mathrm{d}p} + L_3(t)\bar{h}_3(t)\frac{\mathrm{d}\bar{\rho}_3(p)}{\mathrm{d}p} + - L_3(t)\right)\frac{\mathrm{d}p(t)}{\mathrm{d}t}\Bigg\} \\
&\quad + \dot{m}_{\text{out}}(t)h_{\text{out}}(t) - \dot{m}_{23}(t)h_{g,\text{sat}}(t) = \pi D_i\alpha_{i3}L_3(t)T_{\text{wall},3}(t) - \widetilde{T}_{\text{Rfg},3}(t)
\end{aligned}
\tag{12.29}
$$

where, the average density of the refrigerant vapour in the superheated flow segment ($\bar{\rho}_3(t)$) is found by utilizing $\widetilde{T}_{\mathrm{Rfg},3}(t)$ along with $p(t)$ (Isobaric Properties for Ethane 2018). Thereafter, $\bar{\rho}_3(t)$ is utilized along with $p(t)$ to find $\bar{h}_3(t)$ from the database of thermodynamic values (IRC Online Fluid Property Calculator 2018). The density ($\rho_{\mathrm{out}}(t)$) and the specific enthalpy ($h_{\mathrm{out}}(t)$) of superheated refrigerant vapour at the exit of the two-phase heat exchanger, are found by using the fixed temperature of the working fluid at the heat exchanger outlet ($T_{\mathrm{out,HE}}$) (Isobaric Properties for Ethane 2018) and transient pressure $p(t)$.

The energy balance equation for the tube wall of the subcooled segment is given is,

$$c_{\mathrm{wall}}\rho_{\mathrm{wall}}A_{\mathrm{wall}}\left\{L_1\frac{dT_{\mathrm{wall},1}(t)}{\mathrm{d}t}+\left(T_{\mathrm{wall},1}(t)-T_{\mathrm{wall},1,\mathrm{end}}(t)\right)\frac{\mathrm{d}L_1(t)}{\mathrm{d}t}\right\}$$
$$=\alpha_{i1}\pi D_i L_1(t)\left(\tilde{\mathrm{T}}_{\mathrm{Rfg},1}(t)-T_{\mathrm{wall},1}(t)\right)+\alpha_o\pi D_o L_1(t)\left(\tilde{\mathrm{T}}_{\mathrm{HTF}}(t)-T_{\mathrm{wall},1}(t)\right) \quad (12.30)$$

where, $A_{\mathrm{wall}}=\pi(D_o-D_i)$; $T_{\mathrm{wall},1,\mathrm{end}}(t)=T_{\mathrm{wall},1}(t)|_{z=L_1(t)}$.

The average HTF temperature $\left(\widetilde{T}_{\mathrm{HTF}}(t)\right)$ is altered by changing the HTF mass flow rate, which in turn is modulated according to the circulating mass flow rate of the pressurized feed water in the collector loop or the primary heat transfer loop (Majumdar et al. 2018b).

The dynamical energy balance equation for the wall of the two-phase flow segment of evaporator tube is,

$$c_{\mathrm{wall}}\rho_{\mathrm{wall}}A_{\mathrm{wall}}\left\{\begin{array}{l}L_2(t)\frac{\mathrm{d}T_{\mathrm{wall},2}(t)}{\mathrm{d}t}+\left(T_{\mathrm{wall},1,\mathrm{end}}(t)-T_{\mathrm{wall},2}(t)\right)\frac{\mathrm{d}L_1(t)}{\mathrm{d}t}\\ +\left(T_{\mathrm{wall},2}(t)-T_{\mathrm{wall},2,\mathrm{end}}(t)\right)\frac{\mathrm{d}L_2(t)}{\mathrm{d}t}\end{array}\right\}$$
$$=\alpha_{i2}\pi D_i L_2(t)\left(\widetilde{\mathrm{T}}_{\mathrm{Rfg},2}(t)-T_{\mathrm{wall},2}(t)\right)+\alpha_o\pi D_o L_2(t)\left(\widetilde{\mathrm{T}}_{\mathrm{HTF}}(t)-T_{\mathrm{wall},2}(t)\right) \quad (12.31)$$

where, $T_{\mathrm{wall},2,\mathrm{end}}(t)=T_{\mathrm{wall},2}(t)|_{z=L_1(t)+L_2(t)}$ and the boundary condition is taken as (Jensen and Tummescheit 2002),

$$\left.\begin{array}{ll}T_{\mathrm{wall},2,\mathrm{end}}(t)=T_{\mathrm{wall},2}(t) & \textit{if } \frac{dL_2(t)}{\mathrm{d}t}\le 0\\ T_{\mathrm{wall},2,\mathrm{end}}(t)=T_{\mathrm{wall},3}(t) & \textit{if } \frac{\mathrm{d}L_2(t)}{dt}>0\end{array}\right\} \quad (12.32)$$

and

$$\left.\begin{array}{ll}T_{\mathrm{wall},1,\mathrm{end}}(t)=T_{\mathrm{wall},1}(t) & \textit{if } \frac{\mathrm{d}L_1(t)}{\mathrm{d}t}\le 0\\ T_{\mathrm{wall},1,\mathrm{end}}(t)=T_{\mathrm{wall},2}(t) & \textit{if } \frac{\mathrm{d}L_1(t)}{\mathrm{d}t}>0\end{array}\right\} \quad (12.33)$$

The energy balance equation for the wall of the superheated region of heat exchanger tube is given as,

$$c_{\text{wall}}\rho_{\text{wall}}A_{\text{wall}}\left\{L_3\frac{dT_{\text{wall},3}(t)}{\mathrm{d}t}+\left(T_{\text{wall},1,\text{end}}(t)-T_{\text{wall},2}(t)\right)\frac{\mathrm{d}L_1(t)}{\mathrm{d}t}\right.$$
$$\left.+\left(T_{\text{wall},2,\text{end}}(t)-T_{\text{wall},3}(t)\right)\left(\frac{\mathrm{d}L_1(t)}{dt}+\frac{\mathrm{d}L_2(t)}{\mathrm{d}t}\right)\right\}$$
$$=\alpha_{i3}\pi D_iL_3(t)\left(\tilde{\mathrm{T}}_{\text{Rfg},3}(t)-T_{\text{wall},3}(t)\right)+\alpha_o\pi D_oL_3(t)\left(\tilde{\mathrm{T}}_{\text{HTF}}(t)-T_{\text{wall},3}(t)\right) \tag{12.34}$$

The boundary condition is given as (Jensen and Tummescheit 2002),

$$\left.\begin{aligned}T_{\text{wall},2,\text{end}}(t)&=T_{\text{wall},2}(t)\quad \textit{if } \tfrac{dL_2(t)}{\mathrm{d}t}\le 0\\ T_{\text{wall},2,\text{end}}(t)&=T_{\text{wall},3}(t)\quad \textit{if } \tfrac{\mathrm{d}L_2(t)}{\mathrm{d}t}>0\end{aligned}\right\} \tag{12.35}$$

and

$$\left.\begin{aligned}T_{\text{wall},1,\text{end}}(t)&=T_{\text{wall},1}(t)\quad \textit{if } \tfrac{\mathrm{d}L_1(t)}{\mathrm{d}t}\le 0\\ T_{\text{wall},1,\text{end}}(t)&=T_{\text{wall},2}(t)\quad \textit{if } \tfrac{\mathrm{d}L_1(t)}{\mathrm{d}t}>0\end{aligned}\right\} \tag{12.36}$$

**Selected computational results for the transient model**. In order to facilitate the demonstration of the transient characteristics of the dynamic model, a sinusoidal profile for the pumping pressure is assumed. The mathematical expression for the time-varying pressure is given by following the footsteps of relevant mathematical formulation available in published literature (Desideri et al. 2016),

$$p(t)=p_o\left[1+0.01\left(\frac{PPS}{2}\right)\sin(0.3\times 2\pi t)\right] \tag{12.37}$$

where, *PPS* denotes the envelope (in number of percentage) encompassing the peak-to-peak deviation from the mean pressure. In the representative results, an envelope of 0.1% peak-to-peak deviation is assumed about the mean operating pressure ($p_o$), and therefore PPS = 0.1.

In order to solve for the governing Eqs. (12.24)–(12.31) and (12.34), the initial conditions (at $t = 0$) are obtained from the numerical results of the quasi-steady model. The constraints on the length segments are suitably chosen such that a subcooled segment length ($L_1$) of at least $0.015L$ is always ensured across the time-varying profile of $\widetilde{T}_{\text{HTF}}(t)$, in order to ensure that the evaporator tube in the two-phase ORC heat exchanger never faces a dearth of subcooled column. Furthermore, a superheated segment length ($L_3$) of at least $0.0467L$ is ensured as well, to facilitate the desired level of specific enthalpy of the superheated vapour at the outlet of the evaporator tube, at 30 bar. The initial values for the wall segment temperatures ($T_{\text{wall},1}$, $T_{\text{wall},2}$ and $T_{\text{wall},3}$) are chosen as 395, 370 and 430 K, respectively, following the steady state values reported in an earlier work

(Jensen and Tummescheit 2002). Detailed description of the computational scheme can be found in the relevant published work (Majumdar et al. 2018b).

The dynamical simulation of the one-dimensional model demonstrated that the transient fluctuations in the temperatures of the tube wall segments are essentially of similar graphical nature to the fluctuations in the pumping pressure at the inlet of the two-phase evaporator (Majumdar et al. 2018b). Similar observations were found in earlier computational works pertaining to the modeling and simulation of two-phase flows (Bauer 1999).

Figures 12.13, 12.14 and 12.15 represent the transient variations of the wall temperatures of the subcooled, two-phase and superheated segments of the evaporator tube of the two-phase ORC heat exchanger, respectively, for a suitable mass inflow rate of the subcooled ORC refrigerant which will enable generation of at least 750 kWt at the turbine. In the reported work (Majumdar et al. 2018b), while calculating the output power it was assumed that the mass flow rate of the superheated refrigerant steam remains almost the same as the mass flow rate of the subcooled refrigerant entering the narrow evaporator tube. From Figs. 12.13, 12.14, 12.15 it can be evidently observed that the temporal fluctuations in the wall temperature is the largest in the superheated region, whereas the temperature swing is found to be the lowest in the two-phase region. Very sharp transient variations in the wall temperatures of interest is a computational artefact that arise from one of the key assumptions used in the formulation of the moving boundary dynamic model that the axial heat conduction in the tube wall is neglected.

More accurate results can be obtained with proper thermal optimization of the system based on the length on the evaporator tube, working fluid mass flow rate and the heat flux transferred into the working fluid from the hot thermic oil side.

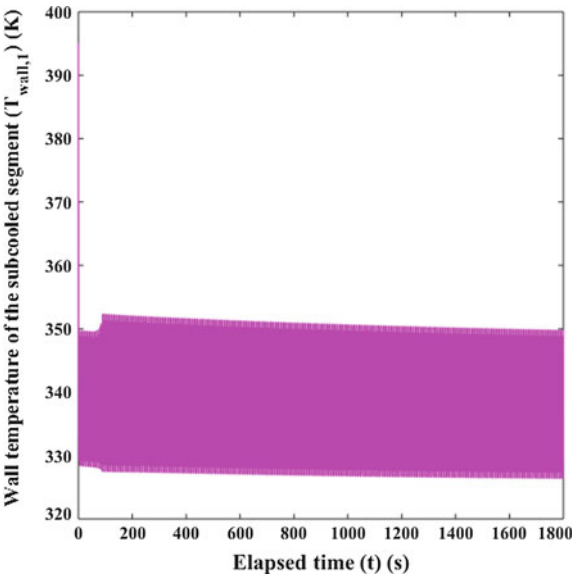


**Fig. 12.13** Transient fluctuations in the subcooled region wall temperature ($T_{wall,1}$) (Majumdar et al. 2018b). (Reproduced with permission from © 2018 Elsevier)

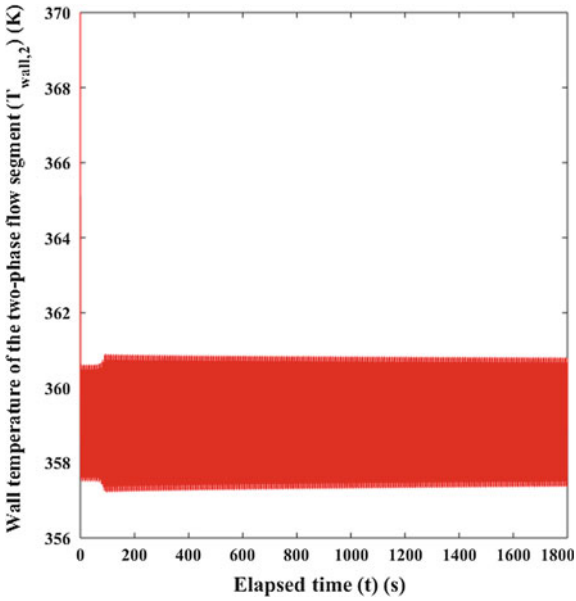


**Fig. 12.14** Transient fluctuations in the two-phase region wall temperature ($T_{wall,2}$) (Majumdar et al. 2018b). (Reproduced with permission from © 2018 Elsevier)

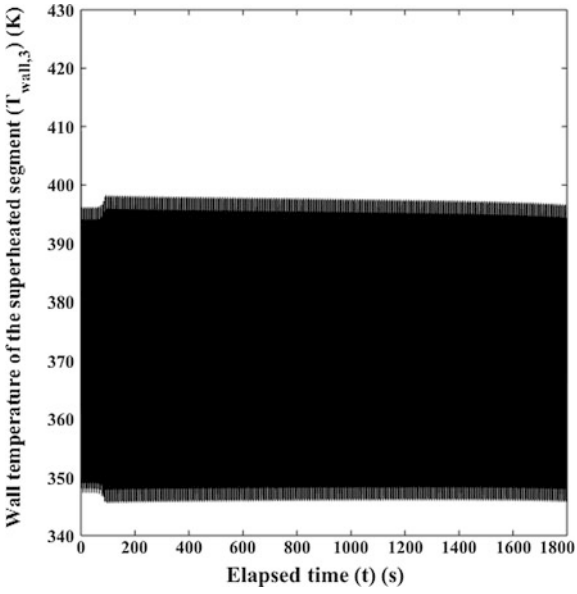


**Fig. 12.15** Transient fluctuations in the superheated region wall temperature ($T_{wall,3}$) (Majumdar et al. 2018b). (Reproduced with permission from © 2018 Elsevier)

### 12.2.4 Moving Boundary Dynamic Model with Inclusion of Momentum Conservation

Momentum conservation equation is introduced to the transient moving boundary model (Jensen and Tummescheit 2002) in order to take into account the effect of pressure drop across the long evaporator tube with a length of the order of 1000 m in real life solar thermal installations. The model is formulated based on the Finite Volume Method (FVM) using staggered grid control volume approach. Figure 12.16 shows the computational control volume with three different regions of the fluid. The following hypotheses are made in the model to incorporate the pressure changing over the successive flow regions (subcooled, two-phase and superheated sections) represented by $P_o(t)$, $P_1(t)$ and $P_2(t)$ in the respective control volumes (figure). A tilt angle ($\alpha$) over the horizontal plane has also been considered. The mass and energy conservations are made in the control volume $CV_{M,Ei}$ whereas the control volume, $CV_{\mathrm{FM},i}$ is used for the momentum conservation. The temporal evaluation of control volume boundaries is discussed in detail in the work reported by Yebra (Yebra et al. 2005). The General Balance Equation (GBE) is expressed as (Jensen and Tummescheit 2002; Todreas and Kazimi 1993),

$$\frac{\mathrm{d}}{\mathrm{d}t}\int_{\forall}\rho\zeta\mathrm{d}\forall+\oint_{S}\rho\zeta(u-u_s)\hat{n}\mathrm{d}S=\int_{\forall}\rho\phi\mathrm{d}\forall+\oint_{S}J\hat{n}\mathrm{d}S \tag{12.38}$$

where $u$ is the fluid velocity, $u_s$ is the CV surface velocity and $\hat{n}$ is the unit normal vector to CV surface. The variables $\{\zeta,\phi,J\}$ takes the form according to the conservation equation as tabulated in Table 12.1. In Table 12.1, $g$ is the

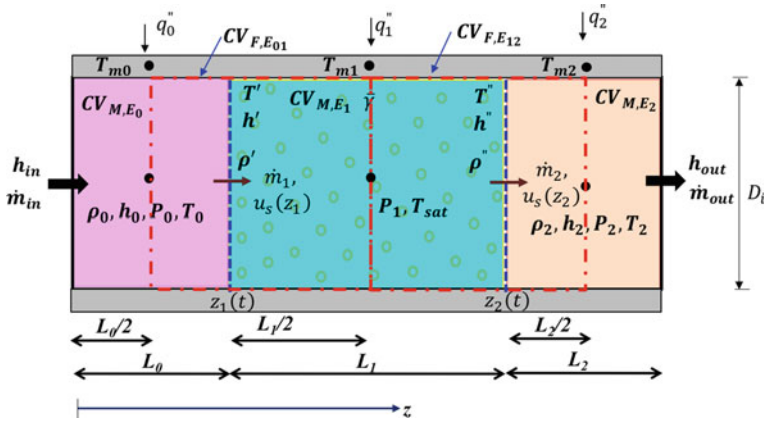


**Fig. 12.16** Computational domain divided into control volumes (dash-dotted lines indicate staggered grid and dotted lines designate standard grid)

**Table 12.1** Variables $\{\zeta, \phi, J\}$ in the conservation equations

| Conservation equation | $\zeta$ | $\phi$ | $J$ |
|---|---|---|---|
| Mass | 1 | 0 | 0 |
| Momentum | $u$ | $g$ | $\bar{\tau} - P\bar{I}$ |
| Energy | $e + \frac{u^2}{2}$ | $gu$ | $-q'' + (\bar{\tau} - P\bar{I})u$ |

acceleration due to gravity, $\tau$ is the surface stress tensor, $I$ is the identity matrix, $q''$ is the energy flux on the surface S, P is the pressure and $e$ is the specific internal energy.

***Momentum conservation***:

The one-dimensional momentum conservation in $z$-direction of evaporator with cross section $A$, can be written as,

$$\begin{aligned} & A\frac{\mathrm{d}\left(\overline{\rho\zeta}\right)}{\mathrm{d}t}(z_2 - z_1) + A\left(\overline{\rho\zeta}\right)\left(\frac{\mathrm{d}z_2}{\mathrm{d}t} - \frac{\mathrm{d}z_1}{\mathrm{d}t}\right) \\ & \quad + A\left[(\rho\zeta(u - u_s))|_{z_2} - (\rho\zeta(u - u_s))|_{z_1}\right] \\ & = A\int_{z_1}^{z_2} \rho\phi dz + \oint_S J\hat{n}\mathrm{d}S \end{aligned} \tag{12.39}$$

For $u_s|_{z_i} = \frac{\mathrm{d}z_i}{\mathrm{d}t}$. The momentum conservation equation turns out to be after substituting the variables $\{\zeta, \phi, J\}$,

$$\begin{aligned} & (z_2 - z_1)\frac{\mathrm{d}\overline{m}}{\mathrm{d}t} + \left(\dot{m}(z_1) - \overline{\dot{m}}\right)\frac{\mathrm{d}z_1}{\mathrm{d}t} - \left(\dot{m}(z_2) - \overline{\dot{m}}\right)\frac{\mathrm{d}z_2}{\mathrm{d}t} \\ & \quad = \dot{I}(z_1) - \dot{I}(z_2) - A\rho g(z_2 - z_1)\sin\alpha - AP_{loss} \\ & \quad + A(P(z_2) - P(z_1)) \end{aligned} \tag{12.40}$$

where, $\overline{\dot{m}}$ is the average mass flow rate in the interval $[z_1, z_2]$ and is expressed as $\frac{1}{(z_2 - z_1)}A\int_{z_1}^{z_2}\dot{m}(z)\mathrm{d}z$ and the mass flow rate $\dot{m}(z_i)$ is calculated at $z_i$. The momentum flux, $\dot{I}(z_i)$ can be evaluated at $z_i$ using $\dot{m}(z_i)|u(z_i)|$. The equivalent pressure of friction forces in control volume can be determined assuming turbulent flow as $P_{\text{loss}} = f\frac{(z_2 - z_1)\overline{\dot{m}}|\overline{\dot{m}}|}{2A^2\rho\left(\overline{\dot{m}}\right)D_{\text{in}}}$. $\rho\left(\overline{\dot{m}}\right)$ takes the form according to the discretization scheme, such as central difference or upwind. The parameters, $P(z_i), f$ and $D_{in}$ are pressure at $z_i$, friction factor and hydraulic diameter, respectively. For two consecutive control volumes, the terms used in Eq. (12.40) have been summarized in Table 12.2.

The momentum equation is solved using the following boundary conditions on $CV_{M,E_i}$-

**Table 12.2** Terms used in Eq. (12.40) for two control volumes $CV_{FM_{0-1}}$ and $CV_{FM_{1-2}}$

| Variable | $CV_{FM_{0-1}}$ | $CV_{FM_{1-2}}$ |
|---|---|---|
| $z_1$ | $\frac{L_0}{2}$ | $L_0 + \frac{L_1}{2}$ |
| $z_2$ | $L_0 + \frac{L_1}{2}$ | $L_0 + L_1 + \frac{L_2}{2}$ |
| $\bar{\dot{m}}$ | $\dot{m}_1$ | $\dot{m}_2$ |
| $\dot{I}(z_1)$ | $\frac{\bar{\dot{m}}(z_1)\lvert\bar{\dot{m}}(z_1)\rvert}{A\rho_0}$ | $\frac{\bar{\dot{m}}(z_1)\lvert\bar{\dot{m}}(z_1)\rvert}{A\rho_1}$ |
| $\dot{I}(z_2)$ | $\frac{\bar{\dot{m}}(z_2)\lvert\bar{\dot{m}}(z_2)\rvert}{A\rho_1}$ | $\frac{\bar{\dot{m}}(z_2)\lvert\bar{\dot{m}}(z_2)\rvert}{A\rho_2}$ |
| $P(z_1)$ | $P_0$ | $P_1$ |
| $P(z_2)$ | $P_1$ | $P_2$ |
| $P_{loss}$ | $f\frac{(L_0-L_1)\dot{m}_1\lvert\dot{m}_1\rvert}{4A^2\rho(\dot{m}_1)D_{\text{in}}}$ | $f\frac{(L_1-L_2)\dot{m}_2\lvert\dot{m}_2\rvert}{4A^2\rho(\dot{m}_2)D_{\text{in}}}$ |
| $\rho(\dot{m}_1)$ | $\frac{\rho_0+\rho_1}{2}$ | |
| $\rho(\dot{m}_2)$ | | $\frac{\rho_1+\rho_2}{2}$ |
| $\dot{m}(z_1)$ | $\frac{\dot{m}_{\text{in}}+\dot{m}_1}{2}$ | $\frac{\dot{m}_1+\dot{m}_2}{2}$ |
| $\dot{m}(z_2)$ | $\frac{\dot{m}_1+\dot{m}_2}{2}$ | $\frac{\dot{m}_2+\dot{m}_{\text{out}}}{2}$ |

$$P(L_0) = \frac{P_0 + P_1}{2}; P(L_0 + L_1) = \frac{P_1 + P_2}{2} \tag{12.41}$$

$$T_w(L_0) = \begin{cases} T_{w0} & \text{if } \frac{\mathrm{d}L_0}{\mathrm{d}t} > 0 \\ T_{w0} & \text{if } \frac{\mathrm{d}L_0}{\mathrm{d}t} \leq 0 \end{cases} \tag{12.42}$$

$$T_w(L_0 + L_1) = \begin{cases} T_{w2} & \text{if } \frac{\mathrm{d}L_1}{\mathrm{d}t} > 0 \\ T_{w2} & \text{if } \frac{\mathrm{d}L_1}{\mathrm{d}t} \leq 0 \end{cases} \tag{12.43}$$

The mass and energy balance equations for the working fluid flowing through the evaporator tube in the three flow regimes of interest are written as follows,

***Subcooled zone***:

$$\begin{aligned} \textbf{\textit{Mass}}: \quad & A(\rho_0 - \rho')\frac{\mathrm{d}L_0}{\mathrm{d}t} + AL_0\left(\frac{\mathrm{d}\rho_0}{\mathrm{d}P}\bigg|_h + \frac{1}{2}\frac{\mathrm{d}\rho_0}{\mathrm{d}h}\bigg|_P \frac{\mathrm{d}h'}{\mathrm{d}P}\right)\frac{\mathrm{d}P_0}{\mathrm{d}t} \\ & + \frac{1}{2}AL_0\frac{\mathrm{d}\rho_0}{\mathrm{d}h}\bigg|_P \frac{\mathrm{d}h_{\text{in}}}{\mathrm{d}t} = \dot{m}_{\text{in}} - \dot{m}_1 \end{aligned} \tag{12.44}$$

$$\begin{aligned} \textbf{\textit{Fluid energy}}: \quad & \frac{1}{2}A(\rho_0(h_{\text{in}} - h') - 2\rho' h' - 2P_0 + 2P(L_0))\frac{\mathrm{d}L_0}{\mathrm{d}t} \\ & + \frac{1}{2}AL_0\left(\rho_0 + \frac{1}{2}(h_{\text{in}} + h')\frac{\mathrm{d}\rho_0}{\mathrm{d}h}\bigg|_P\right)\frac{\mathrm{d}h_{\text{in}}}{\mathrm{d}t} \\ & + \frac{1}{2}AL_0\left(\rho_0\frac{\mathrm{d}h'}{\mathrm{d}P} + (h_{\text{in}} + h')\left(\frac{\mathrm{d}\rho_0}{\mathrm{d}h}\bigg|_P + \frac{1}{2}\frac{\mathrm{d}\rho_0}{\mathrm{d}h}\bigg|_P\frac{\mathrm{d}h'}{\mathrm{d}P} - 2\right)\right)\frac{\mathrm{d}P_0}{\mathrm{d}t} \\ & = \dot{m}_{\text{in}}h_{\text{in}} - \dot{m}_1 h' + \pi D_i L_0 \alpha_{i0}(T_{w0} - T_o) \end{aligned} \tag{12.45}$$

$$\textbf{\textit{Tube energy}}: \quad A_w\rho_w c_{p,w}\left(L_0\frac{\mathrm{d}T_{w0}}{\mathrm{d}t}+(T_{w0}-T_w(L_0))\frac{\mathrm{d}L_0}{\mathrm{d}t}\right) = \pi D_i L_0\alpha_{i0}(T_o-T_{w0})+q_0''L_0 \tag{12.46}$$

***Two-phase zone***:

$$\begin{aligned}\textbf{\textit{Mass}}: \quad & A(\rho'-\rho'')\frac{\mathrm{d}L_0}{\mathrm{d}t}+A(\rho'-\rho'')(1-\bar{\gamma})\frac{\mathrm{d}L_1}{\mathrm{d}t}\\ & +AL_1\left(\bar{\gamma}\frac{\mathrm{d}\rho''}{\mathrm{d}P}+(1-\bar{\gamma})\frac{\mathrm{d}\rho'}{\mathrm{d}P}\right)\frac{\mathrm{d}P_1}{\mathrm{d}t}=\dot{m}_1-\dot{m}_2\end{aligned} \tag{12.47}$$

$$\begin{aligned}\textbf{\textit{Fluid energy}}: \quad & A(\rho''h'-\rho''h''-P(L_0)+P(L_0+L_1))\frac{\mathrm{d}L_0}{\mathrm{d}t}\\ & +A((1-\bar{\gamma})(\rho'h'-\rho''h'')-P_1+P(L_0+L_1))\frac{\mathrm{d}L_1}{\mathrm{d}t}\\ & +AL_1\left(\bar{\gamma}\frac{d(\rho''h'')}{\mathrm{d}P}+(1-\bar{\gamma})\frac{\mathrm{d}(\rho'h')}{\mathrm{d}P}-1\right)\frac{\mathrm{d}P_1}{\mathrm{d}t}\\ & =\dot{m}_1h'-\dot{m}_2h''+\pi D_iL_1\alpha_{i1}(T_{w1}-T_1)\end{aligned} \tag{12.48}$$

$$\begin{aligned}\textbf{\textit{Tube energy}}: \quad & A_w\rho_w c_{p,w}\left(\begin{array}{l}L_1\frac{\mathrm{d}T_{w1}}{dt}+(T_w(L_0)-T_{w1})\frac{\mathrm{d}L_0}{\mathrm{d}t}\\ \qquad +(T_{w1}-T_w(L_0+L_1))\frac{\mathrm{d}L_1}{\mathrm{d}t}\end{array}\right)\\ & =\pi D_iL_1\alpha_{i1}(T_1-T_{w1})+q_1''L_1\end{aligned} \tag{12.49}$$

***Superheated zone***:

$$\begin{aligned}\textbf{\textit{Mass}}: \quad & A(\rho''-\rho_2)\frac{\mathrm{d}L_0}{\mathrm{d}t}+A(\rho''-\rho_2)\frac{\mathrm{d}L_1}{\mathrm{d}t}\\ & +AL_2\left(\tfrac{1}{2}\frac{\mathrm{d}\rho_2}{\mathrm{d}P}\Big|_P\frac{\mathrm{d}h''}{\mathrm{d}P}+\frac{\mathrm{d}\rho_2}{\mathrm{d}P}\Big|_h\right)\frac{\mathrm{d}P_2}{\mathrm{d}t}\\ & +\tfrac{1}{2}AL_2\frac{\mathrm{d}\rho_2}{\mathrm{d}P}\Big|_P\frac{\mathrm{d}h_{\text{out}}}{\mathrm{d}t}=\dot{m}_2-\dot{m}_{\text{out}}\end{aligned} \tag{12.50}$$

$$\begin{aligned}\textbf{\textit{Fluid energy}}: \quad & A\left(\rho''h''-\tfrac{1}{2}\rho_2(h''+h_{\text{out}})+P_2-P(L_0+L_1)\right)\left(\frac{\mathrm{d}L_0}{\mathrm{d}t}+\frac{\mathrm{d}L_1}{dt}\right)\\ & +\tfrac{1}{2}AL_2\left((h''+h_{\text{out}})\left(\tfrac{1}{2}\frac{\mathrm{d}\rho_2}{\mathrm{d}P}\Big|_P\frac{\mathrm{d}h''}{\mathrm{d}P}+\frac{\mathrm{d}\rho_2}{\mathrm{d}P}\Big|_h\right)+\rho_2\frac{\mathrm{d}h''}{\mathrm{d}P}-2\right)\frac{\mathrm{d}P_2}{\mathrm{d}t}\\ & +\tfrac{1}{2}AL_2\left(\rho_2+\tfrac{1}{2}\frac{\mathrm{d}\rho_2}{\mathrm{d}P}\Big|_P(h''+h_{\text{out}})\right)\frac{\mathrm{d}h_{\text{out}}}{\mathrm{d}t}\\ & =\dot{m}_2h''-\dot{m}_{\text{out}}h_{\text{out}}+\pi D_iL_2\alpha_{i2}(T_{w2}-T_2)\end{aligned} \tag{12.51}$$

$$\begin{aligned}\textbf{\textit{Tube energy}}: \quad & A_w\rho_w c_{p,w}\left[L_2\frac{dT_{w2}}{\mathrm{d}t}+(T_w(L_0)-T_{w1})\frac{\mathrm{d}L_0}{\mathrm{d}t}\right.\\ & \left.+(T_w(L_0+L_1)-T_{w2})\left(\frac{dL_0}{\mathrm{d}t}+\frac{\mathrm{d}L_1}{\mathrm{d}t}\right)\right]\\ & =\pi D_iL_2\alpha_{i2}(T_2-T_{w2})+q_2''L_2\end{aligned} \tag{12.52}$$

All the symbols bear the same meaning as mentioned in ref. (Yebra et al. 2005). Computational investigations can be performed by using the above one-dimensional model (Eqs. 12.40–12.52) and by training the initial conditions

according to the experimental findings available from the real-life solar thermal power plants, with a view to comparing the computational cost as well as the accuracy of numerical predictions with the aforementioned reduced order dynamic model.

The dynamic moving boundary model can be improved further by incorporating axial variation in the heat transfer fluid temperature profile in shell and tube heat exchanger and by introducing time-dependent fluctuations in the subcooled refrigerant flow at the heat exchanger entry. Study of the transient moving boundary characteristics for different steady-state mean pressure values and for different extent of the dynamic fluctuations will a facilitate a better understanding about the feasible operating conditions and will help in the instrumentation for the advanced control of the solar thermal load loop.

## References

Aguilar C, White D, Ryan D (2005) Domestic water heating and water heater energy consumption in Canada. Canadian Building Energy End-Use Data and Analysis Centre (CBEEDAC), Edmonton, AB, Report 2005-RP-02

Baddou Y (2017) Solar thermal systems for domestic water heating applications in residential buildings. Efficiency and economic viability analysis of monitored plants. Master Thesis, UEMF-Morocco/UPC Barcelona-Spain

Bauer O (1999) Modelling of two-phase flows with Modelica™. Master Thesis, Department of Automatic Control, Lund Institute of Technology, ISSN 0280-5316, ISRN LUTFD2/TFRT-5639-SE

Beck BT, Wedekind GL (1981) A generalization of the system mean void fraction model for transient two-phase evaporating flows. J Heat Transfer 103:81–85

Becker B, Stogsdill K (1990) A domestic hot water use database. ASHRAE J, 21–25

Behar O, Khellaf A, Mohammedi K (2015) A novel parabolic trough solar collector model—validation with experimental data and comparison to Engineering Equation Solver (EES). Energy Convers Manag 106:268–281

Cruz JB, Muñoz LJY, Bencomo SD, Moya EZ (2013) Modeling and simulation of two-phase flow evaporators for parabolic-trough solar thermal power plants. Gobierno de España, Ministerio de economía y competitividad, ISBN: 978-84-7834-705-6, NIPO: 721-13-044-9, 268 pages

Davidson JH (2005) Low-temperature solar thermal systems: an untapped energy resource in the United States. J Sol Energy Eng 127(3):305–306

Desideri A, Dechesne B, Wronski J, van den Broek M, Gusev S, Lemort V, Quoilin S (2016) Comparison of moving boundary and finite-volume heat exchanger models in the modelica language. Energies 9(5):1–18

Dittus FW, Boelter LMK (1930) Heat transfer in automobile radiators of the tubular type. Univ Calif Publ Eng 2:443–461

Donowski VD, Kandlikar SG (1999) Correlating evaporation heat transfer coefficient of refrigerant R-134a in a plate heat exchanger. Mechanical Engineering Department, Rochester Institute of Technology, Rochester, NY

Du P, Xu Y-F, Li M-L, Cai Z-H (1996) The transient characteristics of parallel flow plate-fin heat exchangers, energy and environment. In: Proceedings of the international conference on energy and environment, ICEE 1996, Begell House Inc, New York, pp 442–447

Eldredge BD, Alleyne AG (2006) Improving the accuracy and scope of control-oriented vapor compression cycle system models. ACRC TR-246, Air Conditioning and Refrigeration Center, University of Illinois Mechanical and Industrial Engineering Department

Endalew A, Abebe K (2012) Numerical modelling and experimental validation of heat tube solar collector for water heating. Master of Science Thesis, Energy Technology, Division of Thermodynamics and Refrigeration

Evarts JC, Swan LG (2013) Domestic hot water consumption estimates for solar thermal system sizing. Energy Build 58:58–65

Fairey P, Parker D (2004) A review of hot water draw profiles used in performance analysis of residential domestic hot water systems. Florida Solar Energy Center/University of Central Florida, Cocoa, FL, Report FSEC-RR-56-04, 20 July 2004

Gnielinski V (1975) Neue Gleichungen für den Wärme- und den Stoffübergang in turbulent durchströmten Rohren und Kanälen. Forschung im Ingenieurwesen (Engineering Research) 41:8–16

Grald EW, MacArthur JW (1992) A moving boundary formulation for modeling time-dependent two-phase flow. Int J Heat Fluid Flow 13:266–272

Heat Exchangers for Solar Water Heating Systems (2018) Available from: https://www.energy.gov/energysaver/heat-exchangers-solar-water-heating-systems. Accessed April 2018

Hobson PA, Norton B (1988) Verified accurate performance simulation model of direct thermosyphon solar energy water heaters. J SolEnergy Eng 110:282–292

Hoevenaars EJ, Crawford CA (2012) Implications of temporal resolution for modelling renewables-based power systems. Renew Energy 41:285–293

Homola CA (2018) Solar domestic hot water heating systems design, installation and maintenance. http://www.asse-plumbing.org/chapters/NOH%20SolarWtrHtg%20Pres.pdf. Accessed April 2018

IRC Online Fluid Property Calculator (2018) https://www.irc.wisc.edu/properties/. Accessed 15 May 2018

Isobaric Properties for Ethane, 1,1,1,2-tetrafluoro- (R134a), NIST Chemistry WebBook, SRD 69, National Institute of Standards and Technology, U.S. Department of Commerce. Accessed 15 May 2018

Jensen JM, Tummescheit H (2002) Moving boundary models for dynamic simulations of two-phase flows. In: Otter M (ed) Proceedings of the 2nd international Modelica conference, Oberpfaffhenhofen, Germany, pp 235–244

Kakaç S, Bergles AE, Fernandes EO (eds) (1988) Two-phase flow heat exchangers, thermal-hydraulic fundamentals and design. NATO ASI Series book series (NSSE), vol 143, Springer, Dordrecht, Print ISBN: 978-94-010-7755-2

Kalogirou S (2009) Thermal performance, economic and environmental life cycle analysis of thermosiphon solar water heaters. Sol Energy 83(1):39–48

Kalogirou SA, Tripanagnostopoulos Y (2006) Hybrid PV/T solar systems for domestic hot water and electricity production. Energy Convers Manag 47:3368–3382

Khan TS, Khan MS, Chyu M-C, Ayub ZH (2010) Experimental investigation of single phase convective heat transfer coefficient in a corrugated plate heat exchanger for multiple plate configurations. Appl Thermal Eng 30:1058–1065

Kim MB, Park CY (2017) An experimental study on single phase convection heat transfer and pressure drop in two brazed plate heat exchangers with different chevron shapes and hydraulic diameters. J Mech Sci Technol 31(5):2559–2571

Koffi PME, Andoh HY, Gbaha P, Touré S, Ado G (2008) Theoretical and experimental study of solar water heater with internal exchanger using thermosiphon system. Energy Convers Manag 49:2279–2290

Lakhani S, Raul A, Saha SK (2017) Dynamic modelling of ORC-based solar thermal power plant integrated with multitube shell and tube latent heat thermal storage system. Appl Therm Eng 123:458–470

Li W, Hrnjak P (2016) Single phase pressure drop and flow distribution in brazed plate heat exchangers. In: 16th international refrigeration and air conditioning conference at Purdue, 11–14 July 2016

Li H, Hrnjak P (2017) Measurement of heat transfer coefficient and pressure drop during evaporation of R134a in new type facility with one pass flow through microchannel tube. Int J Heat Mass Transf 115:502–512

Lunde PJ (1980) Solar thermal engineering: space heating and hot water systems. OSTI ID: 5819885, Unites States

Majumdar R, Saha SK (2018) Quasi-steady state reduced order moving boundary model of ORC heat exchanger for medium temperature solar-thermal systems. In: Proceedings of the international conference on sustainable energy and environmental challenges (SEEC-2018), IISc. Bangalore, India, 01–03 Jan 2018

Majumdar R, Singh S, Saha SK (2018a) Quasi-steady state moving boundary reduced order model of two-phase flow for ORC refrigerant in solar-thermal heat exchanger. Renew Energy 126:830–843

Majumdar R, Saha SK, Singh S (2018b) Evaluation of transient characteristics of medium temperature solar thermal systems utilizing thermal stratification. Appl Energy 224:69–85. https://doi.org/10.1016/j.apenergy.2018.04.083

Manglik RM (2006) On the advancements in boiling, two-phase flow heat transfer, and interfacial phenomena. J Heat Transfer 128(12):1237–1242

Mani A, Rangarajan S (1982) Solar radiation over India. Allied Publishers Private Limited, New Delhi, 647 pages

Mathioulakis E, Belessiotis V (2002) A new heat-pipe type solar domestic hot water system. Sol Energy 72(1):13–20

Mehendale SS (2017) Single-phase heat exchangers. In: Kulacki F (eds) Handbook of thermal science and engineering. Springer, Cham, Online ISBN: 978-3-319-32003-8

Meyer M (2014) Heat transfer and pressure drop in the condensing superheated region with visualization and film thickness measurement. M.S. Thesis, University of Illinois at Urbana-Champaign

Mills D (2004) Advances in solar thermal electricity technology. Sol Energy 76:19–31

MNRE Annual Report: 2006–2007 (2007) Ministry of New and Renewable Energy (MNRE). Government of India, CGO Complex, Lodhi Road, New Delhi

Mongibello L, Bianco N, Di Somma M, Graditi G, Naso V (2014) Numerical simulation of a solar domestic hot water system. In: 32nd UIT (Italian Union of Thermo-fluid-dynamics) heat transfer conference, Journal of Physics: Conference Series, 547

Muley A, Manglik RM (1997) Enhanced heat transfer characteristics of single-phase flows in a plate heat exchanger with mixed Chevron plates. J Enhanced Heat Transf 4(3):187–201. https://doi.org/10.1615/JEnhHeatTransf.v4.i3.30

Natural Resources Canada (NRCan): Survey of household energy use—summary report (December 2005). http://oee.nrcan.gc.ca/Publications/statistics/sheu-summary/pdf/sheu-summary.pdf. Accessed April 2018

Nilpueng K, Wongwises S (2015) Experimental study of single-phase heat transfer and pressure drop inside a plate heat exchanger with a rough surface. Exp Thermal Fluid Sci 68:268–275

Paynter HM, Takahashi Y (1956) A new method of evaluating dynamic response of counter flow and parallel flow heat exchangers. Trans ASME 78:749–758

Pinel P, Cruickshank CA, Beausoleil-Morrison I, Wills A (2011) A review of available methods for seasonal storage of solar thermal energy in residential applications. Renew Sustain Energy Rev 15(7):3341–3359

Pingaud H, Le Lann JM, Koehret B (1989) Steady-state and dynamic simulation of plate fin heat exchangers. Comput Chem Eng 13:577–585

Powell KM, Edgar TF (2012) Modeling and control of a solar thermal power plant with thermal energy storage. Chem Eng Sci 71:138–145

Renewable Energy Solutions, Solar Thermal- Domestic Hot Water Systems (DHWS) (2018) Available from: http://cf.cdn.unwto.org/sites/all/files/docpdf/re28solarthermal-domestichotwatersystemsdhwsfaq.pdf. Accessed April 2018

Roetzel W (1996) Transient analysis in heat exchangers. In: Afgan N et al (eds) New developments in heat exchangers. Gordon and Breach Publishers, Amsterdam, pp 547–575

Roetzel W, Xuan Y (1999) Dynamic behaviour of heat exchangers. In: International series on developments in heat transfer. WIT Press, Boston, 380 pages

Sarbu I, Adam M (2011) Applications of solar energy for domestic hot–water and buildings heating/cooling. Int J Energy 5(2):34–42

Shi R, He T, Peng J, Zhang Y, Zhuge W (2016) System design and control for waste heat recovery of automotive engines based on organic Rankine cycle. Energy 102:276–286

Shinde A, Sankalp A, Pramod KM, Rao PVC, Saha SK (2017) Heat transfer characterization and optimization of latent heat thermal storage system using fins for medium temperature solar applications. J Sol Energy Eng ASME 139:031003-(1-10)

Shoureshi R, McLaughlin K (1984) Modeling and dynamics of two-phase flow heat exchangers using temperature—entropy bond graphs. In: Proceedings of American control conference, San Diego, CA, USA, pp 93–98

Single Phase Fluid Coils (2018) Available from: http://www.srcoils.com/2887wp/wp-content/uploads/2012/06/CW-Coil-Primer.pdf. Accessed April 2018

Solar Thermal Hot Water Systems and Individual Components (2018) STIEBEL ELTRON, http://www.stiebel-eltron-usa.com/products/solar-thermal-hot-water-systems-individual-components. Accessed April 2018]

Sung T, Yun E, Kim HD, Yoon SY, Choi BS, Kim K, Kim J, Jung YB, Kim KC (2016) Performance characteristics of a 200-kW organic Rankine cycle system in a steel processing plant. Appl Energy 183:623–635

Taherian H, Rezania A, Sadeghi S, Ganji DD (2011) Experimental validation of dynamic simulation of the flat plate collector in a closed thermosyphon solar water heater. Energy Convers Manag 52:301–307

Tang R, Cheng Y, Wu M, Li Z, Yu Y (2010) Experimental and modeling studies on thermosiphon domestic solar water heaters with flat-plate collectors at clear nights. Energy Convers Manag 51:2548–2556

Tchuen G, Koholé WY (2017) A numerical investigation of three different thermosyphon solar water heating systems. Int J Ambient Energy, 1–12

Thirugnanasambandam M, Iniyan S, Goic R (2010) A review of solar thermal technologies. Renew Sustain Energy Rev 14(1):312–322

Thome JR (1990) Enhanced boiling heat transfer, Hemisphere, New York, 356 pages

Todreas NE, Kazimi MS (1993) Nuclear systems I, Thermal hydraulic fundamentals. Taylor and Francis, Abingdon

Vélez F, Chejne F, Quijano A (2014) Thermodynamic analysis of R134a in an Organic Rankine cycle for power generation from low temperature sources. DYNA 81:153–159

Voller V, Cross M (1981) Accurate solutions of moving boundary problems using the enthalpy method. Int J Heat Mass Transfer 24:545–556

Wedekind GL, Bhatt BL, Beck BT (1978) A system mean void fraction model for predicting various transient phenomena associated with two-phase evaporating and condensing flows. Int J Multiphase Flow 4:97–114

Weiss W (ed) (2012) Solar heating systems for houses: a design handbook for solar combisystems. Routledge (an imprint of the Taylor & Francis Group), ISBN 1 902916468, 330 pages

Wood AS (1991) A note on the use of the isotherm migration method. J Comput Appl Math 36:371–384

Wormley DN, Masada GY (1982) Evaluation of lumped parameter heat exchanger dynamic models. ASME Paper 82-WA/DSC-16

Yebra LJ (2006) Modelado orientado a objetos con Modelica de plantas de energía solar basadas en colectores cilindro-parabólicos. Ph.D. Thesis, Universidad Nacional de Educación a Distancia (UNED), Madrid, Spain

Yebra LJ, Berenguel M, Dormido S (2005) Extended moving boundary model for two-phase flows. IFAC Proc Volumes 38(1):368–373

Zelzouli K, Guizani A, Kerkeni C (2014) Numerical and experimental investigation of thermosyphon solar water heater. Energy Convers Manag 78:913–922

Zhang W-J, Zhang C-L (2006) A generalized moving boundary model for transient simulation of dry expansion evaporators under larger disturbances. Int J Refrig 29:1119–1127

# Chapter 13
# Shell-and-Tube Latent Heat Thermal Energy Storage (ST-LHTES)


**Amit Shrivastava and Prodyut R. Chakraborty**

**Abstract** Thermal energy storage (TES) unit has become an integral part of thermal energy conservation. As the name implies, the device simply stores heat when energy from the source is available in excess, and releases the same when energy from the source falls short of the requirement. By doing so, such devices deliver heat energy across the temporal barrier, making thermal energy available for extended working hours of solar thermal power plants (STPP). High energy density and stable operation for long duration are desirable qualities which may be found in latent heat thermal energy storage (LHTES) system. To exploit the advantage of LHTES, the most common design reported in the literature is shell-and-tube type latent heat thermal energy storage (ST-LHTES) systems with phase change material filled in shell side, while (heat transfer fluid) HTF flows in the tubes (or vice versa). The present chapter gives a detailed classification of ST-LHTES systems based on geometry, orientation and relative position of PCM and HTF in heat exchanger along with the classification of phase-change materials. Numerical modelling of heat transfer phenomenon is presented along with some simulated results for enhanced PCM, clearly describing the coupling between PCM and HTF domain. Various heat transfer enhancement techniques and parametric analysis have been discussed with challenges and future scope.

**Keywords** Thermal energy storage · Latent heat · Shell and Tube Heat Exchanger Phase change material · Heat transfer fluid · Coupling

A. Shrivastava · P. R. Chakraborty (✉)
Department of Mechanical Engineering, Indian Institute of Technology Jodhpur, Karwad 342037, India
e-mail: pchakraborty@iitj.ac.in



H. Tyagi et al. (eds.), *Advances in Solar Energy Research*, Energy, Environment, and Sustainability, https://doi.org/10.1007/978-981-13-3302-6_13

## 13.1 Introduction

Environmental degradation and energy crisis are the prime motivating factor behind the extensive research work taking place in the field of energy technology. The gap that exists between energy demand and supply is alarmingly increasing, and the trend of this supply-demand mismatch is expected to deteriorate further in near future. The major portion of energy demand is directly addressed by the usage of fossil fuels with adverse impact on the environment. Environment-friendly, clean and renewable energy resources like geothermal, solar, wind and tidal are going to play pivotal role in addressing future energy demand. Efforts are being made to develop these renewable resource-based technologies to be reliable, efficient and economic. Solar thermal is considered to be one of the most promising renewable resources among the others that can be used for the applications requiring direct heating. Solar thermal power plants (STPP) for the production of electricity is also envisaged to be extremely promising, provided it is implemented for large-scale (O ~ GW) electricity production. Since the availability of solar energy is inherently intermittent and unpredictable in nature, there exists a continuous threat of supply-demand mismatch. Hence, the successful deployment of a wide variety of solar thermal applications including STPP depends heavily on suitable TES systems that can address this intermittent and unpredictable supply-demand mismatch.
Based on the storage principle, thermal energy storage can be classified as: (i) sensible heat thermal energy storage (SHTES), (ii) latent heat thermal energy storage (LHTES) and (iii) thermo-chemical energy storage system (TCES). The primary advantage of LHTES is its ability to store (charging) and release (discharging) of thermal energy at near-isothermal conditions and high energy density.

In general, the TES system consists of heat storage medium, Heat transfer fluid (HTF) and containment unit (shell). For LHTES unit, thermal energy is stored in phase-change material (PCM) in the form of latent heat. Variety of phase-change materials and their properties are mentioned in the literature (Sharma et al. 2009; Zalba et al. 2003; Iverson et al. 2012). During the process of charging, heat transfer fluid supplies heat to PCM which causes the PCM to melt, while storing thermal energy in PCM in the form of latent heat. During discharging, the PCM releases thermal energy (latent heat), which is absorbed by the heat transfer fluid causing the PCM to solidify.

Geometrical design of thermal energy storage unit influences the performance parameter of the storage system, namely charging and discharging time, storage capacity, storage volume, effectiveness and the stability of HTF exit temperature. Numerous enclosure designs (containment unit design) have been proposed in the literature like cylindrical, rectangular, multi-material/multi-tank or wavy enclosure (Mao 2016). Among the various designs proposed in the literature, shell-and-tube type is extensively investigated (Morisson et al. 2008; Lakhani et al. 2017; Hosseini et al. 2014; Han et al. 2017).

Shell-and-tube (ST) storage containers may have different orientations with respect to the HTF flow direction, namely horizontal, vertical and inclined. The

most common practice for such heat exchangers is to store the PCM in the annular shell, while HTF flow is maintained through the internal tubing arrangement within the shell. The comparison of cylindrical ST container with other container designs indicates the superiority of this design in terms of faster energy storing capacity, larger heat transfer area, and being less expensive and easy to fabricate (Cao et al. 2018; Longeon et al. 2013).

## 13.2 A Brief Compilation of Available Literature of ST-LHTES Based on Experimental and Simulations Performed

See Table 13.1.

## 13.3 Classification of ST-LHTES

A. **Classification based on geometry**

Extensive study on shell-and-tube heat exchangers has been carried out by several research groups pertaining to the effects of various design-, flow- and material-based parameters on charging and discharging process of the storage unit. The flow parameters are associated with mass flow rate and inlet temperature of HTF. The design parameters involve orientation with respect to HTF flow direction, tubing arrangement and enhancing heat transfer by means of providing extended surface area (fin) for heat transfer. The material base parameters are associated with exploring different types of PCM and HTF, enhanced heat transport properties of PCM and HTF obtained by graphite matrix and nanoparticles. Most of these studies deal with analysing ST configuration with single central tube. However, studies on multi-tube designs are also occasionally reported. A detailed classification is given below based on various factors such as geometry, relative positions of PCM and HTF and orientation of the LHTES unit (Fig. 13.1).

(a) **Single tube in shell ST-LHTES**: This is the most common type of shell-and-tube arrangement adopted for experimental and numerical analysis. In this arrangement, there are two pipes, may or may not be concentric, arranged in such a manner so as to form an annular region between outer (shell) and inner (tube) pipe. In general, PCM fills the annular region and HTF flows through the tube but vice versa studies are also available in the literature.

   i. **Eccentric tube in shell**: In this type of ST-LHTES, shell and tube are arranged in such a manner that there exists an eccentricity between the central axis of tube and of shell such that they are parallel but do not coincide (Fig. 13.2).

**Table 13.1** Experimental and numerical work from literature on ST-LHTES

| Authors/year | Experimental/numerical | PCM/HTF |
|---|---|---|
| Gasia (2017) Experimental (Gasia et al. 2017a) | Effect of fins | Paraffin RT58/water and commercial silicone |
| Tay (2012) Experimental (Tay et al. 2012) | Charging/discharging dynamics for cold storage application | Salt hydrate/aqueous-based fluids with dissolved ionic solids |
| Kibria (2014) Experimental/numerical (Kibria et al. 2014) | Parametric study of conduction dominated phase change process | Paraffin wax/water |
| Hosseini (2014) Experimental/numerical (Hosseini et al. 2014) | Effect of increase in temperature of HTF on charging/discharging | Paraffin RT50/water |
| Seddegh (2018) Experimental/numerical (Seddegh et al. 2018) | Thermal behaviour of conical and cylindrical LHTES systems | Paraffin RT60/water |
| Jian-you (2008) Experimental/numerical (Jian-you 2008) | Triplex concentric tube charging/discharging | *n*-hexacosane/distilled water |
| Longeon (2013) Experimental/numerical (Longeon et al. 2013) | Effect of HTF inlet direction on vertical concentric tube LHTES | Paraffin RT35/water |
| Cao (2018) Experimental/numerical (Cao et al. 2018) | Cycle dynamics with eccentric HTF tube | Lauric acid (LA)/electrical wire-based heating with PID |
| Zhang (2016) Experimental/numerical (Zhang et al. 2016) | Comparative study of nickel foam/composite salt-based LHTES device | Eutectic molten salt ($NaNO_3$ and $KNO_3$)/Therminol 66 |
| Trp (2005) Experimental/numerical (Trp 2005) | HT analysis of phase chance cycle dynamics | Technical grade paraffin Rubitherm RT 30/water |
| Agyenim (2010) Experimental (Agyenim et al. 2010) | Comparative analysis of single and multi-tube in PCM shell | Erythritol/hot oil |
| Gasia (2017) Experimental (Gasia et al. 2017b) | Dynamic melting enhancement technique | Water/potassium formate water solution |
| Akguan (2007) Experimental (Akgün et al. 2007) | Heat transfer enhancement by heat storage geometry and orientation | Paraffin (P1)/water |
| Avci (2013) Experimental (Avci and Yazici 2013) | Charging and discharging behaviour of PCM storage is analysed | Paraffin/distilled water |
| Fornarelli (2017) Numerical (Fornarelli et al. 2017) | Vertical orientation of LHTES device and top to bottom flow of HTF | Molten salt/diathermic oil |
| Parsazadeh (2018) Numerical (Parsazadeh and Duan 2018) | Study on the simultaneous effects of nanoparticles and fins on phase change | Paraffin wax/water |

(continued)

**Table 13.1** (continued)

| Authors/year | Experimental/numerical | PCM/HTF |
|---|---|---|
| Fornarelli (2016) Numerical (Fornarelli et al. 2016) | Melting in vertical LHTES device considering convection and mushy zone constant | Binary eutectic salt ($NaNO_3$–$KNO_3$ 60–40% wt.)/Alusil TR 50 |
| Morisson (2008) Numerical (Morisson et al. 2008) | Analyse LHTES system with reference to DSG (direct steam generation) | Binary eutectic salt composite ($KNO_3$: $NaNO_3$: CEG)/water or vapour |
| Lakhani (2017) Numerical (Lakhani et al. 2017) | Effects of geometric parameters of LHTES on the overall performance | Organic PCM (A164)/ Hytherm 600 |
| Han (2017) Numerical (Han et al. 2017) | Effect of natural convection in different type of shell and tube (charging only) | Eutectic (60wt% $KNO_3$: 40 wt% $NaNO_3$)/air |
| Khan (2016) Numerical (Khan et al. 2016) | Parametric analysis of a novel shell-and-tube geometry | Commercial grade paraffin/ water |
| Seddegh (2016) Numerical (Seddegh et al. 2016) | Comparative analysis of horizontal and vertical orientation of concentric shell-and-tube TES device | Paraffin (RT50)/water |
| Zheng (2018) Numerical (Zheng et al. 2018a) | Effect of eccentricity on melting and solidification in concentric shell-and-tube TES device | *n*-octadecane/air |
| Wang (2016) Numerical (Wang et al. 2016) | Effect of fin on charging/discharging dynamics | N.A. |
| Parsazadeh (2017) Numerical (Parsazadeh and Duan 2017) | Nanoparticle-enhanced heat transfer | Paraffin/water |
| Pahamli (2017) Numerical (Pahamli et al. 2017) | Inclination effect on nanoparticle enhanced PCM | Paraffin RT50/water |
| Jmal (2015) Numerical (Jmal and Baccar 2015) | Solidification of PCM in a finned coaxial tube | Paraffin C18/air |
| Pizzolato (2017) Numerical (Pizzolato et al. 2017) | Topology optimization of fin | NA |
| Xu (2018) Numerical (Xu et al. 2018) | Copper metal foam porous inserts is built and optimized | $Li_2CO_3$–$K_2CO_3$ (mole ratio 62:38)/isothermal heating boundary |
| Zheng (2018) Numerical (Zheng et al. 2018b) | LHTES system with double coil | Paraffin and EG composite PCM/water |
| Yang (2017) Numerical (Yang et al. 2017) | Cycle dynamics based on height, thickness and number of fin | Commercial grade paraffin/ water |

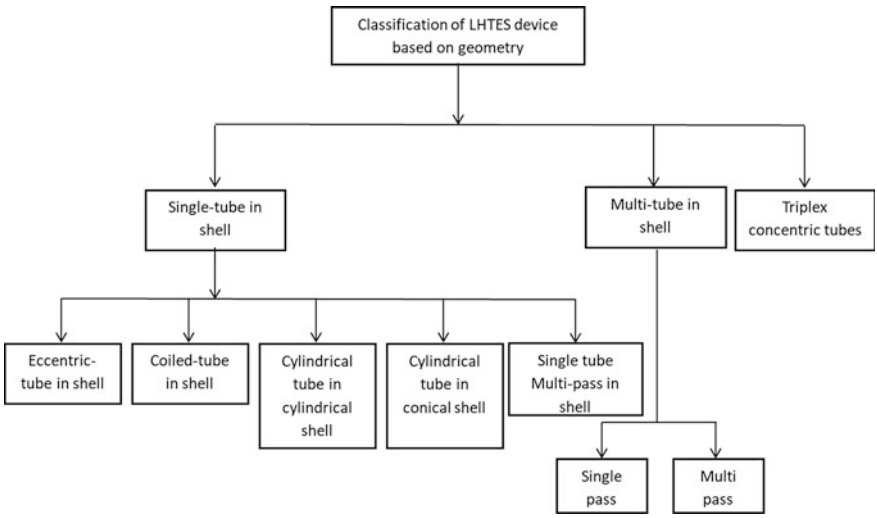


**Fig. 13.1** Classification of LHTES device based on geometry

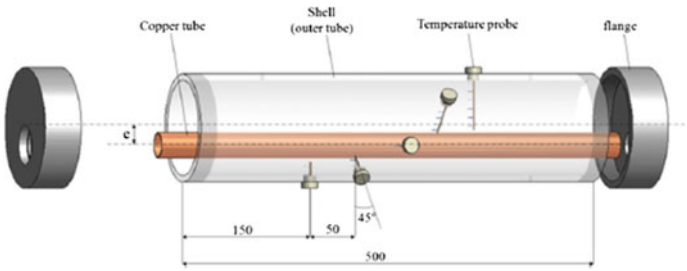


**Fig. 13.2** Eccentric ST-LHTES device (Yazici et al. 2014)

ii. **Coiled tube in shell**: In this arrangement, the inner tube is twisted and turned into a spiral which passes through the cylindrical PCM shell. Depending on the configuration of the inner tube, coiled tube in shell may be classified as single spiral coil tube and double spiral coil tube (Figs. 13.3 and 13.4).
iii. **Cylindrical tube in cylindrical shell**: This type of ST-LHTES consists of two concentric pipes where the cylindrical outer pipe acts as a shell and cylindrical inner pipe acts as a tube.
iv. **Cylindrical tube in conical shell**: This type of ST-LHTES consists of two concentric pipes where the conical outer pipe acts as a shell and cylindrical inner pipe acts as a tube. As per the available literature (Seddegh et al. 2018), storing PCM in the conical annular space incorporates the advantage heat transfer enhancement through natural convection as

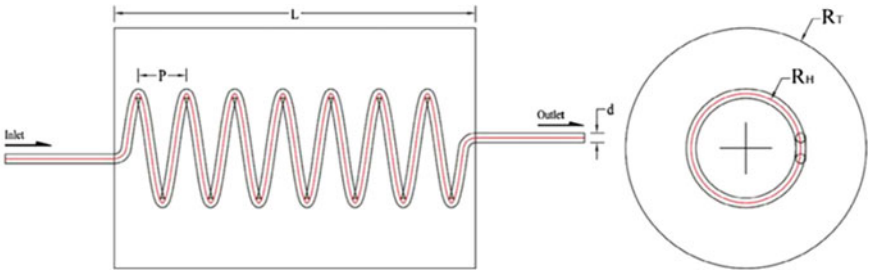


**Fig. 13.3** Schematic diagram of the LTES system with single spiral coil tube (Zheng et al. 2018b)

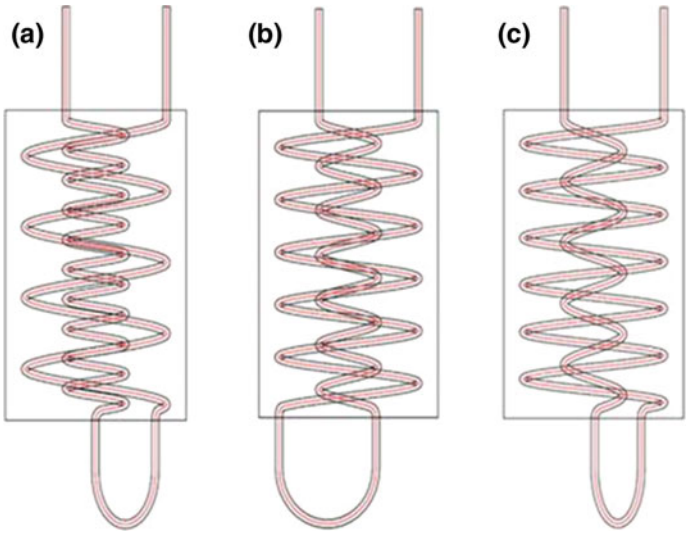


**Fig. 13.4** Schematic diagram of the LHTES system with double spiral coil tube, **a** HT surface area ratio inner tube to outer tube 1:1, **b** 1:2, **c** 1:3 (Zheng et al. 2018b)

compared to storing it in the central pipe. The experimental and numerical results entails that much faster thermal energy storage can be attained with conical shell design as compared to cylindrical shell of the same volume. The conical design being favourable allows natural convection to occur at a larger section of upper volume of the container, enhances heat transfer within PCM to a large extent. However, the discharging process is devoid of any such heat transfer enhancement due to natural convection (Fig. 13.5).

v. **Single-tube multipass in shell**: This arrangement may also be called as '1 shell n tube-pass'. In this type of arrangement, a single-tube runs through the entire length of the shell '*n*' number of times as shown in Fig. 13.6.

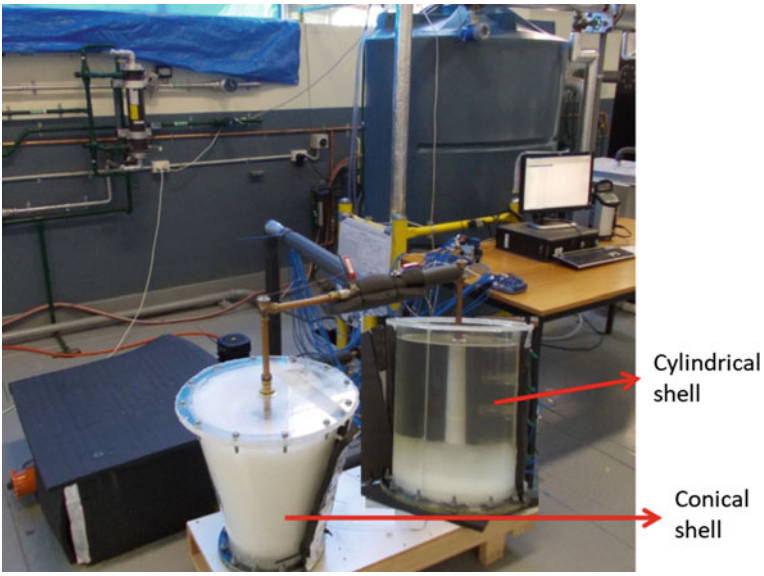


**Fig. 13.5** Photograph of the experimental system (Seddegh et al. 2018)

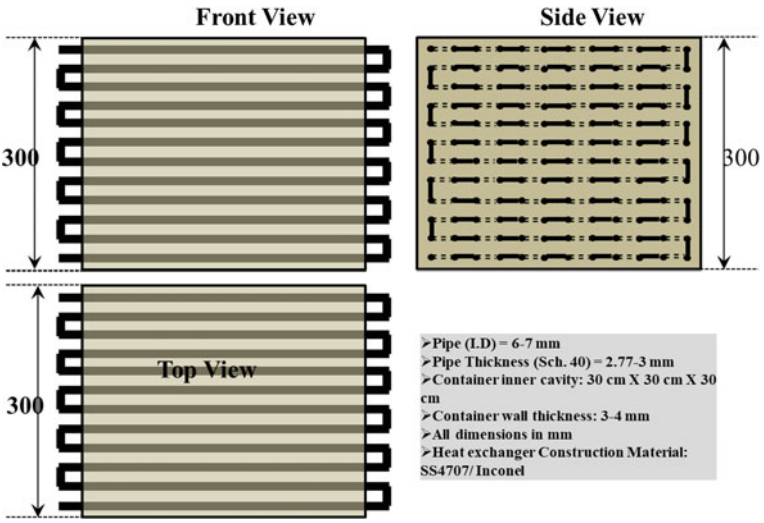


**Fig. 13.6** Front, top and side view of a single-tube multipass in shell

(b) **Multi-tube in shell (single pass)**: In this type of arrangement, a single shell incorporates multiple tubes with all the tubes having their axis parallel to each other as well as parallel to the axis of the shell. Figure 13.7a consists of a cylindrical block of PCM with HTF flowing through a set of parallel tubes traversing the block. A single module is shown in Fig. 13.7b. Often, the conditions assumed in all the tubes are identical, for the sake of simplicity.

(c) **Triplex concentric tube**: Consists of a triple concentric tube where hot heat transfer fluid (HHTF) flows in the annular region between outer tube and middle tube during charging process (malting of PCM) and cold heat transfer fluid (CHTF) flows inside the inner tube during discharging process (solidification of PCM), while PCM is filled in the annular region between the external annular and the inner tube. The design was reported by You (2008), and can be used for energy recovery from waste heat, rejected heat from the condenser of air conditioners and solar energy (Fig. 13.8).

B. **Classification based on relative position of PCM and HTF in the ST-LHTES device**

Based on relative position of PCM and HTF, shell-and-tube LHTES device can be classified as: (i) PCM in shell and HTF in tube side (pipe model) design as shown in Fig. 13.10a and (ii) HTF is in shell and PCM in tube side (cylinder model) design as shown in Fig. 13.10b (Fig. 13.9).

C. **Classification based on orientation**

(a) **Horizontal ST-LHTES**: In horizontal shell-and-tube latent heat thermal energy storage (ST-LHTES) device, the axial flow direction of HTF (in tube or in shell, depending on the relative position of HTF and PCM) is horizontal to the reference plane (Figs. 13.11 and 13.12b).

(b) **Vertical ST-LHTES**: In vertical shell-and-tube latent heat thermal energy storage (ST-LHTES) device, the axial flow direction of HTF (in tube or in shell,

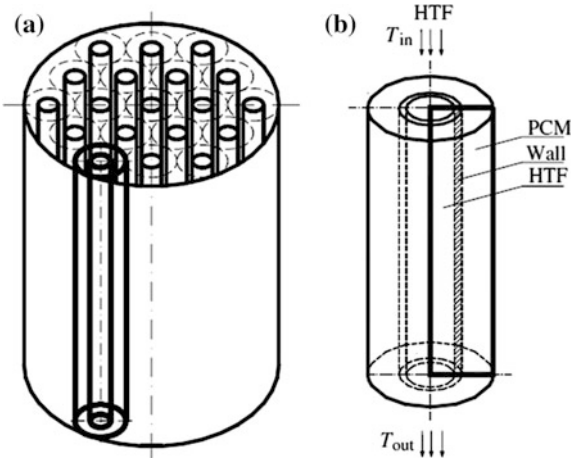


**Fig. 13.7** Multi-tube ST-LHTES: **a** complete system; and **b** single module (Trp 2005)

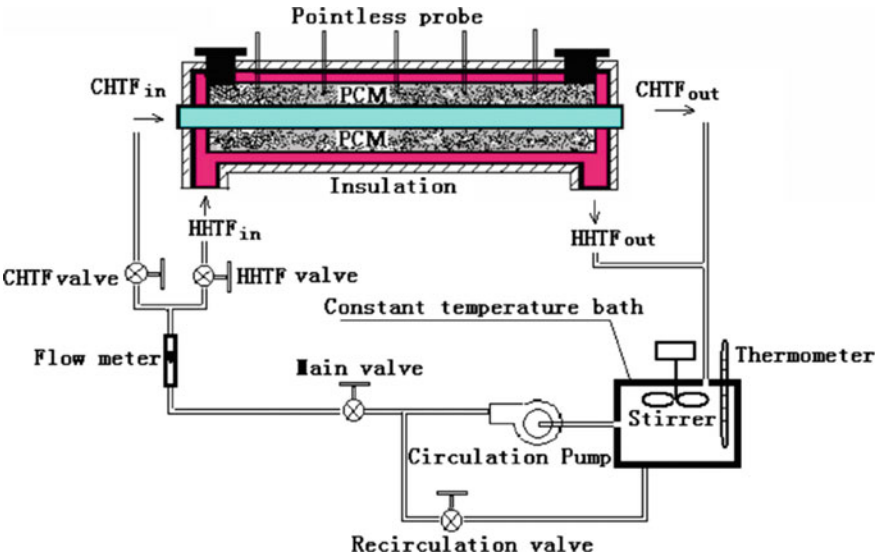


**Fig. 13.8** Schematic diagram of experimental setup (Jian-you 2008)

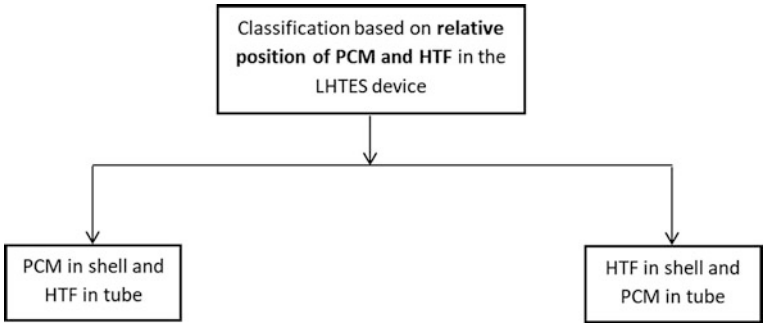


**Fig. 13.9** Classification of LHTES device based on relative position of PCM and HTF

depending on the relative position of HTF and PCM) is vertical to the reference plane (Fig. 13.12a).

(c) **Inclined ST-LHTES**: In inclined shell-and-tube latent heat thermal energy storage (ST-LHTES) device, the axial flow direction of HTF (in tube or in shell, depending on the relative position of HTF and PCM) is inclined at an angle to the reference plane (Fig. 13.12c).

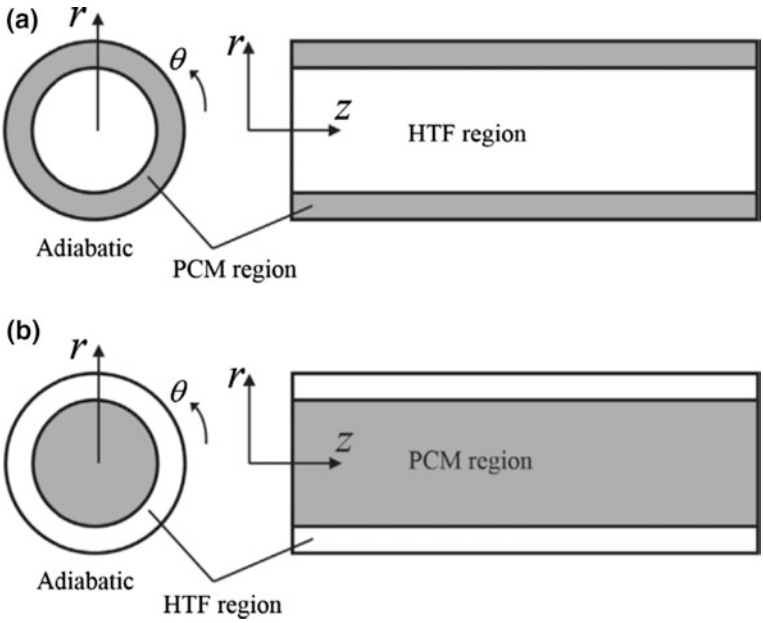


**Fig. 13.10** Physical models of the two shell-and-tube LHTES units. **a** Pipe model, **b** cylinder model (Han et al. 2017)

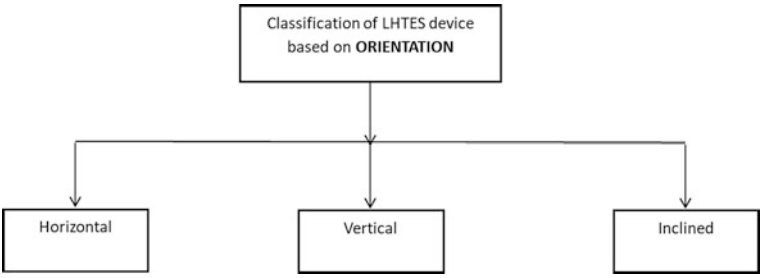


**Fig. 13.11** Classification of ST-LHTES device based on orientation

## 13.4 Application of ST-LHTES

Latent heat thermal energy storage is a relatively new concept in the field of energy storage and retrieval. In order to make the storage and retrieval of thermal energy efficient and convenient, various geometries for the storage have been proposed in the literature. Among them, shell-and-tube geometry has gained extensive research interest mostly due to the fact that design and manufacturing expertise is already state-of-the-art for such heat exchangers, and the expected thermal energy storage

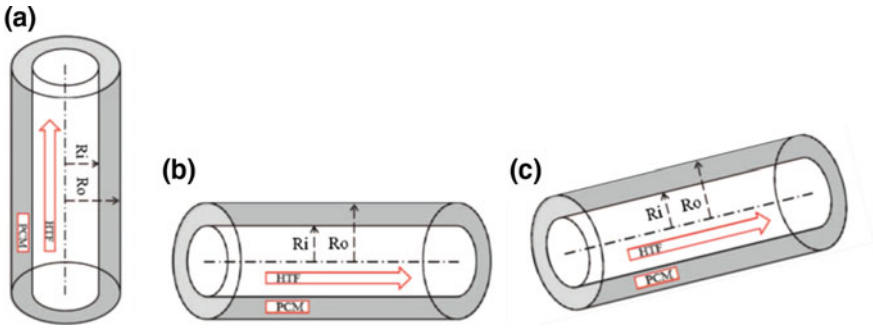


**Fig. 13.12** Classification of ST-LHTES device based on orientation (Han et al. 2017)

efficiencies are acceptably high. Some of the major fields of application for shell-and-tube latent heat thermal energy storage (ST-LHTES) device are

A. **Solar thermal energy**: It is well known that the nature of solar energy is transient, intermittent and unpredictable. To deal with such disparity of supply and demand especially for extended period of operation of solar thermal power plant (STPP), thermal energy storage is a must. As part of the European project DISTOR, Morisson et al. (2008) proposed the concept of direct steam generation (DSG) to be utilized for producing electricity from solar thermal power plants (STPP). Their objective was to conceive, analyse, and, test LHTES adapted to DSG technology for the production of electricity. The geometry chosen by them for this purpose was shell-and-tube LHTES as shown in Fig. 13.13 which shows a single block of shell-and-tube LHTES device and a single HTF tube surrounded by PCM domain used for their numerical analysis.

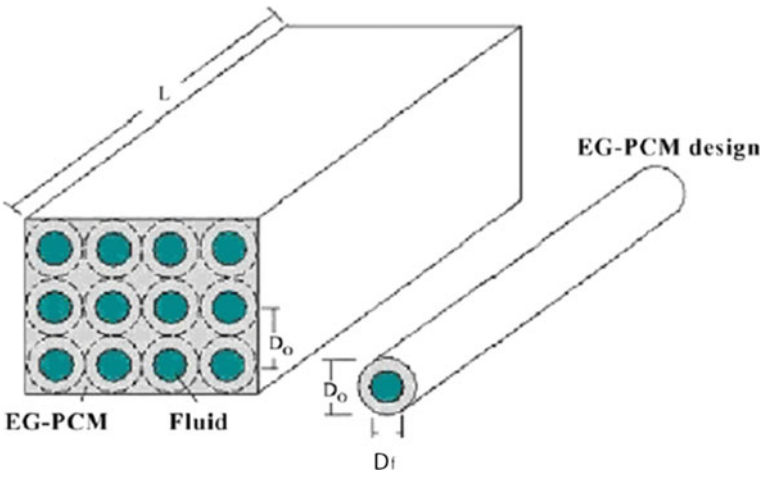


**Fig. 13.13** Shell-and-tube latent heat thermal energy storage (ST-LHTES) block (Morisson et al. 2008)

B. **Industrial waste heat storage**: In general, 'waste heat' can be regarded as heat that is emitted directly into the environment. All industrial processes requiring high-grade energy at higher temperature range produce large amount of unutilized low-grade thermal energy, which is dumped into the environment (Jouhara et al. 2018). Industrial waste heat may be used as a source of heat for some other industrial processes. This may reduce consumption of fossil fuel, and thus helps in curbing the risk of global warming. There are many technologies available in the literature for industrial waste heat recovery such as heat pumps, heat exchangers, heat pipes, boilers, refrigeration cycles, power cycles and heat storage. Thermal energy storage may be regarded as indirect heat recovery technology for collecting waste heat. The energy may be stored at some point of time and released (utilized) at some other time, thus making the energy delivery a time-independent process.
C. **District heating/cooling systems**: District heating/cooling systems consists of one or more thermal energy source/sink, a distribution network of insulated pipes and heat transfer fluid where heat transfer fluid delivers heat to the end users (residential or commercial building). An important unit of district heating/cooling system is a heat storage system which is mainly used to even the rate and time mismatch between the energy sources and sink. Numerous energy sources are studied in literature to be used in such systems such as solar thermal, biomass, combined heat power plant (CHP), industrial waste heat, etc. Numerical simulation for design characterization of a medium scale ST-LHTES device-based district heating system is presented by Colella et al. (2012) in which they have simulated CHP as the source of heat. In their simulation charging of the storage system is achieved by using CHP plants at night, while the stored energy is discharged during the day, when the thermal demand peaks. PCM used in the simulation is paraffin RT100 and HTF is water and several cases of heating demand ranging from 130 to 400 kW is presented.
D. **Mobile Thermal Energy Storage (M-TES)**: Industrial sector of the world accounts for roughly 37% of the global energy consumption. 33% of this industrial energy consumption is regarded as waste heat (Kaizawa et al. 2008). Efforts are directed towards utilizing this waste heat so as to gain energy efficiency, economical advantage as well as reduction in harmful emissions from burning carbon-based fuels. Nature of residential sector is also energy intensive. While district heating (DH) may be applied in community clusters, it may not be feasible for distributed heating due to high initial cost. Mobile thermal energy storage (M-TES) can be a feasible option for such distributed heating requirement (Guo et al. 2016), although it may not be limited to only distributed users and may also be used for community clusters as well as schools, hospitals, etc. (Kaizawa et al. 2008).

As shown in Fig. 13.14, M-TES system consists of a source of waste heat, container for energy transport and end user. In this system, mobile ST-LHTES devices is mounted on a truck, in a container which recovers industrial waste heat and stores it compactly as latent heat of PCM (charging) and distribute it to the end

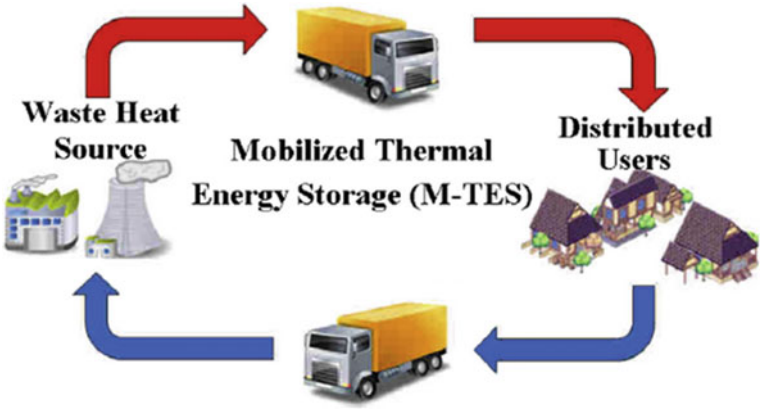


**Fig. 13.14** Schematic of mobilized thermal energy storage (M-TES) system (Guo et al. 2016)

users (discharging, i.e. PCM solidifies and releases energy) situated at distances up to 35 km from the heat source. Once the stored energy is distributed, the storage unit is transported back to the waste heat source and recharged for the next cycle.

## 13.5 Classification of PCM Used in ST-LHTES

Based on the chemical compositions, PCM may be classified as organic, inorganic and eutectic.

There are some specific merits and demerits which may be attributed to the PCM based on their chemical class, which are listed below (Memon 2014) (Fig. 13.15):

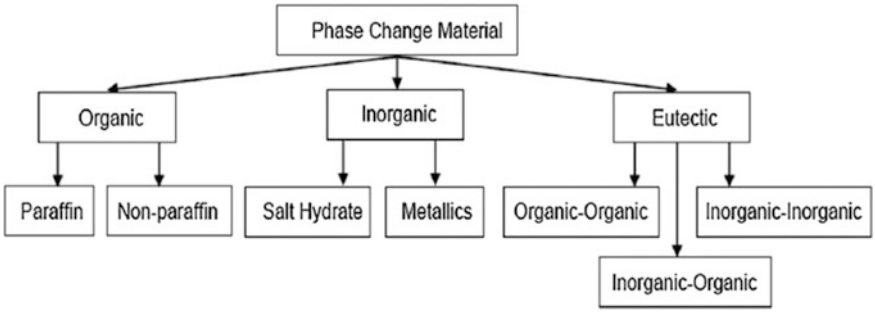


**Fig. 13.15** Classification of PCM (Memon 2014)

A. **Organic PCM**

(a) Points in favour:

- Large variation in phase change temperature (from 20 to 70 °C)
- Chemically inactive
- Devoid of phase segregation
- High thermal stability for large number of phase change cycle
- Low vapour pressure of liquid phase
- Moderate latent heat of freezing/melting (120 J/g up to 210 J/g)
- Higher specific heat as compared to salt hydrates
- Mostly non-corrosive or mildly corrosive in case of fatty acids
- Affordable and economic
- Compatibility with common container materials other than plastics
- Change in volume during phase change process is small
- Negligible supercooling during solidification
- Mostly non-toxic and non-irritant
- Generally stable below 500 °C
- Recyclable

(b) Disadvantages:

- Low thermal conductivity (around 0.2 W/mK)
- Moderately flammable
- Non-compatible with plastic containers

B. **Inorganic PCM—Salt hydrates**

(a) Points in favour:

- Latent heat storage per unit volume is twice as compared to organic materials
- High latent heat of freezing/melting
- Thermal conductivity twice or more as compared to organic PCM (0.5 W/mK)
- Affordable, economic and easily available
- Non-flammable
- Compatibility with plastic container
- Sharp phase change
- Potentially recyclable

(b) Disadvantages:

- Likely to undergo supercooling during freezing
- Possibility of phase segregation during freezing
- Corrosive to most metals
- Might be Irritant
- Vapour pressure is high

- Thermal properties changes gradually after long run of thermal cycling due to oxidation, hydrolysis, thermal decomposition, etc.
- Change in volume during phase change process is large

C. **Eutectic**

(a) Points in favour:

- Isothermal phase transformation
- Thermal energy storage density is slightly above organic PCM

(b) Disadvantages:

- Test data on thermo-physical property is not extensively available.

## 13.6 Selection Criteria for PCM Used in ST-LHTES Device

There are certain properties which the designer look for while selecting PCM for application. The general desirable properties may be summarized as (Memon 2014):

A. **Thermo-physical properties**:

- Phase change temperature should match the suitable operating temperature of the application.
- Large latent heat of fusion ensures large storage density leading to compact storage device.
- Thermal conductivity of the PCM should be high so as to accomplish charging and discharging of PCM within the limited time period.
- PCM should have high specific heat so that additional energy in the form of sensible heat may be stored.
- To avoid containment problem, PCM must not undergo large volume change during phase transition and its vapour pressure must also be small.
- PCM should melt congruently.
- PCM must fulfil the criteria of thermal stability during cyclic operation.

B. **Kinetic properties**:

- During the process of solidification, PCM must have high rate of nucleation so that supercooling of PCM may be avoided.
- High rate of crystal growth promotes optimum heat recovery from the storage system.

C. **Chemical properties**:

- Chemical compatibility with construction/encapsulated materials is a must.

- Degradation of thermal properties after large number of phase change cycles is undesirable.
- Should not be toxic, flammable or explosive.
- Should be non-corrosive to containment material.

D. **Economic properties**:

- It must be affordable, economic and easily available.

E. **Environmental properties**:

- The PCM must be non-polluting and potentially recyclable.

## 13.7 A Brief Compilation of PCM and HTF with Their Properties Used in ST-LHTES Device

See Tables 13.2 and 13.3.

## 13.8 Various Key Performance Indicators Reported for ST-LHTES Device

A. **Average power** (Gasia et al. 2017a).
B. **5-min peak power**: It is defined as the maximum value of the averaged power in 5 min and measured in Watts (Gasia et al. 2017a).
C. **Peak power-to-energy ratio**: It is the ratio between 5-min peak power to the energetic size of the energy store and measured in per hour (Gasia et al. 2017a).
D. **Heat storage rate**: It is the amount of thermal energy stored in the PCM during the process of charging per unit time and measured in watts.
E. **Complete charging/discharging time**: It is the total amount of time elapsed from starting of the charging/discharging process up to the time when complete melting/solidification of the entire PCM has taken place and is measured in second.
F. **Total energy storage capacity**: During charging of PCM, initially, PCM is in solid state below melting point, therefore, it will absorb sensible energy, when it reaches melting temperature, and then energy will be absorbed in the form of latent heat. When the PCM has melted completely, heat storage is in sensible form again. Sum of all these forms of energy absorbed by the PCM during charging is called total energy storage capacity. It is measured in joules.

$$\mathrm{TESC} = \mathrm{SH_I} + \mathrm{LH} + \mathrm{SH_{II}} \tag{13.1}$$

where $\mathrm{SH_I}$, LH and $\mathrm{SH_{II}}$ are sensible heat for solid PCM, latent heat and sensible heat for liquid PCM, respectively.

**Table 13.2** Property table for PCM

| PCM | $T_m$ (°C) | $H$ (kJ/kg) | $\rho$ (kg/m$^3$) | | $c_p$ (kJ/kg K) | | $k$ (W/mK) | | $\mu$ (Ns/m$^2$) | | Refs. |
|---|---|---|---|---|---|---|---|---|---|---|---|
| | | | S | L | S | L | S | L | S | L | |
| Paraffin RT58 | 58 | 160 ± 7% | 880 (15 °C) | 770 at (80 °C) | 2 | | 0.2 | | – | | Gasia et al. (2017a) |
| Paraffin wax | 61 | 190 | 910 | 790 | 2 | 2.15 | 0.24 | 0.22 | 4.738 | 4.108 | Kibria et al. (2014) |
| Paraffin RT60 | 55–61 | 123.5 | 880 | 770 | 2 | | 0.2 | | 0.03705 | | Seddegh et al. (2018) |
| *n*-hexacosane | 56.3 | 255.22 | 770 | | – | | 0.22 | | – | | Jian-you (2008) |
| Paraffin RT35 | 35 | 157 | 880 | 760 | 1.8 | 2.4 | 0.2 | | 2.904 | 2.508 | Longeon et al. (2013) |
| Lauric acid | 44.2 | 174.9 | 862.9 | 856 | 2.3 | – | – | 0.147 | – | – | Cao et al. (2018) |
| Eutectic solar salt $NaNO_3$: $KNO_3$ | 218–228 | 122.89 | 2079 | 1884 | 1.05 ($T \leq 90$ °C) 1.85 ($90 < T \leq 228$ °C) 1.5 ($T > 228$ °C) | | 0.705 | 0.478 | 5.06 | | Zhang et al. (2016) |
| Paraffin Rubitherm RT 30 | 27.54 | 206 | 789 | 750 | 1.8 | 2.4 | 0.18 | 0.19 | – | – | Trp (2005) |
| Erythritol | 117.7 | 339.8 | 1480 (20 °C) | 1300 at 140 (°C) | 1.38 | 2.76 | 0.733 | 0.326 | – | – | Agyenim et al. (2010) |
| Organic PCM (A164) | 168.7 | 249.7 | 1500 | | | 2.01 | 0.45 | | 6.3 | | Lakhani et al. (2017) |
| *n*-octadecane | 27.24 | 248.24 | 770 | | | 2.15 | 0.253 | | 3.1 | | Zheng et al. (2018a) |
| Paraffin C18 | 28–28.5 | 244 | 814 | 774 | 2.15 | 2.18 | 0.15 | 0.148 | 1.221 | 1.161 | Jmal and Baccar (2015) |
| $Li_2CO_3$–$K_2CO_3$ (mole ratio 62:38) | 485.84 | 342 | 1990 | | | 1.6 | 0.6 | | 5.5 | | Xu et al. (2018) |

**Table 13.3** Property table for HTF

| S. no. | HTF | Dynamic viscosity (mPa s) | Thermal conductivity (W/mK) | Specific heat (kJ/kg K) | Density (kg/m$^3$) | Refs. |
|---|---|---|---|---|---|---|
| 1 | Therminol 66 at 20 (°C) | 123.47 | 0.118 | 1.562 | 1008.4 | [50] |
| 2 | Diathermic oil | $e^{((560/T+60)-2.38)}$ | $0.118294 - 0.000033 * T - 0.00000015 * T^2$ | $1496.0 + 3.313 * T + 0.0008970785 * T^2$ | $1020.62 - 0.614254 * T - 0.000321 * T^2$ | Fornarelli et al. (2017) |
| 3 | Alusil TR 50 | $(17.523 * T^{1.529}) * 1000$ | $0.177 - 0.00007 * T$ | $1.2266 + 0.0014 * T$ | $964.6 - 0.6458 * T$ | Fornarelli et al. (2016) |
| 4 | Hytherm 600 | 19.5 | 0.116 | 3.0974 | 720.9 | Lakhani et al. (2017) |
| 5 | Dowtherm A at 20 (°C) | 4.29 | 0.1387 | 1573 | 1056 at 20 (°C) | [51] |

G. **Compactness factor**: It may be defined as the ratio of volume of PCM per unit volume of ST-LHTES device (Gasia et al. 2017b).

$$\mathrm{CF} = \frac{\text{Volume of PCM}}{\text{Volume of STLHTES unit}} \tag{13.2}$$

H. **Local effectiveness**: It is the ratio of actual heat transfer to theoretical heat transfer that can be discharged at any point in time over the complete phase change period (Gasia et al. 2017b).

$$\varepsilon = \frac{\dot{Q}_{\text{experiment}}}{\dot{Q}_{\text{theoric}}} = \frac{T_{\text{HTF,in}} - T_{\text{HTF,out}}}{T_{\text{HTF,in}} - T_{\text{PCM,m}}} \tag{13.3}$$

I. **Average effectiveness**: Average effectiveness over the phase change process may be defined by the average inlet and outlet temperature over the phase change process. The average effectiveness gives an indication of the performance of the effectiveness (Tay et al. 2012).

$$\varepsilon_{\text{avg}} = \frac{T_{\text{in,avg}} - T_{\text{out,avg}}}{T_{\text{in,avg}} - T_{\text{m}}} \tag{13.4}$$

## 13.9 Numerical Modelling

A. **Modelling of PCM domain (considering the PCM composite in shell side with graphite incorporation): liquid fraction updating scheme**:

Numerical modelling of heat transfer between PCM and HTF is a complex problem due to the nonlinear coupling arising out of the absorption or release of latent heat from or to the HTF during melting and freezing processes. Also, the inherent transient nature of phase change process caused by movement of solid–liquid interface causes additional complexity.

Fix grid-based volume averaging method was introduced by Bennon and Incropera (1987) to describe the general form of conservation equations for multiphase transport phenomena which may be written as:

$$\frac{\partial}{\partial t}(g_{\text{k}}\rho_{\text{k}}h_{\text{k}}) + \nabla \cdot (g_{\text{k}}\rho_{\text{k}}\vec{u}_{\text{k}}h_{\text{k}}) = \nabla \cdot (g_{\text{k}}k_{\text{k}}\nabla T) \tag{13.5}$$

where $g$, $h$, $k$, $\rho$, $\vec{u}$ and $T$ represents volume fraction, specific enthalpy, thermal conductivity, mass density, velocity and temperature, respectively, while subscript k represents the phases. Volume averaged density is defined as $\rho = g_{\text{l}}\rho_{\text{l}} + g_{\text{s}}\rho_{\text{s}} + g_{\text{g}}\rho_{\text{g}}$. Where subscripts 1, s and g stand for liquid phase, solid

phase and graphite present in PCM-graphite composite, respectively. By suppressing convection, the general energy conservation equation reduced to:

$$\frac{\partial}{\partial t}(g_k \rho_k h_k) = \nabla \cdot (g_k k_k \nabla T) \tag{13.6}$$

Assuming no shrinkage during phase change of PCM, the following relations are considered:

$\rho_l = \rho_s, f_l = g_l, f_s = g_s, g_l + g_s + g_g = 1$ and $f_l + f_s + f_g = 1$ where $f$ stands for mass fraction.

Applying the volume averaged density, the volume averaged energy conservation equation can be written as

$$\sum \frac{\partial}{\partial t}(g_k \rho_k h_k) = \nabla \cdot (g_k k_k \nabla T) \tag{13.7}$$

Energy conservation Eq. 13.3 may be expanded as

$$\frac{\partial}{\partial t}\left(g_l \rho_l h_l + g_s \rho_s h_s + g_g \rho_g h_g\right) = \nabla \cdot (g_l k_l \nabla T) + \nabla \cdot (g_s k_s \nabla T) + \nabla \cdot \left(g_g k_g \nabla T\right) \tag{13.8}$$

The specific enthalpy for solid phase, liquid phase and graphite can be written as

$$h_s = C_{ps} T \tag{13.9}$$

$$h_l = C_{ps} T_m + h_{sl} + C_{pl}(T - T_m) \tag{13.10}$$

$$h_g = C_{pg} T \tag{13.11}$$

where $C_{ps}$, $C_{pl}$, $C_{pg}$, $h_{sl}$ and $T_m$ are the specific heat capacities of solid PCM, liquid PCM, graphite, specific enthalpy of fusion of PCM and melting temperature of PCM, respectively.

Assuming enthalpy as a function of temperature only, the volume average energy conservation equation may be written as

$$\begin{aligned}\frac{\partial}{\partial t}\left(\rho C_{ps} T\right) = \nabla \cdot (k \nabla T) - \frac{\partial}{\partial t}(\rho f_l h_{sl}) - \frac{\partial}{\partial t}\left[\rho f_l \left(C_{pl} - C_{ps}\right)(T - T_m)\right] \\ - \frac{\partial}{\partial t}\left[\rho f_g \left(C_{pg} - C_{ps}\right) T\right]\end{aligned} \tag{13.12}$$

Source term for the above equation may be written as

$$S_{\mathrm{h}} = -\frac{\partial}{\partial t}(\rho f_{\mathrm{l}} h_{\mathrm{sl}}) - \frac{\partial}{\partial t}\left[\rho f_{\mathrm{l}}\left(C_{\mathrm{pl}} - C_{\mathrm{ps}}\right)(T - T_{\mathrm{m}})\right] - \frac{\partial}{\partial t}\left[\rho f_{\mathrm{g}}\left(C_{\mathrm{pg}} - C_{\mathrm{ps}}\right)T\right] \tag{13.13}$$

Finite volume method-based discretization technique is applied on energy Eq. (13.8) to obtain the following algebraic equation:

$$A_{\mathrm{p}}T_{\mathrm{p}} = \sum A_{\mathrm{nb}}T_{\mathrm{nb}} + A_{\mathrm{p}}^{0}T_{\mathrm{p}}^{0} - B_{\mathrm{p}}f_{\mathrm{lp}} + B_{\mathrm{p}}^{0}f_{\mathrm{lp}}^{0} - C_{\mathrm{p}}f_{\mathrm{lp}}\left(T_{\mathrm{p}} - T_{\mathrm{m}}\right) + C_{\mathrm{p}}^{0}f_{\mathrm{lp}}^{0}\left(T_{\mathrm{p}}^{0} - T_{\mathrm{m}}\right) - D_{\mathrm{p}}T_{\mathrm{p}} + D_{\mathrm{p}}^{0}T_{\mathrm{p}}^{0} \tag{13.14}$$

where

$$B_{\mathrm{P}} = \frac{h_{\mathrm{sl}}}{C_{\mathrm{ps}}} \tag{13.15}$$

$$C_{\mathrm{P}} = \left(\frac{C_{\mathrm{pl}}}{C_{\mathrm{ps}}} - 1\right) \tag{13.16}$$

$$D_{\mathrm{P}} = f_{\mathrm{g}}\left(\frac{C_{\mathrm{pg}}}{C_{\mathrm{ps}}} - 1\right) \tag{13.17}$$

In Eq. (13.14), 'p' and 'np' represents grid point under consideration and neighbouring grid point, respectively, the superscript 0 represent the previous time step value while $f_{\mathrm{lp}}$ represents the liquid fraction of grid point under consideration. Coefficients $A_{\mathrm{p}}$ and $A_{\mathrm{nb}}$ are calculated using power law while $B_{\mathrm{p}}$, $B_{\mathrm{p}}^{0}$, $C_{\mathrm{p}}$, $C_{\mathrm{p}}^{0}$, $D_{\mathrm{p}}$ and $D_{\mathrm{p}}^{0}$ are calculated using forward difference scheme.

To get the liquid fraction updating scheme, Eq. (13.14) can be rewritten for nth and $(n+1)$th iteration step as

$$A_{\mathrm{p}}T_{\mathrm{p}}^{n} = \sum A_{\mathrm{nb}}T_{\mathrm{nb}}^{n} + A_{\mathrm{p}}^{0}T_{\mathrm{p}}^{0} - B_{\mathrm{p}}f_{\mathrm{lp}}^{n} + B_{\mathrm{p}}^{0}f_{\mathrm{lp}}^{0} - C_{\mathrm{p}}f_{\mathrm{lp}}^{n}\left(T_{\mathrm{p}}^{n} - T_{\mathrm{m}}\right) + C_{\mathrm{p}}^{0}f_{\mathrm{lp}}^{0}\left(T_{\mathrm{p}}^{0} - T_{\mathrm{m}}\right) - D_{\mathrm{p}}T_{\mathrm{p}}^{n} + D_{\mathrm{p}}^{0}T_{\mathrm{p}}^{0} \tag{13.18}$$

$$A_{\mathrm{p}}T_{\mathrm{p}}^{n+1} = \sum A_{\mathrm{nb}}T_{\mathrm{nb}}^{n+1} + A_{\mathrm{p}}^{0}T_{\mathrm{p}}^{0} - B_{\mathrm{p}}f_{\mathrm{lp}}^{n+1} + B_{\mathrm{p}}^{0}f_{\mathrm{lp}}^{0} - C_{\mathrm{p}}f_{\mathrm{lp}}^{n+1}\left(T_{\mathrm{p}}^{n+1} - T_{\mathrm{m}}\right) + C_{\mathrm{p}}^{0}f_{\mathrm{lp}}^{0}\left(T_{\mathrm{p}}^{0} - T_{\mathrm{m}}\right) - D_{\mathrm{p}}T_{\mathrm{p}}^{n+1} + D_{\mathrm{p}}^{0}T_{\mathrm{p}}^{0} \tag{13.19}$$

Subtracting Eq. (13.19) from Eq. (13.18), an expression of $f_{\mathrm{lp}}^{n+1}$ is obtained in terms of $A_{\mathrm{p}}$, $D_{\mathrm{p}}$, $C_{\mathrm{p}}$, $f_{\mathrm{lp}}^{n}$, $T_{\mathrm{p}}^{n+1}$ and $T_{\mathrm{m}}$. It should be noted that the effect of

neighbouring points is neglected and the effect is compensated by the use of a relaxation factor $\lambda$ as described by Chakraborty and Dutta (2001). The resulting expression for $f_{\mathrm{lp}}^{n+1}$ is as follows:

$$f_{\mathrm{lp}}^{n+1} = f_{\mathrm{lp}}^{n} + \lambda \left[ \left\{ \frac{A_{\mathrm{p}} + D_{\mathrm{p}} + C_{\mathrm{p}} f_{\mathrm{lp}}^{n}}{B_{\mathrm{p}} + C_{\mathrm{p}} \left( T_{\mathrm{p}}^{n+1} - T_{\mathrm{m}} \right)} \right\} \left( T_{\mathrm{p}}^{n} - T_{\mathrm{p}}^{n+1} \right) \right] \tag{13.20}$$

But during phase change $T_{\mathrm{p}}^{n+1} = T_{\mathrm{m}}$, the final expression for liquid fraction updating scheme is obtained as

$$f_{\mathrm{lp}}^{n+1} = f_{\mathrm{lp}}^{n} + \lambda \left[ \left\{ \frac{A_{\mathrm{p}} + D_{\mathrm{p}} + C_{\mathrm{p}} f_{\mathrm{lp}}^{n}}{B_{\mathrm{p}}} \right\} \left( T_{\mathrm{p}}^{n} - T_{\mathrm{m}} \right) \right] \tag{13.21}$$

The value of relaxation factor ($\lambda$) adopted by Brent et al. (2018) is 0.2. To prevent overshooting and undershooting, the range of liquid fraction is taken as

$$0 \leq f_{\mathrm{l}} \leq \left(1 - f_{\mathrm{g}}\right) \tag{13.22}$$

where '0' corresponds to complete solid PCM and "$\left(1 - f_{\mathrm{g}}\right)$" corresponds to complete liquid PCM while $f_{\mathrm{g}}$ represents the fraction of graphite present in PCM-graphite composite.

For the pure PCM, there is no graphite present in domain under consideration, and the volume averaged energy conservation equation reduce to

$$\begin{aligned} \frac{\partial}{\partial t}\left(\rho C_{\mathrm{ps}} T\right) = \nabla \cdot (k \nabla T) - \frac{\partial}{\partial t}\left(\rho f_{\mathrm{l}} h_{\mathrm{sl}}\right) \\ - \frac{\partial}{\partial t}\left[\rho f_{\mathrm{l}} \left(C_{\mathrm{pl}} - C_{\mathrm{ps}}\right)(T - T_{\mathrm{m}})\right] \end{aligned} \tag{13.23}$$

And the source term will reduce to

$$S_{\mathrm{h}} = -\frac{\partial}{\partial t} \rho f_{\mathrm{l}} h_{\mathrm{sl}} - \frac{\partial}{\partial t}\left[\rho f_{\mathrm{l}} \left(C_{\mathrm{pl}} - C_{\mathrm{ps}}\right)(T - T_{\mathrm{m}})\right] \tag{13.24}$$

Then, the liquid fraction updating scheme will be

$$f_{\mathrm{lp}}^{n+1} = f_{\mathrm{lp}}^{n} + \lambda \left[ \left\{ \frac{A_{\mathrm{p}} + C_{\mathrm{p}} f_{\mathrm{lp}}^{n}}{B_{\mathrm{p}}} \right\} \left( T_{\mathrm{p}}^{n} - T_{\mathrm{m}} \right) \right] \tag{13.25}$$

And the range for liquid fraction to prevent over and undershooting will be

$$0 \leq f_l \leq 1 \tag{13.26}$$

Since the domain under consideration for PCM is cylindrical, volume averaged energy conservation equation in Eq. 13.12 will be applied in polar coordinates as given below:

$$\begin{aligned}\frac{\partial}{\partial t}\left(\rho C_{ps} T\right) = \frac{1}{r}\frac{\partial}{\partial r}\left(r k_r \frac{\partial T}{\partial r}\right) + \frac{\partial}{\partial x}\left(k_x \frac{\partial T}{\partial x}\right) - \frac{\partial}{\partial t}\left(\rho f_l h_{sl}\right) \\ - \frac{\partial}{\partial t}\left[\rho f_l \left(C_{pl} - C_{ps}\right)\left(T - T_m\right)\right] - \frac{\partial}{\partial t}\left[\rho f_g \left(C_{pg} - C_{ps}\right) T\right]\end{aligned} \tag{13.27}$$

Due to non-homogeneity of the PCM material in axial and radial direction, thermal conductivity is calculated at interface as shown by Patankar (1980) (Fig. 13.16)

$$k_e = \frac{1}{\frac{1-f_e}{k_P} + \frac{f_e}{k_E}} \tag{13.28}$$

where

$$f_e = \frac{(\Delta x)_{e+}}{\Delta x_e} \tag{13.29}$$

For an axisymmetric case, the conductive thermal resistance in radial direction will be logarithmic which is incorporated by varying the thermal conductivity in radial direction.

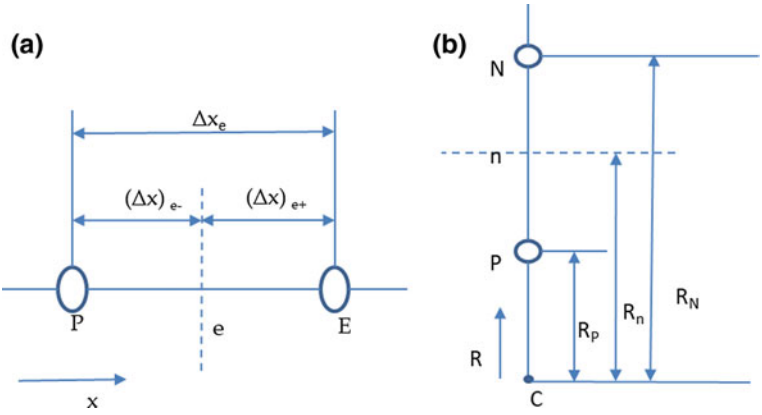


**Fig. 13.16** Distances associated with the interface **a** e, **b** n (Kumar D 2018)

$$k_{\mathrm{n}} = \frac{1}{\frac{1-F_{\mathrm{n}}}{k_{\mathrm{P}}} + \frac{F_{\mathrm{n}}}{k_{\mathrm{N}}}} \tag{13.30}$$

where

$$f_{\mathrm{n}} = \frac{\ln \frac{R_{\mathrm{N}}}{R_{\mathrm{n}}}}{\ln \frac{R_{\mathrm{N}}}{R_{\mathrm{P}}}} \tag{13.31}$$

For numerical simulation of the present case of concentric tubes with composite PCM in the annular region and HTF in inner tube, the following assumptions are made:

(a) HTF domain is assumed to be 1D.
(b) Axial heat conduction in HTF is neglected.
(c) There will not be any phase change for the HTF for the current analysis.
(d) Material properties to be different in solid and liquid phase but are constant in individual phase for PCM.
(e) PCM domain is assumed to be 2D axisymmetric.
(f) Heat transfer within PCM is diffusion dominated.
(g) The effect of shrinkage in PCM is neglected.

B. **Coupling between PCM and HTF domain**:

The procedure of coupling between PCM composite (graphite incorporation) and HTF domain is discussed, where concentric shell-and-tube arrangement is adopted as shown in Fig. 13.17.

The domain considered by the authors consists of a pipe of negligible thickness carrying heat transfer fluid (HTF), which is Therminol vp-1, while being surrounded by phase-change material (PCM), which is solar salt (60% $NaNO_3$: 40%

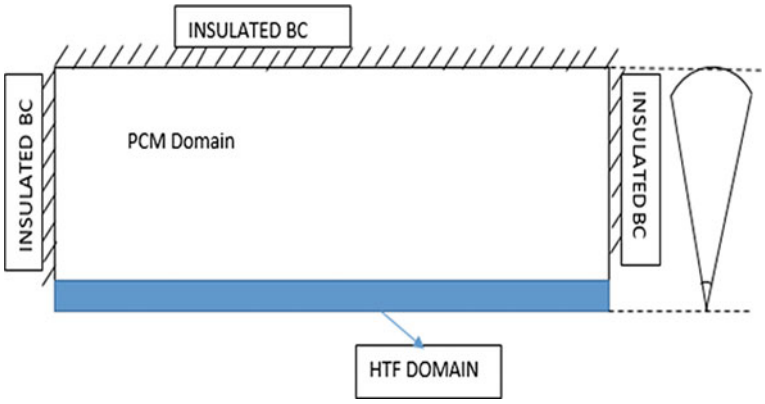


**Fig. 13.17** Axisymmetric computation domain of PCM and HTF (Shrivastava et al. 2018)

$KNO_3$). The PCM domain is considered to be 2D axisymmetric and heat transfer mechanism is diffusion dominated. For the sake of simplicity, a 1D model is considered for the flow of HTF through the inner pipe. Diffusion in the flowing HTF domain and convection in the PCM domain is considered negligible. Coupling of the two domains is performed by source term of HTF energy equation and boundary condition of the PCM domain at the pipe wall.

The volume averaged energy conservation equation for the PCM domain with temperature as the primary dependent variable is given in Eq. 13.27.

Energy conservation equation for HTF is given as

$$\rho_{\mathrm{f}} \frac{\partial}{\partial t}(C_{\mathrm{Pf}} T_{\mathrm{f}}) + \dot{G} \frac{\partial}{\partial x}(C_{\mathrm{Pf}} T_{\mathrm{f}}) = \frac{2}{r} h (T_{\mathrm{wall}} - T_{\mathrm{f}}) \tag{13.32}$$

where subscript f denotes heat transfer fluid (HTF), $\dot{G}$ stands for mass flux (kg/$m^2$ s), $r$ is the radius of pipe, and $h$ is convective heat transfer coefficient between the pipe wall and HTF.

The energy conservation equation of HTF domain was discretized by finite volume method assuming upwind scheme to obtain generalized algebraic Eq. 13.32 and source term denoted by '$b$' (Eq. 13.37).

$$a_{\mathrm{P}} T_{\mathrm{P}} = \left[ \sum a_{\mathrm{nb}} T_{\mathrm{nb}} \right] + b \tag{13.33}$$

$$b = \frac{2}{r} h \Delta x T_{\mathrm{wall}} + \rho C_{\mathrm{Pf}} \Delta x \frac{\mathrm{T_f^o}}{\Delta t} \tag{13.34}$$

Convective heat transfer coefficient $h$ appearing in Eqs. 13.32 and 13.34 are calculated using Gnielinski correlation form Nusselt number (Eq. 13.35).

$$\mathrm{Nu} = \frac{(f/8)(R_{\mathrm{e}} - 1000) P_{\mathrm{r}}}{1.0 + 12.7 (f/8)^{0.5} \left( P_{\mathrm{r}}^{(2/3)} - 1 \right)} \tag{13.35}$$

where friction factor $f$ is defined as

$$f = (0.790 \ln R_{\mathrm{e}} - 1.64)^{-2} \tag{13.36}$$

The coupling is obtained using the following steps:

1. For a given time step, guess pipe wall temperature $T_{\mathrm{w}} = T_{\mathrm{w}}^*$, and solve system of algebraic Eq. 13.5 to obtain HTF temperature distribution $T_{\mathrm{f}}$. A good initial guess for $T_{\mathrm{w}}$ is the wall temperature at the previous time step.
2. Use this $T_{\mathrm{f}}$ to calculate heat rate at the wall from HTF to PCM domain as $q = h_{\mathrm{c}} A (T_{\mathrm{f}} - T_{\mathrm{w}})$ and use heat rate $q$ as the boundary condition for the PCM domain to update temperature distribution in the PCM domain and hence obtain the newly updated value of $T_{\mathrm{w}}$.

3. Repeat steps 1 and 2 until temperature distribution in both the domains converge (Fig. 13.18).

In the case of modelling PCM domain where conduction and natural convection both are significant in heat transfer phenomena.

In addition to the equations previously discussed in Sect. 13.9 (A), continuity and momentum equation have to be solved simultaneously which are given below

$$\frac{\partial \rho}{\partial t} + \nabla \cdot (\rho \vec{u}) = 0 \tag{13.37}$$

$$\frac{\partial}{\partial t}\rho u + \nabla \cdot (\rho \vec{u} u) = -\frac{\partial P}{\partial x} + \nabla \cdot (\mu_l \nabla u) - \frac{\mu_l}{K} u \tag{13.38}$$

$$\frac{\partial}{\partial t}\rho v + \nabla \cdot (\rho \vec{u} v) = -\frac{\partial P}{\partial y} + \nabla \cdot (\mu_l \nabla v) + g(\rho_{ref} - \rho) - \frac{\mu_l v}{K} \tag{13.39}$$

The fourth term appearing in the right-hand side of the above momentum equation represents Darcy term for porous media with permeability coefficient '$K$' defined as in Chakraborty (2017).

$$K = K_0 \left[ \frac{f_l^3 + \varepsilon}{(1 - f_l)^2} \right] \tag{13.40}$$

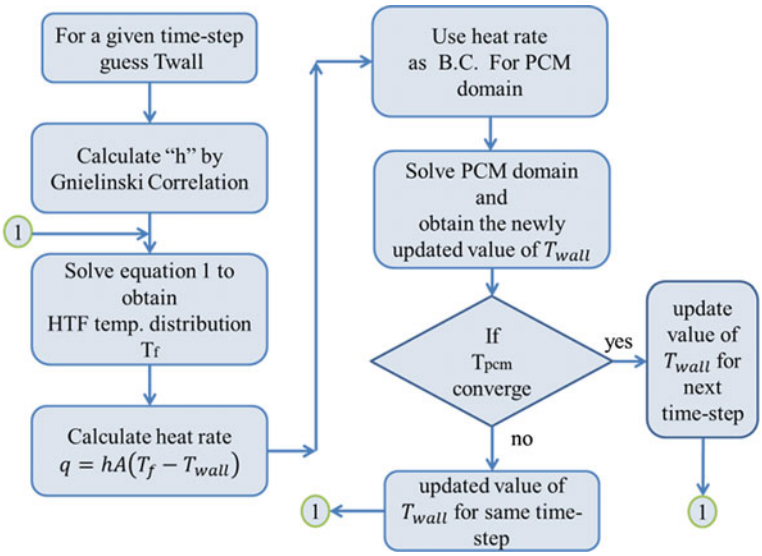


**Fig. 13.18** Flowchart for coupling of PCM and HTF

where $\varepsilon$ has an extremely small value ($<10^{-8}$) retained to avoid errors associated with floating point when $f_l$ approaches zero value and $K_0$ is the permeability constant (Guo et al. 2016). As can be seen from Eq. 13.40, for pure liquid phase, the ratio $\mu_l/K$ becomes zero. With the decrease in liquid fraction ($f_l$) from 1 to 0, the ratio $\mu_l/K$ increases rapidly to an extremely large value.

## 13.10 Results

Figures 13.19 and 13.20 correspond to charging and discharging of the PCM domain by exchanging thermal energy with HTF. In Figs. 13.19a, b and 13.20a, b, PCM does not have graphite while in Figs. 13.19c, d and 13.20c, d, 10% graphite is

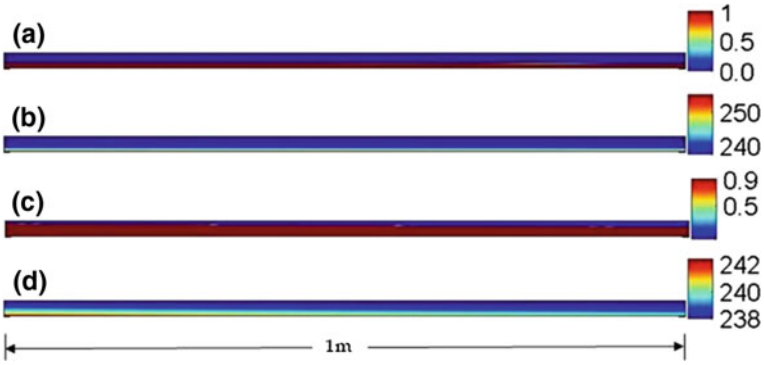


**Fig. 13.19** Charging after 1000 s: **a** Extent of melting with 0% graphite. **b** Temperature distribution with 0% graphite. **c** Extent of melting with 10% graphite. **d** Temperature distribution with 10% graphite (Shrivastava et al. 2018)

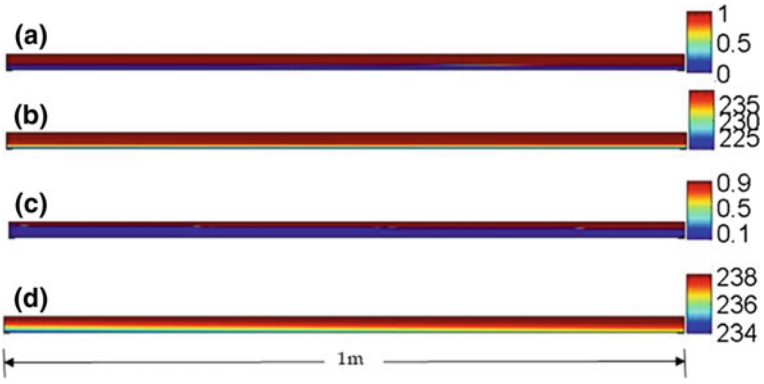


**Fig. 13.20** Discharging after 1000 s: **a** Extent of melting with 0% graphite. **b** Temperature distribution with 0% graphite. **c** Extent of melting with 10% graphite. **d** Temperature distribution with 10% graphite (Shrivastava et al. 2018)

present in the PCM. Incorporation of graphite in PCM renders anisotropic effect in the PCM domain. While thermal conductivity of solar salt (PCM) is taken as constant throughout the domain, anisotropic effects in thermal conductivity of the graphite are considered. Axial thermal conductivity of graphite is taken to be 1.3 W/mK, whereas thermal conductivity of graphite in radial direction is 180.0 W/mK (Chung 2016). As can be seen from Figs. 13.19a, c and 13.20a, c, there is a significant increase in the extent of melting/solidification due to the presence of graphite in PCM for the same time elapse; so it can be concluded that higher effective thermal conductivity of PCM domain promotes much faster charging and discharging rate.

Figure 13.21a, b shows temperature profile of HTF along axial flow direction during charging and discharging, respectively, at 1000th second, and it is evident that at the given instant of time, higher temperature drop/rise for charging/discharging occurs in HTF corresponding to PCM with enhanced thermal conductivity as a result of enhanced heat transfer phenomenon between HTF and PCM domain caused by graphite incorporation.

Figure 13.22a, b shows temperature profile of HTF at the exit of the pipe with respect to time. From Fig. 13.22a, it can be observed that the HTF exit temperature attains a much lower value in the case of enhanced conductivity (PCM-10% graphite composite) as compared to pure PCM case study. The reason being more heat is extraction from HTF by PCM-10% graphite composite. Similarly, from Fig. 13.22b, it can be observed that the HTF exit temperature attains a much higher value in the case of enhanced conductivity (PCM-10% graphite composite) as compared to pure PCM case study, due to higher heat released to HTF by PCM-10% graphite composite.

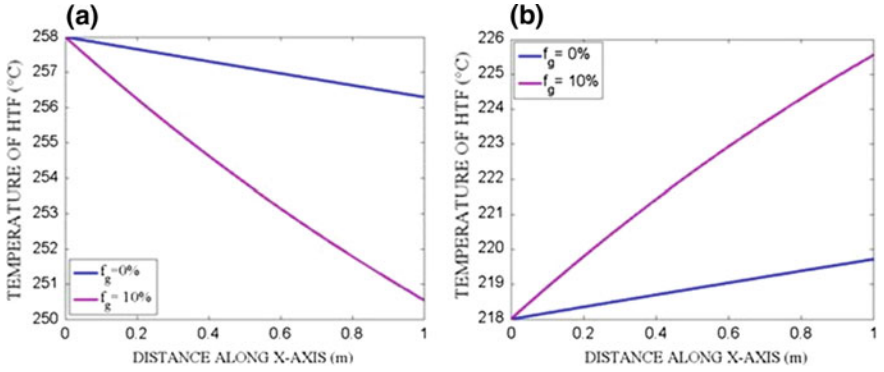


**Fig. 13.21** Temperature of HTF along axial flow direction after 1000 s: **a** Charging. **b** Discharging (Shrivastava et al. 2018)

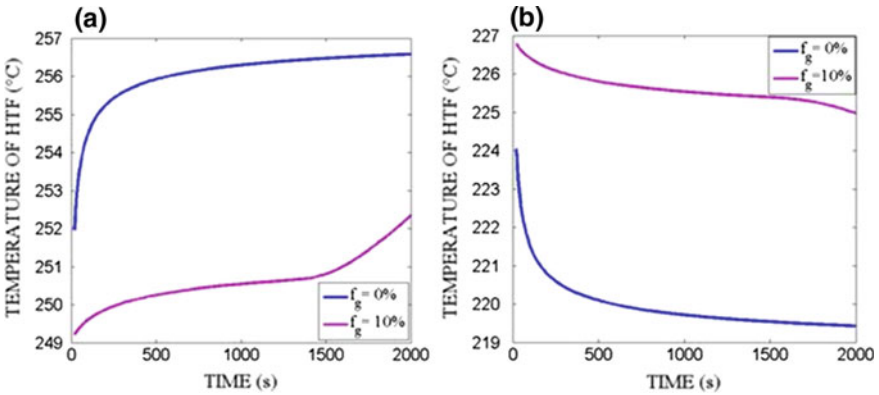


**Fig. 13.22** Temperature variation of HTF at exit of pipe with respect to time: **a** Charging. **b** Discharging (Shrivastava et al. 2018)

## 13.11 Other Techniques of Storage Dynamics Enhancement for ST-LHTES

A. PCM and HTF with nanoparticles (conduction and convection HT).
B. PCM heat transfer enhancement by extended surfaces.
C. Dynamic melting of PCM.

A. **PCM with nanoparticles**:

In general, addition of nanoparticles into the HTF and PCM is expected to improve the overall heat transfer rate between the HTF and the PCM. As a result, the PCM melting process accelerates during charging of the thermal energy storage unit; but, there exists a critical amount of nanoparticle that must be added to PCM. Adding nanoparticles to the PCM below a critical concentration may provide less enhancement effects than optimum. On the other hand, nanoparticles in PCM above the critical concentration limit may lead to poor overall heat transfer and decreased melting rate. One possible explanation for such behaviour may be attributed to increased viscosity of the PCM, leading to reduction in convective heat transfer (Parsazadeh and Duan 2017).

The above observation was re-affirmed by the numerical analysis done by Parsazadeh and Duan (2017). Addition of CuO nanoparticles into the PCM caused an overall depletion of heat transfer rate, leading to longer charging duration in all cases studied (Parsazadeh and Duan 2017). The thermal conductivity enhancement obtained by adding nanoparticle to the PCM is found out to be inadequate to compensate for reduction in natural convection caused by high viscosity of the PCM melt incurred by the addition of nanoparticles to PCM (Parsazadeh and Duan 2017) (Fig. 13.23).

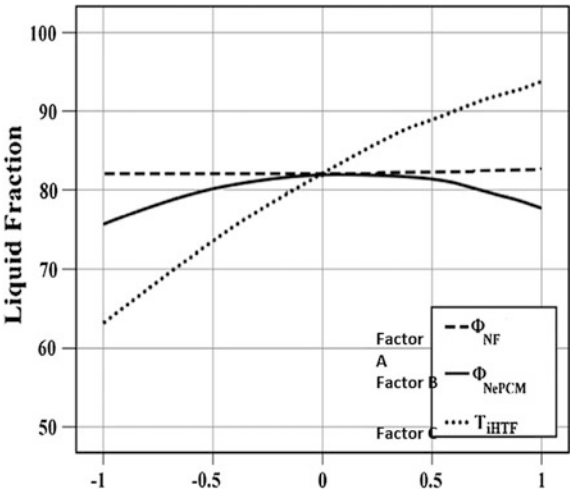


**Fig. 13.23** Impact of factor A (Nanofluid), factor B (NePCM) and factor C ($T_{in,HTF}$) in a coded range on liquid fraction (Parsazadeh and Duan 2017)

A. **PCM heat transfer enhancement by fin**:

A number of numerical and experimental investigations have been performed on melting/solidification of ST-LHTES with fins of various designs and configurations. Commonly, the two types of fins studied are annular and longitudinal fins. Yang et al. (2017), studied the effects of annular fin number, height and thickness on the phase change process, using finite volume-based numerical simulations. Addition of annular fins on the outer surface of the tube carrying HTF enhances the heat conduction between HTF significantly. Also, large number of annular fins may lead to division of the entire space into too many small regions, leading to suppression of local free convection and hence convective heat transfer. Therefore, optimized number of fins must be used to ensure the overall heat transfer enhancement (Yang et al. 2017).

Figure 13.24a, b gives the geometrical details of the annular fin-based ST-LHTES device used in the simulations. The plot in Fig. 13.24c shows the extent of melting with respect to time for the cases having different number of fins. From the plot, it can be clearly seen that time required for complete melting is least for 31 number of fins for the given configuration of ST-LHTES device. Anymore addition of fin may lead to increase in the time period for charging. Incorporation of annular fins in ST-LHTES unit manifests promising potential for heat transfer enhancement during charging or melting process. The complete melting duration could be significantly reduced (by 65%) by means of introducing annular fins in the PCM domain (Yang et al. 2017). The inclusion of optimum number of annular fins improved the combined overall heat transfer rate by enhancing conduction coupled with local free convection (Yang et al. 2017).

Also for the annular fin configuration, Parsazadeh and Duan (2018) studied the effect of 'fin-angle' from −45° to +45° and the effect of fin 'pitch' combined with

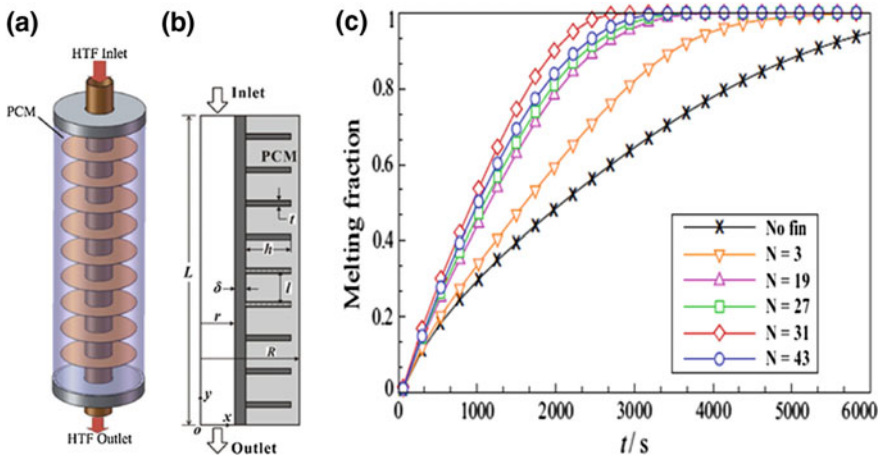


**Fig. 13.24** **a** Schematic of the shell-and-tube LHTES unit with annular fins; **b** computational domain, **c** effect of fin number on melting front evolution (Yang et al. 2017)

the $Al_2O_3$ nanoparticle-enhanced phase-change material (NePCM) as shown in Figs. 13.25 and 13.26.

Based on their numerical simulations, Parsazadeh and Duan (2018) discussed the effect of parameters like nanoparticle concentration, fin angle and pitch on the process of charging. They concluded that during the early stages of heat transfer,

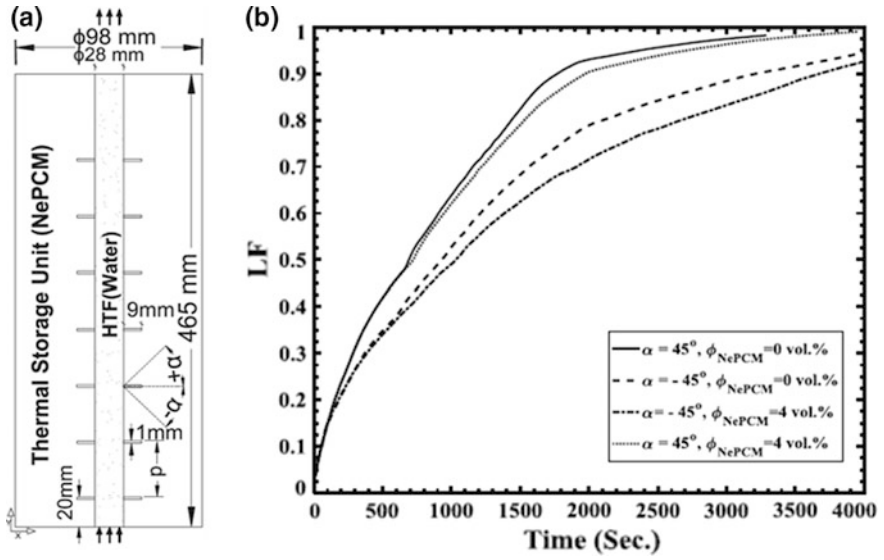


**Fig. 13.25** **a** Schematic of ST-LHTES unit, **b** liquid fraction (LF) over the time for 45 mm pitch '*p*' at various fin angles (Parsazadeh and Duan 2018)

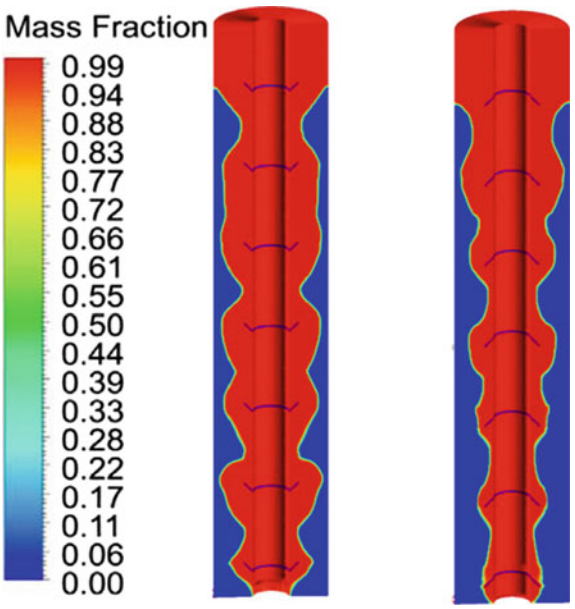


**Fig. 13.26** Liquid fraction (LF) at 1080 s, annular fins −45° and +45° (Parsazadeh and Duan 2018)

i.e. when liquid fraction (f_l) < 0.25, heat conduction plays the dominant role and melting occurs only near the HTF tube wall. During this period, nanoparticle concentration, fin angle and pitch have no significant effect on the melting process but at liquid fraction 0.25, some effects of these parameters are visible, with the effect of fin angle being the most significant. Beyond liquid fraction of 0.70, effects of these parameters become insignificant till all the NePCM melts. The effect of fin pitch during the charging process is relatively negligible on the rate of heat transfer and charging duration.

It is also concluded that a positive fin angle seems to be favouring the charging process. There was an adverse hot spot region seen in the case of −45° fins which was absent for +45° fin. Further altering the fin angle from −45° to +45° leads to the formation of larger and stronger vortices which enhances convective heat transfer, therefore, reduces charging time.

Wang et al. (2016) studied the effect of longitudinal fins on horizontal sleeve tube. Numerical studies were performed in order to understand the effect of fin geometry, i.e. fin length, ratio and angle between neighbour fins, on the charging process of ST-LHTES device.

Figure 13.27a, b, compares the melting of PCM without fin and with four half-scale fins at a neighbour angle of 90°. As can be observed from the 13.27a, b, there is a significant increase in heat transfer and rate of melting due to the impact of longitudinal fins on horizontal tube. For early stages, the melted PCM is near the HTF tube wall and fin. As the time passes by, comparatively more PCM melts in the four-half scale fin unit than no-fin unit due to heat transfer enhancement. From Fig. 13.27a, it can be seen that at 2000s, natural convection vortices are more

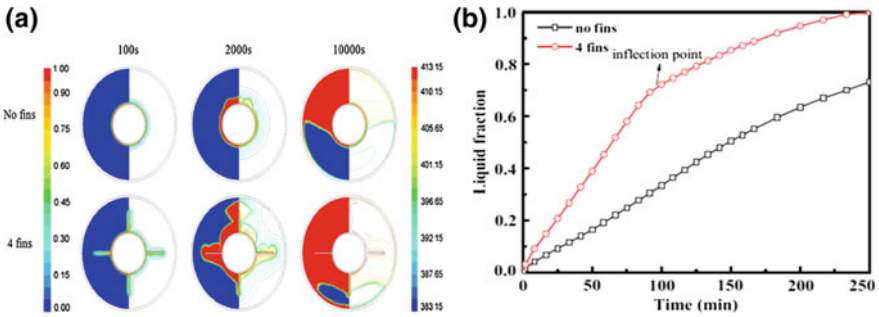


**Fig. 13.27** **a** Contours of liquid fraction and temperature gradient for sleeve tube with no fins and four fins LHTES unit, **b** Liquid fraction of PCM (Wang et al. 2016)

intense in PCM for four half-scale fin unit. An 'inflection point' can be seen in Fig. 13.27b for the four half-scale fin case in the graph above depicting the time when total melting speed reduces as the upper region of the PCM is almost completely melted. Wang et al. (2016) concluded that natural convection has a significant effect on melting process and the most effective angle between neighbouring fins is 60–90° if free convection is considered.

C. **Dynamic melting of PCM**:

Low thermal conductivity of PCM used in ST-LHTES is an undesirable quality, since it reduces heat transfer rate, and thus, increases charging time of the system. Various methods are reported in literature in order to enhance thermal conductivity (reduce thermal resistance) of the PCM, so as to improve performance of the system such as adding external surfaces (fins), heat pipes and adding highly conductive materials such as carbon-based elements, metallic particles elements and nanoparticles with the PCM. Although they have been found to be very effective, their presence in PCM causes a reduction in the energy storage capacity, and compactness factor which in turn leads to hike the fabrication cost of the system.

Dynamic melting is a relatively new concept of enhancing heat transfer in LHTES devices. The heat transport enhancement scheme involves recirculation the liquid PCM melt as the melting process is under progress by means of using a pump. The overall heat transfer coefficient improves due to the incorporation of forced convection in the liquid melt (Gasia et al. 2017b). In dynamic melting of PCM, an external mechanical energy is applied, like a pump, to circulate the already melted PCM within the PCM domain. This results in a significant reduction in the thermal resistance of PCM since force convection becomes the dominating heat transfer mechanism. It becomes quiet evident from the above discussion that the compactness number of the storage system remains constant, as no external elements are added in the PCM, while higher heat transfer rates are achieved. Another added advantage of the method is that phase segregation may be avoided due to continuous movement of the PCM.

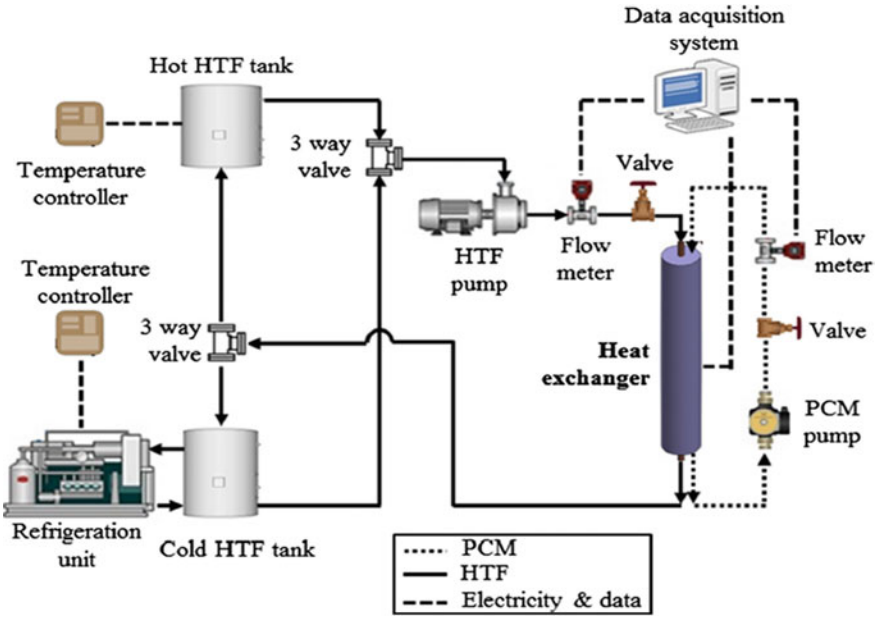


**Fig. 13.28** Schematic view of experimental setup for dynamic melting experiment (Gasia et al. 2017b)

While Fig. 13.28 presents schematic of the experimental setup used, Fig. 13.29 shows the effect of dynamic melting on local effectiveness of ST-LHTES system with respect to the PCM liquid fraction for an HTF flow rate of 1 litre per minute. A baseline test was designed by Gasia et al. (2017b), where dynamic melting was absent and three other cases with 0.5, 1 and 2 L/min flow rate of PCM was selected to study the effect of dynamic melting.

As can be seen from Fig. 13.29, for the baseline test, initially, the effectiveness is high caused by low thermal resistance in the PCM followed by a decreasing trend up to 0.25 liquid fractions and remains nearly constant until the liquid fraction reaches 0.4. Thereafter, convection effects dominate, causing low thermal resistance. At the later stages of melting process, there is a decrease in the effectiveness due to decrease in heat transfer area, as interface between solid–liquid decreases rapidly. The average effectiveness value obtained during the baseline case study is reported to be 0.088 (Gasia et al. 2017b).

At a melt fraction of nearly 0.095, the three dynamic melting starts, and the sudden and sharp decrease in the effectiveness were caused due to mixing of the PCM in the PCM recirculation loop, which was initially at ambient temperature. Soon after this decrease, there is again a sudden and sharp increase of effectiveness due to the recirculation, which resulted in drop of the PCM temperature. Hence, the HTF outlet temperature reduced sharply causing a sharp rise of the effectiveness.

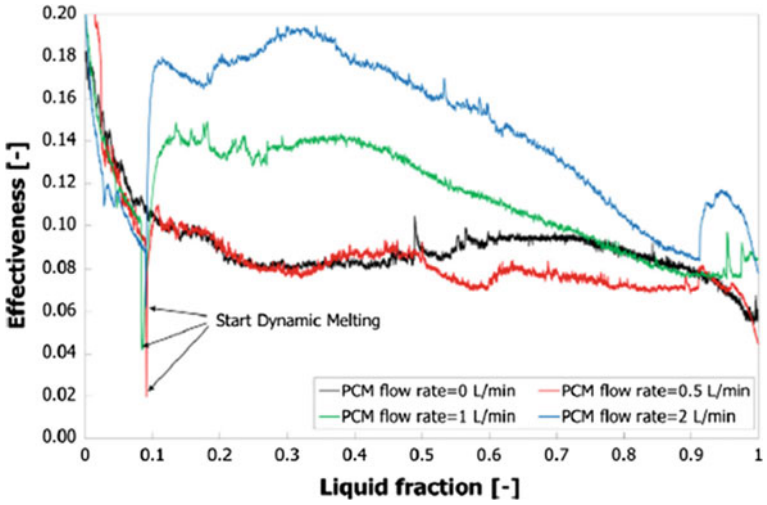


**Fig. 13.29** Local effectiveness evolution during the melting process for HTF flow rate of 1 L/min with and without the influence of the dynamic melting (Gasia et al. 2017b)

At nearly 0.9 liquid fraction, again an increase in effectiveness can be seen which may be attributed to the last piece of solid PCM suddenly melting and reducing the PCM liquid temperature and there by HTF outlet temperature.

Effectiveness of dynamic melting may be directly related to PCM flow rate. It can be clearly seen from Fig. 13.29 that enhancement in heat transfer rate is observed when PCM flow rate was equal to or greater than the HTF flow rate (Gasia et al. 2017b).

## 13.12 Parametric Analysis of Charging/Discharging Dynamics

A. Orientation and inclination effect
B. Effect of HTF inlet direction
C. Eccentricity and variation in HTF inlet temperature

A. **Orientation and Inclination effect**:

Based on combined conduction and convection heat transfer model, Seddegh et al. (2016) did a comparative numerical study on thermal behaviour of vertical and horizontal ST-LHTES unit, using paraffin RT50 as PCM and water as HTF.

Figure 13.30 shows that for the same inlet HTF temperature, total melting time for PCM is less for horizontal configuration as compared to vertical configuration of shell and tube, while HTF inlet direction is from top to bottom in vertical orientation.

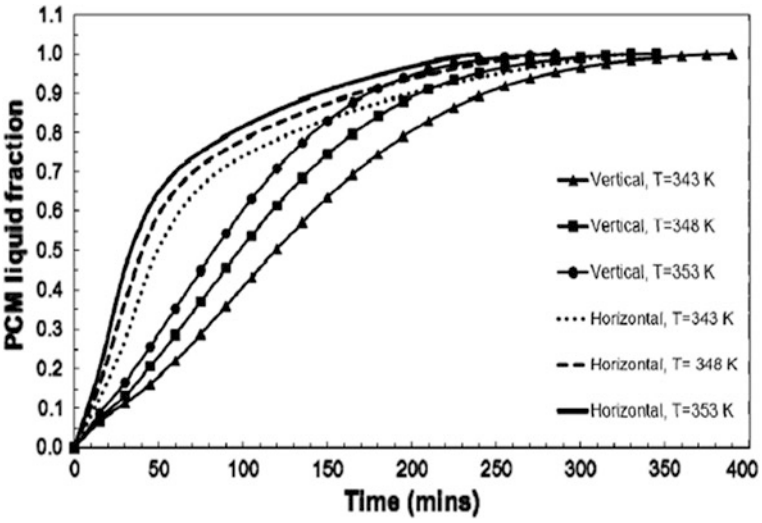


**Fig. 13.30** PCM liquid fraction in vertical and horizontal units during the charging process at different HTF inlet temperatures (Seddegh et al. 2016)

After an experimental investigation conducted by Akgün et al. (2007) on a vertical concentric tube with paraffin (P1) as PCM and water as HTF, it was concluded that enhancement is achieved, for both melting and solidification, by tilting the outer surface of the storage container, or the surface of the outer shell by a tilting angle of 5°. With such an angular arrangement of shell, nearly, a 30% decrease in the total melting time was achieved (Akgün et al. 2007).

B. **Effect of HTF inlet direction**:

Experimental and numerical studies were performed, on vertical shell-and-tube latent heat thermal energy storage system filled with paraffin RT35 in annular region and water flowing as HTF in inner tube, by Longeon et al. (2013). The two configurations compared are: (i) top injection configuration, where the ST-LHTES unit is positioned vertically and the HTF is injected from the top and (ii) Bottom injection configuration, where the ST-LHTES unit is positioned vertically and the HTF is injected from the bottom. Based on the configurations four cases can be described as charging with top inlet, charging with bottom inlet, discharging with top inlet and discharging with bottom inlet.

During charging of PCM with top injection of HTF, solid–liquid melt front moves continuously downwards along the annular region with a 'vessel shape'. This particular shape appears due to the set-up of a natural convection current, after a pure conduction mode as soon as a sufficient layer of PCM is melted. As can be seen from Fig. 13.31a, hot liquid PCM flows upward along the inner HTF tube heating up the top of the heat exchanger and enabling the PCM located in the upper

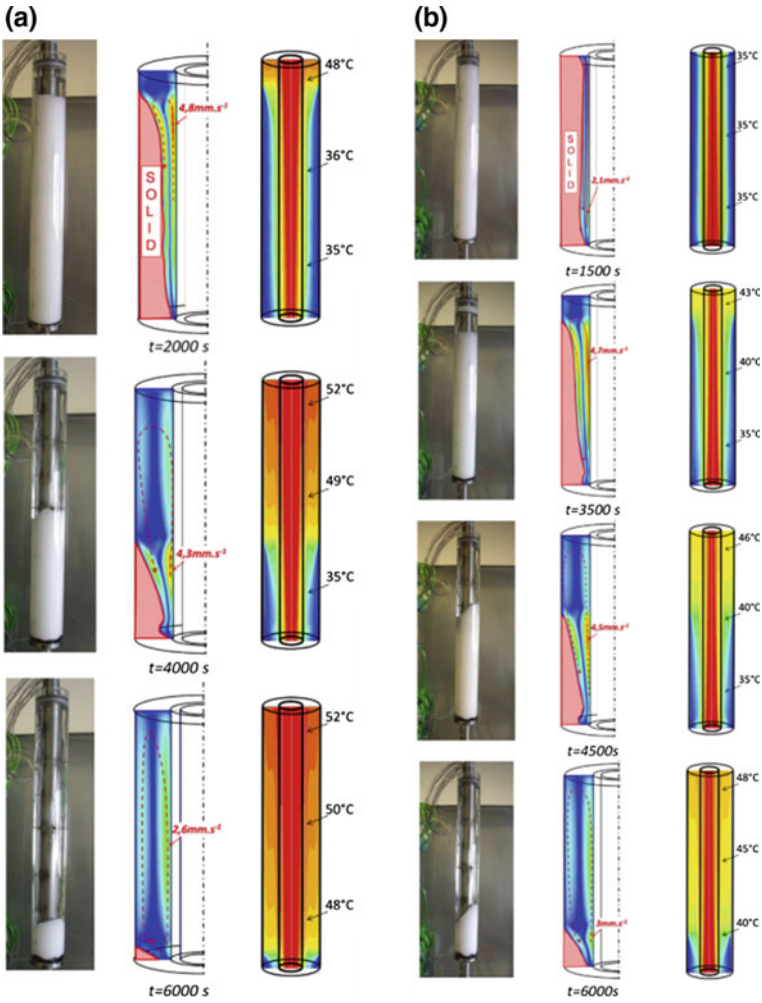


**Fig. 13.31** **a** Melting front shots (left), numerical velocities magnitude in the PCM (middle) and temperature (right) profiles during charge with top HTF injection, **b** during charging with bottom HTF injection (Longeon et al. 2013)

layer to melt. For the present case, thermocline profile can be observed in the annular region of PCM where the hot PCM is at the top and the cold at the bottom.

During the charging of PCM with bottom injection of HTF, the PCM first melts over its whole thickness (complete radial melting of PCM) at the top of the heat exchanger and not at the bottom, as expected. First, a thin layer of PCM melts along the inner HTF tube from bottom to top. After some critical amount of PCM is melted, convection current is set-up (as can be seen from Fig. 13.31b at 1500 s). The natural convection so setup intensifies the heat exchange. The hot PCM fluid

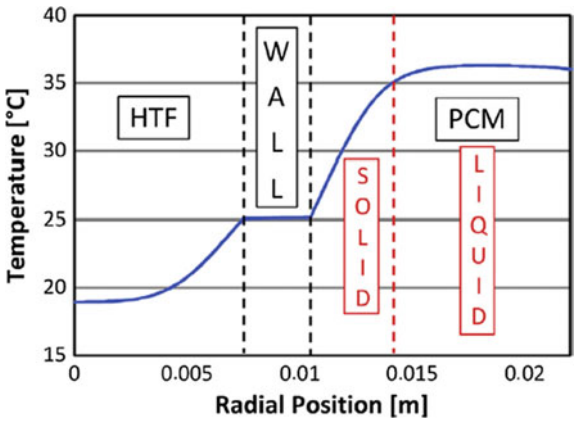


**Fig. 13.32** Radial temperature profile at $t$ = 1000 s in midsection (Longeon et al. 2013)

rising up to the top melts the solid PCM layer at the upper portion. At the end, the solid PCM at the outer radial distances melts due to natural recirculation effects.

During discharging of PCM with HTF bottom inlet, the solid–liquid interface moves up from bottom to top, but, cannot be seen very clearly during the experiment due to the fact that solid PCM appears first around the HTF tube causing visual deformation. Also, melting temperature of PCM being higher than ambient temperature, a thin layer of solid PCM appears against the external cylinder (shell) due to heat loss, causing visual blockage. Analysis of the fluent-based simulation results by Longeon et al. (2013) states that solidification front moves upwards from bottom in an 'oblique shape' and natural convection does not play a significant role. When the solidification starts, a slow convection current is set-up in the liquid PCM and disappears gradually as the solid–liquid front moves up the annular region. The liquid PCM temperature beyond the solidification front remains close to the melting temperature as can be seen in Fig. 13.32. This prevents the setup of natural convection.

During discharging of PCM with HTF inlet from the top, natural convection yet again plays an insignificant role (Longeon et al. 2013).

Longeon et al. (2013) recommends a top HTF injection during charging process and bottom HTF injection during discharging, since the storage unit can be easily managed with top injection during partial charging, since major amount of heat is stored at the upper part of the storage unit, which can be restored easily with a bottom discharge. Another reason for such recommendation is that during solidification voids are formed. If the HTF injection is from bottom for discharging, then any void formed during solidification will be filled by liquid PCM by means of gravity.

C. **Eccentricity and variation of HTF inlet temperature**:

Most of the studies available in the literature are related to 'concentric tubes' for shell-and-tube LHTES device. However, few studies (Cao et al. 2018; Zheng et al. 2018a; Yazici et al. 2014; Avcı et al. 2014) have considered the effect of

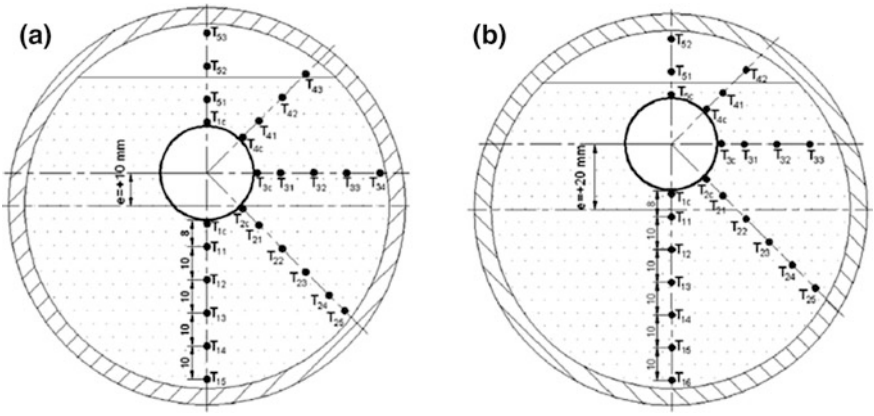


**Fig. 13.33** Points of the temperature measurements inside the PCM for, **a** $e$ = 10 mm, **b** $e$ = 20 mm, (solidification) (Yazici et al. 2014)

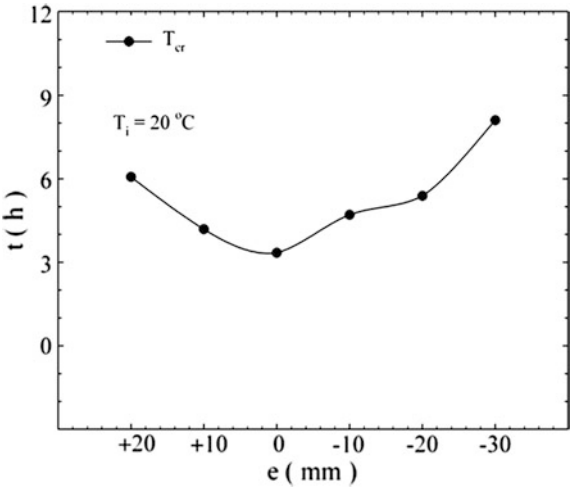


**Fig. 13.34** Solidification time ($t$) versus eccentricity ($e$) (Yazici et al. 2014)

eccentricity on the cycle dynamics of ST-LHTES. In eccentric configuration, the inner tube is shifted somewhat away from the central axis of the shell as shown in Fig. 13.34.

Yazici et al. (2014) studied the effect of eccentricity of HTF tube on solidification of PCM in a horizontal shell-and-tube arrangement experimentally keeping the HTF mass flow rate and inlet temperature constant. Distilled water is used as HTF while P56-58 paraffin wax is used as PCM. The eccentricity of the inner HTF tube is maintained in a manner such that the inner tube centre is vertically aligned to shell central axis (Fig. 13.33). Various values of eccentricity were selected for experiments $(e = -30, -20, -10, 0, 10, 20\,\text{mm})$. Figure 13.33a, b shows

schematic of ST-LHTES with two values of eccentricities. An air gap (15% of the total volume) is maintained at the top of the module such that volumetric expansion of the PCM during melting process can be accommodated.

A critical point in the PCM geometry is referred to that point which takes longest time to solidify. $T_{cr}$ is the temperature of that critical point. As the eccentricity of the HTF tube increases (either in upward or downward direction from the centre of the outer shell), time duration for total solidification gets extended (Fig. 13.34). In other words, lowest solidification time can be obtained for concentric geometry as compared to the eccentric ones. Since, primary objective is to discharge the stored thermal energy within shortest possible time duration, concentric geometries can be considered to be the most favourable design option.

Another experimental study was conducted by Avcı et al. (2014) where melting behaviour of paraffin in a horizontal shell in tube type storage unit was studied. Apart from temporal behaviour of inlet HTF, concentric geometry and effect of three different eccentric geometries were investigated ($e$ = 10, 20, 30 mm) keeping mass flow rate of the HTF constant (280 kg/h).

Critical point temperature for eccentricity 20 mm is shown by $T_{12}$, whereas for the same critical point, the temperature is depicted by $T_{11}$ for eccentricity 30 mm (as shown in Fig. 13.35).

The graph shown in Fig. 13.36 compares the temporal variation of critical points which are very close to the bottom for various eccentricity values. With the increasing eccentricity of the HTF tube in the downwards direction from the central axis of the shell, time required for melting reduces till the eccentricity reaches the critical value.

In the experiment for melting of PCM, Avcı et al. (2014) concluded that at the beginning of the melting process for all configurations, with or without eccentricity, conduction mechanism is the dominant factor for heat transfer at the beginning.

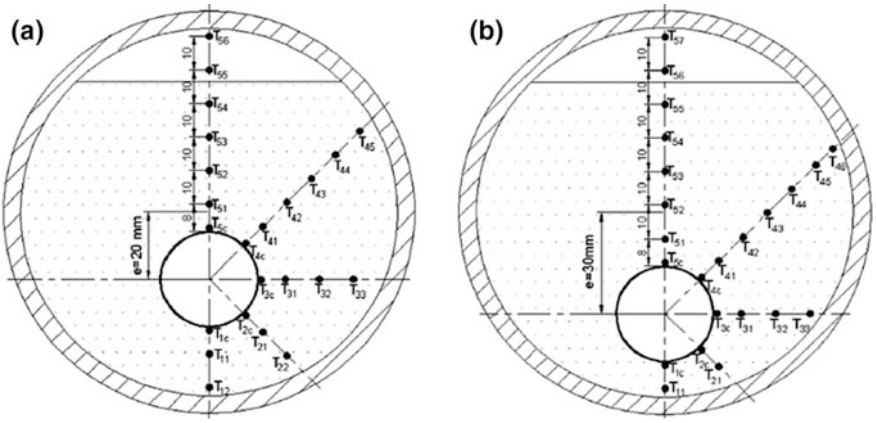


**Fig. 13.35** Points of temperature measurements inside the PCM for melting with eccentricity, **a** $e$ = 20 mm, **b** $e$ = 30 mm (Avcı et al. 2014)

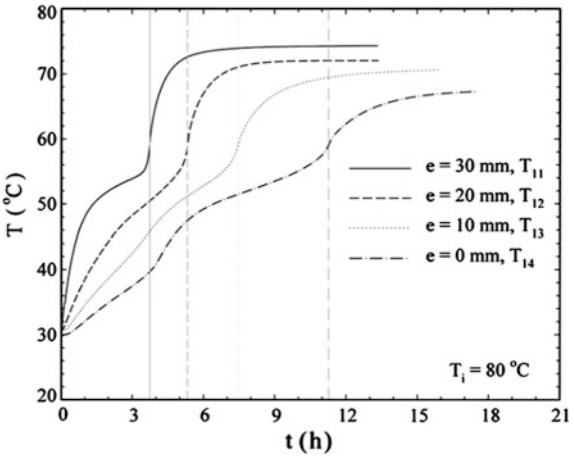


**Fig. 13.36** Effect of eccentricity on transient temperatures of the critical stations for HTF at 80 °C inlet during charging (Avcı et al. 2014)

However, natural convection gradually becomes dominating driving force for heat transfer after the initial stage. For the horizontal concentric shell and tube, melting in the upper half of the annulus region enhanced significantly owing to the effect of natural convection. As the inner tube is moved downwards from the central axis of the shell (i.e. a geometric change from concentric to eccentric), circulation area corresponding to natural convection increases, and therefore, enhancement in melting rate is observed Thus eccentricity intensifies natural convection inside the PCM. Experimental results presented by Avcı et al. (2014) reports 67% decrease of total melting time when compared to concentric cases.

The graph in Fig. 13.37 shows the effect of inlet temperature on melting of PCM. As the inlet temperature of HTF increases melting time is reduced. Least melting time is observed for highest HTF inlet temperature combined with highest eccentricity in downward direction from shell central axis.

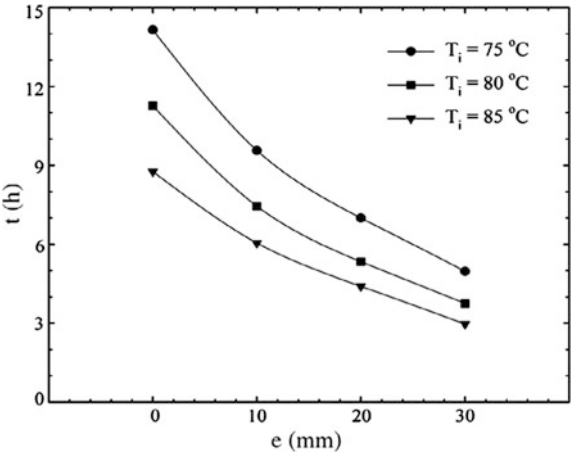


**Fig. 13.37** Effect of eccentricity on the total melting time for different inlet temperatures during charging (Avcı et al. 2014)

It seems obvious that as the eccentricity of HTF tube in the downward direction increases, melting time reduces. However, Zheng et al. (2018a) reported that there exists an optimal eccentricity for the shortest melting time and is linearly dependent on the Rayleigh number. Thus larger eccentricity does not always improve the melting performance.

Figure 13.38 shows the effect of eccentricity (Ec) on the total non-dimensional melting duration represented by Fourier number ($Fo_{tot}$) for two different temperatures of HTF tube wall. The total melting time denotes the length of time between the beginning of heating and the moment when 100% melt fraction is obtained. The Rayleigh numbers Ra for inner tube temperature = 316 K and inner tube temperature = 416 K are 1.63 × 106 and 1.21 × 107, respectively. Based on the simulations performed, Zheng et al. (2018a) concluded that higher value of Rayleigh number (Ra) causes shorter duration of complete melting. Also, there exists an optimum eccentricity for a given Rayleigh number and inner tube temperature, as can be seen from Fig. 13.38.

Figure 13.39 shows the linear variation of optimum eccentricity with respect to Ra, where optimum eccentricity may be defined as the numerical value of eccentricity at which total melting time for the PCM will be minimal. As the Rayleigh number increases, optimum value of eccentricity also increases.

Experimental and numerical parametric analysis was carried out by Kibria et al. (2014) to understand the thermal behaviour of ST-LHTES unit with different flow parameters and system dimensions for both charging and discharging process. The flow parameter and dimensions under consideration are mass flow rates, inlet temperatures of HTF, tube thicknesses and radii, respectively. It was found that the inlet temperature of the HTF influences the solidification and melting of PCM significantly, whereas mass flow rate has negligible influence on phase change.

From the graph in Fig. 13.40a, b, it can be seen that for discharging (solidification of PCM) process rate of heat transfer increases reducing total discharging time of PCM as the inlet temperature of HTF is reduced. Similarly, during charging (melting of PCM) process, rate of heat transfer increases reducing the total charging time of PCM as the HTF inlet temperature is increased (Table 13.4).

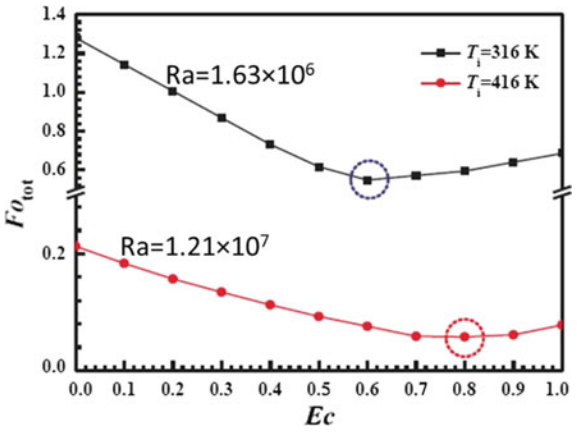


**Fig. 13.38** Total melting time (represented by Fourier number) as a function of eccentricity for different Rayleigh numbers (Zheng et al. 2018a)

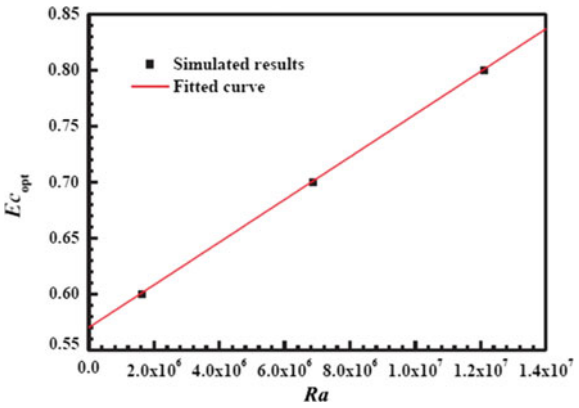


**Fig. 13.39** Optimal eccentricity as a function of Rayleigh number (Zheng et al. 2018a)

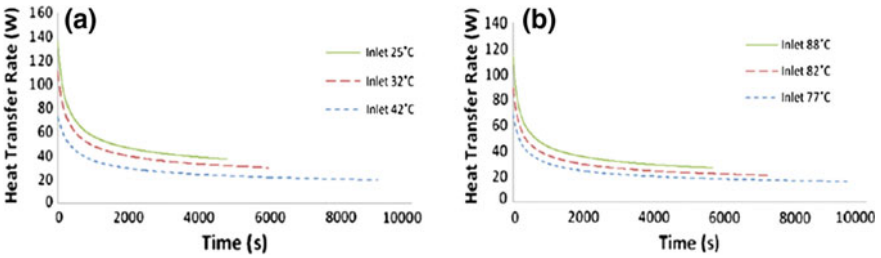


**Fig. 13.40** **a** Heat transfer rate during discharging with different inlet temperatures, **b** heat transfer rate during charging with different inlet temperatures (Kibria et al. 2014)

**Table 13.4** Non-dimensional parameter associated with ST-LHTES

| S. no. | Non-dimensional parameter | Formula | Refs. |
|---|---|---|---|
| 1 | Stefan number (Ste) | $\text{Ste} = \frac{C_P(T_W - T_m)}{\text{LH}}$ | Cao et al. (2018) |
| 2 | Rayleigh number (Ra) | $\text{Ra} = \frac{g\beta d^3(T_W - T_m)}{\alpha\vartheta}$ | Cao et al. (2018) |

where
$C_p$ = Specific heat at constant pressure (J/kg K)
$T_w$ = Inner wall temperature (K)
$T_m$ = Phase change temperature (K)
LH = Latent Heat (J/kg)
$g$ = Acceleration due to gravity (m/s$^2$)
$\beta$ = Expansion coefficient (1/K)
$D$ = Equivalent diameter (m)
$\alpha$ = Thermal diffusivity (m$^2$/s)
$\upsilon$ = Kinematic viscosity (m$^2$/s)

## 13.13 Current Issues, Challenges and Limitations

1. A major drawback in the development of latent heat thermal energy storage systems has been the low thermal conductivities possessed by most phase-change materials (PCMs).
2. Need for an in-depth study into multi-tube ST-LHTES systems.
3. Suboptimal structure of heat exchanger (Zheng et al. 2018b).
4. Most of the work in literature reports about laboratory level experimental setup and simulations. Large-scale industrial level setups are still to be envisaged.

## References

Agyenim F, Eames P, Smyth M (2010) Heat transfer enhancement in medium temperature thermal energy storage system using a multitube heat transfer array. Renew Energy 35(1):198–207

Akgün M, Aydın O, Kaygusuz K (2007) Experimental study on melting/solidification characteristics of a paraffin as PCM. Energy Convers Manage 48(2):669–678

Avci M, Yazici MY (2013) Experimental study of thermal energy storage characteristics of a paraffin in a horizontal tube-in-shell storage unit. Energy Convers Manage 73:271–277

Avcı M, Aydın O, Akgun M (2014) Effect of eccentricity on melting behavior of paraffin in a horizontal tube-in-shell storage unit: an experimental study. Sol Energy 101:291–298

Bennon WD, Incropera FP (1987) A continuum model for momentum, heat and species transport in binary solid-liquid phase change systems—I. Model formulation. Int J Heat Mass Transf 30 (10):2161–2170

Brent AD, Voller VR, Reid KTJ (1988) Enthalpy-porosity technique for modeling convection-diffusion phase change: application to the melting of a pure metal. Num Heat Transf Part A App 13(3):297–318

Cao X, Yuan Y, Xiang B, Haghighat F (2018) Effect of natural convection on melting performance of eccentric horizontal shell and tube latent heat storage unit. Sustain Cities Soc 38:571–581

Chakraborty PR (2017) Enthalpy porosity model for melting and solidification of pure-substances with large difference in phase specific heats. Int Commun Heat Mass Transf 81:183–189

Chakraborty S, Dutta P (2001) A generalized formulation for evaluation of latent heat functions in enthalpy-based macroscopic models for convection-diffusion phase change processes. Metall Mater Trans B 32(3):562–564

Chung DDL (2016) A review of exfoliated graphite. J Mater Sci 51(1):554–568

Colella F, Sciacovelli A, Verda V (2012) Numerical analysis of a medium scale latent energy storage unit for district heating systems. Energy 45(1):397–406

Fornarelli F, Camporeale SM, Fortunato B, Torresi M, Oresta P, Magliocchetti L, Miliozzi A, Santo G (2016) CFD analysis of melting process in a shell-and-tube latent heat storage for concentrated solar power plants. Appl Energy 164:711–722

Fornarelli F, Ceglie V, Fortunato B, Camporeale SM, Torresi M, Oresta P, Miliozzi A (2017) Numerical simulation of a complete charging-discharging phase of a shell and tube thermal energy storage with phase change material. Energy Procedia 126:501–508

Gasia J, Diriken J, Bourke M, Van Bael J, Cabeza LF (2017a) Comparative study of the thermal performance of four different shell-and-tube heat exchangers used as latent heat thermal energy storage systems. Renew Energy 114:934–944

Gasia J, Tay NS, Belusko M, Cabeza LF, Bruno F (2017b) Experimental investigation of the effect of dynamic melting in a cylindrical shell-and-tube heat exchanger using water as PCM. Appl Energy 185:136–145

Guo S, Zhao J, Wang W, Yan J, Jin G, Zhang Z, Gu J, Niu Y (2016) Numerical study of the improvement of an indirect contact mobilized thermal energy storage container. Appl Energy 161:476–486

Han GS, Ding HS, Huang Y, Tong LG, Ding YL (2017) A comparative study on the performances of different shell-and-tube type latent heat thermal energy storage units including the effects of natural convection. Int Commun Heat Mass Transf 88:228–235

Hosseini MJ, Rahimi M, Bahrampoury R (2014) Experimental and computational evolution of a shell and tube heat exchanger as a PCM thermal storage system. Int Commun Heat Mass Transf 50:128–136

Iverson BD, Broome ST, Kruizenga AM, Cordaro JG (2012) Thermal and mechanical properties of nitrate thermal storage salts in the solid-phase. Sol Energy 86(10):2897–2911

Jian-you L (2008) Numerical and experimental investigation for heat transfer in triplex concentric tube with phase change material for thermal energy storage. Sol Energy 82(11):977–985

Jmal I, Baccar M (2015) Numerical study of PCM solidification in a finned tube thermal storage including natural convection. Appl Therm Eng 84:320–330

Jouhara H, Khordehgah N, Almahmoud S, Delpech B, Chauhan A, Tassou SA (2018) Waste heat recovery technologies and applications. Therm Sci Eng Prog 6:268–289

Kaizawa A, Kamano H, Kawai A, Jozuka T, Senda T, Maruoka N, Akiyama T (2008) Thermal and flow behaviors in heat transportation container using phase change material. Energy Convers Manage 49(4):698–706

Khan Z, Khan Z, Tabeshf K (2016) Parametric investigations to enhance thermal performance of paraffin through a novel geometrical configuration of shell and tube latent thermal storage system. Energy Convers Manage 127:355–365

Kibria MA, Anisur MR, Mahfuz MH, Saidur R, Metselaar IHSC (2014) Numerical and experimental investigation of heat transfer in a shell and tube thermal energy storage system. Int Commun Heat Mass Transf 53:71–78

Kumar D (2018) Master of technology thesis. IIT Jodhpur

Lakhani S, Raul A, Saha SK (2017) Dynamic modelling of ORC-based solar thermal power plant integrated with multitube shell and tube latent heat thermal storage system. Appl Therm Eng 123:458–470

Longeon M, Soupart A, Fourmigué JF, Bruch A, Marty P (2013) Experimental and numerical study of annular PCM storage in the presence of natural convection. Appl Energy 112:175–184

Mao Q (2016) Recent developments in geometrical configurations of thermal energy storage for concentrating solar power plant. Renew Sustain Energy Rev 59:320–327

Memon SA (2014) Phase change materials integrated in building walls: a state of the art review. Renew Sustain Energy Rev 31:870–906

Morisson V, Rady M, Palomo E, Arquis E (2008) Thermal energy storage systems for electricity production using solar energy direct steam generation technology. Chem Eng Process 47 (3):499–507

Pahamli Y, Hosseini MJ, Ranjbar AA, Bahrampoury R (2017) Effect of nanoparticle dispersion and inclination angle on melting of PCM in a shell and tube heat exchanger. J Taiwan Inst Chem Eng 81:316–334

Parsazadeh M, Duan X (2017) Numerical and statistical study on melting of nanoparticle enhanced phase change material in a shell-and-tube thermal energy storage system. Appl Therm Eng 111:950–960

Parsazadeh M, Duan X (2018) Numerical study on the effects of fins and nanoparticles in a shell and tube phase change thermal energy storage unit. Appl Energy 216:142–156

Patankar S (1980) Numerical heat transfer and fluid flow. CRC Press, Boca Raton

Pizzolato A, Sharma A, Maute K, Sciacovelli A, Verda V (2017) Design of effective fins for fast PCM melting and solidification in shell-and-tube latent heat thermal energy storage through topology optimization. Appl Energy 208:210–227

Seddegh S, Wang X, Henderson AD (2016) A comparative study of thermal behaviour of a horizontal and vertical shell-and-tube energy storage using phase change materials. Appl Therm Eng 93:348–358

Seddegh S, Tehrani SSM, Wang X, Cao F, Taylor RA (2018) Comparison of heat transfer between cylindrical and conical vertical shell-and-tube latent heat thermal energy storage systems. Appl Therm Eng 130:1349–1362

Sharma A, Tyagi VV, Chen CR, Buddhi D (2009) Review on thermal energy storage with phase change materials and applications. Renew Sustain Energy Rev 13(2):318–345

Shrivastava A, Kumar D, Chakraborty PR (2018) Numerical analysis of latent heat thermal energy storage (LHTES) performance: a 2-D axisymmetric approach. In: Fifth international conference on computational methods for thermal problems, ThermaComp2018, IISc Bangalore, 9–11 July 2018.

Tay NHS, Belusko M, Bruno F (2012) Experimental investigation of tubes in a phase change thermal energy storage system. Appl Energy 90(1):288–297

Trp A (2005) An experimental and numerical investigation of heat transfer during technical grade paraffin melting and solidification in a shell-and-tube latent thermal energy storage unit. Sol Energy 79(6):648–660

Typical Physical, Chemical and Thermal Properties of Therminol 66 by SOLUTIA, applied chemistry, creative solutions

Wang P, Yao H, Lan Z, Peng Z, Huang Y, Ding Y (2016) Numerical investigation of PCM melting process in sleeve tube with internal fins. Energy Convers Manage 110:428–435

Xu Y, Li MJ, Zheng ZJ, Xue XD (2018) Melting performance enhancement of phase change material by a limited amount of metal foam: configurational optimization and economic assessment. Appl Energy 212:868–880

Yang X, Lu Z, Bai Q, Zhang Q, Jin L, Yan J (2017) Thermal performance of a shell-and-tube latent heat thermal energy storage unit: role of annular fins. Appl Energy 202:558–570

Yazici MY, Avci M, Aydin O, Akgun M (2014) On the effect of eccentricity of a horizontal tube-in-shell storage unit on solidification of a PCM. Appl Therm Eng 64(1–2):1–9

Zalba B, Marın JM, Cabeza LF, Mehling H (2003) Review on thermal energy storage with phase change: materials, heat transfer analysis and applications. Appl Therm Eng 23(3):251–283

Zhang P, Ma F, Xiao X (2016) Thermal energy storage and retrieval characteristics of a molten-salt latent heat thermal energy storage system. Appl Energy 173:255–271

Zheng ZJ, Xu Y, Li MJ (2018a) Eccentricity optimization of a horizontal shell-and-tube latent-heat thermal energy storage unit based on melting and melting-solidifying performance. Appl Energy 220:447–454

Zheng X, Xie N, Chen C, Gao X, Huang Z, Zhang Z (2018b) Numerical investigation on paraffin/expanded graphite composite phase change material based latent thermal energy storage system with double spiral coil tube. Appl Therm Eng 137:164–172

# Part IV
# Applications of Solar Energy

# Chapter 14
# Current Trends and Future Roadmap for Solar Fuels


**Gurudayal**

**Abstract** Solar to fuel conversion, if it could be performed in a sustainable manner, has the potential to deliver an alternative to unsustainable use of fossil fuels. Solar fuel production by photoelectrochemical (PEC) approach is a promising solution to address this fundamental and important challenge. To date, research into these approaches has been primarily focused on solar water splitting, which produces hydrogen. Thus, the conversion of $CO_2$ to hydrocarbons that could displace currently used fossil fuels remains as an unmet challenge. Various photoelectrode materials such as $Fe_2O_3$, $BiVO_4$, $WO_3$, $TiO_2$, and $Cu_2O$ have been discussed for solar water splitting. However, their performance for PEC water splitting is limited by poor electronic properties and sluggish charge transfer kinetics that lead to high charge carrier recombination. Nanostructuring, elemental doping, surface passivation, conducting template, cocatalyst, and heterostructure are possible pathways to improve their performance. Whereas only a few reports are available on PEC $CO_2$ reduction. A number of semiconducting photocathodes including Si, GaP, InP, and CdTe have been explored for PEC $CO_2$ reduction reaction ($CO_2$RR), although most of these photocathodes produce only two electron products such as carbon monoxide or formate. This chapter reviews the state-of-the art limitations of various semiconducting photoelectrodes for PEC water splitting and $CO_2$ reduction. Other emerging photoelectrode materials and tandem cell strategies are also discussed for efficient solar fuel production. This chapter concludes with the future prospects on the challenges and research direction in this cutting-edge research of solar fuels devices.

**Keywords** Solar fuels · Water splitting · $CO_2$ reduction · PEC

Gurudayal (✉)
Joint Center for Artificial Photosynthesis and Chemical Sciences Division, Lawrence Berkeley National Laboratory, 1 Cyclotron Road, Berkeley, CA 94720, USA
e-mail: mgurudayal@lbl.gov

Gurudayal
Department of Materials Science and Engineering, University of California Berkeley, Berkeley, CA 94720, USA



H. Tyagi et al. (eds.), *Advances in Solar Energy Research*, Energy, Environment, and Sustainability, https://doi.org/10.1007/978-981-13-3302-6_14

## 14.1 Introduction

The development of sustainable and clean energy sources is critical for persistent human progress among increasing populations and climbing energy demand, as fossil fuel energy relies on finite resources and produces considerable air and water pollution (B.E. Outlook 2016; I.E.A. 2015). Greenhouse gases such as $CO_2$ are rising at alarming levels, leading to catastrophic global consequences in terms of climatic aberrations, natural disasters, and resource scarcity (S.C. Program 2015; Nielander et al. 2015). Solar energy is abundantly available on earth surface although, the foremost challenge is to translate and store into chemical fuels by efficient and cost-effective approaches (W.E. Council 2013). The direct conversion of abundant solar energy to liquid and gaseous fuels via photoelectrochemical (PEC) process is an attractive technology (Ronge et al. 2014; Grätzel 2001; Nozik 1976). PEC cell is able to translate the solar energy efficiently into hydrogen and oxygen by splitting water or reducing $CO_2$ into value-added products such as hydrocarbons and alcohols (Grätzel 2001; Ohashi et al. 1977; Crabtree et al. 2004; Walter et al. 2010; Arai et al. 2015).

More specifically, in PEC cell, water or $CO_2$ molecules are wrecked into hydrogen or hydrocarbons on the surface of semiconducting photocathode and oxygen on the surface of a semiconductor photoanode (Arai et al. 2015; Graves et al. 2011; Kumar et al. 2012; Gurudayal et al. 2014). The photoanode and photocathode materials should have an optimum energy band gap to harvest solar light efficiently, appropriate band edges with respect to water redox and $CO_2$ reduction reactions, decent chemical stability, nontoxicity, and economic viability (Nozik 1976; Kumar et al. 2012; Bak et al. 2002; Bard and Fox 1995; Bolton 1996; Osterloh 2008). Another simplest approach for solar fuels is to connect the solar cells in series with a water-splitting electrochemical cell. Burhan and coworker demonstrated similar architecture by using concentrated photovoltaics with PEM electrolyzer for hydrogen production. Their device exhibits a solar to hydrogen conversion efficiency of 15% with a hydrogen production rate of 218 kW h/kg (Burhan et al. 2017).

Thermodynamically, water splitting and $CO_2$ reduction reactions are an uphill reaction and requiring an energy of around $\sim$1.23 eV because this is equivalent to the Gibbs free energy change for these reactions, i.e., 237.2 kJ/mol (Walter et al. 2010; Hamann 2014; Jones et al. 2014). Whereas, water splitting reaction reactions requires an overpotential of 0.4–0.6 due to slow kinetics and recombination losses (Bassi et al. 2014a). Similarly, $CO_2$ reduction reaction requires even higher overpotential $\sim$1 V due to high energy required to form intermediates production and multiple electrons requirement (Jones et al. 2014; Jinghua et al. 2017).

As compared to the two-electron $H_2$ evolution at the photocathode, 12–18 electrons required to form ethylene, ethanol, and propanol in $CO_2$ reduction (Jones et al. 2014; Jinghua et al. 2017). Whereas, four-electron water oxidation at photoanode is also a rate-limiting reaction in PEC cell (Bard and Fox 1995; Bassi et al. 2014a). Therefore, a highly efficient photocathodes and photoanodes system have to be built to achieve these complicated reactions.

After pioneering work of Fujishima and Honda on $TiO_2$ photoanode for oxygen evolution in PEC water splitting, various photoanode materials such as $Fe_2O_3$, $WO_3$, $BiVO_4$, TaON, $Ta_3N_5$, GaInP, and $Fe_2TiO_5$ have been explored (Fujishima and Honda 1972; Bassi et al. 2014b; Gurudayal et al. 2015a; Wang et al. 2008; Gonçalves et al. 2012; Saito et al. 2013; Kim et al. 2015; Maeda and Domen 2011; Higashi et al. 2012). Metal oxide-based photoanodes have been studied extensively for PEC water splitting because to their semiconducting nature, stability in aqueous solutions, and economic viability (Walter et al. 2010; Tachibana et al. 2012; Ager et al. 2015). Similarly, metal oxide/sulfide-based photocathodes ($Cu_2O$, CuO, $MoS_2$ and ZnS) are also advantageous for an $H_2$ generation in PEC water splitting (Lin et al. 2012; Paracchino et al. 2012; Dias et al. 2015; Joshi et al. 2016; Morales-Guio et al. 2014). Although, metal oxides have wide energy band gap and poor electrical properties as compared with traditional III–V semiconductors and silicon (Alexander et al. 2008). Silicon, III–V, ZnTe, and $Cu_2O$ are the most explored photocathodes for $H_2$ production and $CO_2$ reduction reaction (Wang et al. 2008; Reece et al. 2011; Jang et al. 2016; Bornoz et al. 2014; Yamane et al. 2009; Luo et al. 2015; Rau et al. 2014; Kyu et al. 2014; Kong et al. 2016). However, most of the reported photocathodes produce only two electron products such as carbon monoxide or formic acid, while only a few reports show the multiple electron products (ethylene, ethanol propanol, etc.,) of $CO_2$ reduction reaction (Kyu et al. 2014; Kong et al. 2016; Tae et al. 2017). Finally, the fundamental limitations of the solar to chemical fuel conversion PEC cells are the materials availability, energy conversion efficiency, economic feasibility, and scalability (Crabtree et al. 2004; Murphy et al. 2006; Kudo and Miseki 2009). Here, we discuss the mechanism of PEC water splitting cell, various photoanode/photocathode materials and efficiency for water splitting. This chapter gives insight and future directions to achieve efficient solar-driven fuel production (Table 14.1).

**Table 14.1** Solar to hydrogen conversion (STH) efficiency of various photoanodes

| Photoelectrodes | Energy band gap (eV) | STH (%) | References |
|---|---|---|---|
| $TiO_2$ | 3.0 | 2.2 | Murphy et al. (2006) |
| $BiVO_4$ | 2.4 | 9.1 | Prévot and Sivula (2013) |
| $WO_3$ | 2.7 | 4.8 | Walter et al. (2010) |
| $Fe_2O_3$ | 2.2 | 15 | Prévot and Sivula (2013) |
| $Ta_3N_5$ | 2.1 | 16 | Murphy et al. (2006) |
| $Fe_2TiO_5$ | 2.1 | 16 | Bassi et al. (2014) |
| $Cu_2O$ | 2.0 | 18 | Dias et al. (2015) |

## 14.2 PEC Water Splitting Mechanism

Fujishima and Honda introduced the concept of photoelectrochemical (PEC) water splitting by using $TiO_2$ as a photoanode material (Fujishima and Honda 1972). In principle, PEC water splitting is the conversion of solar energy into hydrogen by using photoelectrodes, water redox couples, sunlight, and external bias. More specifically, water molecules are broken into hydrogen at the photocathode and oxygen at the photoanode in a PEC cell under solar illumination. The overall water splitting mechanism is directed by photo-generated electron and holes are characterized by the following reaction (Grätzel 2001; Bard and Fox 1995; Bolton et al. 1985):

Complete reaction:

$$2H_2O + \text{Light} \rightarrow 2H_2 + O_2 \quad \Delta E = 1.23\ \text{V} \tag{2.1}$$

Water splitting half reaction at photoanode (oxygen evolution reaction, i.e., OER):

$$H_2O + \text{Light} \rightarrow 2H^+ + 1/2O_2 + 2e^- \quad \Delta E = 1.23\ \text{V versus NHE} \tag{2.2}$$

Water splitting half reaction at photocathode (hydrogen evolution reaction, i.e., HER):

$$2H^+ + 2e^- \rightarrow H_2 \quad \Delta E = 0.0\ \text{V versus NHE} \tag{2.3}$$

The redox potentials in water splitting half reactions Eq. (2.2) and (2.3) are at pH 0 condition. Water redox potentials are highly pH dependent and their value changes with electrolyte pH can easily be calculated from the Nernst equation.

Generally, water splitting half reaction performed in a PEC cell (Grätzel 2001). Whereas, a complete water splitting required a tandem PEC cell (Prévot and Sivula 2013; Brillet et al. 2010). Here, we discuss water splitting half reaction PEC cells either using a photoanode or photocathode system. In a PEC cell, a semiconducting photoelectrode (photoanode/photocathode) generates electrons in conduction band and holes in valence band by absorbing a photon (Fig. 14.1). These photo-generated holes can oxidize the water molecule at the photoanode/electrolyte interface. Whereas, photo-generated electrons produce hydrogen at photocathode/electrolyte interface.

When a semiconducting photoelectrode is submerged in an electrolyte, a charge transfer take place between the photoelectrode and the electrolyte until the equilibrium condition is attained (Fig. 14.1). In the case of photoanode, upward band bending occurs at the surface of photoanode to match the Fermi level of the semiconductor with the water redox level. Similarly, downward band banding are formed at the photocathode surface to align the Fermi level with water redox level. Due to this energy level band banding, the concentration of electrons/holes get depleted at the photoanode/photocathode–electrolyte interface and this region is known as the depletion layer (Nozik 1976; Lin et al. 2011). The formation of

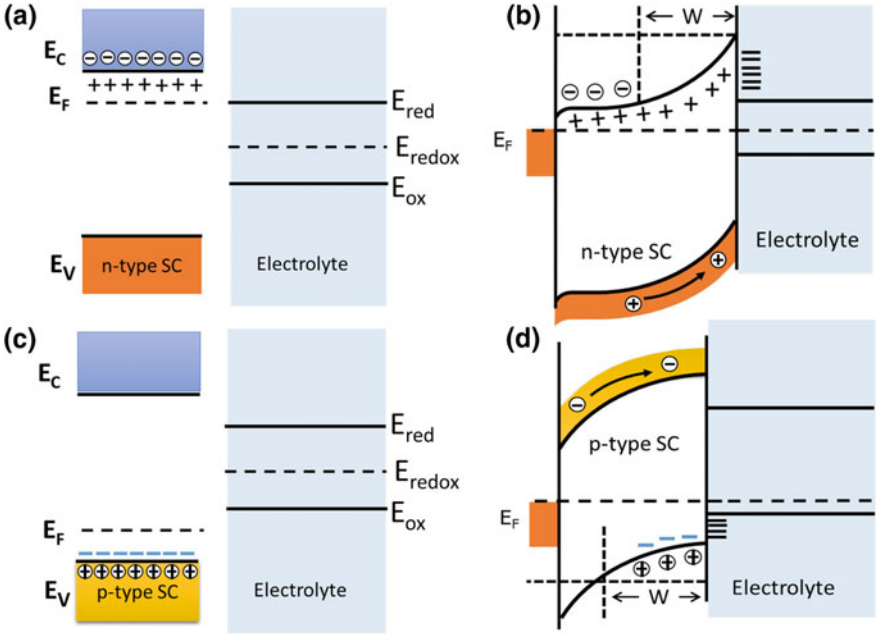


**Fig. 14.1** **a** Separate energy band diagrams of n-type semiconductor and the electrolyte, **b** schematic of submerged and equilibrated energy band diagram of n-type semiconductor, **c** separate energy band diagrams of the p-type semiconductor and the electrolyte, and **d** the submerged and equilibrated energy band diagram of p-type semiconductor. Reprinted from Gurudayal's Ph.D. thesis (Gurudayal 2016)

depletion layer results is an electric field, which is beneficial for charge carrier separation. Figure 14.1a–b shows the energy levels of an isolated and immersed n-type semiconducting photoelectrode and the redox potentials of electrolyte, while Fig. 14.1c–d exhibit the energy levels of isolated and impregnated p-type photocathode and water redox levels.

These photoelectrode materials do not produce required photovoltage to energize the water-splitting reaction (1.23 V) and hence an external bias has to be applied in PEC cell to perform water splitting efficiently. There have been various efforts to materialize an efficient PEC water splitting cell, although there is a large difference between the reported and theoretically predicted efficiencies of PEC cells (Ager et al. 2015; Brillet et al. 2010; Hu et al. 2013; Zhang et al. 2016). This is mainly due to the poor absorption, high recombination, and kinetic losses in photoelectrodes. Many efforts have been devoted to improve the efficiency and to absorb a wide range of light spectrum by making heterostructures and tandem cells (Gurudayal et al. 2015a; Sakai et al. 1988; Mor et al. 2008; Bora et al. 2013a; Wang et al. 2018; Brillet et al. 2012).

## 14.3 Efficiency for PEC Water Splitting

Here, we discuss the several efficiency standards for different photoelectrode materials and PEC cell. Photoelectrode classification and efficiency protocols are essential to implement to directly compare the various PEC systems. There are four standard efficiencies, those facilitate the functioning of photoelectrode materials solar to hydrogen conversion efficiency (STH), applied bias to current conversion efficiency (ABPE), incident photon-to-current conversion efficiency (IPCE), and absorbed photon-to-current conversion efficiency (APCE) (Murphy et al. 2006; Zhang et al. 2016; Doscher et al. 2014).

### *14.3.1 STH Efficiency*

STH efficiency provides the overall efficiency of a PEC water splitting cell under solar illumination. This efficiency has to be measured in two-electrode configuration and in same electrolyte pH. Furthermore, electrolyte solution should not have any sacrificial electron donor because the redox reactions will not reproduce the exact aqueous water splitting condition. STH efficiency is distinct as incident solar energy transformed into chemical energy ($H_2$) and explains as below (Luo et al. 2014; Peharz et al. 2007; Shi et al. 2015):

$$\eta_{\mathrm{STH}} = \left(J_{\mathrm{op}} \times 1.23 \times \mathrm{FE}\right)/P_{\mathrm{Solar}} \tag{3.1a}$$

where $J_{\mathrm{op}}$ is the operating current density (mA $\mathrm{cm}^{-2}$), 1.23 eV is the energy equivalent of Gibbs free energy for water splitting, FE is the Faradaic efficiency of hydrogen and $P_{\mathrm{Solar}}$ is the solar irradiance intensity (100 $\mathrm{mWcm}^{-2}$, AM1.5G).

Practically, solar irradiance intensity has to be normalized with the total illumination area of the device in order to obtain the accurate input power. For photovoltaics-electrochemical cell (PV-EC) based devices, a separate efficiency of each component has to be calculated accurately in order to acquire the solar to hydrogen conversion efficiency (Gurudayal et al. 2017a; Burhan et al. 2018).

$$\eta_{\mathrm{STH}} = \eta_{\mathrm{PV}} \times \eta_{\mathrm{PMU}} \times \eta_{\mathrm{EC}} \tag{3.1b}$$

where $\eta_{\mathrm{PV}}$ is the efficiency of solar cells, $\eta_{\mathrm{PMU}}$ is the efficiency of power management unit and $\eta_{\mathrm{EC}}$ is the efficiency of electrochemical cell.

### *14.3.2 ABPE Efficiency*

A voltage has to be applied between the photoelectrode (working electrode) and counter electrode to provide the extra energy to perform the water splitting. Applied

bias to current conversion efficiency under illumination defines the photoelectrode materials strength to perform the water splitting reaction. The ABPE is explained as below (Murphy et al. 2006):

$$\eta = I_{\mathrm{Ph}}(1.23 - V)/P_{\mathrm{Solar}} \tag{3.2a}$$

where $V$ is the applied Voltage, $I_{\mathrm{Ph}}$ is the photocurrent density at a specific applied voltage, and $P_{\mathrm{Solar}}$ is the intensity of illumination 100 m W $\mathrm{cm}^{-2}$ (AM1.5G). This efficiency is doubtful when the applied voltage exceeds the thermodynamic potential of water splitting (1.23 V). However, ABPE explains the onset potential region of a photoelectrode. ABPE measurements have to be conducted in a two-electrode electrochemical configuration because the potential drop at the counter electrode is unknown in three-electrode configuration. Although, most of the reports show ABPE measured in a three-electrode configuration, where a voltage is applied versus a reference electrode. One can only measure half-cell efficiency in three-electrode electrochemical reaction because the potential drop at the counter electrode is unknown in this arrangement.

### *14.3.3 IPCE Efficiency*

The IPCE defines the photocurrent produced per incident photon with wavelength of solar irradiance. This efficiency is also called an external quantum efficiency (EQE). A photocurrent estimation can be made by integration the IPCE spectra with the standard solar spectrum. IPCE can be explained by three essential processes: (i) charge carrier production per incident photon, (ii) electron-hole separation, and (iii) charge transfer at electrode–electrolyte interface (Gurudayal et al. 2014; Murphy et al. 2006).

$$\mathrm{IPCE} = \mathrm{EQE} = \eta_{(e^- - h^+)} + \eta_{\mathrm{separation}} + \eta_{\mathrm{transport}} \tag{3.3a}$$

The IPCE can also be derived from the ratio of photocurrent with the rate of incident photons per wavelength (Gurudayal et al. 2016; Li et al. 2012).

$$\mathrm{IPCE}(\%) = \left(\left(1240 \times \mathrm{I_{ph}}\right)/\lambda \times \mathrm{J_{Light}}\right) \times 100 \tag{3.3b}$$

where 1240 is an augmentation of $h$ (Planck's constant), $c$ is the speed of light, $I_{\mathrm{ph}}$ is the photocurrent density at a specific wavelength, $\lambda$ is the wavelength of incident light, and $J_{\mathrm{Light}}$ is the irradiance at a particular wavelength.

### 14.3.4 APCE Efficiency

APCE can be defined as internal quantum efficiency and similar to IPCE. APCE accounts the reflection and transmittance losses, whereas IPCE does not. In APCE, we subtract all the optical losses and calculate the efficiency only based on absorbed photons. APCE is a ratio of IPCE and the absorptance of the material (Gurudayal et al. 2014; Murphy et al. 2006).

$$\mathrm{APCE}(\%) = \left((1240 \times I_{\mathrm{Ph}})/\left(\lambda \times J_{\mathrm{Light}} \times 1 - 10^{-A}\right)\right) \times 100 \qquad (3.4a)$$

where 1240 is exponentiation of $h$ (Planck's constant), $c$ is the speed of light, $I_{\mathrm{ph}}$ is the photocurrent density at a specific wavelength, $\lambda$ is the wavelength of illumination light, $J_{\mathrm{light}}$ is the measured irradiance at a specific wavelength, and $A$ is the absorbance of the material.

## 14.4 Photoelectrode Materials for PEC

It is a bottleneck to discover a photoelectrode material for artificial photosynthesis (PEC water splitting), which can mimic the photosynthesis as efficient as a natural leaf (Bak et al. 2002; Maeda and Domen 2011; Kudo and Miseki 2009; Chen et al. 2010). To perform efficient PEC reactions, materials should have excellent stability in an aqueous medium, appropriate energy band levels with water redox potentials, good carrier conductivity, and excellent absorption of the visible spectrum (Kudo and Miseki 2009). A material which can show all these properties is impracticable. In past, numerous semiconducting photoelectrode materials have been discovered but their conduction and valance band potentials are not ideal for water redox levels (Fig. 14.2) (Kudo and Miseki 2009; Bassi et al. 2014c). Consequently, if a material possesses appropriate valance and conduction band edges than the material has a wide energy band gap thus inappropriate for harvesting visible spectrum or not stable in aqueous solution (Chang and Liu 2011; Smith et al. 2015). Metal oxides-based photoelectrodes are widely explored for water splitting because of their favorable semiconducting properties, chemical stability, and economical viability (Alexander et al. 2008; Kudo and Miseki 2009). However, many of them have high energy band gap thus poor absorption of visible light and poor electrical properties (Yamane et al. 2009; Sakai et al. 1988; Hu et al. 2013).

For commercialization, a PEC cell should have an STH efficiency of 10% with a cost of US$ 160/m$^2$ (Keable and Holcroft 2012). This target can be achieved by using earth-abundant materials combined with facile and scalable production methods (Alexander et al. 2008; Brillet et al. 2010).

Essentially, $TiO_2$ has been explored as a photoanode for PEC water splitting but its performance is limited due to high energy band gap (Chang and Liu 2011; Kavan and Grätzel 1995; Zhang et al. 2015). Various attempts have been made to

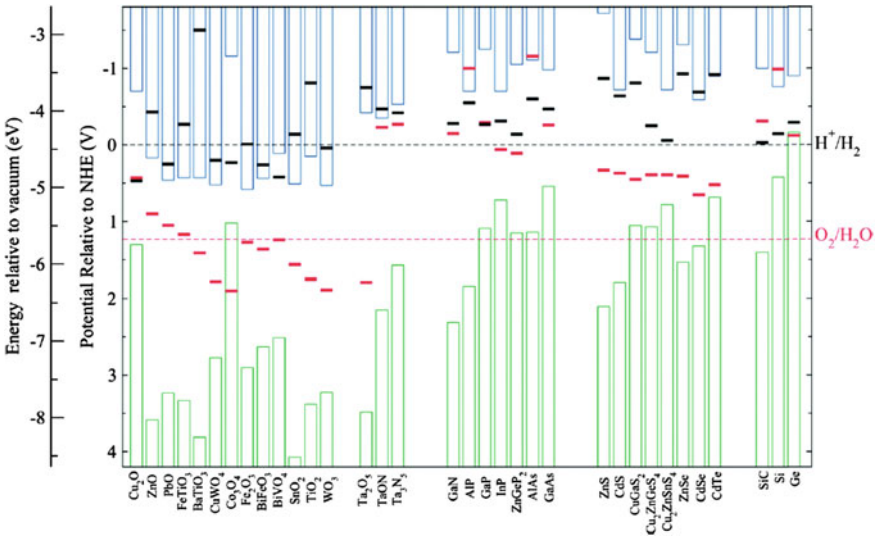


**Fig. 14.2** The energy band positions of various photoelectrodes with respect to water redox potentials. Reprinted with the permission of Royal Society of Chemistry, copyright© 2015 (Smith et al. 2015)

address the poor absorption issue of $TiO_2$ by employing the dyes, with good visible light absorption ability, elemental doping to tune the energy band gap (Cherepy et al. 1997; Park and Bard 2005; Kroeze et al. 2004). $BiVO_4$ is also a photoanode material and widely discussed for PEC water oxidation (Kim et al. 2015; Pihosh et al. 2014). However, researchers achieved 90% of its theoretically anticipated STH efficiency, but this material has poor chemical stability (Pihosh et al. 2015). $WO_3$ is another potential candidate for photoanode material that can perform oxygen evolution reaction under visible light but this material shows low PEC photocurrent performance due to its large energy band gap and poor charge dynamics (Wang et al. 2008; Gonçalves et al. 2012). Oxynitride materials are well-known due to their optimum energy band gap and ideal conduction and valance band edges with water redox levels. Oxynitrides can perform overall water splitting but poor conductivity and charge carrier mobility restrict the PEC performance of these materials (Maeda and Domen 2011). Beyond these metal oxide photoanodes, hematite ($Fe_2O_3$) is the most promising photoanode material (Bassi et al. 2014c; Liao and Carter 2012; Sivula et al. 2011). Hematite shows fundamentally promising effects for PEC water splitting. However, conduction band minima are inappropriate with water reduction potential to reduce water, nevertheless, it is typically used in photoelectrochemical cells that oxidize water into oxygen by using an additional voltage (Sivula et al. 2011; Tallarida et al. 2014).

For photocathode, $Cu_2O$ has been widely studied due to its optimum energy band gap (2.0–2.2 eV) and excellent semiconducting properties such as mobility

but suffer from aqueous stability (Dias et al. 2015; Bornoz et al. 2014; Wang et al. 2018). A protection layer is always required to attain the PEC performance from $Cu_2O$ (Dias et al. 2015). Silicon-based photoelectrodes integrated with various cocatalysts show excellent PEC performance for water splitting but a tradeoff between the cocatalyst loading on the surface of Si and light absorption is a major hurdle.

### *14.4.1 $TiO_2$ Photoanode*

After pioneering work of Fujishima and Honda on $TiO_2$ for PEC water splitting, various researchers extensively explore this material (Fujishima and Honda 1972; Kavan and Grätzel 1995; Park and Bard 2005; Shaner et al. 2016; Yu et al. 2017). $TiO_2$ exhibits wide energy band gap of 3.2 eV, which allow only ultraviolet (UV) light absorption and UV light is only 4% of the solar spectrum reaching on the Earth surface (Fujishima and Honda 1972). Although, its outstanding aqueous stability and low cost makes potentially applicable for PEC water splitting (Chang and Liu 2011). $TiO_2$ nanotube is the superior alternative among $TiO_2$ nanomaterials due to the high surface area to volume ratio. High electron-hole recombination in bulk $TiO_2$ leads to low quantum efficiency (Tsui and Zangari 2013). In order to tackle the recombination losses and light harvesting, materials with smaller band gap were integrated with $TiO_2$ (Shaner et al. 2016). $TiO_2$ black nanoparticles were developed, those show efficient photocatalytic activities without second material integration (Song et al. 2017). Song et al. synthesized black $TiO_2$ nanostructure with high surface area (168.8 $m^2$ g $m^{-1}$) and small particle size (8 nm) for photocatalytic hydrogen generation (Song et al. 2017). This black $TiO_2$ nanostructure exhibits nearly 2.5 times higher solar-driven hydrogen generation rate (56.7 mmol $h^{-1}$ $g^{-1}$) and excellent stability of 70 h under 1 sun illumination than the as prepared $TiO_2$ (Fig. 14.3) (Song et al. 2017). EPR study has been performed to understand the mid-gap states in black $TiO_2$, which are the main reason of light absorption alteration, and thus high photocatalytic properties (Fig. 14.3b) (Song et al. 2017). The size and shape of nanoscale $TiO_2$ can significantly alter the water splitting efficiency (Dantong et al. 2015). Recently, nanostructured $TiO_2$ photoanodes with various cocatalyst shows improved PEC performance (Dantong et al. 2015; Guolei et al. 2012).

### *14.4.2 $Fe_2O_3$ Photoanode*

Hematite is the fourth most ample element on earth (6.3% by weight) (Cornell and Schwertmann 2004). Hematite is a potential photoanode because of its aqueous stability, favorable energy band gap (1.9–2.2 eV), and economic viability (Bassi et al. 2014a; Sivula et al. 2011). Hematite can attain a theoretical maximum STH

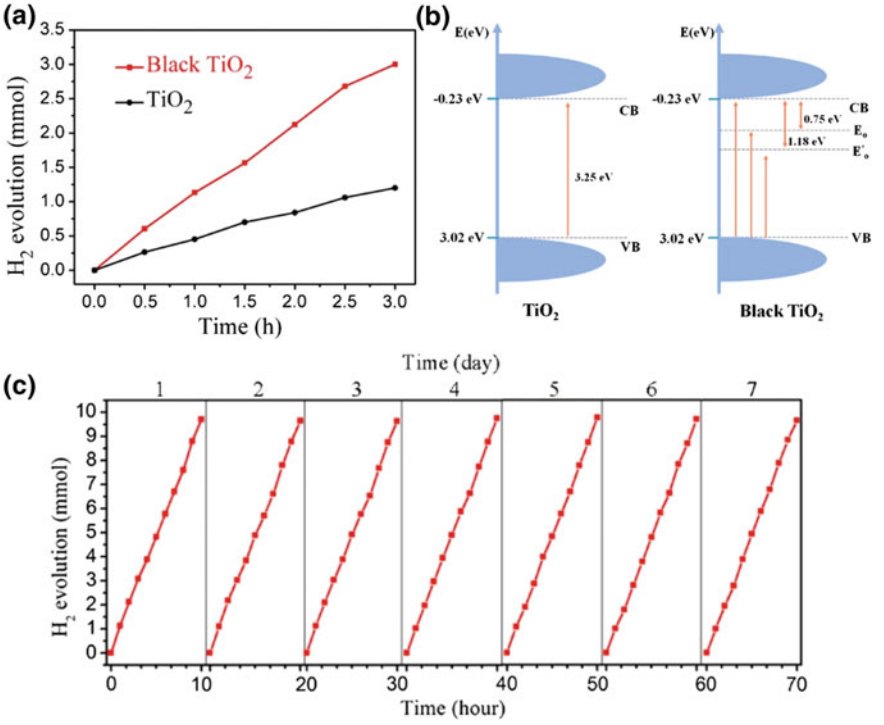


**Fig. 14.3** **a** Photocatalytic hydrogen generation from black and as prepared $TiO_2$ with Pt cocatalyst under the 1 sun illumination, **b** energy band diagram of as prepared and black $TiO_2$. Eo and Eo′ are the possible energy levels corresponding to oxygen vacancies located at 0.73 and 1.18 eV below the CB of $TiO_2$, and **c** stability tests of photocatalytic hydrogen production of black $TiO_2$ for 70 h. Reprinted with the permission of American Chemical Society. Copyright© 2017 (Song et al. 2017)

efficiency of 15% based on its energy band gap, which exceeds the benchmark STH efficiency of 10% essential for large-scale applications (Bassi et al. 2014a; Keable and Holcroft 2012; Sivula et al. 2011). However, the PEC behavior of hematite is constrained by low carrier conductivity, low charge carrier mobility, short minority carrier diffusion length, high absorption depth, and slow charge transfer kinetics at electrode/electrolyte interface leading to high overpotential for water oxidation and poor PEC performance (Bassi et al. 2014a; Sivula et al. 2011; Liao and Carter 2012). Various researchers demonstrated surface and bulk modified hematite photoanode with a significant achievement (Bassi et al. 2014a; Sivula et al. 2011; Bora et al. 2013b; Ling and Li 2014). In recent years, an enormous progress has been made on improving the performance of hematite photoanode since 1978 (Kennedy and Frese 1978; Iordanova et al. 2005; Liao et al. 2011; Gurudayal et al. 2017b). A recent report from Wonyong Choi's group shows 6 mA $cm^{-2}$ current density at 1.23 V versus RHE, which is ~50% of theoretical predicted

photocurrent density based on hematite band gap (Jeon et al. 2017). However, strategies to further improve hematite performance still have to be pursued, for example, by fabricating heterostructures, which incorporate a second material to promote charge separation, charge collection, and surface catalysis (Bassi et al. 2014a).

The use of hematite in thin film or bulk forms is not successful because of the competing requirement of its low minority carrier diffusion length (2–10 nm) and high absorption depth ($\sim$120 nm at 550 nm wavelength) to convert significant amount of incident energy (Beermann et al. 2000; Klahr and Hamann 2011; Gurudayal et al. 2015b). Because of the low hole diffusion length, holes created beyond 5–10 nm of the hematite electrolyte interface can be useful for water oxidation (Gurudayal et al. 2014). A promising photoanode must exhibit low onset potential and high plateau current (Sivula et al. 2011; Ling and Li 2014). In our review paper, we argued that manipulations in nanostructures and doping strategies are necessary to increase the plateau current, while the surface properties of the semiconductor need to be improved to lower the onset potential (Bassi et al. 2014a). In recent times, there has been many advancements in the nanostructure synthesis, bulk, and surface modifications of hematite by forming heterostructures with various materials which overcome the obstacle of low minority carrier diffusion length and achieve improvements in photon absorption (Chou et al. 2013; De Carvalho et al. 2012; Tilley et al. 2010; Mao 2011). Various hematite nanostructures (nanorods, nanowires, cauliflower-type, nanotubes, etc.) have been synthesized by different researchers (Gurudayal et al. 2015b; Tilley et al. 2010; Morrish et al. 2011; Mayer et al. 2012; Wang et al. 2014). The low inherent electrical conductivity of bulk hematite is one limitation that needs to be addressed (Balko and Clarkson 2001; Dunn et al. 2014). These characteristics could be improved by adding suitable dopants to hematite. Various dopants, such as Ti, Zr, Sn, Mn, Ge, and Si are added to replace some of the $Fe^{3+}$ cations, the extra electrons donated to the crystal will increase its conducting electron concentration and retain its n-type conductivity (Gurudayal et al. 2014, 2017b; Liao and Carter 2012; Ling et al. 2011; Glasscock et al. 2007; Sivula et al. 2010; Shen et al. 2012). Elemental doping enhances the PEC performance of hematite by (1) increasing the intrinsic conductivity, (2) generating a shallow donor level below the conduction band minima, which alter the absorption, (3) large cation substitution induces the strain within lattice and thus recombination centers. $Fe^{3+}$ cation has an ionic radii of 55 pm and substituting a cation with larger ionic radii than 55 pm will create additional defects (Gurudayal et al. 2014; Ling and Li 2014; Balko and Clarkson 2001). In our previous study, $Mn^{4+}$ cation were doped in hematite, which has similar ionic radius (53 pm) as $Fe^{3+}$ (55 pm) (Gurudayal et al. 2014). Mn doping improves the PEC performance of hematite by increasing the carrier conductivity without creating the additional defects (similar UV-V is spectra with and without doping) and also enhance the OER kinetics at the electrode/electrolyte interface because of its good OER catalytic property (Fig. 14.4) (Gurudayal et al. 2014).

One of the most commonly used dopants in hematite is Sn which has bigger ionic radii (69 pm) than $Fe^{3+}$ (Ling and Li 2014; Meng et al. 2013). Annamalai and

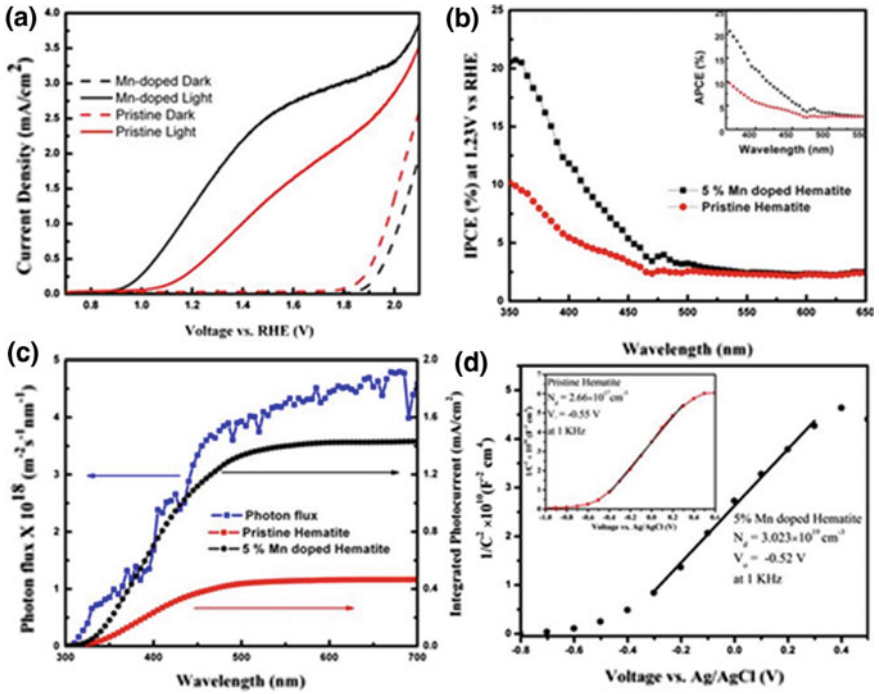


**Fig. 14.4** **a** J–V curve of as prepared and Mn-doped hematite obtained under AM 1.5G illumination and in 1 M NaOH electrolyte solution, **b** IPCE spectrum of undoped and Mn-doped hematite at 1.23 V versus RHE, figure's inset shows APCE spectra, **c** Integrated photocurrent of undoped and Mn-doped hematite, **d** Mott–Schottky plots of undoped in inset and Mn-doped hematite. Reprinted with the permission from Gurudayal et al. (2014). Copyright 2015 American Chemical Society

coworkers show that $Sn^{4+}$ doping improves the photocurrent of hematite and discussed that the $Sn^{4+}$ doping induced a shallow donor level below the conduction band of hematite, which does not contribute to increasing electrical conductivity because of its localized nature (Annamalai et al. 2016). Additionally, $Sn^{4+}$ introduction induces local micro-strain and a decreased Fe–O bond ordering. $Sn^{4+}$ donor dopants in hematite lattices introduce electrons to $Fe^{3+}$ sites and reduce to $Fe^{2+}$. These $Fe^{2+}$ sites can thus improve the electrical conductivity of hematite photoanodes through the polaron hopping (Liao and Carter 2012; Meng et al. 2013; Annamalai et al. 2016; Zhou et al. 2015). Sn can be doped intentionally (Gurudayal et al. 2017b). Alternatively, it could get introduced into hematite by diffusion from FTO glass which is frequently used as the conducting substrate in anodes, during its post-annealing treatments (Ling and Li 2014). Our group recently demonstrated a dual effect of Sn doping (Gurudayal et al. 2017b). Sn doping was achieved by depositing a thin overlayer of $SnO_x$ via atomic layer deposition (ALD) on FeOOH nanorods followed by annealing at 650 °C. This Sn-doped hematite exhibited

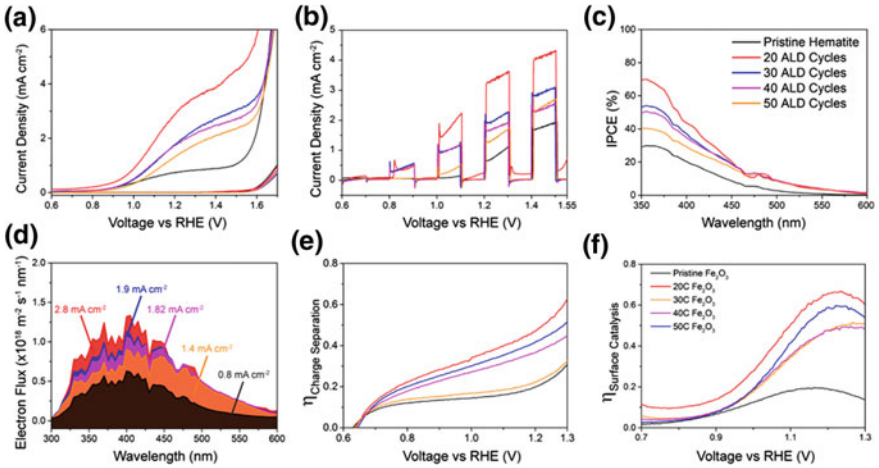


**Fig. 14.5** PEC experimental data obtained in undoped hematite anode and SnOx coated hematite anodes at 20–50 ALD cycles measured under 1 sun illumination (100 mWcm$^{-2}$). **a** J–V curve, **b** chopped photocurrent–potential curve, **c** IPCE action spectrum collected at 1.23 V versus RHE, **d** electron flux and integrated photocurrent from IPCE spectrum previously shown, **e** charge separation efficiency for water oxidation and **f** surface catalysis efficiency for water oxidation. Reprinted with permission from Wiley (Gurudayal et al. 2017b)

3.1 mA cm$^{-2}$ photocurrent density at 1.23 V versus RHE and also showed a cathodic shift in the onset potential when compared to the undoped hematite which was also annealed at 650 °C (Fig. 14.5) (Gurudayal et al. 2017b). High annealing temperatures usually damage the FTO and increase its series resistance, and hence the lower annealing temperature used in this study was beneficial. The annealing temperature could be further reduced by employing two layers of $SnO_2$, an underlayer, and an overlayer to facilitate Sn diffusion from both sides during annealing.

Slow charge transfer kinetics at hematite/electrolyte interface can be tackled by loading cocatalyst or a surface passivation layer (Tilley et al. 2010; Wang et al. 2015; Hisatomi et al. 2011; Klahr et al. 2012). Various surface passivation layers such as $TiO_2$, $Al_2O_3$, $SnO_2$, and $Fe_2O_3$ have been shown beneficial effects of PEC water splitting (Gurudayal et al. 2017b; Jeon et al. 2017; Gurudayal et al. 2015b; Ahmed et al. 2015; Le Formal et al. 2011). Our group shows beneficial effects of $Fe_2O_3$ passivation layer on hematite photoanodes for water splitting (Gurudayal et al. 2015b). This overlayer enhances PEC performance by reducing recombination at electrode/electrolyte interface, which can be distinguished in chronoamperometry analysis (Gurudayal et al. 2015b). A systematic photoelectrochemical impedance analysis revealed that the $Fe_2O_3$ treated hematite exhibit a different and efficient charge transfer behavior than the untreated hematite (Fig. 14.6) (Gurudayal et al. 2015b). $MnO_x$, CoPi, $NiO_x$, and $FeNiO_x$ cocatalyst were also integrated with hematite to enhance the PEC water splitting properties (Bora et al. 2013a; Klahr et al. 2012;

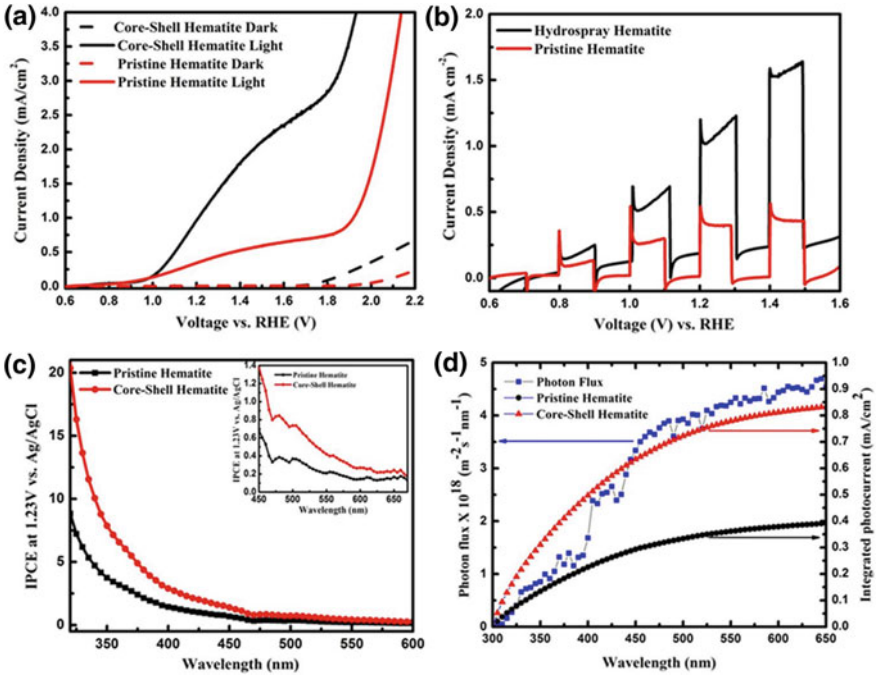


**Fig. 14.6** **a** J–V curve of as prepared and core-shell hematite photoanodes measure under 1 sun illumination, **b** transient photocurrent of as prepared and core-shell hematite photoanodes, **c** IPCE spectrum of as prepared and core-shell hematite photoanodes at 1.23 V versus RHE, and **d** integrated photocurrent from IPCE spectra. Reprinted with the permission from Gurudayal et al. (2015b). Copyright 2015 American Chemical Society

Gurudayal et al. 2016; Li et al. 2012; Morales-Guio et al. 2015). Our group studied the $MnO_x$ nanoparticle coated hematite and compared with CoPi-treated one (Gurudayal et al. 2016). Our study revealed that the $MnO_x$ enhances the charge transfer rate at electrode–electrolyte interface. Whereas, CoPi-treated hematite did not show any change in charge transfer rate, while a decrease in recombination rate was observed (Gurudayal et al. 2016).

### *14.4.3 $Fe_2TiO_5$ Photoanode*

In previous sections, we discussed the strategies employed to improve $Fe_2O_3$-based photoelectrochemical devices by nanostructuring, doping and by surface treatments with thin overlayers and cocatalysts. However, these actions do not address the underlying limitations of hematite namely small minority carrier diffusion length and poor charge transport properties. Although, these limitations have been mitigated somewhat by nanostructuring to increase the space charge layer surface

charge transfer kinetics, and poor OER of hematite are still significant impediments for the realization of commercial PEC cells. This makes it inevitable that we explore new systems with better charge transport properties, longer diffusion length of minority carriers and improved surface reaction kinetics. It has been noted that some complex metal oxides may have desirable properties for consideration as an alternative to hematite (Fatwa and Sean 2017). A report on such complex metal oxides has been recently compiled by Abdi et al. which uncovers a range of materials and their development for application in solar water splitting (Fatwa and Sean 2017). One way to improve the intrinsic properties of $Fe_2O_3$ is to amalgamate with another material, such as $TiO_2$, which inherently has good carrier conductivity and large charge diffusion length (Bassi et al. 2014a). A scrutiny of the Fe–Ti–O ternary system might give indications for an alternative material with the best combination of the desired properties of both $Fe_2O_3$ and $TiO_2$. This is corroborated by the evidence that Ti is an effective dopant to tune the band level positioning in $Fe_2O_3$ (Atabaev et al. 2014). When exploring a novel material for photoabsorber, it is imperative to understand both its bulk and surface characteristics. Surface characteristics are often correlated with the morphology of films and post-deposition treatments, but bulk characteristics depend on the intrinsic electron band and crystal structures.

One candidate material in the Fe–Ti–O ternary system that has received considerable attention in recent times is $Fe_2TiO_5$ pseudobrookite which possesses an orthorhombic structure with a Cmm space group (Gao et al. 2015). $Fe_2TiO_5$ comprises abundant and nontoxic elements and can be produced simply by the oxidation of ilmenite ore at temperatures above 1000 °C with rutile as the byproduct (Gupta et al. 1991). In the form of a film, it has a good thermodynamic and aqueous stability in a wide pH range. Some early reports on $Fe_2TiO_5$ have been on its crystal growth and its characterization (Muranaka et al. 1971; Kōzō et al. 1971). $Fe_2TiO_5$ is an n-type semiconductor and has an energy band gap of around 1.9–2.1 eV which covers a large part of solar spectrum. In a recent report, Guillaume et al. presented a crystal structural analysis for $Fe_2TiO_5$ pseudobrookite composition (Fig. 14.7a) (Seitz et al. 2016).

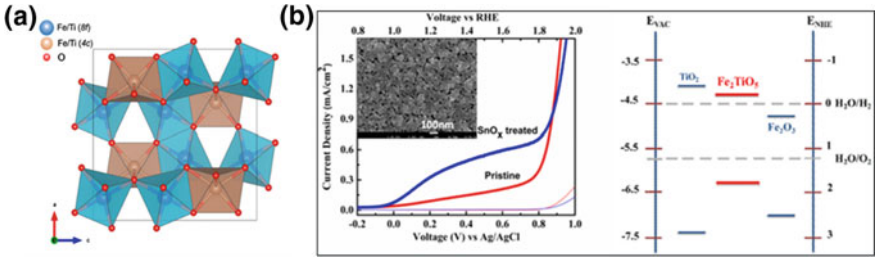


**Fig. 14.7** **a** Representation of Fe and Ti sites in pseudobrookite structure. Reprinted with permission from American Chemical Society (Seitz et al. 2016), and **b** JV plots along with probable band level positions for $Fe_2TiO_5$ films calculated using ultraviolet photoelectron spectroscopy. Reprinted with permission from American Chemical Society (Bassi et al. 2014a)

The important properties such as conductivity, mobility, and carrier lifetime for $Fe_2TiO_5$ have been largely unexplored. Since these properties contribute to the charge transport in bulk and significantly impact on their performance in photoelectrochemical cell, it would be important to characterize them carefully.

Our group also demonstrated the synthesis of pure phase $Fe_2TiO_5$ by a solvothermal technique, using isopropanol as the solvent for the precursors (Bassi et al. 2014a). Nanoporous thin films were synthesized on FTO substrates by this technique and coated with a $SnO_x$ overlayer for surface passivation to investigate its photoelectrochemical performance. It yielded a photocurrent density of 0.35 mA $cm^{-2}$ at 1.23 V versus RHE under 1 sun irradiation. Ultraviolet Photoelectron Spectroscopy (UPS) measurements showed that its band levels straddle the water redox levels with a work function of around 4.77 eV (Fig. 14.7b) (Bassi et al. 2014a). This was later confirmed by Deng et al. who reported a similar valence band of around −6.31 eV for a $Fe_2TiO_5$ layer synthesized by Ti treatment of a hematite layer (Deng et al. 2015).

Although we confirmed that our layer consisted pure phase of $Fe_2TiO_5$, the photocurrent density was still lower than those we obtained in $Fe_2O_3$-based thin films which were of the order of 1 mA $cm^{-2}$ (Bassi et al. 2014a; Deng et al. 2015). This is attributed to the low $Fe_2TiO_5$ film thickness of 150 nm used which is insufficient for significant photon absorption. To realize the full potential of $Fe_2TiO_5$, it is necessary to improve its quantum efficiency. Very recently, Zhang et al. used an iron titanate nanotube array with a $TiO_2$ underlayer and modified it by hydrogen treatment and $FeNiO_x$ cocatalyst to improve its PEC activity (Zhang et al. 2018). The nanotube photoanode achieved a photocurrent density of 0.93 mA $cm^{-2}$ at 1.23 VRHE under 1 sun (100 $mWcm^{-2}$) irradiation with a cathodic shift in photocurrent onset potential of ∼280 mV relative to the pristine nanotube array electrode (Hemin et al. 2017). This is one of the highest performances achieved for a modified iron titanate-based photoanode under standard conditions.

### *14.4.4 $BiVO_4$ Photoanode*

$BiVO_4$ is also a very attractive photoanode because of its suitable energy band gap (2.4 eV) with appropriate valance band edge with respect to water oxidation level (2.4 V vs. RHE), which provides enough potential for photo-generated holes to oxidize water (Fatwa and Sean 2017; Chen et al. 2015a; Qiu et al. 2016). However, the conduction band edge is similar to hematite and not favorable for water reduction (Fatwa and Sean 2017). Fatwa et al. demonstrated a gradient-doped $BiVO_4$ photoanode connected to Si solar cells in tandem configuration for water splitting with a 4.9% solar to hydrogen conversion (STH) efficiency (Fig. 14.8) (Bornoz et al. 2014). Many groups have attempted to enhance the performance of $BiVO_4$ by doping, nanostrcutring, surface overlayers, and heterostructures (Kim et al. 2015; Zhang et al. 2015; Pihosh et al. 2014; Han et al. 2014). Recently, Choi et al. demonstrated the most efficient $BiVO_4$ photoanode with 6.7% STH

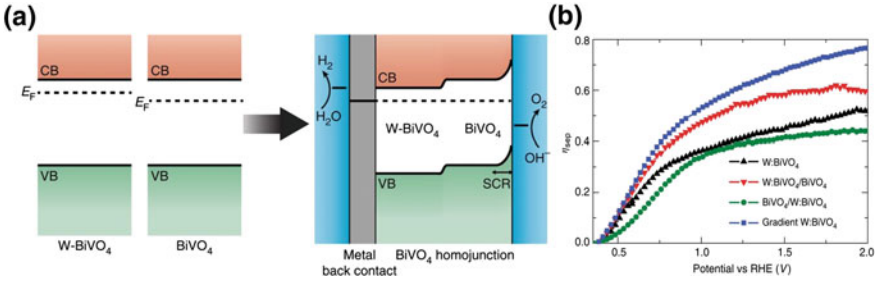


**Fig. 14.8** **a** Isolated and electrolyte submerged energy band schematic of pristine $BiVO_4$ and W-doped $BiVO_4$, **b** charge carrier separation efficiency ($\eta_{sep}$) for 1% W-doped $BiVO_4$, W:$BiVO_4$ homojunction, W:$BiVO_4$ reverse homojunction, and gradient-doped W:$BiVO_4$. Reprinted with the permission of Nature Publishing Group (Abdi et al. 2013). Copyright© 2013

efficiency by making a $BiVO_4/WO_3$ heterostructure (Pihosh et al. 2015). This reported STH efficiency is 90% of the theoretically predicted STH efficiency of $BiVO_4$ photoanode but still less than the predicted STH efficiency (10%) for large-scale setup (Keable and Holcroft 2012). This 10% number can only be achieved by making $BiVO_4$-based heterostructure or by tuning the energy band gap via replacing the cations (Fatwa and Sean 2017).

Anodic photo-corrosion of $BiVO_4$ photoanodes involves the main factor that limits the stability against the PEC water oxidation (Lee and Choi 2018). This photo-corrosion is due to the loss of $V^{5+}$ dissolution from the $BiVO_4$ lattice during the PEC water splitting. Very recently, Dong et al. attempted to stabilize the $BiVO_4$ photoanode during PEC water splitting by intentionally adding the vanadium ions ($V^{5+}$) in electrolyte solution, which inhibits the photo-corrosion of $BiVO_4$. FeOOH/NiOOH oxygen evolution catalyst was also integrated with $BiVO_4$ surface to further boost the solar-driven water splitting performance (Fig. 14.9) (Lee and Choi 2018). By adding FeOOH/NiOOH layer, the photocurrent onset is shifted from 0.47 to 0.24 V versus RHE and a photocurrent plateau of 2.0 mA $cm^{-2}$ at a potential as low as 0.40 V versus RHE is achieved. The maximum photocurrent densities of 4.7 mA $cm^{-2}$ at 1.23 V versus RHE. A stability measurement has also been performed at 0.6 V versus RHE, which shows that the photocurrent slowly increases for first 20 h and then decreases after 40 h, indicating that sample is not stable with time (Fig. 14.9) (Lee and Choi 2018).

### *14.4.5 $WO_3$ Photoanode*

$WO_3$ photoanode brings new opportunities for efficient PEC water splitting (Wang et al. 2008; Gonçalves et al. 2012; Pihosh et al. 2015; Coridan et al. 2013). $WO_3$ has an energy band gap 2.5–2.7 eV, moderate hole diffusion length, good chemical

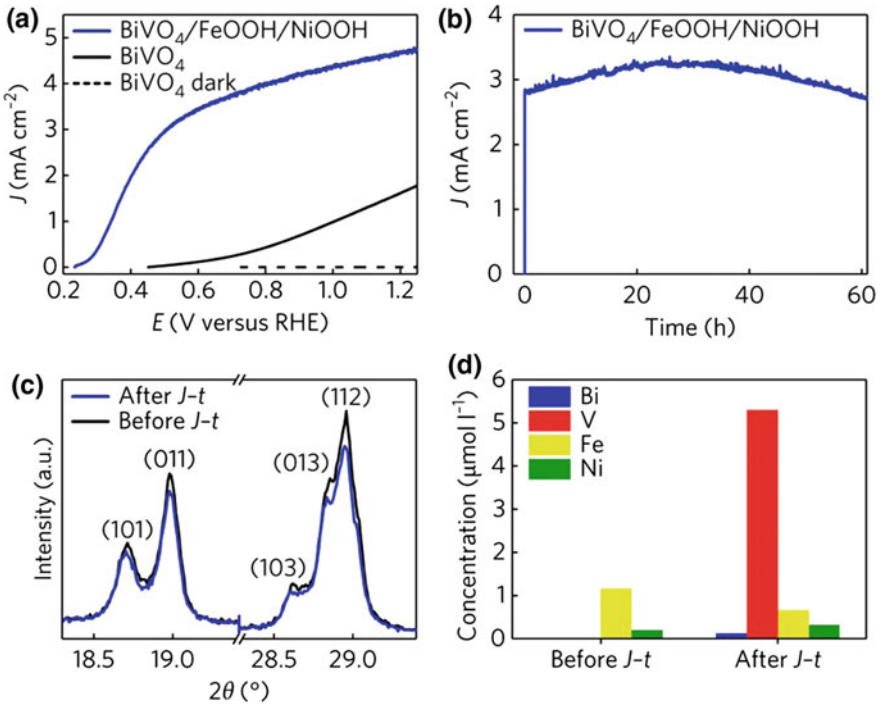


**Fig. 14.9** **a** J–V curve of $BiVO_4$ and $BiVO_4$/FeOOH/NiOOH measured under 1 sun illumination, (100 mW $cm^{-2}$), **b** stability curve of $BiVO_4$/FeOOH/NiOOH at 0.6 V versus RHE, **c** XRD patterns of $BiVO_4$ before and after 60 h stability measurement, and **d** ICP measurement of KB electrolyte solution before and after 60 h stability. Reprinted with the permission of Nature Publishing Group (Lee and Choi 2018). Copyright© 2018

stability in neutral pH, and easy fabrication methods (Gonçalves et al. 2012; Liu et al. 2012). The PEC performance of $WO_3$ varies with the fabrication temperature and underlying conducting substrates (Liu et al. 2012). The photocurrent density increases with increasing temperature. Crystalline phase of $WO_3$ changes to amorphous at high temperature, which results in high bulk recombination, and thus dropping in photocurrent density (Liu et al. 2012; Feng et al. 2016).

Several nanostructures, doping and surface modification of $WO_3$ have been reported by various group to enhance the PEC performance (Wang et al. 2008; Gonçalves et al. 2012; Liu et al. 2012; Kim et al. 2011). $WO_3$ nanoflakes with hierarchical architecture improved photoelectrochemical activity because of the multiple light scattering which facilitates better light absorption and the exposure of active sites resulted in enhanced interfacial charge transfer (Li et al. 2014). Zhang et al. demonstrated a facile method to synthesis oxygen vacancy rich $WO_3$ photoanode for water splitting (Zhang et al. 2018). Oxygen vacancies in $WO_3$ photoanode significantly increase the carrier concentration around seven times than that of pristine $WO_3$ (Fig. 14.10). Additionally, DFT calculations show that a

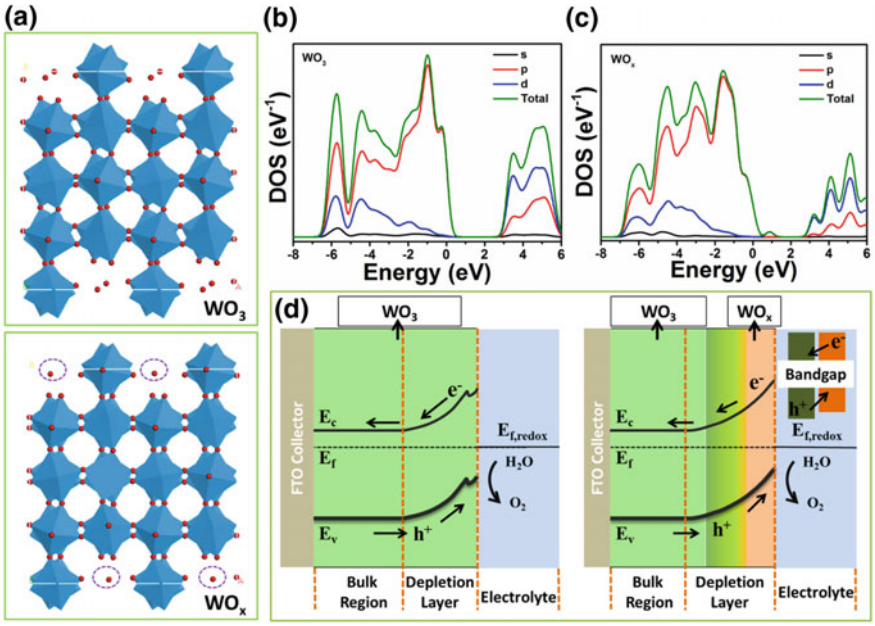


**Fig. 14.10** **a** Augmented geometries of $WO_3$ and $WO_x$, **b** the density of states for $WO_3$ and $WO_x$ **c** the density of states for $WO_x$, and **d** representation of $WO_3$ and $WO_3$-OV photoanodes energetics $WO_x$, with water redox couple for water splitting. Reprinted with the permission of Elsevier (Zhang et al. 2018). Copyright© 2018

$WO_3/WO_x$ heterojunction is formed due to oxygen vacancies, which reduces the charge carrier recombination by enhancing the built-in electric field. Consequently, $WO_3$–OV photoanode exhibit charge carrier separation efficiency of 67.2% and improved photocurrent density of 1.35 mA $cm^{-2}$ at 1.23 V versus RHE, as compared to as prepared $WO_3$ (Fig. 14.11) (Zhang et al. 2018).

Shankara et al. also demonstrated Mo-doped $WO_3$ photoanode for PEC water splitting. Mo doping in $WO_3$ changes its morphology without altering the crystal structure (Kalanur and Seo 2018). The doping of Mo in $WO_3$ decreased the energy band gap of $WO_3$ by creating mid-gap states, and thus increased its light absorption ability (Fig. 14.12). Mo-doped $WO_3$ photoanode shows a twice increase in photocurrent compared to undoped $WO_3$ photoanode under simulated sunlight (Kalanur and Seo 2018).

### *14.4.6 $Ta_3N_5$ Photoanode*

Tantalum nitride ($Ta_3N_5$) has also received significant attention in past years due to its ideal energy band gap (2.1 eV) and aqueous stability (Maeda and Domen 2011;

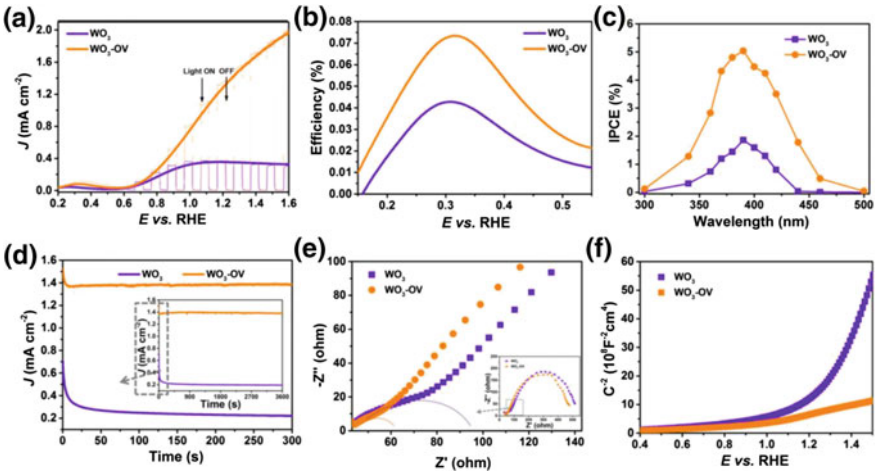


**Fig. 14.11** **a** J–V curve of $WO_3$ and $WO_3$–OV photoanodes under 1 sun illumination, **b** photoconversion efficiency, **c** IPCEs measured at 1.23 V versus RHE, **d** stability photocurrents, **e** Nyquist plot at 1.0 V versus RHE under 1 sun illumination and **f** Mott–Schottky curve of $WO_3$ and $WO_3$–OV photoanodes, respectively. Reprinted with the permission of Elsevier (Zhang et al. 2018). Copyright© 2018

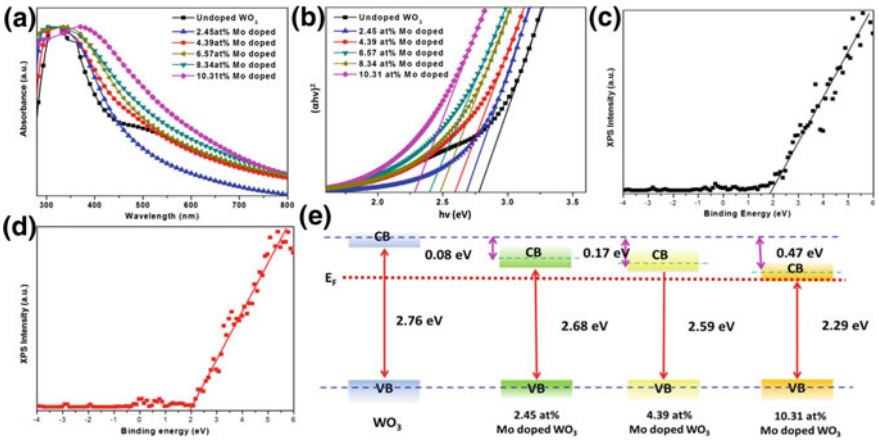


**Fig. 14.12** **a** UV–V is spectra of as prepared and differently Mo-doped $WO_3$ photoanodes, **b** Tauc's plot of $WO_3$ photoanodes, **c**–**d** XPS valence band spectra of pristine and Mo-doped $WO_3$, **e** diagram of energy band alignment of undoped and Mo-doped $WO_3$ plotted by optical and VB edge analysis. Reprinted with the permission of Elsevier (Kalanur and Seo 2018). Copyright© 2018

Higashi et al. 2012; Zhong et al. 2017). $Ta_3N_5$ conduction and valance band edges are also suitable with respect to water redox levels. It has conduction band minima at −0.4 V versus RHE, and valance band maxima at +1.6 V versus RHE, which

allow $Ta_3N_5$ to perform unassisted solar water splitting (Maeda and Domen 2011; Kim et al. 2017; Chun et al. 2003). This material can theoretically split water without any external bias with a maximum solar to hydrogen conversion (STH) efficiency of ~15% (Maeda and Domen 2011; Kim et al. 2017). However, $Ta_3N_5$ suffer from the poor charge transport properties and low light absorption (Maeda and Domen 2011; Kim et al. 2017; Chun et al. 2003; Pinaud et al. 2012). Various strategies have been used to improve the light absorption and charge transport such as nanostructuring, doping, and surface modification (Kim et al. 2017; Pinaud et al. 2012; Liu et al. 2017; Abdel Haleem et al. 2017; Fan et al. 2017a). Predominantly, nanostructured $Ta_3N_5$ photoanode such as nanotubes (NTs), nanorods (NRs) have been extensively investigated (Liu et al. 2017; Abdel Haleem et al. 2017; Sherdil et al. 2015; Yanbo et al. 2013). These 1D nanostructures offer better charge transfer at electrode/electrolyte interface without altering the incident light (Sherdil et al. 2015; Yanbo et al. 2013). Kim et al. demonstrated that the surface boron doping in $Ta_3N_5$ nanocrystals is beneficial for PEC water splitting (Kim et al. 2017). The surface modification with boron significantly enhance the photocurrent and reduce the onset potential for water oxidation (Fig. 14.13) (Kim et al. 2017). This is because surface boron doping reduces the interfacial charge transfer resistance and thus increases the carrier conductivity. The low onset potential is a result of the negative shift of the flat band potential due to boron surface doping (Kim et al. 2017).

### *14.4.7 $Cu_2O$ Photocathode*

Cuprous oxide is one of the most investigated p-type semiconducting photocathode for solar water splitting and $CO_2$ reduction (Lin et al. 2012; Paracchino et al. 2012; Dias et al. 2015; Bornoz et al. 2014; Wang et al. 2018; Tsui and Zangari 2013; Schreier et al. 2015). $Cu_2O$ has a direct energy band gap of 2.0–2.2 eV, which makes it an outstanding solar absorber (Dias et al. 2015). Unfortunately, $Cu_2O$ suffers from poor aqueous stability and also photo-corrosion is limit the PEC performance of $Cu_2O$ (Qi et al. 2016; Luo et al. 2016; Huang et al. 2015; Liu et al. 2005). Various efforts have been made to address the photo-corrosion issue of $Cu_2O$ by using a protection layer on the surface (Fig. 14.14a) (Dias et al. 2015; Paracchino et al. 2011). This layer prevents the direct contact between the $Cu_2O$ surface and the electrolyte. Gratzeal group demonstrated the highly efficient $Cu_2O$ photocathode for $H_2$ generation. $Cu_2O$ was protected against photocathodic corrosion by using a few nanometers thick of Al-doped zinc oxide and titanium oxide layers (Paracchino et al. 2011). The PEC performance of $TiO_2$ protected $Cu_2O$ was further boosted by integrating platinum nanoparticles as a hydrogen evolution catalyst. This system shows a photocurrent density of $-7.6$ mA $cm^{-2}$ at 0 V versus RHE at near neutral pH (Fig. 14.14) (Paracchino et al. 2011). This photocathode shows excellent stability during the water reduction reaction.

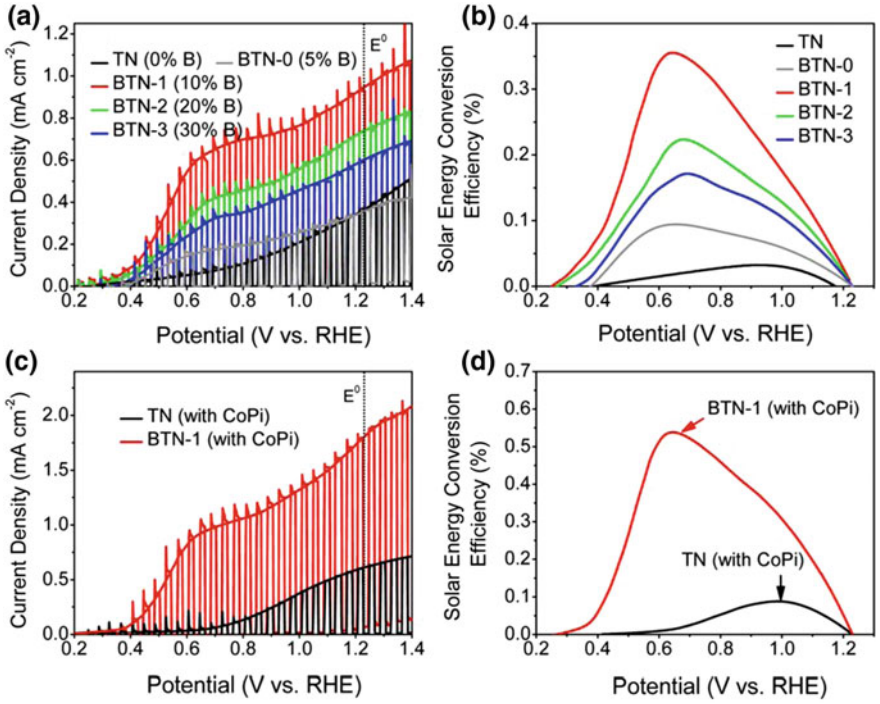


**Fig. 14.13** **a** J–V curve of pristine and B-doped $Ta_3N_5$ photoanodes in 0.1 M $Na_2SO_4$ and 5 M NaOH electrolyte under 1 sun illumination, 100 mWcm$^{-2}$, **b** solar energy conversion efficiency of the photoanodes, **c** chopped current density for $Ta_3N_5$ and 10% B-doped $Ta_3N_5$ photoanodes modified by the CoPi cocatalyst, and **d** solar energy conversion efficiency of $Ta_3N_5$ and 10% B-doped $Ta_3N_5$. Reprinted with the permission of American Chemical Society (Kim et al. 2017). Copyright© 2017

Same group also studied $TiO_2$ protected $Cu_2O$ photocathode integrated with a rhenium bipyridyl catalyst for PEC $CO_2$ reduction into carbon monoxide with 100% faradaic efficiency (Schreier et al. 2015). They found charge transfer limitation from $TiO_2$ to the rhenium bipyridyl catalyst and address this issue by using an organic additive. They propose that the additives act to modify the charge state of the catalyst intermediate to avoid electrostatic repulsion between molecule and semiconductor (Schreier et al. 2015).

### *14.4.8 Si-Based Photocathode/Photoanode*

Silicon has a relatively narrow energy band gap of 1.1 eV, which makes Si is an excellent photoabsorber (Reece et al. 2011; Chen et al. 2011). Silicon does not show any catalytic properties and can easily be photo-corroded in aqueous medium

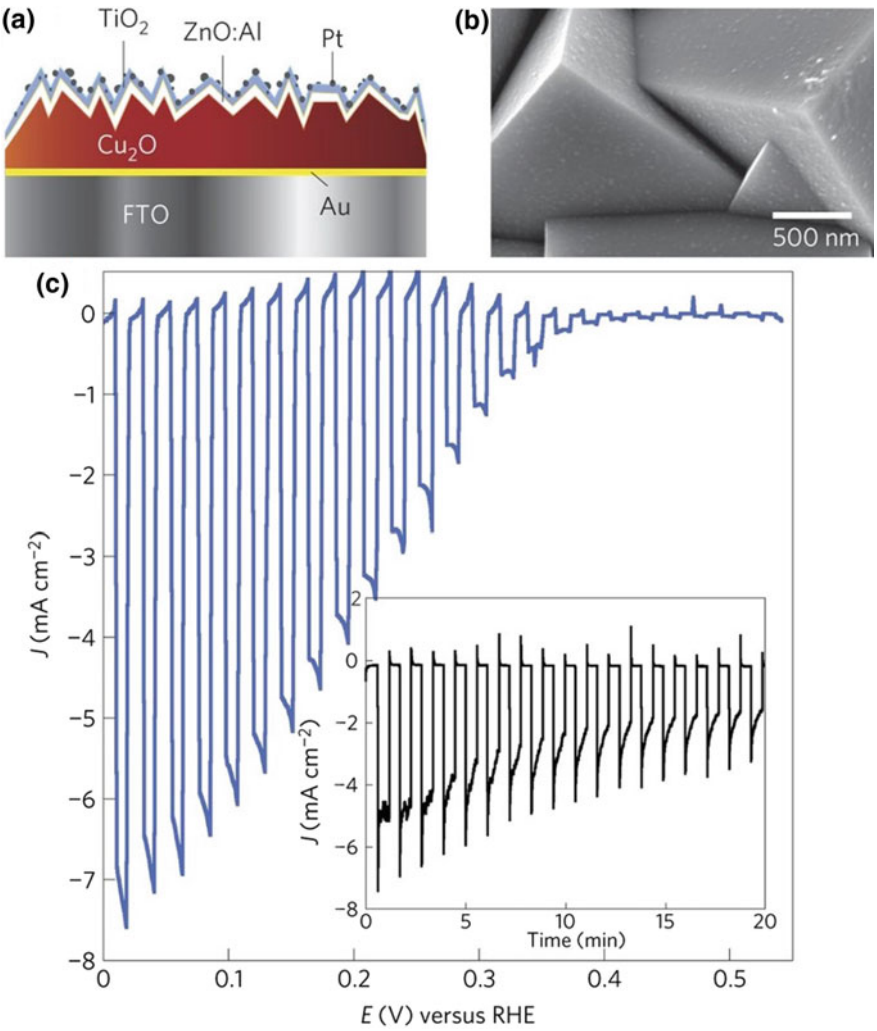


**Fig. 14.14** **a** Schematic diagram of $Cu_2O$ photocathodes deposited with ZnO:Al and $TiO_2$ as a protective layers. **b** SEM image of as deposited $Cu_2O$ photocathode. **c** J–V plot of the FTO/$Cu_2O$/$TiO_2$ photocathodes. Reprinted with the permission of Nature Publishing Group (Paracchino et al. 2011). Copyright© 2011

(Oh et al. 2011; Ji et al. 2014; Fan et al. 2017b). However, protection and catalyst layers integration with Si show an extraordinary water splitting performance (Fan et al. 2017b; Lai et al. 2015; Choi et al. 2014; Benck et al. 2015). Silicon can be used as a photoanode by making an n-type Si with pentavalent doping or photocathode by using p-type doping. Energy band diagrams of isolated and submerged p-type/n-type Si in electrolyte and under illumination (Fig. 14.15) (Chen et al. 2015b; Sun et al. 2014). To date, Si-based photoelectrodes have been

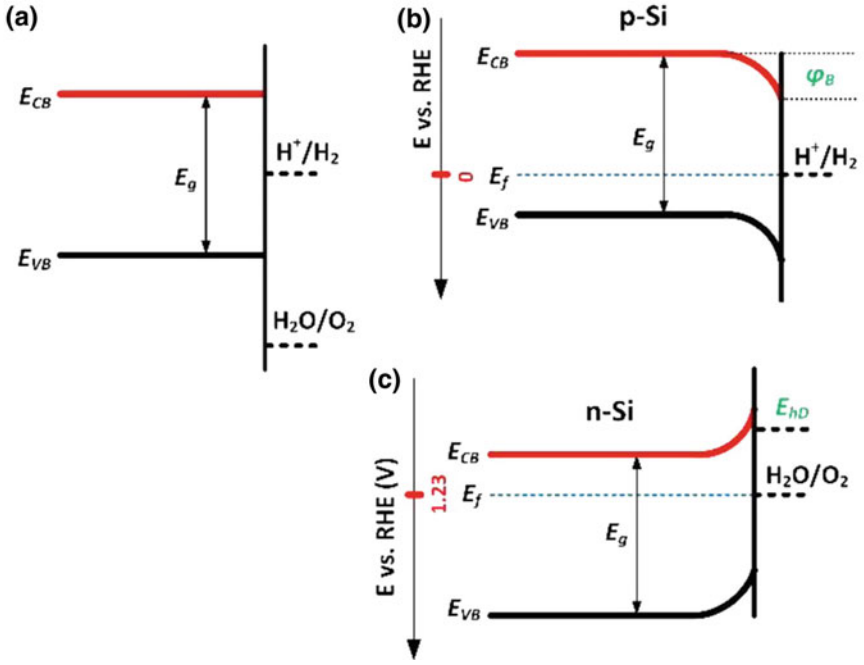


**Fig. 14.15** **a** Si enegetics with water redox potentials at flat band condition in pH 0 solution. **b** Equilibrated energy band diagram of a p-type Si. **c** Energy band diagram of n-type Si under anodic bias. Reprinted with the permission of American Chemical Society (Sun et al. 2014). Copyright© 2014

experimentally studied for PEC water splitting by employing numerous strategies, including: (i) deposition of a protection layer (e.g., $TiO_2$ $Al_2O_3$, $SrTiO_3$, and $Ta_2O_5$), (ii) deposition of cocatalyst for hydrogen evolution reaction (HER) or oxygen evolution reaction (OER) (Yu et al. 2017; Ji et al. 2014; Fan et al. 2017b; Choi et al. 2014; Sun et al. 2014; Wan et al. 2018). Recently, silicon-based photoanodes are extensively explored and several efforts are made to stabilize in alkaline for PEC water splitting (Chen et al. 2015b; Cai et al. 2018). Joel Ager's group demonstrated Si-based photoanode by integrating p-type transparent conducting oxide with n-type Si (Chen et al. 2015b). They have shown that p-type transparent conducting oxides (p-TCOs) can work bifunctionally as a hole selective contact and corrosion protection layer. Employing $np^+$ structure of Si and integrating an active heterogeneous Ni–Fe oxygen evolution catalyst, efficient PEC water splitting can be achieved (Chen et al. 2015b). This system exhibits a high photocurrent density over 25 mA $cm^{-2}$ at 1.23 V versus RHE and an onset potential of 0.95 V versus RHE under 1 sun illumination (Fig. 14.16). This photocathode also shows an excellent stable operation of 72 h in 1 M NaOH for water oxidation. Ekerdt et al. demonstrated a silicon photocathode with a $SrTiO_3$

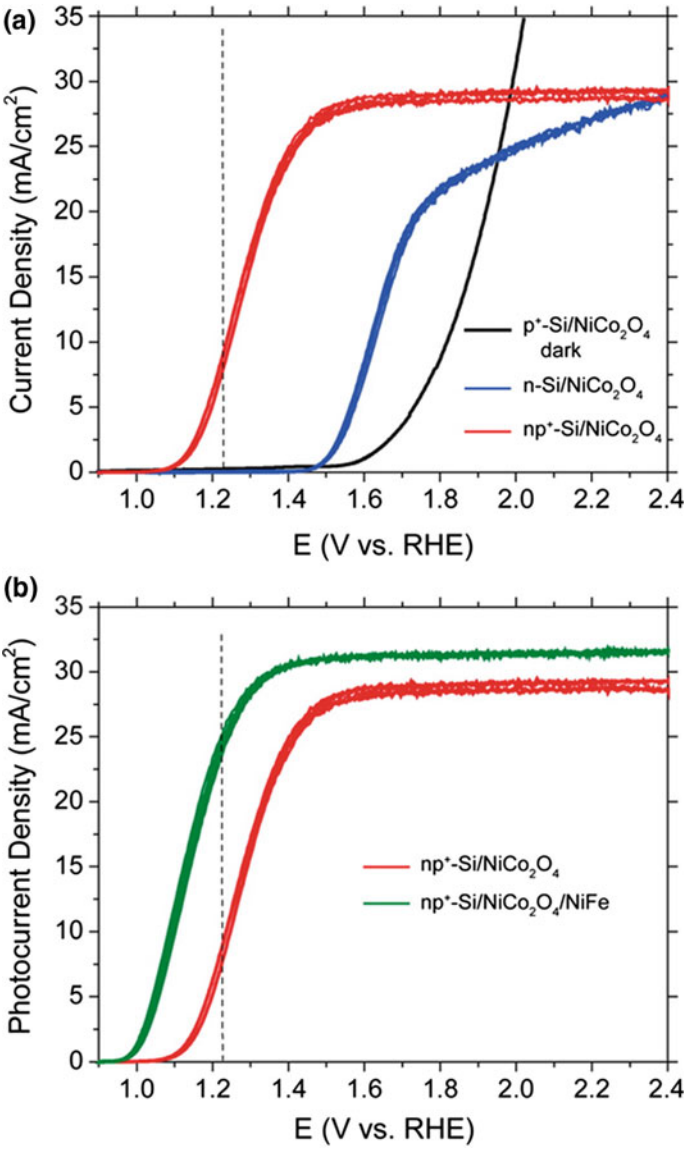


**Fig. 14.16** **a** J–V curve of $p^+$ Si, n-Si, and $np^+$ Si with a 40 nm of p-type $NiCo_2O_4$ protection layer in 1 M KOH and under 1 sun illumination, and **b** photocurrent–potential curve of $NiCo_2O_4$ coated $np^+$ Si with and without a 2 nm Ni–Fe oxygen-evolving catalyst overlayer. Reprinted with the permission of American Chemical Society (Chen et al. 2015b). Copyright© 2015

passivation layer and a mesh-like Ti/Pt HER catalyst for water reduction. This Si photocathode exhibit an extraordinary stability (35 h) in 0.5 M $H_2SO_4$ (Fig. 14.17) (Ji et al. 2014).

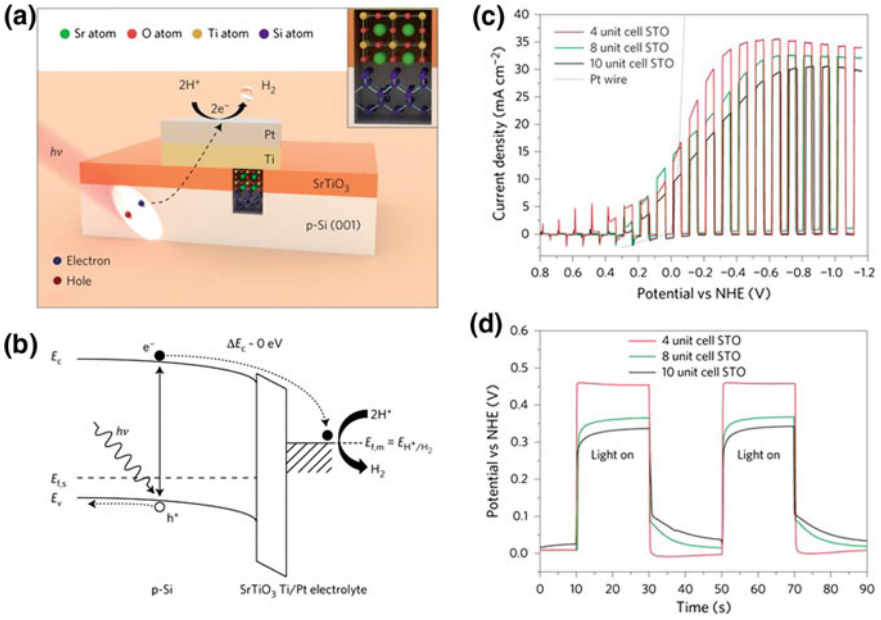


**Fig. 14.17** **a** Schematic of the STO-protected Si photocathode. The inset plot represents the boundary between STO and Si(001), **b** the energy band diagram of p-type Si under illumination, and **c**–**d** linear scan voltammetry and chopped illumination measurements for Pt/Ti/STO/p-Si(001) for various STO thicknesses from four to ten unit cells. Reprinted with the permission of Nature Publishing Group (Ji et al. 2014). Copyright© 2015

In terms of the PEC water splitting, silicon is a standard choice as a photoabsorber because of easy integration with various catalyst and excellent stable operation with protection layer (Ji et al. 2014; Benck et al. 2015; Sun et al. 2014). Chorkendorff and coworkers deposited catalytic $Mo_3S_4$ on p-type silicon and observed the absorption of red light photons (wavelengths > 620 nm) (Seger et al. 2014). They used photolithography to pattern the silicon substrate and create a high surface area structure for solar water splitting. The pillared Si-integrated with $MoS_x$ arrays exhibited higher photocurrent densities as compared to the planar Si at all potentials (Fan et al. 2017b). Si-based nanostructured photocathode is also extensively studied for $CO_2$ reduction (Arai et al. 2015; Kumar et al. 2012; Kyu et al. 2014; Kong et al. 2016; Tae et al. 2017). Although far fewer in number compared to water splitting, there have been a number of recent demonstrations of solar-powered electrochemical $CO_2$ reduction ($CO_2R$), some of which have overall energy conversion efficiencies above 1% (Kong et al. 2016). Also notable are studies which interface molecular catalysts to p-Si to produce two-electron reduction products such as CO (Kong et al. 2016). Mostly, Si photocathode-based reports show only two-electron products production such as carbon monoxide or formate except for a report by Hinogami (Hinogami et al. 1998). Hinogami et al. integrated Cu nanoparticle with Si photocathode and manage to produce ethylene with 10%

faradaic efficiency by PEC $CO_2$ reduction (Hinogami et al. 1998). An example of this type of study is the work of Song and coworkers in which a Si photocathode with a nanoporous Au thin film produced CO with 96% faradaic efficiency (FE) (Tae et al. 2017).

Graphene has also been used as a cocatalyst for selective conversion of $CO_2$ to CO using p-Si nanowire photocathodes (Dong et al. 2016). Choi et al. demonstrated Sn-coupled p-Si nanowire arrays for solar-driven $CO_2$ conversion into formate (Kyu et al. 2014). The Si microwire arrays exhibited a 0.5 V higher anodic onset potential compared to planar p–Si and an approximately twice photocurrent density and formate production. These heterojunction Si microwire/Sn arrays exhibited a five times increase in formate production with faradaic efficiencies of 40% in a single cell and 88% in an H-type cell (Fig. 14.18) (Kyu et al. 2014). Toyota center demonstrated a simple $CO_2$ reduction monolithic device (Arai et al. 2015). The device contains a porous ruthenium complex $CO_2$ reduction catalyst, iridium oxide anode for water oxidation, and a triple-junction amorphous silicon-germanium solar cell. This device exhibits a solar to chemical conversion efficiency of 4.6%, while formate was the only product (Arai et al. 2015).

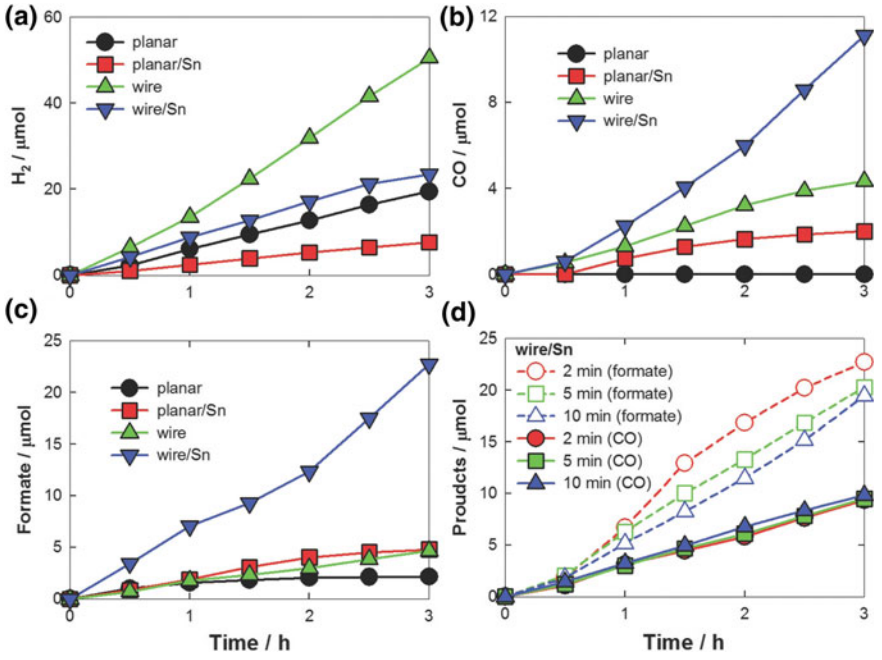


**Fig. 14.18** Products evolution profile of **a** $H_2$, **b** CO, **c** formate, and **d** CO and formate from planar p-Si and p-Si nanowire array photoelectrodes in 0.1 M bicarbonate electrolytes under 1 sun illumination. Reprinted with the permission of Wiley (Kyu et al. 2014). Copyright© 2014

### 14.4.9 III–V Photocathodes

Group III–V semiconductors, GaAs and InP, and related quaternary compounds exhibits favorable properties for PEC water splitting because of their ideal energy band gaps for light absorption, and extraordinary charge carrier mobilities (Wang et al. 2008; Yamane et al. 2009; Licht et al. 2000; Sekimoto et al. 2015; Hu et al. 2014; Kang et al. 2017). Turner et al. reported a monolithic PV–PEC device based on III–V semiconductor (p/n GaAs bottom cell connected to a $GaInP_2$ top cell) for hydrogen production with STH efficiency of 12.6% (Wang et al. 2008; Khaselev and Turner 1998). Furthermore, they also pointed out the common mistakes on STH calculation from similar devices and demonstrated a following balanced in the reported STH efficiency down to 9.3% (Khaselev et al. 2001). Their group also reported $TiO_2$ overlayer for GaAs, and GaInP which acts as a protective layer as well as improved the water oxidation kinetics (Gu et al. 2015). Whereas, these devices use expensive materials, and synthesizes technology such as ALD and sputtering, which limits large-area application. Jaramillo group also displayed a p-$GaInP_2$ photocathode integrated with Molybdenum disulfide ($MoS_2$) for efficient solar-driven $H_2$ production (Britto et al. 2016). $MoS_2$ nanoparticles are promising in protecting $GaInP_2$ and also improve the catalytic performance for HER because $MoS_2$ is highly stable in aqueous solution and also exhibits superior activity for the hydrogen evolution reaction (HER). This system shows a stable operation of 70 h under 1 sun simulated illumination (Fig. 14.19) (Britto et al. 2016). Recently, Jeong et al. reported an Au/ZnO/ZnTe/CdTe core—shell nanorod array photocathode, cobalt—bicarbonate anode, and a $CH_3NH_3PbI_3$ perovskite solar cell in tandem for solar assisted $CO_2$ reduction (Jang et al. 2016). This device harvest light efficiently, as photocathode absorb higher energy photons (2.14 eV) and perovskite solar cell absorbs lower energy photons (1.5 eV). Although this device shows only CO with nominal solar to CO conversion efficiency of 0.35% and a solar to fuel conversion efficiency exceeding 0.43% including $H_2$. Finally, this device performance was reduced by nearly 30% within 3 h (Jang et al. 2016).

## 14.5 Future Directions to Achieve the Efficient PEC Performance

Semiconducting photoelectrodes are an integral part of Photoelectrochemical (PEC) cells, those define the water splitting performance by performing hydrogen evolution reaction (HER) at photocathode and oxygen evolution reaction (OER) at photoanode. Most of the reported photoelectrodes are suffer from various issues such as (1) slow charge transfer kinetics, (2) high recombination losses, (3) inappropriate conduction and valance bad edges with respect to water redox levels, (4) low photovoltage generation than the water thermodynamic potential (1.23 V), (5) poor aqueous stability, and (6) low conductivity. Various researchers have tried

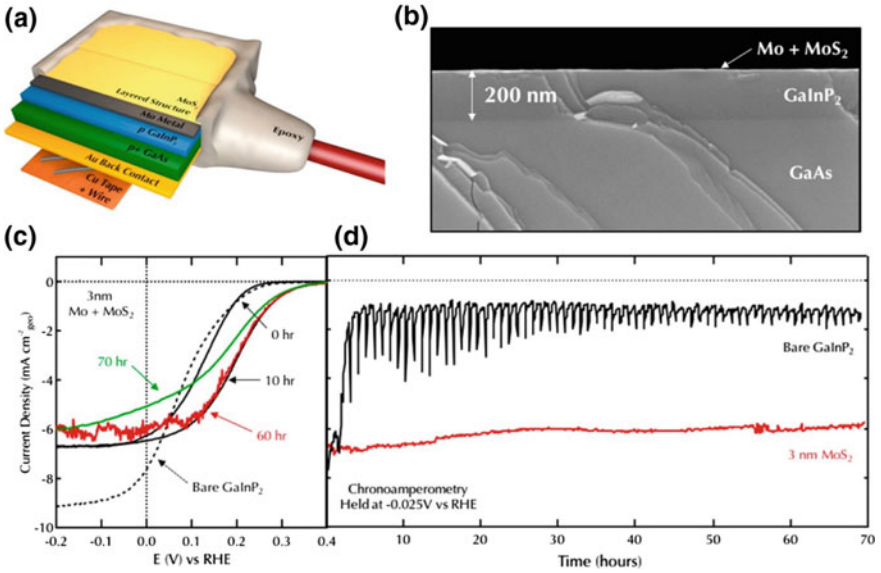


**Fig. 14.19** **a** Schematic of p-$GaInP_2$/$MoS_2$ photocathode. **b** Cross-sectional view of p-$GaInP_2$/$MoS_2$ from SEM image surface region. Electrochemical stability measurements of the bare p-$GaInP_2$ and p-$GaInP_2$/$MoS_2$ photocathodes. **c** J–V curves of p-$GaInP_2$/$MoS_2$ photocathodes, and **d** chronoamperometry measurements at −0.025 V versus RHE with a stability over 70 h. Reprinted with the permission of American Chemical Society (Britto et al. 2016). Copyright© 2016

to address these issues by various modifications of photoelectrodes as (1) integrating cocatalyst to improve the kinetics, (2) surface passivation layers to address the recombination losses, (3) heterostructure fabrication to achieve the band alignment, (4) tandem configuration to generate enough photovoltage for water splitting, (5) integrating protection layers to address the stability issue, and (6) elemental doping to enhance the conductivity. Even after this modification, the experimentally reported efficiencies of most of photoelectrode materials are far from the theoretically predicted efficiencies. This is because all of the above-mentioned modifications are hard to implement previously on all photoelectrode materials. New materials have to be discovered in order to achieve the solar efficient water splitting. JCAP is leading in discovering new materials by using theoretical modeling and synthesizing those in the laboratory (Jiang et al. 2018). Tandem architecture is another approach to achieve the affordable and efficient hydrogen generation by splitting water. In tandem cell configurations (Photoelectrochemical cell-photovoltaic and photoanode–photocathode), the total photovoltage is generated by balancing optical absorption in two or more light absorbers coupled in series for overall water splitting. Additionally, it is hard to realize a single photoelectrode or photoanode–photocathode system to perform both OER and HER in the same pH electrolyte solution. For PEC–PV configuration, the photovoltage

generated from each absorber is important, particularly, the photovoltage output by conventional solar cells is not adequate to perform overall water splitting (Gurudayal et al. 2015a; Zhang et al. 2016). In this context, the relatively large open circuit voltages of the halide perovskite solar cells have made them attractive candidates as the photovoltaic components of solar fuel devices (Gurudayal et al. 2015a, 2017b; Qiu et al. 2016). The multiple light absorber tandem PEC systems can easily harvest a significant portion of the solar spectrum and generate enough voltage to overcome the overpotential and thermodynamical potential for water splitting. In the subsequent sections, different systems using multi photoabsorbers will be deliberated. Finally, a balance between the system complexity, cost, and solar to hydrogen (STH) conversion efficiency has to be considered.

## 14.6 Summary

Recent developments in PEC cells and photoelectrode materials for solar-assisted water splitting are discussed in this chapter. The working mechanism of PEC cells is discussed in order to have a common understanding between various PEC cells and water splitting half-reactions. PEC cell has the potential to generate clean fuels such as hydrogen, methanol, and ethanol by splitting water or reducing carbon dioxide. A standard procedure for efficiency calculation should have to be followed to compare different PEC cells and photoelectrodes performance. Widely studied photoanode materials ($TiO_2$, $Fe_2O_3$, $BiVO_4$, and $WO_3$) and their water oxidation performance by solar water splitting is delivered. Most of these photoanode materials show poor charge transport properties and sluggish charge transfer kinetics at the electrode/electrolyte interface.

To compensate for the deficiencies of these photoanode materials and to further improve, various combinations of many different approaches have been investigated by their PEC performance, researchers over more than 10 years. These are summarized below.

(a) Nanostructuring to compensate for the poor minority carrier diffusion length, (b) Elemental doping with a suitable multivalent elements to increase its inherent bulk conductivity, (c) Integration with a transparent and efficient oxygen evolution reaction cocatalyst, (d) Use of a surface passivation layer to reduce charge recombination at the surface, (e) Fabricating heterostructure with more than one photoanode materials which has appropriate conduction and valance band offsets with respect to water redox levels. This last strategy has not been adopted widely by many researchers possibly because of the difficulty in synthesizing such nanocomposite materials, but this could become a very effective technique.

The significant research efforts in particular hematite-based photoanode developments which shone a light on the benefits of modifications such as nanostructuring, doping, surface passivation, and cocatalyst has increased the photocurrent densities to $\sim 6$ mA $cm^{-2}$, which is $\sim 50\%$ of its theoretical limit. Given the recent success in $WO_3$–$BiVO_4$ core-shell heterostructure photoanodes which gave about

90% of theoretical photocurrent density, we remain optimistic that with the right combination of strategies, these photoanode materials will also be able to realize its theoretical photocurrent density in future. $Ta_3N_5$ exhibits ideal conduction band edges with respect to water redox level and suppose to drive unassisted solar water splitting but slow kinetics and high recombination limit the performance. $Cu_2O$ photocathode has an excellent energy band gap but suffers from photo-corrosion and poor charge transport properties. Many researchers tried to address the photo-corrosion issue by using a protection layer but still not able to achieve the stable performance for HER. Silicon-based photoelectrodes exceeded the 10% STH efficiency number by employing the protection and cocatalyst layers. Although, a careful optimization of passivation layers need to be done to achieve longer stability. A tandem cell has to be designed in such a way that the photovoltage generated by photoabsorbers exceeded the thermodynamic potential of water splitting.

Finally, the laboratory understandings and experiences must be translated into pilot scale PEC devices to demonstrate the commercial viability of the technology.

## References

Abdel Haleem A, Majumder S, Perumandla N, Zahran ZN, Naruta Y (2017) Enhanced performance of pristine $Ta_3N_5$ photoanodes for solar water splitting by modification with Fe–Ni–Co mixed-metal oxide cocatalysts. J Phys Chem C 121:20093–20100

Abdi FF, Han L, Smets AHM, Zeman M, Dam B, van de Krol R (2013) Efficient solar water splitting by enhanced charge separation in a bismuth vanadate-silicon tandem photoelectrode. Nat Commun 4

Ager JW, Shaner MR, Walczak KA, Sharp ID, Ardo S (2015) Experimental demonstrations of spontaneous, solar-driven photoelectrochemical water splitting. Energ Environ Sci 8:2811–2824

Ahmed MG, Kretschmer IE, Kandiel TA, Ahmed AY, Rashwan FA, Bahnemann DW (2015) A facile surface passivation of hematite photoanodes with $TiO_2$ overlayers for efficient solar water splitting. ACS Appl Mater Interfaces 7:24053–24062

Alexander BD, Kulesza PJ, Rutkowska I, Solarska R, Augustynski J (2008) Metal oxide photoanodes for solar hydrogen production. J Mater Chem 18:2298–2303

Annamalai A, Lee HH, Choi SH, Lee SY, Gracia-Espino E, Subramanian A, Park J, Kong K-J, Jang JS (2016) Sn/Be sequentially co-doped hematite photoanodes for enhanced photoelectrochemical water oxidation: effect of Be2 + as co-dopant. Sci Rep 6:23183

Arai T, Sato S, Morikawa T (2015) A monolithic device for $CO_2$ photoreduction to generate liquid organic substances in a single-compartment reactor. Energ Environ Sci 8:1998–2002

Atabaev TS, Ajmal M, Hong NH, Kim H-K, Hwang Y-H (2014) Ti-doped hematite thin films for efficient water splitting. Appl Phys A 118:1539–1542

Bak T, Nowotny J, Rekas M, Sorrell CC (2002) Photo-electrochemical hydrogen generation from water using solar energy. Materials-related aspects. Int J Hydrogen Energ 27:991–1022

Balko BA, Clarkson KM (2001) The effect of doping with Ti(IV) and Sn(IV) on oxygen reduction at hematite electrodes. J Electrochem Soc 148:E85–E91

Bard AJ, Fox MA (1995) Artificial photosynthesis: solar splitting of water to hydrogen and oxygen. Acc Chem Res 28:141–145

Bassi PS, Gurudayal LH, Wong J (2014a) Barber, iron based photoanodes for solar fuel production. Phys Chem Chem Phys 16:11834–11842

Bassi PS, Chiam SY, Barber GJ, Wong LH (2014b) Hydrothermal grown nanoporous iron based titanate, $Fe_2TiO_5$ for light driven water splitting. ACS Appl Mater Interfaces 6:22490–22495
Bassi PS, Gurudayal, Wong LH, Barber WJ (2014c) Iron based photoanodes for solar fuel production. Phys Chem Chem Phys
B.E. Outlook (2016) Outlook to 2035, BP
Beermann N, Vayssieres L, Lindquist SE, Hagfeldt A (2000) Photoelectrochemical studies of oriented nanorod thin films of hematite. J Electrochem Soc 147:2456–2461
Benck JD, Hellstern TR, Britto RJ, Kibsgaard J, Lee SC, Fong KD, Sinclair R, Jaramillo TF (2015) High performance silicon photocathodes for hydrogen production via solar water splitting. Meet Abs, MA2015–01, 2021
Bolton JR (1996) Solar photoproduction of hydrogen: a review. Sol Energ 57:37–50
Bolton JR, Strickler SJ, Connolly JS (1985) Limiting and realizable efficiencies of solar photolysis of water. Nature 316:495–500
Bora DK, Braun A, Erni R, Muller U, Dobeli M, Constable EC (2013a) Hematite-NiO/[small alpha]-$Ni(OH)_2$ heterostructure photoanodes with high electrocatalytic current density and charge storage capacity. Phys Chem Chem Phys 15:12648–12659
Bora DK, Braun A, Constable EC (2013b) "In rust we trust". Hematite-the prospective inorganic backbone for artificial photosynthesis. Energ Environ Sci 6:407–425
Bornoz P, Abdi FF, Tilley SD, Dam B, van de Krol R, Graetzel M, Sivula K (2014) A bismuth vanadate-cuprous oxide tandem cell for overall solar water splitting. J Phys Chem C 118:16959–16966
Brillet J, Cornuz M, Formal FL, Yum J-H, Grätzel M, Sivula K (2010) Examining architectures of photoanode–photovoltaic tandem cells for solar water splitting. J Mater Res 25:17–24
Brillet J, Yum J-H, Cornuz M, Hisatomi T, Solarska R, Augustynski J, Graetzel M, Sivula K (2012) Highly efficient water splitting by a dual-absorber tandem cell. Nat Photon 6:824–828
Britto RJ, Benck JD, Young JL, Hahn C, Deutsch TG, Jaramillo TF (2016) Molybdenum disulfide as a protection layer and catalyst for gallium indium phosphide solar water splitting photocathodes. J Phys Chem Lett 7:2044–2049
Burhan M, Oh SJ, Chua KJE, Ng KC (2017) Solar to hydrogen: compact and cost effective CPV field for rooftop operation and hydrogen production. Appl Energ 194:255–266
Burhan M, Shahzad MW, Oh SJ, Ng KC (2018) A pathway for sustainable conversion of sunlight to hydrogen using proposed compact CPV system. Energ Convers Manag 165:102–112
Cai Q, Hong W, Jian C, Li J, Liu W (2018) High-performance silicon photoanode using nickel/iron as catalyst for efficient ethanol oxidation reaction. ACS Sustain Chem Eng 6:4231–4238
Chang S-M, Liu W-S (2011) Surface doping is more beneficial than bulk doping to the photocatalytic activity of vanadium-doped $TiO_2$. Appl Catal B Environ 101:333–342
Chen Z, Jaramillo TF, Deutsch TG, Kleiman-Shwarsctein A, Forman AJ, Gaillard N, Garland R, Takanabe K, Heske C, Sunkara M, McFarland EW, Domen K, Milled EL, Dinh HN (2010) Accelerating materials development for photoelectrochemical hydrogen production: standards for methods, definitions, and reporting protocols. J Mater Res 25:3–16
Chen YW, Prange JD, Dühnen S, Park Y, Gunji M, Chidsey CED, McIntyre PC (2011) Atomic layer-deposited tunnel oxide stabilizes silicon photoanodes for water oxidation. Nat Mater 10:539–544
Chen Y-S, Manser JS, Kamat PV (2015a) All solution-processed lead halide perovskite-BiVO4 tandem assembly for photolytic solar fuels production. JACS 137:974–981
Chen L, Yang J, Klaus S, Lee LJ, Woods-Robinson R, Ma J, Lum Y, Cooper JK, Toma FM, Wang L-W, Sharp ID, Bell AT, Ager JW (2015b) p-type transparent conducting oxide/n-type semiconductor heterojunctions for efficient and stable solar water oxidation. JACS 137:9595–9603
Cherepy NJ, Smestad GP, Grätzel M, Zhang JZ (1997) Ultrafast electron injection: implications for a photoelectrochemical cell utilizing an anthocyanin dye-sensitized $TiO_2$ nanocrystalline electrode. J Phys Chem B 101:9342–9351

Choi MJ, Jung J-Y, Park M-J, Song J-W, Lee J-H, Bang JH (2014) Long-term durable silicon photocathode protected by a thin $Al_2O_3/SiO_x$ layer for photoelectrochemical hydrogen evolution. J Mater Chem A 2:2928–2933

Chou J-C, Lin S-A, Lee C-Y, Gan J-Y (2013) Effect of bulk doping and surface-trapped states on water splitting with hematite photoanodes. J Mater Chem A 1:5908–5914

Chun W-J, Ishikawa A, Fujisawa H, Takata T, Kondo JN, Hara M, Kawai M, Matsumoto Y, Domen K (2003) Conduction and valence band positions of $Ta_2O_5$, TaON, and $Ta_3N_5$ by UPS and electrochemical methods. J Phys Chem B 107:1798–1803

Coridan RH, Shaner M, Wiggenhorn C, Brunschwig BS, Lewis NS (2013) Electrical and photoelectrochemical properties of $WO_3$/Si tandem photoelectrodes. J Phys Chem C 117:6949–6957

Cornell RM, Schwertmann U (2004) Soils, the iron oxides, pp. 433–474. Wiley-VCH Verlag GmbH & Co. KGaA, Weinheim

Crabtree GW, Dresselhaus MS, Buchanan MV (2004) The hydrogen economy. Phys Today 57:39–44

Dantong Z, Zhi C, Tong G, Feng N, Laishun Q, Yuexiang H (2015) Hydrogen generation from water splitting on $TiO_2$ nanotube-array-based photocatalysts. Energ Technol 3:888–895

De Carvalho VAN, Luz RADS, Lima BH, Crespilho FN, Leite ER, Souza FL (2012) Highly oriented hematite nanorods arrays for photoelectrochemical water splitting. J Power Sources 205:525–529

Deng J, Lv X, Liu J, Zhang H, Nie K, Hong C, Wang J, Sun X, Zhong J, Lee S-T (2015) Thin-Layer $Fe_2TiO_5$ on hematite for efficient solar water oxidation. ACS Nano 9:5348–5356

Dias P, Schreier M, Tilley SD, Luo J, Azevedo J, Andrade L, Bi D, Hagfeldt A, Mendes A, Grätzel M, Mayer MT (2015) Transparent cuprous oxide photocathode enabling a stacked tandem cell for unbiased water splitting. Adv Energ Mater 5, n/a-n/a

Dong YK, Yoonhoo H, Uk S, Junghyun A, Woo LC, Kyoungsuk J, Younghye K, Jimin P, Sug HJ, Ho LJ, Hye-Eun L, Hui-Yun J, Hyungjun K, Tae NK (2016) Graphene quantum sheet catalyzed silicon photocathode for selective $CO_2$ conversion to CO. Adv Funct Mater 26:233–242

Doscher H, Geisz JF, Deutsch TG, Turner JA (2014) Sunlight absorption in water - efficiency and design implications for photoelectrochemical devices. Energ Environ Sci 7:2951–2956

Dunn HK, Feckl JM, Muller A, Fattakhova-Rohlfing D, Morehead SG, Roos J, Peter LM, Scheu C, Bein T (2014) Tin doping speeds up hole transfer during light-driven water oxidation at hematite photoanodes. Phys Chem Chem Phys 16:24610–24620

Fan G, Wang X, Fu H, Feng J, Li Z, Zou Z (2017a) Compensation of band-edge positions in titanium-doped $Ta_3N_5$ photoanode for enhanced water splitting performance: a first-principles insight. Phys Rev Mater 1:035403

Fan R, Mao J, Yin Z, Jie J, Dong W, Fang L, Zheng F, Shen M (2017b) Efficient and stable silicon photocathodes coated with vertically standing nano-$MoS_2$ films for solar hydrogen production. ACS Appl Mater Interfaces 9:6123–6129

Fatwa FA, Sean PB (2017) Recent developments in complex metal oxide photoelectrodes. J Phys D Appl Phys 50:193002

Feng X, Chen Y, Qin Z, Wang M, Guo L (2016) Facile fabrication of sandwich structured $WO_3$ nanoplate arrays for efficient photoelectrochemical water splitting. ACS Appl Mater Interfaces 8:18089–18096

Fujishima A, Honda K (1972) Electrochemical photolysis of water at a semiconductor electrode. Nature 238:37–38

Gao XM, Li MW, Hou YL, Wang CY (2015) Characterisation of $Fe_2TiO_5$ nanocrystallites synthesised via homogeneous precipitation. Mater Res Innovations 19:1–6

Glasscock JA, Barnes PRF, Plumb IC, Savvides N (2007) Enhancement of photoelectrochemical hydrogen production from hematite thin films by the introduction of Ti and Si. J Phys Chem C 111:16477–16488

Gonçalves RH, Leite LDT, Leite ER (2012) Colloidal $WO_3$ nanowires as a versatile route to prepare a photoanode for solar water splitting. Chemsuschem 5:2341–2347

Grätzel M (2001) Photoelectrochemical cells. Nature 414:338–344
Graves C, Ebbesen SD, Mogensen M, Lackner KS (2011) Sustainable hydrocarbon fuels by recycling $CO_2$ and $H_2O$ with renewable or nuclear energy. Renew Sustain Energ Rev 15:1–23
Gu J, Yan Y, Young JL, Steirer KX, Neale NR, Turner JA (2015) Water reduction by a p-GaInP2 photoelectrode stabilized by an amorphous $TiO_2$ coating and a molecular cobalt catalyst. Nat Mater 15:456
Guolei X, Yang-Gang W, Di W, Tianyang L, Jie H, Jun L, Xun W (2012) Size-dependent surface activity of rutile and anatase $TiO_2$ nanocrystals: facile surface modification and enhanced photocatalytic performance. Chem Eur J 18:4759–4765
Gupta SK, Rajakumar V, Grieveson P (1991) Phase transformations during heating of llmenite concentrates. Metall Trans B 22:711–716
Gurudayal (2016) Bulk and surface chemical modification of hematite photoanode for solar water splitting, MSE, NTU Singapore, Singapore, p 193
Gurudayal SY, Chiam MH, Kumar PS, Bassi HL, Seng J, Barber LH (2014) Wong, improving the efficiency of hematite nanorods for photoelectrochemical water splitting by doping with manganese. ACS Appl Mater Interfaces 6:5852–5859
Gurudayal D, Sabba MH, Kumar LH, Wong J, Barber M, Grätzel N (2015a) Mathews, perovskite-hematite tandem cells for efficient overall solar driven water splitting. Nano Lett 15:3833–3839
Gurudayal PM, Chee PP, Boix H, Ge F, Yanan J, Barber LH (2015b) Wong, core-shell hematite nanorods: a simple method to improve the charge transfer in the photoanode for photoelectrochemical water splitting. ACS Appl Mater Interfaces 7:6852–6859
Gurudayal, Donghyuk J, Kyoungsuk J, Hyo-Yong A, Boix PP, Abdi FF, Nripan M, Tae NK, Helena WL (2016) Highly active MnO catalysts integrated onto $Fe_2O_3$ nanorods for efficient water splitting. Adv Mater Interfaces, 3:1600176
Gurudayal J, Bullock DF, Srankó CM, Towle Y, Lum M, Hettick MC, Scott A, Javey J (2017a) Ager, efficient solar-driven electrochemical $CO_2$ reduction to hydrocarbons and oxygenates. Energ Environ Sci 10:2222–2230
Gurudayal RA, John PP, Boix C, Yi C, Shi MC, Scott SA, Veldhuis AM, Minor SM, Zakeeruddin LH, Wong M, Grätzel N (2017b) Mathews, atomically altered hematite for highly efficient perovskite tandem water-splitting devices. Chemsuschem 10:2449–2456
Hamann TW (2014) Water splitting: an adaptive junction. Nat Mater 13:3–4
Han L, Abdi FF, van de Krol R, Liu R, Huang Z, Lewerenz H-J, Dam B, Zeman M, Smets AHM (2014) Efficient water-splitting device based on a bismuth vanadate photoanode and thin-film silicon solar cells. ChemSusChem 7:2832–2838
Hemin Z, Hun KJ, Hyun KJ, Sung LJ (2017) Engineering highly ordered iron titanate nanotube array photoanodes for enhanced solar water splitting activity. Adv Funct Mater 27:1702428
Higashi M, Domen K, Abe R (2012) Highly stable water splitting on oxynitride TaON photoanode system under visible light irradiation. JACS 134:6968–6971
Hinogami R, Nakamura Y, Yae S, Nakato Y (1998) An approach to ideal semiconductor electrodes for efficient photoelectrochemical reduction of carbon dioxide by modification with small metal particles. J Phys Chem B 102:974–980
Hisatomi T, Le Formal F, Cornuz M, Brillet J, Tetreault N, Sivula K, Gratzel M (2011) Cathodic shift in onset potential of solar oxygen evolution on hematite by 13-group oxide overlayers. Energy Environ Sci 4:2512–2515
Hu S, Xiang C, Haussener S, Berger AD, Lewis NS (2013) An analysis of the optimal band gaps of light absorbers in integrated tandem photoelectrochemical water-splitting systems. Energ Environ Sci 6:2984–2993
Hu S, Shaner MR, Beardslee JA, Lichterman M, Brunschwig BS, Lewis NS (2014) Amorphous $TiO_2$ coatings stabilize Si, GaAs, and GaP photoanodes for efficient water oxidation. Science 344:1005–1009
Huang Q, Ye Z, Xiao X (2015) Recent progress in photocathodes for hydrogen evolution. J Mater Chem A 3:15824–15837
I.E.A. (IEA) (2015) Key world energy statics

Iordanova N, Dupuis M, Rosso KM (2005) Charge transport in metal oxides: a theoretical study of hematite α-$Fe_2O_3$. J Chem Phys 122:144305

Jang YJ, Jeong I, Lee J, Lee J, Ko MJ, Lee JS (2016) Unbiased sunlight-driven artificial photosynthesis of carbon monoxide from $CO_2$ using a ZnTe-based photocathode and a perovskite solar cell in Tandem. ACS Nano 10:6980–6987

Jeon TH, Moon G-H, Park H, Choi W (2017) Ultra-efficient and durable photoelectrochemical water oxidation using elaborately designed hematite nanorod arrays. Nano Energ 39:211–218

Ji L, McDaniel MD, Wang S, Posadas AB, Li X, Huang H, Lee JC, Demkov AA, Bard AJ, Ekerdt JG, Yu ET (2014) A silicon-based photocathode for water reduction with an epitaxial $SrTiO_3$ protection layer and a nanostructured catalyst. Nat Nanotechnol 10:84

Jiang C-M, Segev G, Hess LH, Liu G, Zaborski G, Toma FM, Cooper JK, Sharp ID (2018) Composition-dependent functionality of copper vanadate photoanodes. ACS Appl Mater Interfaces 10:10627–10633

Jinghua W, Yang H, Wen Y, Yanguang L (2017) $CO_2$ reduction: from the electrochemical to photochemical approach. Adv Sci 4:1700194

Jones J-P, Prakash GKS, Olah GA (2014) Electrochemical $CO_2$ reduction: recent advances and current trends. Isr J Chem 54:1451–1466

Joshi RK, Shukla S, Saxena S, Lee G-H, Sahajwalla V, Alwarappan S (2016) Hydrogen generation via photoelectrochemical water splitting using chemically exfoliated MoS2 layers. AIP Adv 6:015315

Kalanur SS, Seo H (2018) Influence of molybdenum doping on the structural, optical and electronic properties of $WO_3$ for improved solar water splitting. J Colloid Interface Sci 509:440–447

Kang D, Young JL, Lim H, Klein WE, Chen H, Xi Y, Gai B, Deutsch TG, Yoon J (2017) Printed assemblies of GaAs photoelectrodes with decoupled optical and reactive interfaces for unassisted solar water splitting. Nat Energ 2:17043

Kavan L, Grätzel M (1995) Highly efficient semiconducting $TiO_2$ photoelectrodes prepared by aerosol pyrolysis. Electrochim Acta 40:643–652

Keable J, Holcroft B (2012) Economic and business perspectives. In: van de Krol R, Grätzel M (eds) Photoelectrochemical hydrogen production. Springer, US, Boston, MA, pp 277–292

Kennedy JH, Frese KW Jr (1978) Photo-oxidation of water at alpha-$Fe_2O_3$ electrodes. J Electrochem Soc 125:709–714

Khaselev O, Turner JA (1998) A monolithic photovoltaic-photoelectrochemical device for hydrogen production via water splitting. Science 280:425–427

Khaselev O, Bansal A, Turner JA (2001) High-efficiency integrated multijunction photovoltaic/electrolysis systems for hydrogen production. Int J Hydrogen Energ 26:127–132

Kim JK, Shin K, Cho SM, Lee T-W, Park JH (2011) Synthesis of transparent mesoporous tungsten trioxide films with enhanced photoelectrochemical response: application to unassisted solar water splitting. Energ Environ Sci 4:1465–1470

Kim JH, Jo Y, Kim JH, Jang JW, Kang HJ, Lee YH, Kim DS, Jun Y, Lee JS (2015) Wireless solar water splitting device with robust cobalt-catalyzed, dual-doped BiVO4 photoanode and perovskite solar cell in tandem: a dual absorber artificial leaf. ACS Nano

Kim YW, Cha S, Kwak I, Kwon IS, Park K, Jung CS, Cha EH, Park J (2017) Surface-modified Ta3N5 nanocrystals with boron for enhanced visible-light-driven photoelectrochemical water splitting. ACS Appl Mater Interfaces 9:36715–36722

Klahr BM, Hamann TW (2011) Current and voltage limiting processes in thin film hematite electrodes. J Phys Chem C 115:8393–8399

Klahr B, Gimenez S, Fabregat-Santiago F, Bisquert J, Hamann TW (2012) Photoelectrochemical and impedance spectroscopic investigation of water oxidation with "Co–Pi"-coated hematite electrodes. JACS 134:16693–16700

Kong Q, Kim D, Liu C, Yu Y, Su Y, Li Y, Yang P (2016) Directed assembly of nanoparticle catalysts on nanowire photoelectrodes for photoelectrochemical $CO_2$ reduction. Nano Lett 16:5675–5680

Kōzō I, Shigehisa Y, Yoshichika B, Tetsuya H, Naokazu K, Toshio T, Syōji F (1971) Dielectric Properties of the Mixtures of α-$Fe_2O_3$, $TiO_2$ and $Fe_2TiO_5$. Jpn J Appl Phys 10:1513

Kroeze JE, Savenije TJ, Warman JM (2004) Electrodeless determination of the trap density, decay kinetics, and charge separation efficiency of dye-sensitized nanocrystalline TiO2. JACS 126:7608–7618

Kudo A, Miseki Y (2009) Heterogeneous photocatalyst materials for water splitting. Chem Soc Rev 38:253–278

Kumar B, Llorente M, Froehlich J, Dang T, Sathrum A, Kubiak CP (2012) Photochemical and photoelectrochemical reduction of $CO_2$. Annu Rev Phys Chem 63:541–569

Kyu CS, Unseock K, Seunghoon L, Jin HD, Min JS, Hyunwoong P (2014) Sn-coupled p-Si nanowire arrays for solar formate production from $CO_2$. Adv Energ Mater 4:1301614

Lai Y-H, Park HS, Zhang JZ, Mathews PD, Wright DS, Reisner E (2015) A Si photocathode protected and activated with a Ti and Ni composite film for solar hydrogen production. Chem Eur J 21:3919–3923

Le Formal F, Tetreault N, Cornuz M, Moehl T, Gratzel M, Sivula K (2011) Passivating surface states on water splitting hematite photoanodes with alumina overlayers. Chem Sci 2:737–743

Lee DK, Choi K-S (2018) Enhancing long-term photostability of $BiVO_4$ photoanodes for solar water splitting by tuning electrolyte composition. Nat Energ 3:53–60

Li J, Meng F, Suri S, Ding W, Huang F, Wu N (2012) Photoelectrochemical performance enhanced by a nickel oxide-hematite p-n junction photoanode. Chem Commun 48:8213–8215

Li W, Da P, Zhang Y, Wang Y, Lin X, Gong X, Zheng G (2014) $WO_3$ nanoflakes for enhanced photoelectrochemical conversion. ACS Nano 8:11770–11777

Liao P, Carter EA (2012) Hole transport in pure and doped hematite. J Appl Phys 112:013701

Liao P, Toroker MC, Carter EA (2011) Electron transport in pure and doped hematite. Nano Lett 11:1775–1781

Licht S, Wang B, Mukerji S, Soga T, Umeno M, Tributsch H (2000) Efficient solar water splitting, exemplified by $RuO_2$-catalyzed AlGaAs/Si photoelectrolysis. J Phys Chem B 104:8920–8924

Lin Y, Yuan G, Liu R, Zhou S, Sheehan SW, Wang D (2011) Semiconductor nanostructure-based photoelectrochemical water splitting: a brief review. Chem Phys Lett 507:209–215

Lin C-Y, Lai Y-H, Mersch D, Reisner E (2012) $Cu_2O|NiO_x$ nanocomposite as an inexpensive photocathode in photoelectrochemical water splitting. Chem Sci 3:3482–3487

Ling Y, Li Y (2014) Review of Sn-doped hematite nanostructures for photoelectrochemical water splitting. Part Part Syst Charact 31:1113–1121

Ling Y, Wang G, Wheeler DA, Zhang JZ, Li Y (2011) Sn-doped hematite nanostructures for photoelectrochemical water splitting. Nano Lett 11:2119–2125

Liu YL, Liu YC, Mu R, Yang H, Shao CL, Zhang JY, Lu YM, Shen DZ, Fan XW (2005) The structural and optical properties of $Cu_2O$ films electrodeposited on different substrates. Semicond Sci Technol 20:44

Liu X, Wang F, Wang Q (2012) Nanostructure-based $WO_3$ photoanodes for photoelectrochemical water splitting. Phys Chem Chem Phys 14:7894–7911

Liu J, Luo W, Zhu K, Wen X, Xiu F, Yuan J, Zou Z, Huang W (2017) Cathodic shift of a photo-potential on a $Ta_3N_5$ photoanode by post-heating a $TiO_2$ passivation layer. RSC Adv 7:30650–30656

Luo J, Im J-H, Mayer MT, Schreier M, Nazeeruddin MK, Park N-G, Tilley SD, Fan HJ, Grätzel M (2014) Water photolysis at 12.3% efficiency via perovskite photovoltaics and Earth-abundant catalysts. Science 345:1593–1596

Luo J, Li Z, Nishiwaki S, Schreier M, Mayer MT, Cendula P, Lee YH, Fu K, Cao A, Nazeeruddin MK, Romanyuk YE, Buecheler S, Tilley SD, Wong LH, Tiwari AN, Grätzel M (2015) Targeting ideal dual-absorber tandem water splitting using perovskite photovoltaics and cuinxga1-xSe2 photocathodes. Adv Energ Mater n/a-n/a

Luo J, Steier L, Son M-K, Schreier M, Mayer MT, Grätzel M (2016) $Cu_2O$ nanowire photocathodes for efficient and durable solar water splitting. Nano Lett 16:1848–1857

Maeda K, Domen K (2011) Oxynitride materials for solar water splitting. MRS Bull 36:25–31

Mao A et al (2011) Controlled synthesis of vertically aligned hematite on conducting substrate for photoelectrochemical cells: nanorods versus nanotubes. ACS Appl Mater Interfaces 110518093048092

Mayer MT, Du C, Wang D (2012) Hematite/Si nanowire dual-absorber system for photoelectrochemical water splitting at low applied potentials. JACS 134:12406–12409

Meng X, Qin G, Goddard WA, Li S, Pan H, Wen X, Qin Y, Zuo L (2013) Theoretical understanding of enhanced photoelectrochemical catalytic activity of Sn-doped hematite: anisotropic catalysis and effects of morin transition and Sn doping. J Phys Chem C 117:3779–3784

Mor GK, Varghese OK, Wilke RHT, Sharma S, Shankar K, Latempa TJ, Choi K-S, Grimes CA (2008) p-Type Cu–Ti–O nanotube arrays and their use in self-biased heterojunction photoelectrochemical diodes for hydrogen generation. Nano Lett 8:1906–1911

Morales-Guio CG, Tilley SD, Vrubel H, Grätzel M, Hu X (2014) Hydrogen evolution from a copper(I) oxide photocathode coated with an amorphous molybdenum sulphide catalyst. Nat Commun 5:3059

Morales-Guio CG, Mayer MT, Yella A, Tilley SD, Grätzel M, Hu X (2015) An optically transparent iron nickel oxide catalyst for solar water splitting. JACS 137:9927–9936

Morrish R, Rahman M, MacElroy JMD, Wolden CA (2011) Activation of hematite nanorod arrays for photoelectrochemical water splitting. Chemsuschem 4:474–479

Muranaka S, Shinjo T, Bando Y, Takada T (1971) Mössbauer Study of $Fe_2TiO_5$ and $FeTi_2O_5$. J Phys Soc Jpn 30:890

Murphy AB, Barnes PRF, Randeniya LK, Plumb IC, Grey IE, Horne MD, Glasscock JA (2006) Efficiency of solar water splitting using semiconductor electrodes. Int J Hydrogen Energ 31:1999–2017

Nielander AC, Shaner MR, Papadantonakis KM, Francis SA, Lewis NS (2015) A taxonomy for solar fuels generators. Energ Environ Sci 8:16–25

Nozik AJ (1976) p-n photoelectrolysis cells. Appl Phys Lett 29:150–153

Oh J, Deutsch TG, Yuan H-C, Branz HM (2011) Nanoporous black silicon photocathode for $H_2$ production by photoelectrochemical water splitting. Energ Environ Sci 4:1690–1694

Ohashi K, McCann J, Bockris JOM (1977) Stable photoelectrochemical cells for the splitting of water. Nature 266:610–611

Osterloh FE (2008) Inorganic materials as catalysts for photochemical splitting of water. Chem Mater 20:35–54

Paracchino A, Laporte V, Sivula K, Grätzel M, Thimsen E (2011) Highly active oxide photocathode for photoelectrochemical water reduction. Nat Mater 10:456

Paracchino A, Mathews N, Hisatomi T, Stefik M, Tilley SD, Gratzel M (2012) Ultrathin films on copper(i) oxide water splitting photocathodes: a study on performance and stability. Energ Environ Sci 5:8673–8681

Park JH, Bard AJ (2005) Unassisted water splitting from bipolar Pt/ Dye-sensitized $TiO_2$ photoelectrode arrays. Electrochem Solid-State Lett 8:G371–G375

Peharz G, Dimroth F, Wittstadt U (2007) Solar hydrogen production by water splitting with a conversion efficiency of 18%. Int J Hydrogen Energ 32:3248–3252

Pihosh Y, Turkevych I, Mawatari K, Asai T, Hisatomi T, Uemura J, Tosa M, Shimamura K, Kubota J, Domen K, Kitamori T (2014) Nanostructured $WO_3/BiVO_4$ photoanodes for efficient photoelectrochemical water splitting. Small 10:3692–3699

Pihosh Y, Turkevych I, Mawatari K, Uemura J, Kazoe Y, Kosar S, Makita K, Sugaya T, Matsui T, Fujita D, Tosa M, Kondo M, Kitamori T (2015) Photocatalytic generation of hydrogen by core-shell $WO_3/BiVO_4$ nanorods with ultimate water splitting efficiency. Sci Rep 5:11141

Pinaud BA, Vesborg PCK, Jaramillo TF (2012) Effect of film morphology and thickness on charge transport in $Ta_3N_5$/Ta photoanodes for solar water splitting. J Phys Chem C 116:15918–15924

Prévot MS, Sivula K (2013) Photoelectrochemical tandem cells for solar water splitting. J Phys Chem C 117:17879–17893

Qi H, Wolfe J, Fichou D, Chen Z (2016) $Cu_2O$ photocathode for low bias photoelectrochemical water splitting enabled by NiFe-layered double hydroxide Co-catalyst. Sci Rep 6:30882

Qiu Y, Liu W, Chen W, Chen W, Zhou G, Hsu P-C, Zhang R, Liang Z, Fan S, Zhang Y, Cui Y (2016) Efficient solar-driven water splitting by nanocone $BiVO_4$-perovskite tandem cells. Sci Adv 2

Rau S, Vierrath S, Ohlmann J, Fallisch A, Lackner D, Dimroth F, Smolinka T (2014) Highly efficient solar hydrogen generation—an integrated concept joining III–V solar cells with PEM electrolysis cells. Energ Technol 2:43–53

Reece SY, Hamel JA, Sung K, Jarvi TD, Esswein AJ, Pijpers JJH, Nocera DG (2011) Wireless solar water splitting using silicon-based semiconductors and earth-abundant catalysts. Science 334:645–648

Ronge J, Bosserez T, Martel D, Nervi C, Boarino L, Taulelle F, Decher G, Bordiga S, Martens JA (2014) Monolithic cells for solar fuels. Chem Soc Rev 43:7963–7981

Saito R, Miseki Y, Sayama K (2013) Photoanode characteristics of multi-layer composite BiVO4 thin film in a concentrated carbonate electrolyte solution for water splitting. J Photochem Photobiol A Chem

Sakai Y, Sugahara S, Matsumura M, Nakato Y, Tsubomura H (1988) Photoelectrochemical water splitting by tandem type and heterojunction amorphous silicon electrodes. Can J Chem 66:1853–1856

S.C. Program (2015) Scripps Institutio of Oceanography US San Diago

Schreier M, Gao P, Mayer MT, Luo J, Moehl T, Nazeeruddin MK, Tilley SD, Grätzel M (2015) Efficient and selective carbon dioxide reduction on low cost protected $Cu_2O$ photocathodes using a molecular catalyst. Energ Environ Sci 8:855–861

Seger B, Herbst K, Pedersen T, Abrams B, Vesborg PCK, Hansen O, Chorkendorff I (2014) $Mo_3S_4$ clusters as an effective $H_2$ evolution catalyst on protected Si photocathodes. J Electrochem Soc 161:H722–H724

Seitz G, Penin N, Decoux L, Wattiaux A, Duttine M, Gaudon M (2016) Near the ferric pseudobrookite composition ($Fe_2TiO_5$). Inorg Chem 55:2499–2507

Sekimoto T, Shinagawa S, Uetake Y, Noda K, Deguchi M, Yotsuhashi S, Ohkawa K (2015) Tandem photo-electrode of InGaN with two Si p-n junctions for $CO_2$ conversion to HCOOH with the efficiency greater than biological photosynthesis. Appl Phys Lett 106:073902

Shaner MR, McDowell MT, Pien A, Atwater HA, Lewis NS (2016) Si/$TiO_2$ tandem-junction microwire arrays for unassisted solar-driven water splitting. J Electrochem Soc 163:H261–H264

Shen S, Jiang J, Guo P, Kronawitter CX, Mao SS, Guo L (2012) Effect of Cr doping on the photoelectrochemical performance of hematite nanorod photoanodes. Nano Energ 1:732–741

Sherdil K, Marcos JLS, Jairton D, Sergio RT (2015) Photoelectrochemical study of $Ta_3N_5$ nanotubes for water splitting. IOP Conf Ser Mater Sci Eng 97:012007

Shi X, Zhang K, Shin K, Ma M, Kwon J, Choi IT, Kim JK, Kim HK, Wang DH, Park JH (2015) Unassisted photoelectrochemical water splitting beyond 5.7% solar-to-hydrogen conversion efficiency by a wireless monolithic photoanode/dye-sensitised solar cell tandem device. Nano Energ 13:182–191

Sivula K, Zboril R, Le Formal F, Robert R, Weidenkaff A, Tucek J, Frydrych J, Grätzel M (2010) Photoelectrochemical water splitting with mesoporous hematite prepared by a solution-based colloidal approach. JACS 132:7436–7444

Sivula K, Le Formal F, Grätzel M (2011) Solar water splitting: progress using hematite ($\alpha$–$Fe_2O_3$) photoelectrodes. Chemsuschem 4:432–449

Smith WA, Sharp ID, Strandwitz NC, Bisquert J (2015) Interfacial band-edge energetics for solar fuels production. Energ Environ Sci 8:2851–2862

Song H, Li C, Lou Z, Ye Z, Zhu L (2017) Effective formation of oxygen vacancies in black $TiO_2$ nanostructures with efficient solar-driven water splitting. ACS Sustain Chem Eng 5:8982–8987

Sun K, Shen S, Liang Y, Burrows PE, Mao SS, Wang D (2014) Enabling silicon for solar-fuel production. Chem Rev 114:8662–8719

Tachibana Y, Vayssieres L, Durrant JR (2012) Artificial photosynthesis for solar water-splitting. Nat Photon. 6:511–518

Tae SJ, Hyewon R, Minhyung C, Jaehoon K, Jin-Gyu K, Sung-Yoon C, Jihun O (2017) Nanoporous Au thin films on Si photoelectrodes for selective and efficient photoelectrochemical $CO_2$ reduction. Adv Energ Mater 7:1601103

Tallarida M, Das C, Cibrev D, Kukli K, Tamm A, Ritala M, Lana-Villarreal T, Gómez R, Leskelä M, Schmeisser D (2014) Modification of hematite electronic properties with trimethyl aluminum to enhance the efficiency of photoelectrodes. J Phys Chem Lett 5:3582–3587

Tilley SD, Cornuz M, Sivula K, Grätzel M (2010) Light-inducedwater splitting with hematite: Improved nanostructure and iridium oxide catalysis. Angewandte Chemie Int Ed 49:6405–6408

Tsui LK, Zangari G (2013) The influence of morphology of electrodeposited $Cu_2O$ and $Fe_2O_3$ on the conversion efficiency of $TiO_2$ nanotube photoelectrochemical solar cells. Electrochim Acta 100:220–225

Walter MG, Warren EL, McKone JR, Boettcher SW, Mi Q, Santori EA, Lewis NS (2010) Solar water splitting cells. Chem Rev 110:6446–6473

Wan Y, Karuturi SK, Samundsett C, Bullock J, Hettick M, Yan D, Peng J, Narangari PR, Mokkapati S, Tan HH, Jagadish C, Javey A, Cuevas A (2018) Tantalum oxide electron-selective heterocontacts for silicon photovoltaics and photoelectrochemical water reduction. ACS Energ Lett 3:125–131

Wang H, Deutsch T, Turner JA (2008) Direct water splitting under visible light with nanostructured hematite and WO3 photoanodes and a GaInP2 photocathode. J Electrochem Soc 155:F91–F96

Wang L, Lee C-Y, Mazare A, Lee K, Müller J, Spiecker E, Schmuki P (2014) Enhancing the water splitting efficiency of Sn-Doped hematite nanoflakes by flame annealing. Chem Eur J 20:77–82

Wang Z, Liu G, Ding C, Chen Z, Zhang F, Shi J, Li C (2015) Synergetic effect of conjugated Ni $(OH)_2/IrO_2$ cocatalyst on titanium-doped hematite photoanode for solar water splitting. J Phys Chem C 119:19607–19612

Wang C, Ma B, Cao X, He S, Han J, Wei M, Evans DG, Duan X (2018) Bridge-type interface optimization on a dual-semiconductor heterostructure toward high performance overall water splitting. J Mater Chem A 6:7871–7876

W.E. Council (2013) World energy resources: Solar

Yamane S, Kato N, Kojima S, Imanishi A, Ogawa S, Yoshida N, Nonomura S, Nakato Y (2009) Efficient solar water splitting with a composite "n-Si/p-CuI/n-i-p a-Si/n-p GaP/RuO2" semiconductor electrode. J Phys Chem C 113:14575–14581

Yanbo L, Tsuyoshi T, Dongkyu C, Kazuhiro T, Tsutomu M, Jun K, Kazunari D (2013) Vertically aligned $Ta_3N_5$ nanorod arrays for solar-driven photoelectrochemical water splitting. Adv Mater 25:125–131

Yu Y, Zhang Z, Yin X, Kvit A, Liao Q, Kang Z, Yan X, Zhang Y, Wang X (2017) Enhanced photoelectrochemical efficiency and stability using a conformal $TiO_2$ film on a black silicon photoanode. Nat Energ 2:17045

Zhang X, Zhang B, Cao K, Brillet J, Chen J, Wang M, Shen Y (2015) A perovskite solar cell-$TiO_2$@$BiVO_4$ photoelectrochemical system for direct solar water splitting. J Mater Chem A 3:21630–21636

Zhang K, Ma M, Li P, Wang DH, Park JH (2016) Water splitting progress in tandem devices: moving photolysis beyond electrolysis. Adv Energ Mater, 6 n/a-n/a

Zhang R, Ning F, Xu S, Zhou L, Shao M, Wei M (2018) Oxygen vacancy engineering of $WO_3$ toward largely enhanced photoelectrochemical water splitting. Electrochim Acta 274:217–223

Zhong M, Hisatomi T, Sasaki Y, Suzuki S, Teshima K, Nakabayashi M, Shibata N, Nishiyama H, Katayama M, Yamada T, Domen K (2017) Highly active GaN-stabilized Ta3N5 thin-film photoanode for solar water oxidation. Angew Chem Int Ed 56:4739–4743

Zhou Z, Huo P, Guo L, Prezhdo OV (2015) Understanding hematite doping with group IV elements: a DFT + U study. J Phys Chem C 119:26303–26310

# Chapter 15
# Low GWP Refrigerants for Energy Conservation and Environmental Sustainability


**Kutub Uddin, Bidyut Baran Saha, Kyaw Thu and Shigeru Koyama**

**Abstract** Refrigerant significantly influences the performance of air-conditioning and refrigeration system as well as it has some environmental issues that need to be considered before selection. These systems can be made eco-friendly, if it is powered by solar energy or low-grade thermal energy and they use environment-friendly refrigerants. In this chapter, low GWP (global warming potential) refrigerants have been explored for the domestic air-conditioning applications. Refrigerants with high GWP are mostly used in environment control applications such as heating, ventilation, air-conditioning (HVAC), and refrigeration systems. Some refrigerants contribute to significant environmental issues and the Montreal Protocol and Kyoto Protocol have been signed to address the threats of ozone layer depletion and global warming potential. To fulfil the commitments of Kyoto Protocol, meanwhile, governments in many countries instituted phase-out plan for the use of environmentally harmful gasses in heat pump systems. For instance, EU MAC Directives, F-gas regulation, and Japan METI directives, which clearly declared their target year to use new refrigerant of GWP below 150 for mobile air conditioner and GWP below 750 for the residential air conditioner. Research interest has been stimulated to find alternative refrigerants with low or

Shigeru Koyama: Deceased on August 4, 2018.

K. Uddin · B. B. Saha (✉) · K. Thu
International Institute for Carbon-Neutral Energy Research (WPI-I2CNER), Kyushu University, 744 Motooka, Nishi-ku, Fukuoka 819-0395, Japan
e-mail: saha.baran.bidyut.213@m.kyushu-u.ac.jp

K. Uddin
Faculty of Physics, Jagannath University, Dhaka 1100, Bangladesh

B. B. Saha · K. Thu
Kyushu University Program for Leading Graduate School, Green Asia Education Center Interdisciplinary Graduate School of Engineering Sciences, Kyushu University, Kasuga-Koen 6-1, Kasuga-Shi, Fukuoka 816-8580, Japan

B. B. Saha
Mechanical Engineering Department, Kyushu University, 744 Motooka, Nishi-ku, Fukuoka 819-0395, Japan



H. Tyagi et al. (eds.), *Advances in Solar Energy Research*, Energy, Environment, and Sustainability, https://doi.org/10.1007/978-981-13-3302-6_15

ultra-low GWP for energy conservation and environmental sustainability. Hydrofluoroolefins (HFOs) have a very low environmental impact, and thus HFOs are considering as potential candidates to replace the hydrofluorocarbon (HFC) refrigerants such as R410A, a near-azeotropic mixture of difluoromethane (R-32) and pentafluoroethane (R-125) and is commonly used refrigerant in air-conditioning applications. The limited number of pure fluids sometimes cannot meet the excellent heat transfer criteria due to their low volumetric capacity and moderate flammability or toxicity. Mixing of HFOs and HFCs refrigerants, in this case, allows the adjustment of the most desirable properties of the refrigerant by varying the molar fraction of the components. Different combination of mixture presented here cannot be claimed as the best mixture, but it might be a good choice for further study. This chapter focuses on the research trend in finding low GWP refrigerants and its application in different heat pump system considering the system performance, safety, and the overall environmental impact. The conventional vapor compression system, thermally driven adsorption system, and sorption-compression hybrid system have been taken into consideration.

**Keywords** Global warming potential · Hydrofluoro-olefins (HFOs) Refrigerant blend · Temperature glide · Volumetric capacity

## 15.1 Introduction

The air-conditioning and refrigeration system are widely used in a domestic and industrial application for providing thermal comfort and storage facilities (Calm and Didion 1998). According to the Japan Refrigeration and Air Conditioning Industry Association (JRAIA), the demand for room air conditioners (RAC) is estimated to reach 88.81 million units in 2016 which is 2.9% higher than the previous year. Figure 15.1 presents the huge demand of RAC and in a country or region which reflect the significance of environmental concern in this sector in terms of greenhouse gas emission and electrical energy consumption.

Refrigerants as heat carrier substance significantly influence the performance of the RAC and refrigeration systems. Thermophysical properties of such refrigerants are crucial in designing such a system. Additionally, flammability, toxicity, and environmental friendliness are equally important. From the beginning of commercial production of the system, most of the popular refrigerants such as CFCs and HCFCs possess show excellent system performance. These refrigerants are not flammable and toxic but possess higher ODP and GWP characteristics. Following the Montreal Protocol (1987), a gradual phase-out of refrigerants that deplete the ozone layer has been implemented and are substituted with more environment-friendly refrigerants which have almost zero ODP (UNEP 2016; Benhadid-Dib and Benzaoui 2012). The air-conditioning and refrigeration industry have taken many initiatives after signing the Montreal Protocol to overcome challenges in developing suitable refrigerants to replace the popular CFCs and

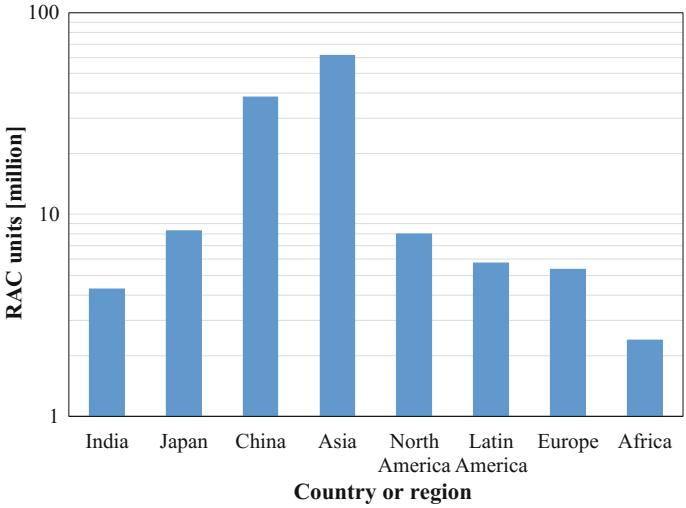


**Fig. 15.1** World room air-conditioning demand (RAC) in 2016 (JRAIA 2017)

HCFCs refrigerants (Calm and Didion 1998; McMullan 2002). Remarkably, the CFCs phase-out has been accomplished in 1996 in the developed countries whilst the targeted deadline for the developing countries is the year 2010 whereas HCFCs phase-out will be accomplished in 2030 or earlier (Powell 2002). Today, most acceptable choice of refrigerants as an alternative to the ozone-depleting refrigerants (CFCs and HCFCs), includes R410A, R134a, R407C, etc., particularly, for residential and automobile air-conditioning systems.

However, the global warming potential (GWP) of these refrigerants are considered very high. For example, hydrofluorocarbon refrigerant R134a and R410A have zero ODP but their GWP values are 1300 and 1900, respectively (Cabello et al. 2015; Xu et al. 2013). Refrigerant R410A has good thermal and transport properties with high volumetric capacity for air-conditioning applications, but it has an unfavorable effect on the environment in case of leakage that might be resulted during maintenance and unavoidable wear and tear. The Kyoto Protocol in 1997 (COP3-1997) (Parties to the Protocol 1998) commits the state parties will reduce the greenhouse gas emission to the atmosphere at least 5% below 1990 levels in the first commitment period, i.e., from 2008 to 2012. In the second commitment period, from 2013 to 2020 (agreed in 2012, known as Doha Amendment to the protocol), 37 countries including the European Union agreed to reduce 18% greenhouse gas emission. According to the European Environment Agency report (2016), the emission of F-gas, which includes HFCs, PFCs, and SF6, will be reduced by two-thirds of its 2014 value by 2030. In the USA, the Montreal Protocol is amended and now is implementing as the Clean Air Act via the US Environment Protection Agency (EPA). The EPA (1990) decided to limit the use of R134a in a newly manufactured light-duty vehicle from the model year 2021 and HVAC units using

HCFC-22 can continue to be serviced until 2020. After the model year 2025, R134a will not be accepted in MVAC system although its production will continue for servicing older vehicles contain R134a. The Australian government has imposed 50 $/kg carbon tax for R410A (Pham and Rajendran 2012).

Finding low GWP refrigerants with excellent energy efficiency has become an urgent task of the present generation whilst the total climate impact associated with refrigerants consists of direct and indirect contributions. Realizing the long-term environmental commitments and to comply with global regulations, the auto industry began to look for new, low GWP air conditioner refrigerants in approximately 2011. There are a number of refrigerants available which have a low environmental impact but not suitable to replace the existing halogenated refrigerants. The phase-out plan of high GWP refrigerants used in domestic and automobile application is listed in Table 15.1.

This chapter will focus both the pure and blend refrigerants which have ultra-low and low GWP but system performance equivalent or better to the existing refrigerant in domestic and automobile air-conditioning application. According to the taxonomy of RTOC 2014 Assessment Report (UNEP 2016), the 100 year GWP levels are classified in five levels which is shown in Table 15.2.

**Table 15.1** Target GWP value for designated product and year of implementation (European Environment Agency 2016; EPA 1990; Pham and Rajendran 2012; Meno 2015; Fukushima and Hashimoto 2015)

| | Designated products | Current Refrigerant and $GWP_{100}$ (IPCC5) | | Targeted GWP | Year of implementation |
|---|---|---|---|---|---|
| Japan | Room air-conditioning | R410A<br>R32 | 1900<br>675 | 750 | 2018 |
| | Mobile air-conditioning | R134a | 1300 | 150 | 2023 |
| USA | Mobile air-conditioning | R12<br>R134a | 10900<br>1300 | | 2021 |
| | Residential air-conditioning/ refrigerator | R22<br>R410A<br>R134a<br>R407C | 1760<br>1900<br>1300<br>1600 | | 2020<br>NA<br>2025<br>NA |
| EU | Mobile air-conditioning | R134a | 1300 | 150 | 2017 |
| | Room air-conditioning | | | 750 | 2021 |
| Canada | Domestic refrigeration | | | 150 | 2025 |
| | AC-chillers | | | 700 | 2025 |

**Table 15.2** Classification of 100 year GWP levels (UNEP 2016)

| 100 year GWP | Classification |
|---|---|
| <30 | Ultra-low or negligible |
| <100 | Very low |
| <300 | Low |
| 300–1000 | Medium |
| >1000 | High |

## 15.2 Refrigerant Selection

Currently, the widely used refrigerant in the domestic air-conditioning system is R410A which has no ODP but higher GWP. Alternative refrigerant with low GWP is desirable to fulfil the directive of Kyoto Protocol and some countries local guideline. Low GWP refrigerant mixture is being studied by many authors around the world considering the system performance, flammability, and toxicity. The refrigerants R32, R1234yf, R1234ze(E), R744, R152a, and hydrocarbon (HC) possesses very low GWP and within safety limit. Sometime refrigerant blend is found suitable to replace the widely used R410A. Blend is usually a mixture of two or more refrigerants. Some characteristics features of the pure refrigerants are furnished in Table 15.3. Along with the GWP and safety limit, the volumetric capacity and cycle performance are equally important. For blend, the temperature glide needs to be under consideration.

### *15.2.1 Global Warming Effect*

$GWP_{100}$ is measured by the amount of heat traps in a refrigerant compared to the heat trap by the same mass of $CO_2$ over 100-year horizon. A clear definition of GWP calculation is to be found in the IPCC's 2001 Third Assessment Report. The widely used refrigerants in domestic and automobile applications are R410A and R134a, have the GWP of 1900 and 1300, respectively. After Kyoto Protocol, research interest on low GWP refrigerant intensified. Initially, HFCs and HFOs are put into the domain. But in most of the cases, single component low GWP cannot meet the requirements to drop-in replacement of R410A. Now refrigerant blend is considering as an alternative refrigerant. Blend are formed by mixing two or more single component refrigerants, the GWP of a refrigerant mixture is calculated as the mass weighted average of GWPs of individual components in the mixture. To respond the international guideline, refrigeration industry is looking for ultra-low GWP refrigerant either pure or blend. The GWP value of the mixture can be adjusted varying the composition of constituents in a mixture. Table 15.4 lists the most widely used refrigerants with respective ODP and GWP in the residential and automobile applications.

**Table 15.3** Main characteristics of some individual refrigerants (Fukushima and Hashimoto 2015; Lemmon et al. 2013; Higashi and Akasaka 2016; Takizawa et al. 2009)

| Refrigerant name | R32 | R1234yf | R1234ze | R1123 | R744 | R152a | R134a | R410A |
|---|---|---|---|---|---|---|---|---|
| Molar mass (kg/kmol) | 52.02 | 114.04 | 114.04 | 82.03 | 44.01 | 66.05 | 102.03 | 72.59 |
| Normal boiling point (°C) | −51.7 | −29.5 | −19.0 | −59.1 | −78.5 | −24.02 | −26.07 | −51.5 |
| Critical temperature (°C) | 78.2 | 94.7 | 109.37 | 58.55 | 30 | 113.26 | 101.06 | 71.34 |
| Critical pressure (MPa) | 5.78 | 3.38 | 3.64 | 4.55 | 7.38 | 4.52 | 4.06 | 4.9 |
| GWP (UNEP 2016) | 677 | <1 | <1 | <1 | 1 | 138 | 1300 | 1900 |
| Atmospheric lifetime | 4.9 yr | 11 d | 18 d | 1.6 d | – | | 14.6 yr | 17 yr |
| Flammability range (vol%) | 13.3–29.3 | 6.2–12.3 | 7.0–9.5 | 10.4–29.3 | – | | | None |
| Burning velocity (cm/s) | 6.7 | 1.5 | | 7 | | | | – |
| Safety class (ASHRAE classification) | A2L | A2L | A2L | – | A1 | A2 | A1 | A1 |

GWP values taken from the IPCC AR5 report (IPCC 2014)

Following the number of components in the blend the GWP can be calculated as:

$$\begin{aligned}\text{GWP of Blend} = {} & \text{Proportion by \% mass of component A} \times \text{GWP of A} \\ & + \text{Proportion by \% mass of component B} \times \text{GWP of B} \\ & + \text{Proportion by \% mass of component C} \times \text{GWP of C}\end{aligned}$$

## 15.2.2 Volumetric Capacity

Volumetric capacity is defined by the cooling capacity per unit of vapor volume at the exit of evaporator. It is calculated by the product of evaporation enthalpy ($\Delta h_{eva}$) and vapor density at evaporator outlet ($\rho_v$). A refrigerant with high volumetric capacity gives high cooling capacity for a given swept volume in compressor (Granryd 2001). Generally, low GWP HFOs have found low volumetric capacity also compared to HFCs. By mixing HFOs with higher volumetric HFCs can solve the problem of low volumetric capacity. So the mixture of high GWP HFCs with low GWP HFOs increases the volumetric capacity but it reduces the GWP. Table 15.5 shows the volumetric capacity of some pure refrigerant at a temperature −3 °C.

**Table 15.4** Most widely used refrigerants with respective ODP and GWP

| | Mostly used refrigerant in the system | Mostly adopting regions | ODP | $GWP_{100}$ (IPCC5) | Comments |
|---|---|---|---|---|---|
| Residential air-conditioning | R22 (Park et al. 2007; Chen and Yu 2008; Park et al. 2008; Park et al. 2009; Park et al. 2009; Joudi and Al-Amir 2014; Devotta et al. 2001) [retrofitting R22 are R134a (GWP-1300), R407C (GWP-1600), R407A (GWP-1900) and R404A (GWP-3900)] | Developing countries | 0.034 | 1760 | Will be banned on January 1, 2020 |
| | R410A (Yun et al. 2006; Mota-Babiloni et al. 2017; Spatz et al. 2004) | Developed countries | 0 | 1900 | |
| | R32 (n.d.) | | 0 | 677 | DAIKIN Tec. introduced |
| Automobile air-conditioning | R134a (Brown et al. 2002; Vaghela 2017; Minjares 2011) | Developed and developing | 0 | 1300 | Replacing R12 and will be banned very soon (Tiwari and Gupta 2011) |
| | R1234yf (Sciance 2013; Navarro-Esbrí et al. 2013; Zilio et al. 2011) | Developed country | 0 | <1 | |

$GWP_{100}$ (IPCC5)-values are taken from the IPCC AR5 report (IPCC 2014) for pure fluids; for mixtures, values are calculated based on the values for pure fluids

Volumetric capacity,

$$VC = h_{\text{eva}} + \rho_v \tag{15.1}$$

### *15.2.3 Flammability and Toxicity*

Most potential refrigerant having lower GWP and toxicity possess higher flammability, which is a problem to replace HCFC refrigerants. A special security arrangement is required to make the system when flammable refrigerant is used. The LFL and UFL (lower and upper flammable limit) range the basic combustion

**Table 15.5** Volumetric capacity of some widely known refrigerant at −3 °C

| Refrigerant | R32 | R1234yf | R1234ze | R1123 | R744 | R152 | R134a | R410A | Propane |
|---|---|---|---|---|---|---|---|---|---|
| Volumetric capacity ($MJ/m^3$) | 5.17 | 1.94 | 1.49 | 5.34 | 12.34 | 2.34 | 2.61 | 4.78 | 3.59 |

**Table 15.6** The flammability limit and burning velocity of the refrigerants

| Property | R1234yf | R1234ze (E) | R32 | Propane (R-290) | R152a | Ammonia (R717) | Ethanol | Gasoline |
|---|---|---|---|---|---|---|---|---|
| Lower flammable limit (vol% air) | 6.2 | 7 | 14.4 | 2.2 | 3.9 | 15 | 3.3 | 1.4 |
| Upper flammable limit (% vol. air) | 12.3 | 9.5 | 29.3 | 10 | 16.9 | 28 | 19 | 7.6 |
| Minimum ignition energy (mJ) | >5000, $<1\times10^4$ | 61,000–64,000 | >30, <100 | 0.25 | 0.38 | 100–300 | 0.65 | 0.29 |
| Heat of combustion (kJ/g) | 10.7 | – | 9.4 | 46.3 | 16.5 | 18.6 | 29.8 | 47 |
| Burning velocity (cm/s) | 1.5 | – | 6.7 | 46 | 23 | 7.2 | 58 | 34 |
| Safety class (ISO 817 and ASHRAE 34) | A2L | A2L | A2L | A3 | A2 | B2L | A3 | A3 |

A—lower chronic toxicity, have an occupation exposure limit of 400 ppm or greater
B—higher chronic toxicity, have an occupation exposure limit of less than 400 ppm
2L—lower flammability, burning velocity not higher than 10 cm/s, the energy of combustion below 19 MJ/kg and not flammable below 3.5% volume concentration

characteristics of flammable refrigerants. ASHRAE (American Society of Heating, Refrigeration and air conditioning) updated two standards, NSI/ASHRAE standard 15 Safety Standard for Refrigeration Systems and standard 34 Designation and Safety Classification of Refrigerants. In the latest version, classification "2L" was added to highlight the lower flammability refrigerants with a maximum burning velocity <10 cm/s which benefit the promotion of HFOs and R32 (Yang and Wu 2013). The burning velocity and safety group of some refrigerants are presented in Table 15.6.

### *15.2.4 Refrigerant Mixture*

To use pure refrigerant in a system is always easy because of its azeotropic nature and the available thermophysical properties. Nowadays, HFO refrigerants get attention due to its suitable properties like extremely low GWP, lower toxicity, and moderate flammability (A2L). But some researcher reported that pure HFOs are not

**Table 15.7** Currently used popular blend refrigerants (UNEP 2016)

| Refrigerant designation | Refrigerant composition (mass %) | Molecular weight | Boiling point (bubble/dew) | Safety class | ODP | $GWP_{100}$ |
|---|---|---|---|---|---|---|
| R404 | R125/143a/134a (44/52/4) | 97.6 | −46.6/−45.8 | A1 | 0 | 3900 |
| R407A | R-32/125/134a (20/40/40) | 90.1 | −45.2/−38.7 | A1 | 0 | 1900 |
| R407C | R32/125/134a (23/25/52) | 86.2 | −43.8/−36.7 | A1 | 0 | 1600 |
| R407F | R32/125/134a (30/30/40) | 82.1 | −46.1/−39.7 | A1 | 0 | 1700 |
| R410A | R32/125 (50/50) | 72.6 | −51.6/−51.5 | A1 | 0 | 1900 |
| R507A | R125/143a (50/50) | 98.9 | −47.1/−47.1 | A1 | 0 | 4000 |

Safety classification follows ANSI/ASHRAE Standard 34-2010
GWP values are calculated based on the values of pure refrigerant from IPCC AR5 report (IPCC 2014)

good choice as an alternative of R410A in residential scale air-conditioning due to their low vapor pressure (Kojima et al. 2015; Barve and Cremaschi 2012; Koyama et al. 2011). The improvement of overall system performance is achieved by many researchers when added with HFC or natural refrigerant (Han et al. 2007; Mota-Babiloni et al. 2015; Maczek et al. 1997; Wu et al. 2009). Refrigerant mixture can solve the problem of very limited number of fluids which have suitable properties. But there is a chance to alter the other properties of mixture. There are three categories of mixtures which can be used as working fluids: azeotropes, near-azeotropes, and non-azeotropes. This chapter highlighted some important parameters of binary and ternary mixture which need to be considered during mixture formation such as temperature glide, volumetric capacity, GWP, and cycle performance. In this chapter, few new mixture properties are presented keeping in mind the performance of widely used R410A (Table 15.7).

### *15.2.5 Temperature Glide*

During the evaporation process, refrigerant begins to boil at a saturated liquid temperature, called bubble point, and ended with saturated vapor pressure, called dew point. At constant pressure, the difference between dew point and bubble point is called temperature glide. Pure refrigerant boils and condenses at a constant temperature so it has no gliding temperature. A mixture of two or more different fluids is classified as azeotropes and has long been used in the refrigeration industry; this refrigerant behaves like a pure refrigerant so it has no gliding temperature. The boiling point and condensation point curves unite at a point at which vapor and liquid have the same concentration. Near-azeotropes have a much greater

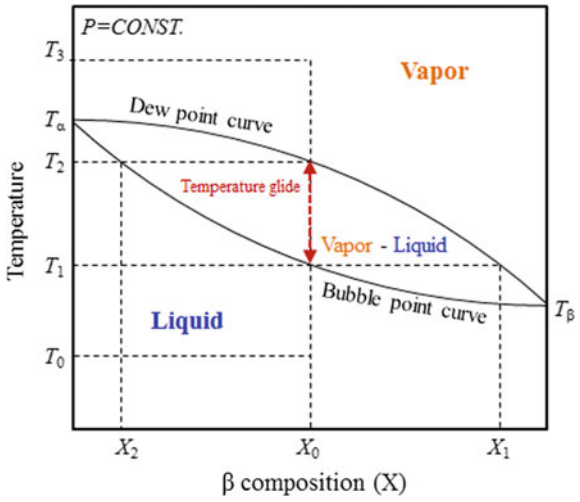


**Fig. 15.2** Phase equilibrium diagram of zeotropic mixtures with the state points of the vapor compression cycle superimposed

potential for drop-in alternatives to HFCs (Morrison and McLinden 1993). The temperature change during evaporation and condensation is negligible (1–2 K) for near-azeotropic mixture. Non-azeotropic (zeotropic) mixtures have a separate curve for bubble point and dew point over the full concentration range. During the evaporation, a more volatile component of the mixture starts to boil first where less volatile component boils at last, so there is a concentration change with temperature, that creates temperature glide (3–20 K). Sometime leakage may alter their composition and properties so as to $T_{glide}$. At composition $X_0$ in Fig. 15.2, the refrigerant begins to boil at $T_1$ and ended at $T_2$ ($T_{glide} = T_2 - T_1$), the temperature varies because the evaporating liquid continuously changing its composition and thus the boiling point.

Temperature glide

$$\Delta T_{glide} = T_{dew} - T_{bulb} \tag{15.2}$$

## *15.2.6 Cycle Performance*

The cycle performance of the refrigerant is very important and can be calculated theoretically and experimentally. The coefficient of performance (COP) can be evaluated theoretically employing thermophysical properties of refrigerant from REFPROP database which contain so many refrigerants. Considering the application area, cycle simulation requires operating condition for the system. As the mixture shows temperature glide during evaporation and condensation, so pressure selection for simple calculation is difficult. Sometimes average values for temperature are considered for evaporation and condensation in the simulation process.

**Table 15.8** Parameter considered for cycle performance calculation

| | |
|---|---|
| Condensation temperature (average) | 30 °C |
| Evaporation temperature (average) | −3 °C |
| Degree of subcool | 0 °C |
| Degree of superheat | 3 °C |
| Adiabatic compression efficiency | 0.85 |
| Thermophysical properties | REFPROP V9.1 |

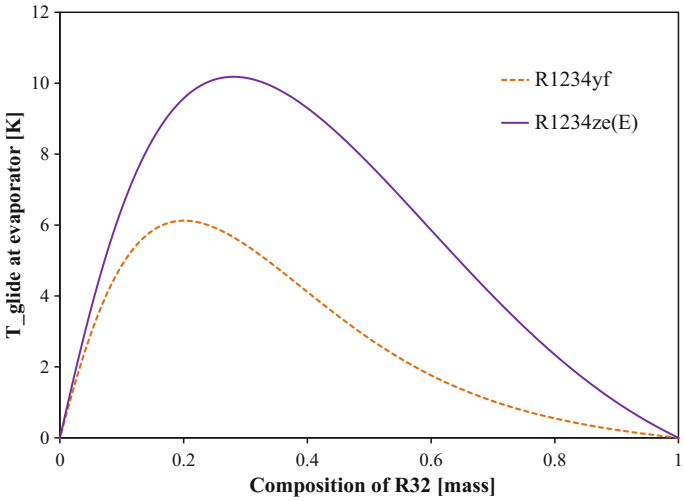


**Fig. 15.3** Temperature glide of two binary mixtures R32/R1234ze and R32/R1234yf

In this chapter, mixture performance are shown using constant operating parameters which are shown in Table 15.8. The following equations can be used where suffix 1, 2, 2a, 3, and 4 are picked from Fig. 15.3.

Coefficient of Performance (COP) for heating of an ideal cycle is presented in Eq. 15.3.

$$COP_{\mathrm{h}} = \frac{h_{2a} - h_3}{h_{2a} - h_1} \tag{15.3}$$

where

$$h_{2a} = \frac{h_2 - h_1}{0.85} + h_1 \tag{15.4}$$

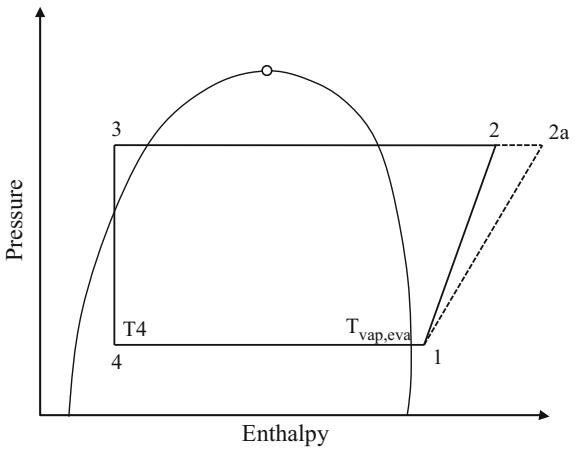


**Fig. 15.4** Basic thermodynamic cycle

For refrigeration or cooling COP,

$$\mathrm{COP_r} = \frac{h_1 - h_4}{h_{2a} - h_1} \tag{15.5}$$

Volumetric capacity during evaporation can be calculated as

$$\mathrm{VC_{eva}} = (h_1 - h_4) \times \rho_1 \tag{15.6}$$

Temperature glide at evaporator can be calculated as shown in Eq. 15.7, where the temperatures are shown in Fig. 15.4. Basic thermodynamic cycle.

$$T_{\mathrm{glide\_eva}(T_4)} = T_{\mathrm{vap,eva}} - T_4 \tag{15.7}$$

## 15.3 Low GWP Refrigerants

There is an urgent need to find a low GWP refrigerant to develop sustainable technologies. The current single component low GWP refrigerant may increase energy consumption, introduce safety risk and sometimes require significant system modification. Refrigerant blend can be an effective alternative to achieve sustainable building technology reducing energy consumption and greenhouse gas emissions by 50% compared to the current best refrigerants. This section discusses the ongoing research activities about some pure and blend refrigerants which are considered as a promising alternative.

## *15.3.1 Pure Refrigerants*

### 15.3.1.1 R1234yf

The R1234yf (CF3CF = CH2) is a refrigerant of GWP < 1. It is low in toxicity and mildly flammable (A2L) (Minor et al. 2010; Honeywell Technical Bulletin 2012). It has no ODP but has excellent life cycle climate performance (LCCP) compared to R134a and R744 (Spatz and Minor 2008). The critical temperature and critical pressure of the refrigerant are 94.7 °C and 3.38 MPa, respectively (Tanaka and Higashi 2010; Akasaka et al. 2010; Lai et al. 2011). In 2007, the SAE International launched CRP 1234 program to investigate the safety and performance of HFO 1234yf for the use in mobile air-conditioning. It has got attention as a prospective alternative candidate of R134a, the mostly used refrigerant in automobiles (Spatz and Minor 2008; SAE-CRP 1234 2009; Lee and Jung 2012) though the performance of R11234yf is slightly lower than R134a (Navarro-Esbrí et al. 2013; Zilio et al. 2011; Qi 2015). General Motors started using R1234yf for vehicles in 2012 (Sciance 2013). However, when this refrigerant is used as an alternative to R410A, it shows lower coefficient of performance (COP) and also it requires larger unit bodies related to R410A (Barve and Cremaschi 2012; Fukuda et al. 2016). Figure 15.5 shows that thermodynamic cycle of R1234yf positioned much lower than R410A. The volumetric capacity of R1234yf is lower compared to R410A. Insufficient production capacity and higher price are another constraints to use this refrigerant in the larger scale.

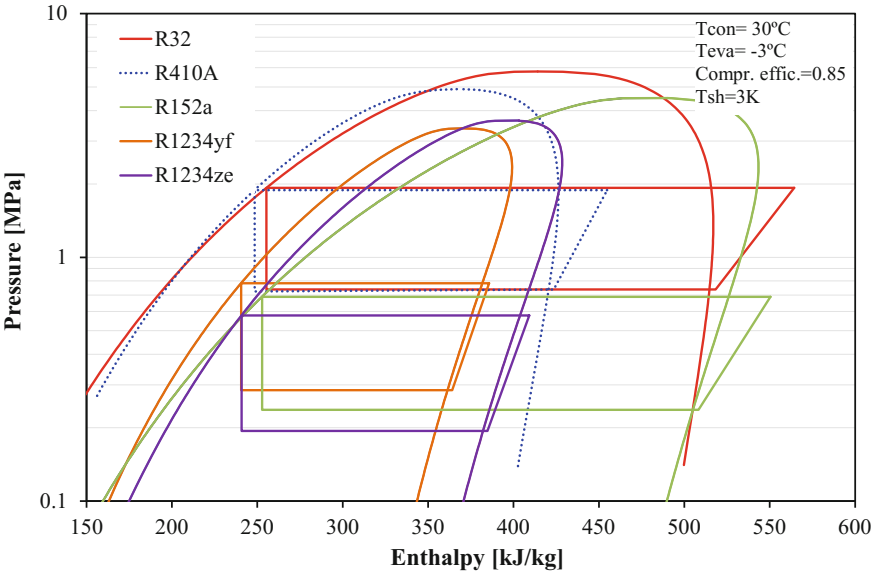


**Fig. 15.5** Comparison of P-h diagram of some pure refrigerant along with thermodynamic cycle

#### 15.3.1.2 R1234ze(E)

The (R1234ze(E) (CF3CH = CHF) got attention due to its ultra-low GWP (<1) and it is investigated as a candidate refrigerant for industrial centrifugal chillers (Ueda et al. 2011; Yang et al. 2015). The critical temperature and critical pressure of the refrigerant are 109.3 °C and 3.63 MPa, respectively (Higashi et al. 2010; Brown et al. 2010). It is a potential refrigerant for high-temperature heat pumps which works as hot dryers and steam generators for industrial purposes, such as the concentration of beverages, sterilization of foods, drying lumber, solvent recovery and distillation of petrochemical products. The possibility of using the refrigerant R1234ze(E) and R1234ze(Z) into high-temperature heat pump system has been investigated by Fukuda et al. (2014). The flammability of the refrigerant was studied by the same authors and found all the properties are suitable for the future application. Brown et al. (2009) predicted the performance potential of R1234ze(Z) in high-temperature heat pumping applications and suggested for further research as a possible alternative of R114. Experimental studies revealed that due to its low volumetric capacity, pure R1234ze(E) is not suitable as an alternative for R410A (Koyama et al. 2011) but it is suitable for turbo refrigeration system if the impeller size of the compressor is enlarged as compared to that of R134a (Koyama et al. 2010a). The energy saving potential of the refrigerant is found to 9–15% compared to R134a (Kabeel et al. 2016; Lai 2014). Figure 15.6 shows the schematic diagram of water-cooled experimental set up which is used to study the performance of new refrigerants and their blends (Fukuda et al. 2016).

Figure 15.7 shows the coefficient of performance (COP) of R1234ze(E) compared to R410A and R32, where it is found that the COP of R1234ze(E) is lower than other two. The COP is the ratio of heat transfer in the condenser or evaporator to the compressor/inverter input and can be estimated based on the cycle level and system level. The $COP_{cycle}$ and the $COP_{system}$ are calculated using the following equations.

Thermodynamic cycle COP for heating,

$$COP_{h\_cycle} = \frac{h_{R,COND\_in} - h_{R,COND\_out}}{h_{COMP\_out} - h_{COMP\_in}} \tag{15.8}$$

Thermodynamic cycle COP for refrigeration,

$$COP_{r\_cycle} = \frac{h_{R,EVA\_out} - h_{R/EVA\_in}}{h_{COMPR,out} - h_{COMPR,in}} \tag{15.9}$$

System COP for heating,

$$COP_{h\_system} = COP_{h\_cycle} \times (\eta_{inv} \cdot \eta_{COMPR}) \tag{15.10}$$

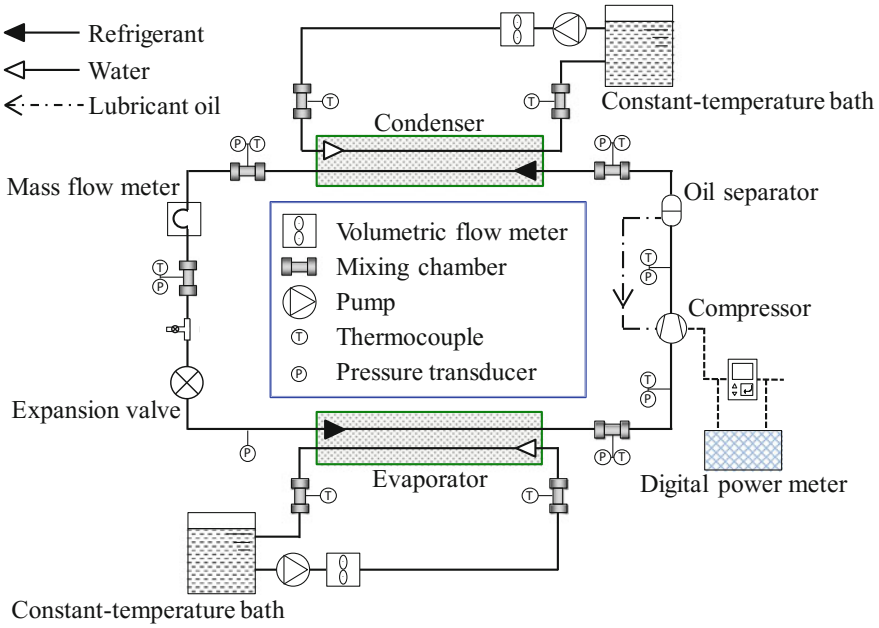


**Fig. 15.6** Experimental set up to test new refrigerant (Koyama et al. 2010a)

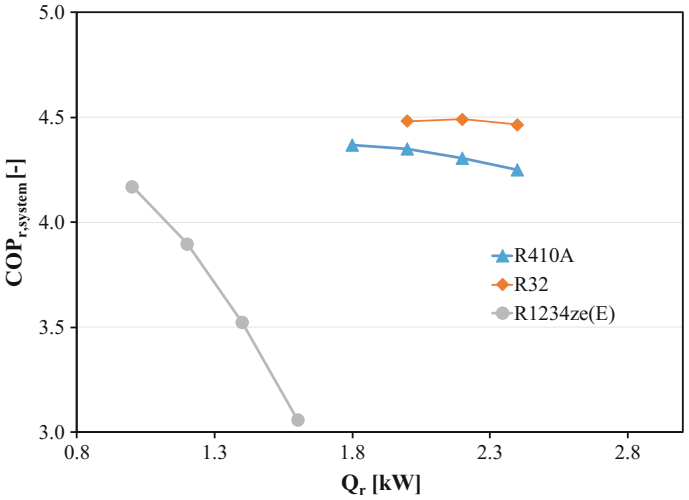


**Fig. 15.7** Variation of coefficient of performance with cooling load

System COP for refrigeration or cooling,

$$\mathrm{COP}_{\mathrm{r\_system}} = \mathrm{COP}_{\mathrm{r\_cycle}} \times (\eta_{\mathrm{inv}} \cdot \eta_{\mathrm{COMPR}}) \tag{15.11}$$

#### 15.3.1.3 R152a

HFC-152a (1,1 difluoroethane, C2H4F2) has been used for many years as a component in refrigerant blends but not as a single compound. The critical temperature and pressure of the refrigerant are 113 °C and 4.52 MPa, respectively (Higashi et al. 1987; Tamatsu et al. 1993; Van Poolen et al. 1997). It has zero ODP. The special advantage of this refrigerant is the low global warming potential (=138, Stocker et al. 2013) and reduced price compared to other HFC and HFO refrigerants. Compared to R134a, R152a possesses very similar volumetric cooling capacity and pressure levels, while the energy efficiency, the mass flow, and the vapor density are even more favorable (SAE-CRP 1234 2009). Bolaji (2010) and Cabello et al. (2015) reported superior system performance of R152a in a vapor compression system while comparing to the experimental result with R134a. Their test results revealed an improvement in COP ranges from 4.7 to 13% with a decrease in cooling capacity of about 0–10%. This refrigerant has been used for a long time as an aerosol spray propellant and foam blowing agent, as well as a component in some refrigerant blends (R401A, R415A, R430A, R500, etc.). However, its flammability is ranked as A2 by ASHRAE (Wilson et al. 2010), and hence flammable hazards could be the major reason in hindering its usage as a pure refrigerant until now.

#### 15.3.1.4 R744

R744 (Carbon dioxide, $CO_2$) is a natural refrigerant used in vapor compressor systems of many types for over 130 years (Pearson 2005; Austin and Sumathy 2011; Bolaji and Huan 2013). The cost of this refrigerant is low and it is not necessary for recovery or disposal but it requires extremely high pressure as it operates at transcritical refrigeration cycle. There is a renewed interest in R744 as it is free of toxicity and flammability (Austin and Sumathy 2011; Maina and Huan 2015). Gustav Lorentzen was the pioneer of the revival of R744 in the early 1990s. Lorentzen and Pettersen (1994) developed a laboratory prototype of car air-conditioning system to evaluate the cycle performance of R744 and R12. Authors suggested that the higher energy density of high-pressure refrigerants may give considerable advantages in terms of cost and practicality due to the reduced dimension and weight. Xue et al. (2010) developed a steady state model of the R744 transcritical cycle for air-conditioning to estimate the heating and cooling performance. The performance of R744 both theoretically and experimentally as well as the comparison with other refrigerants has been conducted by many authors

as a viable alternative of synthetic fluids (Brown et al. 2002; Jing-yang et al. 2003; Girotto et al. 2004; He et al. 2016; Pitarch et al. 2016; Chen et al. 2017). Hwang et al. (2004) measured the performance of different two-stage compressor R744 cycles and found 18–35% improved COP over the basic cycles at 7.2 °C evaporating temperature. Girotto et al. (2004) found a possibility to improve the efficiency of the $CO_2$ system approaching the efficiency of the R404A system though the installation cost is 20% higher. Maina and Huan (2015), and Nekså (2002) reviewed numerous area of applications for R744 including hot water production, commercial refrigeration, and heat pump dryers.

#### 15.3.1.5 HC

HC (hydrocarbon) is a natural refrigerant which offers in general, high efficiency, good miscibility with mineral oils, lower compressor discharge pressure and good heat transfer criteria, but its highly flammable behavior limits the usage of this refrigerant in a larger scale. The use of HCs as refrigerant is confined to Europe because many other countries elsewhere banned the use of flammable gas in the presence of public. Lampugnani and Zgliczynski (1996) studied the performances of R290 in comparison with R22 theoretically and experimentally. The experimental result showed that R290 is an excellent candidate to replace R22 from the thermodynamic point of view. Granryd (2001) reviewed the possibilities and problems of using hydrocarbons as the refrigerant for refrigeration and heat pump applications. It is found a number of HC have favorable characteristics as refrigerants from the thermodynamic and heat transfer point of view. Halimic et al. (2003) concluded in their study that R290 is an attractive alternative to R12 in small domestic refrigerators after correcting technical operation and safety factors. Bjerre and Larsen (2006) evaluated the potential of R600 for household applications and found 10% better performance than R134a. Palm (2008) reviewed the excellent performance of HC comparing R134a, R22, and ammonia. The author suggested that the safety risk can be reduced by designing the systems as hermetic type with the minimum number of connections and a minimum charge of refrigerant or it can be used as an indirect system. Corberán et al. (2008) reviewed the standard of using HC in vapor compression system. It is stated that the IEC355.2.20 standard allows up to approximately 150 g of HC sealed in the typical refrigerator and small freezers are permitted to be located anywhere regardless of the room size incorporating a few special safety measures. This standard has opened the way for some European refrigerator manufacturers to produce household refrigerator with flammable HCs.

#### 15.3.1.6 R32

R32 is a difluoromethane having GWP of 677. The critical temperature and pressure of this refrigerant is 78.2 °C and 5.8 MPa, respectively. Though the safety

class of this refrigerant is 2L, it is higher hazardous than R1234yf due to its faster flame propagation. The volumetric capacity (VC) of R32 is higher than R410A (see Table 15.4) which shows the potentiality of higher COP than R410A. The larger VC reduces the charging amount even to achieve similar COP of that of R410A. The direct equivalent greenhouse gas emission of R32 is also lower due to low charging. But the higher compressor discharge temperature of R32 adversely affects its vast application (Mota-Babiloni et al. 2017; Bolaji 2010; Leck 2010).

### *15.3.2 Refrigerant Blend*

Pure refrigerants for vapor compression systems can be considered convenient due to azeotropic nature and mostly well-developed thermophysical properties. For pure refrigerants, HFOs are good choices in terms of toxicity, flammability, and ultra-low GWP. Bella and Kaemmer (2011) reported that pure HFOs are not efficient alternatives for R410A from the viewpoint of system performance because redesigning the system is required with larger compressor, piping, and heat exchangers. Mixing HFOs with some other refrigerants is one approach to solve the aforementioned problems. Generally, the addition of two or more single component refrigerants is termed as blend, which can be of two types: azeotropic and zeotropic. Azeotropic blends behave like a single component refrigerant, in that they boil and condense at respective constant temperature at any given pressure. Whereas zeotropic blends boil and condense through a range of temperatures at a given pressure. Such temperature range is called "temperature glide" which it is basically the difference between the bubble point and the dew point of the refrigerant compound.

#### 15.3.2.1 Binary Mixtures

The addition of two single component refrigerants is termed as binary mixtures. Figure 15.8 shows the temperate glides of R32/R1234ze(E) binary mixtures at a constant pressure. It can be seen that the temperature glide depends on the mixture component. About 20–30% of R32 in the mixture provides maximum temperature glide.

R32/R1234ze(E)

Figure 15.7 shows that the COP of R1234ze(E) is lower than that of commonly used refrigerant, i.e., R410A and R32, mainly due to the low volumetric capacity and higher pressure drop (Mota-Babiloni et al. 2016). To increase vapor density as well as the performance of R1234ze(E), R32 is normally mixed using various ratios (Koyama et al. 2010a; Wang and Amrane 2014). The various refrigerants mixture and their respective GWP values, typically less than 300. In the cycle performance

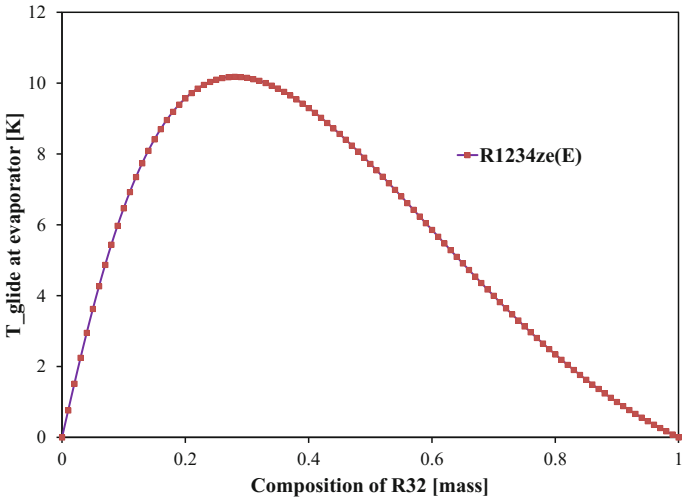


**Fig. 15.8** Temperature glide of a binary mixtures R32/R1234ze(E)

analysis, Koyama et al. (2010b) showed that the addition of R32 (50% mass) with R1234ze(E) improved the volumetric capacity keeping COP higher than that of R410A which suggested this mixture is a strong candidate to replace R410A.

R32/R1234yf

The refrigerant R1234yf can be considered as a promising next-generation refrigerant with its ultra-low GWP and comparable performances with R134a. Hitherto, some shortcomings of R1234yf, especially the volumetric capacity, which is considerably lower than that of R134a. On the other hand, pure R32 is a good choice for residential air-condition but it shows very high temperature at the compressor outlet and considerably higher GWP. So mixing of these two refrigerants offers solutions to overcome their individual shortcomings. In a drop-in experiment, Kojima et al. (2016) studied the performance of this mixture considering the GWP values 300 and 200. The experimental results show the performance of R32/R1234yf binary mixture of 42/58 (by mass) is considerably higher than that of R410A. An irreversible loss by parts and total irreversible loss for different mixtures are also compared where results show that the irreversible loss for R32/R1234yf (42/58) mixture is lower than R32/R1234ze(E) (28/72). Figure 15.9 shows that after mixing with R32, the cycle operation area for binary mixture match with R410A. It seems these mixtures can replace R410A.

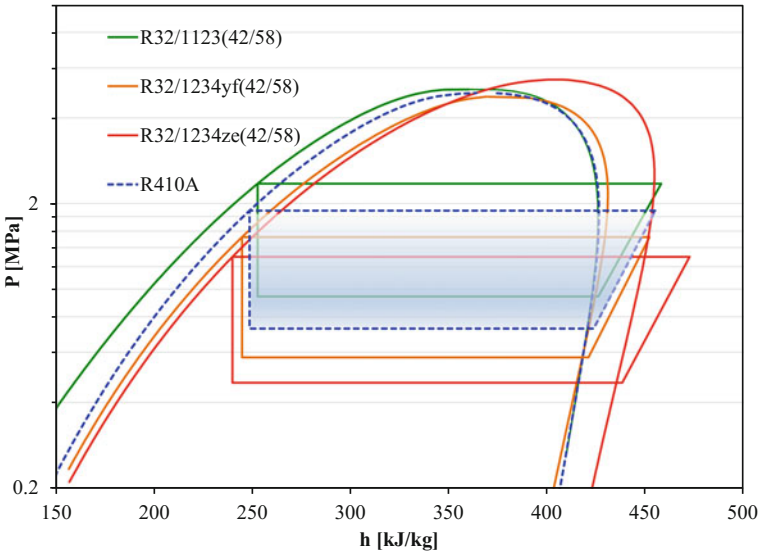


**Fig. 15.9** P-h diagram with thermodynamic cycle for binary mixtures

R32/R1123

In 2014, AGC (Asahi Glass Co., Ltd.) developed a new refrigerant for air-conditioning systems that can reduce GWP further, which adopts hydro-fluoroolefin R1123 as a main component. R1123 (trifluoroethylene) is strongly attractive because of its performance, which is equivalent to that of conventional refrigerants, along with extremely low GWP (=0.3) (Tanaka et al. 2014). Considering the safety and stability, the mixture of R1123 and R32 is considered as an alternative to R410A. According to Asahi Glass Co. Ltd., the new refrigerant mixture is azeotropic and can achieve good performance when replacing R410A for domestic and commercial air-conditioning system (Fukushima and Hashimoto 2015).

HC Mixtures

HC mixtures are environment-friendly natural refrigerants and can be used in the existing systems. Due to high flammable (A3) properties, HC mixtures are preferred to use in a small system where the charged amount is very small compared to halogenated refrigerants. Many researchers studied R290/R600a mixture as a substitute for R12 and found higher COP and refrigeration capacity of the hydro-carbon mixture than R12 (Richardson and Butterworth 1995; Dalkilic and Wongwises 2010; Mani and Selladurai 2008; Jung et al. 2000). Kim et al. (2007, 2008) experimentally studied the mixture of R744/R290 with three different

compositions and found the ratio of 3:1 (by mass) enhanced the COP or 12.8% than that of R744 when the temperature glide matches with the change in fluid temperature. Tian et al. (2015) studied the performance of R32/R290 mixtures (68/32) as a drop-in replacement for R410A and found the COP of the mixture is 6–7% lower than that of R410A, whereas the charge amount is reduced by 30–35%. Mohanraj et al. (2011) reviewed the development of HC mixtures and identified that these mixtures can be suitable alternatives to phase-out halogenated based refrigerants in vapor compression systems.

#### 15.3.2.2 Ternary Mixtures

R744/R32/R1234ze(E)

The binary mixture of R32/R1234yf and R32/R1234ze(E) show better performance than R410A when the mass fraction of R32 is above 50% in the mixtures. The mass fraction of R32 is below 50% in the binary mixture gives the GWP value less than 300; however, the COP drastically decreases as a consequence of the insufficient volumetric capacity. Fukuda et al. (2014, 2016), added R744 into the binary mixture to increase the volumetric capacity. In a drop-in experiment, authors studied the performance of R744/R32/R1234ze(E) mixtures having GWP 300 and GWP 200 and found the COP of GWP 300 mixture is comparable to that of R410A in both heating and cooling modes.

R744/R32/R1234yf

Fukuda et al. (2016) experimentally studied two ternary mixtures by adding R744 into R32/R1234yf mixture to increase the volumetric capacity and then compared the cycle performance with R410A. It is also found that the addition of R744 decreases the GWP but increases the temperature glide. But when the temperature glide of mixtures matches with the temperature changes in the heat sink and heat source during condensation and evaporation, they found that the irreversible loss is minimum. The ternary mixture of GWP nearly 300 show very good performance in both heating and cooling modes which means the ternary mixture of 4/44/52 (by mass) can be used as a drop-in alternative of R410A (Fukuda et al. 2016). Figure 15.10 shows the COPs of the ternary mixtures at optimum charge condition which are comparable with R410A.

Other Ternary Mixture

Maczek et al. (1997) studied R744/R32/R134a (7/31/62) mixture theoretically and experimentally to compare the performance with R22. Authors found the mixture is promising as a drop-in replacement of R22 with 10% better COP suggested using in

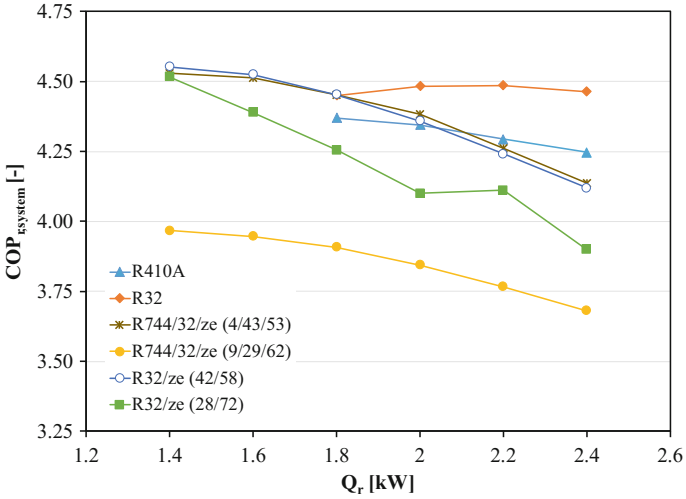


**Fig. 15.10** COP value with cooling load for binary and ternary mixtures

low-temperature heat pump because of its excessive condensing pressure. Hakkaki-fard et al. (2014) theoretically compared the performance of R744/R32/Propane (10/80/10, GWP ∼ 540) mixture with R410A and found the heating capacity of the mixture is higher than that of R410A.

## 15.4 Environmental Sustainability

The conventional vapor compression air-conditioning and refrigeration technology are responsible for both direct and indirect greenhouse gas emission. The warming potential of heat transfer fluid and the input electrical energy to run the system are accountable for environmental sustainability. Here, the emission is calculated considering system lifetime 10 years. Other related data are taken from the "Kyushu Electric Power Environmental Action Report 2013".

### *15.4.1 Direct Emission*

The direct emission is a function of GWP, the charge amount, and the emission due to leakages from the air-conditioning system and those associated with the servicing and equipment disposal. Leakage can be reduced by using a small and tight system with sealed compressor but the servicing and equipment disposal cannot be stopped. Figure 15.11 shows the comparison of GWP for newly proposed binary and

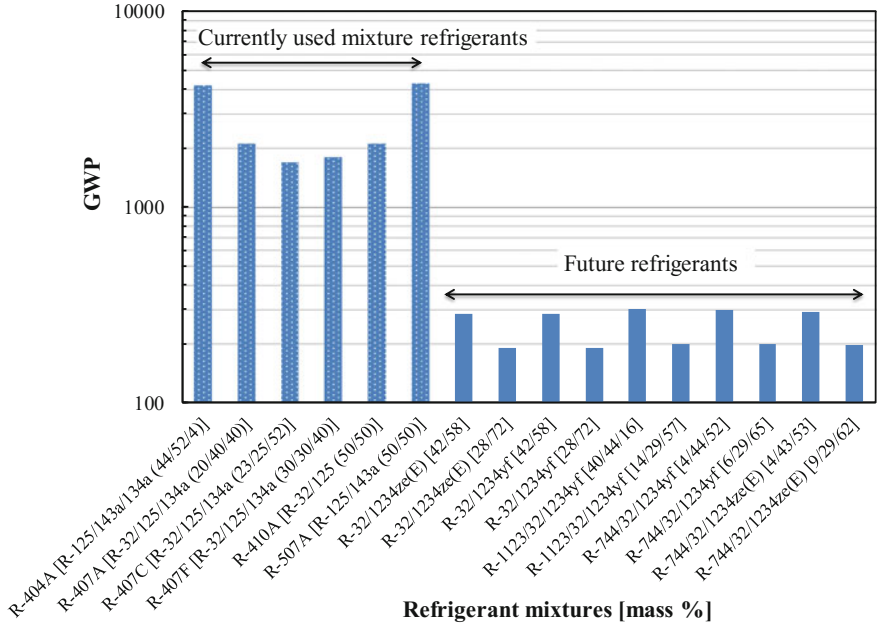


**Fig. 15.11** GWP of some binary and ternary mixtures

ternary mixtures with currently used blend refrigerants. Figure 15.12 shows the direct equivalent $CO_2$ emission for pure refrigerant considering different application area. Figure 15.13 shows the comparison of direction emission among the widely used R410A with newly proposed binary and ternary mixtures when applied in domestic air condition system. It can be seen from these two figures that direct emission significantly reduced when blend refrigerants are considered as an alternative.

$$\text{Direct Emission} = \text{Emission due to leakage} + \text{Emission due to disposal}$$

## *15.4.2 Indirect Emission*

The conventional air-conditioning and refrigeration devices are run by the electricity. The indirect emission is related to the operational activities of the system such as the emission during the production of electricity in a power plant, i.e., kg $CO_2$-equivalent emission generated during production of electrical energy which is consumed by the air-conditioning system. Usually, the higher performance of the

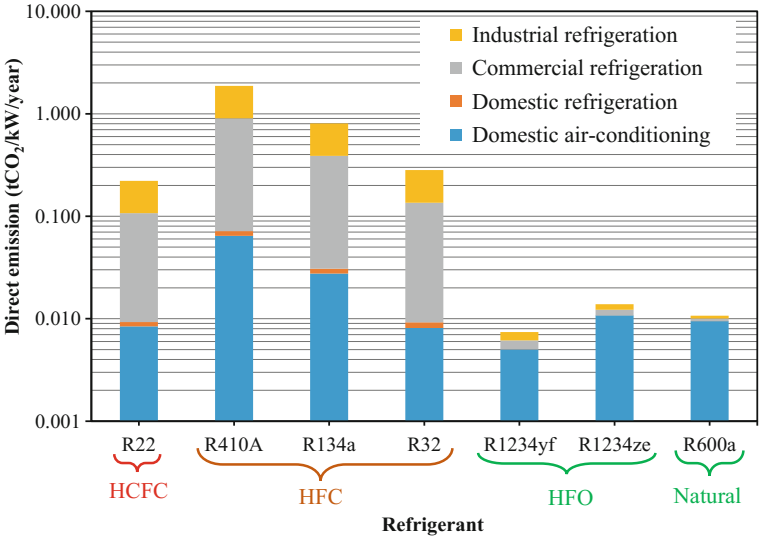


**Fig. 15.12** Direct $CO_2$ equivalent emission for some popular pure refrigerant (Pal et al. 2018)

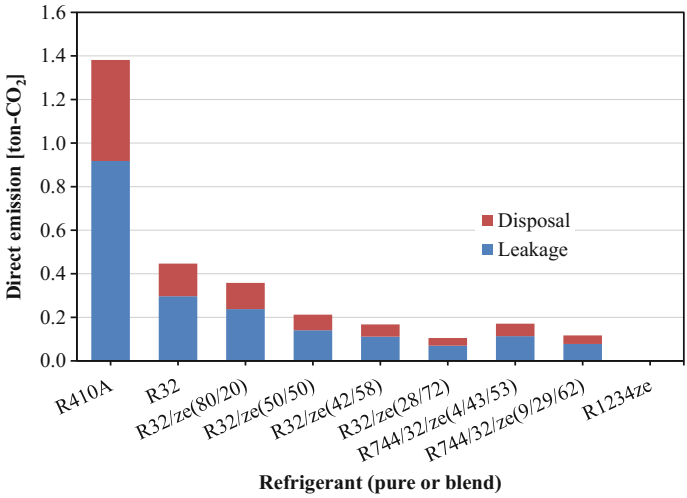


**Fig. 15.13** Direct $CO_2$ equivalent emission for pure and mixture refrigerants

system means lower electricity consumption. The proposed refrigerant blend is attractive not only due to its very low GWP but also its excellent system performance. Figure 15.14 shows the indirect emission considering the annual use for heating is 1183 h and for cooling 1008 h.

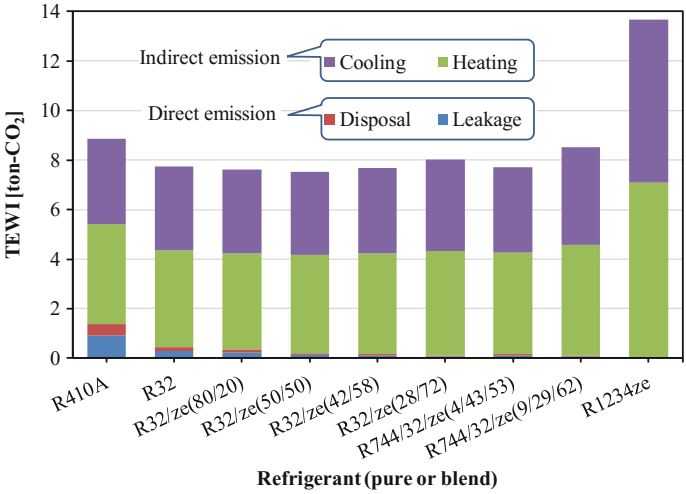


**Fig. 15.14** TEWI for few blend refrigerants in comparison with R410A

$$\text{Indirect Emission} \;=\; \text{System run in cooling mode} + \text{System run in heating mode}$$

The environmental impacts of the air-conditioning and refrigeration system for its lifetime can be calculated by LCCP (Life Cycle Climate performance) or TEWI (Total Equivalent Warming Impact) (Mohanraj et al. 2011; Islam et al. 2017). LCCP accounts the energy embodied in product materials, greenhouse gas emissions during chemical manufacturing, and end of life disposal of the unit which is ignored for the case of TEWI. The small sources of emissions generated over the course of the lifetime of the unit are explicitly accounted for in LCCP. This study compared the TEWI value of blend with widely used R410A to avoid the emission related to the manufacturing of the component of the system.

$$\text{TEWI} = \text{Direct emission} + \text{Indirect emission} \tag{15.12}$$

$$\text{DE} = \text{GWP} \times M \times \left[1 - (1 - \text{a}/100)^{Y}\right] + \text{GWP} \times M \times (1 - \text{a}/100)^{Y} \times (1 - \text{b}/100) \tag{15.13}$$

$$\text{IDE} = c \times Y \times (\text{HC} \times t_{\text{h}}/\text{COP}_{\text{h}} + \text{CC} \times t_{\text{c}}/\text{COP}_{\text{r}}) \tag{15.14}$$

where

$a$ Annual refrigerant leak rate [%/year]
$b$ Refrigerant recovery rate (based on residual refrigerant at disposal) [%]
$c$ Carbon dioxide emission coefficient [kg-$CO_2$/kWh]
CC Rated cooling capacity [kW]
HC Rated heating capacity [kW]

LE Refrigerant leakage during disposal [kg-$CO_2$]
LL Lifetime refrigerant leakage [kg-$CO_2$]
$M$ Refrigerant charge amount [kg]
$t_c$ System use in cooling mode [h/year]
$t_h$ System use in heating mode [h/year]
$Y$ System lifetime [year]

### 15.4.3 Energy Efficiency

Energy efficiency for a refrigeration system is related to the selection of refrigerant, system configuration, and component efficiencies. For a specific refrigerant, there is need of suitable configuration of evaporator, condenser, and compressor to achieve maximum performance. There is different approach to assess the energy efficiency for a specific refrigerant, which are theoretical or semi-theoretical cycle simulations, detailed equipment simulation models and laboratory test of the system. The operating condition, system capacity, and system hardware also influence the energy efficiency. In practice, the cost of the system is another important parameter as the success in the market depends on a cost-performance trade-off.

### 15.4.4 Nonconventional System

There is another approach to building a sustainable environment by changing the design of the vapor compression system. The adsorption cooling/heating system is one of them. This system is able to use natural refrigerants and is driven by renewable or waste energy. Water, ethanol, ammonia, and methanol known as natural refrigerants, are getting attention in domestic and automobile heat pump applications (Saha et al. 1995; El-Sharkawy et al. 2014; Tamainot-Telto et al. 2009; Wang et al. n.d.). These refrigerants have no GWP and toxicity. As the system is driven by waste energy so it is free from direct and indirect greenhouse gas emission. Water (R-718) and ethanol are not familiar refrigerant in vapor compression systems due to poor volumetric efficiency, but they can be considered as popular refrigerants in sorption-based systems (Wang et al. 2014; Uddin et al. 2014). Adsorption cooling systems can be operational utilizing low-temperature heat sources such as solar energy and low-grade process waste heat, e.g., engine exhaust, industrial waste heat (Khan et al. 2006; Kai and Edward 2011). When the system is applied in automobiles, the exhausted heat can be utilized without compromising any mechanical energy output from the engine. Hybrid vapor compression–adsorption system is also feasible when low-grade heat is available (Banker et al. 2008; Uddin et al. 2013). Figure 15.15 shows the conventional mechanical system and nonconventional adsorption heat pump system. The thermal

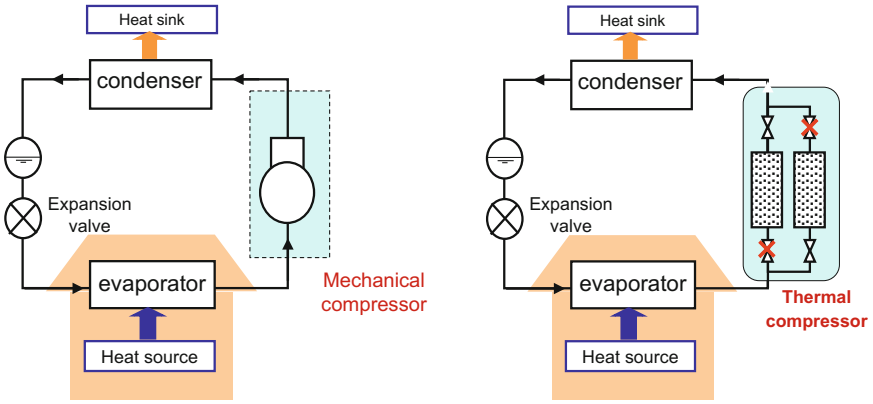


**Fig. 15.15** Conventional mechanical compression system and nonconventional adsorption system

compressor in nonconventional system works based on adsorption and desorption phenomenon.

## 15.5 Summary

To summarize, the most important factors determining the environmental sustainability are the low GWP refrigerant with higher volumetric capacities. Figure 15.16 shows the progression of refrigerants from the beginning of commercial production to current condition. The fourth generation refrigerant should be zero ODP, ultra-low GWP, should have a shorter lifetime in atmosphere, and high efficiency. The HFOs and their mixture can be a good solution to reduce the direct and indirect greenhouse gas emission. The study presented here will help the reader to find a suitable composition of the mixture that is desirable for a specific application.

The adsorption cooling system using natural refrigerant is also a promising alternative to traditional vapor compression system, in terms of primary energy source diversification and reducing the overall environmental effect. Vapor compression and adsorption hybrid system can also be a promising alternative of current mechanical vapor compressor system using conventional refrigerants.

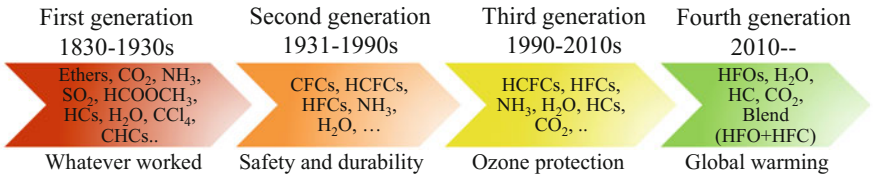


**Fig. 15.16** Refrigerant progression toward sustainable environment

## References


Akasaka R, Tanaka K, Higashi Y (2010) Thermodynamic property modeling for 2,3,3,3-tetrafluoropropene (HFO-1234yf). Int J Refrig 33:52–60. https://doi.org/10.1016/j.ijrefrig.2009.09.004

Austin BT, Sumathy K (2011) Transcritical carbon dioxide heat pump systems: a review. Renew Sustain Energy Rev 15:4013–4029. https://doi.org/10.1016/j.rser.2011.07.021

Banker ND, Dutta P, Prasad M, Srinivasan K (2008) Performance studies on mechanical + adsorption hybrid compression refrigeration cycles with HFC 134a. Int J Refrig 31:1398–1406. https://doi.org/10.1016/j.ijrefrig.2008.03.009

Barve A, Cremaschi L (2012) Drop-in performance of low GWP refrigerants in a heat pump system for residential applications. Int Refrig Air Cond Conf 1–9. Purdue

Bella B, Kaemmer N (2011) An assessment of low GWP refrigerants in different applications. 23rd IIR Congr Refrig 8. Prague, Czech Republic

Benhadid-Dib S, Benzaoui A (2012) Refrigerants and their environmental impact Substitution of hydro chlorofluorocarbon HCFC and HFC hydro fluorocarbon. Search for an adequate refrigerant. Energy Procedia 18:1611–1623. https://doi.org/10.1016/j.egypro.2012.05.096

Bjerre P, Larsen P (2006) Evaluation of N-butane as a potential refrigerant for household compressors. Int Compress Eng Conf 1–6. Purdue

Bolaji BO (2010) Experimental study of R152a and R32 to replace R134a in a domestic refrigerator. Energy 35:3793–3798. https://doi.org/10.1016/j.energy.2010.05.031

Bolaji BO, Huan Z (2013) Ozone depletion and global warming: case for the use of natural refrigerant—a review. Renew Sustain Energy Rev 18:49–54. https://doi.org/10.1016/j.rser.2012.10.008

Brown JS, Yana-motta SF, Domanski PA (2002) Comparative analysis of an automotive air conditioning systems operating with $CO_2$ and R134a. Int J Refrig 25:19–32. https://doi.org/10.1016/s0140-7007(01)00011-1

Brown JS, Zilio C, Cavallini A (2009) The fluorinated olefin R-1234ze(Z) as a high-temperature heat pumping refrigerant. Int J Refrig 32:1412–1422. https://doi.org/10.1016/j.ijrefrig.2009.03.002

Brown JS, Zilio C, Cavallini A (2010) Thermodynamic properties of eight fluorinated olefins. Int J Refrig 33:235–241. https://doi.org/10.1016/j.ijrefrig.2009.04.005

Cabello R, Sánchez D, Llopis R, Arauzo I, Torrella E (2015) Experimental comparison between R152a and R134a working in a refrigeration facility equipped with a hermetic compressor. Int J Refrig 60:92–105. https://doi.org/10.1016/j.ijrefrig.2015.06.021

Calm JM, Didion DA (1998) Trade-offs in refrigerant selections: past, present, and future. Int J Refrig 21:308–321. https://doi.org/10.1016/S0140-7007(97)00089-3

Chen J, Yu J (2008) Performance of a new refrigeration cycle using refrigerant mixture R32/R134a for residential air-conditioner applications. Energy Build 40:2022–2027. https://doi.org/10.1016/j.enbuild.2008.05.003

Chen G, Volovyk O, Zhu D, Ierin V, Shestopalov K (2017) Theoretical analysis and optimization of a hybrid $CO_2$ transcritical mechanical compression—ejector cooling cycle. Int J Refrig 74:86–94. https://doi.org/10.1016/j.ijrefrig.2016.10.002

Corberán JM, Segurado J, Colbourne D, Gonzálvez J (2008) Review of standards for the use of hydrocarbon refrigerants in A/C, heat pump and refrigeration equipment. Int J Refrig 31:748–756. https://doi.org/10.1016/j.ijrefrig.2007.12.007

Dalkilic AS, Wongwises S (2010) A performance comparison of vapour-compression refrigeration system using various alternative refrigerants. Int Commun Heat Mass Transf 37:1340–1349. https://doi.org/10.1016/j.icheatmasstransfer.2010.07.006

Devotta S, Waghmare AV, Sawant NN, Domkundwar BM (2001) Alternatives to HCFC-22 for air conditioners. Appl Therm Eng 21:703–715

El-Sharkawy III, Uddin K, Miyazaki T, Saha BB, Koyama S, Miyawaki J et al (2014) Adsorption of ethanol onto parent and surface treated activated carbon powders. Int J Heat Mass Transf 73:445–455. https://doi.org/10.1016/j.ijheatmasstransfer.2014.02.046

EPA (1990) 40 CFR Part 82—protection of stratospheric ozone: change of listing status for certain substitutes under the significant new alternative policy program. Final Rule. Fed Regist 80:1–91

European Environment Agency (2016) Company reporting for Regulation (EU) No 517/ 2014 on fluorinated greenhouse gases

Fukuda S, Kondou C, Takata N, Koyama S (2014a) Low GWP refrigerants R1234ze(E) and R1234ze(Z) for high temperature heat pumps. Int J Refrig 40:161–173. https://doi.org/10.1016/j.ijrefrig.2013.10.014

Fukuda S, Kondou C, Takata N, Koyama S (2014b) Cycle performance of low GWP refrigerant mixtures R-32/1234ze(E) and R-744/1234ze(E). Asian Conf Refrig Air Cond. Jeju, Korea

Fukuda S, Kojima H, Kondou C, Takata N, Koyama S (2016) Comparative assessment on irreversible losses in heat pumps using R744/R32/R1234yf and R744/R32/R1234ze(E). Sci Technol Built Environ 22:1118–1127. https://doi.org/10.1080/23744731.2016.1206452

Fukushima M, Hashimoto M (2015) Next generation low-GWP refrigerants "AMOLEA-TM". Res Reports. Asahi Glas Co. Ltd

Girotto S, Minetto S, Neksa P (2004) Commercial refrigeration system using $CO_2$ as the refrigerant. Int J Refrig 27:717–723. https://doi.org/10.1016/j.ijrefrig.2004.07.004

Granryd E (2001) Hydrocarbons as refrigerants—an overview. Int J Refrig 24:15–24. https://doi.org/10.1016/S0140-7007(00)00065-7

Hakkaki-fard ALI, Aidoun Z, Ouzzane M (2014) Air-source heat pumps with refrigerant mixtures for cold climates. 11th IEA Heat Pump Conf 1–11. Monteal, Canada

Halimic E, Ross D, Agnew B, Anderson A, Potts I (2003) A comparison of the operating performance of alternative refrigerants. Appl Therm Eng 23:1441–1451. https://doi.org/10.1016/S1359-4311(03)00081-4

Han XH, Wang Q, Zhu ZW, Chen GM (2007) Cycle performance study on R32/R125/R161 as an alternative refrigerant to R407C. Appl Therm Eng 27:2559–2565. https://doi.org/10.1016/j.applthermaleng.2007.01.034

He Y, Deng J, Zheng L, Zhang Z (2016) Performance optimization of a transcritical $CO_2$ refrigeration system using a controlled ejector. Int J Refrig 75:250–261. https://doi.org/10.1016/j.ijrefrig.2016.12.015

Higashi Y, Akasaka R (2016) Measurements of thermodynamic properties for R1123 and R1123 + R32 Mixture. Int Refrig Air Cond Conf Purdue 1–10. Purdue, Indiana

Higashi Y, Ashizawa M, Kabata Y, Majima T, Uematsu M, Watanabe K (1987) Measurements of vapor pressure, vapor-liquid coexistence curve and critical parameters of refrigerant 152a. Trans Japan Soc Mech Eng Ser B 53:1379–1385. https://doi.org/10.1299/kikaib.53.1379

Higashi Y, Tanaka K, Ichikawa T (2010) Critical parameters and saturated densities in the critical region for trans-1,3,3,3-Tetrafluoropropene (HFO-1234ze(E)). J Chem Eng Data 55:1594–1597

Honeywell Technical Bulletin (2012) Honeywell SolsticeTM yf refrigerants

Hwang YH, Celik A, Radermacher R (2004) Performance of $CO_2$ cycles with a two-stage compressor. Int Refrig Air Cond Conf 1–8. Purdue

Islam MA, Srinivasan K, Thu K, Saha BB (2017) Assessment of total equivalent warming impact (TEWI) of supermarket refrigeration systems. Int J Hydrogen Energy 1–11. https://doi.org/10.1016/j.ijhydene.2017.07.035

Jing-yang M, Jiang-ping C, Zhi-jiu C (2003) System design and analysis of trans-critical carbon-dioxide automotive air-conditioning system. J Zhejiang Univ Sci 4:305–308

Joudi KA, Al-Amir QR (2014) Experimental Assessment of residential split type air-conditioning systems using alternative refrigerants to R-22 at high ambient temperatures High ambient performance parameters refrigerants R290 R407C and R410A in residential split A/C systems. Energy Convers Manag 86:496–506. https://doi.org/10.1016/j.enconman.2014.05.036

JRAIA 2017 (2017) World air conditioner demand by region

Jung D, Kim CB, Song K, Park B (2000) Testing of propane/isobutane mixture in domestic refrigerators. Int J Refrig 23:517–527. https://doi.org/10.1016/S0140-7007(99)00084-5

Kabeel AE, Khalil A, Bassuoni MM, Raslan MS (2016) Comparative experimental study of low GWP alternative for R134a in a walk-in cold room. Int J Refrig 69:303–312. https://doi.org/10.1016/j.ijrefrig.2016.06.017

Kai W, Edward AV (2011) New opportunities for solar: adsorption refrigeration. ASHRAE J 14–24

Khan MZI, Alam KCA, Saha BB, Hamamoto Y, Akisawa A, Kashiwagi T (2006) Parametric study of a two-stage adsorption chiller using re-heat—the effect of overall thermal conductance and adsorbent mass on system performance. Int J Therm Sci 45:511–519. https://doi.org/10.1016/j.ijthermalsci.2005.08.003

Kim JH, Cho JM, Lee IH, Lee JS, Kim MS (2007) Circulation concentration of $CO_2$/propane mixtures and the effect of their charge on the cooling performance in an air-conditioning system. Int J Refrig 30:43–49. https://doi.org/10.1016/j.ijrefrig.2006.06.008

Kim JH, Cho JM, Kim MS (2008) Cooling performance of several $CO_2$/propane mixtures and glide matching with secondary heat transfer fluid. Int J Refrig 31:800–806. https://doi.org/10.1016/j.ijrefrig.2007.11.009

Kojima H, Fukuda S, Kondou C, Takata N, Koyama S (2015) Comparative assessment of heat pump cycle operated with R32/R1234ze(E) and R32/R1234yf mixtures. Int Congr Refrig 1–8. Yokohama

Kojima H, Arakaki S, Fukuda S, Takata N, Kondou C, Koyama S (2016) comparative study on heat pump cycle using R32/R1234yf and R744/R32/R1234yf. 8th Asian Conf Refrig Air Cond 8–11. Taiwan

Koyama S, Takata N, Fukuda S (2010a) Drop-in experiments on heat pump cycle using HFO-1234ze(E) and its mixtures with HFC-32. Int Refrig Air Cond Conf 1–7. Purdue

Koyama S, Takata N, Matsuo Y, Yoshitake D, Fukuda S (2010b) Possibility to introduce HFO-1234ze(E) and its mixture with HFC-32 as low-GWP alternatives for heat pump/refrigeration systems. Int Symp Next-generation Air Cond Refrig Technol 1–10. Tokyo

Koyama S, Takata N, Fukuda S (2011) An experimental study on heat pump cycle using zeotropic binary refrigerant of HFO-1234ze(E) and HFC-32. 10th IEA Heat Pump Conf 1–10

Lai NA (2014) Equations of state for HFO-1234ze(E) and their application in the study on refrigeration cycle. Int J Refrig 43:194–202. https://doi.org/10.1016/j.ijrefrig.2013.11.011

Lai NA, Vrabec J, Raabe G, Fischer J, Wendland M (2011) Description of HFO-1234yf with BACKONE equation of state. Fluid Phase Equilib 305:204–211. https://doi.org/10.1016/j.fluid.2011.04.005

Lampugnani G, Zgliczynski M (1996) R290 as a substitute of R502 and R22 in commercial refrigeration and air conditioning. Int Compress Eng Conf 83–88. Purdue

Leck TJ (2010) New high performance, low GWP refrigerants for stationary AC and refrigeration. Int Refrig Air Cond Conf 8

Lee Y, Jung D (2012) A brief performance comparison of R1234yf and R134a in a bench tester for automobile applications. Appl Therm Eng 35:240–242. https://doi.org/10.1016/j.applthermaleng.2011.09.004

Lemmon EW, Huber ML, Mclinden MO (2013) NIST Reference fluid thermodynamic and transport properties—REFPROP (Version 9.1)

Lorentzen G (1994) Revival of carbon dioxide as a refrigerant. Int J Refrig 17:292–301. https://doi.org/10.1016/0140-7007(94)90059-0

Maczek K, Muller J, Wojtas K, Domanski PA (1997) Ternary zeotropic mixture with $CO_2$ component for R-22 heat pump application. CLIMA 2000, Brussels

Maina P, Huan Z (2015) A review of carbon dioxide as a refrigerant in refrigeration technology. S Afr J Sci 111:1–10. https://doi.org/10.17159/sajs.2015/20140258

Mani K, Selladurai V (2008) Experimental analysis of a new refrigerant mixture as drop-in replacement for CFC12 and HFC134a. Int J Therm Sci 47:1490–1495. https://doi.org/10.1016/j.ijthermalsci.2007.11.008

McMullan JT (2002) Refrigeration and the environment—issues and strategies for the future. Int J Refrig 25:89–99. https://doi.org/10.1016/S0140-7007(01)00007-X

Meno A (2015) Laws and regulation for fluorocarbons in Japan. Ministry of Economy, Trade and Industry, Japan

Minjares R (2011) Refrigerants for light-duty passenger vehicle air conditioning systems Technical assessment of alternatives to HFC-134a. Int Counc Clean Transp

Minor BH, Herrmann D, Gravell R (2010) Flammability characteristics of HFO-1234yf. Process Saf Prog 29:150–154. https://doi.org/10.1002/prs.10347

Mohanraj M, Muraleedharan C, Jayaraj S (2011) A review on recent developments in new refrigerant mixtures for vapour compression-based refrigeration, air-conditioning and heat pump units. Int J Energy Res 35:647–669. https://doi.org/10.1002/er.1736

Morrison G, McLinden MO (1993) Azeotropy in refrigerant mixtures. Int J Refrig 16:129–138. https://doi.org/10.1016/0140-7007(93)90069-K

Mota-Babiloni A, Navarro-Esbrí J, Barragán-Cervera Á, Molés F, Peris B (2015) Experimental study of an R1234ze(E)/R134a mixture (R450A) as R134a replacement. Int J Refrig 51:52–58. https://doi.org/10.1016/j.ijrefrig.2014.12.010

Mota-Babiloni A, Navarro-Esbrí J, Molés F, Cervera ÁB, Peris B, Verdú G (2016) A review of refrigerant R1234ze(E) recent investigations. Appl Therm Eng 95:211–222. https://doi.org/10.1016/j.applthermaleng.2015.09.055

Mota-Babiloni A, Navarro-Esbrí J, Makhnatch P, Molés F (2017) Refrigerant R32 as lower GWP working fluid in residential air conditioning systems in Europe and the USA. Renew Sustain Energy Rev 80:1031–1042. https://doi.org/10.1016/j.rser.2017.05.216

Navarro-Esbrí J, Mendoza-Miranda JM, Mota-Babiloni A, Barragán-Cervera A, Belman-Flores JM (2013) Experimental analysis of R1234yf as a drop-in replacement for R134a in a vapor compression system. Int J Refrig 36:870–880. https://doi.org/10.1016/j.ijrefrig.2012.12.014

Nekså P (2002) $CO_2$ heat pump systems. Int J Refrig 25:421–427. https://doi.org/10.1016/S0140-7007(01)00033-0

Pal A, Uddin K, Thu K, Saha BB (2018) Environmental assessment and characteristics of next generation refrigerants. Evergr Jt J Nov Carbon Resour Sci Green Asia Strateg 5:58–66

Palm B (2008) Hydrocarbons as refrigerants in small heat pump and refrigeration systems—a review. Int J Refrig 31:552–563. https://doi.org/10.1016/j.ijrefrig.2007.11.016

Park K-J, Seo T, Jung D (2007) Performance of alternative refrigerants for residential air-conditioning applications. Appl Energy 84:985–991. https://doi.org/10.1016/j.apenergy.2007.05.002

Park KJ, Shim YB, Jung D (2008) Performance of R433A for replacing HCFC22 used in residential air-conditioners and heat pumps. Appl Energy 85:896–900. https://doi.org/10.1016/j.apenergy.2007.11.003

Park KJ, Shim YB, Jung D (2009a) A "drop-in" refrigerant R431A for replacing HCFC22 in residential air-conditioners and heat pumps. Energy Convers Manag 50:1671–1675. https://doi.org/10.1016/j.enconman.2009.03.027

Park KJ, Shim YB, Jung D (2009b) Experimental performance of R432A to replace R22 in residential air-conditioners and heat pumps. Appl Therm Eng 29:597–600. https://doi.org/10.1016/j.applthermaleng.2008.02.019

Parties to the Protocol (1998) Kyoto protocol to the united nations framework convention on climate change

Pearson A (2005) Carbon dioxide—new uses for an old refrigerant. Int J Refrig 28:1140–1148. https://doi.org/10.1016/j.ijrefrig.2005.09.005

Pham H, Rajendran R (2012) R32 and HFOs as low-GWP refrigerants for air conditioning. Int Refrig Air Cond Conf. Purdue, Indiana, 1–10

Pitarch M, Navarro-Peris E, Gonzalvez J, Corberan JM (2016) Analysis and optimisation of different two-stage transcritical carbon dioxide cycles for heating applications. Int J Refrig 70:235–242. https://doi.org/10.1016/j.ijrefrig.2015.08.013

Powell RL (2002) CFC phase-out: have we met the challenge? J Fluor Chem 114:237–250. https://doi.org/10.1016/S0022-1139(02)00030-1

Qi Z (2015) Performance improvement potentials of R1234yf mobile air conditioning system. Int J Refrig 58:35–40. https://doi.org/10.1016/j.ijrefrig.2015.03.019

R-32 (n.d.) Next-generation refrigerant/benefits of daikin technology. Daikin Global. http://www.daikin.com/about/why_daikin/benefits/r-32/. Accessed 4 July 2017

Richardson RN, Butterworth JS (1995) The performance of propane/isobutane mixtures in a vapour-compression refrigeration system. Int J Refrig 18:58–62. https://doi.org/10.1016/0140-7007(94)P3712-A

SAE-CRP1234 (2009) Industry evaluation of low global warning potential refrigerant HFO-1234yf

Saha BB, Boelman EC, Kashiwagi T (1995) Computer simulation of a silica gel water adsorption refrigeration cycle-the influence of operating conditions on cooling output and COP. Am Soc Heating, Refrig Air-Conditioning Eng ASHRAE Trans 101:348–357

Sciance F (2013) The transition from HFC-134a to a low-GWP refrigerant in mobile air conditioners HFO-1234yf. Gen Mot Public Policy Cent 1–15

Spatz M, Minor B (2008) HFO-1234yf low GWP refrigerant : a global sustainable solution for mobile air conditioning 1–26

Spatz MW, Motta SFY, Yana Motta SF (2004) An evaluation of options for replacing HCFC-22 in medium temperature refrigeration systems. Int J Refrig 27:475–483. https://doi.org/10.1016/j.ijrefrig.2004.02.009

Stocker TF, Qin D, Plattner G-K, Tignor MMB, Allen SK, Boschung J et al (2013) Climate change 2013 the physical science basis working group I contribution to the fifth assessment Report of the intergovernmental panel on climate change. Cambridge University Press

Takizawa K, Tokuhashi K, Kondo S (2009) Flammability assessment of CH2 = CFCF3: comparison with fluoroalkenes and fluoroalkanes. J Hazard Mater 172:1329–1338. https://doi.org/10.1016/j.jhazmat.2009.08.001

Tamainot-Telto Z, Metcalf SJ, Critoph RE, Zhong Y, Thorpe R (2009) Carbon-ammonia pairs for adsorption refrigeration applications: ice making, air conditioning and heat pumping. Int J Refrig 32:1212–1229. https://doi.org/10.1016/j.ijrefrig.2009.01.008

Tamatsu T, Sato H, Watanabe K (1993) An equation of state for 1,1-difluoroethane (HFC 152a). Int J Refrig 16:347–352

Tanaka K, Higashi Y (2010) Thermodynamic properties of HFO-1234yf (2,3,3,3-tetrafluoropropene). Int J Refrig 33:474–479. https://doi.org/10.1016/j.ijrefrig.2009.10.003

Tanaka T, Hidekazu O, Katsuya U, Jun I, Otsuka T, Nogami T et al (2014) Development of a new low-GWP refrigerant composed of HFO-1123 (trifluoroethylene). AIChE Annu Meet, Atlanta, GA

Tian Q, Cai D, Ren L, Tang W, Xie Y, He G et al (2015) An experimental investigation of refrigerant mixture R32/R290 as drop-in replacement for HFC410A in household air conditioners. Int J Refrig 57:216–228. https://doi.org/10.1016/j.ijrefrig.2015.05.005

Tiwari A, Gupta RC (2011) Recent development of domestic refrigerator—a review. Int J Eng Sci Technol 3:4233–4239

Uddin K, Miyazaki T, Koyama S, Saha BB (2013) Performance investigation of adsorption-compression hybrid refrigeration system. Int J Air-Conditioning Refrig 21:1350024. https://doi.org/10.1142/S2010132513500247

Uddin K, El-Sharkawy III, Miyazaki T, Saha BB, Koyama S, Kil H-S et al (2014) Adsorption characteristics of ethanol onto functional activated carbons with controlled oxygen content. Appl Therm Eng 72:211–218. https://doi.org/10.1016/j.applthermaleng.2014.03.062

Ueda K, Wajima K, Yokoyama A, Akimasa SA, Kenji U, Kazuki W, Akimasa AS, Yokoyama A (2011) Low GWP refrigerant application for the centrifugal chiller- study for application of HFO-1234ze(E). Trans Japan Soc Refrig Air Cond Eng 28:503–508. https://doi.org/10.11322/tjsrae.28.503

UNEP (2016) Montreal protocol on substances that deplete the ozone layer (report of the technology and economic assessment panel)

Vaghela JK (2017) Comparative evaluation of an automobile air-conditioning system using R134a and its alternative refrigerants. Energy Procedia 109:153–160. https://doi.org/10.1016/j.egypro.2017.03.083

Van Poolen LJ, Holcomb CD, Niesen VG (1997) Critical temperature and density from liquid-vapor coexistence data: application to refrigerants R32, R124, and R152a. Fluid Phase Equilib 129:105–111. https://doi.org/10.1016/S0378-3812(96)03171-8

Wang X, Amrane K (2014) AHRI Low global warming potential alternative refrigerants evaluation program (low-GWP AREP)—summary of phase I testing results. 15th Int Refrig Air Cond Conf 1–10. Purdue

Wang LW, Wu JY, Wang RZ, Xu YX, Wang SG, Li XR (n.d.) Study of the performance of activated carbon–methanol adsorption systems concerning heat and mass transfer. https://doi.org/10.1016/s1359-4311(03)00104-2

Wang D, Zhang J, Yang Q, Li N, Sumathy K (2014) Study of adsorption characteristics in silica gel-water adsorption refrigeration. Appl Energy 113:734–741. https://doi.org/10.1016/j.apenergy.2013.08.011

Wilson DP, Kujak S, Leary JMO, Kennoy DH, Kusmierz A, Patnaik V et al (2010) Designation and Safety Classification of Refrigerants. ANSI/ASHRAE Stand 34-2010 8400:9

Wu J, Chu Y, Hu J, Liu Z (2009) Performance of mixture refrigerant R152a/R125/R32 in domestic air-conditioner. Int J Refrig 32:1049–1057. https://doi.org/10.1016/j.ijrefrig.2008.10.009

Xu X, Hwang Y, Radermacher R (2013) Performance comparison of R410A and R32 in vapor injection cycles. Int J Refrig 36:892–903. https://doi.org/10.1016/j.ijrefrig.2012.12.010

Xue J, Koyama S, Kuwahara K (2010) Performance prediction of a R744 transcritical cycle for air conditioning. Int Symp Next-generation Air Cond Refrig Technol 17–19

Yang Z, Wu X (2013) Retrofits and options for the alternatives to HCFC-22. Energy 59:1–21. https://doi.org/10.1016/j.energy.2013.05.065

Yang Z, Wu X, Tian T (2015) Flammability of Trans-1, 3, 3, 3-tetrafluoroprop-1-ene and its binary blends. Energy 91:386–392. https://doi.org/10.1016/j.energy.2015.08.037

Yun R, Heo JH, Kim Y (2006) Evaporative heat transfer and pressure drop of R410A in microchannels R410A. Int J Refrig 29:92–100. https://doi.org/10.1016/j.ijrefrig.2005.08.005

Zilio C, Brown JS, Schiochet G, Cavallini A (2011) The refrigerant R1234yf in air conditioning systems. Energy 36:6110–6120. https://doi.org/10.1016/j.energy.2011.08.002

# Chapter 16
# Application of Nanofluid-Based Direct Absorption Solar Collector in Once-Through Multistage Flash Desalination System


**Kapil Garg, Vikrant Khullar, Sarit K. Das and Himanshu Tyagi**

**Abstract** Multistage flash (MSF) desalination technique is one of the simplest of thermal desalination methods which requires thermal energy in order to desalinate seawater. This thermal energy can be provided by solar energy harnessed by a direct absorption solar collector (DASC) in which a nanofluid while flowing through the collector absorbs the incident irradiation directly and gets heated to higher temperatures. These collectors are having a relatively higher thermal efficiency (10% higher) as compared to conventional surface-absorption-based solar collectors. In this study, a direct absorption solar collector (DASC) has been used as a heat source for multistage flash (MSF) desalination system having once-through (OT) configuration, and these two systems are coupled using a counterflow type heat exchanger. This direct absorption collector is replaced by surface-absorption-based collector in order to prevent the degradation of thermal performance of surface-absorption-based collector due to high salinity of seawater as in the present case seawater flows through heat exchanger and is getting heated by the nanofluid flowing through direct absorption collector. The aim of the present study is to evaluate the thermal performance of the combined system which is represented by a quantity known as gained output ratio (GOR). The thermal performance or efficiency of the solar collector depends upon various parameters such as thickness of nanofluid layer inside DASC ($H$), length of the collector ($L$), particle volume fraction of nanoparticles ($f_v$), and incident solar energy ($q$) which will affect the performance of the MSF system also. Hence, the performance of the combined system will be evaluated as a function of the collector parameters mentioned above. The gained output ratio is also evaluated as a function of brine rejection temperature

K. Garg (✉) · S. K. Das · H. Tyagi
School of Mechanical, Materials and Energy Engineering,
Indian Institute of Technology Ropar, Rupnagar 140001, Punjab, India
e-mail: kapil.garg@iitrpr.ac.in

V. Khullar
Mechanical Engineering Department, Thapar Institute of Engineering
and Technology, Patiala 147004, Punjab, India



H. Tyagi et al. (eds.), *Advances in Solar Energy Research*, Energy, Environment,
and Sustainability, https://doi.org/10.1007/978-981-13-3302-6_16

($T_b$) and feed seawater temperature ($T_f$) which are parameters associated with the MSF desalination system. The fresh water production rate ($\dot{m}_d$) has also been evaluated as a function of the abovementioned parameters related to the collector and MSF system. A numerical model has been prepared to solve the temperature profile of the DASC system which is solved using finite difference implicit method (FDM) with the help of MATLAB. The numerical model for MSF desalination system is also prepared and solved in MATLAB.

**Keywords** Solar energy · Desalination · Multistage flash · Once-through Nanofluid

## Nomenclature

| | |
|---|---|
| $C_p$ | Specific heat capacity [W/mK] |
| $D$ | Diameter of nanoparticles [nm] |
| $H$ | Height of the solar collector [m] |
| $h$ | Planck constant, $h = 6.6256 \times 10^{-34}$ J-s |
| $h_{conv}$ | Convective heat transfer coefficient [W/m$^2$K] |
| $h_{fg,\ avg}$ | Specific enthalpy of vaporization [J/kg] |
| $I_\lambda$ | Spectral intensity of radiation [W/m$^2$-str-μm] |
| $K$ | Radiative coefficients [m$^{-1}$] |
| $k$ | Thermal conductivity of nanofluid [W/mK] |
| $k_B$ | Boltzmann constant, $k_B = 1.38 \times 10^{-23}$ J/K |
| $L$ | Solar collector length [m] |
| $\dot{m}$ | Mass flow rate [kg/s] |
| $m$ | Normalized refractive index, $m = n + i\kappa$ |
| $N$ | Number of stages of MSF desalination system |
| $n$ | Index of refraction |
| $Q_{transfer}$ | Rate of heat transfer [J/s] |
| $q_r$ | Radiative flux obtained [W/m$^2$] |
| $T$ | Temperature [K] |
| $U$ | Nanofluid velocity [m/s] |
| $W$ | Solar collector width [m] |
| $X$ | Seawater salinity [ppm] |

## Greek Symbols

| | |
|---|---|
| $\varepsilon$ | Heat exchanger effectiveness |
| $\kappa$ | Index of absorption |
| $\lambda$ | Wavelength of incident radiation [μm] |
| $\rho$ | Density [kg/m$^3$] |
| $\tau$ | Transmissivity |
| $\phi$ | Solid angle [str] |

**Subscripts**

| | |
|---|---|
| a | Absorption |
| amb | Ambient |
| b | Brine |
| black | Blackbody |
| conv | Convection |
| d | Distillate |
| e | Extinction |
| f | Feed sea water |
| in | Collector inlet |
| nf | Nanofluid |
| o | Top brine |
| out | Collector outlet |
| r | Radiative |
| st | Stage |

**Abbreviations**

| | |
|---|---|
| BR | Brine recirculation |
| DASC | Direct absorption solar collector |
| FDM | Finite difference method |
| GOR | Gained output ratio |
| MSF | Multistage flash |
| OT | Once-through |

## 16.1 Introduction

Water shortage affects nearly half of the world's population (Miller 2003). The lack of freshwater reservoirs globally along with the ever-increasing rate of population and industrialization, especially in the developing regions of the world necessitates the development of various methods for obtaining the fresh water in order to avoid water scarcity around the globe. Seawater desalination and reusing water are the two possible methods which may help in increasing the amount of fresh water available on the planet. But, out of these two methods, seawater desalination offers a seemingly unlimited, steady supply of high-quality water without disturbing natural freshwater ecosystems (Elimelech and Phillip 2011). The various available methods for seawater desalination are broadly categorized as membrane-based desalination methods and thermal-energy-based desalination methods (Narayan et al. 2010). In the present study, multistage flash (MSF) desalination method has been studied which is a thermal-energy-based desalination process which requires thermal energy to desalinate seawater. The MSF desalination method is one of the

simplest thermal desalination methods which is having several attractive features such as the salinity and high temperature, and the turbidity of feed seawater does not affect the plant operation. Also, it requires less maintenance having long life and can be integrated with power plants to produce both electricity and water (Roy et al. 2017). It can be concluded that due to these attractive features MSF has its special position in Middle East and North African (MENA) countries where it occupies approximately 86% of the total desalination capacity (El-Dessouky and Ettouney 2002). There are two configurations of MSF desalination technique such as once-through (OT) multistage flash desalination process and brine recirculation (BR) multistage flash desalination process, out of which BR-MSF technology is the state-of-the-art MSF desalination technology. In OT-MSF method, none of the portion of brine is reused, and hence all of the brine is rejected to sea, whereas in case of BR-MSF process, some of the portion of brine is rejected and remaining portion is reused which is having higher energy as compared to the incoming feed seawater. MSF desalination plants are installed in many countries and also various researchers have studied this method. El-Dessouky et al. (1995) have presented the steady-state mathematical model for analyzing MSF desalination process which describes the relationships between parameters controlling the cost of produced water to other design and operating variables. The model also takes care of the practical case of constant heat transfer surface area per stage, variation of physical properties of seawater with temperature and salinity, fouling effects, and effects due to presence of non-condensable gases. In another study by El-Dessouky et al. (1998), various configurations of flashing desalination techniques such as single-stage flashing system, once-through multistage flashing system, and brine recirculation multistage flashing system has been studied. The analysis was done to evaluate the performance characteristics of these configurations which include performance ratio, specific heat transfer area, specific flow rate of cooling and feed seawater, salinity, temperature, and specific flow rate of recycled brine. Thomas et al. (1998) have developed the mathematical model and its solution procedure to study the steady and dynamic behavior of MSF desalination plants. It was observed that there is a close agreement between the predicted values and actual plant data. Darwish et al. (1993) have done the second law analysis of recirculating MSF desalination unit and it has been shown that the major energy losses in the process occur during vapor condensation, vapor flashing, and preheating of feed in brine heaters. Al-Wazzan and Al-Modaf (2001) have presented the historical developments of the MSF plants in Kuwait and gained experience over the years concerning plant maintenance and operation.

In conventional MSF desalination plants, thermal energy is required in a huge amount and is supplied in the form of high pressure saturated steam obtained from the coal- and natural-gas-based power plants. As the demand for fresh water is increasing at a faster rate, the amount of desalinated water produced from MSF plants will also increase which may cause burden on the fossil fuels due to increased energy requirements. The use of fossil fuels for obtaining thermal energy for MSF desalination plants will create harmful impact on the environment. Hence, thermal energy may be supplied to MSF plants by utilizing the solar thermal energy

as there are various regions in the world which are having both water scarcity and high incidence of solar energy (Kalogirou 2005). Nafey et al. (2007) have studied a small unit based on flashing desalination process utilizing the flat-plate solar collector. The average accumulative productivity of the system between November to January was reported as 1.04–1.45 kg/day/$m^2$ and in summers it was reported as 5.44–7 kg/day/$m^2$. Kabeel and El-Said (2014) have also studied the flat-plate solar collector based single-stage flashing (SSF) desalination unit. The working fluid inside the solar collector is a copper nanofluid. The gained output ratio (GOR) of the system was reported as 1.058. The gained output ratio (GOR) is the ratio of the latent heat of evaporation of the distillate produced to the total heat absorbed by the fluid inside the solar collector (Narayan et al. 2010). In the solar-energy-based MSF desalination units, surface-absorption-based solar collectors are usually employed to heat the saline water to a desired temperature. The high salinity of the seawater leads to the fouling and scaling of the heat transfer surface area of these collectors due to which thermal performance of these collectors and of the overall system may get affected. This problem can be avoided by replacing the surface-absorption-based solar collectors by direct absorption solar collectors (DASC) and coupling the DASC and MSF desalination unit using a counterflow heat exchanger.

In the present study, a nanofluid-based direct absorption solar collector has been used as a heat source for once-through configuration of multistage flash (MSF) desalination unit. A counterflow heat exchanger of fixed effectiveness value is used in order to combine these two units. The direct absorption solar collector (DASC) is the replacement of surface-absorption-based solar collector due to the issues related to the structural damage of these collectors under the conditions of high incident solar flux, cyclic variations of temperature, and high salinity of seawater. The thermal efficiency of the combined system has been quantified using a factor known as gained output ratio (GOR) as a function of various operating parameters such as particle volume fraction ($f_v$), thickness of the nanofluid layer inside (DASC), solar collector length ($L$), incident solar energy on the collector ($q$), brine rejection temperature ($T_b$), and feed seawater temperature ($T_f$). The effect of abovementioned parameters has also been studied on the distillate production rate ($\dot{m_d}$).

## 16.2 Studied System

The direct absorption solar collector (DASC) based multistage flash (MSF) desalination system having once-through (OT) configuration has been shown in Fig. 16.1. The overall system is a combination of two subsystems which are nanofluid-based direct absorption solar collector (DASC) and once-through (OT) multistage flash (MSF) desalination system and these two subsystems are coupled using a counterflow heat exchanger in which heated nanofluid supplies the thermal energy to preheated saline water which gets heated to a required

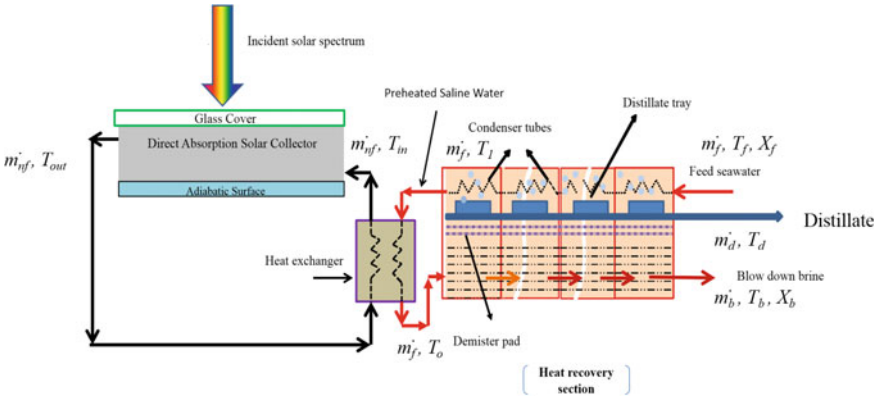


**Fig. 16.1** Schematic of once-through (OT) multistage flash (MSF) desalination system integrated with direct absorption solar collector (DASC) through a counterflow heat exchanger

temperature known as top brine temperature ($T_o$). The solar collector is simply a rectangular channel in which the nanofluid flows and gets heated to higher temperature by absorbing the incident solar flux. The nanofluid is prepared by suspending nanoparticles of certain material such as copper, aluminum, graphite, etc. inside a base fluid (water, ethylene glycol, therminol vp-1, etc.) The solar collector is also having a glass cover at its top having transmissivity, $\tau$, which allows the irradiation to pass through the cover and interacts with the nanofluid. The heat loss occurs from the top layer of nanofluid to the ambient through convection only (radiative losses are neglected) and the bottom surface is made to be highly insulating and transparent such that it does not allow the heat flux to pass through but irradiation passes through the bottom surface. The incident solar radiation having spectral intensity $I_\lambda$, which is considered to be in the wavelength range of 0.1–3 μm interacts with the nanofluid and as the irradiation passes through the nanofluid layers, it gets absorbed by different layers of nanofluid and this absorbed energy appears as the rise in the internal energy of the fluid. Hence, at the outlet of the collector nanofluid will be at relatively higher temperature than at the inlet of collector depending on the various operating parameters.

The second subsystem is the once-through (OT) multistage flash (MSF) desalination system which consists of $N$ number of stages or evacuated chambers which are also called flashing chambers. These flashing chambers are made up of a brine pool, a distillate tray, a demister pad, and condenser tubes. The heated saline water from the heat exchanger at a desired temperature (called top brine temperature) passes through the first flashing chamber which is maintained at a certain operating pressure lower than the saturation pressure at which heated saline water enters the first flashing chamber. Due to decrease in sudden pressure of the saline water, flashing of brine occurs which results in the formation of fresh water vapors from the brine pool. These fresh water vapors then pass through the demister pad which prevents the entrainment of brine droplet into the vapors of

fresh water. These vapors then flow over the condenser tubes at the top of the flashing chamber and lose their latent heat energy to the incoming feed of cold saline water ($M_f$) flowing inside these cooling coils or condenser tubes and gives distillate or pure water stream. The remaining portion of the brine enters the next flashing stage which is maintained at an even lower pressure than the pressure inside the first flashing chamber and due to sudden drop in operating pressure, vapors of fresh water are obtained and ultimately distillate stream as explained earlier. The same process is repeated in the remaining flashing chambers as the brine passes through these evacuated chambers giving the fresh water and at the same time, the latent heat of formed vapors is utilized in heating the incoming feed of cold saline water inside condenser tubes. At the outlet of the last flashing chamber, the remaining brine is rejected to the sea, and hence the process is named as once-through MSF desalination system.

## 16.3 Numerical Modeling of the Proposed System

In the present study, direct absorption solar collector which is employed as a heat source for OT-MSF desalination has been taken as a rectangular channel in which the nanofluid flows which is basically a suspension of copper (Cu) nanoparticles inside the base fluid taken as water. This nanofluid enters the DASC with mass flow rate $\dot{m_{nf}}$ and inlet temperature $T_{in}$, absorbs the incident solar radiation while flowing through the channel. The incident solar spectrum is considered to be in the wavelength range of 0.1–3 μm and spectral intensity for each wavelength ($I_\lambda$) is given by the following Eq. (16.1) (Cengel and Ghajar 2007):

$$I_\lambda = \frac{2hc_o^2}{\lambda^5\left[\exp\left(\frac{hc_o}{k_B\lambda T_{solar}}-1\right)\right]}, \tag{16.1}$$

where $h$ is the Planck's constant, $c_o$ is the speed of light (in vacuum), $k_B$ is the Boltzmann constant, $\lambda$ is the wavelength of incident radiation, and $T_{solar}$ is the blackbody temperature of the sun ($T_{solar}$ = 5800 K). The incident intensity interacts with the nanofluid and is assumed to be varied only as a function of the thickness of nanofluid layer inside DASC or height of the collector ($y$) which is governed by the simplified form of radiative transfer equation (RTE) given as follows (Tyagi et al. 2009; Khullar et al. 2013; Gorji and Ranjbar 2016; Garg et al. 2018a, b):

$$\frac{\partial I_\lambda}{\partial y} = K_{e\lambda,\text{nanofluid}} I_\lambda = -\left(K_{a\lambda,\text{water}} + K_{e\lambda,\text{nanoparticles}}\right) I_\lambda, \tag{16.2}$$

where $K_{e\lambda}$ and $K_{a\lambda}$ are the spectral extinction coefficient and spectral absorption coefficient, respectively. The spectral extinction coefficient for nanoparticles ($K_{e\lambda}$) is the sum of the spectral absorption coefficient ($K_{a\lambda,\ \text{nanoparticles}}$) and spectral

scattering coefficient ($K_{s\lambda,\text{ nanoparticles}}$) represented by the following Eqs. (16.2a) and (16.2b) (Tyagi et al. 2009; Garg et al. 2018a, b):

$$K_{a\lambda,\text{nano}-\text{particles}} = \frac{12\pi f_v}{\lambda}\text{Im}\left\{\frac{m^2-1}{m^2+2}\left[1+\frac{\pi^2 D^2}{15\lambda^2}\left(\frac{m^2-1}{m^2+2}\right)\right]\left(\frac{m^4+27m^2+38}{2m^2+3}\right)\right\}, \tag{16.2a}$$

$$K_{s\lambda,\text{nanoparticles}} = \frac{8\pi^4 D^3 f_v}{\lambda^4}\left|\frac{m^2-1}{m^2+2}\right|^2, \tag{16.2b}$$

where $f_v$ is the amount of nanoparticles inside the base fluid which is known as particle volume fraction, $D$ is the diameter of the nanoparticles, and $m$ (=$n$ + i$\kappa$) is the normalized refractive index of nanoparticles given by the following Eq. (16.2c) (Tyagi et al. 2009; Garg et al. 2018a, b):

$$m = \frac{m_{\text{particles}}}{n_{\text{fluid}}}, \tag{16.2c}$$

where $m_{\text{particles}}$ is the complex refractive index of particles and $n$ is the index of refraction of the base fluid. The spectral absorption coefficient for base fluid is given by the following Eq. (16.2d) (Tyagi et al. 2009; Garg et al. 2018a, b):

$$K_{a\lambda,\text{water}} = \frac{4\pi\kappa}{\lambda}, \tag{16.2d}$$

where $\kappa$ is the index of absorption for base fluid. In the present case, due to small size of nanoparticles under consideration, Rayleigh scattering model has been applied (Tyagi et al. 2009). The absorbed irradiation by the nanofluid appears as the rise in the internal energy of the fluid and thus nanofluid gets heated to higher temperature, $T_{\text{out}}$. This outlet temperature ($T_{\text{out}}$) is calculated by applying the energy balance equation on DASC given as follows (Tyagi et al. 2009; Gorji and Ranjbar 2016; Garg et al. 2017, 2018a):

$$k\frac{\partial^2 T}{\partial y^2} - \frac{\partial q_r}{\partial y} = \rho C_p U\frac{\partial T}{\partial x}, \tag{16.3}$$

where $k$, $\rho$, and $C_p$ are the thermal conductivity, density, and specific heat of the nanofluid which are taken to be equal to that of the base fluid due to very low particle volume fraction considered in the present study and $U$ is the nanofluid velocity. The above energy balance Eq. (16.3) has been solved using the finite difference implicit method (FDM) using MATLAB and it holds some assumptions which are as follows. The nanofluid flows through the collector at a constant velocity, and it loses heat to the ambient through convection only. The radiative flux ($q_r$) absorbed by the nanofluid is given by the following Eq. (16.4) (Tyagi et al. 2009; Khullar et al. 2013; Garg et al. 2017, 2018a):

$$q_r = \iint I_\lambda \mathrm{d}\phi \mathrm{d}\lambda, \tag{16.4}$$

where $\mathrm{d}\phi$ is the solid angle subtended by the sun on the earth. The boundary conditions which are required to solve the above governing Eq. (16.3) can be obtained from (Gorji and Ranjbar 2016; Garg et al. 2018a, b).

The modeling of the OT-MSF desalination unit is based on some assumptions which are as follows:

1. The properties of the seawater are assumed to be equal to the properties of pure water.
2. The effect of non-condensable gases inside the flashing chambers is neglected, and hence the entire mass of the water vapor is assumed to be condensed.
3. The heat loss from the flashing chambers to the ambient is neglected.

The total mass balance and salt balance equations involved in the modeling of the OT-MSF desalination unit are as follows (El-Dessouky and Ettouney 2002):

$$\dot{m}_f = \dot{m}_b + \dot{m}_d, \tag{16.5}$$

$$X_b = \frac{\dot{m}_f X_f}{\dot{m}_b}, \tag{16.6}$$

where $\dot{m}_f$ is the mass flow rate of feed seawater, $\dot{m}_b$ is the mass flow rate of the rejected brine, $\dot{m}_d$ is the mass flow rate of the distillate produced, and $X_b$ and $X_f$ are the salinities of feed seawater and rejected brine. The heated nanofluid with mass flow rate $\dot{m}_{nf}$ and temperature $T_{out}$ supplies the thermal energy to the preheated saline water inside the counterflow heat exchanger. This preheated saline water enters the heat exchanger from the exit of the condenser tubes inside the first flashing chamber having mass flow rate $\dot{m}_f$ and temperature $T_1$ and gets heated to temperature $T_o$ (top brine temperature) at the exit of the heat exchanger. After that the heated saline water at a certain saturation pressure enters into the first flashing chamber where it flashes and produces vapors of fresh water. The top brine temperature $T_o$ is calculated by the following Eq. (16.7):

$$T_o = \frac{Q_{transfer}}{\dot{m}_f C_p} + T_1, \tag{16.7}$$

where $C_p$ is the specific heat capacity of saline water and $Q_{transfer}$ is the heat transfer that takes place between heated nanofluid and preheated saline water inside the heat exchanger and is given by the following Eq. (16.8):

$$Q_{transfer} = \varepsilon \dot{m}_{nf} C_p (T_{out} - T_1), \tag{16.8}$$

where $\varepsilon$ is the effectiveness of the heat exchanger.

The heated saline water with temperature $\dot{m_f}$ and temperature $T_o$ flows through the flashing chambers and produce the distillate stream (including all stages) having mass flow rate $\dot{m_d}$ which is calculated by the following Eq. (16.9) (El-Dessouky and Ettouney 2002; Harandi et al. 2017):

$$\dot{m_d} = \frac{\dot{m_f}\, C_p (NT_{st})}{h_{fg,avg}}, \tag{16.9}$$

where $N$ is the number of stages or flashing chambers in the OT-MSF desalination unit, $T_{st}$ represents the temperature drop of the saline water per flashing stage, and $h_{fg,avg}$ is the average specific enthalpy of vaporization of the fresh water vapors formed in the $N$ stages which is evaluated at the average of the top brine temperature ($T_o$) and brine rejection temperature ($T_b$). The temperature drop of brine per flashing stage is given by the following Eq. (16.10):

$$T_{st} = \frac{T_o - T_b}{N}. \tag{16.10}$$

The temperature of the preheated saline water at the exit of the condenser tubes inside first flashing chamber ($T_1$) is calculated by the following Eq. (16.11):

$$T_1 = T_f + (NT_{st}). \tag{16.11}$$

Finally, the thermal performance of the overall system is quantified by evaluating the gained output ratio (GOR) which is obtained by the following Eq. (16.12) (Prakash Narayan et al. 2013):

$$\text{GOR} = \frac{\dot{m_d}\, h_{fg,avg}}{Q_{transfer}}. \tag{16.12}$$

## 16.4 Results and Discussions

The present section discusses the performance of direct absorption solar collector (DASC) based once-through (OT) multistage flash (MSF) desalination system. The performance index of the combined system is evaluated in the form of gained output ratio (GOR). The gained output ratio (GOR) is defined as the ratio of latent heat of vaporization of distillate produced to the heat transfer rate obtained from the heat exchanger. The gained output ratio (GOR) is evaluated as a function of various parameters such as length of the collector or channel ($L$), thickness of fluid layer ($H$), particle volume fraction of nanoparticles ($f_v$), amount of solar energy received by the collector ($q$), brine rejection temperature ($T_b$), and temperature of feed seawater ($T_f$) independently. The distillate production rate ($\dot{m_d}$) is also measured as a function of these parameters. The numerical model prepared for both solar

collector and MSF system are solved in MATLAB and the steady-state analysis is performed. The values of the various input parameters related to MSF and DASC systems which are used to perform the analysis are as follows. Diameter of copper nanoparticles, $D$ = 5 nm, ambient temperature, $T_{amb}$ = 25 °C, inlet temperature of nanofluid, $T_{in}$ = 60 °C, convective heat transfer coefficient, $h_{conv}$ = 3.5 W/m$^2$ K, mass flow rate of nanofluid, $\dot{m}_{nf}$ = 0.05 kg/s, mass flow rate of feed seawater, $\dot{m}_f$ = 0.1 kg/s, width of the collector, $W$ = 2 m, glass cover transmissivity, $\tau$ = 0.98, and effectiveness of the counterflow heat exchanger, $\varepsilon$ = 0.85.

### 16.4.1 *Effect of Particle Volume Fraction ($f_v$) on Gained Output Ratio (GOR) of the System and Distillate Production Rate ($\dot{m}_d$)*

The variation of gained output ratio (GOR) and distillate production rate ($\dot{m}_d$) as a function of particle volume fraction ($f_v$) of copper nanoparticles is shown in Fig. 16.2. This analysis is done for the nanofluid layer of thickness, $H$ = 10 mm, temperature of feed seawater, $T_f$ = 25 °C, brine rejection temperature, $T_b$ = 40 °C, length of the collector, $L$ = 5 m, and number of stages of OT-MSF desalination unit, $N$ = 20. As shown in Fig. 16.2, the increase in particle volume fraction ($f_v$) leads to an increase in gained output ratio (GOR) and distillate production rate ($\dot{m}_d$). The presence of copper nanoparticles inside the base fluid causes the significant attenuation of incident intensity within the nanofluid and thus internal energy of nanofluid increases. At lower volume fraction, some of the irradiation may able to pass through the nanofluid layer, and hence absorption of incident intensity is less. But with the increase in volume fraction ($f_v$) up to a certain amount for a fixed thickness of nanofluid layer ($H$), the attenuation of incident intensity increases due to increased scattering and absorption of irradiation, and hence the rise in internal energy of the nanofluid is more which increases the temperature of the nanofluid at

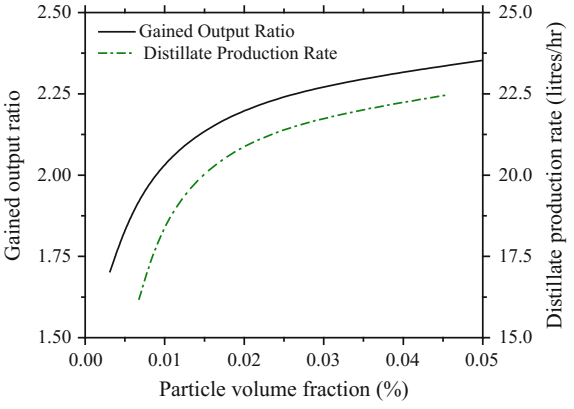


**Fig. 16.2** Effect of particle volume fraction ($f_v$) on the gained output ratio (GOR) and distillate production rate ($\dot{m}_d$)

the collector exit ($T_{out}$). Due to higher outlet temperature of nanofluid at the collector exit, the rate of thermal energy supplied to the preheated brine by the heated nanofluid inside the heat exchanger increases which increases the top brine temperature ($T_o$). The increase in top brine temperature with fixed brine rejection temperature ($T_b$) causes the increase in flashing range ($T_o$–$T_b$) of the brine between the various stages of OT-MSF system. The increase in flashing range leads to the increase in the amount of distillate produced ($\dot{m_d}$), and hence the gained output ratio (GOR) of the overall system. Also, it should be noted that after the volume fraction of 0.025%, the rate of increase in GOR and distillate production rate gets lowered. It is due to the reason that after this value of volume fraction, the rate of increase in collector outlet temperature is low because at a higher volume fraction, the maximum incident intensity gets attenuated within the top layers of the nanofluid, thus unable to reach the bottom layers of nanofluid. Thus, overall temperature of fluid will be lower and so the rate of heat transfer inside the heat exchanger between nanofluid and saline water which ultimately lowers the increment rate of GOR and $\dot{m_d}$.

### 16.4.2 *Effect of Thickness of Nanofluid Layer (H) on Gained Output Ratio (GOR) of the System and Distillate Production Rate ($\dot{m_d}$)*

Figure 16.3 shows the impact of nanofluid layer thickness ($H$) on gained output ratio of the system and distillate production rate ($\dot{m_d}$). This analysis has been done for the particle volume fraction, $f_v = 0.0125\%$, length of the solar collector, $L = 5$ m, temperature of the feed seawater, $T_f = 25$ °C, brine rejection temperature, $T_b = 40$ °C, and number of stages of OT-MSF unit, $N = 20$. It can be observed from Fig. 16.3 that the increase in the thickness of nanofluid layer inside DASC ($H$) increases the gained output ratio and distillate production rate. At a relatively lower thickness of nanofluid layer for a fixed particle volume fraction ($f_v$), this lower thickness of fluid layer may not be able to fully attenuate the incident irradiation and some of the incident intensity gets passed through the bottom surface of the fluid layer and due to this lower absorption of intensity the rise in outlet temperature of the fluid is also lower. The lower outlet nanofluid temperature at the collector exit ($T_{out}$) results in the lower heat transfer rate causing the top brine temperature to decrease to a lower value. As explained earlier, the lower top brine temperature ($T_o$) with a fixed brine rejection temperature ($T_b$) results in lower flashing range, and hence lower distillate production rate ($\dot{m_d}$) and lower gained output ratio (GOR).

Also, the increase in nanofluid layer thickness leads to the increased absorption of incident intensity due to increase in attenuation of the intensity within the fluid

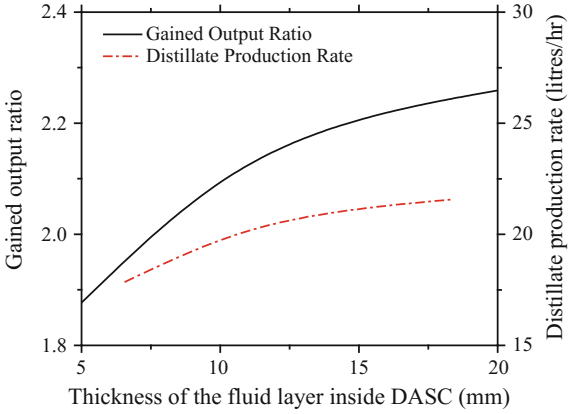


**Fig. 16.3** Effect of thickness of nanofluid layer inside DASC ($H$) on the gained output ratio (GOR) and distillate production rate ($\dot{m}_d$)

layer which increases the temperature of the nanofluid at the collector exit. The higher nanofluid temperature leads to higher top brine temperature and as explained earlier the higher top brine temperature leads to higher GOR and distillate production rate. But, it should also be noted that after the increase in fluid layer thickness beyond 15 mm, the rate of increase in GOR and distillate production rate ($\dot{m}_d$) are lowered. It is due to the reason that at greater thickness of nanofluid layer, all of the incident intensities get absorbed within the top layers and the incident energy does not reach the bottom layers due to which the bottom layers remain colder than the top layers which make the average fluid temperature at collector outlet relatively lower. The lower outlet temperature of nanofluid at collector exit results in lower GOR and distillate production rate ($\dot{m}_d$).

### 16.4.3 *Effect of the Length of Direct Absorption Solar Collector (L) on Gained Output Ratio (GOR) and Distillate Production Rate ($\dot{m}_d$) of the System at Different Values of Brine Rejection Temperature ($T_b$)*

The variation of the gained output ratio (GOR) of the overall system and distillate production rate ($\dot{m}_d$) with solar collector length ($L$) at different values of brine rejection temperature has been shown in Fig. 16.4. The present analysis has been done for the particle volume fraction, $f_v = 0.05\%$, nanofluid layer thickness, $H = 10$ mm, temperature of the feed seawater, $T_f = 25$ °C, and number of stages of OT-MSF unit, $N = 20$.

Figure 16.4 shows that the increase in length of the collector increases the thermal performance of the overall system measured as gained output ratio

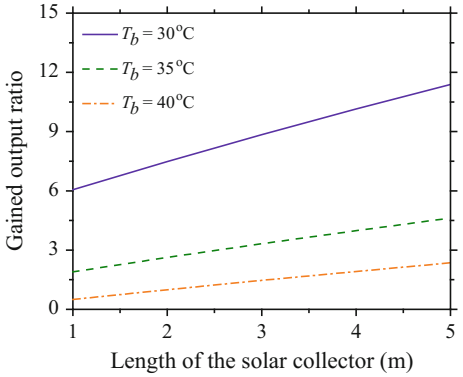


**Fig. 16.4** Effect of the length of direct absorption solar collector ($L$) on the gained output ratio (GOR) for different values of brine rejection temperature ($T_b$)

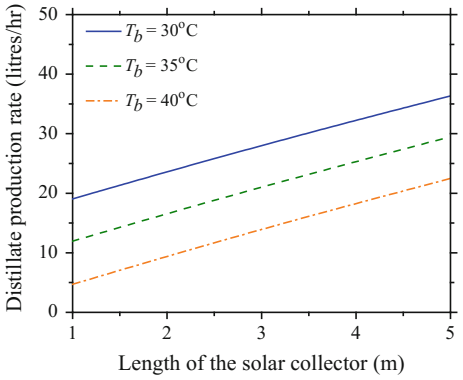


**Fig. 16.5** Impact of the variation of solar collector length ($L$) on the distillate production rate ($\dot{m_d}$) for different values of brine rejection temperature ($T_b$)

(GOR) for different values of brine rejection temperature ($T_b$). When the length of the collector is increased at a fixed brine rejection temperature, the nanofluid with a fixed value of mass flow rate ($\dot{m_{nf}}$) has to flow through the collector for a longer period of time, and hence will absorb the incident energy for this longer period. This will lead to higher outlet temperature of nanofluid ($T_{out}$) which will lead to higher gained output ratio (GOR) and distillate production rate ($\dot{m_d}$) as explained in earlier subsections. It can also be observed from Fig. 16.4 that as the brine rejection temperature is reduced, the increase in gained output ratio (GOR) is much larger. The reduction in brine rejection temperature ($T_b$) increases the flashing range of the brine which leads to the increase in distillate production rate ($\dot{m_d}$), and hence gained output ratio (GOR). Figure 16.5 shows the variation in distillate production rate ($\dot{m_d}$) as a function of the length of the collector for various values of brine rejection temperature ($T_b$).

### 16.4.4 Impact of Incident Solar Energy (q) on the Gained Output Ratio (GOR) and Distillate Production Rate ($\dot{m}_d$) of the System at Different Values of Feed Seawater Temperature ($T_f$)

Figure 16.6 shows the effect of incident solar energy on the gained output ratio (GOR) of the system for different values of feed seawater temperature ($T_f$). The present analysis has been done for the particle volume fraction, $f_v = 0.05\%$, nanofluid layer thickness, $H = 10$ mm, brine rejection temperature, $T_b = 25$ °C, and number of stages of OT-MSF unit, $N = 20$.

It can be observed from Fig. 16.6 that the increase in incident solar energy ($q$) leads to an increase in gained output ratio (GOR). As the amount of incident intensity increases, absorption of irradiation by the nanofluid also increases while flowing through the collector, and hence its temperature will be higher at the outlet of the collector ($T_{out}$). Due to higher outlet temperature of nanofluid ($T_{out}$), there is an increase in heat transfer rate between preheated saline water and nanofluid, and hence the temperature of saline water at the outlet of the heat exchanger (top brine temperature, $T_o$) will be higher. As explained earlier, higher top brine temperature leads to higher gained output ratio and distillate production rate. The increase in feed seawater temperature leads to an increase in gained output ratio (GOR) of the combined system as shown in Fig. 16.6. The high feed seawater temperature ($T_f$) leads to higher heat recovery inside the cooling coils in the flashing chambers, and hence the temperature of the preheated feed seawater at the outlet of the first flashing chamber ($T_1$) will be higher. The higher temperature of preheated feed seawater results in higher $T_o$ due to which flashing range increases and distillate production rate increases ($\dot{m}_d$) which leads to higher gained output ratio (GOR). The variation of distillate production rate ($\dot{m}_d$) as a function of incident solar energy ($q$) for various values of feed seawater temperature is shown in Fig. 16.7.

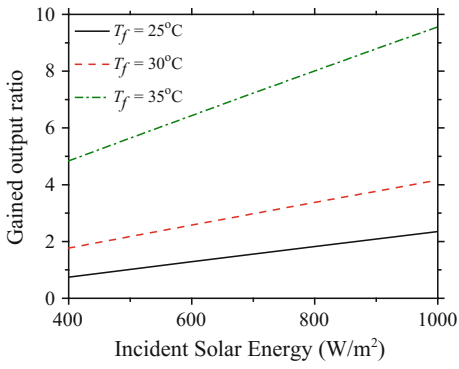


**Fig. 16.6** Impact of the variation in incident solar energy ($q$) on the gained output ratio (GOR) for different values of feed seawater temperature ($T_f$)

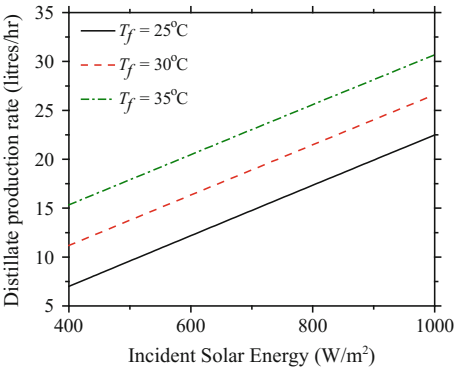


**Fig. 16.7** Impact of the variation in solar energy received by the collector ($q$) on distillate production rate ($\dot{m}_d$) for different values of feed seawater temperature ($T_f$)

## 16.5 Conclusion

A solar-energy-based once-through (OT) multistage flash (MSF) desalination system has been studied in which a nanofluid-based solar collector is used as a heat source. The nanofluid absorbs the incident solar energy directly using the direct absorption principle. The heated nanofluid is used to heat the saline water to a desired temperature inside a counterflow heat exchanger. The numerical model is prepared for both the units (DASC and MSF) and has been solved in MATLAB. The thermal performance of the combined system has been evaluated in the form of gained output ratio (GOR) as a function of various operating parameters such as thickness of nanofluid layer inside DASC ($H$), length of the collector ($L$), particle volume fraction ($f_v$), incident solar energy ($q$), brine rejection temperature ($T_b$), and temperature of feed seawater ($T_f$). The distillate production rate ($\dot{m}_d$) has also been calculated as a function of the abovementioned parameters. It can be concluded that there exits an optimum volume fraction ($f_v$) at which the GOR and distillate production rate is maximum and beyond this optimum value, rate of increment of GOR and distillate production rate gets lowered, when all other parameters are kept constant. Similarly, there also exists an optimum value of thickness of fluid layer ($H$) at which the GOR and distillate production rate ($\dot{m}_d$) is maximum and beyond this optimum thickness value, rate of increment of GOR and distillate production rate starts decreasing when all other input parameters are kept constant. Also, the increase in length of the collector ($L$) and incident solar flux ($q$) increases the gained output ratio and distillate production rate. The reduction in brine rejection temperature and increase in feed seawater temperature lead to an increase in gained output ratio and distillate production rate.

**Acknowledgements** The authors (K. Garg, S. K. Das, and H. Tyagi) wish to acknowledge the support provided by School of Mechanical Material and Energy Engineering at Indian Institute of Technology. Ropar V. K. gratefully acknowledges the support provided by Mechanical Engineering Department, Thapar Institute of Engineering and Technology, Patiala.

## References

Al-Wazzan Y, Al-Modaf F (2001) Seawater desalination in Kuwait using multistage flash evaporation technology historical overview. Desalination 134:257–267

Cengel YA, Ghajar AJ (2007) Heat & mass transfer: a practical approach. McGraw-Hill Education (India) Pvt Limited, New York

Darwish MA, Al-Najem NM, Al-Ahmad MS (1993) Second-law analysis of recirculating multi-stage flash desalting system. Desalination 89:289–309

El-Dessouky HT, Ettouney HM (2002) Fundamentals of salt water desalination, https://doi.org/10.1016/B978-044450810-2/50008-7

El-Dessouky H, Shaban HI, Al-Ramadan H (1995) Steady-state analysis of multi-stage flash desalination process. Desalination 103(3):271–287

El-Dessouky H, Alatiqi I, Ettouney H (1998) Process synthesis: the multi-stage flash desalination system. Desalination 115(2):155–170

Elimelech M, Phillip WA (2011) The future of seawater desalination: energy, technology, and the environment. Science 333(6043):712–717

Garg K, Bhalla V, Khullar V, Das SK, Tyagi H (2017) Performance evaluation of single stage flash evaporation desalination system coupled with nanofluid-based direct. Paper no. IHMTC2017-19-0659. In: 24th national and 2nd international ISHMT-ASTFE heat and mass transfer conference (IHMTC-2017), Hyderabad, India, 27–30 Dec 2017, pp 1–8

Garg K, Khullar V, Das SK, Tyagi H (2018a) Performance evaluation of a brine-recirculation multistage flash desalination system coupled with nanofluid-based direct absorption solar collector. Renew Energy 122:140–151

Garg K, Khullar V, Das SK, Tyagi H (2018b) IMECE2018-87318. In: ASME 2018 international mechanical engineering congress & exposition IMECE2018, 9–15 Nov 2018, Pittsburgh, PA (Accepted)

Gorji TB, Ranjbar AA (2016) A numerical and experimental investigation on the performance of a low-flux direct absorption solar collector (DASC) using graphite, magnetite and silver nanofluids. Sol Energy 135:493–505

Harandi HB, Rahnama M, Jahanshahi Javaran E, Asadi A (2017) Performance optimization of a multi stage flash desalination unit with thermal vapor compression using genetic algorithm. Appl Therm Eng 123:1106–1119

Kabeel AE, El-Said EMS (2014) Applicability of flashing desalination technique for small scale needs using a novel integrated system coupled with nanofluid-based solar collector. Desalination 333(1):10–22

Kalogirou SA (2005) Seawater desalination using renewable energy sources. Prog Energy Combust Sci 31(3):242–281

Khullar V, Tyagi H, Phelan PE, Otanicar TP, Singh H, Taylor RA (2013) Solar energy harvesting using nanofluids-based concentrating solar collector. J Nanotechnol Eng Med 3:1–9

Miller JE (2003) Review of water resources and desalination techniques. Sandia national labs unlimited release report SAND-2003-0800

Nafey AS, Mohamad MA, El-Helaby SO, Saharf MA (2007) Theoretical and experimental study of a small unit for solar desalination using flashing process. Energy Convers Manage 48:528–538

Narayan GP, Sharqawy MH, Summers EK, Lienhard JH, Zubair SM, Antar MA (2010) The potential of solar-driven humidification-dehumidification desalination for small-scale decentralized water production. Renew Sustain Energy Rev 14(4):1187–1201

Prakash Narayan G, St. John MG, Zubair SM, Lienhard JH (2013) Thermal design of the humidification dehumidification desalination system: an experimental investigation. Int J Heat Mass Transf 58(1–2):740–748

Roy Y, Thiel GP, Antar MA, Lienhard JH (2017) The effect of increased top brine temperature on the performance and design of OT-MSF using a case study. Desalination 412:32–38

Thomas PJ, Bhattacharyya S, Patra A, Rao OP (1998) Steady state and dynamic simulation of multi-stage flash desalination plants: a case study. Comput Chem Eng 22(10):1515–1529

Tyagi H, Phelan P, Prasher R (2009) Predicted efficiency of a low-temperature nanofluid-based direct absorption solar collector. J Sol Energy Eng 131(4):041004

# Chapter 17
# Experimental Investigation into the Applicability of Nanoparticles in Purification of Sewage Water Through Usage of Solar Energy


**Virender Ohri and Vikrant Khullar**

**Abstract** In recent years, solar energy driven water desalination/purification systems have been extensively researched with the objective of improving the distillate yield. In these conventional solar driven systems, solar energy heats the water indirectly i.e. in these systems the solar energy is transferred to the water through conduction, resulting in evaporation and hence purification of the water. The present work explores the idea of adding nanoparticles into the wastewater so that solar energy is transferred to water volumetrically, which considerably improves the evaporation rate. Amorphous carbon nanoparticles have been used owing to their high solar weighted absorptivity values. Careful experiments have been carried out to quantify the effect of nanoparticles on the evaporation rate. It was found that optimum level of nanoparticles addition could actually enhance the evaporation rates of the sewage water by $\sim 15\%$. Furthermore, total dissolved solids (TDS) and pH measurements showed considerable improvements, the values being in the range to qualify for drinkable water.

**Keywords** Solar energy · Nanoparticles · Evaporation · Condensation
Sewage water

## Nomenclature

$D$ Mean particle diameter of nanoparticles [nm]
$f_v$ Particle volume fraction inside base fluid
$I_\lambda$ Spectral intensity of sunlight [$Wm^{-2}\mu m^{-1}$]
$K$ Radiative coefficients [$m^{-1}$]
$m$ Normalized refractive index, $m = n + i\kappa$
$n$ Index of refraction
$y$ Distance from the free surface [m]

V. Ohri · V. Khullar (✉)
Mechanical Engineering Department, Thapar Institute of Engineering and Technology, Patiala 147004, Punjab, India
e-mail: vikrant.khullar@thapar.edu



H. Tyagi et al. (eds.), *Advances in Solar Energy Research*, Energy, Environment, and Sustainability, https://doi.org/10.1007/978-981-13-3302-6_17

### Greek Symbols

$k$ Index of absorption
$\lambda$ Wavelength of incident radiation [μm]
$\varphi_m$ Mass fraction of nanoparticles in base fluid [$mgL^{-1}$]

### Subscripts

abs Absorption
$e$ Extinction
imp Impurities
np Nanoparticles
nsw Nanoparticle laden sewage water
pw Pure water
sca Scateering
sw Sewage water
$\lambda$ Spectral

### Abbreviations

DLS Dynamic light scattering
RTE Radiative transfer equation
TDS Total dissolved solids
TEM Transmission electron microscope

## 17.1 Introduction

According to a recent UN (United Nations) World Water Development Report nearly 80% of the wastewater (municipal and industrial waste water) is discharged without any kind of treatment into the environment. Moreover, the existing water treatment technologies are energy intensive and require huge amount of capital cost (Andreozzi et al. 1999; Carlos et al. 2006; Das et al. 2014; Malik et al. 2001; Shannon et al. 2008) and therefore have not able to make significant impact especially in low-income countries. On the other hand water purification through usage of solar energy is a very promising clean low cost method (Aburideh et al. 2012; Hanson et al. 2004; Sharon et al. 2017; Christopher 2017; Panchal 2015). However, these conventional solar desalination systems have relatively low distillate yield and researchers have been working to improve the yield through various modification in the design to effectively improve the two key processes namely evaporation and condensation (Ayber 2009; Sathyamurthy et al. 2016; Panchal and Shah 2014; Balan et al. 2012; Panchal et al. 2015). Clearly, it is imperative to further improve and develop these clean low cost renewable energy based water purification technologies.

The present work explores the idea of improving the former of the two processes through addition of nanoparticles. Addition of nanoparticles has shown to improve the solar absorption capability of the basefluid (Tyagi et al. 2009; Lenert and Wang 2012; Lee et al. 2012; Khullar et al. 2014; Khullar et al. 2017) and hence the evaporation rate (Gan and Qiao 2012; Ishii et al. 2016).

Usually sewage water is contaminated with many solid particles and has unacceptable pH values (McCarty et al. 2011; Qasim 2008). Therefore, firstly, a sample of sewage water was collected and parameters such as total dissolved solids (TDS) and pH were measured. Subsequently, evaporation rate of the sewage water at different nanoparticle volume fractions was carefully measured under an artificial light source (that simulates the sunlight). Two sets of experimental set-ups were employed, which were similar in all respects except for the optical properties of the bottom surface. At the bottom, two extreme conditions were studied namely—black surface and a totally reflective surface (3M solar mirror film). Finally, to collect a sizable amount of distillate, real life outdoor experiments were carried out and the TDS and pH values were measured for the distillate.

## 17.2 Theoretical Basis

### *17.2.1 Basic Idea*

Evaporation of sewage water (and sewage water + nanoparticles) due to direct volumetric interaction with the sunlight depends on host of interdependent parameters and is therefore a highly coupled phenomenon. Parameters such as temperature of the free surface layer and the ambient conditions (temperature and humidity) essentially dictate the evaporation rate. The temperature distribution in general and the free surface temperature in particularly depend on how the sunlight interacts with the working fluid. Sewage water (although highly impure) is relatively transparent in the sunlight wavelength region, therefore not very effective as volumetric absorber. On the other hand, addition of nanoparticles (owing to their excellent solar absorption capabilities) into the sewage water makes it highly absorbing in the sunlight wavelength region. This effectively results in higher temperatures and hence higher evaporation rates.

The more distance sunlight is able to penetrate into the fluid (sewage water in the present work), more uniform is the temperature distribution. On the other hand, addition of nanoparticles (owing to their excellent solar absorption capabilities), result in more pronounced (non-uniform) temperature distribution (and higher surface temperatures). The spatial temperature distribution also depends on the optical properties of the bounding surfaces and is also influenced by the heat transfer mechanisms within the fluid (conduction and convection). Finally, cooling due to evaporation also needs to be incorporated to completely predict the temperature distribution within the fluid.

### 17.2.2 *Quantifying Interaction Between Sunlight and the Nanoparticle Laden Sewage Water*

Sunlight interacts with the nanoparticle laden sewage water through absorption and scattering modes. Figure 17.1 shows the schematic diagram of the evaporation process due to direct interaction of the sunlight with the nanoparticle laden sewage water.

At low volume fractions of nanoparticles (having size comparable to the wavelength of the incident radiation), the interaction of sunlight could be quantified as per simplified form of one dimensional radiative transfer equation (RTE)

$$\frac{\mathrm{d}I_\lambda}{\mathrm{d}y} = -K_{e\lambda,\mathrm{nsw}} I_\lambda \tag{17.1}$$

where $K_{e\lambda,\mathrm{nsw}}$ is the spectral extinction coefficient of the nanoparticle laden sewage water, $y$ is the penetration depth of the sunlight intensity and $I_\lambda$ is the spectral intensity of the incident sunlight.

Extinction of sunlight as it transverse through the nanoparticle laden sewage water takes place both due to absorption and scattering mechanisms. Quantitatively, extinction coefficient could be expressed as

$$K_{e\lambda,\mathrm{nsw}} = K_{\mathrm{abs}\lambda,\mathrm{nsw}} + K_{\mathrm{sca}\lambda,\mathrm{nsw}} \tag{17.2}$$

where $K_{\mathrm{abs}\lambda,\mathrm{nsw}}$, $K_{\mathrm{sca}\lambda}$, nsw are the spectral absorption and scattering coefficients of the nanoparticle laden sewage water respectively.

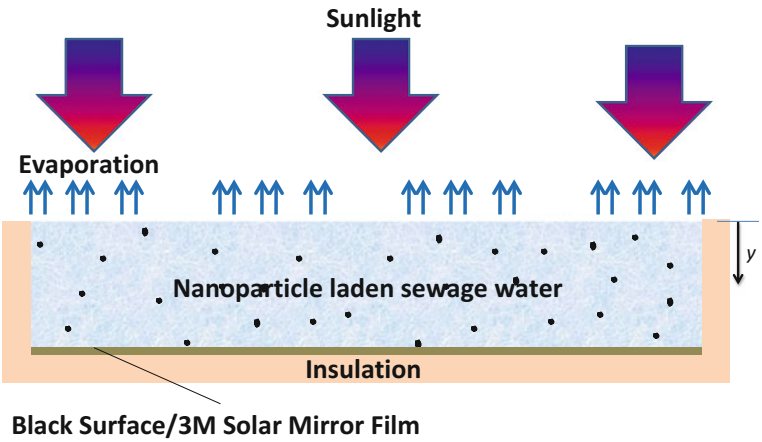


**Fig. 17.1** Schematic showing the evaporation process during direct interaction of the sunlight with the nanoparticle laden sewage water

Furthermore, absorption coefficient of the nanoparticle laden sewage water can be written as

$$K_{\text{abs}\lambda,\text{nsw}} = K_{\text{abs}\lambda,\text{np}+\text{imp}} + K_{\text{abs}\lambda,\text{pw}} \tag{17.3}$$

where $K_{\text{abs}\lambda,\text{np}+\text{imp}}$ is the absorption coefficient of the added nanoparticles and impurities and can be mathematically expressed as

$$K_{\text{abs}\lambda,\text{np}+\text{imp}} = \frac{12\pi f_{\text{v}}}{\lambda}\text{Im}\left\{\frac{m^2-1}{m^2+2}\left[1+\frac{\pi^2 D^2}{15\lambda^2}\left(\frac{m^2-1}{m^2+2}\right)\right]\left(\frac{m^4+27m^2+38}{2m^2+3}\right)\right\} \tag{17.4}$$

and absorption coefficient of the pure water ($K_{\text{abs}\lambda,pw}$) is given as

$$K_{\text{abs}\lambda,\text{pw}} = \frac{4\pi\kappa}{\lambda} \tag{17.5}$$

where $m$ is the normalized spectral complex refractive of the nanoparticles and other impurities and $\alpha$ is the size parameter.

As the size of the nanoparticles and other impurities is comparable to the wavelength of the incident sunlight, therefore independent Rayleigh scattering could explain the scattering mechanism in nanoparticle laden sewage water

$$K_{\text{sca}\lambda,\text{np}+\text{imp}} = \frac{8\pi^4 D^3 f_{\text{v}}}{\lambda^4}\left|\frac{m^2-1}{m^2+2}\right|^2, \tag{17.6}$$

Once the spectral extinction coefficients of nanoparticle laden sewage water have been calculated, next these are employed to quantify the intensity attenuation as the sunlight passes through the nanoparticle laden sewage water. The computation of the attenuation across the entire sunlight spectra gives the energy generation term in the overall energy balance equation.

## 17.3 Experimental Materials and Methods

### *17.3.1 Laboratory Scale Indoor Experiments*

In the present work, amorphous carbon nanoparticles have been employed as these have shown to have broad spectra absorption characteristics (Khullar et al. 2014, 2017). The optical characteristics of these nanoparticles have been described in greater detail elsewhere (Khullar et al. 2017). The nanoparticles have been procured from Sigma Aldrich, and they were found to be of irregular shape with particle size <100 nm. The morphology (size and shape) of nanoparticles [transmission electron microscope (TEM) images, and dynamic light scattering

(DLS) measurements] have been given elsewhere (Khullar et al. 2017). In order to quantify the effect of adding nanoparticles on the evaporation rate, a small container housing the sewage water (and sewage water with various volume fractions of amorphous carbon nanoparticles) was illuminated with an artificial light source (a halogen lamp, color temperature 3400 K in conjunction with a light guide) simulating sunlight. The geometry (miniature cylindrical column, height: 10 mm, diameter: 8 mm) and material (polypropylene) of the container housing the fluid was so chosen that the fluid could absorb maximum amount of energy and nearly all the absorbed energy goes into raising the temperature of the fluid and in changing the phase of the fluid; in other words the aforementioned geometry and material selection ensured that minimum amount of energy goes in heating the walls of the container housing the fluid.

As the light directly interacts with the fluid, it is imperative to carefully engineer the optical properties of the fluid and the bottom surface of the container (housing the fluid). The amount of energy absorbed essentially depends on the penetration depth of the light which in turn depends on the optical properties of the fluid and the optical boundary conditions.

To continuously monitor the evaporation rate, the setups were loaded on to an analytical weighing balance (METTLER TOLEDO XSE104) which could give real time values during the evaporation process. Figure 17.2 shows the pictures as well as the schematics of the experimental setups, which are essentially similar in all respects except for the bottom surfaces.

In our experiment we have used sewage water as the basefluid. To find out difference in evaporation rates at different mass fractions of amorphous carbon nanoparticles, all the experiments were done at similar ambient conditions (ambient

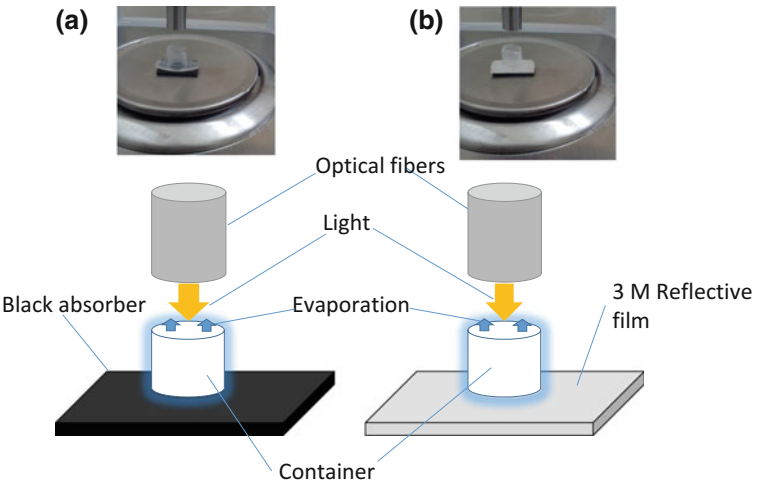


**Fig. 17.2** Photographs and schematics of experimental setups with **a** black and **b** reflective bottom

**Table 17.1** Ambient conditions during the evaporation rate measurement experiments

| Bottom surface | Mass fraction, $mgL^{-1}$ | Ambient temperature °C (error) | Relative humidity, % (error) |
|---|---|---|---|
| Black | 200 | 26.5 (± 0.61) | 71% (± 2.44) |
| | 100 | 26.5 (± 0.70) | 71% (± 6.16) |
| | 50 | 26.6 (± 0.37) | 73.3% (± 0.81) |
| | 0 | 26.7 (± 0.73) | 72.3% (± 4.08) |
| 3M reflective | 200 | 26.8 (± 0.37) | 73.3% (± 1.63) |
| | 100 | 26.5 (± 0.56) | 77% (± 4.24) |
| | 50 | 26.6 (± 0.73) | 70.3% (± 8.98) |
| | 0 | 26.9 (± 0.36) | 68.9% (± 5.79) |

temperatures and relative humidity). The prepared nanofluid was filled into the setups and heated volumetrically with help of a light source connected with optical fibers (light guides). *K* type thermocouples were employed to measure the temperature distribution and the ambient temperature, and a wet and dry bulb hygrometer was used (ZEAL England P501) to measure the relative humidity. Table 17.1 details the ambient temperatures and relative humidity values during the experimentation.

For each mass concentration at least three experiments were carried out to ensure repeatability. This was repeated for both the bottom conditions—black and reflective.

### *17.3.2 Outdoor Experiments Under the Sun*

For getting a sizable amount of distillate, a separate setup has been fabricated which was then employed to produce distillate under the sun. Figure 17.3 shows the photograph and schematic of the same.

There is a small selectively coated (black chrome) metallic container housing the nanofluid (sewage water + amorphous carbon nanoparticles). This container is enveloped with a glass cover which allows the sunlight to interact with the nanofluid as well as serves as the surface on which condensation happens.

Total dissolved solids in sewage and distilled water were calculated experimentally in the lab by evaporating the water and then weighing the residue that left behind after evaporation. pH was measured with a pH meter (THERMO ELECTRON).

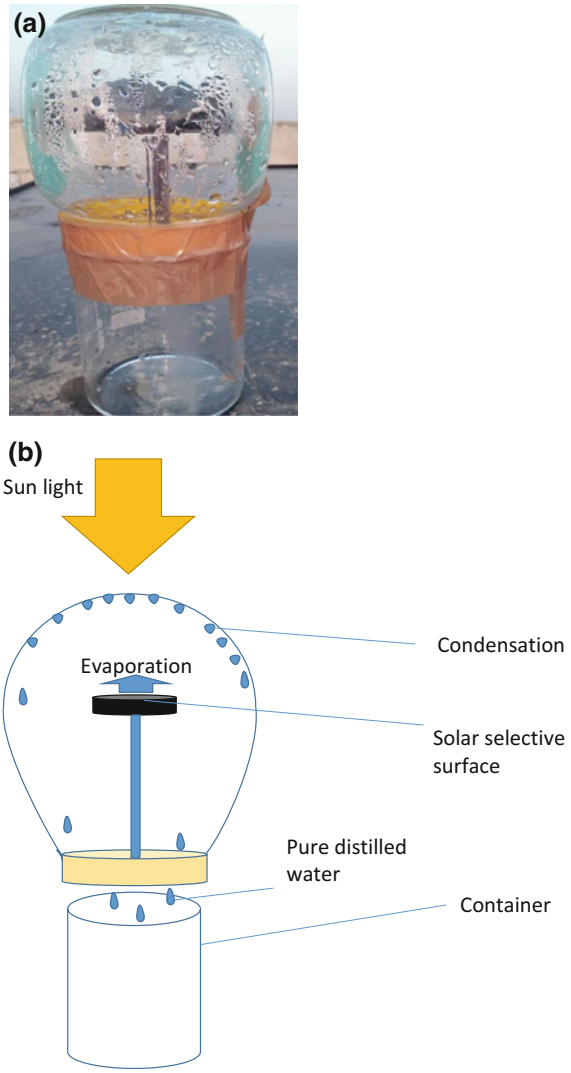


**Fig. 17.3** **a** Photograph and **b** schematic of the experimental setup employed for distillate generation

## 17.4 Results and Discussion

In the indoor (laboratory) experiments, the evaporation rates for the two cases of bottom surfaces (namely black and reflective bottom) at various mass fractions of the nanoparticles have been plotted in Fig. 17.4.

Graphs in Fig. 17.5 clearly reveal that for a given illumination period (22 min in the present study), the total mass evaporated increases with increase in the mass fraction of the nanoparticles. Furthermore, black bottom is far more effective

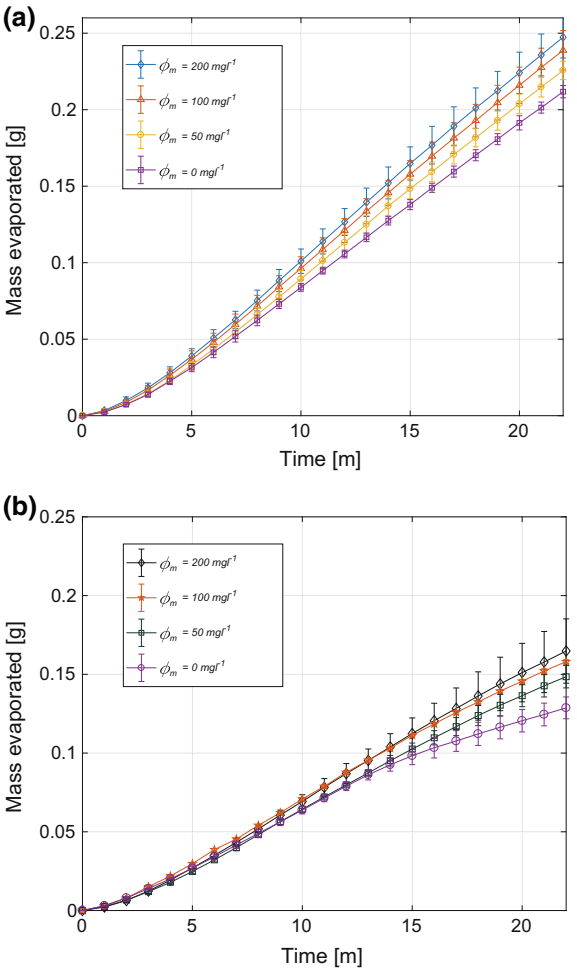


**Fig. 17.4** Graphs showing the mass of water evaporated as a function of time for four different mass fractions of nanoparticles for **a** black bottom and **b** reflective bottom surfaces respectively

(irrespective of nanoparticle addition) than a reflective bottom clearly indicating the criticality of choosing the bottom surface.

Furthermore, in order clearly understand the reasons for evaporation rate enhancements (in the indoor laboratory experiments); temperature distribution in each case was also recorded. Figure 17.6 shows the temperature at top and bottom layer of nanofluid during evaporation for different mass fractions for the black and reflective bottom cases. It is clearly apparent from Fig. 17.6 that there is pronounced temperature spread in case of reflective bottom as compared to the black bottom. This may be attributed to the fact that opposed to black bottom there is no natural convection effects in case of reflective bottom. As the top layer is the hottest part in the case of reflective bottom case, the energy redistribution within the liquid column takes place primarily through conduction. On the other hand, in case of

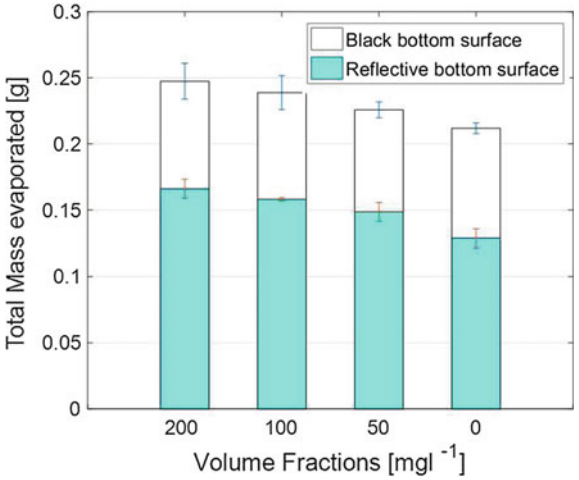


**Fig. 17.5** Mass evaporated as a function of nanoparticle mass fraction for black and reflective bottom cases

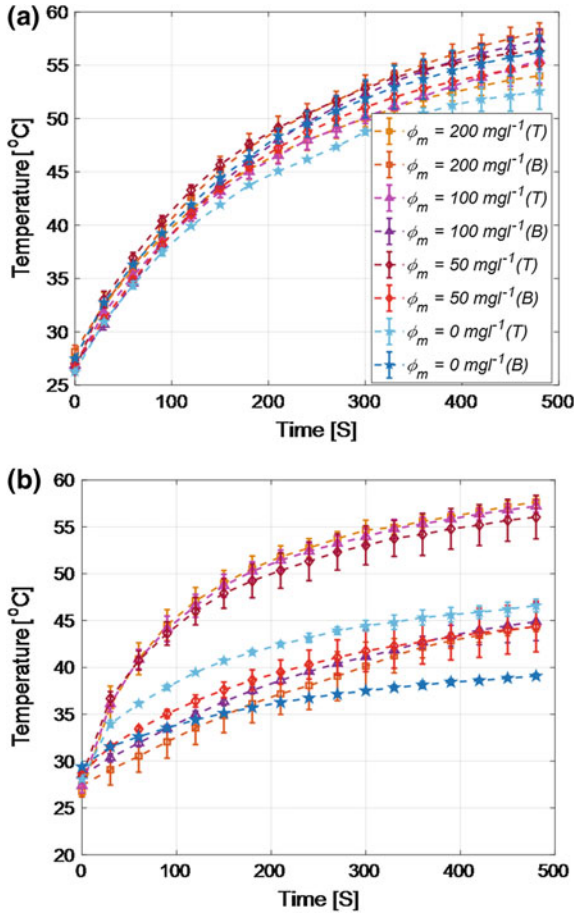


**Fig. 17.6** Graphs showing the temperature at bottom (B) and top (T) layer in nanofluid as a function of time for four different mass fractions of nanofluid having **a** black bottom surface, and **b** reflective bottom surfaces respectively

black bottom surface, the hottest layer being the layer in direct contact with the bottom layer, tends to come up owing to boyancy effects and therefore very little temperature spread across the liquid column.

Also Fig. 17.7 details the average temperatures for the two cases (for various nanoparticle concentrations). It may be observed from these graphs that addition of nanoparticles in case of reflective bottom has more pronounced effect on the average temperature rise as compared to the black bottom case. This could be understood from the fact that in black bottom surface case, essentially two components take part in the absorption process (namely black surface and the amorphos carbon nanoparticles). Whereas in the reflective bottom case, nanoparticles are soley responsible for the absorption of light and hence the temperature gain.

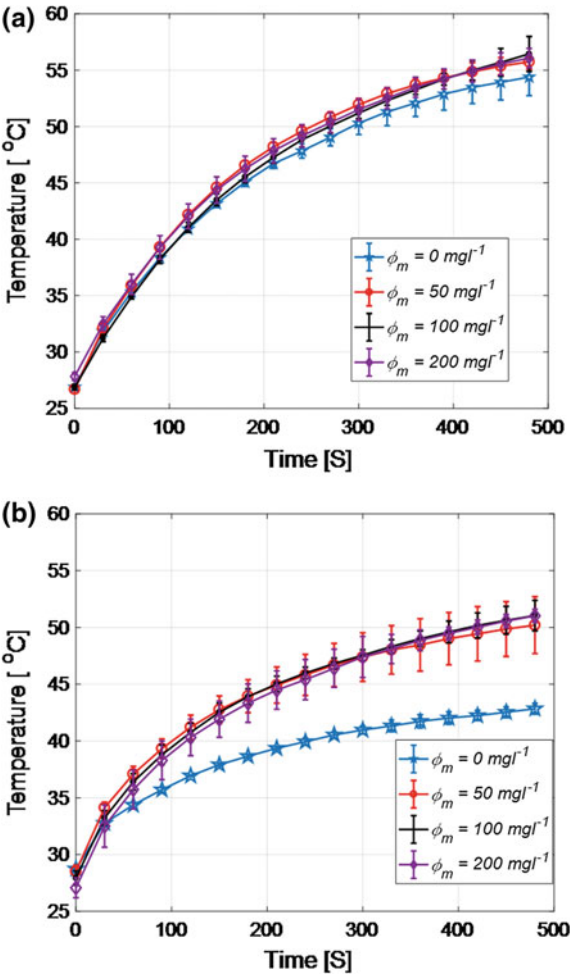


**Fig. 17.7** Graph showing the average temperature in nanofluid as a function of time for four different mass fractions of nanofluid having **a** black bottom surface, and **b** 3M film reflective bottom surface

**Table 17.2** Properties of sewage water sample before and after distillation

| Properties | Sewage water | Distilled water |
|---|---|---|
| Color | Yellowish | Colorless |
| Odor | Stale | Odorless |
| pH | 9.04 | 7.49 |
| TDS | 743 $mgL^{-1}$ | 126.5 $mgL^{-1}$ |

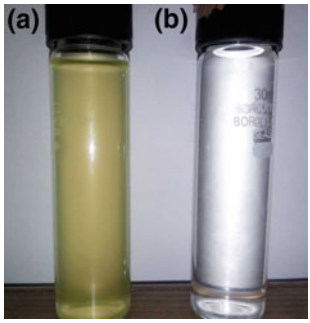


**Fig. 17.8** Photographs of the sewage water sample **a** before and **b** after purification

Finally, Table 17.2 and Fig. 17.8 detail the properties and photographs of the sewage water before and after distillation.

## 17.5 Conclusion

Experimental results indicate that addition of amorphous carbon nanoparticles can effectively improve the evaporation rate of sewage water. Furthermore, if we use black coating at bottom surface in addition of nanoparticles, significant evaporation rates could be achieved. Finally, TDS and pH measurements show that volumetric heating of sewage water in the presence of nanoparticles could indeed prove to be an efficient and reliable method for sewage water purification. Given the encouraging preliminary results, it is worthwhile to investigate further (both theoretically and experimentally) these volumetric heating based sewage water purification systems.

**Acknowledgements** The authors gratefully acknowledge the support provided by Mechanical Engineering Department, Thapar Institute of Engineering and Technology, Patiala, India.

## References

Aburideh H, Deliou A, Abbad B, Alaoui F, Tassalit D, Tigrine Z (2012) An experimental study of a solar still: application on the sea water desalination of Fouka. Procedia Eng 33:475–484

Andreozzi R, Caprio V, Insola A, Marotta R (1999) Advanced oxidation processes (AOP) for water purification and recovery. Catal Today 53:51–59

Ayber HS (2009) A review and comparison of solar distillation: direct and indirect type systems. Desalin Water Treat 10:321–331

Balan R, Chandrasekaran J, Shanmugan S, Janarthanan B, Kumar S (2012) Review on passive solar distillation. Desalin Water Treat 28:217–238

Carlos A, Huitle M, Ferro S (2006) Electrochemical oxidation of organic pollutants for the wastewater treatment: direct and indirect processes. Chem Soc Rev 35:1324–1340

Das R, Ali ME, Hamid SBA, Ramakrishna S, Chowdhury ZZ (2014) Carbon nanotube membranes for water purification: a bright future in water desalination. Desalination 336:97–109

Gan Y, Qiao L (2012) Optical properties and radiation enhanced evaporation of nanofluid fuels containing carbon-based nanostructures. Energy Fuels 26:4224–4230

Gnanaraj SJP, Ramachandran S, Christopher, DS (2017) Enhancing the design to optimize the performance of double basin solar still. Desalination 411:112–123

Hanson A, Zachritz W, Stevens K, Mimbela L, Polka R, Cisneros L (2004) Distillate water quality of a single- basin solar still: laboratory and field work. Solar Energy 76:635–645

Ishii S, Sugavaneshwar RP, Chen K, Dao TD, Nagao T (2016) Solar water heating and vaporization with silicon nanoparticles at Mie resonances. Opt Mater Express 6:640–648

Khullar V, Tyagi H, Hordy N, Otanicar T, Hewakuruppu Y, Modi P, Taylor R (2014) Harvesting solar thermal energy through nanofluid-based volumetric absorption systems. Int J Heat Mass Transf 77:377–384

Khullar V, Tyagi H, Bhalla V (2017) Potential heat transfer fluids (nanofluids) for direct volumetric absorption-based solar thermal systems. J Therm Sci Eng Appl 10(1)

Lee BJ, Park K, Walsh T, Xu L (2012) Radiative heat transfer analysis in plasmonic nanofluids for direct solar thermal absorption. J Solar Energy Eng 134(2):1–6

Lenert A, Wang EN (2012) Optimization of nanofluid volumetric receivers for solar thermal energy conversion. Sol Energy 86(1):253–265

Malik MA, Ghaffar A, Malik SA (2001) Water purification by electrical discharges. Plasma Sources Sci Technol 10:82–91

McCarty PL, Bae J, Kim J (2011) Domestic wastewater treatment as a net energy producer. Environ Sci Technol 45:7100–7106

Panchal HN (2015) Enhancement of distillate output of double basin solar still with vacuum tubes. J King Saud Univ Eng Sci 27:170–175

Panchal HN, Shah PK (2014) Investigation on performance analysis of a novel design of the vacuum tube-assisted double basin solar still: an experimental approach. Int J Ambient Energy

Panchal H, Patel N, Thakkar H (2015) Various techiques for improvement in distillate output from active solar still. Int J Ambient Energy 1–37

Qasim SR (2008) Treatment of domestic sewage by using solar distillation and plant culture. J Environ Sci Health 13:615–627

Sathyamurthy R, Samuel DGH, Nagarajan PK, Arunkumar T (2016) Geometrical variations in solar stills for improving the fresh water yield. Desalin Water Treat 10:1–15

Shannon MA, Bohn PW, Elimelech M, Georgiadis JG, Marin BJ, Mayes AM (2008) Science and technology for water purification in the coming decades. Nat Publishing Group 452:301–310

Sharon H, Reddy KS, KrithikaD, Philip L (2017) Experimental performance investigation of tilted solar still with basin and wick for distillate quality and enviro-economic aspects. Desalination 410:30–54

Tyagi H, Phelan P, Prasher R (2009) Predicted efficiency of a low-temperature nanofluid-based direct absorption solar collector. J Solar Energy Eng 131(4)

# Chapter 18
# Solar Assisted Gasification


**Anirudh Singh, Ankur Kaundal, Raj Krishna Jha, Satvasheel Powar and Atul Dhar**

**Abstract** Gasification is a thermo-chemical conversion process, which is used to gasify any carbonaceous substance. On the application of heat, and/or under a controlled amount of oxygen, carbonaceous substances break down to form the synthetic gas. Use of gasification may be attributed to a wide range of applications, from biomass conversion for energy production to municipal solid waste management. The gasification process is endothermic with an operating temperature range of 480–1650 °C. In conventional gasification process, some part (∼5–20%) of feedstock is burnt in controlled air to supply the process heat. Any auxiliary heating source such as solar heating reduces the heat requirements from partial combustion. Moreover, the side effects of combustion viz. product gas contamination, need for purification attachments, etc. can be partially averted. Higher temperatures of the concentrated solar radiations drive the chemical reaction to the near-complete utilization of carbonaceous content. This chapter discusses different approaches for solar assisted gasification reported in the literature and the future prospects.

**Keywords** Biomass · Gasification · Solar energy · Thermo-chemical Conversion

## 18.1 Introduction

Biomass is a renewable and sustainable source of energy, which is obtained from organic matters. As per International Energy Agency, "Biomass is any organic, i.e. decomposable matter obtained from plants and animals on a renewable basis" (IEA Homepage 2018). Biomass is obtained from living or recently living organisms such as wood, rice husk, and wastes. Biomass differs from fossil fuel in the sense that fossil fuels are obtained from decayed living organisms, and combustion of

A. Singh · A. Kaundal · R. K. Jha · S. Powar · A. Dhar (✉)
School of Engineering, Indian Institute of Technology Mandi,
Mandi 175005, Himachal Pradesh, India
e-mail: add@iitmandi.ac.in



H. Tyagi et al. (eds.), *Advances in Solar Energy Research*, Energy, Environment, and Sustainability, https://doi.org/10.1007/978-981-13-3302-6_18

fossil fuels leads to greater emissions of $CO_2$ whereas biomass is obtained from living organisms and combustion of biomass leads to much lesser $CO_2$ emissions making it "carbon neutral". Carbon neutral here means that as biomass is formed i.e. from living plants, it stores $CO_2$ in its bonds and when it is broken down for fuels it again releases $CO_2$ into atmosphere. This cycle of utilisation of $CO_2$ for formation and release of the same while combustion (or any other process) makes the biomass carbon neutral. Gasification is a thermo-chemical process of converting solid biomass into gaseous fuels, mainly synthetic gas ($CO_2$ + $H_2$). In conventional gasification, the biomass is introduced to a limited quantity of air or sub-stoichiometric air with the required heat for gasification provided by energy released from reactions in the pyro oxidation zone of the gasifier (Reed 1988). In solar assisted gasification, the energy required to gasify the biomass is obtained from solar energy instead of conventional coal-fired plants or auto-thermal processes, thereby producing a greenhouse gas (GHG) neutral fuel and enhancing gasifier efficiency. There is also the possibility of getting producer gas with higher $H_2$ content and lower $CO_2$ emissions. In this chapter, various gasification techniques and solar assisted gasification are discussed.

## 18.2 Biomass as an Alternative Source of Energy

As per the reports of the International Energy Agency, bioenergy provides 14% of the primary energy supply of the world (World Energy Resources 2016). With the limited reserves of fossil fuels and the growing concerns of global warming, biomass can prove to be a viable alternative to the conventional sources of energy. Biofuel is considered as GHG-neutral because the carbon in biomass is bound to be released in the form of $CO_2$ to complete carbon cycle. The burning, gasification, fermentation or any other synthesis process of biomass results in no net increase of $CO_2$. In addition to this, the low sulphur content, ease of availability, shorter life cycle, and lower costs of biomass does make it suitable for being one of the major sources of primary energy. Currently biomass supplies $50 \times 10^{18}$ J of energy per year, which is around 77% of the renewable energy and has a technical capability to provide around 50–1500 EJ per year. Bioenergy contributes 32% of the total primary energy use in India with 70% of the total population (most of from rural parts of the country) dependent on it.[1] Currently, the major contributors are fuelwood, sugarcane bagasse, maize, rice straw, palm oil, animal by products and other forest-based products. From Fig. 18.1, we can infer that woody biomass is the major contributor of biomass at present. However, reports from World Energy Resources (World Energy Council 2016) suggests that the use of agriculture by-products like straw, husks, corn leaves, sugarcane bagasse for bioenergy is

[1]European Business and Technology Centre "Snapshot Biofuels and Bio-Energy in India Biofuels and Bio-Energy in India."

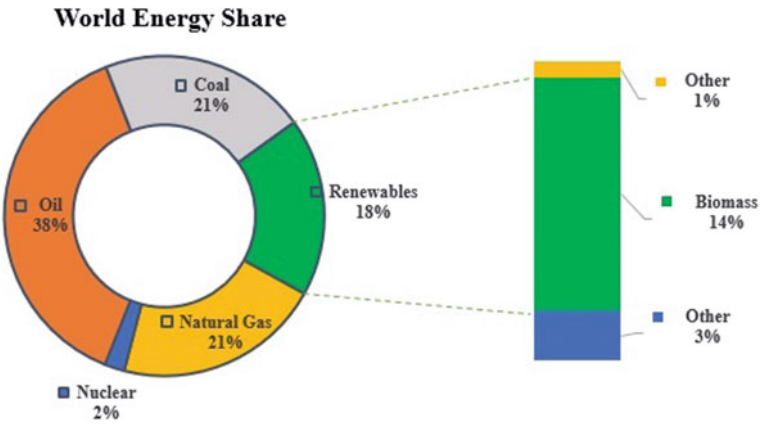


**Fig. 18.1** Share of bioenergy in global primary energy (World Energy Resources 2016)

continuously increasing. The use of municipal and industrial wastes, (which would otherwise be disposed of in landfills) for producing $CH_4$ and other gases not only provides a means of energy production but also reduces GHG emissions and facilitates waste management.

## 18.3 Gasification

Various physical, thermochemical and biochemical processes are applied to produce energy from biomass. Physical processes include densification of biomass by processes like drying, briquetting, and pelletization. Figure 18.2 illustrates various conversion routes that are employed for the utilization of biomass. Gasification has several advantages over other biomass conversion processes. Axelson et al. (2012) found the maximum exergy efficiency of gasification followed by synthesis. Among all the conversion routes, biochemical routes are comparatively slow, produce water-rich products as compared to gasification (Sikarwar et al. 2016). Gasification process involves storing the energy in the form of chemical bonds, which can be utilized later by breaking these bonds (oxidation). Gasification is achieved in the presence of mediums like air, steam, oxygen, carbon dioxide or a mixture of steam and air.

The product gas obtained from air gasification has lower calorific value than that obtained from oxygen gasification (Bridgwater 1995). Gasification can be either direct in which the air is used to generate the heat for pyrolyzing biomass through exothermic reaction (the heat can also be supplied by combustion of volatile tars or from charcoal) or indirect in which the heat from an external source is provided to the reactor. Indirect gasification is more complicated than direct gasification and so

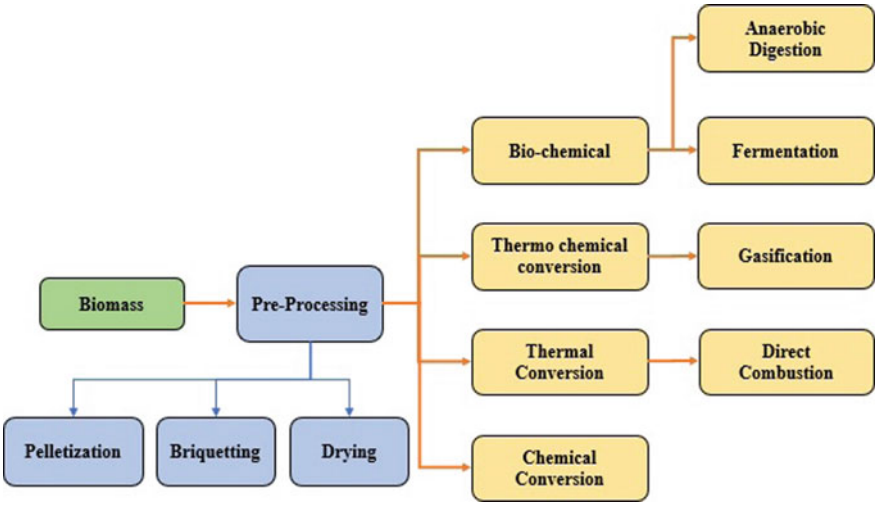


**Fig. 18.2** Conversion routes of biomass

direct gasification is mostly used (Prabowo et al. 2014). Gasification can be represented by the reaction:

$$\text{Biomass} + H_2O + O_2 \rightarrow H_2, CO, CO_2, H_2O, CH_4 + \text{tar} + \text{char} + \text{ash} \quad (1)$$

Following processes occur during gasification of biomass in a gasifier:

1. Drying
2. Pyrolysis
3. Partial combustion
4. Reduction

### *18.3.1 Drying*

There are two types of biomass: wet biomass (molasses, starch and manures) and dry biomass (wood) (Reed 1988). Wet biomass is used for biological processes like fermentation and anaerobic digestion whereas thermal processes function better with biomass with moisture content less than 50%. Usually, raw biomass has moisture content around 60–80% (Paepatung et al. 2009). Increased moisture content leads to decreased biofuel calorific value and increased formation of tar leading to decreased overall system efficiency. The increase in moisture content leads to a decrease in temperature of producer gas causing slow reaction rates and a corresponding decrease in quality of producer gas (Kaushal et al. 2011). Moisture content in biomass should be around 10–25% because inadequate moisture content

reduces the quality of the producer gas (Reed 1988). Drying of the biomass is necessary when its moisture content is greater than 25%.

Drying of biomass is done in two ways: (i) Mechanical drying like centrifuging, filtering, shedding, (ii) Thermal drying with direct or indirect heating.

### 18.3.2 Pyrolysis

Pyrolysis is defined as the thermal breakdown of biomass into smaller molecules like charcoal, tar, wood-oils, and gases (CO, $CO_2$, $H_2$, $CH_4$ and $H_2O$). There is heating of biomass without the presence of air up to around 500 °C. Pyrolysis begins around 200 °C. It is a highly irreversible process. Pyrolysis can either be slow or fast depending upon the heating rate. Slow pyrolysis results in the formation of biochar, takes considerably long time and has longer residence time whereas fast pyrolysis produces mostly bio-oil and has shorter residence time with rapid cooling of vapors (Balat et al. 2009). The product compositions are dependent on the parent biomass, pyrolysis temperature, moisture content and the rate of heating of the biomass. With the increase in temperature, there is an increase in the bio-oil and decrease in Syngas. Kabir et al. (2015) observed maximum yield of bio-oil from Municipal Green Waste occurs at 500–550 °C temperature range.

### 18.3.3 Partial Combustion

The biomass is treated with a limited supply of air for partial combustion. It is one of the exothermic reactions of the gasifiers, which provides the heat for drying, pyrolysis, and reduction. The tar gases and char from pyrolysis serve as a fuel for combustion. The temperature for partial combustion should be high (>1100 °C) (Dayton 2002) to crack or burn the tar present in the gasifier. The solid carbonized fuel reacts with the oxygen of the air to form carbon monoxide.

### 18.3.4 Reduction

The reduction is considered as the reverse process of combustion. In combustion, there is a combination of oxygen with the gases whereas in reduction the oxygen atoms are removed. In the reduction zone $CO_2$ is reduced to CO whereas $H_2O$ is reduced to $H_2$ as described in Eqs. 2 and 3. The various reactions occurring in the reduction zone are Boudouard reaction, Water Gas reaction, Water Shift reaction and the Methanation reaction (Sharma 2008). Reduction zone of a downdraft gasifier can either be cylindrical (Stratified Gasifier) or diverging (Imbert Gasifier).

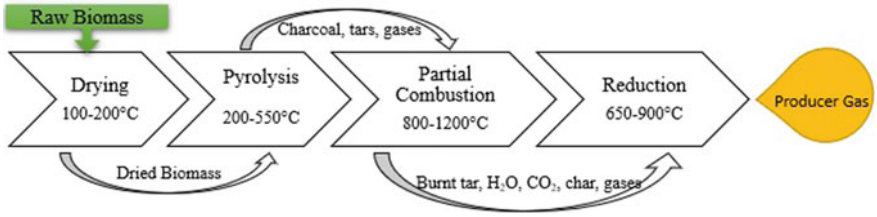


**Fig. 18.3** Gasification process

There is a continuous decrease in the temperature of the producer gas along the length of the reduction zone of the biomass gasifier because most of the reactions in this zone are endothermic (Sharma 2008).

$$C + CO_2 \rightarrow 2CO \tag{2}$$

$$C + H_2O \rightarrow CO + H_2 \tag{3}$$

Figure 18.3 is a summary of all the processes occurring during gasification. The raw biomass is fed to the gasifier to be first dried at around 100 °C with the resulting dried biomass pyrolyzed in absence of air to produce charcoal, tar which undergoes partial combustion at high temperatures and the char obtained undergoes reduction and is further burnt to produce more gaseous species and provide the heat for the reduction reactions. Finally, the exhaust gas is usually obtained at temperatures as high as 800–1000 °C depending on the type of gasifier (Dayton 2002; Kirkels and Verbong 2011; Han and Kim 2008; Overend 1999).

## 18.4 Methods for Improvement in Performance of Gasification Process

There are several methods used to increase the efficiency of a gasifier by either increasing the temperature of gasification or by reducing the carbon dioxide emission. From thermodynamics, we can derive that at higher temperatures we will get high exergy and efficiency improvement such as (a) Molten Salts in Gasifier, (b) Supercritical Water, (c) Plasma Gasification, (d) Solar Gasification employed for improvement in performance of solar gasifiers are discussed in the following subsections.

(a) Molten Salts in Gasifiers

Molten Salts, as the name signifies, are the melted forms of salts which are used in the gasification system directly or indirectly. Usually, the melting point of the salts is 200 °C, and the maximum allowable temperature is kept at 600 °C

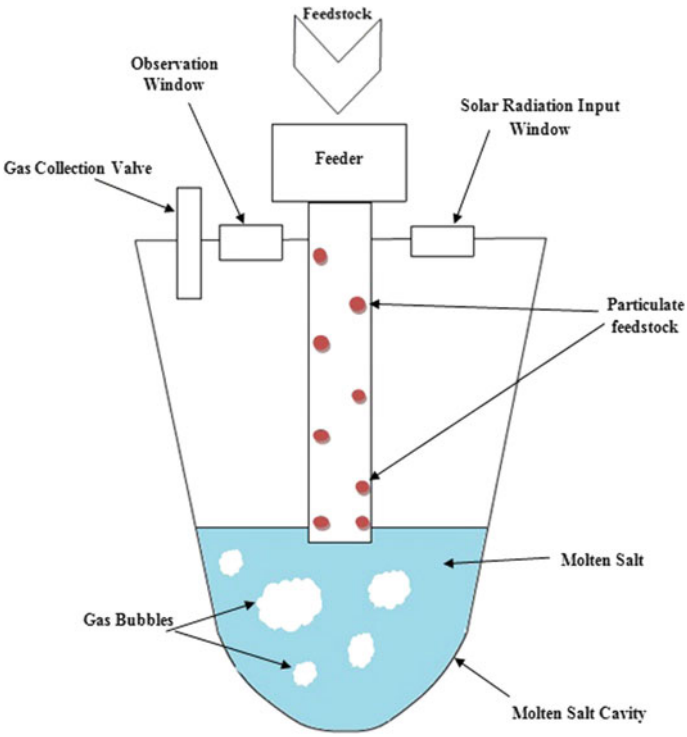


**Fig. 18.4** A simple layout of direct use of molten salts in gasification

(Hasuike et al. 2006). Temperature variation is between 500 and 700 °C (Hasuike et al. 2006). In various research setups molten salts are used mainly by two methods that are:

i. Direct exposure of the biomass to the molten salt

In this method, the feedstock [mostly in particulate form (size 1–2 mm)] is fed into the liquid molten salt, and then the reaction takes place accordingly (Hasuike et al. 2006). Direct injection of particles into the molten salt, enables their fast heating. The molten salts are said to absorb unwanted residual compounds like char, ash and sulfur in the gasification gas (Sugiura et al. 2007; Adinberg et al. 2004). Figure 18.4 shows a simple setup of the system used for molten salt gasification.

ii. Indirect transfer of heat by use of molten salts as a medium

In this method, we heat molten salts by any heat source and then transfer it to the target area. Molten salt is not in direct contact with the biomass. Molten salts provide heat transfer advantage as well as a chemical advantage. Due to the high thermal conductivity of molten salts, the biomass is exposed to the desired amount of heat in the gasifier. The heat transfer also improves between the wall and the

**Table 18.1** Some common molten salts

| Molten salts | Thermal conductivity (W/mK) |
|---|---|
| $NaNO_3$–$KNO_3$ (50–50 mol%) | 0.4215 (Hasuike et al. 2006) |
| $Li_2CO_3$(32%) + $Na_2CO_3$(33%) + $K_2CO_3$(35%) | 0.87 (Hathaway and Davidson 2017) |

biomass because of the convection effect of the fluid (Jin et al. 2005). Due to catalytic action of molten salts, the alkali metals present in the molten salt accelerate the reaction by breaking the β (1,4)—glycosidic bonds found in the cellulose molecules (Jin et al. 2005). The presence of salts has increased the product yield (i.e., the blend of $H_2$ and CO) and has almost nulled the tar yield (Adinberg et al. 2004). Various salts that are used are carbonates and chlorides of Sodium, Zinc, Lithium, and Potassium (Adinberg et al. 2004).

Table 18.1 shows thermal conductivities of some commonly used molten salts.

(b) Supercritical Water

Supercritical water gasification is a technique which is very much favorable for a high moisture content biomass. In supercritical water gasification (SCWG), gasification is performed at high pressures and temperatures. Supercritical water (temperature 374.2 °C and pressure 22.1 MPa) is a single phase that inhibits the characteristics of both liquids and gases. At such high temperatures, the physical properties of water change to a great extent, e.g., decrease in thermal conductivity, density and viscosity (Calzavara et al. 2005). Also, heat exchange is much more effective due to high diffusivity and high transport properties of supercritical water.

The main advantage of supercritical gasification is that we can achieve a complete carbon conversion (Luterbacher et al. 2009). According to Boukis et al. (2002), complete gasification can be achieved at a temperature of 600 °C and pressure of 25 MPa. Moreover, SCWG does not require the removal of moisture from the biomass as it is required in other gasification processes (Luterbacher et al. 2009). According to studies in recent years the yield of desirable syngas composition is directly proportional to the increase in the temperature of the gasifier. Hydrogen yield increases significantly with an increase in temperature whereas the yield of carbon monoxide is highest for high-temperature range (around 920 K) (Voll et al. 2009). Though supercritical gasification has many merits still some disadvantages have to be considered. Char and tar formation is less than the conventional gasification bit due to small apparatus and tubing, that has to be considered. Due to high pressure working and liquids involved, corrosion of the reactor material is also a limiting factor (Boukis et al. 1999; Mitton et al. 2000). Another limitation is the hydrogen exposure of the inner components of the reactor causes the material to weaken and reduce its resistance to withstand high pressure. Aging of a material is defined as change in appearance, deposition of oxide or hydroxide layer on a surface due to continuous exposure to chemicals. Calzavara et al. have described this phenomenon as hydrogen aging in which reactor tubes are damaged due to hydrogen exposure. Due to this reason only, a specific set of geometries and materials can be used for supercritical gasification (Calzavara et al. 2005).

(c) Plasma Gasification

Plasma gasification is high-temperature gasification in which electric heat is used as a heat source for the gasification process. In conventional gasification processes which work around 700–850 °C, considerable amounts of char and tar are produced which are undesirable for the environment and increase the complexity of the process because further treatment is required in that case. However, if we use a high-temperature source the chances of tar production significantly decrease. Recent researches have credited it as the environmentally friendly process (Mountouris et al. 2008). The final product gas is purer than the conventional gasification product gas, and there is no ash at the end of the process. Waste volume is reduced to a great extent (Leal-Quiros 2004). Also, complex feed system is not needed because we can supply feedstock directly without preprocessing.

(d) Solar Gasification

In solar gasification, we use solar energy as the heat source for the gasification process. Various methods are there for the transfer of solar energy on the biomass, but in most studies, direct solar irradiation is used. Due to solar energy, a large portion of useful syngas is saved, which is partially burned in the conventional gasifiers for providing the process heat. The emphasis of this chapter is the use of solar energy in the gasification process, which is described in detail in the next section.

## 18.5 Solar Assisted Gasification

Gasification, as discussed in the previous section is a process of conversion of biomass into useful products by heating at various temperature ranges. However, the main drawback of conventional gasification is that considerable yields of syngas per ton of feedstock are lost because some feedstock is to be combusted to provide energy for pyrolysis (Ravaghi-ardebili et al. 2015). So, there is a need for an external heating source so that the yield of product gas can be increased.

Various researchers around the world have worked to find alternate energy sources, and the most efficient, effective, abundant and reliable source is the solar energy. In solar assisted gasification optical surfaces concentrate solar energy into the reactor such that there is multiple times increment of the solar intensity thereby causing the temperature of the reactor to be higher than 1000 °C. There are various advantages of the solar integration with the biomass gasification. Some of them are:

- For conventional gasification, sometimes we require an oxidizer (such as oxygen) because air is not enough for combustion. However, in solar integration, no such oxidizer is required (Gregg et al. 1980).
- We can achieve almost double the yield of product gas with solar integration as compared to the conventional technique because no coal/biomass is burned in this process (Gregg et al. 1980; Janajreh et al. 2010; Frosch 1981).

- Around 40% of the total solar energy incident on biomass is saved in the product gas thus increasing the stored energy in product gas (Gregg et al. 1980; Janajreh et al. 2010; Zedtwitz and Steinfeld 2003). Taylor et al. (1983) found out that there is an increase in the calorific value of the producer gas by 10–20% with solar gasification due to gasification of charcoal produced during pyrolysis.
- The product gas is almost free of any unwanted effluents and is cleaner (Zedtwitz and Steinfeld 2003). In the case of solar gasification of coal, the $CO_2$ is reduced to approximately one third as compared to the conventional gasification (Kodama et al. 2001; Aoki et al. 2000).
- There are no requirements of heat exchangers (If direct solar irradiation is used) thus the system remains simple.

Since biomass gasification occurs at temperatures below 1300 °C, the concentrated solar reactor used can be of metal alloys instead of ceramic materials used for high temperatures having low thermal shock resistance and cycle lives. Solar energy can be stored in chemical form by using it to drive endothermic chemical reactions to produce liquid fuels. Solar gasification occurs at higher temperatures as compared to conventional gasification with shorter residence time due to which at high temperatures the producer gas is composed mainly of $H_2$, CO, $CO_2$, and $CH_4$ with increased carbon conversion efficiency (Woodruff and Andrews 2008).

### *18.5.1 Solar Energy Collection*

Earth's surface especially in tropical countries (like India) are abundant in direct solar radiations. The big challenge in these countries is to harvest this solar radiation, and many methods have been developed to accomplish this task. Some applications of solar technologies that have been in common use are like solar water heaters, solar cookers, solar dryers, solar air conditioning, solar chimneys etc. (Thirugnanasambandam et al. 2010).

Solar collectors being direct and simple in operation are therefore admitted for providing a power source in the process of gasification. The solar collector is the significant part of any solar thermal system as it collects the solar radiation and passes it on for further processing. This device consists of a collecting arrangement which absorbs the incident radiation (may or may not change its direction) and passes the thermal energy to a carrier medium (mostly a fluid). The principle followed is that the internal energy of a carrier substance is increased by the solar radiation and then this energy is transferred to the required site. Solar collectors are broadly divided into two categories:

1. Concentrating type solar collector—In this type of collector we have a much large catchment area (for solar radiations), and the rays are concentrated on a particular point (or line) where our energy transfer fluid is present. After that, the

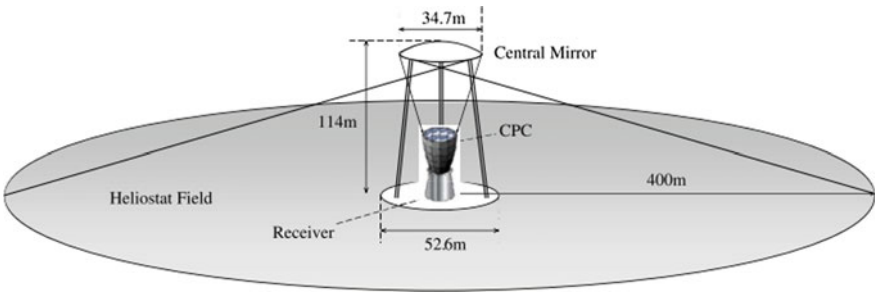


**Fig. 18.5** A simple layout of a heliostat field and solar tower for a particular facility (Hasuike et al. 2006). Reprinted from Solar Energy, Vol 80, Hiroshi Hasuike, Yoshio Yoshizawa, Akio Suzuki, Yutaka Tamaura, 8, Copyright (2006), with permission from Elsevier

heat from high internal energy fluid is transferred to the site of application or can be stored using thermal storage devices.

2. Non-concentrating type solar collector—Here, the area exposed to solar radiations is itself the heat absorbing area. This type of solar concentrator is used for low-temperature applications.

Figure 18.6 shows the various types of solar collectors. Collectors can be simple and of reasonable sizes like the flat plate collectors or evacuated type collectors which commonly find applications in domestic use or their size can extend into hectares like that of a heliostat collector field. Temperature ranges also vary from as low as 30–200 °C (approx.) in the stationary collectors and as high as 100–2000 °C (approx.) in a heliostat field (Kalogirou 2004). In heliostat fields a whole piece of land is covered with reflector mirrors which concentrate solar radiations on a single point which is located at a height and that point's location is properly defined in a solar power tower. Figure 18.5 shows schematic of a solar power tower (Fig. 18.6).

From the review of various papers, it is found that the reactors used are mostly directly irradiated and heliostat fields are most widely used sources of radiation collection method for solar gasification (Gregg et al. 1980; Piatkowski 2009; Arribas et al. 2017).

### *18.5.2 Solar Reactor*

To achieve the gasification reaction, we need a device to concentrate solar radiations on the biomass. These devices are commonly known as solar reactors. Based on the type of irradiation, solar reactors can be divided into two types:

a. Directly Irradiated Solar Reactors
In direct irradiation, radiations directly fall upon the reaction site. In this type, we use an opening (mostly a quartz window) through which our solar radiations

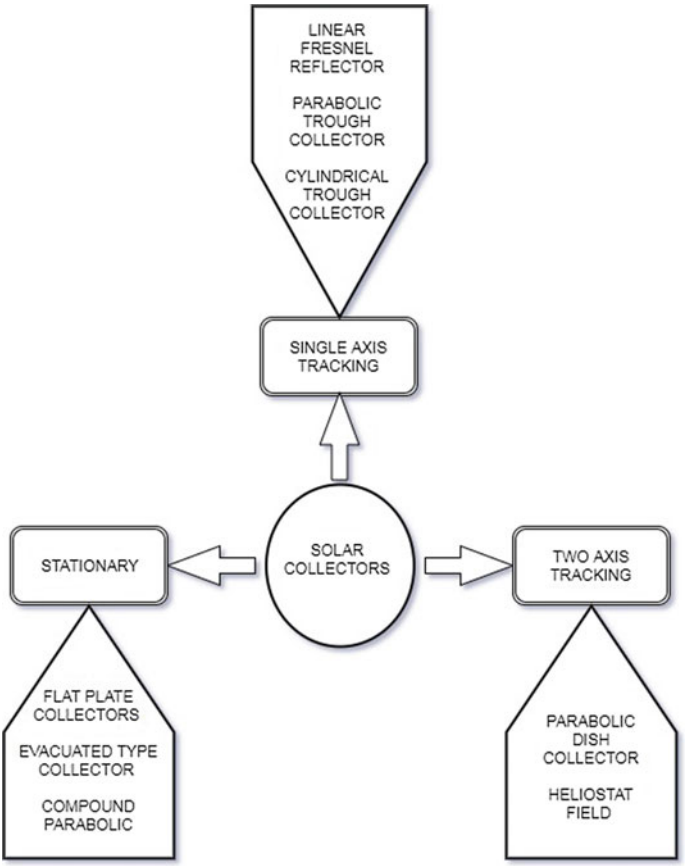


**Fig. 18.6** Types of solar collectors

can pass and irradiate the biomass. It has a more efficient energy transfer as compared to other methods. It enhances photochemical kinetic in adequate conditions. The only disadvantage in this method is to maintain the transparency of the window because with time it alters, and it reduces the efficiency of the reactor to a great extent (Steinfeld et al. 2001). Reactors with silica glass have been reported to be crystallized due to exposure to high temperature. So, the windows are to be cleaned or changed from time to time (Lichty et al. 2010).

b. Indirectly Irradiated Solar Reactor
In this type of solar reactor, heat is absorbed by the cavity of the reactor and then passed on to the reactants. It eliminates the function of the window.

However, due to that, there is less absorption.

A solar reactor is a combination of reaction space where biomass is present and a solar collection system whose role is to collect the solar radiations and focus it on the reaction space.

1. Gasification reactors are considered to be of two types, depending on the source of the energy used for gasification: Autothermal Reactors—In which the energy required for gasification is extracted from the biomass itself. This is itself is the main disadvantage as much of the energy is consumed. This energy can be saved by using an external heat source. Their main advantage is that they have a simple design and construction is cheaper as compared to the advanced versions. They can be easily commercialized if the requirement is quite high.
2. Allothermal Reactors—When some external heat source is used to perform combustion and gasification reactions they are considered to be allothermal gasifiers. Some of the significant disadvantages of these reactors are:

   - Complex design and geometry.
   - In case of solar gasifiers, the reactor body is subjected to intermittent solar radiations, which cause thermal shocks and failure of the body.

Many solutions are there like making a ceramic body and other alloy bodies, but that will increase the manufacturing cost.

Table 18.2 shows the trends of solar reactors (or gasifiers) since the 1980s, in which the concept of solar gasification was started (Antal 1976). Many researchers have tried to fabricate a working solar gasifier. Most of the researches have been lab-based and simulated solar radiation was used. Gregg et al. (1980) published the first research (1980) on a full scale solar gasifier in which packed bed approach was used and biomass was directly irradiated by solar energy. An L shaped reactor was employed to put in effect the gravity feed mechanism as shown in Fig. 18.7. Taylor et al. (1983) has performed solar gasification of two reactors, i.e. packed bed and fluidized bed approaches. Packed bed included a window for solar radiations and in latter, the reactor body was made up of silica glass. Similarly, many tries were made on actual solar radiations. Such as Z'Graggen et al. (2006) has described a reactor using a vortex flow bed of coal particles and direct solar irradiation. In recent trends, Muroyama et al. (2018) have described an indirectly irradiated gasification

**Table 18.2** Research prototypes of solar assisted gasifiers

| Author | Irradiation type | Solar power (kW/m$^2$) | Reactor type |
|---|---|---|---|
| Antal (1976) | Direct | – | Fluidized bed |
| Gregg et al. (1980) | Direct | 32.25 | Packed bed |
| Taylor et al. (1983) | Direct | 4.244 | Packed bed |
| Taylor et al. (1983) | Direct | 14.184 | Fluidized bed |
| Z'Graggen et al. (2006) | Direct | 421.18 | Vortex bed |
| Piatkowski et al. (2009) | Indirect | 2500 | Packed bed |
| Lichty et al. (2010) | Indirect | 2000–2500 | Fixed bed |
| Wieckert et al. (2013) | Direct | 346 | Packed bed |
| Kruesi et al. (2014) | Direct | 1600–2400 | Fixed bed |
| Bellouard et al. (2017) | Indirect | 16,000 | Fixed bed |
| Muroyama et al. (2018) | Indirect | 1091 | Fluidized bed |

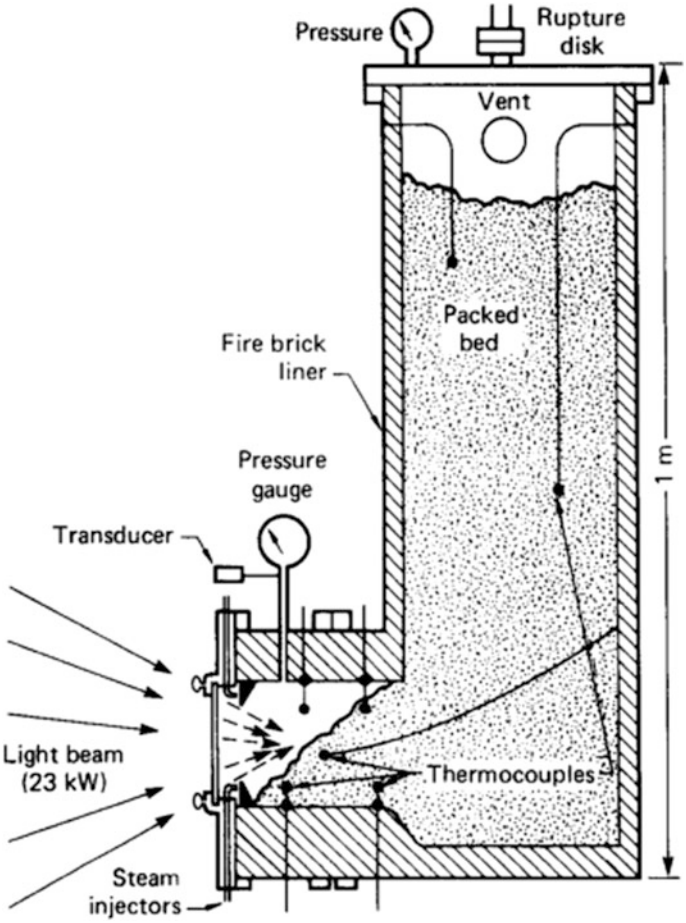


**Fig. 18.7** Reactor design by Gregg et al. (1980). Reprinted from Solar Energy, Vol 25, D. W. Gregg, R. W. Taylor, J. H. Campbell, J. R. Taylor and A. Cotton, Solar Gasification of Coal, Activated Carbon, Coke and Coal and Biomass Mixtures, 12, Copyright (1980), with permission from Elsevier

reactor with simulated solar radiations. Bellouard et al. (2017) have fabricated an indirectly irradiated reactor working on original solar radiations.

Extensive worldwide research has shown that solar driven gasification provides a high quality of syngas. Arribas et al. (2017) selected three feed stocks namely wheat straw, algae and sewage sludge. They used a 7-kW reactor and measured the output gas composition for the different feed stocks. Desirable gases like CO and $H_2$ were highest for wheat straw (37% by vol.) followed by algae (29% by vol.). Methane production was same for all, and $CO_2$ production was highest for algae. The results on sewage were very important because it is very beneficial environmentally.

They also found that product gas obtained in this case is of much good quality than conventionally produced gas (Arribas et al. 2017).

B.J. Hathaway et al. experimented on a molten salt solar reactor and have combined the solar and molten salt methods. They used a 2.2 kW solar reactor though it used simulated radiations from a 6.5 kW xenon short arc lamp. They have used a eutectic blend of lithium, sodium carbonate, and potassium as the molten salts in this setup. At 1218 K they recorded 30% solar conversion efficiency and 47% carbon conversion efficiency. They have claimed to get an efficiency of 55% if the char losses are eliminated (Hathaway 2013).

Quentin Bellouard et al. fabricated a 1 kW reactor for solar driven gasification of biomass. A parabolic solar concentrator with 2 m diameter was employed, and the reactor was tested under real solar insolation. A mixture of spruce and pine wood was used as biomass feedstock, and temperature range for the operation was 1000–1400 °C. The receiver was insulated cavity type made up of graphite, which absorbs the concentrated solar radiations through a small aperture of 15 mm diameter. Biomass was fed by a screw feeder in the high-temperature solar reactor, and output composition was recorded in the aforementioned temperature range. Their results showed the increase of hydrogen production and a decrease in methane production with increasing temperatures. $H_2$/CO molar ratio also showed an increase from 0.45 at 1000 °C to 1.14 at 1400 °C (Bellouard et al. 2017). Solar-to-fuel thermochemical efficiency, which is the ratio of the chemical energy of syngas to the total energy input (solar and calorific value of fuel) up to 28% was recorded in this reactor when wood was heated to 1400 °C.

Z'Graggen et al. have performed the pyrolysis and steam-gasification of petroleum vacuum residue in a 5-kW aerosol flow solar chemical reactor. The operating temperature range in high flux solar furnace was 1147–1294 °C. The feedstock was continuously injected into the reactor's cavity along with a coaxial steam flow. The reactor consists of a cylindrical cavity receiver made up of Inconel, lined with $Al_2O_3$. Aperture was 50 mm diameter circular opening, through which concentrated solar radiations with a concentration ratio of more than 1800 suns enter. The high-quality syngas was produced at 1199 °C with the composition of 68% $H_2$, 15% CO, 14% $CO_2$ and 2% $CH_4$ (Graggen et al. 2008).

### *18.5.3 Methods to Incorporate Solar Heat with Gasifier*

Concentrated solar heat is a highly dense form of solar energy. For an incident irradiance of 1000 W/m$^2$, output radiation flux from parabolic trough collector would be around 45 kW/m$^2$ and same from parabolic dish collector can be up to 1 MW/m$^2$ (Kalogirou 2004), because of its high concentration ratio. This radiation flux can be used to assist the thermo-chemical conversion process going inside the gasifier either through direct heating or carrying the concentrated heat through a circulating fluid. Heat transfer fluids, synthetic oils or molten salt mixtures are generally used to take away the heat from the receiver, which is discussed in

subsequent sections. However, intermediate circulating fluid reduces the efficiency due to heat loss to ambient. Proper insulation is required to minimize this loss. In direct heating through a transparent window, this loss can be averted, but coke, ash and tar formation inside the chamber blacken the window (Janajreh et al. 2010), thereby leaving it no more transparent. Cleaning of this window after regular intervals is necessary for its proper functioning. Various conceptual designs with direct and indirect heating are described below.

#### 18.5.3.1 Gasifier as a Black Body

A black body is characterized by highest absorptivity of thermal radiations. A hole or cavity on the outer surface of an enclosure is treated as a black body. A similar concept can be used here by enclosing a gasifier body inside an outer chamber with a hole or cavity on its surface (Janajreh et al. 2010). Concentrated solar radiations are made to enter the hole, and because of multiple internal reflections they remain entrapped inside the chamber.

Figure 18.8 shows the conceptual design of such gasifier. Entered concentrated radiations heat up the gasifier body uniformly and pave the way for thermo-chemical conversion processes going inside the gasifier. This is the direct method of heating without any heat transfer fluid for exchanging the heat of solar. Usually, flat glass windows are not capable of withstanding the high temperature and pressure inside

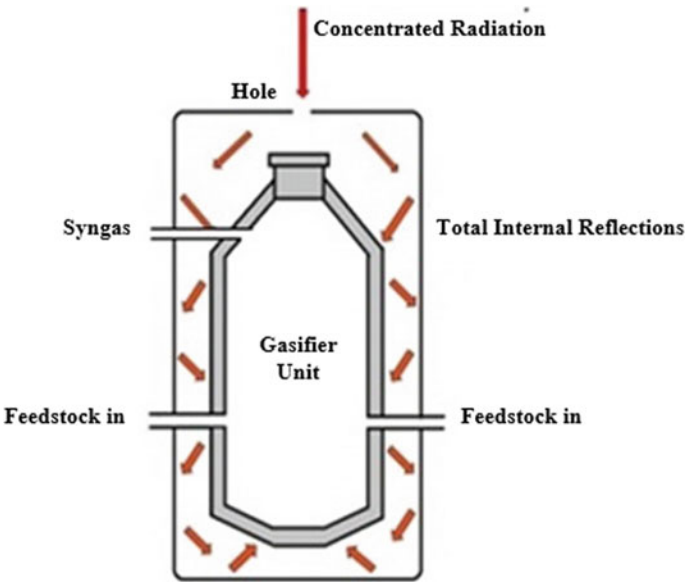


**Fig. 18.8** Gasifier as a black body

the chamber. So, curved glasses are generally employed for this purpose. Meng et al. (2016) studied the use of a curved quartz window and cup-shaped porous absorber to achieve a maximum temperature of 794 °C. Moreover, quartz glass can withstand a temperature of 1000 °C and pressure of 15 bars (Meng et al. 2016). A mixture of air and non-reacting metallic particles is also used as a heat transfer medium.

According to Sarker et al. (2016), recirculating the metallic particles to enhance the heat transfer rate with 10% particle concentration in air can achieve a temperature up to 577 °C.

#### 18.5.3.2 Gasifier Body Surrounded by a Jacket of Molten Salt

The molten salt mixture is an economical way to carry the heat of solar thermal radiations to the desired location. Usual heat transfer oils or synthetic oils can be used below 400 °C, but molten salt mixture can be used in the temperature range of 450–500 °C (Hasuike et al. 2006; Yang and Garimella 2010). Figure 18.9 shows the conceptual design to use molten salt jacket around the gasifier body. For instance, a mixture of $NaNO_3$ and $KNO_3$ in the ratio of 60:40 by weight can be used in solar collector up to 565 °C (Bradshaw and Meeker 1990) with a melting point of 238 °C. One of the problems with the binary mixture is their high melting point, below which they solidify. During off time conditions, the system is highly prone to get choked. To avert this issue, either thermal storage system should be capable enough, or other alternatives in the form of a ternary mixture of $NaNO_3$ and $KNO_3$ with other alkali and alkaline earth nitrates avoids the problem of solidification to a

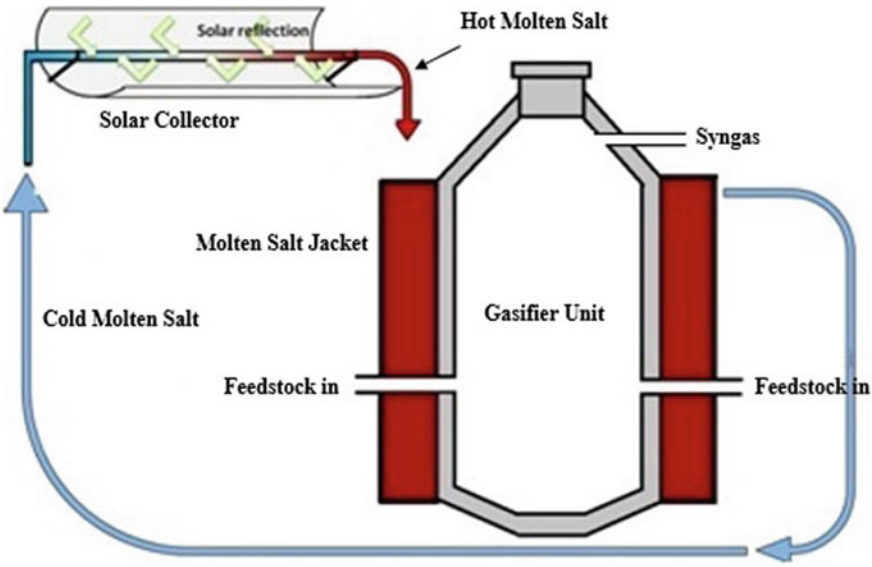


**Fig. 18.9** Gasifier body surrounded by jacket of molten salt

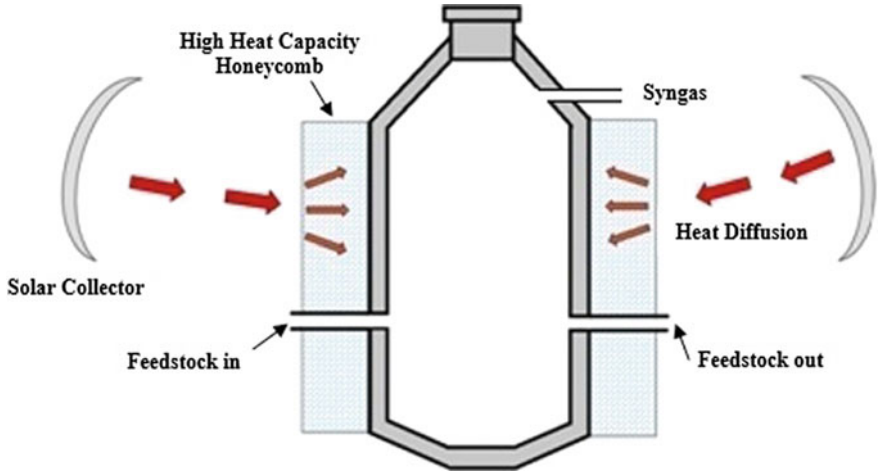


**Fig. 18.10** Gasifier body surrounded by high heat capacity refractory honeycomb

greater extent as their melting point is as low as 120 °C (Bradshaw and Meeker 1990). The commercial salt solution, which is the mixture of $NaNO_3$, $KNO_3$ and $NaNO_2$ in the proportion 7:53:40 respectively has a melting point of 142 °C and operational temperature of 535 °C. Similarly, another salt mixture $NaNO_3$, $KNO_3$ and Ca $(NO_3)_2$ in the proportion 7:45:48 has a melting point of 120 °C and operational temperature of 500 °C (Kearney et al. 2003). These ternary mixtures are easily manageable in terms of solidification. Moreover, the molten salt mixture is cheap and environment-friendly.

In Fig. 18.10, hot molten salt enters the surrounding jacket and leave it after heating the gasifier body. The thermal energy stored in the circulating fluid gets transferred to gasifier body during each cycle. This process assists the chemical reactions going inside the reactor.

#### 18.5.3.3 Use of High Heat Capacity Refractory Honeycomb

Design: According to Frosch (1981), high heat capacity refractory honeycomb can be used to surround gasifier body. Concentrated solar radiations through an optical window are focused on to this as shown in Fig. 18.10. Heat is slowly and uniformly diffused through this honeycomb structure and heats up the gasifier body. The preheated gasifier body assists the thermo-chemical reactions on the way inside the reactor.

Limitations: This kind of reactor has a limitation with geographic locations. This concept is not suitable for a location with less Sun hours, because high heat capacity refractory will take time to get heat diffused through it and as soon as heat reaches the gasifier body sun will set. Hence continuous operation is not possible.

## 18.6 Thermodynamics of Solar Assisted Gasification

In this section we will discuss two aspects, first is about how solar energy is incorporated in gasification reactions and second is the efficiency of the whole gasifiers. Both of these notions are important to get an image of the working of a solar assisted gasifier. The study of such problems, which deals with the involvement of solar energy in chemical processes is named as solar thermochemistry. In this field, we use the two fundamental laws of thermodynamics to get information about a solar thermochemical process, i.e. the first and second laws of thermodynamics. We use the first law to determine how much solar energy is required to perform the reactions. As the critical gasification reactions are endothermic so, this is an important aspect. Studies have found that if the reactions are occurring at high temperatures, then all the energy required for reactions can be provided by solar processes. The second law denotes how well the solar energy is being converted into the fuel (Steinfeld et al. 2001).

The first law is also applied to know the absorption efficiency of the solar reactor. By absorption efficiency, we mean that how much is being used in the reactions that is incident on the feedstock. At higher temperatures, we can say that there will be considerable radiation losses from the cavity, so there is an ample need for analyzing the solar efficiency of the cavity of a solar reactor as defined by Eq. 4 (Fletcher and Moen 1977):

$$\eta_{\text{Absorption}} = \frac{\text{IA}\eta_{\text{a}}\alpha - \text{a}\epsilon\sigma\text{T}_{\text{H}}{}^{4}}{\text{IA}} \tag{4}$$

where,

$I$ Intensity of Solar Radiation (kW/m$^2$)
$A$ Area of Collector (m$^2$)
$\eta_{\text{a}}$ Factor accounting for energy loss due to optical abnormalities
$\alpha$ Absorptivity
$\epsilon$ Emissivity
$\Sigma$ Stefan Boltzmann Constant (Wm$^{-2}$ K$^{-4}$)
$T_H$ Upper temperature limit of cavity (K)

The first term in numerator of Eq. 4 denotes the rate of total solar energy that is being absorbed by the cavity of the reactor. The second term denotes the losses due to re-radiation from the cavity. The denominator denotes the rate of total solar energy falling on the aperture of the solar cavity receiver.

Similarly, by applying the first law of thermodynamics to the gasifier, we express its efficiency in terms of cold gas efficiency as described in Eq. 5. As efficiency is defined as ratio of output and input energy, we consider the energy from feedstock and the energy obtained from the product gas. In Eq. 5, the energies are defined as product of mass flow rate and lower heating value (commonly known as calorific value) of the entity (Piatkowski 2009).

$$\eta_{\text{Cold Gas}} = \frac{\text{LHV}_{\text{Product Gas}} * \dot{M}_{\text{Product Gas}}}{\text{LHV}_{\text{Feedstock}} * \dot{M}_{\text{Feedstock}}} \tag{5}$$

where LHV is the lower heating value. Now if we consider the solar energy input on the gasifier the efficiency becomes

$$\eta_{\text{Solar to Fuel}} = \frac{\text{LHV}_{\text{Product Gas}} * \dot{M}_{\text{Product Gas}}}{\text{LHV}_{\text{Feedstock}} * \dot{M}_{\text{Feedstock}} + Q_{\text{Solar}}} \tag{6}$$

where $Q_{\text{solar}}$ will be additional energy input.

The energy flow chart in case of a solar powered process can be visualized in the following flow chart as shown in Fig. 18.11.

Following are the terms used in Fig. 18.11:

| | |
|---|---|
| $Q_{\text{Solar}}$ | The incident solar energy from the collector |
| $Q_{\text{Absorbed}}$ | Solar energy absorbed by the solar reactor that will be available for use in gasification process |
| $Q_{\text{Reradiation}}$ | The energy which is lost due to reradiation losses. Other losses are negligible in its comparison |
| $Q_{\text{Loss}}$ | Usual energy losses that happen in a thermodynamic system |
| $Q_{\text{Feedstock}}$ | Heat from the combustion of feedstock as little feedstock is consumed in gasification |
| $Q_{\text{Fuel Gas}}$ | Heat from combustion of fuel gas |
| $W_{\text{HE}}$ | Work obtained by combusting the fuel gas in an energy conversion device, in this case, a heat engine |

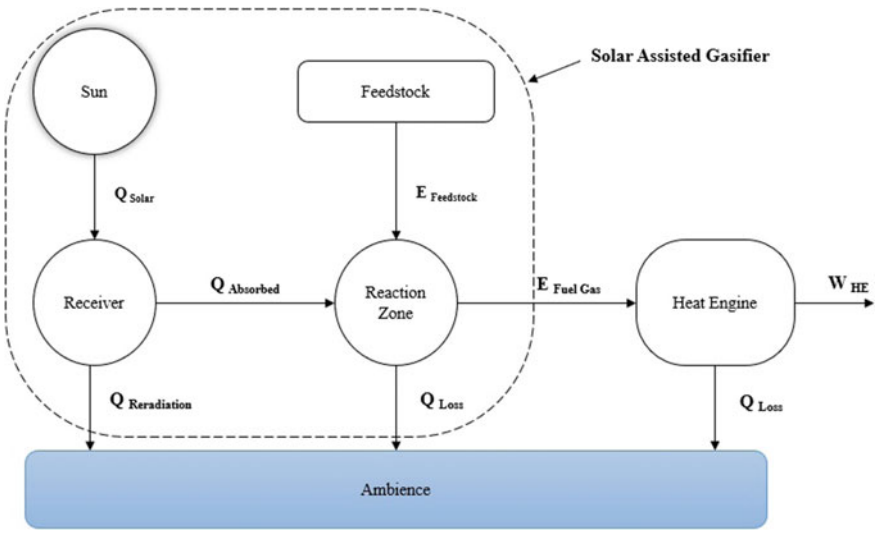


**Fig. 18.11** Thermodynamic aspect of solar assisted gasifier

From above depiction we can speculate the first and second law analysis of a solar assisted gasifier. The dotted line in Fig. 18.11 includes the solar assisted gasifier part. First law includes only the energy balance and thermal efficiencies of the devices. Second law, whereas, depicts how well the solar energy is being converted into fuel. We will try to observe the second law efficiency for a solar assisted system.

The first law can also be written by using Fig. 18.11:

$$\eta_{\text{Absorption}} = \frac{Q_{\text{Solar}} - Q_{\text{Reradiation}}}{Q_{\text{Solar}}} = \frac{Q_{\text{Absorbed}}}{Q_{\text{Solar}}} \tag{7}$$

Now for second law application we will find the exergy efficiency (or second law efficiency) which is defined as minimum available energy divided by the maximum available energy. Let us observe the energy balance around the reaction zone in Fig. 18.11:

$$Q_{\text{Absorbed}} + Q_{\text{Feedstock}} = Q_{\text{Fuel Gas}} + Q_{\text{Loss}} \tag{8}$$

We will induce the concept of available energy which is defined as the maximum work output we can extract from an input heat energy. We can write energy from solar input energy as:

$$Q_{\text{Solar}} = W_{\text{availalble}} + UE \tag{9}$$

UE is the unavailable energy which will be rejected in any case.

The first law efficiency (or thermal efficiency):

$$\eta_{\text{I}} = \frac{W_{\text{HE}}}{Q_{\text{Solar}}} \tag{10}$$

The Carnot efficiency which is considered to be the maximum efficiency of a system if $T_{\text{L}}$ and $T_{\text{H}}$ are the lower and upper limits of the whole system, can be defined as:

$$\eta_{\text{Carnot}} = 1 - \frac{T_{\text{L}}}{T_{\text{H}}} \tag{11}$$

Also, the available energy for the system can be found by using Eq. 11:

$$W_{\text{availalble}} = Q_{\text{Solar}}\left[1 - \frac{T_{\text{L}}}{T_{\text{H}}}\right] \tag{12}$$

Here we used

The second law efficiency (or exergy efficiency) is defined as the ratio of minimum available energy and maximum available energy (or actual available energy). The former is assumed to be the work actually obtained. Thus, we can write:

$$\eta_{\mathrm{II}} = \frac{\text{Minimum available energy}}{\text{Maximum available energy}} = \frac{W_{\mathrm{HE}}}{W_{\mathrm{available}}} \tag{13}$$

Now comparing Eqs. 12 and 13 we get:

$$\eta_{\mathrm{II}} \times \eta_{\mathrm{Carnot}} = \mathrm{I} \tag{14}$$

The above equation will be checked by the following energy balance which is an expanded form of Eq. 8:

$$W_{\mathrm{availalble}} + \mathrm{UE} - Q_{\mathrm{Reradiation}} + Q_{\mathrm{Feedstock}} - Q_{\mathrm{Loss}} = Q_{\mathrm{Fuel\ Gas}} + Q_{\mathrm{Loss}} \tag{15}$$

Now all these equations are made into use when experimental data is tested. Values of particular energy terms are calculated and efficiencies' output values are compared accordingly.

## 18.7 Present Scenario

Use of solar energy to gasify biomass is in its initial phase of development. Few commercial and non-commercial models have been made. The model by Sundrop Fuels uses concentrated solar power from reflective mirrors to heat the furnace consisting of ceramic tubes through which raw biomass is fed and is instantly vaporized to producer gas with high-quality syngas. Lichty et al. (2010) presents a reflective cavity multi-tube prototype reactor with the tubes lined inside an aluminum cavity with heliostat fields as solar concentrators which can attain carbon conversion efficiency as high as 62.8%. Tanaka et al. (2015) present a model with Concentrated Solar Power(CSP) based Integrated Gasification Combined Cycle with a bubbling fluidized bed gasifier and a molten salt heat storage system while the proposed design of Ravaghi-ardebili et al. (2015) uses CSP to produce steam at low temperature($\sim$410 °C) to gasify the biomass in an updraft gasifier. Current challenges faced for integration of solar energy with gasification are: difficulty to maintain transparency of the window on which solar energy is concentrated due to deposition of aerosols, liquids because of phase change during chemical reaction due to which there is a decrease in heat flux, the non-uniform reaction rates of biomass particles and difficult modeling of integrated solar gasification to vary the parameters associated to optimize the processes.

## 18.8 Summary and Outlook

Amid concerns of global warming and depletion of conventional energy sources biomass as an alternative source possesses huge potential. To harness the energy content in biomass, gasification is a promising route for the production of biofuels. Circulating fluidized bed gasifier seems to be viable, particularly for biomass. Moreover, gasification of Municipal Solid Wastes is yet another utility of gasification for solid waste management. As discussed earlier, solar assisted gasification holds multiple advantages over conventional gasification. Sidewise solar concentrator integrated gasifiers provide a feasible solution for reducing the emissions from the gasification process and also help in improving the calorific value of producer gas. Enriched producer gas can be utilized in various applications such as in fuel cells, boilers, generators, transportation and to name a few. In conclusion, integration of solar energy with gasification can be a reliable primary energy source in the near future.

## References

Adinberg R, Epstein M, Karni J (2004) Solar gasification of biomass: a molten salt pyrolysis study. J Solar Energy Eng 126(3):850

Antal J (1976) United States Patent (19)

Aoki A, Ohtake H, Shimizu T, Kitayama Y, Kodama T (2000) Reactive metal-oxide redox system for a two-step thermochemical conversion of coal and water to CO and H 2(25):201–218

Arribas L, Arconada N, González-Fernández C, Löhrl C, González-Aguilar J, Kaltschmitt M, Romero M (2017) Solar-driven pyrolysis and gasification of low-grade carbonaceous materials. Int J Hydrogen Energy 42(19):13598–13606

Axelsson L, Franzén M, Ostwald M, Berndes G, Lakshmi G, Ravindranath NH (2012) "Perspective: Jatropha cultivation in Southern India: assessing farmers' experiences", Biofuels. Bioprod Biorefin 6(3):246–256

Balat M, Balat M, Kirtay E, Balat H (2009) Main routes for the thermo-conversion of biomass into fuels and chemicals. Part 1: pyrolysis systems. Energy Convers Manag 50(12):3147–3157

Bellouard Q, Abanades S, Rodat S, Dupassieux N (2017) A high temperature drop- tube and packed-bed solar reactor for continuous biomass gasification. 100001

Boukis N, Frierich C, Dinjus E (1999) Corrosion of titanium under SCWO—conditions. Recent results, GVC Fachausschuss. In: High Pressure Chemical Engineering, pp 97–98

Boukis N, Diem V, Dinjus E, Galla U (2002).Biomass gasification in supercritical water. In: European conference on biomass for energy, industry and climate protection

Bradshaw RW, Meeker DE (1990) High-temperature stability of ternary nitrate molten salts for solar thermal energy systems. Solar Energy Mater 21(1):51–60

Bridgwater V (1995) The technical and economic feasibility of biomass gasification for power generation. Fuel 74(5):631–653

Calzavara Y, Joussot-Dubien C, Boissonnet G, Sarrade S (2005) Evaluation of biomass gasification in supercritical water process for hydrogen production. Energy Convers Manag 46 (4):615–631

Dayton D (2002) Review of the literature on catalytic biomass tar destruction: milestone completion report, no. December, 2002

Fletcher EA, Moen RL (1977) Hydrogen and oxygen from water. Science 197(4308):1050–1056. https://doi.org/10.1126/science.197.4308.1050

Frosch RA (1981) Solar heated fluidized bed gasification system, United States Patent, Sept 22, 4290779

Graggen AZ, Haueter P, Maag G, Romero M, Steinfeld A (2008) Hydrogen production by steam-gasification of carbonaceous materials using concentrated solar energy—IV. Reactor Experimentation Vac Residue 33:679–684

Gregg DW, Taylor RW, Campbell JH, Taylor JR, Cotton A (1980) Solar gasification of coal, activated carbon coke and coal and biomass mixtures

Han J, Kim H (2008) The reduction and control technology of tar during biomass gasification/pyrolysis: an overview. Renew Sustain Energy Rev 12(2):397–416

Hasuike H, Yoshizawa Y, Suzuki A, Tamaura Y (2006) Study on design of molten salt solar receivers for beam-down solar concentrator. Sol Energy 80(10):1255–1262

Hathaway BJ (2013) Solar gasification of biomass: design and characterization of a molten salt gasification reactor (December)

Hathaway BJ, Davidson JH (2017) Demonstration of a prototype molten salt solar gasification reactor. Sol Energy 142:224–230

IEA Homepage. https://www.iea.org/topics/renewables/bioenergy/. Last accessed 21 May 2018

IRENA. World Energy Resources: Bioenergy 2016. World Energy Counc. 60 (2016) https://doi.org/10.1016/0165-232x(80)90063-4

Janajreh I, Raza SS, Qudaih R, Talab I (2010) Solar assisted gasification: systematic analysis and numerical simulation. Int J Thermal Environ Eng 1(2):81–90

Jin G, Iwaki H, Arai N (2005) Study on the gasification of wastepaper/carbon dioxide catalyzed by molten carbonate salts. Energy 30:1192–1203

Kabir MJ, Chowdhury AA, Rasul MG (2015) Pyrolysis of municipal green waste: a modelling, simulation and experimental analysis. Energies 8(8):7522–7541

Kalogirou SA (2004) Solar thermal collectors and applications. Prog Energy Combust Sci 30

Kalogirou SA (2004) Progress in energy and combustion science, vol 30, pp 231–295

Kaushal P, Proell T, Hofbauer H (2011) Application of a detailed mathematical model to the gasifier unit of the dual fluidized bed gasification plant. Biomass Bioenergy 35(7):2491–2498

Kearney D, Herrmann U, Nava P, Kelly B, Mahoney R, Pacheco J, Cable R, Potrovitza N, Blake D, Price H (2003) Assessment of a molten salt heat transfer fluid in a parabolic trough solar field. J Solar Energy Eng 125(2)

Kirkels AF, Verbong GPJ (2011) Biomass gasification: still promising? A 30-year global overview. Renew Sustain Energy Rev 15(1):471–481

Kodama T, Funatoh A, Shimizu K, Kitayama Y (2001) Kinetics of metal oxide-catalyzed $CO_2$ gasification of coal in a fluidized-bed reactor for solar thermochemical process. Energy Fuels (17):1200–1206

Kruesi M, Jovanovic ZR, Steinfeld A (2014) A two-zone solar—driven gasifier concept: reactor design and experimental evaluation with bagasse particles. Fuel 117:680–687

Leal-Quiros E (2004) Plasma processing of municipal solid waste. Braz J Phys 34:1587–1593

Lichty P, Perkins C, Woodruff B, Bingham C, Weimer A (2010) Rapid high temperature solar thermal biomass gasification in a prototype cavity reactor. J Sol Energy Eng 132(1):11012

Luterbacher J, Froling M, Vogel F, Marechal F, Tester F (2009) Sci Technol 43:1578–1583

Meng XL, Xia X-L, Sun C, Li X-L (2016) Optical transmission characteristics of concentrated solar rays in the VSR using cup-shaped porous absorber. Proc Eng 157:301–308

Mitton D, Yoon J, Cline J, Kim H, Eliaz N, Latanision RM (2000) Corrosion behavior of Ni-based alloys in SCWO systems. Ind Eng Chem Res 39:4689

Mountouris A, Voutsas E, Tassios D (2008) Plasma gasification of sewage sludge: process development and energy optimization. Energy Convers Manag 49:2264–2271

Muroyama AP, Guscetti I, Schieber GL, Haussener S, Loutzenhiser PG (2018) Design and demonstration of a prototype 1.5 kWth hybrid solar/autothermal steam gasifier. Fuel 211:331–340

Overend R (1999) Thermochemical conversion of biomass. Renew Energy Sources Charg Energy Sun Orig Earth-Moon Interact 78:252–258
Paepatung N, Nopharatana A, Songkasiri W (2009) Bio-methane potential of biological solid materials and agricultural wastes. Asian J Energy Environ 10(1):19–27
Piatkowski NSA (2009) Solar gasification of carbonaceous waste feedstocks in a packed-bed reactor—dynamic modeling and experimental validation. In: IFAC Proceedings Volumes (IFAC-PapersOnline), vol 7(PART 1), pp 405–410
Piatkowski N, Wieckert C, Steinfeld A (2009) Experimental investigation of a packed-bed solar reactor for the steam-gasification of carbonaceous feedstocks. Fuel Process Technol 90(3):360–366
Prabowo K, Umeki M, Yan M, Nakamura R, Castaldi MJ, Yoshikawa K (2014) $CO_2$-steam mixture for direct and indirect gasification of rice straw in a downdraft gasifier: laboratory-scale experiments and performance prediction. Appl Energy 113:670–679
Ravaghi-ardebili Z, Manenti F, Corbetta M, Pirola C (2015) Biomass gasification using low-temperature solar driven steam supply. Renew Energy 74:671–680
Reed TB (1988) Downdraft gasifier engine systems handbook of biomass
Sarker MRI, Saha M, Beg RA (2016) A concentrated solar cavity absorber with direct heat transfer through recirculating metallic particles. 50040
Sharma AK (2008a) Equilibrium and kinetic modeling of char reduction reactions in a downdraft biomass gasifier: a comparison. Sol Energy 82(10):918–928
Sharma AK (2008b) Equilibrium modeling of global reduction reactions for a downdraft (biomass) gasifier. Energy Convers Manag 49(4):832–842
Sikarwar VS et al (2016) An overview of advances in biomass gasification. Energy Environ Sci 9 (10):2939–2977
Steinfeld A, Zurich C, Palumbo R (2001) Solar thermochemical process technology. Encycl Phys Sci Technol 15:237–256
Sugiura K, Minami K, Yamauchi M, Morimitsu S, Tanimoto K (2007) Gasification characteristics of organic waste by molten salt. J Power Sources 171(1):228–236
Tanaka Y, Mesfun S, Umeki K, Toffolo A, Tamaura Y (2015) Thermodynamic performance of a hybrid power generation system using biomass gasification and concentrated solar thermal processes q. Appl Energy 160:664–672
Taylor RW, Berjoan R, Coutures P (1983) Solar gasification of carbonaceous materials. Sol Energy 30:513–525
Thirugnanasambandam M, Iniyan S, Goic R (2010) A review of solar thermal technologies. Renew Sustain Energy Rev 14(1):312–322
Voll FAP, Rossi CCRS, Silva C, Guirardello R, Souza ROMA, Cabral VF, Cardozo-Filho L (2009) Thermodynamic analysis of supercritical water gasification of methanol, ethanol, glycerol, glucose and cellulose. Int J Hydrogen Energy 34(24):9737–9744. https://doi.org/10.1016/j.ijhydene.2009.10.017
Wieckert C, Obrist A, Von Zedtwitz P, Maag G, Steinfeld A (2013) Syngas production by thermochemical gasification of carbonaceous waste materials in a 150 kWth packed-bed solar reactor. Energy Fuels 27:4770–4776
Woodruff PB, Andrews L (2008) Synthesis gas production by rapid solar thermal gasification of corn stover. In: 14th Bienn. CSP …, no. March, pp 4–7
World Energy Council (2016) "World Energy Resources: Bioenergy," Main Report
Yang Z, Garimella SV (2010) Thermal analysis of solar thermal energy storage in a molten-salt thermocline. Sol Energy 84(6):974–985
Z'Graggen A et al (2006) Hydrogen production by steam-gasification of petroleum coke using concentrated solar power- II Reactor design, testing, and modeling. Int J Hydrogen Energy 31:797–811
Zedtwitz P, Steinfeld A (2003) The solar thermal gasification of coal—energy conversion efficiency and $CO_2$ mitigation potential. Energy 28:441–456

# Chapter 19
# Solar Thermal Powered Bakery Oven


**Ayushi Mishra, Satvasheel Powar and Atul Dhar**

**Abstract** The bakery process, out of all the food making processes, requires the highest range of processing temperature. Therefore the energy consumption in bakery is also high. The baking process alone consumes about 73% of the total energy consumed in bread production. Currently utilized conventional energy sources affect the surroundings detrimentally. Shifting to renewable energy sources can be a sustainable way. Considering the fact that the process temperature requirements can be fulfilled by the solar thermal energy, we propose a solar thermal based system for bakery oven. This chapter discusses a solar thermal powered bakery oven model. The proposed system integrates bakery oven with a solar parabolic trough collector. Computational fluid dynamics (CFD) analysis of the temperature and air flow distribution inside the oven are undertaken. The CFD results reveal that uniform temperature can be acquired throughout the oven by proper selection of the flow model, along with implementation of realistic boundary conditions. It is also observed that a temperature of 168 °C is achievable inside the oven cavity when the coils surface is maintained at an average temperature of 300 °C, which is achievable employing a 3.2 $m^2$ area of solar parabolic trough collector.

**Keywords** Bakery industry · Solar thermal powered bakery oven
CFD analysis · Temperature distribution

## 19.1 Introduction

The global growth of the bakery sector is around 19% from the year 2010–2015. Whereas in India it is 27% for those five years, accounting for approximately 6% increment annually (Annual report 2015–16). The annual consumption of bread in India in the year 2015 is 3.75 million kg (Annual report 2015–16). Therefore,

A. Mishra · S. Powar (✉) · A. Dhar
School of Engineering, Indian Institute of Technology Mandi,
Mandi 175005, Himachal Pradesh, India
e-mail: satvasheel@iitmandi.ac.in



H. Tyagi et al. (eds.), *Advances in Solar Energy Research*, Energy, Environment, and Sustainability, https://doi.org/10.1007/978-981-13-3302-6_19

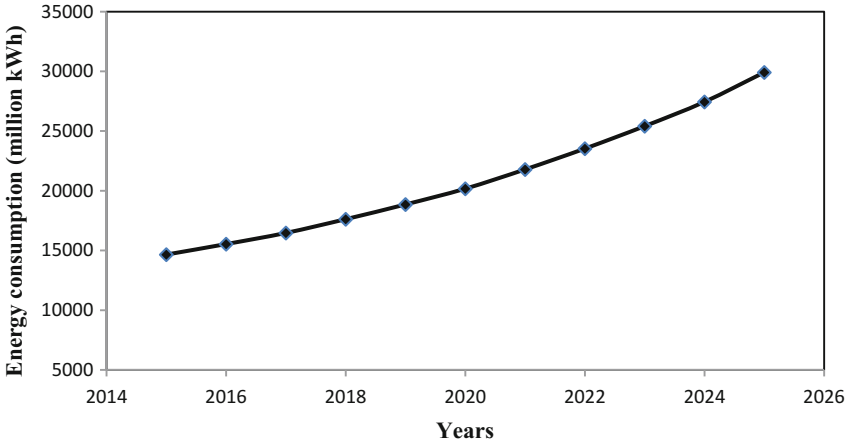


**Fig. 19.1** Energy consumption in food processing (Annual Report 2015–16)

projecting this data non-linearly (based on the available data of 6% increment annually) to 2025, it would be around 6 million kg. Considering the above data, the energy consumption by bakery will also increase at around the same rate. The projected data for energy by the year 2025 has been plotted which results to 30,000 million kWh consumption of energy (see Fig. 19.1). The energy consumption by food processing for the year 2015 has been taken from the annual report of MNRE (2015–16) and the data has been extrapolated based on the growth rate. Extracting this amount of energy from conventional sources will affect the nature detrimentally. The conventional sources are limited in nature and also, they emit many pollutants producing a greenhouse effect in the atmosphere. With this increasing demand for energy, we should shift our focus to energy source that leaves minimal impact on the nature. Solar thermal is one of the suitable solutions to this problem as its' manufacturing, and operating costs are also low, and it does not have any side effects to the surroundings. Therefore, by providing the proposed solution, we are conserving the conventional and limited source of energy and giving a sustainable solution to the problem.

The Indian industrial sector accounts for about 16–20% of the total fuel consumption for thermal energy for different heating applications in the temperature range of 50–250 °C (Suresh and Rao 2017; Fuller 2011; Kalogirou 2003). The conventional fuels (fossil fuels) emit greenhouse gases, which depletes the ozone layer and are responsible for global warming that causes a negative impact on the environment. Solar-power is a renewable and non-polluting energy source, and gaining global attention due to none harmful environmental effect over conventional fuels. Bakery industries demand a maximum temperature of 240 °C for baking to get completed. This temperature can be easily achieved by the integration of solar thermal systems into the bakery system. Conventionally the bakery ovens, for mass production, are either electric powered or fuel powered. With the depleting

source of conventional energy, the researchers are attempting to integrate solar in maximum applications possible. The bakery is also one of those sectors which can get benefited out of the solar energy (Shahzad et al. 2013). Apart from the conventional methods (electric and fuel powered), the heat to the oven can also be provided by a renewable energy source. Since, it is a thermal process, solar thermal utilization would be the best option. In India, solar thermal systems are used for various cooking applications; however, the bakery industry has not integrated solar thermal system so far. The baking temperature influences the quality of the bread as well as its shelf life, making it unsuitable for extended periods.

Differet types of solar thermal collectors have different temperature attinability. The collector type can be selected based on the energy requirements. In a typical bakery processing plant, a significant fraction (73%) of energy use is mostly for process heating (50–250 °C) (Sharma et al. 2017). The non-imaging type concentrating solar collectors such as parabolic dish collector or parabolic trough collector can suffice the energy requirements in bakery (Mbodji and Hajji 2017).

In this chapter a solar thermal based bakery system is proposed. Computational Fluid Dynamics study of the temperature and airflow distribution inside an existing electric oven has been done, and the results are validated. The CFD analysis has also been done for the solar oven considering an average solar insolation for Kamand (Himachal Pradesh, India) location. The predicted temperature distribution inside the baking cavity is presented are based on the Kamand location.

## 19.2 Bakery Processes

A flowchart of the processes in the bakery industry is shown in Fig. 19.2 along with the temperature requirements.

Mixing—The raw materials are mixed in proper proportion for best quality of bread. Table 19.1 shows the proportion of all the raw materials (Zisopoulos et al. 2015).

Molding—The doughs formed are given proper shape and size as required by a loaf of bread.

Proving—It is the stage where the yeast in the bread gives off carbon dioxide and makes the bread rise before baking. It is also called fermenting. It is done at a controlled humidity of 70%.

Baking—The baking time for each batch is determined precisely, through experimental trials, to get the bread cooked just right and outside just brown.

Second Baking- The second baking process is carried out at 180 °C for about 18 min. This process hardens the bread to form rusks.

Conventionally the bread baking ovens are either electric powered or fuel powered for mass production. Based on the data collected during our visit to “Once More Bakery Industry”, it is found that a typical fuel powered bakery oven consumes 0.02 L of fuel per kg of bread making which would be even more in case of

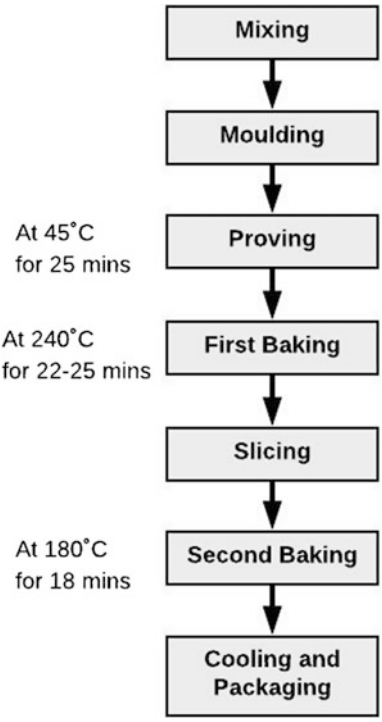


**Fig. 19.2** Processes in bakery

**Table 19.1** Dough composition

| S. No. | Raw material | Composition |
|---|---|---|
| 1. | Wheat flour | 61.7 |
| 2. | Yeast | 0.6 |
| 3. | Salt | 0.9 |
| 4. | Bread improver | 0.6 |
| 5. | Water | 36.1 |

electric oven considering the transmission losses and everything else. In India alone, the daily consumption of bread is around 10 million kg which is even higher in other countries around the globe. The above data gives a clue of global energy consumption by global bakery industry. A working of an electric as well as fuel powered bakery oven has been discussed further to commence a general idea about the existing method of bread production and whether it can be modified to completely solar thermal based bakery oven or even to solar assisted electric bakery oven.

### 19.2.1 Electric Oven

An electrically powered bakery oven depends solemnly on the grid system which has its own drawbacks. The ovens consist of steel heating elements of different capacities on the top and bottom surfaces of the oven. These generally work on natural convection phenomena for heat transfer mechanism which also aids the moisture removal from the oven. The moisture removal from the oven is a vital criterion in the bread making process. A definite amount of moisture must be removed otherwise the bread would be hard from outside but wet on the inner volume, which degrades the bread properties. The moisture will rotten the bread very early. The temperature distribution and heat transfer rate mainly depend on convection and radiation inside the oven. In electric ovens, cooking time and quality are generally dependent on the airflow in the oven. Areas of high velocity accelerate evaporation and heat transfer, hence cooking speed.

### 19.2.2 Fuel Powered Bakery Oven

In a fuel powered bakery oven, the combustion chamber is integrated with the baking chamber itself. The forced air is circulated into the combustion chamber from the atmosphere, and then the hot air along with the flue gases is sent to the baking cavity of the oven where the doughs are placed in trays. The heat transfer in the baking cavity is dominated by forced convection (Khatir et al. 2013). The exhaust from the baking cavity is sent to the heat recovery system where it is used to pre-heat the incoming air to the combustion chamber. A schematic of the air flow in the complete oven is shown in Fig. 19.3.

## 19.3 Solar as an Alternative Source of Energy

It is a known fact that the solar thermal technology uses the sun's energy to generate thermal (heat) energy. Currently, the primary applications for utilizing solar thermal energy are heating water, heating buildings, and heating swimming pools. In general, the majority of the collectors used are flat-plate collectors, in a fixed position (Tian and Zhao 2013). Cooking is not a widely accepted application to solar thermal for household application. Solar assisted cooking is successful in community cooking solutions. Many different types of apparatus are being manufactured for utilizing solar thermal energy for cooking purpose. They are yet to be commercialized to their potential due to many factors including costs, ease of operation, location for energy utilization, and a variation in the solar energy availability.

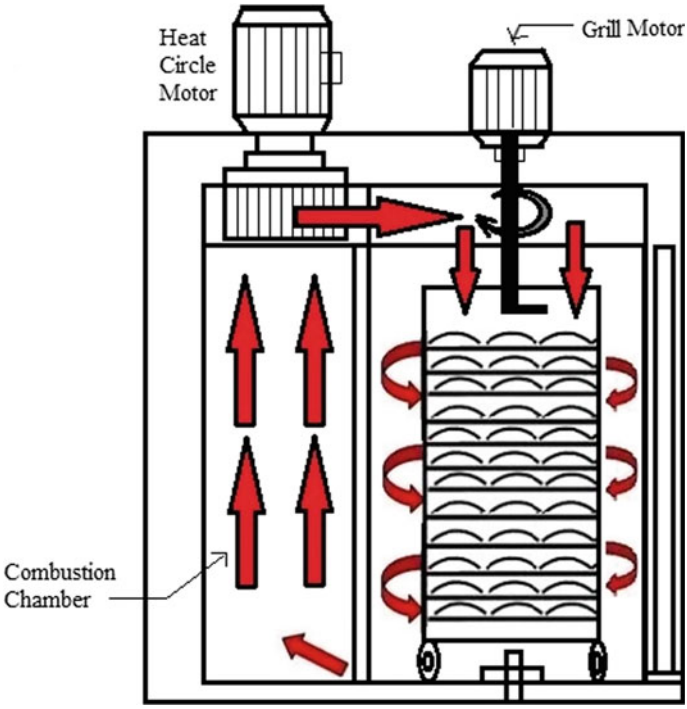


**Fig. 19.3** Schematic of a fuel powered bakery oven

The solar collectors are generally of two types: concentrating and non-concentrating. Concentrating collectors have distinct areas of focusing and intercepting, while non-concentrating collectors have nearly same area of intercept and focus. We obtain high radiation fluxes at the focus of concentrating collectors because they have different areas of intercept and focus; making them suitable for high-temperature applications (Tesfay et al. 2014). A classification of solar thermal collectors is shown in Fig. 19.4 with their working range of temperatures (Kalogirou 2004).

As in the above section, we have seen the working temperature range of different solar collectors; therefore, we conclude that for the bakery industry, which demands a maximum temperature of 240 °C, the best applicable collector is the parabolic trough collector (PTC). The PTC works in the desired temperature range. The output temperature can be as low as 50 °C and as high as 400 °C, with just the variation of the mass flow rate of the working fluid. Compared to parabolic dish collector (PDC), the stagnant temperature for PDC can reach as high as 1500 °C that is indeed undesirable for the case of bakery application. As PTC is most widely used and simple to manufacture than a compound parabolic collector or linear Fresnel collector, therefore, it is more cost effective and readily available.

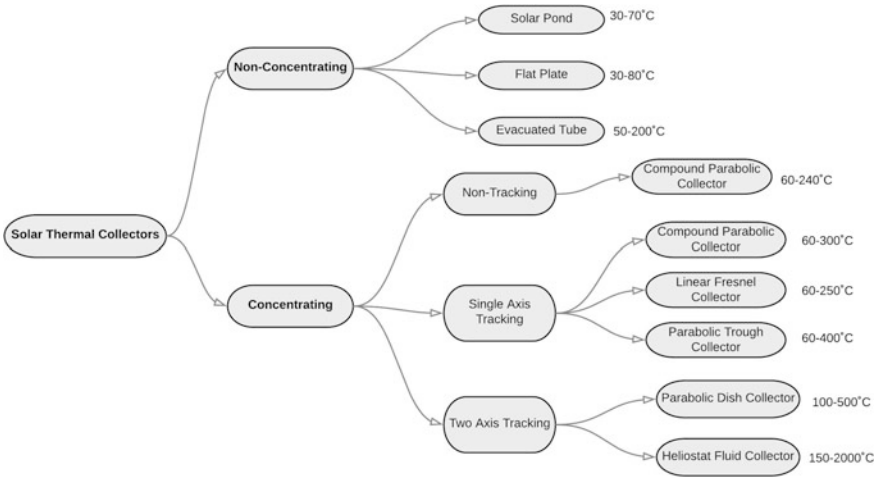


**Fig. 19.4** Classification of solar thermal collectors

## 19.4 Proposed Solar Thermal Bakery System

Figure 19.5 is the proposed design of bakery oven using electric power as the auxiliary source. A model of solar cum electric powered bakery oven integrated with Solar Parabolic Trough Collector is designed. The solar energy will be extracted from the PTC in the form of internal energy of the heat transfer fluid (HTF) (Prasanna and Umanand 2011). This fluid (e.g. Duratherm 600) would be heated up to 300 °C and then circulated to the bakery oven. The oven consists of one baking cavity which is integrated with copper coils having HTF from solar

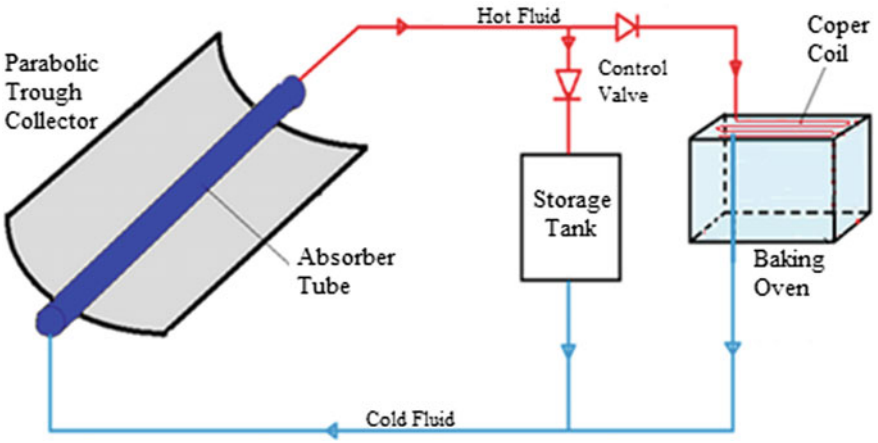


**Fig. 19.5** Schematic of solar thermal powered bakery oven

PTC. For better heat transfer an induced convection fan is introduced into the oven, and the air is circulated back to the oven at a velocity of around 0.75 m/sec.

The main components of the system are:

### 19.4.1 Solar Collector

Solar collectors are the devices that collect solar radiation and convert it into thermal energy for various applications. The major components of the solar parabolic trough collector include the reflector for concentrating solar radiations, absorber to extract the concentrated heat, and heat transport medium.

A parabolic trough collector essentially has a sheet of the reflector bended into the form of a parabolic shape to focus on a line, as shown in Fig. 19.6. There is a black coated receiver pipe at this line focus that is sometimes covered with a vacuum glass tube to reduce heat losses (Duffie et al. 2013), or this may also be covered with another concentric pipe resulting in the tube in tube type arrangement. To collect the incident rays and focus those onto the receiver throughout the day the concentrator requires one axis tracking mechanism. The concentrated radiation which is reflected to the receiver tube gets converted into heat and further starts heating the fluid circulating through it. Figure 19.6 shows a schematic of a parabolic collector with tube in tube receiver. This type of geometry facilitates the inlet and outlet of the HTF from the same side of the receiver tube.

### 19.4.2 Solar Thermal Powered Bakery Oven

The existing electrical bakery oven consists of steel heating elements and convection fan for better heat distribution and proper moisture removal from the oven cavity (Chhanwal et al. 2011). The upper electrical heating elements are replaced with copper coils having heat transfer fluid from the solar PTC and lower heating

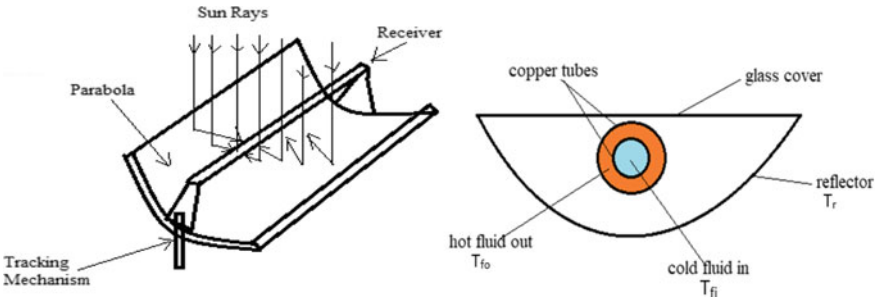


**Fig. 19.6** Solar parabolic trough collector

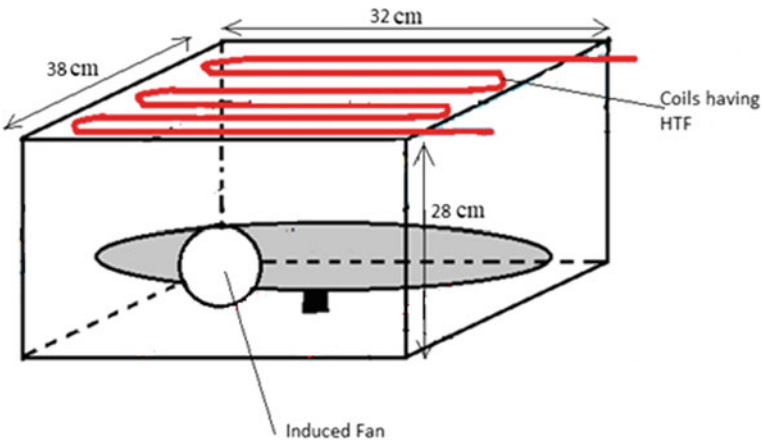


**Fig. 19.7** Solar thermal powered bakery oven

elements are removed, as shown in Fig. 19.7. These coils firstly extract the heat from solar energy through parabolic trough collector and then supply this heat to the bakery oven at a temperature of 300 °C. The exit temperature of the heat transfer fluid is assumed to be 250 °C. Compared to the electric coils, the temperature of the copper coils having HTF does not reach 600 °C.

### *19.4.3 Piping System*

The piping system consists of pipes with proper insulation and flow meters to control the flow of HTF to the oven. For maintaining a proper temperature inside the oven mass flow rate needs to be adjusted as the solar insolation on the PTC keeps varying all-round the day and correspondingly the mass flow varies. Temperature sensors are required to keep track of the temperature at various points in the complete circuit. These temperature sensors are coupled with the flow meters to adjust the mass flow rate with temperature variation and varying solar insolation. The pipes are made of galvanized iron and are properly insulated with ceramic wool.

## 19.5 CFD Analysis

A CFD analysis was carried out treating the copper coils containing heat transfer fluid as an energy source. Annual daily average solar insolation for the Kamand location (650 W/m$^2$) has been taken into account for plotting the temperature profiles. The methodology adopted is discussed further.

Modeling is the process in which a simulation model is built, defining the computational geometry of the region of interest, including the regions of fluid flow, solid regions, internal flow obstacles, surface boundaries, free surfaces interfaces, etc. After modeling the next step is meshing followed by the proper definition of the initial and boundary conditions only then, we can proceed for actual analysis. In the present study modeling of the geometry for CFD analysis has been done using ANSYS Workbench 16.0. The modeled geometry of the solar thermal powered bakery oven has been shown in Fig. 19.8. The solar coils are provided near the top wall of the baking cavity. The inlets and outlet are given at the same wall, where the two rectangles (as shown in Fig. 19.8) are air inlets and the circle is the air outlet.

For convection phenomena and better heat transfer, the inlet and outlet of air are given on the same wall (with boundary conditions as velocity inlet and pressure outlet). The velocity at the inlet is taken in the range of 0.75–1.00 m/sec (measured experimentally from the existing electric oven). For the parametric study, the length of the coils has been taken a variable, and temperature plots are compared for full-length geometry (covering the maximum space) and for having half the above length. The second geometry is shown is Fig. 19.9.

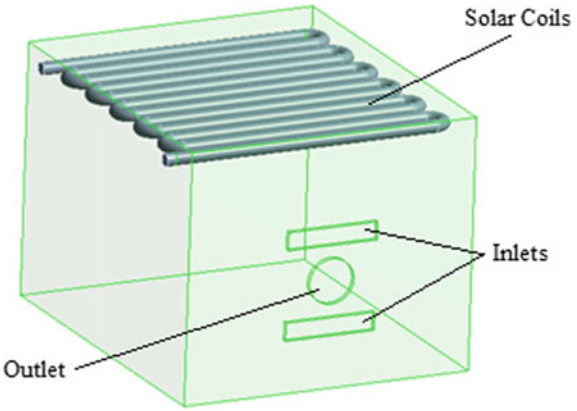


**Fig. 19.8** Solar oven having full-length solar coils

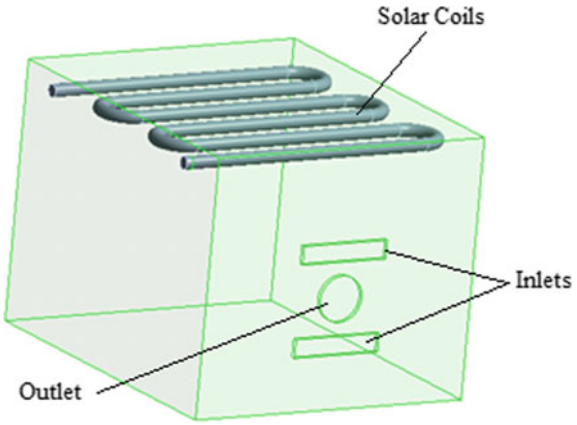


**Fig. 19.9** Solar oven having half length solar coils

Assumptions for CFD Analysis:

1. The conditions during simulations are assumed to be steady state.
2. The energy transfer from the collector to the oven was considered to have 40% losses in the piping system and solar collector.
3. Velocity conditions for both cases are taken to be same.
4. The flow inside the oven is assumed to be laminar because of the low velocities measured experimentally from the electric oven.
5. Heat transfer coefficient from the oven walls is assumed to be constant (10 W/$m^2$-K), which is calculated for an existing electric oven (Cengel et al. 2002; Duffie et al. 2013).

The airflows in the oven are analyzed in three dimensions using the steady-state Navier–Stokes equations (based on momentum conservation, Eqs. 19.2–19.4) (Boulet et al. 2010). The temperature distribution and heat transfer are analyzed using the steady-state Energy equations in three dimensions (Eq. 19.5).

$$\frac{\partial \rho}{\partial t} + \frac{\partial(\rho V_x)}{\partial x} + \frac{\partial(\rho V_y)}{\partial y} + \frac{\partial(\rho V_z)}{\partial z} = 0 \tag{19.1}$$

$$\frac{\partial V_x}{\partial t} + V_x\frac{\partial V_x}{\partial x} + V_y\frac{\partial V_x}{\partial y} + V_z\frac{\partial V_x}{\partial z} = F_x - \frac{1}{\rho}\frac{\partial P}{\partial x} + \frac{\mu}{\rho}\left(\frac{\partial^2 V_x}{\partial x^2} + \frac{\partial^2 V_x}{\partial y^2} + \frac{\partial^2 V_x}{\partial z^2}\right) \tag{19.2}$$

$$\frac{\partial V_y}{\partial t} + V_x\frac{\partial V_y}{\partial x} + V_y\frac{\partial V_y}{\partial y} + V_z\frac{\partial V_y}{\partial z} = F_y - \frac{1}{\rho}\frac{\partial P}{\partial x} + \frac{\mu}{\rho}\left(\frac{\partial^2 V_y}{\partial x^2} + \frac{\partial^2 V_y}{\partial y^2} + \frac{\partial^2 V_y}{\partial z^2}\right) \tag{19.3}$$

$$\frac{\partial V_z}{\partial t} + V_x\frac{\partial V_z}{\partial x} + V_y\frac{\partial V_z}{\partial y} + V_z\frac{\partial V_z}{\partial z} = F_z - \frac{1}{\rho}\frac{\partial P}{\partial x} + \frac{\mu}{\rho}\left(\frac{\partial^2 V_z}{\partial x^2} + \frac{\partial^2 V_z}{\partial y^2} + \frac{\partial^2 V_z}{\partial z^2}\right) \tag{19.4}$$

$$\begin{aligned}\int_{\forall}\frac{\rho}{2}\left(\frac{\partial V^2}{\partial t} + V_x\frac{\partial V^2}{\partial x} + V_y\frac{\partial V^2}{\partial y} + V_z\frac{\partial V^2}{\partial z}\right)d\forall = &\int_{\forall}\left(F_xV_x + F_yV_y + F_zV_z\right)d\forall \\ &+ \int_{\forall}\left[V_x\left(\frac{\partial \sigma_x}{\partial x} + \frac{\partial \tau_{xy}}{\partial y} + \frac{\partial \tau_{xz}}{\partial z}\right)\right. \\ &+ V_y\left(\frac{\partial \sigma_y}{\partial y} + \frac{\partial \tau_{yx}}{\partial x} + \frac{\partial \tau_{yz}}{\partial z}\right) \\ &\left.+ V_z\left(\frac{\partial \sigma_z}{\partial z} + \frac{\partial \tau_{zy}}{\partial y} + \frac{\partial \tau_{zx}}{\partial x}\right)\right]\end{aligned} \tag{19.5}$$

where, $V^2 = V_x^2 + V_y^2 + V_z^2$.

**Table 19.2** System parameters

| | | |
|---|---|---|
| Oven dimensions (cm) | Outer dimensions | 38 × 32 × 28 |
| | Length of solar coil in first case | 377.4 |
| | Length of solar coil in second case | 195.7 |
| Velocity at inlet (m/sec) | 0.75 | |
| Maximum temperature (°C) | First case | 168.6 |
| | Second case | 160.1 |

Table 19.2 discusses the system parameters used for the simulations as well as the resultant maximum temperature attained in both the cases having different coils lengths.

The results of the temperature contours for both the conditions are plotted in Figs. 19.10, 19.11 and 19.12. The results show that the maximum temperature attained in an oven having a full-length coil (377.4 cm) is 168.6 °C and in an oven having half coil length (195.7 cm) is 160.1 °C. The temperature distribution in the central part of the baking cavity is uniform with a maximum temperature difference of 1–2 °C. A comparison of surface temperature of coils in both the cases is also shown in Fig. 19.12. The surface temperature of coils is more in case of an oven having half-length coil that is 409.5 °C and in case of an oven having full-length coil it is 334.8 °C.

## 19.6 Conclusions

A CFD based comparison has been carried out for solar thermal powered bakery oven. Simulations are carried out for the temperature distribution inside a solar thermal powered bakery oven (with two different lengths of solar coils).

The temperature attained in an oven having a full-length coil (which satisfies the symmetry and utilizes maximum space) is more than the oven having a half-length coil. The reason attributed to the above results is the surface area of heat transfer. With more length, there is more contact area between the air and the coils, which results in better heat transfer characteristics from the coils surface.

From the comparison of coil temperature, it is seen that the temperature of the coils is more in the case of an oven having half-length coils. The reason being, an equal amount of energy generation is given to a smaller unit of volume, which results in the higher surface temperature of the coils (as the energy generation is given in terms of Watts/$m^3$).

The temperature attained in the oven in both cases is much below the desired temperature for proper baking of the bread. Therefore, it is not actually possible to bake the bread with the available area of the solar PTC giving only 1248 W of energy. If we want to achieve the desired temperature with the same amount of solar

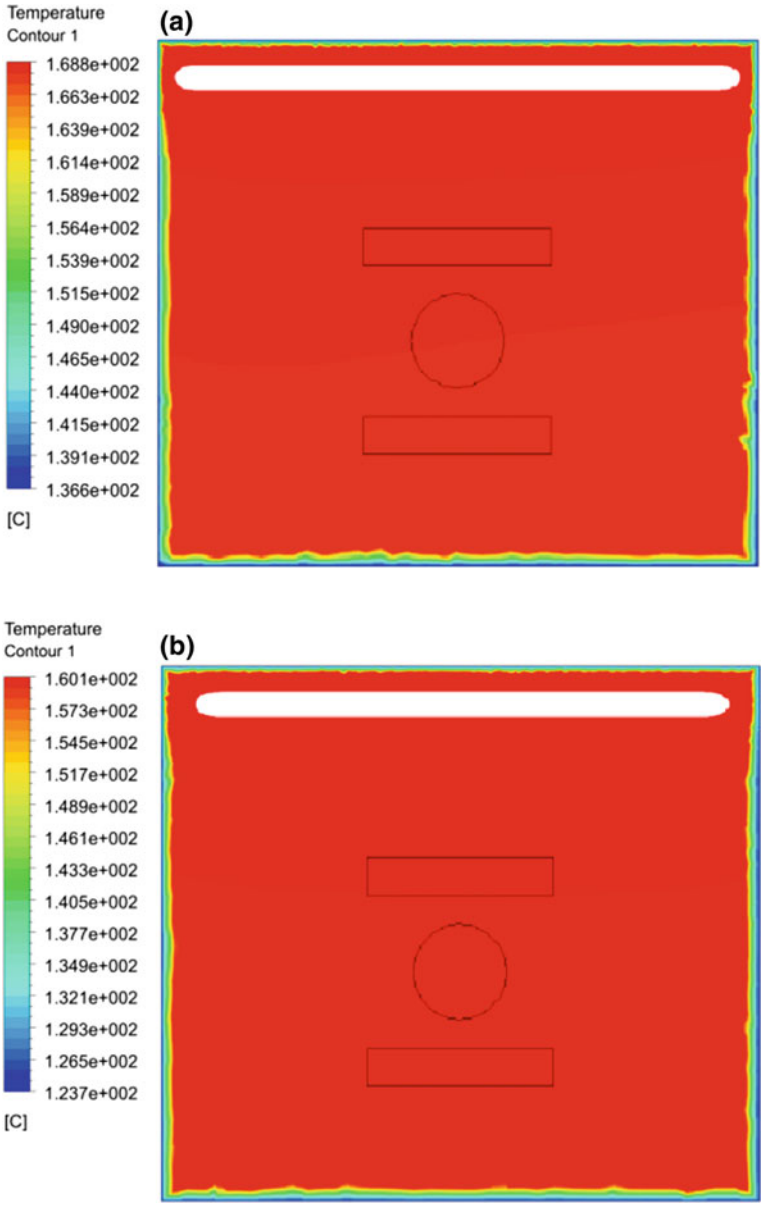


**Fig. 19.10** Comparison of temperature contours at plane parallel to solar coils in case of **a** full-length coil and **b** half length coil

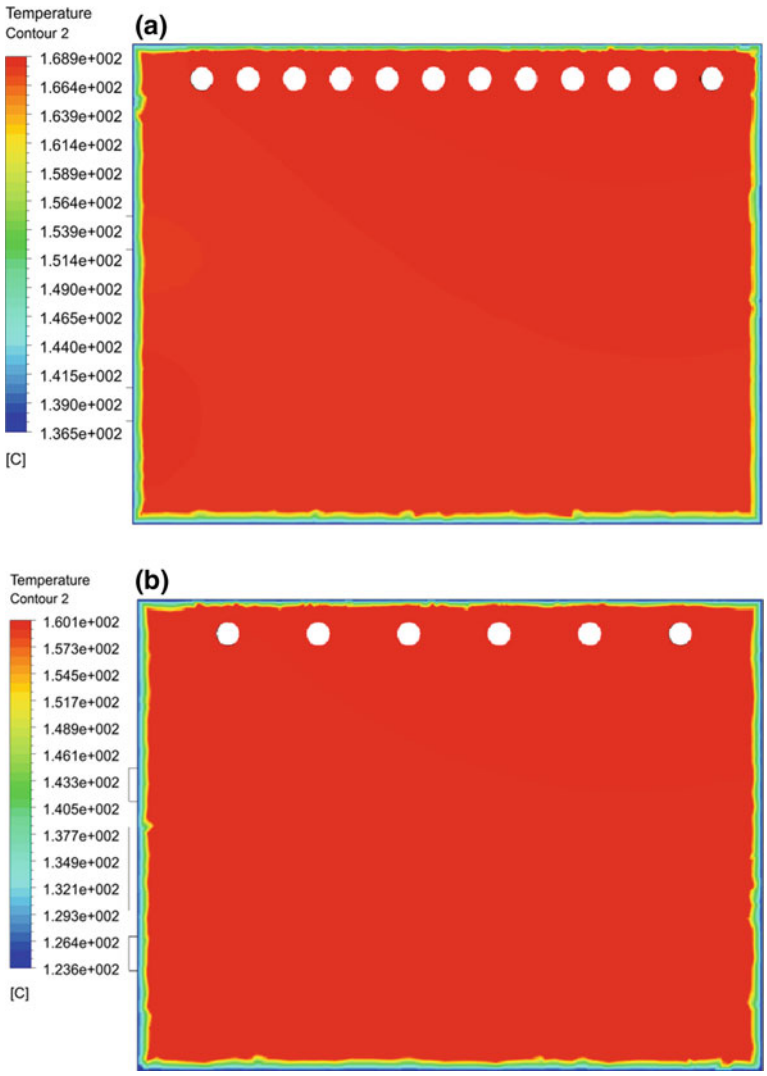


**Fig. 19.11** Comparison of temperature contours at plane perpendicular to solar coils in case of **a** full-length coil and **b** half length coil

collector area then the heat loss coefficient from the surface walls of the bakery oven must be reduced by providing proper insulation materials.

The possible solution is either to increase the surface area of the solar PTC or to integrate the solar thermal powered oven with an auxiliary source (electric energy). Then only a desired temperature of 220–240 °C is possible to achieve inside the oven cavity. Based only on the CFD analysis, the area required to achieve this temperature is around 5 $m^2$ for the same heat loss coefficient from the walls of the bakery oven.

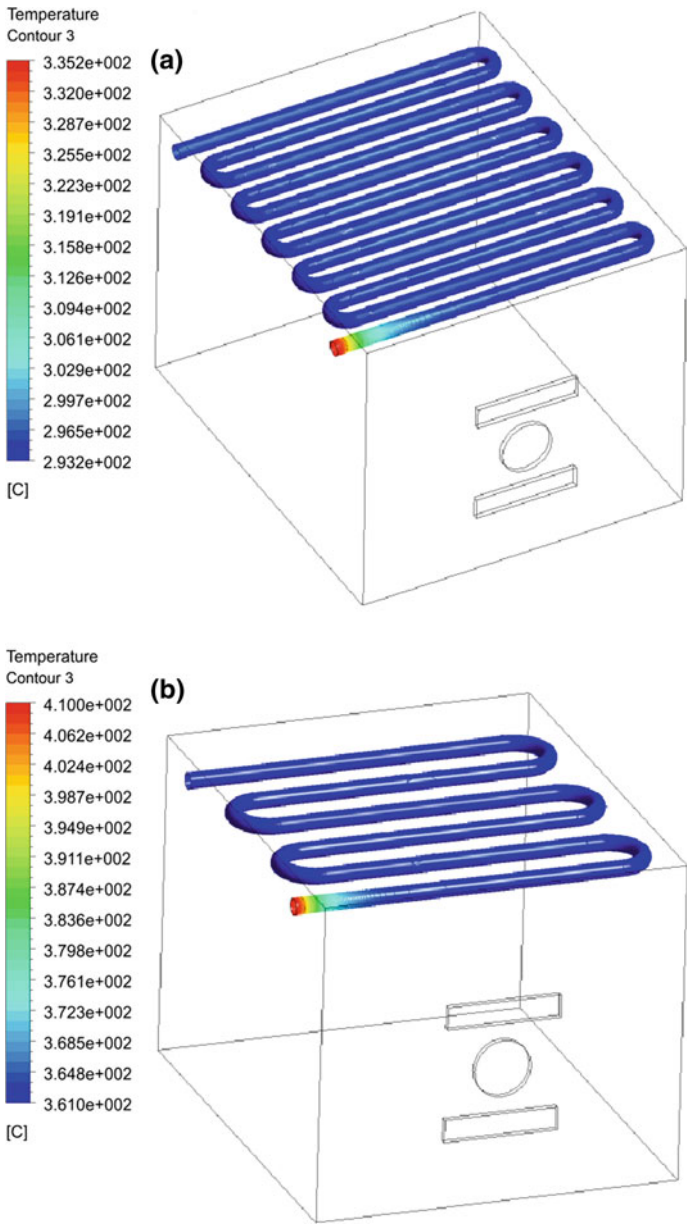


**Fig. 19.12** Comparison of temperature contours of solar coils in case of **a** full-length coil and **b** half length coil

**Acknowledgements** The authors gratefully thank the "Once More Bakery Industry", Rewa, Madhya Pradesh, India for allowing them to visit their industry, learn the processes and techniques involved and collect the required data for the above study.

## References

Annual report 2015–16 on Bakery Product Sales by Euromonitor International
Annual Report 2015–16 by Ministry of Food Processing Industry
Boulet M, Marcos B, Dostie M, Moresoli C (2010) CFD modeling of heat transfer and flow field in a bakery pilot oven. J Food Eng 97(3):393–402
Cengel YA, Boles MA (2002) Thermodynamics: an engineering approach, 8 edn. Mc Graw Hill Education
Chhanwal N, Indrani D, Raghavarao KSMS, Anandharamakrishnan C (2011) Computational fluid dynamics modeling of bread baking process. Food Res Int 44(4):978–983
Duffie JA, Beckman WA (2013) Solar engineering of thermal processes, 4th edn. Willey
Fuller RJ (2011) Solar industrial process heating in Australia e past and current status. Renew Energy 36:216–221
Kalogirou S (2003) The potential of solar industrial process heat applications. Appl Energy 76:337–361
Kalogirou SA (2004) Solar thermal collectors and applications, 30(3)
Khatir Z, Paton J, Thompson H, Kapur N, Toropov V (2013) Optimisation of the energy efficiency of bread-baking ovens using a combined experimental and computational approach. Appl Energy 112:918–927
Mbodji N, Hajji A (2017) Modeling, testing, and parametric analysis of a parabolic solar cooking system with heat storage for indoor cooking. Energy Sustain Soc 7(1)
Prasanna UR, Umanand L (2011) Modeling and design of a solar thermal system for hybrid cooking application. Appl Energy 88(5):1740–1755
Shahzad A, Kanwal T, He M (2013) Design and development of efficient domestic electric cum solar oven. J Basic Appl 296–301
Sharma AK, Sharma C, Mullick SC, Kandpal TC (2017) Potential of solar industrial process heating in dairy industry in India and consequent carbon mitigation. J Clean Prod 140:714–724
Suresh NS, Rao BS (2017) Solar energy for process heating: a case study of select Indian industries. J Clean Prod 151:439–451, May 2011
Tesfay AH, Kahsay MB, Nydal OJ (2014) Design and development of solar thermal Injera baking: steam based direct baking. Energy Procedia 57:2946–2955
Tian Y, Zhao CY (2013) A review of solar collectors and thermal energy storage in solar thermal applications. Appl Energy 104:538–553
Zisopoulos FK, Moejes SN, Rossier-Miranda FJ, Van Der Goot AJ, Boom RM (2015) Exergetic comparison of food waste valorization in industrial bread production. Energy 82:640–649